Signatures of the quantum vacuum

Stefan Yoshi Buhmann

Habilitationsschrift

vorgelegt der

Habilitationskommission
der Fakultät für Mathematik und Physik
der Albert-Ludwigs-Universität Freiburg

April 2019

Acknowledgements

First and foremost, I would like to thank the four mentors which have guided my development as a scientist and whose honest and critical opinion I value beyond measure: Peter Hertel, who has accompanied my introduction to the world of physics from the very beginning; Dirk-Gunnar Welsch, who has inspired me with his dedication to science; Stefan Scheel with whom I have been able to share an extremely productive period of my career; and Andreas Buchleitner, who has helped me navigate the challenges faced by an emerging group leader.

My work has greatly profited from collaborations and exchanges with fellow students, postdocs and colleagues whose names I dare not list in fear of forgetting anyone. In particular, I am grateful to those who have helped form my own group with their unique individual personalities and ideas—I deeply enjoy working with all of you. Akbar Salam has improved this thesis with his critical opinion for which I am very grateful. The remaining errors are all mine.

Finally, I am deeply grateful to my family: my parents and sister, whose care, sympathy, and stalwart solidarity have carried me though many ups and downs; my children, who are a constant source of marvel and inspiration; and my wife, without whose unwavering support none of this would have been possible and who makes every day a little brighter.

Hello to Jason Isaacs.

Contents

List of abbreviations

CP	Casimir–Polder
QED	quantum electrodynamics
VdW	Van der Waals

Outline

In this habilitation thesis, we report on the development of macroscopic quantum electrodynamics as a coherent framework to study the electromagnetic field in environments and its application to quantum vacuum effects such as dispersion forces.

An overview of these efforts and the central findings is provided in Part I. We briefly introduce quantum electrodynamics, the quantum vacuum, and the resulting phenomena with their context and relevance across sciences and technology (Chap. 1). This is followed by a discussion of our main results in the areas of macroscopic quantum electrodynamics (Chap. 2); dispersion forces, ranging from vacuum forces (Chap. 3) and interactions in media (Chap. 4) to excited systems (Chap. 5), thermal (Chap. 6), non-additive and collective effects (Chap. 7); quantum friction (Chap. 8); matter-wave scattering (Chap. 9); and resonance energy transfer (Chap. 10); ending with some concluding remarks (Chap. 11).

Part II contains a selection of key original publications which are grouped and ordered according to their discussion in Part I. The results reported in these publications were obtained while I was a postdoctoral researcher in the groups of E. A. Hinds and S. Scheel at Imperial College London and later junior group leader and Emmy Noether fellow at the University of Freiburg. Some of the articles contain calculations that I have performed entirely myself, sometimes in parallel with colleagues and PhD students from the same group [S1, S2, S3, S4, S10, S11, S12, S13, S21, S22, S23, S26, S28]. For some of the later articles, my role has shifted to conceiving projects and supervising the work of postdocs, PhD, MSc and BSc students while carrying out or checking the respective relevant key steps myself [S5, S6, S7, S8, S9, S14, S15, S16, S17, S18, S19, S20, S24, S25, S27, S29, S30]. In collaborations, experimentalists have complemented my theoretical analysis with experimental details [S8], measurements [S28], and simulations of matter-wave scattering [S28, S29], while theorists have contributed expertise on Rayleigh coefficients [S4, S28], optical properties of topological insulators [S6, S7, S9] polymers [S8], Chern–Simons materials [S10], media [S15], and (polar) molecules [S15, S21], Van der Waals interactions in free space [S11, S12, S14, S19], and numerical computations of thermal Casimir–Polder forces [S23]. A bibliography provides references for my findings that can only be mentioned in passing in Part I. Of these, the publications [P1–P6, P8–P85] were written after my PhD.

Part I.

Perspective

1. Introduction

In the following, we will set the stage for the development of macroscopic quantum electrodynamics and the investigations of some of its consequences, to be laid out in this habilitation thesis. To this end, we introduce quantum electrodynamics as the fundamental theory of light and matter as well as its nonrelativistic offspring quantum optics, molecular, cavity, and macroscopic quantum electrodynamics. We discuss the quantum vacuum as an important concept; its observable consequences such as dispersion forces; and their relevance in physics and beyond.

1.1. Quantum electrodynamics

Quantum electrodynamics (QED) is the fundamental quantum theory of light and its interaction with matter. Originated by Dirac [1], with key advances by Dyson, Feynman, Schwinger, Tomonaga and others [2], it has become one of the most precisely tested theories in physics and a firmly established part of textbook canon [3, 4]. In its original fully relativistically covariant form, it describes light and matter on an equal footing as bosonic and fermionic particles—photons, electrons, protons and neutrons—that can be created, destroyed and transformed in scattering events. Quantum optics [5, 6, 7] or molecular QED [8, 9] is the nonrelativistic version of QED valid for small velocities and energies such that the Coulomb gauge can be employed and matter can be regarded as conserved. Instead, the focus is on the structure and dynamics of photons and their interaction with atoms.

QED in free space can be constructed from classical electrodynamics by means of canonical quantisation (for a compact introduction, see [P3]). To this end, one solves Maxwell's equations by introducing vector and scalar potentials. These fundamental degrees of freedom of the theory are governed by Helmholtz's wave equation. Casting this equation of motion into its equivalent Lagrangian and Hamiltonian forms, quantisation can proceed by means of the correspondence principle upon replacing Poisson brackets of canonically conjugated variables with commutators of their quantised counterparts. Explicit expressions for the quantised electromagnetic field are constructed as superpositions of the classical plane-wave solutions of Helmholtz's equation, the normal modes, multiplied by bosonic creation and annihilation operators. The field can thus be envisaged as an infinite collection of harmonic oscillators, one for each normal mode, whose energies are quantised into discrete units: the photons.

Normal-mode QED is valid in free space, but can easily accommodate for the presence of nonabsorbing bodies whose surfaces enforce boundary conditions. In resonator geometries formed by good conductors, this typically leads to discrete normal modes in the form of standing waves which are the primary subject of cavity QED [10]. Its paradigmatic Jaynes–Cummings model describes the resonant interaction of a single cavity mode with two-level atoms [11]. The highly idealised conditions required for such a simplified description were experimentally realised by coupling Rydberg atoms [12] to a Gaussian mode inside a microwave Fabry–Pérot cavity [13] formed by two curved, highly-reflecting mirrors [14]. In this way, reversible emission and absorption of individual photons by atoms in the form of vacuum Rabi oscillations [15] were observed, accompanied by the formation of entangled

atom–field states.

As shown by Glauber and Lewenstein, normal-mode QED can also be constructed for an arbitrary arrangement of nondispersive non-absorbing dielectric bodies as characterised by a real-valued, frequency-independent permittivity that varies with position [16]. The normal modes in this case solve the wave equation both inside these bodies and in the space between them and obey the boundary conditions of macroscopic electrodynamics [17] governing reflection and transmission at their surface.

Complications arise when attempting to extend the normal-mode framework to absorbing media. In this case, the electromagnetic field is no longer a closed system whose quantum dynamics is governed by a unitary Hamiltonian evolution. Two main solutions to this problem have been developed. The first, phenomenological approach based on linear response theory [18, 19] forgoes explicit field quantisation and instead relates commutators and correlations of the quantised electromagnetic field in the presence of absorbing bodies to the classical Green tensor [20] by virtue of the fluctuation–dissipation theorem [21, 22]. The alternative is the Huttner–Barnett model [23] where a homogeneous absorbing medium is explicitly taken into account in the form of a harmonic-oscillator polarisation field which is coupled to an additional harmonic-oscillator bath responsible for dissipation. The fundamental, polariton-like field–matter excitations of the system emerge after a Fano diagonalisation [24]. The Huttner–Barnett model has been generalised to inhomogeneous dielectric bodies [25, 26, 27], including media with a nonlocal response [28].

Macroscopic QED [29] as developed and used throughout this thesis combines the versatility of the linear response approach with the rigor of the Huttner–Barnett model: it is valid for arbitrary arrangements of linear bodies and media but includes the fluctuation–dissipation theorem for the electromagnetic field as a derivable consequence. The point of departure is Maxwell's equations of classical macroscopic electrodynamics (hence the name macroscopic QED) together with the constitutive relations in linear media. The latter include a responsive component as well as a random noise term associated with material absorption. Solving the resulting wave equation, one finds an electromagnetic field that is created by a fluctuating noise polarisation inside the bodies as propagated by the classical Green tensor. The noise polarisation is closely related to the fundamental polariton-like field–matter excitations of the Huttner–Barnett model. The formalism has been extended to magnetodielectric media where noise magnetisation features alongside noise polarisation [P98, P99]. A variant directly employs the noise polarisation rather than polariton excitations and has been developed for dielectrics [30, 31] and magneto-electrics [32]. A further alternative implements a dissipative bath via auxiliary fields [33] leading to a model whose equivalence has been established explicitly [34]. It has recently been demonstrated that macroscopic QED can be obtained by means of canonical quantisation [35] and can even be formulated for moving and accelerated media [36].

1.2. The quantum vacuum

One of the most striking consequences of QED is the prediction of a nontrivial ground state: the quantum vacuum. As the electric and magnetic fields are noncommuting operators, the Heisenberg uncertainty principle [37] dictates that they cannot simultaneously assume definite values. Instead, the vacuum fields vanish on average, but exhibit nonzero quantum fluctuations. The energy of the quantum vacuum can be understood in close analogy with the ground state of the harmonic oscillator: the energy of each mode of the electromagnetic field is quantised according to $E_n = (n + \frac{1}{2})\hbar\omega$ $(n = 0, 1, \ldots)$ with a nonvanishing ground-state energy $E_0 = \frac{1}{2}\hbar\omega$. The total vacuum energy of the electromagnetic field emerges as

the (divergent) sum over all modes

$$E_{\text{vac}} = \sum_{\nu} \tfrac{1}{2}\hbar\omega_{\nu} \,. \tag{1.1}$$

As the fluctuating vacuum field and its formally infinite energy cannot induce real transitions in a photo detector, a number of indirect consequences have been proposed to illuminate their relevance. These all arise from the interaction of the vacuum field with matter. Its coupling with an electron leads to the anomalous magnetic moment [38, 39], while the ground-state energy of one or two atoms interacting with the quantum vacuum can be used to derive the famous Lamb shift [40, 41] or the interatomic Van der Waals (VdW) potential [42, 43, 44], respectively. Spontaneous radiative decay of an excited atom [45] can be understood as decay which is stimulated by the fluctuating vacuum fields [46]. It has further been speculated that the quantum vacuum might be relevant to cosmology with its energy acting as a source for gravity [47].

Changes to the fluctuating vacuum fields brought about by macroscopic bodies and the associated boundary conditions also lead to a host of observable effects. The Casimir force is probably the prime example [48]: Casimir himself derived this effect by considering how the above vacuum energy is affected by the introduction of two parallel perfectly conducting plates. The modified vacuum energy depends on the separation between the plates, from which he was able to derive the Casimir force by taking the gradient. Other signatures of body-induced modifications of the quantum vacuum include the position-dependent Lamb shift as well as the closely related single-atom Casimir–Polder (CP) potential [44]; the altered spontaneous decay rate in an environment, commonly known as the Purcell effect [49, 50]; and the predicted environment-induced changes to the magnetic moment of the electron [51].

More exotic, and to date largely unobserved, quantum vacuum effects have been predicted for moving objects. Quantum friction is the postulated ultimate limit to friction: a contactless dissipative force between two perfectly smooth plates that move parallel to each other [52]. A constantly accelerated object has been predicted by to perceive the quantum vacuum as a thermal electromagnetic field, a phenomenon known as the Unruh–Davies effect [53, 54]. Periodic motion of the boundaries of a cavity leads to the creation of real photons from the quantum vacuum according to the dynamical Casimir effect [55, 56]. The latter two phenomena are intricately related to Hawking radiation [57] which involves photon-pair creation from the vacuum in a curved or accelerated spacetime.

As a caveat, it should be noted that none of the mentioned indirect consequences are able to confirm the existence of fluctuating vacuum fields and their modification in nontrivial environments beyond any doubt. For instance, the Casimir force has alternatively been derived by Lifshitz from interacting fluctuating polarisations inside the two plates rather than fluctuating fields between them [58], a perspective that is shared by macroscopic QED [S5]. Similarly, it has been shown that both Lamb shift and spontaneous decay can be derived from fluctuating atomic dipoles and their radiation reaction onto themselves via emitted and reabsorbed electromagnetic fields [46]. A detailed analysis has revealed that the attribution of the two effects to vacuum fluctuations versus radiation reaction can be chosen at will by performing the calculations with different operator orderings [59]. Symmetric ordering has been advocated as the most physical choice, which would lead to the conclusion that atomic fluctuations are responsible for the single-atom ground-state Casimir–Polder potential at short distance while field fluctuations dominate in the far-field regime [60]. In any case, all of the described effects arise from interactions of light with matter and are due to quantum ground-state fluctuations, be they uncertainties of the positions of particles as described by quantum mechanics or of electromagnetic fields as predicted by QED.

Very recently, experimentalists have succeeded in directly probing the vacuum fluctuations of the electromagnetic field via their effect on the propagation of an ultrashort laser pulse though a nonlinear crystal [61, 62]. Setups of this kind open the perspective of investigating body-induced modifications to the quantum vacuum and their relevance to the above effects by direct experimental observation.

1.3. Dispersion forces

The effective electromagnetic forces between neutral polarisable objects that were brought forward as possible consequences of the quantum vacuum in the previous section are often subsumed under the general notion of dispersion forces. As these are the focus of a large part of this thesis, it is worth discussing them in more detail (see the monographs and reviews [8, 9, 46, 63, 64, 65, 66, 67, 68, 69, P1, P2, P3, P6, P7] for further information). We will distinguish Casimir forces between bodies [48, 58], CP forces between atoms and bodies [44], and interatomic VdW forces [42, 43, 44].

Dispersion forces are the electromagnetic interactions that always remain, even when removing all isolated charges and (external) electromagnetic fields. Being so persistent, they play a role in many areas of science. In physics and chemistry, they are one of the main binding mechanisms for atoms and molecules, forming the long-range attractive part of the Lennard-Jones potential [70] and modifying the ideal gas law to the Van der Waals equation of state [42]. They are the origin of surface tension [71]; drive the adsorption of atoms to surfaces [72]; and influence the structure and properties of liquids [73] and solids [74]. The stability of colloids is described by Derjaguin–Landau–Verwey–Overbeek theory [75, 76] which relies on dispersion forces as a central ingredient. In astrophysics, dispersion forces have been found to govern the condensation of dust particle in the early stages of planetary formation [77] and to be responsible for the stability of asteroids [78]. The most prominent example of their role in biology is the demonstration that dispersion forces are responsible for the sticky feet of geckos [79]. However, they also play an important role on a cellular level, governing the interaction of molecules within cells, their transport through cell membranes, and cell adhesion [64].

In the context of modern applications and experiments, Casimir forces play an ever-increasing dual beneficial versus detrimental role in nanomechanics: they are responsible for the unwanted effect of stiction, the permanent adhesion of mobile components [80, 81]; but are also the driving principle of the atomic force microscope [82]. Similarly, CP forces limit the miniaturisation and near-surface operation of atomic traps [83], but can also be exploited to guide atoms in matter-wave scattering experiments [84].

Roughly fifty years after the first prediction of the Casimir force, a series of experiments on the basis of torsion pendulums [85], cantilevers [86] and micromechanical oscillators [87] finally succeeded in their high-precision measurement. Subsequent experiments addressed a range of materials [88] and geometries [89, 90], thermal [91, 92], repulsive [93], and lateral Casimir forces [94] and, most recently, the Casimir torque [95]. CP forces have been studied much earlier by atomic-beam deflection [96] and spectroscopic measurements [97], with later findings being concerned with retardation [98], excited atoms [99] and thermal non-equilibrium [100].

Following the original conception by Casimir and Polder, the theory of dispersion forces has been extended to a range of materials and geometries. Theoretical developments of the past two decades include studies of the proximity force approximation that is frequently used in the analysis of the plane–sphere geometry common to most experimental setups [101, 102, 103]; methods based on numerical solutions to Maxwell's equations that can be

used to study more complex geometries [104]; and considerations of new materials such as metamaterials [105] or topological insulators [106]. In view of the complex interrelated dependence of dispersion forces on geometric and material properties, some general principles have been developed to guide, e.g. the search for repulsive dispersion forces to overcome the stiction problem [80, 81]. Examples of such general rules include the opposites-attract theorem according to which the Casimir force between two ground-state bodies in free space that are mirror images of each other and whose response is purely electric is always attractive [107]. This is supplemented by a generalised Earnshaw theorem stating that the dispersion potential of an isotropic particle does not exhibit stable equilibrium points in the free space between other electric bodies [108]. Loopholes to these no-go statements include repulsive dispersion forces predicted for objects with a magnetic or chiral response (see also Chap. 3 of this thesis); for an anisotropic particle above a plate with a hole [109, P51]; or observed inside liquid media (Chap. 4) and for excited objects (Chap. 5).

A number of fundamental questions have led to heated debates involving theorists and experimentalists [P4]. The most prominent one is the discrepancy between measurements and predictions of the Casimir force between metals at finite temperature [91, 92]; this is often referred to as the Drude–plasma debate in honour of the prominent role that conduction electrons and their correct description seem to play [67, 110, 111]. A, at least to date, purely theoretical issue is the Casimir energy of a single compact object [112, 113, 114]. A range of theoretical questions regarding the correct description of Casimir forces in media; the separation dependence of VdW forces between excited atoms; and the existence and velocity-dependence of quantum friction will be addressed in detail in this thesis.

2. Macroscopic quantum electrodynamics

Macroscopic quantum electrodynamics in dispersing and absorbing media forms the basis for studying the impact of light ranging from the quantum vacuum to few and many photons on microscopic and macroscopic matter. We have continuously developed and adapted this theory to incorporate new developments in materials design and to answer new fundamental questions. Major steps include the generalisation to media with a nonreciprocal response, the establishment of duality as a powerful theoretical tool; and the determination of concrete Green tensors and their symmetries.

2.1. Nonreciprocal media

Macroscopic QED in dispersing and absorbing media was originally conceived for isotropic dielectric bodies [29] which can be described by a position- and frequency-dependent (relative) dielectric permittivity $\epsilon(\boldsymbol{r},\omega)$. Motivated by successes in the design and fabrication of metamaterials [115, 116] and electronic [117, 118] as well as photonic [119, 120] topological insulators, we have extended the theory to arbitrary linear media with particular attention to those exhibiting a nonreciprocal response [S1].

The coupling of the electromagnetic field to such media can be described via the nonlocal conductivity tensor $\boldsymbol{Q}(\boldsymbol{r},\boldsymbol{r}',\omega)$ according to Ohm's law in frequency space

$$\hat{\boldsymbol{j}} = \boldsymbol{Q} * \hat{\boldsymbol{E}} + \hat{\boldsymbol{j}}_{\mathrm{n}} \tag{2.1}$$

($*$: spatial convolution), which gives the internal current density $\hat{\boldsymbol{j}}(\boldsymbol{r},\omega)$ as a linear response to the electric field $\hat{\boldsymbol{E}}(\boldsymbol{r},\omega)$ plus a noise current density $\hat{\boldsymbol{j}}_{\mathrm{n}}(\boldsymbol{r},\omega)$. With the aid of Maxwell's equations, one finds that the electric field is in turn generated by the noise currents,

$$\hat{\boldsymbol{E}} = \mathrm{i}\mu_0\omega \boldsymbol{G} * \hat{\boldsymbol{j}}_{\mathrm{n}}\,, \tag{2.2}$$

where the Green tensor $\boldsymbol{G}(\boldsymbol{r},\boldsymbol{r}',\omega)$ plays the role of a propagator; it is the classical solution to a Helmholtz equation. Following the approach developed in Ref. [121] for reciprocal media, an explicit field quantisation can be achieved by invoking the fluctuation–dissipation theorem [21, 22],

$$\Big[\hat{\boldsymbol{j}}_{\mathrm{n}}(\boldsymbol{r},\omega), \hat{\boldsymbol{j}}_{\mathrm{n}}^{\dagger}(\boldsymbol{r}',\omega')\Big] = \frac{\hbar\omega}{\pi}\,\mathcal{R}\mathrm{e}\boldsymbol{Q}(\boldsymbol{r},\boldsymbol{r}',\omega)\delta(\omega-\omega')\,. \tag{2.3}$$

Note that nonreciprocal media possess an asymmetric conductivity tensor which necessitates the use of a generalised real part $\mathcal{R}\mathrm{e}\boldsymbol{Q} = \big(\boldsymbol{Q}+\boldsymbol{Q}^{\dagger}\big)/2$. By taking a formal square root of the right hand side of the above equation, one can finally identify bosonic creation and annihilation operators $\hat{\boldsymbol{f}}^{\dagger}(\boldsymbol{r},\omega)$ and $\hat{\boldsymbol{f}}(\boldsymbol{r},\omega)$ for the polariton-like fundamental excitations of the field–matter system, whose Hamiltonian assumes the form of a collection of harmonic oscillators:

$$\hat{H}_{\mathrm{F}} = \int \mathrm{d}^3 r \int_0^{\infty} \mathrm{d}\omega\, \hbar\omega \hat{\boldsymbol{f}}^{\dagger}\cdot\hat{\boldsymbol{f}}\,. \tag{2.4}$$

In particular when studying magneto-electric, chiral media, or topological insulators, it is advantageous to use an equivalent alternative formulation of macroscopic electrodynamics where linear constitutive relations

$$\hat{\boldsymbol{D}} = \epsilon_0 \boldsymbol{\epsilon} \cdot \hat{\boldsymbol{E}} + \frac{1}{c} \boldsymbol{\xi} \cdot \hat{\boldsymbol{H}} + \hat{\boldsymbol{P}}_{\rm n} + \frac{1}{c} \boldsymbol{\xi} \cdot \hat{\boldsymbol{M}}_{\rm n} \,, \tag{2.5}$$

$$\hat{\boldsymbol{B}} = \frac{1}{c} \boldsymbol{\zeta} \cdot \hat{\boldsymbol{E}} + \mu_0 \boldsymbol{\mu} \cdot \hat{\boldsymbol{H}} + \mu_0 \boldsymbol{\mu} \cdot \hat{\boldsymbol{M}}_{\rm n} \tag{2.6}$$

for the electric and magnetic fields $\hat{\boldsymbol{E}}(\boldsymbol{r},\omega)$ and $\hat{\boldsymbol{B}}(\boldsymbol{r},\omega)$ and excitations $\hat{\boldsymbol{D}}(\boldsymbol{r},\omega)$ and $\hat{\boldsymbol{H}}(\boldsymbol{r},\omega)$ are used in place of Ohm's law. The linear response is governed by the tensor-valued dielectric permittivity $\boldsymbol{\epsilon}(\boldsymbol{r},\omega)$, magnetic permeability $\boldsymbol{\mu}(\boldsymbol{r},\omega)$ and two cross-susceptibilities $\boldsymbol{\xi}(\boldsymbol{r},\omega)$ and $\boldsymbol{\zeta}(\boldsymbol{r},\omega)$, which often feature in their above local forms. The noise current density has been decomposed into a noise polarisation $\hat{\boldsymbol{P}}_{\rm n}(\boldsymbol{r},\omega)$ and magnetisation $\hat{\boldsymbol{M}}_{\rm n}(\boldsymbol{r},\omega)$ according to $\hat{\boldsymbol{j}}_{\rm n} = -{\rm i}\omega\hat{\boldsymbol{P}}_{\rm n} + \boldsymbol{\nabla}\times\hat{\boldsymbol{M}}_{\rm n}$. As a consequence, one distinguishes fundamental electric from magnetic field–matter excitations which are related to noise polarisation and magnetisation, respectively. The emerging alternative formulation of macroscopic QED has the advantages that electric and magnetic effects can be easily identified and that the present media are described by response functions which are readily available from tabulated optical data.

Macroscopic QED in either of its above equivalent forms is valid for nonreciprocal media. A reciprocal response is characterised by symmetric conductivity, permittivity and permeability tensors and cross-susceptibilities which are related via $\boldsymbol{\xi}^{\rm T} = -\boldsymbol{\zeta}$. On the contrary, nonreciprocal media carry an intrinsic arrow of time which may be imprinted onto the system, e.g. via an applied magnetic field, as is the case for most topological insulators; or by motion, with both magnetic field and velocity being odd with respect to time reversal. This has profound consequences in optics as Lorentz reciprocity [122] is violated and sources and fields can no longer be interchanged, *viz.* $\boldsymbol{G}(\boldsymbol{r},\boldsymbol{r}',\omega) \neq \boldsymbol{G}^{\rm T}(\boldsymbol{r}',\boldsymbol{r},\omega)$. Despite this asymmetry, we have been able to show that the Green tensor still satisfies the completeness relation which is so vital for the construction of a workable field quantisation.

In quantum optics, nonreciprocal media can lead to an asymmetric coupling of emitters which can be exploited to enforce unidirectional energy transfer in a chain of atoms [123] or to induce a persistent heat current between three objects held at different temperatures [124]. As we will see in Chap. 3, the directional properties of topological insulators affect the attractive versus repulsive nature of dispersion forces and can even be used to induce Casimir torques.

A number of applications of macroscopic QED to determine quantum vacuum effects will be described in detail in the following chapters. In addition, we have shown that the formalism provides a simple tool to calculate electrostatic Coulomb interactions in complex geometries on the basis of the Green tensor [P28]; and have employed it to predict environment-induced modifications to the electron magnetic moment [P18].

2.2. Duality

Macroscopic QED is primarily concerned with neutral bodies and media with no isolated charges or currents being present. In this case, Maxwell's equations assume their homogeneous form and are symmetric with respect to an exchange of electric and magnetic fields

as can be made apparent by combining these into dual pairs,

$$\boldsymbol{\nabla}\cdot\begin{pmatrix} Z_0\hat{\boldsymbol{D}} \\ \hat{\boldsymbol{B}} \end{pmatrix} = \begin{pmatrix} 0 \\ 0 \end{pmatrix}, \tag{2.7}$$

$$\boldsymbol{\nabla}\times\begin{pmatrix} \hat{\boldsymbol{E}} \\ Z_0\hat{\boldsymbol{H}} \end{pmatrix} - \mathrm{i}\omega \begin{pmatrix} 0 & 1 \\ -1 & 0 \end{pmatrix}\cdot\begin{pmatrix} Z_0\hat{\boldsymbol{D}} \\ \hat{\boldsymbol{B}} \end{pmatrix} = \begin{pmatrix} \boldsymbol{0} \\ \boldsymbol{0} \end{pmatrix} \tag{2.8}$$

($Z_0 = \sqrt{\mu_0/\epsilon_0}$: vacuum impedance). It then becomes obvious that a duality transformation

$$\begin{pmatrix} \boldsymbol{x} \\ \boldsymbol{y} \end{pmatrix} \mapsto \mathcal{D}(\theta)\cdot\begin{pmatrix} \boldsymbol{x} \\ \boldsymbol{y} \end{pmatrix} \qquad \text{with } \mathcal{D}(\theta) = \begin{pmatrix} \cos\theta & \sin\theta \\ -\sin\theta & \cos\theta \end{pmatrix} \tag{2.9}$$

applied to all dual pairs above leaves Maxwell's equations invariant for arbitrary rotation angles θ [17, 125].

We have developed duality into a powerful analytical tool within the context of macroscopic QED by deriving the transformation behaviour of the medium properties and resulting field propagation [S2, P78]. The constitutive relations (2.5)–(2.6) being linear, one finds that the medium reponse functions transform as

$$\begin{pmatrix} \boldsymbol{\epsilon} \\ \boldsymbol{\zeta} \\ \boldsymbol{\xi} \\ \boldsymbol{\mu} \end{pmatrix} \mapsto \mathcal{D}(\theta)\otimes\mathcal{D}(\theta)\cdot\begin{pmatrix} \boldsymbol{\epsilon} \\ \boldsymbol{\zeta} \\ \boldsymbol{\xi} \\ \boldsymbol{\mu} \end{pmatrix}. \tag{2.10}$$

Due to the implied mixing of the purely electric or magnetic response functions with the cross-susceptibilities, one finds a nontrivial interplay of duality and reciprocity. In particular, duality transformations only conserve reciprocity for rotation angles $\theta = n\pi/2$ with integer n, demonstrating that nonreciprocal media generically arise from duality transformations. A prominent example is the perfect electromagnetic conductor [126] which is obtained from the ordinary perfect conductor ($\epsilon \to \infty$) by means of a duality rotation. One arrives at a generalised ideal material with $\epsilon, \mu \to \infty$, $\xi = \zeta = \pm\sqrt{\epsilon\mu} \to \infty$, and a finite ratio $\sqrt{\epsilon/\mu} = \pm\cot\theta$, which continuously interpolates between the perfect electric conductor ($\theta = 0$) and an infinitely permeable medium ($\theta = \pi/2$).

The practical virtue of duality symmetry is the ability to generate new solutions to Maxwell's equations for bodies with a given magneto-electric response from known solutions for bodies with the dual response according to the above relation (2.10). To this end, we introduce electric and magnetic Green tensors according to

$$\boldsymbol{G}_{\mathrm{ee}} = \frac{\mathrm{i}\omega}{c}\,\boldsymbol{G}\,\frac{\mathrm{i}\omega}{c}, \qquad \boldsymbol{G}_{\mathrm{em}} = \frac{\mathrm{i}\omega}{c}\,\boldsymbol{G}\times\overleftarrow{\boldsymbol{\nabla}}', \tag{2.11}$$

$$\boldsymbol{G}_{\mathrm{me}} = \boldsymbol{\nabla}\times\boldsymbol{G}\,\frac{\mathrm{i}\omega}{c}, \quad \boldsymbol{G}_{\mathrm{mm}} = \boldsymbol{\nabla}\times\boldsymbol{G}\times\overleftarrow{\boldsymbol{\nabla}}'. \tag{2.12}$$

One can then obtain new solutions by subjecting these to a duality transformation; in the special case where the arguments $\boldsymbol{r} \neq \boldsymbol{r}'$ are situated in free-space regions, this is simply achieved by applying the transformation (2.10) to $(\boldsymbol{G}_{\mathrm{ee}}, \boldsymbol{G}_{\mathrm{me}}, \boldsymbol{G}_{\mathrm{em}}, \boldsymbol{G}_{\mathrm{mm}})^{\mathrm{T}}$. A simple example is the generation of solutions of magnetostatics such as the magnetic field of a magnetic dipole from the corresponding ones of electrostatics. As we will see in Chap. 3, one can use duality in the context of dispersion forces both as a consistency check and as an elegant means to obtain new dispersion potentials.

2.3. Green tensor

The versatiliy of macroscopic QED is rooted in the use of the Green tensor as a central ingredient: it encodes all relevant information about both the electromagnetic properties of the present bodies and media and their geometry, i.e. their shapes, sizes, and relative positions. General properties of the Green tensor may hence be used to make general statements about QED phenomena such as dispersion forces. One such property is the behaviour with respect to a rescaling of all sizes, distances, and wavelengths by a global factor a: $\boldsymbol{r} \mapsto a\boldsymbol{r}, \omega \mapsto \omega/a$. We have derived the respective scaling behaviour of the Green tensor [S3] from the defining Helmholtz equation which for isotropic media reads

$$\boldsymbol{\nabla} \times \frac{1}{\mu(\boldsymbol{r},\omega)} \boldsymbol{\nabla} \times \boldsymbol{G}(\boldsymbol{r},\boldsymbol{r}',\omega) - \frac{\omega^2}{c^2} \epsilon(\boldsymbol{r},\omega) \boldsymbol{G}(\boldsymbol{r},\boldsymbol{r}',\omega) = \boldsymbol{\delta}(\boldsymbol{r}-\boldsymbol{r}') \,. \tag{2.13}$$

Due to the dispersive nature of medium responses, we have to distinguish two regimes. In the retarded far-field regime of distances and sizes which are much larger than the relevant wavelengths of the electromagnetic field, dispersion can be neglected and the Helmholtz equation implies a $1/a$ scaling of the Green tensor. In the opposite nonretarded regime, we have to distinguish between the electrostatic limit for bodies with a purely electric response, leading to a $1/a^3$ scaling, and the magnetostatic limit for purely magnetic bodies, where a $1/a$ scaling is observed.

When applying the results of macroscopic QED to concrete geometries, the respective explicit Green tensor is required. For bodies with planar [127, 128], spherical [129] and cylindrical symmetries [130] and simple magneto-electric media, analytical solutions are well known and given in terms of vector wave functions [20]. We have generalised such solutions for the paradigmatic case of a planar multilayer system to allow for more general media and periodic surface structures. Such a system is a stack of homogeneous layers with plane parallel interfaces and infinite lateral extension in the xy-plane. The intrinsic symmetry can be exploited by performing a spatial Fourier transformation in this plane, leading to a Weyl expansion [131]

$$\boldsymbol{G}(\boldsymbol{r},\boldsymbol{r}',\omega) = \int \mathrm{d}^2 k^{\parallel} \, \mathrm{e}^{\mathrm{i}\boldsymbol{k}^{\parallel}\cdot(\boldsymbol{r}-\boldsymbol{r}')} \boldsymbol{G}(\boldsymbol{k}^{\parallel}, z, z', \omega) \,. \tag{2.14}$$

Its components are given in terms of generalised Fresnel reflection and transmission coefficients [132] for plane waves which conserve the lateral wave vector $\boldsymbol{k}^{\parallel}$ due to the respective translation symmetry. We have derived these coefficients for the perfect electromagnetic conductor as introduced above [S5]; electronic topological insulators with isotropic cross-susceptibilities ξ and ζ [P47]; and photonic topological insulators with a nonsymmetric permittivity $\boldsymbol{\epsilon}$ [S6]. In all these cases, we have found that reflection and transmission at interfaces mixes the two linear polarisations of incident plane waves. In addition, photonic topological insulators may exhibit a strong dependence of reflection and transmission on the direction of the lateral wave vector. For surfaces with one-dimensional periodic corrugations the continuous translational symmetry is broken, leading to Rayleigh reflection and transmission coefficients [133] which mix lateral wave vectors with $k_x - k_x' = 2\pi n/d$ for integer n where d is the period of the corrugations [134, 135, S4].

The Fresnel and Rayleigh coefficients can assume very intricate forms in the above cases. To alleviate the computational effort while at the same time verifying the consistency, we have derived a set of symmetry relations [S4]. The most general symmetry relation follows from the Schwarz reflection principle for the Green tensor $\boldsymbol{G}(\boldsymbol{r},\boldsymbol{r}',-\omega^*) = \boldsymbol{G}^*(\boldsymbol{r},\boldsymbol{r}',\omega)$ and is valid for arbitrary causal media. In particular, it ensures that the Green tensor is real-valued at purely imaginary frequencies, $\boldsymbol{G}(\boldsymbol{r},\boldsymbol{r}',\mathrm{i}\xi)$. Another set of symmetries for the coefficients

follows from Lorentz reciprocity and hence only holds for reciprocal media. Further symmetries may follow from possible inversion symmetries of the media and interfaces in the xy-plane and an isotropy in this plane, respectively.

3. Vacuum dispersion forces

Dispersion forces as originally conceived by Casimir and Polder [44, 48] are vacuum forces in two respects: they arise when all interacting objects are in their ground state and the electromagnetic field is in its vacuum state; and they refer to objects in free space. The strength and direction of dispersion forces depend on both geometry, i.e. the shape, size, orientation and distances between the objects, and spectral properties, i.e. their electromagnetic response. We have studied both these dependences with a focus on new fundamental effects that arise from nontrivial electromagnetic responses [69].

In the following, we shall describe how Casimir forces between two bodies, CP forces between atoms and bodies, and VdW forces between atoms can be analysed within the framework of macroscopic QED. After presenting specific results for variety of different systems, we will formulate some general principles that govern the behaviour of dispersion forces.

3.1. Casimir forces

As first proposed by Lifshitz [58], the Casimir force on an object is the vacuum expectation value of all electromagnetic stresses acting on its surface ∂V,

$$\boldsymbol{F} = \int_{\partial V} \mathrm{d}\boldsymbol{A}\cdot\langle\boldsymbol{\sigma}\rangle\,. \tag{3.1}$$

In free space, the electromagnetic stress tensor is given by

$$\boldsymbol{\sigma} = \epsilon_0\hat{\boldsymbol{E}}\otimes\hat{\boldsymbol{E}} + \frac{1}{\mu_0}\hat{\boldsymbol{B}}\otimes\hat{\boldsymbol{B}} - \frac{1}{2}\biggl(\epsilon_0\hat{\boldsymbol{E}}^2 + \frac{1}{\mu_0}\hat{\boldsymbol{B}}^2\biggr)\boldsymbol{I} \tag{3.2}$$

($\boldsymbol{I}$: unit tensor). Its vacuum expectation value can be evaluated using either of the two explicit field quantisations presented in Chap. 2 [S5, S6],

$$\langle\boldsymbol{\sigma}(\boldsymbol{r})\rangle = -\frac{\hbar}{\pi}\sum_{\lambda=\mathrm{e,m}}\int_0^\infty \mathrm{d}\xi\bigl[\mathcal{S}\boldsymbol{G}^{(1)}_{\lambda\lambda}(\boldsymbol{r},\boldsymbol{r},\mathrm{i}\xi) - \tfrac{1}{2}\mathrm{tr}\boldsymbol{G}^{(1)}_{\lambda\lambda}(\boldsymbol{r},\boldsymbol{r},\mathrm{i}\xi)\boldsymbol{I}\bigr]\,. \tag{3.3}$$

Note that we have discarded self-interactions by retaining only the scattering part of the Green tensor $\boldsymbol{G}^{(1)}$ which is associated with reflections of the electromagnetic field at the surfaces of present bodies. We have thus generalised earlier findings for the Casimir force [136] to arbitrary arrangements of bodies with a linear electromagnetic response. In particular, the symmetrisation $\mathcal{S}\boldsymbol{G} = \bigl(\boldsymbol{G} + \boldsymbol{G}^{\mathrm{T}}\bigr)/2$ is required in the presence of nonreciprocal materials.

In the paradigmatic case of two infinite parallel surfaces at separation z, one may use the multilayer Green tensor in Weyl decomposition to find a Casimir force per unit area [S5, S6]

$$\boldsymbol{f}(z) = -\frac{\hbar}{4\pi^3}\int_0^\infty \mathrm{d}^2k^\parallel \int_0^\infty \mathrm{d}\xi\,\kappa e^{-2\kappa z}\mathrm{Tr}\Bigl[\mathcal{R}_1\cdot\bigl(1-\mathcal{R}_2\cdot\mathcal{R}_1\mathrm{e}^{-2\kappa z}\bigr)^{-1}\cdot\mathcal{R}_2\Bigr]\boldsymbol{e}_z \tag{3.4}$$

($\kappa = \mathrm{Im}\,k_z$). This generalises Lifshitz's theory [58] to the case of nonreciprocal materials. The reflection matrices $\mathcal{R}_1(\boldsymbol{k}^\parallel,\mathrm{i}\xi)$ and $\mathcal{R}_2(\boldsymbol{k}^\parallel,\mathrm{i}\xi)$ of the two surfaces mix polarisations for

anisotropic or bi-isotropic media. For isotropic media, they reduce to ordinary Fresnel coefficients [132]. Due to the high symmetry of the system, our result assumes the same form as previously derived for the reciprocal case [137].

To demonstrate the scope of the theory, we have applied it to the highly idealised perfect electromagnetic conductor; the recently emerged photonic topological insulator; and a polymer film interacting with a solid substrate. Our investigation of the Casimir force for perfect electromagnetic conductors [S5] was motivated by Boyer's observation that the Casimir force between a perfectly conducting plate and an infinitely permeable one is repulsive [138]. The perfect electromagnetic conductor [126] as introduced in Chap. 2 continuously interpolates between the two ideal materials. We consider two perfect electromagnetic conductor plates, parametrised by duality angles θ_1 and θ_2, respectively. The reflection matrices can be derived from that of a perfect electric conductor by means of a duality transformation. Being independent of both lateral wave vector and frequency, they allow for an analytical solution for the Casimir force [S5]:

$$\boldsymbol{f}(z) = -\frac{\hbar c}{8\pi^2 z^4}\left[\frac{\pi^4}{30} - \Delta\theta^2(\pi-\Delta\theta)^2\right]\boldsymbol{e}_z\,. \tag{3.5}$$

As a signature of global duality invariance (cf. Sect. 3.4 below), the Casimir force only depends on the difference $\Delta\theta = \theta_1 - \theta_2$ between the duality angles. Our result interpolates between Casimir's attractive force for two perfectly conducting plates [48] and Boyer's repulsive result [138] as extreme cases. Remarkably, the integral $\int_0^{\pi/2} \mathrm{d}(\Delta\theta)\,\boldsymbol{f}$ vanishes, showing that attractive and repulsive forces occupy equally large parameter spaces.

Photonic topological insulators exhibit a preferential direction which is imprinted by an external magnetic field [119]. Their anisotropic permitivity $\boldsymbol{\epsilon}$ assumes a block-diagonal form with the components perpendicular to the preferred axis forming an antisymmetric 2×2 matrix. We have studied the Casimir effect for two parallel plates made of such anisotropic nonreciprocal dielectrics [S6]. Determining the reflection coefficients via the boundary conditions for the electromagnetic field at interfaces of anisotropic media [137] and solving the lateral wave vector and frequency integrals numerically, we have been able to show how the strength of the Casimir force between photonic topological insulators can be tuned by means of external magnetic fields. The field-induced enhancement is most pronounced in the highly symmetric situation of magnetic fields pointing perpendicularly out of the surfaces of the topological insulators. In the antisymmetric configuration of one field pointing out of and one into the respective surface, we find a much weaker enhancement, which can be interpreted as a reduction when compared to the average case.

When the external magnetic fields are oriented parallel to the surfaces, the guided plasmon modes become strongly directional as evidenced by a dependence of the reflection coefficients on the direction of the lateral wave vector $\boldsymbol{k}^{\parallel}$. In this case, a Casimir torque can arise between the two topological insulator plates which depends on the relative angle ϕ between the two in-plane magnetic fields. We have derived this torque by first integrating the above Casimir force (3.4) to obtain the Casimir energy E per unit area A according to $\boldsymbol{f} = -\boldsymbol{\nabla}E/A$ [S7]. The torque per unit area then follows by taking the derivative with respect to the angle, $\boldsymbol{\tau}/A = -(\partial/\partial\phi)E/A\boldsymbol{e}_z$. We find that the torque acts to align the two magnetic-field vectors parallel to one another, hence displaying a 2π periodicity in its angle-dependence. This feature distinguishes the Casimir torque between two photonic topological insulators from all other Casimir torques, namely those between birefringent dielectrics [139, 140], electronic topological insulators [141] or corrugated surfaces [142]. In the two latter cases, the surfaces exhibit a distinguished *axis* (as opposed to a distinguished *direction*), so the torque has a periodicity of π. The Casimir torque between two birefringent dielectrics has been observed experimentally only very recently [95], see also Ref. [P8].

As a last example, our investigation of the adhesion of polymer films on solid substrates demonstrates that the Lifshitz's macrosopic theory can be used in conjunction with inputs from microscopic simulations. The study was motivated by the Van der Waals-based dry adhesion of gecko feet to solid surfaces where a hierarchy of flexible hair establishes close contact despite microscopic surface roughness [79]. In a biomimetic approach akin to the recently constructed gecko tape [143], we showed that the flexible chemically inert polymer ethylene-chlorotrifluoroethylene can similarly overcome surface roughness to ensure a large adhesion force [S8]. To this end, we combine the above Lifshitz's result (3.4) with density functional theory calculations of the dielectric permittivity of the polymer film. The same microscopic simulations also help us determine the equilibrium distance of the polymer from the solid substrate. We find adhesion forces ranging from $1.48\,\mathrm{kN/mm^2}$ for silicon dioxide to $2.22\,\mathrm{kN/mm^2}$ for steel. These values for perfectly smooth substrates serve as an upper limit to the forces achievable on rough surfaces. To account for the latter effect, we have alternatively used the proximity force or Derjaguin's approximation which is based on a decomposition into small parallel surface segments [144] and Hamaker's approach which calculates the dispersion force between two objects as a pairwise sum over their volumes [145]. For one-dimensional periodic sawtooth corrugations, we find that the reduction due to surface roughness depends on the opening angle between neighbouring peaks: for narrower angles, the contact between substrate and polymer film is reduced, leading to a smaller adhesion force.

3.2. Casimir–Polder forces

According to Casimir and Polder's original idea, the CP potential can be derived from the position-dependent energy of the atom–field system [44]. Starting from the uncoupled product of the atomic ground state $|0_\mathrm{A}\rangle$ and the quantum vacuum $|0_\mathrm{F}\rangle$, with the latter being the ground state of the field–matter Hamiltonian (2.4), this energy can be obtained using perturbation theory. We have generalised this approach to nonreciprocal media and to a range of atom–field interactions.

The interaction of a purely electric atom with the quantum vacuum in the presence of nonreciprocal media can be described by means of an electric-dipole interaction $\hat{H}_\mathrm{int} = -\hat{\boldsymbol{d}}\cdot\hat{\boldsymbol{E}}(\boldsymbol{r})$ [146, P96]. The leading contribution to the CP potential is of second order in this coupling and involves the emission and reabsorption of one virtual photon. Using the field quantisation of Chap. 2 to evaluate the interaction matrix elements, one finds a ground-state CP potential [S9, S10]

$$U(\boldsymbol{r}) = \frac{\hbar\mu_0}{2\pi}\int_0^\infty \mathrm{d}\xi\,\xi^2 \mathrm{tr}\big[\boldsymbol{\alpha}(\mathrm{i}\xi)\cdot\boldsymbol{G}^{(1)}(\boldsymbol{r},\boldsymbol{r},\mathrm{i}\xi)\big] \tag{3.6}$$

for a ground-state atom with polarisability

$$\boldsymbol{\alpha}(\omega) = \lim_{\delta\to 0+}\frac{1}{\hbar}\sum_k\left(\frac{\boldsymbol{d}_{k0}\otimes\boldsymbol{d}_{0k}}{\omega+\omega_{k0}+\mathrm{i}\delta} - \frac{\boldsymbol{d}_{0k}\otimes\boldsymbol{d}_{k0}}{\omega-\omega_{0k}+\mathrm{i}\delta}\right) \tag{3.7}$$

($\boldsymbol{d}_{0k} = \langle 0_\mathrm{A}|\hat{\boldsymbol{d}}|n_\mathrm{A}\rangle$: electric dipole matrix elements, $\omega_{k0} = (E_k - E_0)/\hbar$: transition frequencies) within an arbitrary environment of nonreciprocal bodies. As in the case of the Casimir force, we have discarded self-interactions by retaining only the scattering part of the Green's tensor. In the special case of an isotropic atom at distance z from a perfectly conducting plate, one recovers Casimir and Polder's original result [44]. For a perfect nonreciprocal plate (i.e. a perfect electromagnetic conductor with duality angle $\theta = \pi/4$), the scattering

Green's tensor is completely antisymmetric and hence the potential of an isotropic atom vanishes. We have shown that to obtain a nonvanishing interaction, one needs to consider an atom with a nonsymmetric polarisability as induced, e.g. by circular dipole moments [S9]. Similar results are obtained when generalising the perfect nonreciprocal plate to an electronic topological insulator [S9] a Chern–Simons medium [S10].

More generally, the interaction of an atom with an electromagnetic and chiral response with the electromagnetic field is described by a coupling [147, 148, P96]

$$\hat{H}_{\rm int} = -\hat{\boldsymbol{d}}\cdot\hat{\boldsymbol{E}}(\boldsymbol{r}) - \hat{\boldsymbol{m}}\cdot\hat{\boldsymbol{B}}(\boldsymbol{r}) - \tfrac{1}{2}\hat{\boldsymbol{B}}(\boldsymbol{r})\cdot\hat{\boldsymbol{\beta}}_{\rm dia}\cdot\hat{\boldsymbol{B}}(\boldsymbol{r}) \tag{3.8}$$

that includes electric- and magnetic-dipole contributions as well as a diamagnetic interaction ($\hat{\boldsymbol{\beta}}_{\rm dia}$: diamagnetic magnetisability). After collecting all contributions to the energy shift which involve the emission and reabsorption of one virtual photon, the total ground-state CP potential can be given as [S9, S10, S11, S12, S13, P64]

$$U(\boldsymbol{r}) = \frac{\hbar}{2\pi\epsilon_0}\sum_{\lambda_1,\lambda_2={\rm e,m}}\int_0^\infty {\rm d}\xi\,{\rm tr}\big[\boldsymbol{\alpha}_{\lambda_1\lambda_2}({\rm i}\xi)\cdot\boldsymbol{G}^{(1)}_{\lambda_2\lambda_1}(\boldsymbol{r},\boldsymbol{r},{\rm i}\xi)\big] \tag{3.9}$$

where we have introduced the electric/magnetic Green tensors (2.11)–(2.12). Here, $\boldsymbol{\alpha}_{\rm ee}$ is the electric polarisability defined above which gives rise to the ordinary CP potential. The magnetic polarisability $\boldsymbol{\alpha}_{\rm mm}$ contains paramagnetic and diamagnetic contributions. The former leads to a repulsive potential near a perfectly conducting plate [S11] in analogy with Boyer's repulsive Casimir force between an infinitely permeable and a perfectly conducting plate [138]. The diamagnetic magnetisability being negative due to Lenz's law [149], it is associated with an opposing, attractive interaction [S12].

The electromagnetic cross-polarisabilities

$$\boldsymbol{\alpha}_{em}(\omega) = \lim_{\delta\to0+}\frac{1}{\hbar c}\sum_k\left(\frac{\boldsymbol{d}_{k0}\otimes\boldsymbol{m}_{0k}}{\omega+\omega_{k0}+{\rm i}\delta} - \frac{\boldsymbol{d}_{0k}\otimes\boldsymbol{m}_{k0}}{\omega-\omega_{k0}+{\rm i}\delta}\right), \tag{3.10}$$

$$\boldsymbol{\alpha}_{em}(\omega) = \lim_{\delta\to0+}\frac{1}{\hbar c}\sum_k\left(\frac{\boldsymbol{m}_{k0}\otimes\boldsymbol{d}_{0k}}{\omega+\omega_{k0}+{\rm i}\delta} - \frac{\boldsymbol{m}_{0k}\otimes\boldsymbol{d}_{k0}}{\omega-\omega_{k0}+{\rm i}\delta}\right) \tag{3.11}$$

($\boldsymbol{m}_{0k} = \langle 0_{\rm A}|\hat{\boldsymbol{m}}|n_{\rm A}\rangle$: magnetic dipole matrix elements) only contribute in the case of reduced atomic or molecular symmetries. Chiral molecules with a broken parity symmetry occur as two distinct right- and left-handed enantiomers which are mirror images of each other. As these molecules are symmetric with respect to time-reversal, Lloyd's theorem states that their cross-polarisabilities are related according to $\boldsymbol{\alpha}_{me} = -\boldsymbol{\alpha}_{em}^{\rm T}$ [150]. We have shown that the associated chiral CP potential is governed by the optical rotatory strength $R_k = {\rm Im}(\boldsymbol{d}_{0k}\cdot\boldsymbol{m}_{k0})$ which takes opposite signs for right- versus left-handed molecules [151]. The chiral CP force is hence attractive or repulsive, depending on the handedness of the molecule [S13, P64]. The effect can be enhanced by means of dynamical self-dressing [P43]. We have shown how discriminatory CP interactions of chiral molecules with chiral surfaces may be exploited for enantiomer separation [P12].

Charge–parity violating effects in atoms, on the contrary, lead to charge–parity-odd cross-polarisabilities such that $\boldsymbol{\alpha}_{me} = \boldsymbol{\alpha}_{em}^{\rm T}$ [152]. We have shown that charge–parity violation thus becomes manifest in the CP interaction of an atom with the surface of a medium whose response is odd under time-reversal, such as a perfect electromagnetic conductor, a Chern–Simons medium, or a topological insulator [S10].

3.3. Van der Waals forces

Van der Waals forces between atoms can also be obtained from the ground-state energy of coupled atom–field system following Casimir and Polder [44]. Based on this idea, we have used macroscopic QED to develop a theory of VdW forces for a range of atom–field interactions that agrees with the results of normal-mode QED in free space, but also accounts for modifications induced by bodies and surfaces.

Point of departure is once more the factorised ground state of the system which now has three components: the ground states $|0_\mathrm{A}\rangle$ and $|0_\mathrm{B}\rangle$ of the two atoms and the quantum vacuum $|0_\mathrm{F}\rangle$. The interaction in electric-dipole approximation $\hat{H}_\mathrm{int} = -\hat{\boldsymbol{d}}_\mathrm{A}\cdot\hat{\boldsymbol{E}}(\boldsymbol{r}_\mathrm{A}) - \hat{\boldsymbol{d}}_\mathrm{B}\cdot\hat{\boldsymbol{E}}(\boldsymbol{r}_\mathrm{B})$ involves the coupling of each atom to the body-assisted field at the respective positions [146, P96]. This interaction induces a shift to the ground-state energy that depends on the positions of both atoms and can hence be identified as the VdW potential. The leading contribution is of fourth order and involves the exchange of two virtual photons between the atoms [8]. The calculation is hence considerably more complex than in the single-atom case as it involves twelve distinct Feynman diagrams [153] instead of just one. Using the quantisation scheme of Chap. 2, one finds [P90]

$$U(\boldsymbol{r}_\mathrm{A},\boldsymbol{r}_\mathrm{B}) = -\frac{\hbar\mu_0^2}{2\pi}\int_0^\infty \mathrm{d}\xi\,\xi^4 \mathrm{tr}\big[\boldsymbol{\alpha}_\mathrm{A}(\mathrm{i}\xi)\cdot\boldsymbol{G}(\boldsymbol{r}_\mathrm{A},\boldsymbol{r}_\mathrm{B},\mathrm{i}\xi)\cdot\boldsymbol{\alpha}_\mathrm{B}(\mathrm{i}\xi)\cdot\boldsymbol{G}(\boldsymbol{r}_\mathrm{B},\boldsymbol{r}_\mathrm{A},\mathrm{i}\xi)\big]\,. \tag{3.12}$$

Unlike the single-atom case, the VdW potential contains the full Green tensor which acts as a propagator for the virtual photons exchanged between the atoms. In free space, the above expression reduces to the well-known result by Casimir and Polder [44].

The theory can be extended to atoms with a more general electromagnetic response by using an interaction of the form (3.8) for each atom. The resulting VdW potential can be expressed in terms of the electric/magnetic Green tensors (2.11)–(2.12) and the electromagnetic polarisabilities of the two atoms [P87, S11, S12, S14],

$$\begin{aligned} U(\boldsymbol{r}_\mathrm{A},\boldsymbol{r}_\mathrm{B}) = -\frac{\hbar}{2\pi\epsilon_0^2}\sum_{\lambda_1,\lambda_2,\lambda_3,\lambda_4=\mathrm{e,m}}\int_0^\infty \mathrm{d}\xi \\ \times \mathrm{tr}\big[\boldsymbol{\alpha}^\mathrm{A}_{\lambda_1\lambda_2}(\mathrm{i}\xi)\cdot\boldsymbol{G}_{\lambda_2\lambda_3}(\boldsymbol{r}_\mathrm{A},\boldsymbol{r}_\mathrm{B},\mathrm{i}\xi)\cdot\boldsymbol{\alpha}^\mathrm{B}_{\lambda_3\lambda_4}(\mathrm{i}\xi)\cdot\boldsymbol{G}_{\lambda_4\lambda_1}(\boldsymbol{r}_\mathrm{B},\boldsymbol{r}_\mathrm{A},\mathrm{i}\xi)\big]\,. \end{aligned} \tag{3.13}$$

In free space, we again recover the normal-mode results for VdW potentials involving para- [154, 155], diamagnetic [156], or chiral molecules [157] whose properties are encoded via the respective polarisabilities. For anisotropic molecules, the VdW potential depends not only on their distance, but also on their orientation as represented by polarisability tensors $\boldsymbol{\alpha}$. We have developed a simplified description of this dependence in terms of effective molecular eccentricities [P24]. Finite-size effects manifest themselves via higher-order multipoles in the interaction Hamiltonian, as we have demonstrated [P21] by including electric quadrupole and octupule transitions in the three-atom Axilrod–Teller potential [158].

The true benefit of the macroscopic-QED description lies in its ability to describe body-induced modifications of the VdW potential. By using the respective Green tensors, we have shown this effect for perfectly conducting, magneto-electric [P87, P90] or chiral plates [S14] and spheres [S11, P85]. This can be understood in terms of image dipoles [17]: a given atom A interacts with both a second atom B and its mirror image behind the surface, where constructive or destructive interference can lead to enhancement or reduction of the VdW potential with respect to the free-space value. This genuine many-body interaction depends on the distances of both atoms from each other and the body as well as the orientation of their line of sight with respect to the surface. For instance, the VdW potential of two electric atoms is reduced by a factor of up to 2/3 in the vicinity of a perfectly conducting plate for parallel alignment and enhanced by up to 8/3 for perpendicular alignment [P90].

3.4. General principles

Our extensive studies of dispersion forces for a range of geometries and material properties allow us to formulate some emerging general principles regarding their scaling behaviour; duality symmetry; attractive versus respulsive nature; and potential use as a probe for material properties.

The macroscopic-QED expressions (3.3), (3.6) and (3.12) for the Casimir, CP and VdW interactions immediately reveal that these do not depend on distance in the form of simple power laws in general. They are all given as integrals of the Green tensor along the positive imaginary frequency axis, so that all frequencies contribute and spectral and geometric dependences become intrinsically intertwined. With the aid of the scaling transformation for the Green tensor derived in Sect. 2.3, we have nevertheless been able to formulate simple scaling laws in two asymptotic regimes [S3]: In the far-field or retarded regime all distances and sizes of the interacting objects are much larger than all characteristic wavelengths of their spectral response such as those associated with the relevant medium resonance, plasma or atomic transition frequencies. In this zone, a combination of our above results with the scaling behaviour of the Green tensor implies that a resizing of all distances and sizes by a factor a leads to a scaling of the Casimir force per unit area as $1/a^4$, of the CP potential as $1/a^4$ and of the VdW potential as $1/a^7$. In the opposite near-field or nonretarded regime, one needs to distinguish whether only electric or only magnetic bodies are present: for electric bodies, the Casimir force scales as $1/a^3$, the Casimir–Polder potential of an electric atom scales as $1/a^3$ and the respective VdW potential as $1/a^6$, while for purely magnetic properties, these interactions are governed by $1/a^3$, $1/a$ and $1/a^6$ power laws, respectively. For configurations characterised by a single distance parameter such as the Casimir force between two plates of infinite thickness, the CP force between an atom and a plate of infinite thickness or the VdW force between two atoms in free space, these scaling laws immediately imply simple power laws as given in Tab. 3.1. For more involved geometries, one can use scaling laws to factorise the distance and size dependences into a power law with respect to a chosen length times a scaling function that only depends on dimensionless parameters.

The above results for dispersion interactions can be combined with the transformation laws of Sect. 2.2 for the Green tensor to prove that dispersion forces in free space are invariant with respect to a global duality transformation [S2, P78]. One example of this is the Casimir force between two perfect electromagnetic conductors [S5]: it depends only on the difference of their duality rotation angles which remains unchanged under such a transformation. The duality invariance can be used as a consistency check or to generate new results for dispersion forces in a given arrangement of magneto-electric objects from known solutions by replacing all electric response functions with their dual magnetic counterparts and vice versa. This is illustrated in Tab. 3.1 where we list signs and power laws of a range of dispersion forces. Note that duality transforms the permittivity to a paramagnetic permeability, which is why

Table 3.1.: Signs and power laws for dispersion forces

Interaction	Retarded regime		Nonretarded regime	
objects	elect.–elect.	elect.–magnet.	elect.–elect.	elect.–magnet.
dual objects	magnet.–magnet.	magnet.–elect.	magnet.–magnet.	magnet.–elect.
Casimir force	$-1/z^4$	$+1/z^4$	$-1/z^3$	$+1/z$
CP potential	$-1/z^4$	$+1/z^4$	$-1/z^3$	$+1/z$
VdW potential	$-1/r^7$	$+1/r^7$	$-1/r^6$	$+1/r^4$

Table 3.2.: Opposites repel—contrary properties associated with repulsive forces

Symmetry and examples	Property	Opposite property
duality		
magneto-electrics	electric	magnetic
parity		
chiral enantiomers	right-handed	left-handed
time reversal		
charge-parity violating molecules	electric and magnetic dipoles parallel	electric and magnetic dipoles antiparallel
photonic topological insulators	magnetic field out of surface	magnetic field into surface
electronic topological insulators	positive axion coupling	negative axion coupling

all asymptotes given in the table refer to para- as opposed to diamagnetic objects.

The attractive and repulsive forces shown in the table together with a host of further findings mentioned in this chapter can be subsumed under a general heuristic law regarding the sign of dispersion forces between ground-state objects in free space: opposites repel. In other words, whenever the possible material properties of the interacting objects occur in pairs that are related via a discrete symmetry (e.g. electric versus magnetic, as related via duality), then two objects that share the same nature will be subject to an attractive dispersion interaction while objects of opposite nature will repel each other. Examples for this rule are listed in Tab. 3.2.

As dispersion forces sensitively depend on the material properties of the interacting objects, one can conversely use these forces as a sensor for the latter. To this end, Curie's symmetry principle needs to be taken into account [159]. Originally formulated for the probing of crystal symmetries, it states that a symmetry of an object can only be probed by means of a reference object serving as a detector which is also sensitive to the same symmetry. For instance, one finds that the chiral interaction of isotropic left- or right-handed molecules with a nonchiral atom vanishes [157], so the VdW interaction with a nonchiral atom can obviously not be used to discriminate enantiomers. One way to circumvent this problem is the use of a second chiral molecule to act as a reference object where one finds that the chiral–chiral VdW force is typically extremely small. We have proposed body-induced interactions as an alternative [S14]: a surface with a chiral response can serve as a reference object by inducing a discriminatory VdW force between a chiral molecule and a nonchiral atom. Further examples for exploiting Curie's symmetry principle are listed in Tab. 3.3 where dispersion forces might serve as probes for material properties with respect to time-reversal and charge–parity symmetries.

Table 3.3.: Use of dispersion interactions for probing for symmetries

Symmetry	Sample	Detector
parity	chiral molecule	chiral molecule, chiral plate
time reversal	electronic topological insulator	circularly polarised atom
	photonic topological insulator	photonic topological insulator
charge–parity	charge–parity violating atom	electronic topological insulator

4. Dispersion forces in media

Dispersion forces in free space are typically only observed under highly idealised laboratory conditions, whereas the forces relevant to physical chemistry or colloid science often act on objects embedded in liquid media. In the following, we will discuss how the theory of the previous chapter can be generalised to address the very specific problems that arise when calculating CP and VdW forces on the one hand or Casimir forces on the other within such settings.

4.1. Casimir–Polder and Van der Waals forces

Macroscopic QED crucially relies on the assumption that all present bodies and media can be modelled via a continuum description that does not resolve their atomic structure. This assumption is intrinsically incompatible with placing a microscopic atom within such a medium. The problems that arise when combining point particles with a continuum theory are most plastically illustrated by the behaviour of spontaneous decay within a medium. The spontaneous decay rate of an excited atom from state $|n\rangle$ to a lower state $|k\rangle$ in an abritrary environment can be calculated by means of macroscopic QED where it turns out to be proportional to the imaginary part of the Green tensor [P6],

$$\Gamma_{nk}(\boldsymbol{r}) = \frac{2\mu_0}{\hbar}\,\omega_{nk}^2 \boldsymbol{d}_{nk}\cdot \mathrm{Im}\,\boldsymbol{G}(\boldsymbol{r},\boldsymbol{r},\omega_{nk})\cdot\boldsymbol{d}_{kn}\,. \tag{4.1}$$

The result agrees with the well-known Einstein rate [45] in free space and becomes modified within a non-absorbing medium. For an absorbing medium however, one finds an unphysical divergent decay rate that stems from the near-field interaction of the atom with the medium in its immediate neighbourhood. This interaction is unphysical as the medium atoms will never occupy the exact same position as the guest atom due to Pauli repulsion. A solution to this problem was given by Onsager's real-cavity model [160]: he proposed to surround the guest atom with a finite spherical free-space cavity that prevents immediate contact with the medium.

Our expressions for CP and VdW forces can formally be applied to atoms embedded in media without encountering any divergences where one finds that the interactions are reduced due to screening. However, the result is not realistic as it neglects the local-field effects associated with the real cavity model. Such a naïve application of macroscopic QED to atoms in media is also not very satisfying on a formal level as it leads to forces that are not duality-invariant. To address these problems, we had shown earlier how the real-cavity model can be implemented within the framework of macroscopic QED by determining the respective Green tensor for the modified setting including spherical cavities around each atom [P88]. Applying this local-field corrected Green tensor to CP and VdW forces, we find that Eqs. (3.6) and (3.12) apply in a medium of permittivity ϵ provided that the free-space electric polarisability α is replaced with the correct effective polarisability [S15]

$$\alpha^* = \left(\frac{3\epsilon}{2\epsilon+1}\right)^2 \alpha\,. \tag{4.2}$$

Determining CP and VdW interactions in water, we find enhancements due to local-field effects within the theoretical upper limits of factors 9/4 or 81/16 for the two cases. We have compared these results with alternative descriptions such as the virtual cavity model or the hard-sphere and finite-size models presented in the next two sections. Our results for dispersion forces in planar multilayer systems [P80] have been used to study the effect of salt ions on the thickness of wetting films on melting ice [P44] and to investigate the potential use of silica [P46] or cellulose [P52] for carbon dioxide capture.

We have generalised the real-cavity model to magnetic atoms where the magnetic polarisability $\alpha_{\rm mm}$ must be replaced by its effective counterpart [S11]

$$\alpha^*_{\rm mm} = \left(\frac{3}{2\mu+1}\right)^2 \alpha_{\rm mm} \tag{4.3}$$

where μ is the permeability of the surrounding medium. With these modifications, CP and VdW forces in media obey duality symmetry.

4.2. Casimir forces

The Casimir force in a medium is fraught with ambiguities, because it has been debated whether the Maxwell (3.3) or the Abraham stress tensor [161]

$$\boldsymbol{\sigma} = \epsilon_0 \hat{\boldsymbol{D}} \otimes \hat{\boldsymbol{E}} + \frac{1}{\mu_0} \hat{\boldsymbol{H}} \otimes \hat{\boldsymbol{B}} - \frac{1}{2}\left(\epsilon_0 \hat{\boldsymbol{D}} \cdot \hat{\boldsymbol{E}} + \frac{1}{\mu_0} \hat{\boldsymbol{H}} \cdot \hat{\boldsymbol{B}}\right) \boldsymbol{I} \tag{4.4}$$

should be used for its derivation. Dzyaloshinkii, Lifshitz and Pitaesvkii's use of the Abraham stress tensor [162] had been criticised by Raabe and Welsch [136] who argued that only the Maxwell stress tensor is compatible with a derivation on the basis of the Lorentz force. This had led to a lively debate [163, 164, 165] where canonical quantisation [166] and arguments from classical electrodynamics [167] had been invoked in favour of the Abraham stress tensor, but Raabe and Welsch insisted on the Lorentz force as the more fundamental concept.

To avoid the potentially problematic definition of the stress tensor in a medium altogether, we have developed a microscopic test of the two approaches, showing that only the Casimir force derived by Dzyaloshinkii, Lifshitz and Pitaesvkii on the basis on the Abraham stress tensor correctly accounts for three-particle VdW interactions between the interacting bodies and the intervening medium [S16]. We have derived the Casimir forces for one or two small spheres inside a medium and shown that they can be given by the CP and VdW expressions (3.6) and (3.12) when replacing the atomic polarisability with the excess polarisability of a dielectric sphere of radius R and permittivity $\epsilon_{\rm s}$ [17],

$$\alpha^*_{\rm s} = 4\pi\epsilon_0\epsilon R^3 \frac{\epsilon_{\rm s} - \epsilon}{\epsilon_{\rm s} + 2\epsilon}\,. \tag{4.5}$$

The excess polarisability becomes negative when the medium is more optically dense than the sphere. This can lead to repulsive forces which are akin to the rising of an air bubble in water in an apparent reversal of gravity. We have predicted that early stages of ice condensation take place below the water surface due to such repulsive Casimir forces [P23]; and that gas hydrates in freezing water may be coated with a thin ice layer, depending on their species [P9].

Introducing the magnetic polarisability of a sphere, we have shown that the Casimir force in a medium as based on the Abraham stress tensor is duality-invariant. As a further application of the Casimir force in a medium, we have pointed out that the interaction between objects embedded in a plasma [P54] bears a striking resemblance to the Yukawa potential [168].

4.3. Synthesis: particles of arbitrary size

The CP and VdW forces determined by the effective polarisability (4.3) of point particles inside cavities seem to be conceptually very different from Casimir forces between macroscopic spheres of polarisability (4.5). To bridge this apparent discrepancy, we have developed the generalised model of a particle of radius R inside a cavity of radius R_c. Its effective polarisablity reduces to those given in the previous two sections in the extremes $R \ll R_c$ (point particle) and $R = R_c$ (macroscopic sphere). Using this model for one [S17] or two such finite-size particles [S15], we find realistic CP and VdW potentials where the particle and cavity radii are obtained from microscopic simulations.

5. Forces on excited systems

The notion of dispersion forces as vacuum forces can be relaxed further by considering excited atoms and bodies, such that real photons contribute. To draw the line between dispersion versus optical forces, we require that only fields emitted by the interacting objects themselves are present. We will discuss the new phenomena that arise when allowing for excitations, including spatially oscillating CP and VdW forces; lateral photon recoil forces on circularly polarised atoms; and repulsive Casimir forces on amplifying bodies.

5.1. Excited and lateral Casimir–Polder forces

An atom in an excited state $|n\rangle$ can spontaneously undergo a downward transition to a state $|k\rangle$ upon emission of a real photon. This is accompanied by a resonant CP potential which selectively depends on the atomic downwards transition frequency ω_{nk} [S9],

$$U_n(\boldsymbol{r}) = -\mu_0 \sum_{k<n} \omega_{nk}^2 \,\mathrm{Re}\big[\boldsymbol{d}_{nk}\cdot\boldsymbol{G}^{(1)}(\boldsymbol{r},\boldsymbol{r},\omega_{nk})\cdot\boldsymbol{d}_{kn}\big]\,. \tag{5.1}$$

In the special case of reciprocal media (such that the Green tensor is symmetric) and real dipole moments (associated with linearly polarised transitions), the real part can be applied to the Green tensor alone and one recovers previous results [169]. The resonant CP potential exhibits spatial oscillations [170] that are analogous to the Drexhage oscillations of the spontaneous decay rate [50] and which have been observed experimentally [171, 172]. For the simple case of an atom in front of a perfectly conducting plate, these can be understood from the behaviour of the electomagnetic field of frequency ω_{nk} that is emitted by the atomic dipole and reflected by the plate: depending on the atom–plate separation z, the reflected plate is either in phase with the dipole, leading to attraction, or out of phase, leading to repulsion. As the total optical path is $2z$, the potential exhibits oscillations between attractive and repulsive regions with a period of half the transition wavelength λ_{nk}. The phase of these oscillations depends on the reflective properties of the plate; we have shown that it is shifted when replacing the perfectly conducting plate with a magneto-electric metamaterial [P76] or a perfectly reflecting nonreciprocal mirror [S9]. The narrow frequency dependence of the resonant CP potential can be exploited in conjunction with a metamaterial superlens [115] to achieve a strong attraction towards the focal plane [P83]. Excited-state CP potentials can further be enhanced by dynamical self-dressing [P39], nonperturbative effects [P50, P53], and resonant coupling to surface polaritons [P56].

Spontaneous decay has recently been demonstrated to acquire a directionality under certain conditions [173, 174, 175]. For instance, an atom undergoing a circularly polarised transition in the vicinity of an optical fibre was found to emit preferentially towards one of the fibre ends [176]. Such directional emission is due to spin–orbit coupling of the electromagnetic field where its spin (as addressed via the circular dipole transition) controls the orbital angular momentum (and hence its spatial structure and emission direction). The effect generally requires a setup with three well-defined mutually perpendicular directions, such as the dipole moment, the atom–fibre separation, and the fibre axis [177]. The question naturally arises whether the recoil associated with directional photon emission could lead to

lateral forces perpendicular to the atom–body separation and whether these are connected to the above resonant CP force. Using earlier methods based on the Lorentz force [P96], we have shown that a resonant lateral CP force [S18]

$$\boldsymbol{F}_n(\boldsymbol{r}) = 2\mu_0 \sum_{k<n} \omega_{nk}^2 \boldsymbol{\nabla} \operatorname{Re}\big[\boldsymbol{d}_{nk} \cdot \boldsymbol{G}^{(1)}(\boldsymbol{r}, \boldsymbol{r}, \omega_{nk}) \cdot \boldsymbol{d}_{kn}\big] \tag{5.2}$$

indeed arises in the presence of directional emission. This force is not a potential force, as the gradient only acts on the first argument of the Green tensor; it instead has the nature of a curl force [178]. The lateral force results from an imbalance of recoil due to photons with momentum $\hbar\boldsymbol{k}^{\parallel}$ emitted with a directional rate $\Gamma_n(\boldsymbol{r}, \boldsymbol{k}^{\parallel})$ [S18],

$$\boldsymbol{F}_n(\boldsymbol{r}) = -\int \mathrm{d}^2 k^{\parallel}\, \hbar\boldsymbol{k}^{\parallel} \Gamma_n(\boldsymbol{r}, \boldsymbol{k}^{\parallel})\,. \tag{5.3}$$

We have applied the formalism to predict recoil forces for a circularly polarised atom in front of a plate [S18] or a fibre [P48]. The former is analogous to the recently proposed lateral force on an excited rotating sphere [179].

5.2. Excited Van der Waals forces

While the spatial oscillations of the CP potential due to interference of emitted and reflected fields mentioned above have been firmly established both theoretically and experimentally, the behaviour of the excited-state VdW potential in the far zone has been subject to controversies until very recently. Some authors had predicted an oscillating potential [180, 181] in close analogy with the CP interaction [182], while others had advocated a strictly monotonous interaction [183, 184]. Alongside others [185, 186, 187], we have addressed this very fundamental problem which had led Power, one of the founding fathers of nonrelativistic QED, to predict his own previous work. Using our approach based on the Lorentz force that is able to address the forces acting on the two atoms individually [P96], we have found a surprising resolution to the puzzle [S19]: the force on an excited atom A in the vicinity of a ground-state atom B oscillates as a function of interatomic separation, while the corresponding force on atom B is monotonous. This answer is in agreement with the observed oscillatory CP potential of an excited atom near a plate, as the corresponding monotonous force on the plate is never detected due to its smallness.

At a first glance, these different separation dependences of the forces between two atoms in free space seem to imply a violation of Newton's third law. The apparent contradiction is resolved when taking into account the recoil of the photon emitted by the excited atom. The presence of atom B induces an asymmetry in the emission of atom A. In close analogy to the mechanism described in the previous section, the oscillating force on the excited atom is then a photon recoil force due to this asymmetric emission, so that the total momentum of the atom–atom–photon system is conserved [188].

5.3. Casimir forces on amplifying media

Inversion-type amplifying media with linear gain that are continuously repumped to a quasi-stationary state can be characterised by a permittivity with a positive imaginary part in some frequency window, $\operatorname{Im}\epsilon(\omega) < 0$, such that electromagnetic waves grow exponentially upon propagation. The quantum statistics of the electromagnetic field in this state can be accounted for within macrosocpic QED by exchanging the roles of creation and annihilation operators in the respective frequency region [189, 190].

We have exploited this to determine the Casimir force in the presence of amplifying media by evaluating the electromagnetic stress tensor (3.2) [S20]. One finds that an additional resonant force component arises which is due to fields emitted by the amplifying bodies and hence expressed as an integrals over their volume as well as their emission spectrum. The volume integral is potentially problematic for the idealised infinitely thick plates paradigmatically considered in Casimir physics [191]. We have hence considered an amplifying plate of finite thickness interacting with a perfectly conducting plate [P68], finding a force that oscillates as a function of separation due to the interference of electromagnetic waves emitted by the amplifying medium and reflected by the conducting plate. The amplitude of these oscillations is reduced as the thickness of the amplifying plate increases due to imperfect phase matching. Our results confirm the possibility of realising repulsive Casimir forces by means of amplifying media that had been conjectured earlier [192].

To illuminate the physical origin of resonant Casimir forces on amplifying media, we have established their connection to CP forces on excited atoms discussed in the previous Sect. 5.1 [S20]. To this end, we have considered an optically dilute amplifying medium consisting of a gas of excited atoms with number density η. In this case, the imaginary part of the permittivity which governs resonant Casimir forces can be related to the polarisability (3.7) of the atoms in an excited state $|n\rangle$ via a linearised Clausius–Mossotti law [17]

$$\operatorname{Im}\epsilon(\omega) = \frac{\eta \operatorname{Im}\alpha_n(\omega)}{\epsilon_0} = \frac{\pi\eta}{3\epsilon_0\hbar}\sum_n |\boldsymbol{d}_{nk}|^2\big[\delta(\omega+\omega_{nk}) - \delta(\omega-\omega_{nk})\big]\,. \tag{5.4}$$

One then finds that the Casimir force is simply the sum of the resonant CP forces (5.1) acting on the excited atoms constituting the amplifying medium:

$$\boldsymbol{F} = -\int \mathrm{d}^3 r\, \eta \boldsymbol{\nabla} U_n(\boldsymbol{r})\,. \tag{5.5}$$

6. Thermal fluctuations

Quantum vacuum forces in a strict sense would require the environment to be prepared at zero kelvin. At finite temperatures, thermal fluctuations of the electromagnetic field complement the zero-point fluctuations. We will discuss how these can lead to a heating of molecules; show that they induce thermal dispersion forces; and discuss in which regimes these play a role.

6.1. Surface-induced heating

An atom prepared in a single ground or excited state and placed in a finite-temperature environment will emit and absorb thermal photons until its internal-state population reaches equilibrium. This non-equilibrium dynamics and its modification due to bodies and surfaces can be studied by means of macroscopic QED. Assuming the electromagnetic field to be in a thermal state of uniform temperature T and considering its interaction with an atom, we have shown that the dynamics of its internal-state populations p_n is governed by the rate equations [S21]

$$\dot{p}_n(t) = -\sum_k \Gamma_{nk} p_n(t) + \sum_k \Gamma_{kn} p_k(t) \tag{6.1}$$

with transition rates

$$\Gamma_{nk}(\boldsymbol{r}) = \begin{cases} \dfrac{2\mu_0}{\hbar}\,\omega_{nk}^2[n(\omega_{nk})+1]\boldsymbol{d}_{nk}\cdot\mathrm{Im}\,\boldsymbol{G}(\boldsymbol{r},\boldsymbol{r},\omega_{nk})\cdot\boldsymbol{d}_{kn} & \text{for } k<n\,, \\ \dfrac{2\mu_0}{\hbar}\,\omega_{kn}^2 n(\omega_{kn})\boldsymbol{d}_{nk}\cdot\mathrm{Im}\,\boldsymbol{G}(\boldsymbol{r},\boldsymbol{r},\omega_{kn})\cdot\boldsymbol{d}_{kn} & \text{for } k>n \end{cases} \tag{6.2}$$

for stimulated emission by and absorption of thermal photons as determined by the Bose–Einstein distribution $n(\omega) = 1/\left[\mathrm{e}^{\hbar\omega/(k_\mathrm{B}T)}-1\right]$ [193, 194]. In free space, one recovers the well-known Einstein A- and B-coefficients [45]. These processes eventually lead to an equilibrium where the atom assumes a thermal state which only depends on the relation between its transition frequencies and the ambient temperature: for $k_\mathrm{B}T \ll \hbar\omega_{nk}$, the final state of the atom is essentially its ground state and thermal photons do not play any important role. In the opposite case, the thermal equilibrium state exhibits appreciable excited-state populations of the atom as maintained by the thermal environment.

The dynamics towards the equilibrium state depends crucially on the material environment as encoded via the Green tensor. We have investigated this Purcell modification of thermal dynamics for polar molecules in the vicinity of metal or dielectric surfaces [S21]. Such molecules exhibit rovibrational excitations that can be excited even at room temperature [195], so that heating becomes a severe obstacle to their coherent manipulation. We have shown that the surface can become the dominant source of heating for distances comparable to the molecular transition wavelength.

6.2. Thermal dispersion forces

Dispersion forces at finite temperature have, for the equilibrium case, traditionally been studied on the basis of Lifshitz theory [162], where one starts by evaluating the finite-temperature expectation value of the stress tensor (3.2). We have pointed out that the resulting Casimir force can only be used to derive the corresponding CP potential

$$U(\boldsymbol{r}) = \mu_0 k_\mathrm{B} T {\sum_{j=0}^{\infty}}' \xi_j^2 \mathrm{tr}\big[\boldsymbol{\alpha}_T(\mathrm{i}\xi_j)\cdot\boldsymbol{G}^{(1)}(\boldsymbol{r},\boldsymbol{r},\mathrm{i}\xi_j)\big] \tag{6.3}$$

by taking the dilute-gas limit for one of the interacting bodies if the thermal-equilibribium polarisability $\boldsymbol{\alpha}_T = \sum_n p_n \boldsymbol{\alpha}_n$ is used rather than the ground-state polarisability [S22]. Note that the impact of thermal photons has led to a replacement of the imaginary-frequency integral by a Matsubara sum [196] whose frequencies $\xi_j = 2\pi k_\mathrm{B} T j/\hbar$ are the poles of the Bose–Einstein distribution.

Even more importantly, Lifshitz theory is unable to describe the transient resonant CP potentials [197, S22, P75]

$$\begin{aligned} U_n(\boldsymbol{r}) = -\mu_0 \sum_{k<n} [n(\omega_{nk})+1]\omega_{nk}^2 \,\mathrm{Re}\big[\boldsymbol{d}_{nk}\cdot\boldsymbol{G}^{(1)}(\boldsymbol{r},\boldsymbol{r},\omega_{nk})\cdot\boldsymbol{d}_{kn}\big] \\ + \mu_0 \sum_{k>n} n(\omega_{kn})\omega_{kn}^2 \,\mathrm{Re}\big[\boldsymbol{d}_{nk}\cdot\boldsymbol{G}^{(1)}(\boldsymbol{r},\boldsymbol{r},\omega_{kn})\cdot\boldsymbol{d}_{kn}\big] \end{aligned} \tag{6.4}$$

which are associated with stimulated emission and absorption, respectively. Weighted with the time-dependent internal-state populations, they arise even for a ground-state atom within a thermal environment. As the atom reaches equilibrium, the resonant contributions mutually cancel and only the equilibrium interaction (6.3) persists. We have studied the full dynamics of the CP force on ground-state polar molecules near a gold surface, showing how an initial resonant potential with Drexhage-type spatial oscillations eventually gives way to the strictly attractive equilibrium potential [P77]. Such oscillations can be considerably enhanced when placing the molecules inside a planar [P74] or cylindrical cavity [P65].

The described non-equilibrium between a single molecule and its uniform thermal environment is in contrast to another possible thermal non-equilibrium which arises if different parts of the environment are held at different temperatures. The latter situation has been predicted [198] and experimentally demonstrated [100] to give rise to strongly enhanced CP forces. We have shown that the two different non-equilibrium scenarios can be subsumed within a single framework where an atom in an arbitrary state interacts with an environment of non-uniform temperature [P71].

6.3. Asymptotics of the Casimir–Polder potential

The dependences of the equilibrium CP potential (6.3) on distance, temperature, and transition frequencies are intrinsically intertwined. Focussing on the distance dependence for a given temperature, one can nevertheless identify distinct asymptotic regimes [S23]. The ambient temperature and the atomic spectrum define two characteristic wavelengths λ_T and λ_{nk}, respectively. For atoms, $\lambda_{nk} \ll \lambda_T$ typically holds at room temperature and below. One can then show that the CP potential near a plane surface scales as $-C_3/z^3$ in the electrostatic near-field regime $z \ll \lambda_{nk}$, falls off more strongly as $-C_4/z^4$ in the far-field regime $\lambda_{nk} \ll z \ll \lambda_T$, and resumes a $-C_{3T}/z^3$ power law in the thermal regime $z \gg \lambda_T$ with a

reduced coefficient $C_{3T} < C_3$. We have shown that these three asymptotes can also be observed for the CP interaction of fullerene molecules with surfaces, which is dominated by electronic transitions [P60]. The situation is fundamentally different for systems dominated by long-wavelength transitions such as polar molecules [S23] or Rydberg atoms [P40, P66]. Here, the order of thermal and transition wavelengths can become reversed, $\lambda_{nk} \gg \lambda_T$ and as a result, the near-field and thermal asymptotes cover a single $-C_3/z^3 = -C_{3T}/z^3$ regime that is valid at all separations, such that a far-field $-C_4/z^4$ behaviour never arises.

The large transition wavelengths of polar molecules and Rydberg atoms have a similarly striking effect on the temperature-dependence of the CP interaction at a given position. For such systems in the near-field regime $z \ll \lambda_{nk}$, one can show that the CP potential near a metal plate becomes approximately independent of temperature due to strong mutual cancellations of resonant and nonresonant contributions [S23]. We have generalised this finding to arbitrary geometries [P63] and applied it to a metal sphere [P62].

7. Non-additive and collective phenomena

Starting from vacuum dispersion forces in Chapter 3, we have increasingly widened this notion to include the effects of media, excitations and thermal fluctuations. Most of these led to new force components that could simply be added to the previous results. Qualitatively new, non-additive effects arise when the interactions of atoms with the quantum vacuum are combined with external laser fields or coherently enhanced via collective effects in an ensemble.

7.1. Laser-induced Casimir–Polder force

Atoms in free space can be trapped in an offresonant external monochromatic laser field $\boldsymbol{E}_{\rm L}(\boldsymbol{r},t) = \left[\boldsymbol{E}_{\rm L}(\boldsymbol{r})\mathrm{e}^{\mathrm{i}\omega_{\rm L}t} + \boldsymbol{E}_{\rm L}^{*}(\boldsymbol{r})\mathrm{e}^{-\mathrm{i}\omega_{\rm L}t}\right]/\sqrt{2}$ [199]. This can be easily shown by calculating the mean energy of the atomic dipole moment interacting with this field according to $\hat{H}_{\rm int} = -\hat{\boldsymbol{d}}\cdot\boldsymbol{E}_{\rm L}(\boldsymbol{r},t)$ within second-order perturbation theory, leading to an optical potential [S24]

$$U_{\rm L}(\boldsymbol{r}) = -\tfrac{1}{2}\alpha(\omega_{\rm L})|\boldsymbol{E}_{\rm L}(\boldsymbol{r})|^2\,. \tag{7.1}$$

For a negative detuning $\Delta = \omega_{\rm L} - \omega_{nk} < 0$, the atomic polarisability $\alpha(\omega_{\rm L})$ is positive and hence the optical potential is attractive towards regions of high intensity. This has been exploited in order to optically trap atoms in a strongly focussed Gaussian laser beam [200].

Optical forces also arise in evanescent fields that emerge on the surface of dielectrics as a result of total internal reflection of a laser beam [201]. In this case, the exponentially decaying repulsive optical force for positive detuning can combine with the attractive CP force (3.6) of the surface to form a potential barrier whose position and height can be controlled via the laser beam. Probing this barrier by means of quantum reflection, it was possible to sensitively measure the CP potential [202, 203].

However, in all these setups, it is generally assumed that the optical and CP potentials, which are due to the interaction of the atomic dipole moment with the laser and surface-assisted vacuum fields, respectively, can be simply added. We have used perturbation theory simultaneously for both these interactions to show that this is not always the case [S24]: an additional laser-induced CP potential arises that is quadratic in both couplings. In the near-field limit and for a two-level atom, this potential can be given as

$$U_{\rm LCP}(\boldsymbol{r}) = U_{\rm L}(\boldsymbol{r})U_{\rm CP}(\boldsymbol{r})\frac{\mathrm{Re}\,r_{\rm p}}{\hbar\Delta}\,, \tag{7.2}$$

where $r_{\rm p}$ is the Fresnel reflection coefficient of the surface for p-polarised waves. The latter can become very large due to surface-plasmon resonances, leading to a strong short-range repulsive potential that dominates over the attractive CP potential near the surface. This can lead to the formation of a stable trapping potential very close to the surface. We have confirmed our results, which generalise [204] and correct earlier findings [205] in the far-field case, by means of a nonperturbative calculation [P19] and an alternative derivation on

the basis of normal-mode QED [P13]. The laser-induced CP potential is analogous to the optical binding potential of nanoparticles [206, 207]. It could be observed in experiments using optically levitated nanoparticles close to a surface. Our initial investigations on the basis of a macroscopic-QED analysis of CP and Coulomb potentials [P28] have shown that the latter dominate the setup at present due to residual charges [P16].

7.2. Collective atom–field interactions

As shown by Dicke, an ensemble of N identical two-level atoms i with transition dipole moment $\boldsymbol{d}$ and individual Pauli operators $\hat{\sigma}_i^+$, $\hat{\sigma}_i^-$ may collectively and coherently interact with the electromagnetic field, provided that they are confined to a region that is much smaller than its relevant wavelengths [208, 209]. In this case, the atom–field interaction may be approximated via

$$\hat{H}_{\rm int} = -\sum_{i=1}^{N} \hat{\boldsymbol{d}}_i \cdot \hat{\boldsymbol{E}}(\boldsymbol{r}_i) = \hat{\boldsymbol{d}} \cdot \hat{\boldsymbol{E}}(\boldsymbol{r}_i) \tag{7.3}$$

where the collective dipole $\hat{\boldsymbol{d}} = \sum_{i=1}^{N} (\boldsymbol{d}\hat{\sigma}_i^- + \boldsymbol{d}^* \hat{\sigma}_i^+) = \boldsymbol{d}\hat{J}^- + \boldsymbol{d}^* \hat{J}^+$ is governed by the algebra of an angular momentum operator $\hat{J}$ with eigenvalue $J = N/2$. The corresponding collective eigenstates of the ensemble, the Dicke states $|J, M\rangle$ $(M = -J, \ldots, J)$ have transition matrix elements

$$\langle J, M | \hat{\boldsymbol{d}} | J, M-1 \rangle = \sqrt{(J+M)(J-M+1)}\, \boldsymbol{d}\,. \tag{7.4}$$

When the atoms initially coherently share N excitations, then the accelerated spontaneous decay between these Dicke states as induced by the collective dipole operator leads to a pronounced burst of the emitted radiation on short timescales, which is commonly known as superradiance. The total energy is of course the same as that emitted by an incoherent ensemble of atoms. It has been predicted that the Purcell effect can enhance superradiance further by means of an environment [210].

In parallel with, but independent of the group of Meystre [211], we have shown that superradiance can also be used to collectively enhance atom–surface interactions [S25]. The effect can be understood from our observation in Chap. 5 that the resonant CP potential (5.1) is a recoil force due to spontaneous emission. By combining it with the above collective dipole moment, we find a time-dependent total potential

$$U(\boldsymbol{r}, t) = \sum_{M=-J}^{J} p_M(t)(J+M)(J-M+1) U_n(\boldsymbol{r}_i) \tag{7.5}$$

that closely follows the superradiance dynamics and whose peak height shows an N^2 scaling with respect to the number of atoms. This increase with respect to the N scaling of the total CP interaction of an incoherent ensemble could be exploited to sensitively detect weak quantum vacuum forces, such as the quantum friction to be discussed in the next Chap. 8, on short time scales, thus decreasing the required interaction length. We have determined the conditions for observing a superradiant enhancement of CP forces, finding that the ensemble must be confined to a region whose veticall extent is smaller than the atomic transition wavelength in the far-field regime or smaller than the atom–surface separation in the near-zone.

In further studies of collective effects, we have shown how the super- and subradiant decay of two coherent emitters near a perfectly conducting plate depends on both the orientation of

their dipole moments and their positions with respect to each other as well as to the surface [P32]; and that strong coupling in a planar cavity can lead to enhanced VdW interactions governed by collective vacuum Rabi frequencies [P11, P25].

8. Quantum friction

The quantum vacuum effects considered so far have all been obtained by averaging the fluctuating field and charge distributions for a given centre-of-mass position of the interacting objects in the spirit of a Born–Oppenheimer approximation. When allowing for uniform motion, quantum friction is expected to arise as a dissipative dispersion force. We will discuss the contributions to and behaviour of Casimir–Polder quantum friction on atoms moving with respect to a body; and propose that this elusive phenomenon might be verified indirectly in the form of velocity-dependent shifts and broadenings of atomic transitions.

8.1. Casimir–Polder forces on moving atoms

Quantum friction was originally proposed for a setting that is an immediate generalisation of the Casimir geometry: two infinite parallel plates that move in the lateral direction with constant velocity [52]. The effect being very small, it has not been observed to date, allowing theoretical controversies regarding its existence and velocity dependence to flourish [212, 213, 214].

The closely related CP friction is predicted to arise when an atom moves parallel to a plane surface [215, 216, 217]. We have studied this effect by considering the Lorentz force on a moving atom that arises from the coupled atom–field dynamics [S26]. In a nonrelativistic calculation to leading order in the atomic centre-of-mass velocity $\boldsymbol{v}$, we have found that velocity-dependent forces arise via three distinct contributions. Firstly, the plate induced shifts and broadenings of the atomic transitions which feature in the CP potential acquire a velocity dependence, as will be discussed in the next section. Secondly, the atomic polarisation couples to its centre-of-mass motion via the Röntgen current [8] which are a part of the electric dipole interaction, with the electric field having been transformed to the atom's co-moving frame: $\hat{H}_{\rm int} = -\hat{\boldsymbol{d}}\cdot\hat{\boldsymbol{E}}' = -\hat{\boldsymbol{d}}\cdot\big(\hat{\boldsymbol{E}} + \boldsymbol{v}\times\hat{\boldsymbol{B}}\big)$. The Röngten contribution is only relevant in the far field and becomes negligible for the near-zone distances where quantum friction is most likely to be detectable. Thirdly, the delay between the emission of electromagnetic fields by the atomic dipole and their back-action onto the atom means that these events takes place at slightly different positions in the case of motion. This delay is responsible for the dominant contribution to CP friction and it has a simple interpretation in terms of image dipoles: the atom interacts with its own image dipole behind the plate which lags slightly behind due to the motion, leading to a dissipative backwards force.

Concentrating on the delay contribution, we have determined quantum friction for ground- and excited-state atoms. For ground-state atoms, we predict a tiny force linear in $\boldsymbol{v}$ that agrees with findings of time-dependent perturbation theory [218], but is at odds with the cubic velocity dependence obtained on the basis of linear response theory [219]. It was later shown that the perturbative result depends very sensitively on the precise trajectory of the moving atom prior to the constant motion [P49] and that the Markov approximation made in our calculation is not always appropriate in the quantum friction setting [220]. We have performed a detailed comparison of the Markovian and perturbative approaches for lateral and normal motion, finding agreement to second order in the atom–field coupling, but discrepancies for higher orders [P34].

For excited atoms interacting with the plasmon mode of a surface, we find resonant quantum friction versus acceleration forces [S26] that are closely analogous to cavity cooling [221]. For an atom whose transition energy is larger than the plasmon energy absorbed by the surface, the excess energy is transformed into kinetic energy, accelerating the atom. In the opposite case of the atomic transition energy being slightly too small, we predict a decelerating quantum friction force.

8.2. Spectroscopic signatures

The motion-induced atomic line shifts and broadenings do not suffer from any ambiguities caused by different model assumptions. We have used the Markov approximation to determine these for arbitrary motion with respect to a plane surface [S27] and our results are in agreement with those from time-dependent perturbation theory [P34]. These indirect signatures of quantum friction have the advantage that they could potentially be measured by means of very sensitive spectroscopic methods [222]. To pursue this prospect, we have analysed the dependence of the level shifts and widths on velocity, atomic and material parameters. Rather surprisingly, their magnitude is not governed by v/c as expected for a relativistic effect, but by the much larger $v/(z\gamma)$ where γ is the width of the relevant medium resonance. Furthermore, we find that the shifts and widths are quadratic in $v/(z\gamma)$ for the original quantum friction setting involving parallel motion, but exhibit a linear scaling for normal motion towards the surface that is much more favourable with regard to detection.

9. Matter-wave diffraction

In the previous chapter, we have studied the impact of motion on dispersion forces. Conversely, these forces influence the motion of atoms. Staying firmly in the quantum realm, we will apply our results regarding Casimir–Polder and optical potentials by showing that they can be combined to facilitate matter-wave interference at a one-dimensional periodic grating; and how Casimir–Polder interactions imprint a phase on atomic matter waves diffracted at compact objects, influencing the Poisson-spot interference pattern that forms behind the scatterer.

9.1. Reflective matter-wave grating

Matter-wave interference at transmissive material or optical gratings [223] is at the heart of current endeavours to push the quantum–classical divide by demonstrating the wave nature of matter for ever more massive and complex particles [224]. We have shown how the ground-state CP potential of Chap. 3 and the optical potential encountered in Chap. 7 can be combined to form a reflective grating for matter-wave interference [S28].

Our setup involves ultracold rubidium atoms incident on a sapphire surface with a periodic array of gold nanowires of rectangular cross-section. The resulting CP potential (3.6) for this geometry can be obtained by using the Green tensor for a plane surface with periodic corrugations in Rayleigh decomposition as described in Sect. 2.3. The potential is attractive and periodic in the lateral direction, being strongest above the gold wires. To achieve a reflective grating, we use a laser beam with negative detuning that is totally internally reflected inside the sapphire substrate and emerges as an evanescent field. The corresponding optical potential (7.1) can be determined using Rayleigh transmission coefficients [134, S4]. One finds a repulsive potential that exponentially decays away from the surface and is periodically modulated in the lateral direction, with weaker optical forces above the gold wires due to shielding. As neither substrate nor wires exhibit any resonances near the laser frequency, the laser-induced CP potential (7.2) can be neglected and one can simply add CP and optical potentials. The result is a complex landscape of alternating attractive CP-dominated potentials above the wires and repulsive regions above the space between them.

An incident matter wave will be classically reflected from regions where the repulsive potential exceeds the initial kinetic energy. This gives rise to a reflective periodic grating for matter-wave interference where atoms attracted to the wires do not contribute to the signal. We have simulated the resulting interference pattern using Fraunhofer diffraction theory [225]. The effective slit width of the matter-wave grating can be tuned by changing the intensity of the repulsive evanescent, where an increase leads to broader reflective strips. The simulations are in good agreement with the experimental observations, so the experiment constitutes a measurement of a lateral CP force above a periodically structured surface.

For high laser intensities, the reflective strips become so large that they overlap and cover the whole area. Our simple description would then imply that no grating-interference pattern can form. The experiment shows that this is not the case. The persisting interference pattern is due to phase imprinting, which has been intensely studied for CP potentials in the context of transmissive gratings [223, 226, 227]. We consider the impact of phase imprinting

on matter-wave diffraction in the next section for a different geometry.

9.2. Poisson spot

The Poisson spot is a bright spot due to constructive interference in the centre of the classical shadow region behind a compact scatterer. Unobserved at the time, it was originally brought forward by Poisson [228] as an argument against Fresnel's wave theory of light [132]. In a turn of events unforeseen by Poisson, the spot now bearing his name was later experimentally demonstrated by Arago [229] and has since become paradigmatic evidence for the wave nature of light and matter.

In the case of light, a compact object simply blocks part of the wave, thus generating the interference pattern. For matter-wave scattering, an additional effect arises: even the transmitted matter waves are affected via the CP potential (3.6) between the scattered atoms and the body. For sufficiently fast atoms, one can use the Wentzel–Kramers–Brillouin approximation [230, 231, 232] to determine the phase shift imprinted on the matter wave along a trajectory at distance ρ from the optical axis [233],

$$\Delta\phi(\rho) = -\frac{1}{\hbar v}\int_{-\infty}^{\infty} \mathrm{d}z\, U(\rho, z)\,. \tag{9.1}$$

We have calculated the CP potential of ground-state indium atoms in the presence of a silicon dioxide sphere by means of the spherical Green tensor [P97] to analyse its impact on the Poisson-spot signal [S29]. We find that the Poisson spot is mainly due to matter waves propagating so close to the sphere surface that we can neglect both retardation and curvature effects, with the latter result confirming the assumptions of previous simulations [234]. One can then find a simple analytical expression for the above phase. Combining this with Fresnel diffraction theory, we find that the CP-imprinted phase leads to a pronounced increase of the Poisson-spot signal. This shows that the CP interaction needs to be taken into account when using the Poisson spot as evidence for the wave nature of matter [235] and that conversely, the Poisson spot can be used as a probe for the former.

We have performed similar investigations for matter-wave scattering of indium atoms or deuterium molecules at silicon nitride and silicon dioxide disks [P33], with the latter observed in recent experiments [236]. Here, curvature effects are again negligible and edge effects mutually cancel, so that the CP potential experienced by the traversing atoms can be approximated with that of an infinite plane surface.

A different environment-induced phenomenon arises when a coherently split beam of electrons passes close to a metal surface [237]. This induces image currents inside the metal, so that the associated which-path information reduces the interference contrast. We have used macroscopic QED to quantify this effect in terms of the conductivity of the metal, showing that path decoherence requires material absorption [P61]. Our theory was later generalised to account for environment-mediated interactions across the two interfering beams [238].

10. Resonance energy transfer

As seen in Chapter 5, the emission of a real photon can lead to spatially oscillating VdW forces for excited atoms. In such scenarios, the photon can also mediate an irreversible energy transfer, changing the internal states of both atoms. We discuss the impact of retardation and environments on the efficiency of a particular resonance energy transfer phenomenon, interatomic Coulombic decay; and describe the effect of a third, mediator atom on the transfer rate.

10.1. Interatomic Coulombic decay

Interatomic Coulombic decay is a recently predicted [239] and experimentally verified [240] fast dissipation channel whereby a highly excited donor ion relaxes and transmits its energy to a neighbouring acceptor atom which becomes ionised. Being a source for slow electrons, this process is believed to be a major contributor to radiation damage in biological tissue [241]. As the name suggests, the process has traditionally been studied in free space on the basis of nonretarded Coulomb interactions [242].

In the mentioned relevant biological scenarios as well as in current experiments with nanodroplets [243], interatomic Coulombic decay takes place in a nontrivial dielectric environment consisting of liquid media and surfaces. Their impact on the efficiency of the process can be described by means of macroscopic QED. To show this, one can determine the rate for the process by means of Fermi's golden rule where the initial state involves the donor ion in an excited state $|m_\mathrm{A}\rangle$, an acceptor ion in state $|n_\mathrm{B}\rangle$ and the electromagnetic fields in its vacuum state $|0_\mathrm{F}\rangle$; while the final state comprises the donor in a lower state $|k_\mathrm{A}\rangle$, the ionised acceptor with one electron in a continuum state $|p_\mathrm{B}\rangle$ and the field again in the vacuum. The matrix element for this process is of second order in the atom–field coupling $\hat{H}_\mathrm{int} = -\hat{\boldsymbol{d}}_\mathrm{A}\cdot\hat{\boldsymbol{E}}(\boldsymbol{r}_\mathrm{A}) - \hat{\boldsymbol{d}}_\mathrm{B}\cdot\hat{\boldsymbol{E}}(\boldsymbol{r}_\mathrm{B})$ and it involves the exchange of a photon between donor and acceptor. Using the field quantisation of Chap. 2, we find that the rate for interatomic Coulombic decay can be given as [S30]

$$\Gamma_{mn}(\boldsymbol{r}_\mathrm{A},\boldsymbol{r}_\mathrm{B}) = -2\pi^2 \sum_{k<m} \Gamma_{mk}\sigma_n(\hbar\omega_{mk})\mathrm{tr}\big[\boldsymbol{G}(\boldsymbol{r}_\mathrm{A},\boldsymbol{r}_\mathrm{B},\omega_{mk})\cdot\boldsymbol{G}^*(\boldsymbol{r}_\mathrm{B},\boldsymbol{r}_\mathrm{A},\omega_{mk})\big]\,. \tag{10.1}$$

This shows that the process depends on the ability of the donour to emit a photon as encoded via the single-atom rate Γ_{mk} (4.1); the progagation of the photon from donor to acceptor as represented by the Green tensor; and the ability of the acceptor to absorb the photon as contained via the absorption cross section σ_n.

When applied in free space by using the respective Green tensor, our formalism demonstrates that the rate exhibits the $1/r^6$ distance scaling in the near zone as known from electrostatic simulations [242]. For distances larger than the wavelength of the exchanged photon, interatomic Coulombic decay becomes a true QED effect with a $1/r^2$ scaling due to the influence of the retarded electromagnetic far field. Interatomic Coulombic decay can thus have a much larger range than previously thought. By using the real-cavity model introduced in Sect. 4.1, we have further been able to show how the rate can be enhanced

or suppressed in a medium such as water or liquid helium due to a combination of screening and local-field effects. Finally, interatomic Coulombic decay near a surface exhibits a modification that sensitively depends on the positioning of both donor and acceptor.

10.2. Three-body effects

Interatomic Coulombic decay is formally closely analogous to resonance energy transfer [244, 245], where the donor becomes ionised rather than excited. This process, which can also be described within the framework of macroscopic QED [246], is known to be sensitive to the presence of a third, mediator atom [247, 248, 249]. A similar three-body phenomenon has very recently been predicted for interatomic Coulombic decay [250]. In this so-called superexchange, a mediator placed in the vicinity of the donor–acceptor pair affects the rate.

We have used the above QED description to analyse the geometry dependence of three-body interatomic Coulombic decay. To this end, one can use a Born expansion of the Green tensor in the presence of a single mediator of polarisability α_C [P92],

$$\boldsymbol{G}(\boldsymbol{r},\boldsymbol{r}',\omega_{mk}) = \boldsymbol{G}^{(0)}(\boldsymbol{r},\boldsymbol{r}',\omega) + \mu_0\omega^2\alpha_\mathrm{C}(\omega)\boldsymbol{G}^{(0)}(\boldsymbol{r},\boldsymbol{r}_\mathrm{C},\omega)\cdot\boldsymbol{G}^{(0)}(\boldsymbol{r}_\mathrm{C},\boldsymbol{r}',\omega) \tag{10.2}$$

with $\boldsymbol{G}^{(0)}$ denoting the free-space Green tensor. Combining this with the above general formula (10.1), we find a three-body rate that agrees with the predictions of molecular dynamics simulations in the near-field regime in the absence of wave-function overlap [250], but extends them to the far-field regime while allowing to study the position dependence analytically [P10].

11. Conclusions

With the research presented in this thesis, we have developed a modern and integrated analysis of the quantum vacuum and some of its consequences. The central tool is macroscopic quantum electrodynamics, an effective nonrelativistic theory of the electromagnetic field in its various states and its interactions with matter in the form of macroscopic objects (bodies, surfaces, media, ...) and microscopic particles (electrons, ions, atoms, molecules, ...) that is consistent with free-space quantum electrodynamics and combines inputs from classical optics in the form of the Green tensor; from atomic and molecular physics in the guise of polarisabilities; and from solid-state physics via material response functions. We have continuously developed this theory in line with current developments and requirements from modern experiments and materials design, including an extension to nonreciprocal media as constituted by topological insulators. We have introduced duality as an important symmetry of the theory and uncovered a deep relation between this symmetry and nonreciprocity.

Starting from dispersion forces as pure quantum vaccum forces in free space, we have successively extended this notion to include intervening media, excited objects, finite temperature, collective phenomena, and centre-of-mass motion. Along the way, very fundamental questions concerning the correct stress tensor to be used for calculating Casimir forces in media or the oscillating nature of the Van der Waals force between excited atoms have been answered and general principles such as an opposites-repel rule for Casimir repulsion and the application of the Curie symmetry principle for using dispersion forces as a probe for optical properties have been uncovered.

Surprising findings include the facts that spin–orbit coupling can lead to lateral dispersions force driven by spontaneous emission; that Casimir–Polder forces may become entirely independent of temperature under certain conditions; and that optical and Casimir–Polder forces can sometimes not be simply added. We have proposed that amplifying could be used to realise repulsive Casimir forces as required to overcome stiction; pointed out that Casimir and Van der Waals forces can be utilised for the separation of chiral enantiomers; and shown how atom–surface interations must be accounted for in order to unambiguously establish the wave nature of matter. Our effective description of atom–light interactions in media has applications in colloid physics and for spectroscopy in the liquid phase.

Our investigations show that a clever combination of ideas and techniques from various fields can be used to predict new quantum effects such as a superradiant enhancement of atom–surface interactions or to facilitate the detection of elusive and exotic phenomena such as quantum friction. Major breakthroughs have been achieved by applying macroscopic quantum electrodynamics beyond its comfort zone and within realms traditionally described by other methods such as interatomic Coulombic decay. Potential for future developments thus lies in the extension of the theory to more exotic quantum phenomena such as the Unruh effect; in its application at the interfaces with other theories such as quantum optics, physical chemistry, attosecond science, Bose–Einstein condensation or colloid physics; and in the monitoring of new developments in atomic, molecular, and materials physics.

A particularly exciting prospect has recently opened with the advent of nonlinear crystal-based scenarios to directly probe the quantum vacuum. This presents new challenges to macroscopic quantum electrodynamics and inspires dreams of one day directly witnessing the fluctuating zero-point electromagnetic field and its role in fuelling what we have been

referring to as vacuum effects. This would turn a mainly mathematic-philosophical concept into a tangible physical phenomenon and would enable us to address the question: how real is a virtual photon?

Part II.

Original publications

1. List of selected publications

Macroscopic quantum electrodynamics

[S1] S. Y. Buhmann, D. T. Butcher, and S. Scheel, Macroscopic quantum electrodynamics in nonlocal and nonreciprocal media, *New J. Phys.*, 14/8 (2012), 083034.

[S2] S. Y. Buhmann and S. Scheel, Macroscopic quantum electrodynamics and duality, *Phys. Rev. Lett.*, 102/14 (2009), 140404.

[S3] S. Y. Buhmann, S. Scheel, and J. Babington, Universal scaling laws for dispersion interactions, *Phys. Rev. Lett.*, 104/7 (2010), 070404.

[S4] S. Y. Buhmann, V. N. Marachevsky, and S. Scheel, Impact of anisotropy on the interaction of an atom with a one-dimensional nanograting, *Int. J. Mod. Phys. A*, 31/2–3 (2016), 1641029.

Vacuum dispersion forces

[S5] S. Rode, R. Bennett, and S. Y. Buhmann, Casimir effect for perfect electromagnetic conductors (PEMCs): A sum rule for attractive/repulsive forces, *New J. Phys.*, 20/4 (2018), 043024.

[S6] S. Fuchs, F. Lindel, R. V. Krems, G. W. Hanson, M. Antezza, and S. Y. Buhmann, Casimir–Lifshitz force for nonreciprocal media and applications to photonic topological insulators, *Phys. Rev. A*, 96/6 (2017), 062505.

[S7] F. Lindel, G. W. Hanson, M. Antezza, and S. Y. Buhmann, Inducing and controlling rotation on small objects using photonic topological materials, *Phys. Rev. A*, 98/14 (2018), 144101.

[S8] J. Klatt, P. Barcellona, R. Bennett, O. S. Bokareva, H. Feth, A. Rasch, P. Reith, and S. Y. Buhmann, Strong Van der Waals adhesion of a polymer film on rough substrates, *Langmuir*, 33/21 (2017), 5298.

[S9] S. Fuchs, J. A. Crosse, and S. Y. Buhmann, Casimir–Polder shift and decay rate in the presence of nonreciprocal media, *Phys. Rev. A*, 95/2 (2017), 023805.

[S10] S. Y. Buhmann, V. N. Marachevsky, and S. Scheel, Charge–parity-violating effects in Casimir–Polder potentials, *Phys. Rev. A*, 98/2 (2018), 022510.

[S11] H. Safari, D.-G. Welsch, S. Y. Buhmann, and S. Scheel, Van der Waals potentials of paramagnetic atoms, *Phys. Rev. A*, 78/6 (2008), 062901.

[S12] S. Y. Buhmann, H. Safari, S. Scheel, and A. Salam, Body-assisted dispersion potentials of diamagnetic atoms, *Phys. Rev. A*, 87/1 (2013), 012507.

[S13] D. T. Butcher, S. Y. Buhmann, and S. Scheel, Casimir–Polder forces between chiral objects, *New J. Phys.*, 14/11 (2012), 113013.

[S14] P. Barcellona, H. Safari, A. Salam, and S. Y. Buhmann, Enhanced chiral discriminatory Van der Waals interactions mediated by chiral surfaces, *Phys. Rev. Lett.*, 118/19 (2017), 193401.

Dispersion forces in media

[S15] J. Fiedler, P. Thiyam, A. Kurumbail, F. A. Burger, M. Walter, C. Persson, I. Brevik, D. F. Parsons, M. Boström, and S. Y. Buhmann, Effective polarizability models, *J. Phys. Chem. A*, 121/51 (2017), 9742.

[S16] F. A. Burger, J. Fiedler, and S. Y. Buhmann, Zero-point electromagnetic stress tensor for studying Casimir forces on colloidal particles in media, *Europhys. Lett.*, 121/2 (2018), 24004.

[S17] A. Sambale, S. Scheel, and S. Y. Buhmann, Casimir–Polder interaction between an atom and a small magnetodielectric sphere, *Phys. Rev. A*, 81/1 (2010), 012509.

Forces on excited systems

[S18] R. R. Q. P. T. Oude Weernink, P. Barcellona, and S. Y. Buhmann, Lateral Casimir–Polder forces by breaking time-reversal symmetry, *Phys. Rev. A*, 97/3 (2018), 032507.

[S19] P. Barcellona, R. Passante, L. Rizzuto, and S. Y. Buhmann, Van der Waals interactions between excited atoms in generic environments, *Phys. Rev. A*, 94/1 (2016), 012705.

[S20] A. Sambale, S. Y. Buhmann, D.-G. Welsch, and D. T. Ho, Impact of amplifying media on the Casimir force, *Phys. Rev. A*, 80/5 (2009), 051801(R).

Thermal fluctuations

[S21] S. Y. Buhmann, M. R. Tarbutt, S. Scheel, and E. A. Hinds, Surface-induced heating of cold polar molecules, *Phys. Rev. A*, 78/5 (2008), 052901.

[S22] S. Y. Buhmann and S. Scheel, Thermal Casimir–Polder forces: Equilibrium and nonequilibrium forces, *Phys. Rev. Lett.*, 100/25 (2008), 253201.

[S23] S. Å. Ellingsen, S. Y. Buhmann, and S. Scheel, Temperature-invariant Casimir–Polder forces despite large thermal photon numbers, *Phys. Rev. Lett.*, 104/22 (2010), 223003.

Non-additive and collective phenomena

[S24] S. Fuchs, R. Bennett, R. V. Krems, and S. Y. Buhmann, Nonadditivity of optical and Casimir–Polder potentials, *Phys. Rev. Lett.*, 121/8 (2018), 083603.

[S25] S. Fuchs and S. Y. Buhmann, Purcell–Dicke enhancement of the Casimir–Polder potential, *Europhys. Lett.*, 124/3 (2018), 34003.

Quantum friction

[S26] S. Scheel and S. Y. Buhmann, Casimir–Polder forces on moving atoms, *Phys. Rev. A*, 80/4 (2009), 042902.

[S27] J. Klatt, R. Bennett, and S. Y. Buhmann, Spectroscopic signatures of quantum friction, *Phys. Rev. A*, 94/6 (2016), 063803.

Matter-wave diffraction

[S28] H. Bender, C. Stehle, C. Zimmermann, S. Slama, J. Fiedler, S. Scheel, S. Y. Buhmann, and V. N. Marachevsky, Probing atom–surface interactions by diffraction of Bose–Einstein condensates, *Phys. Rev. X*, 4 (2014), 011029.

[S29] J. L. Hemmerich, R. Bennett, T. Reisinger, S. Nimmrichter, J. Fiedler, H. Hahn, H. Gleiter, and S. Y. Buhmann, Impact of Casimir–Polder interaction on Poisson-spot diffraction at a dielectric sphere, *Phys. Rev. A*, 94/2 (2016), 023621.

Resonance energy transfer

[S30] J. L. Hemmerich, R. Bennett, and S. Y. Buhmann, The influence of retardation and dielectric environments on interatomic Coulombic decay, *Nature Commun.*, 9 (2018), 2934.

New Journal of Physics
The open-access journal for physics

Macroscopic quantum electrodynamics in nonlocal and nonreciprocal media

Stefan Yoshi Buhmann[1,3], **David T Butcher**[1] **and Stefan Scheel**[1,2]

[1] Quantum Optics and Laser Science, Blackett Laboratory, Imperial College London, Prince Consort Road, London SW7 2AZ, UK
[2] Institut für Physik, Universität Rostock, Universitätsplatz 3, D-18051 Rostock, Germany
E-mail: s.buhmann@imperial.ac.uk

New Journal of Physics **14** (2012) 083034 (12pp)
Received 6 July 2012
Published 29 August 2012
Online at http://www.njp.org/
doi:10.1088/1367-2630/14/8/083034

Abstract. We formulate macroscopic quantum electrodynamics in the most general linear, absorbing media. In particular, Onsager reciprocity is not assumed to hold. The field quantization is based on the source-quantity representation of the electromagnetic field in terms of the dyadic Green's tensor. For media with a nonlocal response, a description in terms of a complex conductivity tensor is employed. As an alternative description, we introduce the permittivity, permeability and magnetoelectric susceptibilities to obtain an explicitly duality-invariant scheme. We find that duality invariance only holds as a continuous symmetry when nonreciprocal responses are allowed for.

[3] Author to whom any correspondence should be addressed.

Contents

1. Introduction

The linear response of a macroscopic material to externally applied electromagnetic fields can go beyond the scope of simple descriptions via electric permittivities and magnetic permeabilities [1]. In particular, cross-susceptibilities naturally arise in chiral (meta-) materials [2], topological insulators [3] or moving media [4]. In the latter case nonlocal responses arise [5] with the additional complication that Onsager reciprocity [6] fails to hold. Onsager reciprocity, the electrodynamic manifestation of time-reversal symmetry, would also be violated in Tellegen media [7], including the recently proposed perfect electromagnetic conductor that continuously interpolates between a perfect conductor and an infinitely permeable material [8].

Chiral metamaterials with cross-susceptibilities have been constructed based on nanoscale chiral objects, such as a helix [9]. This leads to a discriminatory response of the medium to left- and right-circularly polarized light. This central feature of chiral media is important in biological systems due to the prevalence of left-handed objects in the processes crucial to life [10]. Furthermore, chiral meta-materials have been discussed as candidates for repulsive Casimir forces [11]. It should be noted that repulsive forces for magnetoelectric media were originally discussed for dielectric plates interacting with magnetic plates [12]. To implement these effects with metamaterials, the anisotropic response of the medium needs to be taken into account [13].

Topological insulators are a novel class of materials which behave as insulators in their bulk phase but allow for conduction on the surface [14, 15]. Time reversal symmetry is an important feature which ensures an extremely high stability of the surface currents. The latter make topological insulators a promising candidate for quantum computing [16]. It has recently been predicted that topological insulators [3] (or materials with a Chern–Simons interaction [17]) could be used to realize repulsive Casimir forces. A related phenomenon is the fractional quantum hall effect where the Hall current takes fractional values due to electron–electron interactions [18]. This medium can be nonlocal [19] and in contrast to topological insulators it can violate time-reversal symmetry [20] and hence Onsager reciprocity.

The impact of electric versus magnetic material properties can be studied in a systematic way by means of a duality transformation [21]. It has recently been shown that macroscopic QED [22] in isotropic magnetoelectrics obeys a discrete duality symmetry [23]. This has immediate consequences for dispersion forces in free space.

The successes in the realization of the above mentioned novel materials open the perspective on a range of new quantum phenomena related to photon-induced matter interactions, quantum dynamics and (possibly irreversible) quantum-light propagation. To make such studies possible, we will construct a quantum theory of the electromagnetic field in the most general linear absorbing media, including nonlocal, bianisotropic and Onsager reciprocity violating materials. A recent theory based on canonical quantization is a valuable step in this direction [24], which does not yet consider the most general nonlocal media (apart from the above mentioned moving media).

In addition, our theory shall answer the question under which circumstances duality can be realized as a continuous symmetry of the Maxwell equations in media; and it will shed light on the generalizations necessary to discuss moving media and quantum friction.

2. Field quantization in nonlocal media

We begin by recalling a quantization procedure of the electromagnetic field in the presence of an absorbing medium. For alternative methods for the quantization procedure, see [25–27] and references therein. In a linearly responding medium, the effect of an external electromagnetic field on the matter can be given by Ohm's law in its most general form

$$\mathbf{j}_{\mathrm{in}}(\mathbf{r},t)=\int_{-\infty}^{\infty}\mathrm{d}\tau\int\mathrm{d}^3r'\,\mathbf{Q}(\mathbf{r},\mathbf{r}',\tau)\cdot\mathbf{E}(\mathbf{r}',t-\tau)+\mathbf{j}_{\mathrm{N}}(\mathbf{r},t). \tag{1}$$

Here, $\mathbf{Q}(\mathbf{r},\mathbf{r}',\tau)$ is the conductivity tensor and $\mathbf{j}_{\mathrm{N}}(\mathbf{r},t)$ is the random noise current required to fulfil the fluctuation–dissipation theorem (17) as given below. Causality requires that $\mathbf{Q}(\mathbf{r},\mathbf{r}',\tau)=\mathbf{0}$ for $c\tau<|\mathbf{r}-\mathbf{r}'|$, in particular for all $\tau<0$ [28]. In frequency space, Ohm's law takes the simpler form

$$\mathbf{j}_{\mathrm{in}}(\mathbf{r},\omega)=\int\mathrm{d}^3r'\,\mathbf{Q}(\mathbf{r},\mathbf{r}',\omega)\cdot\mathbf{E}(\mathbf{r}',\omega)+\mathbf{j}_{\mathrm{N}}(\mathbf{r},\omega) \tag{2}$$

with

$$\mathbf{Q}(\mathbf{r},\mathbf{r}',\omega)=\int_{0}^{\infty}\mathrm{d}\tau\,\mathrm{e}^{\mathrm{i}\omega\tau}\mathbf{Q}(\mathbf{r},\mathbf{r}',\tau). \tag{3}$$

As a result of the causality requirement the conductivity obeys the Schwarz reflection principle,

$$\mathbf{Q}^*(\mathbf{r},\mathbf{r}',\omega)=\mathbf{Q}(\mathbf{r},\mathbf{r}',-\omega^*)\quad\forall\,\mathbf{r},\mathbf{r}',\omega. \tag{4}$$

Quantization is achieved by specifying the commutator

$$[\hat{\mathbf{j}}_{\mathrm{N}}(\mathbf{r},\omega),\hat{\mathbf{j}}_{\mathrm{N}}^{\dagger}(\mathbf{r}',\omega')]=\frac{\hbar\omega}{\pi}\,\mathcal{R}\mathrm{e}[\mathbf{Q}(\mathbf{r},\mathbf{r}',\omega)]\delta(\omega-\omega'), \tag{5}$$

where we have introduced generalized real and imaginary parts of a tensor field according to

$$\mathcal{R}\mathrm{e}\mathbf{T}(\mathbf{r},\mathbf{r}')=\tfrac{1}{2}\big[\mathbf{T}(\mathbf{r},\mathbf{r}')+\mathbf{T}^{\dagger}(\mathbf{r}',\mathbf{r})\big], \tag{6}$$

$$\mathcal{I}\mathrm{m}\mathbf{T}(\mathbf{r},\mathbf{r}')=\frac{1}{2\mathrm{i}}\big[\mathbf{T}(\mathbf{r},\mathbf{r}')-\mathbf{T}^{\dagger}(\mathbf{r}',\mathbf{r})\big]. \tag{7}$$

They reduce to ordinary real and imaginary parts for orthogonal tensor fields that are reciprocal, i.e. $\mathbf{T}^{\mathsf{T}}(\mathbf{r}', \mathbf{r}) = \mathbf{T}(\mathbf{r}, \mathbf{r}')$. The other nontrivial current commutators follow alternatively via the rules $[\hat{b}, \hat{a}] = -[\hat{a}, \hat{b}]$ or $[\hat{a}^\dagger, \hat{b}^\dagger] = -[\hat{a}, \hat{b}]^\dagger$;

$$\left[\hat{\mathbf{j}}_{\mathrm{N}}^\dagger(\mathbf{r}, \omega), \hat{\mathbf{j}}_{\mathrm{N}}(\mathbf{r}', \omega')\right] = -\frac{\hbar\omega}{\pi}\,\mathcal{R}\mathrm{e}[\mathbf{Q}^*(\mathbf{r}, \mathbf{r}', \omega)]\delta(\omega - \omega') = -\frac{\hbar\omega}{\pi}\,\mathcal{R}\mathrm{e}[\mathbf{Q}^{\mathsf{T}}(\mathbf{r}', \mathbf{r}, \omega)]\delta(\omega - \omega'). \tag{8}$$

The fact that the right-hand side of this expression is a Hermitian tensor field guarantees the consistency of the commutation relations.

Combining Ohm's law with Maxwell's equations [$\mathrm{i}\,\omega\hat{\rho}_{\mathrm{in}}(\mathbf{r}, \omega) = \nabla \cdot \hat{\mathbf{j}}_{\mathrm{in}}(\mathbf{r}, \omega)$]

$$\nabla \cdot \hat{\mathbf{E}}(\mathbf{r}, \omega) = \frac{\hat{\rho}_{\mathrm{in}}(\mathbf{r}, \omega)}{\varepsilon_0}, \quad \nabla \times \hat{\mathbf{E}}(\mathbf{r}, \omega) - \mathrm{i}\,\omega\hat{\mathbf{B}}(\mathbf{r}, \omega) = \mathbf{0}, \tag{9}$$

$$\nabla \cdot \hat{\mathbf{B}}(\mathbf{r}, \omega) = 0, \quad \nabla \times \hat{\mathbf{B}}(\mathbf{r}, \omega) + \frac{\mathrm{i}\,\omega}{c^2}\hat{\mathbf{E}}(\mathbf{r}, \omega) = \mu_0\hat{\mathbf{j}}_{\mathrm{in}}(\mathbf{r}, \omega), \tag{10}$$

one finds that the electric field obeys a generalized inhomogeneous Helmholtz equation of the form

$$\left[\nabla \times \nabla \times - \frac{\omega^2}{c^2}\right]\hat{\mathbf{E}}(\mathbf{r}, \omega) - \mathrm{i}\,\mu_0\omega \int \mathrm{d}^3r'\mathbf{Q}(\mathbf{r}, \mathbf{r}', \omega) \cdot \hat{\mathbf{E}}(\mathbf{r}', \omega) = \mathrm{i}\,\mu_0\omega\hat{\mathbf{j}}_{\mathrm{N}}(\mathbf{r}, \omega). \tag{11}$$

With the help of the Green function $\mathbf{G}(\mathbf{r}, \mathbf{r}', \omega)$ of the Helmholtz equation, defined by

$$\left[\nabla \times \nabla \times - \frac{\omega^2}{c^2}\right]\mathbf{G}(\mathbf{r}, \mathbf{r}', \omega) - \mathrm{i}\,\mu_0\omega \int \mathrm{d}^3s\,\mathbf{Q}(\mathbf{r}, \mathbf{s}, \omega) \cdot \mathbf{G}(\mathbf{s}, \mathbf{r}', \omega) = \boldsymbol{\delta}(\mathbf{r} - \mathbf{r}'), \tag{12}$$

where $\mathbf{G}(\mathbf{r}, \mathbf{r}', \omega) \to \mathbf{0}$ for $|\mathbf{r} - \mathbf{r}'| \to \infty$, the formal solution to the integro-differential equation (11) reads

$$\hat{\mathbf{E}}(\mathbf{r}, \omega) = \mathrm{i}\,\mu_0\omega[\mathbf{G}(\omega) \star \hat{\mathbf{j}}_{\mathrm{N}}(\omega)](\mathbf{r}). \tag{13}$$

Here, $[\mathbf{G} \star \hat{\mathbf{j}}_{\mathrm{N}}]$ is an abbreviation denoting the spatial convolution

$$[\mathbf{G} \star \hat{\mathbf{j}}_{\mathrm{N}}](\mathbf{r}) \equiv \int \mathrm{d}^3r'\,\mathbf{G}(\mathbf{r}, \mathbf{r}') \cdot \hat{\mathbf{j}}_{\mathrm{N}}(\mathbf{r}').$$

By virtue of its definition (12), the Green tensor inherits the Schwarz reflection principle from the conductivity tensor (4),

$$\mathbf{G}^*(\mathbf{r}, \mathbf{r}', \omega) = \mathbf{G}(\mathbf{r}, \mathbf{r}', -\omega^*) \quad \forall\, \mathbf{r}, \mathbf{r}', \omega. \tag{14}$$

However, as a major departure from previous treatments, we do not require the conductivity to obey reciprocity, i.e. the relation $\mathbf{Q}^{\mathsf{T}}(\mathbf{r}', \mathbf{r}, \omega) = \mathbf{Q}(\mathbf{r}, \mathbf{r}', \omega)$ does not necessarily hold. As a consequence, the Green tensor will not obey the Onsager principle, i.e. the relation

$$\mathbf{G}^{\mathsf{T}}(\mathbf{r}', \mathbf{r}, \omega) = \mathbf{G}(\mathbf{r}, \mathbf{r}', \omega) \tag{15}$$

will not hold in general. Recall that the Onsager principle, applied to electromagnetic field propagation, states a reversibility of optical paths [6]. According to (13), the Green tensor governs the relation between a source current j at $\mathbf{r}'$ along a direction $\mathbf{e}_2$ and the generated electric field E at $\mathbf{r}$ along a direction $\mathbf{e}_1$. If (15) holds, then the Onsager principle states that the roles of source and field can be reversed. A source current j at $\mathbf{r}$ along a direction $\mathbf{e}_1$ would

then give rise to an electric field E at $\mathbf{r}'$ along a direction $\mathbf{e}_2$. In a configuration involving nonreciprocal media, this is not necessarily the case. Despite the extension to nonreciprocal media, it is still possible to derive the useful integral relation (appendix)

$$\mu_0\omega[\mathbf{G}(\omega)\star\mathcal{R}\mathrm{e}\mathbf{Q}(\omega)\star\mathbf{G}^\dagger(\omega)](\mathbf{r},\mathbf{r}')=\mathcal{I}\mathrm{m}\,\mathbf{G}(\mathbf{r},\mathbf{r}',\omega). \tag{16}$$

It generalizes the result from [29] to the case where Onsager reciprocity does not hold.

The theory thus far is analogous to classical electromagnetism in an absorbing medium under the assumption of classical fluctuating current sources, $\hat{\mathbf{j}}_\mathrm{N}\mapsto\mathbf{j}_\mathrm{N}$. Their strengths are governed by the fluctuation–dissipation theorem in the classical (high-temperature) limit [30].

Introducing the ground state $|\{0\}\rangle$ of the medium-field system according to $\hat{\mathbf{j}}_\mathrm{N}(\mathbf{r},\omega)|\{0\}\rangle=\mathbf{0}$, the currents satisfy the fluctuation–dissipation theorem as an immediate consequence of (5),

$$\langle\{\Delta\hat{\mathbf{j}}_\mathrm{N}(\mathbf{r},\omega),\Delta\hat{\mathbf{j}}_\mathrm{N}^\dagger(\mathbf{r}',\omega')\}\rangle=\frac{\hbar}{\pi}\mathcal{I}\mathrm{m}[\mathrm{i}\,\omega\mathbf{Q}(\mathbf{r},\mathbf{r}',\omega)]\delta(\omega-\omega'). \tag{17}$$

Combining (5) and (13), one finds that the fluctuations of the electric field are also consistent with the fluctuation–dissipation theorem, as required:

$$\langle\{\Delta\hat{\mathbf{E}}(\mathbf{r},\omega),\Delta\hat{\mathbf{E}}^\dagger(\mathbf{r}',\omega')\}\rangle=\frac{\hbar}{\pi}\mathcal{I}\mathrm{m}\big[\mu_0\omega^2\mathbf{G}(\mathbf{r},\mathbf{r}',\omega)\big]\delta(\omega-\omega'). \tag{18}$$

In order to verify the canonical equal-time commutation relations, we introduce the vector potential for the electromagnetic field in the Coulomb gauge, $\hat{\mathbf{A}}(\mathbf{r},\omega)=\hat{\mathbf{E}}^\perp(\mathbf{r},\omega)/(\mathrm{i}\,\omega)$ ($\perp$: transverse part). Using (5) and (13), one finds

$$\big[\hat{\mathbf{E}}(\mathbf{r},\omega),\hat{\mathbf{A}}^\dagger(\mathbf{r}',\omega')\big]=\frac{\mathrm{i}\hbar\mu_0\omega}{\pi}\mathcal{I}\mathrm{m}[\mathbf{G}^\perp(\mathbf{r},\mathbf{r}',\omega)]\delta(\omega-\omega') \tag{19}$$

and hence

$$\big[\hat{\mathbf{E}}(\mathbf{r}),\hat{\mathbf{A}}(\mathbf{r}')\big]=\frac{\hbar\mu_0}{2\pi}\int_{-\infty}^{\infty}\mathrm{d}\omega\,\omega\big[\mathbf{G}^\perp(\mathbf{r},\mathbf{r}',\omega)+{}^\perp\mathbf{G}^\mathsf{T}(\mathbf{r}',\mathbf{r},\omega)\big], \tag{20}$$

where the Schwarz reflection principle (14) has been used. Use has been made of the left- and right-sided transverse projections, which are defined, respectively, as

$${}^\perp\boldsymbol{T}=\boldsymbol{\delta}^\perp\star\boldsymbol{T},\quad \boldsymbol{T}^\perp=\boldsymbol{T}\star\boldsymbol{\delta}^\perp. \tag{21}$$

Closing the integration contour in the upper half of the complex ω plane, where the Green's function is analytic, and using the asymptote $(\omega^2/c^2)\mathbf{G}(\mathbf{r},\mathbf{r}',\omega)\to-\boldsymbol{\delta}(\mathbf{r}-\mathbf{r}')$ for $|\omega|\to\infty$, one finds the canonical commutation relation from free-space QED,

$$\big[\hat{\mathbf{E}}(\mathbf{r}),\hat{\mathbf{A}}(\mathbf{r}')\big]=\frac{\mathrm{i}\hbar}{\varepsilon_0}\boldsymbol{\delta}^\perp(\mathbf{r}-\mathbf{r}'), \tag{22}$$

as required. We now introduce the bosonic creation and annihilation operators of the matter-field system, $\hat{\mathbf{f}}^\dagger$ and $\hat{\mathbf{f}}$ according to the prescription

$$\hat{\mathbf{j}}_\mathrm{N}(\omega)=\sqrt{\frac{\hbar\omega}{\pi}}\,\mathbf{R}(\omega)\star\hat{\mathbf{f}}(\omega), \tag{23}$$

where $\mathbf{R}$ is a square root of the positive definite tensor field $\mathcal{R}\mathrm{e}[\mathbf{Q}]$,

$$\mathbf{R}(\omega)\star\mathbf{R}^\dagger(\omega)=\mathcal{R}\mathrm{e}[\mathbf{Q}(\omega)]. \tag{24}$$

This solution is only unique up to a unitary matrix which does not affect the physical results [29]. Together with equation (5), this ensures bosonic commutation relations,

$$[\hat{\mathbf{f}}(\mathbf{r},\omega),\hat{\mathbf{f}}^{\dagger}(\mathbf{r}',\omega')]=\boldsymbol{\delta}(\mathbf{r}-\mathbf{r}')\delta(\omega-\omega'). \tag{25}$$

The Hamiltonian of the medium-field system is then

$$\hat{H}_{\mathrm{F}}=\int \mathrm{d}^3r\int_0^{\infty}\mathrm{d}\omega\,\hbar\omega\,\hat{\mathbf{f}}^{\dagger}(\mathbf{r},\omega)\cdot\hat{\mathbf{f}}(\mathbf{r},\omega). \tag{26}$$

It leads to the free evolution of the dynamical variables as $\hat{\mathbf{f}}(\mathbf{r},\omega,t)=\hat{\mathbf{f}}(\mathbf{r},\omega)\,\mathrm{e}^{-\mathrm{i}\,\omega t}$; hence Maxwell's equations for the electromagnetic-field operators in the Heisenberg picture are valid by construction.

3. Field quantization in terms of electric and magnetic response functions

The properties of media with spatially nonlocal or local responses can alternatively be described by their permittivity, permeability and magnetoelectric susceptibilities. To begin, it is convenient to cast the inhomogeneous Maxwell equations (10) into the forms (we drop the spatial and frequency arguments from now on)

$$\nabla\cdot\hat{\mathbf{D}}=0,\qquad \nabla\times\hat{\mathbf{H}}+\mathrm{i}\,\omega\hat{\mathbf{D}}=\mathbf{0} \tag{27}$$

with

$$\hat{\mathbf{D}}=\varepsilon_0\hat{\mathbf{E}}+\hat{\mathbf{P}},\qquad \hat{\mathbf{H}}=\frac{1}{\mu_0}\hat{\mathbf{B}}-\hat{\mathbf{M}}. \tag{28}$$

The polarization and magnetization fields respond linearly to the electric and magnetic fields,

$$\hat{\mathbf{P}}=\varepsilon_0(\boldsymbol{\varepsilon}-\boldsymbol{\xi}\star\boldsymbol{\mu}^{-1}\star\boldsymbol{\zeta}-\mathbf{I})\star\hat{\mathbf{E}}+Z_0^{-1}\boldsymbol{\xi}\star\boldsymbol{\mu}^{-1}\star\hat{\mathbf{B}}+\hat{\mathbf{P}}_{\mathrm{N}}, \tag{29}$$

$$\hat{\mathbf{M}}=Z_0^{-1}\boldsymbol{\mu}^{-1}\star\boldsymbol{\zeta}\star\hat{\mathbf{E}}+\mu_0^{-1}(\mathbf{I}-\boldsymbol{\mu}^{-1})\star\hat{\mathbf{B}}+\hat{\mathbf{M}}_{\mathrm{N}}. \tag{30}$$

The medium is characterized by its permittivity, $\boldsymbol{\varepsilon}(\mathbf{r},\mathbf{r}',\omega)$, its permeability, $\boldsymbol{\mu}(\mathbf{r},\mathbf{r}',\omega)$ and its magnetoelectric susceptibilities, $\boldsymbol{\xi}(\mathbf{r},\mathbf{r}',\omega)$ and $\boldsymbol{\zeta}(\mathbf{r},\mathbf{r}',\omega)$. $\hat{\mathbf{P}}_{\mathrm{N}}(\mathbf{r},\omega)$ and $\hat{\mathbf{M}}_{\mathrm{N}}(\mathbf{r},\omega)$ denote the noise polarization and noise magnetization, respectively, and $Z_0=\sqrt{\mu_0/\varepsilon_0}$ is the vacuum impedance. In the case of nonlocal media the permittivity, permeability and magnetoelectric susceptibilities are functions of two independent spatial variables, whereas in a locally responding media they read $\boldsymbol{\varepsilon}(\mathbf{r},\mathbf{r}',\omega)=\boldsymbol{\varepsilon}(\mathbf{r},\omega)\boldsymbol{\delta}(\mathbf{r}-\mathbf{r}')$, $\boldsymbol{\mu}(\mathbf{r},\mathbf{r}',\omega)=\boldsymbol{\mu}(\mathbf{r},\omega)\boldsymbol{\delta}(\mathbf{r}-\mathbf{r}')$, $\boldsymbol{\xi}(\mathbf{r},\mathbf{r}',\omega)=\boldsymbol{\xi}(\mathbf{r},\omega)\boldsymbol{\delta}(\mathbf{r}-\mathbf{r}')$ and $\boldsymbol{\zeta}(\mathbf{r},\mathbf{r}',\omega)=\boldsymbol{\zeta}(\mathbf{r},\omega)\boldsymbol{\delta}(\mathbf{r}-\mathbf{r}')$. By combining (28)–(30), the constitutive relations can be given in the more familiar form (see [31] for the nonconducting case)

$$\hat{\mathbf{D}}=\varepsilon_0\boldsymbol{\varepsilon}\star\hat{\mathbf{E}}+c^{-1}\boldsymbol{\xi}\star\hat{\mathbf{H}}+\hat{\mathbf{P}}_{\mathrm{N}}+c^{-1}\boldsymbol{\xi}\star\hat{\mathbf{M}}_{\mathrm{N}}, \tag{31}$$

$$\hat{\mathbf{B}}=c^{-1}\boldsymbol{\zeta}\star\hat{\mathbf{E}}+\mu_0\boldsymbol{\mu}\star\hat{\mathbf{H}}+\mu_0\boldsymbol{\mu}\star\hat{\mathbf{M}}_{\mathrm{N}}, \tag{32}$$

where the notational distinction between locally and nonlocally responding media as given above applies.

In order to distinguish reciprocal magnetoelectric susceptibilities from nonreciprocal ones, as previously discussed in the nondispersive case [32], one commonly writes $\boldsymbol{\xi}=\boldsymbol{\chi}^{\mathsf{T}}-\mathrm{i}\boldsymbol{\kappa}^{\mathsf{T}}$ and

$\boldsymbol{\zeta} = \boldsymbol{\chi} + \mathrm{i}\boldsymbol{\kappa}$. The chirality tensor $\boldsymbol{\kappa} = (\boldsymbol{\zeta} - \boldsymbol{\xi}^{\mathsf{T}})/(2\mathrm{i})$ represents the reciprocal magnetoelectric response; whereas the nonreciprocal magnetoelectric tensor $\boldsymbol{\chi} = (\boldsymbol{\zeta} + \boldsymbol{\xi}^{\mathsf{T}})/2$ vanishes for a reciprocal medium.

By combining Maxwell's equations with the constitutive relations (31) and (32), we note that the respective Green tensor is the solution to equation (12) with

$$\mathbf{Q} = (\mathrm{i}\,\mu_0\omega)^{-1}\nabla\times(\boldsymbol{\mu}^{-1} - \mathbf{I})\times\overleftarrow{\nabla} + Z_0^{-1}\nabla\times\boldsymbol{\mu}^{-1}\star\boldsymbol{\zeta} + Z_0^{-1}\boldsymbol{\xi}\star\boldsymbol{\mu}^{-1}\times\overleftarrow{\nabla} - \mathrm{i}\varepsilon_0\omega(\boldsymbol{\varepsilon} - \boldsymbol{\xi}\star\boldsymbol{\mu}^{-1}\star\boldsymbol{\zeta} - \mathbf{I}) \tag{33}$$

and

$$\hat{\mathbf{j}}_{\mathrm{N}} = -\mathrm{i}\,\omega\hat{\mathbf{P}}_{\mathrm{N}} + \nabla\times\hat{\mathbf{M}}_{\mathrm{N}}, \tag{34}$$

where $[\mathbf{T}\times\overleftarrow{\nabla}]_{ij}(\mathbf{r},\mathbf{r}') = \epsilon_{jkl}\partial'_l T_{ik}(\mathbf{r},\mathbf{r}')$ denotes a derivative acting on the second argument of a tensor function. The Green tensor for the electric field (13) solves

$$\left[\nabla\times\boldsymbol{\mu}^{-1}\star\nabla\times - \frac{\mathrm{i}\,\omega}{c}\nabla\times\boldsymbol{\mu}^{-1}\star\boldsymbol{\zeta} + \frac{\mathrm{i}\,\omega}{c}\boldsymbol{\xi}\star\boldsymbol{\mu}^{-1}\star\nabla - \frac{\omega^2}{c^2}(\boldsymbol{\varepsilon} - \boldsymbol{\xi}\star\boldsymbol{\mu}^{-1}\star\boldsymbol{\zeta})\right]\star\mathbf{G} = \boldsymbol{\delta}. \tag{35}$$

The commutation relations for $\hat{\mathbf{P}}_{\mathrm{N}}$ and $\hat{\mathbf{M}}_{\mathrm{N}}$ can be deduced by substituting the real parts of (33) and (34) into (5),

$$\left[\hat{\mathbf{P}}_{\mathrm{N}}(\mathbf{r},\omega), \hat{\mathbf{P}}^{\dagger}_{\mathrm{N}}(\mathbf{r}',\omega')\right] = \frac{\varepsilon_0\hbar}{\pi}\mathcal{I}\mathrm{m}\left\{\boldsymbol{\varepsilon}(\omega) - [\boldsymbol{\xi}(\omega)\star\boldsymbol{\mu}^{-1}(\omega)\star\boldsymbol{\zeta}(\omega)]\right\}(\mathbf{r},\mathbf{r}')\delta(\omega-\omega'), \tag{36}$$

$$\left[\hat{\mathbf{P}}_{\mathrm{N}}(\mathbf{r},\omega), \hat{\mathbf{M}}^{\dagger}_{\mathrm{N}}(\mathbf{r}',\omega')\right] = \frac{\hbar}{2\pi\mathrm{i}Z_0}\left\{[\boldsymbol{\xi}(\omega)\star\boldsymbol{\mu}^{-1}(\omega)] - [\boldsymbol{\zeta}^{\dagger}(\omega)\star\boldsymbol{\mu}^{-1\dagger}(\omega)]\right\}(\mathbf{r},\mathbf{r}')\delta(\omega-\omega'), \tag{37}$$

$$\left[\hat{\mathbf{M}}_{\mathrm{N}}(\mathbf{r},\omega), \hat{\mathbf{P}}^{\dagger}_{\mathrm{N}}(\mathbf{r}',\omega')\right] = \frac{\hbar}{2\pi\mathrm{i}Z_0}\left\{[\boldsymbol{\mu}^{-1}(\omega)\star\boldsymbol{\zeta}(\omega)] - [\boldsymbol{\mu}^{-1\dagger}(\omega)\star\boldsymbol{\xi}^{\dagger}(\omega)]\right\}(\mathbf{r},\mathbf{r}')\delta(\omega-\omega'), \tag{38}$$

$$\left[\hat{\mathbf{M}}_{\mathrm{N}}(\mathbf{r},\omega), \hat{\mathbf{M}}^{\dagger}_{\mathrm{N}}(\mathbf{r}',\omega')\right] = -\frac{\hbar}{\pi\mu_0}\mathcal{I}\mathrm{m}[\boldsymbol{\mu}^{-1}(\mathbf{r},\mathbf{r}',\omega)]\delta(\omega-\omega'). \tag{39}$$

We now introduce the bosonic creation and annihilation operators with commutation relations

$$\left[\hat{\mathbf{f}}_{\lambda}(\mathbf{r},\omega), \hat{\mathbf{f}}^{\dagger}_{\lambda'}(\mathbf{r}',\omega')\right] = \delta_{\lambda\lambda'}\boldsymbol{\delta}(\mathbf{r}-\mathbf{r}')\delta(\omega-\omega'), \quad (\lambda,\lambda' = e,m) \tag{40}$$

according to

$$\begin{pmatrix}\hat{\mathbf{P}}_{\mathrm{N}}\\ \hat{\mathbf{M}}_{\mathrm{N}}\end{pmatrix} = \sqrt{\frac{\hbar}{\pi}}\,\mathcal{R}\star\begin{pmatrix}\hat{\mathbf{f}}_e\\ \hat{\mathbf{f}}_m\end{pmatrix}, \tag{41}$$

where the (6×6)-matrix $\mathcal{R}$ is a root of

$$\mathcal{R}\star\mathcal{R}^{\dagger} = \begin{pmatrix}\varepsilon_0\mathcal{I}\mathrm{m}[\boldsymbol{\varepsilon} - \boldsymbol{\xi}\star\boldsymbol{\mu}^{-1}\star\boldsymbol{\zeta}] & \dfrac{\boldsymbol{\xi}\star\boldsymbol{\mu}^{-1} - \boldsymbol{\zeta}^{\dagger}\star\boldsymbol{\mu}^{-1\dagger}}{2\mathrm{i}Z_0}\\ \dfrac{\boldsymbol{\mu}^{-1}\star\boldsymbol{\zeta} - \boldsymbol{\mu}^{-1\dagger}\star\boldsymbol{\xi}^{\dagger}}{2\mathrm{i}Z_0} & -\dfrac{\mathcal{I}\mathrm{m}[\boldsymbol{\mu}^{-1}]}{\mu_0}\end{pmatrix}. \tag{42}$$

The Hamiltonian of the body–field system is again quadratic and diagonal in the bosonic variables,

$$\hat{H}_{\mathrm{F}} = \sum_{\lambda=e,m}\int \mathrm{d}^3 r\int_0^{\infty}\mathrm{d}\omega\,\hbar\omega\,\hat{\mathbf{f}}^{\dagger}_{\lambda}(\mathbf{r},\omega)\cdot\hat{\mathbf{f}}_{\lambda}(\mathbf{r},\omega). \tag{43}$$

Note that (28)–(30) imply a separation of the internal current density into electric and magnetic parts, $\hat{\mathbf{j}}_{\rm in} = -\mathrm{i}\,\omega\hat{\mathbf{P}} + \nabla\times\hat{\mathbf{M}}$. This separation and the resulting explicit field quantization is not unique in spatially dispersive (i.e. nonlocal) media, as the magnetization field can be absorbed into the transverse part of the polarization field [28]. While a local magnetoelectric medium can always be described in terms of a (nonlocal) conductivity without reference to magnetic properties, the equivalent description in terms of a local permittivity, permeability and cross-susceptibility is much more accessible. These parameters are often known experimentally and they allow for a classification of electromagnetic responses.

4. Duality invariance

An electromagnetic system separated into distinct electric and magnetic causes and effects can be subject to a duality transformation operation, that is, a global exchange of the electric and magnetic properties. A system invariant under such an operation is said to possess duality invariance as a symmetry [21]. This symmetry can be exploited in order to simplify the computation of dispersion forces involving, say magnetizable media, from known dispersion forces between polariable media [23].

By introducing dual-pair notation $(\hat{\mathbf{E}}^{\mathsf{T}}, Z_0\hat{\mathbf{H}}^{\mathsf{T}})^{\mathsf{T}}$, $(Z_0\hat{\mathbf{D}}^{\mathsf{T}}, \hat{\mathbf{B}}^{\mathsf{T}})^{\mathsf{T}}$, we may write the Maxwell equations (9) and (27) in the compact form

$$\nabla\cdot\begin{pmatrix} Z_0\hat{\mathbf{D}} \\ \hat{\mathbf{B}}\end{pmatrix} = \begin{pmatrix} 0 \\ 0\end{pmatrix}, \tag{44}$$

$$\nabla\times\begin{pmatrix} \hat{\mathbf{E}} \\ Z_0\hat{\mathbf{H}}\end{pmatrix} - \mathrm{i}\,\omega\begin{pmatrix} 0 & 1 \\ -1 & 0\end{pmatrix}\begin{pmatrix} Z_0\hat{\mathbf{D}} \\ \hat{\mathbf{B}}\end{pmatrix} = \begin{pmatrix} \mathbf{0} \\ \mathbf{0}\end{pmatrix}. \tag{45}$$

The constitutive relations (31) and (32) in condensed form read

$$\begin{pmatrix} Z_0\hat{\mathbf{D}} \\ \hat{\mathbf{B}}\end{pmatrix} = \frac{1}{c}\begin{pmatrix} \boldsymbol{\varepsilon} & \boldsymbol{\xi} \\ \boldsymbol{\zeta} & \boldsymbol{\mu}\end{pmatrix}\star\begin{pmatrix} \hat{\mathbf{E}} \\ Z_0\hat{\mathbf{H}}\end{pmatrix} + \mathcal{A}\star\begin{pmatrix} Z_0\hat{\mathbf{P}}_{\rm N} \\ \mu_0\hat{\mathbf{M}}_{\rm N}\end{pmatrix} \tag{46}$$

with

$$\mathcal{A} = \begin{pmatrix} \mathbf{I} & \boldsymbol{\xi} \\ 0 & \boldsymbol{\mu}\end{pmatrix}. \tag{47}$$

Maxwell's equations are invariant under duality transformations

$$\begin{pmatrix} \mathbf{x} \\ \mathbf{y}\end{pmatrix}^{\circledast} = D(\theta)\begin{pmatrix} \mathbf{x} \\ \mathbf{y}\end{pmatrix}, \quad D(\theta) = \begin{pmatrix} \cos\theta & \sin\theta \\ -\sin\theta & \cos\theta\end{pmatrix}, \tag{48}$$

because $D(\theta)$ is a symplectic matrix. From the constitutive relations, as shown in (46), we find the transformed medium response functions

$$\begin{pmatrix} \boldsymbol{\varepsilon} \\ \boldsymbol{\zeta} \\ \boldsymbol{\xi} \\ \boldsymbol{\mu}\end{pmatrix}^{\circledast} = \mathcal{D}(\theta)\begin{pmatrix} \boldsymbol{\varepsilon} \\ \boldsymbol{\zeta} \\ \boldsymbol{\xi} \\ \boldsymbol{\mu}\end{pmatrix} \tag{49}$$

with

$$\mathcal{D}(\theta) = D(\theta)\otimes D(\theta) \tag{50}$$

as well as

$$\begin{pmatrix} Z_0\hat{\mathbf{P}}_\mathrm{N} \\ \mu_0\hat{\mathbf{M}}_\mathrm{N} \end{pmatrix}^{\circledast} = \mathcal{A}^{\circledast -1} \star D(\theta)\mathcal{A} \star \begin{pmatrix} Z_0\hat{\mathbf{P}}_\mathrm{N} \\ \mu_0\hat{\mathbf{M}}_\mathrm{N} \end{pmatrix}, \tag{51}$$

where

$$\mathcal{A}^{-1} = \begin{pmatrix} \boldsymbol{I} & -\boldsymbol{\xi}\cdot\boldsymbol{\mu}^{-1} \\ \mathbf{0} & \boldsymbol{\mu}^{-1} \end{pmatrix}. \tag{52}$$

It is worth discussing a few special cases of bianisotropic media, their characteristic features and behaviour under duality transformations:

Local media [$\boldsymbol{\varepsilon}(\mathbf{r},\mathbf{r}',\omega) = \boldsymbol{\varepsilon}(\mathbf{r},\omega)\delta(\mathbf{r}-\mathbf{r}')$, similarly for the other response functions]: Convolution operators reduce to ordinary matrix products, compatible with all other special cases below.

Isotropic media ($\boldsymbol{\varepsilon} = \varepsilon\mathbf{I}$, $\boldsymbol{\mu} = \mu\mathbf{I}$, $\boldsymbol{\xi} = \boldsymbol{\zeta} = \mathbf{0}$): Onsager reciprocity (15) holds; $\hat{\mathbf{P}}_\mathrm{N}$ and $\hat{\mathbf{M}}_\mathrm{N}^\dagger$ commute; generalized real and imaginary parts reduce to ordinary ones; discrete duality symmetry.

Bi-isotropic media ($\boldsymbol{\varepsilon} = \varepsilon\mathbf{I}$, $\boldsymbol{\mu} = \mu\mathbf{I}$, $\boldsymbol{\xi} = \xi\mathbf{I}$, $\boldsymbol{\zeta} = \zeta\mathbf{I}$): generalized real and imaginary parts in (36) and (39) reduce to ordinary ones; continuous duality symmetry.

Anisotropic media ($\boldsymbol{\xi} = \boldsymbol{\zeta} = \mathbf{0}$): $\hat{\mathbf{P}}_\mathrm{N}$ and $\hat{\mathbf{M}}_\mathrm{N}^\dagger$ commute; discrete duality symmetry.

Reciprocal media ($\boldsymbol{\varepsilon}^\mathsf{T} = \boldsymbol{\varepsilon}$, $\boldsymbol{\xi}^\mathsf{T} = -\boldsymbol{\zeta}$, $\boldsymbol{\mu}^\mathsf{T} = \boldsymbol{\mu}$): (15) holds; generalized real and imaginary parts reduce to ordinary ones; discrete duality symmetry.

Here, discrete duality symmetry means that the rotation angle is restricted to values $\theta = n\pi/2$ with $n \in \mathbb{Z}$. Note that duality is only realized as a continuous symmetry when Onsager-violation is allowed for. Notably, a reduction in reciprocity symmetry leads to an enhancement of duality symmetry.

In order to derive transformation laws for the Green tensor, we combine (9), (11), (28), (30) and (34) to write

$$\begin{pmatrix} \hat{\mathbf{E}} \\ Z_0\hat{\mathbf{H}} \end{pmatrix} = -c\mathcal{B} \star \mathcal{G} \star \begin{pmatrix} Z_0\hat{\mathbf{P}}_\mathrm{N} \\ \mu_0\hat{\mathbf{M}}_\mathrm{N} \end{pmatrix}, \tag{53}$$

$$\mathcal{B} = \begin{pmatrix} \boldsymbol{I} & \mathbf{0} \\ -\boldsymbol{\mu}^{-1}\star\boldsymbol{\zeta} & \boldsymbol{\mu}^{-1} \end{pmatrix}, \tag{54}$$

$$\mathcal{G} = \begin{pmatrix} \mathbf{G}_{ee} & \mathbf{G}_{em} \\ \mathbf{G}_{me} & \mathbf{G}_{mm} + \boldsymbol{\mu} \end{pmatrix}, \tag{55}$$

where we have introduced the shorthand notations $\mathbf{G}_{ee} = (\mathrm{i}\,\omega/c)\mathbf{G}(\mathrm{i}\,\omega/c)$, $\mathbf{G}_{em} = (\mathrm{i}\,\omega/c)\mathbf{G} \times \overleftarrow{\nabla}'$, $\mathbf{G}_{me} = \nabla \times \mathbf{G}(\mathrm{i}\,\omega/c)$ and $\mathbf{G}_{mm} = \nabla \times \mathbf{G} \times \overleftarrow{\nabla}'$. The transformed Green's tensors follow by applying duality transformations on both sides of this equation,

$$\mathcal{G}^{\circledast} = \mathcal{B}^{\circledast -1} \star D(\theta)\mathcal{B} \star \mathcal{G} \star \mathcal{A}^{-1} \star D^{-1}(\theta)\mathcal{A}^{\circledast}, \tag{56}$$

where

$$\mathcal{B}^{-1} = \begin{pmatrix} \boldsymbol{I} & \mathbf{0} \\ -\boldsymbol{\mu}^{-1}\star\boldsymbol{\zeta} & \boldsymbol{\mu}^{-1} \end{pmatrix}. \tag{57}$$

In the special case of $\mathbf{r}$ and $\mathbf{r}'$ being in free space, we have $\mathcal{A}, \mathcal{B} = \mathcal{I}$, so that $\mathcal{G}^{\circledast} = D(\theta)\mathcal{G}\star D^{-1}(\theta)$ and hence

$$\begin{pmatrix} \mathbf{G}_{ee} \\ \mathbf{G}_{em} \\ \mathbf{G}_{em} \\ \mathbf{G}_{mm} + \boldsymbol{\delta} \end{pmatrix}^{\circledast} = \mathcal{D}(\theta) \begin{pmatrix} \mathbf{G}_{ee} \\ \mathbf{G}_{em} \\ \mathbf{G}_{em} \\ \mathbf{G}_{mm} + \boldsymbol{\delta} \end{pmatrix}. \tag{58}$$

The Green tensors then transform like the medium response functions with (50).

5. Conclusion

Based on the general Ohm's law, we have quantized the electromagnetic field in the presence of nonlocal, nonreciprocal media which satisfies (i) the canonical commutation relations from free-space QED; (ii) the linear fluctuation–dissipation theorem; and (iii) the macroscopic Maxwell equations. A key feature of the scheme is the symmetrization of tensor fields via generalized real and imaginary parts, which is necessary whenever Onsager reciprocity does not hold. Their presence in the fluctuation–dissipation theorem is the key to avoiding restrictions on the allowed medium response.

For nonlocal and local bianisotropic media we have shown that quantization can alternatively be performed by the introduction of permittivity, permeability and magnetoelectric susceptibilities. When the latter do not vanish, the noise polarization and magnetization do not commute. We have explicitly determined the behaviour of the fields and response functions under duality transformations. The full continuous transformation group applies for bianisotropic and bi-isotropic media, but reduces to a discrete symmetry for isotropic, anisotropic and/or reciprocal media.

The scheme lays the foundation for exact studies of quantum phenomena such as dispersion forces, Förster energy transfer or environment-assisted molecular transition rates in the presence of motion or novel media with chiral or nonreciprocal properties. Moving media are a prime example for the occurrence of nonreciprocal material properties [28] which have to be thoroughly accounted for in order to understand, e.g. quantum friction. CP violation in atoms or molecules is manifest in their nonreciprocal cross-polarizability. The Curie principle, stating that certain interactions between two partners (atoms, molecules, bodies, etc) require them to possess similar properties, then allows for a detection of CP violation via atom–surface interactions provided the surface exhibits a corresponding nonreciprocity.

Acknowledgment

This work was supported by the UK Engineering and Physical Sciences Research Council (EPSRC).

Appendix. Integral relation for the Green tensor

To derive the integral relation (16) for the Green tensor, we write the Helmholtz equation (12) as

$$\hat{\mathbf{H}} \cdot \hat{\mathbf{G}} = \hat{\mathbf{I}}, \tag{A.1}$$

where $\langle \mathbf{r}|\hat{\mathbf{G}}|\mathbf{r}'\rangle = \mathbf{G}(\mathbf{r}, \mathbf{r}', \omega)$ and $\langle \mathbf{r}|\hat{\mathbf{H}}|\mathbf{r}'\rangle = [\nabla \times \nabla \times -\omega^2/c^2]\boldsymbol{\delta}(\mathbf{r} - \mathbf{r}') - \mathrm{i}\,\mu_0\omega\mathbf{Q}(\mathbf{r}, \mathbf{r}', \omega)$. The Green operator is the right-inverse and, within any group of invertible operators, also the left-inverse of the Helmholtz operator,

$$\hat{\mathbf{G}} \cdot \hat{\mathbf{H}} = \hat{\mathbf{I}}. \tag{A.2}$$

From this relation and its Hermitian conjugate we find that

$$\hat{\mathbf{G}} \cdot (\hat{\mathbf{H}} - \hat{\mathbf{H}}^\dagger) \cdot \hat{\mathbf{G}}^\dagger = \hat{\mathbf{G}}^\dagger - \hat{\mathbf{G}}. \tag{A.3}$$

In coordinate space this relation reads

$$\mu_0\omega \int \mathrm{d}^3 s \int \mathrm{d}^3 s'\, \mathbf{G}(\mathbf{r}, \mathbf{s}, \omega) \cdot \mathcal{R}\mathrm{e}\mathbf{Q}(\mathbf{s}, \mathbf{s}', \omega) \cdot \mathbf{G}^\dagger(\mathbf{r}', \mathbf{s}', \omega) = \mathcal{I}\mathrm{m}\,\mathbf{G}(\mathbf{r}, \mathbf{r}', \omega) \tag{A.4}$$

which in convolution notation takes the form of equation (16).

References

[1] Lindell L V, Sihvola A H, Tretyakov S A and Viitanen A J 1994 *Electromagnetic Waves in Chiral and Bi-Isotropic Media* (Norwood, MA: Artech House)
Hehl F H and Obukhov Y N 2003 *Foundations of Classical Electrodynamics* (Boston, MA: Birkhäuser)
Hehl F H and Obukhov Y N 2005 *Phys. Lett.* A **334** 249

[2] Ishimaru A, Lee S W, Kuga Y and Jandhyala V 2003 *IEEE Trans. Antennas Propag.* **51** 2550
Yannopapas V 2006 *J. Phys.: Condens. Matter* **18** 6883
Thiel M, Rill M S, von Freymann G and Wegener M 2009 *Adv. Mater.* **21** 4680

[3] Grushin A G and Cortijo A 2011 *Phys. Rev. Lett.* **106** 020403

[4] McKenzie J F 1967 *Proc. Phys. Soc.* **91** 532

[5] Horsley S A R 2012 *Phys. Rev.* A **86** 023830

[6] Onsager L 1931 *Phys. Rev.* **37** 405

[7] Tellegen B D H 1948 *Philips Res. Rep.* **3** 81

[8] Lindell I V and Sihvola A H 2005 *J. Electromagn. Waves Appl.* **19** 861

[9] Gansel J K, Thiel M, Rill M S, Decker M, Bade K, Saile V, von Freymann G, Linden S and Wegener M 2009 *Science* **325** 1513

[10] Hentschel M, Schäferling M, Weiss T, Liu N and Giessen H 2012 *Nano Lett.* **12** 2542

[11] Zhao R, Zhou J, Koschny T, Economou E N and Soukoulis C M 2009 *Phys. Rev. Lett.* **103** 103602

[12] Henkel C and Joulain K 2005 *Europhys. Lett.* **72** 929
Tomaš M S 2005 *Phys. Lett.* A **342** 381

[13] Rosa F S S, Dalvit D A R and Milonni P W 2008 *Phys. Rev. Lett.* **100** 183602

[14] Kane C L and Mele E J 2005 *Phys. Rev. Lett.* **95** 226801

[15] Hsieh D, Qian D, Wray L, Xia Y, Hor Y S, Cava R J and Hasan M Z 2008 *Nature* **452** 970

[16] Hasan M Z and Kane C L 2010 *Rev. Mod. Phys.* **82** 3045

[17] Marachevsky V N and Pis'mak Y M 2010 *Phys. Rev.* D **81** 065005

[18] Abanin D A, Skachko I, Du X, Andrei E Y and Levitov L S 2010 *Phys. Rev.* B **81** 115410

[19] Wang J K and Goldman V J 1992 *Phys. Rev.* B **45** 13479

[20] Tang E, Mei J and Wen X 2011 *Phys. Rev. Lett.* **106** 236802

[21] Silberstein L 1907 *Ann. Phys.* **327** 579
Rainich G Y 1925 *Trans. Am. Math. Soc.* **27** 106
Misner C W and Wheeler J A 1957 *Ann. Phys.* **2** 525

[22] Scheel S and Buhmann S Y 2008 *Acta Phys. Slovaca* **58** 675

[23] Buhmann S Y and Scheel S 2009 *Phys. Rev. Lett.* **102** 140404

[24] Horsley S A R 2011 *Phys. Rev.* A **84** 063822

[25] Philbin T G 2010 *New J. Phys.* **12** 123008
[26] Suttorp L G and Wubs M 2004 *Phys. Rev.* A **70** 013816
[27] Tip A, Knöll L, Scheel S and Welsch D-G 2001 *Phys. Rev.* A **63** 043806
[28] Melrose D B 2008 *Quantum Plasmadynamics* (New York: Springer)
[29] Raabe C, Scheel S and Welsch D-G 2007 *Phys. Rev.* A **75** 053813
[30] Stratonovich R L 1992 *Nonlinear Nonequilibrium Thermodynamics I: Linear and Nonlinear Fluctuation–Dissipation Theorems* (Berlin: Springer)
[31] Kong J A 1972 *Proc. IEEE* **60** 1036
[32] Shen J Q 2008 *J. Opt. Soc. Am.* B **25** 1864

PRL 102, 140404 (2009) PHYSICAL REVIEW LETTERS week ending 10 APRIL 2009

Macroscopic Quantum Electrodynamics and Duality

Stefan Yoshi Buhmann and Stefan Scheel

Quantum Optics and Laser Science, Blackett Laboratory, Imperial College London, Prince Consort Road, London SW7 2AZ, United Kingdom

(Received 13 June 2008; published 10 April 2009)

We discuss under what conditions the duality between electric and magnetic fields is a valid symmetry of macroscopic quantum electrodynamics. It is shown that Maxwell's equations in the absence of free charges satisfy duality invariance on an operator level, whereas this is not true for Lorentz forces and atom-field couplings in general. We prove that derived quantities such as Casimir forces, local-field corrected decay rates, as well as van der Waals potentials are invariant with respect to a global exchange of electric and magnetic quantities. This exact symmetry can be used to deduce the physics of new configurations on the basis of already established ones.

DOI: 10.1103/PhysRevLett.102.140404 PACS numbers: 12.20.−m, 34.35.+a, 42.50.Ct, 42.50.Nn

In the past, studies of phenomena of quantum electrodynamics (QED) have often been restricted to purely electric systems, because effects associated with magnetic properties are considerably smaller for materials occurring in nature. Two developments have recently triggered an increased interest in such magnetic effects: The first was the suggestion [1] and subsequent fabrication [2] of artificial metamaterials with controllable electric permittivity ε and magnetic permeability μ, where left-handed materials (LHMs) with negative real parts of ε and μ are of particular interest. As had been pointed out already in 1968 [3], the basis vectors of an electromagnetic wave propagating inside such a medium form a left-handed triad, implying negative refraction. Motivated by the progress in metamaterial fabrication, researchers have intensively studied their potentials, leading to proposals of a perfect lens with subwavelength resolution [4] as well as cloaking devices [5] and predictions of an unusual behavior of the decay of one or two atoms in the presence of LHMs [6,7].

Another, closely related motivation for considering magnetic systems was due to the fact that dispersion forces [8] have gained an increasing influence on micromechanical devices where they often lead to undesired effects such as stiction [9]. The question naturally arose whether LHMs could be exploited to modify or even change the sign of dispersion forces. Forces on excited systems might indeed be influenced by LHMs [10]. Ground-state forces are not as easily manipulated because they depend on the medium response at all frequencies, whereas the Kramers-Kronig relations imply that LHMs can only be realized in limited frequency windows. However, the controllable magnetic properties available in metamaterials can still have a large impact on dispersion forces: The dispersion forces between electric and magnetic atoms [11] or bodies [12] differ both in sign and power laws from those between only electric ones. Searching for repulsive dispersion forces, interactions of electric or magnetic atoms [13], plates [14,15] and atoms with plates [16,17] have been studied; more complex problems such as atom-atom interactions in the presence of a magnetoelectric bulk medium [18], plate [19] or sphere [20] have also been addressed. Reductions or even sign changes of the forces have been predicted for such scenarios and have been attributed primarily to large permeabilities rather than left-handed properties.

Metamaterials have thus considerably increased the parameter space at one's disposal for manipulating phenomena of QED. An efficient use of this new freedom requires the formulation of general statements of what might be achieved and what is impossible in principle. Working in this direction, upper bounds for the strength of attractive and repulsive Casimir forces have been formulated [15] and it has been proven that the force between two mirror-symmetric purely electric bodies is always attractive [21]. In the present Letter, we establish another such general principle on the basis of the duality of Maxwell's equations under an exchange of electric and magnetic fields [22,23], also known as electric or magnetic reciprocity within a generalized framework of classical electrodynamics [24]. In particle physics, duality has been discussed as a symmetry of the $\mathcal{N} = 4$ supersymmetric Yang-Mills theory [25]. We will prove its validity in the context of macroscopic QED [6,8] and show that under certain conditions, quantities such as decay rates and dispersion forces are invariant with respect to a global exchange of electric and magnetic properties. The parameter space to be considered in the search for optimal geometries and materials will thus be effectively halved.

We begin by verifying duality for macroscopic QED in the absence of free charges and currents. We group the fields into dual pairs $(\sqrt{\varepsilon_0}\hat{\boldsymbol{E}}, \sqrt{\mu_0}\hat{\boldsymbol{H}})$, $(\sqrt{\mu_0}\hat{\boldsymbol{D}}, \sqrt{\varepsilon_0}\hat{\boldsymbol{B}})$ and $(\sqrt{\mu_0}\hat{\boldsymbol{P}}, \sqrt{\varepsilon_0}\mu_0\hat{\boldsymbol{M}})$, so that Maxwell's equations read

$$\boldsymbol{\nabla} \cdot \begin{pmatrix} \sqrt{\mu_0}\hat{\boldsymbol{D}} \\ \sqrt{\varepsilon_0}\hat{\boldsymbol{B}} \end{pmatrix} = \begin{pmatrix} 0 \\ 0 \end{pmatrix}, \tag{1}$$

$$\boldsymbol{\nabla} \times \begin{pmatrix} \sqrt{\varepsilon_0}\hat{\boldsymbol{E}} \\ \sqrt{\mu_0}\hat{\boldsymbol{H}} \end{pmatrix} + \frac{\partial}{\partial t} \begin{pmatrix} 0 & 1 \\ -1 & 0 \end{pmatrix} \begin{pmatrix} \sqrt{\mu_0}\hat{\boldsymbol{D}} \\ \sqrt{\varepsilon_0}\hat{\boldsymbol{B}} \end{pmatrix} = \begin{pmatrix} \boldsymbol{0} \\ \boldsymbol{0} \end{pmatrix} \tag{2}$$

with

$$\begin{pmatrix} \sqrt{\mu_0}\hat{\boldsymbol{D}} \\ \sqrt{\varepsilon_0}\hat{\boldsymbol{B}} \end{pmatrix} = \frac{1}{c}\begin{pmatrix} \sqrt{\varepsilon_0}\hat{\boldsymbol{E}} \\ \sqrt{\mu_0}\hat{\boldsymbol{H}} \end{pmatrix} + \begin{pmatrix} \sqrt{\mu_0}\hat{\boldsymbol{P}} \\ \sqrt{\varepsilon_0}\mu_0\hat{\boldsymbol{M}} \end{pmatrix}. \quad (3)$$

Maxwell's equations are invariant under the general SO(2) duality transformation

$$\begin{pmatrix} \boldsymbol{x} \\ \boldsymbol{y} \end{pmatrix}^{\star} = \mathcal{D}(\theta)\begin{pmatrix} \boldsymbol{x} \\ \boldsymbol{y} \end{pmatrix}, \quad \mathcal{D}(\theta) = \begin{pmatrix} \cos\theta & \sin\theta \\ -\sin\theta & \cos\theta \end{pmatrix}, \quad (4)$$

which may equivalently be expressed as a U(1) transformation when introducing complex Riemann-Silberstein fields [22]. The invariance of Maxwell's equations under this rotation can be verified by multiplying Eqs. (1)–(3) by $\mathcal{D}(\theta)$ and using the fact that $\mathcal{D}(\theta)$ commutes with the symplectic matrix in Eq. (2). Note that the grouping into dual pairs is solely due to the mathematical structure of the equations and is in contrast to the fact that $\hat{\boldsymbol{E}}$, $\hat{\boldsymbol{B}}$ and $\hat{\boldsymbol{D}}$, $\hat{\boldsymbol{H}}$ are the pairs of physically corresponding quantities.

For it to be a valid symmetry of the electromagnetic field, duality must also be consistent with the constitutive relations. In the presence of linear, local, isotropic, dispersing and absorbing media, the constitutive relations in frequency space can be given as

$$\begin{pmatrix} \sqrt{\mu_0}\hat{\boldsymbol{D}} \\ \sqrt{\varepsilon_0}\hat{\boldsymbol{B}} \end{pmatrix} = \frac{1}{c}\begin{pmatrix} \varepsilon & 0 \\ 0 & \mu \end{pmatrix}\begin{pmatrix} \sqrt{\varepsilon_0}\hat{\boldsymbol{E}} \\ \sqrt{\mu_0}\hat{\boldsymbol{H}} \end{pmatrix} + \begin{pmatrix} 1 & 0 \\ 0 & \mu \end{pmatrix}\begin{pmatrix} \sqrt{\mu_0}\hat{\boldsymbol{P}}_N \\ \sqrt{\varepsilon_0}\mu_0\hat{\boldsymbol{M}}_N \end{pmatrix}, \quad (5)$$

where $\varepsilon = \varepsilon(\boldsymbol{r}, \omega)$ and $\mu = \mu(\boldsymbol{r}, \omega)$ denote the relative electric permittivity and magnetic permeability of the media and $\hat{\boldsymbol{P}}_N$ and $\hat{\boldsymbol{M}}_N$ are the noise polarization and magnetization which necessarily arise in the presence of absorption. Invariance of the constitutive relations (5) under the duality transformation requires that

$$\begin{aligned} \begin{pmatrix} \varepsilon^{\star} & 0 \\ 0 & \mu^{\star} \end{pmatrix} &= \mathcal{D}(\theta)\begin{pmatrix} \varepsilon & 0 \\ 0 & \mu \end{pmatrix}\mathcal{D}^{-1}(\theta) \\ &= \begin{pmatrix} \varepsilon\cos^2\theta + \mu\sin^2\theta & (\mu - \varepsilon)\sin\theta\cos\theta \\ (\mu - \varepsilon)\sin\theta\cos\theta & \varepsilon\sin^2\theta + \mu\cos^2\theta \end{pmatrix}. \end{aligned} \quad (6)$$

This condition is trivially fulfilled if $\varepsilon = \mu$ (including both free space and the perfect lens, $\varepsilon = \mu = -1$ [4]), where duality is a continuous symmetry. For media with a nontrivial impedance, the condition (6) only holds for $\theta = n\pi/2$ with $n \in \mathbb{Z}$. The presence of such media thus reduces the continuous symmetry to a discrete symmetry with four distinct members, whose group structure is that of $\mathbb{Z}_4$. For $\theta = n\pi/2$, Eqs. (5) and (6) imply the transformations

$$\begin{pmatrix} \varepsilon \\ \mu \end{pmatrix}^{\star} = \begin{pmatrix} \cos^2\theta & \sin^2\theta \\ \sin^2\theta & \cos^2\theta \end{pmatrix}\begin{pmatrix} \varepsilon \\ \mu \end{pmatrix}, \quad (7)$$

$$\begin{pmatrix} \sqrt{\mu_0}\hat{\boldsymbol{P}}_N \\ \sqrt{\varepsilon_0}\mu_0\hat{\boldsymbol{M}}_N \end{pmatrix}^{\star} = \begin{pmatrix} \cos\theta & \mu\sin\theta \\ -\varepsilon^{-1}\sin\theta & \cos\theta \end{pmatrix}\begin{pmatrix} \sqrt{\mu_0}\hat{\boldsymbol{P}}_N \\ \sqrt{\varepsilon_0}\mu_0\hat{\boldsymbol{M}}_N \end{pmatrix}. \quad (8)$$

Maxwell's equations (1) and (2), together with the constitutive relations (5) for the electromagnetic field in the absence of free charges and currents, are thus invariant under the discrete duality transformations $\theta = n\pi/2$, $n \in \mathbb{Z}$ given by Eqs. (4), (7), and (8). This is not only true for the equations of motion, but clearly must also hold on a Hamiltonian level. To see this explicitly, recall that the Hamiltonian of the medium-assisted field is given by $\hat{H}_F = \sum_{\lambda=e,m}\int d^3r \int_0^{\infty} d\omega \hbar\omega \hat{\boldsymbol{f}}_{\lambda}^{\dagger}(\boldsymbol{r}, \omega)\cdot\hat{\boldsymbol{f}}_{\lambda}(\boldsymbol{r}, \omega)$ [6] where the fundamental bosonic fields $\hat{\boldsymbol{f}}_{\lambda}$ are related to the noise terms via

$$\begin{pmatrix} \sqrt{\mu_0}\hat{\underline{\boldsymbol{P}}}_N \\ \sqrt{\varepsilon_0}\mu_0\hat{\underline{\boldsymbol{M}}}_N \end{pmatrix} = \sqrt{\frac{\hbar}{\pi c^2}}\begin{pmatrix} i\sqrt{Im\varepsilon} & 0 \\ 0 & \sqrt{Im\mu}/|\mu| \end{pmatrix}\begin{pmatrix} \hat{\boldsymbol{f}}_e \\ \hat{\boldsymbol{f}}_m \end{pmatrix}. \quad (9)$$

Combining Eqs. (7)–(9), one finds that the fundamental fields transform as

$$\begin{pmatrix} \hat{\boldsymbol{f}}_e \\ \hat{\boldsymbol{f}}_m \end{pmatrix}^{\star} = \begin{pmatrix} \cos\theta & -i(\mu/|\mu|)\sin\theta \\ -i(|\varepsilon|/\varepsilon)\sin\theta & \cos\theta \end{pmatrix}\begin{pmatrix} \hat{\boldsymbol{f}}_e \\ \hat{\boldsymbol{f}}_m \end{pmatrix} \quad (10)$$

for $\theta = n\pi/2$, so that $\hat{H}_F^{\star} = \hat{H}_F$. It is sufficient to focus on the single duality transformation $\theta = \pi/2$ as summarized in Table I, which is a generator of the whole group.

Let us next turn our attention to Lorentz forces and the coupling of the medium-assisted field to charged particles: We recall that the operator Lorentz force on a neutral body occupying a volume V can be given as [8]

$$\begin{aligned} \hat{\boldsymbol{F}} = \int_{\partial V} d\boldsymbol{A}\cdot\Big\{&\varepsilon_0\hat{\boldsymbol{E}}(\boldsymbol{r})\hat{\boldsymbol{E}}(\boldsymbol{r}) + \frac{1}{\mu_0}\hat{\boldsymbol{B}}(\boldsymbol{r})\hat{\boldsymbol{B}}(\boldsymbol{r}) - \frac{1}{2}\Big[\varepsilon_0\hat{\boldsymbol{E}}^2(\boldsymbol{r}) \\ &+ \frac{1}{\mu_0}\hat{\boldsymbol{B}}^2(\boldsymbol{r})\Big]\mathbf{I}\Big\} - \varepsilon_0\frac{d}{dt}\int_V d^3r\hat{\boldsymbol{E}}(\boldsymbol{r})\times\hat{\boldsymbol{B}}(\boldsymbol{r}) \end{aligned} \quad (11)$$

($\mathbf{I}$: unit tensor), while that on a neutral atom with polarization $\hat{\boldsymbol{P}}_A$ and magnetization $\hat{\boldsymbol{M}}_A$ reads [8,26]

$$\begin{aligned} \hat{\boldsymbol{F}} = \boldsymbol{\nabla}_A\int d^3r[&\hat{\boldsymbol{P}}_A(\boldsymbol{r})\cdot\hat{\boldsymbol{E}}(\boldsymbol{r}) + \hat{\boldsymbol{M}}_A(\boldsymbol{r})\cdot\hat{\boldsymbol{B}}(\boldsymbol{r}) + \hat{\boldsymbol{P}}_A(\boldsymbol{r}) \\ &\times\dot{\hat{\boldsymbol{r}}}_A\cdot\hat{\boldsymbol{B}}(\boldsymbol{r})] + \frac{d}{dt}\int d^3r\hat{\boldsymbol{P}}_A(\boldsymbol{r})\times\hat{\boldsymbol{B}}(\boldsymbol{r}). \end{aligned} \quad (12)$$

The coupling of one or more atoms to the medium-assisted electromagnetic field can in the multipolar coupling scheme be implemented via [8,19]

TABLE I. Effect of the duality transformation with $\theta = \pi/2$.

Partners	Transformation	
$\hat{\boldsymbol{E}}$, $\hat{\boldsymbol{H}}$:	$\hat{\boldsymbol{E}}^{\star} = c\mu_0\hat{\boldsymbol{H}}$,	$\hat{\boldsymbol{H}}^{\star} = -\hat{\boldsymbol{E}}/(c\mu_0)$
$\hat{\boldsymbol{D}}$, $\hat{\boldsymbol{B}}$:	$\hat{\boldsymbol{D}}^{\star} = c\varepsilon_0\hat{\boldsymbol{B}}$,	$\hat{\boldsymbol{B}}^{\star} = -\hat{\boldsymbol{D}}/(c\varepsilon_0)$
$\hat{\boldsymbol{P}}$, $\hat{\boldsymbol{M}}$:	$\hat{\boldsymbol{P}}^{\star} = \hat{\boldsymbol{M}}/c$,	$\hat{\boldsymbol{M}}^{\star} = -c\hat{\boldsymbol{P}}$
$\hat{\boldsymbol{P}}_A$, $\hat{\boldsymbol{M}}_A$:	$\hat{\boldsymbol{P}}_A^{\star} = \hat{\boldsymbol{M}}_A/c$,	$\hat{\boldsymbol{M}}_A^{\star} = -c\hat{\boldsymbol{P}}_A$
$\hat{\boldsymbol{d}}$, $\hat{\boldsymbol{m}}$:	$\hat{\boldsymbol{d}}^{\star} = \hat{\boldsymbol{m}}/c$,	$\hat{\boldsymbol{m}}^{\star} = -c\hat{\boldsymbol{d}}$
$\hat{\boldsymbol{P}}_N$, $\hat{\boldsymbol{M}}_N$:	$\hat{\boldsymbol{P}}_N^{\star} = \mu\hat{\boldsymbol{M}}_N/c$,	$\hat{\boldsymbol{M}}_N^{\star} = -c\hat{\boldsymbol{P}}_N/\varepsilon$
$\hat{\boldsymbol{f}}_e$, $\hat{\boldsymbol{f}}_m$:	$\hat{\boldsymbol{f}}_e^{\star} = -i(\mu/\|\mu\|)\hat{\boldsymbol{f}}_m$,	$\hat{\boldsymbol{f}}_m^{\star} = -i(\|\varepsilon\|/\varepsilon)\hat{\boldsymbol{f}}_e$
ε, μ:	$\varepsilon^{\star} = \mu$,	$\mu^{\star} = \varepsilon$
α, β:	$\alpha^{\star} = \beta/c^2$,	$\beta^{\star} = c^2\alpha$

$$\hat{H}_{AF} = -\int d^3r[\hat{\boldsymbol{P}}_A(\boldsymbol{r})\cdot\hat{\boldsymbol{E}}(\boldsymbol{r}) + \hat{\boldsymbol{M}}_A(\boldsymbol{r})\cdot\hat{\boldsymbol{B}}(\boldsymbol{r}) + m_A^{-1}\hat{\boldsymbol{P}}_A(\boldsymbol{r})\times\hat{\boldsymbol{p}}_A\cdot\hat{\boldsymbol{B}}(\boldsymbol{r})], \quad (13)$$

when neglecting diamagnetic interactions. Using the transformation behavior given in Table I, it is immediately clear that neither the Lorentz forces on bodies or atoms nor the atom-field interactions are duality invariant on an operator level. Even for atoms and bodies at rest with time-independent fields, duality invariance is prohibited by the unavoidable noise polarization and magnetization in the constitutive relations (5).

That said, we will now show that effective quantities derived from the above operator Lorentz forces and atom-field couplings do obey duality invariance when considering atoms and bodies at rest not embedded in a medium. In particular, we will consider the Casimir force [27]

$$\boldsymbol{F} = -\frac{\hbar}{\pi}\int_0^\infty d\xi\int_{\partial V} d\boldsymbol{A}\cdot\Big\{\mathbf{G}^{(1)}_{ee}(\boldsymbol{r},\boldsymbol{r},i\xi) + \mathbf{G}^{(1)}_{mm}(\boldsymbol{r},\boldsymbol{r},i\xi) - \frac{1}{2}\mathrm{Tr}[\mathbf{G}^{(1)}_{ee}(\boldsymbol{r},\boldsymbol{r},i\xi) + \mathbf{G}^{(1)}_{mm}(\boldsymbol{r},\boldsymbol{r},i\xi)]\mathbf{I}\Big\}, \quad (14)$$

the single- and two-atom van der Waals (vdW) potentials [8,17,28]

$$U(\boldsymbol{r}_A) = \frac{\hbar}{2\pi\varepsilon_0}\int_0^\infty d\xi\Big[\alpha(i\xi)\mathrm{Tr}\mathbf{G}^{(1)}_{ee}(\boldsymbol{r}_A,\boldsymbol{r}_A,i\xi) + \frac{\beta(i\xi)}{c^2}\mathrm{Tr}\mathbf{G}^{(1)}_{mm}(\boldsymbol{r}_A,\boldsymbol{r}_A,i\xi)\Big] \quad (15)$$

and

$$U(\boldsymbol{r}_A,\boldsymbol{r}_B) = -\frac{\hbar}{2\pi\varepsilon_0^2}\int_0^\infty d\xi\,\mathrm{Tr}\Big\{\alpha_A(i\xi)\alpha_B(i\xi)\mathbf{G}_{ee}(\boldsymbol{r}_A,\boldsymbol{r}_B,i\xi)\cdot\mathbf{G}_{ee}(\boldsymbol{r}_B,\boldsymbol{r}_A,i\xi) + \alpha_A(i\xi)\frac{\beta_B(i\xi)}{c^2}\mathbf{G}_{em}(\boldsymbol{r}_A,\boldsymbol{r}_B,i\xi)\cdot\mathbf{G}_{me}(\boldsymbol{r}_B,\boldsymbol{r}_A,i\xi) + \frac{\beta_A(i\xi)}{c^2}\alpha_B(i\xi)\mathbf{G}_{me}(\boldsymbol{r}_A,\boldsymbol{r}_B,i\xi)\cdot\mathbf{G}_{em}(\boldsymbol{r}_B,\boldsymbol{r}_A,i\xi) + \frac{\beta_A(i\xi)}{c^2}\frac{\beta_B(i\xi)}{c^2}\mathbf{G}_{mm}(\boldsymbol{r}_A,\boldsymbol{r}_B,i\xi)\cdot\mathbf{G}_{mm}(\boldsymbol{r}_B,\boldsymbol{r}_A,i\xi)\Big\} \quad (16)$$

(α, β: atomic polarizability, magnetizability) and the atomic decay rate [6,29]

$$\Gamma_n(\boldsymbol{r}_A) = \frac{2}{\hbar\varepsilon_0}\sum_{k<n}\Big[\boldsymbol{d}_{kn}\cdot\mathrm{Im}\mathbf{G}_{ee}(\boldsymbol{r}_A,\boldsymbol{r}_A,\omega_{nk})\cdot\boldsymbol{d}_{nk} + \frac{\boldsymbol{m}_{kn}}{c}\cdot\mathrm{Im}\mathbf{G}_{mm}(\boldsymbol{r}_A,\boldsymbol{r}_A,\omega_{nk})\cdot\frac{\boldsymbol{m}_{nk}}{c}\Big] \quad (17)$$

($|n\rangle$: initial atomic state, ω_{nk}: atomic transition frequencies; $\boldsymbol{d}_{nk}$, $\boldsymbol{m}_{nk}$: electric, magnetic dipole matrix elements). Here, $\mathbf{G}^{(1)}$ is the scattering part of the classical Green tensor, where a left index e, m indicates that $\mathbf{G}$ is multiplied by $i\omega/c = -\xi/c$ or $\boldsymbol{\nabla}\times$ from the left and a right index e, m denotes multiplication with $i\omega/c = -\xi/c$ or $\times\overleftarrow{\boldsymbol{\nabla}}'$ from the right. The Casimir force and the single-atom vdW force are the ground-state averages of the above operator Lorentz forces, while the atomic potentials and rates follow from the atom-field coupling.

To prove the duality invariance of the above quantities (14)–(17), we note that the Casimir force depends solely on the classical Green tensor

$$\Big[\boldsymbol{\nabla}\times\frac{1}{\mu(\boldsymbol{r},\omega)}\boldsymbol{\nabla}\times - \frac{\omega^2}{c^2}\varepsilon(\boldsymbol{r},\omega)\Big]\mathbf{G}(\boldsymbol{r},\boldsymbol{r}',\omega) = \boldsymbol{\delta}(\boldsymbol{r}-\boldsymbol{r}'), \quad (18)$$

while vdW forces and decay rates also depend on α, β, $\hat{\boldsymbol{d}}$ and $\hat{\boldsymbol{m}}$. While the transformation behavior of the latter quantities under duality follows immediately from that of ε, μ, $\hat{\boldsymbol{P}}_A$ and $\hat{\boldsymbol{M}}_A$ (see Table I), the transformed Green tensor, which is the solution to Eq. (18) with ε and μ exchanged, can be determined as follows: We first note that Maxwell's equations (1) and (2) together with the constitutive relations (5) are uniquely solved by [6]

$$\hat{\underline{\boldsymbol{E}}}(\boldsymbol{r},\omega) = -\varepsilon_0^{-1}\int d^3r'\mathbf{G}_{ee}(\boldsymbol{r},\boldsymbol{r}',\omega)\cdot\hat{\underline{\boldsymbol{P}}}_N(\boldsymbol{r}',\omega) - c\mu_0\int d^3r'\mathbf{G}_{em}(\boldsymbol{r},\boldsymbol{r}',\omega)\cdot\hat{\underline{\boldsymbol{M}}}_N(\boldsymbol{r}',\omega), \quad (19)$$

$$\hat{\underline{\boldsymbol{B}}}(\boldsymbol{r},\omega) = -c\mu_0\int d^3r'\mathbf{G}_{me}(\boldsymbol{r},\boldsymbol{r}',\omega)\cdot\hat{\underline{\boldsymbol{P}}}_N(\boldsymbol{r}',\omega) - \mu_0\int d^3r'\mathbf{G}_{mm}(\boldsymbol{r},\boldsymbol{r}',\omega)\cdot\hat{\underline{\boldsymbol{M}}}_N(\boldsymbol{r}',\omega), \quad (20)$$

$$\hat{\underline{\boldsymbol{D}}}(\boldsymbol{r},\omega) = -\frac{\varepsilon(\boldsymbol{r},\omega)}{c}\int d^3r'\mathbf{G}_{em}(\boldsymbol{r},\boldsymbol{r}',\omega)\cdot\hat{\underline{\boldsymbol{M}}}_N(\boldsymbol{r}',\omega) - \int d^3r'[\varepsilon(\boldsymbol{r},\omega)\mathbf{G}_{ee}(\boldsymbol{r},\boldsymbol{r}',\omega) - \boldsymbol{\delta}(\boldsymbol{r}-\boldsymbol{r}')]\cdot\hat{\underline{\boldsymbol{P}}}_N(\boldsymbol{r}',\omega), \quad (21)$$

$$\hat{\underline{\boldsymbol{H}}}(\boldsymbol{r},\omega) = -\frac{c}{\mu(\boldsymbol{r},\omega)}\int d^3r'\mathbf{G}_{me}(\boldsymbol{r},\boldsymbol{r}',\omega)\cdot\hat{\underline{\boldsymbol{P}}}_N(\boldsymbol{r}',\omega) - \int d^3r'\Big[\frac{\mathbf{G}_{mm}(\boldsymbol{r},\boldsymbol{r}',\omega)}{\mu(\boldsymbol{r},\omega)} + \boldsymbol{\delta}(\boldsymbol{r}-\boldsymbol{r}')\Big]\cdot\hat{\underline{\boldsymbol{M}}}_N(\boldsymbol{r}',\omega). \quad (22)$$

The invariance of Maxwell's equations implies that this solution remains valid after applying the duality transformation. Taking duality transforms of Eqs. (19) and (20), the unknown transformed Green tensor appears on the right-hand side of these equations, whereas the transformations of all other quantities occurring in the equations can be determined with the aid of Table I. After using Eqs. (19)–(22) to express the resulting fields on the left-hand side in terms of $\hat{\underline{\boldsymbol{P}}}_N$ and $\hat{\underline{\boldsymbol{M}}}_N$ and equating coefficients, one obtains the following transformation rules:

$$\mathbf{G}^{\star}_{ee}(\boldsymbol{r},\boldsymbol{r}',\omega) = \mu^{-1}(\boldsymbol{r},\omega)\mathbf{G}_{mm}(\boldsymbol{r},\boldsymbol{r}',\omega)\mu^{-1}(\boldsymbol{r}',\omega) + \mu^{-1}(\boldsymbol{r},\omega)\boldsymbol{\delta}(\boldsymbol{r}-\boldsymbol{r}'), \quad (23)$$

$$\mathbf{G}^{\star}_{em}(\boldsymbol{r},\boldsymbol{r}',\omega) = -\mu^{-1}(\boldsymbol{r},\omega)\mathbf{G}_{me}(\boldsymbol{r},\boldsymbol{r}',\omega)\varepsilon(\boldsymbol{r}',\omega), \quad (24)$$

$$\mathbf{G}^{\star}_{me}(\boldsymbol{r},\boldsymbol{r}',\omega) = -\varepsilon(\boldsymbol{r},\omega)\mathbf{G}_{em}(\boldsymbol{r},\boldsymbol{r}',\omega)\mu^{-1}(\boldsymbol{r}',\omega), \quad (25)$$

$$\mathbf{G}^{\star}_{mm}(\boldsymbol{r},\boldsymbol{r}',\omega) = \varepsilon(\boldsymbol{r},\omega)\mathbf{G}_{ee}(\boldsymbol{r},\boldsymbol{r}',\omega)\varepsilon(\boldsymbol{r}',\omega) - \varepsilon(\boldsymbol{r},\omega)\boldsymbol{\delta}(\boldsymbol{r}-\boldsymbol{r}'). \quad (26)$$

The duality invariance of dispersion forces and decay rates follows immediately. Using Eqs. (23) and (26) and noting that the δ function does not contribute to the scattering part of the Green tensor, it is seen that the Casimir force (14) on a body is unchanged when globally exchanging ε and μ, provided that the body is located in free space. The duality invariance of the vdW potentials (15) and (16) also follows from the transformation rules (23)–(26). This invariance with respect to a simultaneous exchange $\varepsilon \leftrightarrow \mu$ and $\alpha \leftrightarrow \beta/c^2$ again only holds if $\varepsilon(\boldsymbol{r}_{A/B}) = \mu(\boldsymbol{r}_{A/B}) = 1$. In contrast to the Casimir force, this does not mean that the atom has to be located in vacuum, but merely implies that for atoms embedded in media, local-field corrections must be included via the real-cavity model in order to insure invariance [30].

Duality invariance can be used to obtain the full functional dependence of dispersion forces in given scenarios on the atomic and medium parameters from knowledge of the respective dual scenario. For instance, it has recently been shown that in the retarded limit the vdW potential of two polarizable atoms reads $U(r_{AB}) = -1863\hbar c\alpha_A\alpha_B\varepsilon^2/[64\pi^3\varepsilon_0^2\sqrt{\varepsilon\mu}(2\varepsilon+1)^4 r_{AB}^7]$ when including local-field corrections [30]. Making the replacements $\alpha \to \beta/c^2$, $\varepsilon \leftrightarrow \mu$, one can immediately infer $U(r_{AB}) = -1863\hbar c\mu_0^2\beta_A\beta_B\mu^2/[64\pi^3\sqrt{\varepsilon\mu}(2\mu+1)^4 r_{AB}^7]$ for magnetizable atoms. The utility of this principle becomes even more apparent for complex problems like the interaction of two atoms in the presence of a magnetoelectric object [19,20]. Finally, using the fact that two purely electric, mirror-symmetric bodies always attract [21], we can immediately conclude that so do two purely magnetic ones.

In addition, Eqs. (23) and (26) imply the duality invariance of the decay rate (17) since the δ functions do not contribute to the imaginary part of the Green tensor; again, local-field corrections have to be included for atoms embedded in media. This symmetry can be exploited, e.g., to obtain magnetically driven spin-flip rates of atoms in specific environments from known electric-dipole driven decay rates.

In conclusion, we have shown that dispersion forces on atoms and bodies as well as decay rates of atoms are duality invariant, provided that the bodies are located in free space at rest and that local-field corrections are taken into account when considering (stationary) atoms embedded in a medium. The established symmetry operation of globally exchanging electric and magnetic body and atom properties is a powerful tool for obtaining new results on the basis of already established ones. The invariance can easily be extended to other effective quantities of macroscopic QED such as frequency shifts, heating rates or energy transfer rates.

This work was supported by the Alexander von Humboldt Foundation and the UK Engineering and Physical Sciences Research Council. S. Y. B. is grateful to F. W. Hehl and T. Kästner for discussions.

[1] J. B. Pendry *et al.*, IEEE Trans. Microwave Theory Tech. **47**, 2075 (1999).
[2] D. R. Smith *et al.*, Phys. Rev. Lett. **84**, 4184 (2000).
[3] V. G. Veselago, Sov. Phys. Usp. **10**, 509 (1968).
[4] J. B. Pendry, Phys. Rev. Lett. **85**, 3966 (2000).
[5] U. Leonhardt, Science **312**, 1777 (2006).
[6] Ho Trung Dung *et al.*, Phys. Rev. A **68**, 043816 (2003).
[7] J. Kästel and M. Fleischhauer, Phys. Rev. A **71**, 011804(R) (2005).
[8] S. Y. Buhmann and D.-G. Welsch, Prog. Quantum Electron. **31**, 51 (2007).
[9] F. M. Serry, D. Walliser, and G. J. Maclay, J. Appl. Phys. **84**, 2501 (1998).
[10] A. Sambale *et al.*, Phys. Rev. A **78**, 053828 (2008).
[11] G. Feinberg and J. Sucher, J. Chem. Phys. **48**, 3333 (1968).
[12] T. H. Boyer, Phys. Rev. A **9**, 2078 (1974).
[13] C. Farina, F. C. Santos, and A. C. Tort, Am. J. Phys. **70**, 421 (2002).
[14] V. Hushwater, Am. J. Phys. **65**, 381 (1997).
[15] C. Henkel and K. Joulain, Europhys. Lett. **72**, 929 (2005).
[16] S. Y. Buhmann, Ho Trung Dung, and D.-G. Welsch, J. Opt. B **6**, S127 (2004).
[17] S. Y. Buhmann *et al.*, Eur. Phys. J. D **35**, 15 (2005).
[18] S. Spagnolo, D. A. R. Dalvit, and P. W. Milonni, Phys. Rev. A **75**, 052117 (2007).
[19] H. Safari *et al.*, Phys. Rev. A **74**, 042101 (2006).
[20] H. Safari *et al.*, Phys. Rev. A **77**, 053824 (2008).
[21] O. Kenneth and I. Klich, Phys. Rev. Lett. **97**, 160401 (2006).
[22] L. Silberstein, Ann. Phys. (Leipzig) **327**, 579 (1907).
[23] G. Y. Rainich, Trans. Am. Math. Soc. **27**, 106 (1925); C. W. Misner and J. A. Wheeler, Ann. Phys. (N.Y.) **2**, 525 (1957).
[24] F. H. Hehl and Y. N. Obukhov, *Foundations of Classical Electrodynamics* (Birkhäuser, Boston, 2003).
[25] C. Montonen and D. Olive, Phys. Lett. B **72**, 117 (1977).
[26] S. Y. Buhmann *et al.*, Phys. Rev. A **70**, 052117 (2004).
[27] C. Raabe and D.-G. Welsch, Phys. Rev. A **71**, 013814 (2005).
[28] H. Safari *et al.*, Phys. Rev. A **78**, 062901 (2008).
[29] A. Salam, Int. Rev. Phys. Chem. **27**, 405 (2008).
[30] A. Sambale *et al.*, Phys. Rev. A **75**, 042109 (2007).

PRL 104, 070404 (2010) PHYSICAL REVIEW LETTERS week ending 19 FEBRUARY 2010

Universal Scaling Laws for Dispersion Interactions

Stefan Yoshi Buhmann,[1] Stefan Scheel,[1] and James Babington[2]

[1]*Quantum Optics and Laser Science, Blackett Laboratory, Imperial College London, Prince Consort Road, London SW7 2AZ, United Kingdom*

[2]*Laboratoire de Physique et Modélisation des Milieux Condensés, Université Joseph Fourier and CNRS, Maison des Magistères, BP 166, 38042 Grenoble, France*

(Received 1 December 2009; published 19 February 2010)

We study the scaling behavior of dispersion potentials and forces under very general conditions. We prove that a rescaling of an arbitrary geometric arrangement by a factor a changes the atom–atom and atom–body potentials in the long-distance limit by factors $1/a^7$ and $1/a^4$, respectively, and the Casimir force per unit area by $1/a^4$. In the short-distance regime, electric and magnetic bodies lead to different scaling behavior. As applications, we present scaling functions for two atom–body potentials and display the equipotential lines of a plate-assisted two-atom potential.

DOI: 10.1103/PhysRevLett.104.070404 PACS numbers: 12.20.−m, 34.35.+a, 42.50.Ct, 42.50.Nn

Scaling laws play a prominent role in the formulation of many physical problems and occur naturally when studying critical phenomena in particle physics, condensed matter, and statistical mechanics. One example is percolation theory [1], which has found applications in understanding forest fires, oil-field extraction, and even measurement-based quantum computing [2].

Dispersion forces are effective quantum electromagnetic forces between neutral, but polarizable objects [3,4]. Casimir and Polder found that dispersion forces are governed by simple power laws in the long-distance limit [5]: The potential of a ground state atom at a distance z_A from a perfectly conducting plate and that of two ground state atoms separated by a distance r_{AB} are proportional to $1/z_A^4$ and $1/r_{AB}^7$, respectively, while the force per unit area between two perfectly conducting plates at separation z follows a $1/z^4$ law. Dispersion forces have since been studied for various bodies of simple shapes such as semi-infinite half spaces [6], plates of finite thickness [7,8], cylinders [9], and spheres [10,11]. In all of these cases, simple scaling laws have been found for the long- and short-distance limits.

For electrostatic or gravitational interactions, power laws for the forces between extended objects follow immediately by a volume integration of $1/r$ potentials. Dispersion forces, on the contrary, are due to an infinite hierarchy of microscopic N-point potentials [12], leading to a nontrivial geometry dependence. Many-body effects and the nontrivial dependence on geometry are at the heart of current endeavors to gain a thorough theoretical [13] and experimental understanding [14] of the Casimir effect and to exploit it in nanotechnology applications [15]. The lack of simple analytical solutions for dispersion forces in complex scenarios necessitates general qualitative laws for what is achievable. Along these lines, it has been proven that mirror-symmetric arrangements always lead to attractive Casimir forces [16], and duality invariance has been established as a tool to study magnetoelectric effects [17]. Scaling laws of the kind observed for simple objects would be a powerful addition to this toolbox of general laws, provided that they can be formulated beyond the special cases mentioned above.

With this in mind, we will demonstrate in this Letter that for objects of arbitrary shapes, dispersion interactions in the long- and short-distance limits obey scaling laws, and we will identify the respective scaling powers. Our proof relies on the known dependence of dispersion potentials on the atomic polarizability $\alpha(\omega)$, body permittivity $\varepsilon(\boldsymbol{r}, \omega)$, and permeability $\mu(\boldsymbol{r}, \omega)$, where the latter determines the electromagnetic Green tensor

$$\left[\boldsymbol{\nabla} \times \frac{1}{\mu(\boldsymbol{r}, \omega)} \boldsymbol{\nabla} \times - \frac{\omega^2}{c^2} \varepsilon(\boldsymbol{r}, \omega)\right] \mathbf{G}(\boldsymbol{r}, \boldsymbol{r}', \omega) = \boldsymbol{\delta}(\boldsymbol{r} - \boldsymbol{r}'). \tag{1}$$

In terms of these quantities, the Casimir–Polder (CP) potential of a single electric ground state atom and the van der Waals (vdW) potential of two such atoms read

$$U(\boldsymbol{r}_A) = \frac{\hbar \mu_0}{2\pi} \int_0^\infty d\xi \xi^2 \alpha_A(i\xi) \mathrm{Tr} \mathbf{G}^{(1)}(\boldsymbol{r}_A, \boldsymbol{r}_A, i\xi) \tag{2}$$

($\mathbf{G} = \mathbf{G}^{(0)} + \mathbf{G}^{(1)}$; bulk and scattering parts) and

$$U(\boldsymbol{r}_A, \boldsymbol{r}_B) = -\frac{\hbar \mu_0^2}{2\pi} \int_0^\infty d\xi \xi^4 \alpha_A(i\xi) \alpha_B(i\xi) \times \mathrm{Tr}[\mathbf{G}(\boldsymbol{r}_A, \boldsymbol{r}_B, i\xi) \cdot \mathbf{G}(\boldsymbol{r}_B, \boldsymbol{r}_A, i\xi)], \tag{3}$$

respectively, and the Casimir force on a body of volume V is given by $\boldsymbol{F} = \int_{\partial V} d\boldsymbol{A} \cdot \mathbf{T}(\boldsymbol{r})$ with

$$\mathbf{T}(\boldsymbol{r}) = -\frac{\hbar}{\pi} \int_0^\infty d\xi \left\{ \left[\frac{\xi^2}{c^2} \mathbf{G}^{(1)}(\boldsymbol{r}, \boldsymbol{r}, i\xi) + \boldsymbol{\nabla} \times \mathbf{G}^{(1)}(\boldsymbol{r}, \boldsymbol{r}, i\xi) \times \overleftarrow{\boldsymbol{\nabla}}' \right] - \frac{1}{2} \mathrm{Tr} \left[\frac{\xi^2}{c^2} \mathbf{G}^{(1)}(\boldsymbol{r}, \boldsymbol{r}, i\xi) + \boldsymbol{\nabla} \times \mathbf{G}^{(1)}(\boldsymbol{r}, \boldsymbol{r}, i\xi) \times \overleftarrow{\boldsymbol{\nabla}}' \right] \mathbf{I} \right\} \tag{4}$$

($\mathbf{I}$: unit tensor) [4]. We will first define the general scaling problem and then solve it separately in the long- and short-distance cases.

The scaling problem.—Consider an arbitrary arrangement of linearly responding bodies characterized by their permittivity $\varepsilon(\boldsymbol{r}, \omega)$ and permeability $\mu(\boldsymbol{r}, \omega)$, with one or two atoms at positions $\boldsymbol{r}_A$ and $\boldsymbol{r}_B$ [Fig. 1(i)]. The scaled arrangement (scaling factor $a \neq 0$) is described by the permittivity and permeability

$$\bar{\varepsilon}(\boldsymbol{r}, \omega) = \varepsilon(\boldsymbol{r}/a, \omega), \qquad \bar{\mu}(\boldsymbol{r}, \omega) = \mu(\boldsymbol{r}/a, \omega), \tag{5}$$

with the atomic positions being scaled accordingly: $\bar{\boldsymbol{r}}_A = a\boldsymbol{r}_A$, $\bar{\boldsymbol{r}}_B = a\boldsymbol{r}_B$ [Fig. 1(ii)].

Interactions for long distances.—We speak of the long-distance regime when all distances are much larger than the wavelengths of the atomic and medium response functions. In this case, we can approximate the latter by their static values, $\alpha(\omega) \simeq \alpha$, $\varepsilon(\boldsymbol{r}, \omega) \simeq \varepsilon(\boldsymbol{r})$, $\mu(\boldsymbol{r}, \omega) \simeq \mu(\boldsymbol{r})$, so the Green tensor is determined by

$$\left[\boldsymbol{\nabla} \times \frac{1}{\mu(\boldsymbol{r})}\boldsymbol{\nabla} \times - \frac{\omega^2}{c^2}\varepsilon(\boldsymbol{r})\right]\mathbf{G}(\boldsymbol{r}, \boldsymbol{r}', \omega) = \boldsymbol{\delta}(\boldsymbol{r} - \boldsymbol{r}'). \tag{6}$$

The Green tensor of the scaled arrangement obeys

$$\left[\boldsymbol{\nabla} \times \frac{1}{\bar{\mu}(\boldsymbol{r})}\boldsymbol{\nabla} \times - \frac{\omega^2}{c^2}\bar{\varepsilon}(\boldsymbol{r})\right]\bar{\mathbf{G}}(\boldsymbol{r}, \boldsymbol{r}', \omega) = \boldsymbol{\delta}(\boldsymbol{r} - \boldsymbol{r}'). \tag{7}$$

By renaming $\boldsymbol{r} \mapsto a\boldsymbol{r}$, $\omega \mapsto \omega/a$ and using Eq. (5) and $\delta(a\boldsymbol{r}) = \delta(\boldsymbol{r})/a^3$, we find that

$$\left[\boldsymbol{\nabla} \times \frac{1}{\mu(\boldsymbol{r})}\boldsymbol{\nabla} \times - \frac{\omega^2}{c^2}\varepsilon(\boldsymbol{r})\right]a\bar{\mathbf{G}}(a\boldsymbol{r}, a\boldsymbol{r}', \omega/a) = \boldsymbol{\delta}(\boldsymbol{r} - \boldsymbol{r}'). \tag{8}$$

Comparison with Eq. (6) reveals the scaling

$$\bar{\mathbf{G}}(a\boldsymbol{r}, a\boldsymbol{r}', \omega/a) = (1/a)\mathbf{G}(\boldsymbol{r}, \boldsymbol{r}', \omega). \tag{9}$$

Substitution into the CP potential (2) leads to

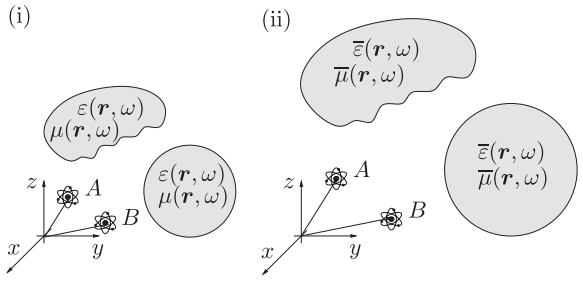

FIG. 1. (i) Original and (ii) scaled configurations of bodies and atoms ($a = 1.4$).

$$\begin{aligned}\bar{U}(a\boldsymbol{r}_A) &= \frac{\hbar\mu_0\alpha_A}{2\pi}\int_0^\infty d\xi\xi^2 \mathrm{Tr}\bar{\mathbf{G}}^{(1)}(a\boldsymbol{r}_A, a\boldsymbol{r}_A, i\xi) \\ &= \frac{\hbar\mu_0\alpha_A}{2\pi}\int_0^\infty \frac{d\xi}{a}\frac{\xi^2}{a^2}\,\mathrm{Tr}\bar{\mathbf{G}}^{(1)}(a\boldsymbol{r}_A, a\boldsymbol{r}_A, i\xi/a) \\ &= (1/a^4)U(\boldsymbol{r}_A).\end{aligned} \tag{10}$$

The CP force thus scales as $\bar{\boldsymbol{F}}(a\boldsymbol{r}_A) = (1/a^5)\boldsymbol{F}(\boldsymbol{r}_A)$. Analogously, Eq. (9) can be used to derive the following scaling laws for the vdW potential (3) and the Casimir force per unit area (4),

$$\bar{U}(a\boldsymbol{r}_A, a\boldsymbol{r}_B) = (1/a^7)U(\boldsymbol{r}_A, \boldsymbol{r}_B), \tag{11}$$

$$\bar{\mathbf{T}}(a\boldsymbol{r}) = (1/a^4)\mathbf{T}(\boldsymbol{r}), \tag{12}$$

so the total Casimir force behaves as $\bar{\boldsymbol{F}} = (1/a^2)\boldsymbol{F}$.

Interactions for short distances.—In the short-distance or nonretarded regime, all distances are much smaller than the characteristic atomic and medium wavelengths. A simple example shows that here no universal scaling law exists in the general case: The nonretarded CP potential of an atom at distance z_A from a magnetoelectric half space reads [8]

$$U(z_A) = -\frac{C_3}{z_A^3} + \frac{C_1}{z_A}, \tag{13}$$

which is incompatible with a relation of the form (10).

However, scaling laws can still be formulated by distinguishing between purely electric and purely magnetic environments. For purely electric bodies, the Green tensor (1) can be given by the Dyson equation [4]

$$\begin{aligned}\mathbf{G}(\boldsymbol{r}, \boldsymbol{r}', \omega) = \mathbf{G}^{(0)}(\boldsymbol{r}, \boldsymbol{r}', \omega) + \frac{\omega^2}{c^2} \\ \times \int d^3s\chi(\boldsymbol{s}, \omega)\mathbf{G}^{(0)}(\boldsymbol{r}, \boldsymbol{s}, \omega)\cdot\mathbf{G}(\boldsymbol{s}, \boldsymbol{r}', \omega)\end{aligned} \tag{14}$$

($\chi = \varepsilon - 1$) where

$$\begin{aligned}\mathbf{G}^{(0)}(\boldsymbol{r}, \boldsymbol{r}', \omega) = -\frac{c^2 e^{i\omega\rho/c}}{4\pi\omega^2\rho^3}\left\{\left[1 - i\frac{\omega\rho}{c} - \left(\frac{\omega\rho}{c}\right)^2\right]\mathbf{I}\right. \\ \left. - \left[3 - 3i\frac{\omega\rho}{c} - \left(\frac{\omega\rho}{c}\right)^2\right]\boldsymbol{e}_\rho\boldsymbol{e}_\rho\right\} \\ - \frac{c^2}{3\omega^2}\boldsymbol{\delta}(\boldsymbol{\rho})\end{aligned} \tag{15}$$

($\boldsymbol{\rho} = \boldsymbol{r} - \boldsymbol{r}'$) is the free-space Green tensor. In the short-distance limit $\omega\rho/c \ll 1$, the latter reduces to

$$\mathbf{G}^{(0)}(\boldsymbol{r}, \boldsymbol{r}', \omega) = -\frac{c^2[\mathbf{I} - 3\boldsymbol{e}_\rho\boldsymbol{e}_\rho]}{4\pi\omega^2\rho^3} - \frac{c^2}{3\omega^2}\boldsymbol{\delta}(\boldsymbol{\rho}). \tag{16}$$

Starting from the analogous Dyson equation for the scaled Green tensor, we make the substitutions $\boldsymbol{r} \mapsto a\boldsymbol{r}$, $\boldsymbol{r}' \mapsto a\boldsymbol{r}'$, and $\boldsymbol{s} \mapsto a\boldsymbol{s}$. After using Eq. (5) and the scaling

$\mathbf{G}^{(0)}(a\boldsymbol{r}, a\boldsymbol{r}', \omega) = (1/a^3)\mathbf{G}^{(0)}(\boldsymbol{r}, \boldsymbol{r}', \omega)$ of Eq. (16), a comparison with (14) reveals the scaling

$$\bar{\mathbf{G}}(a\boldsymbol{r}, a\boldsymbol{r}', \omega) = (1/a^3)\mathbf{G}(\boldsymbol{r}, \boldsymbol{r}', \omega) \tag{17}$$

for the full Green tensor. Substitution into Eqs. (2)–(4) immediately implies the scaling laws

$$\bar{U}(a\boldsymbol{r}_A) = (1/a^3)U(\boldsymbol{r}_A), \tag{18}$$

$$\bar{U}(a\boldsymbol{r}_A, a\boldsymbol{r}_B) = (1/a^6)U(\boldsymbol{r}_A, \boldsymbol{r}_B), \tag{19}$$

$$\bar{\mathbf{T}}(a\boldsymbol{r}) = (1/a^3)\mathbf{T}(\boldsymbol{r}) \tag{20}$$

where we have used the fact that $\mathbf{G}^{(1)}$ dominates over $\boldsymbol{\nabla} \times \mathbf{G}^{(1)} \times \overleftarrow{\boldsymbol{\nabla}}'$ in the short-distance limit.

For an arrangement of purely magnetic bodies, the nonretarded Green tensor obeys the Dyson equation

$$\mathbf{G}^{(1)}(\boldsymbol{r}, \boldsymbol{r}', \omega) = \int d^3s\,\zeta(\boldsymbol{s}, \omega)[\mathbf{G}^{(0)}(\boldsymbol{r}, \boldsymbol{s}, \omega) \times \overleftarrow{\boldsymbol{\nabla}}_s] \cdot [\boldsymbol{\nabla}_s \times \mathbf{G}^{(0)}(\boldsymbol{s}, \boldsymbol{r}', \omega) + \boldsymbol{\nabla}_s \times \mathbf{G}^{(1)}(\boldsymbol{s}, \boldsymbol{r}', \omega)] \tag{21}$$

($\zeta = 1/\mu - 1$) with nonretarded free-space Green tensors

$$\boldsymbol{\nabla} \times \mathbf{G}^{(0)}(\boldsymbol{r}, \boldsymbol{r}', \omega) = -\mathbf{G}^{(0)}(\boldsymbol{r}, \boldsymbol{r}', \omega) \times \overleftarrow{\boldsymbol{\nabla}}' = -\frac{\boldsymbol{e}_\rho \times \mathbf{I}}{4\pi\rho^2}. \tag{22}$$

We read off $(1/a^2)$ scalings for $\boldsymbol{\nabla} \times \mathbf{G}^{(0)}$ and $\mathbf{G}^{(0)} \times \overleftarrow{\boldsymbol{\nabla}}'$, so following similar steps as above, the Dyson Eq. (21) together with Eq. (5) implies

$$\bar{\mathbf{G}}^{(1)}(a\boldsymbol{r}, a\boldsymbol{r}', \omega) = (1/a)\mathbf{G}^{(1)}(\boldsymbol{r}, \boldsymbol{r}', \omega). \tag{23}$$

Using Eq. (2), the nonretarded CP potential scales as

$$\bar{U}(a\boldsymbol{r}_A) = (1/a)U(\boldsymbol{r}_A) \tag{24}$$

for purely magnetic bodies. The vdW potential (3) contains contributions from the bulk and scattering Green tensors with different scalings. We separate it into a free-space part $U^{(0)}$ that contains only $\mathbf{G}^{(0)}$ and scales according to Eq. (19) and a body-induced part $U^{(1)}$. The latter is dominated by the mixed terms $\mathbf{G}^{(0)}\mathbf{G}^{(1)}$ for purely magnetic bodies in the short-distance limit; it scales as

$$\bar{U}^{(1)}(a\boldsymbol{r}_A, a\boldsymbol{r}_B) = (1/a^4)U^{(1)}(\boldsymbol{r}_A, \boldsymbol{r}_B). \tag{25}$$

The Casimir force (4) is dominated by $\boldsymbol{\nabla} \times \mathbf{G}^{(1)} \times \overleftarrow{\boldsymbol{\nabla}}'$ with its $(1/a^3)$ scaling for purely magnetic bodies, so that

$$\bar{\mathbf{T}}(a\boldsymbol{r}) = (1/a^3)\mathbf{T}(\boldsymbol{r}). \tag{26}$$

Applications.—In the simplest situations where dispersion forces depend on a single distance parameter, the scaling laws directly determine the dependence on that parameter. For instance, the long-distance scaling laws (10)–(12) imply the power laws for dispersion interactions involving atoms and perfectly conducting plates mentioned above.

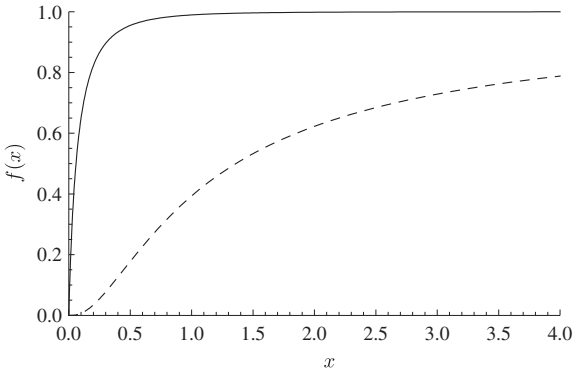

FIG. 2. Scale functions for the potential of an atom in front of a Si plate (solid line) and near a perfectly conducting sphere (dashed line).

For a class of geometries involving a distance parameter z and a single size parameter d, the scaling laws can be employed to write potentials and forces in the form $(C_k/z^k)f(d/z)$, all relevant information being contained in the scaling function $f(x)$. In Fig. 2, we display the scaling functions for the potential of an atom at distance z_A from a Si plate of thickness d ($x = d/z_A$) in the long-distance limit [8] and for the nonretarded potential of a perfectly conducting sphere of radius R ($x = R/z_A$) [11].

The plate potential reaches its half-space limit with associated $1/z_A^4$ asymptote already for $x = d/z_A \gtrsim 0.5$, showing that finite thickness effects can be neglected for moderately thick plates even for dielectrics. For very thin plates with $x = d/z_A \lesssim 0.1$, the scale function of the plate is linear for small x, implying a $x/z_A^4 \propto 1/z_A^5$ potential. A rather abrupt change between the two power laws occurs between the two extremes.

The scale function of the sphere saturates much more slowly to its large-x asymptote where a $1/z_A^3$ half-space

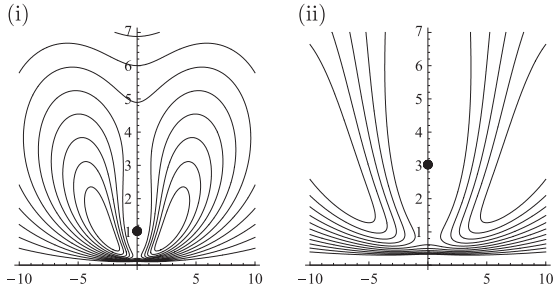

FIG. 3. Retarded vdW potential next to a perfectly conducting plate. Atom B is held at different fixed positions (large dot). The thick contour denotes $U/U^{(0)} = 1$, values are increasing towards the exterior of this contour in steps of 0.02.

TABLE I. Scaling laws for the CP potential, free-space, and body-induced vdW potentials and the Casimir pressure.

Distance	Long	Short	
Bodies	Magnetoelectric	Electric	Magnetic
$U(\boldsymbol{r}_A)$	$1/a^4$	$1/a^3$	$1/a$
$U^{(0)}(\boldsymbol{r}_A, \boldsymbol{r}_B)$	$1/a^7$	$1/a^6$	$1/a^6$
$U^{(1)}(\boldsymbol{r}_A, \boldsymbol{r}_B)$	$1/a^7$	$1/a^6$	$1/a^4$
$\mathbf{T}(\boldsymbol{r})$	$1/a^4$	$1/a^3$	$1/a^3$

potential is observed. This indicates that proximity force approximations [18] should be used with care. The scale function of the sphere potential is cubic for small x, corresponding to a $x^3/z_A^3 \propto 1/z_A^6$ asymptote.

As a more complex example, we consider the vdW potential of two atoms A and B in front of a perfectly conducting plate in the long-distance limit [19]. In Fig. 3(i), we show the plate-induced enhancement of the potential with respect to its free-space value for a given distance of atom B from the plate. The results for a different distance can then be obtained from a scaling transformation cf. Fig. 3(ii). The plate is seen to enhance the interatomic interaction in two lobe-shaped regions to the left and right of atom B. This implies that for a thin slab of an atomic gas at distance z from the plate, the atom–atom correlation function will be enhanced at interatomic distances $r \simeq 2.5z$ corresponding to the centers of the lobes. By virtue of scale invariance, this holds for all z that are compatible with the long-distance limit.

Summary and perspective.—By considering the scaling behavior for the respective Green tensors, we have derived universal scaling laws for dispersion interactions in the long- and short-distance limits as summarized in Table I. Scaling laws indicate the absence of a characteristic length scale of the system. For dispersion potentials, the typical interatomic distances and the wavelengths of atomic and body response functions give two such characteristic length scales. The nonretarded scaling laws are hence only valid for distances well between these two length scales while the long-range one is restricted to distances well above the latter.

The scaling laws may be used to deduce the functional dependence of dispersion forces in the case where they depend on only a single parameter. In more complex cases, the knowledge of a potential for a body of given size can be used to infer the potential for a similar body of different size. In particular, equipotential lines are invariant under a scale transformation. More complex applications include bodies with surface roughness. The duality invariance of dispersion forces [17] can be used to extend our results to magnetic atoms.

This work was supported by the Alexander von Humboldt Foundation, the UK Engineering and Physical Sciences Research Council, the SCALA programme of the European commission, and the CNRS.

[1] A. Aharony and D. Stauffer, *Introduction to Percolation Theory* (Taylor & Francis, London, 1994).
[2] K. Kieling *et al.*, Phys. Rev. Lett. **99**, 130501 (2007).
[3] K. A. Milton, J. Phys. A **37**, R209 (2004); M. B. Bordag *et al.*, *Advances in the Casimir Effect* (Oxford University Press, Oxford, 2009).
[4] S. Scheel and S. Y. Buhmann, Acta Phys. Slovaka **58**, 675 (2008).
[5] H. B. G. Casimir and D. Polder, Phys. Rev. **73**, 360 (1948); H. B. G. Casimir, Proc. K. Ned. Akad. Wet. **51**, 793 (1948).
[6] C. Henkel and K. Joulain, Europhys. Lett. **72**, 929 (2005); M. S. Tomaš, Phys. Lett. A **342**, 381 (2005).
[7] M. Boström and B. E. Sernelius, Phys. Rev. B **61**, 2204 (2000); E. V. Blagov *et al.*, Phys. Rev. B **71**, 235401 (2005).
[8] S. Y. Buhmann *et al.*, Phys. Rev. A **72**, 032112 (2005).
[9] M. J. Mehl and W. L. Schaich, Phys. Rev. A **21**, 1177 (1980); I. V. Bondarev and P. Lambin, Phys. Rev. B **72**, 035451 (2005).
[10] A. M. Marvin and F. Toigo, Phys. Rev. A **25**, 782 (1982); V. N. Marachevsky, Theor. Math. Phys. **131**, 468 (2002); S. Y. Buhmann *et al.*, J. Opt. B **6**, S127 (2004).
[11] M. M. Taddei *et al.*, arXiv:0903.2091.
[12] P. W. Milonni and P. B. Lerner, Phys. Rev. A **46**, 1185 (1992); S. Y. Buhmann and D.-G. Welsch, Appl. Phys. B **82**, 189 (2006).
[13] A. Lambrecht and V. N. Marachevsky, Phys. Rev. Lett. **101**, 160403 (2008); R. Messina *et al.*, Phys. Rev. A **80**, 022119 (2009).
[14] A. Roy and U. Mohideen, Phys. Rev. Lett. **82**, 4380 (1999).
[15] A. Ashourvan *et al.*, Phys. Rev. E **75**, 040103(R) (2007); Phys. Rev. Lett. **98**, 140801 (2007).
[16] O. Kenneth and I. Klich, Phys. Rev. Lett. **97**, 160401 (2006).
[17] S. Y. Buhmann and S. Scheel, Phys. Rev. Lett. **102**, 140404 (2009).
[18] J. Błocki *et al.*, Ann. Phys. (N.Y.) **105**, 427 (1977).
[19] S. Spagnolo *et al.*, Phys. Rev. A **73**, 062117 (2006).

International Journal of Modern Physics A
Vol. 31, Nos. 2 & 3 (2016) 1641029 (10 pages)

DOI: 10.1142/S0217751X16410293

Impact of anisotropy on the interaction of an atom with a one-dimensional nano-grating

Stefan Yoshi Buhmann

Physikalisches Institut, Albert-Ludwigs-Universität Freiburg, Hermann-Herder-Str. 3, D-79104 Freiburg, Germany
Freiburg Institute for Advanced Studies, Albert-Ludwigs-Universität Freiburg, Albertstraße 19, D-79104 Freiburg, Germany

Valery N. Marachevsky

Department of Theoretical Physics, Saint Petersburg State University, Ulianovskaya 1, Petrodvorets, 198504 St. Petersburg, Russia
maraval@mail.ru

Stefan Scheel

Institut für Physik, Universität Rostock, Albert-Einstein-Straße 23, D-18059 Rostock, Germany

Received 14 September 2015
Revised 26 October 2015
Published 19 January 2016

We study the interaction of an atom with a one-dimensional nano-grating within the framework of macroscopic QED, with special emphasis on possible anisotropic contributions. To this end, we first derive the scattering Green's tensor of the grating by means of a Rayleigh expansion and discuss its symmetry properties and asymptotes. We then determine the Casimir–Polder potential of an atom with the grating. In particular, we find that strong anisotropy can lead to a repulsive Casimir–Polder potential in the normal direction.

Keywords: Casimir–Polder potential; material grating; Rayleigh scattering.

PACS numbers: 34.35.+a, 37.10.Vz, 42.50.Nn, 42.25.Gy

1. Introduction

Dispersion forces such as the Casimir–Polder interaction between microscopic particles (atoms and molecules) with macroscopic bodies are prototypical forces that result from quantum vacuum fluctuations of a physical quantity, in this case the electromagnetic field.[1,2] Their magnitude depends sensitively on the geometry of the macroscopic body and the optical response of both particle and medium. In the

simplest case of flat surfaces and isotropic optical response the Casimir–Polder force is usually attractive and perpendicular to the surface. However, in more complex geometries this force can be modified to a large extent. For example, surfaces with gratings can induce force components that are parallel to the (spatially averaged) interface. This has been shown for Casimir forces between corrugated surfaces[3–6] as well as for Casimir–Polder forces.[7–11]

Moreover, the sign of the dispersion force can be reversed. A repulsive force with associated equilibrium, at least in the form of a saddle point, has been predicted for objects above a metal plate with a circular hole[12–15] and near wedges.[16] Apart from geometry, non-equilibrium situations such as resonant Casimir–Polder interactions of excited atoms can provide transient repulsion.[17,18] In this article, we will show how a strong anisotropic optical response of an atom can lead to a repulsive Casimir–Polder force normal to a one-dimensional grating structure.

From a theoretical point of view, to compute an electromagnetic dispersion force means to determine the scattering properties of a surface, typically in terms of reflection matrices that enter a mode expansion[3,19] or, equivalently, a Green's tensor construction.[20] Here we use the dyadic Green's tensor expansion in terms of Rayleigh reflection coefficients to investigate the interaction of an anisotropic atom with a one-dimensional periodic surface.

2. Green's Tensor of a Surface with One-Dimensional Periodic Profile

We require the scattering Green's tensor $\mathbf{G}^{(1)}(\boldsymbol{r}, \boldsymbol{r}', \omega)$ for source point $\boldsymbol{r}'$ and field point $\boldsymbol{r}$ being situated in the vacuum half space above a nano-grating $(y, y' > 0)$ (see Fig. 1). The grating displays a periodic surface profile $f(x) \in [-h, 0]$ in the x-direction with period d, $f(x + d) = f(x)$ and height h while being translationally invariant in the z-direction. To construct the Green's tensor, we employ a plane-wave

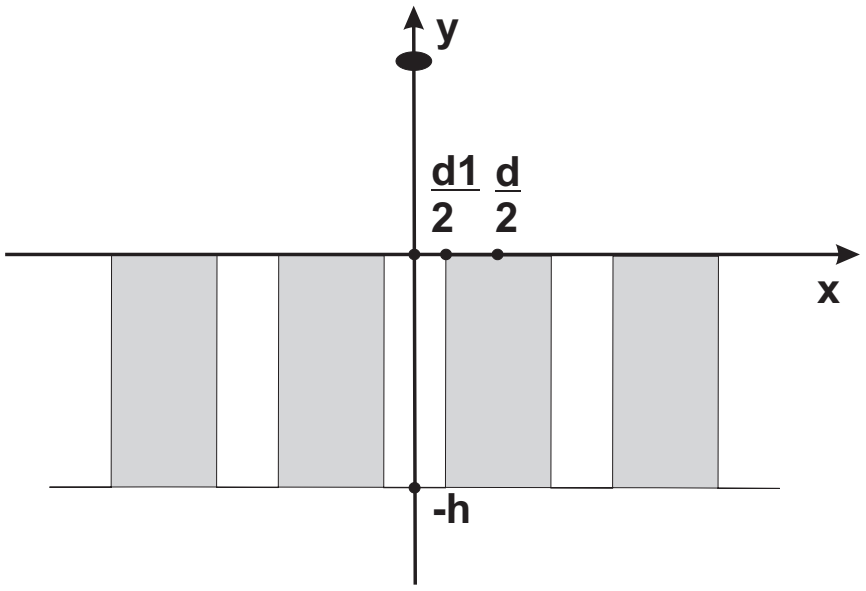

Fig. 1. An atom (black ellipse) at position $(0, y, z)$ above a one-dimensional rectangular grating.

basis which is adapted to the symmetry of the system. Wave vectors for upward (+) and downward (-) moving waves are parametrized as $\boldsymbol{k}_\pm = (k_x^m, \pm k_y^m, k_z)$. Their x-components are decomposed according to $k_x^m = k_x + mq$ into a continuous part $k_x \in [-q/2, q/2]$ that lies within the first Brillouin zone and a discrete part comprised of integer multiples $m \in \mathbb{Z}$ of the reciprocal lattice vector $q = 2\pi/d$. The z-component takes arbitrary continuous values $k_z \in \mathbb{R}$ while the y-component then follows from the dispersion relation:

$$k_y^m = k_y^m(k_x, k_z, \omega) = \lim_{\delta \to 0_+} \sqrt{\frac{\omega^2}{c^2}(1 + \mathrm{i}\delta) - (k_x^m)^2 - k_z^2} \quad \text{with } \operatorname{Im} k_y^m > 0. \tag{1}$$

For each such wave vector $\boldsymbol{k}_\pm = \boldsymbol{k}_{m\pm}(k_x, k_z, \omega)$, we choose two perpendicular polarisation vectors $\boldsymbol{e}_{m\pm}^E$ and $\boldsymbol{e}_{m\pm}^H$ such that only the respective electric and magnetic fields exhibit non-vanishing y-components, respectively:

$$\boldsymbol{e}_{m\pm}^E(k_x, k_z, \omega) = \frac{c}{\omega\sqrt{\omega^2/c^2 - k_z^2}} \begin{pmatrix} -k_x^m k_z \\ \mp k_y^m k_z \\ \omega^2/c^2 - k_z^2 \end{pmatrix}, \tag{2}$$

$$\boldsymbol{e}_{m\pm}^H(k_x, k_z, \omega) = \frac{1}{\sqrt{\omega^2/c^2 - k_z^2}} \begin{pmatrix} \mp k_y^m \\ k_x^m \\ 0 \end{pmatrix}. \tag{3}$$

These vectors are obviously normalized, $\boldsymbol{e}_{m\pm}^E \cdot \boldsymbol{e}_{m\pm}^E = \boldsymbol{e}_{m\pm}^H \cdot \boldsymbol{e}_{m\pm}^H = 1$ and orthogonal to each other, $\boldsymbol{e}_{m\pm}^E \cdot \boldsymbol{e}_{m\pm}^H = 0$, as well as to the unit wave vector $\boldsymbol{e}_{\boldsymbol{k}\pm} = \boldsymbol{k}_\pm/|\boldsymbol{k}_\pm|$, $\boldsymbol{e}_{m\pm}^E \cdot \boldsymbol{e}_{\boldsymbol{k}\pm} = \boldsymbol{e}_{m\pm}^H \cdot \boldsymbol{e}_{\boldsymbol{k}\pm} = 0$. The three orthonormal vectors form a right-handed triad, $\boldsymbol{e}_{m\pm}^H \times \boldsymbol{e}_{m\pm}^E = \boldsymbol{e}_{\boldsymbol{k}\pm}$.

With these preparations at hand, the required scattering Green's tensor can be given as

$$\mathbf{G}^{(1)}(\boldsymbol{r}, \boldsymbol{r}', \omega) = \frac{\mathrm{i}}{8\pi^2} \int_{-q/2}^{q/2} \mathrm{d}k_x \sum_{m,n=-\infty}^{\infty} \int_{-\infty}^{\infty} \mathrm{d}k_z \sum_{\sigma,\sigma'=E,H} \times \frac{\mathrm{e}^{\mathrm{i}[k_x^m x - k_x^n x' + k_y^m y + k_y^n y' + k_z(z-z')]}}{k_y^n} \boldsymbol{e}_{m+}^\sigma R_{mn}^{\sigma\sigma'} \boldsymbol{e}_{n-}^{\sigma'}. \tag{4}$$

The Rayleigh reflection coefficients $R_{mn}^{\sigma\sigma'} = R_{mn}^{\sigma\sigma'}(k_x, k_z, \omega)$ conserve k_x and k_z of the incident wave, but they mix polarizations σ, σ' as well as diffraction orders m, n.[21,22] In general, they have to be calculated numerically by integrating the Maxwell equations within the grating ($-h < y < 0$) and imposing conditions of continuity at its upper and lower boundaries.[3–5,9] For a rectangular grating (Fig. 1), the formalism for computing the Rayleigh coefficients is presented in Appendix A. Before we proceed, let us derive some symmetry properties of the reflection coefficients as well as consider the asymptotes of small and large grating periods.

2.1. *Symmetry properties*

Schwarz reflection principle. Like every causal response function, the scattering Green's tensor obeys the Schwarz reflection principle $\mathbf{G}^{(1)}(\boldsymbol{r},\boldsymbol{r}',-\omega^*) = \mathbf{G}^{(1)*}(\boldsymbol{r},\boldsymbol{r}',\omega)$.[1] Applying this to Eq. (4) leads to

$$R^{\sigma\sigma'}_{-m-n}(-k_x,-k_z,-\omega^*) = R^{\sigma\sigma'*}_{mn}(k_x,k_z,\omega). \tag{5}$$

Onsager reciprocity. Provided that the grating consists of a medium which obeys time-reversal symmetry,[23] the scattering Green's tensor fulfils Onsager reciprocity $\mathbf{G}^{(1)}(\boldsymbol{r}',\boldsymbol{r},\omega) = \mathbf{G}^{(1)\mathrm{T}}(\boldsymbol{r},\boldsymbol{r}',\omega)$. This implies

$$\frac{R^{\sigma\sigma'}_{-n-m}(-k_x,-k_z,\omega)}{k_y^m} = \pm\frac{R^{\sigma'\sigma}_{mn}(k_x,k_z,\omega)}{k_y^n} \quad \text{for } \sigma=\sigma', \sigma\neq\sigma'. \tag{6}$$

Grating symmetries. Finally, we consider symmetries imposed by the geometry of the grating. The invariance of the grating with respect to an inversion of the z coordinate implies that the diagonal/off-diagonal Rayleigh coefficients are even/odd functions of k_z, respectively:

$$R^{\sigma\sigma'}_{mn}(k_x,-k_z,\omega) = \pm R^{\sigma\sigma'}_{mn}(k_x,k_z,\omega) \quad \text{for } \sigma=\sigma', \sigma\neq\sigma'. \tag{7}$$

For a symmetric grating with $f(-x)=f(x)$, we further have

$$R^{\sigma\sigma'}_{-m-n}(-k_x,k_z,\omega) = \pm R^{\sigma\sigma'}_{mn}(k_x,k_z,\omega) \quad \text{for } \sigma=\sigma', \sigma\neq\sigma' \tag{8}$$

by virtue of the x-inversion symmetry.

Further symmetries can be obtained by combining the above. For instance, Eqs. (5) and (6) imply $R^{\sigma\sigma'*}_{nm}(k_x,k_z,\mathrm{i}\xi)/k_y^m = \pm R^{\sigma'\sigma}_{mn}(k_x,k_z,\mathrm{i}\xi)/k_y^n$ for $\sigma=\sigma'$, $\sigma\neq\sigma'$ at purely imaginary frequencies $\omega=\mathrm{i}\xi$.

2.2. *Asymptotes*

The exponential factors $\mathrm{e}^{\mathrm{i}k_y^m y}$ and $\mathrm{e}^{\mathrm{i}k_y^n y'}$ become either exponentially damped or rapidly oscillating whenever $|k_y^m|y>1$ or $|k_y^n|y'>1$, respectively. In the limit where the grating period is small with respect to the distances of source and field points from the grating, $d\ll y,y'$, this implies that the Rayleigh sums in Eq. (4) are effectively limited to small values. To leading order $m=n=0$, we have

$$\begin{aligned}\mathbf{G}^{(1)}(\boldsymbol{r},\boldsymbol{r}',\omega) &= \frac{\mathrm{i}}{8\pi^2}\int_{-q/2}^{q/2}\mathrm{d}k_x\,\mathrm{e}^{\mathrm{i}k_x(x-x')}\int_{-\infty}^{\infty}\mathrm{d}k_z\frac{\mathrm{e}^{\mathrm{i}k_y^0(y+y')+\mathrm{i}k_z(z-z')}}{k_y^0}\\ &\quad\times\sum_{\sigma,\sigma'=E,H}\boldsymbol{e}^{\sigma}_{0+}R^{\sigma\sigma'}_{00}\boldsymbol{e}^{\sigma'}_{0-}\\ &= \frac{\mathrm{i}}{8\pi^2}\int_{-q/2}^{q/2}\mathrm{d}k_x\int_{-\infty}^{\infty}\mathrm{d}k_z\,\frac{\mathrm{e}^{2\mathrm{i}k_y^0 y}}{k_y^0}\sum_{\sigma,\sigma'=E,H}\boldsymbol{e}^{\sigma}_{0+}R^{\sigma\sigma'}_{00}\boldsymbol{e}^{\sigma'}_{0-}\end{aligned} \tag{9}$$

in the coincidence limit $\boldsymbol{r}=\boldsymbol{r}'$. This asymptote of the scattering Green's tensor is thus translationally invariant along the x-direction and it is described by the

effective properties of the grating averaged over one period. The leading correction to this x-independent Green's tensor is a harmonic variation in qx which is due to terms $m = 0$, $n = \pm 1$ and $n = 0$, $m = \pm 1$. In particular for a symmetric grating, this correction is proportional to $\cos(qx)$ in the coincidence limit.

In the opposite extreme of the grating period being very large with respect to the distances of source and field points from the grating, $d \gg y, y'$, very large Rayleigh reflection orders $m, n \gg 1$ contribute. We thus have $k_x^m \approx mq$, $k_y^m(k_x, k_z, \omega) \approx k_y^m(0, k_z, \omega)$, so that the polarization unit vectors and reflection coefficients can be approximated by $\boldsymbol{e}_{m\pm}^{\sigma}(k_x, k_z, \omega) \approx \boldsymbol{e}_{m\pm}^{\sigma}(0, k_z, \omega)$ and $R_{mn}^{\sigma\sigma'}(k_x, k_z, \omega) \approx R_{mn}^{\sigma\sigma'}(0, k_z, \omega)$. Carrying out the remaining k_x-integral, the scattering Green's tensor assumes the asymptotic form

$$\mathsf{G}^{(1)}(\boldsymbol{r}, \boldsymbol{r}', \omega) \simeq \frac{\mathrm{i}\sin[\pi(x - x')/d]}{4\pi^2(x - x')} \sum_{m,n=-\infty}^{\infty} \mathrm{e}^{\mathrm{i}q(mx - nx')} \times \int_{-\infty}^{\infty} \mathrm{d}k_z \frac{\mathrm{e}^{\mathrm{i}(k_y^m y + k_y^n y') + \mathrm{i}k_z(z - z')}}{k_y^{n-}} \sum_{\sigma,\sigma'=E,H} R_{mn}^{\sigma\sigma'} \boldsymbol{e}_{m+}^{\sigma} \boldsymbol{e}_{n-}^{\sigma'}. \quad (10)$$

3. Casimir–Polder Potential Above a Surface with One-Dimensional Periodic Profile

Within leading-order perturbation theory, the CP potential of a ground-state atom within an arbitrary structure is given as[24]

$$U(\boldsymbol{r}) = \frac{\hbar\mu_0}{2\pi} \int_0^{\infty} \mathrm{d}\xi\, \xi^2 \mathrm{Tr}[\boldsymbol{\alpha}(\mathrm{i}\xi) \cdot \mathsf{G}^{(1)}(\boldsymbol{r}, \boldsymbol{r}, \mathrm{i}\xi)], \quad (11)$$

where

$$\boldsymbol{\alpha}(\omega) = \lim_{\epsilon \to 0+} \frac{1}{\hbar} \sum_k \left(\frac{\boldsymbol{d}_{k0} \boldsymbol{d}_{0k}}{\omega + \omega_k + \mathrm{i}\epsilon} - \frac{\boldsymbol{d}_{0k} \boldsymbol{d}_{k0}}{\omega - \omega_k + \mathrm{i}\epsilon} \right) \quad (12)$$

is the ground-state polarisability of the atom as given in terms of its transition frequencies $\omega_k = (E_k - E_0)/\hbar$ and dipole matrix elements $\boldsymbol{d}_{mn}$. Using the Green's tensor (4) from the previous section, we find the CP potential of an atom above a one-dimensional grating as

$$U(\boldsymbol{r}) = \frac{\hbar\mu_0}{16\pi^3} \int_0^{\infty} \mathrm{d}\xi\, \xi^2 \int_{-q/2}^{q/2} \mathrm{d}k_x \sum_{m,n=-\infty}^{\infty} \mathrm{e}^{\mathrm{i}q(m-n)x} \int_{-\infty}^{\infty} \mathrm{d}k_z \frac{\mathrm{e}^{-(\kappa_m + \kappa_n)y}}{\kappa_n} \times \sum_{\sigma,\sigma'=E,H} R_{mn}^{\sigma\sigma'} \boldsymbol{e}_{m+}^{\sigma} \cdot \boldsymbol{\alpha}(\mathrm{i}\xi) \cdot \boldsymbol{e}_{n-}^{\sigma'} \quad (13)$$

with $R_{mn}^{\sigma\sigma'} = R_{mn}^{\sigma\sigma'}(k_x, k_z, \mathrm{i}\xi)$ and

$$\kappa_m = \kappa_m(k_x, k_z, \mathrm{i}\xi) = \sqrt{\frac{\xi^2}{c^2} + (k_x^m)^2 + k_z^2}\,. \quad (14)$$

In the limit $d \ll y$ of small grating period, we use the asymptote (9) of the Green's tensor to find the x-independent potential

$$U(\boldsymbol{r}) = \frac{\hbar\mu_0}{16\pi^3}\int_0^\infty \mathrm{d}\xi\,\xi^2 \int_{-q/2}^{q/2}\mathrm{d}k_x \int_{-\infty}^{\infty}\mathrm{d}k_z\,\frac{\mathrm{e}^{-2\kappa_0 y}}{\kappa_0}\sum_{\sigma,\sigma'=E,H} R_{00}^{\sigma\sigma'}\,\boldsymbol{e}_{0+}^{\sigma}\cdot\boldsymbol{\alpha}(\mathrm{i}\xi)\cdot\boldsymbol{e}_{0-}^{\sigma'}. \tag{15}$$

For large grating period $d \gg y$, Eq. (10) leads to

$$U(\boldsymbol{r}) = \frac{\hbar\mu_0}{8\pi^2 d}\int_0^\infty \mathrm{d}\xi\,\xi^2 \sum_{m,n=-\infty}^{\infty}\mathrm{e}^{\mathrm{i}q(m-n)x}\int_{-\infty}^{\infty}\mathrm{d}k_z\,\frac{\mathrm{e}^{-(\kappa_m+\kappa_n)y}}{\kappa_n}\sum_{\sigma,\sigma'=E,H} R_{mn}^{\sigma\sigma'} \times \boldsymbol{e}_{m+}^{\sigma}\cdot\boldsymbol{\alpha}(\mathrm{i}\xi)\cdot\boldsymbol{e}_{n-}^{\sigma'} \tag{16}$$

with $k_x = 0$ taken in all expressions inside the integrand.

4. Casimir–Polder Potential Above a One-Dimensional Rectangular Grating

We study a ground-state Rb atom above a rectangular Au grating as shown in Fig. 1. The grating consists of a periodic array of rectangular bars of height $h = 20\,\mathrm{nm}$ and width $2\,\mu\mathrm{m}$ with separation $d_1 = 2\,\mu\mathrm{m}$, so that the grating period is $d = 4\,\mu\mathrm{m}$. The atom–grating potential is derived by numerically integrating Eq. (13) with the Rayleigh coefficients as given in Appendix A. To study the effect of possible anisotropies on the potential, we separate the latter into contributions from $\alpha_{xx}(\omega) = \alpha_{yy}(\omega) = \alpha_{zz}(\omega) = \alpha(\omega)$ where $\alpha(\omega)$ is the ground-state polarizability

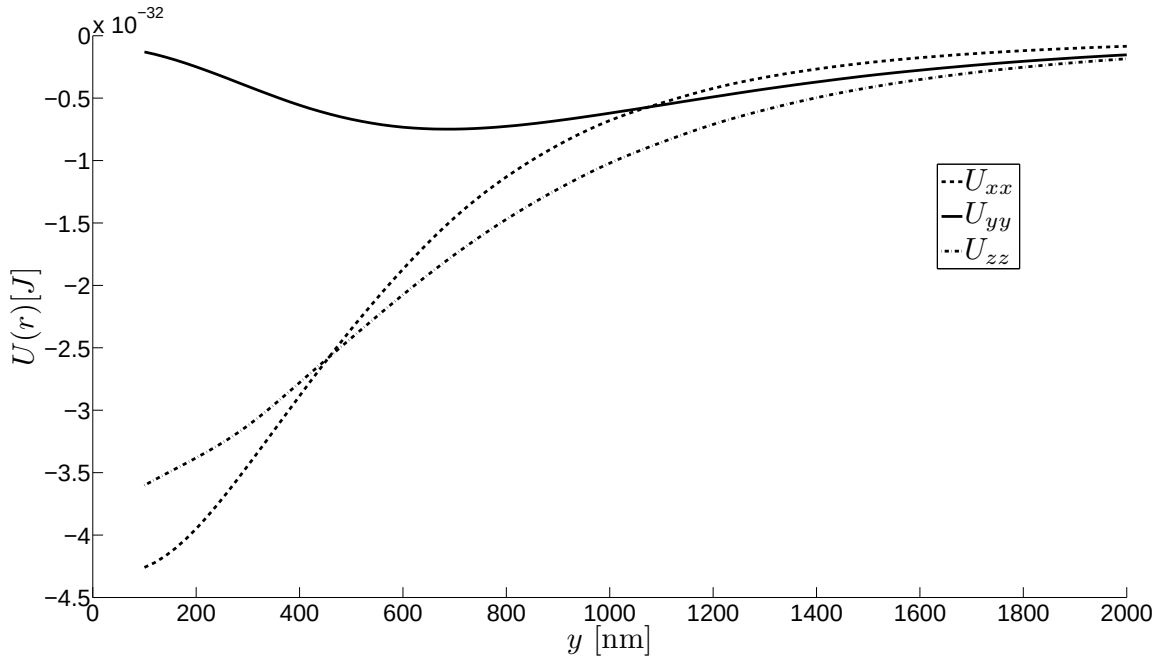

Fig. 2. Contributions to the Casimir–Polder potential of a ground-state Rb atom above an Au grating as shown in Fig. 1.

of the Rb atom: $U(\boldsymbol{r}) = U_{xx}(\boldsymbol{r}) + U_{yy}(\boldsymbol{r}) + U_{zz}(\boldsymbol{r})$. The resulting potentials at $x = 0$ are shown in Fig. 2. We find that the component U_{yy} leads to a repulsive Casimir–Polder potential in normal direction at separations $y \lesssim 700\,\text{nm}$. This is the first demonstration of a repulsive Casimir–Polder potential for a grating geometry.

In many cases of interest, a full numerical calculation of the potential is neither desirable nor needed. For short atom-grating separations, the asymptotic expression (16) gives reliable results. In Fig. 3, we show a comparison of the full numerical calculation according to Eq. (13) (thick lines) with the short-distance asymptote (16) (thin lines) at a fixed atom-grating distance of $y = 700\,\text{nm}$. The obvious appearance of a non-sinusoidal lateral force across the grating implies in particular that the repulsive U_{yy} component at $x = 0$ leads to an unstable, saddle-point equilibrium in accordance with the generalized Earnshaw theorem.[25] One further notices that the short-distance (or large grating) approximation already provides very accurate results already at $y = 700\,\text{nm}$. At smaller separations of $y = 300\,\text{nm}$, the difference between exact and approximate potentials are within the thickness of the lines.

For the components of a Rb atom potential at a distance $y = 700\,\text{nm}$ from a flat Au 20 nm width slab one gets $U_{xx} = U_{zz} = -2.04 \cdot 10^{-31} J$, $U_{yy} = -2.22 \cdot 10^{-31} J$, which is also the proximity force approximation[26,27] result for the components of a potential of a Rb atom located above grating Au bars. At very small distances the Casimir-Polder potential of the atom is oscillating between the values given by a proximity force approximation, i.e. between zero (above the slits) and the value for a thin gold plate (above the bars). This picture remains qualitatively valid up to distances of the order of the grating period.

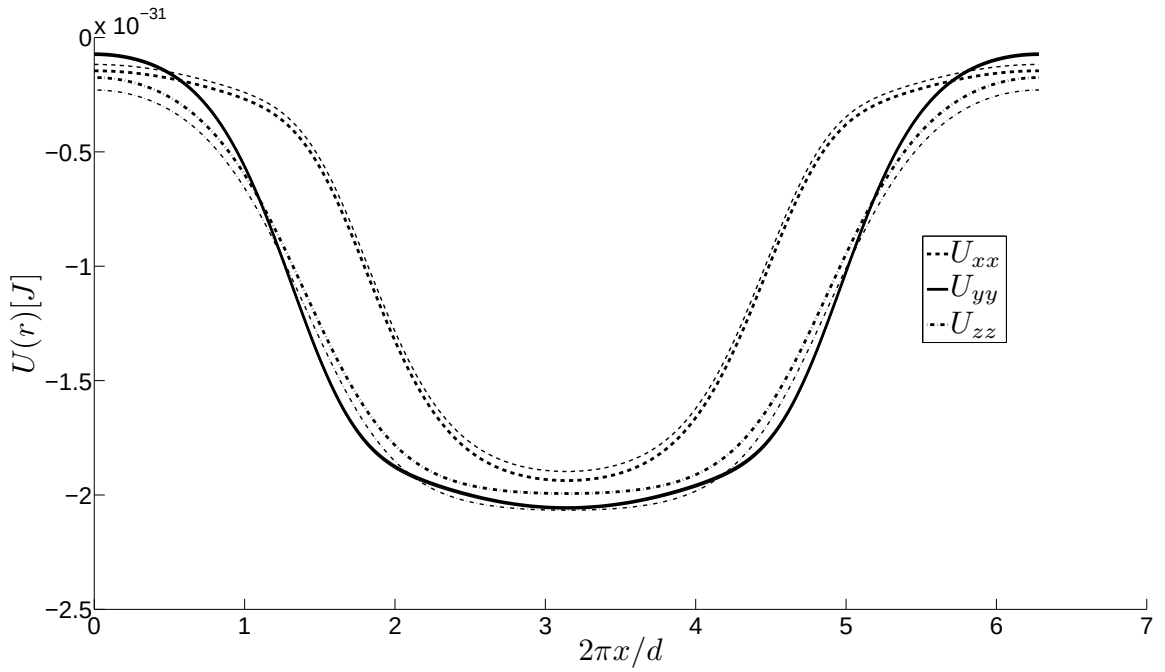

Fig. 3. Casimir–Polder potential of a ground-state Rb atom at fixed distance $y = 700$ nm above an Au grating as a function of lateral position. Thick lines: exact numerical results from Eq. (13). Thin lines: asymptotes from Eq. (16).

5. Conclusions

We have shown that it is possible to generate repulsive Casimir–Polder forces above material gratings using anisotropic atoms. Our calculation was based on the Green's tensor expansion of the electromagnetic field which, using a Rayleigh expansion, yields both a numerically exact result as well as analytically tractable asymptotes for small and large gratings. Surprisingly, the short-distance (or large grating) asymptote becomes already accurate at a distance of 700 nm above a grating with a 4 μm period.

Acknowledgments

SYB was supported by the DFG (grant BU 1803/3-1) and the Freiburg Institute for Advanced Studies. VNM was partially supported by grants of Saint Petersburg State University 11.38.237.2015 and 11.38.660.2013. VNM thanks the participants of the 9th Friedmann Seminar for interesting discussions; it is a pleasure to thank the organizers for an excellent Seminar.

Appendix A. Rayleigh Reflection Coefficients for a Rectangular Grating

In the following, we determine the Rayleigh reflection coefficients for the rectangular grating depicted in Fig. 1. To this end, we express the electromagnetic fields above and below the grating for incident waves of polarisation σ' according to Eqs. (2) and (3) as (the factor $\mathrm{e}^{-\mathrm{i}\omega t+\mathrm{i}k_z z}$ is omitted for brevity)

$$E_z(x,y) = \mathrm{e}^{\mathrm{i}k_x^m x-\mathrm{i}k_y^m y}\delta_{E\sigma'} + \sum_{n=-\infty}^{\infty} R_{nm}^{E\sigma'}\mathrm{e}^{\mathrm{i}k_x^n x+\mathrm{i}k_y^n y}, \tag{A.1}$$

$$H_z(x,y) = \mathrm{e}^{\mathrm{i}k_x^m x-\mathrm{i}k_y^m y}\delta_{H\sigma'} + \sum_{n=-\infty}^{\infty} R_{nm}^{H\sigma'}\mathrm{e}^{\mathrm{i}k_x^n x+\mathrm{i}k_y^n y} \tag{A.2}$$

for $y > 0$ and

$$E_z(x,y) = \sum_{n=-\infty}^{\infty} T_{nm}^{E\sigma'}\mathrm{e}^{\mathrm{i}k_x^n x-\mathrm{i}k_y^n y}, \tag{A.3}$$

$$H_z(x,y) = \sum_{n=-\infty}^{\infty} T_{nm}^{H\sigma'}\mathrm{e}^{\mathrm{i}k_x^n x-\mathrm{i}k_y^n y} \tag{A.4}$$

for $y < -h$, respectively. For simplicity, we take $c = 1$ throughout this Appendix.

In the region $-h \le y \le 0$ one can write $E_z(x,y) = \sum_{n=-\infty}^{\infty} E_z^n(y)\exp(\mathrm{i}k_x^n x)$, analogous decompositions hold for the other components of the electromagnetic field. It is convenient to denote by $[E]$ the $2N+1$-component vector with components E_N, $E_{N-1}, \ldots, E_0, \ldots, E_{-N+1}$, E_{-N}. We further introduce a diagonal $(2N+1)\times(2N+1)$-matrix

$$\Lambda = \mathrm{diag}(k_x^N, k_x^{N-1}, \ldots, k_x^0, \ldots, k_x^{-(N-1)}, k_x^{-N}). \tag{A.5}$$

The Maxwell equations in the region $-h \le y \le 0$ can then be written as[22]

$$\frac{\partial[E_z]}{\partial y} - \mathrm{i}k_z[E_y] = \mathrm{i}\omega[H_x], \qquad \frac{\partial[H_z]}{\partial y} - \mathrm{i}k_z[H_y] = -\mathrm{i}\omega[D_x], \tag{A.6}$$

$$\mathrm{i}k_z[E_x] - i\Lambda[E_z] = \mathrm{i}\omega[H_y], \qquad \mathrm{i}k_z[H_x] - i\Lambda[H_z] = -\mathrm{i}\omega[D_y], \tag{A.7}$$

$$\mathrm{i}\Lambda[E_y] - \frac{\partial[E_x]}{\partial y} = \mathrm{i}\omega[H_z], \qquad \mathrm{i}\Lambda[H_y] - \frac{[H_x]}{\partial y} = -\mathrm{i}\omega[D_z]. \tag{A.8}$$

Writing $[\boldsymbol{D}] = Q[\boldsymbol{E}]$ and using the results of Ref. 28, one has for a rectangular grating:

$$Q = \begin{pmatrix} \|\frac{1}{\varepsilon}\|^{-1} & 0 & 0 \\ 0 & \|\varepsilon\| & 0 \\ 0 & 0 & \|\varepsilon\| \end{pmatrix}. \tag{A.9}$$

Here, $\|\varepsilon\|$ is a Toeplitz matrix defined as

$$\|\varepsilon\| = \begin{pmatrix} \varepsilon_0 & \varepsilon_1 & \varepsilon_2 & \cdots & \varepsilon_{2N} \\ \varepsilon_{-1} & \varepsilon_0 & \varepsilon_1 & \cdots & \varepsilon_{2N-1} \\ \varepsilon_{-2} & \varepsilon_{-1} & \varepsilon_0 & \cdots & \varepsilon_{2N-2} \\ \cdots & \cdots & \cdots & \cdots & \cdots \\ \varepsilon_{-2N} & \varepsilon_{-2N+1} & \varepsilon_{-2N+2} & \cdots & \varepsilon_0 \end{pmatrix}, \tag{A.10}$$

where ε_n is a Fourier coefficient of the periodic function $\varepsilon(x+d) = \varepsilon(x)$:

$$\varepsilon(x) = \sum_{n=-\infty}^{+\infty} \exp\Big(\frac{i2\pi nx}{d}\Big)\varepsilon_n. \tag{A.11}$$

In order to solve the above system of equations, we proceed as follows. Equation (A.7) implies $[E_y] = \|\varepsilon\|^{-1}(\Lambda[H_z] - k_z[H_x])/\omega$, which can be substituted into equations (A.6) and (A.8) to eliminate $[E_y]$. Similarly, Eq. (A.7) leads to $[H_y] = (k_z[E_x] - \Lambda[E_z])/\omega$, which can be substituted into equations (A.6) and (A.8) to eliminate $[H_y]$. As a result, the Maxwell equations in the region $-h \le y \le 0$ can be rewritten as

$$\frac{\partial}{\partial y}\begin{pmatrix} [E_x] \\ [E_z] \\ [H_x] \\ [H_z] \end{pmatrix} = M \begin{pmatrix} [E_x] \\ [E_z] \\ [H_x] \\ [H_z] \end{pmatrix}, \tag{A.12}$$

where the matrix M is defined as

$$M = \mathrm{i}\begin{pmatrix} 0 & 0 & -\frac{k_z}{\omega}\Lambda\|\varepsilon\|^{-1} & \frac{1}{\omega}\Lambda\|\varepsilon\|^{-1}\Lambda - \omega I \\ 0 & 0 & -\frac{k_z^2}{\omega}\|\varepsilon\|^{-1} + \omega I & \frac{k_z}{\omega}\|\varepsilon\|^{-1}\Lambda \\ \frac{k_z}{\omega}\Lambda & \omega\|\varepsilon\| - \frac{1}{\omega}\Lambda^2 & 0 & 0 \\ \frac{k_z^2}{\omega}I - \omega\|\frac{1}{\epsilon}\|^{-1} & -\frac{k_z}{\omega}\Lambda & 0 & 0 \end{pmatrix}. \tag{A.13}$$

Knowing the transmitted fields (A.3) and (A.4) at $y = -h$, one can determine the fields at $y = 0$ by integrating Eq. (A.12) from $-h$ to 0. Imposing the continuity conditions on all Fourier components of $[E_x], [E_z], [H_x], [H_z]$ at $y = 0$, one then determines the Rayleigh reflection and transmission coefficients.

References

1. S. Y. Buhmann, *Dispersion Forces I*: *Macroscopic Quantum Electrodynamics and Ground-State Casimir, Casimir–Polder and van der Waals Forces* (Springer, Heidelberg, 2012).
2. V. N. Marachevsky, *J. Phys. A*: *Math. Theor.* **45**, 374021 (2012).
3. A. Lambrecht and V. N. Marachevsky, *Phys. Rev. Lett.* **101**, 160403 (2008).
4. A. Lambrecht and V. N. Marachevsky, *Int. J. Mod. Phys. A* **24**, 1789 (2009).
5. H.-C. Chiu, G. L. Klimchitskaya, V. N. Marachevsky, V. M. Mostepanenko and U. Mohideen, *Phys. Rev. B* **80**, 121402(R) (2009); *Phys. Rev. B* **81**, 115417 (2010).
6. R. B. Rodrigues, P. A. Maia Neto, A. Lambrecht and S. Reynaud, *Phys. Rev. Lett.* **96**, 100402 (2006).
7. R. Messina, D. A. R. Dalvit, P. A. Maia Neto, A. Lambrecht and S. Reynaud, *Phys. Rev. A* **80**, 022119 (2009).
8. A. M. Contreras-Reyes, R. Guérout, P. A. Maia Neto, D. A. R. Dalvit, A. Lambrecht and S. Reynaud, *Phys. Rev. A* **82**, 052517 (2010).
9. H. Bender, C. Stehle, C. Zimmermann, S. Slama, J. Fiedler, S. Scheel, S. Y. Buhmann and V. N. Marachevsky, *Phys. Rev. X* **4**, 011029 (2014).
10. R. Bennett, *Phys. Rev. A* **92**, 022503 (2015).
11. G. Bimonte, T. Emig and M. Kardar, *Phys. Rev. D* **90**, 081702(R) (2014); *Phys. Rev. D* **92**, 025028 (2015).
12. M. Levin, A. P. McCauley, A. W. Rodriguez, M. T. H. Reid and S. G. Johnson, *Phys. Rev. Lett.* **105**, 090403 (2010).
13. C. Eberlein and R. Zietal, *Phys. Rev. A* **83**, 052514 (2011).
14. K. A. Milton, E. K. Abalo, P. Parashar, N. Pourtolami, I. Brevik and S. A. Ellingsen, *J. Phys. A* **45**, 374006 (2012).
15. K. A. Milton, E. K. Abalo, P. Parashar, N. Pourtolami, I. Brevik, S. A. Ellingsen, S. Y. Buhmann and S. Scheel, *Phys. Rev. A* **91**, 042510 (2015).
16. K. A. Milton, E. K. Abalo, P. Parashar, N. Pourtolami, I. Brevik and S. A. Ellingsen, *Phys. Rev. A* **83**, 062507 (2011).
17. H. Failache, S. Saltiel, M. Fichet, D. Bloch and M. Ducloy, *Phys. Rev. Lett.* **83**, 5467 (1999).
18. S. Y. Buhmann and S. Scheel, *Phys. Rev. Lett.* **100**, 253201 (2008).
19. P. S. Davids, F. Intravaia, F. S. S. Rosa and D. A. R. Dalvit, *Phys. Rev. A* **82**, 062111 (2010).
20. S. Scheel and S. Y. Buhmann, *Acta Phys. Slov.* **58**, 675 (2008).
21. O. M. Rayleigh, *Proc. Roy. Soc. A* **79**, 399 (1907).
22. D. Maystre (ed.) *Selected Papers on Diffraction Gratings* (SPIE, Bellingham, 1993); R. Petit (ed.), *Electromagnetic Theory of Gratings* (Springer-Verlag, Berlin, 1980); M. C. Hutley, *Diffraction Gratings* (Academic Press, London, 1982); E. G. Loewen and E. Popov, *Diffraction Gratings and Applications* (Marcel Dekker, New York, 1997).
23. S. Y. Buhmann, D. T. Butcher and S. Scheel, *New J. Phys.* **14**, 083034 (2012).
24. S. Y. Buhmann, L. Knöll, D.-G. Welsch and T. D. Ho, *Phys. Rev. A* **70**, 052117 (2004).
25. S. J. Rahi, M. Kardar and T. Emig, *Phys. Rev. Lett.* **105**, 070404 (2010).
26. B. V. Derjaguin, I. I. Abrikosova and E. M. Lifshitz, *Q. Rev. Chem. Soc.* **10**, 295 (1956).
27. J. Błoccki, J. Randrup, W. J. Światecki and C. F. Tsang, *Ann. Phys.* **105**, 427 (1977).
28. L. Li, *J. Opt. Soc. Am. A* **13**, 1870 (1996).

IOP Publishing New J. Phys. 20 (2018) 043024 https://doi.org/10.1088/1367-2630/aaaa44

New Journal of Physics
The open access journal at the forefront of physics

Deutsche Physikalische Gesellschaft DPG
IOP Institute of Physics

Published in partnership with: Deutsche Physikalische Gesellschaft and the Institute of Physics

OPEN ACCESS

RECEIVED
4 October 2017

REVISED
20 December 2017

ACCEPTED FOR PUBLICATION
24 January 2018

PUBLISHED
16 April 2018

PAPER

Casimir effect for perfect electromagnetic conductors (PEMCs): a sum rule for attractive/repulsive forces

Stefan Rode[1], **Robert Bennett**[1] **and Stefan Yoshi Buhmann**[1,2]

[1] Physikalisches Institut, Albert-Ludwigs-Universität Freiburg, Hermann-Herder-Str. 3, D-79104 Freiburg, Germany
[2] Freiburg Institute for Advanced Studies, Albert-Ludwigs-Universität Freiburg, Albertstr. 19, D-79104 Freiburg, Germany

E-mail: stefan.rode511@web.de

Keywords: perfect electromagnetic conductor (PEMC), Casimir effect, nonreciprocal media, duality, Casimir repulsion

Abstract

We discuss the Casimir effect for boundary conditions involving perfect electromagnetic conductors, which interpolate between perfect electric conductors and perfect magnetic conductors. Based on the corresponding reciprocal Green's tensor we construct the Green's tensor for two perfectly reflecting plates with magnetoelectric coupling (non-reciprocal media) within the framework of macroscopic quantum electrodynamics. We calculate the Casimir force between two arbitrary perfect electromagnetic conductor plates, resulting in a universal analytic expression that connects the attractive Casimir force with the repulsive Boyer force. We relate the results to a duality symmetry of electromagnetism.

1. Introduction

Nonvanishing zero-point energies are a pervasive feature of quantum mechanics and quantum field theory. The fact that energy fluctuations of the vacuum lead to physically observable macroscopic forces was first discovered by Hendrik Casimir in [1], who calculated the attractive force between two uncharged metallic plates due to the fluctuations of the electromagnetic field, which turned out to be given by the simple expression

$$f_{\mathrm{attr}} = -\frac{\hbar c \pi^2}{240 d^4} \tag{1}$$

for plates separated by a distance d. The origin of this force is the non-vanishing expectation value of the squared electric and magnetic fields in the vacuum state, which is then modified by the presence of surfaces. These vacuum fluctuations give rise to various forms of matter-vacuum interaction. The inverse fourth-power distance-dependence leads to negligibly small forces on large distance scales. However, in the nanometre regime the Casimir effect and other vacuum fluctuation induced forces can become significant or even dominant. In particular, the Casimir force poses a challenge for constructing microelectromechanical systems [2]. It causes effects such as stiction [3, 4], which is the permanent adhesion of two nano-structural elements. In order to remove such impeding effects, possible ways of manipulating the Casimir force between bodies have been pursued.

Of particular interest are repulsive Casimir forces [5]. The first result in this field was obtained by Boyer in [6], who considered an assembly of two parallel plates, one of them perfectly conducting, the other one perfectly permeable. He found the Casimir force to be repulsive in this case and showed that the ratio of his result to the attractive force calculated by Casimir reads

$$f_{\mathrm{rep}} = -\frac{7}{8} f_{\mathrm{attr}}. \tag{2}$$

It has also been theoretically shown that the magnitude of the Casimir force between two plates of any magnetodielectric properties has to fall between the result of Casimir and the result of Boyer [7], which we shall confirm here.

Due to the difficulty of realising materials whose permeability is perfect or nearly perfect, other ways of implementing repulsive Casimir forces have been considered. Kenneth and Klich [8] have discussed the

IOP Publishing New J. Phys. 20 (2018) 043024 S Rode et al

opportunities of materials with non-trivial but finite magnetic susceptibilities for instance. As another approach the Casimir forces on materials with polarisation-twisting effects have been studied. In particular the vacuum interaction properties of topological insulators [9, 10] and of chiral metamaterials [11, 12], have been investigated for generalised boundary conditions [13]. For the case of a scalar field confined by Robin boundary conditions, the Casimir force has been obtained to be either repulsive or attractive [14], as is also the case for thin films described as Chern–Simons boundaries [15, 16]. Here we will study perfect electromagnetic conductors (PEMCs) as introduced by Lindell and Sihvola [17], which are an idealised class of nonreciprocal polarisation-mixing materials whose response is characterised by a single parameter M. We will calculate the Casimir force between two PEMC plates in terms of this parameter, which will allow us to continuously vary the Casimir force between the two extremal values.

From a more fundamental point of view, the Casimir force in PEMC media is of interest because of its close relation to duality invariance. It has been shown [18, 19] that a linear magnetodielectric medium breaks the duality invariance that holds for the free Maxwell equations, causing them to instead have a discrete $\mathbb{Z}_4$-symmetry. Allowing material response that violates Lorentz-reciprocity restores duality invariance [20]—PEMC media provide these properties. For this reason we will determine the relation between the PEMC parameter M and the duality angle of a perfect conductor to obtain a coherent picture of the impact of duality transformations on Casimir forces.

2. The Casimir force on nonreciprocal bodies

The Green's tensor $\mathbb{G} = \mathbb{G}(\mathbf{r}, \mathbf{r}', \omega)$ of Maxwell's equations in a region with tensor-valued permittivity $\varepsilon = \varepsilon(\mathbf{r}, \omega)$, permeability $\mu = \mu(\mathbf{r}, \omega)$ and cross-polarisabilities $\zeta = \zeta(\mathbf{r}, \omega)$ and $\xi = \xi(\mathbf{r}, \omega)$ (discussed in detail in section 3) is defined to satisfy [20]:

$$\left[\nabla \times \frac{1}{\mu}\nabla \times - \frac{\mathrm{i}\omega}{c}\nabla \times \frac{\zeta}{\mu} + \frac{\mathrm{i}\omega}{c}\frac{\xi}{\mu}\nabla \times - \frac{\omega^2}{c^2}\left(\varepsilon - \frac{\xi\zeta}{\mu}\right)\right]\mathbb{G} = \mathbb{I}\delta(\mathbf{r} - \mathbf{r}') \tag{3}$$

subject to appropriate boundary conditions, and where $\mathbb{I}$ is the three-dimensional identity matrix. Then, quantised electromagnetic fields can be constructed via [21]

$$\hat{\mathbf{E}}(\mathbf{r}, \omega) = \mathrm{i}\mu_0\omega \int \mathrm{d}^3\mathbf{r}'\mathbb{G}(\mathbf{r}, \mathbf{r}', \omega) \cdot \hat{\mathbf{j}}_{\mathrm{N}}(\mathbf{r}', \omega) \tag{4}$$

where $\hat{\mathbf{j}}_{\mathrm{N}}$ is a noise-current source, and here we have taken $\omega > 0$, but the corresponding negative frequency fields can be constructed by hermitian conjugation. The noise current $\hat{\mathbf{j}}_{\mathrm{N}}$ is given explicitly in terms of noise polarisation $\hat{\mathbf{P}}_{\mathrm{N}}$ and noise magnetisation $\hat{\mathbf{M}}_{\mathrm{N}}$ by

$$\hat{\mathbf{j}}_{\mathrm{N}}(\mathbf{r}, \omega) = -\mathrm{i}\omega\hat{\mathbf{P}}_{\mathrm{N}} + \nabla \times \hat{\mathbf{M}}_{\mathrm{N}} \tag{5}$$

with

$$\begin{pmatrix}\hat{\mathbf{P}}_{\mathrm{N}} \\ \hat{\mathbf{M}}_{\mathrm{N}}\end{pmatrix} = \sqrt{\frac{\hbar}{\pi}}\mathcal{S}\begin{pmatrix}\hat{\mathbf{f}}_e \\ \hat{\mathbf{f}}_m\end{pmatrix}, \qquad \mathcal{S}\mathcal{S}^\dagger = \begin{pmatrix}\varepsilon_0\,\mathrm{Im}(\varepsilon - \xi\mu^{-1}\zeta) & (2\mathrm{i}\mu Z_0)^{-1}(\xi - \zeta^*) \\ (2\mathrm{i}\mu Z_0)^{-1}(\zeta - \xi^*) & -\mathrm{Im}(\mu^{-1})/\mu_0\end{pmatrix}, \tag{6}$$

where $Z_0 = \sqrt{\mu_0/\varepsilon_0}$ denotes the impedance of free space. Here and throughout we use the convention that 3×3 matrices in position space (tensors) are represented by 'open-face' symbols ($\mathbb{A}$, $\mathbb{B}$ etc), while 2×2 matrices acting in polarisation or duality space are represented by 'calligraphic' symbols ($\mathcal{A}$, $\mathcal{B}$ etc). The quantities $\hat{\mathbf{f}}_\lambda$ are bosonic quasiparticle excitations satisfying:

$$[\hat{\mathbf{f}}_\lambda(\mathbf{r}, \omega), \hat{\mathbf{f}}^\dagger_{\lambda'}(\mathbf{r}', \omega')] = \delta_{\lambda\lambda'}\delta(\mathbf{r} - \mathbf{r}')\delta(\omega - \omega')\mathbb{I}, \qquad (\lambda = e, m) \tag{7}$$

with all other commutators being zero. From a macroscopic point of view the Casimir force $\mathbf{F}$ between arbitrary bodies can be interpreted as the ground-state expectation value of the Lorentz force, or equivalently by an integral over the Maxwell stress tensor $\hat{\mathbb{T}}$:

$$\mathbf{F} = \int_{\partial V} \mathbf{dA} \cdot \langle\hat{\mathbb{T}}\rangle \tag{8}$$

with ∂V being the boundary of a volume enclosing the body on which the force is to be calculated, and the stress tensor is

$$\hat{\mathbb{T}} = \varepsilon_0\hat{\mathbf{E}} \otimes \hat{\mathbf{E}} + \frac{1}{\mu_0}\hat{\mathbf{B}} \otimes \hat{\mathbf{B}} - \frac{1}{2}\left(\varepsilon_0\hat{\mathbf{E}}^2 + \frac{1}{\mu_0}\hat{\mathbf{B}}^2\right)\mathbb{I}, \tag{9}$$

where the fields are obtained from equation (4) together with $\hat{\mathbf{B}} = (\mathrm{i}\omega)^{-1}\nabla \times \hat{\mathbf{E}}$. We can now evaluate the expectation value in the vacuum state $|\{0\}\rangle$ of the noise current quanta $\hat{\mathbf{f}}_\lambda$ by using $\hat{\mathbf{f}}_\lambda|\{0\}\rangle = 0$ and the

IOP Publishing New J. Phys. 20 (2018) 043024 S Rode et al

commutator (7) above. We will also use an integral relation that can be derived from the definition (3) of the Green's tensor [20, 22]

$$\mathfrak{Im}[\mathbb{G}(\mathbf{r}, \mathbf{r}', \omega)] = \mu_0 \int \mathrm{d}^3\mathbf{s}\mathbb{G}(\mathbf{r}, \mathbf{s}, \omega)(\mathrm{i}\omega, \times\overleftarrow{\nabla}) \cdot \mathcal{S} \cdot \mathcal{S}^\dagger \cdot (\mathrm{i}\omega, \nabla\times)^{\mathrm{T}}\mathbb{G}^{*\mathrm{T}}(\mathbf{r}', \mathbf{s}, \omega)\ , \tag{10}$$

where

$$\mathfrak{Im}[\mathbb{A}] \equiv \frac{1}{2\mathrm{i}}(\mathbb{A} - \mathbb{A}^\dagger) \tag{11}$$

is the generalised imaginary part of a tensor. Employing equation (10) as well as the electric field given by equation (4), one obtains in agreement with [11] the vacuum expectation values of the dyadic products appearing in equation (9) in Fourier space:

$$\langle \hat{\mathbf{E}}(\mathbf{r}, \omega) \otimes \hat{\mathbf{E}}(\mathbf{r}', \omega')\rangle = \frac{\mu_0\omega^2\hbar}{\pi}\mathfrak{Im}[\mathbb{G}(\mathbf{r}, \mathbf{r}', \omega)]\delta(\omega - \omega'). \tag{12}$$

This relation is essentially a form of the fluctuation–dissipation theorem, as first shown under very general conditions in [23]. Its role is to link the field correlations required for evaluation of the quantum stress tensor and the classical Green's function of the medium. Using similar relations for the remaining terms in equation (9), transforming back to position space and rotating to imaginary frequencies u yields

$$\begin{aligned}\langle\hat{\mathbb{T}}\rangle = -\frac{\hbar}{2\pi}\int_0^\infty du \int_{\partial V} dA \cdot \Bigg\{ &\frac{\xi^2}{c^2}[\mathbb{G}^{(1)}(\mathbf{r}, \mathbf{r}, \mathrm{i}u) + \mathbb{G}^{(1)\mathrm{T}}(\mathbf{r}, \mathbf{r}, \mathrm{i}u)] \\ &+ \vec{\nabla} \times [\mathbb{G}^{(1)}(\mathbf{r}, \mathbf{r}', \mathrm{i}u) + \mathbb{G}^{(1)\mathrm{T}}(\mathbf{r}', \mathbf{r}, \mathrm{i}u)] \times \overleftarrow{\nabla}'|_{\mathbf{r}'\to\mathbf{r}} \\ &- \mathrm{tr}\left[\frac{\xi^2}{c^2}[\mathbb{G}^{(1)}(\mathbf{r}, \mathbf{r}, \mathrm{i}u)] + \vec{\nabla} \times [\mathbb{G}^{(1)}(\mathbf{r}, \mathbf{r}', \mathrm{i}u)]\times\overleftarrow{\nabla}'|_{\mathbf{r}'\to\mathbf{r}}\right]\mathbb{I}\Bigg\},\end{aligned} \tag{13}$$

from which the force can be computed by means of equation (8). In this formula the Green's tensor has been replaced by its scattering part $\mathbb{G}^{(1)}$ defined via

$$\mathbb{G} = \mathbb{G}^{(0)} + \mathbb{G}^{(1)}, \tag{14}$$

where $\mathbb{G}^{(0)}$ is the bulk part of the Green's tensor, which does not contribute to the Casimir force regardless of the system's geometry. In addition we exploit the fact that [20]

$$\lim_{|\omega|\to\infty} \mathbb{G}^{(0)}(\mathbf{r}, \mathbf{r}') = \lim_{|\omega|\to\infty} \mathbb{G}(\mathbf{r}, \mathbf{r}') = -\mathbb{I}\delta(\mathbf{r} - \mathbf{r}') \tag{15}$$

which functions as a cutoff for high frequencies, allowing one to obtain a finite result. Note in particular that we did not assume the validity of the Lorentz reciprocity condition $\mathbb{G}(\mathbf{r}, \mathbf{r}', \omega) = \mathbb{G}^{\mathrm{T}}(\mathbf{r}', \mathbf{r}, \omega)$, which is connected with time reversal invariance [20]. We hence have derived an expression for the Casimir force of arbitrary nonreciprocal bodies, which can also be obtained as a particular case of results for general magneto-dielectrics (see, for example, [24, 25]).

3. Bi-isotropic media and PEMCs

In order to obtain a tuneable Casimir force we will consider a class of materials whose reflection behaviour is in some sense intermediate between the extreme cases of the perfect electric conductor (PEC) and perfect magnetic conductor (PMC), which are respectively characterised by infinite permittivity ε or infinite permeability μ. These materials are known as bi-isotropic (see, for example, [18]), and in macroscopic quantum electrodynamics the response of such a medium is conveniently described by four material constants; the familiar ε and μ, as well as two cross-polarizabilities ξ and ζ. In principle all these quantities are permitted to be tensor-valued, which leads to the more general case of bi-anisotropic media. We will confine ourselves to bi-isotropic media, in which the material response shows no direction-dependence. This means that the four material constants are scalar (or pseudo-scalar) valued and fulfil the constitutive relations

$$\hat{\mathbf{D}} = \varepsilon_0\varepsilon\hat{\mathbf{E}} + \frac{1}{c}\xi\hat{\mathbf{H}}, \tag{16}$$

$$\hat{\mathbf{B}} = \mu_0\mu\hat{\mathbf{H}} + \frac{1}{c}\zeta\hat{\mathbf{E}}, \tag{17}$$

where we have chosen our definitions in such a way that all four material constants are dimensionless. For a fundamental theory of linear material response see [26].

IOP Publishing New J. Phys. 20 (2018) 043024 S Rode et al

3.1. Duality transformation

By allowing for nonzero (or even infinite) cross-polarisabilities ξ and ζ we achieve an interpolation between PECs and PMCs. To do this we note that Maxwell's equations for classical fields in media in the absence of free charges of currents can be arranged in the following way

$$\nabla \cdot \begin{pmatrix} Z_0\mathbf{D} \\ \hat{\mathbf{B}} \end{pmatrix} = 0, \tag{18}$$

$$\nabla \times \begin{pmatrix} \mathbf{E} \\ Z_0\mathbf{H} \end{pmatrix} + \mathrm{i}\omega \begin{pmatrix} 0 & 1 \\ -1 & 0 \end{pmatrix} \begin{pmatrix} Z_0\mathbf{D} \\ \mathbf{B} \end{pmatrix} = 0. \tag{19}$$

These equations are invariant under an SO(2) transformation, i.e. they remain valid when the vectors of fields are multiplied with a matrix of the form

$$\mathcal{D} = \begin{pmatrix} \cos(\theta) & \sin(\theta) \\ -\sin(\theta) & \cos(\theta) \end{pmatrix}. \tag{20}$$

The fields forming a vector in this formalism are called dual partners. The constitutive relations for the quantised fields then read [19]

$$\begin{pmatrix} Z_0\hat{\mathbf{D}} \\ \hat{\mathbf{B}} \end{pmatrix} = \frac{1}{c} \begin{pmatrix} \varepsilon & \xi \\ \zeta & \mu \end{pmatrix} \begin{pmatrix} \hat{\mathbf{E}} \\ Z_0\hat{\mathbf{H}} \end{pmatrix} + \begin{pmatrix} 1 & \xi \\ 0 & \mu \end{pmatrix} \begin{pmatrix} Z_0\mathbf{P}_\mathrm{N} \\ \mu_0\mathbf{M}_\mathrm{N} \end{pmatrix}, \tag{21}$$

where the noise polarisation $\hat{\mathbf{P}}_\mathrm{N}$ and magnetisation polarisation $\hat{\mathbf{M}}_\mathrm{N}$ are related to the noise current $\hat{\mathbf{j}}_\mathrm{N}$. Note that in case of reciprocal materials the reduced number of degrees of freedom stemming from having $\xi = -\zeta$ leads to the constraint that θ has to be a integer multiple of $\pi/2$, in which case the continuous symmetry of duality invariance hence reduces to a discrete $\mathbb{Z}_4$-symmetry [19]. The consideration of polarisation of polarisation-mixing material constants ξ and ζ, however, restores the continuity of duality invariance [20].

3.2. Perfect electromagnetic conductors (PEMC)

We will now focus on PEMCs as a special case of bi-isotropic materials. The concept of PEMCs has been introduced by Lindell and Sihvola [17, 27, 28], finding applications in waveguide and antenna engineering [29]. At a boundary with normal vector $\mathbf{n}$ the PEMC reflection properties are defined via

$$\mathbf{n} \cdot (Z_0\mathbf{D} - M\mathbf{B}) = 0, \tag{22}$$

$$\mathbf{n} \times (Z_0\mathbf{H} + M\mathbf{E}) = 0. \tag{23}$$

They show a transmission-free, polarisation-mixing reflection behaviour [17]. The pseudoscalar material parameter M interpolates between PEC ($M \to \infty$) and PMC ($M = 0$ boundaries). We can now relate M to the magnetoelectric material constants introduced in the previous section by comparing equations (22) and (23) with the general constitutive relations (21). One arrives at

$$\xi = \zeta = \pm\sqrt{\mu\varepsilon}\,, \tag{24}$$

$$M = \frac{\xi}{\mu} = \pm\sqrt{\frac{\varepsilon}{\mu}} \tag{25}$$

in the limit $\mu \to \infty$, $\varepsilon \to \infty$, with M being finite. In other words, a PEMC is a very specific limiting case of a bi-isotropic medium with a strong response. Though it is not obvious from equations (24) and (25), these equations are consistent with reciprocal media for the PEC ($\varepsilon \to \infty$, ζ, $\xi \ll \varepsilon$) and PMC ($\mu \to \infty$, ζ, $\xi \ll \mu$) limits, as detailed in [17]. As pointed out by Dzyaloshinskii [30] and further investigated in [31], Cr_2O_3 is a naturally occurring crystal with a weak nonreciprocal cross-polarisability. The close analogy of such an electromagnetic response with that of the PEMC as well as the Tellegen medium and the axion field in particle physics is also discussed in [32]

PEMC materials can be seen as the dual transform of a PEC by a finite duality transformation angle θ. Transforming the PEC-boundary conditions

$$\mathbf{n} \cdot \mathbf{B}^* = \mathbf{n} \cdot [-\sin(\theta)Z_0\mathbf{D} + \cos(\theta)\mathbf{B}] = 0, \tag{26}$$

$$\mathbf{n} \times \mathbf{E}^* = \mathbf{n} \times [\sin(\theta)Z_0\mathbf{H} + \cos(\theta)\mathbf{E}] = 0 \tag{27}$$

directly gives equations (22) and (23) if the identification

$$M = \cot(\theta) \tag{28}$$

is made and the positive sign in equations (24) and (25) is taken. This means that the PEC case corresponds to $\theta = 0$ and the PMC case to $\theta = \pi/2$, with all other cases appearing for intermediate angles in the range $(0, \pi/2)$. If the negative sign were included in equations (24) and (25), the angle θ would instead be equal to $-\pi/2$ for the PMC, running to $\theta = 0$ for the PEC.

IOP Publishing New J. Phys. 20 (2018) 043024 S Rode et al

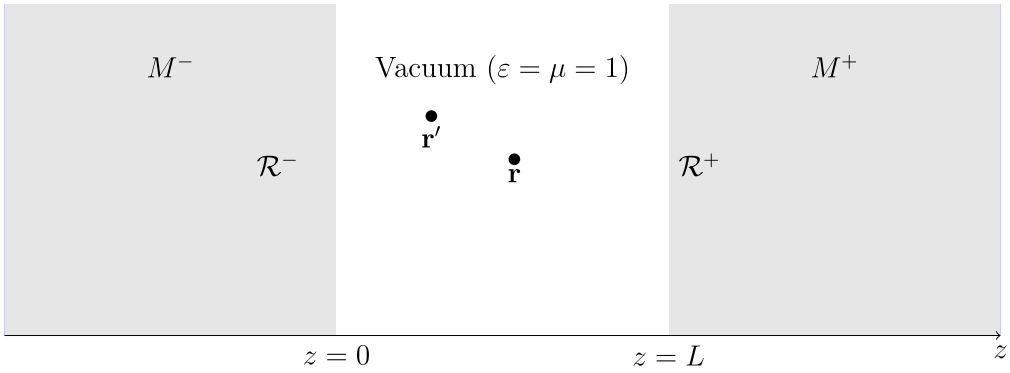

Figure 1. Three-layer system with perfectly reflecting, cross-polarising boundary surfaces at $z = 0$ and $z = L$.

4. The Green's tensor of two PEMC plates

In order to apply our general result (13) to two PEMC plates, we first need to find the respective Green's tensor for the setup specified in figure 1.

4.1. General structure of the Green's tensor

The reflection properties of a nonreciprocal plate are described by four reflection coefficients r_{ss}, r_{sp}, r_{ps}, r_{pp} corresponding to all possible combinations of the polarisation directions (s or p) of the incoming and outgoing light. Here the index p denotes an electric field polarisation parallel to the plane of incidence (transverse-magnetic (TM) polarisation), while s indicates perpendicular polarisation (transverse-electric (TE) polarisation). The reflected wave $\mathbf{v}_{\text{refl}}$ corresponding to a general incident wave $\mathbf{v}_{\text{inc}}$ at a boundary described by these four coefficients can therefore be represented as a matrix multiplication:

$$\mathbf{v}_{\text{refl}} = \mathcal{R} \cdot \mathbf{v}_{\text{inc}} = \begin{pmatrix} r_{ss} & r_{sp} \\ r_{ps} & r_{pp} \end{pmatrix} \cdot \begin{pmatrix} v_s \\ v_p \end{pmatrix}. \tag{29}$$

A setup consisting of two plates is considered as a three-layer system, where we require the Green's tensor for all positions in the middle layer. This consists of waves travelling from $\mathbf{r}$ to $\mathbf{r}'$ and being reflected any number of times, which can be elegantly taken into account by means of a Neumann series, as is well-known (see, for example, [33]). For matrices $\mathcal{R}^{\pm}$ representing two plates being located at $z = 0$ ($\mathcal{R}^-$) and $z = L$ ($\mathcal{R}^+$) respectively we define

$$\mathcal{D}^{\pm}_{\sigma_i\sigma_j} = \left[\sum_{n=0}^{\infty} (\mathcal{R}^{\pm} \cdot \mathcal{R}^{\mp})^n \cdot (\mathrm{e}^{-2\mathrm{i}k^{\perp}L})^n\right]_{\sigma_i\sigma_j} = (\mathcal{I} - \mathcal{R}^{\pm} \cdot \mathcal{R}^{\mp}\mathrm{e}^{-2\mathrm{i}k^{\perp}L})^{-1}_{\sigma_i\sigma_j} \tag{30}$$

with σ_i, σ_j denoting the polarisation directions s and p and $\mathcal{I}$ is the two-dimensional identity matrix. Using the general form of the Green's tensor we obtain the result

$$\begin{aligned} \mathbb{G}^{(1)}(\mathbf{r}, \mathbf{r}', \omega) \;=\; & \frac{1}{8\pi^2} \int \frac{\mathrm{d}^2k^{\parallel}}{k^{\perp}} \mathrm{e}^{\mathrm{i}\mathbf{k}^{\parallel}(\mathbf{r}-\mathbf{r}')} \\ & \times [\mathbf{e}^{+} \cdot \mathcal{R}^{+} \cdot (\mathcal{D}^{-})^{-1} \cdot \mathcal{R}^{-} \cdot \mathbf{e}^{+\mathrm{T}} \mathrm{e}^{\mathrm{i}k^{\perp}(2L+z-z')} + \mathbf{e}^{-} \cdot \mathcal{R}^{-} \cdot (\mathcal{D}^{+})^{-1} \cdot \mathcal{R}^{+} \cdot \mathbf{e}^{-\mathrm{T}} \mathrm{e}^{\mathrm{i}k^{\perp}(2L-z+z')} \\ & + \mathbf{e}^{-} \cdot \mathcal{R}^{-} \cdot (\mathcal{D}^{+})^{-1} \cdot \mathbf{e}^{+\mathrm{T}} \mathrm{e}^{\mathrm{i}k^{\perp}(z+z')} + \mathbf{e}^{+} \cdot \mathcal{R}^{+} \cdot (\mathcal{D}^{-})^{-1} \cdot \mathbf{e}^{-\mathrm{T}} \mathrm{e}^{\mathrm{i}k^{\perp}(2L-z-z')}], \end{aligned} \tag{31}$$

where $\mathbf{e}^{\pm} = (\mathbf{e}^{\pm}_s, \mathbf{e}^{\pm}_p)$, with

$$\mathbf{e}^{\mp}_s = \mathbf{e}^{\mp}_s = \mathbf{e}_{k^{\parallel}} \times \mathbf{e}_z, \quad \mathbf{e}^{\mp}_p = 1/k(k^{\parallel}\mathbf{e}_z \mp k^{\perp}\mathbf{e}_{k^{\parallel}}) \quad \mathbf{k} = k^{\parallel}\mathbf{e}_{k^{\parallel}} + k^{\perp}\mathbf{e}_{k^{\perp}}. \tag{32}$$

Note that the matrix multiplication is performed in (s, p)-space. The Green's tensor's spatial components are obtained by the outer product of the respective polarisation vectors. In this expression the first two terms account for an even number of multiple reflections between $\mathbf{r}$ and $\mathbf{r}'$, while odd numbers of reflections contribute to the final two terms. Similarly to the case of reciprocal materials [21], it turns out that the terms representing an odd number of reflections do not contribute to the Casimir force.

IOP Publishing New J. Phys. 20 (2018) 043024 S Rode et al

4.2. PEMC reflection matrices

The boundary conditions (22) and (23) for the fields lead to polarisation-mixing effects at a PEMC boundary. In terms of the magnetoelectric constants these reflection coefficients for radiation incident from medium 1 onto medium 2 are given by [10]

$$r_{ss} = \frac{(k_1^\perp - \mu k_2^\perp)\Omega_\varepsilon - k_1^\perp k_2^\perp \xi^2}{(k_1^\perp + \mu k_2^\perp)\Omega_\varepsilon + k_1^\perp k_2^\perp \xi^2}, \tag{33}$$

$$r_{ps} = \frac{-2\mu k_1^\perp k_2^\perp \xi}{(k_1^\perp + \mu k_2^\perp)\Omega_\varepsilon + k_1^\perp k_2^\perp \xi^2} = r_{sp}, \tag{34}$$

$$r_{pp} = \frac{\left[k_1^\perp - \left(\varepsilon - \frac{\xi^2}{\mu}\right)k_2^\perp\right]\Omega_\mu - k_1^\perp k_2^\perp \xi^2}{\left[k_1^\perp + \left(\varepsilon - \frac{\xi^2}{\mu}\right)k_2^\perp\right]\Omega_\mu + k_1^\perp k_2^\perp \xi^2}, \tag{35}$$

with $\Omega_\mu = \mu(k_1^\perp + \mu k_2^\perp)$, $\Omega_\varepsilon = \mu[k_1^\perp + (\varepsilon - \xi^2/\mu)k_2^\perp]$ and $k_i^\perp$ representing the component of the wave vector perpendicular to the interface. In the PEMC-limit, with all response functions going to infinity and $M = \sqrt{\varepsilon/\mu}$, one obtains in matrix form:

$$\mathcal{R} = \begin{pmatrix} r_{ss} & r_{sp} \\ r_{ps} & r_{pp} \end{pmatrix} = \frac{1}{1+M^2}\begin{pmatrix} 1-M^2 & -2M \\ -2M & M^2-1 \end{pmatrix} \tag{36}$$

which is independent of the incoming wave vector.

Introducing the corresponding duality transformation angle θ via equation (28), one obtains for two plates:

$$\mathcal{R}^\pm = \begin{pmatrix} -\cos(2\theta^\pm) & \sin(2\theta^\pm) \\ \sin(2\theta^\pm) & \cos(2\theta^\pm) \end{pmatrix} \tag{37}$$

with $\theta^\pm$ being the respective duality transformation angle that defines the properties of each plate. We can now also calculate the corresponding multiple-reflection contributions to obtain

$$(\mathcal{D}^\pm)^{-1} = \frac{b}{1 - 2b\cos(2\delta) + b^2}\begin{pmatrix} b - \cos(2\delta) & \sin(2\delta) \\ -\sin(2\delta) & b - \cos(2\delta) \end{pmatrix} \tag{38}$$

with $b = \mathrm{e}^{-2\mathrm{i}k^\perp L}$ and $\delta = \theta^+ - \theta^-$.

5. Casimir force between two PEMC plates

In order to solve the Green's tensor integral we introduce polar coordinates $(k^\parallel, \varphi)$ for the two-dimensional integral over $\mathbf{k}^\parallel$. This simplifies the calculation considerably because the reflection matrices as well as $D^\pm$ and $D^\mp$ do not depend on φ, the angular dependence appears only in the dyadic product of the polarisation vectors, which may be straightforwardly integrated.

We can compute a force $\mathrm{d}\mathbf{F}/\mathrm{d}A$ per unit area from the stress tensor via equation (8). Making use of the fact that $\mathrm{d}\mathbf{A} \| \mathbf{e}_z$, we have

$$\begin{aligned} \mathbf{f} = \frac{\mathrm{d}\mathbf{F}}{\mathrm{d}A} &= -\frac{1}{A}\int_{\partial V} \mathrm{d}\mathbf{A} \cdot \langle \mathbb{T} \rangle \\ &= -\frac{\hbar}{2\pi}\int_0^\infty \mathrm{d}u \sum_{j=x,y,z} (\langle \mathbb{T} \rangle_{jz}\, \mathbf{e}_j)\Big|_{z=L}, \end{aligned} \tag{39}$$

where $\langle \mathbb{T} \rangle$ is given by (13). The symmetry of the problem requires that $\mathbf{f}$ has no x- or y- components which can indeed be seen from the fact that no combination of the polarisation vectors yields a x–z- or y–z-component when integrated over φ. We will hence suppress the fact that $\mathbf{f}$ is a vector and just calculate its absolute value.

We now insert our obtained Green's tensor (31) into (13) and observe that the contributions from the terms containing curls equal the contributions from those without. After setting $\kappa = \mathrm{i}k^\perp$, transforming to polar co-ordinates $k^\parallel = \kappa\cos(\phi)$, $u/c = \kappa\sin(\phi)$ and carrying out the trivial angular integration we get

$$f = \frac{\hbar c}{4\pi^2}\int_0^\infty \mathrm{d}\kappa\ \kappa^3\ \mathrm{e}^{-2\kappa L}\,\mathrm{Tr}\,[\mathcal{R}^+ \cdot (\mathcal{D}^-)^{-1} \cdot \mathcal{R}^- + \mathcal{R}^- \cdot (\mathcal{D}^+)^{-1} \cdot \mathcal{R}^+]. \tag{40}$$

This generalisation of Lifshitz's formula for planar systems [34] agrees with results for reciprocal polarisation-mixing plates such as gratings [35–37], which is itself a consequence of the general validity of the fluctuation–dissipation theorem. Remarkably, the result is hence insensitive to the fact that the plates are non-reciprocal at this level.

IOP Publishing New J. Phys. 20 (2018) 043024 S Rode et al

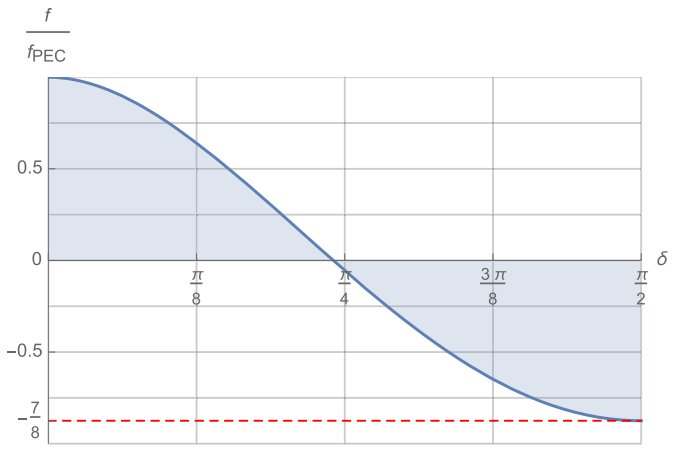

Figure 2. Casimir force between two PEMC plates normalised to the original result of Casimir in terms of their duality phase shift $\delta = \theta^+ - \theta^-$.

Substituting $x = \kappa L$ and performing the matrix multiplications we find the following integral

$$f = -\frac{\hbar c}{\pi^2 L^4}\int_0^\infty \mathrm{d}x\; x^3 \frac{\mathrm{e}^{2x}\cos(2\delta) - 1}{1 - 2\mathrm{e}^{2x}\cos(2\delta) + \mathrm{e}^{4x}}$$
$$= -\frac{\hbar c}{\pi^2 L^4}\int_0^\infty \mathrm{d}x\; x^3 \left(\frac{\frac{1}{2}\mathrm{e}^{2x}(\mathrm{e}^{2\mathrm{i}\delta} + \mathrm{e}^{-2\mathrm{i}\delta})}{(1 - \mathrm{e}^{2x}\mathrm{e}^{2\mathrm{i}\delta})(1 - \mathrm{e}^{2x}\mathrm{e}^{-2\mathrm{i}\delta})} - \frac{1}{(1 - \mathrm{e}^{2x}\mathrm{e}^{2\mathrm{i}\delta})(1 - \mathrm{e}^{2x}\mathrm{e}^{-2\mathrm{i}\delta})} \right) \tag{41}$$

which can be analytically integrated to finally obtain our main result

$$f(\theta^+, \theta^-) = -\frac{3\hbar c}{8\pi^2 L^4}\,\mathrm{Re}\,(\mathrm{Li}_4[\mathrm{e}^{2\mathrm{i}(\theta^+ - \theta^-)}]), \tag{42}$$

where we have made use of the polylogarithm function $\mathrm{Li}_n(z) = \sum_{k=1}^\infty z^k/k^n$. Our result (42) immediately demonstrates an invariance of the Casimir force under duality transforms of material parameters; it only depends on the difference of the PEMC angles, so a simultaneously applied duality transformation does not change the Casimir force. Thus we may write $f(\theta^+, \theta^-) = f(\theta^+ - \theta^-) = f(\delta)$. We can easily check that this is indeed compatible with the results of Casimir and Boyer via

$$\mathrm{Re}\;\mathrm{Li}_4(\mathrm{e}^{\mathrm{i}\phi}) = \sum_{k=1}^\infty \frac{\cos^k(k\phi)}{k^4} = \frac{\pi^4}{90} - \frac{\pi^2\phi^2}{12} + \frac{\pi\phi^3}{12} - \frac{\phi^4}{48}, \tag{43}$$

where we used de Moivre's identity followed by formula (27.8.6(3)) of [38] (see also [39], (25.12(ii))), giving

$$f(\delta) = -\frac{\hbar c}{8\pi^2 L^4}\left[\frac{\pi^4}{30} - \delta^2(\pi - \delta)^2\right]. \tag{44}$$

Then we obtain the special cases of Casimir ($\delta = 0$, corresponding to any choice of identical plates)

$$f(0) = -\frac{\hbar c}{240\pi^2 L^4} \tag{45}$$

and Boyer ($\delta = \pi/2$)

$$f(\pi/2) = \frac{7}{8}\cdot\frac{\hbar c}{240\pi^2 L^4}. \tag{46}$$

We show the results for intermediate angles in figure 2. It is seen that there is some value δ_{crit} for which there is no Casimir force, solving equation (44) for this gives

$$\delta_{\mathrm{crit}} = \frac{\pi}{2}\left(1 - \sqrt{1 - 2\sqrt{\frac{2}{15}}}\right) \approx 0.96\cdot\frac{\pi}{4}. \tag{47}$$

In the case of a scalar field under Robin boundary conditions, it has previously been shown numerically that such a 'zero-force' parameter exists between the extreme cases of attraction and repulsion [14], here we extend this to the electromagnetic field as well as finding an analytic value for δ_{crit}. It is also interesting to notice that the following holds

IOP Publishing New J. Phys. 20 (2018) 043024 S Rode et al

$$\int_0^{\pi/2} \mathrm{d}\delta f(\delta) = 0, \tag{48}$$

so even though the force is not symmetric around the central angle $\delta = \pi/4$, the enclosed areas to the left and the right of the zero-force angle δ_{crit} are equal. Thus our result represents a sum rule for the Casimir force for PEMCs; the sum of Casimir forces over the entire PEMC parameter space is zero.

6. Conclusion

In order to calculate the Casimir force between two PEMC plates we have constructed the Green's tensor for two nonreciprocal plates in terms of their reflection properties. The result is duality invariant as well as it is compatible with the theorem derived by Kenneth and Klich that the Casimir force between identical bodies is always attractive [8]. It also verifies for a certain class of local nonreciprocal media described in section 2 the prediction that the Casimir force between two plates of any possible material will fall in between the results of Casimir and Boyer [7], which had thus far only been shown for magnetodielectrics. The derived Green's tensor is hence also applicable for different lossless material classes. In particular the focus might go to perfectly reflecting chiral materials ($\xi = -\zeta$ in terms of material constants) to explore the full parameter space of the Casimir effect.

For more realistic scenarios of course the corrections due to imperfect reflection or non-zero temperature are of high interest. For these cases the derived PEMC case can be viewed as a theoretical upper limit for the Casimir force since we assumed the reflection coefficients as well as the PEMC parameter to be frequency independent, and calculated the force at zero temperature. In less idealised cases one would expect the resulting Casimir force to lie somewhere 'under the curve' for the respective value of θ.

Acknowledgments

We would like to thank F Hehl for inspiring this work and S Fuchs, F Lindel, A Sihvola, C Henkel and M Bordag for stimulating discussions. The authors would like to thank an anonymous referee for a large number of constructive comments. We acknowledge financial support from the Deutsche Forschungsgemeinschaft via grants BU1803/3-1 and GRK 2079/1. RB and SYB additionally acknowledge support from the Alexander von Humboldt foundation, and SYB acknowledges support from the Freiburg Institute of Advanced Studies (FRIAS).

References

[1] Casimir H B G 1948 On the attraction between two perfectly conducting plates *Proc. K. Ned. Akad.* **360** 793–5
[2] Serry F M, Walliser D and Maclay G J 1995 The anharmonic Casimir oscillator (ACO)-the Casimir effect in a model microelectromechanical system *J. Microelectromech. Syst.* **4** 193–205
[3] Tas N, Sonnenberg T, Jansen H, Legtenberg R and Elwenspoek M 1996 Stiction in surface micromachining *J. Micromech. Microeng.* **6** 385–97
[4] Buks E and Roukes M L 2001 Stiction, adhesion energy, and the Casimir effect in micromechanical systems *Phys. Rev.* B **63** 033402
[5] Woods L M, Dalvit D A R, Tkatchenko A, Rodriguez-Lopez P, Rodriguez A W and Podgornik R 2016 Materials perspective on Casimir and van der Waals interactions *Rev. Mod. Phys.* **88** 045003
[6] Boyer T H 1974 Van der Waals forces and zero-point energy for dielectric and permeable materials *Phys. Rev.* A **9** 2078–84
[7] Henkel C and Joulain K 2005 Casimir force between designed materials: what is possible and what not *Europhys. Lett.* **72** 929–35
[8] Kenneth O, Klich I, Mann A and Revzen M 2002 Repulsive casimir forces *Phys. Rev. Lett.* **89** 033001
[9] Grushin A G and Cortijo A 2011 Tunable Casimir repulsion with three-dimensional topological insulators *Phys. Rev. Lett.* **106** 020403
[10] Fuchs S, Crosse J A and Buhmann S Y 2017 Casimir–Polder shift and decay rate in the presence of nonreciprocal media *Phys. Rev.* A **95** 023805
[11] Butcher D T, Buhmann S Y and Scheel S 2012 Casimir–Polder forces between chiral objects *New J. Phys.* **14** 113013
[12] Rosa F S S, Dalvit D A R and Milonni P W 2008 Casimir–Lifshitz theory and metamaterials *Phys. Rev. Lett.* **100** 183602
[13] Asorey M and Muñoz-Castañeda J M 2013 Attractive and repulsive Casimir vacuum energy with general boundary conditions *Nucl. Phys.* B **874** 852–76
[14] Romeo A and Saharian A A 2002 Casimir effect for scalar fields under Robin boundary conditions on plates *J. Phys. A. Math. Gen.* **35** 1297–320
[15] Markov V N and Pis'mak Y M 2006 Casimir effect for thin films in QED *J. Phys. A. Math. Gen.* **39** 6525–32
[16] Marachevsky V N 2017 Casimir effect for Chern–Simons layers in the vacuum *Theor. Math. Phys.* **190** 315–20
[17] Lindell I V and Sihvola A H 2005 Perfect electromagnetic conductor *J. Electromagn. Waves Appl.* **19** 861–9
[18] Serdyukov A, Semchenko I, Tretyakov S and Sihvola A 2001 *Electromagnetics of Bi-Anisotropic Materials: Theory and Applications* (Amsterdam: Gordon and Breach Science)
[19] Buhmann S Y and Scheel S 2009 Macroscopic quantum electrodynamics and duality *Phys. Rev. Lett.* **102** 140404
[20] Buhmann S Y, Butcher D T and Scheel S 2012 Macroscopic quantum electrodynamics in nonlocal and nonreciprocal media *New J. Phys.* **14** 083034
[21] Buhmann S Y 2012 *Dispersion Forces I—Macroscopic Quantum Electrodynamics and Ground-state Casimir, Casimir–Polder and van der Waals Forces* (*Springer Tracts in Modern Physics* vol 247) (Berlin: Springer)
[22] Eckhardt W 1982 First and second fluctuation–dissipation-theorem in electromagnetic fluctuation theory *Opt. Commun.* **41** 305–9

[23] Agarwal G S 1975 Quantum electrodynamics in the presence of dielectrics and conductors: I. Electromagnetic-field response functions and black-body fluctuations in finite geometries *Phys. Rev.* A **11** 230–42
[24] Kheirandish F, Soltani M and Sarabadani J 2010 Casimir force in the presence of a medium *Phys. Rev.* A **81** 052110
[25] Philbin T G 2011 Casimir effect from macroscopic quantum electrodynamics *New J. Phys.* **13** 063026
[26] Hehl F W and Obukhov Y N 2003 *Foundations of Classical Electrodynamics: Charge, Flux, and Metric* (Basel: Birkhäuser)
[27] Lindell I V and Sihvola A H 2005 Transformation method for problems involving perfect electromagnetic conductor (PEMC) structures *IEEE Trans. Antennas Propag.* **53** 3005–11
[28] Lindell I V and Sihvola A H 2005 Realization of the PEMC boundary *IEEE Trans. Antennas Propag.* **53** 3012–8
[29] Sihvola A H and Lindell I V 2008 Perfect electromagnetic conductor medium *Ann. Phys.* **17** 787–802
[30] Dzyaloshinskii I E 1960 On the magneto-electrical effect in antiferromagnets *J. Exp. Theor. Phys.* **37** 881
[31] Hehl F W, Obukhov Y N, Rivera J-P and Schmid H 2008 Relativistic analysis of magnetoelectric crystals: extracting a new 4-dimensional P odd and T odd pseudoscalar from Cr_2O_3 data *Phys. Lett.* A **372** 1141–6
[32] Zhang R Y, Zhai Y W, Lin S R, Zhao Q, Wen W and Ge M L 2015 Time circular birefringence in time-dependent magnetoelectric media *Sci. Rep.* **5** 13673
[33] Chew W 1995 *Waves and Fields in Inhomogeneous Media* (Piscataway, NJ: IEEE)
[34] Lifshitz E M 1956 The theory of molecular attractive forces between solids *J. Exp. Theor. Phys.* **2** 73–83
[35] Lambrecht A and Marachevsky V N 2008 Casimir interaction of dielectric gratings *Phys. Rev. Lett.* **101** 160403
[36] Contreras-Reyes A M, Guérout R, Maia Neto P A, Dalvit D A R, Lambrecht A and Reynaud S 2010 Casimir–Polder interaction between an atom and a dielectric grating *Phys. Rev.* A **82** 052517
[37] Bender H, Stehle C, Zimmermann C, Slama S, Fiedler J, Scheel S, Buhmann S Y and Marachevsky V N 2014 Probing atom-surface interactions by diffraction of Bose–Einstein condensates *Phys. Rev.* X **4** 011029
[38] Abramowitz M and Stegun I A 1970 *Handbook of Mathematical Functions: With Formulas, Graphs, and Mathematical tables* (New York: Dover)
[39] Olver F W J *et al NIST Digital Library of Mathematical Functions*, http://dlmf.nist.gov/, (Release 1.0.16 of 2017-09-18)

PHYSICAL REVIEW A **96**, 062505 (2017)

Casimir-Lifshitz force for nonreciprocal media and applications to photonic topological insulators

Sebastian Fuchs,[1,2] Frieder Lindel,[1,2] Roman V. Krems,[2] George W. Hanson,[3] Mauro Antezza,[4,5] and Stefan Yoshi Buhmann[1,6]

[1]*Physikalisches Institut, Albert-Ludwigs-Universität Freiburg, Hermann-Herder-Straße 3, 79104 Freiburg, Germany*

[2]*Department of Chemistry, University of British Columbia, Vancouver, British Columbia V6T 1Z1, Canada*

[3]*Department of Electrical Engineering, University of Wisconsin-Milwaukee, 3200 North Cramer Street, Milwaukee, Wisconsin 53211, USA*

[4]*Laboratoire Charles Coulomb, UMR 5221 Université de Montpellier and CNRS, F-34095 Montpellier, France*

[5]*Institut Universitaire de France, 1 rue Descartes, F-75231 Paris Cedex 05, France*

[6]*Freiburg Institute for Advanced Studies, Albert-Ludwigs-Universität Freiburg, Albertstraße 19, 79104 Freiburg, Germany*

(Received 14 July 2017; published 14 December 2017)

Based on the theory of macroscopic quantum electrodynamics, we generalize the expression of the Casimir force for nonreciprocal media. The essential ingredient of this result is the Green's tensor between two nonreciprocal semi-infinite slabs, including a reflexion matrix with four coefficients that mixes optical polarizations. This Green's tensor does not obey Lorentz's reciprocity and thus violates time-reversal symmetry. The general result for the Casimir force is analyzed in the retarded and nonretarded limits, concentrating on the influences arising from reflections with or without change of polarization. In a second step, we apply our general result to a photonic topological insulator whose nonreciprocity stems from an anisotropic permittivity tensor, namely InSb. We show that there is a regime for the distance between the slabs where the magnitude of the Casimir force is tunable by an external magnetic field. Furthermore, the strength of this tuning depends on the orientation of the magnetic field with respect to the slab surfaces.

DOI: 10.1103/PhysRevA.96.062505

I. INTRODUCTION

The Casimir force in its original meaning is an attractive force between two parallel, uncharged, and conducting plates in vacuum. In quantum field theory this effect can be traced back to vacuum fluctuations of the electromagnetic field. Thus, Casimir [1] originally computed the force between two perfectly conducting plates based on vacuum field fluctuations. This force scales as $1/z^4$, where z is the distance between the plates. Here, we explore how the Casimir force is modified for nonreciprocal medium and if, in the case of topological insulators, it can be tuned by a magnetic field. This work is stimulated by recent progress of the experiments aimed at the study of the quantum Hall effect, topological insulators, and nonreciprocal materials in general [2]. The unusual optical properties of nonreciprocal materials have, to the best of our knowledge, not been taken into account in previous treatments of dispersion interactions. Yet, they may change the sign and/or the scaling of the Casimir force. The theory derived here provides a general framework for the analysis of the Casimir force in a variety of experimentally relevant setups.

We compute the Casimir force as the ground-state expectation value of the Lorentz force between two bodies characterized by the charge density and the current density [3]. The electric field and the charge density are mutually correlated since a fluctuating charge density induces fluctuating electric fields and vice versa. This process intertwining the fluctuating charge density and the electric field is responsible for the occurrence of a nonvanishing net force between two bodies, namely the Casimir force. The same applies to the current density and the magnetic field. The Lifshitz approach [4] considers two dielectric half spaces, which show randomly fluctuating polarizations. It is noteworthy that the ground-state expectation values of the electric field, the magnetic field, the charge density, and the current density vanish. In the absence of correlations, the expectation value of the Lorentz force would vanish and there would be no net force.

We apply the theory of macroscopic quantum electrodynamics (QED), which incorporates the influence of material properties by a permittivity and a permeability [3,5,6] to compute the Casimir force. The Green's tensor represents the propagator between the fluctuating noise currents and the quantized electric and magnetic fields. Using this theory, the Casimir force for magnetodielectric bodies has been computed in Ref. [7]. The theoretical extension of macroscopic (QED) for arbitrary nonlocal and nonreciprocal linear media was carried out in Refs. [8,9]. In the case of nonreciprocal media, the electric and magnetic fields are coupled in a way that violates time-reversal symmetry [9]. In QED this means that the electric field fluctuations and their source, namely noise currents, are not interchangeable. Thus, the Green's tensor violates Lorentz's reciprocity principle [10,11].

We consider two semi-infinitely extended plates with a separation of length L and the respective Green's tensor contains four contributions from an even and an odd number of reflections for outgoing waves to the right and the left direction [12,13]. This result for the Green's tensor is extended to nonreciprocal materials. After deriving a general expression for the Casimir force in nonreciprocal media, we apply the result to a photonic topological insulator. Whereas the axion topological insulator, cf. Refs. [2,14–16], couples electric and magnetic fields by a quantized axion coupling, which is usually much smaller than the electric and magnetic properties of the material, the photonic topological insulator [17] shows an anisotropic permittivity, which is responsible for the nonreciprocity of the material. According to Ref. [9], a dielectric material is reciprocal if the permittivity is a symmetric tensor. This is not typically given in case of the anisotropic permittivity of a photonic topological insulator which hence violates Lorentz's reciprocity principle. To calculate the Casimir force, we compute the reflection coefficients for the material with a general approach for biaxial, anisotropic magnetodielectrics [18]. We also analyze the dependence of a

static magnetic field on the Casimir force. In this context, the influence of the surface phonon and surface plasmon polaritons on the heat transfer has been studied for aluminum in Ref. [19] and for InSb in Ref. [20].

This paper is structured as follows: The basic principles and expressions of macroscopic QED for nonreciprocal media are outlined in Sec. II. Due to the violation of Lorentz's reciprocity principle, new definitions for the real and imaginary parts of the Green's tensor are introduced and a generalized Helmholtz equation containing a conductivity tensor is presented. Section III generalizes the concept of Casimir force based on the Lorentz force for nonreciprocal media, where Lorentz's reciprocity does not hold anymore. Section IV is dedicated to the derivation of the Green's tensor for two semi-infinite and nonreciprocal half-spaces. The final result is given in terms of reflection matrices comprising four types of reflection coefficients with equal and alternating polarization. Afterwards, the Green's tensor is used to compute the Casimir force for this geometry. Section V explains the anisotropic structure of the permittivity of the photonic topological insulator and outlines the material properties of the permittivity for InSb. Moreover, it provides the reflection coefficients for the photonic topological insulator. Finally, Sec. VI shows analytical results for the Casimir force in the nonretarded limit and analyzes the retarded limit for a medium with anisotropic permittivity. In the second part the dependence of the Casimir force on the magnetic field is studied. The impact of the diagonal and off-diagonal elements of the reflection matrix on the force as well as the change of sign of the field is discussed. It is pointed out how the external magnetic field changes the main contributions of the Casimir force from surface phonon and surface plasmon polaritons to hyperbolic modes.

II. MACROSCOPIC QED FOR NONRECIPROCAL MEDIA

The theory of macroscopic QED, cf. Refs. [3,21], incorporates material properties in terms of the macroscopic permittivity and permeability. This theory is consistent with the classical theory of macroscopic electrodynamics and satisfies Maxwell's equations, the fluctuation-dissipation theorem and free-space quantum electrodynamics. In contrast to the case of a reciprocal material, time-reversal symmetry is not preserved in nonreciprocal media. To account for this, the mathematical framework has to be adjusted [9].

Lorentz's reciprocity principle for tensors, e.g., the Green's tensor $\mathbf{G}$, does not allow for the violation of time-reversal symmetry, which can be expressed as

$$\mathbf{G}^{\mathrm{T}}(\mathbf{r}',\mathbf{r},\omega) \neq \mathbf{G}(\mathbf{r},\mathbf{r}',\omega). \tag{1}$$

Physically, this means that in a nonreciprocal material a source at $\mathbf{r}'$ does not create the same field at $\mathbf{r}$ that a source at $\mathbf{r}$ would create at $\mathbf{r}'$. A consequence of the breaking of this essential principle is the new definition of real and imaginary parts of a tensor,

$$\begin{aligned}\Re[\mathbf{G}(\mathbf{r},\mathbf{r}',\omega)] &= \frac{1}{2}[\mathbf{G}(\mathbf{r},\mathbf{r}',\omega) + \mathbf{G}^{*\mathrm{T}}(\mathbf{r}',\mathbf{r},\omega)],\\ \Im[\mathbf{G}(\mathbf{r},\mathbf{r}',\omega)] &= \frac{1}{2i}[\mathbf{G}(\mathbf{r},\mathbf{r}',\omega) - \mathbf{G}^{*\mathrm{T}}(\mathbf{r}',\mathbf{r},\omega)].\end{aligned} \tag{2}$$

In the following, the expressions for Ohm's law, the Helmholtz equations, and the electric and magnetic field terms have to be redefined to account for the peculiarities of nonreciprocal materials.

Ohm's law describes the linear response of matter in an external electromagnetic field and reads in frequency space

$$\hat{\mathbf{j}}_{\mathrm{in}}(\mathbf{r},\omega) = \int d^3r' \mathbf{Q}(\mathbf{r},\mathbf{r}',\omega)\cdot\hat{\mathbf{E}}(\mathbf{r}',\omega) + \hat{\mathbf{j}}_{\mathrm{N}}(\mathbf{r},\omega). \tag{3}$$

This term is a convolution of the conductivity tensor $\mathbf{Q}(\mathbf{r},\mathbf{r}',\omega)$ and the quantized electric field $\hat{\mathbf{E}}(\mathbf{r}',\omega)$. $\hat{\mathbf{j}}_{\mathrm{in}}$ represents the internal current density and $\hat{\mathbf{j}}_{\mathrm{N}}(\mathbf{r},\omega)$ is the noise current density. Broken reciprocity now states that $\mathbf{Q}^{\mathrm{T}}(\mathbf{r}',\mathbf{r},\omega) \neq \mathbf{Q}(\mathbf{r},\mathbf{r}',\omega)$. By making use of Ohm's law (3), the continuity relation in the frequency domain combining the noise charge density $\hat{\rho}_{\mathrm{in}}$ and the noise current density $\hat{\mathbf{j}}_{\mathrm{in}}$, $i\omega\hat{\rho}_{\mathrm{in}}(\mathbf{r},\omega) = \overrightarrow{\nabla}\cdot\hat{\mathbf{j}}_{\mathrm{in}}(\mathbf{r},\omega)$, and Maxwell's equations in the frequency domain,

$$\begin{aligned}\overrightarrow{\nabla}\cdot\hat{\mathbf{E}}(\mathbf{r},\omega) &= \frac{\hat{\rho}_{\mathrm{in}}(\mathbf{r},\omega)}{\epsilon_0},\\ \overrightarrow{\nabla}\cdot\hat{\mathbf{B}}(\mathbf{r},\omega) &= 0,\\ \overrightarrow{\nabla}\times\hat{\mathbf{E}}(\mathbf{r},\omega) - i\omega\hat{\mathbf{B}}(\mathbf{r},\omega) &= 0,\\ \overrightarrow{\nabla}\times\hat{\mathbf{B}}(\mathbf{r},\omega) + \frac{i\omega}{c^2}\hat{\mathbf{E}}(\mathbf{r},\omega) &= \mu_0\hat{\mathbf{j}}_{\mathrm{in}}(\mathbf{r},\omega),\end{aligned} \tag{4}$$

we find the inhomogeneous Helmholtz equation for the electric field,

$$\begin{aligned}&\left[\overrightarrow{\nabla}\times\overrightarrow{\nabla}\times - \frac{\omega^2}{c^2}\right]\hat{\mathbf{E}}(\mathbf{r},\omega)\\ &\quad - i\mu_0\omega\int d^3r'\mathbf{Q}(\mathbf{r},\mathbf{r}',\omega)\cdot\hat{\mathbf{E}}(\mathbf{r}',\omega) = i\mu_0\omega\hat{\mathbf{j}}_{\mathrm{N}}(\mathbf{r},\omega).\end{aligned} \tag{5}$$

The formal solution to this inhomogeneous differential equation,

$$\hat{\mathbf{E}}(\mathbf{r},\omega) = i\mu_0\omega\int d^3r'\mathbf{G}(\mathbf{r},\mathbf{r}',\omega)\cdot\hat{\mathbf{j}}_{\mathrm{N}}(\mathbf{r}',\omega), \tag{6}$$

combines the Green's tensor with the properties stated in Eqs. (1) and (2). The Green's tensor fulfills the relation $\mathbf{G}(\mathbf{r},\mathbf{r}',\omega)\to\mathbf{0}$ for $|\mathbf{r}-\mathbf{r}'|\to\infty$ and the Schwarz reflection principle,

$$\mathbf{G}^*(\mathbf{r},\mathbf{r}',\omega) = \mathbf{G}(\mathbf{r},\mathbf{r}',-\omega^*)\ \ \forall\,\mathbf{r},\mathbf{r}',\omega. \tag{7}$$

The respective equation for the magnetic field reads according to Eq. (4)

$$\hat{\mathbf{B}}(\mathbf{r},\omega) = \mu_0\overrightarrow{\nabla}\times\int d^3r'\mathbf{G}(\mathbf{r},\mathbf{r}',\omega)\cdot\hat{\mathbf{j}}_{\mathrm{N}}(\mathbf{r}',\omega). \tag{8}$$

The conductivity tensor $\mathbf{Q}$ from Eq. (3) and the Green's tensor from Eq. (6) are related by

$$\begin{aligned}&\mu_0\omega\int d^3s\int d^3s'\mathbf{G}(\mathbf{r},\mathbf{s},\omega)\cdot\Re[\mathbf{Q}(\mathbf{s},\mathbf{s}',\omega)]\cdot\mathbf{G}^{*T}(\mathbf{r}',\mathbf{s}',\omega)\\ &\quad = \Im[\mathbf{G}(\mathbf{r},\mathbf{r}',\omega)],\end{aligned} \tag{9}$$

where the definitions of the real and imaginary parts (2) are applied. The noise current $\hat{\mathbf{j}}_{\mathrm{N}}$ from Ohm's law (3) and the

expression of the electric field (6) is defined as

$$\hat{\mathbf{j}}_{\mathrm{N}}(\mathbf{r},\omega) = \sqrt{\frac{\hbar\omega}{\pi}} \int d^3r' \mathbf{R}(\mathbf{r},\mathbf{r}',\omega) \cdot \hat{\mathbf{f}}(\mathbf{r}',\omega), \tag{10}$$

with the connection between the conductivity matrix $\mathbf{Q}$ and the $\mathbf{R}$-tensor given by

$$\int d^3r' \mathbf{R}(\mathbf{r},\mathbf{r}',\omega) \cdot \mathbf{R}^{*T}(\mathbf{r}'',\mathbf{r}',\omega) = \Re[\mathbf{Q}(\mathbf{r},\mathbf{r}'',\omega)]. \tag{11}$$

The definition in Eq. (11) ensures that the fluctuation-dissipation theorem is obeyed. The noise current $\hat{\mathbf{j}}_{\mathrm{N}}$ (10) contains the creation and annihilation operators $\hat{\mathbf{f}}^\dagger$ and $\hat{\mathbf{f}}$, which satisfy the commutation relation,

$$[\hat{\mathbf{f}}(\mathbf{r},\omega),\hat{\mathbf{f}}^\dagger(\mathbf{r}',\omega')] = \boldsymbol{\delta}(\mathbf{r}-\mathbf{r}')\delta(\omega-\omega'). \tag{12}$$

The ground-state expectation value of the creation and annihilation operators is given by

$$\langle \hat{\mathbf{f}}(\mathbf{r},\omega)\hat{\mathbf{f}}^\dagger(\mathbf{r}',\omega')\rangle = \boldsymbol{\delta}(\mathbf{r}-\mathbf{r}')\delta(\omega-\omega'). \tag{13}$$

Equation (13) will be used to derive an expression for the Casimir force for nonreciprocal material in Sec. III. Afterwards we apply this general formula to the specific geometry of two semi-infinite slabs and derive the corresponding Green's tensor as solution of the Helmholtz equation (5) with Eq. (6) in Sec. IV.

III. CASIMIR FORCE FOR NONRECIPROCAL MEDIA

Based on the results from Sec. II the Casimir force can be derived by using the Lorentz force acting on the internal charge $\hat{\rho}_{\mathrm{in}}$ and current densities $\hat{\mathbf{j}}_{\mathrm{in}}$ of a body,

$$\hat{\mathbf{F}} = \int_V d^3r (\hat{\rho}_{\mathrm{in}}\hat{\mathbf{E}} + \hat{\mathbf{j}}_{\mathrm{in}} \times \hat{\mathbf{B}}). \tag{14}$$

By using Maxwell's equations (4), these quantities can be expressed in terms of the electric and magnetic fields $\hat{\mathbf{E}}$ (6) and $\hat{\mathbf{B}}$ (8), where the frequency components of the electric field $\hat{\mathbf{E}}(\mathbf{r},\omega)$ and the total field $\hat{\mathbf{E}}(\mathbf{r})$ are connected by the expression

$$\hat{\mathbf{E}}(\mathbf{r}) = \int_0^\infty d\omega[\hat{\mathbf{E}}(\mathbf{r},\omega) + \hat{\mathbf{E}}^\dagger(\mathbf{r},\omega)]. \tag{15}$$

A similar expression also holds for the magnetic field components $\hat{\mathbf{B}}(\mathbf{r},\omega)$. The Casimir force is the ground-state expectation value of the Lorentz force [3]. We apply the relation for vectors such as the electric and magnetic fields, exemplified for the electric field as $\overrightarrow{\nabla}\mathbf{E}^2 = 2(\mathbf{E}\cdot\overrightarrow{\nabla})\mathbf{E} + 2\mathbf{E}\times(\overrightarrow{\nabla}\times\mathbf{E})$ and note that the time-derivative of the ground-state average of the term $\hat{\mathbf{E}}(\mathbf{r}) \times \hat{\mathbf{B}}(\mathbf{r})$ vanishes. Thus, we obtain an expression for the Casimir force

$$\mathbf{F} = \int_{\partial V} d\mathbf{A} \cdot \langle \epsilon_0 \hat{\mathbf{E}}(\mathbf{r})\hat{\mathbf{E}}(\mathbf{r}') + \frac{1}{\mu_0}\hat{\mathbf{B}}(\mathbf{r})\hat{\mathbf{B}}(\mathbf{r}') - \frac{1}{2}\left[\epsilon_0 \hat{\mathbf{E}}(\mathbf{r})\cdot\hat{\mathbf{E}}(\mathbf{r}') - \frac{1}{\mu_0}\hat{\mathbf{B}}(\mathbf{r})\cdot\hat{\mathbf{B}}(\mathbf{r}')\right]\mathbf{1}\rangle_{\mathbf{r}'\to\mathbf{r}}, \tag{16}$$

where $\mathbf{1}$ represents the unit matrix. The transition $\mathbf{r}' \to \mathbf{r}$ is necessary because we must not include self-forces. Equation (16) holds both for reciprocal and nonreciprocal material and serves as a starting point for the following calculations.

We compute the expectation values of the electric and magnetic field components by making use of Eqs. (6), (8), (9), (10), (11) and use the results for the expectation values of the creation and annihilation operators (13),

$$\begin{aligned}\langle \hat{\mathbf{E}}(\mathbf{r})\hat{\mathbf{E}}(\mathbf{r}')\rangle &= \int_0^\infty d\omega \frac{\hbar\mu_0\omega^2}{\pi}\Im[\mathbf{G}(\mathbf{r},\mathbf{r}',\omega)],\\ \langle \hat{\mathbf{B}}(\mathbf{r})\hat{\mathbf{B}}(\mathbf{r}')\rangle &= -\int_0^\infty d\omega \frac{\hbar\mu_0}{\pi}\overrightarrow{\nabla}\times\Im[\mathbf{G}(\mathbf{r},\mathbf{r}',\omega)]\times\overleftarrow{\nabla}'.\end{aligned} \tag{17}$$

The frequency integrals over the Green's tensor expressions can be evaluated further in the complex plane. By using the Schwarz reflection principle (7) and neglecting the values of the Green's tensor for large frequencies, $\lim_{|\omega|\to\infty}\frac{\omega^2}{c^2}\mathbf{G} = 0$, the expression for the Casimir force (16) at the frequency $\omega = i\xi$ yields

$$\begin{aligned}\mathbf{F} = -\frac{\hbar}{2\pi}\int_0^\infty d\xi \int_{\partial V} d\mathbf{A}\cdot\Big\{&\frac{\xi^2}{c^2}\mathbf{G}^{(1)}(\mathbf{r},\mathbf{r}',i\xi)\\ &+\frac{\xi^2}{c^2}\mathbf{G}^{(1)\mathrm{T}}(\mathbf{r}',\mathbf{r},i\xi) + \overrightarrow{\nabla}\times\mathbf{G}^{(1)}(\mathbf{r},\mathbf{r}',i\xi)\times\overleftarrow{\nabla}'\\ &+\overrightarrow{\nabla}\times\mathbf{G}^{(1)\mathrm{T}}(\mathbf{r}',\mathbf{r},i\xi)\times\overleftarrow{\nabla}' - \mathrm{Tr}\Big[\frac{\xi^2}{c^2}\mathbf{G}^{(1)}(\mathbf{r},\mathbf{r}',i\xi)\\ &+\overrightarrow{\nabla}\times\mathbf{G}^{(1)}(\mathbf{r},\mathbf{r}',i\xi)\times\overleftarrow{\nabla}'\Big]\mathbf{1}\Big\}_{\mathbf{r}'\to\mathbf{r}}.\end{aligned} \tag{18}$$

This is the first main result of this paper because Eq. (18) generalizes the expression for the Casimir force to nonreciprocal media and holds for arbitrary geometrical properties. It differs from the respective result for reciprocal material by the presence of the transposed Green's tensor. In case of reciprocal material, Lorentz's reciprocity (1) holds and there is no need for using the transposed version of the Green's tensor.

In Sec. IV, the Green's tensor for the specific geometry of two semi-infinite plates, which are isotropic on the surface, is derived. Afterwards, Eq. (18) is applied to this specific geometry.

IV. GREEN'S TENSOR AND CASIMIR FORCE FOR TWO PLANAR SURFACES

Having derived the general equations for the extension of the Casimir force to nonreciprocal materials, the scattering part of the Green's tensor for a setup consisting of two infinitely extended slabs separated by a distance L is analyzed in this Section. The scattering part of the Green's tensor $\mathbf{G}^{(1)}$ of one planar surface is the integral over $\mathbf{k}^\parallel$ and contains the sum over the polarizations σ of the incoming plane waves,

$$\mathbf{a}_{k\pm\sigma} = \mathbf{e}_{\sigma\pm}e^{i(\mathbf{k}^\parallel\cdot\mathbf{r}\pm k^\perp z)}, \tag{19}$$

and the respective sum over the polarizations σ' of the outgoing wave,

$$\mathbf{c}_{k\pm\sigma'} = \frac{i}{8\pi^2 k^\perp}\mathbf{e}_{\sigma'\pm}e^{-i(\mathbf{k}^\parallel\cdot\mathbf{r}'\pm k^\perp z')}. \tag{20}$$

Here we split the total wave vector $\mathbf{k}$ into its parallel component $\mathbf{k}^\parallel$, consisting of its x (k_x) and y components (k_y), and its z component $k^\perp$. The unit vectors of perpendicular polarization

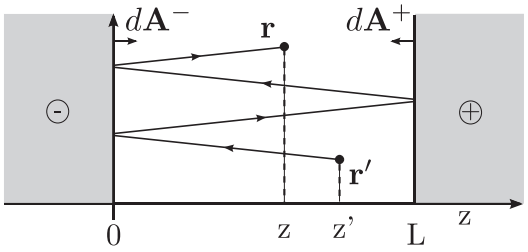

FIG. 1. Sketch of the two semi-infinite half spaces with their boundaries at $z = 0$ and $z = L$. The left half space is denoted by a minus sign and the right one by a plus sign. Moreover, the vectors $d\mathbf{A}^-$ and $d\mathbf{A}^+$ are orthogonal to the interfaces. The source point is located at $\mathbf{r}'$ and the field point at $\mathbf{r}$. There are three reflections in total. The outgoing wave goes in the left direction and the incoming one goes to the right.

$\mathbf{e}_{s\pm}$ and parallel polarization $\mathbf{e}_{p\pm}$ are expressed in terms of the part of the wave vector parallel to the interface ($\mathbf{e}_{k^\parallel}$) and perpendicular to it ($\mathbf{e}_z$),

$$\mathbf{e}_{s\pm} = \mathbf{e}_{k^\parallel} \times \mathbf{e}_z = \frac{1}{k^\parallel}\begin{pmatrix} k_y \\ -k_x \\ 0 \end{pmatrix},$$

$$\mathbf{e}_{p\pm} = \frac{1}{k}(k^\parallel \mathbf{e}_z \mp k^\perp \mathbf{e}_{k^\parallel}) = \frac{1}{k}\begin{pmatrix} \mp\frac{k^\perp}{k^\parallel}k_x \\ \mp\frac{k^\perp}{k^\parallel}k_y \\ k^\parallel \end{pmatrix}. \tag{21}$$

The indices $\pm$ in the unit vectors in Eq. (21) refer to the directions of incoming and outgoing waves. In principle we can distinguish between four different possibilities which contribute to the final expression of the Green's tensor: odd or even number of reflections and an outgoing wave going to the left or right. A reflection coefficient $r^\pm_{\sigma,\sigma'}$ is added for each reflection at the left and the right boundary, where the polarizability can be switched. The index $+(-)$ refers to a reflection at the right (left) boundary. All combinations contribute to the final expression of the Green's tensor.

The sketch in Fig. 1 shows three reflections, which appear in the Green's tensor beginning at the right. The Green's tensor is computed in the gap between the two semi-infinite plates with the boundaries at $z = 0$ and $z = L$ and contains the unit vectors $\mathbf{e}_{\sigma+}\mathbf{e}_{\sigma'-}$. The source of the wave is located at position $\mathbf{r}'$ and the field point is situated at $\mathbf{r}$, respectively. When the outgoing wave starts at the source at z' and ends at 0, the direction of the wave vector $k^\perp$ is negative leading to a contribution of $e^{ik^\perp z'}$. A reflection with possible change of polarizability takes place at the left boundary. The subsequent path from 0 to L in the positive direction gives $e^{ik^\perp L}$ and so does the following negative path from L to 0 after another reflection at the right boundary again. After the third reflection on the left side the final part from 0 to z is positive again giving rise to the factor $e^{ik^\perp z}$.

The following expression contains the terms for one and three reflections,

$$e^{ik^\perp(z+z')}r^-_{\sigma,\sigma'} + \sum_{\sigma_1,\sigma_2} r^-_{\sigma,\sigma_1} r^+_{\sigma_1,\sigma_2} r^-_{\sigma_2,\sigma'} e^{2ik^\perp L} e^{ik^\perp(z+z')} + \cdots \tag{22}$$

By introducing the reflection matrices for the right boundary $\mathscr{R}^+$ and the left boundary $\mathscr{R}^-$,

$$\mathscr{R}^+ = \begin{pmatrix} r^+_{s,s} & r^+_{s,p} \\ r^+_{p,s} & r^+_{p,p} \end{pmatrix};\quad \mathscr{R}^- = \begin{pmatrix} r^-_{s,s} & r^-_{s,p} \\ r^-_{p,s} & r^-_{p,p} \end{pmatrix}. \tag{23}$$

Equation (22) for an infinite number of reflections can be rewritten as

$$e^{ik^\perp(z+z')}\left[\mathscr{R}^- \cdot \sum_{n=0}^{\infty}(\mathscr{R}^+ \cdot \mathscr{R}^- e^{2ik^\perp L})^n\right]_{\sigma,\sigma'}. \tag{24}$$

Analogous to the geometric sum for scalars, we define the infinite Neumann series under the assumption $|r^\pm_{\sigma,\sigma'}| \leqslant 1$ as

$$\begin{aligned}(\mathscr{D}^+)^{-1} &= \sum_{n=0}^{\infty}(\mathscr{R}^+ \cdot \mathscr{R}^- e^{2ik^\perp L})^n \\ &= [1 - \mathscr{R}^+ \cdot \mathscr{R}^- e^{2ik^\perp L}]^{-1}, \\ (\mathscr{D}^-)^{-1} &= \sum_{n=0}^{\infty}(\mathscr{R}^- \cdot \mathscr{R}^+ e^{2ik^\perp L})^n \\ &= [1 - \mathscr{R}^- \cdot \mathscr{R}^+ e^{2ik^\perp L}]^{-1}.\end{aligned} \tag{25}$$

After carrying out the same steps for the three other combinations, the Green's tensor eventually reads

$$\begin{aligned}\mathbf{G}^{(1)}(\mathbf{r},\mathbf{r}',\omega) = \frac{i}{8\pi^2}\int d^2k^\parallel \frac{1}{k^\perp} e^{i\mathbf{k}^\parallel\cdot(\mathbf{r}-\mathbf{r}')}\Bigg[& e^{ik^\perp(z+z')}(\mathbf{e}_{s+},\mathbf{e}_{p+})\cdot\mathscr{R}^-\cdot(\mathscr{D}^+)^{-1}\cdot\begin{pmatrix}\mathbf{e}_{s-}\\ \mathbf{e}_{p-}\end{pmatrix} \\ & + e^{2ik^\perp L}e^{-ik^\perp(z+z')}(\mathbf{e}_{s-},\mathbf{e}_{p-})\cdot\mathscr{R}^+\cdot(\mathscr{D}^-)^{-1}\cdot\begin{pmatrix}\mathbf{e}_{s+}\\ \mathbf{e}_{p+}\end{pmatrix} \\ & + e^{2ik^\perp L}e^{ik^\perp(z-z')}(\mathbf{e}_{s+},\mathbf{e}_{p+})\cdot\mathscr{R}^-\cdot(\mathscr{D}^+)^{-1}\cdot\mathscr{R}^+\cdot\begin{pmatrix}\mathbf{e}_{s+}\\ \mathbf{e}_{p+}\end{pmatrix} \\ & + e^{2ik^\perp L}e^{-ik^\perp(z-z')}(\mathbf{e}_{s-},\mathbf{e}_{p-})\cdot\mathscr{R}^+\cdot(\mathscr{D}^-)^{-1}\cdot\mathscr{R}^-\cdot\begin{pmatrix}\mathbf{e}_{s-}\\ \mathbf{e}_{p-}\end{pmatrix}\Bigg].\end{aligned} \tag{26}$$

The scattering Green's tensor for a multilayer system for reciprocal media was derived in Ref. [13]. Equation (26) is the most general expression of the scattering part of the Green's tensor for the setup shown in Fig. 1. The first two terms in Eq. (26) represent the contributions from an odd number of reflections containing one reflection coefficient apart from the infinite

series. The last two terms are the contributions stemming from an even number of reflections showing two reflection coefficients apart from the series expression. Equation (26) contains several sums over polarizations allowing for a change of polarization at each boundary. The unit vectors show the direction of the outgoing and incoming waves.

To express the Green's tensor (26) in Cartesian coordinates, the two-dimensional integral over the parallel component of the wave vector is transformed to

$$\int d^2k^{\parallel} = \int_0^{\infty} dk^{\parallel} k^{\parallel} \int_0^{2\pi} d\phi. \tag{27}$$

If the reflection coefficients show a specific symmetry, depend only on the absolute value of the parallel component of the wave vector $r_{\sigma,\sigma'} = r_{\sigma,\sigma'}(k^{\parallel})$ and are independent of the angle ϕ, then the angular contribution can be evaluated using the relations

$$\begin{aligned}
\int_0^{2\pi} d\phi \mathbf{e}_{s\pm}\mathbf{e}_{s\pm} &= \int_0^{2\pi} d\phi \mathbf{e}_{s\pm}\mathbf{e}_{s\mp} = \pi[\mathbf{e}_x\mathbf{e}_x + \mathbf{e}_y\mathbf{e}_y],\\
\int_0^{2\pi} d\phi \mathbf{e}_{p\pm}\mathbf{e}_{p\pm} &= \frac{\pi}{k^2}[(k^{\perp})^2(\mathbf{e}_x\mathbf{e}_x + \mathbf{e}_y\mathbf{e}_y) + 2(k^{\parallel})^2\mathbf{e}_z\mathbf{e}_z],\\
\int_0^{2\pi} d\phi \mathbf{e}_{p\pm}\mathbf{e}_{p\mp} &= \frac{\pi}{k^2}[-(k^{\perp})^2(\mathbf{e}_x\mathbf{e}_x + \mathbf{e}_y\mathbf{e}_y) + 2(k^{\parallel})^2\mathbf{e}_z\mathbf{e}_z],\\
\int_0^{2\pi} d\phi \mathbf{e}_{s\pm}\mathbf{e}_{p\pm} &= \frac{\pi k^{\perp}}{k}[\mp\mathbf{e}_x\mathbf{e}_y \pm \mathbf{e}_y\mathbf{e}_x],\\
\int_0^{2\pi} d\phi \mathbf{e}_{s\pm}\mathbf{e}_{p\mp} &= \frac{\pi k^{\perp}}{k}[\pm\mathbf{e}_x\mathbf{e}_y \mp \mathbf{e}_y\mathbf{e}_x].
\end{aligned} \tag{28}$$

In Sec. V, the Casimir force is applied to a photonic topological insulator with a magnetic field pointing in the z direction, for which Eq. (28) and $r_{\sigma,\sigma'} = r_{\sigma,\sigma'}(k^{\parallel})$ hold. For a magnetic field in the xy plane, this expression would not hold anymore and one would need to use the more general expression in Eq. (26).

From these relations, it is apparent that the final expression of the Green's tensor shows diagonal contributions and a xy component. There are no off-diagonal contributions involving the z component, which is essential for the calculation of the Casimir force for the setup in Fig. 1.

Equation (18) is evaluated for the case of two semi-infinite planes by inserting the expression for the Green's tensor (26). In contrast to the respective result for reciprocal material [3] this expression includes the transposed Green's tensor. This is a consequence of the specific definition of the real and imaginary parts for nonreciprocal media (2). Since only the diagonal elements of the Greens tensor are nonzero due to the geometry consisting of two nonreciprocal planar infinite surfaces separated by vacuum, the expression of the Casimir force (18) does not differ in form from the respective reciprocal one. The nonreciprocity of the Casimir force arises from the specific expressions for the diagonal elements of the Green's tensor, containing the reflection matrices (23).

To compute the contribution of the Casimir force (18) stemming from the magnetic field (8), one has to apply the operators $\overrightarrow{\nabla}$ and $\overleftarrow{\nabla}$ to the unit vectors (21) from the left and the right, respectively, with $\overrightarrow{\nabla}\times \to i\mathbf{k}_{\pm}$ and $\times\overleftarrow{\nabla} \to -i\mathbf{k}_{\pm}$. The unit vectors are related as the following:

$$i\mathbf{k}_{\pm}\times\mathbf{e}_{s\pm} = \frac{\xi}{c}\mathbf{e}_{p\pm},\quad i\mathbf{k}_{\pm}\times\mathbf{e}_{p\pm} = -\frac{\xi}{c}\mathbf{e}_{s\pm}. \tag{29}$$

After the substitution $k^{\perp} = i\kappa^{\perp}$ we finally obtain

$$\begin{aligned}
\overrightarrow{\nabla}\times\mathbf{G}^{(1)}(\mathbf{r},\mathbf{r}',i\xi)\times\overleftarrow{\nabla}' = \frac{\xi^2}{8\pi^2c^2}\int d^2k^{\parallel}\frac{1}{\kappa^{\perp}}e^{i\mathbf{k}^{\parallel}\cdot(\mathbf{r}-\mathbf{r}')}\Bigg[&e^{-\kappa^{\perp}(z+z')}(\mathbf{e}_{p+},-\mathbf{e}_{s+})\cdot\mathscr{R}^{-}\cdot(\mathscr{D}^{+})^{-1}\cdot\begin{pmatrix}\mathbf{e}_{p-}\\-\mathbf{e}_{s-}\end{pmatrix}\\
&+e^{-2\kappa^{\perp}L}e^{\kappa^{\perp}(z+z')}(\mathbf{e}_{p-},-\mathbf{e}_{s-})\cdot\mathscr{R}^{+}\cdot(\mathscr{D}^{-})^{-1}\cdot\begin{pmatrix}\mathbf{e}_{p+}\\-\mathbf{e}_{s+}\end{pmatrix}\\
&+e^{-2\kappa^{\perp}L}e^{-\kappa^{\perp}(z-z')}(\mathbf{e}_{p+},-\mathbf{e}_{s+})\cdot\mathscr{R}^{-}\cdot(\mathscr{D}^{+})^{-1}\cdot\mathscr{R}^{+}\cdot\begin{pmatrix}\mathbf{e}_{p+}\\-\mathbf{e}_{s+}\end{pmatrix}\\
&+e^{-2\kappa^{\perp}L}e^{\kappa^{\perp}(z-z')}(\mathbf{e}_{p-},-\mathbf{e}_{s-})\cdot\mathscr{R}^{+}\cdot(\mathscr{D}^{-})^{-1}\cdot\mathscr{R}^{-}\cdot\begin{pmatrix}\mathbf{e}_{p-}\\-\mathbf{e}_{s-}\end{pmatrix}\Bigg].
\end{aligned} \tag{30}$$

The Casimir force for the setup in Fig. 1 is the force on the right plate situated at $z = L$. Due to our geometry the surface vector of the right plane points ourwards $d\mathbf{A} = -dA\mathbf{e}_z$. Since the surface has infinite extensions in the x and y directions, the total Casimir force $\mathbf{F}$ diverges. Thus, we restrict ourselves to the calculation of the surface force density $\mathbf{f}$, which is equivalent to the Casimir pressure. Due to this geometry, the resulting term of the Casimir force only contains contributions in the z direction. Since the z contributions of the Green's tensor (26) do not show any mixing terms with the x or y components (28), the zz component of the Casimir force is the only relevant one.

Since the term of the Casimir force (18) shows the trace over the Green's tensor, one has to use the xx and yy components of the Green's tensor (26) beside its zz component. After making use of the relation $\xi^2 = (\kappa^{\perp})^2 - (k^{\parallel})^2$, the Casimir force per unit area eventually reads

$$\begin{aligned}
\mathbf{f} = -\frac{\hbar}{4\pi^2}\int_0^{\infty} d\xi \int_0^{\infty} dk^{\parallel}k^{\parallel}\kappa^{\perp}e^{-2\kappa^{\perp}L}\\
\times \mathrm{Tr}[\mathscr{R}^{-}\cdot(\mathscr{D}^{+})^{-1}\cdot\mathscr{R}^{+} + \mathscr{R}^{+}\cdot(\mathscr{D}^{-})^{-1}\cdot\mathscr{R}^{-}]\mathbf{e}_z.
\end{aligned} \tag{31}$$

Since $\mathbf{f}$ always points in the z direction, it is convenient to work with the scalar Casimir force f defined by $\mathbf{f} = f\mathbf{e}_z$. It

contains only terms that have their origins in an even number of reflections at the boundaries. Besides, the polarizations of the outgoing and incoming wave are the same, which does not necessarily mean that there is no polarization change between the first and the last reflection at the boundaries.

Carrying out both sums over polarizations, one can find a more explicit form of Eq. (31),

$$\mathbf{f} = -\frac{\hbar}{2\pi^2}\int_0^\infty d\xi \int_0^\infty dk^\parallel k^\parallel \kappa^\perp \times e^{-2\kappa^\perp L}\frac{a - 2e^{-2\kappa^\perp L}b}{1 - e^{-2\kappa^\perp L}a + e^{-4\kappa^\perp L}b}\mathbf{e}_z, \tag{32}$$

with

$$\begin{aligned} a &= r^-_{\mathrm{s,s}} r^+_{\mathrm{s,s}} + r^-_{\mathrm{p,p}} r^+_{\mathrm{p,p}} + r^-_{\mathrm{p,s}} r^+_{\mathrm{s,p}} + r^-_{\mathrm{s,p}} r^+_{\mathrm{p,s}}, \\ b &= (r^+_{\mathrm{s,p}} r^+_{\mathrm{p,s}} + r^+_{\mathrm{s,s}} r^+_{\mathrm{p,p}})(r^-_{\mathrm{s,p}} r^-_{\mathrm{p,s}} + r^-_{\mathrm{s,s}} r^-_{\mathrm{p,p}}). \end{aligned} \tag{33}$$

In the following, this general expression of the Casimir force for nonreciprocal material (31) or (32) is evaluated for the case of the photonic topological insulator InSb. Besides, it can also be used to reproduce the well-known results for the Casimir force for two perfectly conducting reciprocal mirrors with reflection coefficients $r^\pm_{\mathrm{s,s}} = -1$, $r^\pm_{\mathrm{p,p}} = +1$ and $r^\pm_{\mathrm{p,s}} = r^\pm_{\mathrm{s,p}} = 0$ and two perfectly reflecting nonreciprocal mirrors with $r^\pm_{\mathrm{s,p}} = r^\pm_{\mathrm{p,s}} = -1$ and $r^\pm_{\mathrm{s,s}} = r^\pm_{\mathrm{p,p}} = 0$. In both cases, we obtain the final result,

$$\mathbf{f} = -\frac{\pi^2\hbar c}{240\,L^4}\mathbf{e}_z. \tag{34}$$

The Casimir force between one perfectly conducting and one perfectly permeable plate with the reflection coefficients $r^-_{\mathrm{s,s}} = r^-_{\mathrm{p,p}} = -1$, $r^-_{\mathrm{p,p}} = r^-_{\mathrm{s,s}} = 1$, and $r^\pm_{\mathrm{s,p}} = r^\pm_{\mathrm{p,s}} = 0$ reads

$$\mathbf{f} = \frac{7\pi^2\hbar c}{1920\,L^4}\mathbf{e}_z \tag{35}$$

and is repulsive, cf. Ref. [22]. The sign of the Casimir force thus depends on the material used. The Casimir force for a perfect electromagnetic conductor (PEMC) is computed in Ref. [23] and the two cases described above can be seen as limitting cases for PEMC-angles of 0 and $\pi/2$, respectively.

The central result (31) can be applied to all kinds of nonreciprocal materials as long as their reflection coefficients are independent of the angle ϕ. Both axion topological insulators, cf. Refs. [2,24], and photonic topological insulators with perpendicular bias fulfill this property. The Casimir force between axion topological insulators with frequency-dependent permittivity and permeability and frequency-independent axion coupling was studied in Ref. [14], leading to the prediction of repulsive Casimir forces. A later treatment with a more involved material model [16] incorporates a frequency dependent axion coupling.

Similar to the topological insulators, the Casimir force between two parallel planar Chern-Simons layers with a vacuum gap in between is studied in Refs. [25,26]. The boundary conditions for the electromagnetic fields are derived in Ref. [26] leading to reflection and transmission coefficients which mix the polarizability. The resulting Casimir force can be switched from attractive to repulsive.

In Sec. VI, Eq. (31) is applied to a photonic topological insulator (PTI), whose material model is outlined in Sec. V.

V. THEORETICAL MODEL OF THE PHOTONIC TOPOLOGICAL INSULATOR

A photonic topological insulator (PTI) shows a mixing of polarizations, cf. Eq. (23), which stems from the PTI's anisotropic permittivity $\boldsymbol{\epsilon}$, cf. Sec. V A. A specific material model for the permittivity is based on InSb and is explained in Sec. V B. Afterwards, the reflection coefficients (23) needed for the calculation of the Casimir force are derived in Sec. V C.

A. Antisymmetric Permittivity

The mixing of polarizations stems from the PTI's anisotropic permittivity $\boldsymbol{\varepsilon}$, which has the form of a nonsymmetric tensor,

$$\boldsymbol{\varepsilon} = \begin{pmatrix} \varepsilon_{xx} & \varepsilon_{xy} & 0 \\ -\varepsilon_{xy} & \varepsilon_{xx} & 0 \\ 0 & 0 & \varepsilon_{zz} \end{pmatrix}. \tag{36}$$

We assume a constant unit permeability $\mu = 1$. Furthermore, all magnetoelectric cross susceptibilities are zero ($\zeta = \xi = 0$). The permittivity tensor (36) of such materials is antisymmetric and thus violates Lorentz's reciprocity principle (1) and consequently time-reversal symmetry.

This model is studied in the Voigt configuration, where the surface is perpendicular to the bias magnetic field $\mathbf{B}$ [17]. The normal vector of the interface is parallel to the z axis. In this particular case we find that the system is symmetric in the xy plane because its ε tensor (36) is rotationally invariant around the z axis for an arbitrary angle ϕ,

$$\mathbf{R}^{\mathrm{T}} \cdot \boldsymbol{\varepsilon} \cdot \mathbf{R} = \boldsymbol{\varepsilon}, \quad \text{with} \quad \mathbf{R} = \begin{pmatrix} \cos(\phi) & \sin(\phi) & 0 \\ -\sin(\phi) & \cos(\phi) & 0 \\ 0 & 0 & 1 \end{pmatrix}. \tag{37}$$

A particular challenge is the fact that in a PTI neither solely perpendicularly (s) nor solely parallelly (p) polarized waves are solutions of Maxwell's equations. Thus, a more general approach is needed to find the electric field in the PTI. Mathematically this procedure is similar to the one for biaxial, anisotropic magnetodielectics [18] and is presented in Sec. V C.

B. Material model for the Permittivity based on InSb

We compute the Casimir force of the PTI for a specific material model, which is based on n-doped InSb with an external static magnetic field pointing in z direction, $\mathbf{B} = B\mathbf{e}_z$. As was already mentioned in Sec. IV, the magnetic field pointing in the z direction is an essential condition for using Eq. (31). This material has been investigated in Ref. [27], and more recently with a higher doping in Ref. [28]. It has been used to study the near-field heat transfer by various authors, cf. Refs. [20,29,30]. The entries of the permittivity tensor (36)

for this specific model read

$$\varepsilon_{xx} = \varepsilon_{\text{inf}}\left\{\frac{\omega_{\text{p}}^2(\omega+i\gamma)}{\omega\left[\omega_c^2-(\omega+i\gamma)^2\right]}+\frac{\omega_{\text{L}}^2-\omega_{\text{T}}^2}{-i\Gamma\omega+\omega_{\text{T}}^2-\omega^2}+1\right\},$$
$$\varepsilon_{zz} = \varepsilon_{\text{inf}}\left\{-\frac{\omega_{\text{p}}^2}{\omega(\omega+i\gamma)}+\frac{\omega_{\text{L}}^2-\omega_{\text{T}}^2}{-i\Gamma\omega-\omega^2+\omega_{\text{T}}^2}+1\right\}, \quad (38)$$
$$\varepsilon_{xy} = \frac{i\varepsilon_{\text{inf}}\omega_c\omega_{\text{p}}^2}{\omega\left[\omega_c^2-(\omega+i\gamma)^2\right]}.$$

The plasma and cyclotron frequencies are given by

$$\omega_{\text{p}} = \sqrt{\frac{nq_e^2}{\varepsilon_{\text{inf}}m^\star\varepsilon_0}}, \quad \omega_c = \frac{Bq_e}{m^\star}, \quad (39)$$

where q_e is the electron charge and $m^\star$ its reduced mass. Γ represents the phonon damping constant and γ is the free carrier damping constant. Throughout this paper we will use the following values for the material constants which have been measured in Ref. [27]: $\omega_{\text{L}} = 3.62\times10^{13}$ rad/s, $\omega_{\text{T}} = 3.39\times10^{13}$ rad/s, $\Gamma = 5.65\times10^{11}$ rad/s, $\gamma = 3.39\times10^{12}$ rad/s, $n = 1.07\times10^{17}$ cm^{-3}, $m^\star = 0.022\,m_e$, where m_e is the electron mass. Additionally, Ref. [27] used $\varepsilon_{\text{inf}} = 15.7$, but since we are integrating over all frequencies equally we have to set $\varepsilon_{\text{inf}} = 1$ to ensure convergence. Physically this means we are neglecting certain resonances of $\varepsilon(\omega)$ and only take contributions from the ones at ω_{T} and ω_c into account. Since we are interested in the influence of the off-diagonal elements of $\boldsymbol{\varepsilon}$ on the Casimir force this seems to be a reasonable simplification, because the other resonances are not contributing to ε_{xy}.

Note that the cyclotron frequency ω_c is proportional to the external magnetic field, so by changing its direction from $+\mathbf{e}_z$ to $-\mathbf{e}_z$ one can change the sign of ω_c. This results in a sign change of the offdiagonal elements of $\boldsymbol{\varepsilon}$ as one can see in Eq. (38) and this is equivalent to applying the time reversal operator.

The permittivity model for InSb (38) with Eq. (39) is closely related to the one for a single-component magnetic plasma biased with an external static magnetic field $\mathbf{B} = B_z\mathbf{e}_z$, which is examined in Refs. [17,31]. By setting the damping constants γ and Γ equal to zero and if $\omega_{\text{L}} = \omega_{\text{T}}$, Eq. (38) reduces to the model of the magnetic plasma. One could consider different parameter ranges with this material, e.g., for ω_{p}. This model often applies to gas plasmas, because phonon contributions are ignored, but it is considered to be the simplistic model of a free-carrier material subject to a bias field.

C. Reflection coefficients

We consider a single interface, where the half space $z<0$ is vacuum and the half space $z>0$ is a PTI. In Ref. [18] the field in the vacuum is described by general amplitudes e, where the indices i and r refer to the incoming and reflected waves and the indices s and p specify the polarization. We define a s-polarized wave by $\mathbf{E}\parallel\mathbf{e}_y$ and a p-polarized one by $\mathbf{B}\parallel\mathbf{e}_y$. Using Maxwell's equations in cgs-units,

$$\vec{\nabla}\times\mathbf{E} = -\frac{1}{c}\frac{\partial}{\partial t}\mathbf{H}, \quad \vec{\nabla}\times\mathbf{H} = \frac{1}{c}\frac{\partial}{\partial t}(\boldsymbol{\varepsilon}\cdot\mathbf{E}), \quad (40)$$

and setting $\varepsilon = 1$ in the vacuum the equations for a general incoming wave with $\mathbf{k} = (k^x,0,k_i^\perp)^{\text{T}}$ read

$$\mathbf{E}_i = \left[e_{\text{s},i}\mathbf{e}_y + e_{\text{p},i}\frac{c}{\omega}(k_i^\perp\mathbf{e}_x - k^x\mathbf{e}_z)\right]e^{i(k^xx+k_i^\perp z-\omega t)},$$
$$\mathbf{H}_i = \left[e_{\text{p},i}\mathbf{e}_y - e_{\text{s},i}\frac{c}{\omega}(k_i^\perp\mathbf{e}_x - k^x\mathbf{e}_z)\right]e^{i(k^xx+k_i^\perp z-\omega t)},$$
$$\mathbf{E}_r = \left[e_{\text{s},r}\mathbf{e}_y - e_{\text{p},r}\frac{c}{\omega}(k_i^\perp\mathbf{e}_x + k^x\mathbf{e}_z)\right]e^{i(k^xx-k_i^\perp z-\omega t)},$$
$$\mathbf{H}_r = \left[e_{\text{p},r}\mathbf{e}_y + e_{\text{s},r}\frac{c}{\omega}(k_i^\perp\mathbf{e}_x + k^x\mathbf{e}_z)\right]e^{i(k^xx-k_i^\perp z-\omega t)}. \quad (41)$$

Since our setup is xy symmetric we assumed without loss of generality $\mathbf{k}^\parallel = k^x\mathbf{e}_x$ and we have used $k_i^\perp = -k_r^\perp$.

Due to the structure of the $\boldsymbol{\varepsilon}$-tensor the s- and p-polarized contributions cannot be separated from each other any longer. Thus in a more general approach plane waves are assumed

$$\mathbf{E} = \begin{pmatrix}e_x(z)\\e_y(z)\\e_z(z)\end{pmatrix}e^{i(k^xx-\omega t)}, \quad \mathbf{H} = \begin{pmatrix}h_x(z)\\h_y(z)\\h_z(z)\end{pmatrix}e^{i(k^xx-\omega t)}. \quad (42)$$

k^x is conserved across the interface. The z components of Maxwell's equations (40) read

$$h_z = \frac{c}{\omega}k^xe_y, \quad e_z = -\frac{c}{\omega\varepsilon_{zz}}k^xh_y, \quad (43)$$

and can be inserted into the x,y contributions. For these components we introduce the vector $\mathbf{u}$ with $u_1 = e_x$, $u_2 = e_y$, $u_3 = h_x$, and $u_4 = h_y$. By assuming the ansatz $u_j = u_j(0)e^{ik^\perp z}$ for the single components with $k^\perp$ as the z contribution of the wave vector in the PTI one obtains again from Eq. (40),

$$\mathsf{L}\cdot\mathbf{u} = -\frac{c}{\omega}k^\perp\mathbf{u}, \quad (44)$$

with

$$\mathsf{L} = \begin{pmatrix}0 & 0 & 0 & -1+\frac{c^2}{\omega^2\varepsilon_{zz}}(k^x)^2\\ 0 & 0 & 1 & 0\\ -\varepsilon_{xy} & \varepsilon_{xx}-\frac{c^2}{\omega^2}(k^x)^2 & 0 & 0\\ -\varepsilon_{xx} & -\varepsilon_{xy} & 0 & 0\end{pmatrix}. \quad (45)$$

To find nontrivial solutions one has to solve the equation $\det(\mathsf{L}+\frac{\omega k^\perp}{c}\mathbf{1}) = 0$ leading to the dispersion relations,

$$k^{\perp(m)} = \pm\frac{\omega}{c}\frac{1}{\sqrt{2}}\sqrt{A+B\pm\sqrt{(A-B)^2+4C}}, \quad (46)$$

with

$$A = \varepsilon_{xx}\left[1-\frac{c^2}{\omega^2\varepsilon_{zz}}(k^x)^2\right],$$
$$B = \varepsilon_{xx}-\frac{c^2}{\omega^2}(k^x)^2, \quad (47)$$
$$C = -\left[1-\frac{c^2}{\omega^2\varepsilon_{zz}}(k^x)^2\right]\varepsilon_{xy}^2,$$

for the four mathematical solutions $m = 1,2,3,4$, corresponding to the four possible combinations of signs in Eq. (46). Since solutions with $\text{Re}(k^{\perp(m)}) < 0$ would result in waves propagating in negative z direction we can neglect these solutions for the transmitted wave propagating in the positive z direction. Let $k^{\perp(1)}$ and $k^{\perp(2)}$ be the two solutions with positive

real parts and neglect the other two ones and we finally arrive at the expression for the transmitted components of **E** and **H** parallel to the surface,

$$\begin{pmatrix}\mathbf{E}_t\\ \mathbf{H}_t\end{pmatrix} = e^{i(k^x x-\omega t)}\sum_{m=1,2}\mathbf{u}^{(m)}(0)e^{ik^{\perp(m)}z}. \tag{48}$$

According to the continuity relations, the parallel components of the electric and magnetic fields **E** and **H**, i.e., the x, y components, at the interface between vacuum and the topological insulator are continuous. Since this set of four equations is under-determined we start by expressing e_y, h_x, and h_y in terms of e_x using Eq. (45),

$$\begin{aligned}\alpha^{(m)} &\equiv \frac{e_y^{(m)}(0)}{e_x^{(m)}(0)} = \frac{L_{23}L_{31}}{\frac{c^2\left(k^{\perp(m)}\right)^2}{\omega^2} - L_{23}L_{32}},\\ \beta^{(m)} &\equiv \frac{h_x^{(m)}(0)}{e_x^{(m)}(0)} = -\frac{\omega}{ck^{\perp(m)}}L_{31} - \frac{\omega}{ck^{\perp(m)}}L_{32}\alpha^{(m)},\\ \gamma^{(m)} &\equiv \frac{h_y^{(m)}(0)}{e_x^{(m)}(0)} = -\frac{\omega}{ck^{\perp(m)}}L_{41} - \frac{\omega}{ck^{\perp(m)}}L_{31}\alpha^{(m)}.\end{aligned} \tag{49}$$

These equations are inserted into the boundary conditions and one obtains

$$\underbrace{\begin{pmatrix}-1 & 0 & \alpha^{(1)} & \alpha^{(2)}\\ \frac{ck_i^\perp}{\omega} & 0 & -\beta^{(1)} & -\beta^{(2)}\\ 0 & \frac{ck_i^\perp}{\omega} & 1 & 1\\ 0 & -1 & \gamma^{(1)} & \gamma^{(2)}\end{pmatrix}}_{\equiv\mathbf{M}}\cdot\begin{pmatrix}e_{\mathrm{s},r}\\ e_{\mathrm{p},r}\\ e_x^{(1)}\\ e_x^{(2)}\end{pmatrix} = \begin{pmatrix}e_{\mathrm{s},i}\\ \frac{ck_i^\perp}{\omega}e_{\mathrm{s},i}\\ \frac{ck_i^\perp}{\omega}e_{\mathrm{p},i}\\ e_{\mathrm{p},i}\end{pmatrix}. \tag{50}$$

We now assume the incoming wave separately for s- ($e_{\mathrm{p},i}=0$, $e_{\mathrm{s},i}\neq 0$) or p-polarization ($e_{\mathrm{s},i}=0, e_{\mathrm{p},i}\neq 0$) and solve for the reflected amplitudes to finally obtain the reflection coefficients by help of Kramers rule,

$$\begin{aligned}r_{\mathrm{s,s}} &= \frac{e_{\mathrm{s},r}}{e_{\mathrm{s},i}} = \frac{\det(\mathbf{M}_1)}{\det(\mathbf{M})},\\ r_{\mathrm{p,s}} &= \frac{e_{\mathrm{p},r}}{e_{\mathrm{s},i}} = \frac{\det(\mathbf{M}_2)}{\det(\mathbf{M})},\\ r_{\mathrm{s,p}} &= \frac{e_{\mathrm{s},r}}{e_{\mathrm{p},i}} = \frac{\det(\mathbf{M}_3)}{\det(\mathbf{M})},\\ r_{\mathrm{s,s}} &= \frac{e_{\mathrm{p},r}}{e_{\mathrm{p},i}} = \frac{\det(\mathbf{M}_4)}{\det(\mathbf{M})},\end{aligned} \tag{51}$$

with the matrices

$$\mathbf{M}_1 = \begin{pmatrix}1 & 0 & \alpha^{(1)} & \alpha^{(2)}\\ \frac{ck_i^\perp}{\omega} & 0 & -\beta^{(1)} & -\beta^{(2)}\\ 0 & \frac{ck_i^\perp}{\omega} & 1 & 1\\ 0 & -1 & \gamma^{(1)} & \gamma^{(2)}\end{pmatrix},$$

$$\mathbf{M}_2 = \begin{pmatrix}-1 & 1 & \alpha^{(1)} & \alpha^{(2)}\\ \frac{ck_i^\perp}{\omega} & \frac{ck_i^\perp}{\omega} & -\beta^{(1)} & -\beta^{(2)}\\ 0 & 0 & 1 & 1\\ 0 & 0 & \gamma^{(1)} & \gamma^{(2)}\end{pmatrix},$$

$$\mathbf{M}_3 = \begin{pmatrix}0 & 0 & \alpha^{(1)} & \alpha^{(2)}\\ 0 & 0 & -\beta^{(1)} & -\beta^{(2)}\\ \frac{ck_i^\perp}{\omega} & \frac{ck_i^\perp}{\omega} & 1 & 1\\ 1 & -1 & \gamma^{(1)} & \gamma^{(2)}\end{pmatrix},$$

$$\mathbf{M}_4 = \begin{pmatrix}-1 & 0 & \alpha^{(1)} & \alpha^{(2)}\\ \frac{ck_i^\perp}{\omega} & 0 & -\beta^{(1)} & -\beta^{(2)}\\ 0 & \frac{ck_i^\perp}{\omega} & 1 & 1\\ 0 & 1 & \gamma^{(1)} & \gamma^{(2)}\end{pmatrix}. \tag{52}$$

Since $\det(\mathbf{M}_2) = \det(\mathbf{M}_3)$, the off-diagonal reflection coefficients are equal, $r_{\mathrm{s,p}} = r_{\mathrm{p,s}}$. According to Ref. [32], a medium obeys Lorentz's reciprocity, which is called Onsager reciprocity in Ref. [32], if and only if $r_{\sigma,\sigma}(-\mathbf{k}^\parallel,) = r_{\sigma,\sigma}(\mathbf{k}^\parallel)$ and $r_{\sigma,\bar\sigma}(-\mathbf{k}^\parallel,) = -r_{\bar\sigma,\sigma}(\mathbf{k}^\parallel)$ with $\sigma = \mathrm{s}, \mathrm{p}$ and $\bar\sigma = \mathrm{p}, \mathrm{s}$, respectively. This condition is not fulfilled since we instead have $r_{\mathrm{s,p}} = r_{\mathrm{p,s}}$.

Moreover, by changing the sign of ε_{xy}, which is equivalent to applying the time-reversal operator, we obtain: $r_{\sigma,\bar\sigma} \to -r_{\sigma,\bar\sigma}$ and $r_{\sigma,\sigma} \to r_{\sigma,\sigma}$. By setting $\varepsilon_{xy} = 0$ we find that the reflection coefficients simplify to the case of a uniaxial out of plane metamaterial [18], where $r_{\mathrm{p,s}} = r_{\mathrm{s,p}} = 0$ and the nonreciprocity vanishes. By assuming the model described by Eq. (38) for InSb we can change the sign of $r_{\sigma,\bar\sigma}$ simply by changing the sign of the magnetic field and moreover, by switching the magnetic field on and off we can switch between a reciprocal and a nonreciprocal case.

Furthermore, we consider the case where we exchange the positions of the TI and the vacuum which is equivalent to changing the z coordinate to $-z$. We still consider the incoming wave to propagate in the vacuum but this time in the $-z$ direction before it is reflected by the TI. So in this case we have to exchange $k^\perp \to -k^\perp$ and $k^{\perp(m)} \to -k^{\perp(m)}$, which causes $r_{\sigma,\bar\sigma} \to -r_{\sigma,\bar\sigma}$ and $r_{\sigma,\sigma} \to r_{\sigma,\sigma}$. This is exactly the same result as the one we obtained by exchanging $B \to -B$. This can be understood by analyzing a rotation by angle π around an arbitrary axis in the x-y plane of our whole system. This rotation should leave the reflection coefficients invariant and is carried out by exchanging $k^\perp \to -k^\perp$, $k^{\perp(m)} \to -k^{\perp(m)}$, and $B \to -B$. We conclude that the parameter governing the reflection coefficients is the projection of the magnetic field onto the outward normal vector of the TI surface, cf. Fig. 1.

VI. RESULTS

In Sec. VI A we first find general characteristics of the Casimir force between two infinite PTI half spaces separated by vacuum with a general permittivity tensor (36) and a permeability of $\mu = 1$. Second, in Sec. VI B we calculate and analyze the Casimir force for the InSb model (38).

A. Analytical results in the retarded and nonretarded limits

In this subsection the near field (nonretarded) and the far field (retarded) limits are analyzed. In the retarded limit we assume that $\omega_{\mathrm{res}}L/c \gg 1$ and find that the term $e^{-2\xi L/c}$ restricts the frequency dependence: $0 \leqslant \xi \leqslant c/(2L) \ll \omega_{\mathrm{res}}$. ω_{res} stands for the smallest relevant plasma or resonance frequency associated with the medium. So we can approximate $\varepsilon(i\xi) \backsimeq \varepsilon(0)$. We insert different static values for $\varepsilon_{ij}(i\xi = 0)$

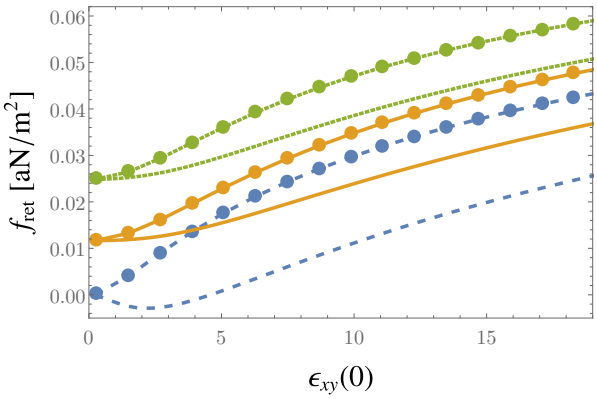

FIG. 2. Numerically calculated Casimir force density for different static values of ε_{ii} as a function of ε_{xy} at a fixed gap distance of $L = 10$ mm. The dashed lines correspond to $\varepsilon_{xx} = 3$ and $\varepsilon_{zz} \to \infty$, the solid lines to $\varepsilon_{xx} = \varepsilon_{zz} = 3$ and the dotted ones to $\varepsilon_{xx} = \varepsilon_{zz} = 1$. Lines with (without) circles correspond to the case with $B^+ = B^-$ ($B^+ = -B^-$) in each case.

into Eq. (31) and calculate the Casimir force density at a fixed distance $L = 10$ mm. We obtain for the reflection coefficients $r_{\rm s,p} = r_{\rm p,s} \to 0$ and $r_{\rm s,s} = -r_{\rm p,p} \to -1$ if $\varepsilon_{xx} \to \pm\infty$ or $\varepsilon_{xy} \to \pm\infty$ and for $i\xi \to 0$. Thus, the material behaves like a perfect conductor in the retarded limit and its Casimir force is given by Eq. (34). Especially for materials with a frequency dependence of ε_{xy} or ε_{xx} similar to the Drude model we find this divergence at $i\xi = 0$.

Figure 2 shows the Casimir force for several static values of the permittivity tensor with ε_{xx}, $\varepsilon_{xy} \neq \pm\infty$ for $i\xi = 0$. We further distinguish between the two cases $\varepsilon^+_{xy} = \pm\varepsilon^-_{xy}$, where ε^+_{xy}, ε^-_{xy} are the xy entry of the permittivity tensor in the left and right half space, respectively. We can see that we only find repulsive Casimir forces if $|\varepsilon_{xy}| \lesssim 5$, $\varepsilon^+_{xy} = -\varepsilon^-_{xy}$ and $\varepsilon_{xx} = \varepsilon_{zz} \cong 1$ in the retarded limit. The reason is that ε_{xy} does not only contribute to $r_{\sigma,\bar\sigma}$ but also to $r_{\sigma,\sigma}$. Especially for higher values of ε_{xy} it contributes more to $r_{\sigma,\sigma}$ than to $r_{\sigma,\bar\sigma}$, which results in an attractive Casimir force density. Nevertheless, there is a strong dependence of $f_{\rm ret}$ on the relative sign and magnitude of $\varepsilon^\pm_{xy}(0)$. So the Casimir force of a PTI in the retarded limit $f_{\rm ret}$ can be tuned by changing the external magnetic field if ε_{xx}, $\varepsilon_{xy} \neq \pm\infty$ for $i\xi = 0$.

In the nonretarded limit one cannot neglect the frequency dependence of the permittivity. Instead one can assume that $k^\parallel \gg \omega/c$. In this case one obtains the simplified dispersion relations $k_i^\perp \cong ik^\parallel$, $k^{\perp(1)} \cong i\sqrt{\frac{\varepsilon_{xx}(i\xi)}{\varepsilon_{zz}(i\xi)}}k^\parallel$ and $k^{\perp(2)} \cong ik^\parallel$. Taking only the highest-order terms in $k^\parallel$ into account one finds $r_{\rm s,s} \propto 1/(k^\parallel)^2 \cong 0$ and $r_{\rm s,p}, r_{\rm p,s} \propto 1/k^\parallel \cong 0$. This is in accordance with the reciprocal case in which one finds $r_{\rm s,s} \cong 0$ in the nonretarded limit as well. So the only remaining term is $r_{\rm p,p}$ and its expression to highest order in $k^\parallel$ is given by

$$r_{\rm p,p} = \frac{\sqrt{\varepsilon_{xx}(i\xi)\varepsilon_{zz}(i\xi)} - 1}{\sqrt{\varepsilon_{xx}(i\xi)\varepsilon_{zz}(i\xi)} + 1}. \tag{53}$$

The Casimir force in the nonretarded limit $f_{\rm nret}$ reduces to a much simpler expression,

$$f_{\rm nret} = -\frac{\hbar}{8\pi^2 L^3}\int_0^\infty d\xi\, {\rm Li}_3\left[\left(\frac{\sqrt{\varepsilon_{xx}(i\xi)\varepsilon_{zz}(i\xi)} - 1}{\sqrt{\varepsilon_{xx}(i\xi)\varepsilon_{zz}(i\xi)} + 1}\right)^2\right]. \tag{54}$$

Interestingly, this short-distance approximation is independent of ε_{xy} and closely related to the case of an isotropic material where now the geometric mean $\sqrt{\varepsilon_{xx}\varepsilon_{zz}}$ appears in place of the isotropic permittivity. Similar results have first been found for the Casimir-Polder interaction between an atom and a uniaxial material, which is isotropic on the interface plane and where the optic axis coincides with the anisotropic direction [33–35].

Since applying the time-reversal operator only changes the sign of ε_{xy}, the solution in the nonretarded limit is unaffected by changing the direction of the external magnetic field $B^\pm$. This does not mean, that $f_{\rm nret}$ does not change as well by tuning the external magnetic field, because ε_{ii} can still depend on, e.g., B^2 as in the model of InSb. Furthermore, we find that $f_{\rm nret}$ is proportional to $1/L^3$ for short distances as in the reciprocal case.

B. B-dependence of the Casimir force

After exploring the general characteristics of the Casimir force between two semi-infinite half spaces of the PTI separated by a layer of vacuum with thickness L, we analyze the force for the material model of InSb (38). We especially want to concentrate on how the force depends on the bias magnetic fields applied to the right $\mathbf{B}^+$ and left $\mathbf{B}^-$ half spaces where $\mathbf{B}^\pm$ is always perpendicular to the interfaces between PTI and the vacuum. Furthermore, let us note that we found in Sec. V C that the sign of $r_{\sigma,\bar\sigma}$ depends on the projection of the applied magnetic fields onto the outward normal vector of the surfaces. So we define the projected external magnetic field of the left ($^-$) and the right ($^+$) interface as $B^\pm = \mathbf{B}^\pm \cdot d\mathbf{A}^\pm$. Here $d\mathbf{A}^\pm$ is the normal vector of the right and left half space with $d\mathbf{A}^+ = -\mathbf{e}_z$ and $d\mathbf{A}^- = \mathbf{e}_z$, cf. Fig. 1. That means that with this definition the signs of $r^+_{\sigma,\bar\sigma}$ and $r^-_{\sigma,\bar\sigma}$ are the same for $B^+ = B^-$ and they are opposite for $B^+ = -B^-$. So we will further differentiate between $B^+ = \pm B^-$ because we expected different results for the Casimir force in the two cases after the previous discussion.

The problem of realizing magnetic fields with opposite directions in the two half-spaces in an experiment has been described in Ref. [36]. One can cover the PTI with a thin ferromagnetic layer on which the influence on the Casimir force is negligible. Another way is to dope the PTI with magnetic impurities [37], although the material response tensor would need to be modified. Figure 3 shows the numerical results for the Casimir force as a function of the gap distance L for the two cases $B = 0$ T and $B^+ = -B^- = 20$ T. It can be seen that the influence of the bias magnetic field is small on this logarithmic scale. Nevertheless we find here that the influence vanishes for large values of L because the two graphs overlap in that region but they split at intermediate distances and stay separated even in the nonretarded limit.

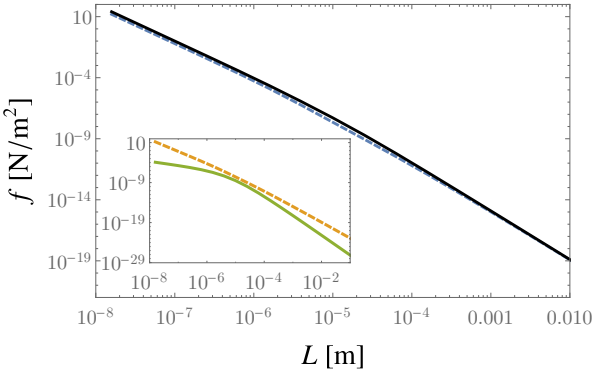

FIG. 3. The Casimir force density f has been calculated using Eq. (31) for the InSb model (38) as a function of the gap distance L in the main plot without applied magnetic field (solid line) and for the case $B^- = -B^+ = 20$ T (dashed line). Additionally, f was plotted only considering contributions from reflections with f_{off} (solid line) or without f_{diag} (dashed line) change of polarization in the inset for the case $B^- = -B^+ = 20$ T. Since $f_{\text{off}} < 0$, the negative value $-f_{\text{off}}$ was plotted.

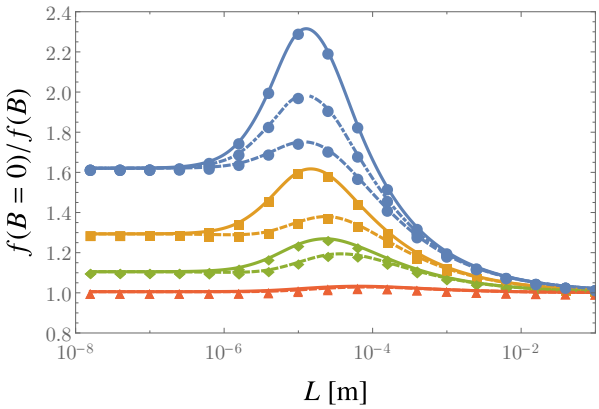

FIG. 4. Numerically calculated ratio between the Casimir force density with and without external magnetic field $f(B=0)/f(B)$ as a function of the gap distance L and for different magnetic fields $B = 1$ T (triangles), 5 T (diamonds), 10 T (squares), 20 T (bullets). Furthermore, we distinguished between the cases with $B^+ = B^-$ (dashed lines) and $B^+ = -B^-$ (solid lines). For $B = 20$ T we also plotted the numerical result in case of $r_{\text{s,p}}, r_{\text{p,s}} = 0$ (dashed and dotted line) and so here the only nonvanishing contributions arise from $r_{\text{s,s}}$, $r_{\text{p,p}}$.

Furthermore, we analyze which one of the reflection coefficients is responsible for the main contribution of the Casimir force density. The contributions of the off-diagonal (diagonal) terms f_{off} (f_{diag}) are depicted in Fig. 3, which has been calculated by setting $r_{\text{s,s}} = r_{\text{p,p}} = 0$ ($r_{\text{s,p}} = r_{\text{p,s}} = 0$). Therefore, only reflections where the polarization does change (does not change) are considered. As expected for the case of $B^+ = -B^-$, f_{off} is purely repulsive, whereas f_{diag} is attractive. But since $|f_{\text{diag}}| > |f_{\text{off}}|$ the total Casimir force is attractive and mainly dominated by contributions from $r_{\text{s,s}}$, $r_{\text{p,p}}$. At intermediate distances the influence of $r_{\text{s,p}} = r_{\text{p,s}}$ is probably not negligible because the yellow and green graphs are getting close to each other at around 10^{-5} m. So at this point we expect to find differences for $B^+ = \pm B^-$ because for the case $B^+ = B^-$, f_{off} would have the same absolute value but a different sign as for $B^+ = -B^-$ as explained at the beginning of this section.

To analyze the B-dependence in greater detail, Fig. 4 shows the relation $f(B=0)/f(B)$ as a function of the gap distance. As expected we find a constant value of 1 in the retarded limit and $f(B=0)/f(B) \neq 1$ at intermediate distances and in the nonretarded limit. Here the fraction $f(B=0)/f(B)$ increases if B increases. Interestingly, there is a peak at around 10^{-5} m where we find a reduction of the Casimir force by a factor of up to 2.3 for $B = 20$ T. The height of that peak depends additionally on whether the two magnetic fields are pointing in the same direction or not. So at intermediate distances we can see clearly the effect of nonreciprocity. Now the question arises if that peak is only caused by $r_{\text{s,p}}$ and $r_{\text{p,s}}$. From the dotted and dashed lines in Fig. 4 one can see a sensitive region at around $L = 10^{-5}$ m, even if $r_{\text{s,p}} = r_{\text{p,s}} = 0$ and it is enhanced or reduced depending on $\text{sgn}(B^+) = -\text{sgn}(B^-)$ (solid lines) or $\text{sgn}(B^+) = \text{sgn}(B^-)$ (dashed lines), respectively, if $r_{\text{s,p}}, r_{\text{p,s}} \neq 0$ again.

In particular, the case $\text{sgn}(B^+) = -\text{sgn}(B^-)$ can be attributed to a repulsive Casimir force component (the force being reduced), while $\text{sgn}(B^+) = \text{sgn}(B^-)$ corresponds to an attractive force. There is an analogy to the attractive Casimir force between two perfectly conducting or two perfectly permeable plates and the repulsive Casimir force between one perfectly conducting and one perfectly permeable plate, cf. Sec. IV. Reference [22] connects this behavior to the attractive Van-der-Waals force between two purely electrically polarizable particles or two purely magnetically polarizable particles and the repulsive force between one purely electrically polarizable and one purely magnetically polarizable particle. This can be extended to the attractive Casimir-Polder force of an electrically polarizable particle to a perfectly conducting wall and the repulsion of the magnetically polarizable particle from the wall [22]. Moreover, there is a similar feature in the Casimir-Polder potential between a circularly polarized atom and an axion topological insulator, where the axion contribution stemming from a coupling between the electric and the magnetic field decreases the effect of the ordinary Casimir-Polder potential [38].

In the nonretarded limit f is reduced by a constant factor depending on the strength of the magnetic field only. That can be understood analytically by noting that f_{nret} does not depend on ε_{xy} and thus is invariant under a sign change of one of the magnetic fields. Using Eq. (54) we can plot $\tilde{f}_{\text{nret}} = f_{\text{nret}}(B=0)/f_{\text{nret}}(B)$ as a function of the magnetic field, which is shown in Fig. 5 for a gap distance of $L = 10^{-9}$ m. $\tilde{f}_{\text{nret}}$ increases with increasing bias magnetic field until it saturates at around 40 T where the reduction factor has almost reached 2.

To understand the shifting of f in the nonretarded limit for an increasing magnetic field we can analyze the Casimir force as a function of $k^{\parallel}$ and ω in the nonretarded limit. The result is very similar to the one obtained for the near field heat transfer discussed in Ref. [20]. The Casimir force density does

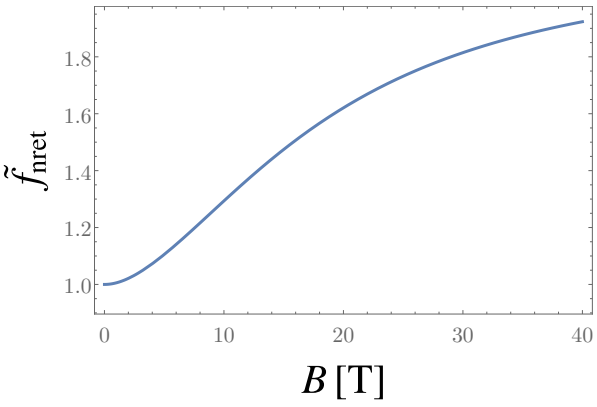

FIG. 5. The Casimir force in the nonretarded limit approximation f_{nret} has been evaluated numerically for a fixed gap distance of $L = 1$ nm as a function of the magnetic field $B = B^{\pm}$. Afterwards the ratio $\tilde{f}_{\mathrm{nret}} = f_{\mathrm{nret}}(B = 0)/f_{\mathrm{nret}}(B)$ has been computed and plotted. As one can see here this reduction factor $\tilde{f}_{\mathrm{nret}}$ increases with increasing magnetic field until it saturates at around $B \cong 40$ T at $\tilde{f}_{\mathrm{nret}} \cong 2$.

not depend on ε_{xy} for $k^x \gg \omega/c$, cf. Eq. (54), and the only nonvanishing reflection coefficient is $r_{\mathrm{p,p}}$. So one finds the following relation between k^x and ω in the nonretarded limit for surface phonon (SPhPs) and surface plasmon polaritons (SPPs), cf. Ref. [20],

$$k^x = \frac{1}{L}\ln\left(\frac{\sqrt{\varepsilon_{xx}(\omega)\varepsilon_{zz}(\omega)}-1}{\sqrt{\varepsilon_{xx}(\omega)\varepsilon_{zz}(\omega)}+1}\right), \tag{55}$$

if $\mathrm{Re}(\varepsilon_{xx})$, $\mathrm{Re}(\varepsilon_{zz}) < 0$. This equation can also be found by setting the denominator of the multiple reflections in the nonretarded limit $1 - r^{+}_{\mathrm{p,p}} r^{-}_{\mathrm{p,p}} e^{2\kappa^{\perp} L}$ equal to zero.

Furthermore, the general dispersion relations simplify to

$$\begin{aligned} k_1^{\perp} &= \sqrt{\varepsilon_{xx}\frac{\omega^2}{c^2} - (k^x)^2}, \\ k_2^{\perp} &= \sqrt{\varepsilon_{xx}\frac{\omega^2}{c^2} - \frac{\varepsilon_{xx}}{\varepsilon_{zz}}(k^x)^2}, \end{aligned} \tag{56}$$

where the second equation can also be brought to the form

$$\frac{\omega^2}{c^2} = \frac{(k_2^{\perp})^2}{\varepsilon_{xx}} + \frac{(k^x)^2}{\varepsilon_{zz}}. \tag{57}$$

This describes hyperbolic modes for $\mathrm{Re}(\varepsilon_{xx})\mathrm{Re}(\varepsilon_{zz}) < 0$, where one can further distinguish between hyperbolic modes with $\mathrm{Re}(\varepsilon_{xx}) > 0$ and $\mathrm{Re}(\varepsilon_{zz}) < 0$ (HMI) and modes with $\mathrm{Re}(\varepsilon_{xx}) < 0$ and $\mathrm{Re}(\varepsilon_{zz}) > 0$ (HMII). Interestingly, these modes are therefore propagating within the material and evanescent in the vacuum and therefore frustrated internal reflections.

Figure 6 shows $f(\omega, k^{\parallel})$ for different values of B. At $B = 0$ the main contribution of the Casimir force is due to SPPs and SPhPs. By increasing the magnetic field this contribution gets less intense and is shifted to lower k^x values. Furthermore, the region $\mathrm{Re}(\varepsilon_{xx})$, $\mathrm{Re}(\varepsilon_{zz}) < 0$, where these modes are allowed, becomes smaller until it vanishes completely at around $B = 16$ T.

On the other hand, there are increasing contributions from hyperbolic modes with stronger magnetic fields, which can be found at a broad range of ω and k^x values equally and which are restricted to $\mathrm{Re}(\varepsilon_{xx})\mathrm{Re}(\varepsilon_{zz}) < 0$. In summary, we found that the Casimir force is dominated by SPPs and SPhPs for small magnetic fields in the nonretarded limit, whereas the main contributions stem from hyperbolic modes for bigger values of B. So the decrease of f is due to the fact that the contributions of hyperbolic modes at high fields are smaller than the ones of SPPs and SPhPs at small magnetic fields.

To see all the effects described in this section one needs large magnetic fields up to 20 T. In the following we investigate if the necessary value of the magnetic field is smaller if we used different values for the parameters [especially n and $m^{\star}$ and so ω_{p} in our material model, cf. Eq. (38)]. Therefore, we plot the Casimir force at a fixed distance $L = 10$ nm in the nonretarded limit for different magnetic fields as a function of ω_{p}. The result is shown in Fig. 7. It can be seen that there are mainly two limits for the Casimir force which are independent of B. One is reached at high values of ω_{p}. In this case $\omega_{\mathrm{p}} \gg \omega_c$ and there is no difference whether there is a magnetic field or not. Whereas in the other limit for small values of ω_{p} and so for $\omega_c \gg \omega_{\mathrm{p}}$ the Casimir force has reached a minimal value, which is different from $f(B = 0)$. It depends on the value of ω_{p}, where the transition from one limit to the other happens.

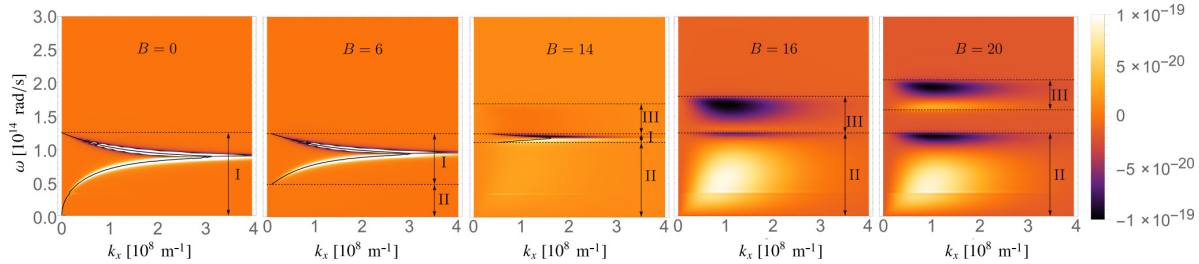

FIG. 6. The Casimir force density in the nonretarded limit approximation is plotted as a function of ω and k^x for different magnetic fields $B = B^{\pm}$ and with $L = 10$ nm, similar to Ref. [20]. Additionally, the dispersion relations for surface cavity modes are plotted with black solid lines in the ω-$k^{\parallel}$ plane. Furthermore, one can find different regions I, II, III, in each figure separated by black dotted lines. In region I we have $\mathrm{Re}(\varepsilon_{xx})$,$\mathrm{Re}(\varepsilon_{zz}) < 0$, and so this is the region with surface phonon and surface plasmon polaritons. In regions II and III there is $\mathrm{Re}(\varepsilon_{xx})\mathrm{Re}(\varepsilon_{zz}) < 0$ and we can find the hyperbolic modes HMI (II) and HMII (III), respectively.

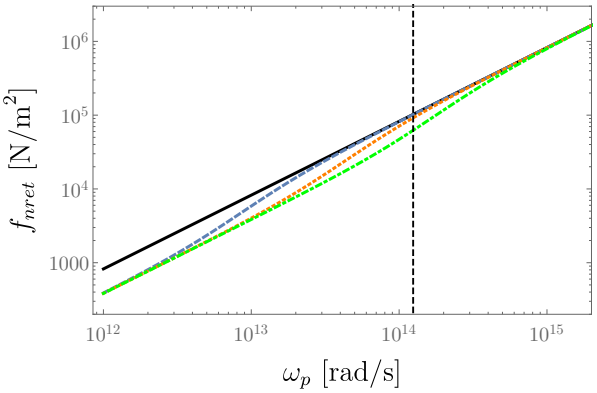

FIG. 7. Casimir force density in the nonretarded limit f_{nret} for a fixed gap distance $L = 1$ nm as a function of the plasma frequency ω_{p} for different fixed values of $B^{\pm} = 0$ T (solid line), 1 T (dashed line), 5 T (dotted line), and 20 T (dashed and dotted line).

The dotted vertical line shows the value of ω_{p}, which we used in all of our calculations so far. For smaller values of ω_{p} a weaker magnetic field would influence the Casimir force in the same way.

C. Casimir repulsion for a model inspired by Iron Garnet

The second model inspired by iron garnet, was introduced in Ref. [39] and examined in Ref. [17]. The respective elements of the permittivity tensor (36) read

$$\varepsilon_{xx} = 1 - \frac{\omega_0\omega_e}{\omega^2 - \omega_0^2},$$
$$\varepsilon_{zz} = 1, \tag{58}$$
$$\varepsilon_{xy} = -\varepsilon_{yx} = \frac{\omega\omega_e}{\omega^2 - \omega_0^2}.$$

In this model, $|\omega_0|$ is the resonance frequency and ω_e is the resonance strength. According to Ref. [39], the condition

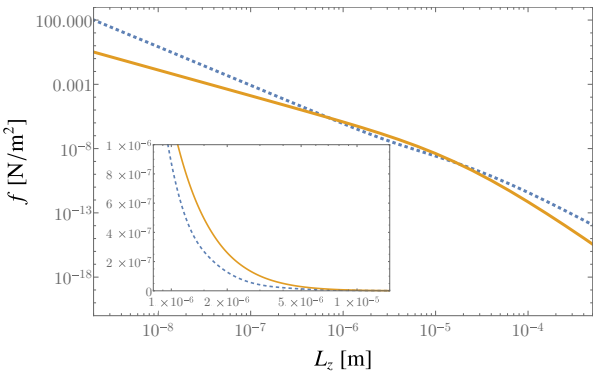

FIG. 8. The different contributions from reflection with $(-f_{\text{off}})$ (solid line) or without (f_{diag}) (dashed line) a change of polarization at the interface are plotted separately for the parameters $\omega_e = \pm 7.7 \times 10^{12}\, 2\pi/\text{s}$ and $\omega_0 = \pm 1.3 \times 10^{10}\, 2\pi/\text{s}$ and additionally $\omega_0\omega_e < 0$ in both half spaces. Since $f_{\text{off}} < 0$ we plotted $-f_{\text{off}}$. There is a region where $|f_{\text{off}}| > |f_{\text{diag}}|$ (see inset) and so that is where we expect to find a total repulsive Casimir force, cf. Fig. 9.

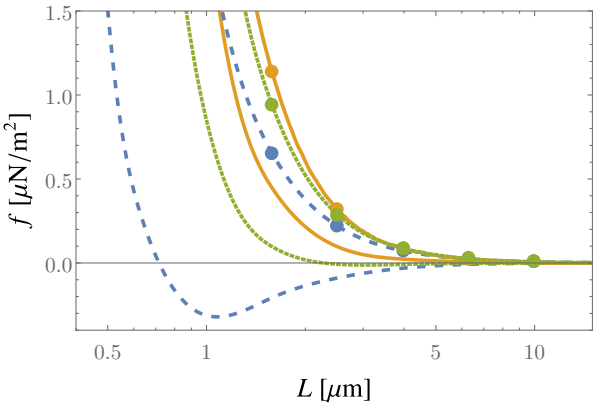

FIG. 9. The Casimir force density of a PTI for the model similar to iron garnet as a function of the gap distance. We used in both half spaces $\omega_e = \pm 7.7 \times 10^{12}\, 2\pi/\text{s}$ and $\omega_0 = \pm 1.3 \times 10^{m_2}\, 2\pi/\text{s}$ and different values for $m_2 = 10$ (dashed), 11 (dotted), and 12 (solid). Additionally, we distinguished between the two cases where first $\omega_0, \omega_e > 0$ in both half spaces (without circles) and second $\omega_0, \omega_e < 0$ in only one of the half spaces and $\omega_0, \omega_e > 0$ in the other one (with circles).

$\omega_e\omega_0 > 0$ has to be fulfilled. One finds from Eq. (58) that by changing the sign of ω_e and ω_0 one can achieve $\varepsilon_{xy} \to -\varepsilon_{xy}$, whereas the diagonal elements ε_{ii} do not change their signs.

So far there is no experimental evidence for a real material with such a permittivity. The exact B-field dependence of $\boldsymbol{\varepsilon}$ is unknown. Nevertheless, we consider it as an alternative hypothetical model which can be compared to the one of InSb and which shows a different aspect concerning the Casimir force.

Similar to Sec. VI B, we calculate the Casimir force numerically by using the permittivity values similar to iron garnet (58) and insert them into Eq. (31). First we have a look at the different contributions only from reflections with (f_{off}) or without (f_{diag}) change of polarizations, for the case where ω_0, $\omega_e < 0$ in both of the half spaces. The result is shown in Fig. 8. We find that in the retarded and nonretarded limit $|f_{\text{off}}| < f_{\text{diag}}$ for InSb, whereas the reflections with a change of polarization dominate at intermediate distances. So we expect the force to be repulsive in that region. This assumption is confirmed in Fig. 9. So there is a region at around 2×10^{-7} m $< L < 10^{-4}$ m, where we can switch between a repulsive and an attractive force simply by changing the sign of ω_0 and ω_e in one of the half spaces.

VII. CONCLUSION

We have derived a general expression for the Casimir force density between two nonreciprocal semi-infinite half spaces. This derivation is based on an extension of the theory of macroscopic quantum electrodynamics for nonreciprocal material.

This general expression is applied to a photonic topological insulator with a permittivity tensor with off-diagonal elements. First we have derived the reflection coefficients and investigated the Casimir force based on the general expression

of the permittivity tensor. The reflection coefficients with a polarization flip at the interface change signs by switching from a positive to a negative magnetic field in only one of the half spaces. Whereas the material behaves like a perfect conductor in the retarded limit if $\varepsilon_{xx} \to \pm\infty$ or $\varepsilon_{xy} \to \pm\infty$ for $i\xi \to 0$, the reflection coefficient for parallel polarization dominates in the nonretarded limit and we give an analytical result for the Casimir force.

We then applied the Casimir force formalism to the material model of InSb. We found a dependence of the Casimir force on the magnitude of the magnetic field at small distances. The polarization changing reflection coefficients were shown to be responsible for a repulsive force only if the signs of the magnetic fields in the two half spaces differ, whereas the other components cause an attractive force regardless of the sign. Nevertheless, this model never allows for a repulsive net force. Only a reduction of the magnitude of the Casimir force can be observed if an external magnetic field is applied. This can be explained by studying the force in the nonretarded limit. In this case the Casimir force is dominated by surface phonon and surface plasmon polaritons at small magnetic fields, whereas they are outperformed by hyperbolic modes at larger magnetic fields. The ratio between the Casimir force without applied field and the force with magnetic field shows a maximum at a critical distance of $L = 10^{-5}$ m where the Casimir force for the InSb model is reduced by a factor of about 2 at 10 T. Additionally in this regime of intermediate distances the magnitude of the Casimir force strongly depends on the relative sign of the magnetic fields in the two half spaces.

Finally, the Casimir force was studied for a model inspired by iron garnet. In this case the impact of the polarization changing reflection coefficients is stronger than the terms which do not change the polarization at intermediate distances. This makes it possible to achieve repulsive Casimir forces.

ACKNOWLEDGMENTS

We thank Diego Dalvit, Robert Bennett, and Stefan Rode for discussions. This work was supported by the German Research Foundation (DFG, Grants No. BU 1803/3-1 and No. GRK 2079/1). S.F. and F.L. are grateful for the hospitality at the Chemistry Department of the University of British Columbia, where this work was mostly done. S.Y.B. is grateful for support by the Freiburg Institute of Advanced Studies.

S.F. and F.L. contributed equally to this work.

[1] H. B. G. Casimir, Proc. K. Ned. Akad. Wet. **51**, 793 (1948).
[2] M. Z. Hasan and C. L. Kane, Rev. Mod. Phys. **82**, 3045 (2010).
[3] S. Y. Buhmann, *Dispersion Forces I—Macroscopic Quantum Electrodynamics and Ground-State Casimir, Casimir–Polder and van der Waals Forces* (Springer, Berlin/Heidelberg, 2012).
[4] E. M. Lifshitz, Sov. Phys. JETP **2**, 73 (1956).
[5] S. Scheel and S. Y. Buhmann, Acta Phys. Slovaca **58**, 675 (2008).
[6] H. T. Dung, L. Knöll, and D.-G. Welsch, Phys. Rev. A **57**, 3931 (1998).
[7] C. Raabe and D.-G. Welsch, Phys. Rev. A **71**, 013814 (2005).
[8] C. Raabe, S. Scheel, and D.-G. Welsch, Phys. Rev. A **75**, 053813 (2007).
[9] D. T. Butcher, S. Y. Buhmann, and S. Scheel, New J. Phys. **14**, 113013 (2012).
[10] H. A. Lorentz, Amsterdammer Akademie der Wetenschappen **4**, 176 (1896).
[11] L. Onsager, Phys. Rev. **37**, 405 (1931).
[12] L. Li, P. Kooi, M. Leong, and T. Yeo, J. Electromagn. Waves. Appl. **8**, 663 (1994).
[13] M. S. Tomaš, Phys. Rev. A **51**, 2545 (1995).
[14] A. G. Grushin and A. Cortijo, Phys. Rev. Lett. **106**, 020403 (2011).
[15] W. Nie, R. Zeng, Y. Lan, and S. Zhu, Phys. Rev. B **88**, 085421 (2013).
[16] P. Rodriguez-Lopez and A. G. Grushin, Phys. Rev. Lett. **112**, 056804 (2014).
[17] G. W. Hanson, S. Gangaraj, and A. Nemilentsau, arXiv:1602.02425 (2016).
[18] F. S. S. Rosa, D. A. R. Dalvit, and P. W. Milonni, Phys. Rev. A **78**, 032117 (2008).
[19] K. Joulain, J.-P. Mulet, F. Marquier, R. Carminati, and J.-J. Greffet, Surf. Sci. Rep. **57**, 59 (2005).
[20] E. Moncada-Villa, V. Fernandez-Hurtado, F. J. Garcia-Vidal, A. Garcia-Martin, and J. C. Cuevas, Phys. Rev. B **92**, 125418 (2015).
[21] S. Y. Buhmann, *Dispersion Forces II—Many-Body Effects, Excited Atoms, Finite Temperature and Quantum Friction* (Springer, Berlin/Heidelberg, 2012).
[22] T. H. Boyer, Phys. Rev. A **9**, 2078 (1974).
[23] S. Rode, R. Bennett, and S. Y. Buhmann, arXiv:1710.01509 (2017).
[24] F. Wilczek, Phys. Rev. Lett. **58**, 1799 (1987).
[25] V. N. Markov and Y. M. Pis'mak, J. Phys. A: Math. Gen. **39**, 6525 (2006).
[26] V. N. Marachevsky, Theor. Math. Phys. **190**, 315 (2017).
[27] E. Palik, R. Kaplan, R. Gammon, H. Kaplan, R. Wallis, and J. Quinn, Phys. Rev. B **13**, 2497 (1976).
[28] S. Law, R. Liu, and D. Wasserman, J. Vac. Sci. Technol. B **32**, 052601 (2014).
[29] P. Ben-Abdallah, Phys. Rev. Lett. **116**, 084301 (2016).
[30] L. Zhu and S. Fan, Phys. Rev. Lett. **117**, 134303 (2016).
[31] J. A. Bittencourt, *Fundamentals of Plasma Physics* (Springer, New York, 2004).
[32] S. Y. Buhmann, V. N. Marachevsky, and S. Scheel, Int. J. Mod. Phys. A **31**, 1641029 (2016).
[33] M. Fichet, F. Schuller, D. Bloch, and M. Ducloy, Phys. Rev. A **51**, 1553 (1995).
[34] L. Bruch and H. Watanabe, Surf. Sci. **65**, 619 (1977).
[35] T. Kihara and N. Honda, J. Phys. Soc. Jpn. **20**, 15 (1965).
[36] A. G. Grushin, P. Rodriguez-Lopez, and A. Cortijo, Phys. Rev. B **84**, 045119 (2011).
[37] Y. Cheng, Q. Zhang, and U. Schwingenschlögl, Phys. Rev. B **89**, 155429 (2014).
[38] S. Fuchs, J. A. Crosse, and S. Y. Buhmann, Phys. Rev. A **95**, 023805 (2017).
[39] M. G. Silveirinha, Phys. Rev. B **92**, 125153 (2015).

PHYSICAL REVIEW B **98**, 144101 (2018)

Inducing and controlling rotation on small objects using photonic topological materials

Frieder Lindel,[1] George W. Hanson,[2] Mauro Antezza,[3,4] and Stefan Yoshi Buhmann[1,5]

[1]*Physikalisches Institut, Albert-Ludwigs-Universität Freiburg, Hermann-Herder-Straße 3, 79104 Freiburg, Germany*

[2]*Department of Electrical Engineering, University of Wisconsin–Milwaukee, 3200 N. Cramer Street, Milwaukee, Wisconsin 53211, USA*

[3]*Laboratoire Charles Coulomb, UMR 5221 Université de Montpellier and CNRS, 34095 Montpellier, France*

[4]*Institut Universitaire de France, 1 rue Descartes, 75231 Paris Cedex 5, France*

[5]*Freiburg Institute for Advanced Studies, Albert-Ludwigs-Universität Freiburg, Albertstraße 19, 79104 Freiburg, Germany*

(Received 19 March 2018; revised manuscript received 10 August 2018; published 1 October 2018)

Photonic topological insulator plates violate Lorentz reciprocity, which leads to a directionality of surface-guided modes. This in-plane directionality can be imprinted via an applied magnetic field. On the basis of macroscopic quantum electrodynamics in nonreciprocal media, we show that two photonic topological insulator surfaces are subject to a tunable, magnetic-field-dependent Casimir torque. Due to the directionality, this torque exhibits a unique 2π periodicity, in contradistinction to the Casimir torques encountered for reciprocal uniaxial birefringent media or corrugated surfaces which are π periodic. Remarkably, the torque direction and strength can be externally driven *in situ* by simply applying a magnetic field on the system, and we show that this can be exploited to induce a control of the rotation of small objects. Our predictions are relevant for nano-optomechanical experiments and devices.

DOI: 10.1103/PhysRevB.98.144101

I. INTRODUCTION

The Casimir force was originally proposed as an attractive force between two perfectly conducting plates due to a reduced virtual photon pressure in the space between the plates [1,2]. Subsequently, the Casimir force for objects consisting of anisotropic materials or possessing anisotropic surfaces like birefringent plates [3], magnetodielectric metamaterials [4], and corrugated metals [5] was studied. Since all those materials have a distinguishable axis in the plane of the plates, it is natural to ask whether the Casimir energy depends on the relative angle between the two axes when bringing two anisotropic surfaces together. It turns out that, indeed, one obtains a Casimir torque [3,5–9]. There have been successful measurements of the lateral Casimir force, which is closely related to the Casimir torque [10–14]. More recently, there also have been several promising proposals for experiments with the goal to measure the Casimir torque between birefringent materials [15–17].

A material which is able to break rotational symmetry and which is of great interest at the moment is the topological insulator (TI) [18]. Topological insulators behave like regular insulators in their bulk but possess conducting surface states. Originally proposed for electronic states, it was shown more recently that they also exist in so-called photonic topological insulators (PTIs) [19–22] such as magnetized plasma [23–25]. One of the most striking features of TIs is that there exist unidirectional waves on the surfaces of these materials which turn out to be immune to backscattering [26,27]. Due to this directionality of the edge states PTIs not only have a distinguishable axis like, e.g., birefringent materials, but their axes also possess a distinguished *direction*. This feature has been of great interest and was used to construct devices like directional wave guides [27], optical isolators, and circulators.

Now the natural question arises regarding what quantum optical effects emerge when exploiting the directionality or nonreciprocity in PTIs. This question has been addressed by previous authors before: they studied the influence of the presence of a PTI on the entanglement of a two-level system [28]. In Refs. [29–31] the normal and lateral Casimir-Polder force acting on an atom close to a vacuum/PTI interface was analyzed; a huge anisotropic thermal magnetoresistance was obtained in the near-field radiative heat transfer between two spherical particles consisting of a PTI in Ref. [32]. A persistent unidirectional heat current was found between three objects at thermal equilibrium [33,34]; also the Casimir force has been studied for two infinite half-spaces consisting of PTIs in Ref. [35]. All those works showed that there exist interesting new features in quantum optics arising from the interplay of the quantized electromagnetic field with PTIs. However, the unidirectional features of PTIs have not yet been seen to manifest in Casimir torques between two macroscopic objects.

II. CASIMIR TORQUE

In this paper, we want to show how the unidirectionality and nonreciprocity of PTI plates manifest in the Casimir force and torque. To this end, we will show in the following that, in addition to a normal component of the Casimir force, there exists a non-negligible Casimir torque whose magnitude and direction are tunable by the external magnetic fields. Furthermore, due to the directionality of the topological surface states, we find that this torque is 2π periodic with respect to the relative angle between the two bias magnetic fields, in sharp contrast to the π periodicity occurring for reciprocal bianisotropic media. We also discuss how the tunability of the Casimir torque can be exploited in nanomechanical schemes to induce rotation.

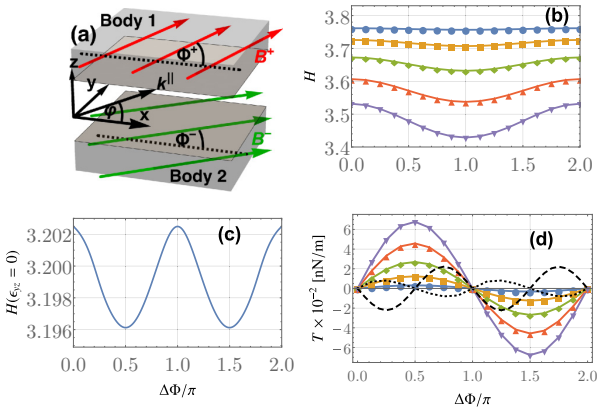

FIG. 1. In (a) we show the setup under the consideration consisting of two semi-infinite half-spaces filled with a PTI. Additionally, in each half-space there is an applied external magnetic field $\mathbf{B}^+$ and $\mathbf{B}^-$. The fields are in the xy plane and are parametrized by the angles Φ^+ and Φ^- between $\mathbf{B}^+$ and $\mathbf{B}^-$ and the x axis, respectively. In (b) we plot the dimensionless Hamaker constant H as a function of $\Delta\Phi$ for different values of $B = 1, 2, 3, 4, 5$ T (dots, squares, diamonds, triangles, and upside-down triangles, respectively). In (c) we again use the $\boldsymbol{\epsilon}$ tensor in Eq. (1) with the only exception being that we set $\epsilon_{yz} = 0$ to obtain a description of a normal anisotropic medium ($B = 5$ T). The Casimir torque $T(\Delta\Phi)$ is plotted in (d) for different magnetic fields, where the same shapes correspond to the same values of B as in (b). Additionally, we plot the Casimir torque for the material model in (c) (dotted line) and for a setup where the two PTI half-spaces are replaced by one barium titanate and one quartz half-space (dashed line). In (b) and (c) we use $L = 100$ nm.

A. Setup

We study a setup consisting of two semi-infinite half-spaces separated by a vacuum with separation L and filled with PTIs where a bias magnetic field is applied to each half-space [see Fig. 1(a)]. The PTI is implemented by a magnetized plasma with an applied bias magnetic field $\mathbf{B}$ as an example of a gyrotropic material which is described by a permittivity tensor of the form [36]

$$\boldsymbol{\epsilon} = \begin{pmatrix} \epsilon_{xx} & 0 & 0 \\ 0 & \epsilon_{zz} & \epsilon_{yz} \\ 0 & -\epsilon_{yz} & \epsilon_{zz} \end{pmatrix},$$
$$\epsilon_{yz}(\omega) = \frac{i\omega_c\omega_p^2}{\omega\left[\omega_c^2 - (\omega + i\gamma)^2\right]},$$
$$\epsilon_{zz}(\omega) = 1 + \frac{\omega_L^2 - \omega_T^2}{-i\Gamma\omega + \omega_T^2 - \omega^2} + \frac{\omega_p^2(\omega + i\gamma)}{\omega\left[\omega_c^2 - (\omega + i\gamma)^2\right]}, \tag{1}$$
$$\epsilon_{xx}(\omega) = 1 + \frac{\omega_L^2 - \omega_T^2}{-i\Gamma\omega + \omega_T^2 - \omega^2} - \frac{\omega_p^2}{\omega(\omega + i\gamma)}$$

if $\mathbf{B}$ points in the x direction. This is easily generalized for arbitrary directions of the magnetic field by simply rotating $\boldsymbol{\epsilon}$. The plasma and cyclotron frequencies are given by $\omega_p = \sqrt{nq_e^2/(m^\star\epsilon_0)}$ and $\omega_c = Bq_e/m^\star$, respectively, where q_e is the electron charge, $m^\star$ is its reduced mass, n is the free-electron density, and γ is the free-carrier damping constant. Furthermore, Γ represents the phonon damping constant, and ω_L and ω_T are the longitudinal and transverse optic-phonon frequencies, respectively. Throughout this paper we will use the following values for the material constants of InSb which have been measured in Ref. [36]: $\omega_L = 3.62 \times 10^{13}$ rad/s, $\omega_T = 3.39 \times 10^{13}$ rad/s, $\Gamma = 5.65 \times 10^{11}$ rad/s, $\gamma = 3.39 \times 10^{12}$ rad/s, $n = 1.07 \times 10^{17}\,\mathrm{cm}^{-3}$, $m^\star = 0.022m_e$, where m_e is the electron mass. Although we choose a specific PTI model here, our findings are general and can be applied to other specific PTI realizations.

B. Basic formulas

We first have to derive a general expression for the Casimir torque T of our system which is usually obtained from the Casimir energy E of the system. To build on previous results we use the intermediate result in Eq. (18) of Ref. [35] as obtained using macroscopic QED in nonreciprocal media [37]:

$$\mathbf{F} = -\frac{\hbar}{2\pi}\int_0^\infty d\xi \int_{\partial V} d\mathbf{A}\left\{\frac{2\xi^2}{c^2}\mathscr{S}[\mathbf{G}^{(1)}(\mathbf{r},\mathbf{r}',i\xi)] + 2\nabla\times\mathscr{S}[\mathbf{G}^{(1)}(\mathbf{r},\mathbf{r}',i\xi)]\times\overleftarrow{\nabla}'\right.$$
$$\left. -\mathrm{Tr}\left[\frac{\xi^2}{c^2}\mathbf{G}^{(1)}(\mathbf{r},\mathbf{r}',i\xi) + \nabla\times\mathbf{G}^{(1)}(\mathbf{r},\mathbf{r}',i\xi)\times\overleftarrow{\nabla}'\right]\mathbf{I}\right\}_{\mathbf{r}'\to\mathbf{r}}. \tag{2}$$

Here we have introduced the symmetrization $\mathscr{S}$ of a tensor defined by $\mathscr{S}[\mathbf{G}(\mathbf{r},\mathbf{r}',\omega)] = (1/2)[\mathbf{G}(\mathbf{r},\mathbf{r}',\omega) + \mathbf{G}^{\mathrm{T}}(\mathbf{r}',\mathbf{r},\omega)]$. Furthermore, $\xi = -i\omega$, where ω is the frequency of the electromagnetic wave, $\mathbf{I}$ is the unit tensor, ∂V is any infinite planar surface in the vacuum gap between the two planar bodies, $d\mathbf{A}$ is its surface element, and $\mathbf{r}$ and $\mathbf{r}'$ are arbitrary points on the surface of body 1. Most importantly, $\mathbf{G}^{(1)}(\mathbf{r},\mathbf{r}',i\xi)$ is the scattering Green's tensor [38] of our setup. It can be expressed using the reflection coefficients of the vacuum/PTI interfaces calculated in Appendix A and the different components of the wave vector $\mathbf{k} = (\mathbf{k}^{\parallel,T}, k_z = i\kappa)^{\mathrm{T}}$ satisfying $\mathbf{k}^2 = -\xi^2/c^2$, where c is the speed of light in vacuum. The full expression of $\mathbf{G}^{(1)}(\mathbf{r},\mathbf{r}',i\xi)$ and its derivation can be found in Appendix A.

Using these results, we find first of all, as expected, that there is no lateral force in the ground state of the system, and thus the x and y components of $\mathbf{F}$ are zero. Furthermore, in Appendix B we find a general expression for the normal component of $\mathbf{F}$ per unit area A which we define as $f \equiv F_z/A$, where F_z is the z component of $\mathbf{F}$. This result is not shown here since we are interested only in the near-field behavior of our system. Thus we want to analyze f further under

the assumption $\xi/c \ll k^{\parallel}$, which is often referred to as the nonretarded limit and becomes valid for small separations $L \ll c/\omega_{\rm ch}$, where $\omega_{\rm ch}$ is the highest characteristic frequency of the permittivity tensor (compare Ref. [38]). To estimate the value of $\omega_{\rm ch}$ for our specific material model in Eq. (1) we take a closer look at the monotonically decreasing function $\chi_{ij}(i\xi)/[\chi_{ij}(i\xi)+2]$, with $\chi_{ij}(i\xi) = \epsilon_{ij}(i\xi) - \delta_{ij}$. The condition

$$\frac{\chi_{ij}(i\omega_{\rm ch})}{\chi_{ij}(i\omega_{\rm ch})+2} = \frac{1}{2} \tag{3}$$

gives a good estimate of the characteristic frequency $\omega_{\rm ch}$. Neglecting absorption effects and phonon contributions. one obtains from Eq. (3)

$$ij = xx,\ zz \Rightarrow \omega_{\rm ch} \simeq \frac{\omega_p}{\sqrt{2}}, \tag{4}$$

$$ij = yz \Rightarrow \omega_{\rm ch} \simeq \sqrt[3]{\omega_p \omega_c}, \tag{5}$$

where we also assumed $\omega_c \ll \omega_p$, which is true for magnetic fields B of the order of a few teslas. Therefore we conclude that the nonretarded limit approximation is valid for distances $L \ll c\sqrt{2}/\omega_{\rm p} = 3.4\,\mu$m. Note, however, that this estimation for the validity of the nonretarded limit approximation is true only for our specific material model as given in Eq. (1), which includes only two medium resonances.

Under this assumption the reflection coefficients simplify significantly to $r^{\pm}_{\rm s,s} \simeq r^{\pm}_{\rm s,p} \simeq r^{\pm}_{\rm s,p} \simeq 0$ and

$$r^{\pm}_{\rm pp}(\omega) \simeq \frac{-2 + D \mp 2i\epsilon_{yz}\sin(\Phi^{\pm}-\varphi)}{2 + D \mp 2i\epsilon_{yz}\sin(\Phi^{\pm}-\varphi)},$$
$$D = \sqrt{2\epsilon_{zz}\{\epsilon_{zz} + \epsilon_{\rm xx} + (\epsilon_{\rm xx} - \epsilon_{zz})\cos[2(\Phi^{\pm}-\varphi)]\}}. \tag{6}$$

Here φ is defined by $\mathbf{k}^{\parallel} = k^{\parallel}(\sin(\varphi), \cos(\varphi))^{\rm T}$, with $k^{\parallel} \equiv |\mathbf{k}^{\parallel}|$ [compare Fig. 1(a)], and the $\pm$ symbol indicates the reflection at the lower and upper half-spaces, respectively. Note that this reflection coefficient is not real even when evaluated at imaginary frequencies $\omega = i\xi$ due to the terms proportional to $\epsilon_{\rm yz}$. But since this term also flips sign under $\mathbf{k}^{\parallel} \to -\mathbf{k}^{\parallel}$, the Schwarz reflection principle $\mathbf{G}^{(1)}(\mathbf{r}, \mathbf{r}', i\xi) = \mathbf{G}^{(1)\star}(\mathbf{r}, \mathbf{r}', i\xi)$ is obeyed, which, according to [39], implies $r^{\star}_{\rm pp}(\mathbf{k}^{\parallel}, i\xi) = r_{\rm pp}(-\mathbf{k}^{\parallel}, i\xi)$. Thus it is ensured that the Green's tensor and therefore the Casimir force are real.

Finally, using the previous result of the reflection coefficients in the nonretarded limit, f simplifies to

$$f = -\frac{\hbar}{16\pi^3 L^3}\int_0^{\infty} d\xi \int_0^{2\pi} d\varphi\ {\rm Li}_3[r^{+}_{\rm pp}(i\xi) r^{-}_{\rm pp}(i\xi)], \tag{7}$$

where $\rm Li_3$ is the polylogarithm of order 3. As in the reciprocal case [38] and for a magnetized plasma with a bias magnetic field perpendicular to the interface [35], we find a simple $f \propto 1/L^3$ behavior in the nonretarded limit. Therefore we can easily calculate the Casimir energy E per unit area in the nonretarded limit from Eq. (B19) by integrating f with respect to L and eventually find $E = L\,f/2$. From this result we can now calculate the Casimir torque $T = -\partial E/(\partial\Delta\Phi)$, where $\Delta\Phi = \Phi^{-} - \Phi^{+}$.

III. RESULTS AND DISCUSSION

Next, we want to analyze our previous results for the Casimir force, energy, and torque. To this end, in Fig. 1(b), we display the dimensionless Hamaker constant defined by $H \equiv \int_0^{\infty}(d\xi/\omega_p)\int_0^{2\pi} d\varphi {\rm Li}_3[r^{+}_{\rm pp} r^{-}_{\rm pp}]$ at a fixed gap distance $L = 100$ nm. Note that one can easily retrieve f, E, and T from H via $f = -\omega_p\hbar H/16\pi^3 L^3$, $E = -\omega_p\hbar H/32\pi^3 L^2$, and $T = (\omega_p\hbar/32\pi^3 L^2)\partial H/(\partial\Delta\Phi)$. Before discussing the qualitative features of these results let us discuss the magnitude of the torque. As depicted in Fig. 1(d), the Casimir torque at zero temperature for two semi-infinite PTI half-spaces reaches the same order of magnitude as the one for quartz or calcite half-spaces kept parallel to a barium titanate half-space. Those examples for birefringent plates were studied in Ref. [15], and we have used the same model for the permittivity, including the same values for the constants measured in Ref. [40] to reproduce these results. More concretely, this means that the torque for the PTI setup reaches a maximal torque of about 67 pN/m with $B = 5$ T, whereas the quartz (calcite)–barium titanate setup reaches 22 pN/m (317 pN/m). Nevertheless, the Casimir torque between two corrugated metals is three orders of magnitude larger [5]. Note that these torques are all periodic under a rotation of π of one of the plates around its normal component since their distinguished axes are not directional. On the contrary, we see in Fig. 1(b) that $H(\Delta\Phi)$ is 2π periodic with a maximum (minimum) when the two magnetic fields $B^{\pm}$ point in the same (opposite) direction. This result is therefore qualitatively different from the ones observed when dealing with birefringent half-spaces with one in-plane optical anisotropy [15] [compare the dashed line in Fig. 1(d)] or corrugated metals [5]. Heuristically, this new periodicity can be explained by the fact that not only does our material model have a distinguished axis, but this axis also has a direction.

The angle dependence of the Casimir energy can be understood in more detail by studying the contributions of different surface-plasmon polaritons (SPPs) which dominate in the nonretarded limit [41]. To this end, we take a closer look at the spectral decomposition of the Casimir energy evaluated at real frequencies $\tilde{H}(\omega) \equiv \int_0^{2\pi} d\varphi\ {\rm Im}\{{\rm Li}_3[r^{+}_{\rm pp}(\omega) r^{-}_{\rm pp}(\omega)]\}$, which allows us to see which surface modes contribute the most to the Casimir energy. The total Casimir energy is simply the integral over this spectral energy density, $H = \int_0^{\infty}(d\omega/\omega_p)\tilde{H}(\omega)$, and therefore $E, f \propto \int_0^{\infty} d\omega\ \tilde{H}(\omega)$, as can be seen from contour-integral techniques.

The central ingredient to the spectral Casimir energy density is the SPPs of the individual plates, which are resonances of the respective reflection coefficients $r^{+}_{\rm pp}(\omega)$ and $r^{-}_{\rm pp}(\omega)$. The frequencies of the SPPs are easily found by setting the denominators in the reflection coefficients (6) to zero, which upon using Eq. (1) and neglecting the photon contribution leads to the dispersion relations

$$\Omega^{\pm}(\Phi^{\pm}-\varphi) = \tfrac{1}{4}\Big\{\sqrt{6\omega_c^2 + 8\omega_p^2 + 2\omega_c^2\cos[2(\Phi^{\pm}-\varphi)]} \pm 2\omega_c\sin[\Phi^{\pm}-\varphi]\Big\} \tag{8}$$

in the lossless limit, as also found in Ref. [29]. The single-plate SPPs are illustrated by the dotted and dashed lines in

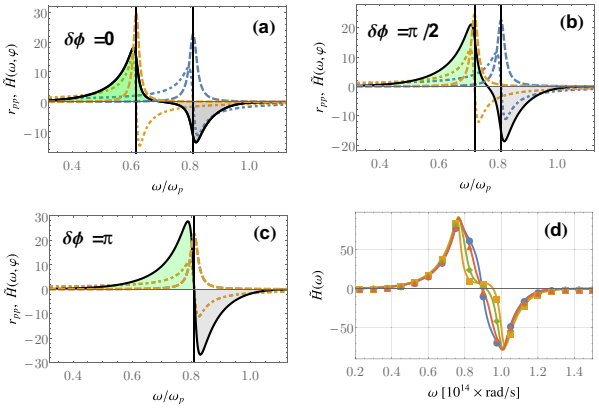

FIG. 2. Contributions of surface-plasmon polaritons (SPPs) to the Casimir energy. (a)–(c) Single-plate SPPs $\mathrm{Re}[r_{\mathrm{pp}}^{\pm}(\omega)]$ (dotted lines) and $\mathrm{Im}[r_{\mathrm{pp}}^{\pm}(\omega)]$ (dashed lines) and angle-resolved spectral energy density $\tilde{H}(\omega,\varphi)$ (solid lines) with $\Phi^{+}-\varphi=\pi/2$ and $\Delta\Phi=0,\pi/2,\pi$, respectively. $\mathrm{Re}[r_{\mathrm{pp}}^{+}(\omega)]$ and $\mathrm{Im}[r_{\mathrm{pp}}^{+}(\omega)]$ correspond to the curves with the resonance at higher frequencies, whereas $\mathrm{Re}[r_{\mathrm{pp}}^{-}(\omega)]$ and $\mathrm{Im}[r_{\mathrm{pp}}^{-}(\omega)]$ correspond to the ones with a lower resonance frequency ($\Omega^{+}>\Omega^{-}$ in this case); the two single-plate SPP frequencies $\Omega^{\pm}(\Phi^{\pm}-\varphi)$ as given by Eq. (8) are indicated as vertical lines. (d) Total spectral energy density $\tilde{H}(\omega)$ with $\Delta\Phi=0,\pi/4,\pi/2,\pi$ (dots, triangles, diamonds, and squares, respectively). For all plots we have used $B=3$ T.

Figs. 2(a)–2(c) for selected combinations of magnetic field and wave vector directions. In particular, we see that the SPP frequencies of the two plates coincide in the special case $\Delta\Phi=\pi$ [Fig. 2(c)].

When the two plates are brought in close proximity, as is the case in the nonretarded limit considered, the single-plate SPPs combine to form symmetric and antisymmetric coupled SPPs [41]. Mathematically, this can be seen from the Casimir spectral energy density. Using $\mathrm{Li}_3[z]\approx\zeta(3)\,z$ for $z\ll 1$, where ζ is the Riemann zeta function, we find $\tilde{H}(\omega)\approx\zeta(3)\{\mathrm{Im}[r_{\mathrm{pp}}^{+}(\omega)]\mathrm{Re}[r_{\mathrm{pp}}^{-}(\omega)]+\mathrm{Im}[r_{\mathrm{pp}}^{-}(\omega)]\mathrm{Re}[r_{\mathrm{pp}}^{+}(\omega)]\}$. We can clearly see how $\tilde{H}(\omega,\varphi)$ is built up from the products $\mathrm{Im}[r_{\mathrm{pp}}^{\pm}(\omega)]\mathrm{Re}[r_{\mathrm{pp}}^{\mp}(\omega)]$ in Figs. 2(a)–2(c). As illustrated by the solid lines in Figs. 2(a)–2(c), the symmetric coupled SPPs give the dominant positive contribution to the Casimir energy (left peak), while the antisymmetric coupled SPPs give a smaller negative contribution (right dip). As further seen in the figures, the difference between the positive and negative contributions is quite pronounced for $\Delta\Phi=0$ [Fig. 2(a)], leading to a large net Casimir energy. The splitting is reduced for larger angles [Fig. 2(b)] until, eventually, the single-plate SPPs coincide for $\Delta\Phi=\pi$ and the two coupled SPPs become very close in frequency and similar in magnitude. For this case, we have a smaller Casimir energy.

Our observations remain valid for general combinations of magnetic field and wave vector directions and thus also when integrating over all wave vector directions $\varphi\in[0,2\pi]$ to obtain the total spectral energy density $\tilde{H}(\omega)$. As seen from Fig. 2(d), this energy density has quite a complex profile as it is the sum over contributions from many SPPs with different resonant frequencies. Nevertheless, we again find that positive and negative contributions are the most different in magnitude for $\Delta\Phi=0$ (dots), leading to a large total Casimir energy. As the angle difference increases towards $\Delta\Phi=\pi$ (squares), the positive and negative contributions become more similar in magnitude, and the total Casimir energy decreases.

IV. APPLICATION

The advantage of having an *in situ* tunability of the torque can be exploited for nanomechanical schemes. For instance, we consider a setup of two nanodisks as depicted in Fig. 3(a). This system is an example of a new mechanism (compare Ref. [47]) to generate a motor with small moving parts. As shown, the relative angle between the two applied magnetic fields is given by $\Delta\Phi(t)=\Phi^{-}(t)-\theta(t)$. The dependence of the torque T on the relative angle between the applied magnetic fields is well approximated by $T(\Delta\Phi)\cong T_0\sin(\Delta\Phi)$ [compare Fig. 1(d)], where $T_0=67\,\mathrm{pN/m}$ if $B^{+}=B^{-}=5$ T. Thus the equation of motion for the rotation of the upper disk neglecting finite-size effects, retardation, and friction is given by

$$\frac{d^2\theta}{dt^2}=\frac{2T_0}{lr^2\rho_{\mathrm{InSb}}}\sin[\Phi^{-}(t)-\theta(t)]. \tag{9}$$

The result of the numerical solution of Eq. (9) can be found in Fig. 3(b). As we can see, if we let the tunable magnetic field $\mathbf{B}^{-}$ rotate with an angular velocity of up to 0.75 rad/s, the upper plate will follow the direction of $\mathbf{B}^{-}$ and start to rotate with the same angular velocity of almost one full 2π rotation per second. If $\mathbf{B}^{-}$ rotates faster than 0.75 rad/s, the

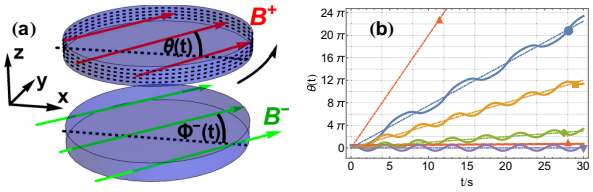

FIG. 3. (a) Scheme for inducing rotation via Casimir torques. As shown, there are two disks with the same size as considered in Ref. [16], namely, with radius $r=20\,\mu$m and thickness $d=20\,\mu$m consisting of InSb, which has a mass density of $\rho_{\mathrm{InSb}}=5.59\,\mathrm{g/cm^3}$ [42]. They are held at a distance of $L=100$ nm from each other so that the nonretarded limit assumption and the assumption of having two semi-infinite half-spaces apply for the idealized medium response assumed. Furthermore, $\mathbf{B}^{+}$ is a static magnetic field which is attached to the disk, i.e., via magnetic coating [43–46]. Thus its angle with the x axis Φ^{+} only changes if the whole disk rotates and the rotation of the upper disk is described by the angle $\theta(t)\equiv\Phi^{+}(t)$. In the lower disk there is a magnetic field $\mathbf{B}^{-}$ whose direction described by the angle $\Phi^{-}(t)$ may change over time, although the plate is fixed. In (b) we show the numerical solution to Eq. (9) with $B^{+}=B^{-}=5$ T for the cases $\Phi^{-}(t)=0.75\pi t, 0.4\pi t, 0.1\pi t, 2\pi t, 0$ (dot, square, diamond, triangle, and upside-down triangle, respectively) with solid lines. Additionally, we plot $\Phi^{-}(t)=0.75\pi t, 0.4\pi t, 0.1\pi t, 2\pi t, 0$ (also indicated by the dot, square, diamond, triangle, and upside-down triangle, respectively) describing the rotation of $\mathbf{B}^{-}$ with dot-dashed lines.

upper disk cannot follow the direction of $\mathbf{B}^-$, and therefore it barely rotates (triangle). Here r and l are the radius of the upper disk and its thickness, respectively.

V. SUMMARY

To summarize, we have found a Casimir torque between topological-insulator plates whose direction and magnitude are tunable by an external bias magnetic field. We have further shown that in the nonretarded limit this torque is dominated by SPPs which are directional, and therefore it is symmetric only under a rotation of 2π of one of the plates around its normal component. This unique periodicity, in contrast to the typical π periodicity for ordinary birefringent media, is a clear signature of nonreciprocity. We have shown how the tunability of the torque between two InSb disks can be exploited to set one of the disks into rotation, which offers new possibilities for measurements and nanomechanical applications of the Casimir torque on small objects.

ACKNOWLEDGMENTS

We acknowledge helpful discussions with F. Intravaia and A. Belyanin. This work was supported by the German Research Foundation (DFG, Grants No. BU 1803/3-1 and No. GRK 2079/1). S.Y.B. is grateful for support from the Freiburg Institute of Advanced Studies (FRIAS).

APPENDIX A: GREEN'S TENSOR FOR TWO SEMI-INFINITE HALF-SPACES OF PTI

In this appendix, we derive an expression for the Casimir force between two half-spaces filled with photonic topological materials separated by vacuum and with distinct in-plane bias magnetic fields in each of the half-spaces [see Fig. 1(a)]. To this end, we first calculate the Green's tensor for this setup here as the essential ingredient for the Casimir force calculated in Appendix B.

The following derivation of the Green's tensor $\mathbf{G}^{(1)}(\mathbf{r}, \mathbf{r}', \omega)$ is very similar to the ones given in Refs. [4,35]. As a starting point we can use the intermediate result of Ref. [35] in their Eq. (26):

$$\begin{aligned}\mathbf{G}^{(1)}(\mathbf{r}, \mathbf{r}', \omega) = \frac{i}{8\pi^2}\int d^2k^{\parallel}\frac{1}{k_z}e^{i\mathbf{k}^{\parallel}\cdot(\mathbf{r}-\mathbf{r}')}\Big[&e^{ik_z(z+z')}(\mathbf{e}_{s+},\ \mathbf{e}_{p+})\cdot\mathscr{R}^-\cdot(\mathscr{D}^+)^{-1}\cdot\begin{pmatrix}\mathbf{e}_{s-}\\ \mathbf{e}_{p-}\end{pmatrix}\\ &+e^{2ik_zL}e^{-ik_z(z+z')}(\mathbf{e}_{s-},\ \mathbf{e}_{p-})\cdot\mathscr{R}^+\cdot(\mathscr{D}^-)^{-1}\cdot\begin{pmatrix}\mathbf{e}_{s+}\\ \mathbf{e}_{p+}\end{pmatrix}\\ &+e^{2ik_zL}e^{ik_z(z-z')}(\mathbf{e}_{s+},\ \mathbf{e}_{p+})\cdot\mathscr{R}^-\cdot(\mathscr{D}^+)^{-1}\cdot\mathscr{R}^+\cdot\begin{pmatrix}\mathbf{e}_{s+}\\ \mathbf{e}_{p+}\end{pmatrix}\\ &+e^{2ik_zL}e^{-ik_z(z-z')}(\mathbf{e}_{s-},\ \mathbf{e}_{p-})\cdot\mathscr{R}^+\cdot(\mathscr{D}^-)^{-1}\cdot\mathscr{R}^-\cdot\begin{pmatrix}\mathbf{e}_{s-}\\ \mathbf{e}_{p-}\end{pmatrix}\Big].\end{aligned} \tag{A1}$$

Here we have split the wave vector $\mathbf{k} = (\mathbf{k}^{\parallel,T}, k_z)^{\mathrm{T}}$ into its components parallel ($\mathbf{k}^{\parallel}$) and perpendicular (k_z) to the plates, and the polarization vectors $\mathbf{e}_{s\pm}$, $\mathbf{e}_{p\pm}$ and the multiple reflection matrices $\mathscr{D}^{\pm}$ are defined by

$$\mathbf{e}_{s\pm} = \mathbf{e}_{k^{\parallel}} \times \mathbf{e}_z = \frac{1}{k^{\parallel}}\begin{pmatrix}k_y\\ -k_x\\ 0\end{pmatrix}, \tag{A2}$$

$$\mathbf{e}_{p\pm} = \frac{1}{k}(k^{\parallel}\mathbf{e}_z \mp k_z\mathbf{e}_{k^{\parallel}}) = \frac{1}{k}\begin{pmatrix}\mp\frac{k_z}{k^{\parallel}}k_x\\ \mp\frac{k_z}{k^{\parallel}}k_y\\ k^{\parallel}\end{pmatrix}, \tag{A3}$$

$$(\mathscr{D}^{\pm})^{-1} = \sum_{n=0}^{\infty}\left(\mathscr{R}^{\pm}\cdot\mathscr{R}^{\mp}e^{2ik^{\perp}L}\right)^n = \left[1-\mathscr{R}^{\pm}\cdot\mathscr{R}^{\mp}e^{2ik^{\perp}L}\right]^{-1}. \tag{A4}$$

We are left with the task of calculating the reflection matrices

$$\mathscr{R}^{\pm} = \begin{pmatrix}r^{\pm}_{s,s} & r^{\pm}_{s,p}\\ r^{\pm}_{p,s} & r^{\pm}_{p,p}\end{pmatrix} \tag{A5}$$

to find $\mathbf{G}^{(1)}(\mathbf{r}, \mathbf{r}', \omega)$. Here $r^{+}_{\sigma\sigma'}$ ($r^{-}_{\sigma\sigma'}$) is the reflection coefficient for a σ'-polarized incoming wave which is reflected off body 1 (body 2; see Fig. 1 in the main text) as a σ-polarized wave.

We are going to calculate $\mathscr{R}^+$ first and retrieve $\mathscr{R}^-$ from symmetry considerations. To find $\mathscr{R}^+$ we first find appropriate expressions for the electric and magnetic fields in vacuum and in the PTI by making use of Maxwell's equations. Afterwards, we can obtain $\mathscr{R}^+$ from the continuity relations at the interface.

We start with the permittivity tensor for body 1, which is given by

$$\boldsymbol{\epsilon} = \begin{pmatrix}\epsilon_{xx} & 0 & 0\\ 0 & \epsilon_{zz} & \epsilon_{yz}\\ 0 & -\epsilon_{yz} & \epsilon_{zz}\end{pmatrix} \tag{A6}$$

if the external magnetic field $\mathbf{B}^+$ points in the x direction. Note that we have $\epsilon_{yy} = \epsilon_{zz}$ and $\epsilon_{yz} = -\epsilon_{zy}$. We generalize this expression to arbitrary directions Φ^+ of $\mathbf{B}^+$ (see Fig. 1 in the main text) in the xy plane by rotating $\boldsymbol{\epsilon}$ by an angle of Φ^+ around the z axes. Furthermore, we consider a general wave vector $\mathbf{k} = (k^{\parallel}\cos\varphi, k^{\parallel}\sin\varphi, k_z)^T$, but by rotating $\boldsymbol{\epsilon}$ by an angle of $-\varphi$ we get without loss of generality $\mathbf{k} = (k^{\parallel}, 0, k_z)^T$, which simplifies the following calculation

significantly. So the permittivity tensor eventually reads

$$\widetilde{\boldsymbol{\epsilon}} = \begin{pmatrix} \frac{1}{2}\{\epsilon_{xx}+\epsilon_{zz}+(\epsilon_{xx}-\epsilon_{zz})\cos[2(\Phi^+-\varphi)]\} & \frac{1}{2}(\epsilon_{xx}-\epsilon_{zz})\sin[2(\Phi^+-\varphi)] & -\epsilon_{yz}\sin[\Phi^+-\varphi] \\ \frac{1}{2}(\epsilon_{xx}-\epsilon_{zz})\sin[2(\Phi^+-\varphi)] & \frac{1}{2}\{\epsilon_{xx}+\epsilon_{zz}+(\epsilon_{zz}-\epsilon_{xx})\cos[2(\Phi^+-\varphi)]\} & \epsilon_{yz}\cos\left[\Phi^+-\varphi\right] \\ \epsilon_{yz}\sin[\Phi^+-\varphi] & -\epsilon_{yz}\cos[\Phi^+-\varphi] & \epsilon_{zz} \end{pmatrix} \tag{A7}$$

in the rotated frame. As expected, it depends on only the relative angle between the magnetic field and the wave vector. Note that this form of the permittivity tensor is different from the one considered in Ref. [35]. Nevertheless, the general procedure to find $\mathscr{R}^{\pm}$ is analogous.

Now we make a plane wave ansatz for the field in the vacuum layer given by

$$\begin{aligned} \mathbf{E}_{\mathrm{i}} &= \left[e_{\mathrm{s,i}}\mathbf{e}_y + e_{\mathrm{p,i}}\frac{c}{\omega\epsilon}(k_{z,\mathrm{i}}\mathbf{e}_x - k^{\parallel}\mathbf{e}_z)\right]e^{i(k^{\parallel}x+k_{z,\mathrm{i}}z-\omega t)}, \\ \mathbf{H}_{\mathrm{i}} &= \left[e_{\mathrm{p,i}}\mathbf{e}_y - e_{\mathrm{s,i}}\frac{c}{\omega}(k_{z,\mathrm{i}}\mathbf{e}_x - k^{\parallel}\mathbf{e}_z)\right]e^{i(k^{\parallel}x+k_{z,\mathrm{i}}z-\omega t)}, \\ \mathbf{E}_{\mathrm{r}} &= \left[e_{\mathrm{s,r}}\mathbf{e}_y - e_{\mathrm{p,r}}\frac{c}{\omega\epsilon}(k_{z,\mathrm{i}}\mathbf{e}_x + k^{\parallel}\mathbf{e}_z)\right]e^{i(k^{\parallel}x-k_{z,\mathrm{i}}z-\omega t)}, \\ \mathbf{H}_{\mathrm{r}} &= \left[e_{\mathrm{p,r}}\mathbf{e}_y + e_{\mathrm{s,r}}\frac{c}{\omega}(k_{z,\mathrm{i}}\mathbf{e}_x + k_x\mathbf{e}_z)\right]e^{i(k^{\parallel}x-k_{z,\mathrm{i}}z-\omega t)}, \end{aligned} \tag{A8}$$

which satisfies Maxwell's equations

$$\nabla\times\mathbf{E} = -\frac{1}{c}\frac{\partial}{\partial t}\mathbf{H}, \quad \nabla\times\mathbf{H} = \frac{1}{c}\frac{\partial}{\partial t}(\boldsymbol{\epsilon}\cdot\mathbf{E}), \tag{A9}$$

with $\boldsymbol{\epsilon} = \mathbf{I}$ since the wave propagates in vacuum. In Eq. (A8) $e_{\sigma,\mathrm{i}}$ and $e_{\sigma,\mathrm{r}}$ are unknown complex-valued amplitudes of the fields, where the subscripts i and r indicate the incident and reflected waves, respectively. To eventually find the reflection coefficients we also need to find a way to describe the field within the PTI. Due to the structure of $\widetilde{\boldsymbol{\epsilon}}$ in Eq. (A7) Maxwell's equations in Eq. (A9) mix s- and p-polarized waves within the PTI. Therefore an ansatz as in Eq. (A8) is not possible, and thus in a more general approach plane waves are assumed in the form

$$\mathbf{E} = \begin{pmatrix} e_x(z) \\ e_y(z) \\ e_z(z) \end{pmatrix} e^{i(k^{\parallel}x-\omega t)}, \quad \mathbf{H} = \begin{pmatrix} h_x(z) \\ h_y(z) \\ h_z(z) \end{pmatrix} e^{i(k^{\parallel}x-\omega t)}. \tag{A10}$$

Note that $k^{\parallel}$ is conserved across the interface. The z components of Maxwell's equations (A9) read

$$h_z(z) = \frac{c}{\omega}k^{\parallel}e_y(z), \tag{A11}$$

$$e_z(z) = \frac{1}{\epsilon_{zz}}\left[-\frac{c}{\omega}k^{\parallel}h_y(z) + \widetilde{\epsilon}_{xz}e_x(z) + \widetilde{\epsilon}_{yz}e_y(z)\right] \tag{A12}$$

and can be inserted into the x, y contributions. For these components we introduce the vector $\mathbf{u}$ with $u_1 = e_x$, $u_2 = e_y$, $u_3 = h_x$, and $u_4 = h_y$. By assuming the ansatz $u_j = u_j(0)e^{ik_z^{(m)}z}$ for the single components with $k_z^{(m)}$ as the z contribution of the wave vector in the PTI one obtains again from Eq. (A9)

$$\mathbf{L}\cdot\mathbf{u} = -\frac{c}{\omega}k_z^{(m)}\mathbf{u}, \tag{A13}$$

with

$$\mathbf{L} = \begin{pmatrix} -k^{\parallel}c\widetilde{\epsilon}_{\mathrm{xz}}/(\omega\widetilde{\epsilon}_{\mathrm{zz}}) & -k^{\parallel}c\widetilde{\epsilon}_{\mathrm{yz}}/(\omega\widetilde{\epsilon}_{\mathrm{zz}}) & 0 & -1+(ck^{\parallel}/\omega)^2 1/\widetilde{\epsilon}_{\mathrm{zz}}) \\ \widetilde{\epsilon}_{\mathrm{xy}}+\widetilde{\epsilon}_{\mathrm{yz}}\widetilde{\epsilon}_{\mathrm{xz}}/\widetilde{\epsilon}_{\mathrm{zz}} & \widetilde{\epsilon}_{\mathrm{yy}}+\widetilde{\epsilon}_{\mathrm{yz}}^2/\widetilde{\epsilon}_{\mathrm{zz}}-(\omega/ck^{\parallel})^2 & 0 & -\omega\widetilde{\epsilon}_{\mathrm{yz}}/(ck^{\parallel}\widetilde{\epsilon}_{\mathrm{zz}}) \\ -\tilde{\epsilon}_{xy} & \tilde{\epsilon}_{xx}-\frac{c^2}{\omega^2}(k^{\parallel})^2 & 0 & 0 \\ -\tilde{\epsilon}_{xx}-\widetilde{\epsilon}_{\mathrm{xz}}^2/\widetilde{\epsilon}_{\mathrm{zz}} & -\widetilde{\epsilon}_{xy}-\widetilde{\epsilon}_{\mathrm{yz}}\widetilde{\epsilon}_{\mathrm{xz}}/\widetilde{\epsilon}_{\mathrm{zz}} & 0 & \omega\widetilde{\epsilon}_{\mathrm{xz}}/(ck^{\parallel}\widetilde{\epsilon}_{\mathrm{zz}}) \end{pmatrix}. \tag{A14}$$

To find nontrivial solutions one has to solve the relation $\det[\mathbf{L}+\mathbf{I}\,\omega k_z^{(m)}/c] = 0$, leading to the dispersion relations

$$\begin{aligned} k_z^{(m)} &= \pm\frac{\omega}{c}\frac{1}{2l\sqrt{\epsilon_{zz}}}\sqrt{U_1+U_2\cos[2(\Phi^+-\varphi)] \pm \sqrt{\frac{1}{2}\{U_3+U_4\cos[2(\Phi^+-\varphi)]+U_2^2\cos[4(\Phi^+-\varphi)]\}}}, \\ U_1 &= -3\epsilon_{zz}+\epsilon_{xx}(2l^2\epsilon_{zz}-1)+2l^2\left(\epsilon_{yz}^2+\epsilon_{zz}^2\right), \quad U_2 = \epsilon_{zz}-\epsilon_{xx}, \\ U_3 &= 6\epsilon_{zz}^2-8l^2\epsilon_{zz}\left(\epsilon_{yz}^2+\epsilon_{zz}^2\right)+8l^4\left(\epsilon_{yz}^2+\epsilon_{zz}^2\right)^2+8l^2\epsilon_{zz}^3(\epsilon_{zz}l^2-1)-2\epsilon_{xx}\left[3\epsilon_{zz}+4l^2\left(\epsilon_{yz}^2-2\epsilon_{zz}^2\right)+8l^2\epsilon_{zz}\left(\epsilon_{yz}^2+\epsilon_{zz}^2\right)\right], \\ U_4 &= 4\left\{\epsilon_{xx}^2(1-2l^2\epsilon_{zz})-2\epsilon_{xx}\left[\epsilon_{zz}+l^2\left(\epsilon_{yz}^2-2\epsilon_{zz}^2\right)\right]+\epsilon_{zz}\left[\epsilon_{zz}-2l^2\left(\epsilon_{yz}^2+\epsilon_{zz}^2\right)\right]\right\} \end{aligned} \tag{A15}$$

for the four mathematical solutions $m = 1, 2, 3, 4$, corresponding to the possible combinations of signs in Eq. (A15) with the dimensionless quantity $l = \omega/(c\,k^{\parallel})$. Note that these dispersion relations agree with the ones found in Ref. [29]. Since solutions with $\mathrm{Im}[k^{\perp(m)}] > 0$ would result in waves propagating in the negative z direction, we can neglect these solutions for the transmitted wave propagating in the positive z direction. Let $k^{\perp(1)}$ and $k^{\perp(2)}$ be the two solutions with a positive real part; then neglecting the other two, we finally arrive at the expression for the transmitted components of $\mathbf{E}$ and $\mathbf{H}$ parallel to the surface,

$$\begin{pmatrix}\mathbf{E}_\mathrm{t}\\ \mathbf{H}_\mathrm{t}\end{pmatrix} = e^{i\left(k^{\parallel}x-\omega t\right)}\sum_{m=1,2}\mathbf{u}^{(m)}(0)e^{ik^{\perp(m)}z}. \tag{A16}$$

According to the continuity relations, the parallel components of the electric and magnetic fields $\mathbf{E}$ and $\mathbf{H}$, i.e., the x, y components, at the interface between vacuum and the topological insulator are continuous. To simplify this set of four equations we start by expressing e_y, h_x, and h_y in terms of e_x using Eqs. (A13) and (A14),

$$\begin{aligned}\alpha^{(m)} &\equiv \frac{e_y^{(m)}(0)}{e_x^{(m)}(0)} = \frac{(ck^{\perp(m)}/\omega + L_{11} - L_{31})L_{44}/L_{14}}{L_{32} - L_{12}\,L_{34}/L_{14} - (k^{\perp(m)}c/\omega)^2},\\ \beta^{(m)} &\equiv \frac{h_x^{(m)}(0)}{e_x^{(m)}(0)} = -\frac{-ck^{\perp(m)}}{\omega}\alpha^{(m)},\\ \gamma^{(m)} &\equiv \frac{h_y^{(m)}(0)}{e_x^{(m)}(0)} = \frac{-ck^{\perp(m)}/\omega - L_{11} - L_{12}\alpha^{(m)}}{L_{41}}.\end{aligned} \tag{A17}$$

These equations are inserted into the boundary conditions, and one obtains

$$\underbrace{\begin{pmatrix}-1 & 0 & \alpha^{(1)} & \alpha^{(2)}\\ \frac{ck_\mathrm{i}^{\perp}}{\omega} & 0 & -\beta^{(1)} & -\beta^{(2)}\\ 0 & \frac{ck_\mathrm{i}^{\perp}}{\omega} & 1 & 1\\ 0 & -1 & \gamma^{(1)} & \gamma^{(2)}\end{pmatrix}}_{\equiv\,\mathbf{M}}\begin{pmatrix}e_{\mathrm{s,r}}\\ e_{\mathrm{p,r}}\\ e_x^{(1)}\\ e_x^{(2)}\end{pmatrix} = \begin{pmatrix}e_{\mathrm{s,i}}\\ \frac{ck_\mathrm{i}^{\perp}}{\omega}e_{\mathrm{s,i}}\\ \frac{ck_\mathrm{i}^{\perp}}{\omega}e_{\mathrm{p,i}}\\ e_{\mathrm{p,i}}\end{pmatrix}. \tag{A18}$$

We now assume the incoming wave to be s ($e_{\mathrm{p,i}} = 0,\ e_{\mathrm{s,i}} \neq 0$) or p polarized ($e_{\mathrm{s,i}} = 0,\ e_{\mathrm{p,i}} \neq 0$) separately and solve for the reflected amplitudes to finally obtain the reflection coefficients with the help of Cramer's rule:

$$r_{\mathrm{s,s}}^{+} = \frac{e_{\mathrm{s,r}}}{e_{\mathrm{s,i}}} = \frac{\det(\mathbf{M}_1)}{\det(\mathbf{M})}, \tag{A19}$$

$$r_{\mathrm{p,s}}^{+} = \frac{e_{\mathrm{p,r}}}{e_{\mathrm{s,i}}} = \frac{\det(\mathbf{M}_2)}{\det(\mathbf{M})}, \tag{A20}$$

$$r_{\mathrm{s,p}}^{+} = \frac{e_{\mathrm{s,r}}}{e_{\mathrm{p,i}}} = \frac{\det(\mathbf{M}_3)}{\det(\mathbf{M})}, \tag{A21}$$

$$r_{\mathrm{s,s}}^{+} = \frac{e_{\mathrm{p,r}}}{e_{\mathrm{p,i}}} = \frac{\det(\mathbf{M}_4)}{\det(\mathbf{M})}, \tag{A22}$$

with the matrices

$$\mathbf{M}_1 = \begin{pmatrix}1 & 0 & \alpha^{(1)} & \alpha^{(2)}\\ \frac{ck_\mathrm{i}^{\perp}}{\omega} & 0 & -\beta^{(1)} & -\beta^{(2)}\\ 0 & \frac{ck_\mathrm{i}^{\perp}}{\omega} & 1 & 1\\ 0 & -1 & \gamma^{(1)} & \gamma^{(2)}\end{pmatrix}, \tag{A23}$$

$$\mathbf{M}_2 = \begin{pmatrix}-1 & 1 & \alpha^{(1)} & \alpha^{(2)}\\ \frac{ck_\mathrm{i}^{\perp}}{\omega} & \frac{ck_\mathrm{i}^{\perp}}{\omega} & -\beta^{(1)} & -\beta^{(2)}\\ 0 & 0 & 1 & 1\\ 0 & 0 & \gamma^{(1)} & \gamma^{(2)}\end{pmatrix}, \tag{A24}$$

$$\mathbf{M}_3 = \begin{pmatrix}0 & 0 & \alpha^{(1)} & \alpha^{(2)}\\ 0 & 0 & -\beta^{(1)} & -\beta^{(2)}\\ \frac{ck_\mathrm{i}^{\perp}}{\omega} & \frac{ck_\mathrm{i}^{\perp}}{\omega} & 1 & 1\\ 1 & -1 & \gamma^{(1)} & \gamma^{(2)}\end{pmatrix}, \tag{A25}$$

$$\mathbf{M}_4 = \begin{pmatrix}-1 & 0 & \alpha^{(1)} & \alpha^{(2)}\\ \frac{ck_\mathrm{i}^{\perp}}{\omega} & 0 & -\beta^{(1)} & -\beta^{(2)}\\ 0 & \frac{ck_\mathrm{i}^{\perp}}{\omega} & 1 & 1\\ 0 & 1 & \gamma^{(1)} & \gamma^{(2)}\end{pmatrix}. \tag{A26}$$

Having found the reflection coefficients for waves reflected at body 1 ($\mathscr{R}^{+}$), we can easily derive the ones reflected by body 2 ($\mathscr{R}^{-}$). To this end one simply has to invert the direction of the z coordinate ($z \to -z$) and therefore replace $\epsilon_{yz} \to -\epsilon_{yz}$, $k_z \to -k_z$, and $k_z^{(m)} \to -k_z^{(m)}$. Thus we have

$$r_{\sigma\sigma'}^{-} = r_{\sigma\sigma'}^{+}|_{\epsilon_{yz}\to-\epsilon_{yz},\ k_z\to-k_z,\ k_z^{(m)}\to-k_z^{(m)}}. \tag{A27}$$

We also want to calculate the reflection coefficients in the nonretarded limit by assuming $k^{\parallel} \gg \omega/c$. In this limit we find from Eqs. (A19), (A20), (A21), (A22), and (A27)

$$r_{\mathrm{s,s}}^{\pm} \simeq r_{\mathrm{s,p}}^{\pm} \simeq r_{\mathrm{p,s}}^{\pm} \simeq 0, \tag{A28}$$

$$r_{\mathrm{pp}}^{\pm}(\omega) \simeq \frac{-2 + D \mp 2i\epsilon_{yz}\sin(\Phi^{\pm} - \varphi)}{2 + D \mp 2i\epsilon_{yz}\sin(\Phi^{\pm} - \varphi)}, \tag{A29}$$

$$D = \sqrt{2\epsilon_{zz}\{\epsilon_{zz} + \epsilon_{\mathrm{xx}} + (\epsilon_{\mathrm{xx}} - \epsilon_{zz})\cos\left[2(\Phi^{\pm} - \varphi)\right]\}}. \tag{A30}$$

Finally, we can insert the results for the reflection coefficients found in Eqs. (A19), (A20), (A21), (A22), and (A27) into Eq. (A1) to find a fully analytic expression for the Green's tensor of our setup. In the next section we want to use this result to calculate the Casimir force.

APPENDIX B: CASIMIR FORCE BETWEEN TWO INFINITE HALF-SPACES OF A PTI

The starting point for the calculation of the Casimir force between two infinite half-spaces of a PTI separated by a layer

of vacuum of thickness L can be found in Eq. (18) of [35]:

$$\mathbf{F} = -\frac{\hbar}{2\pi}\int_0^\infty d\xi \int_{\partial V} d\mathbf{A}\cdot\Bigg(\underbrace{\left\{\frac{2\xi^2}{c^2}\mathscr{S}[\mathbf{G}^{(1)}(\mathbf{r},\mathbf{r}',i\xi)] + 2\nabla\times\mathscr{S}[\mathbf{G}^{(1)}(\mathbf{r},\mathbf{r}',i\xi)]\times\overleftarrow{\nabla}'\right\}_{\mathbf{r}'\to\mathbf{r}}}_{\equiv\,\mathbf{S}^{(1)}(\mathbf{r},i\xi)}$$
$$-\mathrm{Tr}\left[\frac{\xi^2}{c^2}\mathbf{G}^{(1)}(\mathbf{r},\mathbf{r}',i\xi) + \nabla\times\mathbf{G}^{(1)}(\mathbf{r},\mathbf{r}',i\xi)\times\overleftarrow{\nabla}'\right]_{\mathbf{r}'\to\mathbf{r}}\mathbf{I}\Bigg). \tag{B1}$$

Here ∂V is any infinite planar surface in the vacuum gap between the two planar bodies, and $d\mathbf{A}$ is its surface element, whose sign depends on the body on which $\mathbf{F}$ acts. First, we want to calculate the 3×3 tensor $\mathbf{S}^{(1)}(\mathbf{r},i\xi)$ from whose entries $S^{(1)}_{ij}(\mathbf{r},i\xi)$ we obtain the surface force density $\mathbf{f}$ acting on body 1 using Eq. (B1) via

$$\mathbf{f} = \frac{\hbar}{2\pi}\int_0^\infty d\xi\,\frac{1}{2}\left[S^{(1)}_{zz}(\mathbf{r},i\xi) - S^{(1)}_{xx}(\mathbf{r},i\xi) - S^{(1)}_{yy}(\mathbf{r},i\xi)\right]\mathbf{e}_z + S^{(1)}_{zx}(\mathbf{r},i\xi)\mathbf{e}_x + S^{(1)}_{zy}(\mathbf{r},i\xi)\mathbf{e}_y, \tag{B2}$$

where we used $d\mathbf{A} = -dA\mathbf{e}_z$. To find $\mathbf{S}^{(1)}(\mathbf{r},i\xi)$ we are going to calculate its different components step by step. That means, in the following, we are going to calculate $\mathbf{G}^{(1)T}(\mathbf{r}',\mathbf{r},\omega)$, $\mathbf{G}^{(1)}(\mathbf{r},\mathbf{r}',\omega)+\mathbf{G}^{(1)T}(\mathbf{r}',\mathbf{r},\omega)$, and $\nabla\times[\mathbf{G}^{(1)}(\mathbf{r},\mathbf{r}',\omega)+\mathbf{G}^{(1)T}(\mathbf{r}',\mathbf{r},\omega)]\times\overleftarrow{\nabla}'$ subsequently.

First, we rewrite the Green's tensor given in Eq. (A1) by inserting the reflection matrices as found in Eq. (A5) and expanding the scalar products to obtain

$$\mathbf{G}^{(1)}(\mathbf{r},\mathbf{r}',\omega) = \frac{1}{8\pi^2}\int d^2\mathbf{k}^\parallel \frac{e^{i\mathbf{k}^\parallel\cdot(\mathbf{r}-\mathbf{r}')}}{\kappa}\sum_{\sigma,\sigma'}\Bigg[\mathbf{e}^\sigma_+\mathbf{e}^{\sigma'}_- e e^{-\kappa(z+z')}\underbrace{\sum_{\sigma_1}\frac{r^-_{\sigma\sigma_1}}{D^+_{\sigma_1\sigma'}}}_{\equiv \mathrm{I}_{\sigma\sigma'}(\mathbf{k}^\parallel)} + \mathbf{e}^\sigma_-\mathbf{e}^{\sigma'}_+ e^{\kappa(z+z')}e^{-2\kappa L}\underbrace{\sum_{\sigma_1}\frac{r^+_{\sigma\sigma_1}}{D^-_{\sigma_1\sigma'}}}_{\equiv \mathrm{II}_{\sigma\sigma'}(\mathbf{k}^\parallel)}$$
$$+\mathbf{e}^\sigma_+\mathbf{e}^{\sigma'}_+ e^{-\kappa(z-z'+2L)}\underbrace{\sum_{\sigma_1,\sigma_2}\frac{r^-_{\sigma\sigma_1}r^+_{\sigma_2\sigma'}}{D^+_{\sigma_1\sigma_2}}}_{\equiv \mathrm{III}_{\sigma\sigma'}(\mathbf{k}^\parallel)} + \mathbf{e}^\sigma_-\mathbf{e}^{\sigma'}_- e^{-\kappa(z'-z+2L)}\underbrace{\sum_{\sigma_1,\sigma_2}\frac{r^+_{\sigma\sigma_1}r^-_{\sigma_2\sigma'}}{D^-_{\sigma_1\sigma_2}}}_{\mathrm{IV}_{\sigma\sigma'}(\mathbf{k}^\parallel)}\Bigg]. \tag{B3}$$

Here we have replaced $k_z = i\kappa$, and the polarization indices are σ, σ', σ_1, $\sigma_2 = s, p$. Furthermore, $D^\pm_{\sigma_1\sigma_2} = (\mathscr{D}^\pm)_{\sigma_1\sigma_2}$ refers to components of the matrix $\mathscr{D}^\pm$ defined in Eq. (A4).

To obtain $\mathbf{S}^{(1)}(\mathbf{r},i\xi)$, in the second step, we calculate $\mathbf{G}^{(1)\mathrm{T}}(\mathbf{r}',\mathbf{r},i\xi)$. Because of the switching of $\mathbf{r}'$ and $\mathbf{r}$ we have to substitute $\mathbf{k}^\parallel\to-\mathbf{k}^\parallel$ to ensure that the term $e^{i\mathbf{k}^\parallel\cdot(\mathbf{r}-\mathbf{r}')}$ stays the same. Using the fact that $\mathbf{e}^\pm_p\to\mathbf{e}^\mp_p$ and $\mathbf{e}^\pm_s\to-\mathbf{e}^\pm_s=-\mathbf{e}^\mp_s$ for $\mathbf{k}^\parallel\to-\mathbf{k}^\parallel$, we therefore get

$$\mathbf{G}^{(1)\mathrm{T}}(\mathbf{r}',\mathbf{r},i\xi) = \frac{1}{8\pi^2}\int d^2\mathbf{k}^\parallel\frac{e^{i\mathbf{k}^\parallel\cdot(\mathbf{r}-\mathbf{r}')}}{\kappa}\sum_{\sigma,\sigma'}\{(-1)^{\sigma\sigma'}[\mathbf{e}^\sigma_+\mathbf{e}^{\sigma'}_- e^{-\kappa(z+z')}\,\mathrm{I}_{\sigma'\sigma}(-\mathbf{k}^\parallel) + \mathbf{e}^\sigma_-\mathbf{e}^{\sigma'}_+ e^{\kappa(z+z'-2L)}\,\mathrm{II}_{\sigma'\sigma}(-\mathbf{k}^\parallel)$$
$$+\mathbf{e}^\sigma_-\mathbf{e}^{\sigma'}_- e^{-\kappa(z'-z+2L)}\,\mathrm{III}_{\sigma'\sigma}(-\mathbf{k}^\parallel) + \mathbf{e}^\sigma_+\mathbf{e}^{\sigma'}_+ e^{\kappa(z'-z-2L)}\,\mathrm{IV}_{\sigma'\sigma}(-\mathbf{k}^\parallel)]\}. \tag{B4}$$

Here we also relabel $\sigma\leftrightarrow\sigma'$ and introduce $(-1)^{\sigma\sigma'}$, given by

$$(-1)^{\sigma\sigma'} = \begin{cases} 1 & \text{if } \sigma=\sigma', \\ -1 & \text{if } \sigma\neq\sigma'. \end{cases} \tag{B5}$$

As a side note, we want to mention here that by comparing Eqs. (B3) and (B4), one finds that Onsager's reciprocity, i.e., $\mathbf{G}^{(1)\mathrm{T}}(\mathbf{r}',\mathbf{r},i\xi) = \mathbf{G}^{(1)}(\mathbf{r},\mathbf{r}',i\xi)$, holds if

$$(-1)^{\sigma\sigma'}R_{\sigma'\sigma}(-\mathbf{k}^\parallel) = R_{\sigma\sigma'}(\mathbf{k}^\parallel), \quad R = \mathrm{I},\,\mathrm{II},\,\mathrm{III},\,\mathrm{IV}. \tag{B6}$$

Note that a similar expression has also been found in Ref. [39] for one-dimensional nanogratings. Nevertheless, in the setup considered here Eq. (B6) is not satisfied, and hence Onsager reciprocity is violated. Continuing with finding an expression for

$\mathbf{S}^{(1)}(\mathbf{r}, i\xi)$, we combine Eqs. (B3) and (B4) and obtain

$$\begin{aligned}\mathbf{G}^{(1)}(\mathbf{r},\mathbf{r}',i\xi)+\mathbf{G}^{(1)\mathrm{T}}(\mathbf{r}',\mathbf{r},i\xi)=\frac{1}{8\pi^2}\int d^2\mathbf{k}^{\parallel}\frac{e^{i\mathbf{k}^{\parallel}\cdot(\mathbf{r}-\mathbf{r}')}}{\kappa}\sum_{\sigma,\sigma'}\{&\mathbf{e}_+^{\sigma}\mathbf{e}_-^{\sigma'}e^{-\kappa(z+z')}\left[(-1)^{\sigma\sigma'}\mathrm{I}_{\sigma'\sigma}(-\mathbf{k}^{\parallel})+\mathrm{I}_{\sigma\sigma'}(\mathbf{k}^{\parallel})\right]\\&+\mathbf{e}_-^{\sigma}\mathbf{e}_+^{\sigma'}e^{\kappa(z+z'-2L)}\left[(-1)^{\sigma\sigma'}\mathrm{II}_{\sigma'\sigma}(-\mathbf{k}^{\parallel})+\mathrm{II}_{\sigma\sigma'}(\mathbf{k}^{\parallel})\right]\\&+\mathbf{e}_-^{\sigma}\mathbf{e}_-^{\sigma'}e^{-\kappa(z'-z+2L)}\left[(-1)^{\sigma\sigma'}\mathrm{III}_{\sigma'\sigma}(-\mathbf{k}^{\parallel})+\mathrm{III}_{\sigma\sigma'}(\mathbf{k}^{\parallel})\right]\\&+\mathbf{e}_+^{\sigma}\mathbf{e}_+^{\sigma'}e^{\kappa(z'-z-2L)}\left[(-1)^{\sigma\sigma'}\mathrm{IV}_{\sigma'\sigma}(-\mathbf{k}^{\parallel})+\mathrm{IV}_{\sigma\sigma'}(\mathbf{k}^{\parallel})\right]\}.\end{aligned}\tag{B7}$$

Next, we need to evaluate the curls. This can be done by realizing that the operators ∇ and $\overleftarrow{\nabla}$ reduce to $\nabla\to i\mathbf{k}_{\pm}$ and $\overleftarrow{\nabla}\to -i\mathbf{k}_{\pm}$, where $\mathbf{k}_{\pm}=\mathbf{k}^{\parallel}\pm i\kappa\mathbf{e}_z$. Using $i\mathbf{k}_{\pm}\times\mathbf{e}_{\mathrm{s}\pm}=\frac{\xi}{c}\mathbf{e}_{\mathrm{p}\pm}$, $i\mathbf{k}_{\pm}\times\mathbf{e}_{\mathrm{p}\pm}=-\frac{\xi}{c}\mathbf{e}_{\mathrm{s}\pm}$, we find that $\nabla\times\mathscr{S}[\mathbf{G}^{(1)}(\mathbf{r},\mathbf{r}',i\xi)]\times\overleftarrow{\nabla}'$ is obtained from $\mathscr{S}[\mathbf{G}^{(1)}(\mathbf{r},\mathbf{r}',i\xi)]$ by simply replacing all $\mathbf{e}_{\pm}^{\sigma\sigma'}\to\mathbf{e}_{\pm}^{\bar{\sigma}\bar{\sigma}'}\xi^2(-1)^{\sigma\sigma'}/c^2$, where $\bar{\sigma}$ is defined by $\bar{s}=p$ and $\bar{p}=s$. We can combine this result with Eq. (B7) to find

$$\begin{aligned}\mathbf{S}^{(1)}(\mathbf{r},i\xi)=\frac{\xi^2}{8\pi^2c^2}\int d^2\mathbf{k}^{\parallel}\frac{e^{i\mathbf{k}^{\parallel}\cdot(\mathbf{r}-\mathbf{r}')}}{\kappa}\sum_{\sigma,\sigma'}\{&\underbrace{[\mathbf{e}_+^{\sigma}\mathbf{e}_-^{\sigma'}+\mathbf{e}_-^{\sigma'}\mathbf{e}_+^{\sigma}+(-1)^{\sigma\sigma'}(\mathbf{e}_+^{\bar{\sigma}}\mathbf{e}_-^{\bar{\sigma}'}+\mathbf{e}_-^{\bar{\sigma}'}\mathbf{e}_+^{\bar{\sigma}})]}_{\equiv\,\mathbf{Q}^{(1)}}[e^{-2\kappa z}\mathrm{I}_{\sigma\sigma'}(\mathbf{k}^{\parallel})+e^{2\kappa(z-L)}\mathrm{II}_{\sigma'\sigma}(\mathbf{k}^{\parallel})]\\&+e^{-2\kappa L}\underbrace{[\mathbf{e}_-^{\sigma}\mathbf{e}_-^{\sigma'}+\mathbf{e}_+^{\sigma'}\mathbf{e}_+^{\sigma}+(-1)^{\sigma\sigma'}(\mathbf{e}_-^{\bar{\sigma}}\mathbf{e}_-^{\bar{\sigma}'}+\mathbf{e}_+^{\bar{\sigma}'}\mathbf{e}_+^{\bar{\sigma}})]}_{\equiv\,\mathbf{Q}^{(2)}}[\mathrm{III}_{\sigma\sigma'}(\mathbf{k}^{\parallel})+\mathrm{IV}_{\sigma'\sigma}(\mathbf{k}^{\parallel})]\}.\end{aligned}\tag{B8}$$

Here, in the last step, we substituted $\mathbf{k}^{\parallel}\to-\mathbf{k}^{\parallel}$ back in some of the terms to find the two tensor valued prefactors $\mathbf{Q}^{(1)}$ and $\mathbf{Q}^{(2)}$ corresponding to terms with odd and even numbers of reflections, respectively. To eventually be able to evaluate Eq. (B2) we need to calculate the outer products in $\mathbf{Q}^{(1)}$ and $\mathbf{Q}^{(2)}$ in Cartesian coordinates. With the help of Eq. (A2) we find

$$\mathbf{e}_{\mp}^{\mathrm{p}}\mathbf{e}_{\pm}^{\mathrm{p}}=\frac{c^2}{\xi^2(k^{\parallel})^2}\begin{pmatrix}-\kappa^2k_x^2 & -\kappa^2k_xk_y & \pm i(k^{\parallel})^2\kappa k_x\\ -\kappa^2k_xk_y & -\kappa^2k_y^2 & \pm i(k^{\parallel})^2\kappa k_y\\ \mp i(k^{\parallel})^2\kappa k_x & \mp i(k^{\parallel})^2\kappa k_y & -(k^{\parallel})^4\end{pmatrix},\tag{B9}$$

$$\mathbf{e}_{\pm}^{\mathrm{p}}\mathbf{e}_{\pm}^{\mathrm{p}}=\frac{c^2}{\xi^2(k^{\parallel})^2}\begin{pmatrix}\kappa^2k_x^2 & \kappa^2k_xk_y & \pm i(k^{\parallel})^2\kappa k_x\\ \kappa^2k_xk_y & \kappa^2k_y^2 & \pm i(k^{\parallel})^2\kappa k_y\\ \pm i(k^{\parallel})^2\kappa k_x & \pm i(k^{\parallel})^2\kappa k_y & -(k^{\parallel})^4\end{pmatrix},\tag{B10}$$

$$\mathbf{e}_{\pm}^{\mathrm{s}}\mathbf{e}_{\pm}^{\mathrm{s}}=\mathbf{e}_{\pm}^{\mathrm{s}}\mathbf{e}_{\mp}^{\mathrm{s}}=\frac{1}{(k^{\parallel})^2}\begin{pmatrix}k_y^2 & -k_xk_y & 0\\ -k_xk_y & k_x^2 & 0\\ 0 & 0 & 0\end{pmatrix},\tag{B11}$$

$$\mathbf{e}_{+}^{\mathrm{s}}\mathbf{e}_{\pm}^{\mathrm{p}}=\mathbf{e}_{-}^{\mathrm{s}}\mathbf{e}_{\pm}^{\mathrm{p}}=(\mathbf{e}_{\pm}^{\mathrm{s}}\mathbf{e}_{+}^{\mathrm{s}})^{\mathrm{T}}=(\mathbf{e}_{\pm}^{\mathrm{p}}\mathbf{e}_{-}^{\mathrm{s}})^{\mathrm{T}}\tag{B12}$$

$$=\frac{c}{\xi(k^{\parallel})^2}\begin{pmatrix}\mp\kappa k_xk_y & \mp\kappa k_y^2 & i(k^{\parallel})^2k_y\\ \pm\kappa k_x^2 & \pm\kappa k_xk_y & -i(k^{\parallel})^2k_x\\ 0 & 0 & 0\end{pmatrix}.\tag{B13}$$

Comparing Eq. (B8) with Eq. (B2), we see that we need to evaluate the terms $(Q_{zz}^{(i)}-Q_{xx}^{(i)}-Q_{yy}^{(i)})/2$, $Q_{zx}^{(i)}$, and $Q_{zy}^{(i)}$. Using Eqs. (B9)–(B13) and the dispersion relation $(k^{\parallel})^2-\kappa^2=-\xi^2/c^2$, we eventually find

$$\left(Q_{zz}^{(1)}-Q_{xx}^{(1)}-Q_{yy}^{(1)}\right)/2=Q_{zx}^{(1)}=Q_{zy}^{(1)}=0,\tag{B14}$$

$$Q_{zx}^{(2)}=Q_{zy}^{(2)}=0,\tag{B15}$$

$$\left(Q_{zz}^{(2)}-Q_{xx}^{(2)}-Q_{yy}^{(2)}\right)/2=-\frac{2c^2}{\xi^2}\kappa^2.\tag{B16}$$

Equation (B14) shows that all terms with an odd number of reflections do not contribute to the Casimir force, whereas Eq. (B15) tells us that there is no lateral Casimir force, i.e., a nonzero x or y component of $\mathbf{f}$. Finally, using Eqs. (B2), (B8), and

(B14)–(B16), we find the final result for the Casimir force density acting on body 1:

$$\mathbf{f} = -\frac{\hbar}{8\pi^3}\int_0^\infty d\xi \int d^2\mathbf{k}^\parallel \kappa e^{-2\kappa L}[\mathrm{III}_{pp}(\mathbf{k}^\parallel) + \mathrm{IV}_{pp}(\mathbf{k}^\parallel) + \mathrm{III}_{ss}(\mathbf{k}^\parallel) + \mathrm{IV}_{ss}(\mathbf{k}^\parallel)]\mathbf{e}_z \tag{B17}$$

$$= -\frac{\hbar}{8\pi^3}\int_0^\infty d\xi \int_0^{2\pi} d\varphi \int_0^\infty dk^\parallel \kappa e^{-2\kappa L}\mathrm{Tr}[\mathscr{R}^- \cdot (\mathscr{D}^+)^{-1} \cdot \mathscr{R}^+ + \mathscr{R}^+ \cdot (\mathscr{D}^-)^{-1} \cdot \mathscr{R}^-]\mathbf{e}_z. \tag{B18}$$

Note that this result differs from the one obtained in Ref. [35] only by the fact that in Eq. (B18) we cannot carry out the $d\varphi$ integral due to the φ dependence of the reflection coefficients, whereas in Ref. [35] the media were isotropic in the plane of the surfaces and hence this integral simply gave a factor of 2π.

In the nonretarded limit the reflection coefficients simplify significantly according to Eqs. (A28) and (A30), and thus Eq. (B18) reduces to

$$\mathbf{f} = -\frac{\hbar}{16\pi^3 L^3}\int_0^\infty d\xi \int_0^{2\pi} d\varphi \int_0^\infty d\kappa\, \kappa^2 \frac{r_{\mathrm{pp}}^+(i\xi)r_{\mathrm{pp}}^-(i\xi)e^{-2\kappa L}}{1 - r_{\mathrm{pp}}^+(i\xi)r_{\mathrm{pp}}^-(i\xi)e^{-2\kappa L}}\mathbf{e}_z$$

$$= -\frac{\hbar}{16\pi^3 L^3}\int_0^\infty d\xi \int_0^{2\pi} d\varphi\ \mathrm{Li}_3[r_{\mathrm{pp}}^+(i\xi)r_{\mathrm{pp}}^-(i\xi)]\mathbf{e}_z. \tag{B19}$$

[1] H. B. G. Casimir, Proc. K. Ned. Akad. Wet. **51**, 793 (1948).
[2] I. E. Dzyaloshinskii, E. M. Lifshitz, and L. P. Pitaevskii, Adv. Phys. **10**, 165 (1961).
[3] S. J. van Enk, Phys. Rev. A **52**, 2569 (1995).
[4] F. S. S. Rosa, D. A. R. Dalvit, and P. W. Milonni, Phys. Rev. A **78**, 032117 (2008).
[5] R. B. Rodrigues, P. A. M. Neto, A. Lambrecht, and S. Reynaud, Europhys. Lett. **76**, 822 (2006).
[6] Y. S. Barash, Radiophys. Quantum Electron. (Engl. Transl.) **21**, 1138 (1978).
[7] T. G. Philbin and U. Leonhardt, Phys. Rev. A **78**, 042107 (2008).
[8] J. C. Torres-Guzmán and W. L. Mochán, J. Phys. A **39**, 6791 (2006).
[9] P. Thiyam, P. Parashar, K. V. Shajesh, O. I. Malyi, M. Boström, K. A. Milton, I. Brevik and C. Persson, Phys. Rev. Lett. **120**, 131601 (2018).
[10] F. Chen, U. Mohideen, G. L. Klimchitskaya, and V. M. Mostepanenko, Phys. Rev. Lett. **88**, 101801 (2002).
[11] F. Chen, U. Mohideen, G. L. Klimchitskaya, and V. M. Mostepanenko, Phys. Rev. A **66**, 032113 (2002).
[12] F. Chen, B. Harris, A. Roy, and U. Mohideen, Int. J. Mod. Phys. A **17**, 711 (2002).
[13] H. C. Chiu, G. L. Klimchitskaya, V. N. Marachevsky, V. M. Mostepanenko, and U. Mohideen, Phys. Rev. B **80**, 121402 (2009).
[14] H. C. Chiu, G. L. Klimchitskaya, V. N. Marachevsky, V. M. Mostepanenko, and U. Mohideen, Phys. Rev. B **81**, 115417 (2010).
[15] J. N. Munday, D. Iannuzzi, Y. Barash, and F. Capasso, Phys. Rev. A **71**, 042102 (2005).
[16] D. Iannuzzi, M. Lisanti, J. N. Munday, and F. Capasso, Solid State Commun. **135**, 618 (2005).
[17] X. Chen and J. C. H. Spence, Phys. Status Solidi B **248**, 2064 (2011).
[18] M. Z. Hasan and C. L. Kane, Rev. Mod. Phys. **82**, 3045 (2010).
[19] S. Raghu and F. D. M. Haldane, Phys. Rev. A **78**, 033834 (2008).
[20] S. A. Hassani Gangaraj, M. G. Silveirinha, and G. W. Hanson, IEEE J. Multiscale Multiphys. Comput. Tech. **2**, 3 (2017).
[21] L. Lu, J. D. Joannopoulos, and M. Soljačić, Nat. Photonics **8**, 821 (2014).
[22] A. B. Khanikaev, S. Hossein Mousavi, W.-K. Tse, M. Kargarian, A. H. MacDonald, and G. Shvets, Nat. Mater. **12**, 233 (2012).
[23] W. Gao, B. Yang, M. Lawrence, F. Fang, B. Béri, and S. Zhang, Nat. Commun. **7**, 12435 (2016).
[24] M. G. Silveirinha, Phys. Rev. B **92**, 125153 (2015).
[25] M. G. Silveirinha, Phys. Rev. B **94**, 205105 (2016).
[26] A. R. Davoyan and N. Engheta, Phys. Rev. Lett. **111**, 257401 (2013).
[27] F. D. M. Haldane and S. Raghu, Phys. Rev. Lett. **100**, 013904 (2008).
[28] S. A. H. Gangaraj, G. W. Hanson, and M. Antezza, Phys. Rev. A **95**, 063807 (2017).
[29] M. G. Silveirinha, S. A. Gangaraj, G. W. Hanson, and M. Antezza, Phys. Rev. A **97**, 022509 (2018).
[30] S. A. H. Gangaraj, G. W. Hanson, M. Antezza, and M. G. Silveirinha, Phys. Rev. B **97**, 201108(R) (2018).
[31] S. A. H. Gangaraj, M. G. Silveirinha, G. W. Hanson, M. Antezza, and F. Monticone, Phys. Rev. B **98**, 125146 (2018).
[32] R. M. Abraham Ekeroth, P. Ben-Abdallah, J. C. Cuevas, and A. García-Martín, ACS Photonics **5**, 705 (2018).
[33] L. Zhu and S. Fan, Phys. Rev. Lett. **117**, 134303 (2016).
[34] M. G. Silveirinha, Phys. Rev. B **95**, 115103 (2017).
[35] S. Fuchs, F. Lindel, R. V. Krems, G. W. Hanson, M. Antezza, and S. Y. Buhmann, Phys. Rev. A **96**, 062505 (2017).
[36] E. D. Palik, R. Kaplan, R. W. Gammon, H. Kaplan, R. F. Wallis, and J. J. Quinn, Phys. Rev. B **13**, 2497 (1976).
[37] S. Y. Buhmann, D. T. Butcher, and S. Scheel, New J. Phys. **14**, 083034 (2012).
[38] S. Y. Buhmann, *Dispersion Forces: Many-Body Effects, Excited Atoms, Finite Temperature and Quantum Friction* (Springer, Heidelberg, 2012).
[39] S. Y. Buhmann, V. N. Marachevsky, and S. Scheel, Int. J. Mod. Phys. A **31**, 1641029 (2016).

[40] L. Bergstrom, Adv. Colloid Interface Sci. **70**, 125 (1997).
[41] C. Henkel, K. Joulain, J.-P. Mulet, and J.-J. Greffet, Phys. Rev. A **69**, 023808 (2004).
[42] T. B. Bateman, H. J. McSkimin, and J. M. Whelan, J. Appl. Phys. **30**, 544 (1959).
[43] A. G. Grushin, P. Rodriguez-Lopez, and A. Cortijo, Phys. Rev. B **84**, 045119 (2011).
[44] T. Osaka, M. Dakai, K. Hayashi, K. Ohashi, M. Saito, and K. Yamada, Nature (London) **392**, 796 (1998).
[45] X. L. Qi, T. L. Hughes, and S. C. Zhang, Phys. Rev. B **78**, 195424 (2008).
[46] X. L. Qi, R. Li, J. Zang, and S. C. Zhang, Science **323**, 1184 (2009).
[47] K. Kim, X. Xu, J. Guo, and D. L. Fan, Nat. Commun. **5**, 3632 (2014).

LANGMUIR Article
pubs.acs.org/Langmuir

Strong van der Waals Adhesion of a Polymer Film on Rough Substrates

Juliane Klatt,*[,†] Pablo Barcellona,[†] Robert Bennett,[†] Olga S. Bokareva,[‡] Hagen Feth,[§] Andreas Rasch,[§] Patrick Reith,[§] and Stefan Yoshi Buhmann[†,⊥]

[†]Physikalisches Institut, Albert-Ludwigs-Universität Freiburg, Hermann-Herder-Str. 3, 79104 Freiburg, Germany
[‡]Institut für Physik, Universität Rostock, Albert-Einstein-Str. 23-24, 18059 Rostock, Germany
[§]TrueDyne Sensors AG, Christoph-Merian-Ring 20, 4153 Reinach, Switzerland
[⊥]Freiburg Institute for Advanced Studies, Albert-Ludwigs-Universität Freiburg, Albertstr. 19, 79104 Freiburg, Germany

Supporting Information

ABSTRACT: We propose that chemically inert polymeric films can enhance van der Waals (vdW) forces in the same way as nanofabrication of biomimetic adhesive materials. For the vdW adhesion of an ethylene-chlorotrifluoroethylene (ECTFE) film on rough metal and dielectric substrates, we present a model that combines microscopic quantum-chemistry simulations of the polymer response functions and the equilibrium monomer−substrate distance with a macroscopic quantum-electrodynamics calculation of the Casimir force between the polymer film and the substrate. We predict adhesive forces up to 2.22 kN/mm^2, where the effect is reduced by substrate roughness and for dielectric surfaces.

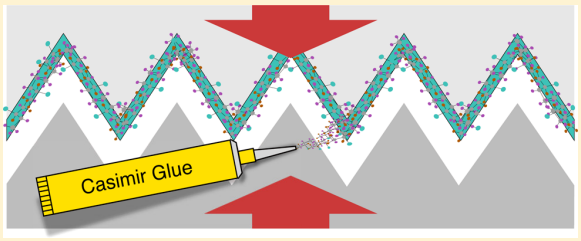

The discovery that van der Waals (vdW) forces are responsible for the remarkable sticking properties of gecko feet on dry surfaces[1] has inspired the nanofabrication of biomimetic adhesive materials. Organorods[2] and nanopillars[3] exhibit the flexibility of gecko-feet setae, hence providing close contact with the substrate in order to enhance the vdW attraction. Fundamentally, vdW forces are caused by quantum charge-density fluctuations and arise whenever two neutral, but polarizable, objects are brought in proximity. Unlike chemical binding forces, they do not require immediate contact to ensure notable attraction. However, their strong power-law decay with increasing distance makes them most effective in micro- to nanoranges. They have not only been measured with high accuracy,[4] but have also been found responsible for stiction in nanofabrication.[5] Measurements of Casimir−vdW forces typically involve well-separated solid-state objects at distances where a correct theoretical description requires accounting for the retarded quantum electromagnetic field.[6] For plane metal or dielectric surfaces, this is achieved by the Lifshitz theory.[7] The effect of surface roughness on the interaction has been studied experimentally and theoretically, both for obtaining a more realistic understanding[8,9] and in view of potential applications of the lateral Casimir force arising between two periodically corrugated surfaces.[10] A very recent study of the force between corrugated surfaces has revealed discrepancies between experiment and theory that remain unresolved to date.[11] In all of the mentioned studies, the surfaces are well separated, so that their corrugations are not intertwined and their interaction due to electromagnetic field fluctuations can be studied by means of scattering theory.[12,13]

We propose to exploit the flexibility of a polymer film to ensure close contact and hence high adhesive force on a solid substrate. In particular, ECTFE is a partially fluorinated polymer whose semicrystalline films have been experimentally demonstrated to exhibit a resistance against permeation of water[14] and also high chemical resistance.[15] Wettability measurements of ECTFE in polar liquids have revealed a considerable influence of vdW forces on the ECTFE−liquid interaction.[16] Our proposed setup of a such a polymer film sticking to a solid surface operates in a very different regime than the traditional Casimir setups. The polymer is expected to come into close contact with the substrate so that effects of retardation are negligible. The adhesion force per unit area between two smooth surfaces separated by a distance z is hence given by the nonretarded limit of the Lifshitz formula: $\vec{f}(z) = -(C_3/z^3)\vec{e}_z$ with a coefficient[7]

$$C_3 = \frac{\hbar}{8\pi^2}\int_0^\infty \mathrm{d}\omega \mathrm{Li}_3\left[\frac{\varepsilon_1(i\omega)-1}{\varepsilon_1(i\omega)+1}\frac{\varepsilon_2(i\omega)-1}{\varepsilon_2(i\omega)+1}\right] \quad (1)$$

Here, $\mathrm{Li}_3(x) = \sum_{k=1}^{\infty} x^k/k^3$ is the polylogarithm and $\varepsilon_1(\omega)$ and $\varepsilon_2(\omega)$ are the dielectric permittivities at angular frequency ω of polymer film and substrate, respectively. The Lifshitz formula is originally expressed as an integral over real frequencies with the

Received: April 22, 2017
Published: May 10, 2017

DOI: 10.1021/acs.langmuir.7b01381
Langmuir 2017, 33, 5298−5303

permittivities being strongly oscillating functions. For mathematical convenience, we have used a Wick rotation to equivalently express the C_3 coefficient as an integral over purely imaginary frequencies $I\omega$ with $\omega > 0$. The integrand is then much easier to evaluate numerically, as it is a monotonously decreasing function. To illustrate the use of such imaginary-frequency integrals, we first quote the formula for the closely related van der Waals potential between two ground-state atoms

$$U(\mathbf{r}_{AB}) = -\frac{1}{24\pi^2\epsilon_0^2 r_{AB}^6}\sum_{k,l}\frac{|\mathbf{d}_{0k}^A|^2|\mathbf{d}_{0l}^B|^2}{E_{0k}^A + E_{0l}^B} \equiv -\frac{C_6}{r_{AB}^6} \tag{2}$$

Here, r_{AB} is the distance between the atoms, and the sum represents virtual transitions of atoms A and B from their ground states to excited states l, k with transition energies E_{0k}^A and E_{0l}^B, respectively. The respective dipole-matrix elements are denoted as $\mathbf{d}_{0k}^A$ and $\mathbf{d}_{0l}^B$. The potential $U(\mathbf{r}_{AB})$ can be expressed as an integral over frequency

$$U(\mathbf{r}_{AB}) = -\frac{3\hbar}{16\pi^3\epsilon_0^2 r_{AB}^6}\int_0^\infty d\omega \alpha_A(i\omega)\alpha_B(i\omega) \tag{3}$$

where

$$\alpha_A(i\omega) = \frac{2}{3}\frac{E_{0k}^A|\mathbf{d}_{0k}^A|^2}{(E_{0k}^A)^2 + \hbar^2\omega^2} \tag{4}$$

describes the polarizability of atom A at imaginary frequencies (similarly for atom B).

In eq 1 we have neglected the effect of thermal fluctuations of the electromagnetic field and that of spatial dispersion. The assumption of a spatially local response implies the use of dielectric functions $\epsilon_1(\omega)$ and $\epsilon_2(\omega)$, which depend on the wave vector $\mathbf{k}$ only via its absolute value $|\mathbf{k}| = \omega/c$. A spatially nonlocal response and thermal effects combined have been shown to modify the Casimir force by a factor of 2 at distances larger than the thermal wavelength.[17] At room temperature, the thermal wavelength assumes a value of about 48 μm and is, hence, much smaller than the distances considered here. The effect of nonlocal responses has also been studied at smaller distances where it was found that, depending on the model used, the force may be increased or decreased on a percent level.[18] Finally, we note that, for moderate roughness, one may expect the polymers to adapt to the surface profile of the substrate, so that the corrugated surfaces of the interacting objects intertwine (see Figure 1).

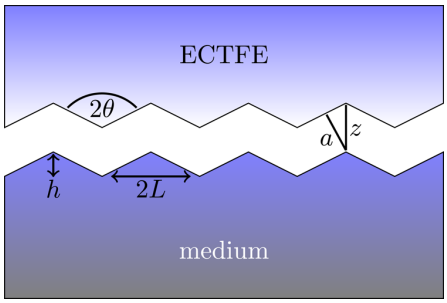

Figure 1. Setup: One-dimensional periodic sawtooth corrugations. The roughness is characterized by the mean distance between peaks, $2L$, and their average height, h, related via the angle $\theta = \arctan\left(\frac{L}{h}\right)$.

While the optical properties of common solid substrates are well studied and tabulated,[19] those of polymer species require microscopic simulations. Periodic simulations of long polymer chains packed in a box have been performed, see, for example, ref 20. However, in order to reproduce vibrational frequencies, polarizabilities, and polymerization mechanisms, careful investigations of monomeric or dimeric units are often applied instead, where the molecular properties are evaluated by quantum chemical methods[21,22] or via combined quantum and molecular mechanical approaches.[23] In the following, we will estimate the total adhesive force of ECTFE films on different substrates by combining macroscopic Lifshitz theory with microscopic simulations of the polymer response function. We begin by determining the polarizability of the polymer and the equilibrium distance of its monomers from different substrate media. Combining this information, we will determine the maximum total adhesive force for perfectly smooth substrates and finally study the effect of surface roughness on this force.

Let us start by determining the dielectric response of ECTFE. Microscopically, it is encoded in the dynamical polarizability $\alpha(i\omega)$ at imaginary frequencies. We are interested in the average dielectric properties of a large ensemble of ECTFE chains of various lengths and resort to a simple model: we study the polarizability of simple ECTFE monomers and represent the ensemble as a set of such monomeric units with random orientations. We calculate the monomer polarisibilities by means of combining quantum chemical methods[24−27] as described in Supporting Information, A. To check the validity of the assumption that the polarizability of the polymers can be decomposed into those of single monomers, we compare monomer and dimer polarizabilities. After averaging over orientations, the isotropic polarizability of the dimer is almost equal to twice that of the monomer (Figure 2), justifying our model.

As a second microscopic ingredient, we require the equilibrium distance between the ECTFE polymer and the substrate, as determined from a competition between local chemical binding and long-range dispersion forces. We evaluate the covalent interactions between ECTFE monomers and substrate surfaces by means of quantum chemistry, as described in the Supporting Information.[28−31] Beginning with the case of a (001) silicon surface with 2−1 reconstruction, three starting positions of monomer relative to the surface are chosen, leading to three different optimal structures for each case. The corresponding equilibrium distances are displayed in Figure 2. They range from 2.6−3.7 Å for all cases, justifying the use of a single parameter for further modeling: a rotationally averaged value for the equilibrium surface−monomer separation, given as

$$a = \frac{1}{6}(4r_{\text{orientation 1}} + r_{\text{orientation 2}} + r_{\text{orientation 3}}) \tag{5}$$

Due to sterical reasons and possible surface defects, the monomer units in the polymer chain will have a certain distribution of distances to the silicon surface. To account for this effect, the dependence of the binding energy on the distance between monomer and cluster has been studied. We find that the interaction in all cases is weak, with binding energies being close to zero, because no stable chemical bonds are formed. The binding energy rapidly decreases with the increase of distance between the monomer unit and the surface. We conclude that the total adhesion force is dominated by dispersive binding. We assume the presence of similar orientations for surface−monomer complexes with other

DOI: 10.1021/acs.langmuir.7b01381
Langmuir 2017, 33, 5298−5303

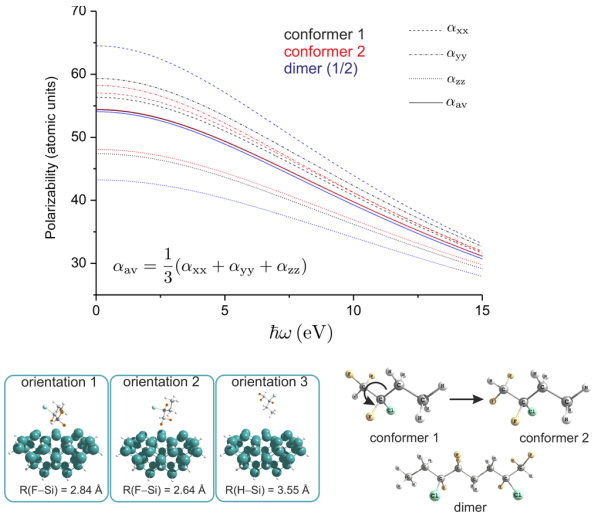

Figure 2. ECTFE monomers: Upper panel: Dynamical polarizabilities $\alpha(i\omega)$ of ECTFE monomer and dimer units at imaginary frequencies. After averaging over orientations, the isotropic polarizability of the dimer is almost equal to twice that of the monomer. This justifies the assumption that the polarizability of the polymers can be decomposed into those of single monomers. Lower right panel: Three-dimensional structures corresponding to the two conformers of the ECTFE monomer and the dimer. Lower left panel: Three starting positions of monomer relative to a (001) silicon surface with 2−1 reconstruction and corresponding equilibrium distances. The latter are in a of 2.6−3.7 Å for all cases, justifying the use of a single parameter.

substrate materials. To transfer our results to different substrates, a correction accounting for size-effects is introduced (see Supporting Information, B). The obtained equilibrium distances for all substrates are summarized in Table 1.

Table 1. Adhesion Forces: Equilibrium Distances, C_3 Coefficients, and Casimir Forces per Unit Area (Obtained from Exact Theory and Pairwise Approximation) for ECTFE Films on Various Substrates[a]

substrate	a (Å)	C_3 (mP μm^3)	C_3^{pw} (mP μm^3)	f (kN/mm^2)	f^{pw} (kN/mm^2)
silicon dioxide	2.48	22.5	26.5	1.48	1.74
silicon	2.95	38.2	50.9	1.49	1.98
gold	3.16	51.2	68.4	1.62	2.17
steel	2.93	55.9	76.1	2.22	3.03

[a]Silicon dioxide, which has the weakest C_3 coefficient, has the smallest equilibrium distance, thus, considerably enhancing the total force. Also, the fairly large equilibrium separation of gold has had the effect of reducing its total adhesion force, which is now more similar to that of silicon rather than that of steel. Therefore, both the force coefficient and equilibrium separation are equally relevant in determining the total force.

We chose to study four different substrate materials that are widely used: silicon, silicon dioxide, gold and steel. To obtain the required permittivities at imaginary frequencies as featured in eq 1, we start from optical data, as tabulated in ref 19, and apply a Kramers−Kronig transformation. For the two metals, the hence-obtained curves are well fitted with an asymmetric two-resonance product model that combines a Drude term for the response of the conduction electrons with a Drude-Lorentz term for that of the valence electrons. For the dielectrics, we use additive single- or two-resonance Drude-Lorentz models instead. The obtained fit parameters can be found in Table III of section C of the Supporting Information. For the ECTFE film, we use the Clausius-Mosotti formula[32] that relates its permittivity ε to the simulated polarizability: $\alpha\eta/\varepsilon_0 = 3(\varepsilon - 1)/(\varepsilon + 2)$, where η is the number density of particles. In Figure 3, we display the dimensionless polarizability $3(\varepsilon - 1)/(\varepsilon + 2)$ for all materials under study.

The figure reveals that the polarizabilities of the dielectrics ECTFE and silicon dioxide show a similar response in terms of the imaginary-axis polarizabilities. On the other hand, the metals gold and steel and the metalloid silicon all display a high static polarizability, with the polarizability of gold dropping fastest with increasing frequency. As the dispersive adhesion force depends on the integrated polarizabilities, one may hence expect this force to be significantly smaller for gold than for steel and silicon.

Using the optical data, we can now evaluate the dispersion force coefficients (eq 1) for ECTFE films on each of the four substrate materials. Using the equilibrium separations a between ECTFE monomers and the various substrates, we can hence determine the respective adhesive dispersion force $\vec{f} = \vec{f}(a)$. The results are shown in Table 1, where for comparison, we have also given the approximate values obtained from a pairwise-additive approach. The findings are illustrated in Figure 3 which displays the dispersion force as a function of separation with the respective equilibrium separations indicated. One notes that silicon dioxide, which has the weakest force coefficient, has the smallest equilibrium distance, thus, enhancing the total force. As a result, the series silicon dioxide−silicon−gold−steel of increasing adhesive dispersion forces retains its order, but the relative differences between the substrates are less pronounced than they are for the force coefficients. The difference between forces for silicon dioxide and steel is a factor of 1.5. In addition, we note that the large equilibrium separation of gold has had the effect of reducing its total adhesion force, which is now more similar to that of silicon rather than that of steel. To summarize, the force coefficient and equilibrium separation are both equally relevant in determining the strength of the total adhesion force.

Realistic substrates exhibit roughness. We here address the question how this influences the adhesive force. As a model system, we study the one-dimensional periodic sawtooth corrugations as depicted in Figure 1. The roughness is characterized by the mean distance between peaks, $2L$, and their average height, h, related via the angle $\theta = \arctan(L/h)$. We assume the polymer film to be sufficiently elastic such that its shape adapts to the substrate surface. The effect of roughness will be cast into a correction factor λ which relates the average force per unit area of a rough surface to that of a perfectly smooth one via $\vec{f}(a,L,\theta) = \lambda(a,L,\theta)\vec{f}(a,L,\pi/2)$. The roughness exhibited by real materials can be accounted for via the proximity force approximation (PFA).[33] Here, irregular geometries are approximated by piecewise parallel ones, each subject to the Lifshitz force per unit area for infinitely extended plates. One way to treat the peaks of our model is to approximate their profile by small plane-parallel steps. The effective Casimir force is then obtained from eq 1 and it carries a correction factor

$$\lambda(\theta) = \sin^3\theta \leq 1 \qquad (6)$$

DOI: 10.1021/acs.langmuir.7b01381
Langmuir 2017, 33, 5298−5303

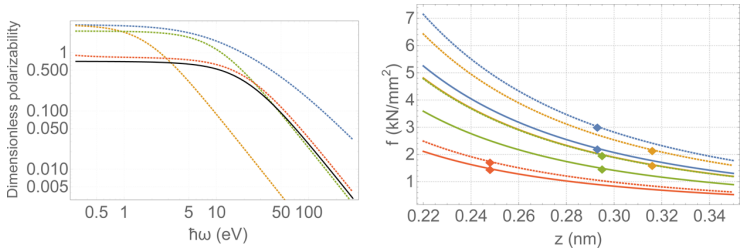

Figure 3. Adhesive force: Left: Dimensionless polarizabilities of all materials studied. From top to bottom: steel (blue), gold (orange), silicon (green), silicon dioxide (red), and ECTFE (black). The polarizabilities of the dielectrics ECTFE and silicon dioxide show a similar response. On the other hand, the metals gold and steel and the metalloid silicon all display a high static polarizability. Right: Total adhesive forces f per unit area as a function of the ECTFE−substrate separation. Solid and dashed lines correspond to exact theory and pairwise approximation, respectively. Diamonds indicate the respective equilibrium separations for the various substrates. Colors: steel (blue), gold (orange), silicon (green), silicon dioxide (red).

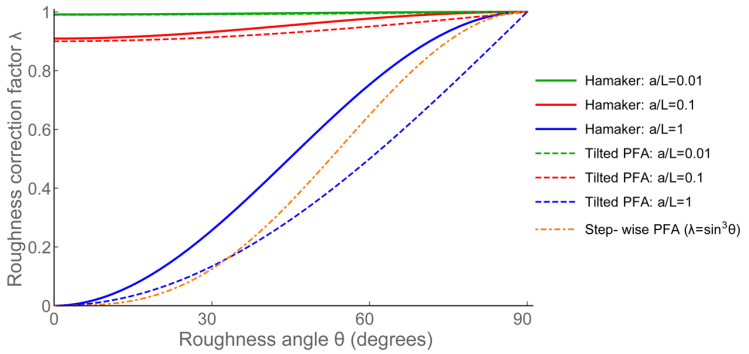

Figure 4. Surface roughness: Roughness correction λ which relates the average dispersion force per unit area of a rough surface to that of a perfectly smooth one via $\tilde{f}(a,L,\theta) = \lambda(a,L,\theta)\tilde{f}(a,L,\pi/2)$. Shown in the figure are three different approximations: first, the Hamaker approximation (solid lines), with the parameter $a/L = 0.01$ (green, uppermost solid line), 0.1 (red, middle solid line), and 1 (blue, lowest solid line); second, we show the tilted-surface proximity force approximation (dashed lines) with the same choices of a/L; and third, we include the stepwise proximity force approximation (dot-dashed line).

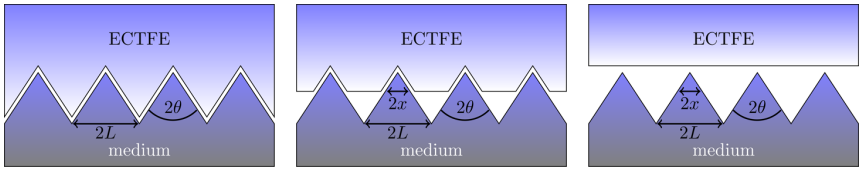

Figure 5. Complete, partial, and no contact. The left panel depicts the ideal of a perfectly elastic polymer film, which is completely pulled into the substrate's asperities by the adhesive force and hence is in perfect contact with the substrate. The middle panel instead depicts partial contact while the right panel depicts the extreme of a perfectly inelastic film, which does not give in to the substrate's asperities at all and therefore has only pointlike contact with the latter.

In this simple treatment, λ only depends on θ and becomes arbitrarily small for very rough surfaces. This may be understood from a reduced contact due to enhanced distance in the z-direction as the ECTFE film gets pushed away from the substrate for steep corrugations. An alternative way of employing the PFA is to decompose the model peaks into their tilted parallel sections. The length of such sections equals $L/\sin\theta - a/\tan\theta$. Combined with the tilting factor, $\sin\theta$ this leads to

$$\lambda(\theta, L, a) = 1 - \frac{a}{L}\cos\theta \leq 1 \tag{7}$$

For strong roughness, the effective force does not necessarily vanish but rather depends on the ratio of equilibrium distance a to mean separation of peaks $2L$. In this model, the roughness-reduction of the force is due to a reduction of contact area. The angle-dependence of λ for both models is illustrated in Figure 4.

As an alternative method, we study the effect of roughness via the Hamaker approximation,[34] which reproduces the two-body contribution to the geometry-dependence (see Supporting Information, D). The corresponding result, also displayed in Figure 4, agrees with the tilted-surface PFA for small values of a/L. For large values of a/L, it lies in between the predictions from the stepwise-profile PFA and the tilted-surface PFA. We note that $\lambda \leqslant 1$ in all cases, meaning that roughness always reduces the adhesion force.

Finally, we want to address the assumption of complete contact between the ECTFE film and the substrate, which was made throughout this work. As depicted in Figure 5, complete contact means that the ECTFE film is perfectly pulled into the substrate's asperities by the adhesion force and hence is nowhere separated further than its respective equilibrium distance a from the roughness peaks of the substrate, regardless

DOI: 10.1021/acs.langmuir.7b01381
Langmuir 2017, 33, 5298−5303

of the roughness profile. This corresponds to the ideal case of a perfectly elastic polymer film. The opposite extreme of a perfectly inelastic film would instead not adjust at all to the substrate's roughness and hence have only point-like contact with it. This effect evidently affects the strength of the van der Waals adhesion between the ECTFE film and the substrate.[35] Our predictions for such forces as presented in Table 1 only hold for the case of complete contact. This is motivated by the process of applying the ECTFE film to the substrate, during which the film is actually heated, causing it to adopt the shape of the roughness of the substrate as its zero-stress configuration.

Nevertheless, one may consider the situation in which no heating is performed. Whether the ECTFE then adjusts to the shape of the substrate depends on the elastic modulus σ of ECTFE on the one hand and the adhesive force per area f between ECTFE and the respective substrate on the other hand. The elastic modulus is defined as the ratio between the applied stress f and the resulting strain $\delta l/l$ of the material to which the stress is applied,

$$\sigma = \frac{f}{\delta l/l} \tag{8}$$

Here, δl refers to a change in length. Now, at any point at a lateral distance x from a roughness peak of the interface, there is the competition between elastic energy lost,

$$E_{\mathrm{el}} = \frac{\sigma}{2}\left(\frac{x}{\tan\theta}\right)^2 \tag{9}$$

and adhesive energy gained,

$$E_{\mathrm{adh}} = 3C_3 \sin\theta\left(\frac{1}{a^2} - \frac{1}{(x\cos\theta + a)^2}\right) \tag{10}$$

when bending into the substrate's asperities. Depending on which of the two dominates, ECTFE at a lateral distance x from a peak does or does not stick to the substrate. For the simplified geometry considered here, this leads to a correction or filling factor $\kappa = \tilde{x}^2/L^2$, with $\tilde{x}$ being the distance x from a peak at which loss and gain balance. Such filling factors are given in Figure 6 for the elasticity modulus σ = 1655 MPa of ECTFE[36] and micron-scale roughness, $L = 10^{-6}$ m. Such filling factors depend on the respective C_3 coefficient, the equilibrium distance a, roughness angle θ, and absolute roughness scale L. This figure illustrates that from $\theta = 10°$ onward, perfect contact may be presupposed for all substrates considered here.

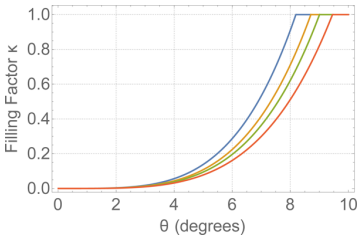

Figure 6. Filling factor and critical angle: Filling factors for steel (blue), gold (orange), and silicon/silicon dioxide (green/red). The elasticity modul σ = 1655 MPa of ECTFE[36] and micron roughness, $L = 10^{-6}$ m, were used. The filling factors depend on the respective C_3 coefficient, the equilibrium distance a, roughness angle θ, and absolute roughness scale L.

To conclude, we have shown that chemically inert polymer films such as ECTFE can be used to achieve high van der Waals adhesion forces on dielectric or metallic substrates. We have predicted these forces by combining quantum-chemistry simulations of the polymers microscopic properties with a macroscopic quantum electrodynamics calculation of the Lifshitz force between polymer film and substrate. A simple model of one-dimensional corrugations implies that substrate roughness will diminish the adhesion force. This model operates in a new regime of distances being comparable to or even smaller than the length scales characterizing the corrugations. The predicted forces are based on the assumption that the polymer film is sufficiently flexible to follow the substrate surface profile and achieve contact distances equal to those found for monomers. They thus have to be regarded as an upper bound to the forces found on practical implementations. To get a more precise estimate of the latter, further simulations of the microscopic structure of the polymer film will be necessary.

■ ASSOCIATED CONTENT

Supporting Information

The Supporting Information is available free of charge on the ACS Publications website at DOI: 10.1021/acs.langmuir.7b01381.

Detailed account of the Hamaker approximation and the determination of material parameters (PDF).

■ AUTHOR INFORMATION

Corresponding Author

*E-mail: juliane.klatt@physik.uni-freiburg.de.

ORCID

Olga S. Bokareva: 0000-0002-2313-7996

Notes

The authors declare no competing financial interest.

■ ACKNOWLEDGMENTS

The authors thank C. Blattert for discussions. J.K., P.B., R.B., and S.Y.B. gratefully acknowledge financial support by the German Research Foundation (Grant BU1803/3-1), and S.Y.B. was also supported by the Freiburg Institute for Advanced Studies (FRIAS).

■ REFERENCES

(1) Autumn, K.; Sitti, M.; Liang, Y. A.; Peattie, A. M.; Hansen, W. R.; Sponberg, S.; Kenny, T. W.; Fearing, R.; Israelachvili, J. N.; Full, R. J. Evidence for van der Waals adhesion in gecko setae. *Proc. Natl. Acad. Sci. U. S. A.* **2002**, *99*, 12252−6.

(2) Northen, M. T.; Turner, K. L. A batch fabricated biomimetic dry adhesive. *Nanotechnology* **2005**, *16*, 1159−1166.

(3) Lee, H.; Lee, B. P.; Messersmith, P. B. A reversible wet/dry adhesive inspired by mussels and geckos. *Nature* **2007**, *448*, 338−41.

(4) Lamoreaux, S. K. Demonstration of the Casimir Force in the 0.6 to 6 μ m Range. *Phys. Rev. Lett.* **1997**, *78*, 5−8.

(5) Serry, F. M.; Walliser, D.; Maclay, G. J. The role of the casimir effect in the static deflection and stiction of membrane strips in microelectromechanical systems (MEMS). *J. Appl. Phys.* **1998**, *84*, 2501−2506.

(6) Casimir, H. On the attraction between two perfectly conducting plates. *Proc. K. Ned. Akad.* **1948**, *360*, 793−795.

(7) Lifshitz, E. The Theory of Molecular Attractive Forces between Solids. *J. Exp. Theor. Phys.* **1956**, *2*, 73−83.

DOI: 10.1021/acs.langmuir.7b01381
Langmuir 2017, 33, 5298−5303

(8) Roy, A.; Mohideen, U. Demonstration of the Nontrivial Boundary Dependence of the Casimir Force. *Phys. Rev. Lett.* **1999**, *82*, 4380−4383.
(9) Chan, H. B.; Bao, Y.; Zou, J.; Cirelli, R. A.; Klemens, F.; Mansfield, W. M.; Pai, C. S. Measurement of the Casimir Force between a Gold Sphere and a Silicon Surface with Nanoscale Trench Arrays. *Phys. Rev. Lett.* **2008**, *101*, 030401.
(10) Ashourvan, A.; Miri, M.; Golestanian, R. Noncontact Rack and Pinion Powered by the Lateral Casimir Force. *Phys. Rev. Lett.* **2007**, *98*, 140801.
(11) Intravaia, F.; Koev, S.; Jung, I. W.; Talin, A. A.; Davids, P. S.; Decca, R. S.; Aksyuk, V. A.; Dalvit, D. A. R.; López, D. Strong Casimir force reduction through metallic surface nanostructuring. *Nat. Commun.* **2013**, *4*, 793−796.
(12) Rodrigues, R. B.; Neto, P. A. M.; Lambrecht, A.; Reynaud, S. Lateral Casimir Force beyond the Proximity-Force Approximation. *Phys. Rev. Lett.* **2006**, *96*, 100402.
(13) Lambrecht, A.; Neto, P. A. M.; Reynaud, S. The Casimir effect within scattering theory. *New J. Phys.* **2006**, *8*, 243.
(14) Hansen, C. M. Water transport and condensation in fluoropolymer films. *Prog. Org. Coat.* **2001**, *42*, 167−178.
(15) Ausimont Halar ECTFE:Chemical resistance data [Online]; http://www.integument.com/Portals/34/Files/Chemical-Resistance/ectfe.pdf.
(16) Lee, S.; Park, J. S.; Lee, T. R. The wettability of fluoropolymer surfaces: Influence of surface dipoles. *Langmuir* **2008**, *24*, 4817−4826.
(17) Sernelius, B. E. Finite-temperature Casimir force between metal plates: full inclusion of spatial dispersion resolves a long-standing controversy. *J. Phys. A: Math. Gen.* **2006**, *39*, 6741.
(18) Esquivel-Sirvent, R.; Villarreal, C.; Mochán, W. L.; Contreras-Reyes, A. M.; Svetovoy, V. B. Spatial dispersion in Casimir forces: A brief review. *J. Phys. A: Math. Gen.* **2006**, *39*, 6323.
(19) Palik, E. D. *Handbook of Optical Constants of Solids*; Academic Press, 1985.
(20) Han, B.; Jiao, M.; Li, C.; Zhang, C.; Wu, Z.; Wang, Y.; Zhang, H. QM/MD simulations on the role of SiO2 in polymeric insulation materials. *RSC Adv.* **2016**, *6*, 555−562.
(21) Smith, S. M.; Markevitch, A. N.; Romanov, D. A.; Li, X.; Levis, R. J.; Schlegel, H. B. Static and Dynamic Polarizabilities of Conjugated Molecules and Their Cations. *J. Phys. Chem. A* **2004**, *108*, 11063−11072.
(22) Mavroudakis, E.; Cuccato, D.; Dossi, M.; Comino, G.; Moscatelli, D. Quantum Chemistry Investigation of Fluorinated Polymer Systems of Industrial Interest. *J. Phys. Chem. A* **2014**, *118*, 238−247.
(23) Kupfer, S.; Zedler, L.; Guthmuller, J.; Bode, S.; Hager, M. D.; Schubert, U. S.; Popp, J.; Gräfe, S.; Dietzek, B. Self-healing mechanism of metallopolymers investigated by QM/MM simulations and Raman spectroscopy. *Phys. Chem. Chem. Phys.* **2014**, *16*, 12422.
(24) University of Karlsruhe and Forschungszentrum Karlsruhe. *TURBOMOLE V6.2*; TURBOMOLE GmbH, 2010.
(25) Becke, A. D. Density-functional exchange-energy approximation with correct asymptotic behavior. *Phys. Rev. A: At., Mol., Opt. Phys.* **1988**, *38*, 3098−3100.
(26) Lee, C.; Yang, W.; Parr, R. G. Development of the Colle-Salvetti correlation-energy formula into a functional of the electron density. *Phys. Rev. B: Condens. Matter Mater. Phys.* **1988**, *37*, 785−789.
(27) Dunning, T. H. Gaussian basis sets for use in correlated molecular calculations. I. The atoms boron through neon and hydrogen. *J. Chem. Phys.* **1989**, *90*, 1007−1023.
(28) Hehre, W. J.; Ditchfield, R.; Pople, J. A. Self-Consistent Molecular Orbital Methods. XII. Further Extensions of Gaussian-Type Basis Sets for Use in Molecular Orbital Studies of Organic Molecules. *J. Chem. Phys.* **1972**, *56*, 2257.
(29) Frisch, M. J.; Trucks, G. W.; Schlegel, H. B.; Scuseria, G. E.; Robb, M. A.; Cheeseman, J. R.; Scalmani, G.; Barone, V.; Mennucci, B.; Petersson, G. A.; Nakatsuji, H.; Caricato, M.; Li, X.; Hratchian, H. P.; Izmaylov, A. F.; Bloino, J.; Zheng, G.; Sonnenberg, J. L.; Hada, M.; Ehara, M.; Toyota, K.; Fukuda, R.; Hasegawa, J.; Ishida, M.; Nakajima, T.; Honda, Y.; Kitao, O.; Nakai, H.; Vreven, T.; Montgomery, J. A., Jr.; Peralta, J. E.; Ogliaro, F.; Bearpark, M.; Heyd, J. J.; Brothers, E.; Kudin, K. N.; Staroverov, V. N.; Kobayashi, R.; Normand, J.; Raghavachari, K.; Rendell, A.; Burant, J. C.; Iyengar, S. S.; Tomasi, J.; Cossi, M.; Rega, N.; Millam, J. M.; Klene, M.; Knox, J. E.; Cross, J. B.; Bakken, V.; Adamo, C.; Jaramillo, J.; Gomperts, R.; Stratmann, R. E.; Yazyev, O.; Austin, A. J.; Cammi, R.; Pomelli, C.; Ochterski, J. W.; Martin, R. L.; Morokuma, K.; Zakrzewski, V. G.; Voth, G. A.; Salvador, P.; Dannenberg, J. J.; Dapprich, S.; Daniels, A. D.; Farkas, Ö.; Foresman, J. B.; Ortiz, J. V.; Cioslowski, J.; Fox, D. J. *Gaussian09*, Revision E.01; Gaussian, Inc., 2009.
(30) Boys, S.; Bernardi, F. The calculation of small molecular interactions by the differences of separate total energies. Some procedures with reduced errors. *Mol. Phys.* **1970**, *19*, 553−566.
(31) Jansen, H.; Ros, P. Non-empirical molecular orbital calculations on the protonation of carbon monoxide. *Chem. Phys. Lett.* **1969**, *3*, 140−143.
(32) Jackson, J. D. *Classical Electrodynamics*; Wiley, 1975.
(33) Derjaguin, B. V.; Abrikosova, I. I.; Lifshitz, E. M. Direct measurement of molecular attraction between solids separated by a narrow gap. *Q. Rev., Chem. Soc.* **1956**, *10*, 295−329.
(34) Hamaker, H. The London-van der Waals attraction between spherical particles. *Physica* **1937**, *4*, 1058−1072.
(35) Zilberman, S.; Persson, B. Adhesion between elastic bodies with rough surfaces. *Solid State Commun.* **2002**, *123*, 173−177.
(36) Solvay, Halar ECTFE: Design and Processing Guide [Online]; http://www.solvay.com/en/binaries/Halar-ECTFE-Design-and-Processing-Guide_EN-227532.pdf.

DOI: 10.1021/acs.langmuir.7b01381
Langmuir 2017, 33, 5298−5303

PHYSICAL REVIEW A **95**, 023805 (2017)

Casimir-Polder shift and decay rate in the presence of nonreciprocal media

Sebastian Fuchs,[1] J. A. Crosse,[2] and Stefan Yoshi Buhmann[1,3]
[1]*Physikalisches Institut, Albert-Ludwigs-Universität Freiburg, Hermann-Herder-Straße 3, 79104 Freiburg, Germany*
[2]*Department of Electrical and Computer Engineering, National University of Singapore, 4 Engineering Drive 3, 117583, Singapore*
[3]*Freiburg Institute for Advanced Studies, Albert-Ludwigs-Universität Freiburg, Albertstraße 19, 79104 Freiburg, Germany*
(Received 19 May 2016; published 2 February 2017)

We calculate the Casimir–Polder frequency shift and decay rate for an atom in front of a nonreciprocal medium by using macroscopic quantum electrodynamics. The results are a generalization of the respective quantities for matter with broken time-reversal symmetry which does not fulfill the Lorentz reciprocity principle. As examples, we contrast the decay rates, the resonant and nonresonant frequency shifts of a perfectly conducting (reciprocal) mirror with those of a perfectly reflecting nonreciprocal mirror. We find different power laws for the distance dependence of all quantities in the retarded and nonretarded limits. As an example of a more realistic nonreciprocal medium, we investigate a topological insulator subject to a time-symmetry-breaking perturbation.

DOI: 10.1103/PhysRevA.95.023805

I. INTRODUCTION

The Casimir–Polder force [1], like the van der Waals and the Casimir forces [2], is a dispersion force [3,4]. This weak electromagnetic force was studied by using a variety of different methods. The lifetime and the frequency shift of an atom in its ground state or excited state near a flat surface, which causes the Casimir–Polder force, are analyzed by using a quantum-mechanical linear-response formalism in Refs. [5,6]. This is exemplified for a perfect conductor and a metal plate.

The Casimir–Polder force can also be viewed as result of noise currents composed of noise polarization and noise magnetization in matter, which act as a source for a quantized electromagnetic field. These fields can be expanded in terms of the classical electromagnetic Green's tensor for the Helmholtz equation [7–12]. By computing the interaction of an atom with this field one can compute the effect of material bodies on the internal properties of the atom. The Casimir–Polder force is a result of the level shift of the atom induced by this field. In this theoretical framework, materials are described macroscopically by electromagnetic physical quantities and therefore this approach is known as macroscopic quantum electrodynamics (QED) [3,4,13]. Casimir–Polder potentials have been investigated for graphene [14], metamaterials [15,16], and Rydberg atoms near metallic surfaces [17].

In bi-isotropic media electric and magnetic fields are coupled to each other and the general expressions of the constitutive relations read $\mathbf{D} = \varepsilon_0 \boldsymbol{\epsilon} \star \mathbf{E} + \frac{1}{c}\boldsymbol{\xi} \star \mathbf{H}$ and $\mathbf{B} = \frac{1}{c}\boldsymbol{\zeta} \star \mathbf{E} + \mu_0 \boldsymbol{\mu} \star \mathbf{H}$ (where $\star$ denotes a spatial convolution) with the cross susceptibilities $\boldsymbol{\xi}$ and $\boldsymbol{\zeta}$. If a material shows imaginary cross susceptibilities, the material is called chiral [18,19]. The radiation of a dipole in proximity to a thin [20] and a thick chiral layer [21] has already been studied. References [22,23] study the interaction between a chiral molecule in front of a chiral half space [23] and a chiral nanosphere [22]. The decay rate of spontaneous emission is computed in a direct way by using the electric and magnetic dipole moments, their induced counterparts, and the respective fields.

A bi-isotropic medium is called nonreciprocal if the mixing parameters have a real-valued contribution, e.g., a topological insulator which breaks time-reversal symmetry. In the theory of macroscopic QED, Lorentz's reciprocity principle stating the reversibility of optical paths, i.e., the symmetry with respect to an exchange of positions and orientations of sources and fields, holds for reciprocal material (Lorentz reciprocity being a particular case of the Onsager reciprocity from statistical physics [24]). Thus these materials preserve time-reversal symmetry. To study Casimir–Polder potentials for nonreciprocal media, which violate Lorentz's reciprocity relation [25], the theory of macroscopic QED was generalized to include these cross susceptibilities [26]. In this paper, we investigate the Casimir–Polder frequency shift and decay rate for a nonreciprocal medium.

Topological insulators [27–29] are time-symmetric materials which are characterized by an insulating bulk and protected conducting surface states and have been observed in three-dimensional (3D) materials which exhibit sufficiently strong spin-orbit coupling to induce band inversion [30]. These materials can be used to realize axion media. To do this one needs to introduce a time-reversal-symmetry-breaking perturbation to the surface, either via ferromagnetic dopants [31,32] or an external static magnetic field [33]. Such a perturbation opens a gap on the surface, converting the surface conductor into a full insulator and leads to a nontrivial electromagnetic response—in particular the electric and the magnetic fields $\mathbf{E}$ and $\mathbf{B}$ are able to mix [31].

This magneto-electric effect can be described by adding an axion Lagrangian density term $\mathscr{L}_{\text{axion}} = \alpha/(4\pi^2)\theta(\mathbf{r},\boldsymbol{\omega})\mathbf{E}\cdot\mathbf{B}$ to the usual electromagnetic Lagrangian density [34]. Here, α is the fine-structure constant and $\theta(\mathbf{r},\boldsymbol{\omega})$ is the space- and time-dependent axion coupling. The axion coupling θ vanishes in a trivial insulator but takes odd integer values of π in a time-reversal-symmetry-broken topological insulator, with the value and sign of the integer related to the strength and direction of the time-symmetry-breaking perturbation. Physically, this describes a quantum Hall effect on the surface of the topological insulator [31]. The lowest Hall plateau leads to an axion coupling of $\pm\pi$. Changing the size of the perturbation will not change the axion coupling until the next Hall plateau is reached, whereupon the axion coupling will increase to $\pm 3\pi$. Further changes to the perturbation would result in even higher axion couplings as the relevant Hall plateaus are reached. It has been previously shown that the mixing of the electric and magnetic fields by the axion coupling

has a significant effect on the Casimir force [35] and, as we will show in Sec. IV, it also modifies the Casimir–Polder shift.

Optical properties, e.g., reflective and transmissive properties, Fresnel formulas, Brewster angle, and the Goos–Hänchen effect of these materials have been studied theoretically in Refs. [36,37]. Reference [38] derives electric fields and dipole moments for stratified isorefractive Tellegen media (purely-real-valued coupling parameter between electric and magnetic field) with the Green's tensor method. One consequence of isorefractive media is the parallelism of the incident and transmitted beam. As for layered topological insulators with a time-reversal-symmetry-breaking perturbation, potential applications are broad; for example, a waveguide that induces polarization rotations due to the magneto-electric effect and mixes the electric and magnetic induction fields at the material's surface [39].

In our context, Casimir repulsion is of specific interest, e.g., the Casimir repulsion for magnetodielectric metamaterials predicted in Refs. [40–42]. Specifically, repulsive dispersion forces for a setup containing topological insulators are discussed in Ref. [35], such as Casimir forces between three-dimensional topological insulators. Based on this approach, it is shown in Ref. [43] that there is a critical band gap where the Casimir force switches from attractive to repulsive. The influence of unusual material properties, such as those of the topological insulator, on dispersion forces is emphasized in the recent review [44]. The Casimir–Polder interaction between an atom and a graphene surface with an applied magnetic field is studied in Ref. [45]. The authors observe plateau-like discontinuities of the Casimir–Polder interaction energy for specific values of the magnetic field and at low temperatures. This effect is traced back to the quantum Hall effect and is thus closely connected to our approach. We are going to apply the extended theory of macroscopic QED for nonreciprocal media to calculate frequency shifts and atomic decay rates of an atom in front of a topological insulator by directly using the electromagnetic properties derived in Ref. [46].

This paper on the Casimir–Polder shift and decay rate in the presence of nonreciprocal media is organized as follows: The time-dependent electric field is calculated in the framework of macroscopic QED for nonreciprocal media in Sec. II. This result is reached alternatively by a direct quantization of the noise current or by expressing noise polarization and magnetization through electromagnetic response functions and is needed for studying the internal atomic dynamics. This is described in Sec. III where the modified equations for the frequency shift and decay rate for nonreciprocal media are presented. In Sec. IV, the results are applied to a perfectly reflecting nonreciprocal mirror and a topological insulator described by an axion coupling. In this context, we distinguish between a pure nonreciprocal topological insulator and material properties similar to Bi_2Se_3. Finally, we discuss the possibility of switching between an attractive and a repulsive force.

II. THE TIME-DEPENDENT ELECTRIC FIELD

A nonreciprocal medium violates time-reversal symmetry and, hence, the Lorentz reciprocity principle for the Green's tensor [25] does not hold

$$\mathbf{G}^{\mathrm{T}}(\mathbf{r}',\mathbf{r},\omega) \neq \mathbf{G}(\mathbf{r},\mathbf{r}',\omega). \tag{1}$$

This necessitates new definitions for the real and imaginary parts of the Green's tensor $\mathbf{G}$

$$\mathcal{R}[\mathbf{G}(\mathbf{r},\mathbf{r}')] = \frac{1}{2}[\mathbf{G}(\mathbf{r},\mathbf{r}') + \mathbf{G}^{*\mathrm{T}}(\mathbf{r}',\mathbf{r})], \tag{2}$$

$$\mathcal{I}[\mathbf{G}(\mathbf{r},\mathbf{r}')] = \frac{1}{2i}[\mathbf{G}(\mathbf{r},\mathbf{r}') - \mathbf{G}^{*\mathrm{T}}(\mathbf{r}',\mathbf{r})]. \tag{3}$$

Thus the violation of Lorentz's principle calls for a modified mathematical description of macroscopic quantum electrodynamics (QED) for nonreciprocal media. Whereas the framework of macroscopic QED is described in Refs. [3,13], the modified approach for nonreciprocal media is outlined in Ref. [26]. The internal dynamics of an atom with reciprocal media is discussed in Refs. [4,8].

The general expression for the electric field reads

$$\hat{\mathbf{E}}(\mathbf{r}) = \int_0^\infty d\omega[\hat{\mathbf{E}}(\mathbf{r},\omega) + \hat{\mathbf{E}}^\dagger(\mathbf{r},\omega)], \tag{4}$$

with frequency components in Fourier space

$$\begin{aligned}\hat{\mathbf{E}}(\mathbf{r},\omega) &= i\mu_0\omega[\mathbf{G} \star \hat{\mathbf{j}}_{\mathrm{N}}](\mathbf{r},\omega) \\ &= i\mu_0\omega \int d^3r'\mathbf{G}(\mathbf{r},\mathbf{r}',\omega)\cdot\hat{\mathbf{j}}_{\mathrm{N}}(\mathbf{r}',\omega),\end{aligned} \tag{5}$$

where $\star$ denotes a spatial convolution. The noise current density $\hat{\mathbf{j}}_{\mathrm{N}}$ is governed by the quantum fluctuations occurring in the medium and its average vanishes $\langle\hat{\mathbf{j}}_{\mathrm{N}}\rangle = \mathbf{0}$. $\hat{\mathbf{j}}_{\mathrm{N}}$ can either be quantized directly, as is outlined in Sec. II A, or it can be represented by noise polarization $\hat{\mathbf{P}}_{\mathrm{N}}$ and magnetization $\hat{\mathbf{M}}_{\mathrm{N}}$ and the respective electric and magnetic fields are quantized separately yielding creation and annihilation operators for each field. We dedicate Sec. II B to the second method using electric and magnetic response functions.

To obtain an expression for the time-dependent electric field (4), we have to find a solution for the time-dependent creation and annihilation operators first. This procedure is carried out both for a noise-current-based schema and a polarization-magnetization-founded method. The Hamiltonian $\hat{H}$ for the atom-field system is composed of the atomic part $\hat{H}_{\mathrm{A}}$, the field part $\hat{H}_{\mathrm{F}}$, and a contribution for the atom-field interaction $\hat{H}_{\mathrm{AF}}$: $\hat{H} = \hat{H}_{\mathrm{A}} + \hat{H}_{\mathrm{F}} + \hat{H}_{\mathrm{AF}}$. The atomic part $\hat{H}_{\mathrm{A}}$,

$$\hat{H}_{\mathrm{A}} = \sum_n E_n \hat{A}_{nn}, \tag{6}$$

incorporates the eigenenergy E_n for each atomic energy level and the atomic flip operator $\hat{A}_{mn} = |m\rangle\langle n|$. Resembling a harmonic oscillator, $\hat{H}_{\mathrm{F}}$ comprises the integral over all the frequency-dependent number operators of the field-medium system and can be cast in the two aforementioned ways; cf. Secs. II A and II B. The interaction Hamiltonian $\hat{H}_{\mathrm{AF}}$, which couples the atomic dipole to the electromagnetic field, reads

$$\hat{H}_{\mathrm{AF}} = -\hat{\mathbf{d}}\cdot\hat{\mathbf{E}}(\mathbf{r}_A) = -\sum_{m,n}\hat{A}_{mn}\mathbf{d}_{mn}\cdot\hat{\mathbf{E}}(\mathbf{r}_A) \tag{7}$$

and contains the electric-dipole operator $\hat{\mathbf{d}} = \sum_{m,n}\mathbf{d}_{mn}\hat{A}_{mn}$. $\mathbf{r}_{\mathrm{A}}$ is the position of the atom. Since $\hat{H}_{\mathrm{A}}$ commutes with the field operators, only the commutation relations for the field

Hamiltonian $\hat{H}_{\mathrm{F}}$ and the interaction Hamiltonian $\hat{H}_{\mathrm{AF}}$ have to be studied to find the expression for the electric field (4). The field operators' equations of motion will be solved in the two different ways and inserted into Eq. (5), thus giving a final expression for the electric field in the presence of an atom.

A. Electric field in noise-current-based schema

In this first approach, the noise current is quantized directly by expressions for the field operators. Ohm's Law in frequency space,

$$\hat{\mathbf{j}}_{\mathrm{in}}(\mathbf{r},\boldsymbol{\omega}) = [\mathbf{Q} \star \hat{\mathbf{E}}](\mathbf{r},\boldsymbol{\omega}) + \hat{\mathbf{j}}_{\mathrm{N}}(\mathbf{r},\boldsymbol{\omega}), \tag{8}$$

describes the effect of the electric field $\hat{\mathbf{E}}(\mathbf{r},\boldsymbol{\omega})$ on a linearly responding medium where $\mathbf{Q}$ is the conductivity matrix. Hence, the Helmholtz equation reads

$$\left[\overrightarrow{\nabla} \times \overrightarrow{\nabla} \times - \frac{\boldsymbol{\omega}^2}{c^2}\right]\mathbf{G}(\mathbf{r},\mathbf{r}',\boldsymbol{\omega}) - i\mu_0\boldsymbol{\omega}[\mathbf{Q} \star \mathbf{G}](\mathbf{r},\mathbf{r}'\boldsymbol{\omega}) = \boldsymbol{\delta}(\mathbf{r}-\mathbf{r}'). \tag{9}$$

This equation is formally solved by the Green's tensor $\mathbf{G}$ with $\mathbf{G} \to \mathbf{0}$ for $|\mathbf{r}-\mathbf{r}'| \to \infty$.

We quantize the noise-current density $\hat{\mathbf{j}}_{\mathrm{N}}$ in Eq. (5) directly by writing it in terms of creation and annihilation operators $\hat{\mathbf{f}}^{\dagger}$ and $\hat{\mathbf{f}}$

$$\hat{\mathbf{j}}_{\mathrm{N}}(\mathbf{r},\boldsymbol{\omega}) = \sqrt{\frac{\hbar\boldsymbol{\omega}}{\pi}}[\mathbf{R} \star \hat{\mathbf{f}}](\mathbf{r},\boldsymbol{\omega}), \tag{10}$$

where $\mathbf{R}$ is related to the real part of the conductivity tensor $\mathbf{Q}$

$$[\mathbf{R} \star \mathbf{R}^{*\mathrm{T}}](\mathbf{r},\mathbf{r}',\boldsymbol{\omega}) = \mathcal{R}[\mathbf{Q}(\mathbf{r},\mathbf{r}',\boldsymbol{\omega})]. \tag{11}$$

The Heisenberg equation of motion for the annihilation operator $\hat{\mathbf{f}}$

$$\dot{\hat{\mathbf{f}}}(\mathbf{r},\boldsymbol{\omega}) = \frac{1}{i\hbar}[\hat{\mathbf{f}}(\mathbf{r},\boldsymbol{\omega}),\hat{H}], \tag{12}$$

upon using the field Hamiltonian $\hat{H}_{\mathrm{F}}$,

$$\hat{H}_{\mathrm{F}} = \int d^3r \int_0^{\infty} d\boldsymbol{\omega}\hbar\boldsymbol{\omega}\hat{\mathbf{f}}^{\dagger}(\mathbf{r},\boldsymbol{\omega}) \cdot \hat{\mathbf{f}}(\mathbf{r},\boldsymbol{\omega}), \tag{13}$$

and the interaction Hamiltonian $\hat{H}_{\mathrm{AF}}$ (7) by using Eq. (5),

$$\hat{H}_{\mathrm{AF}} = -\sum_{m,n}\int_0^{\infty} d\boldsymbol{\omega} i\mu_0\boldsymbol{\omega}\sqrt{\frac{\hbar\boldsymbol{\omega}}{\pi}}\hat{A}_{mn}\mathbf{d}_{mn} \times \{[\mathbf{G} \star \mathbf{R} \star \hat{\mathbf{f}}](\mathbf{r}_A,\boldsymbol{\omega}) - [\mathbf{G}^* \star \mathbf{R}^* \star \hat{\mathbf{f}}^{\dagger}](\mathbf{r}_A,\boldsymbol{\omega})\}, \tag{14}$$

gives the solution of the annihilation operator $\hat{\mathbf{f}}$

$$\hat{\mathbf{f}}(\mathbf{r},\boldsymbol{\omega},t) = e^{-i\boldsymbol{\omega}(t-t_0)}\hat{\mathbf{f}}(\mathbf{r},\boldsymbol{\omega}) + \frac{\mu_0\boldsymbol{\omega}}{\hbar}\sqrt{\frac{\hbar\boldsymbol{\omega}}{\pi}}\sum_{m,n}\int_{t_0}^{t} dt' \times e^{-i\boldsymbol{\omega}(t-t')}[\mathbf{G} \star \mathbf{R}]^{*\mathrm{T}}(\mathbf{r}_A,\mathbf{r},\boldsymbol{\omega}) \cdot \mathbf{d}_{mn}\hat{A}_{mn}. \tag{15}$$

Substituting the results into Eq. (10) and using Eq. (11) and the expression

$$\mathcal{I}[\mathbf{G}(\mathbf{r},\mathbf{r}',\boldsymbol{\omega})] = \mu_0\boldsymbol{\omega}[\mathbf{G} \star \mathcal{R}[\mathbf{Q}] \star \mathbf{G}^{*\mathrm{T}}](\mathbf{r},\mathbf{r}',\boldsymbol{\omega}), \tag{16}$$

leads to an expression for the electric field in nonreciprocal media

$$\hat{\mathbf{E}}(\mathbf{r},\boldsymbol{\omega},t) = e^{-i\boldsymbol{\omega}(t-t_0)}\hat{\mathbf{E}}(\mathbf{r},\boldsymbol{\omega}) + i\frac{\mu_0\boldsymbol{\omega}^2}{\pi}\sum_{m,n}\int_{t_0}^{t} dt' \times e^{-i\boldsymbol{\omega}(t-t')}\mathcal{I}[\mathbf{G}(\mathbf{r},\mathbf{r}_A,\boldsymbol{\omega})] \cdot \mathbf{d}_{mn}\hat{A}_{mn}, \tag{17}$$

which differs from the usual expression for reciprocal media only by the definition of the imaginary part of the Green's tensor (3) [4].

B. Electric field in polarization-magnetization-based schema

The components of the electric field $\hat{\mathbf{E}}(\mathbf{r},\boldsymbol{\omega})$ can also be calculated in terms of electric and magnetic response functions, i.e., polarization and magnetization [26]. The constitutive relations for the electric displacement field $\hat{\mathbf{D}}$ and the magnetic induction field $\hat{\mathbf{B}}$ are given by [26]

$$\hat{\mathbf{D}} = \varepsilon_0\boldsymbol{\epsilon} \star \hat{\mathbf{E}} + \frac{1}{c}\boldsymbol{\xi} \star \hat{\mathbf{H}} + \hat{\mathbf{P}}_{\mathrm{N}} + \frac{1}{c}\boldsymbol{\xi} \star \hat{\mathbf{M}}_{\mathrm{N}}, \tag{18}$$

$$\hat{\mathbf{B}} = \frac{1}{c}\boldsymbol{\zeta} \star \hat{\mathbf{E}} + \mu_0\boldsymbol{\mu} \star \hat{\mathbf{H}} + \mu_0\boldsymbol{\mu} \star \hat{\mathbf{M}}_{\mathrm{N}}, \tag{19}$$

where the tensor $\boldsymbol{\epsilon}$ is the permittivity, $\boldsymbol{\mu}$ is the permeability and $\boldsymbol{\xi}$ and $\boldsymbol{\zeta}$ represent the magneto-electric cross susceptibilities. The noise polarization $\hat{\mathbf{P}}_{\mathrm{N}}$ and noise magnetization $\hat{\mathbf{M}}_{\mathrm{N}}$ form the noise current $\hat{\mathbf{j}}_{\mathrm{N}}$

$$\hat{\mathbf{j}}_{\mathrm{N}}(\mathbf{r},\boldsymbol{\omega}) = -i\boldsymbol{\omega}\hat{\mathbf{P}}_{\mathrm{N}}(\mathbf{r},\boldsymbol{\omega}) + \overrightarrow{\nabla} \times \hat{\mathbf{M}}_{\mathrm{N}}(\mathbf{r},\boldsymbol{\omega}) = (-i\boldsymbol{\omega}, \quad \overrightarrow{\nabla} \times) \cdot \begin{pmatrix} \hat{\mathbf{P}}_{\mathrm{N}}(\mathbf{r},\boldsymbol{\omega}) \\ \hat{\mathbf{M}}_{\mathrm{N}}(\mathbf{r},\boldsymbol{\omega}) \end{pmatrix}. \tag{20}$$

The noise polarization and noise magnetization can be expressed in terms of the creation and annihilation operators for the electric and the magnetic fields $\hat{\mathbf{f}}_{\mathrm{e}}$, $\hat{\mathbf{f}}_{\mathrm{e}}^{\dagger}$, $\hat{\mathbf{f}}_{\mathrm{m}}$, and $\hat{\mathbf{f}}_{\mathrm{m}}^{\dagger}$

$$\begin{pmatrix} \hat{\mathbf{P}}_{\mathrm{N}} \\ \hat{\mathbf{M}}_{\mathrm{N}} \end{pmatrix} = \sqrt{\frac{\hbar}{\pi}}\mathscr{R} \star \begin{pmatrix} \hat{\mathbf{f}}_{\mathrm{e}} \\ \hat{\mathbf{f}}_{\mathrm{m}} \end{pmatrix}. \tag{21}$$

The Green's tensor $\mathbf{G}$ from Eq. (5) solves the respective Helmholtz equation

$$-\mu_0(-i\boldsymbol{\omega}, \quad \overrightarrow{\nabla} \times) \star \mathscr{M} \star \begin{pmatrix} i\boldsymbol{\omega} \\ \overrightarrow{\nabla} \times \end{pmatrix} \star \mathbf{G} = \delta, \tag{22}$$

with the matrix

$$\mathscr{M} = \begin{pmatrix} \varepsilon_0(\boldsymbol{\epsilon} - \boldsymbol{\xi} \star \boldsymbol{\mu}^{-1} \star \boldsymbol{\zeta}) & \frac{\boldsymbol{\xi} \star \boldsymbol{\mu}^{-1}}{Z_0} \\ \frac{\boldsymbol{\mu}^{-1} \star \boldsymbol{\zeta}}{Z_0} & -\frac{\boldsymbol{\mu}^{-1}}{\mu_0} \end{pmatrix}. \tag{23}$$

The Helmholtz equation reduces to the standard form [3] if all cross susceptibilities are set to 0. The tensor $\mathscr{R}$ is related to the matrix $\mathscr{M}$ via

$$\mathscr{R} \star \mathscr{R}^{*T} = \mathcal{I}[\mathscr{M}]. \tag{24}$$

The conductivity matrix $\mathbf{Q}$ can also be expressed in terms of $\mathscr{M}$

$$\mathbf{Q} = \frac{1}{i\boldsymbol{\omega}}(-i\boldsymbol{\omega}, \quad \overrightarrow{\nabla} \times) \star \left[\mathscr{M} - \begin{pmatrix} \varepsilon_0 & 0 \\ 0 & -\frac{1}{\mu_0} \end{pmatrix}\right] \star \begin{pmatrix} i\boldsymbol{\omega} \\ - \times \overleftarrow{\nabla} \end{pmatrix}. \tag{25}$$

Calculations of the equations of motion of the creation and annihilation operators require the field Hamiltonian $\hat{H}_\mathrm{F}$,

$$\hat{H}_\mathrm{F} = \sum_{\lambda=\mathrm{e,m}} \int d^3r \int_0^\infty d\omega \hbar\omega \hat{\mathbf{f}}^\dagger_\lambda(\mathbf{r},\omega)\cdot\hat{\mathbf{f}}_\lambda(\mathbf{r},\omega), \tag{26}$$

and the interaction Hamiltonian $\hat{H}_\mathrm{AF}$ (7). Inserting Eqs. (4), (5), (20), and (21) into Eq. (7) enables us to solve the linear and inhomogeneous differential equation of the field operators

$$\begin{aligned}\begin{pmatrix}\hat{\mathbf{f}}_\mathrm{e}(\mathbf{r},\omega,t)\\ \hat{\mathbf{f}}_\mathrm{m}(\mathbf{r},\omega,t)\end{pmatrix} &= e^{-i\omega(t-t_0)}\begin{pmatrix}\hat{\mathbf{f}}_\mathrm{e}(\mathbf{r},\omega)\\ \hat{\mathbf{f}}_\mathrm{m}(\mathbf{r},\omega)\end{pmatrix} + \frac{\mu_0\omega}{\hbar}\sqrt{\frac{\hbar}{\pi}}\sum_{m,n}\int_0^{t_0} dt' \\ &\times [\mathbf{G}\star(-i\omega,\overrightarrow{\nabla}\times)\star\mathscr{R}]^{*\mathrm{T}}(\mathbf{r}_A,\mathbf{r},\omega) \\ &\times e^{-i\omega(t-t')}\cdot\mathbf{d}_{mn}\hat{A}_{mn},\end{aligned} \tag{27}$$

which can be inserted into Eqs. (21), (20), and (5) again. After using Eqs. (25) and (16) again, the final expression for $\hat{\mathbf{E}}(\mathbf{r},\omega)$ yields

$$\begin{aligned}\hat{\mathbf{E}}(\mathbf{r},\omega,t) &= e^{-i\omega(t-t_0)}\hat{\mathbf{E}}(\mathbf{r},\omega) + i\frac{\mu_0\omega^2}{\pi}\sum_{m,n}\int_{t_0}^{t} dt' e^{-i\omega(t-t')} \\ &\times \mathcal{I}[\mathbf{G}(\mathbf{r},\mathbf{r}_A,\omega)]\cdot\mathbf{d}_{mn}\hat{A}_{mn}\end{aligned} \tag{28}$$

and agrees perfectly with the result from Sec. II A [Eq. (17)].

III. INTERNAL ATOMIC DYNAMICS: FREQUENCY SHIFT AND DECAY RATE

The internal atomic dynamics can be described by the Heisenberg equations of motion for the atomic flip operator

$$\dot{\hat{A}}_{mn} = \frac{1}{i\hbar}[\hat{A}_{mn},\hat{H}] = \frac{1}{i\hbar}[\hat{A}_{mn},\hat{H}_\mathrm{A}] + \frac{1}{i\hbar}[\hat{A}_{mn},\hat{H}_\mathrm{AF}], \tag{29}$$

which includes only the atomic Hamiltonian $\hat{H}_\mathrm{A}$ and the interaction Hamiltonian $\hat{H}_\mathrm{AF}$ because the field Hamiltonian $\hat{H}_\mathrm{F}$ commutes with the atomic flip operator. This approach follows the procedure for a reciprocal surface outlined in Ref. [4] and is now extended to nonreciprocal media [26].

This leads to

$$\begin{aligned}\dot{\hat{A}}_{mn} &= i\omega_{mn}\hat{A}_{mn} + \frac{i}{\hbar}\sum_k\int_0^\infty d\omega \\ &\times [(\hat{A}_{mk}\mathbf{d}_{nk} - \hat{A}_{kn}\mathbf{d}_{km})\cdot\hat{\mathbf{E}}(\mathbf{r}_A,\omega) \\ &+ \hat{\mathbf{E}}^\dagger(\mathbf{r}_A,\omega)\cdot(\mathbf{d}_{nk}\hat{A}_{mk} - \mathbf{d}_{km}\hat{A}_{kn})].\end{aligned} \tag{30}$$

$\hat{A}_{mn}$ is dominated by oscillations with frequencies $\tilde{\omega}_{mn} = \omega_{mn} + \delta\omega_{mn}$, where ω_{mn} is the atom's eigenfrequency and $\delta\omega_{mn}$ is the shift owing to interaction with nearby material bodies (Casimir–Polder shift). The electric field is given in Eqs. (17) or (28). The time integral in the electric field can be formally evaluated in the Markov approximation where we neglect the slow nonoscillatory dynamics of the atomic flip operator $\hat{A}_{mn}$ during the time interval $t_0 \leqslant t' \leqslant t$ and set $\hat{A}_{mn}(t') \simeq \exp[i\tilde{\omega}_{mn}(t'-t)]\hat{A}_{mn}(t)$, where we have anticipated the result $\tilde{\omega}_{mn} = -\tilde{\omega}_{nm}$. In the long-time limit $t\to\infty$ the time integral reduces to $\hat{A}_{mn}(t)\int_{t_0}^t dt' \exp[-i(\omega-\tilde{\omega}_{nm})(t-t')] \simeq \hat{A}_{mn}(t)[\pi\delta(\omega-\tilde{\omega}_{nm}) - i\mathscr{P}/(\omega-\tilde{\omega}_{nm})]$, where $\mathscr{P}$ is the Cauchy principle value and the limits of the frequency integral will lead to the appearance of the Heaviside step-function Θ.

By defining the coefficient

$$\begin{aligned}\mathbf{C}_{mn} &= \frac{\mu_0}{\hbar}\Theta(\tilde{\omega}_{nm})\tilde{\omega}_{nm}^2\mathcal{I}[\mathbf{G}(\mathbf{r}_\mathrm{A},\mathbf{r}_\mathrm{A},\tilde{\omega}_{nm})]\cdot\mathbf{d}_{mn} \\ &- i\frac{\mu_0}{\pi\hbar}\mathscr{P}\int_0^\infty d\omega\frac{1}{\omega-\tilde{\omega}_{nm}}\omega^2\mathcal{I}[\mathbf{G}(\mathbf{r}_\mathrm{A},\mathbf{r}_\mathrm{A},\omega)]\cdot\mathbf{d}_{mn},\end{aligned} \tag{31}$$

Eq. (30) can be cast into the form

$$\begin{aligned}\dot{\hat{A}}_{mn}(t) &= i\omega_{mn}\hat{A}_{nm}(t) + \frac{i}{\hbar}\sum_k\int_0^\infty d\omega \\ &\times \{e^{-i\omega(t-t_0)}[\hat{A}_{mk}(t)\mathbf{d}_{nk} - \hat{A}_{kn}(t)\mathbf{d}_{km}]\cdot\hat{\mathbf{E}}(\mathbf{r}_\mathrm{A},\omega) \\ &+ e^{i\omega(t-t_0)}\hat{\mathbf{E}}^\dagger(\mathbf{r}_\mathrm{A},\omega)\cdot[\mathbf{d}_{nk}\hat{A}_{mk}(t) - \mathbf{d}_{km}\hat{A}_{kn}(t)]\} \\ &- \sum_{k,l}[\mathbf{d}_{nk}\cdot\mathbf{C}_{kl}\hat{A}_{ml}(t) - \mathbf{d}_{km}\cdot\mathbf{C}_{nl}\hat{A}_{kl}(t)] \\ &+ \sum_{k,l}[\mathbf{d}_{nk}\cdot\mathbf{C}^*_{ml}\hat{A}_{lk}(t) - \mathbf{d}_{km}\cdot\mathbf{C}^*_{kl}\hat{A}_{ln}(t)],\end{aligned} \tag{32}$$

where we have used the identity $\mathcal{I}[\mathbf{G}^*(\mathbf{r}_\mathrm{A},\mathbf{r}_\mathrm{A},\omega)] = \mathcal{I}[\mathbf{G}^\mathrm{T}(\mathbf{r}_\mathrm{A},\mathbf{r}_\mathrm{A},\omega)]$, which can be derived from Eq. (3).

Next, we take expectation values of Eq. (32) and assume the electromagnetic field to be prepared in its ground state at initial time t_0 which implies $\hat{\mathbf{E}}(\mathbf{r},\omega)|\{0\}\rangle = \mathbf{0}$. Therefore, the free terms of the electric field $\hat{\mathbf{E}}(\mathbf{r},\omega)$ and $\hat{\mathbf{E}}^\dagger(\mathbf{r},\omega)$ do not contribute to the dynamics of the average value of the atomic flip operator and are discarded.

Since we assume the atom to be free of quasidegenerate transitions, the set of differential equations for the atomic flip operator's expectation value can be decoupled. Moreover, the atom is unpolarized in each of its energy eigenstates, $\hat{\mathbf{d}}_{nn} = 0$, which is guaranteed by atomic selection rules [4]. As a result of these assumptions, the fast-oscillating off-diagonal flip operators decouple from the nonoscillating diagonal ones as well as from each other [4].

By making use of Eq. (3) we find that the two terms $\mathbf{d}_{nk}\cdot\mathcal{I}[\mathbf{G}(\mathbf{r}_A,\mathbf{r}_A,\omega)]\cdot\mathbf{d}_{kn} = \mathcal{I}[\mathbf{d}_{nk}\cdot\mathbf{G}(\mathbf{r}_A,\mathbf{r}_A,\omega)\cdot\mathbf{d}_{kn}]$ and $\mathbf{d}_{kn}\cdot\mathcal{I}[\mathbf{G}^\mathrm{T}(\mathbf{r}_A,\mathbf{r}_A,\omega)]\cdot\mathbf{d}_{nk} = \mathcal{I}[\mathbf{d}_{nk}\cdot\mathbf{G}(\mathbf{r}_A,\mathbf{r}_A,\omega)\cdot\mathbf{d}_{kn}]$ are equal and real.

With the help of these relations we identify the decay rate

$$\Gamma_{nk} = \frac{2\mu_0}{\hbar}\tilde{\omega}_{nk}^2\mathcal{I}[\mathbf{d}_{nk}\cdot\mathbf{G}(\mathbf{r}_A,\mathbf{r}_A,\tilde{\omega}_{nk})\cdot\mathbf{d}_{kn}] \tag{33}$$

and the frequency shift

$$\begin{aligned}\delta\omega_{nk} &= -\frac{\mu_0}{\pi\hbar}\mathscr{P}\int_0^\infty d\omega\frac{1}{\omega-\tilde{\omega}_{nk}}\omega^2 \\ &\times\mathcal{I}[\mathbf{d}_{nk}\cdot\mathbf{G}^{(1)}(\mathbf{r}_A,\mathbf{r}_A,\omega)\cdot\mathbf{d}_{kn}].\end{aligned} \tag{34}$$

Here, the Green's tensor $\mathbf{G}$ has been split into a bulk part $\mathbf{G}^{(0)}$ and a scattering part $\mathbf{G}^{(1)}$. The Lamb shift due to the free-space Green's tensor $\mathbf{G}^{(0)}$ is already included in the transition frequency ω_{mn}, which refers solely to the atom and does not take the material properties of surrounding matter into account. The remaining frequency shift stems from the presence of electromagnetic bodies around the atom.

Finally, the expectation value for the atomic flip operator for the nondiagonal terms yields

$$\langle\dot{\hat{A}}_{mn}(t)\rangle = i\boldsymbol{\omega}_{mn}\langle\hat{A}_{mn}(t)\rangle + \sum_k\left(-\frac{1}{2}\Gamma_{nk} - i\delta\boldsymbol{\omega}_{nk}\right)\langle\hat{A}_{mn}(t)\rangle + \sum_k\left(-\frac{1}{2}\Gamma_{mk} + i\delta\boldsymbol{\omega}_{mk}\right)\langle\hat{A}_{mn}(t)\rangle. \quad (35)$$

We define $\delta\boldsymbol{\omega}_n = \sum_k \delta\boldsymbol{\omega}_{nk}$ and $\Gamma_n = \sum_{k<n}\Gamma_{nk}$—the Θ function in Eq. (31) determines the order of summation indices—and the shifted transition frequency as

$$\tilde{\boldsymbol{\omega}}_{mn} = \boldsymbol{\omega}_{mn} + \delta\boldsymbol{\omega}_m - \delta\boldsymbol{\omega}_n, \quad (36)$$

which verifies our previous assumption $\tilde{\boldsymbol{\omega}}_{mn} = -\tilde{\boldsymbol{\omega}}_{nm}$. Thus Eq. (32) for the diagonal terms has the simple form

$$\langle\dot{\hat{A}}_{nn}(t)\rangle = -\Gamma_n\langle\hat{A}_{nn}(t)\rangle + \sum_{k>n}\Gamma_{kn}\langle\hat{A}_{kk}(t)\rangle. \quad (37)$$

Since the shifted frequency $\tilde{\boldsymbol{\omega}}_{nk}$ appears in $\delta\boldsymbol{\omega}_{nk}$ itself, the frequency shift is given as a self-consistent result from the implicit equation.

The frequency shift (34) can be simplified further by making use of the definition of the imaginary part (3), the Schwarz principle which is still valid for nonreciprocal media,

$$\mathbf{G}^*(\mathbf{r}_A,\mathbf{r}_A,\boldsymbol{\omega}) = \mathbf{G}(\mathbf{r}_A,\mathbf{r}_A,-\boldsymbol{\omega}^*), \quad (38)$$

and a substitution $\boldsymbol{\omega}\to-\boldsymbol{\omega}$ in the second integral having its origin in Eq. (3). The integral contours along the positive and negative real axes have one pole each and are evaluated in the complex plane. The path along the quarter circle does not give a contribution because $\lim_{|\omega|\to 0}\mathbf{G}^{(1)}(\mathbf{r},\mathbf{r}',\boldsymbol{\omega})\boldsymbol{\omega}^2/c^2 = 0$. The part along the imaginary axis leads to the nonresonant frequency shift

$$\delta\boldsymbol{\omega}_{nk}^{\mathrm{nres}} = \frac{\mu_0}{\pi\hbar}\int_0^\infty d\xi\,\frac{\xi^3}{\xi^2+\tilde{\boldsymbol{\omega}}_{nk}^2}\mathcal{I}[\mathbf{d}_{nk}\cdot\mathbf{G}^{(1)}(\mathbf{r}_A,\mathbf{r}_A,i\xi)\cdot\mathbf{d}_{kn}] - \frac{\mu_0}{\pi\hbar}\int_0^\infty d\xi\,\frac{\xi^2\tilde{\boldsymbol{\omega}}_{nk}}{\xi^2+\tilde{\boldsymbol{\omega}}_{nk}^2} \times\mathcal{R}[\mathbf{d}_{nk}\cdot\mathbf{G}^{(1)}(\mathbf{r}_A,\mathbf{r}_A,i\xi)\cdot\mathbf{d}_{kn}], \quad (39)$$

with a Green's function $\mathbf{G}$ with imaginary frequency $\boldsymbol{\omega}\to i\xi$. This expression resembles the frequency shift of the Casimir–Polder force for an atom in its ground state [3]. It comes from the exchange of virtual photons between the atom and the material body. This entirely quantum-mechanical interpretation can be extended for an atom in an arbitrary state. The matrix-vector product of the Green's tensor and the dipole moments is real for a reciprocal medium and therefore only the second contribution remains in this case.

The evaluation of the poles gives the resonant contribution associated with real-photon emission and a real-frequency expression $\tilde{\boldsymbol{\omega}}_{nk}$

$$\delta\boldsymbol{\omega}_{nk}^{\mathrm{res}} = -\frac{\mu_0}{\hbar}\tilde{\boldsymbol{\omega}}_{nk}^2\mathcal{R}[\mathbf{d}_{nk}\cdot\mathbf{G}^{(1)}(\mathbf{r}_A,\mathbf{r}_A,\tilde{\boldsymbol{\omega}}_{nk})\cdot\mathbf{d}_{kn}]. \quad (40)$$

In case of the resonant frequency shift, the Green's tensor $\mathbf{G}$ in Eq. (40) contains discrete frequencies for the real atomic transitions to a lower energy state, which can only occur for excited atoms and is related to real exchange photons.

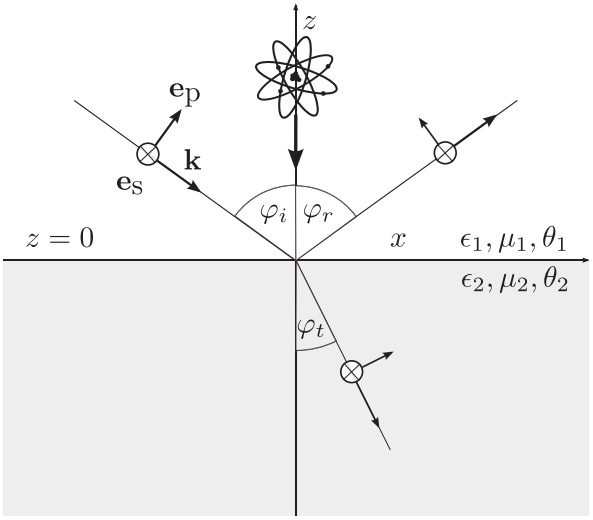

FIG. 1. Sketch of an atom in front of a medium with electric and magnetic properties and an axion coupling. The direction of incoming parallely polarized light $\mathbf{e}_\mathrm{p}$ and perpendicularly polarized light $\mathbf{e}_\mathrm{s}$ are shown.

The sum of the resonant and nonresonant frequency shifts $\delta\boldsymbol{\omega}_{nk}$ over all indices k can be identified with the total position-dependent Casimir–Polder potential. Its derivative with respect to position is the Casimir–Polder force between the atom and the nonreciprocal medium, which is caused by the atom's level-shift due to the body's presence.

IV. APPLICATIONS AND RESULTS

Having derived expressions for the atomic rate of spontaneous decay (33) and nonresonant and resonant frequency shifts [Eqs. (39) and (40)], we contrast a perfectly reflecting nonreciprocal mirror with a perfectly conducting mirror. Afterward we compare this to a topological insulator from Ref. [46]. Figure 1 shows a sketch of an atom in front of a medium having electric, magnetic properties and an axion coupling. The scattering part of the Green's tensor $\mathbf{G}^{(1)}$ of a single planar surface has the form [46]

$$\mathbf{G}^{(1)}(\mathbf{r},\mathbf{r}',\boldsymbol{\omega}) = \frac{i}{8\pi^2}\int d^2k^\parallel\frac{1}{k^\perp}\sum_{\sigma=\mathrm{s,p}}\sum_{\sigma'=\mathrm{s,p}}r_{\sigma,\sigma'} \times\mathbf{e}_{\sigma+}\mathbf{e}_{\sigma'-}e^{i\mathbf{k}^\parallel(\mathbf{r}-\mathbf{r}')}e^{ik^\perp(z+z')}, \quad (41)$$

with the two unit vectors $\mathbf{e}_{\sigma+}$ and $\mathbf{e}_{\sigma'-}$ representing the polarizations of incident (σ') and reflected waves (σ). The reflective coefficient $r_{\sigma,\sigma'}$ takes the mixing of the incoming and outgoing polarizations σ' and σ into account. The indices p and s refer to parallel or perpendicular polarization, respectively. $\mathbf{k}^\parallel$ represents the parallel component of the wave vector, $\mathbf{k}^\perp$ is its perpendicular component, and z is the vertical distance to the surface.

According to Curie's principle a system consisting of a crystal and an external influence, each having a specific symmetry, only maintains the symmetries that are shared by both the crystal and the external influence [47]. Hence our choice of

dipole moments must be such that the atom is sensitive to the violated time-reversal symmetry of a perfectly reflecting nonreciprocal mirror. To study possible effects of nonreciprocity, we assume circularly polarized dipole moments

$$\mathbf{d}_{10} = \frac{d}{\sqrt{2}}\begin{pmatrix}1\\ i\\ 0\end{pmatrix}, \quad \mathbf{d}_{01} = \frac{d}{\sqrt{2}}\begin{pmatrix}1\\ -i\\ 0\end{pmatrix}, \tag{42}$$

which are not invariant if the direction of time is reversed $t \to -t$.

A. Perfectly conducting mirror

Let us first investigate the atomic decay rate (33) and the nonresonant and resonant frequency shift (39), (40) for a perfectly conducting mirror. The energy shift of a hydrogen atom between two conducting plates has been studied in Refs. [48,49] and one can obtain the interaction between an atom and a single plate if one plate is shifted to infinity. Reference [50] shows the radiative decay rate of an atom in front of a perfect mirror, where the dipole is either parallel or perpendicular to the mirror. These approaches are based on perturbation theory.

The reflective coefficients for a perfectly conducting mirror are $r_{\mathrm{p,p}} = 1$, $r_{\mathrm{s,s}} = -1$, and $r_{\mathrm{s,p}} = r_{\mathrm{p,s}} = 0$. This set of coefficients is obtained from the reflective coefficients for a general material in the limit $\varepsilon \to \infty$, which is explained in greater detail in Sec. IV C. In this case the Green's tensor (41) contains only diagonal terms with $\mathbf{G}^{(1)}_{xx} = \mathbf{G}^{(1)}_{yy}$

$$\mathbf{G}^{(1)}_{xx}(\mathbf{r},\mathbf{r},\boldsymbol{\omega}) = \left(-\frac{1}{8\pi z} - i\frac{c}{16\pi\boldsymbol{\omega}z^2} + \frac{c^2}{32\pi\boldsymbol{\omega}^2 z^3}\right)e^{\frac{2i\boldsymbol{\omega}z}{c}}. \tag{43}$$

The nondiagonal elements of the Green's tensor vanish. The atomic decay rate (33) for circularly polarized dipole moments (42) hence reads

$$\Gamma^{(1)}_{10} = \frac{\mu_0\tilde{\boldsymbol{\omega}}^2_{10}d^2}{4\pi\hbar}\left[-\frac{1}{z}\sin\left(\frac{2\tilde{\boldsymbol{\omega}}_{10}z}{c}\right) - \frac{c}{2\tilde{\boldsymbol{\omega}}_{10}z^2}\cos\left(\frac{2\tilde{\boldsymbol{\omega}}_{10}z}{c}\right) + \frac{c^2}{4\tilde{\boldsymbol{\omega}}^2_{10}z^3}\sin\left(\frac{2\tilde{\boldsymbol{\omega}}_{10}z}{c}\right)\right]. \tag{44}$$

Figure 2 shows the atomic decay rate (44) scaled by the free-space decay rate

$$\Gamma^{(0)}_{10} = \frac{\mu_0\tilde{\boldsymbol{\omega}}^3_{10}d^2}{3\pi\hbar c}. \tag{45}$$

Moreover we study the asymptotic behavior of the decay rate and distinguish between the retarded limit ($\tilde{\boldsymbol{\omega}}_{10}z/c \gg 1$) and the nonretarded limit ($\tilde{\boldsymbol{\omega}}_{10}z/c \ll 1$). The decay rate decays asymptotically in the retarded limit with $-[\mu_0\tilde{\boldsymbol{\omega}}^2_{10}d^2\sin(2\tilde{\boldsymbol{\omega}}_{10}z/c)]/[4\pi\hbar z]$.

At $z = 0$, in the nonretarded limit, the decay rate has a value of $-\Gamma^{(0)}_{10}$ (Fig. 2). The total decay rate Γ_{10} of a dipole parallel to a perfectly conducting mirror is a sum of the free-space part $\Gamma^{(0)}_{10}$ and the body-induced part $\Gamma^{(1)}_{10}$ and is equal to $\Gamma_{10} = \Gamma^{(0)}_{10} + \Gamma^{(1)}_{10} = 0$ on the surface of the mirror at $z = 0$. This can be explained by an image dipole with equal strength and opposite direction induced by the original one so that the two dipoles cancel, leading to vanishing radiative decay.

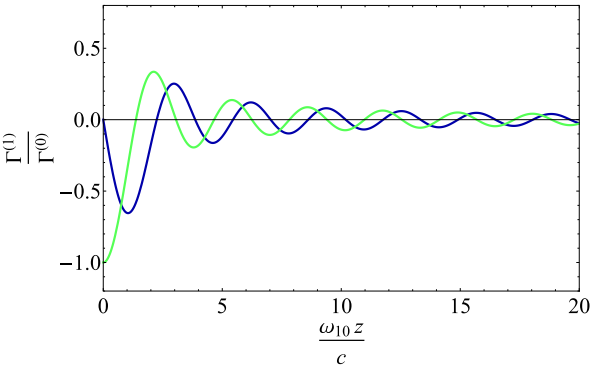

FIG. 2. Atomic decay rates $\Gamma^{(1)}$ scaled by the free-space decay rate $\Gamma^{(0)}$ (45) for a circularly polarized two-level atomic dipole in front of a perfectly conducting mirror (green line) and a perfectly reflecting nonreciprocal mirror (blue line).

The frequency shift is composed of a resonant and a nonresonant contribution

$$\begin{aligned}\delta\boldsymbol{\omega}_{10} &= \delta\boldsymbol{\omega}^{\mathrm{res}}_{10} + \delta\boldsymbol{\omega}^{\mathrm{nres}}_{10}\\ &= \frac{\mu_0\tilde{\boldsymbol{\omega}}^2_{10}d^2}{8\pi\hbar}\left[\frac{1}{z}\cos\left(\frac{2\tilde{\boldsymbol{\omega}}_{10}z}{c}\right) - \frac{c}{2\tilde{\boldsymbol{\omega}}_{10}z^2}\sin\left(\frac{2\tilde{\boldsymbol{\omega}}_{10}z}{c}\right) - \frac{c^2}{4\tilde{\boldsymbol{\omega}}^2_{10}z^3}\cos\left(\frac{2\tilde{\boldsymbol{\omega}}_{10}z}{c}\right)\right]\\ &\quad + \frac{\mu_0 d^2}{8\pi^2\hbar}\int_0^\infty d\xi\,\frac{\tilde{\boldsymbol{\omega}}_{10}\xi^2}{\tilde{\boldsymbol{\omega}}^2_{10}+\xi^2}\left(\frac{1}{z} + \frac{c}{2\xi z^2} + \frac{c^2}{4\xi^2 z^3}\right)e^{-\frac{2\xi z}{c}},\end{aligned} \tag{46}$$

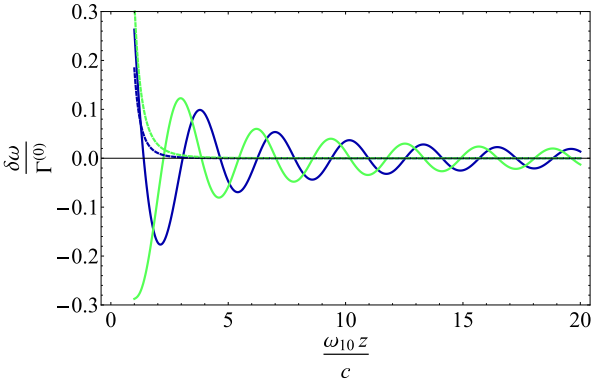

FIG. 3. Frequency shifts $\delta\boldsymbol{\omega}$ scaled by the free-space decay rate $\Gamma^{(0)}$ (45) for a circularly polarized two-level atomic dipole in front of a perfectly reflecting nonreciprocal mirror and a perfectly conducting mirror. The resonant frequency shift $\delta\boldsymbol{\omega}^{\mathrm{res}}$ of the perfectly conducting mirror (green line) and the resonant frequency shift of the perfectly reflecting nonreciprocal mirror (blue line) show oscillations. The nonresonant frequency shift $\delta\boldsymbol{\omega}^{\mathrm{nres}}$ of the perfectly conducting mirror (dashed green line) and the perfectly reflecting nonreciprocal mirror (dashed blue line) decay monotonically with distance.

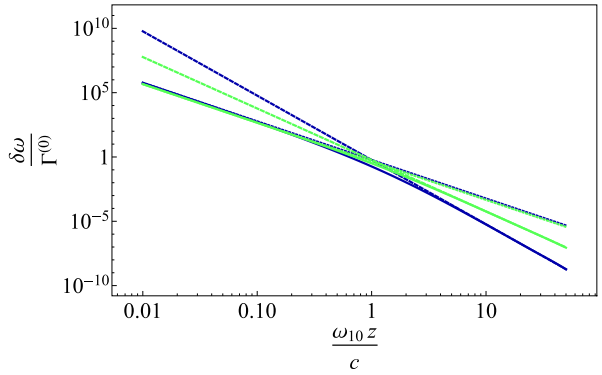

FIG. 4. Double-logarithmic plot for the nonresonant frequency shift $\delta\boldsymbol{\omega}^{\mathrm{nres}}$ of the perfectly conducting mirror (green line), its retarded limit (green dashed line), and its nonretarded limit (green dotted line). The perfectly reflecting nonreciprocal mirror (blue line), its retarded limit (blue dashed line), and its nonretarded limit (blue dotted line) are depicted in the same figure.

which are shown in Fig. 3. The retarded and nonretarded limits of the nonresonant frequency shift (46) read

$$\delta\boldsymbol{\omega}_{10}^{\mathrm{nres}} = \begin{cases} \dfrac{d^2 c}{16\pi^2\varepsilon_0\hbar\tilde{\boldsymbol{\omega}}_{10}z^4}, & \dfrac{\tilde{\boldsymbol{\omega}}_{10}z}{c} \gg 1 \\ \dfrac{d^2}{64\pi\varepsilon_0\hbar z^3}, & \dfrac{\tilde{\boldsymbol{\omega}}_{10}z}{c} \ll 1, \end{cases} \tag{47}$$

and are depicted in a double-logarithmic plot in Fig. 4. The asymptotic limits of the resonant frequency shift (46) read

$$\delta\boldsymbol{\omega}_{10}^{\mathrm{res}} = \begin{cases} \dfrac{\mu_0\tilde{\boldsymbol{\omega}}_{10}^2 d^2}{8\pi\hbar z}\cos\left(\dfrac{2\tilde{\boldsymbol{\omega}}_{10}z}{c}\right), & \dfrac{\tilde{\boldsymbol{\omega}}_{10}z}{c} \gg 1 \\ -\dfrac{d^2}{32\pi\varepsilon_0\hbar z^3}, & \dfrac{\tilde{\boldsymbol{\omega}}_{10}z}{c} \ll 1 \end{cases} \tag{48}$$

and are shown in Fig. 3 as well.

B. Perfectly reflecting nonreciprocal mirror

The reflection coefficients for incoming perpendicular or parallel polarization and outgoing perpendicular or parallel polarization $r_{\mathrm{s,s}}$ and $r_{\mathrm{p,p}}$ are set equal to 0, whereas the mixing terms $r_{\mathrm{s,p}}$ and $r_{\mathrm{p,s}}$ can be chosen to be either 1 or -1 thus generating a perfectly reflecting nonreciprocal mirror. In this section, we restrict ourselves to the case $r_{\mathrm{s,p}} = r_{\mathrm{p,s}} = -1$. These reflective coefficients are the specific case of a perfect electromagnetic conductor (PEMC) with parameter $M = 1$ [51–53], which is explained in Sec. IV C. The Green's tensor (41) is antisymmetric under these conditions: $\mathbf{G}^{(1)\mathrm{T}}(\mathbf{r},\mathbf{r}',\boldsymbol{\omega}) = -\mathbf{G}^{(1)}(\mathbf{r}',\mathbf{r},\boldsymbol{\omega})$. Thus the diagonal terms of the Green's tensor vanish and only the nondiagonal terms remain. By interchanging the indices of the nondiagonal terms, $\mathbf{G}^{(1)}_{xz}(\mathbf{r},\mathbf{r}') = \mathbf{G}^{(1)}_{zx}(\mathbf{r},\mathbf{r}')$ and $\mathbf{G}^{(1)}_{yz}(\mathbf{r},\mathbf{r}') = \mathbf{G}^{(1)}_{zy}(\mathbf{r},\mathbf{r}')$ keep their signs, whereas $\mathbf{G}^{(1)}_{xy}(\mathbf{r},\mathbf{r}') = -\mathbf{G}^{(1)}_{yx}(\mathbf{r},\mathbf{r}')$ shows a sign change. This behavior is exactly opposite if the arguments of the nondiagonal terms are interchanged. Therefore $\mathbf{G}^{(1)}_{xz}$ and $\mathbf{G}^{(1)}_{yz}$ have to vanish by setting $\mathbf{r} = \mathbf{r}'$ and only $\mathbf{G}^{(1)}_{xy} = -\mathbf{G}^{(1)}_{yx}$ has finite values. The final result after integrating yields

$$\mathbf{G}^{(1)}_{xy}(\mathbf{r},\mathbf{r},\boldsymbol{\omega}) = \left(-\frac{1}{8\pi z} - i\frac{c}{16\pi\boldsymbol{\omega}z^2}\right)e^{\frac{2i\boldsymbol{\omega}z}{c}}. \tag{49}$$

By using the circularly polarized dipole moments (42), we obtain for the atomic decay rate

$$\Gamma^{(1)}_{10} = \frac{\mu_0\tilde{\boldsymbol{\omega}}_{10}^2 d^2}{4\pi\hbar}\left[\frac{1}{z}\cos\left(\frac{2\tilde{\boldsymbol{\omega}}_{10}z}{c}\right) - \frac{c}{2\tilde{\boldsymbol{\omega}}_{10}z^2}\sin\left(\frac{2\tilde{\boldsymbol{\omega}}_{10}z}{c}\right)\right], \tag{50}$$

which is shown in Fig. 2. The decay rate of a perfectly reflecting nonreciprocal mirror is equal to zero for small values of $\tilde{\boldsymbol{\omega}}_{10}z/c$ (nonretarded limit). The function decays asymptotically in the retarded limit with $[\mu_0\tilde{\boldsymbol{\omega}}_{10}^2 d^2\cos(2\tilde{\boldsymbol{\omega}}_{10}z/c)]/[4\pi\hbar z]$.

The frequency shift is shown in Fig. 3 and consists of a resonant and a nonresonant contribution

$$\begin{aligned}\delta\boldsymbol{\omega}_{10} &= \delta\boldsymbol{\omega}_{10}^{\mathrm{res}} + \delta\boldsymbol{\omega}_{10}^{\mathrm{nres}} \\ &= \frac{\mu_0\tilde{\boldsymbol{\omega}}_{10}^2 d^2}{8\pi\hbar}\left[\frac{1}{z}\sin\left(\frac{2\tilde{\boldsymbol{\omega}}_{10}z}{c}\right) + \frac{c}{2\tilde{\boldsymbol{\omega}}_{10}z^2}\cos\left(\frac{2\tilde{\boldsymbol{\omega}}_{10}z}{c}\right)\right] \\ &\quad + \frac{\mu_0 d^2}{8\pi^2\hbar}\int_0^\infty d\xi\,\frac{\xi^3}{\xi^2 + \tilde{\boldsymbol{\omega}}_{10}^2}\left(\frac{1}{z} + \frac{c}{2\xi z^2}\right)e^{-\frac{2\xi z}{c}}.\end{aligned} \tag{51}$$

In the retarded and nonretarded limits the nonresonant part has the asymptotic behavior,

$$\delta\boldsymbol{\omega}_{10}^{\mathrm{nres}} = \begin{cases} \dfrac{d^2 c^2}{16\pi^2\varepsilon_0\hbar\tilde{\boldsymbol{\omega}}_{10}^2 z^5}, & \dfrac{\tilde{\boldsymbol{\omega}}_{10}z}{c} \gg 1 \\ \dfrac{d^2}{16\pi^2\varepsilon_0\hbar z^3}, & \dfrac{\tilde{\boldsymbol{\omega}}_{10}z}{c} \ll 1, \end{cases} \tag{52}$$

which is shown in a double-logarithmic plot in Fig. 4. The resonant part has the limits

$$\delta\boldsymbol{\omega}_{10}^{\mathrm{res}} = \begin{cases} \dfrac{\mu_0\tilde{\boldsymbol{\omega}}_{10}^2 d^2}{8\pi\hbar z}\sin\left(\dfrac{2\tilde{\boldsymbol{\omega}}_{10}z}{c}\right), & \dfrac{\tilde{\boldsymbol{\omega}}_{10}z}{c} \gg 1 \\ \dfrac{\mu_0\tilde{\boldsymbol{\omega}}_{10}d^2 c}{16\pi\hbar z^2}, & \dfrac{\tilde{\boldsymbol{\omega}}_{10}z}{c} \ll 1. \end{cases} \tag{53}$$

By comparing both the decay rates and the resonant frequency shifts in Figs. 2 and 3, a phase shift by $\pi/2$ between the respective curves of the perfectly conducting mirror and the perfectly reflecting nonreciprocal mirror is apparent, as can also be read off from the first terms in Eqs. (44), (46), (50), and (51). This is the additional phase shift implied by the reflection of s- into p-polarized waves. The scaling behavior of the decay rates and the resonant frequency shifts in the retarded limit is the same. The decay of the resonant frequency shift in the nonretarded limit is proportional to z^{-3} for the perfectly conducting mirror and z^{-2} for the perfectly reflecting nonreciprocal mirror. As for the nonresonant frequency shift (46) and (51), the perfectly reflecting nonreciprocal mirror decays with z^{-5} in contrast to z^{-4} for the perfectly conducting mirror in the retarded limit. The scaling behavior in the nonretarded limit is z^{-3} for both media.

The term z^{-1} of the total frequency shift, the sum of the resonant and the nonresonant part, will dominate in the retarded limit both for the perfectly conducting mirror and

the perfectly reflecting nonreciprocal mirror. As for the total frequency shift in the nonretarded limit, there is a dominant z^{-3} scaling behavior for both ideal materials.

C. Topological insulator

Reference [46] studies the electromagnetic behavior of a topological insulator. Permittivity, permeability, and the magneto-electric cross susceptibilities for this material mentioned in Eq. (23) are assigned according to

$$\boldsymbol{\epsilon} - \boldsymbol{\xi} \star \boldsymbol{\mu}^{-1} \star \boldsymbol{\zeta} \to \epsilon, \quad \boldsymbol{\xi} \star \boldsymbol{\mu}^{-1} \to \frac{\alpha}{\pi}\theta(\mathbf{r},\boldsymbol{\omega}),$$
$$\boldsymbol{\mu}^{-1} \star \boldsymbol{\zeta} \to \frac{\alpha}{\pi}\theta(\mathbf{r},\boldsymbol{\omega}), \quad \boldsymbol{\mu}^{-1} \to \mu^{-1}, \tag{54}$$

so that Eq. (19) takes the form

$$\hat{\mathbf{D}} = \varepsilon_0\varepsilon\hat{\mathbf{E}} + \frac{\alpha}{\pi}\frac{\theta(\mathbf{r},\boldsymbol{\omega})}{\mu_0 c}\hat{\mathbf{B}} + \hat{\mathbf{P}}_{\mathrm{N}}, \tag{55}$$

$$\hat{\mathbf{H}} = -\frac{\alpha}{\pi}\frac{\theta(\mathbf{r},\boldsymbol{\omega})}{\mu_0 c}\hat{\mathbf{E}} + \frac{1}{\mu_0\mu}\hat{\mathbf{B}} - \hat{\mathbf{M}}_{\mathrm{N}}. \tag{56}$$

Reflective coefficients $r_{\sigma,\sigma'}$ mentioned in Eq. (41) for bi-isotropic media are shown in Ref. [54] and are applied to the specific case of a topological insulator with time-reversal-breaking symmetry in Ref. [46] by making use of the relations in Eq. (54)

$$r_{\mathrm{s,s}} = \frac{(\mu k_1^\perp - k_2^\perp)\mu(\varepsilon k_1^\perp + k_2^\perp) - k_1^\perp k_2^\perp \Delta^2}{(\mu k_1^\perp + k_2^\perp)\mu(\varepsilon k_1^\perp + k_2^\perp) + k_1^\perp k_2^\perp \Delta^2},$$
$$r_{\mathrm{p,s}} = \frac{2k_1^\perp k_2^\perp \mu\Delta}{(\mu k_1^\perp + k_2^\perp)\mu(\varepsilon k_1^\perp + k_2^\perp) + k_1^\perp k_2^\perp \Delta^2},$$
$$r_{\mathrm{p,p}} = \frac{(\mu k_1^\perp + k_2^\perp)\mu(\varepsilon k_1^\perp - k_2^\perp) + k_1^\perp k_2^\perp \Delta^2}{(\mu k_1^\perp + k_2^\perp)\mu(\varepsilon k_1^\perp + k_2^\perp) + k_1^\perp k_2^\perp \Delta^2},$$
$$r_{\mathrm{s,p}} = \frac{2k_1^\perp k_2^\perp \mu\Delta}{(\mu k_1^\perp + k_2^\perp)\mu(\varepsilon k_1^\perp + k_2^\perp) + k_1^\perp k_2^\perp \Delta^2}. \tag{57}$$

In these equations, $k_1^\perp$ and $k_2^\perp$ refer to the perpendicular part of the wave vector in medium 1 and 2 and Δ is given by

$$\Delta = \alpha\frac{1}{\pi}(\theta_2 - \theta_1), \tag{58}$$

where α represents the fine-structure constant and θ_1 and θ_2 are the axion coupling constants in the two media. The first medium is assumed to be vacuum ($\mu_1 = \varepsilon_1 = 1, \theta_1 = 0$) and only the second medium has specific electromagnetic properties μ, ε, and θ.

The reflective coefficients (57) reduce to the respective ones for the perfectly conducting mirror in Sec. IV A by setting the axion coupling to $\Delta = 0$ and the other parameters to $\mu_1 = \mu_2 = 1$ and $\varepsilon_1 = 1$. In the limit $\varepsilon_2 \to \infty$, the reflective coefficients for a perfect electrical conductor ($r_{\mathrm{p,p}} = 1$, $r_{\mathrm{s,s}} = -1$, and $r_{\mathrm{s,p}} = r_{\mathrm{p,s}} = 0$) are obtained.

The reflective coefficients of the perfectly reflecting nonreciprocal mirror from Sec. IV B can also be generated from Eq. (57) with the help of Eq. (54). Medium 1 is treated as vacuum and in medium 2 the cross susceptibilities $\boldsymbol{\zeta}$ and $\boldsymbol{\xi}$ are treated as scalars and are set equal to each other, $\zeta = \xi$. The boundary conditions for the perfect electromagnetic conductor

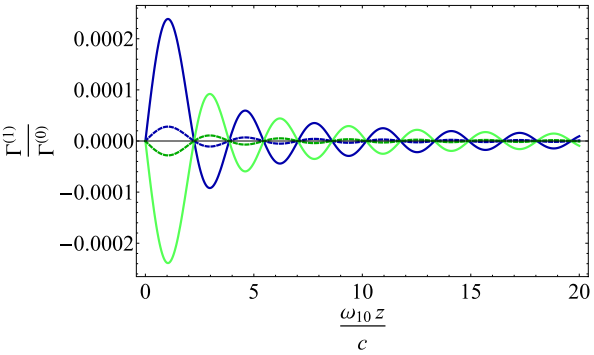

FIG. 5. Atomic decay rates $\Gamma^{(1)}$ for a circularly polarized two-level atomic dipole in front of a topological insulator with $\theta = \pi$ (45) (green line) and $\theta = -\pi$ (blue line) and $\varepsilon = \mu = 1$ scaled by the free-space decay rate $\Gamma^{(0)}$. The difference between the decay rate for Bi_2Se_3 with axion contribution ($\varepsilon = 16$, $\mu = 1$) and the respective decay rate without axion contribution is depicted for an axion coupling of $\theta = \pi$ (green dotted line) and $\theta = -\pi$ (blue dotted line).

(PEMC) read [51–53]

$$\mathbf{n}\cdot\left[\sqrt{\frac{\mu_0}{\varepsilon_0}}\hat{\mathbf{D}} - M\hat{\mathbf{B}}\right] = 0,$$
$$\mathbf{n}\times\left[M\hat{\mathbf{E}} + \sqrt{\frac{\mu_0}{\varepsilon_0}}\hat{\mathbf{H}}\right] = 0, \tag{59}$$

where we have introduced the PEMC parameter $M = \xi/\mu$ and $\mathbf{n}$ represents a unit vector perpendicular to the interface. These conditions imply reflection coefficients

$$r_{\mathrm{s,s}} = \frac{1-M^2}{1+M^2}, \quad r_{\mathrm{p,s}} = r_{\mathrm{s,p}} = \frac{-2M}{1+M^2}, \quad r_{\mathrm{p,p}} = \frac{M^2-1}{1+M^2}, \tag{60}$$

showing that the perfectly reflecting nonreciprocal mirror ($r_{\mathrm{s,s}} = r_{\mathrm{p,p}} = 0$ and $r_{\mathrm{s,p}} = r_{\mathrm{p,s}} = -1$) is a PEMC with parameter $M = 1$. The general PEMC reflection coefficients are recovered from Eq. (57) with Eq. (54) in the limit $\varepsilon, \mu, \xi \to \infty$ while imposing the PEMC condition $\xi^2 - \varepsilon\mu = 0$.

In Ref. [55], the rate of spontaneous decay for an atom close to a topological insulator with axion coupling is also considered. In that work, a linear dipole transition is chosen which is perpendicular or parallel to the surface. In this case, the general expression for the decay rate, unlike Eq. (33), is identical to that for reciprocal material without making use of the definition of the imaginary part of the Green's tensor (3). As a result, the phenomenon is insensitive to the specific time-reversal-symmetry-breaking properties of the topological insulator, as explained above.

Due to the small value of the fine-structure constant α and the small effect on the reflection coefficients (57), we first study a purely axion medium by setting $\varepsilon = 1$ and $\mu = 1$. Figure 5 shows the atomic decay rate for $\theta = \pi$ and $\theta = -\pi$. Figure 6 depicts the respective resonant part of the frequency shift. The results for the decay rate and the resonant frequency shift resemble the respective curves of the perfectly reflecting nonreciprocal mirror in Figs. 2 and 3, but are scaled by $\Delta/2$. This ratio can be easily read off in the retarded and nonretarded

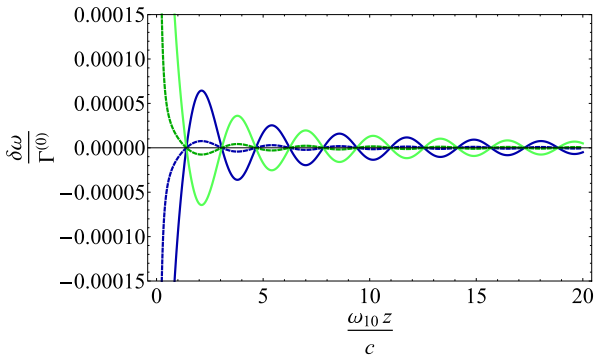

FIG. 6. Resonant frequency shift $\delta\boldsymbol{\omega}^{\mathrm{res}}$ for a circularly polarized two-level atomic dipole in front of a topological insulator (45) with $\theta = \pi$ (green line) and $\theta = -\pi$ (blue line) and $\varepsilon = \mu = 1$ scaled by the free-space decay rate $\Gamma^{(0)}$. The difference between the resonant frequency shift for Bi_2Se_3 with axion contribution ($\varepsilon = 16$, $\mu = 1$) and the respective frequency shift without axion contribution is depicted for an axion coupling of $\theta = \pi$ (green dotted line) and $\theta = -\pi$ (blue dotted line).

limits. The reflective coefficients (57) in the retarded limit read

$$\begin{aligned} r_{\mathrm{s,s}}^{\mathrm{ret}} &= \frac{(1-\varepsilon)-\Delta^2}{(1+n)^2+\Delta^2}, \\ r_{\mathrm{p,s}}^{\mathrm{ret}} &= \frac{-2\Delta}{(1+n)^2+\Delta^2}, \\ r_{\mathrm{p,p}}^{\mathrm{ret}} &= \frac{-(1-\varepsilon)+\Delta^2}{(1+n)^2+\Delta^2} = -r_{\mathrm{s,s}}^{\mathrm{ret}}, \\ r_{\mathrm{s,p}}^{\mathrm{ret}} &= \frac{-2\Delta}{(1+n)^2+\Delta^2} = r_{\mathrm{p,s}}^{\mathrm{ret}}, \end{aligned} \tag{61}$$

with the refractive index $n = \sqrt{\varepsilon}$. The decay rate and resonant frequency shift with the purely axion contribution in the retarded limit are given by

$$\begin{aligned} \Gamma_{10}^{(1)\mathrm{ret}}(\varepsilon = 1, \theta = \pi) &= \frac{\mu_0 \tilde{\boldsymbol{\omega}}_{10}^2 d^2}{4\pi\hbar z} \cos\left(\frac{2\tilde{\boldsymbol{\omega}}_{10} z}{c}\right)\frac{\Delta}{2}, \\ \delta\boldsymbol{\omega}_{10}^{\mathrm{res,ret}}(\varepsilon = 1, \theta = \pi) &= \frac{\mu_0 \tilde{\boldsymbol{\omega}}_{10}^2 d^2}{8\pi\hbar z} \sin\left(\frac{2\tilde{\boldsymbol{\omega}}_{10} z}{c}\right)\frac{\Delta}{2}. \end{aligned} \tag{62}$$

The same procedure is carried out in the nonretarded limit and the respective reflective coefficients (57) are

$$\begin{aligned} r_{\mathrm{s,s}}^{\mathrm{nonret}} &= \frac{-\Delta^2}{2(\varepsilon+1)+\Delta^2}, \\ r_{\mathrm{p,s}}^{\mathrm{nonret}} &= \frac{-2\Delta}{2(\varepsilon+1)+\Delta^2}, \\ r_{\mathrm{p,p}}^{\mathrm{nonret}} &= \frac{2(\varepsilon-1)+\Delta^2}{2(\varepsilon+1)+\Delta^2}, \\ r_{\mathrm{s,p}}^{\mathrm{nonret}} &= \frac{-2\Delta}{2(\varepsilon+1)+\Delta^2} = r_{\mathrm{p,s}}^{\mathrm{nonret}}. \end{aligned} \tag{63}$$

The respective decay rate and resonant frequency shift for the purely axion contribution in the nonretarded limit read

$$\begin{aligned} \Gamma_{10}^{(1)\mathrm{nonret}}(\varepsilon = 1, \theta = \pi) &= -\frac{\mu_0 \tilde{\boldsymbol{\omega}}_{10} d^2 c}{8\pi\hbar z^2}\frac{\Delta}{2}, \\ \delta\boldsymbol{\omega}_{10}^{\mathrm{res,nonret}}(\varepsilon = 1, \theta = \pi) &= \frac{\mu_0 \tilde{\boldsymbol{\omega}}_{10} d^2 c}{16\pi\hbar z^2}\frac{\Delta}{2}. \end{aligned} \tag{64}$$

Next, we look at general material properties similar to Bi_2Se_3, where we take $\varepsilon = 16$ and $\mu = 1$ [46]. We compare the case with axion coupling of $\theta = \pi$ and without axion coupling $\theta = 0$. Because of the small value of α, the reflective coefficients $r_{\mathrm{p,s}}$ and $r_{\mathrm{s,p}}$ do not have a big impact on the decay rate and the frequency shift. The decay rate and resonant frequency shift in the retarded limit are calculated by inserting the reflective coefficients (61) into Eqs. (33) and (40)

$$\begin{aligned} \Gamma_{10}^{(1)\mathrm{ret}} &= \frac{\mu_0 \tilde{\boldsymbol{\omega}}_{10}^2 d^2}{4\pi\hbar}\left[-\frac{1}{z}\sin\left(\frac{2\tilde{\boldsymbol{\omega}}_{10} z}{c}\right) r_{\mathrm{p,p}}^{\mathrm{ret}} \right. \\ &\quad \left. - \frac{1}{z}\cos\left(\frac{2\tilde{\boldsymbol{\omega}}_{10} z}{c}\right) r_{\mathrm{s,p}}^{\mathrm{ret}}\right], \\ \delta\boldsymbol{\omega}_{10}^{\mathrm{res,ret}} &= \frac{\mu_0 \tilde{\boldsymbol{\omega}}_{10}^2 d^2}{8\pi\hbar}\left[\frac{1}{z}\cos\left(\frac{2\tilde{\boldsymbol{\omega}}_{10} z}{c}\right) r_{\mathrm{p,p}}^{\mathrm{ret}} \right. \\ &\quad \left. - \frac{1}{z}\sin\left(\frac{2\tilde{\boldsymbol{\omega}}_{10} z}{c}\right) r_{\mathrm{s,p}}^{\mathrm{ret}}\right]. \end{aligned} \tag{65}$$

The difference in the decay rate and the resonant frequency shift between the cases with and without axion coupling in the retarded limit and for $\Delta \ll 1$ yields

$$\begin{aligned} \Delta\Gamma_{10}^{(1)\mathrm{ret}} &\equiv \Gamma_{10}^{(1)\mathrm{ret}}(\theta = \pi) - \Gamma_{10}^{(1)\mathrm{ret}}(\theta = 0) \\ &= \frac{\mu_0 \tilde{\boldsymbol{\omega}}_{10}^2 d^2}{4\pi\hbar z}\cos\left(\frac{2\tilde{\boldsymbol{\omega}}_{10} z}{c}\right)\frac{2\Delta}{(1+n)^2}, \\ \Delta\delta\boldsymbol{\omega}_{10}^{\mathrm{res,ret}} &\equiv \delta\boldsymbol{\omega}_{10}^{\mathrm{res,ret}}(\theta = \pi) - \delta\boldsymbol{\omega}_{10}^{\mathrm{res,ret}}(\theta = 0) \\ &= \frac{\mu_0 \tilde{\boldsymbol{\omega}}_{10}^2 d^2}{8\pi\hbar z}\sin\left(\frac{2\tilde{\boldsymbol{\omega}}_{10} z}{c}\right)\frac{2\Delta}{(1+n)^2}. \end{aligned} \tag{66}$$

In the limit of $\Delta \ll 1$, the scaling factor for Eq. (66) for $\varepsilon = 16$ with respect to the purely axion material in the retarded limit (62) is $4/25$.

The decay rate and resonant frequency shift in the nonretarded limit are obtained by inserting Eq. (63) into Eqs. (33) and (40)

$$\begin{aligned} \Gamma_{10}^{(1)\mathrm{nonret}} &= \frac{\mu_0 \tilde{\boldsymbol{\omega}}_{10}^2 d^2}{4\pi\hbar}\left[\frac{c}{2\tilde{\boldsymbol{\omega}}_{10} z^2} r_{\mathrm{s,p}}^{\mathrm{nonret}} + \frac{c^2}{4\tilde{\boldsymbol{\omega}}_{10}^2 z^3} r_{\mathrm{p,p}}^{\mathrm{nonret}}\right], \\ \delta\boldsymbol{\omega}_{10}^{\mathrm{res,nonret}} &= \frac{\mu_0 \tilde{\boldsymbol{\omega}}_{10}^2 d^2}{8\pi\hbar}\left[-\frac{c}{2\tilde{\boldsymbol{\omega}}_{10} z^2} r_{\mathrm{s,p}}^{\mathrm{nonret}} - \frac{c^2}{4\tilde{\boldsymbol{\omega}}_{10}^2 z^3} r_{\mathrm{p,p}}^{\mathrm{nonret}}\right]. \end{aligned} \tag{67}$$

The differential effects of the axion coupling on the decay rate and the resonant frequency shift for the nonretarded limit are given by

$$\begin{aligned} \Delta\Gamma_{10}^{(1)\mathrm{nonret}} &\equiv \Gamma_{10}^{(1)\mathrm{nonret}}(\theta = \pi) - \Gamma_{10}^{(1)\mathrm{nonret}}(\theta = 0) \\ &= -\frac{\mu_0 \tilde{\boldsymbol{\omega}}_{10} d^2 c}{8\pi\hbar z^2}\frac{\Delta}{\varepsilon+1}, \end{aligned}$$

$$\Delta\delta\boldsymbol{\omega}_{10}^{\mathrm{res,nonret}} \equiv \delta\boldsymbol{\omega}_{10}^{\mathrm{res,nonret}}(\theta=\pi) - \delta\boldsymbol{\omega}_{10}^{\mathrm{res,nonret}}(\theta=0) = \frac{\mu_0\tilde{\boldsymbol{\omega}}_{10}d^2c}{16\pi\hbar z^2}\frac{\Delta}{\varepsilon+1}. \tag{68}$$

The respective scaling factor of Eq. (68) with respect to Eq. (64) in the nonretarded limit for $\varepsilon = 16$ is $2/17$. The difference in the atomic decay rate and the resonant frequency shift between these two cases follows the same form of the purely axion atomic decay rate and frequency shift and can be compared with that. The scaling factors are gauged in the retarded and nonretarded limit (cf. Figs. 5 and 6).

The nonresonant frequency shift (39) for the topological insulator contains frequency-dependent permeability and permittivity $\varepsilon(i\xi)$ and $\mu(i\xi)$. Without knowing the exact behavior of these quantities we can only approximate the nonresonant frequency shift in the retarded and nonretarded limits. Since the resonant frequency shift always dominates in the retarded limit, we restrict ourselves to gauge the nonretarded limit. For a purely nonreciprocal medium with $\varepsilon = 1$, we obtain

$$\delta\boldsymbol{\omega}_{10}^{\mathrm{nres,nonret}}(\varepsilon=1,\theta=\pi) = \frac{d^2}{16\pi^2\varepsilon_0\hbar z^3}\frac{\Delta}{2}. \tag{69}$$

The result for a general medium reads

$$\delta\boldsymbol{\omega}_{10}^{\mathrm{nres,nonret}} = \frac{\mu_0 d^2}{8\pi^2\hbar}\int_0^\infty d\xi\,\frac{\xi^2}{\xi^2+\tilde{\boldsymbol{\omega}}_{10}^2}e^{-\frac{2\xi z}{c}} \times\left\{-\frac{\xi}{z}r_{\mathrm{s,p}}^{\mathrm{nonret}} - \frac{c}{2z^2}r_{\mathrm{s,p}}^{\mathrm{nonret}} + \frac{c^2\tilde{\boldsymbol{\omega}}_{10}}{4\xi^2 z^3}r_{\mathrm{p,p}}^{\mathrm{nonret}}\right\}. \tag{70}$$

Because of the strong effect of ε compared with Δ the terms with $r_{\mathrm{p,p}}^{\mathrm{nonret}}$ (63) do not have to be considered for the difference between the topological insulator with and without axion coupling. Only $r_{\mathrm{s,p}}^{\mathrm{nonret}}$ remains and is inserted into Eq. (39). For $\xi\to\infty$, $\varepsilon(i\xi)\to 1$. After performing the ξ integral, we obtain the final result for the difference of the nonresonant frequency shift of the topological insulator in the nonretarded limit,

$$\Delta\delta\boldsymbol{\omega}_{10}^{\mathrm{nres,nonret}} \equiv \delta\boldsymbol{\omega}_{10}^{\mathrm{nres,nonret}}(\theta=\pi) - \delta\boldsymbol{\omega}_{10}^{\mathrm{nres,nonret}}(\theta=0) = \frac{d^2}{16\pi^2\varepsilon_0\hbar z^3}\frac{\Delta}{\varepsilon+1}. \tag{71}$$

The total frequency shift of the resonant and nonresonant parts of the topological insulator scales with z^{-1} in the nonretarded limit. An experimental distinction from another material is difficult (cf. Sec. IV B).

In case of an extremely large axion coupling, the reflective coefficients (57) reduce to the values $r_{\mathrm{s,s}} = -1$ and $r_{\mathrm{p,p}} = 1$. Both the decay rates, the resonant frequency shift, and the nonresonant frequency shift approximate the results of the perfectly conducting mirror; cf. Figs. 2 and 3.

Note that for each of the interacting time-reversal-symmetry-breaking subsystems, atom and medium, there are two possible choices regarding their internal sense of time. For the atom, they correspond to clockwise versus counterclockwise circular dipole transitions and can be related to one another via $\mathbf{d}\to\mathbf{d}^*$. For the medium, the two possible internal senses of time are related via $\Delta\to-\Delta$ or $r_{\mathrm{s,p}}$, $r_{\mathrm{p,s}}\to -r_{\mathrm{s,p}}$, $-r_{\mathrm{p,s}}$. We thus have four possible combinations of t-odd atoms interacting with nonreciprocal media. The other three possible combinations can be obtained from the particular choice considered here by changing the internal arrow of time in atom, medium or both, where each such change reverses the signs of frequency shift and body-assisted decay rate.

Due to the internal connection between the frequency shift and the Casimir–Polder force, one can also switch from an attractive to a repulsive force between atom and medium.

V. SUMMARY

We have applied macroscopic QED to derive expressions for the Casimir–Polder frequency shift and spontaneous decay rate for nonreciprocal media, which violate Lorentz's reciprocity principle and therefore break time-reversal symmetry. Consequently, real and imaginary parts of the Green's tensor for nonreciprocal media have to be redefined by using the adjoint tensor instead of the complex-conjugate one.

Based on the interaction Hamiltonian between the atom, the field and the nonreciprocal medium, an expression for the electric field has been obtained in two alternative ways. First, noise currents can be quantized directly yielding one set of field operators for the combined electric and magnetic fields. According to the second approach the noise currents can be divided into contributions for the polarization and the magnetization giving rise to cross correlations between electric and magnetic fields. The result for the electric field has enabled us to study the internal atomic dynamics. By making use of the redefined real and imaginary parts of a tensor, we obtain general expressions for the atomic decay rate and the frequency shift, which can be split into a resonant and a nonresonant contribution, representing generalizations for nonreciprocal media.

As an example, we have investigated the decay rate and frequency shift for a two-level atom with circularly polarized dipole moments in order to be able to detect the broken time-reversal symmetry. First, a perfectly conducting mirror has been compared with a perfectly reflecting nonreciprocal mirror yielding different polynomial scaling behavior. Whereas the nonresonant frequency shift of the perfectly conducting mirror decays with z^{-4} in the retarded limit, it scales with z^{-5} in case of the perfectly reflecting nonreciprocal mirror. In the nonretarded limit both scale with z^{-3}. As for the resonant frequency shift, there is a z^{-1} behavior for both materials in the retarded limit and in the nonretarded limit they differ again: the perfectly conducting mirror scales with z^{-3}, the perfectly reflecting nonreciprocal mirror with z^{-2}.

Second, we have investigated a time-reversal-symmetry-broken topological insulator, whose electromagnetic properties are described by an axion coupling and whose reflective coefficients depend on the wave vector. Due to the small impact of the axion part, we have restricted ourselves to a medium of pure axion behavior by setting $\varepsilon = 1$ and compared this to the difference quantities between included axion coupling and without axion coupling for a material similar to Bi_2Se_3. We find a qualitatively similar behavior and determine scaling factors between the two cases in the retarded and nonretarded

limits. Finally, we can switch the sign of the decay rate and the frequency shift of the topological insulator both by reversing the direction of the oscillating dipole moments and by changing the sign of the axion coupling. This opens the door for switching between attractive and repulsive Casimir–Polder forces.

ACKNOWLEDGMENTS

We would like to thank A. Sihvola, Tobias Brünner, and Robert Bennett for discussions. This work was supported by the German Research Foundation (DFG, Grants No. BU 1803/3-1 and No. GRK 2079/1). S.Y.B. is grateful for support by the Freiburg Institute of Advanced Studies.

[1] H. Casimir and D. Polder, Phys. Rev. **73**, 360 (1948).
[2] H. B. G. Casimir, Proc. K. Ned. Acad Wet. **51**, 793 (1948).
[3] S. Y. Buhmann, *Dispersion Forces I - Macroscopic Quantum Electrodynamics and Ground-State Casimir, Casimir–Polder and van der Waals Forces* (Springer, Berlin, Heidelberg, 2012).
[4] S. Y. Buhmann, *Dispersion Forces II - Many-Body Effects, Excited Atoms, Finite Temperature and Quantum Friction* (Springer, Berlin, Heidelberg, 2012).
[5] J. M. Wylie and J. E. Sipe, Phys. Rev. A **30**, 1185 (1984).
[6] J. M. Wylie and J. E. Sipe, Phys. Rev. A **32**, 2030 (1985).
[7] H. T. Dung, L. Knöll, and D.-G. Welsch, Phys. Rev. A **57**, 3931 (1998).
[8] S. Y. Buhmann, L. Knöll, D.-G. Welsch, and H. T. Dung, Phys. Rev. A **70**, 052117 (2004).
[9] S. Y. Buhmann and D.-G. Welsch, Prog. Quantum Electron. **31**, 51 (2007).
[10] S. Scheel and S. Y. Buhmann, Acta Phys. Slovaca **58**, 675 (2008).
[11] B.-S. Skagerstam, P. K. Rekdal, and A. H. Vaskinn, Phys. Rev. A **80**, 022902 (2009).
[12] W. C. Chew, *Waves and Fields in Inhomogeneous Media*, Series on Electromagnetic Waves (IEEE Press, New York, 1995).
[13] L. Knöll, S. Scheel, and D. G. Welsch, in *Coherence and Statistics of Photons and Atoms*, edited by J. Perina (Wiley, New York, 2001).
[14] C. Eberlein and R. Zietal, Phys. Rev. A **86**, 062507 (2012).
[15] J. Xu, M. Alamri, Y. Yang, S.-Y. Zhu, and M. S. Zubairy, Phys. Rev. A **89**, 053831 (2014).
[16] C. Henkel and K. Joulain, Europhys. Lett. **72**, 929 (2005).
[17] J. A. Crosse, S. A. Ellingsen, K. Clements, S. Y. Buhmann, and S. Scheel, Phys. Rev. A **82**, 010901 (2010).
[18] V. Yannopapas, J. Phys.: Condens. Matter **18**, 6883 (2006).
[19] M. Thiel, M. S. Rill, G. von Freymann, and M. Wegener, Adv. Mater. **21**, 4680 (2009).
[20] D. V. Guzatov and V. V. Klimov, Quantum Electron. **44**, 1112 (2014).
[21] D. V. Guzatov and V. V. Klimov, Quantum Electron. **44**, 873 (2014).
[22] V. V. Klimov, D. V. Guzatov, and M. Ducloy, Europhys. Lett. **97**, 47004 (2012).
[23] D. Guzatov, V. Klimov, and N. Poprukailo, J. Exp. Theor. Phys. **116**, 531 (2013).
[24] L. Onsager, Phys. Rev. **37**, 405 (1931).
[25] H. A. Lorentz, Verhandelingen en bijdragen uitgegeven door de Afeeling Natuurkunde, Koninklijke Nederlandse Akademie van Wetenschappen te Amsterdam **4**, 176 (1896).
[26] S. Y. Buhmann, D. T. Butcher, and S. Scheel, New J. Phys. **14**, 083034 (2012).
[27] S.-Q. Shen, Natl. Sci. Rev. **1**, 49 (2014).
[28] B. A. Bernevig, T. L. Hughes, and S. C. Zhang, Science **314**, 1757 (2006).
[29] M. Z. Hasan and C. L. Kane, Rev. Mod. Phys. **82**, 3045 (2010).
[30] H. Zhang, L. C. X., X. L. Qi, X. Dai, Z. Fang, and S. C. Zhang, Nat. Phys. **5**, 438 (2009).
[31] X.-L. Qi, R. Li, J. Zang, and S.-C. Zhang, Science **323**, 1184 (2009).
[32] Y. L. Chen, J.-H. Chu, J. G. Analytis, Z. K. Liu, K. Igarashi, H.-H. Kuo, X. L. Qi, S. K. Mo, M. R. G., D. H. Lu, M. Hashimoto, T. Sasagawa, S. C. Zhang, I. R. Fisher, Z. Hussain, and Z. X. Shen, Science **329**, 659 (2010).
[33] J. Maciejko, X.-L. Qi, H. D. Drew, and S.-C. Zhang, Phys. Rev. Lett. **105**, 166803 (2010).
[34] F. Wilczek, Phys. Rev. Lett. **58**, 1799 (1987).
[35] A. G. Grushin and A. Cortijo, Phys. Rev. Lett. **106**, 020403 (2011).
[36] M.-C. Chang and M.-F. Yang, Phys. Rev. B **80**, 113304 (2009).
[37] Z. W. Zuo, D. B. Ling, L. Sheng, and D. Y. Xing, Phys. Lett. A **377**, 2909 (2013).
[38] F. R. Prudêncio, S. A. Matos, and C. R. Paiva, IEEE Trans. Antennas Propag. **62**, 4637 (2014).
[39] J. A. Crosse, arXiv:1510.06130.
[40] F. S. S. Rosa, D. A. R. Dalvit, and P. W. Milonni, Phys. Rev. Lett. **100**, 183602 (2008).
[41] F. S. S. Rosa, D. A. R. Dalvit, and P. W. Milonni, Phys. Rev. A **78**, 032117 (2008).
[42] R. Zhao, J. Zhou, T. Koschny, E. N. Economou, and C. M. Soukoulis, Phys. Rev. Lett. **103**, 103602 (2009).
[43] L. Chen and S. Wan, Phys. Rev. B **84**, 075149 (2011).
[44] L. M. Woods, D. A. R. Dalvit, A. Tkatchenko, P. Rodriguez-Lopez, A. W. Rodriguez, and R. Podgornik, Rev. Mod. Phys. **88**, 045003 (2016).
[45] T. Cysne, W. J. M. Kort-Kamp, D. Oliver, F. A. Pinheiro, F. S. S. Rosa, and C. Farina, Phys. Rev. A **90**, 052511 (2014).
[46] J. A. Crosse, S. Fuchs, and S. Y. Buhmann, Phys. Rev. A **92**, 063831 (2015).
[47] P. Curie, J. Phys. Theor. Appl. **3**, 393 (1894).
[48] G. Barton, Proc. R. Soc. London, Ser. A **320**, 251 (1970).
[49] G. Barton, Proc. R. Soc. London, Ser. A **367**, 117 (1979).
[50] *Advances in Atomic, Molecular, and Optical Physics*, edited by D. Bates and B. Bederson (Academic Press, Inc., San Diego, 1991), Vol. 28.
[51] A. Sihvola and I. V. Lindell, Ann. Phys. (Berlin, Ger.) **17**, 787 (2008).
[52] I. V. Lindell and A. H. Sihvola, J. Electromagnet. Wave. **19**, 861 (2005).
[53] I. V. Lindell and A. H. Sihvola, IEEE Trans. Antennas Propag. **53**, 3005 (2005).
[54] A. H. Sihvola, A. Viitanen, I. Lindell, and S. Tretyakov, *Electromagnetic Waves in Chiral and Bi-Isotropic Media* (Artech House Antenna Library, Boston, London, 1994).
[55] G. Song, J.-P. Xu, and Y.-P. Yang, EPL **105**, 64001 (2014).

PHYSICAL REVIEW A **98**, 022510 (2018)

Charge-parity-violating effects in Casimir-Polder potentials

Stefan Yoshi Buhmann*
Physikalisches Institut, Albert-Ludwigs-Universität Freiburg, Hermann-Herder-Straße 3, 79104 Freiburg, Germany and Freiburg Institute for Advanced Studies, Albert-Ludwigs-Universität Freiburg, Albertstraße 19, 79104 Freiburg, Germany

Valery N. Marachevsky†
Department of Theoretical Physics, Saint Petersburg State University, Ulianovskaya 1, Petrodvorets, 198504 St. Petersburg, Russia

Stefan Scheel‡
Institut für Physik, Universität Rostock, Albert-Einstein-Straße 23, D-18059 Rostock, Germany

(Received 2 March 2018; published 15 August 2018)

We demonstrate under which conditions a violation of the charge-parity (*CP*) symmetry in molecules will manifest itself in the Casimir-Polder interaction of these with a magnetodielectric surface. Charge-parity violation induces a specific electric-magnetic cross polarizability in a molecule that is not chiral, but time-reversal (*T*) symmetry violating. As we show, a detection of such an effect via the Casimir-Polder potential requires a material medium that is also sensitive to time reversal, i.e., it must exhibit a nonreciprocal electromagnetic response. As simple examples of such media, we consider a perfectly reflecting nonreciprocal mirror that is a special case of a perfect electromagnetic conductor, as well as a Chern-Simons medium. In addition, we show that Chern-Simons and related media can induce unusual atom-surface interactions for anisotropic molecules with and without a chiral response.

DOI: 10.1103/PhysRevA.98.022510

I. INTRODUCTION

The Casimir effect is an effective electromagnetic force between polarizable objects that is induced by the recently directly observed vacuum fluctuations of the quantum electromagnetic field [1]. Originally conceived by Casimir as an attractive force between two perfectly conducting mirrors [2], recent progress in material design and control has placed Casimir forces between materials exhibiting both more realistic and more complex electromagnetic responses in a focus of interest [3]. *Inter alia*, (para)magnetic media [4,5], chiral materials [6], topological insulators [7,8] and graphene [9,10] have been studied.

A major driving force behind such investigations continues to be the search for repulsive Casimir forces to overcome stiction in nanotechnology [11]. Inspired by Boyer's observation that the force between a perfectly conducting plate and an infinitely permeable one is repulsive [12], it was theoretically predicted that repulsion persists for combinations of purely electric and magnetic media with a more realistic response. Quite generally, repulsive Casimir forces arise whenever the nature of the electromagnetic response of the two interacting objects is diametrically opposite in a certain sense, for example, if the objects show electric versus magnetic responses, have opposite chirality, or represent topological insulators with different internal arrows of time.

Casimir-Polder forces between an atom or a molecule and a macroscopic body are a closely related type of dispersion force [13] and hence subject to the same phenomenology regarding their dependence on the electromagnetic nature of the interacting objects. However, they are (i) a local effect due to the small size of one of the two interacting objects, and (ii) they can be measured with far higher accuracy due to the superior techniques in manipulating and controlling single atoms or molecules [14]. This suggests that Casimir-Polder forces might (i) serve as a probe of the molecule's or the body's properties rather than a force that is to be manipulated and overcome, and that (ii) this probe could be applied to access very exotic properties of matter. In particular, we intend to apply this idea to the phenomenon of charge-parity violation in molecules, asking the hypothetical question: Would a potential charge-parity violation in a molecule become manifest in its Casimir-Polder interaction with a macroscopic body and, if so, under what conditions?

One of the fundamental symmetries of the standard model of particle physics is the invariance under combined charge (*C*), parity (*P*), and time (*T*) reversal. However, a physical system need not be invariant under each of these three symmetries individually. Examples of parity nonconservation include processes involving the weak force such as the β decay [15,16]. The weak interaction is also responsible for the broken parity invariance in rovibrational spectra of chiral molecules [17,18]. The antiferromagnet Cr_2O_3, on the other hand, is an example of a *P*-odd and *T*-odd system that exhibits a pseudoscalar response (see Ref. [19] and references therein) which provides a template for perfect electromagnetic conductors [20]. In the search for physics beyond the standard model, weak-scale

*stefan.buhmann@physik.uni-freiburg.de
†maraval@mail.ru
‡stefan.scheel@uni-rostock.de

supersymmetry would induce a *CP* violation that is reflected in an intrinsic electron dipole moment (EDM) of neutrons or electrons (see Ref. [21] for a review). Recent experiments place an upper limit of $|d_e| < 8.7 \times 10^{-29} e$ cm on the electron EDM [22].

Within a field-theoretic setting, it is known that a Chern-Simons interaction violates both *P* and *T* symmetries [23,24]. The Casimir interaction between two flat Chern-Simons layers was studied in Refs. [25–28], with its main feature being the prediction of both attractive and repulsive regimes of the Casimir force between Chern-Simons layers separated by a vacuum slit. A physical example showing an effective Chern-Simons interaction is a quantum Hall system consisting of a two-dimensional (2D) electron gas [29]. The coupling constant of the Chern-Simons action is different for each quantum Hall plateau, with its value being determined by the external magnetic field perpendicular to the quantum Hall layer. The implication is that the Casimir-Polder potential will be quantized at the quantum Hall plateaus [30].

In this article, we investigate the Casimir-Polder potential for an anisotropic molecule in the presence of a flat Chern-Simons layer. It is known that the *CP*-even part of the Casimir-Polder potential is quadratic in the coupling constant of the Chern-Simons layer [31]. On the other hand, the *CP*-odd part of the Casimir-Polder potential, which we derive here, is linear in the coupling constant. The sign of the Chern-Simons coupling can be altered by reversing the direction of an external magnetic field. As a result, the *CP*-odd part of the Casimir-Polder potential can be extracted from measurements at any plateau of a quantum Hall system performed at external magnetic fields with alternating spatial directions.

The article is organized as follows. We begin with a discussion of atom-field coupling and the resulting Casimir-Polder interaction potentials in the presence of nonreciprocal media. As a particular example, we consider a planar Chern-Simons layer that gives rise to nonreciprocal effects. In the following, we then construct the Casimir-Polder potentials for molecules with various anisotropic, asymmetric polarizabilities, including the particular case of *CP*-odd molecules. We close the article with some concluding remarks. Details regarding the Chern-Simons action and its influence on Maxwell's equations have been delegated to the Appendix.

II. ATOM-FIELD COUPLING

The Curie dissymmetry principle [32] suggests that *CP*-odd atomic properties can only couple to environments which are also *T* odd, i.e., nonreciprocal, so that the Green's tensor does not necessarily fulfill the Onsager relation $\mathbf{G}^{\mathsf{T}}(\boldsymbol{r}',\boldsymbol{r},\omega) = \mathbf{G}(\boldsymbol{r},\boldsymbol{r}',\omega)$ regarding the reversibility of optical paths [33]. This suggests a novel possibility for the detection of *CP*-odd atomic properties by studying the electromagnetic interaction of a *CP*-odd molecule with a macroscopic Chern-Simons layer by means of the Casimir-Polder potential.

The interaction of a molecule *A* with the electromagnetic field can be described by the multipolar Hamiltonian in long-wavelength approximation as [34]

$$\hat{H}_{\mathrm{AF}} = -\hat{\boldsymbol{d}}\cdot\hat{\boldsymbol{E}}(\boldsymbol{r}_A) - \hat{\boldsymbol{m}}\cdot\hat{\boldsymbol{B}}(\boldsymbol{r}_A) \tag{1}$$

($\hat{\boldsymbol{d}}, \hat{\boldsymbol{m}}$: molecular electric and magnetic dipole moments; $\boldsymbol{r}_A$: position) when neglecting the diamagnetic interaction. The position-dependent Casimir-Polder potential can be derived within second-order perturbation theory by replacing the full propagator of the electromagnetic field $\mathbf{G}$ with its scattering part $\mathbf{G}^{(1)}$ [34,35]. A general technique for calculating the Casimir-Polder potential in an arbitrary gauge of the vector potential was developed in Ref. [31], with example calculations in different gauges being provided in Ref. [35]. In the following, we will derive contributions to the Casimir-Polder potential from electric-electric and electric-magnetic terms in the presence of a planar Chern-Simons layer.

A. Casimir-Polder potential for a nonmagnetic molecule

The Casimir-Polder potential [13] for a nonmagnetic ground-state molecule arises from the second-order energy shift

$$U_{ee}(\boldsymbol{r}_A) = \frac{\hbar\mu_0}{2\pi}\int_0^\infty d\xi\,\xi^2\,\mathrm{tr}[\boldsymbol{\alpha}(i\xi)\cdot\mathbf{G}^{(1)}(\boldsymbol{r}_A,\boldsymbol{r}_A,i\xi)], \tag{2}$$

where

$$\boldsymbol{\alpha}(\omega) = \lim_{\epsilon\to 0+}\frac{1}{\hbar}\sum_k\left[\frac{\boldsymbol{d}_{k0}\boldsymbol{d}_{0k}}{\omega+\omega_k+i\epsilon} - \frac{\boldsymbol{d}_{0k}\boldsymbol{d}_{k0}}{\omega-\omega_k+i\epsilon}\right] \tag{3}$$

is the molecular polarizability, and $\mathbf{G}^{(1)}$ is the scattering part of the electromagnetic Green's tensor. In order to make the influence of nonreciprocal media more explicit, we decompose the polarizability and Green's tensors into their respective symmetric and antisymmetric parts,

$$U_{ee}(\boldsymbol{r}_A) = \frac{\hbar\mu_0}{2\pi}\int_0^\infty d\xi\,\xi^2\,\mathrm{tr}\big[\boldsymbol{\alpha}_S(i\xi)\cdot\mathbf{G}_S^{(1)}(\boldsymbol{r}_A,\boldsymbol{r}_A,i\xi) + \boldsymbol{\alpha}_A(i\xi)\cdot\mathbf{G}_A^{(1)}(\boldsymbol{r}_A,\boldsymbol{r}_A,i\xi)\big]. \tag{4}$$

The first term is the ordinary Casimir-Polder potential in environments respecting the Onsager theorem [36,37]. The second term is due to the presence of nonreciprocal media; it only arises for molecules with an anisotropic, asymmetric polarizability. Examples for its relevance are the recently considered interaction of an atom with a plate exhibiting a Chern-Simons interaction [31] or with a topological-insulator plate [38].

It is instructive to study the effects of *P* and *CP* violation due to the presence of a flat Chern-Simons layer at $z = 0$ described by the action

$$S = \frac{a}{2}\int dt\,dx\,dy\,\varepsilon^{\nu\rho\sigma}A_\nu F_{\rho\sigma}, \tag{5}$$

with a dimensionless parameter a. The scattering part of a Green's function $\mathbf{G}^{(1)}$ above ($z_A > 0$) a Chern-Simons plate in the gauge $A_0 = 0$ mixes *s*- and *p*-polarized waves,

$$\mathbf{G}^{(1)}(\boldsymbol{r},\boldsymbol{r}',i\xi) = \frac{1}{8\pi^2}\int\frac{d^2q}{\beta}\,e^{i\boldsymbol{q}\cdot(\boldsymbol{r}-\boldsymbol{r}')-\beta(z+z')}(\boldsymbol{e}_s^+\boldsymbol{e}_s^- r_s + \boldsymbol{e}_p^+\boldsymbol{e}_p^- r_p + \boldsymbol{e}_p^+\boldsymbol{e}_s^- r_{s\to p} + \boldsymbol{e}_s^+\boldsymbol{e}_p^- r_{p\to s}) \tag{6}$$

($\boldsymbol{q}\perp\boldsymbol{e}_z$, $\beta = \sqrt{\xi^2/c^2+q^2}$), where the polarization unit vectors for the *s*- and *p*-polarized waves read $\boldsymbol{e}_s^\pm = \boldsymbol{e}_q\times\boldsymbol{e}_z$,

$\boldsymbol{e}_p^{\pm} = -(c/\xi)(iq\boldsymbol{e}_z \pm \beta\boldsymbol{e}_q)]$ and the respective reflection coefficients of the half space are given in the Appendix.

The symmetric part of the polarizability leads in this case to a potential equal to the Casimir-Polder potential in front of a perfectly conducting plate multiplied by a factor $a^2/(1+a^2)$. The asymmetric part of the polarizability yields an additional interaction with the Chern-Simons plate [31], viz.,

$$U_{\rm as}(z_A) = \frac{\hbar}{32\pi^2\varepsilon_0 c}\frac{a}{1+a^2}\int_0^{+\infty} d\xi\,\epsilon_{jlz}\alpha_{jl}(i\xi)\xi \times\left(1+2\frac{\xi z_A}{c}\right)e^{-2\xi z_A/c}. \tag{7}$$

In the retarded limit, $\omega_k z_A/c \gg 1$, the potential (7) leads to an $1/z_A^5$ asymptote,

$$U_{\rm as}(z_A) = -\frac{c^2}{8\pi^2\varepsilon_0 z_A^5}\frac{a}{1+a^2}\sum_k \frac{{\rm Im}(d_{0k,x}d_{k0,y})}{\omega_k^2}, \tag{8}$$

whereas at short separations, $\omega_k z_A/c \ll 1$, it is well approximated by a $1/z_A^3$ potential,

$$U_{\rm as}(z_A) = -\frac{1}{16\pi^2\varepsilon_0 z_A^3}\frac{a}{1+a^2}\sum_k {\rm Im}(d_{0k,x}d_{k0,y}). \tag{9}$$

The limiting cases of a perfectly reflecting, nonreciprocal mirror ($r_{s\to p}=\pm1, r_{p\to s}=\pm1, r_s=0, r_p=0$) can be immediately obtained from Eqs. (7)–(9) by substituting $a/(1+a^2)\to\pm1$. The latter is a specific example of a perfect electromagnetic conductor and emerges from a perfect electric conductor by means of a duality transformation [20].

B. Casimir-Polder potential for a molecule with *CP*-odd cross polarizabilities

For an electromagnetic molecule, both electric and magnetic dipole couplings contribute to the atom-field interaction (1). Beyond the purely electric interaction, we are now interested in the part of the Casimir-Polder potential due to the second-order energy shift arising from mixed electric-magnetic transitions,

$$\begin{aligned} U_{CP}(\boldsymbol{r}_A) &= U_{em}(\boldsymbol{r}_A) + U_{me}(\boldsymbol{r}_A) \\ &= -\frac{\hbar\mu_0}{2\pi}\int_0^{\infty} d\xi\,\xi\Big\{{\rm tr}\big[\boldsymbol{\chi}_{me}(i\xi)\cdot\ \mathbf{G}^{(1)}(\boldsymbol{r}_A,\boldsymbol{r}_A,i\xi)\overleftarrow{\nabla}'\big] \\ &\quad + {\rm tr}[\boldsymbol{\chi}_{em}(i\xi)\cdot\nabla\times\ \mathbf{G}^{(1)}(\boldsymbol{r}_A,\boldsymbol{r}_A,i\xi)]\Big\}, \end{aligned} \tag{10}$$

where we have introduced the cross polarizabilities

$$\boldsymbol{\chi}_{em}(\omega) = \lim_{\epsilon\to0}\frac{1}{\hbar}\sum_k\left[\frac{\boldsymbol{d}_{k0}\boldsymbol{m}_{0k}}{\omega+\omega_k+i\epsilon} - \frac{\boldsymbol{d}_{0k}\boldsymbol{m}_{k0}}{\omega-\omega_k+i\epsilon}\right], \tag{11}$$

$$\boldsymbol{\chi}_{me}(\omega) = \lim_{\epsilon\to0}\frac{1}{\hbar}\sum_k\left[\frac{\boldsymbol{m}_{k0}\boldsymbol{d}_{0k}}{\omega+\omega_k+i\epsilon} - \frac{\boldsymbol{m}_{0k}\boldsymbol{d}_{k0}}{\omega-\omega_k+i\epsilon}\right]. \tag{12}$$

It is customary to decompose the Hamiltonian $\hat{H}_A = \hat{H}_0 + \hat{V}^{CP}$ of the atomic subsystem into *CP*-even and -odd parts [39]. We can use perturbation theory to express the eigenstates $|n\rangle$ and energies E_n of $\hat{H}_A$ in terms of the eigenstates $|n^0\rangle$ and energies E_n^0 of $\hat{H}_0$. Assuming that $\langle n|\hat{V}^{CP}|n\rangle \equiv V_{nn}^{CP} = 0$ [39], we have $E_n = E_n^0$ in linear order in $\hat{V}^{CP}$, while the eigenstates acquire linear shifts due to the *CP*-odd interaction,

$$|n\rangle = |n^0\rangle + \sum_l |l^0\rangle\frac{\langle l^0|\hat{V}^{CP}|n^0\rangle}{E_n^0 - E_l^0}. \tag{13}$$

To linear order in $\hat{V}^{CP}$, we can hence expand

$$\begin{aligned} \boldsymbol{d}_{0k}\boldsymbol{m}_{k0} = &-\sum_l\frac{V_{0l}^{CP}\boldsymbol{d}_{kl}^0\boldsymbol{m}_{0k}^0}{\hbar\omega_l^0} - \sum_l\frac{\boldsymbol{d}_{0l}^0 V_{lk}^{CP}\boldsymbol{m}_{k0}^0}{\hbar(\omega_l^0-\omega_k^0)} \\ &- \sum_l\frac{\boldsymbol{d}_{0k}^0 V_{kl}^{CP}\boldsymbol{m}_{l0}^0}{\hbar(\omega_l^0-\omega_k^0)} - \sum_l\frac{\boldsymbol{d}_{0k}^0\boldsymbol{m}_{kl}^0 V_{l0}^{CP}}{\hbar\omega_l^0}, \end{aligned} \tag{14}$$

with the definitions $\omega_k^0 = (E_k^0 - E_0^0)/\hbar$, $\boldsymbol{d}_{nm}^0 = \langle n^0|\hat{\boldsymbol{d}}|m^0\rangle$, $\boldsymbol{m}_{nm}^0 = \langle n^0|\hat{\boldsymbol{m}}|m^0\rangle$, and $V_{nm}^{CP} = \langle n^0|\hat{V}^{CP}|m^0\rangle$.

Substituting this result into Eq. (11), relabeling $l \leftrightarrow k$ in the third term, and using the identity

$$\begin{aligned} &\frac{1}{(\omega_l^0-\omega_k^0)(\omega_k^0\pm\omega+i\epsilon)} + \frac{1}{(\omega_l^0-\omega_k^0)(\omega_l^0\pm\omega+i\epsilon)} \\ &\quad = \frac{1}{(\omega_k^0\pm\omega+i\epsilon)(\omega_l^0\pm\omega+i\epsilon)} \end{aligned} \tag{15}$$

results in the expression

$$\begin{aligned} \boldsymbol{\chi}_{em}(\omega) = &\lim_{\epsilon\to0}\frac{1}{\hbar}\sum_{k,l}\left[\frac{V_{0l}^{CP}\boldsymbol{d}_{kl}^0\boldsymbol{m}_{0k}^0}{\omega_l^0(\omega+\omega_k^0+i\epsilon)} - \frac{V_{0l}^{CP}\boldsymbol{d}_{lk}^0\boldsymbol{m}_{k0}^0}{\omega_l^0(\omega-\omega_k^0+i\epsilon)}\right] \\ &+ \lim_{\epsilon\to0}\frac{1}{\hbar}\sum_{k,l}\left[\frac{\boldsymbol{d}_{l0}^0 V_{lk}^{CP}\boldsymbol{m}_{0k}^0}{(\omega+\omega_l^0+i\epsilon)(\omega+\omega_k^0+i\epsilon)}\right. \\ &\left. - \frac{\boldsymbol{d}_{0l}^0 V_{lk}^{CP}\boldsymbol{m}_{k0}^0}{(\omega-\omega_l^0+i\epsilon)(\omega-\omega_k^0+i\epsilon)}\right] \\ &+ \lim_{\epsilon\to0}\frac{1}{\hbar}\sum_{k,l}\left[\frac{\boldsymbol{d}_{k0}^0\boldsymbol{m}_{lk}^0 V_{l0}^{CP}}{\omega_l^0(\omega+\omega_k^0+i\epsilon)} - \frac{\boldsymbol{d}_{0k}^0\boldsymbol{m}_{kl}^0 V_{l0}^{CP}}{\omega_l^0(\omega-\omega_k^0+i\epsilon)}\right]. \end{aligned} \tag{16}$$

For a *CP*-odd system, the electric and magnetic transition dipole matrix elements have a vanishing relative phase, so that $\boldsymbol{\chi}_{me} = \boldsymbol{\chi}_{em}^{\mathsf{T}}$. Due to this symmetry, it is clear that the cross polarizabilities of a *CP*-odd system do not lead to an interaction with a perfectly conducting plate. However, they do provide an interaction with a Chern-Simons layer as well as with a perfectly reflecting nonreciprocal mirror. To evaluate this contribution of the cross polarizabilities of a *CP*-odd molecule to the Casimir-Polder interaction with a nonreciprocal medium, we use Eq. (10) with $\chi_{jl} \equiv \chi_{em,jl} = \chi_{me,lj}$ to find

$$\begin{aligned} U_{CP}(z_A) = &\frac{\hbar}{32\pi^2\varepsilon_0 c z_A^3}\frac{a}{1+a^2}\int_0^{\infty} d\xi\, e^{-2\xi z_A/c} \\ &\times\left\{[\chi_{xx}(i\xi)+\chi_{yy}(i\xi)]\left(1+2\frac{\xi z_A}{c}+4\frac{\xi^2 z_A^2}{c^2}\right)\right. \\ &\left. +2\chi_{zz}(i\xi)\left(1+2\frac{\xi z_A}{c}\right)\right\}. \end{aligned} \tag{17}$$

Note that the symmetry of the cross polarizabilities implies that $\chi_{jl}(i\xi) = \frac{1}{\hbar}\sum_k \frac{2\omega_k}{\omega_k^2+\xi^2} d_{k0,j}m_{0k,l}$, where $d_{k0,j}m_{0k,l}$ is a real

number. In the retarded limit, $\omega_k z_A/c \gg 1$, the approximation $\chi_{jl}(i\xi) \simeq \chi_{jl}(0)$ leads to the asymptote

$$U_{CP}(z_A) = \frac{\hbar}{16\pi^2\varepsilon_0 z_A^4}\frac{a}{1+a^2} \times \big[\chi_{xx}(0)+\chi_{yy}(0)+\chi_{zz}(0)\big]. \quad (18)$$

In the opposite nonretarded limit, we may approximate

$$U_{CP}(z_A) = \frac{\hbar}{32\pi^2\varepsilon_0 c z_A^3}\frac{a}{1+a^2}\int_0^\infty d\xi \times \big[\chi_{xx}(i\xi)+\chi_{yy}(i\xi)+2\chi_{zz}(i\xi)\big]. \quad (19)$$

The limiting case of a perfectly reflecting, nonreciprocal mirror ($r_{s\to p}=\pm1, r_{p\to s}=\pm1, r_s=0, r_p=0$) can be immediately obtained from Eqs. (17)–(19) by replacing $a/(1+a^2)\to\pm1$.

Upon substitution, $\boldsymbol{\chi}\to\boldsymbol{\alpha}$, the potential (17) coincides with the well-known Casimir-Polder potential [13] of a purely electric atom in front of a perfectly conducting plate, apart from a factor of two. This correspondence can be easily understood from the duality of electric and magnetic fields [33]. Under a duality transformation by an angle $\theta/4$, a perfectly conducting plate transforms into a perfect nonreciprocal reflector [20], while a purely dielectric atom transforms into one with cross polarizabilities. The factor of two stems from the fact that two cross polarizabilities contribute to U_{CP} as opposed to the single electric polarizability contributing to the ordinary Casimir-Polder potential.

Let us compare the magnitude of the *CP*-odd ground-state potential with that of the Casimir-Polder potential of an ordinary, purely electric atom. We note that when going from the ordinary to the *CP*-odd case, one electric dipole moment d is replaced by m/c, while the other electric dipole moment of the order of $d\sim ea_0$ (e: electron charge; a_0: Bohr radius) is replaced by the *CP*-odd electron EDM d_{CP}. The first replacement leads to a reduction by a factor of roughly the fine-structure constant $m/(cd)\sim\alpha$, while the second yields a factor $d_{CP}/(ea_0)\approx 1.6\times10^{-20}$ according to the most recent upper limit [22]. The *CP*-odd ground-state potential is thus smaller than the ordinary Casimir-Polder potential by a factor of roughly 10^{-22}.

In order to potentially use the Casimir-Polder potential as a probe for *CP*-odd effects, one needs to enhance the effect by means of cavity QED. To this end, consider an excited atom in resonance with a cavity. Starting from the known resonant Casimir-Polder frequency shift of an excited atom in state n [40],

$$\Delta f = -\frac{\mu_0}{h}\sum_{k<n}\omega_{nk}^2 \boldsymbol{d}_{nk}\,\mathrm{Re}\;\mathbf{G}^{(1)}(\boldsymbol{r}_A,\boldsymbol{r}_A,\omega_{nk})\cdot\boldsymbol{d}_{kn}, \quad (20)$$

and applying the above replacements $d\mapsto m/c$, $d\mapsto d_{CP}$, we estimate the *CP*-odd resonant frequency shift to be of the order of

$$\Delta f_{CP}\sim\frac{\mu_0}{h}\omega^2\frac{m}{c}\,\mathrm{Re}\,G d_{CP}. \quad (21)$$

The Green's tensor scales as $\mathrm{Re}\,G\sim Q\omega/c$, where Q is the quality factor of the cavity [41]. In addition, we take into account the EDM enhancement which arises in heavy paramagnetic atoms so that $d_{CP}\sim K d_e$, where K is the atomic enhancement factor and $d_e\approx1.6\times10^{-20}ea_0$ is the electron EDM, as above. In addition, we estimate $\omega\sim E_\mathrm{R}/\hbar$, where E_R is the Rydberg energy and, once more, $m/c\sim ea_0\alpha$. Combining these estimates and noting that the EDM enhancement factor can reach values of up to 10^3 [24] and that Q factors of up to 10^{11} have been reported, a frequency shift of the order of 50 Hz becomes conceivable, which is within reach of current experimental resolution [18]. Note that such a cavity-QED setup based on *CP*-odd Casimir-Polder shifts would easily outperform a number of early experiments that have placed upper limits on the electron EDM using paramagnetic atoms in a conventional setup. Here, the reported constraints range from $d_e\approx4\times10^{-5}ea_0$ in the 1950s [42] to $d_e\approx8\times10^{-19}ea_0$ in the early 1990s [43] (see Ref. [24] for an overview).

C. Chern-Simons interaction with chiral molecules

For chiral, time-reversal invariant molecules, Lloyd's theorem states that electric and magnetic transitions carry a relative phase factor, $i=e^{i\pi/2}$ [44], so that the relation $\boldsymbol{\chi}_{me}=-\boldsymbol{\chi}_{em}^\mathsf{T}$ holds between the cross polarizabilities. The case of an isotropic chiral polarizability and the respective chiral Casimir-Polder potential was studied in Ref. [45]. Here we demonstrate that the interaction of a molecule with an anisotropic, asymmetric chiral polarizability and nonchiral media leads to an additional component of the Casimir-Polder potential. As an example, we evaluate this component of the Casimir-Polder potential for a molecule with anisotropic, asymmetric chiral polarizability in front of a Chern-Simons layer.

Using Eq. (10), one obtains the Chern-Simons interaction with P-odd chiral molecules now satisfying $\chi_{jl}\equiv\chi_{em,jl}=-\chi_{me,lj}$,

$$U_P(z_A) = -\frac{\hbar}{64\pi^2\varepsilon_0 z_A^4}\frac{a^2}{1+a^2}\int_0^{+\infty}d\xi\,\epsilon_{jlz}\chi_{jl}(i\xi) \times\frac{e^{-2\xi z_A/c}}{\xi}\left(3+6\frac{\xi z_A}{c}+8\frac{\xi^2 z_A^2}{c}+8\frac{\xi^3 z_A^3}{c}\right), \quad (22)$$

where a summation over j,l is implied. Note that due to the symmetry $\chi_{em,jl}=-\chi_{me,lj}$, one can write $\chi_{jl}(i\xi)=\frac{1}{\hbar}\sum_k\frac{2\xi}{\omega_k^2+\xi^2}\mathrm{Im}(d_{k0,j}m_{0k,l})$, where $d_{k0,j}m_{0k,l}$ is purely imaginary. As a result, in the retarded limit, $\omega_k z_A/c\gg1$, we obtain

$$U_P(z_A) = -\frac{c}{4\pi^2\varepsilon_0 z_A^5}\frac{a^2}{1+a^2}\sum_k\frac{\epsilon_{jlz}\mathrm{Im}(d_{k0,j}m_{0k,l})}{\omega_k^2}. \quad (23)$$

In the opposite nonretarded limit, we may approximate

$$U_P(z_A) = -\frac{3\hbar}{64\pi^2\varepsilon_0 z_A^4}\frac{a^2}{1+a^2}\int_0^{+\infty}d\xi\,\frac{\epsilon_{jlz}\chi_{jl}(i\xi)}{\xi} = -\frac{3}{64\pi\varepsilon_0 z_A^4}\frac{a^2}{1+a^2}\sum_k\frac{\epsilon_{jlz}\mathrm{Im}(d_{k0,j}m_{0k,l})}{\omega_k}. \quad (24)$$

In the limit $a\to\pm\infty$, we obtain the potential of a chiral molecule in front of a perfectly conducting plate. Note, however, that the quantity $\chi_{xy}(i\xi)-\chi_{yx}(i\xi)$ should be different from zero to obtain a nonvanishing potential.

III. CONCLUSIONS

With regard to answering our central question, we have shown that charge-parity-violating effects in molecules can indeed be manifest in their Casimir-Polder interaction with a surface. As anticipated from the Curie dissymmetry principle, this requires the surface to also possess *CP*-odd or *T*-odd properties. We have shown this explicitly for a nonreciprocal perfect reflector as an example of a perfect electromagnetic conductor medium, as well as for a Chern-Simons medium. The result in the former case is strikingly similar in form to the well-known formula by Casimir and Polder, which can readily be understood from the duality invariance of QED in the absence of free charges or currents.

In addition, we have shown that Chern-Simons media lead to a different Casimir-Polder potential for anisotropic chiral molecules. In this case, the respective power laws of the potential in the short- and long-distance limits differ from those previously predicted for isotropic molecules. Our findings can be generalized to topological insulator media, where we expect similar new potential components for *CP*-odd or anisotropic molecules.

Although the *CP*-odd polarizability that induces the respective ground-state potential is very small [46], the resonant Casimir-Polder potential for an excited atom may be considerably larger. We have estimated that using an optimal combination of a high-Q cavity and a strong EDM enhancement factor as found in heavy paramagnetic atoms, the *CP*-odd resonant Casimir-Polder frequency shift is within reach of current experimental resolution, even when taking into account the most recent upper limits on the electron EDM.

ACKNOWLEDGMENTS

We would like to thank V. Flambaum, O. P. Sushkov, A. N. Petrov, and L. V. Skripnikov for discussions. S.Y.B. is grateful for support by the German Research Foundation (DFG, Grant No. BU 1803/3-1) and by the Freiburg Institute of Advanced Studies. V.N.M. carried out research using computational resources provided by the Computer Center of SPbU through a Saint Petersburg State University Grant No. 11.40.538.2017.

APPENDIX: DIFFRACTION FROM A PLANAR CHERN-SIMONS LAYER

The action for a planar Chern-Simons layer at $z = 0$ has the form [see Eq. (5)]

$$S = \frac{a}{2}\int dt\, dx\, dy\, \varepsilon^{z\nu\rho\sigma} A_\nu F_{\rho\sigma}, \tag{A1}$$

where the current due to the Chern-Simons interaction is $J^\nu = a\varepsilon^{z\nu\rho\sigma} F_{\rho\sigma}$. Maxwell's equations for the electromagnetic field in the presence of the action (A1) are subsequently modified to

$$\partial_\mu F^{\mu\nu} + a\,\varepsilon^{z\nu\rho\sigma} F_{\rho\sigma}\delta(z) = 0. \tag{A2}$$

From Eq. (A2), the continuity conditions follow as (see, e.g., Ref. [47])

$$E_z|_{z=0^+} - E_z|_{z=0^-} = -2a H_z|_{z=0}, \tag{A3}$$

$$H_x|_{z=0^+} - H_x|_{z=0^-} = 2a E_x|_{z=0}, \tag{A4}$$

$$H_y|_{z=0^+} - H_y|_{z=0^-} = 2a E_y|_{z=0}. \tag{A5}$$

Consider an s-polarized plane electromagnetic wave impinging onto a planar Chern-Simons layer at $z = 0$,

$$E_x = \exp(-ik_z z) + r_s \exp(ik_z z),\ z > 0, \tag{A6}$$

$$E_x = t_s \exp(-ik_z z),\ z < 0, \tag{A7}$$

$$H_x = r_{s\to p} \exp(ik_z z),\ z > 0, \tag{A8}$$

$$H_x = t_{s\to p} \exp(-ik_z z),\ z < 0, \tag{A9}$$

where the factor $\exp[i(\omega/c)t + ik_y y]$ is omitted for simplicity. From the continuity condition (A4), it follows that

$$r_{s\to p} - t_{s\to p} = 2a\, t_s. \tag{A10}$$

From the continuity condition $E_x|_{z=0^+} = E_x|_{z=0^-}$, one obtains

$$1 + r_s = t_s. \tag{A11}$$

The continuity condition $E_y|_{z=0^+} = E_y|_{z=0^-}$ and the Maxwell equation $E_y = -\frac{1}{i\omega}\partial_z H_x$ yield

$$r_{s\to p} = -t_{s\to p}. \tag{A12}$$

From the continuity condition (A5) and the Maxwell equation $H_y = \frac{1}{i\omega}\partial_z E_x$, one gets

$$1 - r_s - t_s = -2a\, t_{s\to p}. \tag{A13}$$

By solving (A10)–(A13), one obtains the reflection and transmission coefficients of an s-polarized wave as

$$\begin{aligned} r_s &= -\frac{a^2}{1+a^2}, \quad t_s = \frac{1}{1+a^2}, \\ r_{s\to p} &= \frac{a}{1+a^2}, \quad t_{s\to p} = -\frac{a}{1+a^2}. \end{aligned} \tag{A14}$$

By a duality transformation, i.e., by exchanging the fields E, H as well as the indices s, p in Eqs. (A6)–(A9), we obtain the reflection and transmission coefficients for the diffraction of a p-polarized wave as

$$\begin{aligned} r_p &= \frac{a^2}{1+a^2}, \quad t_p = \frac{1}{1+a^2}, \\ r_{p\to s} &= \frac{a}{1+a^2}, \quad t_{p\to s} = \frac{a}{1+a^2}. \end{aligned} \tag{A15}$$

[1] C. Riek *et al.*, Science **350**, 420 (2015).
[2] H. B. G. Casimir, Proceedings of the Koninklijke Nederlandse Akademie van Wetenschappen **51**, 793 (1948).
[3] L. M. Woods *et al.*, Rev. Mod. Phys. **88**, 045003 (2016).
[4] O. Kenneth, I. Klich, A. Mann, and M. Revzen, Phys. Rev. Lett. **89**, 033001 (2002).

[5] C. Henkel and K. Joulain, Europhys. Lett. **72**, 929 (2005).
[6] R. Zhao, J. Zhou, T. Koschny, E. N. Economou, and C. M. Soukoulis, Phys. Rev. Lett. **103**, 103602 (2009).
[7] A. G. Grushin and A. Cortijo, Phys. Rev. Lett. **106**, 020403 (2011).
[8] B.-S. Lu, Phys. Rev. B **97**, 045427 (2018).
[9] M. Bordag, I. V. Fialkovsky, D. M. Gitman, and D. V. Vassilevich, Phys. Rev. B **80**, 245406 (2009).
[10] I. V. Fialkovsky, V. N. Marachevsky, and D. V. Vassilevich, Phys. Rev. B **84**, 035446 (2011).
[11] F. M. Serry, D. Walliser, and G. J. Maclay, J. Appl. Phys. **84**, 2501 (1998).
[12] T. H. Boyer, Phys. Rev. **180**, 19 (1969).
[13] H. B. G. Casimir and D. Polder, Phys. Rev. **73**, 360 (1948).
[14] J. Fortágh and C. Zimmermann, Rev. Mod. Phys. **79**, 235 (2007).
[15] T. D. Lee and C. N. Yang, Phys. Rev. **104**, 254 (1956).
[16] C. S. Wu, E. Ambler, R. W. Hayward, D. D. Hoppes, and R. P. Hudson, Phys. Rev. **105**, 1413 (1957).
[17] M. Quack and J. Stohner, Phys. Rev. Lett. **84**, 3807 (2000).
[18] B. Darquié *et al.*, Chirality **22**, 870 (2010).
[19] F. W. Hehl, Yu. N. Obukhov, J.-P. Rivera, and H. Schmid, Phys. Lett. A **372**, 1141 (2008).
[20] A. H. Sihvola and I. Lindell, Ann. Phys. **17**, 787 (2008).
[21] M. Pospelov and A. Ritz, Ann. Phys. **318**, 119 (2005).
[22] J. Baron *et al.*, Science **343**, 269 (2014).
[23] I. B. Khriplovich, *Parity Nonconservation in Atomic Phenomena* (Gordon and Breach, Philadelphia, 1991).
[24] I. B. Khriplovich and S. K. Lamoreaux, *CP Violation Without Strangeness: Electric Dipole Moments of Particles, Atoms, and Molecules* (Springer, New York, 1997).
[25] V. N. Markov and Yu. M. Pis'mak, J. Phys. A: Math. Gen. **39**, 6525 (2006).
[26] V. N. Marachevsky, Theor. Math. Phys. **190**, 315 (2017).
[27] V. N. Marachevsky, arXiv:1802.06523.
[28] I. Fialkovsky, N. Khusnutdinov, and D. Vassilevich, Phys. Rev. B **97**, 165432 (2018).
[29] R. Jackiw, Phys. Rev. D **29**, 2375 (1984).
[30] T. Cysne, W. J. M. Kort-Kamp, D. Oliver, F. A. Pinheiro, F. S. S. Rosa, and C. Farina, Phys. Rev. A **90**, 052511 (2014).
[31] V. N. Marachevsky and Yu. M. Pis'mak, Phys. Rev. D **81**, 065005 (2010).
[32] P. Curie, J. Phys. Theor. Appl. **3**, 393 (1894).
[33] S. Y. Buhmann, D. T. Butcher, and S. Scheel, New J. Phys. **14**, 083034 (2012).
[34] S. Scheel and S. Y. Buhmann, Acta Physica Slovaka **58**, 675 (2008).
[35] V. N. Marachevsky, J. Phys. A: Math. Theor. **45**, 374021 (2012).
[36] J. M. Wylie and J. E. Sipe, Phys. Rev. A **30**, 1185 (1984).
[37] C. Henkel, K. Joulain, J.-P. Mulet, and J.-J. Greffet, J. Opt. A: Pure Appl. Opt. **4**, S109 (2002).
[38] S. Fuchs, J. A. Crosse, and S. Y. Buhmann, Phys. Rev. A **95**, 023805 (2017).
[39] A. Derevianko and M. G. Kozlov, Adv. At. Mol. Opt. Phys. **58**, 77 (2010).
[40] S. Y. Buhmann, L. Knöll, D.-G. Welsch, and H. T. Dung, Phys. Rev. A **70**, 052117 (2004).
[41] S. Esfandiarpour, H. Safari, R. Bennett, and S. Y. Buhmann, J. Phys. B: At. Mol. Opt. Phys. **51**, 094004 (2018).
[42] E. M. Purcell and N. F. Ramsey, Phys. Ref. **78**, 807 (1950).
[43] E. D. Commins, S. B. Ross, D. DeMille, and B. C. Regan, Phys. Rev. A **50**, 2960 (1994).
[44] S. P. Lloyd, Phys. Rev. **81**, 161 (1951).
[45] D. T. Butcher, S. Y. Buhmann, and S. Scheel, New J. Phys. **14**, 113013 (2012).
[46] V. V. Flambaum, J. S. M. Ginges, and G. Mititelu, arXiv:nucl-th/0010100.
[47] D. Yu. Pis'mak, Yu. M. Pis'mak, and F. J. Wegner, Phys. Rev. E **92**, 013204 (2015).

PHYSICAL REVIEW A **78**, 062901 (2008)

van der Waals potentials of paramagnetic atoms

Hassan Safari and Dirk-Gunnar Welsch
Theoretisch-Physikalisches Institut, Friedrich-Schiller-Universität Jena, Max-Wien-Platz 1, 07743 Jena, Germany

Stefan Yoshi Buhmann and Stefan Scheel
Quantum Optics and Laser Science, Blackett Laboratory, Imperial College London, Prince Consort Road, London SW7 2BW, United Kingdom

(Received 23 September 2008; published 3 December 2008)

We study single- and two-atom van der Waals interactions of ground-state atoms which are both polarizable and paramagnetizable in the presence of magnetoelectric bodies within the framework of macroscopic quantum electrodynamics. Starting from an interaction Hamiltonian that includes particle spins, we use leading-order perturbation theory to express the van der Waals potentials in terms of the polarizability and magnetizability of the atom(s). To allow for atoms embedded in media, we also include local-field corrections via the real-cavity model. The general theory is applied to the potential of a single atom near a half space and that of two atoms embedded in a bulk medium or placed near a sphere, respectively.

DOI: 10.1103/PhysRevA.78.062901 PACS number(s): 34.35.+a, 34.20.−b, 12.20.−m, 42.50.Nn

I. INTRODUCTION

The dispersion interaction between neutral and (unpolarized) atoms or molecules—commonly known as the van der Waals (vdW) interaction—is, together with Casimir-Polder and Casimir forces, one of the consequences of zero-point fluctuations in quantum electrodynamics (QED) (for a recent review, see Ref. [1]). The interaction potential of two polarizable atoms in free space was first studied for small distances (nonretarded limit) by London using second-order perturbation theory [2]. In this limit the result is an attractive potential proportional to r^{-6} with r being the interatomic distance. The London formula was extended to arbitrary distances by Casimir and Polder using fourth-order perturbation theory within the framework of QED [3]. They found an attractive potential proportional to r^{-7} for large separations (retarded limit) where the potential is due to the ground-state fluctuations of both the atomic dipole moments and the electromagnetic far field. Casimir and Polder also considered the potential of a polarizable atom in the presence of a perfectly conducting wall [3]. The result is an attractive potential which shows a z^{-3} dependence in the nonretarded limit and is proportional to z^{-4} in the retarded limit (z being the atom-wall separation).

In the three-atom case, a nonadditive term prevents the potential from just being the sum of three pairwise contributions; it was first calculated in the nonretarded limit [4,5] and extended to arbitrary interatomic distances [6]. Later, a general formula for the nonadditive N-atom vdW potential was obtained by summing the responses of each atom to the electromagnetic field produced by the other atoms [7], or alternatively, by calculating the zero-point energy difference of the electromagnetic field with and without the atoms [8].

The theory was extended to magnetic atoms by Feinberg and Sucher [9] who studied the retarded interaction of two electromagnetic atoms based on a calculation of photon scattering amplitudes; their results were later reproduced by Boyer [10] using a zero-point energy technique. In this limit, the interaction potential of a polarizable atom and a magnetizable one was found to be repulsive and proportional to r^{-7}. Later on, Feinberg and Sucher extended their formula to arbitrary distances [11]. In particular, in the nonretarded limit the potential of the mentioned atoms is found to be repulsive and proportional to r^{-4}. The retarded Feinberg-Sucher potential was extended to atoms with crossed electric-magnetic polarizabilities on the basis of a duality argument [12]. For the single-atom case, the atom-wall potential, calculated in Ref. [3] in the retarded limit, has been generalized to atoms with both electric and magnetic polarizabilities [10], showing that a magnetically polarizable atom in a distance l from a conducting wall is repelled by that wall due to a potential proportional to l^{-4}. A full QED treatment has been invoked to study the potential of an excited magnetic atom placed inside a planar cavity for all distance regimes [13].

In order to extend the theory of atom-atom interactions to the case of magnetoelectrics being present, the effect of the bodies on the fluctuating electromagnetic field must be taken into account. A general formula expressing the vdW potential between two polarizable ground-state atoms in the presence of electric bodies in terms of the Green tensor of the body-assisted electromagnetic field was obtained using linear response theory [14] and later reproduced by treating the effect of the bodies semiclassically [15]. Recently, an analogous formula for two polarizable atoms interacting in the presence of magnetoelectric bodies was derived by using fourth-order perturbation theory within the framework of macroscopic QED [16], it was later generalized to N atoms [17]. For atoms that are embedded in a host body or medium, the local electromagnetic field experienced by them differs from the macroscopic one. Hence, the theory of vdW interactions must be modified by taking local-field corrections into account. One approach to this problem is the real-cavity model, where one assumes that each guest atom is surrounded by a small, empty, spherical cavity [18]. It has been used to study local-field corrections to the spontaneous decay rate of an atom embedded in an arrangement of magnetoelectric bodies and/or media [19] and was recently applied to obtain local-field corrected formulas for one-atom and two-atom vdW potentials of polarizable atoms within such geometries [20].

In this article, we generalize the theory of ground-state single- and two-atom vdW potentials in the presence of arbitrarily shaped magnetoelectric bodies to atoms exhibiting both polarizabilities and (para)magnetizabilities. Such a theory includes and generalizes the recently studied potential of two polarizable and magnetizable bodies embedded in a bulk magnetoelectric medium [21]. This article is organized as follows. In Sec. II, the multipolar atom-field interaction Hamiltonian is derived for atoms that are both electric and (para)magnetic. In Sec. III, general expressions for single- and two-atom potentials are derived using perturbation theory. Local-field corrections are considered in Sec. IV, while in Sec. V, we apply our theory by studying the examples of (i) an atom in the presence of a half space, (ii) two atoms in bulk media, and (iii) two atoms in the presence of a sphere. A summary is given in Sec. VI.

II. ATOM-FIELD INTERACTIONS IN THE PRESENCE OF SPINS

The interaction of individual atoms with medium-assisted electromagnetic fields has extensively been discussed for spinless atoms [16,22–24]. In order to correctly describe the paramagnetic properties of an atom, it is crucial to include the spins of its constituents in the considerations. A neutral atom (or molecule) A thus has to be regarded as being a collection of (nonrelativistic) particles $\alpha \in A$ which in addition to their charges q_α ($\Sigma_{\alpha\in A} q_\alpha = 0$), masses m_α, positions $\hat{\mathbf{r}}_\alpha$, canonically conjugate momenta $\hat{\mathbf{p}}_\alpha$ have spins $\hat{\mathbf{s}}_\alpha$. The particle spins give rise to magnetic dipole moments $\gamma_\alpha \hat{\mathbf{s}}_\alpha$, where γ_α is the gyromagnetic ratio of particle α [$\gamma_e = -e g_e/(2m_e)$ for electrons with $-e$, electron charge; $g_e \simeq 2$, electron g factor; m_e, electron mass]. While leaving the atomic charge density

$$\hat{\rho}_A(\mathbf{r}) = \sum_{\alpha\in A} q_\alpha \delta(\mathbf{r} - \hat{\mathbf{r}}_\alpha) \tag{1}$$

and polarization

$$\hat{\mathbf{P}}_A(\mathbf{r}) = \sum_{\alpha\in A} q_\alpha \hat{\bar{\mathbf{r}}}_\alpha \int_0^1 d\sigma \delta(\mathbf{r} - \hat{\mathbf{r}}_A - \sigma \hat{\bar{\mathbf{r}}}_\alpha) \tag{2}$$

unaffected, the spin magnetic moments do contribute to the atomic current density and magnetization, so that the expressions given in Refs. [23,24] for spinless particles generalize to

$$\hat{\mathbf{j}}_A(\mathbf{r}) = \sum_{\alpha\in A} \frac{q_\alpha}{2} [\dot{\hat{\mathbf{r}}}_\alpha \delta(\mathbf{r} - \hat{\mathbf{r}}_\alpha) + \delta(\mathbf{r} - \hat{\mathbf{r}}_\alpha)\dot{\hat{\mathbf{r}}}_\alpha] - \sum_{\alpha\in A} \gamma_\alpha \hat{\mathbf{s}}_\alpha \times \boldsymbol{\nabla} \delta(\mathbf{r} - \hat{\mathbf{r}}_\alpha) \tag{3}$$

and

$$\hat{\mathbf{M}}_A(\mathbf{r}) = \sum_{\alpha\in A} \frac{q_\alpha}{2} \int_0^1 d\sigma \sigma [\delta(\mathbf{r} - \hat{\mathbf{r}}_A - \sigma \hat{\bar{\mathbf{r}}}_\alpha) \hat{\bar{\mathbf{r}}}_\alpha \times \dot{\hat{\bar{\mathbf{r}}}}_\alpha - \dot{\hat{\bar{\mathbf{r}}}}_\alpha \times \hat{\bar{\mathbf{r}}}_\alpha \delta(\mathbf{r} - \hat{\mathbf{r}}_A - \sigma \hat{\bar{\mathbf{r}}}_\alpha)] + \sum_{\alpha\in A} \gamma_\alpha \hat{\mathbf{s}}_\alpha \delta(\mathbf{r} - \hat{\mathbf{r}}_\alpha). \tag{4}$$

In Eqs. (2) and (4), $\hat{\bar{\mathbf{r}}}_\alpha = \hat{\mathbf{r}}_\alpha - \hat{\mathbf{r}}_A$ denotes the position of the αth particle relative to the center-of-mass position

$$\hat{\mathbf{r}}_A = \sum_{\alpha\in A} \frac{m_\alpha}{m_A} \hat{\mathbf{r}}_\alpha \tag{5}$$

($m_A = \Sigma_{\alpha\in A} m_\alpha$), with the associated momenta being

$$\hat{\bar{\mathbf{p}}}_\alpha = \hat{\mathbf{p}}_\alpha - \frac{m_\alpha}{m_A} \hat{\mathbf{p}}_A \tag{6}$$

and $\hat{\mathbf{p}}_A = \Sigma_{\alpha\in A} \hat{\mathbf{p}}_\alpha$, respectively. Since the current density associated with the spins is transverse, the continuity equation $\dot{\hat{\rho}}_A + \boldsymbol{\nabla}\cdot\hat{\mathbf{j}}_A = 0$ remains valid. In addition, the atomic charge and current densities can still be related to the atomic polarization and magnetization via

$$\hat{\rho}_A = -\boldsymbol{\nabla}\cdot\hat{\mathbf{P}}_A, \tag{7}$$

$$\hat{\mathbf{j}}_A = \dot{\hat{\mathbf{P}}}_A + \boldsymbol{\nabla}\times\hat{\mathbf{M}}_A + \hat{\mathbf{j}}_{\mathrm{Ro}} \tag{8}$$

as in the case of spinless particles, since the particle spins lead to equal contributions on the left- and right-hand sides of Eq. (8), as an inspection of Eqs. (3) and (4) shows. In Eq. (8),

$$\hat{\mathbf{j}}_{\mathrm{Ro}} = \frac{1}{2} \boldsymbol{\nabla} \times [\hat{\mathbf{P}}_A \times \dot{\hat{\mathbf{r}}}_A - \dot{\hat{\mathbf{r}}}_A \times \hat{\mathbf{P}}_A] \tag{9}$$

is the Röntgen current density associated with the center-of-mass motion of the atom [25,26]. Further atomic quantities of interest are the atomic electric and magnetic dipole moments

$$\hat{\mathbf{d}}_A = \sum_{\alpha\in A} q_\alpha \hat{\bar{\mathbf{r}}}_\alpha = \sum_{\alpha\in A} q_\alpha \hat{\mathbf{r}}_\alpha \tag{10}$$

and

$$\hat{\mathbf{m}}_A = \sum_{\alpha\in A} \left[\frac{q_\alpha}{2} \hat{\bar{\mathbf{r}}}_\alpha \times \dot{\hat{\bar{\mathbf{r}}}}_\alpha + \gamma_\alpha \hat{\mathbf{s}}_\alpha \right], \tag{11}$$

which emerge from the atomic polarization (2) and magnetization (4) in the long-wavelength approximation, as we will see later on. The first and second terms in Eq. (11) obviously represent the orbital angular momentum and spin contributions to the magnetic dipole moment.

In order to account for the interaction of the spins with the magnetic field, a Pauli term has to be included in the minimal-coupling Hamiltonian given in Ref. [16] for spinless atoms interacting with the quantized electromagnetic field in the presence of linearly responding magnetoelectric bodies, viz.,

$$\hat{H} = \sum_{\lambda=e,m} \int d^3r \int_0^\infty d\omega \hbar\omega \hat{\mathbf{f}}_\lambda^\dagger(\mathbf{r},\omega)\cdot\hat{\mathbf{f}}_\lambda(\mathbf{r},\omega) + \sum_{\alpha\in UA} \frac{[\hat{\mathbf{p}}_\alpha - q_\alpha \hat{\mathbf{A}}(\hat{\mathbf{r}}_\alpha)]^2}{2m_\alpha} + \sum_{\substack{\alpha,\beta\in UA \\ \alpha\neq\beta}} \frac{q_\alpha q_\beta}{8\pi\varepsilon_0|\hat{\mathbf{r}}_\alpha - \hat{\mathbf{r}}_\beta|} + \sum_{\alpha\in UA} q_\alpha\hat{\varphi}(\hat{\mathbf{r}}_\alpha) - \sum_{\alpha\in UA}\gamma_\alpha\hat{\mathbf{s}}_\alpha\cdot\hat{\mathbf{B}}(\hat{\mathbf{r}}_\alpha). \quad (12)$$

The first term in Eq. (12) is the energy of the electromagnetic field and the bodies, expressed in terms of bosonic (collective) variables $\hat{\mathbf{f}}_\lambda(\mathbf{r},\omega)$ and $\hat{\mathbf{f}}_\lambda^\dagger(\mathbf{r},\omega)$ ($\lambda, \lambda' \in \{e,m\}$, with e, m denoting electric and magnetic excitations), the second term is the kinetic energy of the charged particles constituting the atoms, the third and fourth terms denote their mutual and body-assisted Coulomb potentials, respectively, and the last term is the newly introduced Pauli interaction of the particle spins with the body-assisted magnetic field. Note that the scalar potential $\hat{\varphi}$, the vector potential $\hat{\mathbf{A}}$, and the induction field $\hat{\mathbf{B}}$ are thought of as being expressed in terms of the fundamental bosonic fields $\hat{\mathbf{f}}_\lambda$ and $\hat{\mathbf{f}}_\lambda^\dagger$ [24,27].

To verify the consistency of the Hamiltonian (12), we need to show that it leads to the correct Maxwell equations for the electromagnetic field and the Newton equations for the particles. As in the case of spinless particles, the total electromagnetic field can be given by

$$\hat{\boldsymbol{\mathcal{E}}} = \hat{\mathbf{E}} - \sum_A \boldsymbol{\nabla}\hat{\varphi}_A, \quad \hat{\boldsymbol{\mathcal{B}}} = \hat{\mathbf{B}}, \quad (13)$$

$$\hat{\boldsymbol{\mathcal{D}}} = \hat{\mathbf{D}} - \varepsilon_0\sum_A \boldsymbol{\nabla}\hat{\varphi}_A, \quad \hat{\boldsymbol{\mathcal{H}}} = \hat{\mathbf{H}}, \quad (14)$$

where $\hat{\mathbf{E}}$, $\hat{\mathbf{B}}$, $\hat{\mathbf{D}}$, and $\hat{\mathbf{H}}$ are the body-assisted electromagnetic-field strengths [24,27], and

$$\hat{\varphi}_A(\mathbf{r}) = \sum_{\alpha\in A} \frac{q_\alpha}{4\pi\varepsilon_0|\mathbf{r} - \hat{\mathbf{r}}_\alpha|} \quad (15)$$

is the Coulomb potential due to atom A. Since the atomic charge density (1) is not affected by the particle spins either, the Maxwell equations

$$\boldsymbol{\nabla}\cdot\hat{\boldsymbol{\mathcal{B}}} = 0, \quad (16)$$

$$\boldsymbol{\nabla}\cdot\hat{\boldsymbol{\mathcal{D}}} = \sum_A \hat{\rho}_A, \quad (17)$$

which are not governed by the system Hamiltonian, are not changed by the presence of spins. It is obvious that the Maxwell equation

$$\boldsymbol{\nabla}\times\hat{\boldsymbol{\mathcal{E}}} + \dot{\hat{\boldsymbol{\mathcal{B}}}} = 0 \quad (18)$$

also remains unchanged, because the Pauli interaction term commutes with the $\hat{\boldsymbol{\mathcal{B}}}$ field and hence its inclusion does not lead to an additional contribution in Heisenberg's equation of motion $\dot{\hat{\boldsymbol{\mathcal{B}}}} = (i/\hbar)[\hat{H}, \hat{\boldsymbol{\mathcal{B}}}]$. As implied by the commutation relation [27]

$$[\hat{D}_i(\mathbf{r}), \hat{A}_j(\mathbf{r}')] = i\hbar\delta_{ij}^\perp(\mathbf{r} - \mathbf{r}') \quad (19)$$

[$\delta_{ij}^\perp(\mathbf{r})$, transverse δ function], the Pauli interaction does lead to an additional contribution

$$\frac{i}{\hbar}\left[-\sum_{\alpha\in UA}\gamma_\alpha\hat{\mathbf{s}}_\alpha\cdot\hat{\mathbf{B}}(\hat{\mathbf{r}}_\alpha), \hat{\boldsymbol{\mathcal{D}}}(\mathbf{r})\right] = -\sum_{\alpha\in UA}\gamma_\alpha\hat{\mathbf{s}}_\alpha\times\boldsymbol{\nabla}\delta(\mathbf{r} - \hat{\mathbf{r}}_\alpha) \quad (20)$$

in the Heisenberg equation of motion $\dot{\hat{\boldsymbol{\mathcal{D}}}} = (i/\hbar)[\hat{H}, \hat{\boldsymbol{\mathcal{D}}}]$, which coincides with the spin-induced component of $\hat{\mathbf{j}}_A$ [second term in Eq. (3)]. Hence, the Maxwell equation

$$\boldsymbol{\nabla}\times\hat{\boldsymbol{\mathcal{H}}} - \dot{\hat{\boldsymbol{\mathcal{D}}}} = \sum_A \hat{\mathbf{j}}_A \quad (21)$$

holds in the presence of spin when using the amended atomic current density (3).

Next, consider the equations of motion for the charged particles. Using the Hamiltonian (12), we have

$$\dot{\hat{\mathbf{r}}}_\alpha = \frac{1}{m_\alpha}[\hat{\mathbf{p}}_\alpha - q_\alpha\hat{\mathbf{A}}(\hat{\mathbf{r}}_\alpha)], \quad (22)$$

as in the absence of spins. Equation (22) implies that the Pauli interaction gives rise to a contribution

$$\frac{i}{\hbar}\left[-\sum_{\beta\in UA}\gamma_\beta\hat{\mathbf{s}}_\beta\cdot\hat{\mathbf{B}}(\hat{\mathbf{r}}_\beta), m_\alpha\dot{\hat{\mathbf{r}}}_\alpha\right] = \gamma_\alpha\boldsymbol{\nabla}_\alpha[\hat{\mathbf{s}}_\alpha\cdot\hat{\mathbf{B}}(\hat{\mathbf{r}}_\alpha)] \quad (23)$$

to $m_\alpha\ddot{\hat{\mathbf{r}}}_\alpha = (i/\hbar)[\hat{H}, m_\alpha\dot{\hat{\mathbf{r}}}_\alpha]$. Combining this with the contributions from the spin-independent part of the Hamiltonian [27], we arrive at

$$m_\alpha\ddot{\hat{\mathbf{r}}}_\alpha = q_\alpha\hat{\boldsymbol{\mathcal{E}}}(\hat{\mathbf{r}}_\alpha) + \frac{q_\alpha}{2}[\dot{\hat{\mathbf{r}}}_\alpha\times\hat{\boldsymbol{\mathcal{B}}}(\hat{\mathbf{r}}_\alpha) - \hat{\boldsymbol{\mathcal{B}}}(\hat{\mathbf{r}}_\alpha)\times\dot{\hat{\mathbf{r}}}_\alpha] + \gamma_\alpha\boldsymbol{\nabla}_\alpha[\hat{\mathbf{s}}_\alpha\cdot\hat{\boldsymbol{\mathcal{B}}}(\hat{\mathbf{r}}_\alpha)]. \quad (24)$$

The first two terms on the right-hand side of this equation represent the Lorentz force on the charged particles while the third term is the Zeeman force resulting from the action of the magnetic field on the particle spins. We have thus successfully established a Hamiltonian [Eq. (12)] describing the interaction of one or more atoms with the electromagnetic field in the presence of magnetoelectric bodies which generates the correct Maxwell equations for the fields and the correct Newton equations for the particles.

Due to the rather large number of atom-field and even atom-atom interaction terms, the Hamiltonian (12) may be not very practical as a starting point for calculations. As an alternative, we use the multipolar-coupling Hamiltonian which for neutral atoms follows from a Power-Zienau-Woolley transformation [28,29],

$$\hat{O}' = \hat{U}\hat{O}\hat{U}^\dagger \quad (25)$$

with

$$\hat{U} = \exp\left[\frac{i}{\hbar}\int d^3r \sum_A \hat{\mathbf{P}}_A \cdot \hat{\mathbf{A}}\right] \tag{26}$$

upon expressing the Hamiltonian (12) in terms of the transformed variables. The only difference with respect to the case of spinless particles is the Pauli interaction term, which is invariant under the transformation since $\hat{\mathbf{B}}' = \hat{\mathbf{B}}$ and $\hat{\mathbf{s}}'_\alpha = \hat{\mathbf{s}}_\alpha$. The multipolar-coupling Hamiltonian can thus be given in the form of

$$\hat{H} = \hat{H}'_F + \sum_A \hat{H}'_A + \sum_A \hat{H}'_{AF}, \tag{27}$$

where

$$\hat{H}'_F = \sum_{\lambda=e,m} \int d^3r \int_0^\infty d\omega \hbar\omega \hat{\mathbf{f}}'^{\dagger}_\lambda(\mathbf{r},\omega)\cdot\hat{\mathbf{f}}'_\lambda(\mathbf{r},\omega), \tag{28}$$

$$\hat{H}'_A = \sum_{\alpha\in A}\frac{\hat{\mathbf{p}}'^2_\alpha}{2m_\alpha} + \frac{1}{2\varepsilon_0}\int d^3r \hat{\mathbf{P}}'^2_A = \frac{\hat{\mathbf{p}}'^2_A}{2m_A} + \sum_{\alpha\in A}\frac{\hat{\tilde{\mathbf{p}}}'^2_\alpha}{2m_\alpha} + \frac{1}{2\varepsilon_0}\int d^3r \hat{\mathbf{P}}'^2_A = \frac{\hat{\mathbf{p}}'^2_A}{2m_A} + \sum_n E_A^{n'}|n'_A\rangle\langle n'_A|, \tag{29}$$

with $|n'_A\rangle$ and $E_A^{n'}$ denoting, respectively, the eigenstates and eigenvalues of $\hat{H}'_A$, and

$$\hat{H}'_{AF} = -\int d^3r(\hat{\mathbf{P}}'_A\cdot\hat{\mathbf{E}}' + \hat{\mathbf{M}}'_A\cdot\hat{\mathbf{B}}') + \int d^3r\frac{\hat{\mathbf{p}}'_A}{m_A}\cdot\hat{\mathbf{P}}'_A\times\hat{\mathbf{B}}' + \sum_{\alpha\in A}\frac{1}{2m_\alpha}\left[\int d^3r\hat{\Xi}'_\alpha\times\hat{\mathbf{B}}'\right]^2, \tag{30}$$

with

$$\hat{\mathbf{M}}'_A(\mathbf{r}) = \sum_{\alpha\in A}\frac{q_\alpha}{2m_\alpha}\int_0^1 d\sigma\sigma[\delta(\mathbf{r}-\hat{\mathbf{r}}'_A-\sigma\hat{\tilde{\mathbf{r}}}'_\alpha)\hat{\tilde{\mathbf{r}}}'_\alpha\times\hat{\tilde{\mathbf{p}}}'_\alpha - \hat{\tilde{\mathbf{p}}}'_\alpha\times\hat{\tilde{\mathbf{r}}}'_\alpha\delta(\mathbf{r}-\hat{\mathbf{r}}'_A-\sigma\hat{\tilde{\mathbf{r}}}'_\alpha)] + \sum_{\alpha\in A}\gamma_\alpha\hat{\mathbf{s}}'_\alpha\delta(\mathbf{r}-\hat{\mathbf{r}}'_\alpha) \tag{31}$$

being the canonical magnetization and

$$\hat{\Xi}'_\alpha(\mathbf{r}) = \frac{m_\alpha}{m_A}\hat{\mathbf{P}}'_A(\mathbf{r}) + q_\alpha\hat{\tilde{\mathbf{r}}}'_\alpha\int_0^1 d\sigma\sigma\delta(\mathbf{r}-\hat{\mathbf{r}}'_A-\sigma\hat{\tilde{\mathbf{r}}}'_\alpha) - \frac{m_\alpha}{m_A}\sum_{\beta\in A}q_\beta\hat{\tilde{\mathbf{r}}}'_\beta\int_0^1 d\sigma\sigma\delta(\mathbf{r}-\hat{\mathbf{r}}'_A-\sigma\hat{\tilde{\mathbf{r}}}'_\beta). \tag{32}$$

In the long-wavelength approximation, the atom-field coupling Hamiltonian reduces to

$$\hat{H}'_{AF} = -\hat{\mathbf{d}}'_A\cdot\hat{\mathbf{E}}'(\hat{\mathbf{r}}'_A) - \hat{\mathbf{m}}'_A\cdot\hat{\mathbf{B}}'(\hat{\mathbf{r}}'_A) + \frac{\hat{\mathbf{p}}'_A}{m_A}\cdot\hat{\mathbf{d}}'_A\times\hat{\mathbf{B}}'(\hat{\mathbf{r}}'_A) + \sum_{\alpha\in A}\frac{q_\alpha^2}{8m_\alpha}[\hat{\tilde{\mathbf{r}}}'_\alpha\times\hat{\mathbf{B}}'(\hat{\mathbf{r}}'_A)]^2 + \frac{3}{8m_A}[\hat{\mathbf{d}}'_A\times\hat{\mathbf{B}}'(\hat{\mathbf{r}}'_A)]^2, \tag{33}$$

where

$$\hat{\mathbf{d}}'_A = \sum_{\alpha\in A}q_\alpha\hat{\tilde{\mathbf{r}}}'_\alpha = \sum_{\alpha\in A}q_\alpha\hat{\mathbf{r}}'_\alpha \tag{34}$$

and

$$\hat{\mathbf{m}}'_A = \sum_{\alpha\in A}\left[\frac{q_\alpha}{2m_\alpha}\hat{\tilde{\mathbf{r}}}'_\alpha\times\hat{\tilde{\mathbf{p}}}'_\alpha + \gamma_\alpha\hat{\mathbf{s}}'_\alpha\right] \tag{35}$$

are the atomic electric and (canonical) magnetic dipole moments, respectively. In Eq. (33), the first and the second terms are the electric and magnetic dipole interaction, respectively, the third term is the Röntgen interaction associated with center-of-mass motion, and the last two terms are generalized diamagnetic interactions. The Röntgen interaction becomes important when studying dissipative forces such as quantum friction [30]. In this work, we are mainly interested in the interaction of atoms at given center-of-mass positions $\mathbf{r}_A$ featuring electric as well as paramagnetic properties which, upon discarding the last three terms in Eq. (33), can be described by the interaction Hamiltonian

$$\hat{H}'_{AF} = -\hat{\mathbf{d}}'_A\cdot\hat{\mathbf{E}}'(\mathbf{r}_A) - \hat{\mathbf{m}}'_A\cdot\hat{\mathbf{B}}'(\mathbf{r}_A). \tag{36}$$

We conclude this section by recalling some relations that will be needed for the calculation of vdW potentials. The electromagnetic fields $\hat{\mathbf{E}}'$ and $\hat{\mathbf{B}}'$ are expressed in terms of the fundamental bosonic fields

$$[\hat{\mathbf{f}}'_\lambda(\mathbf{r},\omega),\hat{\mathbf{f}}'^{\dagger}_{\lambda'}(\mathbf{r}',\omega')] = \delta_{\lambda\lambda'}\delta(\omega-\omega')\boldsymbol{\delta}(\mathbf{r}-\mathbf{r}'), \tag{37}$$

$$[\hat{\mathbf{f}}'_\lambda(\mathbf{r},\omega),\hat{\mathbf{f}}'_{\lambda'}(\mathbf{r}',\omega')] = \mathbf{0} \tag{38}$$

$(\lambda,\lambda'\in\{e,m\})$ according to

$$\hat{\mathbf{E}}'(\mathbf{r}) = \sum_{\lambda=e,m}\int d^3r'\int_0^\infty d\omega\mathbf{G}_\lambda(\mathbf{r},\mathbf{r}',\omega)\cdot\hat{\mathbf{f}}'_\lambda(\mathbf{r}',\omega) + \text{H.c.}, \tag{39}$$

$$\hat{\mathbf{B}}'(\mathbf{r}) = \sum_{\lambda=e,m}\int d^3r'\int_0^\infty\frac{d\omega}{i\omega}\boldsymbol{\nabla}\times\mathbf{G}_\lambda(\mathbf{r},\mathbf{r}',\omega)\cdot\hat{\mathbf{f}}'_\lambda(\mathbf{r}',\omega) + \text{H.c.}, \tag{40}$$

where the quantities $\mathbf{G}_\lambda(\mathbf{r},\mathbf{r}',\omega)$ are related to the classical Green tensor $\mathbf{G}(\mathbf{r},\mathbf{r}',\omega)$ as

$$\mathbf{G}_e(\mathbf{r},\mathbf{r}',\omega) = i\frac{\omega^2}{c^2}\sqrt{\frac{\hbar}{\pi\varepsilon_0}\,\mathrm{Im}\,\varepsilon(\mathbf{r}',\omega)}\mathbf{G}(\mathbf{r},\mathbf{r}',\omega), \tag{41}$$

$$\mathbf{G}_m(\mathbf{r},\mathbf{r}',\omega) = i\frac{\omega}{c}\sqrt{\frac{\hbar}{\pi\varepsilon_0}\frac{\mathrm{Im}\,\mu(\mathbf{r}',\omega)}{|\mu(\mathbf{r}',\omega)|^2}}[\boldsymbol{\nabla}'\times\mathbf{G}(\mathbf{r}',\mathbf{r},\omega)]^{\mathsf{T}}. \tag{42}$$

For an arbitrary arrangement of linearly responding magnetoelectric bodies described by a permittivity $\varepsilon(\mathbf{r},\omega)$ and a permeability $\mu(\mathbf{r},\omega)$, the Green tensor obeys the differential equation

$$\left[\boldsymbol{\nabla}\times\frac{1}{\mu(\mathbf{r},\omega)}\boldsymbol{\nabla}\times-\frac{\omega^2}{c^2}\varepsilon(\mathbf{r},\omega)\right]\mathbf{G}(\mathbf{r},\mathbf{r}',\omega)=\boldsymbol{\delta}(\mathbf{r}-\mathbf{r}'),\tag{43}$$

has the useful properties

$$\mathbf{G}^*(\mathbf{r},\mathbf{r}',\omega)=\mathbf{G}(\mathbf{r},\mathbf{r}',-\omega^*),\tag{44}$$

$$\mathbf{G}(\mathbf{r},\mathbf{r}',\omega)=\mathbf{G}^{\mathsf{T}}(\mathbf{r}',\mathbf{r},\omega),\tag{45}$$

and satisfies the integral relation [27]

$$\sum_{\lambda=e,m}\int d^3s\,\mathbf{G}_\lambda(\mathbf{r},\mathbf{s},\omega)\cdot\mathbf{G}_\lambda^{*\mathsf{T}}(\mathbf{r}',\mathbf{s},\omega)=\frac{\hbar\mu_0}{\pi}\omega^2\,\mathrm{Im}\,\mathbf{G}(\mathbf{r},\mathbf{r}',\omega).\tag{46}$$

The ground state $|\{0'\}\rangle$ of $\hat{H}_F'$ is defined by the relation $\hat{\mathbf{f}}_\lambda'(\mathbf{r},\omega)|\{0'\}\rangle=\mathbf{0}$ for all $\lambda,\mathbf{r},\omega$. Since we will exclusively work with the multipolar-coupling Hamiltonian, we will henceforth drop the primes indicating the Power-Zienau-Woolley transformation.

III. VAN DER WAALS POTENTIALS

According to the well-known concept of Casimir and Polder [31], vdW forces on ground-state atoms can be derived from the associated vdW potentials, which in turn can be deduced from a perturbative calculation of the position-dependent parts of energy shift induced by the atom-field coupling.

A. Single-atom potential

Let us consider a neutral ground-state atom A at a position $\mathbf{r}_A$ in the presence of arbitrarily shaped magnetoelectric bodies. With the atom-field interaction Hamiltonian given by Eq. (36) (recall that we have dropped all primes), the vdW potential of the atom follows from the second-order energy shift

$$\Delta E=-\sum_{I\neq 0}\frac{\langle 0|\hat{H}_{AF}|I\rangle\langle I|\hat{H}_{AF}|0\rangle}{E_I-E_0},\tag{47}$$

where $|0\rangle=|0_A\rangle|\{0\}\rangle$ denotes the quantum state where both atoms and the body-assisted electromagnetic field are in their ground states. Note that the summation in Eq. (47) includes position and frequency integrals. Recalling the interaction Hamiltonian (36), we see that only intermediate states $|I\rangle$ in which the atom is in an excited state and a single quantum of the fundamental fields is excited contribute to the sum and hence Eq. (47) may be specified as

$$\Delta E=-\frac{1}{\hbar}\sum_k\sum_{\lambda=e,m}\int d^3r\int_0^\infty\frac{d\omega}{\omega_A^k+\omega}\times|\langle 0_A|\langle\{0\}|\hat{H}_{AF}|\mathbf{1}_\lambda(\mathbf{r},\omega)\rangle|k_A\rangle|^2\tag{48}$$

$[\omega_A^k=(E_A^k-E_A^0)/\hbar,\ |\mathbf{1}_\lambda(\mathbf{r},\omega)\rangle=\hat{\mathbf{f}}_\lambda^\dagger(\mathbf{r},\omega)|\{0\}\rangle]$. Using the expansions (39) and (40) as well as the commutation relations (37) and (38), the matrix elements of the interaction Hamiltonian (36) are found to be

$$\langle 0_A|\langle\{0\}|\hat{H}_{AF}|\mathbf{1}_\lambda(\mathbf{r},\omega)\rangle|k_A\rangle=-\mathbf{d}_A^{n0}\cdot\mathbf{G}_\lambda(\mathbf{r}_A,\mathbf{r},\omega)-\frac{\mathbf{m}_A^{0k}\cdot\boldsymbol{\nabla}_A\times\mathbf{G}_\lambda(\mathbf{r}_A,\mathbf{r},\omega)}{i\omega}\tag{49}$$

$[\mathbf{d}_A^{0k}=\langle 0_A|\hat{\mathbf{d}}_A|k_A\rangle,\ \mathbf{m}_A^{0k}=\langle 0_A|\hat{\mathbf{m}}_A|k_A\rangle]$.

With ΔE being quadratic in the matrix elements, there are three classes of contributions to the energy shift. The contribution involving two electric-dipole transitions is known to lead to the electric single-atom vdW potential [32]

$$U_e(\mathbf{r}_A)=\frac{\hbar\mu_0}{2\pi}\int_0^\infty d\xi\xi^2\,\mathrm{tr}[\boldsymbol{\alpha}_A(i\xi)\cdot\mathbf{G}^{(1)}(\mathbf{r}_A,\mathbf{r}_A,i\xi)]=\frac{\hbar\mu_0}{2\pi}\int_0^\infty d\xi\xi^2\alpha_A(i\xi)\mathrm{tr}\,\mathbf{G}^{(1)}(\mathbf{r}_A,\mathbf{r}_A,i\xi),\tag{50}$$

where $\mathbf{G}^{(1)}$ is the scattering part of the Green tensor, and

$$\boldsymbol{\alpha}_A(\omega)=\lim_{\epsilon\to 0}\frac{2}{\hbar}\sum_k\frac{\omega_A^k\mathbf{d}_A^{0k}\mathbf{d}_A^{k0}}{(\omega_A^k)^2-\omega^2-i\omega\epsilon}=\lim_{\epsilon\to 0}\frac{2}{3\hbar}\sum_k\frac{\omega_A^k|\mathbf{d}_A^{0k}|^2}{(\omega_A^k)^2-\omega^2-i\omega\epsilon}\mathbf{I}=\alpha_A(\omega)\mathbf{I}\tag{51}$$

(with $\mathbf{I}$ denoting the unit tensor) is the atomic ground-state polarizability. The second lines in Eqs. (50) and (51) are valid for isotropic atoms.

The contribution ΔE_m to ΔE which involves two magnetic-dipole transitions can be calculated by substituting the second term in Eq. (49) into Eq. (48) and using the integral relation (46), resulting in

$$\Delta E_m=\frac{\mu_0}{\pi}\sum_k\int_0^\infty\frac{d\omega}{\omega_A^k+\omega}\times[\mathbf{m}_A^{0k}\cdot\boldsymbol{\nabla}\times\mathrm{Im}\,\mathbf{G}(\mathbf{r},\mathbf{r}',\omega)\times\overleftarrow{\boldsymbol{\nabla}}'\cdot\mathbf{m}_A^{k0}]_{\mathbf{r}=\mathbf{r}'=\mathbf{r}_A}\tag{52}$$

$[(\mathbf{T}\times\overleftarrow{\boldsymbol{\nabla}})^{\mathsf{T}}=-\boldsymbol{\nabla}\times\mathbf{T}^{\mathsf{T}}]$. The relevant, position-dependent part of ΔE_m is obtained by replacing the Greens tensor with its scattering part. After writing $\mathrm{Im}\,\mathbf{G}=(\mathbf{G}-\mathbf{G}^*)/(2i)$, making use of Eq. (44), and transforming the integral along the real axis into ones along the purely imaginary axis (cf. Ref. [23]), the resulting magnetic single-atom potential reads

$$U_m(\mathbf{r}_A)=\frac{\hbar\mu_0}{2\pi}\int_0^\infty d\xi\,\mathrm{tr}[\beta_A(i\xi)\cdot\mathbf{L}^{(1)}(\mathbf{r}_A,\mathbf{r}_A,i\xi)]=\frac{\hbar\mu_0}{2\pi}\int_0^\infty d\xi\beta_A(i\xi)\mathrm{tr}\,\mathbf{L}^{(1)}(\mathbf{r}_A,\mathbf{r}_A,i\xi),\tag{53}$$

where

$$\mathbf{L}(\mathbf{r},\mathbf{r}',\omega)=\boldsymbol{\nabla}\times\mathbf{G}(\mathbf{r},\mathbf{r}',\omega)\times\overleftarrow{\boldsymbol{\nabla}}'\tag{54}$$

[note that $\mathbf{L}^{(1)}$ refers to $\mathbf{G}^{(1)}$], and

TABLE I. The intermediate states contributing to the two-atom vdW interaction according to Eq. (57) together with the energy denominators, where we have used the short-hand notations $|1_{(\mu)}\rangle=|1_{\lambda_\mu i_\mu}(\mathbf{r}_\mu,\omega_\mu)\rangle$, $|1_{(\mu)}1_{(\nu)}\rangle=|1_{\lambda_\mu i_\mu}(\mathbf{r}_\mu,\omega_\mu)1_{\lambda_\nu i_\nu}(\mathbf{r}_\nu,\omega_\nu)\rangle$.

Case	$\|\mathrm{I}\rangle$	$\|\mathrm{II}\rangle$	$\|\mathrm{III}\rangle$	Denominator
(1)	$\|k_A,0_B\rangle\|1_{(1)}\rangle$	$\|0_A,0_B\rangle\|1_{(2)}1_{(3)}\rangle$	$\|0_A,l_B\rangle\|1_{(4)}\rangle$	$D_{1a}=(\omega_A^k+\omega')(\omega'+\omega)(\omega_B^l+\omega')$, $D_{1b}=(\omega_A^k+\omega')(\omega'+\omega)(\omega_B^l+\omega)$
(2)	$\|k_A,0_B\rangle\|1_{(1)}\rangle$	$\|k_A,l_B\rangle\|\{0\}\rangle$	$\|0_A,l_B\rangle\|1_{(2)}\rangle$	$D_2=(\omega_A^k+\omega')(\omega_A^k+\omega_B^l)(\omega_B^l+\omega)$
(3)	$\|k_A,0_B\rangle\|1_{(1)}\rangle$	$\|k_A,l_B\rangle\|\{0\}\rangle$	$\|k_A,0_B\rangle\|1_{(2)}\rangle$	$D_3=(\omega_A^k+\omega')(\omega_A^k+\omega_B^l)(\omega_A^k+\omega)$
(4)	$\|k_A,0_B\rangle\|1_{(1)}\rangle$	$\|k_A,l_B\rangle\|1_{(2)}1_{(3)}\rangle$	$\|0_A,l_B\rangle\|1_{(4)}\rangle$	$D_4=(\omega_A^k+\omega')(\omega_A^k+\omega_B^l+\omega'+\omega)(\omega_B^l+\omega')$
(5)	$\|k_A,0_B\rangle\|1_{(1)}\rangle$	$\|k_A,l_B\rangle\|1_{(2)}1_{(3)}\rangle$	$\|k_A,0_B\rangle\|1_{(4)}\rangle$	$D_5=(\omega_A^k+\omega')(\omega_A^k+\omega_B^l+\omega'+\omega)(\omega_A^k+\omega)$
(6)	$\|0_A,l_B\rangle\|1_{(1)}\rangle$	$\|0_A,0_B\rangle\|1_{(2)}1_{(3)}\rangle$	$\|k_A,0_B\rangle\|1_{(4)}\rangle$	$D_{6a}=(\omega_B^l+\omega')(\omega'+\omega)(\omega_A^k+\omega')$, $D_{6b}=(\omega_B^l+\omega')(\omega'+\omega)(\omega_A^k+\omega)$
(7)	$\|0_A,l_B\rangle\|1_{(1)}\rangle$	$\|k_A,l_B\rangle\|\{0\}\rangle$	$\|k_A,0_B\rangle\|1_{(2)}\rangle$	$D_7=(\omega_B^l+\omega')(\omega_A^k+\omega_B^l)(\omega_A^k+\omega)$
(8)	$\|0_A,l_B\rangle\|1_{(1)}\rangle$	$\|k_A,l_B\rangle\|\{0\}\rangle$	$\|0_A,l_B\rangle\|1_{(2)}\rangle$	$D_8=(\omega_B^l+\omega')(\omega_A^k+\omega_B^l)(\omega_B^l+\omega)$
(9)	$\|0_A,l_B\rangle\|1_{(1)}\rangle$	$\|k_A,l_B\rangle\|1_{(2)}1_{(3)}\rangle$	$\|k_A,0_B\rangle\|1_{(4)}\rangle$	$D_9=(\omega_B^l+\omega')(\omega_A^k+\omega_B^l+\omega'+\omega)(\omega_A^k+\omega')$
(10)	$\|0_A,l_B\rangle\|1_{(1)}\rangle$	$\|k_A,l_B\rangle\|1_{(2)}1_{(3)}\rangle$	$\|0_A,l_B\rangle\|1_{(4)}\rangle$	$D_{10}=(\omega_B^l+\omega')(\omega_A^k+\omega_B^l+\omega'+\omega)(\omega_B^l+\omega)$

$$\beta_A(\omega)=\lim_{\epsilon\to 0}\frac{2}{\hbar}\sum_k\frac{\omega_A^k\mathbf{m}_A^{0k}\mathbf{m}_A^{k0}}{(\omega_A^k)^2-\omega^2-i\omega\epsilon}$$

$$=\lim_{\epsilon\to 0}\frac{2}{3\hbar}\sum_k\frac{\omega_A^k|\mathbf{m}_A^{0k}|^2}{(\omega_A^k)^2-\omega^2-i\omega\epsilon}\mathbf{I}=\beta_A(\omega)\mathbf{I} \quad (55)$$

is the atomic ground-state magnetizability. The second lines in Eqs. (53) and (55) are again valid for isotropic atoms.

We restrict our considerations to nonchiral atoms and molecules whose energy eigenstates can be chosen to be eigenstates of the parity operator. Contributions to the energy shift that contain one electric-dipole transition and one magnetic-dipole transition can then be excluded, since $\hat{\mathbf{d}}_A$ is odd and $\hat{\mathbf{m}}_A$ is even under spatial reflection. Hence, the total vdW potential of a single ground-state atom that is both polarizable and (para)magnetizable and is placed within an arbitrary environment of magnetoelectric bodies reads

$$U(\mathbf{r}_A)=U_e(\mathbf{r}_A)+U_m(\mathbf{r}_A), \quad (56)$$

with U_e and U_m being given by Eqs. (50) and (53), respectively. To our knowledge, the magnetic part of this potential has been derived for the first time in this general form.

B. Two-atom potential

We now consider two neutral ground-state atoms A and B at given positions $\mathbf{r}_A$ and $\mathbf{r}_B$ in the presence of arbitrarily shaped magnetodielectric bodies. The two-atom vdW potential follows from the fourth-order energy shift

$$\Delta E=-\sum_{\mathrm{I,II,III}\neq 0}\frac{\langle 0|\hat{H}_{AF}+\hat{H}_{BF}|\mathrm{III}\rangle\langle\mathrm{III}|\hat{H}_{AF}+\hat{H}_{BF}|\mathrm{II}\rangle}{(E_{\mathrm{III}}-E_0)}$$

$$\times\frac{\langle\mathrm{II}|\hat{H}_{AF}+\hat{H}_{BF}|\mathrm{I}\rangle\langle\mathrm{I}|\hat{H}_{AF}+\hat{H}_{BF}|0\rangle}{(E_{\mathrm{II}}-E_0)(E_{\mathrm{I}}-E_0)}, \quad (57)$$

where $|0\rangle=|0_A\rangle|0_B\rangle|\{0\}\rangle$ is the ground state of the combined atom-field system. With the interaction Hamiltonian being given by Eq. (36), the summands in Eq. (57) vanish unless the intermediate states $|\mathrm{I}\rangle$ and $|\mathrm{III}\rangle$ are such that one of the atoms and a single quantum of the fundamental fields are excited. The intermediate states $|\mathrm{II}\rangle$ correspond to one of the following three types of states: (i) both atoms are in the ground state and two field quanta are excited, (ii) both atoms are excited and no field quantum is excited, and (iii) both atoms are excited and two field quanta are excited. All the possible intermediate states together with the respective energy denominators are listed in Table I. In addition to the matrix element (49), an evaluation of Eq. (57) hence requires matrix elements of the interaction Hamiltonian (36) which involve transitions of the body-assisted field between single- and two-quantum excited states. Recalling the definitions (39) and (40) as well as the commutation relations (37) and (38), one finds

$$\langle k_A|\langle 1_{\lambda_1 i_1}(\mathbf{r}_1,\omega_1)|\hat{H}_{AF}|1_{\lambda_2 i_2}(\mathbf{r}_2,\omega_2)1_{\lambda_3 i_3}(\mathbf{r}_3,\omega_3)\rangle|0_A\rangle$$

$$=-\frac{\delta_{(13)}}{\sqrt{2}}[\mathbf{d}_A^{k0}\cdot\mathbf{G}_{\lambda_2}(\mathbf{r}_A,\mathbf{r}_2,\omega_2)]_{i_2}$$

$$-\frac{\delta_{(12)}}{\sqrt{2}}[\mathbf{d}_A^{k0}\cdot\mathbf{G}_{\lambda_3}(\mathbf{r}_A,\mathbf{r}_3,\omega_3)]_{i_3}$$

$$+\frac{i\delta_{(13)}}{\omega_2\sqrt{2}}[\mathbf{m}_A^{k0}\cdot\boldsymbol{\nabla}_A\times\mathbf{G}_{\lambda_2}(\mathbf{r}_A,\mathbf{r}_2,\omega_2)]_{i_2}$$

$$+\frac{i\delta_{(12)}}{\omega_3\sqrt{2}}[\mathbf{m}_A^{k0}\cdot\boldsymbol{\nabla}_A\times\mathbf{G}_{\lambda_3}(\mathbf{r}_A,\mathbf{r}_3,\omega_3)]_{i_3} \quad (58)$$

with $|\mathbf{1}_\lambda(\mathbf{r},\omega)\mathbf{1}_{\lambda'}(\mathbf{r}',\omega')\rangle=\frac{1}{\sqrt{2}}\hat{\mathbf{f}}_\lambda^\dagger(\mathbf{r},\omega)\hat{\mathbf{f}}_{\lambda'}^\dagger(\mathbf{r}',\omega')|\{0\}\rangle$ and

$$\delta_{(\mu\nu)}=\delta_{\lambda_\mu\lambda_\nu}\delta_{i_\mu i_\nu}(\mathbf{r}_\mu-\mathbf{r}_\nu)\delta(\omega_\mu-\omega_\nu). \quad (59)$$

The two-atom potential follows from those contributions to the energy shift (57) in which each atom undergoes exactly two transitions. As in the single-atom case, we distinguish different classes of contributions according to the elec-

tric or magnetic nature of those transitions. Those involving only electric transitions of both atoms are known to lead to the electric-electric vdW potential [16]

$$U_{ee}(\mathbf{r}_A,\mathbf{r}_B) = -\frac{\hbar\mu_0^2}{2\pi}\int_0^\infty d\xi\xi^4 \times \mathrm{tr}[\boldsymbol{\alpha}_A(i\xi)\cdot\mathbf{G}(\mathbf{r}_A,\mathbf{r}_B,i\xi)\cdot\boldsymbol{\alpha}_B(i\xi)\cdot\mathbf{G}(\mathbf{r}_B,\mathbf{r}_A,i\xi)] = -\frac{\hbar\mu_0^2}{2\pi}\int_0^\infty d\xi\xi^4\alpha_A(i\xi)\alpha_B(i\xi) \times \mathrm{tr}[\mathbf{G}(\mathbf{r}_A,\mathbf{r}_B,i\xi)\cdot\mathbf{G}(\mathbf{r}_B,\mathbf{r}_A,i\xi)] \quad (60)$$

[recall Eq. (51)], where the second equality is valid for isotropic atoms.

Next, we calculate the electric-magnetic vdW potential U_{em}, which is due to the contributions of atom A undergoing electric transitions and atom B undergoing magnetic transitions. Each of the possible intermediate-state combinations listed in Table I contributes to U_{em}, where we begin with the intermediate states of case (1). Substituting the respective matrix elements from Eqs. (49) and (58) into Eq. (57) and using the integral relation (46), we find

$$\Delta E_{em}^{(1)} = -\frac{\mu_0^2}{\hbar\pi^2}\sum_{k,l}\int_0^\infty d\omega\omega\int_0^\infty d\omega'\omega'\left(\frac{1}{D_{1a}}+\frac{1}{D_{1b}}\right) \times\{[\mathbf{d}_A^{0k}\cdot\mathrm{Im}\,\mathbf{G}(\mathbf{r}_A,\mathbf{r}_B,\omega)\times\tilde{\boldsymbol{\nabla}}_B\cdot\mathbf{m}_B^{0l}] \times[\mathbf{m}_B^{0l}\cdot\boldsymbol{\nabla}_B\times\mathrm{Im}\,\mathbf{G}(\mathbf{r}_B,\mathbf{r}_A,\omega')\cdot\mathbf{d}_A^{0k}]\}, \quad (61)$$

with the energy denominators D_{1a} and D_{1b} being given in Table I. Without loss of generality, we have assumed that the matrix elements of the electric- and magnetic-dipole operators are real-valued quantities. One can then easily find that the contributions $\Delta E_{em}^{(k)}$ ($k\in\{2,3,\ldots,10\}$) from the other possible intermediate-state combinations differ from Eq. (61) only with respect to their energy denominators and signs. Case (6) leads to two terms with different energy denominators $1/D_{6a}+1/D_{6b}$, just the same as case (1), while all other cases only give rise to a single term each. Furthermore, the contributions from cases (3)–(5) and (8)–(10) differ in sign from Eq. (61). The electric-magnetic vdW potential can be found as the sum of all contributions $U_{em}(\mathbf{r}_A,\mathbf{r}_B)=\Sigma_k\Delta E_{em}^{(k)}$. In analogy to Ref. [16] it can be seen that the denominator sum

$$\frac{1}{D_{1a}}+\frac{1}{D_{1b}}+\frac{1}{D_2}-\frac{1}{D_3}-\frac{1}{D_4}-\frac{1}{D_5} +\frac{1}{D_{6a}}+\frac{1}{D_{6b}}+\frac{1}{D_7}-\frac{1}{D_8}-\frac{1}{D_9}-\frac{1}{D_{10}} \quad (62)$$

can be replaced by

$$\frac{4(\omega_A^k+\omega_B^l+\omega)}{(\omega_A^k+\omega_B^l)(\omega_A^k+\omega)(\omega_B^l+\omega)}\left(\frac{1}{\omega+\omega'}+\frac{1}{\omega-\omega'}\right), \quad (63)$$

under the double frequency integral in Eq. (61), where we have used the definitions of the denominators in Table I and exploited the fact that the remaining integrand is symmetric with respect to an exchange of ω and ω'. This results in

$$U_{em}(\mathbf{r}_A,\mathbf{r}_B) = -\frac{4\mu_0^2}{\hbar\pi^2}\sum_{k,l}\frac{1}{\omega_A^k+\omega_B^l}\int_0^\infty d\omega\int_0^\infty d\omega' \times\frac{\omega\omega'(\omega_A^k+\omega_B^l+\omega)}{(\omega_A^k+\omega)(\omega_B^l+\omega)}\left(\frac{1}{\omega+\omega'}+\frac{1}{\omega-\omega'}\right) \times\{[\mathbf{d}_A^{0k}\cdot\mathrm{Im}\,\mathbf{G}(\mathbf{r}_A,\mathbf{r}_B,\omega)\times\tilde{\boldsymbol{\nabla}}_B\cdot\mathbf{m}_B^{0l}] \times[\mathbf{m}_B^{0l}\cdot\boldsymbol{\nabla}_B\times\mathrm{Im}\,\mathbf{G}(\mathbf{r}_B,\mathbf{r}_A,\omega')\cdot\mathbf{d}_A^{0k}]\}. \quad (64)$$

The integral over ω' can be performed by using the identity $\mathrm{Im}\,\mathbf{G}=(\mathbf{G}-\mathbf{G}^*)/(2i)$ and Eq. (44) to yield [16]

$$\int_0^\infty d\omega'\omega'\left(\frac{1}{\omega+\omega'}+\frac{1}{\omega-\omega'}\right)\mathrm{Im}\,\mathbf{G}(\mathbf{r}_B,\mathbf{r}_A,\omega') = -\frac{\pi}{2}\omega[\mathbf{G}(\mathbf{r}_B,\mathbf{r}_A,\omega)+\mathbf{G}^*(\mathbf{r}_B,\mathbf{r}_A,\omega)]. \quad (65)$$

After substituting Eq. (65) into Eq. (64) and transforming the ω integrals by means of contour-integral techniques to run along the positive imaginary axis, one obtains

$$U_{em}(\mathbf{r}_A,\mathbf{r}_B) = \frac{\hbar\mu_0^2}{2\pi}\int_0^\infty d\xi\xi^2\mathrm{tr}[\boldsymbol{\alpha}_A(i\xi)\cdot\mathbf{K}^{\mathsf{T}}(\mathbf{r}_B,\mathbf{r}_A,i\xi) \cdot\boldsymbol{\beta}_B(i\xi)\cdot\mathbf{K}(\mathbf{r}_B,\mathbf{r}_A,i\xi)] = \frac{\hbar\mu_0^2}{2\pi}\int_0^\infty d\xi\xi^2\alpha_A(i\xi)\beta_B(i\xi) \times\mathrm{tr}[\mathbf{K}^{\mathsf{T}}(\mathbf{r}_B,\mathbf{r}_A,i\xi)\cdot\mathbf{K}(\mathbf{r}_B,\mathbf{r}_A,i\xi)], \quad (66)$$

where

$$\mathbf{K}(\mathbf{r},\mathbf{r}',\omega) = \boldsymbol{\nabla}\times\mathbf{G}(\mathbf{r},\mathbf{r}',\omega), \quad (67)$$

and the second equality holds for isotropic atoms. Obviously, the magnetic-electric potential $U_{me}(\mathbf{r}_A,\mathbf{r}_B)$, which is due to all contributions of atom A undergoing magnetic transitions and atom B undergoing electric transitions, can be obtained from Eq. (66) by interchanging A and B on the right-hand side of this equation. The magnetic-magnetic potential U_{mm}, associated with magnetic transitions of both atoms, can be found in a procedure analogous to the one outlined above for deriving Eq. (66), resulting in

$$U_{mm}(\mathbf{r}_A,\mathbf{r}_B) = -\frac{\hbar\mu_0^2}{2\pi}\int_0^\infty d\xi \times\mathrm{tr}[\boldsymbol{\beta}_A(i\xi)\cdot\mathbf{L}(\mathbf{r}_A,\mathbf{r}_B,i\xi)\cdot\boldsymbol{\beta}_B(i\xi)\cdot\mathbf{L}(\mathbf{r}_B,\mathbf{r}_A,i\xi)] = -\frac{\hbar\mu_0^2}{2\pi}\int_0^\infty d\xi\beta_A(i\xi)\beta_B(i\xi) \times\mathrm{tr}[\mathbf{L}(\mathbf{r}_A,\mathbf{r}_B,i\xi)\cdot\mathbf{L}(\mathbf{r}_B,\mathbf{r}_A,i\xi)], \quad (68)$$

where the second equality again holds for isotropic atoms.

We have thus calculated all those contributions to the energy shift where both atoms undergo exactly two transitions of the same type (electric and/or magnetic). The remaining contributions of one or both atoms undergoing an electric and a magnetic transition can again be excluded from a parity argument for the nonchiral atoms under consideration in

this work (for the interaction of two chiral molecules in free space, see Ref. [33]). The total two-atom vdW potential of two polarizable and (para)magnetizable atoms placed within an arbitrary environment of magnetoelectric bodies is hence given by

$$U(\mathbf{r}_A,\mathbf{r}_B) = U_{ee}(\mathbf{r}_A,\mathbf{r}_B) + U_{em}(\mathbf{r}_A,\mathbf{r}_B) + U_{me}(\mathbf{r}_A,\mathbf{r}_B) + U_{mm}(\mathbf{r}_A,\mathbf{r}_B), \tag{69}$$

together with Eqs. (60), (66), and (68) (the diamagnetic contribution to the dispersion potential of two atoms in free space is discussed in Refs. [33–35]).

IV. LOCAL-FIELD CORRECTIONS

The single- and two-atom potentials given in Sec. III refer to atoms that are not embedded in media, i.e., $\varepsilon(\mathbf{r}_{A(B)},\omega)=\mu(\mathbf{r}_{A(B)},\omega)=1$. When considering guest atoms inside a host medium, one needs to include local-field corrections to account for the difference between the macroscopic electromagnetic field and the local field experienced by the guest atoms. A possible way to treat local-field effects is offered by the real-cavity model [18], where small spherical free-space cavities of radius R_c surrounding the atoms are introduced. As shown in Ref. [19], the local-field corrected forms of the Green tensor read, in leading order of $\omega R_c/c$,

$$\mathbf{G}_{\mathrm{loc}}(\mathbf{r}_A,\mathbf{r}_B,\omega) = \frac{3\varepsilon_A}{2\varepsilon_A+1}\mathbf{G}(\mathbf{r}_A,\mathbf{r}_B,\omega)\frac{3\varepsilon_B}{2\varepsilon_B+1}, \tag{70}$$

$$\mathbf{G}^{(1)}_{\mathrm{loc}}(\mathbf{r}_A,\mathbf{r}_A,\omega) = \frac{\omega}{2\pi c}\left\{\frac{\varepsilon_A-1}{2\varepsilon_A+1}\frac{c^3}{\omega^3R_c^3} + \frac{3}{5}\frac{\varepsilon_A^2(5\mu_A-1)-3\varepsilon_A-1}{(2\varepsilon_A+1)^2}\frac{c}{\omega R_c} + i\left[\frac{3\varepsilon_A n_A^3}{(2\varepsilon_A+1)^2}-\frac{1}{3}\right]\right\}\mathbf{I} + \left(\frac{3\varepsilon_A}{2\varepsilon_A+1}\right)^2\mathbf{G}^{(1)}(\mathbf{r}_A,\mathbf{r}_A,\omega), \tag{71}$$

where $\varepsilon_{A(B)}=\varepsilon(\mathbf{r}_{A(B)},\omega)$ and $\mu_{A(B)}=\mu(\mathbf{r}_{A(B)},\omega)$, respectively, are the permittivity and permeability of the unperturbed host medium at the position of the guest atom $A(B)$ ($n_{A(B)}=\sqrt{\varepsilon_{A(B)}\mu_{A(B)}}$) and $\mathbf{G}$ is the uncorrected Green tensor. Inserting the corrected Green tensor into Eqs. (50) and (60), one obtains the local-field corrected electric contributions to the single- and two-atom vdW potentials [20]

$$U_e(\mathbf{r}_A) = \frac{\hbar\mu_0}{2\pi}\int_0^\infty d\xi\xi^2\left[\frac{3\varepsilon_A(i\xi)}{2\varepsilon_A(i\xi)+1}\right]^2 \times \mathrm{tr}[\boldsymbol{\alpha}_A(i\xi)\cdot\mathbf{G}^{(1)}(\mathbf{r}_A,\mathbf{r}_A,i\xi)] \tag{72}$$

[we have discarded the position-independent first term on the right-hand side of Eq. (71)] and

$$U_{ee}(\mathbf{r}_A,\mathbf{r}_B) = -\frac{\hbar\mu_0^2}{2\pi}\int_0^\infty d\xi\xi^4 \times\left[\frac{3\varepsilon_A(i\xi)}{2\varepsilon_A(i\xi)+1}\right]^2\left[\frac{3\varepsilon_B(i\xi)}{2\varepsilon_B(i\xi)+1}\right]^2 \times \mathrm{tr}[\boldsymbol{\alpha}_A(i\xi)\cdot\mathbf{G}(\mathbf{r}_A,\mathbf{r}_B,i\xi)\cdot\boldsymbol{\alpha}_B(i\xi)\cdot\mathbf{G}(\mathbf{r}_B,\mathbf{r}_A,i\xi)]. \tag{73}$$

For magnetic atoms the vdW potentials depend on spatial derivatives of the Green tensor. Hence, the respective local-field corrected tensors cannot be derived directly from Eqs. (70) and (71) because the correction procedure does not commute with these derivatives. As shown in Appendix A, the required local-field corrected forms of the tensors $\mathbf{L}$ [Eq. (54)] and $\mathbf{K}$ [Eq. (67)] within leading order of $\omega R_c/c$ are given by

$$\mathbf{L}^{(1)}_{\mathrm{loc}}(\mathbf{r}_A,\mathbf{r}_A,\omega) = -\frac{\omega^3}{2\pi c^3}\left\{\frac{\mu_A-1}{2\mu_A+1}\frac{c^3}{\omega^3R_c^3} + \frac{3}{5}\frac{\mu_A^2(5\varepsilon_A-1)-3\mu_A-1}{(2\mu_A+1)^2}\frac{c}{\omega R_c} + i\left[\frac{3\mu_A n_A^3}{(2\mu_A+1)^2}-\frac{1}{3}\right]\right\}\mathbf{I} + \left(\frac{3}{2\mu_A+1}\right)^2\mathbf{L}^{(1)}(\mathbf{r}_A,\mathbf{r}_A,\omega), \tag{74}$$

$$\mathbf{L}_{\mathrm{loc}}(\mathbf{r}_A,\mathbf{r}_B,\omega) = \frac{3}{2\mu_A+1}\mathbf{L}(\mathbf{r}_A,\mathbf{r}_B,\omega)\frac{3}{2\mu_B+1}, \tag{75}$$

and

$$\mathbf{K}_{\mathrm{loc}}(\mathbf{r}_A,\mathbf{r}_B,\omega) = \frac{3}{2\mu_A+1}\mathbf{K}(\mathbf{r}_A,\mathbf{r}_B,\omega)\frac{3\varepsilon_B}{2\varepsilon_B+1}. \tag{76}$$

Replacing in Eq. (53) $\mathbf{L}^{(1)}$ with $\mathbf{L}^{(1)}_{\mathrm{loc}}$ from Eq. (74), we obtain the local-field corrected magnetic single-atom potential

$$U_m(\mathbf{r}_A) = \frac{\hbar\mu_0}{2\pi}\int_0^\infty d\xi\left[\frac{3}{2\mu_A(i\xi)+1}\right]^2 \times\mathrm{tr}[\boldsymbol{\beta}_A(i\xi)\cdot\mathbf{L}^{(1)}(\mathbf{r}_A,\mathbf{r}_A,i\xi)], \tag{77}$$

where a position-independent term has been discarded, as in the electric case. To obtain the local-field corrected contributions U_{em} and U_{mm} to the two-atom vdW potential, we replace $\mathbf{K}$ and $\mathbf{L}$ with $\mathbf{K}_{\mathrm{loc}}$ and $\mathbf{L}_{\mathrm{loc}}$ in Eqs. (66) and (68), respectively, leading to

$$U_{em}(\mathbf{r}_A,\mathbf{r}_B)=\frac{\hbar\mu_0^2}{2\pi}\int_0^\infty d\xi\xi^2\left[\frac{3\varepsilon_A(i\xi)}{2\varepsilon_A(i\xi)+1}\right]^2\left[\frac{3}{2\mu_B(i\xi)+1}\right]^2\mathrm{tr}[\boldsymbol{\alpha}_A(i\xi)\cdot\mathbf{K}^{\mathsf{T}}(\mathbf{r}_B,\mathbf{r}_A,i\xi)\cdot\boldsymbol{\beta}_B(i\xi)\cdot\mathbf{K}(\mathbf{r}_B,\mathbf{r}_A,i\xi)] \tag{78}$$

and

$$U_{mm}(\mathbf{r}_A,\mathbf{r}_B)=-\frac{\hbar\mu_0^2}{2\pi}\int_0^\infty d\xi\left[\frac{3}{2\mu_A(i\xi)+1}\right]^2\left[\frac{3}{2\mu_B(i\xi)+1}\right]^2\mathrm{tr}[\boldsymbol{\beta}_A(i\xi)\cdot\mathbf{L}(\mathbf{r}_A,\mathbf{r}_B,i\xi)\cdot\boldsymbol{\beta}_B(i\xi)\cdot\mathbf{L}(\mathbf{r}_B,\mathbf{r}_A,i\xi)]. \tag{79}$$

Recall that $U_{me}(\mathbf{r}_A,\mathbf{r}_B)$ can be obtained from Eq. (78) by interchanging A and B on the right-hand side of this equation. Needless to say that Eqs. (72), (73), and (77)–(79) reduce to Eqs. (50), (60), (53), (66), and (68), respectively, when the atoms are situated in free space so that $\varepsilon_{A(B)}=\mu_{A(B)}=1$.

V. EXAMPLES

We now apply the theory to some illustrative examples and compare the results with the familiar results for nonmagnetic atoms, with special emphasis on whether the total potentials for electromagnetic atoms are invariant under a global duality transformation $\varepsilon\leftrightarrow\mu$, $c^2\alpha\leftrightarrow\beta$ [36]. It will turn out that atoms situated in free space do respect this symmetry for the examples studied, while atoms embedded in media only do when the local-field corrections are taken into account.

A. Single-atom potential: Half space

First, we consider an isotropic atom A at a distance z_A away from a magnetoelectric half space of permittivity $\varepsilon(\omega)$ and permeability $\mu(\omega)$ and choose the coordinate system such that the z axis is perpendicular to the half space that occupies the region $z\leqslant 0$. Assuming that $\mathbf{r}$ and $\mathbf{r}'$ refer to two points in the free-space region $z>0$, we have [37]

$$\mathbf{G}^{(1)}(\mathbf{r},\mathbf{r}',\omega)=\int d^2q\frac{e^{i(\mathbf{w}_+\cdot\mathbf{r}-\mathbf{w}_-\cdot\mathbf{r}')}}{8\pi^2 b}\times\left[\frac{\mu(\omega)b-b_0}{\mu(\omega)b+b_0}\mathbf{e}_s\mathbf{e}_s+\frac{\varepsilon(\omega)b-b_0}{\varepsilon(\omega)b+b_0}\mathbf{e}_p^+\mathbf{e}_p^-\right] \tag{80}$$

$[\mathbf{w}_\pm=\mathbf{q}\pm ib\mathbf{e}_z,\mathbf{q}\perp\mathbf{e}_z]$, where

$$b=\sqrt{q^2-\frac{\omega^2}{c^2}},\quad b_0=\sqrt{q^2-n^2(\omega)\frac{\omega^2}{c^2}} \tag{81}$$

$[q=|\mathbf{q}|, n(\omega)=\sqrt{\varepsilon(\omega)\mu(\omega)}$, Re b, Re $b_0>0]$, and the polarization vectors $\mathbf{e}_s$ and $\mathbf{e}_p$ are defined by $(\mathbf{e}_q=\mathbf{q}/q)$

$$\mathbf{e}_s=\mathbf{e}_q\times\mathbf{e}_z,\quad \mathbf{e}_p^\pm=\frac{c}{\omega}(q\mathbf{e}_z\mp ib\mathbf{e}_q). \tag{82}$$

As shown in Ref. [37], substitution of $\mathbf{G}^{(1)}$ from Eq. (80) into Eq. (50) yields for the electric part U_e of the single-atom vdW potential

$$U_e(\mathbf{r}_A)=\frac{\hbar\mu_0^2}{8\pi^2}\int_0^\infty d\xi\xi^2\alpha_A(i\xi)\int_0^\infty dq\frac{q}{b}e^{-2bz_A}\times\left[\frac{\mu(i\xi)b-b_0}{\mu(i\xi)b+b_0}-\frac{\varepsilon(i\xi)b-b_0}{\varepsilon(i\xi)b+b_0}\left(1+2q^2\frac{c^2}{\xi^2}\right)\right]. \tag{83}$$

In the nonretarded limit of the atom-surface separation being small with respect to the characteristic atomic and medium wavelengths, Eq. (83) simplifies to

$$U_e(z_A)=-\frac{\hbar}{16\pi^2\varepsilon_0 z_A^3}\int_0^\infty d\xi\alpha_A(i\xi)\frac{\varepsilon(i\xi)-1}{\varepsilon(i\xi)+1}+\frac{\mu_0\hbar}{16\pi^2 z_A}\int_0^\infty d\xi\xi^2\alpha_A(i\xi)\left\{\frac{\varepsilon(i\xi)-1}{\varepsilon(i\xi)+1}+\frac{\mu(i\xi)-1}{\mu(i\xi)+1}+\frac{2\varepsilon(i\xi)[n^2(i\xi)-1]}{[\varepsilon(i\xi)+1]^2}\right\}. \tag{84}$$

In contrast, in the retarded limit of large atom-surface separation one finds that

$$U_e(z_A)=-\frac{3\hbar c\alpha_A(0)}{64\pi^2\varepsilon_0 z_A^4}\int_1^\infty dv\left[\left(\frac{2}{v^2}-\frac{1}{v^4}\right)\times\frac{\varepsilon(0)v-\sqrt{n^2(0)-1+v^2}}{\varepsilon(0)v+\sqrt{n^2(0)-1+v^2}}-\frac{1}{v^4}\frac{\mu(0)v-\sqrt{n^2(0)-1+v^2}}{\mu(0)v+\sqrt{n^2(0)-1+v^2}}\right]. \tag{85}$$

To calculate the magnetic part U_m of the single-atom vdW potential, we first combine Eqs. (80) and (54) to

$$\mathbf{L}^{(1)}(\mathbf{r},\mathbf{r}',\omega)=-\frac{\omega^2}{c^2}\int d^2q\frac{e^{i(\mathbf{w}_+\cdot\mathbf{r}-\mathbf{w}_-\cdot\mathbf{r}')}}{8\pi^2 b}\times\left[\frac{\varepsilon(\omega)b-b_0}{\varepsilon(\omega)b+b_0}\mathbf{e}_s\mathbf{e}_s+\frac{\mu(\omega)b-b_0}{\mu(\omega)b+b_0}\mathbf{e}_p^+\mathbf{e}_p^-\right]. \tag{86}$$

Comparing Eqs. (53) [together with Eq. (86)] and (50) [together with Eq. (80)], we see that the magnetic part U_m can be found from the electric part U_e in Eq. (83) by replacing α_A and ε, with β_A/c^2 and μ, respectively, in agreement with the duality principle [36]. Needless to say that this symmetry also holds for the retarded and nonretarded limits.

B. Two-atom potential: Bulk medium

As a second example, we consider two isotropic atoms A and B embedded in an infinitely extended bulk medium of permittivity $\varepsilon(\omega)$ and permeability $\mu(\omega)$. To illustrate the relevance of the local-field corrections, let us first consider the uncorrected two-atom potential. By using the bulk-material tensors as given in Eqs. (A3) and (A7), and calculating

$$\mathbf{K}_{\text{bulk}}^{\mathsf{T}}(\mathbf{r}_B,\mathbf{r}_A,\omega) = -\mathbf{K}_{\text{bulk}}(\mathbf{r}_B,\mathbf{r}_A,\omega) = \frac{\mu(\omega)e^{ikl}}{4\pi l^2}(1-ikl)\mathbf{e}_l\times\mathbf{I} \tag{87}$$

($\mathbf{l}=\mathbf{r}_B-\mathbf{r}_A$, $l=|\mathbf{l}|$, $\mathbf{e}_l=\mathbf{l}/l$), which follows from Eq. (67) together with Eq. (A3), the potentials (60), (66), and (68) take the form

$$U_{ee}(\mathbf{r}_A,\mathbf{r}_B) = -\frac{\hbar}{16\pi^3\varepsilon_0^2 l^6}\int_0^\infty d\xi\alpha_A(i\xi)\alpha_B(i\xi)\frac{g[n(i\xi)\xi l/c]}{\varepsilon^2(i\xi)}, \tag{88}$$

$$U_{em}(\mathbf{r}_A,\mathbf{r}_B) = \frac{\hbar\mu_0^2}{16\pi^3 l^4}\int_0^\infty d\xi\xi^2\alpha_A(i\xi)\beta_B(i\xi) \times \mu^2(i\xi)h[n(i\xi)\xi l/c], \tag{89}$$

and

$$U_{mm}(\mathbf{r}_A,\mathbf{r}_B) = -\frac{\hbar\mu_0^2}{16\pi^3 l^6}\int_0^\infty d\xi\beta_A(i\xi)\beta_B(i\xi) \times \mu^2(i\xi)g[n(i\xi)\xi l/c], \tag{90}$$

where

$$g(x) = e^{-2x}(3+6x+5x^2+2x^3+x^4), \tag{91}$$

$$h(x) = e^{-2x}(1+2x+x^2). \tag{92}$$

We see that due to the factors $\varepsilon^{-2}(i\xi)$ and $\mu^2(i\xi)$, the uncorrected quantities U_{ee} and U_{mm} do not transform into one another under the duality transformation $\varepsilon\leftrightarrow\mu$, $c^2\alpha\leftrightarrow\beta$. The same is true for the pair U_{em} and U_{me}. As a consequence, the uncorrected total two-atom potential (69) violates duality symmetry.

By contrast, the local-field corrected two-atom potential does obey the duality symmetry. From Eqs. (73), (78), and (79) [together with Eqs. (A3), (87), and (A7)] we find that

$$U_{ee}(\mathbf{r}_A,\mathbf{r}_B) = -\frac{\hbar}{16\pi^3\varepsilon_0^2 l^6}\int_0^\infty d\xi\alpha_A(i\xi)\alpha_B(i\xi) \times \frac{81\varepsilon^2(i\xi)}{[2\varepsilon(i\xi)+1]^4}g[n(i\xi)\xi l/c], \tag{93}$$

$$U_{em}(\mathbf{r}_A,\mathbf{r}_B) = \frac{\hbar\mu_0^2}{16\pi^3 l^4}\int_0^\infty d\xi\xi^2\alpha_A(i\xi)\beta_B(i\xi) \times \frac{81\varepsilon^2(i\xi)\mu^2(i\xi)}{[2\varepsilon(i\xi)+1]^2[2\mu(i\xi)+1]^2}h[n(i\xi)\xi l/c], \tag{94}$$

and

$$U_{mm}(\mathbf{r}_A,\mathbf{r}_B) = -\frac{\hbar\mu_0^2}{16\pi^3 l^6}\int_0^\infty d\xi\beta_A(i\xi)\beta_B(i\xi) \times \frac{81\mu^2(i\xi)}{[2\mu(i\xi)+1]^4}g[n(i\xi)\xi l/c]. \tag{95}$$

Inspection of Eqs. (93)–(95) then reveals that the duality transformation $\varepsilon\leftrightarrow\mu$, $c^2\alpha\leftrightarrow\beta$ results in

$$U_{ee}(\mathbf{r}_A,\mathbf{r}_B) \leftrightarrow U_{mm}(\mathbf{r}_A,\mathbf{r}_B), \tag{96}$$

$$U_{em}(\mathbf{r}_A,\mathbf{r}_B) \leftrightarrow U_{me}(\mathbf{r}_A,\mathbf{r}_B), \tag{97}$$

so the total vdW potential (69) is invariant under the duality transformation. The result clearly shows that (i) the inclusion of local-field effects is essential for obtaining duality-consistent results and that (ii) the real-cavity model is an appropriate tool for achieving this goal.

It is instructive to inspect the nonretarded and retarded limits of Eqs. (93)–(95). In the nonretarded limit where the atom-atom separation is small in comparison to the characteristic atomic and medium wavelengths, the approximations $g[n(i\xi)\xi l/c]\simeq g(0)$ and $h[n(i\xi)\xi l/c]\simeq h(0)$ result in

$$U_{ee}(\mathbf{r}_A,\mathbf{r}_B) = \frac{-3\hbar}{16\pi^3\varepsilon_0^2 l^6}\int_0^\infty d\xi\alpha_A(i\xi)\alpha_B(i\xi)\frac{81\varepsilon^2(i\xi)}{[2\varepsilon(i\xi)+1]^4}, \tag{98}$$

$$U_{em}(\mathbf{r}_A,\mathbf{r}_B) = \frac{\hbar\mu_0^2}{16\pi^3 l^4}\int_0^\infty d\xi\xi^2\alpha_A(i\xi)\beta_B(i\xi) \times \frac{81\varepsilon^2(i\xi)\mu^2(i\xi)}{[2\varepsilon(i\xi)+1]^2[2\mu(i\xi)+1]^2}, \tag{99}$$

$$U_{mm}(\mathbf{r}_A,\mathbf{r}_B) = \frac{-3\hbar\mu_0^2}{16\pi^3 l^6}\int_0^\infty d\xi\beta_A(i\xi)\beta_B(i\xi)\frac{81\mu^2(i\xi)}{[2\mu(i\xi)+1]^4}. \tag{100}$$

In the retarded limit, the quantities α, β, ε, and μ can be replaced by their static values, leading to

$$U_{ee}(\mathbf{r}_A,\mathbf{r}_B) = -\frac{23\hbar c\alpha_A(0)\alpha_B(0)}{64\pi^3\varepsilon_0^2 l^7}\frac{81\varepsilon^2(0)}{n(0)[2\varepsilon(0)+1]^4}, \tag{101}$$

$$U_{em}(\mathbf{r}_A,\mathbf{r}_B) = \frac{7\hbar c\mu_0\alpha_A(0)\beta_B(0)}{64\pi^3\varepsilon_0 l^7}\frac{81n(0)}{[2\varepsilon(0)+1]^2[2\mu(0)+1]^2}, \tag{102}$$

$$U_{mm}(\mathbf{r}_A,\mathbf{r}_B) = -\frac{23\hbar c\mu_0^2\beta_A(0)\beta_B(0)}{64\pi^3 l^7}\frac{81\mu^2(0)}{n(0)[2\mu(0)+1]^4}. \tag{103}$$

Compared with two atoms in free space, one notices that the medium modifies the magnitudes of the interatomic potentials but does not change their signs. Inspection of Eqs. (93) and (95) reveals that the medium always leads to a reduction of U_{ee} and U_{mm}. In the nonretarded limit, U_{ee} is only influenced by the electric properties of the medium and U_{mm} only by the magnetic ones [cf. Eqs. (98) and (100)]. In contrast, U_{em} and U_{me} are diminished by the medium in the retarded limit, Eq. (102), but are enhanced by a factor of up to 81/16 in the nonretarded limit [cf. Eq. (99)].

In the retarded limit, the influence of the medium on all four types of potentials is very similar. The coupling of each atom to the field is screened by a factor $9\varepsilon(0)/[2\varepsilon(0)+1]^2$ for polarizable atoms, and a factor $9\mu(0)/[2\mu(0)+1]^2$ for magnetizable atoms. In addition, the reduced speed of light in the medium leads to a further reduction of the potential by a factor $n(0)$.

It should be pointed out that the uncorrected potentials U_{em} and U_{mm} as given by Eqs. (89) and (90) differ from the corresponding results given in Ref. [21] by factors of μ^{-4} and μ^{-2}, respectively. The discrepancy is due to the different atom-field couplings employed: While our calculation is based on a magnetic coupling of the form $\mathbf{m}\cdot\hat{\mathbf{B}}$, an $\mathbf{m}\cdot\hat{\mathbf{H}}$ coupling is used in Ref. [21]. The potentials derived therein thus do not follow from a Hamiltonian that is demonstrably consistent with the Maxwell equations and generates the correct equations of motion for the charged particles inside the atoms, whereas both of these requirements have been verified for the Hamiltonian (27) together with (28), (29), and (36) employed in this work. Furthermore, in spite of the use of an $\mathbf{m}\cdot\hat{\mathbf{H}}$ coupling, the contribution due to the noise magnetization contained in $\hat{\mathbf{H}}$ (cf. Refs. [23,24]) was not discussed. The discrepancy would not have been noticeable if local-field corrections had been taken into account in Ref. [21]: When applying local-field corrections to the potentials stated therein, one recovers our local-field corrected Eqs. (94) and (95) since the appropriate magnetic local-field correction factors are $3\mu(i\xi)/[2\mu(i\xi)+1]$ in that case, as opposed to the factors $3/[2\mu(i\xi)+1]$ arising in our calculation.

C. Two-atom potential: Sphere

Finally, let us consider two isotropic atoms A and B in the presence of a homogeneous sphere of radius R, permittivity $\varepsilon(\omega)$, and permeability $\mu(\omega)$. According to the decomposition of the Green tensor into a free-space part and a scattering part, each contribution to the two-atom vdW potential $U(\mathbf{r}_A,\mathbf{r}_B)$, Eq. (69), can be decomposed into three parts labeled by the superscripts (0), (1), and (2), respectively, denoting the contribution from the free-space part of the Green tensor, the cross term of the free-space part and the scattering part of the Green tensor, and the scattering part of the Green tensor,

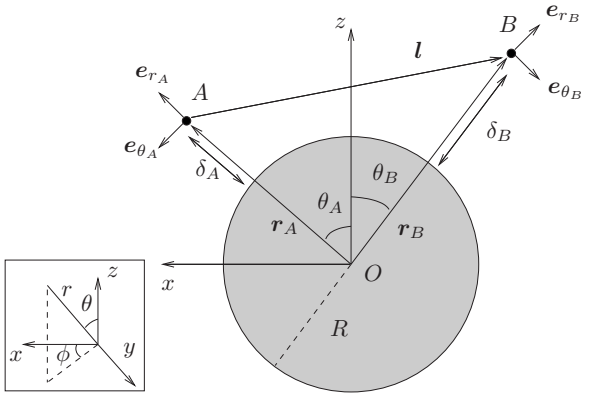

FIG. 1. Two atoms A and B in the presence of a sphere ($\theta_A+\theta_B=\Theta$).

$$U(\mathbf{r}_A,\mathbf{r}_B) = U^{(0)}(\mathbf{r}_A,\mathbf{r}_B) + U^{(1)}(\mathbf{r}_A,\mathbf{r}_B) + U^{(2)}(\mathbf{r}_A,\mathbf{r}_B). \tag{104}$$

The potential contributions arising from the free-space part of the Green tensor can be found from Eqs. (93)–(95) by setting $\varepsilon=\mu=1$. In the body-induced part of the interaction potential

$$U^b(\mathbf{r}_A,\mathbf{r}_B) = U^{(1)}(\mathbf{r}_A,\mathbf{r}_B) + U^{(2)}(\mathbf{r}_A,\mathbf{r}_B), \tag{105}$$

which arises from the scattering part of the Green tensor, the contributions $U_{ee}^{(1)}$ and $U_{ee}^{(2)}$ to U^b can be taken from Ref. [38], and the contributions $U_{mm}^{(1)}$ and $U_{mm}^{(2)}$ to U^b can then be obtained from $U_{ee}^{(1)}$ and $U_{ee}^{(2)}$ by the transformation $\alpha\to\beta/c^2$, $\varepsilon\leftrightarrow\mu$, as sketched in Appendix B. We may therefore focus on the calculation of the body-induced mixed contributions

$$U_{em}^{(1)}(\mathbf{r}_A,\mathbf{r}_B) = \frac{\hbar\mu_0^2}{\pi}\int_0^\infty d\xi\xi^2\alpha_A(i\xi)\beta_B(i\xi) \times \mathrm{tr}[\mathbf{K}^{(0)\mathsf{T}}(\mathbf{r}_B,\mathbf{r}_A,i\xi)\cdot\mathbf{K}^{(1)}(\mathbf{r}_B,\mathbf{r}_A,i\xi)], \tag{106}$$

$$U_{em}^{(2)}(\mathbf{r}_A,\mathbf{r}_B) = \frac{\hbar\mu_0^2}{2\pi}\int_0^\infty d\xi\xi^2\alpha_A(i\xi)\beta_B(i\xi) \times \mathrm{tr}[\mathbf{K}^{(1)\mathsf{T}}(\mathbf{r}_B,\mathbf{r}_A,i\xi)\cdot\mathbf{K}^{(1)}(\mathbf{r}_B,\mathbf{r}_A,i\xi)]. \tag{107}$$

For this purpose, we choose the coordinate system such that its origin coincides with the center of the sphere (Fig. 1). The scattering part of the tensor $\mathbf{K}(\mathbf{r}_B,\mathbf{r}_A,\omega)$ can be given in the form (Appendix B)

$$\mathbf{K}^{(1)}(\mathbf{r}_B,\mathbf{r}_A,\omega)=\frac{ik_0}{4\pi r_A r_B}\sum_{n=1}^{\infty}(2n+1)\Bigg\{r_A B_n^M Q_n P_n'(\gamma)\sin\Theta\mathbf{e}_{r_B}\mathbf{e}_{\phi_A}+\frac{1}{n(n+1)}[r_A B_n^M Q_n^B F_n(\gamma)-r_B B_n^N Q_n^A P_n'(\gamma)]\mathbf{e}_{\theta_B}\mathbf{e}_{\phi_A}$$
$$+r_B B_n^N Q_n P_n'(\gamma)\sin\Theta\mathbf{e}_{\phi_B}\mathbf{e}_{r_A}+\frac{1}{n(n+1)}[r_B B_n^N Q_n^A F_n(\gamma)-r_A B_n^M Q_n^B P_n'(\gamma)]\mathbf{e}_{\phi_B}\mathbf{e}_{\theta_A}\Bigg\} \tag{108}$$

[$k_0=\omega/c$; $r_{A(B)}=|\mathbf{r}_{A(B)}|$; $\gamma=\cos\Theta$; $\Theta=\theta_A+\theta_B$, angular separation between the two atoms with respect to the origin of the coordinate system], where

$$B_n^M(\omega)=-\frac{\mu(\omega)[y_0 j_n(y_0)]' j_n(y)-[y j_n(y)]' j_n(y_0)}{\mu(\omega)[y_0 h_n^{(1)}(y_0)]' j_n(y)-[y j_n(y)]' h_n^{(1)}(y_0)}, \tag{109}$$

$$B_n^N(\omega)=-\frac{\varepsilon(\omega)[y_0 j_n(y_0)]' j_n(y)-[y j_n(y)]' j_n(y_0)}{\varepsilon(\omega)[y_0 h_n^{(1)}(y_0)]' j_n(y)-[y j_n(y)]' h_n^{(1)}(y_0)}, \tag{110}$$

$$Q_n=h_n^{(1)}(k_0 r_A)h_n^{(1)}(k_0 r_B), \tag{111}$$

$$Q_n^A=h_n^{(1)}(k_0 r_B)[z h_n^{(1)}(z)]'_{z=k_0 r_A}, \tag{112}$$

$$Q_n^B=h_n^{(1)}(k_0 r_A)[z h_n^{(1)}(z)]'_{z=k_0 r_B}, \tag{113}$$

$$F_n(x)=n(n+1)P_n(x)-xP_n'(x) \tag{114}$$

[$P_n(x)$, Legendre polynomial; $y_0=k_0 R$; $y=n(\omega)y_0$]. Further, $\mathbf{e}_r$, $\mathbf{e}_\theta$, and $\mathbf{e}_\phi$ are the mutually orthogonal unit vectors pointing in the directions of radial distance r, polar angle θ, and azimuthal angle ϕ, respectively (Fig. 1). In order to facilitate further evaluations, it is convenient to represent the free-space part $\mathbf{K}^{(0)}$, which can be obtained from Eq. (87) for $\mu=1$ and $k=k_0$, in the same spherical coordinate system as the scattering part,

$$\mathbf{K}^{(0)}(\mathbf{r}_B,\mathbf{r}_A,iu)=\frac{1}{4\pi l^3}e^{ik_0 l}(1-ik_0 l)(r_A\sin\Theta\mathbf{e}_{r_B}\mathbf{e}_{\phi_A}+l_B\mathbf{e}_{\theta_B}\mathbf{e}_{\phi_A}+r_B\sin\Theta\mathbf{e}_{\phi_B}\mathbf{e}_{r_A}+l_A\mathbf{e}_{\phi_B}\mathbf{e}_{\theta_A}), \tag{115}$$

where $l_A(l_B)$ is the component of $\mathbf{l}$ in the direction of $\mathbf{r}_A(-\mathbf{r}_B)$,

$$l_A=r_B\cos\Theta-r_A,\quad l_B=r_A\cos\Theta-r_B. \tag{116}$$

Using Eqs. (108) and (115) in Eqs. (106) and (107), we derive

$$U_{em}^{(1)}(\mathbf{r}_A,\mathbf{r}_B)=-\frac{\hbar\mu_0^2}{16\pi^3 c l^3 r_A r_B}\sum_{n=1}^{\infty}\frac{(2n+1)}{n(n+1)}\int_0^\infty d\xi\xi^3\alpha_A(i\xi)\beta_B(i\xi)e^{-l\xi/c}\left(1+\frac{l\xi}{c}\right)\{n(n+1)\sin^2\Theta[r_A^2 B_n^M(i\xi)+r_B^2 B_n^N(i\xi)]Q_n P_n'(\gamma)$$
$$+r_A B_n^M(i\xi)Q_n^B[l_B F_n(\gamma)-l_A P_n'(\gamma)]+r_B B_n^N(i\xi)Q_n^A[l_A F_n(\gamma)-l_B P_n'(\gamma)]\}, \tag{117}$$

$$U_{em}^{(2)}(\mathbf{r}_A,\mathbf{r}_B)=\frac{\hbar\mu_0^2}{32\pi^3 c^2 r_A^2 r_B^2}\sum_{n,n'=1}^{\infty}\frac{(2n'+1)(2n+1)}{n'(n'+1)n(n+1)}\int_0^\infty d\xi\xi^4\alpha_A(i\xi)\beta_B(i\xi)\{n'(n'+1)n(n+1)Q_{n'}Q_n\sin^2\Theta$$
$$\times P_{n'}'(\gamma)P_n'(\gamma)[r_A^2 B_{n'}^M(i\xi)B_n^M(i\xi)+r_B^2 B_{n'}^N(i\xi)B_n^N(i\xi)]+[r_B^2 B_{n'}^N(i\xi)B_n^N(i\xi)Q_{n'}^A Q_n^A+r_A^2 B_{n'}^M(i\xi)B_n^M(i\xi)Q_{n'}^B Q_n^B]$$
$$\times[F_{n'}(\gamma)F_n(\gamma)+P_{n'}'(\gamma)P_n'(\gamma)]-2r_A r_B B_{n'}^M(i\xi)B_n^N(i\xi)Q_{n'}^B Q_n^A[P_{n'}'(\gamma)F_n(\gamma)+P_n'(\gamma)F_{n'}(\gamma)]\}. \tag{118}$$

As before, $U_{me}^{(1)}(\mathbf{r}_A,\mathbf{r}_B)$ and $U_{me}^{(2)}(\mathbf{r}_A,\mathbf{r}_B)$ can be obtained from Eqs. (117) and (118) by interchanging A and B. Inspection of Eqs. (117) and (118) reveals that this is equivalent to the interchanging $\alpha\leftrightarrow\beta/c^2$ and $\varepsilon\leftrightarrow\mu$, which shows that the combination $U_{em}(\mathbf{r}_A,\mathbf{r}_B)+U_{me}(\mathbf{r}_A,\mathbf{r}_B)$ is invariant under the duality transformation. Recalling that $Uee(\mathbf{r}A,\mathbf{r}B)+Umm(\mathbf{r}A,\mathbf{r}B)$ also obeys the duality symmetry, the total potential $U(\mathbf{r}_A,\mathbf{r}_B)$ is duality invariant.

Further analytical evaluation of the body-induced part of the potential is possible in the limiting cases of large and small spheres. In the case of a large sphere,

$$\delta_{A'} \equiv r_{A'} - R \ll R \quad (A' = A,B), \tag{119}$$

$$l \ll R \Rightarrow \Theta \ll 1 \tag{120}$$

[where the second condition in Eq. (120) follows from the first one by virtue of $2R\sin(\Theta/2) \leqslant l$, cf. Fig. 1], we derive (Appendix C)

$$\begin{aligned} U^b_{em}(\mathbf{r}_A,\mathbf{r}_B) = {} & \frac{\hbar\mu_0^2}{32\pi^3 l^3 l_+^4 (l_+ + \delta_+)^2}\{2l_+(l_+ + \delta_+)^2 \\ & \times[(X^2 - \delta_-\delta_+)J_{10} + (X^2 + \delta_-\delta_+)J_{01}] \\ & + l^3(2l_+^2 + X^2)(J_{20} + J_{02}) + 4l^3(X^2 - l_+\delta_+)J_{11}\}, \end{aligned} \tag{121}$$

where $X = R\Theta$, $\delta_\pm = \delta_B \pm \delta_A$, $l_+ = \sqrt{X^2 + \delta_+^2}$, and

$$J_{kl} = \int_0^\infty d\xi \xi^2 \alpha_A(i\xi)\beta_B(i\xi)\left[\frac{\varepsilon(i\xi)-1}{\varepsilon(i\xi)+1}\right]^k\left[\frac{\mu(i\xi)-1}{\mu(i\xi)+1}\right]^l. \tag{122}$$

In the case of a small sphere, $R \ll r_{A'}$ $(A' = A,B)$, the main contribution to the frequency integrals in Eqs. (117) and (118) comes from the region where $\xi \ll c/R$, so that U^b_{em} can be approximated by the term $n=1$ in Eq. (117) (cf. Ref. [38]), leading to

$$\begin{aligned} U^b_{em}(\mathbf{r}_A,\mathbf{r}_B) = {} & \frac{\hbar\mu_0^3 c^2}{64\pi^4 l^3 r_A^3 r_B^3}\int_0^\infty d\xi \xi^2 \alpha_A(i\xi)\beta_B(i\xi)e^{-(r_A+r_B+l)\xi/c} \\ & \times(1 + l\xi/c)\Big\{[2r_B(1 + r_A\xi/c)\sin^2\Theta \\ & + (l_B - l_A\cos\Theta)a(r_A\xi/c)](1 + r_B\xi/c)r_B\alpha_{\mathrm{sp}}(i\xi) \\ & + [2r_A(1 + r_B\xi/c)\sin^2\Theta + (l_A - l_B\cos\Theta) \\ & \times a(r_B\xi/c)](1 + r_A\xi/c)r_A\frac{\beta_{\mathrm{sp}}(i\xi)}{c^2}\Big\}, \end{aligned} \tag{123}$$

where

$$\alpha_{\mathrm{sp}}(\omega) = 4\pi\varepsilon_0 R^3\frac{\varepsilon(\omega)-1}{\varepsilon(\omega)+2}, \tag{124}$$

$$\beta_{\mathrm{sp}}(\omega) = \frac{4\pi}{\mu_0}R^3\frac{\mu(\omega)-1}{\mu(\omega)+2}, \tag{125}$$

and

$$a(x) = 1 + x + x^2. \tag{126}$$

It is worth mentioning that the nonadditive interaction potential of three atoms [polarizable atom A, magnetizable atom B, and a third atom C of polarizability $\alpha_C(\omega)$ and magnetizability $\beta_C(\omega)$] in free space may be obtained from Eq. (123) by replacing $\alpha_{\mathrm{sp}}(\omega) \to \alpha_C(\omega)$ and $\beta_{\mathrm{sp}}(\omega) \to \beta_C(\omega)$. By adding $U^b_{ee}(\mathbf{r}_A,\mathbf{r}_B)$ from Ref. [38] and $U^b_{mm}(\mathbf{r}_A,\mathbf{r}_B)$ (cf. Appendix B), one can obtain the nonadditive potential of three atoms, each being simultaneously polarizable and magnetizable.

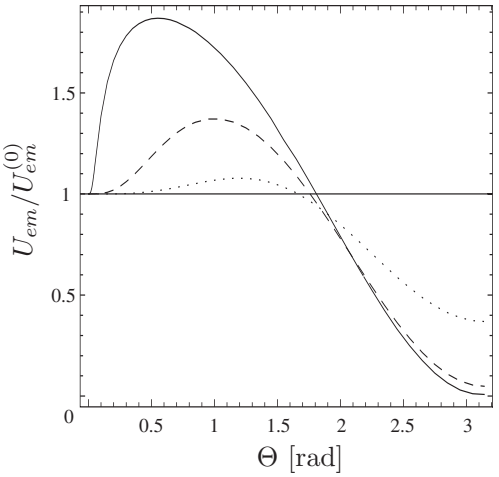

FIG. 2. The vdW potential of a polarizable and a magnetizable two-level atom (transition frequency ω_{10}) in the presence of an electric sphere of radius $R = c/\omega_{10}$ ($\omega_{P_e}/\omega_{10}=3$, $\omega_{T_e}/\omega_{10}=1$, $\gamma_e/\omega_{10}=0.001$) is shown as a function of the angular atom-atom separation Θ. The values of $r_A = r_B$ are $1.03c/\omega_{10}$ (solid line), $1.3c/\omega_{10}$ (dashed line), and $2c/\omega_{10}$ (dotted line).

Let us finally present some numerical results illustrating the effect of a medium-sized magnetoelectric sphere on the vdW potential of two two-level atoms with equal transition frequencies. We again focus on the case where atom A is polarizable and atom B is magnetizable. The corresponding results for two polarizable atoms are given in Ref. [16], from which, by duality, the analogous results for two magnetizable atoms can be inferred (see Appendix B). Figures 2 and 3 show the ratio $U_{em}/U^{(0)}_{em}$ obtained by numerical computation of Eq. (104) together with Eqs. (94) (for $\varepsilon = \mu = 1$), (92), (117), and (118), with the permittivity and permeability of the sphere being approximated by single-resonance Drude-Lorentz models,

$$\varepsilon(\omega) = 1 + \frac{\omega_{P_e}^2}{\omega_{T_e}^2 - \omega^2 - i\gamma_e\omega}, \tag{127}$$

$$\mu(\omega) = 1 + \frac{\omega_{P_m}^2}{\omega_{T_m}^2 - \omega^2 - i\gamma_m\omega}. \tag{128}$$

In Fig. 2, two atoms at equal distances $r_A = r_B$ from an electric sphere are considered and the ratio $U_{em}/U^{(0)}_{em}$ is shown as a function of the angular separation Θ of the atoms, for three different values of the atom-sphere separation. It is seen that the presence of the sphere can lead to enhancement or reduction of the potential, depending upon Θ. To be more specific, $U_{em}/U^{(0)}_{em}$ first increases with Θ, attains a maximum, and then decreases with increasing Θ to eventually become minimal at $\Theta = \pi$ when the atoms are positioned at opposite sides of the sphere. Whereas the position of the maximum shifts with the atom-sphere separation, the minimum is always observed at $\Theta = \pi$. Note that a magnetic in-

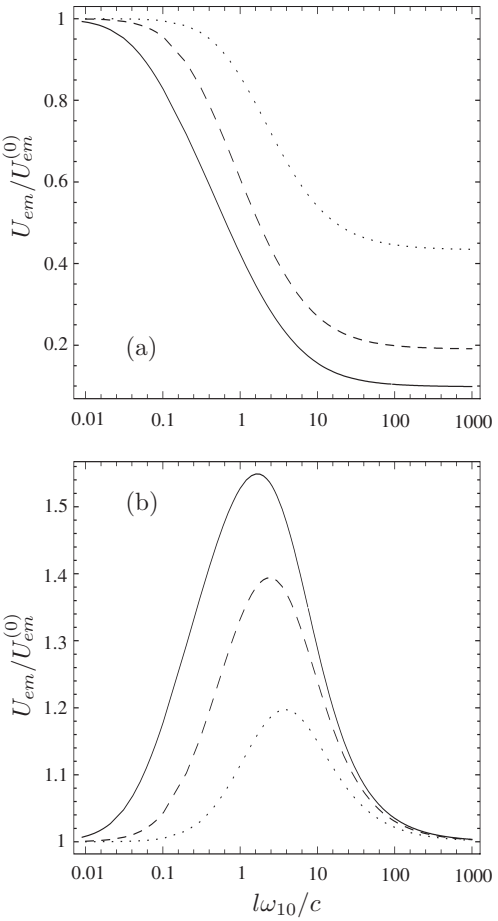

FIG. 3. The vdW interaction potential of two atoms with parameters as in Fig. 2 in the presence of (a) the same electric sphere as in Fig. 2, and (b) an analogous magnetic sphere as a function of the atom-atom distance l for $\Theta=0$ and $r_B=r_A+l$. The values of r_A are $1.03c/\omega_{10}$ (solid line), $1.1c/\omega_{10}$ (dashed line), $1.3c/\omega_{10}$ (dotted line).

stead of an electric sphere would lead to the same behavior because of duality.

Figure 3 shows the dependence of the ratio $U_{em}/U_{em}^{(0)}$ on the separation distance l between the two atoms for a configuration where the atoms are on a straight line through the center of a sphere (i.e., $\Theta=0$), with the polarizable atom A being closer to the sphere than the magnetizable atom B. Note that in contrast to the previous configuration, in this case an electric and a magnetic sphere do not lead to equivalent results by means of duality, because the positions of the electric and magnetic atoms are not equivalent. From Fig. 3(a) it is seen that in the case of an electric sphere the interaction potential is reduced compared to its value in free space; the ratio $U_{em}/U_{em}^{(0)}$ decreases with increasing l and approaches an asymptotic limit that depends to the distance between atom A and the sphere. In contrast, from Fig. 3(b) it is seen that in the case of a magnetic sphere the interaction potential is enhanced compared to its value in free space, and a pronounced maximum of the ratio $U_{em}/U_{em}^{(0)}$ is observed. For large atom-atom distances, $U_{em}/U_{em}^{(0)}$ approaches an asymptotic limit that is independent of the distance between atom A and the sphere.

VI. SUMMARY AND CONCLUDING REMARKS

We have extended the framework of macroscopic QED to paramagnetic atoms by introducing a Pauli term in the atom-field interaction. We have verified the consistency of our generalized Hamiltonian by showing that it generates Maxwell's equations and the correct equations of motion for charged particles with spin. On the basis of this Hamiltonian, we have employed leading-order perturbation theory to generalize the theory of body-assisted one- and two-atom van der Waals potentials of polarizable atoms to those that are both polarizable and magnetizable. It is seen that, with respect to each atom, the generalized potential can be considered as a superposition of contributions associated with the atomic polarizabilities and magnetizabilities. We have extended the scope of our theory to atoms that are embedded in media by implementing local-field corrections via the real-cavity model. We have found that local-field effects give rise to correction factors that depend on the permeability of the host medium for magnetizable atoms rather than the permittivity, as is the case for polarizable atoms.

We have applied the theory to the single-atom potential of an atom in the presence of a magnetoelectric half space and to the two-atom potential of atoms embedded in a bulk magnetoelectric medium or placed near a magnetoelectric sphere. The potential of a magnetizable atom in the presence of a half space has been found to be very similar to the known respective potential of a polarizable one. We have shown that a bulk medium does not change the sign of the two-atom interaction, but can lead to enhancements and reductions, whereby in the nonretarded limit the potentials of two polarizable or two magnetizable atoms is only influenced by the electric and magnetic medium properties, respectively. For the two-atom potential in the presence of a sphere, the case of two magnetizable atoms was demonstrated to be analogous to the known case of two polarizable, so we have focussed on the sphere-assisted interaction of a polarizable atom with a magnetizable one. We have obtained analytic results for a very large sphere (in which case the potential coincides with that of a half space) and a very small sphere (where the potential is analogous to the nonadditive three-atom interaction potential in free space, with the sphere taking the role of a third atom). Numerical results have been obtained for medium-sized spheres, where the sphere gives rise to enhancements and reductions of the potential, depending on the geometric arrangement of atoms and sphere: In particular, when the atoms are placed at equal distances from the sphere, the potential is enhanced (reduced) for small (large) separation angles between the atoms, while a linear arrangement of the atoms and the sphere (with the polarizable atom being closer to the sphere) leads to reduction (enhancement) for a electric (magnetic) sphere.

For the examples involving atoms in free space, we have explicitly verified invariance with respect to a global interchange of $\varepsilon \leftrightarrow \mu$ and $c^2\alpha \leftrightarrow \beta$, in agreement with the duality

properties investigated in Ref. [36]. The case of two atoms in a bulk medium has further revealed that this duality invariance only holds when accounting for local-field corrections.

ACKNOWLEDGMENTS

This work was supported by the Alexander von Humboldt Foundation and the UK Engineering and Physical Sciences Research Council. H.S. would like to thank the ministry of Science, Research, and Technology of Iran for the financial support. S.Y.B. is grateful to G. Barton and A. Salam for discussions.

APPENDIX A: LOCAL-FIELD CORRECTED TENSORS L AND K

The local-field corrected version of the tensor $\mathbf{L}$ defined by Eq. (54) can be derived in complete analogy to the derivation of Eqs. (70) and (71), which was given in Refs. [19,20]. For this purpose we recall that the first term in Eq. (71), i.e., the position-independent part of $\mathbf{G}^{(1)}_{\mathrm{loc}}(\mathbf{r}_A,\mathbf{r}_A,\omega)$, stems from the scattering Green tensor $\mathbf{G}^{(1)}_{\mathrm{cav}}(\mathbf{r}_A,\mathbf{r}_A,\omega)$ with position $\mathbf{r}_A$ at the center of a small spherical cavity of radius R_c which is embedded in an infinitely extended bulk material of permittivity ε_A and permeability μ_A. The respective tensor $\mathbf{L}^{(1)}_{\mathrm{cav}}(\mathbf{r}_A,\mathbf{r}_A,\omega)$ reads [39]

$$\mathbf{L}^{(1)}_{\mathrm{cav}}(\mathbf{r}_A,\mathbf{r}_A,\omega) = -\frac{i\omega^3}{6\pi c^3}C(\omega)\mathbf{I}, \tag{A1}$$

where

$$C(\omega) = -\frac{\mu_A h_1^{(1)}(z)[z_0 h_1^{(1)}(z_0)]' - h_1^{(1)}(z_0)[z h_1^{(1)}(z)]'}{\mu_A h_1^{(1)}(z)[z_0 j_1(z_0)]' - j_1(z_0)[z h_1^{(1)}(z)]'} \tag{A2}$$

[$z_0=\omega R_c/c$, $z=n_A z_0$; the primes indicate derivatives with respect to z_0 and z], with $j_1(x)$ and $h_1^{(1)}(x)$ being the first-kind spherical Bessel and first-kind spherical Hankel functions.

The local-field correction factors multiplying $\mathbf{G}$ in Eqs. (70) and (71) are determined by comparing the Green tensor $\mathbf{G}_{\mathrm{cav}}(\mathbf{r},\mathbf{r}_A,\omega)$ (with $\mathbf{r}_A$ at the center of the cavity and $\mathbf{r}$ at an arbitrary position outside the cavity) with the bulk Green tensor $\mathbf{G}_{\mathrm{bulk}}(\mathbf{r},\mathbf{r}_A,\omega)$ of an infinite homogeneous medium without the cavity,

$$\mathbf{G}_{\mathrm{bulk}}(\mathbf{r},\mathbf{r}_A,\omega) = -\frac{c^2\mathbf{e}^{ik\rho}}{4\pi\varepsilon_A\omega^2\rho^3}\{a(-ik\rho)\mathbf{I} - b(-ik\rho)\mathbf{e}_\rho\mathbf{e}_\rho\} \tag{A3}$$

with

$$a(x) = 1 + x + x^2, \quad b(x) = 3 + 3x + x^2 \tag{A4}$$

[$k=n_A\omega/c$, $\rho=|\mathbf{r}-\mathbf{r}_A|$, $\mathbf{e}_\rho=(\mathbf{r}-\mathbf{r}_A)/\rho$]. In the present case, the required tensor $\mathbf{L}_{\mathrm{cav}}(\mathbf{r},\mathbf{r}_A,\omega)$ reads [39]

$$\mathbf{L}_{\mathrm{cav}}(\mathbf{r},\mathbf{r}_A,\omega) = \frac{\mathbf{e}^{ik\rho}}{4\pi n_A^2\rho^3}D(\omega)\{a(-ik\rho)\mathbf{I} - b(-ik\rho)\mathbf{e}_\rho\mathbf{e}_\rho\} \tag{A5}$$

where

$$D(\omega) = \frac{\mu_A\{h_1^{(1)}(z_0)[z_0 j_1(z_0)]' - j_1(z_0)[z_0 h_1^{(1)}(z_0)]'\}}{\mu_A h_1^{(1)}(z)[z_0 j_1(z_0)]' - j_1(z_0)[z h_1^{(1)}(z)]'}, \tag{A6}$$

and from Eq. (A3), $\mathbf{L}_{\mathrm{bulk}}(\mathbf{r},\mathbf{r}_A,\omega)$ can be found to be

$$\mathbf{L}_{\mathrm{bulk}}(\mathbf{r},\mathbf{r}_A,\omega) = \frac{\mu_A\mathbf{e}^{ik\rho}}{4\pi\rho^3}\{a(-ik\rho)\mathbf{I} - b(-ik\rho)\mathbf{e}_\rho\mathbf{e}_\rho\}. \tag{A7}$$

Comparing Eqs. (A5) and (A7), we can conclude that, on using similar arguments as in Refs. [19,20], the magnetic local-field correction factor is given by $D/(\mu_A n_A^2)$. Combining this with Eq. (A1) and following the line of reasoning of Refs. [19,20], we expand all the terms within leading order in $\omega R_c/c$ to obtain the local-field corrected tensors $\mathbf{L}_{\mathrm{loc}}$ and $\mathbf{L}^{(1)}_{\mathrm{loc}}$ in the form of Eqs. (74) and (75). Equation (76) follows in complete analogy.

APPENDIX B: GREEN TENSORS L AND K FOR A SPHERE

The free-space part $\mathbf{L}^{(0)}$ of the magnetic-magnetic tensor is the special case $\varepsilon=\mu=1$ of the respective bulk Green tensor (A7); it obviously coincides with $-(\omega/c)^2\mathbf{G}^{(0)}$ [which is a special case of the bulk Green tensor (A3)]. According to its definition (54), the scattering part of $\mathbf{L}$ can be found from [39]

$$\begin{aligned}\mathbf{G}^{(1)}(\mathbf{r},\mathbf{r}',\omega) = \frac{ik_0}{4\pi}\sum_{n=1}^{\infty}\frac{2n+1}{n(n+1)}\sum_{m=0}^{n}(2-\delta_{0m})\frac{(n-m)!}{(n+m)!}\\ \times\sum_{p=\pm1}[B_n^M(\omega)\mathbf{M}_{nm,p}(\mathbf{r},k_0)\mathbf{M}_{nm,p}(\mathbf{r}',k_0)\\ + B_n^N(\omega)\mathbf{N}_{nm,p}(\mathbf{r},k_0)\mathbf{N}_{nm,p}(\mathbf{r}',k_0)],\end{aligned} \tag{B1}$$

where B_n^M and B_n^N are defined by Eqs. (109) and (110), $\mathbf{M}_{nm,p}$ and $\mathbf{N}_{nm,p}$ are even ($p=+1$) and odd ($p=-1$) spherical wave vector functions and in spherical coordinates can be expressed in terms of spherical Hankel functions of the first kind $h_n^{(1)}(x)$ and Legendre functions $P_n^m(x)$ as

$$\begin{aligned}\mathbf{M}_{nm,\pm1}(\mathbf{r},k) = \mp\frac{m}{\sin\theta}h_n^{(1)}(kr)P_n^m(\cos\theta)\begin{Bmatrix}\sin\\ \cos\end{Bmatrix}(m\phi)\mathbf{e}_\theta\\ - h_n^{(1)}(kr)\frac{dP_n^m(\cos\theta)}{d\theta}\begin{Bmatrix}\cos\\ \sin\end{Bmatrix}(m\phi)\mathbf{e}_\phi,\end{aligned} \tag{B2}$$

$$\begin{aligned}\mathbf{N}_{nm,\pm1}(\mathbf{r},k) = \frac{n(n+1)}{kr}h_n^{(1)}(kr)P_n^m(\cos\theta)\begin{Bmatrix}\cos\\ \sin\end{Bmatrix}(m\phi)\mathbf{e}_r\\ + \frac{1}{kr}\frac{d[rh_n^{(1)}(kr)]}{dr}\left[\frac{dP_n^m(\cos\theta)}{d\theta}\begin{Bmatrix}\cos\\ \sin\end{Bmatrix}(m\phi)\mathbf{e}_\theta\right.\\ \left.\mp\frac{m}{\sin\theta}P_n^m(\cos\theta)\begin{Bmatrix}\sin\\ \cos\end{Bmatrix}(m\phi)\mathbf{e}_\phi\right].\end{aligned} \tag{B3}$$

They are related to each other via

$$\nabla\times\mathbf{M}_{nm,\pm1}(\mathbf{r},k) = k\mathbf{N}_{nm,\pm1}(\mathbf{r},k), \tag{B4}$$

$$\nabla \times \mathbf{N}_{nm,\pm 1}(\mathbf{r},k) = k\mathbf{M}_{nm,\pm 1}(\mathbf{r},k). \tag{B5}$$

Substituting Eq. (B1) into Eq. (54) and making use of the relations (B4) and (B5) one sees that $\mathbf{L}^{(1)}$ and $-(\omega/c)^2\mathbf{G}^{(1)}$ [and consequently $\mathbf{L}$ and $-(\omega/c)^2\mathbf{G}$] can be converted into one another by interchanging B_n^M and B_n^N, or equivalently interchanging ε and μ. With this knowledge, a comparison between Eqs. (60) and (68) reveals that U_{mm} may be obtained from U_{ee} by replacing α with β/c^2 and interchanging $\varepsilon \leftrightarrow \mu$.

The scattering part of tensor $\mathbf{K}$ may be found by substituting Eq. (B1) in Eq. (67) and making use of relations (B4) and (B5),

$$\mathbf{K}^{(1)}(\mathbf{r},\mathbf{r}',\omega) = \frac{ik_0^2}{4\pi}\sum_{n=1}^{\infty}\frac{2n+1}{n(n+1)}\sum_{m=0}^{n}(2-\delta_{0m})\frac{(n-m)!}{(n+m)!} \times \sum_{p=\pm 1}[B_n^M\mathbf{N}_{nm,p}(\mathbf{r},k_0)\mathbf{M}_{nm,p}(\mathbf{r}',k_0) + B_n^N\mathbf{M}_{nm,p}(\mathbf{r},k_0)\mathbf{N}_{nm,p}(\mathbf{r}',k_0)]. \tag{B6}$$

Assuming, without loss of generality, that the coordinate system is chosen such that its origin coincides with the center of the sphere and the two atoms are located in the xz plane as shown in Fig. 1,

$$\mathbf{r}_A = (r_A,\theta_A,0), \quad \mathbf{r}_B = (r_B,\theta_B,\pi), \tag{B7}$$

the summations over m and p in Eq. (B6) can be performed in a way similar to Ref. [38], leading to

$$\sum_{m=0}^{n}\sum_{p=\pm 1}(2-\delta_{0m})\frac{(n-m)!}{(n+m)!}\mathbf{N}_{nm,p}(\mathbf{r}_B,k_0)\mathbf{M}_{nm,p}(\mathbf{r}_A,k_0) = \frac{1}{k_0 r_B}\{n(n+1)Q_n\sin\Theta P_n'(\gamma)\mathbf{e}_{r_B}\mathbf{e}_{\phi_A} + Q_n^B F_n(\gamma)\mathbf{e}_{\theta_B}\mathbf{e}_{\phi_A} - Q_n^B P_n'(\gamma)\mathbf{e}_{\phi_B}\mathbf{e}_{\theta_A}\}, \tag{B8}$$

$$\sum_{m=0}^{n}\sum_{p=\pm 1}(2-\delta_{0m})\frac{(n-m)!}{(n+m)!}\mathbf{M}_{nm,p}(\mathbf{r}_B,k_0)\mathbf{N}_{nm,p}(\mathbf{r}_A,k_0) = \frac{1}{k_0 r_A}\{-Q_n^A P_n'(\gamma)\mathbf{e}_{\theta_B}\mathbf{e}_{\phi_A} + n(n+1)Q_n\sin\Theta \times P_n'(\gamma)\mathbf{e}_{\phi_B}\mathbf{e}_{r_A} + Q_n^A F_n(\gamma)\mathbf{e}_{\phi_B}\mathbf{e}_{\theta_A}\}. \tag{B9}$$

Combining Eqs. (B6), (B8), and (B9) we arrive at Eq. (108) for the Green tensor.

APPENDIX C: LIMITING CASE OF A LARGE SPHERE

In the limiting case of a large sphere where the conditions (119) and (120) are met, the leading contributions to Eqs. (117) and (118) come from terms with $n \gg 1$ (see Ref. [32]), for which the spherical Bessel and Hankel functions can be approximated by

$$j_n(z) = \frac{z^2}{(2n+1)!!}\left(1-\frac{z^2}{4n+6}\right) \tag{C1}$$

and

$$h_n^{(1)}(z) = -i\frac{(2n-1)!!}{z^{n+1}}\left(1+\frac{z^2}{4n-2}\right). \tag{C2}$$

Hence, Eqs. (109) and (110) are approximated by

$$B_n^M(\omega) = \frac{2in(R\omega/c)^{2n+1}}{[(2n+1)!!]^2}\frac{\mu(\omega)-1}{\mu(\omega)+1} \tag{C3}$$

and

$$B_n^N(\omega) = \frac{2in(R\omega/c)^{2n+1}}{[(2n+1)!!]^2}\frac{\varepsilon(\omega)-1}{\varepsilon(\omega)+1}, \tag{C4}$$

and Eqs. (111)–(113) approximately reduce to

$$Q_n = -\left(\frac{c}{\omega}\right)^{2n+2}\frac{[(2n-1)!!]^2}{(r_A r_B)^{n+1}}, \tag{C5}$$

$$Q_n^A = Q_n^B = -nQ_n. \tag{C6}$$

In order to illustrate the application of the approximation scheme to the tensor $\mathbf{K}^{(1)}$ given by Eq. (108) let us consider, for example, the component $K_{r\phi}^{(1)}$. Making use of Eqs. (C3) and (C5) we find that

$$K_{r\phi}^{(1)}(\mathbf{r}_B,\mathbf{r}_A,\omega) = \frac{X}{4\pi R^3}\frac{\mu(\omega)-1}{\mu(\omega)+1}\frac{t^2}{(1-2tg+t^2)^{3/2}} \tag{C7}$$

$[t=R^2/(r_A r_B)]$ where the identity

$$\sum_{n=1}^{\infty}t^n P_n(\gamma) = \frac{1}{\sqrt{1-2tg+t^2}} - 1 \tag{C8}$$

has been used. Recalling condition (119), we have

$$t^k = 1 - k\frac{\delta_A+\delta_B}{R} + \frac{k(k+1)}{2}\frac{\delta_A^2+\delta_B^2}{R^2} + k^2\frac{\delta_A\delta_B}{R^2} \tag{C9}$$

implying that

$$1-2t\gamma+t^2 \simeq \Theta^2 + \frac{(\delta_A+\delta_B)^2}{R^2} = \frac{l_+^2}{R^2}. \tag{C10}$$

Using Eq. (C10) in (C7) we end up with

$$K_{r\phi}^{(1)}(\mathbf{r}_B,\mathbf{r}_A,\omega) = \frac{X}{4\pi l_+^3}\frac{\mu(\omega)-1}{\mu(\omega)+1}. \tag{C11}$$

The other components of $\mathbf{K}^{(1)}$ can be evaluated in a similar way. Substituting the resulting expressions for $\mathbf{K}^{(1)}$ into Eqs. (106) and (107), and summing them in accordance with Eq. (105) leads to Eq. (121).

[1] A. Salam, Int. Rev. Phys. Chem. **27**, 405 (2008).
[2] F. London, Z. Phys. **63**, 245 (1930).
[3] H. B. G. Casimir, Proc. K. Ned. Akad. Wet. **51**, 793 (1948).
[4] B. M. Axilrod and E. Teller, J. Chem. Phys. **11**, 299 (1943).
[5] B. M. Axilrod, J. Chem. Phys. **17**, 1349 (1949).
[6] M. R. Aub and S. Zienau, Proc. R. Soc. London, Ser. A **257**, 464 (1960).
[7] E. A. Power and T. Thirunamachandran, Proc. R. Soc. London, Ser. A **401**, 267 (1985).
[8] E. A. Power and T. Thirunamachandran, Phys. Rev. A **50**, 3929 (1994).
[9] G. Feinberg and J. Sucher, J. Chem. Phys. **48**, 3333 (1968).
[10] T. H. Boyer, Phys. Rev. **180**, 19 (1969).
[11] G. Feinberg and J. Sucher, Phys. Rev. A **2**, 2395 (1970).
[12] E. Lubkin, Phys. Rev. A **4**, 416 (1971).
[13] M. Babiker and G. Barton, Proc. R. Soc. London, Ser. A **326**, 255 (1972).
[14] A. D. McLachlan, Mol. Phys. **7**, 381 (1964).
[15] J. Mahanty and B. W. Ninham, J. Phys. A **6**, 1140 (1973).
[16] H. Safari, S. Y. Buhmann, D.-G. Welsch, and Ho Trung Dung, Phys. Rev. A **74**, 042101 (2006).
[17] S. Y. Buhmann, H. Safari, D.-G. Welsch, and Ho Trung Dung, Open Syst. Inf. Dyn. **13**, 427 (2006).
[18] L. Onsager, J. Am. Chem. Soc. **58**, 1486 (1936).
[19] Ho Trung Dung, S. Y. Buhmann, and D.-G. Welsch, Phys. Rev. A **74**, 023803 (2006).
[20] A. Sambale, S. Y. Buhmann, D.-G. Welsch, and M. S. Tomaš, Phys. Rev. A **75**, 042109 (2007).
[21] S. Spagnolo, D. A. R. Dalvit, and P. W. Milonni, Phys. Rev. A **75**, 052117 (2007).
[22] L. Knöll, S. Scheel, and D.-G. Welsch, in *Coherence and Statistics of Photons and Atoms*, edited by J. Peřina (Wiley, New York, 2001), p. 1.
[23] S. Y. Buhmann, L. Knöll, D.-G. Welsch, and Ho Trung Dung, Phys. Rev. A **70**, 052117 (2004).
[24] S. Y. Buhmann and D.-G. Welsch, Prog. Quantum Electron. **31**, 51 (2007).
[25] C. Baxter, M. Babiker, and R. Loudon, Phys. Rev. A **47**, 1278 (1993).
[26] D. P. Craig and T. Thirunamachandran, *Molecular Quantum Electrodynamics* (Dover, New York, 1998).
[27] Ho Trung Dung, S. Y. Buhmann, L. Knöll, D.-G. Welsch, S. Scheel, and J. Kästel, Phys. Rev. A **68**, 043816 (2003).
[28] E. A. Power and S. Zienau, Philos. Trans. R. Soc. London, Ser. A **251**, 427 (1959).
[29] R. G. Woolley, Proc. R. Soc. London, Ser. A **321**, 557 (1971).
[30] A. A. Kyasov and G. V. Dedkov, Surf. Sci. **463**, 11 (2001).
[31] H. B. G. Casimir and D. Polder, Phys. Rev. **73**, 360 (1948).
[32] S. Y. Buhmann, Ho Trung Dung, T. Kampf, and D.-G. Welsch, Eur. Phys. J. D **35**, 15 (2005).
[33] J. K. Jenkins, A. Salam, and T. Thirunamachandran, Phys. Rev. A **50**, 4767 (1994).
[34] A. Salam, Int. J. Quantum Chem. **78**, 437 (2000).
[35] A. Salam, J. Phys. B **33**, 2181 (2000).
[36] S. Y. Buhmann and S. Scheel, e-print arXiv:0806.2211.
[37] S. Y. Buhmann, D.-G. Welsch, and T. Kampf, Phys. Rev. A **72**, 032112 (2005).
[38] H. Safari, D.-G. Welsch, Ho Trung Dung, and S. Y. Buhmann, Phys. Rev. A **77**, 053824 (2008).
[39] L.-W. Li, P.-S. Kooi, M.-S. Leong, and T.-S. Yeo, IEEE Trans. Microwave Theory Tech. **42**, 2302 (1994).

PHYSICAL REVIEW A **87**, 012507 (2013)

Body-assisted dispersion potentials of diamagnetic atoms

Stefan Yoshi Buhmann
Quantum Optics and Laser Science, Blackett Laboratory, Imperial College London, Prince Consort Road, London SW7 2AZ, United Kingdom

Hassan Safari
Photonics Group, Kerman Graduate University of Technology, Ending of Haft-Bagh Highway, Kerman, Iran

Stefan Scheel
Institut für Physik, Universität Rostock, Universitätsplatz 3, D-18051 Rostock, Germany, and Quantum Optics and Laser Science, Blackett Laboratory, Imperial College London, Prince Consort Road, London SW7 2AZ, United Kingdom

A. Salam
Department of Chemistry, Wake Forest University, Winston-Salem, North Carolina 27109, USA
(Received 14 September 2012; published 15 January 2013)

We derive Casimir-Polder and van der Waals potentials of one or two atoms with diamagnetic properties in an arbitrary environment of magnetoelectric bodies. The calculations are based on macroscopic quantum electrodynamics and leading-order perturbation theory. For the examples of an atom and a perfect mirror and two atoms in free space, we show that diamagnetic dispersion potentials have the same sign as their electric counterparts but can exhibit quite different distance dependences.

DOI: 10.1103/PhysRevA.87.012507 PACS number(s): 31.30.jh, 34.20.−b, 12.20.−m, 42.50.Nn

I. INTRODUCTION

The issue of electrodynamics in magnetodielectrics is a long-standing one [1]. It ranges from the form and propagation of Maxwell fields in such media to their absorption and emission characteristics, as well as to the numerous other optical properties that they exhibit. One curious aspect, recently confirmed by fabrication of periodic arrays of thin metallic wires [2–4], is the existence of left-handed materials, so called because the electric, magnetic, and direction of propagation vectors form a left-handed triad, resulting in a metamaterial with a negative refractive index. Another interesting aspect is the nature of interparticle interactions in media with electrical permittivity, magnetic permeability, or both. This has its origins in the work of Casimir [5], subsequently spawning a wide variety of related phenomena categorized under Casimir-like effects [6–9] and including the Casimir-Polder (CP) dispersion potential [10].

The understanding and computation of van der Waals forces (vdW) for chemical, physical, and biological systems is of fundamental importance and widespread interest as they manifest in vacuum, gaseous, or condensed phases. These vary from semiclassical treatments yielding the London dispersion formula to quantum field theoretic approaches where radiative effects are properly accounted for and result in Casimir energy shifts. Perhaps the best-known example of a fundamental theory that automatically includes retardation is quantum electrodynamics (QED). Two often-used versions include macroscopic [11–14] and microscopic [15,16] QED, their prefixes aptly describing their general range of applicability. In the former variant, the body-assisted electromagnetic field is evaluated by quantizing the radiation field and the dispersive and absorptive medium. This enables the body-induced atomic energy shift to be computed, which is interpreted as the potential of the force. From this, pair and many-body interaction energies can also be calculated. This has been successfully carried out for both electrically polarizable [17] and paramagnetically susceptible [18] systems. Effects of an intermediate medium can also be accounted for [18–20].

Microscopic Coulomb gauge QED constructed via quantization of the free electromagnetic field has also been used successfully to evaluate atom-field and atom-atom interactions in a vacuum. In the latter situation this has included recalculation of the CP potential and its extension to higher multipole moment contributions, such as magnetic dipole, electric quadrupole, and diamagnetic couplings [21–27]. Unexpected results ensue such as the discriminatory nature of the interaction between two chiral (optically active) molecules, the repulsive form of the ground-state dispersion energy shift between an electrically polarizable atom and a paramagnetically susceptible one, and that in the near-zone, the electric-diamagnetic contribution to this potential is larger than the corresponding limit arising from the electric-paramagnetic term [23].

In this paper a systematic study is performed on the CP potentials of a diamagnetic atom and its vdW potentials with another and with an atom that is either electrically or paramagnetically polarizable in a medium comprised of magnetodielectric bodies using macroscopic QED theory. Interest in contributions arising from diamagnetic coupling has been due to their importance when computing highly accurate potentials for alkali metal atom dimers [28], where it has been found that the electric-diamagnetic and paramagnetic-diamagnetic terms can be larger than the electric-paramagnetic and paramagnetic-paramagnetic energy shifts. The article is organized as follows. Section II briefly describes the quantized body-assisted Maxwell field operators in the medium, their expression in terms of the Green's-function solution of the Helmholtz equation, and the writing of the total-system Hamiltonian. Electric and total magnetic contributions to the single-atom CP shift and for an atom placed in front of a perfectly reflecting mirror are obtained in Sec. III. Presented

in Sec. IV are diagrammatic perturbation theory results for the dispersion pair potential when at least one of the atoms is diamagnetic. Corresponding free-field interaction energies are also given, and these are briefly compared with results obtained via microscopic QED. In all of the cases examined, the asymptotic limits of the energy shift in the near and far zones, corresponding to nonretarded and retarded regimes, are found and compared with previously obtained limiting forms for electric, paramagnetic, and electric-paramagnetic interactions. A short summary is given in Sec. V.

II. QUANTIZATION SCHEME

Consider one or two atoms (or molecules) with internal Hamiltonians ($\xi = A, B$)

$$\hat{H}_\xi = \sum_n E_\xi^n |n_\xi\rangle\langle n_\xi| \tag{1}$$

which are placed at positions $\boldsymbol{r}_\xi$ within an arbitrary arrangement of linearly, locally, and isotropically responding magnetoelectric bodies, described by a Kramers-Kronig consistent permittivity $\varepsilon(\boldsymbol{r},\omega)$ and permeability $\mu(\boldsymbol{r},\omega)$. Upon introducing bosonic variables $\hat{\boldsymbol{f}}_\lambda^\dagger(\boldsymbol{r},\omega)$ and $\hat{\boldsymbol{f}}_\lambda(\boldsymbol{r},\omega)$, which are creation and annihilation operators for the elementary electric ($\lambda = e$) and magnetic ($\lambda = m$) excitations of the system of bodies and electromagnetic field and obey the bosonic commutation relations

$$[\hat{\boldsymbol{f}}_\lambda(\boldsymbol{r},\omega), \hat{\boldsymbol{f}}_{\lambda'}^\dagger(\boldsymbol{r}',\omega')] = \boldsymbol{\delta}(\boldsymbol{r}-\boldsymbol{r}')\delta_{\lambda\lambda'}\delta(\omega-\omega') \tag{2}$$

and

$$[\hat{\boldsymbol{f}}_\lambda(\boldsymbol{r},\omega), \hat{\boldsymbol{f}}_{\lambda'}(\boldsymbol{r}',\omega')] = [\hat{\boldsymbol{f}}_\lambda^\dagger(\boldsymbol{r},\omega), \hat{\boldsymbol{f}}_{\lambda'}^\dagger(\boldsymbol{r}',\omega')] = \boldsymbol{0}, \tag{3}$$

the body-field Hamiltonian takes the form [12]

$$\hat{H}_F = \sum_{\lambda=e,m} \int d^3r \int_0^\infty d\omega \hbar\omega \hat{\boldsymbol{f}}_\lambda^\dagger(\boldsymbol{r},\omega)\cdot\hat{\boldsymbol{f}}_\lambda(\boldsymbol{r},\omega). \tag{4}$$

The ground state of $\hat{H}_F$ can obviously be defined by

$$\hat{\boldsymbol{f}}_\lambda(\boldsymbol{r},\omega)|\{0\}\rangle = 0 \quad \forall\lambda,\boldsymbol{r},\omega. \tag{5}$$

Within the multipolar coupling scheme, the interaction of each atom with the body-assisted electromagnetic field is given by [29]

$$\hat{H}_{\xi F} = \hat{H}_{\xi F}^e + \hat{H}_{\xi F}^p + \hat{H}_{\xi F}^d. \tag{6}$$

Here the three terms are the electric, paramagnetic and diamagnetic interactions,

$$\hat{H}_{\xi F}^e = -\hat{\boldsymbol{\mu}}_\xi \cdot \hat{\boldsymbol{E}}(\boldsymbol{r}_\xi), \tag{7}$$

$$\hat{H}_{\xi F}^p = -\hat{\boldsymbol{m}}_\xi \cdot \hat{\boldsymbol{B}}(\boldsymbol{r}_\xi), \tag{8}$$

$$\hat{H}_{\xi F}^d = \sum_{\alpha\in\xi} \frac{q_\alpha^2}{8m_\alpha}[\hat{\tilde{\boldsymbol{r}}}_\alpha \times \hat{\boldsymbol{B}}(\boldsymbol{r}_\xi)]^2, \tag{9}$$

with $\hat{\boldsymbol{\mu}}_\xi$ and $\hat{\boldsymbol{m}}_\xi$ being the respective atomic electric and magnetic dipole operators and q_α, m_α, and $\hat{\tilde{\boldsymbol{r}}}_\alpha$ denoting the charges, masses, and positions relative to the center of mass of the particles contained in the atoms. Note that electric quadrupole and even octupole contributions can easily be included in the formalism; they have recently been shown to affect the CP potential of Rydberg atoms close to surfaces [30].

Introducing the atomic diamagnetizability operator as

$$\hat{\boldsymbol{\beta}}_\xi^d = -\sum_{\alpha\in\xi} \frac{q_\alpha^2}{4m_\alpha}\left(\hat{\tilde{\boldsymbol{r}}}_\alpha^2\mathbf{I} - \hat{\tilde{\boldsymbol{r}}}_\alpha\hat{\tilde{\boldsymbol{r}}}_\alpha\right) \tag{10}$$

and using the identity $[\boldsymbol{a}\times\boldsymbol{b}]^2 = \boldsymbol{b}\cdot(\boldsymbol{a}^2\mathbf{I} - \boldsymbol{a}\boldsymbol{a})\cdot\boldsymbol{b}$, the diamagnetic interaction Hamiltonian may be cast in the form

$$\hat{H}_{\xi F}^d = -\tfrac{1}{2}\hat{\boldsymbol{B}}(\boldsymbol{r}_\xi)\cdot\hat{\boldsymbol{\beta}}_\xi^d\cdot\hat{\boldsymbol{B}}(\boldsymbol{r}_\xi). \tag{11}$$

The ground-state diamagnetizability of an atom is given by the expectation value

$$\begin{aligned}\boldsymbol{\beta}_\xi^d \equiv \langle\hat{\boldsymbol{\beta}}_\xi^d\rangle &= -\sum_{\alpha\in\xi}\frac{q_\alpha^2}{4m_\alpha}\langle 0_\xi|\hat{\tilde{\boldsymbol{r}}}_\alpha^2\mathbf{I} - \hat{\tilde{\boldsymbol{r}}}_\alpha\hat{\tilde{\boldsymbol{r}}}_\alpha|0_\xi\rangle \\ &= -\sum_{\alpha\in\xi}\frac{q_\alpha^2}{6m_\alpha}\langle\hat{\tilde{\boldsymbol{r}}}_\alpha^2\rangle\mathbf{I} \equiv \beta_\xi^d\mathbf{I},\end{aligned} \tag{12}$$

where the last line holds for isotropic atoms.

The total Hamiltonian of the atom(s) interacting with the electromagnetic field in the presence of the bodies takes the form

$$\hat{H} = \sum_{\xi=A,B}\hat{H}_\xi + \hat{H}_F + \sum_{\xi=A,B}\hat{H}_{\xi F}. \tag{13}$$

The electric and magnetic field operators can be expanded in terms of the bosonic operators $\hat{\boldsymbol{f}}_\lambda^\dagger(\boldsymbol{r},\omega)$ and $\hat{\boldsymbol{f}}_\lambda(\boldsymbol{r},\omega)$ as

$$\hat{\boldsymbol{E}}(\boldsymbol{r}) = \sum_{\lambda=e,m}\int d^3r' \int_0^\infty d\omega\, \mathbf{G}_\lambda(\boldsymbol{r},\boldsymbol{r}',\omega)\cdot\hat{\boldsymbol{f}}_\lambda(\boldsymbol{r}',\omega) + \text{H.c.}, \tag{14}$$

$$\hat{\boldsymbol{B}}(\boldsymbol{r}) = \sum_{\lambda=e,m}\int d^3r' \int_0^\infty \frac{d\omega}{i\omega}\,\boldsymbol{\nabla}\times\mathbf{G}_\lambda(\boldsymbol{r},\boldsymbol{r}',\omega)\cdot\hat{\boldsymbol{f}}_\lambda(\boldsymbol{r}',\omega) + \text{H.c.} \tag{15}$$

The expansion coefficients $\mathbf{G}_\lambda$ are related to the classical Green tensor $\mathbf{G}$ by

$$\mathbf{G}_e(\boldsymbol{r},\boldsymbol{r}',\omega) = i\frac{\omega^2}{c^2}\sqrt{\frac{\hbar}{\pi\varepsilon_0}\,\text{Im}\varepsilon(\boldsymbol{r}',\omega)}\,\mathbf{G}(\boldsymbol{r},\boldsymbol{r}',\omega), \tag{16}$$

$$\mathbf{G}_m(\boldsymbol{r},\boldsymbol{r}',\omega) = i\frac{\omega}{c}\sqrt{\frac{\hbar}{\pi\varepsilon_0}\frac{\text{Im}\mu(\boldsymbol{r}',\omega)}{|\mu(\boldsymbol{r}',\omega)|^2}}[\boldsymbol{\nabla}'\times\mathbf{G}(\boldsymbol{r}',\boldsymbol{r},\omega)]^{\mathsf{T}}; \tag{17}$$

and the Green tensor is the unique solution to the Helmholtz equation

$$\left[\boldsymbol{\nabla}\times\frac{1}{\mu(\boldsymbol{r},\omega)}\boldsymbol{\nabla}\times - \frac{\omega^2}{c^2}\varepsilon(\boldsymbol{r},\omega)\right]\mathbf{G}(\boldsymbol{r},\boldsymbol{r}',\omega) = \boldsymbol{\delta}(\boldsymbol{r}-\boldsymbol{r}') \tag{18}$$

together with the boundary condition

$$\mathbf{G}(\boldsymbol{r},\boldsymbol{r}',\omega)\to\boldsymbol{0} \quad \text{for} \quad |\boldsymbol{r}-\boldsymbol{r}'|\to\infty. \tag{19}$$

Just like the permittivity and permeability, the Green tensor is an analytic function in the upper half of the complex frequency

plane and fulfils the Schwarz reflection principle:

$$\mathbf{G}(\boldsymbol{r},\boldsymbol{r}',-\omega^*)=\mathbf{G}^*(\boldsymbol{r},\boldsymbol{r}',\omega). \tag{20}$$

In addition, it obeys the Onsager-Lorentz reciprocity,

$$\mathbf{G}(\boldsymbol{r}',\boldsymbol{r},\omega)=\mathbf{G}^{\mathsf{T}}(\boldsymbol{r},\boldsymbol{r}',\omega), \tag{21}$$

and the useful integral relation

$$\sum_{\lambda=e,m}\int d^3s\,\mathbf{G}_\lambda(\boldsymbol{r},\boldsymbol{s},\omega)\cdot\mathbf{G}_\lambda^{*\mathsf{T}}(\boldsymbol{r}',\boldsymbol{s},\omega)=\frac{\hbar\mu_0}{\pi}\,\omega^2\mathrm{Im}\mathbf{G}(\boldsymbol{r},\boldsymbol{r}',\omega) \tag{22}$$

holds.

III. CASIMIR-POLDER POTENTIAL OF A SINGLE ATOM

In this section, we calculate the CP force on a single atom in the presence of magnetoelectric bodies, discarding the label A wherever possible. According to Casimir and Polder, the force can be derived from the associated CP potential $U(\boldsymbol{r}_A)$

$$\boldsymbol{F}=-\boldsymbol{\nabla}U(\boldsymbol{r}_A), \tag{23}$$

which in turn can be identified as the position-dependent part of the energy shift ΔE due to the atom-field coupling

$$U(\boldsymbol{r}_A)=\Delta E(\boldsymbol{r}_A). \tag{24}$$

A. Perturbation theory

We assume the atom-field system to be prepared in the uncoupled ground state $|0_A\rangle|\{0\}\rangle$ and calculate the energy shift due to the atom-field coupling within leading-order perturbation theory. Let us first study a purely diamagnetic atom, whose CP potential is due to the first-order energy shift associated with the diamagnetic part of the atom-field interaction (11),

$$\Delta E=\langle\{0\}|\langle 0_A|-\tfrac{1}{2}\,\hat{\boldsymbol{B}}(\boldsymbol{r}_A)\cdot\hat{\boldsymbol{\beta}}^d\cdot\hat{\boldsymbol{B}}(\boldsymbol{r}_A)|0_A\rangle|\{0\}\rangle. \tag{25}$$

Normally, CP energy shifts only arise in second-order perturbation theory. However, due to the diamagnetic interaction Hamiltonian being quadratic in the magnetic induction field already, the first perturbation order contributes. It can be easily evaluated by using the magnetic-field expression, (15), the bosonic commutation relations, (2) and (3), and the integral relation, (22), resulting in

$$\Delta E=\frac{\hbar\mu_0}{2\pi}\int_0^\infty d\omega\,\mathrm{tr}[\boldsymbol{\beta}^d\cdot\mathrm{Im}\mathbf{G}_{mm}(\boldsymbol{r}_A,\boldsymbol{r}_A,\omega)] \tag{26}$$

with

$$\mathbf{G}_{mm}(\boldsymbol{r},\boldsymbol{r}',\omega)=\boldsymbol{\nabla}\times\mathbf{G}(\boldsymbol{r},\boldsymbol{r}',\omega)\times\overleftarrow{\boldsymbol{\nabla}}'. \tag{27}$$

For an atom in a free-space region, the CP potential can be extracted from this energy shift by separating the Green tensor into its bulk and scattering parts,

$$\mathbf{G}(\boldsymbol{r},\boldsymbol{r}',\omega)=\mathbf{G}^{(0)}(\boldsymbol{r},\boldsymbol{r}',\omega)+\mathbf{G}^{(1)}(\boldsymbol{r},\boldsymbol{r}',\omega), \tag{28}$$

and discarding the constant energy shift associated with the translationally invariant bulk part by making the replacement $\mathbf{G}\mapsto\mathbf{G}^{(1)}$. The result can be simplified by converting the integral over real frequencies to another along the imaginary axis in the complex frequency plane. To this end, we first write

$$\int_0^\infty d\omega\,\mathrm{Im}\mathbf{G}(\boldsymbol{r},\boldsymbol{r}',\omega)=\mathrm{Im}\int_0^\infty d\omega\,\mathbf{G}(\boldsymbol{r},\boldsymbol{r}',\omega). \tag{29}$$

The integral on the right-hand side can be replaced by an integral along the positive imaginary axis ($\omega\mapsto i\xi$) plus a vanishing integral along infinite quarter-circles via Cauchy's theorem. Using the fact that $\mathbf{G}(\mathrm{i}\xi)$ is real-valued for a real ξ, as can be inferred from Schwarz reflection principle, (20), one finds

$$\begin{aligned}U_d(\boldsymbol{r}_A)&=\frac{\hbar\mu_0}{2\pi}\int_0^\infty d\xi\,\mathrm{tr}\big[\boldsymbol{\beta}^d\cdot\mathbf{G}^{(1)}_{mm}(\boldsymbol{r}_A,\boldsymbol{r}_A,\mathrm{i}\xi)\big]\\&=\frac{\hbar\mu_0}{2\pi}\int_0^\infty d\xi\,\beta^d\mathrm{tr}\mathbf{G}^{(1)}_{mm}(\boldsymbol{r}_A,\boldsymbol{r}_A,\mathrm{i}\xi).\end{aligned} \tag{30}$$

The last line in Eq. (30) holds for isotropic atoms. For an atom with an additional nontrivial electric and paramagnetic response, the respective electric and paramagnetic interactions in the coupling Hamiltonian, (6), also need to be taken into account. As shown previously, they give rise to second-order energy shifts such that the electric and paramagnetic CP potentials are given by [18]

$$\begin{aligned}U_e(\boldsymbol{r}_A)&=\frac{\hbar}{2\pi\varepsilon_0}\int_0^\infty d\xi\,\mathrm{tr}\big[\boldsymbol{\alpha}(i\xi)\cdot\mathbf{G}^{(1)}_{ee}(\boldsymbol{r}_A,\boldsymbol{r}_A,i\xi)\big]\\&=\frac{\hbar}{2\pi\varepsilon_0}\int_0^\infty d\xi\,\alpha(i\xi)\mathrm{tr}\mathbf{G}^{(1)}_{ee}(\boldsymbol{r}_A,\boldsymbol{r}_A,i\xi),\end{aligned} \tag{31}$$

$$\begin{aligned}U_p(\boldsymbol{r}_A)&=\frac{\hbar\mu_0}{2\pi}\int_0^\infty d\xi\,\mathrm{tr}\big[\boldsymbol{\beta}^p(i\xi)\cdot\mathbf{G}^{(1)}_{mm}(\boldsymbol{r}_A,\boldsymbol{r}_A,i\xi)\big]\\&=\frac{\hbar\mu_0}{2\pi}\int_0^\infty d\xi\,\beta^p(i\xi)\mathrm{tr}\mathbf{G}^{(1)}_{mm}(\boldsymbol{r}_A,\boldsymbol{r}_A,i\xi)\end{aligned} \tag{32}$$

with

$$\mathbf{G}_{ee}(\boldsymbol{r},\boldsymbol{r},\omega)=-\frac{\omega^2}{c^2}\mathbf{G}(\boldsymbol{r},\boldsymbol{r},\omega) \tag{33}$$

and

$$\begin{aligned}\boldsymbol{\alpha}(\omega)&=\lim_{\epsilon\to0}\frac{2}{\hbar}\sum_k\frac{\omega_A^k\boldsymbol{\mu}_A^{0k}\boldsymbol{\mu}_A^{k0}}{(\omega_A^k)^2-\omega^2-i\omega\epsilon}\\&=\lim_{\epsilon\to0}\frac{2}{3\hbar}\sum_k\frac{\omega_A^k|\boldsymbol{\mu}_A^{0k}|^2}{(\omega_A^k)^2-\omega^2-\mathrm{i}\omega\epsilon}\mathbf{I}=\alpha(\omega)\mathbf{I},\end{aligned} \tag{34}$$

$$\begin{aligned}\boldsymbol{\beta}^p(\omega)&=\lim_{\epsilon\to0}\frac{2}{\hbar}\sum_k\frac{\omega_A^k\boldsymbol{m}_A^{0k}\boldsymbol{m}_A^{k0}}{(\omega_A^k)^2-\omega^2-i\omega\epsilon}\\&=\lim_{\epsilon\to0}\frac{2}{3\hbar}\sum_k\frac{\omega_A^k|\boldsymbol{m}_A^{0k}|^2}{(\omega_A^k)^2-\omega^2-i\omega\epsilon}\mathbf{I}=\beta^p(\omega)\mathbf{I}\end{aligned} \tag{35}$$

[$\omega_A^k=(E_A^k-E_A^0)/\hbar$, $\boldsymbol{\mu}_A^{0k}=\langle 0|\hat{\boldsymbol{\mu}}_A|k\rangle$, $\boldsymbol{m}_A^{0k}=\langle 0|\hat{\boldsymbol{m}}_A|k\rangle$] denoting the polarizability and paramagnetizability of the atom, respectively. Introducing the total magnetizability

$$\boldsymbol{\beta}(\omega)=\boldsymbol{\beta}^p(\omega)+\boldsymbol{\beta}^d=[\beta^p(\omega)+\beta^d]\mathbf{I}=\beta(\omega)\mathbf{I}, \tag{36}$$

the magnetic part of the CP potential reads

$$\begin{aligned} U_m(\boldsymbol{r}_A) &= U_p(\boldsymbol{r}_A) + U_d(\boldsymbol{r}_A) \\ &= \frac{\hbar\mu_0}{2\pi}\int_0^\infty d\xi\, \mathrm{tr}\big[\boldsymbol{\beta}(i\xi)\cdot\mathbf{G}^{(1)}_{mm}(\boldsymbol{r}_A,\boldsymbol{r}_A,i\xi)\big] \\ &= \frac{\hbar\mu_0}{2\pi}\int_0^\infty d\xi\, \beta(i\xi)\mathrm{tr}\big[\mathbf{G}^{(1)}_{mm}(\boldsymbol{r}_A,\boldsymbol{r}_A,i\xi)\big] \end{aligned} \tag{37}$$

and the total CP potential is given by

$$U(\boldsymbol{r}_A) = U_e(\boldsymbol{r}_A) + U_m(\boldsymbol{r}_A). \tag{38}$$

We have thus generalized previous results for the CP potential of an atom with electric and paramagnetic properties to one that also exhibits nontrivial diamagnetic properties. It is found that despite the different interaction terms and perturbative orders (first order instead of second order), the extension to a diamagnetic atom can be obtained formally by including the diamagnetic contribution in the magnetizability, $\boldsymbol{\beta}^p(\omega) \mapsto \boldsymbol{\beta}(\omega) = \boldsymbol{\beta}^p(\omega) + \boldsymbol{\beta}^d$. In particular, the local-field corrected potentials for atoms embedded in a medium as derived in Ref. [18] remain valid with this replacement.

By introducing $\boldsymbol{\alpha}^e(\omega) = \boldsymbol{\alpha}(\omega)$, $\boldsymbol{\alpha}^m(\omega) = \boldsymbol{\beta}(\omega)/c^2$, the electric and magnetic parts of the CP potential can be given in the compact notation

$$\begin{aligned} U_\lambda(\boldsymbol{r}_A) &= \frac{\hbar}{2\pi\varepsilon_0}\int_0^\infty d\xi \mathrm{tr}\big[\boldsymbol{\alpha}^\lambda(i\xi)\cdot\mathbf{G}^{(1)}_{\lambda\lambda}(\boldsymbol{r}_A,\boldsymbol{r}_A,i\xi)\big] \\ &= \frac{\hbar}{2\pi\varepsilon_0}\int_0^\infty d\xi\, \alpha^\lambda(i\xi)\mathrm{tr}\mathbf{G}^{(1)}_{\lambda\lambda}(\boldsymbol{r}_A,\boldsymbol{r}_A,i\xi) \end{aligned} \tag{39}$$

($\lambda = e,m$).

There are two important differences between the diamagnetic and the paramagnetic magnetizabilities which will have an impact on the associated potentials. First, the diamagnetizability has an opposite sign with respect to the paramagnetizability, which is a consequence of the Lenz rule. Second, in contrast to the paramagnetizability, which obeys the usual Kramers-Kronig relations, the diamagnetizability is independent of frequency.

B. Application: Atom in front of a perfectly reflecting mirror

Let us consider an isotropic atom at distance z_A from a perfectly reflecting planar mirror. The magnetoelectric properties of the mirror are characterized by $\varepsilon = \infty$ ($\mu = \infty$) for a perfectly conducting (infinitely permeable) plate. The Green tensor reads [31]

$$\boldsymbol{G}^{(1)}(\boldsymbol{r},\boldsymbol{r}',i\xi) = \pm\frac{1}{8\pi^2}\int\frac{d^2q}{b}\, e^{i(\boldsymbol{q}_+\cdot\boldsymbol{r}-\boldsymbol{q}_-\cdot\boldsymbol{r}')}(\boldsymbol{e}_p^+\boldsymbol{e}_p^- - \boldsymbol{e}_s\boldsymbol{e}_s) \tag{40}$$

($\boldsymbol{q}_\pm = \boldsymbol{q} \pm ib\boldsymbol{e}_z$, $\boldsymbol{q}\perp\boldsymbol{e}_z$, $q = |\boldsymbol{q}|$, $b = \sqrt{q^2+\xi^2/c^2}$), with the upper (lower) sign corresponding to a perfectly conducting (infinitely permeable) plate and the polarization vectors $\boldsymbol{e}_s$ and $\boldsymbol{e}_p$ being defined by ($\boldsymbol{e}_q = \boldsymbol{q}/q$)

$$\boldsymbol{e}_s = \boldsymbol{e}_q\times\boldsymbol{e}_z, \quad \boldsymbol{e}_p^\pm = \frac{c}{\xi}(-iq\boldsymbol{e}_z \mp b\boldsymbol{e}_q). \tag{41}$$

Evaluating the double curl of the Green tensor, we find that $\mathbf{G}^{(1)}_{mm}(\boldsymbol{r},\boldsymbol{r}',i\xi)$ is equal to $-\xi^2c^{-2}\mathbf{G}^{(1)}(\boldsymbol{r},\boldsymbol{r}',i\xi)$. Substituting this into Eq. (30) and carrying out the $\boldsymbol{q}$ integral, one finds

$$\begin{aligned} U_d(z_A) = \pm\frac{\hbar\mu_0\beta^d}{16\pi^2 z_A^3}\int_0^\infty d\xi\, e^{-2z_A\xi/c} \\ \times\left(1 + 2\frac{z_A\xi}{c} + 2\frac{z_A^2\xi^2}{c^2}\right). \end{aligned} \tag{42}$$

After performing the ξ integral, we find an attractive (repulsive) CP potential,

$$U_d(z_A) = \pm\frac{3\hbar\mu_0 c\beta^d}{32\pi z_A^4} = \mp\frac{3\hbar\mu_0 c}{32\pi z_A^4}\sum_{\alpha\in A}\frac{q_\alpha^2}{6m_\alpha}\langle\hat{\boldsymbol{r}}_\alpha^2\rangle, \tag{43}$$

of a diamagnetic atom in front of a perfectly conducting (permeable) plate. It is given by a universal $1/z_A^4$ power law.

In Table I, we compare this result with the known findings for electric and paramagnetic atoms. We recall that electric and paramagnetic atoms interact with conducting and permeable plates according to an "equals attract, opposites repel" rule: An electric plate attracts electric atoms while repelling (para)magnetic atoms, with corresponding results for a (para)magnetic plate. In contrast to this, diamagnetic potentials carry a sign that is opposite to that of their paramagnetic counterparts. This is due to the Lenz rule as encoded in the minus sign in the diamagnetic magnetizability, (12). The diamagnetic CP potential thus has the same sign as the corresponding electric potential.

Another difference is the fact that the wavelengths of electric and paramagnetic dipole transitions divide the CP potential into two asymptotic regimes: the nonretarded regime of distances smaller than these wavelengths and the opposite, retarded regime. The CP potential follows two distinct $1/z_A^3$

TABLE I. Signs and asymptotic power laws of the ground-state CP potential of an electric, paramagnetic, or diamagnetic atom with a perfectly reflecting plate.

	Plate			
	Perfectly conducting		Infinitely permeable	
Atom	Retarded limit	Nonretarded limit	Retarded limit	Nonretarded limit
Electric	$-\frac{1}{z_A^4}$	$-\frac{1}{z_A^3}$	$+\frac{1}{z_A^4}$	$+\frac{1}{z_A^3}$
Paramagnetic	$+\frac{1}{z_A^4}$	$+\frac{1}{z_A^3}$	$-\frac{1}{z_A^4}$	$-\frac{1}{z_A^3}$
Diamagnetic	$-\frac{1}{z_A^4}$		$+\frac{1}{z_A^4}$	

and $1/z_A^4$ power laws in these regimes, respectively. On the other hand, the frequency-independent diamagnetic magnetizability lacks an intrinsic length scale. As a result, the CP interaction with a perfectly reflecting plate follows a retarded $1/z_A^4$ power law at all distances.

IV. TWO-ATOM VAN DER WAALS INTERACTION

Similarly to the single-atom case, the body-assisted vdW force between two atoms can be derived from the two-atom vdW potential $U(\boldsymbol{r}_A,\boldsymbol{r}_B)$, which is that part of the energy shift depending on the positions of both atoms,

$$U(\boldsymbol{r}_A,\boldsymbol{r}_B) = \Delta E(\boldsymbol{r}_A,\boldsymbol{r}_B). \tag{44}$$

A. Perturbation theory

Again, we assume the atom-field system to be in its uncoupled ground state $|0_A\rangle|0_B\rangle|\{0\}\rangle$, but now we have to calculate the leading-order two-atom energy shift. We begin with two purely diamagnetic atoms, in which case the vdW potential follows from the second-order energy shift

$$\Delta_2 E = \sum_{\phi\neq 0} \frac{\langle 0|\hat{H}^d_{AF}+\hat{H}^d_{BF}|\phi\rangle\langle\phi|\hat{H}^d_{AF}+\hat{H}^d_{BF}|0\rangle}{E_0-E_\phi}. \tag{45}$$

Note that the first-order energy shift just leads to the sum of two diamagnetic CP potentials as discussed in Sec. III A. Due to the diamagnetic interaction Hamiltonian's being quadratic in the fields, the vdW shift already appears in second-order perturbation theory rather than in fourth order as for electric and paramagnetic dipole transitions.

The numerator of the term in Eq. (45), when read from right to left, represents processes in which the system starts from its ground state, goes to a state $|\phi\rangle$ due to a first atom-field interaction, and, finally, returns to its ground state in the course of a second interaction. As the interaction Hamiltonian is quadratic in the magnetic field, the intermediate state $|\phi\rangle$ must involve the field in its ground state or exhibit two field excitations (photons). Only the latter case leads to a genuine two-atom interaction,

$$|\phi\rangle = |0_A\rangle|0_B\rangle|1_{\lambda i}(\boldsymbol{r},\omega),1_{\lambda' i'}(\boldsymbol{r}',\omega')\rangle, \tag{46}$$

with the two-photon state being defined by

$$|1_{\lambda i}(\boldsymbol{r},\omega),1_{\lambda' i'}(\boldsymbol{r}',\omega')\rangle = \frac{1}{\sqrt{2}}\hat{f}^\dagger_{\lambda' i'}(\boldsymbol{r}',\omega')\hat{f}^\dagger_{\lambda i}(\boldsymbol{r},\omega)|\{0\}\rangle. \tag{47}$$

The photons must have been emitted by one of the atoms and then absorbed by the other. This is schematically illustrated in Fig. 1, where the solid lines and the dashed lines represent the atoms and the photons, respectively (where time progresses in the upwards direction). Note that the formal sum in Eq. (45) involves sums over λ, λ', i, and i' as well as integrals over $\boldsymbol{r}$, $\boldsymbol{r}'$, ω, and ω'. We begin with the contribution $\Delta_2 E_{(i)}$ to the energy shift corresponding to Fig. 1(i), where atom A emits two photons and atom B absorbs them, i.e., where the second matrix element in the perturbative energy shift, (45), is due to the diamagnetic interaction of atom A and the first one is due to that of atom B. The required two-photon emission matrix

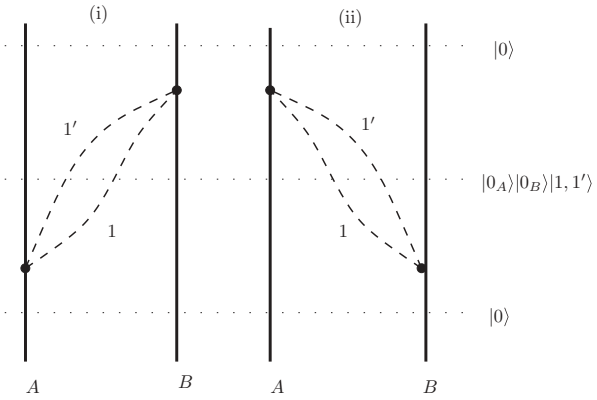

FIG. 1. Contributions to the vdW interaction of two diamagnetic atoms.

element for atom A takes the form

$$\langle\phi|\hat{H}^d_{AF}|0\rangle = \frac{-\beta^d_{Ajk}}{2\sqrt{2}}\langle\{0\}|\hat{f}_{\lambda' i'}(\boldsymbol{r}',\omega')\hat{f}_{\lambda i}(\boldsymbol{r},\omega)\hat{B}_j(\boldsymbol{r}_A) \times \hat{B}_k(\boldsymbol{r}_A)|\{0\}\rangle, \tag{48}$$

where Eqs. (11), (46), and (47) have been used. The two-photon absorption matrix element $\langle 0|\hat{H}^d_{BF}|\phi\rangle$ can be obtained by taking the complex conjugate of the above and replacing the labels A with B. After substituting Eq. (15) for the magnetic field and making use of the commutation relations, (2) and (3), the respective term in Eq. (45) reads

$$\begin{aligned}&\frac{\langle 0|\hat{H}^d_{BF}|\phi\rangle\langle\phi|\hat{H}^d_{AF}|0\rangle}{E_0-E_\phi}\\ &= -\frac{1}{2\omega^2\omega'^2\hbar(\omega+\omega')}\\ &\quad\times \mathrm{tr}\big\{\boldsymbol{\beta}^d_A\cdot\big[\boldsymbol{\nabla}_A\times\mathbf{G}^*_\lambda(\boldsymbol{r}_A,\boldsymbol{r},\omega)\cdot\mathbf{G}^{\mathsf{T}}_{\lambda'}(\boldsymbol{r}_B,\boldsymbol{r},\omega)\times\boldsymbol{\nabla}_B\big]\\ &\quad\cdot\boldsymbol{\beta}^d_B\cdot\big[\boldsymbol{\nabla}_B\times\mathbf{G}_{\lambda'}(\boldsymbol{r}_B,\boldsymbol{r}',\omega')\cdot\mathbf{G}^{*\mathsf{T}}_{\lambda}(\boldsymbol{r}_A,\boldsymbol{r}',\omega')\times\boldsymbol{\nabla}_A\big]\big\}.\end{aligned} \tag{49}$$

At this stage, performing the integrals over $\boldsymbol{r}$ and $\boldsymbol{r}'$ included in Eq. (45) by means of the integral relation (22) results in

$$\begin{aligned}\Delta_2 E_{(i)} = -\frac{\hbar\mu_0^2}{2\pi^2}\int_0^\infty d\omega\int_0^\infty d\omega'\frac{1}{\omega+\omega'}\\ \times\mathrm{tr}\big[\boldsymbol{\beta}^d_A\cdot\mathrm{Im}\,\mathbf{G}_{mm}(\boldsymbol{r}_A,\boldsymbol{r}_B,\omega)\\ \cdot\boldsymbol{\beta}^d_B\cdot\mathrm{Im}\,\mathbf{G}_{mm}(\boldsymbol{r}_B,\boldsymbol{r}_A,\omega')\big]\end{aligned} \tag{50}$$

[recall Eq. (27)]. It can easily be seen that contribution (ii) as depicted in Fig. 1(ii) is exactly the same. We hence find

$$\begin{aligned}U_{dd}(\boldsymbol{r}_A,\boldsymbol{r}_B) = -\frac{\hbar\mu_0^2}{\pi^2}\int_0^\infty d\omega\int_0^\infty d\omega'\frac{1}{\omega+\omega'}\\ \times\mathrm{tr}\big[\boldsymbol{\beta}^d_A\cdot\mathrm{Im}\,\mathbf{G}_{mm}(\boldsymbol{r}_A,\boldsymbol{r}_B,\omega)\\ \cdot\boldsymbol{\beta}^d_B\cdot\mathrm{Im}\,\mathbf{G}_{mm}(\boldsymbol{r}_B,\boldsymbol{r}_A,\omega')\big].\end{aligned} \tag{51}$$

As for the single-atom potential, the result can be simplified via contour-integral techniques. We first write

$$\int_0^\infty\frac{d\omega'}{\omega+\omega'}\mathrm{Im}\mathbf{G}_{mm}(\omega') = \mathrm{Im}\int_0^\infty\frac{d\omega'}{\omega+\omega'}\mathbf{G}_{mm}(\omega') \tag{52}$$

and use the fact that the Green tensor is analytic in the upper half of the complex frequency plane including the real axis. Hence, we may replace the integral with an integral along the positive imaginary frequency axis and use the Schwarz reflection principle, (20), to obtain

$$\int_0^\infty \frac{d\omega'}{\omega+\omega'}\,\mathrm{Im}\mathbf{G}_{mm}(\omega') = \int_0^\infty d\xi\,\frac{\omega}{\omega^2+\xi^2}\,\mathbf{G}_{mm}(i\xi). \quad (53)$$

Substituting this result into Eq. (51), we next evaluate the integral over ω,

$$\int_0^\infty d\omega\,\frac{\omega\mathrm{Im}\mathbf{G}_{mm}(\omega)}{\omega^2+\xi^2} = \mathrm{Im}\int_0^\infty d\omega\,\frac{\omega\mathbf{G}_{mm}(\omega)}{\omega^2+\xi^2}. \quad (54)$$

The integrand on the right-hand side has a simple pole at $\omega = i\xi$ in the upper half of the complex frequency plane. Again using Cauchy's theorem, we transform this integral into a principal value integral along the positive imaginary axis, an integral along an infinitesimal half-circle around the pole, and a (vanishing) integral along an infinite quarter-circle. The first integral is real, while the second integral results in $(i\pi/2)\mathbf{G}_{mm}(i\xi)$, so that

$$\begin{aligned}&\int_0^\infty d\omega\,\frac{\omega\mathrm{Im}\mathbf{G}_{mm}(\omega)}{\omega^2+\xi^2}\\ &= \mathrm{Im}\left[P\int_0^\infty dv\,\frac{v\mathbf{G}_{mm}(iv)}{v^2-\xi^2} + i\frac{\pi}{2}\,\mathbf{G}_{mm}(i\xi)\right]\\ &= \frac{\pi}{2}\,\mathbf{G}_{mm}(i\xi)\end{aligned} \quad (55)$$

(P: principal value). After substituting this result together with Eq. (53) into Eq. (51), we find the CP potential of two diamagnetic atoms,

$$\begin{aligned}U_{dd}(\boldsymbol{r}_A,\boldsymbol{r}_B) &= -\frac{\hbar\mu_0^2}{2\pi}\int_0^\infty d\xi\,\mathrm{tr}\big[\boldsymbol{\beta}_A^d\cdot\mathbf{G}_{mm}(\boldsymbol{r}_A,\boldsymbol{r}_B,i\xi)\\ &\quad\cdot\boldsymbol{\beta}_B^d\cdot\mathbf{G}_{mm}(\boldsymbol{r}_B,\boldsymbol{r}_A,i\xi)\big]\\ &= -\frac{\hbar\mu_0^2}{2\pi}\int_0^\infty d\xi\,\beta_A^d\beta_B^d\\ &\quad\times\mathrm{tr}[\mathbf{G}_{mm}(\boldsymbol{r}_A,\boldsymbol{r}_B,i\xi)\cdot\mathbf{G}_{mm}(\boldsymbol{r}_B,\boldsymbol{r}_A,i\xi)],\end{aligned} \quad (56)$$

where the second equality holds for isotropic atoms.

Let us consider next the interaction of a diamagnetic atom A with an electric atom B. It can be seen easily that the leading two-atom energy shift is of third order in this case,

$$\Delta_3 E = \sum_{\phi,\psi\neq 0}\frac{\langle 0|\hat{H}_{\mathrm{int}}|\psi\rangle\langle\psi|\hat{H}_{\mathrm{int}}|\phi\rangle\langle\phi|\hat{H}_{\mathrm{int}}|0\rangle}{(E_\psi-E_0)(E_\phi-E_0)} \quad (57)$$

with

$$\hat{H}_{\mathrm{int}} = \hat{H}_{AF}^d + \hat{H}_{BF}^e = -\tfrac{1}{2}\hat{\boldsymbol{B}}(\boldsymbol{r}_A)\cdot\hat{\boldsymbol{\beta}}_A^d\cdot\hat{\boldsymbol{B}}(\boldsymbol{r}_A) - \hat{\boldsymbol{\mu}}_B\cdot\hat{\boldsymbol{E}}(\boldsymbol{r}_B). \quad (58)$$

The relevant intermediate states $|\phi\rangle$ and $|\psi\rangle$ can easily be determined with the help of the diagrams in Fig. 2. Let us begin with Fig. 2(i), which corresponds to the the case where atom A emits two photons and atom B absorbs them one after another, so the relevant intermediate states are

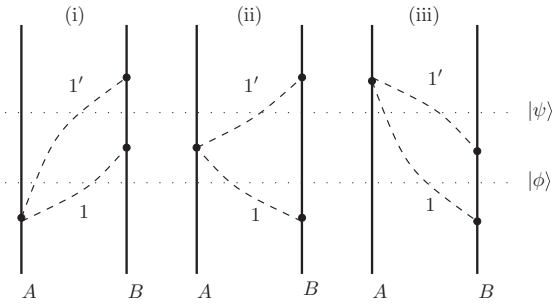

FIG. 2. Contributions to the vdW interaction of a diamagnetic atom A with an electric atom B.

$$|\phi\rangle = |0_A\rangle|0_B\rangle|1_{\lambda i}(\boldsymbol{r},\omega),1_{\lambda' i'}(\boldsymbol{r}',\omega')\rangle, \quad (59)$$

$$|\psi\rangle = |0_A\rangle|n_B\rangle|1_{\lambda'' i''}(\boldsymbol{r}'',\omega'')\rangle. \quad (60)$$

In the two-photon emission matrix element, $\hat{H}_{\mathrm{int}}$ has to be replaced with $\hat{H}_{AF}^d$. This leads, as outlined following Eq. (48), to

$$\begin{aligned}\langle\phi|\hat{H}_{AF}^d|0\rangle = -\frac{1}{\sqrt{2}\omega\omega'}&\mathbf{G}_\lambda^{*\mathsf{T}}(\boldsymbol{r}_A,\boldsymbol{r},\omega)\times\overleftarrow{\nabla}_A\cdot\boldsymbol{\beta}_A^d\cdot\nabla_A\\ &\times\mathbf{G}_{\lambda'}^*(\boldsymbol{r}_A,\boldsymbol{r}',\omega'),\end{aligned} \quad (61)$$

while in the other two matrix elements, $\hat{H}_{\mathrm{int}}$ has to be replaced with $\hat{H}_{BF}^e$. This yields

$$\begin{aligned}&\langle\psi|-\hat{\boldsymbol{\mu}}_B\cdot\hat{\boldsymbol{E}}(\boldsymbol{r}_B)|\phi\rangle\\ &= \frac{-1}{\sqrt{2}}\big\{\big[\boldsymbol{\mu}_B^{n0}\cdot\mathbf{G}_\lambda(\boldsymbol{r}_B,\boldsymbol{r},\omega)\big]_i\delta_{\lambda'\lambda''}\delta_{i'i''}\delta(\boldsymbol{r}'-\boldsymbol{r}'')\delta(\omega'-\omega'')\\ &\quad+\big[\boldsymbol{\mu}_B^{n0}\cdot\mathbf{G}_{\lambda'}(\boldsymbol{r}_B,\boldsymbol{r}',\omega')\big]_{i'}\delta_{\lambda\lambda''}\delta_{ii''}\delta(\boldsymbol{r}-\boldsymbol{r}'')\delta(\omega-\omega'')\big\},\end{aligned} \quad (62)$$

$$\langle 0|-\hat{\boldsymbol{\mu}}_B\cdot\hat{\boldsymbol{E}}(\boldsymbol{r}_B)|\psi\rangle = -\big[\boldsymbol{\mu}_B^{0n}\cdot\mathbf{G}_{\lambda''}(\boldsymbol{r}_B,\boldsymbol{r}'',\omega'')\big]_{i''}, \quad (63)$$

where expression (14) for the electric field and commutation relations (2) and (3) have been used. Substituting these matrix elements into Eq. (57) and performing the integrals over $\boldsymbol{r}$, $\boldsymbol{r}'$, and $\boldsymbol{r}''$ using the integral relation, (22), we find the contribution of Fig. 2(i) to the energy shift to be

$$\begin{aligned}&\Delta_3 E_{(\mathrm{i})}\\ &= \frac{\mu_0^2}{\pi^2}\int_0^\infty d\omega\int_0^\infty d\omega'\,\frac{\omega\omega'}{(\omega+\omega')(\omega_B^n+\omega)}\\ &\quad\times\big[\boldsymbol{d}_B^{0n}\cdot\mathrm{Im}\mathbf{K}^{\mathsf{T}}(\boldsymbol{r}_A,\boldsymbol{r}_B,\omega)\cdot\boldsymbol{\beta}_A^d\cdot\mathrm{Im}\,\mathbf{K}(\boldsymbol{r}_A,\boldsymbol{r}_B,\omega')\cdot\boldsymbol{d}_B^{n0}\big],\end{aligned} \quad (64)$$

where

$$\mathbf{K}(\boldsymbol{r},\boldsymbol{r}',\omega) = \nabla\times\mathbf{G}(\boldsymbol{r},\boldsymbol{r}',\omega). \quad (65)$$

The contribution to the energy shift from Figs. 2(ii) and 2(iii) result in terms similar to Eq. (64) except that the energy denominator $(\omega+\omega')(\omega_B^n+\omega)$ has to be replaced with $(-\omega_B^n-\omega')(\omega_B^n+\omega)$ for Fig. 2(ii) and with $(\omega+\omega')(\omega_B^n+\omega')$ for Fig. 2(iii). Summing all contributions, we find

$$\Delta_3 E = \frac{2\mu_0^2}{\pi^2}\int_0^\infty d\omega \int_0^\infty \frac{d\omega'\,\omega_B^n \omega\omega'}{(\omega_B^n+\omega)(\omega+\omega')(\omega_B^n+\omega')} \times\big[\boldsymbol{d}_B^{0n}\cdot \mathrm{Im}\,\mathbf{K}^{\mathsf{T}}(\boldsymbol{r}_A,\boldsymbol{r}_B,\omega)\cdot\boldsymbol{\beta}_A^d\cdot \mathrm{Im}\,\mathbf{K}(\boldsymbol{r}_A,\boldsymbol{r}_B,\omega')\cdot\boldsymbol{d}_B^{n0}\big]. \tag{66}$$

By transforming the ω' integral by means of contour integral to run along the positive imaginary axis,

$$\int_0^\infty d\omega' \frac{\omega' \mathrm{Im}\,\mathbf{K}(\omega')}{(\omega+\omega')(\omega_B^n+\omega')} = \int_0^\infty d\xi \frac{\xi^2(\omega_B^n+\omega)\mathbf{K}(i\xi)}{(\omega^2+\xi^2)\big[(\omega_B^n)^2+\xi^2\big]}, \tag{67}$$

and then performing the ω integral in the way explained before Eq. (55), one obtains

$$\begin{aligned} U_{de}(\boldsymbol{r}_A,\boldsymbol{r}_B) &= \frac{\hbar\mu_0^2}{2\pi}\int_0^\infty d\xi\,\xi^2 \mathrm{tr}\big[\boldsymbol{\beta}_A^d\cdot\mathbf{K}(\boldsymbol{r}_A,\boldsymbol{r}_B,i\xi) \cdot\boldsymbol{\alpha}_B(i\xi)\cdot\mathbf{K}^{\mathsf{T}}(\boldsymbol{r}_A,\boldsymbol{r}_B,i\xi)\big] \\ &= \frac{\hbar\mu_0^2}{2\pi}\int_0^\infty d\xi\,\xi^2\beta_A^d\,\alpha_B(i\xi) \times \mathrm{tr}[\mathbf{K}(\boldsymbol{r}_A,\boldsymbol{r}_B,i\xi)\cdot\mathbf{K}^{\mathsf{T}}(\boldsymbol{r}_A,\boldsymbol{r}_B,i\xi)], \end{aligned} \tag{68}$$

where definition (34) has been used and the second equality holds for isotropic atoms. Our result, (68), for the vdW potential of a diamagnetic atom A with an electric atom B may be written in the form $(\boldsymbol{\beta}_A^d \equiv c^2\boldsymbol{\alpha}_A^d)$

$$\begin{aligned} U_{de}(\boldsymbol{r}_A,\boldsymbol{r}_B) &= -\frac{\hbar}{2\pi\varepsilon_0^2}\int_0^\infty d\xi\,\mathrm{tr}\big[\boldsymbol{\alpha}_A^d\cdot\mathbf{G}_{me}(\boldsymbol{r}_A,\boldsymbol{r}_B,i\xi) \cdot\boldsymbol{\alpha}_B^e(i\xi)\cdot\mathbf{G}_{em}(\boldsymbol{r}_B,\boldsymbol{r}_A,i\xi)\big] \\ &= -\frac{\hbar}{2\pi\varepsilon_0^2}\int_0^\infty d\xi\,\alpha_A^d\,\alpha_B^e(i\xi) \times\mathrm{tr}[\mathbf{G}_{me}(\boldsymbol{r}_A,\boldsymbol{r}_B,i\xi)\cdot\mathbf{G}_{em}(\boldsymbol{r}_B,\boldsymbol{r}_A,i\xi)], \end{aligned} \tag{69}$$

where

$$\mathbf{G}_{me}(\boldsymbol{r},\boldsymbol{r}',\omega) = \frac{i\omega}{c}\mathbf{K}(\boldsymbol{r},\boldsymbol{r}',\omega) = \frac{i\omega}{c}\nabla\times\mathbf{G}(\boldsymbol{r},\boldsymbol{r}',\omega), \tag{70}$$

$$\mathbf{G}_{em}(\boldsymbol{r},\boldsymbol{r}',\omega) = \frac{-i\omega}{c}\mathbf{K}^{\mathsf{T}}(\boldsymbol{r}',\boldsymbol{r},\omega) = \frac{i\omega}{c}\mathbf{G}(\boldsymbol{r},\boldsymbol{r}',\omega)\times\overleftarrow{\nabla}'. \tag{71}$$

Obviously, the interaction between an electric atom A and a diamagnetic atom B is given by the right-hand side of Eq. (68) with the labels A and B interchanged.

The vdW potential of a diamagnetic atom A with a paramagnetic one B can be calculated in a completely analogous way. The lowest-order energy shift is again given by third-order perturbation theory, with the possible intermediate states given again as depicted in the diagrams in Fig. 2. The result is $(\beta_A^p \equiv c^2\alpha_A^p)$

$$\begin{aligned} U_{dp}(\boldsymbol{r}_A,\boldsymbol{r}_B) &= -\frac{\hbar}{2\pi\varepsilon_0^2}\int_0^\infty d\xi\,\mathrm{tr}\big[\boldsymbol{\alpha}_A^d\cdot\mathbf{G}_{mm}(\boldsymbol{r}_A,\boldsymbol{r}_B,i\xi) \cdot\boldsymbol{\alpha}_B^p(i\xi)\cdot\mathbf{G}_{mm}(\boldsymbol{r}_B,\boldsymbol{r}_A,i\xi)\big] \\ &= -\frac{\hbar}{2\pi\varepsilon_0^2}\int_0^\infty d\xi\,\alpha_A^d\,\alpha_B^p(i\xi) \times\mathrm{tr}[\mathbf{G}_{mm}(\boldsymbol{r}_A,\boldsymbol{r}_B,i\xi)\cdot\mathbf{G}_{mm}(\boldsymbol{r}_B,\boldsymbol{r}_A,i\xi)]. \end{aligned} \tag{72}$$

We have thus generalized the body-assisted vdW potential to allow for atoms with a diamagnetic response. Recalling the previously derived interaction of two paramagnetic atoms [18], we again observe that the generalization can be achieved by replacing the paramagnetizability of each atom with the total magnetizability, $\boldsymbol{\beta}^p(\omega)\mapsto\boldsymbol{\beta}(\omega)=\boldsymbol{\beta}^p(\omega)+\boldsymbol{\beta}^d$. The complete vdW potential of two atoms with nontrivial electric, paramagnetic, and diamagnetic properties can thus be given as

$$U(\boldsymbol{r}_A,\boldsymbol{r}_B) = \sum_{\lambda,\lambda'=e,m} U_{\lambda\lambda'}(\boldsymbol{r}_A,\boldsymbol{r}_B), \tag{73}$$

with

$$\begin{aligned} U_{\lambda\lambda'}(\boldsymbol{r}_A,\boldsymbol{r}_B) &= -\frac{\hbar}{2\pi\varepsilon_0^2}\int_0^\infty d\xi\,\mathrm{tr}\big[\boldsymbol{\alpha}_A^\lambda(i\xi)\cdot\mathbf{G}_{\lambda\lambda'}(\boldsymbol{r}_A,\boldsymbol{r}_B,i\xi) \cdot\boldsymbol{\alpha}_B^{\lambda'}(i\xi)\cdot\mathbf{G}_{\lambda'\lambda}(\boldsymbol{r}_B,\boldsymbol{r}_A,i\xi)\big] \\ &= -\frac{\hbar}{2\pi\varepsilon_0^2}\int_0^\infty d\xi\,\alpha_A^\lambda(i\xi)\,\alpha_B^{\lambda'}(i\xi) \times\mathrm{tr}\big[\mathbf{G}_{\lambda\lambda'}(\boldsymbol{r}_A,\boldsymbol{r}_B,i\xi)\cdot\mathbf{G}_{\lambda'\lambda}(\boldsymbol{r}_B,\boldsymbol{r}_A,i\xi)\big]. \end{aligned} \tag{74}$$

Again, this implies that previous results for local-field corrected vdW potentials [18] remain valid for diamagnetic atoms.

B. Application: Two atoms in free space

As the simplest example of the two-atom interaction, let us consider two isotropic atoms A and B interacting with each other in free space. The Green tensor reads (see, e.g., Ref. [12])

$$\mathbf{G}^{(0)}(\boldsymbol{r}_A,\boldsymbol{r}_B,i\xi) = \frac{c^2}{4\pi\xi^2 l^3}[f(l\xi/c)\mathbf{I} - g(l\xi/c)\boldsymbol{e}_l\boldsymbol{e}_l]\mathrm{e}^{-l\xi/c} \tag{75}$$

$(\boldsymbol{r}_A\neq\boldsymbol{r}_B)$, where $\boldsymbol{l}=\boldsymbol{r}_A-\boldsymbol{r}_B$, $l=|\boldsymbol{l}|$, $\boldsymbol{e}_l=\boldsymbol{l}/l$, and

$$f(x)=1+x+x^2, \quad g(x)=3+3x+x^2. \tag{76}$$

Evaluating the curls as contained in definitions (27), (70), and (71), one easily finds

$$\mathbf{G}_{ee}^{(0)}(\boldsymbol{r}_A,\boldsymbol{r}_B,i\xi) = \mathbf{G}_{mm}^{(0)}(\boldsymbol{r}_A,\boldsymbol{r}_B,i\xi) = \frac{\xi^2}{c^2}\mathbf{G}^{(0)}(\boldsymbol{r}_A,\boldsymbol{r}_B,i\xi), \tag{77}$$

$$\begin{aligned} \mathbf{G}_{me}^{(0)}(\boldsymbol{r}_A,\boldsymbol{r}_B,i\xi) &= -\mathbf{G}_{em}^{(0)}(\boldsymbol{r}_A,\boldsymbol{r}_B,i\xi) \\ &= \frac{\xi}{4\pi cl^2}(1+l\xi/c)\mathrm{e}^{-l\xi/c}\boldsymbol{e}_l\times\mathbf{I}. \end{aligned} \tag{78}$$

Substituting these into Eqs. (74) and (73) we obtain a total free-space vdW potential,

$$U(\boldsymbol{r}_A,\boldsymbol{r}_B) = U(l) = \frac{\hbar\mu_0^2}{16\pi^3}\Big\{ -\frac{1}{l^6}\int_0^\infty d\xi\,[c^4\alpha_A(i\xi)\alpha_B(i\xi) + \beta_A(i\xi)\beta_B(i\xi)]h_1(l\xi/c) + \frac{1}{l^4}\int_0^\infty d\xi\,\xi^2[\alpha_A(i\xi)\beta_B(i\xi) + \beta_A(i\xi)\alpha_B(i\xi)]h_2(l\xi/c)\Big\}, \tag{79}$$

where

$$h_1(x) = (3+6x+5x^2+2x^3+x^4)e^{-2x}, \tag{80}$$

$$h_2(x) = (1+2x+x^2)e^{-2x}. \tag{81}$$

As expected from the results in Sec. IV A, this result has the same form as the previously derived potential between electric and paramagnetic atoms [18], except that here the total magnetizability appears in place of the paramagnetic one.

It is of particular interest to inspect the behavior of the interaction potential in the nonretarded (retarded) limits, where the atom-atom separation is small (large) compared to the respective atomic wavelengths. We focus here on the contribution of the atomic diamagnetizabilities to the potential, given by Eq. (79) with $\beta(i\xi) \mapsto \beta^d$.

The interaction potential between a diamagnetic atom A and an electric atom B, using the explicit expression for the polarizability, (34), in Eq. (79), is found to be an attractive potential in the form

$$U_{de}(l) = -\frac{\mu_0^2|\beta_A^d|}{24\pi^3 l^4}\sum_k \omega_B^k|\boldsymbol{\mu}_B^{0k}|^2\int_0^\infty d\xi\,\frac{\xi^2}{\xi^2+(\omega_B^k)^2}\,h_2(l\xi/c). \tag{82}$$

To achieve the limiting cases mentioned above, we note that in the ξ integral, $\omega_B^k \ll \xi$ ($\omega_B^k \gg \xi$) holds in the nonretarded (retarded) limit. This leads to an l^{-5}-dependent and an l^{-7}-dependent potential for the nonretarded and retarded limits, respectively, as follows:

$$U_{de}^{\rm nr}(l) = -\frac{5\mu_0^2 c|\beta_A^d|}{96\pi^3 l^5}\sum_k \omega_B^k|\boldsymbol{\mu}_B^{0k}|^2, \tag{83}$$

$$U_{de}^{\rm r}(l) = -\frac{7\mu_0^2 c^3|\beta_A^d|}{96\pi^3 l^7}\sum_k \frac{|\boldsymbol{\mu}_B^{0k}|^2}{\omega_B^k} = -\frac{7\hbar\mu_0^2 c^3}{64\pi^3 l^7}\,|\beta_A^d|\alpha_B(0). \tag{84}$$

The diamagnetic-paramagnetic part of the two-atom interaction in free space is seen to be repulsive. It reads

$$U_{dp}(l) = \frac{\mu_0^2|\beta_A^d|}{24\pi^3 l^6}\sum_k \omega_B^k|\boldsymbol{m}_B^{0k}|^2\int_0^\infty d\xi\,\frac{1}{\xi^2+(\omega_B^k)^2}\,h_1(l\xi/c), \tag{85}$$

where Eq. (35) is used for the paramagnetizability of atom B. For the nonretarded limit Eq. (85) exhibits an l^{-6} dependence,

$$U_{dp}^{\rm nr}(l) = \frac{\mu_0^2|\beta_A^d|}{16\pi^2 l^6}\sum_k |\boldsymbol{m}_B^k|^2 = \frac{\mu_0^2|\beta_A^d|\langle\boldsymbol{m}_B^2\rangle}{16\pi^2 l^6}, \tag{86}$$

while in the retarded limit it tends to an l^{-7}-dependent potential,

$$U_{dp}^{\rm r}(l) = \frac{23\mu_0^2 c|\beta_A^d|}{96\pi^3 l^7}\sum_k \frac{|\boldsymbol{m}_B^{0k}|^2}{\omega_B^k} = \frac{23\hbar\mu_0^2 c}{64\pi^3 l^7}\,|\beta_A^d|\beta_B^p(0). \tag{87}$$

Finally, the diamagnetic-diamagnetic two-atom interaction in free space shows a unique attractive l^{-7} dependence for any arbitrary range of atom-atom separation, due to the frequency independence of diamagnetizabilities. As can be obtained from Eq. (79), it is given by

$$U_{dd}(l) = -\frac{23\hbar\mu_0^2 c}{64\pi^3 l^7}\,\beta_A^d\beta_B^d. \tag{88}$$

In Table II, we compare the signs and asymptotic power law of the vdW potentials involving diamagnetic atoms with the known results for purely electric or paramagnetic atoms [18]. We observe that the replacement of a paramagnetic atom with a diamagnetic one leads to a sign change of the vdW interaction as predicted by the Lenz rule. In addition, the frequency independence of the diamagnetic magnetizability leads to new asymptotic power laws, e.g., $1/l^5$ for the nonretarded electric-diamagnetic interaction. This result is in between the $1/l^6$ and the $1/l^4$ asymptotes found for the electric-electric and electric-paramagnetic cases.

C. Comparison with microscopic QED

It is instructive to compare the results obtained in this section for the vdW dispersion interaction between atoms in free space when either one or both species is diamagnetic using body-assisted fields with the result derived using microscopic QED. In this second approach it is common to use the well-established molecular QED theory [15,16]. For two

TABLE II. Signs and asymptotic power laws of ground-state van der Waals potentials of electric, paramagnetic, or diamagnetic atoms in free space.

	Atom A					
	Electric		Paramagnetic		Diamagnetic	
Atom B	Retarded limit	Nonretarded limit	Retarded limit	Nonretarded limit	Retarded limit	Nonretarded limit
Electric	$-\frac{1}{l^7}$	$-\frac{1}{l^6}$	$+\frac{1}{l^7}$	$+\frac{1}{l^4}$	$-\frac{1}{l^7}$	$-\frac{1}{l^5}$
Paramagnetic	$+\frac{1}{l^7}$	$+\frac{1}{l^4}$	$-\frac{1}{l^7}$	$-\frac{1}{l^6}$	$+\frac{1}{l^7}$	$+\frac{1}{l^6}$
Diamagnetic	$-\frac{1}{l^7}$	$-\frac{1}{l^5}$	$+\frac{1}{l^7}$	$+\frac{1}{l^6}$	$-\frac{1}{l^7}$	

mutually interacting particles A and B in vacuum coupled to the radiation field, the total Hamiltonian is written in the form of Eq. (13) with $\hat{H}_\xi$ given by Eq. (1). In the multipolar coupling scheme, the Hamiltonian operator for the free electromagnetic field is expressed as

$$\hat{H}_F = \frac{1}{2}\int d^3r \left[\frac{1}{\varepsilon_0}\hat{\boldsymbol{d}}^2(\boldsymbol{r}) + \frac{1}{\mu_0}\hat{\boldsymbol{b}}^2(\boldsymbol{r})\right] = \sum_{\boldsymbol{k},\lambda}\left[\hat{a}^{(\lambda)\dagger}(\boldsymbol{k})\hat{a}^{(\lambda)}(\boldsymbol{k}) + \frac{1}{2}\right]\hbar\omega, \tag{89}$$

where $\hat{\boldsymbol{d}}(\boldsymbol{r})$ and $\hat{\boldsymbol{b}}(\boldsymbol{r})$ are second quantized microscopic electric displacement and magnetic field operators, respectively. They are commonly written as a mode sum in terms of vacuum boson annihilation and creation operators $\hat{a}^{(\lambda)}(\boldsymbol{k})$ and $\hat{a}^{(\lambda)\dagger}(\boldsymbol{k})$ for a photon of wave vector $\boldsymbol{k}$, polarization index λ, and circular frequency $\omega = ck$, as in the second equality of Eq. (89). Analogous to Eq. (6) with Eqs. (7)–(9), the atom-field coupling Hamiltonian for the dispersion interactions of interest is

$$\hat{H}_{\xi F} = -\varepsilon_0^{-1}\hat{\boldsymbol{\mu}}_\xi \cdot \hat{\boldsymbol{d}}(\boldsymbol{r}_\xi) - \hat{\boldsymbol{m}}_\xi \cdot \hat{\boldsymbol{b}}(\boldsymbol{r}_\xi) + \sum_{\alpha\in\xi}\frac{q_\alpha^2}{8m_\alpha}[\hat{\tilde{\boldsymbol{r}}}_\alpha \times \hat{\boldsymbol{b}}(\boldsymbol{r}_\xi)]^2. \tag{90}$$

It is worth noting the explicit appearance in the last two expressions of the electric displacement field operator. This is a direct consequence of adopting the multipolar framework, where the field momentum canonically conjugate to the vector potential is proportional to $\hat{\boldsymbol{d}}(\boldsymbol{r})$ instead of to the electric field itself. This is a common feature of the microscopic and macrocopic approaches. In the latter, the quantized field $\hat{\boldsymbol{E}}(\mathbf{r})$ also refers to the Power-Zienau transformed electric field operator that has to be regarded as a displacement field with respect to the atomic polarization [12].

Dispersion potentials between a diamagnetic atom and an electrically polarizable and a magnetically susceptible atom, and between two diamagnetic atoms, may be computed in a manner similar to that already detailed. As before, the latter interaction is obtained via second-order perturbation theory and is depicted in Fig. 1, while the former two occur to third order and are described in Fig. 2. Matrix elements are evaluated using unperturbed product atom-field states $|n_\xi\rangle|m(\boldsymbol{k},\lambda)\rangle = |n_\xi; m(\boldsymbol{k},\lambda)\rangle$, where a number state representation is used to signify the number of photons present, in this case m.

As expected, results identical to Eqs. (82), (85), and (88) are found for the vdW dispersion potentials between a diamagnetic and an electric atom, between a diamagnetic and a paramagnetic one, and between two diamagnetic atoms, valid for the entire range of separation distance vector $\boldsymbol{l}$ beyond wave-function overlap of the two centers and extending out to infinity. Explicit details of this calculation may be found in Ref. [25], and the respective energy shifts are given by Eqs. (3.7), (3.20), and (3.43) in that paper. Furthermore, identical near- and far-zone asymptotic limits clearly follow in each case. The connection with the macroscopic approach can be established by computing all necessary field expectation values and evaluating them using the free-space Green tensor, (75).

V. DISCUSSION AND SUMMARY

We have calculated CP and vdW potentials of atoms with nontrivial diamagnetic properties in the presence of arbitrary magnetoelectric bodies on the basis of macroscopic QED and leading-order perturbation theory. The nonlinear interaction generating the diamagnetic interaction is quite different from the paramagnetic coupling and it leads to different perturbative orders. Nevertheless, we have found that diamagnetic atomic properties lead to dispersion potentials which formally resemble those of paramagnetic atoms where the diamagnetic magnetizability appears in place of the paramagnetic one. We have explicitly shown this correspondence for one- and two-atom potentials, but it is expected to hold for multiatom vdW potentials as well.

However, the fact that the diamagnetic magnetizability is negative and frequency independent leads to diamagnetic potentials that differ in signs and power laws from their paramagnetic counterparts. Diamagnetic dispersion interactions carry the same sign as the well-known electric potentials, which implies that diamagnetism alone cannot be used to realize repulsive potentials. The unique power laws resulting from the frequency independence imply that diamagnetic potentials have their strongest influence at short range.

ACKNOWLEDGMENTS

We thank G. Barton for discussions. This work was supported by the UK Engineering and Physical Sciences Research Council.

[1] L. D. Landau and E. M. Lifshitz, *Electrodynamics of Continuous Media* (Pergamon, Oxford, 1960).
[2] D. R. Smith, W. J. Padilla, D. C. Vier, S. C. Nemat-Nasser, and S. Schultz, Phys. Rev. Lett. **84**, 4184 (2000).
[3] R. A. Shelby, D. R. Smith, and S. Schultz, Science **292**, 77 (2001).
[4] R. Marqués, J. Martel, F. Mesa, and F. Medina, Phys. Rev. Lett. **89**, 183901 (2002).
[5] H. B. G. Casimir, Proc. Kon. Nederland. Akad. Wetensch. B **51**, 793 (1948).
[6] K. A. Milton, J. Phys. A **37**, R209 (2004).
[7] M. Bordag, G. L. Klimchitskaya, U. Mohideen, and V. M. Mostepanenko, *Advances in the Casimir Effect* (Oxford University Press, New York, 2009).
[8] D. Dalvit, P. Milonni, D. Roberts, and F. da Rosa (eds.), *Casimir Physics*, *Lecture Notes in Physics, Vol. 834* (Springer, Heidelberg, 2011).
[9] C. Hertlein, L. Helden, A. Gambassi, S. Dietrich, and C. Bechinger, Nature (London) **451**, 172 (2007).
[10] H. B. G. Casimir and D. Polder, Phys. Rev. **73**, 360 (1948).
[11] S. Y. Buhmann and D.-G. Welsch, Prog. Quantum Electron. **31**, 51 (2007).

[12] S. Scheel and S. Y. Buhmann, Acta Phys. Slovaca **58**, 675 (2008).
[13] T. G. Philbin, New J. Phys. **12**, 123008 (2010).
[14] S. A. R. Horsley, Phys. Rev. A **84**, 063822 (2011).
[15] D. P. Craig and T. Thirunamachandran, *Molecular Quantum Electrodynamics* (Academic Press, London, 1984).
[16] A. Salam, *Molecular Quantum Electrodynamics* (John Wiley & Sons, Upper Saddle River, NJ, 2010).
[17] H. Safari, S. Y. Buhmann, D.-G. Welsch, and H. T. Dung, Phys. Rev. A **74**, 042101 (2006).
[18] H. Safari, D.-G. Welsch, S. Y. Buhmann, and S. Scheel, Phys. Rev. A **78**, 062901 (2008).
[19] A. Sambale, S. Y. Buhmann, D.-G. Welsch, and M. S. Tomaš, Phys. Rev. A **75**, 042109 (2007).
[20] S. Spagnolo, D. A. R. Dalvit, and P. W. Milonni, Phys. Rev. A **75**, 052117 (2007).
[21] C. Mavroyannis and M. J. Stephen, Mol. Phys. **5**, 629 (1962).
[22] T. Thirunamachandran, Phys. Scripta, T **21**, 123 (1988).
[23] J. K. Jenkins, A. Salam, and T. Thirunamachandran, Phys. Rev. A **50**, 4767 (1994).
[24] A. Salam and T. Thirunamachandran, J. Chem. Phys. **104**, 5094 (1996).
[25] A. Salam, J. Phys. B **33**, 2181 (2000).
[26] A. Salam, Int. J. Quantum Chemistry **73**, 487 (2000).
[27] J. F. Babb, Adv. At. Mol. Opt. Phys. **59**, 1 (2010).
[28] M. Marinescu and L. You, Phys. Rev. A **59**, 1936 (1999).
[29] S. Y. Buhmann, L. Knöll, D. G. Welsch, and H. T. Dung, Phys. Rev. A **70**, 052117 (2004).
[30] J. A. Crosse, S. Å. Ellingsen, K. Clements, S. Y. Buhmann, and S. Scheel, Phys. Rev. A **82**, 010901(R) (2010).
[31] M. S. Tomaš, Phys. Rev. A **51**, 2545 (1995).

New Journal of Physics
The open access journal for physics

Casimir–Polder forces between chiral objects

David T Butcher[1,3], **Stefan Yoshi Buhmann**[1] **and Stefan Scheel**[1,2]

[1] Quantum Optics and Laser Science, Blackett Laboratory, Imperial College London, Prince Consort Road, London SW7 2AZ, UK

[2] Institut für Physik, Universität Rostock, Universitätsplatz 3, D-18051 Rostock, Germany

E-mail: david.butcher05@imperial.ac.uk

New Journal of Physics **14** (2012) 113013 (19pp)
Received 20 September 2012
Published 8 November 2012
Online at http://www.njp.org/
doi:10.1088/1367-2630/14/11/113013

Abstract. The chiral component of the Casimir–Polder potential is derived within the framework of macroscopic quantum electrodynamics. It is shown to exist only if the particle and the medium are both chiral. Furthermore, the chiral component of the Casimir–Polder potential can be attractive or repulsive, depending on the chirality of the molecule and the medium. The theory is applied to a cavity geometry in the non-retarded limit with the intention of enantiomer separation. For a ground state molecule the chiral component is dominated by the electric component and thus no explicit separation will happen. If the molecule is initially in an excited state the electric component of the Casimir–Polder force can be suppressed by an appropriate choice of material and the chiral component can select the molecule based on its chirality, allowing enantiomeric separation to occur.

[3] Author to whom any correspondence should be addressed.

Contents

1. Introduction

A three-dimensional object that cannot be superimposed on its mirror image is said to be chiral, these distinct mirror images are called enantiomers. Spectroscopically, enantiomers have identical properties and distinguishing between the two is not trivial. The characteristic feature of chiral objects is the manner of their interactions with other chiral objects. For example, the refractive indices of left- and right-handed circularly polarized light are different in a chiral medium, therefore the two polarizations will propagate at different speeds. The difference in velocity is related to the phenomenon of circular dichroism, where the wave with the 'slower' polarization is absorbed more strongly as it travels through the medium [1].

Many of the processes crucial to life involve chiral molecules whose chiral identity plays a central role in their chemical reactions, the incorrect enantiomer reacting differently and not producing the required result. In nature these molecules only occur as one enantiomer and are not found as the other, thus the reactions only occur when the correct enantiomer is present. In contrast, artificial production creates both enantiomers in equal proportions. Therefore it is important to be able to distinguish between enantiomers and ultimately to be able to separate a racemic (containing both enantiomers) mixture into an enantiomerically pure sample.

A frequently used method to separate enantiomers in an industrial setting is chiral chromotography. The initial racemic solution is passed through a column packed with a resolving agent, which is usually an enzyme and by necessity has to be chiral. This either retards, or stops, the progress of one of the enantiomers passing through the column but crucially not for the other and thus allows the solution to be separated. From an optical viewpoint it has been proposed that a racemic sample can be purified by use of coordinated laser pulses, which use a two-step process to initially drive different transitions in the enantiomers before converting one into the other [2]. It has recently been calculated that in the presence of a chiral carbon nanotube

the enantiomers of alanine possess different absorption energies and it was theorized that this could lead to a method of discrimination [3]. Furthermore, it has been shown that the van der Waals dispersion force between molecules can be enantiomer selective [4, 5]. Here we propose the use of another dispersion force, the Casimir–Polder force [6], as a method of distinguishing and ultimately separating enantiomers.

Casimir–Polder forces occur due to fluctuations in the quantum vacuum between objects, in this case it is between a particle and a macroscopic body. This force can be decomposed into an electric component that is solely dependent upon the electric dipole moments of the particle, the magnetic component of the force is likewise defined. We show that there is a third component that depends upon an interaction of the molecule's electric and magnetic dipole moments and this describes the particle's chiral response in the chiral component of the Casimir–Polder force. For the purpose of discrimination, the force on enantiomers must be different, this means that a chiral medium is required to produce the chiral-selective behaviour.

Chiral molecules occur frequently in nature and there has been much research done to calculate the relevant transition values either *ab initio* [7, 8], or through a twisted arc model for simple chiral molecules [9]. Recent technological developments have allowed for the creation of chiral fullerenes such as C_{76} [10], chiral carbon nanotubes [3] and chiral metamaterials [11]. Chiral metamaterials can be made from structures such as a gold helix [12], which shows a broadband electromagnetic response; a woodpile structure [13], a gold bar construction [14], which exhibit a negative refractive index in certain frequency ranges; and gold dots [15], which can be tuned during construction to give a desired response. Recently it has been shown that superchiral electromagnetic fields [16] can arise in planar chiral metamaterials. These fields can generate a much larger dissymmetry between the effective refractive indices for adsorbed chiral molecules on left- and right-handed materials than circularly polarized light and a solution of chiral molecules [17]. Chiral metamaterials have also been proposed as a method of producing repulsive Casimir forces [18].

In this article we derive the chiral component of the Casimir–Polder potential within the framework of macroscopic quantum electrodynamics [19]. We show that inherent to this potential is the requirement that the particle and the medium both exhibit a chiral response. The theory is applied to the case of a chiral molecule in a cavity between two chiral metamaterials in the non-retarded limit, where we show a possible route towards enantiomer separation.

The article is organized as follows. The quantized description of the electromagnetic field in a chiral medium is given in section 2.1, followed by the derivation of the chiral component of the Casimir–Polder force in section 2.2. This is applied to the case of a chiral molecule near a boundary; a perfect chiral mirror is considered in section 3.1 and a chiral metamaterial in section 3.2. We illustrate the theory by examining a chiral molecule in a cavity made of chiral metamaterials, considering a molecule initially in the ground state in section 4.1 and initially in an excited state in section 4.2. We provide some concluding remarks in section 5.

2. Formalism

In order to derive the chiral component of the Casimir–Polder potential in a general form, field quantization in an absorbing chiral medium is required. This quantization is the basis for describing the electric and magnetic fields and the subsequent formulation of an important integral relation, which is needed for the calculation of the Casimir–Polder potential.

2.1. Chiral media

The constitutive relations for the electromagnetic fields in the presence of a classical, non-dissipative chiral medium are given by

$$\mathbf{D} = \varepsilon_0 \boldsymbol{\varepsilon} \star \mathbf{E} - \frac{\mathrm{i}}{c} \boldsymbol{\kappa}^{\mathrm{T}} \star \mathbf{H} \tag{1}$$

and

$$\mathbf{B} = \frac{\mathrm{i}}{c} \boldsymbol{\kappa} \star \mathbf{E} + \mu_0 \boldsymbol{\mu} \star \mathbf{H}, \tag{2}$$

where $\boldsymbol{\varepsilon}$ and $\boldsymbol{\mu}$ are the relative permittivity and permeability tensors and $\boldsymbol{\kappa}$ is the chirality tensor, a magnetoelectric susceptibility. The chiral susceptibility of the medium has the effect of 'rotating' a magnetic effect to contribute towards an electric response and vice versa. The $\star$ is a notational shorthand for a spatial convolution, i.e. $[\boldsymbol{X} \star \boldsymbol{Y}](\mathbf{r}, \mathbf{r}') = \int \mathrm{d}^3\mathbf{s}\, \boldsymbol{X}(\mathbf{r}, \mathbf{s}) \cdot \boldsymbol{Y}(\mathbf{s}, \mathbf{r}')$. For non-locally responding media the permittivity, permeability and chiral susceptibilities take the form $\boldsymbol{\varepsilon}(\mathbf{r}, \mathbf{r}', \omega)$, etc, where the two spatial variables are independent. This reduces to the form $\boldsymbol{\varepsilon}(\mathbf{r}, \omega)\delta(\mathbf{r} - \mathbf{r}')$ in a locally responding medium. The medium is assumed to be reciprocal, i.e. $\boldsymbol{\varepsilon}(\mathbf{r}, \mathbf{r}') = \boldsymbol{\varepsilon}^{\mathrm{T}}(\mathbf{r}', \mathbf{r})$ and $\boldsymbol{\mu}(\mathbf{r}, \mathbf{r}') = \boldsymbol{\mu}^{\mathrm{T}}(\mathbf{r}', \mathbf{r})$.

The Casimir–Polder force requires field quantization in a medium due to its explicit quantum nature. In an absorbing medium, the quantum version of the constitutive relations are given as [20]

$$\hat{\mathbf{D}} = \varepsilon_0 \boldsymbol{\varepsilon} \star \hat{\mathbf{E}} - \frac{\mathrm{i}}{c} \boldsymbol{\kappa}^{\mathrm{T}} \star \hat{\mathbf{H}} + \hat{\mathbf{P}}_{\mathrm{N}} - \frac{\mathrm{i}}{c} \boldsymbol{\kappa}^{\mathrm{T}} \star \hat{\mathbf{M}}_{\mathrm{N}} \tag{3}$$

and

$$\hat{\mathbf{B}} = \frac{\mathrm{i}}{c} \boldsymbol{\kappa} \star \hat{\mathbf{E}} + \mu_0 \boldsymbol{\mu} \star \hat{\mathbf{H}} + \mu_0 \boldsymbol{\mu} \star \hat{\mathbf{M}}_{\mathrm{N}}. \tag{4}$$

The terms $\hat{\mathbf{P}}_{\mathrm{N}}$ and $\hat{\mathbf{M}}_{\mathrm{N}}$ are the noise polarization and magnetization respectively, they describe the dissipation in the medium and form a Langevin noise current

$$\hat{\mathbf{j}}_{\mathrm{N}}(\mathbf{r}, \omega) = -\mathrm{i}\,\omega \hat{\mathbf{P}}_{\mathrm{N}}(\mathbf{r}, \omega) + \nabla \times \hat{\mathbf{M}}_{\mathrm{N}}(\mathbf{r}, \omega). \tag{5}$$

The wave equation for the electric field in the chiral medium is then

$$\left[\nabla \times \boldsymbol{\mu}^{-1} \star \nabla \times + \frac{\omega}{c}(\nabla \times \boldsymbol{\mu}^{-1} \star \boldsymbol{\kappa} + \boldsymbol{\kappa}^{\mathrm{T}} \star \boldsymbol{\mu}^{-1} \star \nabla \times) - \frac{\omega^2}{c^2}(\boldsymbol{\varepsilon} - \boldsymbol{\kappa}^{\mathrm{T}} \star \boldsymbol{\mu}^{-1} \star \boldsymbol{\kappa})\right] \star \hat{\mathbf{E}} = \mathrm{i}\,\omega\mu_0 \hat{\mathbf{j}}_{\mathrm{N}} \tag{6}$$

and the Green's tensor, $\boldsymbol{G}(\mathbf{r}, \mathbf{r}', \omega)$, is the fundamental solution to the above inhomogeneous Helmholtz equation

$$\left\{\left[\nabla \times \boldsymbol{\mu}^{-1} \star \nabla \times + \frac{\omega}{c}(\nabla \times \boldsymbol{\mu}^{-1} \star \boldsymbol{\kappa} + \boldsymbol{\kappa}^{\mathrm{T}} \star \boldsymbol{\mu}^{-1} \star \nabla \times) - \frac{\omega^2}{c^2}(\boldsymbol{\varepsilon} - \boldsymbol{\kappa}^{\mathrm{T}} \star \boldsymbol{\mu}^{-1} \star \boldsymbol{\kappa})\right] \star \boldsymbol{G}\right\}(\mathbf{r}, \mathbf{r}') = \boldsymbol{\delta}(\mathbf{r} - \mathbf{r}'). \tag{7}$$

The Green's tensor obeys the Schwarz reflection principle

$$\boldsymbol{G}^*(\mathbf{r}, \mathbf{r}', \omega) = \boldsymbol{G}(\mathbf{r}, \mathbf{r}', -\omega^*), \tag{8}$$

which ensures reality of $\boldsymbol{G}(\mathbf{r}, \mathbf{r}', t)$, and inherits compliance with the Onsager condition for reciprocal media from the medium response functions, i.e.

$$\boldsymbol{G}(\mathbf{r}, \mathbf{r}', \omega) = \boldsymbol{G}^{\mathrm{T}}(\mathbf{r}', \mathbf{r}, \omega). \tag{9}$$

The wave equation and its Green's-tensor solution uniquely define the electric field (in coordinate space) as

$$\hat{\mathbf{E}}(\mathbf{r},\omega) = \mathrm{i}\,\omega\mu_0 \int \mathrm{d}^3\mathbf{r}'\boldsymbol{G}(\mathbf{r},\mathbf{r}',\omega)\cdot\hat{\mathbf{j}}_{\mathrm{N}}(\mathbf{r}',\omega) \tag{10}$$

and the magnetic induction field as

$$\hat{\mathbf{B}}(\mathbf{r},\omega) = \mu_0 \int \mathrm{d}^3\mathbf{r}'\nabla\times\boldsymbol{G}(\mathbf{r},\mathbf{r}',\omega)\cdot\hat{\mathbf{j}}_{\mathrm{N}}(\mathbf{r}',\omega). \tag{11}$$

To describe a general dissipative chiral medium, it is necessary to introduce the fundamental degrees of freedom of the field–medium system. Starting with the commutation relations for the noise polarization and magnetization [20]

$$[\hat{\mathbf{P}}_{\mathrm{N}}(\mathbf{r},\omega),\hat{\mathbf{P}}^{\dagger}_{\mathrm{N}}(\mathbf{r}',\omega')] = \frac{\varepsilon_0\hbar}{\pi}\{\mathrm{Im}[\boldsymbol{\varepsilon}(\omega)-\boldsymbol{\kappa}^{\mathrm{T}}(\omega)\star\boldsymbol{\mu}^{-1}(\omega)\star\boldsymbol{\kappa}(\omega)]\}(\mathbf{r},\mathbf{r}')\delta(\omega-\omega'), \tag{12}$$

$$[\hat{\mathbf{P}}_{\mathrm{N}}(\mathbf{r},\omega),\hat{\mathbf{M}}^{\dagger}_{\mathrm{N}}(\mathbf{r}',\omega')] = \frac{\hbar}{\mathrm{i}\,Z_0\pi}\{\mathrm{Im}[\boldsymbol{\kappa}^{\mathrm{T}}(\omega)\star\boldsymbol{\mu}^{-1}(\omega)]\}(\mathbf{r},\mathbf{r}')\delta(\omega-\omega'), \tag{13}$$

$$[\hat{\mathbf{M}}_{\mathrm{N}}(\mathbf{r},\omega),\hat{\mathbf{P}}^{\dagger}_{\mathrm{N}}(\mathbf{r}',\omega')] = -\frac{\hbar}{\mathrm{i}\,Z_0\pi}\{\mathrm{Im}[\boldsymbol{\mu}^{-1}(\omega)\star\boldsymbol{\kappa}(\omega)]\}(\mathbf{r},\mathbf{r}')\delta(\omega-\omega'), \tag{14}$$

$$[\hat{\mathbf{M}}_{\mathrm{N}}(\mathbf{r},\omega),\hat{\mathbf{M}}^{\dagger}_{\mathrm{N}}(\mathbf{r}',\omega')] = -\frac{\hbar}{\mu_0\pi}\mathrm{Im}[\boldsymbol{\mu}^{-1}(\mathbf{r},\mathbf{r}',\omega)]\delta(\omega-\omega'), \tag{15}$$

the noise polarization and magnetization can be decomposed into

$$\begin{pmatrix}\hat{\mathbf{P}}_{\mathrm{N}}\\ \hat{\mathbf{M}}_{\mathrm{N}}\end{pmatrix} = \sqrt{\frac{\hbar}{\pi}}\,\mathcal{R}\star\begin{pmatrix}\hat{\mathbf{f}}_{\mathrm{e}}\\ \hat{\mathbf{f}}_{\mathrm{m}}\end{pmatrix}, \tag{16}$$

where $\mathcal{R}$ is the 'square root' of the 6×6 response tensor,

$$\mathcal{R}\star\mathcal{R}^{\dagger} = \begin{pmatrix}\varepsilon_0\,\mathrm{Im}[\boldsymbol{\varepsilon}-\boldsymbol{\kappa}^{\mathrm{T}}\star\boldsymbol{\mu}^{-1}\star\boldsymbol{\kappa}] & \dfrac{\mathrm{Im}[\boldsymbol{\kappa}^{\mathrm{T}}\star\boldsymbol{\mu}^{-1}]}{\mathrm{i}\,Z_0}\\ -\dfrac{\mathrm{Im}[\boldsymbol{\mu}^{-1}\star\boldsymbol{\kappa}]}{\mathrm{i}\,Z_0} & -\dfrac{\mathrm{Im}[\boldsymbol{\mu}^{-1}]}{\mu_0}\end{pmatrix}, \tag{17}$$

which describes the dissipative properties of the medium, where $Z_0 = \sqrt{\frac{\mu_0}{\varepsilon_0}}$. For a passive, isotropic medium the response functions are restricted by $(\mathrm{Im}[\kappa])^2 < \mathrm{Im}[\varepsilon]\mathrm{Im}[\mu]$ [21]. The vector fields $\hat{\mathbf{f}}_{\mathrm{e}}(\mathbf{r},\omega)$ and $\hat{\mathbf{f}}_{\mathrm{m}}(\mathbf{r},\omega)$ are the bosonic annihilation operators for the matter–electromagnetic field system and with the creation operators they obey the commutation relation

$$[\hat{\mathbf{f}}_{\lambda}(\mathbf{r},\omega),\hat{\mathbf{f}}^{\dagger}_{\lambda'}(\mathbf{r}',\omega')] = \delta_{\lambda\lambda'}\boldsymbol{\delta}(\mathbf{r}-\mathbf{r}')\delta(\omega-\omega') \tag{18}$$

with $\lambda,\lambda' = \mathrm{e},\mathrm{m}$. By rewriting the electric and magnetic fields as

$$\hat{\mathbf{E}}(\mathbf{r},\omega) = \sum_{\lambda=\mathrm{e},\mathrm{m}}\int \mathrm{d}^3\mathbf{r}'\boldsymbol{G}_{\lambda}(\mathbf{r},\mathbf{r}',\omega)\cdot\hat{\mathbf{f}}_{\lambda}(\mathbf{r}',\omega), \tag{19}$$

$$\hat{\mathbf{B}}(\mathbf{r},\omega) = \sum_{\lambda=\mathrm{e},\mathrm{m}}\int \mathrm{d}^3\mathbf{r}'\nabla\times\boldsymbol{G}_{\lambda}(\mathbf{r},\mathbf{r}',\omega)\cdot\hat{\mathbf{f}}_{\lambda}(\mathbf{r}',\omega) \tag{20}$$

and making use of (16) and (17) it can be shown that

$$\begin{pmatrix} \boldsymbol{G}_{\mathrm{e}}(\mathbf{r},\mathbf{r}',\omega) \\ \boldsymbol{G}_{\mathrm{m}}(\mathbf{r},\mathbf{r}',\omega) \end{pmatrix} = -\mathrm{i}\,\mu_0\omega\sqrt{\frac{\hbar}{\pi}}[\boldsymbol{G}(\omega)\star\begin{pmatrix} \mathrm{i}\,\omega \\ \times\overleftarrow{\nabla} \end{pmatrix}\cdot\mathcal{R}(\omega)](\mathbf{r},\mathbf{r}'), \tag{21}$$

where the operation $\times\overleftarrow{\nabla}$ refers to taking the derivatives of the second spatial variable and mathematically is described as $[\boldsymbol{T}\times\overleftarrow{\nabla}]_{ij}(\mathbf{r},\mathbf{r}') = \epsilon_{jkl}\partial'_l T_{ik}(\mathbf{r},\mathbf{r}')$.

We can now derive the following integral relation:

$$\sum_{\lambda=\mathrm{e,m}}\int \mathrm{d}^3\mathbf{s}\boldsymbol{G}_\lambda(\mathbf{r},\mathbf{s},\omega)\cdot\boldsymbol{G}^\dagger_\lambda(\mathbf{r}',\mathbf{s},\omega) = \frac{\hbar\mu_0\omega^2}{\pi}\mathrm{Im}\,\boldsymbol{G}(\mathbf{r},\mathbf{r}',\omega), \tag{22}$$

see appendix A.

2.2. *Chiral Casimir–Polder potential*

To derive the Casimir–Polder potential we start with the interaction Hamiltonian in multipolar coupling and long wavelength approximation, describing the interaction of a molecule with the electric and magnetic fields [19]

$$\hat{H}_{\mathrm{AF}} = -\hat{\mathbf{d}}\cdot\hat{\mathbf{E}}(\mathbf{r}_A) - \hat{\mathbf{m}}\cdot\hat{\mathbf{B}}(\mathbf{r}_A), \tag{23}$$

where diamagnetic interactions have been neglected. Initially the particle can be either in its ground state or an excited state and the energy shift due to the atom–field interaction, (23), is given by

$$\Delta E = \sum_{I\neq N}\frac{\langle N|\hat{H}_{\mathrm{AF}}|I\rangle\langle I|\hat{H}_{\mathrm{AF}}|N\rangle}{E_N - E_I}. \tag{24}$$

When multiplying out the matrix elements it is important to note that the cross terms involving both electric and magnetic dipole interactions do not vanish and are in fact responsible for the chiral interaction, i.e. $\langle N|-\hat{\mathbf{d}}\cdot\hat{\mathbf{E}}(\mathbf{r}_A)|I\rangle\langle I|-\hat{\mathbf{m}}\cdot\hat{\mathbf{B}}(\mathbf{r}_A)|N\rangle$ and $\langle N|-\hat{\mathbf{m}}\cdot\hat{\mathbf{B}}(\mathbf{r}_A)|I\rangle\langle I|-\hat{\mathbf{d}}\cdot\hat{\mathbf{E}}(\mathbf{r}_A)|N\rangle \neq 0$.

The initial state is denoted by $|N\rangle = |n\rangle|\{0\}\rangle$ and the intermediate states $|I\rangle = |k\rangle\hat{\mathbf{f}}^\dagger_\lambda(\mathbf{r},\omega)|\{0\}\rangle$ where $|\{0\}\rangle$ denotes the ground state of the matter–field system (upon which the bosonic creation operators $\hat{\mathbf{f}}^\dagger_\lambda(\mathbf{r},\omega)$ act) and $|n\rangle$ and $|k\rangle$ represent the initial and intermediate energy levels of the particle. The summation in (24) contains sums over molecular transitions, the polarization modes of the electromagnetic fields and integrals over all space and positive frequencies

$$\sum_{I\neq N}\to\sum_k\sum_{\lambda=\mathrm{e,m}}\int\mathrm{d}^3\mathbf{r}\,\mathcal{P}\int_0^\infty\mathrm{d}\omega$$

($\mathcal{P}$: principal value). Using the definitions of the electric (19) and magnetic induction (20) fields it can be shown that

$$\langle N|-\hat{\mathbf{d}}\cdot\hat{\mathbf{E}}(\mathbf{r}_A)|I\rangle = -\mathbf{d}_{nk}\cdot\boldsymbol{G}_\lambda(\mathbf{r}_A,\mathbf{r},\omega), \tag{25}$$

$$\langle N|-\hat{\mathbf{m}}\cdot\hat{\mathbf{B}}(\mathbf{r}_A)|I\rangle = -\frac{\mathbf{m}_{nk}\cdot\nabla\times\boldsymbol{G}_\lambda(\mathbf{r}_A,\mathbf{r},\omega)}{\mathrm{i}\,\omega}, \tag{26}$$

where the electric dipole transition matrix elements are $\langle n|\hat{\mathbf{d}}|k\rangle = \mathbf{d}_{nk}$ and $\langle n|\hat{\mathbf{m}}|k\rangle = \mathbf{m}_{nk}$ the corresponding magnetic dipole moment matrix elements.

The electric and magnetic components of the Casimir–Polder potential are well known and the result can be found in [19]. Here we focus on the terms containing a single curl operation and a dependency on the electric and magnetic transition matrix elements as it is these terms that give rise to the chiral component of the Casimir–Polder potential:

$$\Delta E_{\mathrm{c}} = \frac{\mu_0}{\pi}\sum_k \mathcal{P}\int_0^\infty \frac{\mathrm{i}d\omega\,\omega}{\omega_{kn}+\omega}\Big[\mathbf{d}_{nk}\cdot \mathrm{Im}[\boldsymbol{G}(\mathbf{r}_A,\mathbf{r}_A,\omega)]\times \overleftarrow{\nabla}'\cdot\mathbf{m}_{kn} + \mathbf{m}_{nk}\cdot\nabla\times \mathrm{Im}[\boldsymbol{G}(\mathbf{r}_A,\mathbf{r}_A,\omega)]\cdot\mathbf{d}_{kn}\Big], \tag{27}$$

the transition frequencies are defined as $\omega_{kn} = \omega_k - \omega_n$. The Casimir–Polder potential is the position dependent part of the total energy shift, $\Delta E = \Delta E_0 + U(\mathbf{r}_A)$, and so its only contribution arises from the scattering part of the Green's function, $\boldsymbol{G}^{(1)}(\mathbf{r},\mathbf{r}',\omega)$.

The imaginary part of the Green's tensor is written as $\mathrm{Im}[\boldsymbol{G}(\mathbf{r}_A,\mathbf{r}_A,\omega)] = \frac{1}{2\mathrm{i}}[\boldsymbol{G}(\mathbf{r}_A,\mathbf{r}_A,\omega) - \boldsymbol{G}^*(\mathbf{r}_A,\mathbf{r}_A,\omega)]$. When the molecule is not initially in the ground state care needs to be taken of the poles that occur for transitions to states of lower energy than the initial state. By using contour integration techniques the off-resonant part of the Casimir–Polder potential can be obtained in terms of an integral over imaginary frequencies, whereas the resonant part is due to the residue at the poles. The result is

$$\begin{aligned}\Delta E_{\mathrm{c}} = -\frac{\mu_0\hbar}{2\pi}\int_0^\infty \mathrm{d}\xi\,\xi(\mathrm{tr}[\Gamma_{\mathrm{em}}(\mathrm{i}\,\xi)\cdot\boldsymbol{G}^{(1)}(\mathbf{r}_A,\mathbf{r}_A,\mathrm{i}\,\xi)\times\overleftarrow{\nabla}'] + \mathrm{tr}[\Gamma_{\mathrm{me}}(\mathrm{i}\,\xi)\cdot\nabla\times\boldsymbol{G}^{(1)}(\mathbf{r}_A,\mathbf{r}_A,\mathrm{i}\,\xi)])\\ + \mathrm{i}\,\mu_0\sum_k \Theta(\omega_{nk})\omega_{nk}(\mathbf{d}_{nk}\cdot\mathrm{Re}[\boldsymbol{G}^{(1)}(\mathbf{r}_A,\mathbf{r}_A,\omega_{nk})]\times\overleftarrow{\nabla}'\cdot\mathbf{m}_{kn}\\ + \mathbf{m}_{nk}\cdot\nabla\times\mathrm{Re}[\boldsymbol{G}^{(1)}(\mathbf{r}_A,\mathbf{r}_A,\omega_{nk})]\cdot\mathbf{d}_{kn}),\end{aligned} \tag{28}$$

where

$$\boldsymbol{\Gamma}_{\mathrm{em}}(\mathrm{i}\,\xi) = \frac{1}{\hbar}\sum_k\left(\frac{\mathbf{m}_{kn}\otimes\mathbf{d}_{nk}}{\omega_{kn}+\mathrm{i}\,\xi} - \frac{\mathbf{m}_{kn}\otimes\mathbf{d}_{nk}}{\omega_{kn}-\mathrm{i}\,\xi}\right), \tag{29}$$

$$\boldsymbol{\Gamma}_{\mathrm{me}}(\mathrm{i}\,\xi) = \frac{1}{\hbar}\sum_k\left(\frac{\mathbf{d}_{kn}\otimes\mathbf{m}_{nk}}{\omega_{kn}+\mathrm{i}\,\xi} - \frac{\mathbf{d}_{kn}\otimes\mathbf{m}_{nk}}{\omega_{kn}-\mathrm{i}\,\xi}\right) \tag{30}$$

are chiral susceptibility tensors and $\Theta(\omega_{nk})$ is a step function which is zero if $\omega_{nk} < 0$, i.e. for a transition to a higher energy state. For an isotropic particle ($\mathbf{d}\otimes\mathbf{m} = \frac{\mathbf{d}\cdot\mathbf{m}}{3}\mathbf{I}$), (29) and (30) both reduce to

$$\Gamma(\mathrm{i}\,\xi) = -\frac{2}{3\hbar}\sum_k \frac{\xi\ R_{nk}}{(\omega_{kn})^2+\xi^2}. \tag{31}$$

The term R_{nk} is the optical rotatory strength and is defined as

$$R_{nk} = \mathrm{Im}(\mathbf{d}_{nk}\cdot\mathbf{m}_{kn}). \tag{32}$$

It describes the interaction between electric and magnetic dipole moments in a molecule and, crucially, left and right-handed enantiomers differ in the sign of R_{nk} for a particular transition.

To further simplify (28), it can be shown that

$$\mathrm{tr}[\boldsymbol{G}(\mathbf{r}_A,\mathbf{r}_A,\omega)\times\overleftarrow{\nabla}'] = -\mathrm{tr}[\nabla\times\boldsymbol{G}(\mathbf{r}_A,\mathbf{r}_A,\omega)], \tag{33}$$

where the Onsager reciprocity relation (9) has been used. For the real part of the Green's function an equivalent expression holds. We can now write the chiral component of the Casimir–Polder potential as

$$U_{\mathrm{c}}(\mathbf{r}_A) = -\frac{\hbar\mu_0}{\pi}\int_0^\infty \mathrm{d}\xi\ \xi\Gamma(\mathrm{i}\,\xi)\mathrm{tr}[\nabla\times\boldsymbol{G}^{(1)}(\mathbf{r}_A,\mathbf{r}_A,\mathrm{i}\,\xi)] + \frac{2\mu_0}{3}\sum_k \Theta(\omega_{nk})\omega_{nk}R_{nk}\,\mathrm{tr}[\nabla\times\mathrm{Re}[\boldsymbol{G}^{(1)}(\mathbf{r}_A,\mathbf{r}_A,\omega_{nk})]]. \tag{34}$$

The requirement that a chiral object is needed to be able to distinguish between the chiral states of another object is fulfilled. As (34) shows we must have a chiral medium and a chiral molecule. If either the medium ($\mathrm{tr}[\nabla\times\boldsymbol{G}^{(1)}(\mathbf{r}_A,\mathbf{r}_A,\mathrm{i}\,\xi)]=0$), or the particle ($R_{nk}=0$) is achiral there will not be a chiral component to the Casimir–Polder potential. This can be thought of as a generalization to the Curie dissymmetry principle (originally formulated for crystal symmetries) and one may say: the Casimir–Polder potential cannot distinguish between molecules of different handedness if the medium does not possess chiral properties itself.

For reference, the off-resonant electric and magnetic Casimir–Polder potentials [19] and their resonant parts are

$$U_{\mathrm{e}}(\mathbf{r}_A) = \frac{\hbar\mu_0}{2\pi}\int_0^\infty \mathrm{d}\xi\ \xi^2\,\mathrm{tr}[\boldsymbol{\alpha}(\mathrm{i}\,\xi)\cdot\boldsymbol{G}^{(1)}(\mathbf{r}_A,\mathbf{r}_A,\mathrm{i}\,\xi)] - \mu_0\sum_k \Theta(\omega_{nk})\omega_{nk}^2\mathbf{d}_{nk}\cdot\mathrm{Re}[\boldsymbol{G}^{(1)}(\mathbf{r}_A,\mathbf{r}_A,\omega_{nk})]\cdot\mathbf{d}_{kn} \tag{35}$$

and

$$U_{\mathrm{m}}(\mathbf{r}_A) = \frac{\hbar\mu_0}{2\pi}\int_0^\infty \mathrm{d}\xi\ \mathrm{tr}[\boldsymbol{\beta}(\mathrm{i}\,\xi)\cdot\nabla\times\boldsymbol{G}^{(1)}(\mathbf{r}_A,\mathbf{r}_A,\mathrm{i}\,\xi)\times\overleftarrow{\nabla}'] + \mu_0\sum_k \Theta(\omega_{nk})\mathbf{m}_{nk}\cdot\nabla\times\mathrm{Re}[\boldsymbol{G}^{(1)}(\mathbf{r}_A,\mathbf{r}_A,\omega_{nk})]\times\overleftarrow{\nabla}'\cdot\mathbf{m}_{kn}, \tag{36}$$

where

$$\boldsymbol{\alpha}(\mathrm{i}\,\xi) = \frac{1}{\hbar}\sum_k\left(\frac{\mathbf{d}_{kn}\otimes\mathbf{d}_{nk}}{\omega_{kn}+\mathrm{i}\,\xi}+\frac{\mathbf{d}_{nk}\otimes\mathbf{d}_{kn}}{\omega_{kn}-\mathrm{i}\,\xi}\right) \tag{37}$$

and

$$\boldsymbol{\beta}(\mathrm{i}\,\xi) = \frac{1}{\hbar}\sum_k\left(\frac{\mathbf{m}_{kn}\otimes\mathbf{m}_{nk}}{\omega_{kn}+\mathrm{i}\,\xi}+\frac{\mathbf{m}_{nk}\otimes\mathbf{m}_{kn}}{\omega_{kn}-\mathrm{i}\,\xi}\right) \tag{38}$$

are the usual electric and magnetic susceptibilities.

3. Chiral particle near a chiral halfspace

First we consider a chiral particle in free space near halfspace containing an isotropic chiral medium (figure 1). To compute the Casimir–Polder potential as given in (34) the scattering part of the Green's function for a source in free space near an isotropic chiral medium is required.

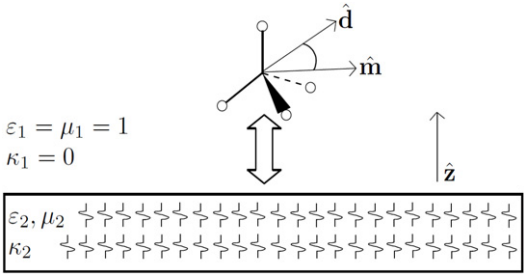

Figure 1. Chiral molecule in free space near a chiral medium. The chiral molecule will have a different group or base (denoted by ○) at the end of each bond, breaking the mirror symmetry. The boundary between the halfspaces is the (x, y) plane at $z = 0$. The isotropic chiral medium fills the space with $z < 0$ (labelled region 2) and $z > 0$ is the free-space (region 1).

The wave vectors travelling in the achiral region 1 are the standard free-space wave vectors

$$k_1^2 = \left(\frac{\omega}{c}\right)^2, \quad k_{1z}^2 = k_1^2 - k_{1q}^2, \tag{39}$$

where $k_q^2 = k_x^2 + k_y^2$. Within the chiral medium the wavevectors are

$$(k_2^{\mathrm{R}})^2 = \left(\frac{\omega}{c}\right)^2 (\kappa_2 + \sqrt{\varepsilon_2 \mu_2})^2, \tag{40}$$

$$(k_2^{\mathrm{L}})^2 = \left(\frac{\omega}{c}\right)^2 (-\kappa_2 + \sqrt{\varepsilon_2 \mu_2})^2, \tag{41}$$

$$(k_{2z}^P)^2 = (k_2^P)^2 - (k_{2q})^2, \tag{42}$$

where $P = \mathrm{R}, \mathrm{L}$ and refers to the right and left circular polarization of the wave, respectively.

The scattering part of the dyadic Green's function for a reflection from the achiral/chiral interface can be found in [22] as

$$\boldsymbol{G}(\mathbf{r}, \mathbf{r}', \omega) = \frac{\mathrm{i}}{8\pi^2} \frac{c}{\omega} \int \mathrm{d}\mathbf{k}_{1\mathrm{q}} \frac{k_1}{k_{1z}} \mathrm{e}^{\mathrm{i}(\mathbf{k}_{1\mathrm{q}} \cdot (\mathbf{r}_{\mathrm{q}} - \mathbf{r}'_{\mathrm{q}}) + k_{1z}(z+z'))} \Big[\mathbf{e}_{\mathrm{s}} \mathbf{e}_{\mathrm{s}} R^{(\mathrm{s,s})}$$

$$+ \mathbf{e}_{\mathrm{s}} \mathbf{e}_{\mathrm{p}}(-k_{1z}) R^{(\mathrm{s,p})} + \mathbf{e}_{\mathrm{p}}(k_{1z}) \mathbf{e}_{\mathrm{s}} R^{(\mathrm{p,s})} + \mathbf{e}_{\mathrm{p}}(k_{1z}) \mathbf{e}_{\mathrm{p}}(-k_{1z}) R^{(\mathrm{p,p})} \Big], \tag{43}$$

where

$$\mathbf{e}_{\mathrm{s}} = \frac{1}{k_q}(k_y \mathbf{x} - k_x \mathbf{y}) \tag{44}$$

and

$$\mathbf{e}_{\mathrm{p}}(\pm k_z) = \frac{1}{k}(\mp k_z \mathbf{k}_q + k_q \mathbf{z}) \tag{45}$$

are the polarization unit vectors for s and p polarized waves. The reflection coefficients $R^{(\mathrm{s,s})}$, $R^{(\mathrm{s,p})}$, $R^{(\mathrm{p,s})}$ and $R^{(\mathrm{p,p})}$ are typically dependent on the wave vectors given above and the medium response functions.

In this geometry the chiral component for the Casimir–Polder potential is

$$U_{\rm c}(z_A) = \frac{\hbar\mu_0}{4\pi^2 c}\int_0^\infty {\rm d}\xi\ \xi^2\Gamma({\rm i}\,\xi)\int_{\frac{\xi}{c}}^\infty {\rm d}\tilde{k}_{1z}\,{\rm e}^{-2\tilde{k}_{1z}z_A}\left[\left(\frac{2\tilde{k}_{1z}^2c^2}{\xi^2}-1\right)R^{({\rm s,p})}({\rm i}\,\xi)+R^{({\rm p,s})}({\rm i}\,\xi)\right]$$
$$-\frac{\mu_0}{12\pi^2 c}\sum_k \Theta(\omega_{nk})\omega_{nk}^2 R_{nk}{\rm Re}\int {\rm d}\mathbf{k}_{1q}\frac{{\rm e}^{{\rm i}2k_{1z}z_A}}{k_{1z}}$$
$$\times\left[\left(\frac{2k_{1z}^2c^2}{\omega_{nk}^2}-1\right)R^{({\rm s,p})}(\omega_{nk})+R^{({\rm p,s})}(\omega_{nk})\right], \tag{46}$$

the details of this calculation can be found in appendix B.

3.1. Perfect chiral mirror

As a purely theoretical construct we consider the potential between an isotropic molecule and an idealized medium that we have dubbed a 'perfect chiral mirror', whose reflection coefficients are $R^{({\rm s,p})}$, $R^{({\rm p,s})}=\pm1$ and therefore $R^{({\rm s,s})}$, $R^{({\rm p,p})}=0$. This represents reflections where perpendicularly polarized waves are completely reflected into parallel polarized waves and vice versa. For a chiral medium that rotates the polarization clockwise (with regard to the incoming wave—labelled 'right-handed') the reflection coefficients are $R^{({\rm s,p})}=1$ and $R^{({\rm p,s})}=-1$ and for an anticlockwise polarization rotation (labelled 'left-handed') they are $R^{({\rm s,p})}=-1$ and $R^{({\rm p,s})}=1$. When the molecule is initially in its ground state, applying these reflection coefficients to (46) results in

$$U(z_A) = \pm\frac{\hbar Z_0}{8\pi^2 z_A^3}\int_0^\infty {\rm d}\xi\ \Gamma({\rm i}\,\xi)\,{\rm e}^{-2\frac{\xi}{c}z_A}\left(\frac{2\xi z_A}{c}+1\right), \tag{47}$$

where the '+' (upper sign) refers to the right-handed medium and '−' (lower sign) refers to the left-handed medium. To examine how the spatial separation between the chiral particle and the chiral halfspace affects the chiral potential, we take the far-distance (retarded) and close-distance (non-retarded) limits of (47).

In the retarded limit where $z_A\omega_{\rm min}/c\gg1$ ($\omega_{\rm min}$ is the minimum relevant particle transition frequency), the cross polarizability, $\Gamma({\rm i}\,\xi)$, approaches the static limit and can be approximated by $\Gamma({\rm i}\,\xi)\approx\Gamma'(0)\xi$. The potential becomes

$$U(z_A) = \mp\frac{Z_0c^2}{16\pi^2 z_A^5}\sum_k\frac{R_{0k}}{(\omega_{k0})^2}. \tag{48}$$

In the non-retarded limit where $z_A\omega_{\rm max}/c\ll1$ ($\omega_{\rm max}$ is the maximum relevant particle transition frequency) the potential becomes

$$U(z_A) = \pm\frac{Z_0}{12\pi^2 z_A^3}\sum_k R_{0k}\ln\left(\frac{\omega_{k0}z_A}{c}\right), \tag{49}$$

where use has been made of the relationship

$$\int_a^b {\rm d}x\frac{x}{a^2+x^2}\approx-\ln a,\quad \text{for } a\ll1.$$

The results show a spatial scaling behaviour in the retarded and non-retarded limit that is different to the cases seen for dielectric or magnetic media in this geometry. An interesting

consequence of such a medium is that in this simple geometry the electric and magnetic components of the Casimir–Polder potential would vanish. It should be noted that the potential can be attractive or repulsive depending on the medium and particle in question, in contrast to the purely attractive potentials that usually arise in this geometry. The chiral identity of both objects determines the character of the potential. The lack of electric and magnetic components of the Casimir–Polder potential and the existence of repulsive forces means that perfect chiral mirrors used in a cavity or Fabry–Pérot geometry could be used to separate enantiomers. We believe that the results represent a theoretical upper bound for the chiral Casimir–Polder potential, however, they are physically unrealizable. This is because it would require a medium that completely rotates the polarization of the incident waves and perfectly reflects the waves. Typically, the chirality of a medium will be restricted to $\kappa^2 < \varepsilon\mu$, which would exclude a perfect chiral mirror.

3.2. Isotropic chiral medium

For all realistic media, the reflection coefficients are not unity as there will always be transmission and losses from the fields as they are reflected. The reflection coefficients for an isotropic medium are given in [22], after taking the non-retarded limit they are

$$R^{(\mathrm{s,p})} = -R^{(\mathrm{p,s})} = \frac{2\mathrm{i}\,\kappa_2}{\varepsilon_2\mu_2 - \kappa_2^2 + \varepsilon_2 + \mu_2 + 1}, \tag{50}$$

$$R^{(\mathrm{s,s})} = \frac{\varepsilon_2\mu_2 - \kappa_2^2 - \varepsilon_2 + \mu_2 - 1}{\varepsilon_2\mu_2 - \kappa_2^2 + \varepsilon_2 + \mu_2 + 1} \tag{51}$$

and

$$R^{(\mathrm{p,p})} = \frac{\varepsilon_2\mu_2 - \kappa_2^2 + \varepsilon_2 - \mu_2 - 1}{\varepsilon_2\mu_2 - \kappa_2^2 + \varepsilon_2 + \mu_2 + 1}. \tag{52}$$

By setting $\kappa_2 = 0$ the cross reflection coefficients disappear and $R^{(\mathrm{s,s})}$, $R^{(\mathrm{p,p})}$ revert to the standard Fresnel reflection coefficients in the non-retarded limit.

We can now obtain the chiral-corrected electric component and the chiral component of the Casimir–Polder potential in the non-retarded limit. The off-resonant terms read

$$U_{\mathrm{eO}}(z_A) = -\frac{\hbar}{16\pi^2\varepsilon_0 z_A^3}\int_0^\infty \mathrm{d}\xi\ \alpha(\mathrm{i}\,\xi)\left[\frac{\varepsilon_2\mu_2 - \kappa_2^2 + \varepsilon_2 - \mu_2 - 1}{\varepsilon_2\mu_2 - \kappa_2^2 + \varepsilon_2 + \mu_2 + 1}\right], \tag{53}$$

$$U_{\mathrm{cO}}(z_A) = \frac{\hbar Z_0}{4\pi^2 z_A^3}\int_0^\infty \mathrm{d}\xi\ \Gamma(\mathrm{i}\,\xi)\left[\frac{\mathrm{i}\,\kappa_2}{\varepsilon_2\mu_2 - \kappa_2^2 + \varepsilon_2 + \mu_2 + 1}\right], \tag{54}$$

where all response functions are dependent on complex frequency, i.e. $\varepsilon_2 = \varepsilon_2(\mathrm{i}\,\xi)$, $\mu_2 = \mu_2(\mathrm{i}\,\xi)$ and $\kappa_2 = \kappa_2(\mathrm{i}\,\xi)$. The resonant terms are

$$U_{\mathrm{eR}}(z_A) = -\frac{1}{24\pi\varepsilon_0 z_A^3}\sum_k \Theta(\omega_{nk})|d_{nk}|^2 \mathrm{Re}\left[\frac{\varepsilon_2\mu_2 - \kappa_2^2 + \varepsilon_2 - \mu_2 - 1}{\varepsilon_2\mu_2 - \kappa_2^2 + \varepsilon_2 + \mu_2 + 1}\right], \tag{55}$$

$$U_{\mathrm{cR}}(z_A) = \frac{Z_0}{6\pi z_A^3}\sum_k \Theta(\omega_{nk}) R_{nk} \mathrm{Im}\left[\frac{\mathrm{i}\,\kappa_2}{\varepsilon_2\mu_2 - \kappa_2^2 + \varepsilon_2 + \mu_2 + 1}\right], \tag{56}$$

where the response functions in (55) and (56) are taken at the transition frequency, ω_{nk} i.e. $\varepsilon_2 = \varepsilon_2(\omega_{nk})$, $\mu_2 = \mu_2(\omega_{nk})$ and $\kappa_2 = \kappa_2(\omega_{nk})$. As a consistency check, setting $\mu_2 = 1$ and letting $\kappa_2 \to 0$ in the off-resonant contribution the results for the electric component of the Casimir–Polder potential between a particle and a dielectric in [19] are recovered.

4. Chiral cavity

To examine whether the Casimir–Polder force can be used to distinguish between enantiomers, we consider a chiral molecule in free space between two chiral media which differ only in their handedness. To illustrate this we have selected a chiral metamaterial whose parameters have been published in [13] as the chiral medium due to the strong chirality that can be obtained from metamaterials. To characterize the medium a single-resonance Drude–Lorentz model is used for $\varepsilon(\omega)$ and $\mu(\omega)$ and the Condon model [1, 23] is used for $\kappa(\omega)$. These are

$$\varepsilon(\omega) = 1 - \frac{\omega_{\mathrm{p}}^2}{\omega^2 - \omega_E^2 + \mathrm{i}\,\gamma_E\omega}, \tag{57}$$

$$\mu(\omega) = 1 - \frac{\omega_m^2}{\omega^2 - \omega_B^2 + \mathrm{i}\,\gamma_B\omega} \tag{58}$$

and

$$\kappa(\omega) = \frac{a\omega}{\omega^2 - \omega_C^2 + \mathrm{i}\,\gamma_C\omega}. \tag{59}$$

The constants $\omega_{\mathrm{p}}, \omega_m$ and a represent the oscillator strengths for the dipole transitions responsible for ε, μ and the rotatory strength associated with κ, respectively. The remaining constants are the resonant frequencies and damping factors for the permittivity (ω_E, γ_E), permeability (ω_B, γ_B) and the chirality (ω_C, γ_C) of the medium.

For the chiral molecule, dimethyl disulphide $(CH_3)_2S_2$ has been chosen. The dipole and rotatory strengths for each transition have been numerically calculated for various orientations [7]. As an example, we have chosen the first transition when the orientation between the two CH_3–S–S planes is 90°. The transition frequency is $\omega_{nk} = 9.17 \times 10^{15}\,\mathrm{s}^{-1}$, dipole strength $|\mathbf{d}_{nk}|^2 = 8.264 \times 10^{-60}\,(\mathrm{C\,m})^2$ and the rotatory strength is $R_{nk} = 3.328 \times 10^{-64}$ $\mathrm{C}^2\,\mathrm{m}^3\,\mathrm{s}^{-1}$.

4.1. Ground-state force

In the non-retarded limit, multiple reflections between the halfspaces are not considered and the forces on the molecule for each halfspace are simply added. From the Casimir–Polder potentials for the electric (53) and chiral (54) components we can obtain the forces ($\mathbf{F} = -\nabla U$) acting on the molecule. The two halfspaces are identical except for their chirality, characterized by a, which is negative for one of the halfspaces and positive for the other. We assume that the molecule has only two energy levels, i.e. only one transition is considered.

By considering a separation between the halfspaces of 100 nm we obtain the results shown in figures 2 and 3. The electric component of the Casimir–Polder force (figure 2) is always attractive towards both halfspaces. In this geometry these forces are equal and opposite, so when computing the electric component of the total force (in the non-retarded limit) on the molecule, the halfspace closest to the molecule will provide the dominant contribution to this

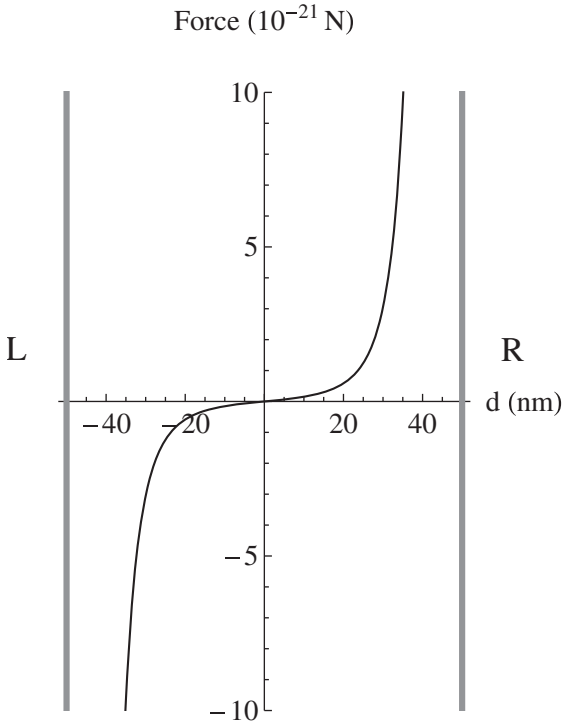

Figure 2. The electric component of the Casimir–Polder force. The molecule is attracted to both halfspaces with the stronger attraction coming from the closest halfspace. The vertical lines denote the boundaries of the metamaterial, the gap between is freespace where the molecule is located. The parameters obtained from [13] are $\omega_p = 5.47 \times 10^{14}\,s^{-1}$, $\omega_m = 3.06 \times 10^{14}\,s^{-1}$, $a = -3.61 \times 10^{14}\,s^{-1}$, $\omega_E = \omega_B = \omega_C = 4.96 \times 10^{14}\,s^{-1}$, $\gamma_E = \gamma_B = 2.51 \times 10^{13}\,s^{-1}$ and $\gamma_C = -2.58 \times 10^{13}\,s^{-1}$.

total force. By implication, when the molecule is in the centre (i.e. equal distance from both halfspaces), the electric components of the Casimir–Polder force cancel and the net contribution to the total Casimir–Polder force is zero. It should be noted that the difference in the chirality of the halfspaces does not effect the electric force from either halfspace and hence the combined electric component of the total force.

By looking at the chiral component of the Casimir–Polder force (figure 3) one obtains an attractive force between the chiral molecule and one of the halfspaces (to the left hand side) and a repulsive force between the chiral molecule and the other halfspace (to the right hand side). Furthermore, the total chiral component of the force does not disappear at the midpoint between the halfspaces.

Figures 2 and 3 show that the electric component of the Casimir–Polder force is many orders of magnitude larger than the chiral component and will dominate interactions. The exception to this is the central region between the halfspaces, where the overall electric component is reduced sufficiently to allow the chiral component to become the dominant force. However, the width of this central region is smaller than the molecule. This means that for a particle initially in the ground state the Casimir–Polder force, in the current geometry, would not be able to distinguish between enantiomers and subsequently separate them.

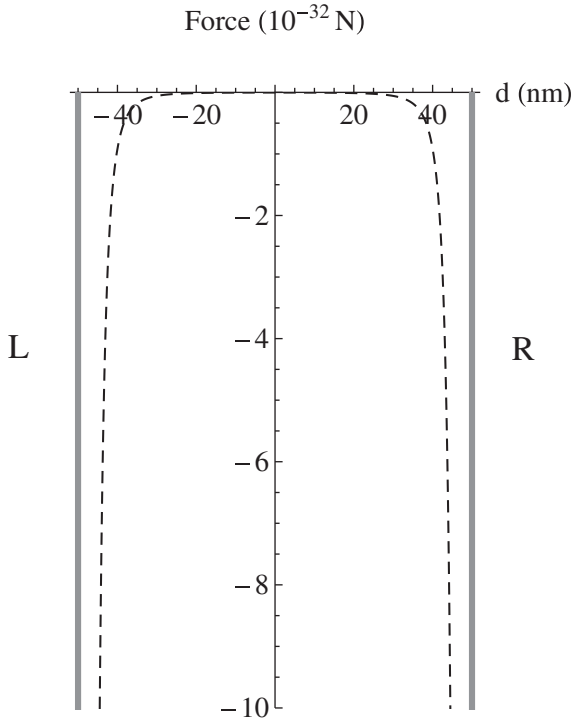

Figure 3. The chiral component of the Casimir–Polder force. The molecule is attracted to the left hand side halfspace and there is a repulsive force between the molecule and the right hand side halfspace.

The difference in orders of magnitude of the force components can be traced to separate origins. With regard to the chiral molecule the optical rotatory strength is orders of magnitude smaller than the electric dipole transition matrix element, $R_{nk}/c \lesssim 10^{-11}|\mathbf{d}_{nk}|^2$. This can be understood by the fact that the magnetic dipole moment appears at a higher-order of the multipole expansion than the electric dipole moment. Looking at the chiral medium, the chirality is slightly smaller than the permittivity, but this difference is enhanced by the structure of the reflection coefficients.

4.2. Excited-state force

In order to overcome the dominance of the electric dipole force, it is helpful to consider other molecular initial states. If the molecule is initially in an excited state the resonant contribution to the force needs to be considered. In this scenario, the off-resonant part of the electric component of the Casimir–Polder force is repulsive whereas the direction of the chiral off-resonant component is dependent on the chiral identity of the molecule and material in question. A metamaterial can be constructed such that for a given transition frequency the resonant contribution to the electric component of the Casimir–Polder force will counteract the off-resonant contribution. By creating a cavity with two such metamaterials, identical except for their chirality, a chiral molecule initially in an excited state can be separated from its enantiomer. This is because the suppression of the electric component of the Casimir–Polder force allows the chiral component of the force to attract an enantiomer to the corresponding

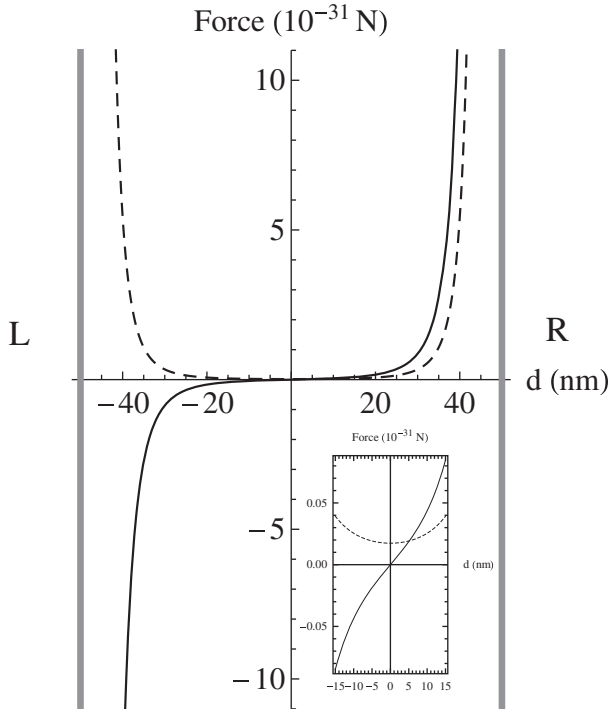

Figure 4. The total electric component of the Casimir–Polder force (black line) and the total chiral component (dashed line). The components of the force are of equal magnitude, with the chiral contribution larger in the centre and the electric contribution larger towards the halfspaces. The parameters are chosen as $\omega_E = \omega_B = \omega_C = \frac{\omega_p}{2}$, $\gamma_E = \gamma_B = -\gamma_C = \frac{\omega_p}{10^3}$, $a = -\frac{\omega_p}{3}$ and $\omega_m = \frac{\omega_p}{5}$. The inset in the bottom right shows a magnification of the centre region between −15 and 15 nm.

halfspace while it is being repelled from the opposite halfspace without the electric component dominating.

As a proof of principle the metamaterials parameters are chosen as suitable multiples of the plasma frequency and the values for the optical rotatory strength and dipole strength are as given above and the metamaterials are separated by 100 nm of free space.

The results are shown in figure 4. As can be seen, for a particular transition frequency a suppression of the electric component of the Casimir–Polder force sufficient to allow enantiomer separation can be obtained. The chiral component is the dominant contribution in the central region (≈10 nm) of the cavity (see the inset to figure 4), meaning that the direction of the force acting on a chiral molecule in this region will be dependent on its chirality. Therefore enantiomers that pass at low speeds through the centre of the cavity will be attracted or repelled in opposite directions and will be separated based on their chirality. As the total electric component of the Casimir–Polder force is attractive, the separated enantiomers will continue to be drawn towards opposite halfspaces even when not in the central region.

It is important to note that, although the chirality of the metamaterials has not changed, the chiral component of the Casimir–Polder force is now acting in the opposite direction. This is

due to the resonant part of the chiral force, which is larger than the off-resonant part and acts against it.

5. Conclusion

The chiral component of the Casimir–Polder potential has been derived within the framework of macroscopic QED. The results show that the medium and particle in question must both be chiral, otherwise this potential does not exist. Furthermore, this potential is sensitive to the chirality of the objects in question and can be attractive or repulsive.

By initially considering a perfect chiral mirror, it was found that in the retarded limit the chiral component of the Casimir–Polder potential scales as $1/(z_A)^5$ with the molecule–surface distance whereas for the non-retarded limit the spatial scaling is $1/(z_A)^3\ln(z_A)$. As already alluded to, it is unlikely that this could be realized in a real material, due to the requirement for perfect reflection *and* complete rotation of the incident wave polarization. When the chiral medium does not exhibit perfect reflectance the chiral potential is slightly diminished and in the non-retarded limit the spatial scaling was found to be $1/(z_A)^3$.

In the geometry where a chiral molecule, initially in the ground state, is located between two halfspaces of opposite chirality it was found that the chiral component of the Casimir–Polder force is attractive towards one halfspace and repulsive from the other. However, the electric component of the Casimir–Polder force between the molecule and the halfspaces dominates over the chiral component. Therefore, in this geometry, it would not be possible to distinguish between enantiomers because the indiscriminate attractive electric force dominates over any chiral effects.

If the molecule is initially in an excited state it was found that the material properties can be tuned such that the resonant contribution to the electric component of the Casimir–Polder force almost completely suppresses the off-resonant contribution. Enantiomers in the centre between the halfspaces would then experience an overall force whose direction is dependent on the chiral identity of the molecule. This chiral force will draw the molecule towards a particular halfspace with its enantiomer attracted to the other side of the cavity. This distinction between enantiomers will allow them to be separated by the Casimir–Polder force.

Acknowledgments

The authors would like to thank K Hornberger and J Trost for useful discussions. The research was funded by the UK Engineering and Physical Sciences Research Council (EPSRC).

Appendix A. Integral relation

We begin by evaluating the left hand side of the integral equation (22). By taking the product of (21) with its hermitian conjugate we arrive at the term

$$\boldsymbol{G}_{\mathrm{e}} \star \boldsymbol{G}_{\mathrm{e}}^{\dagger} + \boldsymbol{G}_{\mathrm{m}} \star \boldsymbol{G}_{\mathrm{m}}^{\dagger} = (\mu_0\omega)^2 \frac{\hbar}{\pi} \boldsymbol{G} \star \begin{pmatrix} \mathrm{i}\,\omega \\ \times \overleftarrow{\nabla} \end{pmatrix} \cdot \mathcal{R} \star \mathcal{R}^{\dagger} \cdot \begin{pmatrix} \mathrm{i}\,\omega \\ \times \overleftarrow{\nabla} \end{pmatrix}^{\dagger} \star \boldsymbol{G}^{\dagger}. \tag{A.1}$$

Substituting in (17) leads to

$$\sum_{\lambda=\mathrm{e,m}} \boldsymbol{G}_\lambda \star \boldsymbol{G}_\lambda^\dagger = \frac{\hbar\mu_0\omega^2}{\pi}\Big[\boldsymbol{G}\star\Big[\frac{\omega^2}{c^2}\mathrm{Im}[\boldsymbol{\varepsilon}-\boldsymbol{\kappa}^{\mathrm{T}}\star\boldsymbol{\mu}^{-1}\star\boldsymbol{\kappa}]+\frac{\omega}{c}(\times\overleftarrow{\nabla}\cdot\mathrm{Im}[\boldsymbol{\mu}^{-1}\star\boldsymbol{\kappa}]$$

$$-\mathrm{Im}[\boldsymbol{\kappa}^{\mathrm{T}}\star\boldsymbol{\mu}^{-1}]\cdot\nabla\times)+\times\overleftarrow{\nabla}\cdot\mathrm{Im}[\boldsymbol{\mu}^{-1}]\cdot\nabla\times\Big]\star\boldsymbol{G}^\dagger\Big]. \tag{A.2}$$

By comparing (A.2) with the noise polarization and magnetization commutators (12)–(15) it can be seen that this reduces to

$$\sum_{\lambda=\mathrm{e,m}} \boldsymbol{G}_\lambda(\omega)\star\boldsymbol{G}_\lambda^\dagger(\omega) = \frac{\hbar\mu_0\omega^2}{\pi}\Big[\boldsymbol{G}(\omega)\star\Big[\hat{\mathbf{j}}_{\mathrm{N}}(\omega),\hat{\mathbf{j}}_{\mathrm{N}}^\dagger(\omega)\Big]\star\boldsymbol{G}^\dagger(\omega)\Big]. \tag{A.3}$$

It is known that [20]

$$\Big[\hat{\mathbf{j}}_{\mathrm{N}}(\mathbf{r},\omega),\hat{\mathbf{j}}_{\mathrm{N}}^\dagger(\mathbf{r}',\omega')\Big] = \frac{\hbar\omega}{\pi}\mathrm{Re}[\boldsymbol{Q}(\mathbf{r},\mathbf{r}',\omega)]\delta(\omega-\omega'), \tag{A.4}$$

where $\boldsymbol{Q}$ is a complex conductivity tensor. This leads to the general form of the integral relation [20]

$$\left(\frac{\hbar\mu_0\omega^2}{\pi}\right)\mu_0\omega[\boldsymbol{G}(\omega)\star\mathrm{Re}\ \boldsymbol{Q}(\omega)\star\boldsymbol{G}^\dagger(\omega)](\mathbf{r},\mathbf{r}') = \frac{\hbar\mu_0\omega^2}{\pi}\mathrm{Im}\,\boldsymbol{G}(\mathbf{r},\mathbf{r}',\omega). \tag{A.5}$$

Therefore,

$$\sum_\lambda[\boldsymbol{G}_\lambda(\omega)\star\boldsymbol{G}_\lambda^\dagger(\omega)](\mathbf{r},\mathbf{r}') = \frac{\hbar\mu_0\omega^2}{\pi}\mathrm{Im}\,\boldsymbol{G}(\mathbf{r},\mathbf{r}',\omega), \tag{A.6}$$

which in coordinate space is

$$\sum_\lambda\int \mathrm{d}^3\mathbf{s}\boldsymbol{G}_\lambda(\mathbf{r},\mathbf{s},\omega)\cdot\boldsymbol{G}_\lambda^\dagger(\mathbf{r}',\mathbf{s},\omega) = \frac{\hbar\mu_0\omega^2}{\pi}\mathrm{Im}\boldsymbol{G}(\mathbf{r},\mathbf{r}',\omega), \tag{A.7}$$

as required.

Appendix B. Dyadic Green's function calculation

To obtain the chiral component of the Casimir–Polder force we require the terms for $\mathrm{tr}[\nabla\times\boldsymbol{G}(\mathbf{r}_A,\mathbf{r}_A,\mathrm{i}\,\xi)]$ and $\mathrm{tr}[\nabla\times\mathrm{Re}[\boldsymbol{G}(\mathbf{r}_A,\mathbf{r}_A,\omega_{nk})]]$. It is known from dyadic algebra that [24]

$$\mathbf{u}\times\mathbf{ab} = (\mathbf{u}\times\mathbf{a})\mathbf{b}, \tag{B.1}$$

where $\mathbf{ab}$ is a dyadic product and subsequently $(\mathbf{u}\times\mathbf{a})\mathbf{b}$ is also a dyadic product. Applying (B.1) to (43) results in

$$\nabla\times\mathbf{e}_{\mathrm{s}} = -\mathrm{i}\,k\mathbf{e}_{\mathrm{p}}(k_z), \tag{B.2}$$

$$\nabla\times\mathbf{e}_{\mathrm{p}}(k_z) = \mathrm{i}\,k\mathbf{e}_{\mathrm{s}}, \tag{B.3}$$

where $\nabla\to(\mathrm{i}\,k_x,\mathrm{i}\,k_y,\mathrm{i}\,k_z)$. Taking the trace of the dyadic Green's function is equivalent to taking the dot product between the dyads,

$$\mathbf{e}_{\mathrm{s}}\cdot\mathbf{e}_{\mathrm{p}}(-k_z) = \mathbf{e}_{\mathrm{p}}(k_z)\cdot\mathbf{e}_{\mathrm{s}} = 0, \tag{B.4}$$

$$\mathbf{e}_{\mathrm{s}} \cdot \mathbf{e}_{\mathrm{s}} = 1, \quad \mathbf{e}_{\mathrm{p}}(k_z) \cdot \mathbf{e}_{\mathrm{p}}(-k_z) = 1 - \frac{2k_z^2}{k^2}. \tag{B.5}$$

To calculate the off-resonant contribution the integration variable is changed to

$$\int \mathrm{d}\mathbf{k}_{\mathrm{q}} \to \int_0^{2\pi} \mathrm{d}\theta \int_0^{\infty} \mathrm{d}k_q k_q \to -2\pi \int_{\frac{\omega}{c}}^{\infty} \mathrm{d}k_z k_z,$$

the wavevectors in complex frequency ($\omega \to \mathrm{i}\,\xi$) become

$$k_1 = \mathrm{i}\frac{\xi}{c} = \mathrm{i}\tilde{k}_1, \quad k_{1z} = \mathrm{i}\tilde{k}_{1z} \tag{B.6}$$

with

$$\tilde{k}_{1z} = \sqrt{\left(\frac{\xi}{c}\right)^2 + \left(k_{1q}\right)^2} \tag{B.7}$$

in the achiral halfspace and

$$\begin{aligned} k_2^{\mathrm{R}} &= \mathrm{i}\left(\frac{\xi}{c}\right)\left(\kappa_2 + \sqrt{\varepsilon_2\mu_2}\right) = \mathrm{i}\tilde{k}_2^{\mathrm{R}}, \\ k_2^{\mathrm{L}} &= \mathrm{i}\left(\frac{\xi}{c}\right)\left(-\kappa_2 + \sqrt{\varepsilon_2\mu_2}\right) = \mathrm{i}\tilde{k}_2^{\mathrm{L}}, \\ k_{2z}^{P} &= \mathrm{i}\,\tilde{k}_{2z}^{P}, \\ \tilde{k}_{2z}^{P} &= \sqrt{\left(\tilde{k}_2^{P}\right) + \left(k_{2q}\right)^2} \end{aligned} \tag{B.8}$$

in the chiral halfspace.

References

[1] Condon E U 1937 *Rev. Mod. Phys.* **9** 432
[2] Král P, Thanopulos I, Shapiro M and Cohen D 2003 *Phys. Rev. Lett.* **90** 033001
[3] Vardanega D, Picaud F and Giradet C 2007 *Surf. Sci.* **601** 3818
[4] Trost J and Hornberger K 2009 *Phys. Rev. Lett.* **103** 023202
[5] Craig D P and Thirunamachandran T 1984 *Molecular Quantum Electrodynamics* (New York: Academic)
[6] Casimir H B G and Polder D 1948 *Phys. Rev.* **73** 360
[7] Rauk A 1984 *J. Am. Chem. Soc.* **106** 6517
[8] Crawford T D 2006 *Theor. Chem. Acc.* **115** 227
[9] Trost J and Hornberger K 2007 *Chem. Phys.* **335** 115
[10] Ettl R, Chao I, Diederich F and Whetten R L 1991 *Nature* **353** 149
[11] Soukoulis C M and Wegener M 2011 *Nature Photon.* **5** 523
[12] Gansel J K, Thiel M, Rill M S, Decker M, Bade K, Saile V, von Freymann G, Linden S and Wegener M 2009 *Science* **325** 1513
[13] Rill M S, Kriegler C E, Thiel M, von Freymann G, Linden S and Wegener M 2009 *Opt. Lett.* **34** 16
[14] Zhang S, Park Y-S, Li J, Lu X, Zhang W and Zhang X 2009 *Phys. Rev. Lett.* **102** 023901
[15] Hentschel M, Schäferling M, Weiss T, Liu N and Giessen H 2012 *Nano Lett.* **12** 2542
[16] Tang Y and Cohen A E 2010 *Phys. Rev. Lett.* **104** 163901
[17] Hendry E, Carpy T, Johnston J, Popland M, Mikhaylovskiy R V, Lapthorn A J, Kelly S M, Barron L D, Gadegaard N and Kadodwala M 2010 *Nature Nanotechnol.* **5** 783

[18] Zhao R, Zhou J, Koschny Th, Economou E N and Soukoulis C M 2009 *Phys. Rev. Lett.* **103** 103602
[19] Scheel S and Buhmann S Y 2008 *Acta Phys. Slovaca* **58** 675
[20] Buhmann S Y, Butcher D T and Scheel S 2012 *New J. Phys.* **14** 083034
[21] Guérin F 1994 *PIER* **9** 31
[22] Ali S M, Habashy T M and Kong J A 1992 *J. Opt. Soc. Am.* A **9** 413
[23] Tsitsas N L, Lakhtakia A and Frantzeskakis D J 2011 *J. Phys. A: Math. Theor.* **44** 435203
[24] Chen H C 1983 *Theory of Electromagnetic Waves: A Coordinate-Free Approach* (New York: McGraw-Hill)

PRL 118, 193401 (2017) PHYSICAL REVIEW LETTERS week ending 12 MAY 2017

Enhanced Chiral Discriminatory van der Waals Interactions Mediated by Chiral Surfaces

Pablo Barcellona,[1,*] Hassan Safari,[2,†] A. Salam,[3,‡] and Stefan Yoshi Buhmann[1,4,§]
[1]Physikalisches Institut, Albert-Ludwigs-Universität Freiburg, Hermann-Herder-Straße 3, 79104 Freiburg, Germany
[2]Physics and Photonics Department, Graduate University of Advanced Technology, P.O. Box 76315-117, Mahan, Kerman, Iran
[3]Department of Chemistry, Wake Forest University, Winston-Salem, North Carolina 27109, USA
[4]Freiburg Institute for Advanced Studies, Albert-Ludwigs-Universität Freiburg, Albertstraße 19, 79104 Freiburg, Germany
(Received 10 June 2016; revised manuscript received 23 January 2017; published 11 May 2017)

We predict a discriminatory interaction between a chiral molecule and an achiral molecule which is mediated by a chiral body. To achieve this, we generalize the van der Waals interaction potential between two ground-state molecules with electric, magnetic, and chiral response to nontrivial environments. The force is evaluated using second-order perturbation theory with an effective Hamiltonian. Chiral media enhance or reduce the free interaction via many-body interactions, making it possible to measure the chiral contributions to the van der Waals force with current technology. The van der Waals interaction is discriminatory with respect to enantiomers of different handedness and could be used to separate enantiomers. We also suggest a specific geometric configuration where the electric contribution to the van der Waals interaction is zero, making the chiral component the dominant effect.

DOI: 10.1103/PhysRevLett.118.193401

Introduction.—Casimir and van der Waals (vdW) forces are electromagnetic interactions between neutral macroscopic bodies and/or molecules due to the quantum fluctuations of the electromagnetic field [1–3]. In particular, the attractive vdW potential between two electrically polarizable particles was first derived by Casimir and Polder using the minimal-coupling Hamiltonian [2]. Molecules can also exhibit magnetic [4–7] and chiral polarizabilities [4,8,9] and their contribution to the vdW force can be repulsive.

The aim of this work is the study of the interaction between chiral molecules in the presence of a chiral magnetodielectric body. Chiral molecules lack any center of inversion or plane of symmetry. Hence they exist as two distinct enantiomers, left handed and right handed, which are related to space inversion. Because of their low symmetry they have distinctive interactions with light. In a chiral solution the refractive indices for circularly polarized light of different handedness are different. Hence a chiral solution can rotate the plane of polarization of light with an angle related to the concentration of the solution (optical rotation) [10–12], or absorb left- and right-circularly polarized light at different rates (circular dichroism) [13]. All of these phenomena are related to the optical rotatory strength, defined in terms of electric ($\mathbf{d}_{nk}$) and magnetic ($\mathbf{m}_{nk}$) dipole moment matrix elements [14]:

$$R_{nk} = \mathrm{Im}(\mathbf{d}_{nk} \cdot \mathbf{m}_{kn}). \tag{1}$$

The rotatory strength changes sign under spatial inversion. Hence the contributions of the vdW force containing the rotatory strength are discriminatory with respect to the handedness of enantiomers [8,15,16]. According to the Curie dissymmetry principle [17], the handedness of an enantiomer can only be detected by means of a second reference object which is also chiral ("it takes a thief to catch a thief"). This second object can be either a second chiral molecule, or in our case, a chiral medium.

Such discriminatory features could play an important role in the separation of enantiomers [15], which nowadays is achieved with other methods like Coulomb explosion imaging [18], rotational spectroscopy [19], and liquid chromatography [20].

Previously, the vdW interaction between two chiral molecules was considered in free space [8]. In this scenario the chiral part of the vdW force is several orders of magnitude smaller than the purely electric contribution. We will show that this is no longer true when the chiral molecules are near a magnetodielectric body which exhibits chiral properties. Chiral media can be realized experimentally using tunable metamaterials [21], made from structures such as a gold helix [22] or a twisted woodpile [23], where large optical activity requires the lack of a mirror plane parallel to the substrate. These media will enhance or reduce the vdW potential via many-body interactions [24,25]. Note that evidence for three-body dispersion forces has recently been found for the critical Casimir effect [26].

This Letter is organized as follows. We first develop an effective Hamiltonian in order to derive the vdW potential between two chiral molecules near magnetodielectric bodies. We then study the interaction between two chiral molecules in free space and subsequently introduce a chiral plate in order to enhance the chiral contribution.

van der Waals potential.—In order to consider the vdW interaction of chiral molecules with a generic body, field quantization in an absorbing chiral medium is required [15]. We introduce the vector field $\hat{\mathbf{f}}_\sigma(\mathbf{r},\omega)$ as the bosonic annihilation operator for the electric ($\sigma = 0$) and magnetic

PRL 118, 193401 (2017) PHYSICAL REVIEW LETTERS week ending 12 MAY 2017

($\sigma = 1$) excitations, respectively. They obey the commutation relation $[\hat{\mathbf{f}}_\sigma(\mathbf{r},\omega), \hat{\mathbf{f}}^\dagger_{\sigma'}(\mathbf{r}',\omega')] = \delta_{\sigma\sigma'}\boldsymbol{\delta}(\mathbf{r}-\mathbf{r}')\delta(\omega-\omega')$. Denoting by $|\{0\}\rangle$ the vacuum state of the electromagnetic field, $\hat{\mathbf{f}}_\sigma(\mathbf{r},\omega)|\{0\}\rangle = 0\ \forall\sigma,\mathbf{r},\omega$, the excited photonic states are obtained by repeated action of the creation operator on the vacuum state. For instance, a two-photon excited state is given as $(1/\sqrt{2})\hat{\mathbf{f}}^\dagger_\sigma(\mathbf{r},\omega)\hat{\mathbf{f}}^\dagger_{\sigma'}(\mathbf{r}',\omega')|\{0\}\rangle = |\mathbf{1}_\sigma(\mathbf{r},\omega), \mathbf{1}_{\sigma'}(\mathbf{r}',\omega')\rangle$. Introducing the frequency component of the fields by $\hat{\mathbf{E}}(\mathbf{r}) = \int_0^\infty d\omega\hat{\mathbf{E}}(\mathbf{r},\omega) + \text{H.c.}$, which for the free field in the Heisenberg picture are simply Fourier components, we may write the electric field in terms of the bosonic annihilation operators as

$$\hat{\mathbf{E}}(\mathbf{r},\omega) = \int d^3\mathbf{r}' \sum_{\sigma=0,1} \mathbf{G}_\sigma(\mathbf{r},\mathbf{r}',\omega)\cdot\hat{\mathbf{f}}_\sigma(\mathbf{r}',\omega) \tag{2}$$

and $\hat{\mathbf{B}}(\mathbf{r},\omega) = \nabla\times\hat{\mathbf{E}}(\mathbf{r},\omega)/i\omega$ with the tensors $\mathbf{G}_\sigma$ being defined in terms of the Green's tensor $\mathbf{G}$ according to Ref. [15]. The Green's tensor contains all geometrical as well as magnetodielectric properties of the environment via the frequency-dependent relative permittivity, relative permeability, and chiral susceptibility. It satisfies a useful integral relation with the mode tensors $\mathbf{G}_\sigma$:

$$\sum_{\sigma=0,1}\int d^3\mathbf{s}\mathbf{G}_\sigma(\mathbf{r},\mathbf{s},\omega)\cdot\mathbf{G}^{*\top}_\sigma(\mathbf{r}',\mathbf{s},\omega) = \frac{\hbar\mu_0}{\pi}\omega^2\text{Im}\mathbf{G}(\mathbf{r},\mathbf{r}',\omega), \tag{3}$$

where μ_0 is the vacuum permeability.

The interaction between atoms (or molecules) and the field may be described by an effective interaction Hamiltonian [27], which represents processes where two photons are created or annihilated at the same time:

$$\hat{H}_{AF} = -\frac{1}{2}\alpha_{ij}E_iE_j - \frac{1}{2}\chi_{ij}(E_iB_j - B_jE_i), \tag{4}$$

where α is the electric polarizability and $\chi = \chi^{em}$ represents the chiral polarizability. It can be expressed in terms of the electric and magnetic dipole moments:

$$\chi(\omega) = \frac{1}{\hbar}\sum_k\left(\frac{\mathbf{d}_{k0}\mathbf{m}_{0k}}{\omega^A_k+\omega} + \frac{\mathbf{d}_{0k}\mathbf{m}_{k0}}{\omega^A_k-\omega}\right), \tag{5}$$

where $\omega^A_k = (E^A_k - E^A_0)/\hbar$ is the transition frequency between the excited state k and the ground state. In writing the effective Hamiltonian we have considered chiral molecules which respect time-reversal symmetry. In this case, Lloyd's theorem states that electric dipole moments are real, while magnetic dipole moments are purely imaginary [28]. We thus have $\chi^{me} = -\chi^{em\top}$. The chiral polarizability describes a mixed electric-magnetic response where an applied magnetic field contributes to an electric dipole moment in the atom:

$$\hat{\mathbf{d}} = \boldsymbol{\alpha}(\omega)\cdot\hat{\mathbf{E}}(\omega) + \boldsymbol{\chi}(\omega)\cdot\hat{\mathbf{B}}(\omega),$$
$$\hat{\mathbf{m}} = -\boldsymbol{\chi}^\top(\omega)\cdot\hat{\mathbf{E}}(\omega). \tag{6}$$

Thus the direction of the electric dipole moment is slightly rotated with respect to the direction of the electric field. The chiral polarizability is discriminatory since it changes sign between different enantiomers. It vanishes for achiral molecules because of parity.

With the interaction Hamiltonian being quadratic in the fundamental operators $\hat{\mathbf{f}}_\lambda$ and $\hat{\mathbf{f}}^\dagger_\lambda$, it is seen that the energy shift describing the interaction between the two molecules A and B can be obtained from second order perturbation theory

$$\Delta E_{(2)} = -\sum_I \frac{\langle 0|\hat{H}_{\text{int}}|I\rangle\langle I|\hat{H}_{\text{int}}|0\rangle}{E_I - E_0} \equiv U(\mathbf{r}_A,\mathbf{r}_B), \tag{7}$$

where $|0\rangle \equiv |0\rangle_A|0\rangle_B|\{0\}\rangle$ and $\hat{H}_{\text{int}} = \hat{H}_{AF} + \hat{H}_{BF}$. The intermediate state $|I\rangle$ corresponds to a state in which both molecules are in their ground state with two virtual photons being present. The relevant two-photon processes are represented by the Feynman diagrams in Fig. 1. The collective sum in Eq. (7) runs over both discrete and continuous parameters. Using the interaction Hamiltonian (4), making use of the integral relation (3), and simplifying the resulting expression using the contour integral technique in the complex frequency plane, the purely electric and electric-chiral energy shifts take the final forms

$$U^{EE}(\mathbf{r}_A,\mathbf{r}_B) = -\frac{\hbar\mu_0^2}{2\pi}\int_0^\infty d\xi\xi^4\text{Tr}\{\boldsymbol{\alpha}_A(i\xi)\cdot\mathbf{G}(\mathbf{r}_A,\mathbf{r}_B,i\xi)\cdot\boldsymbol{\alpha}_B(i\xi)\cdot\mathbf{G}(\mathbf{r}_B,\mathbf{r}_A,i\xi)\} \tag{8a}$$

$$U^{CE}(\mathbf{r}_A,\mathbf{r}_B) = \frac{\hbar\mu_0^2}{\pi}\int_0^\infty d\xi\xi^3\text{Tr}\{\boldsymbol{\chi}_A(i\xi)\cdot\nabla_A\times\mathbf{G}(\mathbf{r}_A,\mathbf{r}_B,i\xi)\cdot\boldsymbol{\alpha}_B(i\xi)\cdot\mathbf{G}(\mathbf{r}_B,\mathbf{r}_A,i\xi)\}. \tag{8b}$$

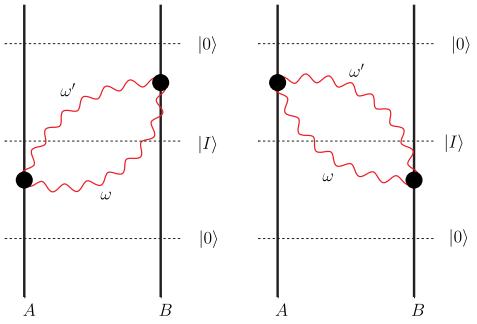

FIG. 1. van der Waals force between two molecules: two-photon exchange.

Resonant terms in the molecular frequencies have been avoided by means of infinitesimal imaginary shifts. The purely electric (achiral) contribution is well known in literature [7,29]. Other terms contributing to the total van der Waals interaction are given in the Supplemental Material [30].

Chiral molecules in free space.—To apply our general results to free space, one uses the bulk Green's tensor

$$\mathbf{G}^{(0)}(\mathbf{r}_A,\mathbf{r}_B,i\xi)=\frac{c^2e^{-\xi r/c}}{4\pi\xi^2r^3}\left[a\left(\frac{\xi r}{c}\right)\mathbf{I}-b\left(\frac{\xi r}{c}\right)\mathbf{e}_\mathbf{r}\mathbf{e}_\mathbf{r}\right], \quad (9)$$

where c is the speed of light, $\mathbf{r}=\mathbf{r}_B-\mathbf{r}_A$, $r=|\mathbf{r}|$, $\mathbf{e}_\mathbf{r}=\mathbf{r}/r$, $a(x)=1+x+x^2$, and $b(x)=3+3x+x^2$.

The order of magnitude of a specific contribution of the vdW energy is roughly given by the respective polarizability, and thus depends on the numbers of electric and magnetic dipole moments. An electric dipole has an order of magnitude of ea_B, where a_B is the Bohr radius, while the magnetic moment has an order of magnitude of the Bohr magneton $e\hbar/2m$. Hence $[(m/c)/d]$ is of the order of the fine-structure constant. The leading order contribution is that from the purely electric term, which contains four electric dipole moments.

The next-to-leading term is the chiral-electric contribution $U^{CE}(r)$, which contains three electric and one magnetic dipole moments. However, if the chiral polarizability of the molecule is isotropic, $U^{CE}(r)=0$. This vanishing interaction is a consequence of the Curie dissymmetry principle [17]: the vdW potential cannot distinguish the handedness of the chiral molecule if the other molecule is not chiral.

The next-order terms contain two electric and two magnetic dipole moments: $U^{\mathrm{EM}}(r)$ and $U^{CC}(r)$. For isotropic polarizabilities, it has been shown that [8,9]:

$$U^{CC}(r)=\frac{\hbar}{8\pi^3\epsilon_0^2r^6}\int_0^\infty d\xi\frac{\chi_A(i\xi)}{c}\frac{\chi_B(i\xi)}{c}l\left(\frac{\xi r}{c}\right), \quad (10)$$

where $l(x)=e^{-2x}(3+6x+4x^2)$ and ϵ_0 is the vacuum permittivity. The interaction scales as r^{-6} in the nonretarded limit, but decreases more rapidly in the far zone (r^{-9}) due to the finite velocity of light. This result can be obtained in our formalism by using the vacuum Green's tensor.

Because the purely electric energy contains four electric dipole moments and U^{CC} contains two electric and two magnetic dipole moments, the latter is roughly 4 orders of magnitude smaller than the former. This shows the necessity to use magnetodielectric bodies to make the chiral contribution appreciable. While $U^{CE}(r)$ is strictly zero in free space for isotropic molecules, this is no longer true with general material environments, which exhibit chiral properties.

Chiral molecules near a perfect chiral plate.—With the introduction of a body, the fluctuations of the electromagnetic field are influenced by the presence of the boundary. The interaction between chiral molecules is a two-photon exchange, where photons can be reflected by the body's surface (Fig. 2). The total Green's tensor is the sum of the bulk (free-space) Green's tensor $\mathbf{G}^{(0)}$ and the scattering Green's tensor of the plate $\mathbf{G}^{(1)}$, that accounts for the reflection of the electromagnetic field from surfaces: $\mathbf{G}=\mathbf{G}^{(0)}+\mathbf{G}^{(1)}$.

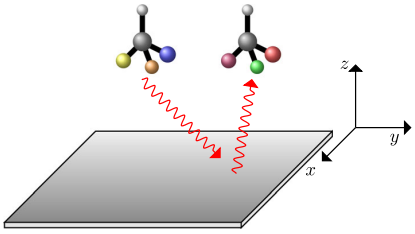

FIG. 2. Medium-assisted vdW interaction between two molecules: direct or indirect exchange of two photons.

If one species is chiral and the other one is achiral we need a chiral surface to observe a discriminatory effect. The simplest surface is a perfect chiral plate which reflects a p-polarized wave to an s-polarized wave and *vice versa* with reflection coefficients $r_{s\to p}$ and $r_{p\to s}$. This is a limit of a chiral plate, which may be approached for metamaterials with large optical activity. In other words, it rotates the polarization of an incoming wave by an angle of $\pm\pi/2$ when looking along the direction of the wave vector. Its scattering Green's tensor reads

$$\begin{aligned}\mathbf{G}^{(1)}(\mathbf{r}_A,\mathbf{r}_B,i\xi)=&\frac{1}{8\pi^2}\int_0^{2\pi}d\varphi\int_0^\infty dk^\parallel\frac{k^\parallel}{\kappa^\perp}e^{-\kappa^\perp z_+}\\&\times e^{-ik^\parallel(x\cos\varphi+y\sin\varphi)}\\&\times(\mathbf{e}_{p+}\mathbf{e}_{s-}r_{s\to p}+\mathbf{e}_{s+}\mathbf{e}_{p-}r_{p\to s}),\end{aligned} \quad (11)$$

where $x=x_B-x_A$, $y=y_B-y_A$, $z_+=z_A+z_B$, and we have introduced the polarization unit vectors $\mathbf{e}_{s\pm}=(\sin\varphi,-\cos\varphi,0)$, $\mathbf{e}_{p\pm}=(c/\xi)(\mp\kappa^\perp\cos\varphi,\mp\kappa^\perp\sin\varphi,-ik^\parallel)$. The parallel and perpendicular components of the wave vector, $k^\parallel$ and $\kappa^\perp$, are related via $\kappa^\perp=\sqrt{\xi^2/c^2+k^{\parallel2}}$. For a plate of positive chirality $r_{s\to p}=-1$, $r_{p\to s}=1$, and for a plate of negative chirality $r_{s\to p}=1$, $r_{p\to s}=-1$.

The perfect chiral plate has no influence on the purely electric contribution, which reduces to the well-known electric van der Waals interaction in free space. Instead, it influences the leading-order chiral contribution, which in the nonretarded limit (all distances much lower than the relevant atomic transition wavelength) reads

$$\begin{aligned}U^{CE}_{\mathrm{nr}}=&\pm\frac{\hbar}{16\pi^3\epsilon_0^2}\int_0^\infty d\xi\frac{\chi_A(i\xi)}{c}\alpha_B(i\xi)\\&\times\frac{r^2[2r_+^2-3(x^2+y^2)]-3r_+^2(x^2+y^2)}{r^5r_+^5},\end{aligned} \quad (12)$$

PRL 118, 193401 (2017) PHYSICAL REVIEW LETTERS week ending 12 MAY 2017

where $r_+ = \sqrt{x^2 + y^2 + z_+^2}$. If the two species are chiral, there is another discriminatory term U^{CC} which is, however, much smaller than U^{CE}.

Consider, for example, the interaction between a rubidium atom and the chiral molecule 3-methylcyclopentanone (3-MCP) [32,33]. The molecule 3-MCP has a particularly small electric dipole moment and a magnetic dipole moment comparable to the Bohr magneton; this kind of system is suitable to observe enhanced chiral effects.

We suppose the position of the molecule A is fixed and we write the resulting energy in terms of the interparticle separation $\mathbf{r} = \mathbf{r}_B - \mathbf{r}_A$; $U(\mathbf{r}_A, \mathbf{r}_A + \mathbf{r})$. The total force acting on B is $\mathbf{F} = -\nabla_{\mathbf{r}} U(\mathbf{r}_A, \mathbf{r}_A + \mathbf{r})$ and its direction differs from $\mathbf{r}$ because of the presence of the additional surface. We choose, without loss of generality, a coordinate system such that the plate corresponds to the $z = 0$ plane, both species lie in the $x = 0$ plane with the coordinates of molecule A being $\mathbf{r}_A = (0, 0, z_A)$. The degree of attractiveness is quantified by using the parameter $\mathbf{e}_{\mathbf{r}} \cdot \mathbf{F}$, where $\mathbf{e}_{\mathbf{r}} = \mathbf{r}/r$.

A three-dimensional plot shows the relative importance between electric and chiral contributions for a plate of negative chirality (see Fig. 3). The chiral contribution is maximally enhanced when both species are aligned parallel to the surface ($z = 0$), having a large distance along the y direction ($y/z_A \gg 1$). In this case the chiral contribution is attractive and one order of magnitude smaller than the purely electric contribution ($\mathbf{e}_{\mathbf{r}} \cdot \mathbf{F}^{CE}/\mathbf{e}_{\mathbf{r}} \cdot \mathbf{F}^{EE} \simeq 6.75\%$). When both species are aligned perpendicular to the surface ($y = 0$) and have a large distance along the z direction ($z/z_A \gg 1$), the chiral contribution is repulsive and 2 orders of magnitude smaller than the electric contribution ($\mathbf{e}_{\mathbf{r}} \cdot \mathbf{F}^{CE}/\mathbf{e}_{\mathbf{r}} \cdot \mathbf{F}^{EE} \simeq -3.37\%$).

Our chiral contribution could be observed in Rydberg molecules, which have large dipole moments and therefore strong van der Waals interactions [34]. We expect a strongly enhanced interaction between a Rydberg molecule and a chiral molecule, which does not have to be in a Rydberg state. On the other hand it has been recognized that it is possible to create chiral Rydberg molecules, exciting moving Rydberg atoms of rubidium by two right- or two left-circularly polarized photons [35]. Such systems could be used in a proof-of-principle experiment. If two identical chiral Rydberg molecules are exposed to a resonant laser, the laser can cause the system to oscillate between the ground state and the excited states. From the oscillations of the molecular populations it is possible to deduce the van der Waals interaction. The experiment has been performed with rubidium atoms where C_6 (van der Waals coefficient of the energy $U = -C_6/r^6$) has been determined with an accuracy of 2.7% for the excited Rydberg state $n = 62$ [36]. Note that if one molecule is absorbed onto the surface the strength of the interaction is even higher because of the influence of the substrate on the molecular polarizability, as shown in Ref. [37].

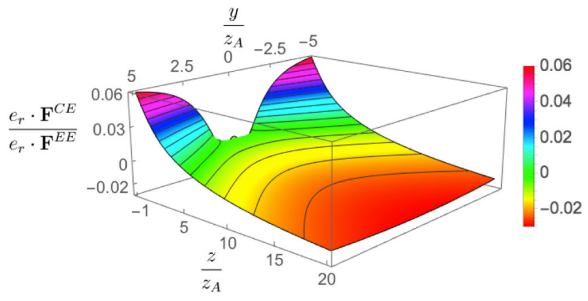

FIG. 3. $\mathbf{e}_{\mathbf{r}} \cdot \mathbf{F}^{CE}/\mathbf{e}_{\mathbf{r}} \cdot \mathbf{F}^{EE}$ for a rubidium atom (atom B) and the chiral molecule 3-MCP (molecule A).

Most importantly, the chiral contribution is discriminatory: it changes sign if we substitute a chiral molecule with its enantiomer or a positive chiral plate with a negative one. Hence by determining whether the free interaction is enhanced or reduced by the presence of the plate, it could be possible to identify the handedness of the chiral molecule. This discriminatory effect also suggests configurations, where the nonchiral contributions of the van der Waals force completely vanish, but not the chiral contributions. Fig. 4 shows such possible geometry. Three species are in the symmetry axis of a cavity composed of two identical chiral plates. We are interested in the force acting on the middle achiral atom B. This experiment allows us to establish if the two chiral molecules A and C have the same handedness. If A and C have the same handedness then the force acting on B is strictly zero; this is no longer true if they are opposite enantiomers because of chiral discriminatory contributions of the vdW force. This interaction is enantiomer selective because atom B will be attracted or repelled from molecule A depending on the handedness of the latter. Hence if we know the handedness of one chiral molecule we are able to determine the handedness of the other one with this experiment. Note that the recently predicted exponential suppression of the electric vdW potential in a parallel mirror cavity [38] or in a planar waveguide [39] might further assist the observability of the chiral component. Three-body discriminatory chiral contributions are also present in the cavity configuration; however, they are smaller with respect to the analyzed two-body contributions.

Alternatively, in scattering experiments one commonly has molecular beams of chiral molecules containing both enantiomers in equal proportions. This molecular beam can

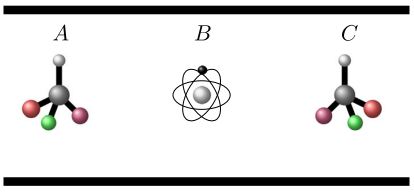

FIG. 4. Three species parallel in the symmetry axis of a cavity.

travel near a gas of chiral molecules of one handedness, prepared, for example, with liquid chromatography. The interactions with the gas molecules will lead to a separation of the trajectories of the molecules in the beam, depending on their handedness. This trajectory imaging technique has been already used for rubidium Rydberg atoms [40].

Conclusions.—Our model, which combines time-independent perturbation theory with an effective-Hamiltonian approach, has allowed us to study the influence of material environments on the vdW interaction involving chiral molecules.

We see that surfaces with chiral properties can significantly enhance chiral contributions. The chiral contribution can be repulsive unlike the purely electric force which is always attractive. For some positions the plate enhances the free interaction (attractive chiral contribution) and for other positions it reduces the interaction (repulsive chiral contribution).

Second, the chiral force is discriminatory with respect to enantiomers of different handedness, this opening an interesting perspective on the separation of enantiomers. We suggest symmetric configurations where we selectively cancel the purely electric contribution, but not the chiral components: this selective cancellation is a direct consequence of the nondiscriminatory nature of electric and magnetic interactions, and the discriminatory nature of the chiral components.

This work was supported by the Deutsche Forschungsgemeinschaft (Grants No. BU 1803/3–1 and No. GRK 2079/1) and the Freiburg Institute for Advanced Studies (FRIAS).

*pablo.barcellona@physik.uni-freiburg.de
†h.safari@kgut.ac.ir
‡salama@wfu.edu
§stefan.buhmann@physik.uni-freiburg.de

[1] H. B. G. Casimir, Proc. K. Ned. Akad. Wet. **51**, 793 (1948).
[2] H. B. G. Casimir and D. Polder, Phys. Rev. **73**, 360 (1948).
[3] P. W. Milonni, *The Quantum Vacuum* (Academic Press, San Diego, 1994).
[4] C. Mavroyannis and M. J. Stephen, Mol. Phys. **5**, 629 (1962).
[5] G. Feinberg and J. Sucher, J. Chem. Phys. **48**, 3333 (1968).
[6] G. Feinberg and J. Sucher, Phys. Rev. A **2**, 2395 (1970).
[7] H. Safari, D.-G. Welsch, S. Y. Buhmann, and S. Scheel, Phys. Rev. A **78**, 062901 (2008).
[8] J. K. Jenkins, A. Salam, and T. Thirunamachandran, Phys. Rev. A **50**, 4767 (1994).
[9] A. Salam, *Molecular Quantum Electrodynamics* (Wiley, Hoboken, 2010).
[10] L. Rosenfeld, Z. Phys. **52**, 161 (1929).
[11] P. W. Atkins and L. D. Barron, Proc. R. Soc. A **304**, 303 (1968).
[12] E. A. Power and T. Thirunamachandran, J. Chem. Phys. **55**, 5322 (1971).
[13] E. A. Power and T. Thirunamachandran, J. Chem. Phys. **60**, 3695 (1974).
[14] D. P. Craig and T. Thirunamachandran, *Molecular Quantum Electrodynamics* (Dover, New York, 1998).
[15] D. T. Butcher, S. Y. Buhmann, and S. Scheel, New J. Phys. **14**, 113013 (2012).
[16] S. Y. Buhmann, *Dispersion Forces I* (Springer, Heidelberg, 2012).
[17] P. Curie, J. Phys. Theor. Appl. **3**, 393 (1894).
[18] M. Pitzer, M. Kunitski, A. S. Johnson, T. Jahnke, H. Sann, F. Sturm, L. Ph. H. Schmidt, H. Schmidt-Böcking, R. Dörner, J. Stohner, J. Kiedrowski, M. Reggelin, S. Marquardt, A. Schieer, R. Berger, and M. S. Schöffler, Science **341**, 1096 (2013).
[19] V. A. Shubert, D. Schmitz, C. Prez, C. Medcraft, A. Krin, S. R. Domingos, D. Patterson, and M. Schnell, J. Phys. Chem. Lett. **7**, 341 (2016).
[20] K. Kimata, K. Hosoya, T. Araki, and N. Tanaka, Anal. Chem. **69**, 2610 (1997).
[21] C. M. Soukoulis and M. Wegener, Nat. Photonics **5**, 523 (2011).
[22] J. K. Gansel, M. Thiel, M. S. Rill, M. Decker, K. Bade, V. Saile, G. von Freymann, S. Linden, and M. Wegener, Science **325**, 1513 (2009).
[23] M. S. Rill, C. E. Kriegler, M. Thiel, G. von Freymann, S. Linden, and M. Wegener, Opt. Lett. **34**, 19 (2009).
[24] K. V. Shajesh and M. Schaden, Int. J. Mod. Phys. Conf. Ser. **14**, 521 (2012).
[25] K. A. Milton, E. Abalo, P. Parashar, and K. V. Shajesh, Nuovo Cimento C **36**, 183 (2013).
[26] S. Paladugu, A. Callegari, Y. Tuna, L. Barth, S. Dietrich, A. Gambassi, and G. Volpe, Nat. Commun. **7**, 11403 (2016).
[27] R. Passante, E. A. Power, and T. Thirunamachandran, Phys. Lett. A **249**, 77 (1998).
[28] S. P. Lloyd, Phys. Rev. **81**, 161 (1951).
[29] H. Safari, S. Y. Buhmann, D. G. Welsch, and H. T. Dung, Phys. Rev. A **74**, 042101 (2006).
[30] See Supplemental Material at http://link.aps.org/supplemental/10.1103/PhysRevLett.118.193401 for a more detailed derivation of van der Waals forces involving electric, magnetic and chiral molecules, which includes Ref. [31].
[31] S. Y. Buhmann and S. Scheel, Phys. Rev. Lett. **102**, 140404 (2009).
[32] D. A. Steck, Rubidium 87D line data, http://steck.us/alkalidata.
[33] D. Kröner, J. Phys. Chem. A **115**, 14510 (2011).
[34] J. A. Crosse, S. A. Ellingsen, K. Clements, S. Y. Buhmann, and S. Scheel, Phys. Rev. A **82**, 010901 (2010).
[35] N. I. Hammer, F. Gao, R. M. Pagni, and R. N. Compton, J. Phys. Chem. **117**, 4299 (2002).
[36] L. Beguin, A. Vernier, R. Chicireanu, T. Lahaye, and A. Browaeys, Phys. Rev. Lett. **110**, 263201 (2013).
[37] S. Kawai, A. S. Foster, T. Björkman, S. Nowakowska, J. Björk, F. Federici Canova, L. H. Gade, T. A. Jung, and E. Meyer, Nat. Commun. **7**, 11559 (2016).
[38] R. de Melo e Souza, W. J. M. Kort-Kamp, F. S. S. Rosa, and C. Farina, Phys. Rev. A **91**, 052708 (2015).
[39] H. R. Haakh and S. Scheel, Phys. Rev. A **91**, 052707 (2015).
[40] N. Thaicharoen, A. Schwarzkopf, and G. Raithel, Phys. Rev. A **92**, 040701 (2015).

THE JOURNAL OF PHYSICAL CHEMISTRY A
Article
Cite This: J. Phys. Chem. A 2017, 121, 9742−9751
pubs.acs.org/JPCA

Effective Polarizability Models

Johannes Fiedler,[*,†] Priyadarshini Thiyam,[*,‡,§] Anurag Kurumbail,[∥] Friedrich A. Burger,[†] Michael Walter,[†,⊥,#] Clas Persson,[‡,§] Iver Brevik,[∥] Drew F. Parsons,[*,¶] Mathias Boström,[*,∥] and Stefan Y. Buhmann[*,†,▽]

[†]Physikalisches Institut, Albert-Ludwigs-Universität Freiburg, Hermann-Herder-Strasse 3, 79104 Freiburg, Germany
[‡]Department of Materials Science and Engineering, KTH, Royal Institute of Technology, SE-100 44 Stockholm, Sweden
[§]Centre for Materials Science and Nanotechnology, Department of Physics, University of Oslo, P.O. Box 1048, Blindern, NO-0316 Oslo, Norway
[∥]Department of Energy and Process Engineering, Norwegian University of Science and Technology, NO-7491 Trondheim, Norway
[⊥]FIT Freiburg Centre for Interactive Materials and Bioinspired Technologies, Georges-Köhler-Allee 105, 79110 Freiburg, Germany
[#]Fraunhofer IWM, Wöhlerstrasse 11, D-79108 Freiburg i. Br., Germany
[¶]School of Engineering and IT, Murdoch University, 90 South Street, Murdoch, WA 6150, Australia
[▽]Freiburg Institute for Advanced Studies, Albert-Ludwigs-Universität Freiburg, Albertstrasse 19, 79104 Freiburg, Germany

ABSTRACT: Theories for the effective polarizability of a small particle in a medium are presented using different levels of approximation: we consider the virtual cavity, real cavity, and the hard-sphere models as well as a continuous interpolation of the latter two. We present the respective hard-sphere and cavity radii as obtained from density-functional simulations as well as the resulting effective polarizabilities at discrete Matsubara frequencies. This enables us to account for macroscopic media in van der Waals interactions between molecules in water and their Casimir−Polder interaction with an interface.

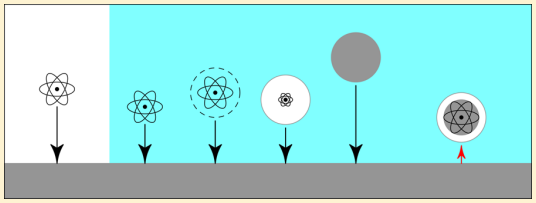

INTRODUCTION

The optical behavior of a small object dissolved in a medium is of interest for a large number of investigations, such as optofluids,[1] medium-assisted density-functional theory (DFT),[2] nanomedicine,[3] hydrogen storage,[4] bio-organics,[5] and photodynamic therapy.[6] The impact of a cavity around the particles is large compared to the typically studied situations where the particles are considered without an environment.

In this fundamental study we derive different models for the effective polarizability of small particles in a medium. The level of accuracy for six different approximations will be discussed and our results exploited to calculate Casimir−Polder forces in a medium. The new theoretical results are then applied to greenhouse gas molecules,[7] and other gas molecules, dissolved in water. After water vapor and carbon dioxide, methane and nitrous oxide are the most important long-lived greenhouse gases in the atmosphere. Release of greenhouse gases from surfaces in water is influenced by the Casimir−Polder interaction. To estimate the Casimir−Polder binding gas particles to surfaces, one needs to have accurate effective polarizabilities of the greenhouse gas molecules in water. As input parameters in our models, we require the frequency-dependent polarizability of the molecules in a vacuum, hard-sphere radii, cavity radii in water, and the dielectric function of water. We use ab initio quantum chemical calculations to accurately calculate the frequency-dependent polarizabilities of different gas molecules in a vacuum. The result is given as a set of parametrized functions, which enables easy access in future investigations that require these molecular polarizabilities. We also provide the theory for determining the molecular radii and cavity radii of different greenhouse gas molecules in water.

These parametrized functions and tabulated data for radii, together with the new theories and tabulated dielectric function of water for discrete Matsubara frequencies, enable us to calculate the effective polarizability of gas molecules in water. This is a key quantity needed in future studies of binding or release of gas molecules near solid−water interfaces. As an illustrative example we consider the nonretarded van der Waals potential of two molecules in water and their Casimir−Polder potential near a perfect metal surface to illustrate the impact of the different cavity models. Therefore, we treat the environment as a continuous medium as a kind of ensemble average of its constitutions. Due to this reason we focus on single-particle interactions, as they are valid for dilute gases. Further investigations on few- and many-particle interaction embedded in a cavity can be performed additionally.[8−11] This enables us to compare how sensitive the results are to different approximations done when the effective polarizability is evaluated. It turns out that the theoretical sensitivity can be quite large; even the sign of the force on molecules close to a

Received: October 13, 2017
Revised: November 21, 2017
Published: November 29, 2017

The Journal of Physical Chemistry A Article

Table 1. Weights (α_j [10^{-42} A^2 s^4 kg^{-1}] in SI-Units Which Transform to CGS Units via $[\alpha_{SI}] = 4\pi\epsilon_0 10^{-30}$ Å^3) and Characteristic Frequencies (ω_j [10^{16} rad s^{-1}] in SI-Units, Which Transform to CGS Units via $[\omega_{SI}] = 2\pi e/\hbar$ eV) for Five-Mode London Fits of the Dynamic Polarizabilities of Four Greenhouse Gas Molecules CH_4, CO_2, N_2O, and O_3 and Other Atmospheric Gas Molecules

	mode 1		mode 2		mode 3		mode 4		mode 5	
	α_1	ω_1	α_2	ω_2	α_3	ω_3	α_4	ω_4	α_5	ω_5
CH_4	89.3	1.75	137.5	2.56	41.2	4.42	2.78	10	0.18	48.3
CO_2	131.7	1.95	116	3.14	41.5	6.2	6.43	13.3	0.43	51.5
N_2O	121.5	1.64	146.2	54.9	54.9	5.59	8.05	12.3	0.41	53.9
O_3	72	0.89	130	2.28	98.7	4.32	21	9.82	0.89	36.5
O_2	38	1.37	85.4	2.78	41.1	5.42	8.16	10.9	0.76	29.5
N_2	90	2.14	10	3.27	29.9	5.92	3.55	13.2	0.23	60.5
CO	49.1	1.43	120	2.46	41.7	4.95	6.89	11	0.39	45.7
NO_2	16.5	0.63	124	1.65	134.1	3.57	28.8	8.39	1.19	31.6
H_2S	55.1	1.12	99	3.25	251.6	1.86	2.33	9.58	0.98	34.2

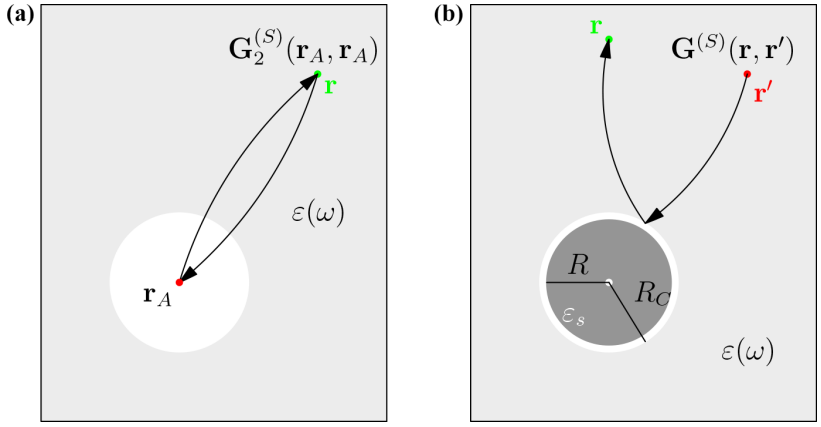

Figure 1. (a) Sketch of Onsager's real cavity model. A particle (red dot) at position $\mathbf{r}_A$ is embedded in a medium with dielectricity $\varepsilon(\omega)$ (grey area) surrounded by a spherical vacuum cavity (white area). The scattering process from an external point $\mathbf{r}$ (green dot) is separated into the propagation to and back from the particle. (b) Sketch of Onsager's real cavity model for finite size particles. A spherical particle with radius R and the dielectric function ε_s is embedded in a medium with $\varepsilon(\omega)$ (grey area) surrounded by a spherical vacuum cavity (white area) with radius R_C. The scattering process from an external point $\mathbf{r}'$ (red dot) to another point $\mathbf{r}$ (green dot).

metal surface can change if we go from one effective polarizability model to another. There is thus a need for experimental information to identify the best model.

FREE-SPACE POLARIZABILITY OF GAS MOLECULES

The Casimir–Polder energy is determined from the effective polarizability of a molecule in a medium at imaginary frequencies $i\xi$. Each of the models of effective polarizability considered in this manuscript describes a different representation of the transformation induced by the medium on the underlying dynamic polarizability $\alpha(i\xi_n)$ of the given molecule in a vacuum (the free-space polarizability). We have computed the free-space polarizability of each molecule by quantum chemical methods. The closed-shell gas molecules, CH_4, CO_2, N_2O, O_3, N_2, CO, and H_2S were calculated at the coupled cluster singles and doubles (CCSD) level of theory[12] using Molpro.[13] The open-shell (paramagnetic) molecules O_2 and NO_2 were calculated using Turbomole[14] at a density functional theory (DFT) level with a hybrid PBE0 functional.[15] Ground states involved higher spin states, O_2 having spin multiplicity 3 (two unpaired electrons), NO_2 with multiplicity 2 (one unpaired electron). For both CCSD and DFT/PBE0 calculations we employed an augmented correlation-consistent basis set, aug-cc-pVQZ.[16] The geometry of each molecule was optimized by energy minimization before evaluating its polarizability. The full anisotropic polarizability tensor was evaluated, and anisotropic effects are known to have an impact on Casimir–Polder interactions.[17,18] However, for simplicity we use the isotropic average, $\alpha = (\alpha_{xx} + \alpha_{yy} + \alpha_{zz})/3$, in this manuscript.

Quantum chemical calculations of dynamic polarizabilities were performed at the Matsubara frequencies $i\xi_n = i2\pi k_B T n/\hbar$ for $T = 298.15$ K with $n = 0, 1, ..., 2100$. It is convenient to represent the polarizability at an arbitrary imaginary frequency $i\xi$ by fitting the polarizability modes to an oscillator model

$$\alpha(i\xi) = \sum_j \frac{\alpha_j}{1 + (\xi/\omega_j)^2} \quad (1)$$

A five-mode fit has previously been found to describe the dynamic polarizability accurately to a 0.02% relative error.[19] The adjusted parameters for a five-mode model fitted to agree with the free-space polarizability obtained from ab initio calculations are given in Table 1.

DOI: 10.1021/acs.jpca.7b10159
J. Phys. Chem. A 2017, 121, 9742–9751

The Journal of Physical Chemistry A Article

CASIMIR–POLDER AND VAN DER WAALS POTENTIAL

The Casimir–Polder force arises when a small particle comes close to a dielectric surface.[20] It is caused by the fluctuations of the ground-state electromagnetic field.[21] Performing the field quantisation and applying second-order perturbation theory to the dipole-electric field Hamiltonian $\hat{H} = -\hat{\mathbf{d}}\cdot\hat{\mathbf{E}}$ for the ground state of the field and particle, one finds the Casimir–Polder potential acting on a particle located at $\mathbf{r}_A$[21,22]

$$U_{CP}(\mathbf{r}_A) = \mu_0 k_B T \sum_{n=0}^{\infty}{}' \xi_n^2 \alpha(i\xi_n)\ \mathrm{tr}[\mathbf{G}^{(S)}(\mathbf{r}_A,\mathbf{r}_A,i\xi_n)] \tag{2}$$

with the Boltzmann constant k_B, the vacuum permeability μ_0, the particle polarizability $\alpha(i\xi)$ at imaginary frequencies $i\xi$, the primed sum means that the zeroth term has to be weighted by $^1/_2$ and the scattering part of the dyadic Green's function $\mathbf{G}^{(S)}$, which satisfies the vector Helmholtz equation

$$\nabla \times \nabla \times \mathbf{G}(\mathbf{r},\mathbf{r}',\omega) - \frac{\omega^2}{c^2}\varepsilon(\mathbf{r},\omega)\,\mathbf{G}(\mathbf{r},\mathbf{r}',\omega) = \boldsymbol{\delta}(\mathbf{r}-\mathbf{r}') \tag{3}$$

with the relative permittivity $\varepsilon(\mathbf{r},\omega)$. The dyadic Green function can be separated into the free propagation through the bulk medium $\mathbf{G}^{(0)}$ and the scattering part $\mathbf{G}^{(S)}$, $\mathbf{G} = \mathbf{G}^{(0)} + \mathbf{G}^{(S)}$. The Casimir–Polder potential, eq 2, shall be understood due to a virtual photon with frequency $i\xi$ being created by the particle at $\mathbf{r}_A$ and backscattered at the dielectric surface as expressed by the scattering Green function. The strength of its fraction to the Casimir–Polder potential is weighted by the polarizability of the particle. Because the fluctuations of the fields ensue at all frequencies, a superposition of all scattering processes results in the Casimir–Polder potential.

Assuming that the particle is located in the nonretarded regime in front of planar surface, the Casimir–Polder potential reduces to the established C_3-potential. This situation is described by the scattering Green function for a planar two-layer system[23]

$$\mathbf{G}(\mathbf{r},\mathbf{r},\omega) = \frac{c^2}{32\pi\omega^2\varepsilon(\omega)z^3}\frac{\varepsilon_H(\omega)-\varepsilon(\omega)}{\varepsilon_H(\omega)+\varepsilon(\omega)}\,\mathrm{diag}(1,1,2) \tag{4}$$

with the dielectric function ε_H describing the electric response of the half-space. A perfectly conducting plate requires the limit $\varepsilon_H(\omega) \to \infty$. Due to the separation of spatial and frequency dependencies of the scattering Green function, the Casimir–Polder potential, eq 2, simplifies to the well-known result

$$U_{CP}(z) = -\frac{C_3}{z^3} \qquad C_3 = \frac{k_B T}{8\pi\varepsilon_0}\sum_{n=0}^{\infty}{}' \frac{\alpha(i\xi_n)}{\varepsilon(i\xi_n)} \tag{5}$$

In analogy, the van der Waals potential describing the interaction between two neutral, but polarizable particles can be derived via the fourth-order perturbation of the two-particle dipole-electric field Hamiltonian $\hat{H} = -\hat{\mathbf{d}}_A\cdot\hat{\mathbf{E}} - \hat{\mathbf{d}}_B\cdot\hat{\mathbf{E}}$, which will be performed for ground-state fields and particles. It results in[21,22]

$$U_{vdW}(\mathbf{r}_A,\mathbf{r}_B) = -k_B T \mu_0^2 \sum_{n=0}^{\infty}{}' \xi_n^4 \alpha_A(i\xi_n)\,\alpha_B(i\xi_n) \times \mathrm{tr}[\mathbf{G}(\mathbf{r}_A,\mathbf{r}_B,i\xi_n)\cdot\mathbf{G}(\mathbf{r}_B,\mathbf{r}_A,i\xi_n)] \tag{6}$$

which has to be read from right to left, and is due to a virtual photon which is created at particle A, propagates to particle B, where it interacts with its polarizability, and is backscattered to particle A. Again, the sum (integral) over all two-photon exchanges results in the van der Waals potential. According to the nonretarded Casimir–Polder potential, the nonretarded Green function[21]

$$\mathbf{G}(\mathbf{r}_A,\mathbf{r}_B,\omega) = -\frac{1}{4\pi k^2(\omega)\varrho^3}(\mathbf{I} - 3\mathbf{e}_\varrho \otimes \mathbf{e}_\varrho) \tag{7}$$

with $\boldsymbol{\varrho} = \mathbf{r}_B - \mathbf{r}_A$, $\varrho = |\boldsymbol{\varrho}|$, $\mathbf{e}_\varrho = \boldsymbol{\varrho}/\varrho$, and $k^2(\omega) = \varepsilon(\omega)\omega^2/c^2$, for the propagation through a bulk medium can be applied. This results in

$$U_{vdW}(r) = -\frac{C_6}{r^6} \qquad C_6 = \frac{3k_B T}{8\pi^2\varepsilon_0^2}\sum_{n=0}^{\infty}{}' \frac{\alpha_A(i\xi_n)\,\alpha_B(i\xi_n)}{\varepsilon^2(i\xi_n)} \tag{8}$$

where r denotes the distance between particle A and B.

The advantage of these formulas is the separation into particle properties $\alpha(i\xi)$ and the scattering processes $\mathbf{G}^{(S)}(\mathbf{r}_A,\mathbf{r}_A,i\xi)$. To describe the Casimir–Polder interaction in media, the scattering Green function changes its properties with respect to the dielectric function of the medium and to the geometrical shape of the cavity around the particle, which gives rise to additional resonances due to the cavity modes. Two different pictures for the consideration of the scattering processes will be used in describing the influence of a cavity effectively. In the first case, the particle is centered in the cavity and the scattering through the cavity's boundary is considered; see Figure 1a. Assuming that the scattering processes between the surface and the particle–cavity system are dominated by a single scattering effect (we neglect multiple scattering effects), the Green function factorizes into a bulk propagation $\mathbf{G}$ (here: in water) and an effective transmission coefficient $R(\omega)$, which has to be found, through the cavity's surface, which includes the properties of the cavity and yields[24]

$$\mathbf{G}_{cav}(\mathbf{r},\mathbf{r}',\omega) = R(\omega)\,\mathbf{G}(\mathbf{r},\mathbf{r}',\omega) \tag{9}$$

Due to the linearity of the Casimir–Polder potential, eq 2, in the polarizability and the scattering Green function, an excess polarizability can be defined as

$$\alpha^*(i\xi) = R(i\xi)\,\alpha(i\xi) \tag{10}$$

In the second picture, we reverse the optical paths and describe the scattering effect as an effective reflection at a sphere, which means that the corresponding initial and final points are located outside the sphere; see Figure 1b. The propagation is again represented by the free propagation in a bulk medium. Thus, we can write

$$\mathbf{G}_{cav}(\mathbf{r},\mathbf{r}',\omega) = \mathbf{G}(\mathbf{r},\mathbf{R},\omega)\cdot\alpha^*(\omega)\cdot\mathbf{G}(\mathbf{R},\mathbf{r}',\omega) \tag{11}$$

where $\mathbf{R}$ is a point at the spherical cavity's surface and the excess polarizability $\alpha^*(\omega)$. In the following we analyze different models for such excess polarizabilities. To apply eqs 5 and 8, the free-space polarizability has to be exchanged by the excess polarizability[25]

$$\alpha(i\xi) \to \alpha^*(i\xi) \tag{12}$$

DOI: 10.1021/acs.jpca.7b10159
J. Phys. Chem. A 2017, 121, 9742–9751

POLARIZABILITY OF PARTICLES EMBEDDED IN A MEDIUM

In the following we introduce the established models estimating the effective electric polarizability of a particle embedded in a medium. First, we start with the virtual cavity model, which results in the Clausius−Mossotti relation. We continue with the real cavity model, where we consider two different configurations. One describes the effective polarizability by treating the particle as a point-like object which leads to the Onsager's real cavity model. In analogy, the hard-sphere model corresponds to Onsager's real cavity model and uses a spatially spread out dielectric function over the complete cavity volume. This yields the vanishing of the vacuum layer. An interpolation between both real cavity models modeling finite-size particles is also considered.

Table 2. Summary of the Polarizability Models

model	$\alpha^* =$
free space	α
local-field corrected, eq 19	$\left(\frac{\varepsilon+2}{3}\right)^2\alpha$
Onsager, eq 24	$\left(\frac{3\varepsilon}{1+2\varepsilon}\right)^2\alpha$
hard sphere, eq 33	$4\pi\varepsilon_0 R_s^3\frac{\varepsilon_s-\varepsilon}{\varepsilon_s+2\varepsilon}$
finite size, eq 36	$\alpha_C^* + \alpha\left(\frac{3\varepsilon}{1+2\varepsilon}\right)^2\frac{1}{1+\alpha_C^*\alpha/(8\pi^2\varepsilon_0^2 R_C^6\varepsilon)}$

Clausius−Mossotti Relation and Virtual Cavity Model. The Clausius−Mossotti relation describes the relation between the microscopic quantity polarizability and the macroscopic quantity dielectric function. It is also known as the virtual cavity model, as or local-field corrections, because it describes the increase of the electric field in the presence of a dielectric sphere with radius R. By considering the fields inside and outside the sphere $\mathbf{E}'$ and $\mathbf{E}$, respectively, one finds that the local field around the sphere increases by[26]

$$\mathbf{E}' = \mathbf{E} + \frac{1}{3\varepsilon_0}\mathbf{P} \tag{13}$$

with the polarization of the sphere $\mathbf{P}$. Using the relation that the polarization is the electric response of an externally applied electric field

$$\mathbf{P} = \varepsilon_0[\varepsilon(\omega) - 1]\mathbf{E} \tag{14}$$

and that the polarization is the response to the application of the local electric field to the sphere

$$\mathbf{P} = \alpha\eta\mathbf{E}' \tag{15}$$

with the number density η of atoms inside the sphere and the polarizability, one finds the polarizability of a sphere as

$$\alpha = 4\pi\varepsilon_0 R^3\frac{\varepsilon(\omega) - 1}{\varepsilon(\omega) + 2} \tag{16}$$

This equation is the Clausius−Mossotti relation and means that the electric response, expressed by the polarizability α, of a sphere with radius R is given by the product of its volume and the Mie reflection.

Furthermore, the local-field correction due to the presence of a spherical object, eq 13, together with the polarization, eq 14, leads us to write the local electric field at the sphere as

$$\mathbf{E}' = \left(\frac{\varepsilon(\omega) + 2}{3}\right)\mathbf{E} \tag{17}$$

This results in that the self-correlation between the local electric field[21]

$$\begin{aligned}\langle\hat{\mathbf{E}}'(\mathbf{r},\omega)\otimes\hat{\mathbf{E}}'^{\dagger}(\mathbf{r}',\omega')\rangle &= \left(\frac{\varepsilon(\omega)+2}{3}\right)^2\langle\hat{\mathbf{E}}(\mathbf{r},\omega)\otimes\hat{\mathbf{E}}^{\dagger}(\mathbf{r}',\omega')\rangle \\ &= \left(\frac{\varepsilon(\omega)+2}{3}\right)^2\frac{\hbar}{\pi\varepsilon_0}\frac{\omega^2}{c^2}\,\mathrm{Im}\,\mathbf{G}(\mathbf{r},\mathbf{r}',\omega)\delta(\omega-\omega')\end{aligned} \tag{18}$$

Hence, the local-field-corrected excess polarizability can be written as

$$\alpha^*(\omega) = \left(\frac{\varepsilon(\omega)+2}{3}\right)^2\alpha(\omega) \equiv \alpha_{\mathrm{virt}} \tag{19}$$

which we denote by α_{virt}.

Onsager's Real Cavity Model. Onsager's real cavity model considers a spherical vacuum bubble around a particle at position $\mathbf{r}_A$ embedded in a medium with permittivity $\varepsilon(\omega)$.[27] Figure 1a illustrates the arrangement. The scattering Green function for a spherical two-layered system with final and source points in the outer layer can be found in refs 28 and 29. The boundary conditions entering the reflection coefficients read as $z = kR_C$ and $z_s = k_sR_C$ with the cavity radius R_C and the absolute values of the wave vector inside and outside of the sphere k_s and k, respectively. Considering a single scattering event starting outside the cavity toward its center and back scattering, these processes can be described with the Born series expansion.[22] The scattering Green function can be expressed as[24]

$$\mathbf{G}_2^{(S)}(\mathbf{r}_A,\mathbf{r}_A,\omega) = R(\omega)\,\mathbf{G}_{\mathrm{bulk}}^{(S)}(\mathbf{r}_A,\mathbf{r}_A,\omega) \tag{20}$$

where $\mathbf{G}_{\mathrm{bulk}}^{(S)}$ denotes the scattering Green function for a bulk medium with the permittivity of the outer layer and the transmission coefficient[24,30]

$$\sqrt{R(\omega)} = \frac{\mathrm{i}}{z_s[j_1(z_s)[zh_1^{(1)}(z)]' - \varepsilon(\omega)[z_sj_1(z_s)]'h_1^{(1)}(z)]} \tag{21}$$

with the spherical Bessel and first kind Hankel functions j_n and $h_n^{(1)}$, respectively, which yields the exact excess polarizability

$$\alpha^*(\omega) = -\alpha(\omega)\frac{1}{z_s^2}\times\left(\frac{1}{j_1(z_s)[zh_1^{(1)}(z)]' - \varepsilon(\omega)[z_sj_1(z_s)]'h_1^{(1)}(z)}\right)^2 \tag{22}$$

Applying the Taylor series expansion assuming that the cavity radius R_C is small compared to the relevant wavelengths, $R_C \ll k^{-1}, k_s^{-1}$, to this transmission coefficient results in

$$\sqrt{R(\omega)} \approx \frac{3\varepsilon(\omega)}{1+2\varepsilon(\omega)} - \frac{3}{10}\frac{\varepsilon(\omega)[10\varepsilon^2(\omega) - 9\varepsilon(\omega) - 1]}{[1+2\varepsilon(\omega)]^2}\left(\frac{\omega R_C}{c}\right)^2 \tag{23}$$

DOI: 10.1021/acs.jpca.7b10159
J. Phys. Chem. A 2017, 121, 9742−9751

and leads to the famous excess polarizability for small radius R_C

$$\alpha^*(\omega) = \alpha(\omega)\left(\frac{3\varepsilon(\omega)}{1+2\varepsilon(\omega)}\right)^2 \equiv \alpha_{\mathrm{Ons}} \tag{24}$$

which is denoted by α_{Ons}. For small but finite radii, a Taylor expansion

$$\alpha^*(\omega) = \alpha(\omega)\frac{3\varepsilon(\omega)}{1+2\varepsilon(\omega)}\left[\frac{3\varepsilon(\omega)}{1+2\varepsilon(\omega)} - 2\left(\frac{3}{10}\frac{\varepsilon(\omega)[10\varepsilon^2(\omega)-9\varepsilon(\omega)-1]}{[1+2\varepsilon(\omega)]^2}\right)\left(\frac{\omega R_C}{c}\right)^2\right] \tag{25}$$

shows that this approximation works for typical cavity radii. It has an agreement of more than 99% compared with the exact solution. The corresponding frequency of the cavity mode can be estimated as $\omega_c = c/R_C$, with the speed of light c. Typical values for the cavity radius are on the order of several Angstroms which result in a cavity mode of the order of 10^{18} rad s^{-1}, where typical materials are transparent.

Onsager's Real Cavity Model for Finite-Size Particles. The Onsager real cavity model for spatially extended particles can be described by a spherical three-layer system.[31] The inner layer represents the particle, the outer layer the surrounding medium, and the second layer between both denotes the vacuum cavity. The description of this arrangement is similar to Onsager's real cavity model. Again, a scattering process at the outer boundary has to be described that follows the same scattering Green function for a spherically layered system[29] whereas the reflection coefficients need to be exchanged by the one for a three-layered system which read[28,32]

$$\tilde{r}_{32} = r_{32} + \frac{t_{23}r_{21}t_{32}}{1 - r_{23}r_{21}} \tag{26}$$

which denotes the multiple reflection coefficients at the second boundary with the transmission and reflection coefficient t_{ij} and r_{ij}, respectively, between the i-th and j-th layer[24,28,32]

$$r_{i,i+1} = \frac{\sqrt{\varepsilon_{i+1}\mu_i}H_n^{(1)}(k_{i+1}a)\,H_n^{(1)\prime}(k_ia) - \sqrt{\varepsilon_i\mu_{i+1}}H_n^{(1)\prime}(k_{i+1}a)\,H_n^{(1)}(k_ia)}{\sqrt{\varepsilon_i\mu_{i+1}}J_n(k_ia)\,H_n^{(1)\prime}(k_{i+1}a) - \sqrt{\varepsilon_{i+1}\mu_i}H_n^{(1)}(k_{i+1}a)\,J_n'(k_ia)} \tag{27}$$

$$t_{i,i+1} = \frac{\mathrm{i}\varepsilon_{i+1}\sqrt{\frac{\mu_{i+1}}{\varepsilon_i}}}{\sqrt{\varepsilon_i\mu_{i+1}}J_n(k_ia)\,H_n^{(1)\prime}(k_{i+1}a) - \sqrt{\varepsilon_{i+1}\mu_i}H_n^{(1)}(k_{i+1}a)\,J_n'(k_ia)} \tag{28}$$

$$r_{i+1,i} = \frac{\sqrt{\varepsilon_{i+1}\mu_i}J_n(k_{i+1}a)\,J_n'(k_ia) - \sqrt{\varepsilon_i\mu_{i+1}}J_n(k_ia)\,J_n'(k_{i+1}a)}{\sqrt{\varepsilon_i\mu_{i+1}}J_n(k_ia)\,H_n^{(1)\prime}(k_{i+1}a) - \sqrt{\varepsilon_{i+1}\mu_i}H_n^{(1)}(k_{i+1}a)\,J_n'(k_ia)} \tag{29}$$

$$t_{i+1,i} = \frac{\mathrm{i}\varepsilon_i\sqrt{\frac{\mu_i}{\varepsilon_{i+1}}}}{\sqrt{\varepsilon_i\mu_{i+1}}J_n(k_ia)\,H_n^{(1)\prime}(k_{i+1}a) - \sqrt{\varepsilon_{i+1}\mu_i}H_n^{(1)}(k_{i+1}a)\,J_n'(k_ia)} \tag{30}$$

with $J_n(x) = xj_n(x)$ and $H_n^{(1)}(x) = xh_n^{(1)}(x)$ and a denotes the position of the boundary between the i-th and $(i+1)$-th layer. Again, the comparison of the exact Green function for the spherically layered system with that for the bulk propagation, eq 11, results in the excess polarizability that reads in general

$$\alpha^*(\omega) = -\mathrm{i}\frac{6\pi\varepsilon_0}{\sqrt{\varepsilon}}\frac{c^3}{\omega^3}\tilde{r}_{32} \tag{31}$$

Note that the dielectric function of the inner sphere is connected to the corresponding polarizability via the Clausius–Mossotti relation, eq 16. Assuming a small radius of the cavity and of the particle, the vector wave functions reduce to the first order ($n = 1$), because all other terms vanish for a centered particle. The reflection coefficient for a purely electric field, eq 26, can be expand into a series expansion for small radii R and R_C

$$\tilde{r}_{32} \approx B_1^N = \frac{2\mathrm{i}}{3}\left(\sqrt{\varepsilon\mu}\frac{\omega}{c}\right)^3\left[{R_C}^3\frac{1-\varepsilon}{1+2\varepsilon} + \frac{9\varepsilon R^3(\varepsilon_s-1)/(2\varepsilon+1)}{(\varepsilon_s+2)(2\varepsilon+1)+2(\varepsilon_s-1)(1-\varepsilon)R^3/{R_C}^3}\right] \tag{32}$$

where R and R_C denote the radii of the particle and the cavity, respectively. In analogy to the virtual cavity model, it can be considered as the electromagnetic scattering at a sphere with radius R_s and permittivity ε_s embedded in a medium ε. Considering the electric fields through a dielectric sphere with ε_s and radius R_s embedded in a medium ε, one finds an excess polarizability ($R_s \to R_C$)

$$\alpha^* = 4\pi\varepsilon_0\varepsilon{R_s}^3\frac{\varepsilon_s-\varepsilon}{\varepsilon_s+2\varepsilon} \equiv \alpha_{\mathrm{HS}} \tag{33}$$

which is the Mie coefficient and is denoted α_{HS}, meaning that the hard-sphere polarizability arises when the vacuum layer vanishes. Using this result, one can define excess polarizabilities in the three-layer model. One is the free-space polarizability for the sphere surrounded by vacuum

$$\alpha_s = 4\pi\varepsilon_0 R^3\frac{\varepsilon_s-1}{\varepsilon_s+2} \tag{34}$$

and the excess one for the cavity

$$\alpha_C^* = 4\pi\varepsilon_0\varepsilon{R_C}^3\frac{1-\varepsilon}{1+2\varepsilon} \tag{35}$$

Substituting eqs 34 and 35 in eq 33 the excess polarizability for the three-layered system simplifies to

$$\alpha_{S+C}^* = \alpha_C^* + \alpha_s\left(\frac{3\varepsilon}{2\varepsilon+1}\right)^2\frac{1}{1+\alpha_C^*\alpha_s/(8\pi^2\varepsilon_0^2{R_C}^6\varepsilon)} = \alpha_C^* + \alpha_s^* \equiv \alpha_{\mathrm{fs}} \tag{36}$$

which we denote by α_{fs} and the dressed polarizability α_s^*. The performed approximation agrees with the exact values with a confidence of more than 99% for small molecules. Due to the multiple reflections occurring here the quality of the series expansion strongly depends on the radii R and R_C. It can be imagined that, for larger objects, such as a fullerene, this approximation might fail because of the increase of the multiple reflection term. Table 2 summarizes the different effective polarizability models.

We note the appearance of the prefactor ε in the effective polarizabilities of the sphere in eq 33 (and for the cavity in eq 35), suggesting that the effective polarizability of a molecule is generally larger in a more polar medium. This contrasts with the effective polarizability presented by Netz,[33] which does not contain the prefactor ε. This apparent contradiction arises

DOI: 10.1021/acs.jpca.7b10159
J. Phys. Chem. A 2017, 121, 9742–9751

because of alternative possible definitions of what the effective polarizability means. The effective polarizability may be thought of as the linear relationship between an external electric field and the dipole (embedded in a medium) induced in a molecule by that field.[26] The polarization field **P**, thought of as the field generated by that induced dipole, has the same value regardless of the definition of the induced dipole. In the picture we have presented here, we have defined the effective polarizability such that the polarization field corresponds to an induced dipole located inside the medium with ε. Netz, by contrast, adopted a definition of the effective polarizability that generates the same polarization field *as if* the corresponding induced dipole was located in a vacuum, rather than in the medium. In other words, the definition depends on whether we take the effective polarizability to refer to an effective induced dipole in medium or in a vacuum. The difference matters in the evaluation of the van der Waals energy, whether the latter treats the medium explicitly (cf. the appearance of ε in the van der Waals parameters eq 5 or eq 8) in section below or whether, as in Netz's approach, the van der Waals energy is evaluated as if the field is in a vacuum. In our case (effective induced dipole in a medium), ε in the effective polarizability cancels with that in denominator of the van der Waals parameters. In Netz's case (effective induced dipole in a vacuum), the factors of ε are never present. The net van der Waals energy is the same either way (the two definitions were incorrectly mixed in ref 19, resulting in an underestimate of van der Waals parameters). We suggest that the approach of effective-dipole-in-medium provides a more natural or more general definition of the effective polarizability, because in the three-layered system ε cannot be simply lifted out from eq 36.

CAVITY RADIUS FOR GAS MOLECULES IN WATER

To apply the model of eq 36, we need to estimate R and R_C for the molecules under investigation. The definition of the cavity radius R_C is under discussion in the literature[34] and is often based on fits to solvation energies.[35,36] More generally, it is possible to compute the probability distribution $p(R_C,T)$ of cavities with radius R_C in a solvent at temperature T,[37−40] with the cavity energy for a given radius equal to $-kT \ln p(R_C,T)$. The cavity radius for a given ion may be extracted from the ion-solvent radial distribution function $g(r)$, or more specifically the ion-oxygen rdf in the case of water.[41,42] The position of the first peak in $g(r)$ has been used to determine ion solvation energies[43] and partial molar volumes.[44] It follows from the temperature dependence of $g(r)$ that, in general, the cavity radius can be expected to depend on temperature, as observed in solvation radii determined from measurement of ion conductivity.[45] Table 3 lists the cavity volumes V_C and corresponding radii $R_C = (3V_C/4\pi)^{1/3}$ that were obtained from the cavity definition in the recently developed continuum solvent model implemented in the GPAW package.[2,46] The generally nonspherical cavity with a smooth boundary is obtained from an effective repulsive potential that describes the interaction between the continuum of the water solvent and the solute molecule. This potential leads to an effective solvent distribution function $0 \le g \le 1$ that can be related to measurable partial molar volumes at the limit of infinite dilution through the compressibility equation.[47] Using this connection to fit the effective potential, only a single parameter is needed to predict the volumes of various test molecules in water in good agreement to experiment.[2] The cavity volume V_C is obtained by an integration over the solvent excluded volume $1 - g$.

Table 3. Cavity Volume V_C (in General Not Spherical), Cavity Radii R_C (Spherical Approximation), and Hard-Sphere Radii R of Four Greenhouse Gases CH_4, CO_2, N_2O, and O_3 and Other Atmospheric Gas Molecules

gas	V_C (Å^3)	R_C (Å)	R (Å)
CH_4	47.00	2.239	1.655
CO_2	62.28	2.459	1.723
N_2O	58.83	2.413	1.991
O_3	58.79	2.412	1.984
O_2	43.84	2.187	1.300
N_2	44.98	2.206	1.409
CO	51.31	2.305	1.966
NO_2	58.33	2.406	1.986
H_2S	52.73	2.326	2.030

The hard-sphere radii R describe the effective spherical radius for the volume occupied by the electron cloud of the molecules,[48] defined as the volume within which the electron density exceeds 0.001 electrons/bohr^3 (evaluated using Gaussian[49]). The cavity radii R_C, by contrast, correspond to the position at which the electron density of the solvent molecules becomes significant (i.e., the position in space where the dielectric medium starts to respond to an external field).[43,44]

The success of polarizable continuum models in the description of solvent effects, ranging from ground-state to excited-state properties, shows that considering the solvent as a continuum is appropriate down to the atomic scale. Dynamic effects arising from averaging over the solvent molecules' movements can be conveniently included into the effective continuum.

APPLICATIONS: EFFECTIVE POLARIZABILITIES FOR GAS MOLECULES IN WATER

The effective polarizabilities determine the strength and sign for van der Waals potentials and Casimir−Polder potentials of gas molecules dissolved in water near surfaces or in bulk water. The free-space polarizabilities and the resulting effective polarizabilities for two different dissolved gas molecules (using the models described in previous sections) are shown in Figure 2. It is the expectation that the effective polarizability of a molecule in a medium is less than its corresponding free-space polarizability because it reflects the difference between the dielectric function in a sphere and the surrounding media (water). This is not observed in the simpler models α_{vir}, eq 19 and α_{Ons}, eq 24. The most sophisticated model α_{fs}, eq 36, accounts for a small polarizable sphere (with a size modeled by the hard-sphere radius R) inside a vacuum bubble (with radius modeled by the cavity radius R_C). Here the presence of a vacuum layer means that the effective polarizability may become negative in some frequency regions. This is obviously so, because a simple vacuum bubble is less polarizable than the surrounding water. We observe that the closer the values for the hard-sphere radius and cavity radius are, the less negative the effective polarizability will be. To illustrate the impact of the different results, we determine the expected van der Waals and Casimir−Polder parameters for the different molecules.

Note that the Casimir−Polder (C_3) parameters in Table 3 correspond to more attraction in free space than any of the C_3 parameters using the effective polarizability models in water.[50]

DOI: 10.1021/acs.jpca.7b10159
J. Phys. Chem. A 2017, 121, 9742−9751

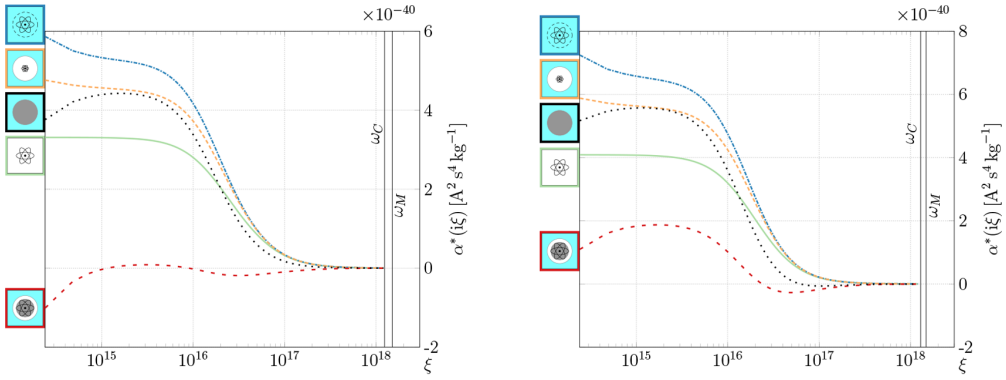

Figure 2. Polarizabilities (green) and effective polarizabilities for (a) N_2O and (b) H_2S. We compare the local-field-corrected model, following eq 19, α_{virt} (blue), the Onsager real cavity model, following eq 24, α_{Ons} (orange), the hard-sphere model α_{HS}, eq 33 (black), and Onsager's real cavity model for finite-size particles, eq 36, α_{fs} (red). In addition, the corresponding cavity modes $\omega_C = c/R_C$ and the hard-sphere modes with respect to the molecule radius $\omega_M = c/R$ are drawn as straight lines.

Table 4. C_3 Coefficients in 10^{-49} J m^3 for the Different Gases in a Vacuum,[a] in a Medium without a Cavity,[b] with the Local-Field Correction (Virtual Cavity),[c] with Onsager's Real Cavity,[d] for the Real Cavity with Finite Size of the Particles,[e] and with the Hard-Sphere Cavity Model[f]

gas	vacuum	medium	loc corr	Onsager	finite size	hard sphere
CH_4	2.69	2.01	2.56	2.36	−0.78	3.07
CO_2	3.61	2.8	3.46	3.23	−0.96	5.71
N_2O	3.81	2.94	3.65	3.4	−0.54	2.29
O_3	3.75	2.92	3.6	3.36	−0.58	2.25
O_2	2.28	1.79	2.19	2.05	−0.91	7.59
N_2	2.38	1.85	2.28	2.13	−0.9	5.72
CO	2.44	1.87	2.34	2.17	−1.29	0.1
NO_2	3.56	2.76	3.41	3.18	−0.73	1.89
H_2S	3.35	2.45	3.21	2.91	−0.57	1.05

[a]Eq 5 with $\varepsilon(\omega) = 1$ and the free-space polarizability. [b]Eq 5 with $\varepsilon(\omega) = \varepsilon_{water}(\omega)$ and the free-space polarizability. [c]Using eq 5 with $\varepsilon(\omega) = \varepsilon_{water}(\omega)$, the polarizability follows from eq 19. [d]Using eq 5 with $\varepsilon(\omega) = \varepsilon_{water}(\omega)$ and the polarizability follows from eq 24. [e]Using eq 5 with $\varepsilon(\omega) = \varepsilon_{water}(\omega)$ and the polarizability follows from eq 36. [f]Eq 33.

Table 5. C_6 Coefficients in 10^{-79} J m^6 for the Different Gases in a Vacuum,[a] in a Medium without a Cavity,[b] with the Local-Field Correction (Virtual Cavity),[c] with Onsager's Real Cavity,[d] for the Real Cavity with Finite Size of the Particles,[e] and with the Hard-Sphere Cavity Model[f]

gas	vacuum	medium	loc corr	Onsager	finite size	hard sphere
CH_4	116.71	48.95	155.66	79.04	6.35	230.33
CO_2	161.5	71.88	205.2	112.31	12.42	452.31
N_2O	188.44	82.58	245.01	130.07	7	94.63
O_3	168.7	75.01	224.46	117.06	7.85	75.4
O_2	58.02	26.61	72.78	40.88	11.16	678.26
N_2	70.29	31.52	88.03	49.07	9.33	448.07
CO	79.39	34.47	104.2	54.56	16.33	7.84
NO_2	155.27	68.87	203.93	107.68	8.95	59.28
H_2S	215.27	85.37	311.73	141.94	15.25	92.75

[a]Eq 8 with $\varepsilon(\omega) = 1$ and the free-space polarizability. [b]Eq 8 with $\varepsilon(\omega) = \varepsilon_{water}(\omega)$ and the free-space polarizability. [c]Using eq 8 with $\varepsilon(\omega) = \varepsilon_{water}(\omega)$, the polarizability follows from eq 19. [d]Using eq 8 with $\varepsilon(\omega) = \varepsilon_{water}(\omega)$ and the polarizability follows from eq 24. [e]Using eq 8 with $\varepsilon(\omega) = \varepsilon_{water}(\omega)$ and the polarizability follows from eq 36. [f]Eq 33.

The reason is partly the large repulsive contribution from the zero-frequency Matsubara term due to the high value for the dielectric constant of water. However, it is not only the zeroth frequency that gives repulsion. Figure 2 shows the effective polarizabilities for methane and nitrous oxide. On the basis of the three-layer model, two subclasses of molecules can be found: one with a purely negative effective polarizability, where CH_4, CO_2, O_2, O_3, N_2, CO, and CO_2 belong, and one with also positive contributions N_2O and H_2S. This is caused by the optical density of water. In eq 36, α_C^* is always negative and the dressed polarizability α_s^* can dominate it to generate a positive result. This is a direct consequence of the ratio of the optical densities for the considered materials. One needs to account for many frequencies where the polarizability is either positive (attractive) or negative (repulsive). A repulsive dispersion force based on the same argumentation was found in previous works by Elbaum and Schick.[51] It turns out that the Onsager's real cavity model for finite-size particles even predicts repulsion between a molecule in water and a perfect metal surface. This is in contrast to the other models in water. We suggest to test the validity of the different effective polarizability models experimentally. For instance, the different predicted Casimir–Polder forces can be experimentally verified by balancing them against gravity. On the basis of the C_3 coefficients given in Table 4, a solution of H_2S can be brought horizontally toward a metal surface. Due to the repulsive force, expected for the finite-size and the hard-sphere model, the molecules will stabilize at a certain distance due to the equilibrium of the Casimir–Polder and the gravitational forces. The results for the van der Waals (C_6) parameters are no less interesting and differ by an order of magnitude between the different models. Interactions between equal molecules and between unequal molecular pairs are given in Tables 5 and 6, respectively.

IMPACT OF PARTICLE SIZE

The polarizabilities in this model vary strongly between different molecules: although the polarizability for H_2S is only negative for high frequencies, the polarizability of CH_4 is also negative for the first two Matsubara frequencies. One main difference between H_2S and CH_4 can be found in Table 3. H_2S

DOI: 10.1021/acs.jpca.7b10159
J. Phys. Chem. A 2017, 121, 9742–9751

Table 6. C_6 Coefficients in 10^{-79} J m^6 for the Different Combinations of Interacting Particles Using the Three-Layer Model, Eq 36

	CH_4	CO_2	N_2O	O_3	O_2	N_2	CO	NO_2	H_2S
CH_4	6.35	7.65	6.4	6.4	5.85	5.99	7.84	6.77	7.33
CO_2		12.4	8.28	9.51	11.3	10.6	13.7	10.4	4.39
N_2O			7	7.13	6.36	6.42	8.09	7.41	6.91
O_3				7.85	8.09	7.76	9.94	8.32	5.27
O_2					11.2	10.1	13.3	9.15	0.76
N_2						9.33	12.2	8.69	2.05
CO							16.3	11.2	2.83
NO_2								8.95	4.89
H_2S									15.2

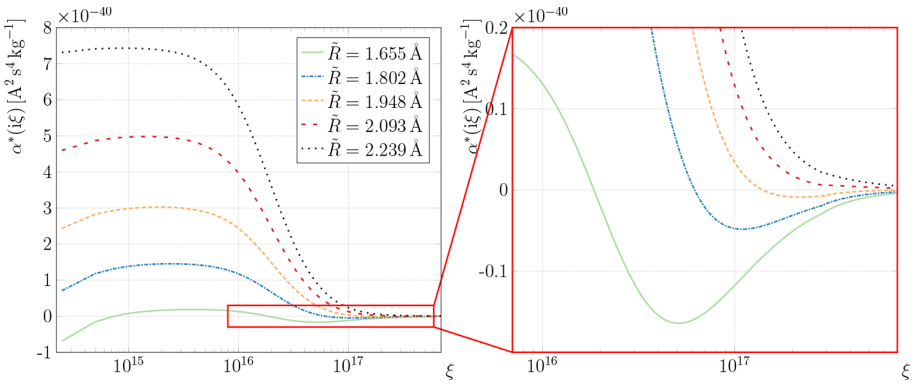

Figure 3. Excess polarizability in the real cavity model for finite-size particles (36) for a toy-methane molecule with the polarizability given by eq 37. The radius of the toy-methane sphere is varied between the original radius and the cavity radius, given in Table 3. One sees a transition from partially negative to purely positive polarizabilities.

has a larger sphere radius compared to the cavity radius. Thus, when the sphere radius of CH_4 is enlarged, the polarizability should also become positive for the first two Matsubara frequencies. To verify this, we calculate the leading order excess polarizability eq 36 for different sphere radii. The permittivity of the CH_4 sphere is fixed using eq 34 with the original sphere radius R = 1.655 Å, and the sphere radius $\tilde{R}$ is then varied between the original one and the cavity radius R_C = 2.239 Å (for $R = R_C$, one obtains the hard-sphere polarizability eq 33 with $R \to R_C$). This means we use a radius-dependent polarizability for the methane sphere, given by

$$\alpha_s(\tilde{R}) = 4\pi\varepsilon_0\tilde{R}^3\frac{\varepsilon_s(R) - 1}{\varepsilon_s(R) + 2} \tag{37}$$

By varying the radius, one indeed sees a transition to positive excess polarizabilities for small frequencies in Figure 3. Furthermore, the excess polarizability becomes positive for all frequencies for $\tilde{R} \geq 2.033$ Å.

CONCLUSIONS

We have demonstrated that accurate estimates of the effective polarizability in a medium, and the related Casimir−Polder and van der Waals potentials, may require a new theory. Such a theory has been worked out in the present paper. However, even more urgent is to test predictions of the real cavity model for finite-size particles in a medium. We predict that molecules may be either attracted or pushed away from a metal surface depending on the effective polarizability model. Testing these predictions should pave the way for improved modeling of van der Waals interactions in a medium.

When the effective polarizability of small particles is calculated—a subject closely related to Casimir Polder and van der Waals potentials—the presence of a dielectric environment implies complications that are at present not very well understood. In the present paper we have approached this problem from a phenomenological viewpoint, making use of various parameter-based models. In essence they consist of (1) the virtual cavity model, implying the Clausius−Mossotti relation; (2) the real cavity model, which in itself can be divided into two subclasses, the first treating the particle as a point-like object surrounded by a spherical cavity volume that denotes the original Onsager cavity model, and the being a finite-size model of the particle that is now assumed to be surrounded by an annular cavity volume and is an extension of the Onsager model. Its limit when the particle radius reaches the cavity radius is the hard-sphere model. We calculated the interaction in terms of scattering Green functions for a spherical three-layer system.

The Green function technique was applied to several greenhouse gas molecules as examples. Effective polarizabilities for gas molecules in water were calculated. To illustrate the sensitivity of the formalism with respect to the input parameters, we analyzed also a real cavity model for finite-size particles for a toy-methane model.

As a striking demonstration of the sensitivity of the formalism, we found that molecules can be attracted to, or be pushed away from, a metal surface depending on which effective polarizability model is used. There is thus an obvious need for testing these parameter-dependent theories against experiments to improve the modeling of van der Waals interactions in media.

DOI: 10.1021/acs.jpca.7b10159
J. Phys. Chem. A 2017, 121, 9742−9751

A decisive model cannot be made on this theoretical level. We note that only the finite-size and hard-sphere models are able to produce repulsive forces, and such forces have indeed been observed in some cases for the related Casimir force.[52] Further, the finite-size model is the most detailed description as it takes into account both the finite particle size and the exclusion volume. To improve this model, the hard cavity boundary has to be adapted to realistic cavity profiles and the constraint to centered particles has to be discarded. On the basis of the results, an experimental improvement is given by measuring the expected van der Waals and Casimir−Polder forces. However, deeper theoretical investigations are required to transform the results to measurable spectra, such as refractive indices or molecular extinctions. To describe realistic scenarios, further investigations are required with respect to the anisotropy of particles, which results in nonspherical cavities, and to the cavity's boundary as described by a continuous profile.[2]

AUTHOR INFORMATION

Corresponding Authors

*J. Fiedler. E-mail: johannes.fiedler@physik.uni-freiburg.de.
*P. Thiyam. E-mail: thiyam@kth.se.
*D. F. Parsons. E-mail: d.parsons@murdoch.edu.au.
*M. Boström. E-mail: mathias.a.bostrom@ntnu.no.
*S. Y. Buhmann. E-mail: stefan.buhmann@physik.uni-freiburg.de.

ORCID

Johannes Fiedler: 0000-0002-2179-0625
Michael Walter: 0000-0001-6679-2491
Drew F. Parsons: 0000-0002-3956-6031

Notes

The authors declare no competing financial interest.

ACKNOWLEDGMENTS

We acknowledge support from the Research Council of Norway (Project 250346). This research was undertaken with the assistance of resources and services from the National Computational Infrastructure (NCI), which is supported by the Australian Government. We gratefully acknowledge support by the German Research Council (grant BU1803/3-1, S.Y.B. and J.F.) the Research Innovation Fund by the University of Freiburg (S.Y.B., J.F. and M.W.) and the Freiburg Institute for Advanced Studies (S.Y.B.).

REFERENCES

(1) Minzioni, P.; Osellame, R.; Sada, C.; Zhao, S.; Omenetto, F. G.; Gylfason, K. B.; Haraldsson, T.; Zhang, Y.; Ozcan, A.; Wax, A.; et al. Roadmap for optofluidics. *J. Opt.* **2017**, *19*, 093003.
(2) Held, A.; Walter, M. Simplified continuum solvent model with a smooth cavity based on volumetric data. *J. Chem. Phys.* **2014**, *141*, 174108.
(3) Dellinger, A.; Zhou, Z.; Connor, J.; Madhankumar, A. B.; Pamujula, S.; Sayes, C. M.; Kepley, C. L. Application of fullerenes in nanomedicine: an update. *Nanomedicine* **2013**, *8*, 1191−1208.
(4) Pupysheva, O. V.; Farajian, A. A.; Yakobson, B. I. Fullerene Nanocage Capacity for Hydrogen Storage. *Nano Lett.* **2008**, *8*, 767−774.
(5) Cheng, Q.; Aravind, A.; Buckley, M.; Gifford, A.; Parvin, B. Functionalized Buckyballs for Visualizing Microbial Species in Different States and Environments. *Sci. Rep.* **2015**, *5*, 13685.
(6) Mroz, P.; Tegos, G. P.; Gali, H.; Wharton, T.; Sarna, T.; Hamblin, M. R. Photodynamic therapy with fullerenes. *Photochem. Photobiol. Sci.* **2007**, *6*, 1139−1149.
(7) Thiyam, P.; Persson, C.; Parsons, D.; Huang, D.; Buhmann, S.; Boström, M. Trends of CO2 adsorption on cellulose due to van der Waals forces. *Colloids Surf., A* **2015**, *470*, 316−321.
(8) Ben-Yaakov, D.; Andelman, D.; Podgornik, R. Dielectric decrement as a source of ion-specific effects. *J. Chem. Phys.* **2011**, *134*, 074705.
(9) Démery, V.; Dean, D. S.; Podgornik, R. Electrostatic interactions mediated by polarizable counterions: Weak and strong coupling limits. *J. Chem. Phys.* **2012**, *137*, 174903.
(10) Buhmann, S. Y.; Safari, H.; Trung Dung, H.; Welsch, D. G. Two-atom van der Waals interaction between polarizable/magnetizable atoms near magnetoelectric bodies. *Opt. Spectrosc.* **2007**, *103*, 374−387.
(11) Ninham, B. W.; Pashley, R. M.; Nostro, P. L. Surface forces: Changing concepts and complexity with dissolved gas, bubbles, salt and heat. *Curr. Opin. Colloid Interface Sci.* **2017**, *27*, 25−32.
(12) Hampel, C.; Peterson, K. A.; Werner, H.-J. A comparison of the efficiency and accuracy of the quadratic configuration interaction (QCISD), coupled cluster (CCSD), and Brueckner coupled cluster (BCCD) methods. *Chem. Phys. Lett.* **1992**, *190*, 1−12.
(13) Werner, H.-J.; Knowles, P. J.; Knizia, G.; Manby, F. R.; Schütz, M.; Celani, P.; Korona, T.; Lindh, R.; Mitrushenkov, A.; Rauhut, G.; et al. *MOLPRO*, version 2012.1, a package of ab initio programs, 2012; http://www.molpro.net.
(14) *TURBOMOLE* V6.4 2012, a development of University of Karlsruhe and Forschungszentrum Karlsruhe GmbH, 1989−2007, TURBOMOLE GmbH, since 2007; available from http://www.turbomole.com.
(15) Adamo, C.; Barone, V. Toward reliable density functional methods without adjustable parameters: The PBE0 model. *J. Chem. Phys.* **1999**, *110*, 6158−6170.
(16) Peterson, K. A.; Dunning, T. H., Jr. Accurate correlation consistent basis sets for molecular core−valence correlation effects: The second row atoms Al−Ar, and the first row atoms B−Ne revisited. *J. Chem. Phys.* **2002**, *117*, 10548−10560.
(17) Parsons, D. F.; Deniz, V.; Ninham, B. W. Nonelectrostatic interactions between ions with anisotropic ab initio dynamic polarisabilities. *Colloids Surf., A* **2009**, *343*, 57−63.
(18) Thiyam, P.; Parashar, P.; Shajesh, K. V.; Persson, C.; Schaden, M.; Brevik, I.; Parsons, D. F.; Milton, K. A.; Malyi, O. I.; Boström, M. Anisotropic contribution to the van der Waals and the Casimir-Polder energies for CO2 and CH4 molecules near surfaces and thin films. *Phys. Rev. A: At., Mol., Opt. Phys.* **2015**, *92*, 052704.
(19) Parsons, D. F.; Ninham, B. W. Importance of Accurate Dynamic Polarizabilities for the Ionic Dispersion Interactions of Alkali Halides. *Langmuir* **2010**, *26*, 1816−1823.
(20) Casimir, H. B. G.; Polder, D. The Influence of Retardation on the London-Van der Waals Forces. *Phys. Rev.* **1948**, *73*, 360−372.
(21) Buhmann, S. Y. *Dispersion Forces I: Macroscopic Quantum Electrodynamics*; Springer Tracts in Modern Physics; Springer: Berlin, 2012.
(22) Buhmann, S. Y. *Dispersion Forces II: Many-Body Effects, Excited Atoms, Finite Temperature and Quantum Friction*; Springer Tracts in Modern Physics; Springer: Berlin, 2012.
(23) Fiedler, J.; Scheel, S. Casimir-Polder potentials on extended molecules. *Ann. Phys.* **2015**, *527*, 570−579.
(24) Sambale, A.; Buhmann, S. Y.; Welsch, D.-G.; Tomaš, M.-S. Local-field correction to one- and two-atom van der Waals interactions. *Phys. Rev. A: At., Mol., Opt. Phys.* **2007**, *75*, 042109.
(25) Burger, F.; Fiedler, J.; Buhmann, S. Y. Zero-point energy-momentum in media and its consequences for dispersion forces. Submitted for publication.
(26) Jackson, J. D. *Classical Electrodynamics*; Wiley: New York, 1998.
(27) Onsager, L. Electric Moments of Molecules in Liquids. *J. Am. Chem. Soc.* **1936**, *58*, 1486−1493.

DOI: 10.1021/acs.jpca.7b10159
J. Phys. Chem. A 2017, 121, 9742−9751

(28) Li, L.-W.; Kooi, P.-S.; Leong, M.-S.; Yee, T.-S. Electromagnetic dyadic Green's function in spherically multilayered media. *IEEE Trans. Microwave Theory Tech.* **1994**, *42*, 2302−2310.
(29) Tomaš, M. S. Local-field corrections to the decay rate of excited molecules in absorbing cavities: The Onsager model. *Phys. Rev. A: At., Mol., Opt. Phys.* **2001**, *63*, 053811.
(30) Abramowitz, M.; Stegun, I. A. *Handbook of mathematical functions with formulas, graphs, and mathematical tables*; Dover: New York, 1972; Vol. *9*.
(31) Sambale, A.; Buhmann, S. Y.; Scheel, S. Casimir-Polder interaction between an atom and a small magnetodielectric sphere. *Phys. Rev. A: At., Mol., Opt. Phys.* **2010**, *81*, 012509.
(32) Chew, W. C. *Waves and Fields in Inhomogenous Media*; Wiley-IEEE Press, 1995.
(33) Netz, R. R. Water and ions at interfaces. *Curr. Opin. Colloid Interface Sci.* **2004**, *9*, 192−197.
(34) Tomasi, J.; Mennucci, B.; Cammi, R. Quantum Mechanical Continuum Solvation Models. *Chem. Rev.* **2005**, *105*, 2999−3094.
(35) Floris, F. M.; Tomasi, J.; Ahuir, J. L. P. Dispersion and repulsion contributions to the solvation energy: Refinements to a simple computational model in the continuum approximation. *J. Comput. Chem.* **1991**, *12*, 784−791.
(36) Sánchez, V. M.; Sued, M.; Scherlis, D. A. First-principles molecular dynamics simulations at solid-liquid interfaces with a continuum solvent. *J. Chem. Phys.* **2009**, *131*, 174108.
(37) Pratt, L. R.; Chandler, D. Theory of the hydrophobic effect. *J. Chem. Phys.* **1977**, *67*, 3683−3704.
(38) Lynden-Bell, R. M.; Giovambattista, N.; Debenedetti, P. G.; Head-Gordon, T.; Rossky, P. J. Hydrogen bond strength and network structure effects on hydration of non-polar molecules. *Phys. Chem. Chem. Phys.* **2011**, *13*, 2748−2757.
(39) Shi, Y.; Beck, T. L. Length scales and interfacial potentials in ion hydration. *J. Chem. Phys.* **2013**, *139*, 044504.
(40) Galib, M.; Duignan, T. T.; Misteli, Y.; Baer, M. D.; Schenter, G. K.; Hutter, J.; Mundy, C. J. Mass density fluctuations in quantum and classical descriptions of liquid water. *J. Chem. Phys.* **2017**, *146*, 244501.
(41) Marcus, Y. Ionic radii in aqueous solutions. *Chem. Rev.* **1988**, *88*, 1475−1498.
(42) Dinpajooh, M.; Matyushov, D. V. Free energy of ion hydration: Interface susceptibility and scaling with the ion size. *J. Chem. Phys.* **2015**, *143*, 044511.
(43) Duignan, T. T.; Parsons, D. F.; Ninham, B. W. A Continuum Model of Solvation Energies Including Electrostatic, Dispersion, and Cavity Contributions. *J. Phys. Chem. B* **2013**, *117*, 9421−9429.
(44) Duignan, T. T.; Parsons, D. F.; Ninham, B. W. A Continuum Solvent Model of the Partial Molar Volumes and Entropies of Ionic Solvation. *J. Phys. Chem. B* **2014**, *118*, 3122−3132.
(45) Krumgal'z, B. S. The nature of temperature changes in the short-range-order solvation of ions depending on solvent structure. *J. Struct. Chem.* **1973**, *13*, 727−731.
(46) Enkovaara, J.; Rostgaard, C.; Mortensen, J. J.; Chen, J.; Dułak, M.; Ferrighi, L.; Gavnholt, J.; Glinsvad, C.; Haikola, V.; Hansen, H. A.; et al. Electronic structure calculations with GPAW: a real-space implementation of the projector augmented-wave method. *J. Phys.: Condens. Matter* **2010**, *22*, 253202.
(47) Kirkwood, J. G.; Buff, F. P. The Statistical Mechanical Theory of Solutions. I. *J. Chem. Phys.* **1951**, *19*, 774−777.
(48) Parsons, D. F.; Ninham, B. W. Ab Initio Molar Volumes and Gaussian Radii. *J. Phys. Chem. A* **2009**, *113*, 1141−1150.
(49) Frisch, M. J.; Trucks, G. W.; Schlegel, H. B.; Scuseria, G. E.; Robb, M. A.; Cheeseman, J. R.; Scalmani, G.; Barone, V.; Mennucci, B.; Petersson, G. A.; et al. *Gaussian 09*, Revision D.01; Gaussian Inc.: Wallingford, CT, 2013.
(50) Dagastine, R. R.; Prieve, D. C.; White, L. R. The Dielectric Function for Water and Its Application to van der Waals Forces. *J. Colloid Interface Sci.* **2000**, *231*, 351−358.
(51) Elbaum, M.; Schick, M. Application of the theory of dispersion forces to the surface melting of ice. *Phys. Rev. Lett.* **1991**, *66*, 1713−1716.
(52) Munday, J. N.; Capasso, F.; Parsegian, V. A. Measured long-range repulsive Casimir−Lifshitz forces. *Nature* **2009**, *457*, 170−173.

DOI: 10.1021/acs.jpca.7b10159
J. Phys. Chem. A 2017, 121, 9742−9751

A Letters Journal Exploring the Frontiers of Physics

January 2018

EPL, **121** (2018) 24004
doi: 10.1209/0295-5075/121/24004

www.epljournal.org

Zero-point electromagnetic stress tensor for studying Casimir forces on colloidal particles in media

Friedrich Anton Burger[1], Johannes Fiedler[1] and Stefan Yoshi Buhmann[1,2]

[1] *Physikalisches Institut, Albert-Ludwigs-Universität Freiburg - Hermann-Herder-Str. 3, 79104 Freiburg, Germany*
[2] *Freiburg Institute for Advanced Studies, Albert-Ludwigs-Universität Freiburg - Albertstr. 19, 79104 Freiburg, Germany*

received 20 November 2017; accepted in final form 1 March 2018
published online 20 March 2018

PACS 42.50.Ct – Quantum description of interaction of light and matter; related experiments
PACS 42.50.Nn – Quantum optical phenomena in absorbing, amplifying, dispersive and conducting media; cooperative phenomena in quantum optical systems
PACS 77.22.Ch – Permittivity (dielectric function)

Abstract – We address the question of the correct electromagnetic stress tensor in media and its consequences for the Casimir force. The latter being due to the zero-point momentum of the electromagnetic field, competing approaches based on the Abraham or Maxwell stress tensor lead to different predictions. We consider the test scenario of two colloidal spherical particles submerged in a dielectric medium and use three criteria to distinguish the two approaches: we show that the Abraham stress tensor, and not the Maxwell stress tensor, leads to a Casimir force that is form-equivalent to Casimir-Polder and van der Waals forces, obeys duality as a fundamental symmetry and is consistent with microscopic many-body calculations. On this basis, we derive general formulas for the dispersion forces on one and between two colloidal particles in arbitrary liquid-media environments in terms of their dipole polarisabilities, allowing for more elaborate theoretical descriptions and bridging the gap between microscopic and macroscopic accounts.

The momentum of the electromagnetic field in media has been subject to an old debate which has recently attracted renewed interest [1–5]. This is due to the very fundamental significance of these quantities in the context of optical forces on particles in media, which prominently feature in experimental schemes for measuring Casimir forces [6] or the critical Casimir effect [7], where laser fields in media are part of the experimental setup. In the former case, they are further also relevant to the predicted Casimir force itself [8,9] as well as a hypothesised vacuum Casimir momentum transfer [10,11]. Early works amongst others go back to Abraham [12] and Minkowski [13]. For the case of isotropic media (we also restrict our analysis to isotropic media in this article), Abraham proposed a stress tensor [14]

$$\mathbf{T}_{\mathrm{A}}(\mathbf{r},t) = \mathbf{D}(\mathbf{r},t)\otimes\mathbf{E}(\mathbf{r},t) + \mathbf{H}(\mathbf{r},t)\otimes\mathbf{B}(\mathbf{r},t) - \frac{1}{2}\Big[\mathbf{D}(\mathbf{r},t)\cdot\mathbf{E}(\mathbf{r},t) + \mathbf{H}(\mathbf{r},t)\cdot\mathbf{B}(\mathbf{r},t)\Big]\mathbb{I}, \quad (1)$$

describing the flux of field momentum, which coincided with the result by Minkowski.

Experiments on the electromagnetic stress tensor in media have mostly been performed by measuring the deformation of dielectric fluids in the electromagnetic field, for example when exposed to a laser beam [15,16], or inside a capacitor [14,17,18]. In such stationary setups, the electromagnetic force density on charges is determined by the stress tensor according to

$$\mathbf{f}(\mathbf{r},t) = \nabla\cdot\mathbf{T}(\mathbf{r},t). \quad (2)$$

The question of the correct momentum of the electromagnetic field in media is also important for the subject of dispersion forces where one calculates mean forces between bodies in media in the presence of the zero-point electromagnetic field. The dispersion force on a body of volume V based on eq. (2) reads

$$\mathbf{F} = \int_V \mathrm{d}^3 r \langle\hat{\mathbf{f}}(\mathbf{r})\rangle = \int_{\partial V} \mathrm{d}\mathbf{A}\cdot\langle\hat{\mathbf{T}}(\mathbf{r})\rangle. \quad (3)$$

Dzyaloshinskii, Lifshitz and Pitaevskii first came up with a theory capable of describing dispersion forces between

plates immersed in homogeneous media at mechanical equilibrium [8], generalising the result by Lifshitz for plates in vacuum [19]. Mechanical equilibrium implies that forces on the medium itself are balanced by pressure gradients within the medium. Dzyaloshinskii and co-workers claimed that the Abraham-Minkowski stress tensor (1) is the correct choice for determining the Casimir force (3) under these assumptions (for simplicity, we will only refer to it as Abraham stress tensor in the following).

In 2005, Raabe and Welsch proposed an alternative way to derive dispersion forces between bodies in media [9]. Calculating the mean Lorentz force acting on the internal charges and currents of a body of interest, they found the dispersion force between bodies in media to be given by eq. (3) together with the Maxwell stress tensor

$$\mathbf{T}_{\mathrm{M}}(\mathbf{r},t) = \varepsilon_0\mathbf{E}(\mathbf{r},t)\otimes\mathbf{E}(\mathbf{r},t) + \frac{1}{\mu_0}\mathbf{B}(\mathbf{r},t)\otimes\mathbf{B}(\mathbf{r},t) - \frac{1}{2}\Big[\varepsilon_0\mathbf{E}^2(\mathbf{r},t) + \frac{1}{\mu_0}\mathbf{B}^2(\mathbf{r},t)\Big]\mathbb{I}, \tag{4}$$

being of the same form as the Maxwell stress tensor for the free-space electromagnetic field [20], but refering to the macroscopic electromagnetic fields in this case. Their result is in clear contradiction to that of Dzyaloshinskii, Lifshitz and Pitaevskii. Note that works by Philbin based on canonical quantisation [21] and by Brevik and Ellingsen based on classical electrodynamics [22] favour the Abraham stress tensor and that the correctness of calculating forces in macroscopic electrodynamics based on the Lorentz force has been doubted by Robinson [23]. Raabe and Welsch regard their theory to be in consensus with microscopic dispersion forces such as van der Waals and Casimir-Polder forces [24–26].

Pitaevskii has argued that the approach by Raabe and Welsch is not complete due to its disregarding of the medium pressure and is thus not able to describe equilibrated media [27]. In contrast, Raabe and Welsch view the latter point as an advantage of their theory, as their not pressure-corrected dispersion forces may constitute a framework for analysing Casimir-induced pressures within the intervening medium. In a dilute-gas limit, such forces would emerge as the well-known Casimir-Polder forces between the medium atoms and the bodies.

Casimir forces between bodies in media have been measured using a surface force apparatus [28–30] or atomic force microscope [31–33], often with a special focus on repulsive forces [34–36]. However, due to uncertainties in the force measurements and the optical data required to theoretically predict the forces, it is unclear whether current experiments are able to unambiguously discriminate between the two models.

In this article, we instead present a theoretical analysis where we investigate the question of the correct approach in a pragmatic way. We analyse the dispersion interaction between two small magneto-dielectric spheres in a homogeneous magneto-dielectric medium for the two theories and check which of the two approaches is on the same footing as the microscopic dispersion forces. Small spheres are well studied [37–39] and are particularly well suited for comparing macroscopic to microscopic dispersion forces: small spheres are only dipole-polarisable and are thus directly comparable to microscopic dipole-polarisable objects. Furthermore, the assumption of smallness facilitates the calculations and leads to more transparent results. The unique result for the dispersion force on small spherical particles in an arbitrary environment that emerges from our calculation may serve as a basis for studies in colloid physics [40].

We employ three criteria:

i) the correspondence to the Casimir-Polder and van der Waals force,

ii) the behaviour under duality transformation and

iii) the consistency with the microscopic theory based on summing van der Waals and Axilrod-Teller interactions.

Finally, we also analyse whether the approach by Raabe and Welsch leads to forces on a medium in presence of a single sphere. This could indicate that their force, which unlike the force by Dzyaloshinskii, Lifshitz and Pitaevskii does not include balancing forces, is not buoyancy-corrected (the notion of buoyancy can be understood here in analogy to the case of a body inside water in the gravitational field).

Employing the quantisation scheme introduced in [41], one finds for the zero-point expectation values of the electric-field stress tensor components

$$\begin{aligned}\langle\mathbf{E}(\mathbf{r})\otimes\mathbf{E}(\mathbf{r})\rangle &= \frac{\hbar}{\varepsilon_0\pi}\int_0^\infty \mathrm{d}\omega\frac{\omega^2}{\mathrm{c}^2}\mathrm{Im}\mathbf{G}(\mathbf{r},\mathbf{r}',\omega)\Big|_{r'=r},\\ \langle\mathbf{D}(\mathbf{r})\otimes\mathbf{E}(\mathbf{r})\rangle &= \frac{\hbar}{\pi}\int_0^\infty \mathrm{d}\omega\frac{\omega^2}{\mathrm{c}^2}\mathrm{Im}\left\{\varepsilon(\mathbf{r},\omega)\mathbf{G}(\mathbf{r},\mathbf{r}',\omega)\right\}\Big|_{r'=r},\end{aligned} \tag{5}$$

and analogous results for the magnetic fields. $\mathbf{G}(\mathbf{r},\mathbf{r}',\omega)$ denotes the electromagnetic Green's tensor which describes the propagation of the electromagnetic field from a source point $\mathbf{r}'$ to a field point $\mathbf{r}$. It is the solution to the differential equation

$$\left[\nabla\times\frac{1}{\mu(\mathbf{r},\omega)}\nabla\times - \frac{\omega^2}{\mathrm{c}^2}\varepsilon(\mathbf{r},\omega)\right]\mathbf{G}(\mathbf{r},\mathbf{r}',\omega) = \boldsymbol{\delta}(\mathbf{r}-\mathbf{r}'). \tag{6}$$

We subtract the bulk part $\mathbf{G}^{(0)}$ of the Green's tensor, which is connected to the position-independent Lamb shift [42] and does not contribute to forces between bodies, and only use the scattering part $\mathbf{G}^{(1)}$ in the following: $\mathbf{G}\to\mathbf{G}-\mathbf{G}^{(0)}=\mathbf{G}^{(1)}$. Also performing a Wick rotation on the complex frequency plane [43], eq. (3) with the

Abraham and the Maxwell stress tensors becomes

$$\mathbf{F}_{[\mathrm{A]M}} = -\frac{\hbar}{\pi}\int_0^\infty \mathrm{d}\xi \int \mathrm{d}\mathbf{A}\cdot\Bigg\{\frac{\xi^2}{\mathrm{c}^2}[\varepsilon(\mathbf{r},\mathrm{i}\xi)]\mathbf{G}^{(1)}(\mathbf{r},\mathbf{r},\mathrm{i}\xi) + \frac{1}{[\mu(\mathbf{r},\mathrm{i}\xi)]}\nabla\times\mathbf{G}^{(1)}(\mathbf{r},\mathbf{r}',\mathrm{i}\xi)\times\overleftarrow{\nabla}\Big|_{r'=r} - \frac{1}{2}\mathbb{I}\,\mathrm{tr}\left(\frac{\xi^2}{\mathrm{c}^2}[\varepsilon(\mathbf{r},\mathrm{i}\xi)]\mathbf{G}^{(1)}(\mathbf{r},\mathbf{r},\mathrm{i}\xi) + \frac{1}{[\mu(\mathbf{r},\mathrm{i}\xi)]}\nabla\times\mathbf{G}^{(1)}(\mathbf{r},\mathbf{r}',\mathrm{i}\xi)\times\overleftarrow{\nabla}\Big|_{r'=r}\right)\Bigg\}, \quad (7)$$

respectively. The results for the two stress tensors only differ via the factors of ε and $1/\mu$ in square brackets which only occur when using the Abraham stress tensor.

To calculate the dispersion force between two small spheres in a homogeneous medium, one has to find the scattering Green's tensor $\mathbf{G}^{(1)}(\mathbf{R},\mathbf{R},\mathrm{i}\xi)$ for this geometry, where $\mathbf{R}$ denotes positions on the surface of the sphere we are integrating over. To this end, we use the method of Born expansion to obtain the Green's tensor of a small sphere with the position arguments on its surface in presence of other background bodies and the medium. Within this method, one has to sum over all possible propagations of (virtual) photons from a source point to a field point to obtain the Green's tensor [44]. The Born expansion for an electric body (volume V, permittivity ε_B) in a homogeneous dielectric (ε) reads (for brevity, the frequency arguments are omitted in the following)

$$\mathbf{G}^{(1)}(\mathbf{r},\mathbf{r}') = \sum_{k=1}^{\infty}(-1)^k\frac{\xi^{2k}}{\mathrm{c}^{2k}}(\Delta\varepsilon)^k\int_V \mathrm{d}^3s_1\ldots\int_V \mathrm{d}^3s_k \times\mathbf{G}^{(0)}(\mathbf{r},\mathbf{s}_1)\cdot\mathbf{G}^{(0)}(\mathbf{s}_1,\mathbf{s}_2)\ldots\mathbf{G}^{(0)}(\mathbf{s}_k,\mathbf{r}'), \quad (8)$$

with $\Delta\varepsilon = \varepsilon_\mathrm{B} - \varepsilon$. An analogous formula can be given for magnetic bodies. As the sphere is small compared to the distance to other bodies, the contribution from paths involving multiple scattering between the bodies and the small sphere are negligible. Three different classes of photon paths remain. A representative of each class and also an example of a negligible path are depicted in fig. 1 for one background body. Summing all paths from the three classes, one obtains the Green's tensor

$$\mathbf{G}^{(1)}_{\odot_1}(\mathbf{R},\mathbf{R}) = \mathbf{G}^{(1)}(\mathbf{R},\mathbf{R}) - \frac{\xi^2\alpha_1^*}{\mathrm{c}^2\varepsilon_0}\Big[\mathbf{G}^{(0)}(\mathbf{R},\mathbf{r}_1)\cdot\mathbf{G}^{(1)}(\mathbf{r}_1,\mathbf{R}) + \mathbf{G}^{(1)}(\mathbf{R},\mathbf{r}_1)\cdot\mathbf{G}^{(0)}(\mathbf{r}_1,\mathbf{R})\Big] - \mu_0\beta_1^*\Big[\mathbf{G}^{(0)}(\mathbf{R},\mathbf{r}_1)\times\overleftarrow{\nabla}_1\cdot\nabla_1 \times\mathbf{G}^{(1)}(\mathbf{r}_1,\mathbf{R}) + \mathbf{G}^{(1)}(\mathbf{R},\mathbf{r}_1)\times\overleftarrow{\nabla}_1\cdot\nabla_1\times\mathbf{G}^{(0)}(\mathbf{r}_1,\mathbf{R})\Big]. \quad (9)$$

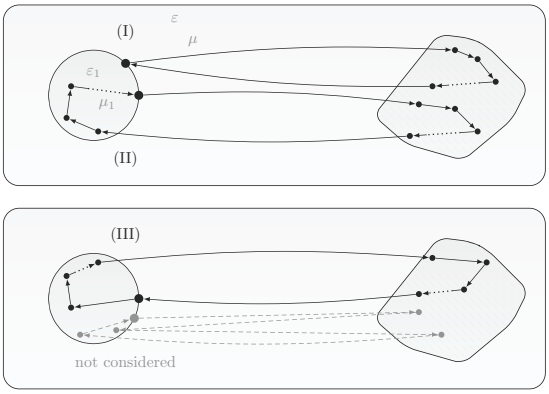

Fig. 1: For a small sphere, all relevant paths contributing to the Green's tensor either only involve scattering events in the background bodies (I), or involve scattering events in the background bodies and subsequently in the small sphere (II), or the other way round (III).

The first term, the Green's tensor for the background bodies, arises from class (I), the term in the second line arises from class (II) and the term in the third line arises from class (III). The remaining terms come from the analogue magnetic contribution. $\mathbf{r}_1$ denotes the centre of the sphere. α_1^* and β_1^* are the electric and magnetic excess dipole polarisabilities of the sphere [45], given by

$$\alpha_1^* = 4\pi\varepsilon_0\varepsilon R_1^3\frac{\varepsilon_1-\varepsilon}{\varepsilon_1+2\varepsilon} \quad\text{and}\quad \beta_1^* = \frac{4\pi R_1^3}{\mu_0\mu}\frac{\mu_1-\mu}{\mu_1+2\mu}. \quad (10)$$

Here, ε_1 and μ_1 denote the sphere's permittivity and permeability, while ε and μ are the respective properties of the medium. Equation (9) generalises the result of Sambale *et al.* [37] and can be used to study light-scattering phenomena involving small spheres, such as optical forces [6], Förster energy transfer [46] or solar cells [47].

A second small sphere with centre at $\mathbf{r}_2$ is now introduced by specifying the background Green's tensor in eq. (9) to be the one of a second small sphere using the result of Sambale *et al.* [37]

$$\mathbf{G}^{(1)}_{\odot_2}(\mathbf{r},\mathbf{r}') = -\frac{\alpha_2^*\xi^2}{\varepsilon_0\mathrm{c}^2}\mathbf{G}^{(0)}(\mathbf{r},\mathbf{r}_2)\cdot\mathbf{G}^{(0)}(\mathbf{r}_2,\mathbf{r}') - \mu_0\beta_2^*\mathbf{G}^{(0)}(\mathbf{r},\mathbf{r}_2)\times\overleftarrow{\nabla}_2\cdot\nabla_2\times\mathbf{G}^{(0)}(\mathbf{r}_2,\mathbf{r}'). \quad (11)$$

Inserting eq. (9) into eq. (7), evaluating the surface integrals using leading-order Taylor expansions in $\mathbf{R}-\mathbf{r}_1$, specifying the background Green's tensor to be given by (11), and by explicitly inserting the bulk Green's tensor in the non-retarded limit [41], one obtains the dispersion forces between two small spheres in the non-retarded limit, where the spheres are close compared to the wavelengths of the relevant transition frequencies. The corresponding

dispersion potentials read

$$U_{\mathrm{A[M]}}(r_{12}) = \frac{C_{6,\mathrm{A[M]}}}{r_{12}^6} \text{ with}$$
$$C_{6,\mathrm{A[M]}} = -\frac{3\hbar}{16\pi^3}\int_0^\infty \mathrm{d}\xi \left(\frac{\alpha_1^*\alpha_2^*}{\varepsilon_0^2\varepsilon^{2\,[+1]}} + \mu_0^2\mu^{2[+1]}\beta_1^*\beta_2^*\right) \tag{12}$$

and $r_{12} \equiv ||\mathbf{r}_1 - \mathbf{r}_2||$. The results for the two stress tensors only differ in the exponents of the medium response functions ε and μ, the additional powers in the square brackets only occur when using the Maxwell stress tensor.

Having found the force between two small spheres in a homogeneous medium on the basis of both stress tensors, we can now analyse the results by employing three criteria.

i) *Correspondence criterion*: The only properties of the two spheres entering eq. (12) are the excess dipole polarisabilities. By replacing these excess dipole polarisabilities by molecular ones, one should obtain the van der Waals potential of two molecules in a homogeneous medium. Explicitly inserting the bulk Green's tensor of a homogeneous medium in the non-retarded limit in ref. [48], one sees that this is the case for the Abraham potential, but not for the Maxwell potential.

One may wonder whether it is possible to redefine the excess polarisabilities (10) in such a way that the Maxwell potential obeys the correspondence criterion. However, this will lead to inconsistencies when requiring a formal correspondence to also hold for the Casimir-Polder potential. This can be seen by analysing the force on a small sphere in a medium in front of a perfectly reflecting surface, obtained by specifying the background Green's tensor in (9) to represent this system. The resulting C_3 coefficients read

$$C_{3,\mathrm{A[M]}} = -\frac{\hbar}{16\pi^2}\int_0^\infty \mathrm{d}\xi \left(\frac{\alpha_1^*}{\varepsilon_0\varepsilon^{1[+1]}} - \mu_0\mu^{1[+1]}\beta_1^*\right); \tag{13}$$

the Abraham result again fits the corresponding Casimir-Polder result. It is not possible to rescale the excess polarisabilities (10) in such a way that the Maxwell approach holds for eqs. (12) and (13) simultaneously, the former would demand the scaling factor $1/\sqrt{\varepsilon}$ for the electric excess polarisability whereas the latter would demand the factor $1/\varepsilon$.

ii) *Duality criterion*: The macroscopic Maxwell equations are symmetric with respect to a duality transformation which exchanges electric and magnetic fields [41]. This symmetry is also obeyed by the van der Waals force and the Casimir-Polder force: the electric and magnetic contributions transform into each other and the total forces are invariant. A macroscopic dispersion potential which also incorporates this symmetry is thus favourable. Exchanging the response functions ε and μ for the medium and the two spheres in eq. (12) together with eq. (10), one sees that the Abraham potential obeys duality invariance, while the Maxwell potential does not.

iii) *Microscopic criterion*: Finally, we investigate which of the two potentials is consistent with the microscopic theory obtained by summing all microscopic potentials which are involved in the interaction between the two spheres. This analysis is restricted to the electric parts of the potentials. We take into account the two-particle van der Waals potentials and the three-particle Axilrod-Teller potentials.

The electric van der Waals potential between two molecules with polarisabilities α and α' is given by

$$U_{\mathrm{vdW}}(\mathbf{r},\mathbf{r}') = -\frac{3\hbar}{16\pi^3\varepsilon_0^2}\int_0^\infty \mathrm{d}\xi\alpha\alpha'\frac{1}{||\mathbf{r}-\mathbf{r}'||^6}. \tag{14}$$

The contribution of the van der Waals potentials to the potential between two spheres in a medium can be obtained by identifying the part of the energy arising from all van der Waals interactions which depends on the finite distance of the spheres. This method was found by Hamaker [38]. It yields $U_{\mathrm{Ham}}(r_{12}) = C_{6,\mathrm{Ham}}/r_{12}^6$ with

$$C_{6,\mathrm{Ham}} = -\frac{\hbar R_1^3 R_2^3}{3\pi}\int_0^\infty \mathrm{d}\xi \Big[\eta_1\alpha_1\eta_2\alpha_2 - \eta_1\alpha_1\eta\alpha - \eta\alpha\eta_2\alpha_2 + \eta^2\alpha^2\Big], \tag{15}$$

where α_1, α_2 and α are the polarisabilities of the molecules in the two spheres and the medium and η_1, η_2 and η the corresponding molecular number densities.

The Axilrod-Teller potential between three molecules with polarisabilities α, α' and α'' is given by [49]

$$U_{\mathrm{AT}}(\mathbf{r},\mathbf{r}',\mathbf{r}'') = \frac{3\hbar}{64\pi^4\varepsilon_0^3}\int_0^\infty \mathrm{d}\xi\alpha\alpha'\alpha'' \times \frac{1+3\cos\theta\cos\theta'\cos\theta''}{||\mathbf{r}-\mathbf{r}'||^2||\mathbf{r}'-\mathbf{r}''||^3||\mathbf{r}''-\mathbf{r}||^3}, \tag{16}$$

where the angles are the ones of the triangle formed by the three molecules. The calculation of the three-particle contribution to the potential between two spheres in a medium for the case when two molecules are in separate spheres and the third one is in the medium yields $U_{3\mathrm{p}}(r_{12}) = C_{6,3\mathrm{p}}/r_{12}^6$ with

$$C_{6,3\mathrm{p}} = \frac{2\hbar R_1^3 R_2^3}{9\pi\varepsilon_0^3}\int_0^\infty \mathrm{d}\xi\ \eta_1\alpha_1\eta_2\alpha_2\eta\alpha. \tag{17}$$

The dispersion potential between two spheres, given by eq. (12) for the two approaches, should coincide with the sum of all microscopic potentials between the involved molecules. This identification is obtained by means of the Clausius-Mossotti law [50], which links the macroscopic susceptibility χ to the molecular polarisability α. For dilute bodies, it reads $\eta\alpha/\varepsilon_0 = \chi$. Hence, an expansion of the C_6 coefficient in eq. (12) in orders of χ_1, χ_2 and χ should yield the microscopic contributions in this case. Up to the third order in χ_1, χ_2 and χ and by only taking into account the term proportional to $\chi_1\,\chi_2\,\chi$ in the third order as depicted in fig. 2, one obtains

$$C_{6,\mathrm{A[M]}} = C_{6,\mathrm{Ham}} + [5/2]C_{6,3\mathrm{p}}. \tag{18}$$

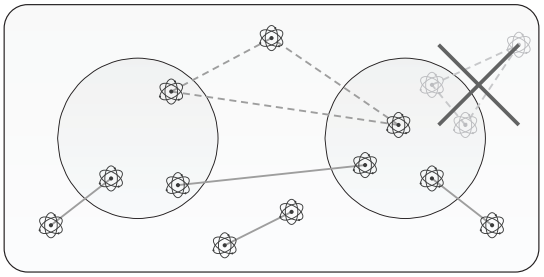

Fig. 2: For comparing $C_{6,\mathrm{A[M]}}$ with $C_{6,\mathrm{Ham}}$ and $C_{6,3\mathrm{p}}$, all terms of quadratic order in χ_1, χ_2 and χ, representing all possible van der Waals interactions between molecules in the two spheres and the medium, are taken into account. In the third order, only the term proportional to $\chi_1\,\chi_2\,\chi$ is connected to U_{3p}, given by eq. (17). Other contributions, such as the depicted term which is proportional to $\chi_2^2\,\chi$, are neglected for this comparison.

Both, the Abraham and the Maxwell potential, yield the correct two-particle Hamaker contribution, while only the Abraham potential also comes with the correct three-particle contribution whereas the Maxwell potential overestimates it by a factor of 5/2.

It could still be possible that the Maxwell potential between two small spheres in a medium is not representing the full potential but excluding buoyancy corrections coming from the surrounding medium. However, this is not the case: the Maxwell potential, like the Abraham potential, vanishes when replacing one of the spheres by a spherical volume of the medium since the corresponding excess polarisabilities in (12) vanish in both cases.

The preceding analysis leads us to the conclusion that the approach by Dzyaloshinskii, Lifshitz and Pitaevskii on the basis of the Abraham stress tensor is confirmed for the geometry of two small spheres in a homogeneous medium. The force is of the same structure as the microscopic van der Waals and Casimir-Polder forces and is symmetric under exchange of electric and magnetic contributions. Furthermore, we have shown that it can at least up to three-particle interactions be viewed as the sum of all microscopic dispersion forces between the contributing molecules.

Our result confirms the use of the theory by Dzyaloshinskii, Lifshitz and Pitaevskii in studies of the melting of bodies [51] and the wetting of surfaces [52]. Here, one is interested in the dispersion interaction of a body, coated by a layer of melted material or liquid, with the surrounding air. Another recently considered application is the formation of ice crystals under water [53].

The approach by Raabe and Welsch on the basis of the Maxwell stress tensor on the other hand is not fulfilling these criteria. Furthermore, contrary to their findings for a planar geometry, their approach does not lead to forces on an initially homogeneous medium in the presence of a small sphere. By definition, this is also the case for the theory based on the Abraham stress tensor and it is thus not possible to calculate such forces on the medium using the present theory. The calculation of many-body dispersion forces in a medium as induced by a nearby solid body remains an important open question which could be relevant, *inter alia*, to the atmosphere capture by small asteroids.

We conclude this article by presenting a more general form of the preceeding analysis of dispersion forces on colloidal particles. Having established eq. (1) as the correct stress tensor, a combination of eqs. (7) and (9) leads to the dispersion potential for a colloid in a homogeneous medium in the presence of other bodies represented by $\mathbf{G}$ reading

$$U(\mathbf{r}_1) = \frac{\hbar}{2\pi}\int_0^\infty \mathrm{d}\xi \Big[\frac{\xi^2\alpha_1^*}{\mathrm{c}^2\varepsilon_0}\,\mathrm{tr}\,\mathbf{G}^{(1)}(\mathbf{r}_1,\mathbf{r}_1) + \mu_0\beta_1^*\,\mathrm{tr}\,\nabla\times\mathbf{G}^{(1)}(\mathbf{r}_1,\mathbf{r}')\times\overleftarrow{\nabla}'\big|_{r'=r_1}\Big]. \quad (19)$$

Further specifying $\mathbf{G}$ to comprise another small sphere using [37], the dispersion potential of two colloids in a homogeneous medium, possibly in the presence of other bodies, is given by

$$U(\mathbf{r}_1,\mathbf{r}_2) = -\frac{\hbar}{2\pi}\int_0^\infty \mathrm{d}\xi \Big[\frac{\xi^4\alpha_1^*\alpha_2^*}{\mathrm{c}^4\varepsilon_0^2}\,\mathrm{tr}\,\mathbf{G}(\mathbf{r}_1,\mathbf{r}_2)\cdot\mathbf{G}(\mathbf{r}_2,\mathbf{r}_1) + \mu_0^2\beta_1^*\beta_2^*\,\mathrm{tr}\,\nabla_1\times\mathbf{G}(\mathbf{r}_1,\mathbf{r}_2)\times\overleftarrow{\nabla}_2\cdot\nabla_2\times\mathbf{G}(\mathbf{r}_2,\mathbf{r}_1)\times\overleftarrow{\nabla}_1\Big]. \quad (20)$$

These formulas have been derived neglecting retardation. Note that there are definitions of the excess dipole polarisabilities of small spherical particles alternative to ours. Netz and Sambale introduce the electric excess polarisability without the prefactor ε [37,54], relating the polarisation field of the particle to a dipole in vacuum. The definition in eq. (10) on the other hand relates the polarisation field of the particle to a dipole in a medium. Our analysis shows that only this way a formal correspondence to microscopic dispersion forces can be established.

Colloids described by eqs. (19) and (20) do not necessarily have to be represented by homogeneous spheres using eq. (10). One can also apply other colloid models and use the according excess polarisabilities following the convention of the present paper as discussed above. In this framework, one can describe the interaction of colloids without having to make the additive approximations one encounters in microscopic calculations.

* * *

We thank R. Corkery, C. Henkel and V. Shatokhin for stimulating discussions. SYB and JF gratefully acknowledge support by the German Research Council (grant BU1803/3-1), the University of Freiburg (Research Innovation Fund) and the Freiburg Institute for Advanced Studies (SYB).

REFERENCES

[1] Obukhov Y. N. and Hehl F. W., *Phys. Lett. A*, **311** (2003) 277.
[2] Pfeifer R. N. C., Nieminen T. A., Heckenberg N. R. and Rubinsztein-Dunlop H., *Rev. Mod. Phys.*, **79** (2007) 1197.
[3] Richter F., Florian M. and Henneberger K., *EPL*, **81** (2008) 67005.
[4] Toptygin I. N., *Phys. Usp.*, **60** (2017) 1007.
[5] Rubinsztein-Dunlop H., Forbes A., Berry M. V., Dennis M. R., Andrews D. L., Mansuripur M., Denz C., Alpmann C., Banzer P., Bauer T., Karimi E., Marucci L., Padgett M., Ritsche-Marte M., Litchinitser N. M., Bigelow N. P., Rosales-Guzmán C., Belmonte A., Torres J. P., Neely T. W., Baker M., Gordon R., Stilgoe A. B., Romero J., White A. G., Fickler R., Willner A. E., Xie G., Mcmorran B. and Weiner A. M., *J. Opt.*, **19** (2017) 013001.
[6] Ether D. S. jr., Pires L. B., Umrath S., Martinez D., Ayala Y., Pontes B., de S. Araújo G. R., Frases S., Ingold G.-L., Rosa F. S. S., Viana N. B., Nussenzveig H. M. and Maia Neto P. A., *EPL*, **112** (2015) 44001.
[7] Hertlein C., Helden L., Gambassi A., Dietrich S. and Bechinger C., *Nature*, **451** (2008) 172.
[8] Dzyaloshinskii I. E., Lifshitz E. M. and Pitaevskii L. P., *Sov. Phys. Usp.*, **4** (1961) 153.
[9] Raabe C. and Welsch D. G., *Phys. Rev. A*, **71** (2005) 013814.
[10] van Tiggelen B. A., Rikken G. L. J. A. and Krstić V., *Phys. Rev. Lett.*, **96** (2006) 130402.
[11] Donaire M., van Tiggelen B. A. and Rikken G. L. J. A., *Phys. Rev. Lett.*, **111** (2013) 143602.
[12] Abraham M., *Rend. Circ. Mat. Palermo*, **28** (1909) 1.
[13] Minkowski H., *Math. Ann.*, **68** (1910) 472.
[14] Brevik I., *Phys. Rep.*, **52** (1979) 133.
[15] Casner A. and Delville J.-P., *Phys. Rev. Lett.*, **90** (2003) 144503.
[16] Hallanger A., Brevik I., Haaland S. and Sollie R., *Phys. Rev. E*, **71** (2005) 056601.
[17] Goetz H. and Zahn W., *Z. Phys.*, **151** (1958) 202.
[18] Hakim S. S. and Higham J. B., *Proc. R. Soc.*, **80** (1962) 190.
[19] Lifshitz E. M., *Sov. Phys. J.*, **2** (1956) 73.
[20] Jackson J. D., *Classical Electrodynamics* (Wiley, New York) 1998.
[21] Philbin T. G., *New J. Phys.*, **13** (2011) 063026.
[22] Brevik I. and Ellingsen S. A., *Phys. Rev. A*, **79** (2009) 027801.
[23] Robinson F. N. H., *Phys. Rep.*, **16** (1975) 313.
[24] Raabe C. and Welsch D. G., *Phys. Rev. A*, **80** (2009) 067801.
[25] Raabe C. and Welsch D. G., *Phys. Rev. A*, **73** (2006) 063822.
[26] Raabe C. and Welsch D. G., *Phys. Rev. A*, **73** (2006) 047802.
[27] Pitaevskii L. P., *Phys. Rev. A*, **73** (2006) 047801.
[28] Horn R. G., Evans D. F. and Ninham B. W., *J. Phys. Chem.*, **92** (1988) 3531.
[29] Afshar-Rad T., Bailey A. I., Luckham P. F., Mcnaughtan W. and Chapman D., *Biochim. Biophys. Acta (BBA)*, **915** (1987) 101.
[30] Claesson P. M., Dedinaite A., Bergenståhl B., Campbell B. and Christenson H., *Langmuir*, **13** (1997) 1682.
[31] Munday J. N., Capasso F., Parsegian V. A. and Bezrukov S. M., *Phys. Rev. A*, **78** (2008) 032109.
[32] Ducker W. A., Senden T. J. and Pashley R. M., *Nature*, **353** (1991) 239.
[33] Senden T. J. and Drummond C. J., *Colloids Surf. A*, **94** (1995) 29.
[34] Hutter J. L. and Bechhoefer J., *J. Appl. Phys.*, **73** (1993) 4123.
[35] Milling A., Mulvaney P. and Larson I., *J. Colloid Interface Sci.*, **180** (1996) 460.
[36] Munday J. N., Capasso F. and Parsegian V. A., *Nature*, **457** (2009) 170.
[37] Sambale A., Buhmann S. Y. and Scheel S., *Phys. Rev. A*, **81** (2010) 012509.
[38] Hamaker H. C., *Physica IV*, **10** (1937) 1058.
[39] Langbein D., *Theory of van der Waals Attraction* (Springer-Verlag, Heidelberg, Berlin) 1974.
[40] Boinovich L., *Curr. Opin. Colloid Interface Sci.*, **15** (2010) 297.
[41] Buhmann S. Y., *Dispersion Forces I: Macroscopic Quantum Electrodynamics and Ground-State Casimir, Casimir–Polder and van der Waals Forces* (Springer-Verlag, Heidelberg, Berlin) 2012.
[42] Lamb W. E. jr. and Retherford R. C., *Phys. Rev.*, **72** (1947) 241.
[43] Wick G. C., *Phys. Rev.*, **96** (1954) 1124.
[44] Buhmann S. Y. and Welsch D. G., *Appl. Phys. B*, **82** (2006) 189.
[45] Mclachlan A. D., *Discuss. Faraday Soc.*, **40** (1965) 239.
[46] Dung H. T., Knöll L. and Welsch D.-G., *Phys. Rev. A*, **65** (2002) 043813.
[47] Efthymios K., Ross D., Mcintosh K. R. and Richards B. S., *Sol. Energy Mater. Sol. Cells*, **93** (2009) 0927.
[48] Safari H., Welsch D. G., Buhmann S. Y. and Scheel S., *Phys. Rev. A*, **78** (2008) 062901.
[49] Axilrod B. M. and Teller E., *J. Chem. Phys.*, **11** (1943) 299.
[50] Van Rysselberghe P., *J. Phys. Chem.*, **36** (1932) 1152.
[51] Tartaglino U., Zykova-Timan T., Ercolessi F. and Tosatti E., *Phys. Rep.*, **411** (2005) 291.
[52] Jacobs K., Seemann R. and Herminghaus S., in *Polymer Thin Films*, edited by Tsui O. K. C. and Russell T. P. (World Scientific, Singapore) 2008, pp. 243–265.
[53] Thiyam P., Fiedler J., Buhmann S. Y., Persson C., Brevik I., Boström M. and Parsons D. F., *Ice pasticles sink below the water surface due to a balance of salt, van der waals and buoyancy forces*, submitted to *J. Phys. Chem.*
[54] Netz R. R., *Curr. Opin. Colloid Interface Sci.*, **9** (2004) 192.

PHYSICAL REVIEW A **81**, 012509 (2010)

Casimir-Polder interaction between an atom and a small magnetodielectric sphere

Agnes Sambale
Theoretisch-Physikalisches Institut, Friedrich-Schiller-Universität Jena, Max-Wien-Platz 1, D-07743 Jena, Germany

Stefan Yoshi Buhmann and Stefan Scheel
Quantum Optics and Laser Science, Blackett Laboratory, Imperial College London, Prince Consort Road, London SW7 2BW, United Kingdom
(Received 27 August 2009; published 28 January 2010)

On the basis of macroscopic quantum electrodynamics and point-scattering techniques, we derive a closed expression for the Casimir-Polder force between a ground-state atom and a small magnetodielectric sphere in an arbitrary environment. To allow for the presence of both bodies and media, local-field corrections are taken into account. Our results are compared with the known van der Waals force between two ground-state atoms. To continuously interpolate between the two extreme cases of a single atom and a macroscopic sphere, we also derive the force between an atom and a sphere of variable radius that is embedded in an Onsager local-field cavity. Numerical examples illustrate the theory.

DOI: 10.1103/PhysRevA.81.012509 PACS number(s): 31.30.jh, 12.20.−m, 34.20.−b, 42.50.Wk

I. INTRODUCTION

Van der Waals (vdW) dispersion forces are effective electromagnetic forces that arise between polarizable objects as a consequence of correlated quantum fluctuations [1–10]. Postulated as early as 1873 to account for deviations from the ideal gas law [11], they were theoretically understood only much later in 1930, when London derived them from the electrostatic Coulomb interaction of charge fluctuations [12]. London found that two atoms of polarizabilities $\alpha_A(\omega)$ and $\alpha_B(\omega)$ at a distance r_{AB} are subject to a vdW potential

$$U(r_{AB}) = -\frac{3\hbar}{16\pi^3\varepsilon_0^2 r_{AB}^6}\int_0^\infty \mathrm{d}\xi\,\alpha_A(i\xi)\alpha_B(i\xi). \qquad (1)$$

Important progress was made in 1948 by Casimir and Polder, who included fluctuations of the transverse electromagnetic field and obtained a full quantum electrodynamic description of dispersion forces [13]. Their result reduces to the London formula in the electrostatic limit but is given by

$$U(r_{AB}) = -\frac{23\hbar c\alpha_A(0)\alpha_B(0)}{64\pi^3\varepsilon_0^2 r_{AB}^7} \qquad (2)$$

for distances much larger than the relevant atomic transition wavelengths.

Casimir arrived at his famous results while studying the properties of colloidal solutions [14]. These results illustrate the importance of dispersion forces to colloid science, which deals with the (inter alia vdW) interactions between small clusters of particles in free space [15] and, more often, with the different forces in colloidal suspensions. For example, (attractive) dispersion forces between spherical micro- and macro-objects embedded in a liquid [16] usually diminish the stability of such suspensions and may even cause clustering or flocculation [17]. The introduction of small amounts of highly charged nanoparticles gives rise to competing repulsive forces, thus balancing the stability of the suspension [18]. Stable mechanical suspensions might also be created with fluid-separated macro-objects such as eccentric cylinders by means of repulsive dispersion forces [19]. Note that in addition to dispersion and electrostatic forces, critical Casimir forces due to concentration fluctuations [20], chemical effects such as hydration and solvation, hydrophobic forces, and steric repulsion [21,22] and depletion [23] also influence the interaction of the colloidal particles.

Dispersion forces play a similar role in biology, where they contribute to the organization of molecules [24–26], cell adhesion [24,25,27,28], and the interaction of molecules with cell membranes [25,27]. They are also of interest in atomic force microscopy [29].

A large variety of models has been used in the past to study vdW forces between small polarizable objects [16]. Interacting atoms have been studied on a microscopic level as neutral arrangements of point charges [12,13], as sketched in Fig. 1(i). Larger systems can be treated by considering collections of such polarizable point objects [Fig. 1(ii)], in which a pairwise-sum method is often employed [30]. Investigations of the polarizability of N-atom nanoclusters of various sizes and shapes have shown that an additive relation, $\alpha_{\mathrm{clust}} = N\alpha_A$, does not hold in general but is valid for spherical clusters [31]. Microscopic approaches have to be contrasted with macroscopic descriptions in which continuous objects of polarizable matter are characterized by their permittivity [Fig. 1(iii)], and an intervening medium can be accounted for in the same spirit. One commonly distinguishes the additive Hamaker method [32] from the more elaborate Lifshitz theory, which includes many-body interactions [33,34].

A hybrid approach consists of a microscopic treatment of interacting atoms, combined with a macroscopic description of an intervening medium. To reconcile the microscopic and macroscopic pictures, local-field effects are included by assuming the atoms to be surrounded by small free-space cavities, an approach known as the Onsager real-cavity model [35]; see Fig. 1(iv). As found by studying the behavior of the classical Green tensor $\mathbf{G}$ for

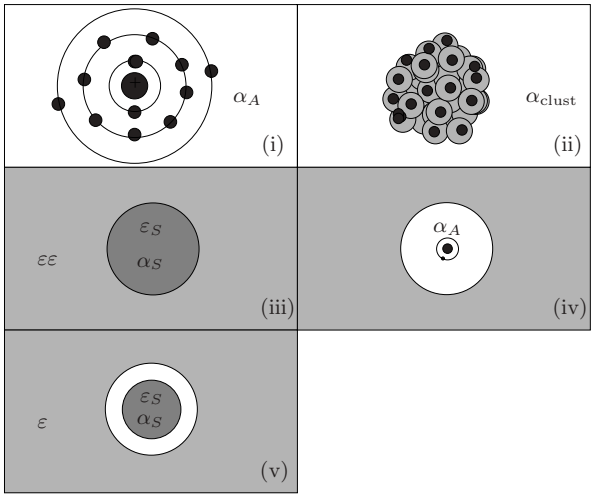

FIG. 1. Models of polarizable systems: (i) neutral arrangement of point charges (atom), (ii) cluster of atoms, (iii) dielectric sphere inside medium, (iv) atom in empty cavity surrounded by medium (Onsager real-cavity model), and (v) dielectric sphere in empty cavity surrounded by medium.

the electromagnetic field in conjunction with the real-cavity model [36], the vdW potential of two atoms at positions $\mathbf{r}_A$ and $\mathbf{r}_B$ in an arbitrary environment can be given as [37]

$$U(\mathbf{r}_A,\mathbf{r}_B) = -\frac{\hbar\mu_0^2}{2\pi}\int_0^\infty \mathrm{d}\xi\ \xi^4\alpha_A(i\xi)\alpha_B(i\xi) \times\left[\frac{3\varepsilon_A(i\xi)}{2\varepsilon_A(i\xi)+1}\right]^2\left[\frac{3\varepsilon_B(i\xi)}{2\varepsilon_B(i\xi)+1}\right]^2 \times \mathrm{Tr}[\mathbf{G}(\mathbf{r}_A,\mathbf{r}_B,i\xi)\cdot\mathbf{G}(\mathbf{r}_B,\mathbf{r}_A,i\xi)], \quad (3)$$

where local-field correction factors explicitly appear.

To compare the microscopic, local-field corrected approach of Fig. 1(iv) with the macroscopic one shown in Fig. 1(iii), in this work we study the Casimir-Polder (CP) interaction of a ground-state atom with a magnetodielectric sphere of variable size in the presence of arbitrary magnetoelectric background media on basis of macroscopic quantum electrodynamics (QED). Our considerations are related to free-space results obtained earlier for the interaction of an atom with curved surfaces [38] and dielectric [39] and perfectly conducting spheres [40]; compare with the nonretarded vdW potential of a ground-state atom inside and outside a dielectric or metallic spherical shell as calculated in Ref. [41]. In addition, we consider the interaction of an atom with a magnetodielectric sphere inside an Onsager cavity [Fig. 1(v)]. By changing the radius of the sphere, this construction allows us to study the transition between a microscopic pointlike object and a macroscopic one.

The article is organized as follows. In Sec. II, we recall the basic equations concerning ground-state CP potentials. In Sec. II A, we show how the Green tensors of a magnetodielectric full sphere or a sphere within an Onsager cavity can be written as functions of the Green tensors of the environment without the sphere. The results are then used to study the atom-sphere potentials, which are compared with the vdW interaction between two ground-state atoms (Sec. II B). As an example, we evaluate the interaction between an atom and molecules of different sizes in a bulk medium. A summary is given in Sec. III.

II. ATOM-SPHERE INTERACTION

In order to derive an expression for the CP interaction between a (ground-state) atom and a magnetodielectric sphere in the presence of an arbitrary medium environment, we start from the familiar formulas for the electric (U_e) and magnetic (U_m) CP potentials of a ground-state atom of polarizability

$$\alpha_A(\omega) = \lim_{\epsilon\to 0}\frac{2}{3\hbar}\sum_k \frac{\omega_{k0}|\mathbf{d}_{0k}|^2}{\omega_{k0}^2-\omega^2-i\omega\epsilon} \quad (4)$$

(where ω_{k0} are transition frequencies and $\mathbf{d}_{0k}$ are electric dipole matrix elements) and magnetizability

$$\beta_A(\omega) = \lim_{\epsilon\to 0}\frac{2}{3\hbar}\sum_k \frac{\omega_{k0}|\mathbf{m}_{0k}|^2}{\omega_{k0}^2-\omega^2-i\omega\epsilon} \quad (5)$$

(where $\mathbf{m}_{0k}$ are magnetic dipole matrix elements) that are placed at an arbitrary position $\mathbf{r}_A$ within an environment of locally and linearly responding magnetoelectric bodies or media [characterized by their permittivity $\varepsilon(\mathbf{r}_A,\omega)$ and permeability $\mu(\mathbf{r}_A,\omega)$] [7,37,42]:

$$U_e(\mathbf{r}_A) = \frac{\hbar\mu_0}{2\pi}\int_0^\infty \mathrm{d}\xi\ \xi^2\alpha_A(i\xi)\left[\frac{3\varepsilon_A(i\xi)}{2\varepsilon_A(i\xi)+1}\right]^2 \times \mathrm{Tr}\mathbf{G}^{(1)}(\mathbf{r}_A,\mathbf{r}_A,i\xi) \quad (6)$$

and

$$U_m(\mathbf{r}_A) = \frac{\hbar\mu_0}{2\pi}\int_0^\infty \mathrm{d}\xi\beta_A(i\xi)\left[\frac{3}{2\mu_A(i\xi)+1}\right]^2 \times \mathrm{Tr}[\nabla\times\mathbf{G}^{(1)}(\mathbf{r}_A,\mathbf{r}_A,i\xi)\times\overleftarrow{\nabla}'], \quad (7)$$

with $\varepsilon_A(\omega)\equiv\varepsilon(\mathbf{r}_A,\omega)$, $\mu_A(\omega)\equiv\mu(\mathbf{r}_A,\omega)$. These expressions explicitly allow for the atom to be embedded in a medium environment where the relevant local-field corrections have been accounted for via the Onsager real-cavity model [35,36]. The scattering Green tensor $\mathbf{G}^{(1)}(\mathbf{r},\mathbf{r}',\omega)$ fully accounts for the position, size, and shape of all bodies and media as well as their magnetoelectric properties and is defined by the differential equation

$$\left[\nabla\times\frac{1}{\mu(\mathbf{r},\omega)}\nabla\times-\frac{\omega^2}{c^2}\varepsilon(\mathbf{r},\omega)\right]\mathbf{G}(\mathbf{r},\mathbf{r}',\omega)=\delta(\mathbf{r}-\mathbf{r}'), \quad (8)$$

with the condition $\mathbf{G}(\mathbf{r},\mathbf{r}',\omega)\to\mathbf{0}$ for $|\mathbf{r}-\mathbf{r}'|\to\infty$. In this work, the body interacting with the atom is a magnetodielectric sphere whose Green tensor we analyze in the following.

A. Decomposition of the Green tensor

Two methods may be envisaged to study the CP potential of an atom in the presence of a magnetodielectric sphere and an arbitrary environment of additional bodies and media. First, one could work with the Green tensor of the combined sphere-environment system [Fig. 2(i)] directly, which may be very

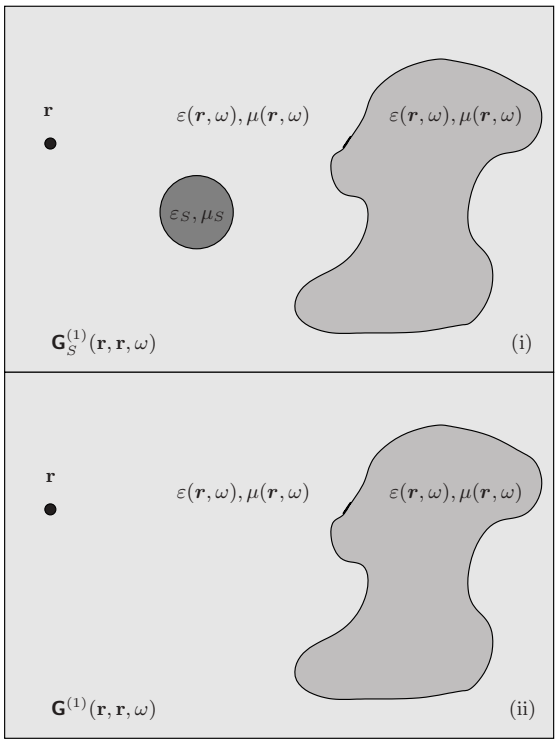

FIG. 2. (i) Green tensor of the combined system of magnetodielectric sphere and arbitrary background environment and (ii) Green tensor of the same system without the sphere.

complicated; even if an analytical expression of the Green tensor is known, the resulting expressions for the potentials are hard to evaluate and do not allow for an explicit discussion of the influence of the sphere. In this work, we therefore follow a second, alternative approach: We show how the Green tensor of the full arrangement including the sphere, $\mathbf{G}_S^{(1)}(\mathbf{r},\mathbf{r},\omega)$, can be related to the Green tensor without the sphere [Fig. 2(ii)]; $\mathbf{G}^{(1)}(\mathbf{r},\mathbf{r},\omega)$ describes only the background environment. To establish such a relation, we use methods similar to those developed for studying local-field corrections [36,37,42]. The crucial assumption for using these point-scattering techniques is that the effective radius of the sphere is small compared with the relevant wavelengths of the electromagnetic field.

1. Full sphere

Assuming that the functions $\varepsilon(\mathbf{r},\omega)$ and $\mu(\mathbf{r},\omega)$ describe the magnetoelectric properties of the environment, the introduction of a homogeneous magnetodielectric sphere with radius R centered at $\mathbf{r}_S$, permittivity $\varepsilon_S(\omega)$, and permeability $\mu_S(\omega)$ leads to the new functions

$$\varepsilon_S(\mathbf{r},\omega),\,\mu_S(\mathbf{r},\omega) = \begin{cases} \varepsilon_S(\omega),\,\mu_S(\omega) & \text{for } |\mathbf{r}-\mathbf{r}_S| \leqslant R, \\ \varepsilon(\mathbf{r},\omega),\,\mu(\mathbf{r},\omega) & \text{elsewhere.} \end{cases} \tag{9}$$

The Green tensor $\mathbf{G}_S^{(1)}(\mathbf{r},\mathbf{r},\omega)$ of sphere plus environment is hence the solution to the differential equation (8) with $\varepsilon_S(\mathbf{r},\omega)$ and $\mu_S(\mathbf{r},\omega)$ in place of $\varepsilon(\mathbf{r},\omega)$ and $\mu(\mathbf{r},\omega)$.

As discussed in Refs. [36,37], for a small sphere it is sufficient to consider first the special case of a homogeneous, bulk environment, which is then generalized to arbitrary environments at the end of the section. The required scattering Green tensor of the sphere with center $\mathbf{r}_S = \mathbf{0}$ inside a bulk medium of permittivity $\varepsilon(\omega)$ and permeability $\mu(\omega)$ can be written in the form [43]

$$\begin{aligned} \mathbf{G}_S^{(1)}(\mathbf{r},\mathbf{r}',\omega) = \frac{i\mu k}{4\pi}\sum_{p=\pm}\sum_{l=1}^{\infty}\sum_{m=0}^{n}(2-\delta_{m0}) \\ \times \frac{2l+1}{l(l+1)}\frac{(l-m)!}{(l+m)!} \\ \times \left[B_l^M \mathbf{M}_{lmp}(k,\mathbf{r})\mathbf{M}_{lmp}(k,\mathbf{r}') \right. \\ \left. + B_l^N \mathbf{N}_{lmp}(k,\mathbf{r})\mathbf{N}_{lmp}(k,\mathbf{r}')\right], \end{aligned} \tag{10}$$

where $k = \sqrt{\varepsilon\mu}\omega/c$, $\mathbf{M}_{lmp}$, $\mathbf{N}_{lmp}$ denote even (+) and odd (−) spherical vector wave functions with total angular momentum l and z projection m, and $B_l^{M,N}$ are the associated coefficients for reflection at the surface of the sphere. Explicit forms for $\mathbf{M}_{lmp}$, $\mathbf{N}_{lmp}$, and $B_l^{M,N}$ can be found in Refs. [43,44].

In the limit of a small sphere with $|k_S R|, |kR| \ll 1$ ($k_S = \sqrt{\varepsilon_S\mu_S}\omega/c$), we have

$$B_l^{M,N} = O\left(\frac{\omega R}{c}\right)^{2l+1}, \tag{11}$$

and so the dominant contribution to the Green tensor is due to the $l = 1$ terms. The respective vector wave functions are given by

$$\begin{aligned} \mathbf{M}_{1m\pm}(k,\mathbf{r}) = \mp\frac{m}{\sin\theta}h_1^{(1)}(kr)P_1^m(\cos\theta)\begin{Bmatrix}\sin m\phi\\ \cos m\phi\end{Bmatrix}\mathbf{e}_\theta \\ - h_1^{(1)}(kr)\frac{\mathrm{d}P_1^m(\cos\theta)}{\mathrm{d}\theta}\begin{Bmatrix}\cos m\phi\\ \sin m\phi\end{Bmatrix}\mathbf{e}_\phi \end{aligned} \tag{12}$$

and

$$\begin{aligned} \mathbf{N}_{1m\pm}(\mathbf{r}) = 2\frac{h_1^{(1)}(kr)}{kr}P_1^m(\cos\theta)\begin{Bmatrix}\cos m\phi\\ \sin m\phi\end{Bmatrix}\mathbf{e}_r \\ + \frac{1}{kr}\frac{\mathrm{d}\left[krh_1^{(1)}(kr)\right]}{d(kr)}\frac{\mathrm{d}P_1^m(\cos\theta)}{\mathrm{d}\theta}\begin{Bmatrix}\cos m\phi\\ \sin m\phi\end{Bmatrix}\mathbf{e}_\theta \\ \mp\frac{m}{\sin\theta}P_1^m(\cos\theta)\frac{1}{kr}\frac{\mathrm{d}\left[krh_1^{(1)}(kr)\right]}{d(kr)}\begin{Bmatrix}\sin m\phi\\ \cos m\phi\end{Bmatrix}\mathbf{e}_\phi, \end{aligned} \tag{13}$$

where the $P_1^m(x)$ are associated Legendre polynomials and $h_1^{(1)}(x)$ is a spherical Hankel function of the first kind. The $l = 1$ reflection coefficients in the small-sphere limit $|k_S R|, |kR| \ll 1$ are given by

$$B_1^M = \frac{2i}{3}\left(\sqrt{\varepsilon\mu}\frac{\omega R}{c}\right)^3\frac{\mu_S-\mu}{\mu_S+2\mu}, \tag{14}$$

$$B_1^N = \frac{2i}{3}\left(\sqrt{\varepsilon\mu}\frac{\omega R}{c}\right)^3\frac{\varepsilon_S-\varepsilon}{\varepsilon_S+2\varepsilon}. \tag{15}$$

We can further evaluate the p and m sums for $l=1$ using $P_1^0(\cos\theta)=\cos\theta$ and $P_1^1(\cos\theta)=-\sin\theta$ to obtain

$$\sum_{p=\pm1}\sum_{m=0}^{1}(2-\delta_{m0})\frac{(1-m)!}{(1+m)!}\mathbf{M}_{1mp}(\mathbf{r})\mathbf{M}_{1mp}(\mathbf{r})=h^2[\mathbf{I}-\mathbf{e}_r\mathbf{e}_r] \tag{16}$$

and

$$\sum_{p=\pm1}\sum_{m=0}^{1}(2-\delta_{m0})\frac{(1-m)!}{(1+m)!}\mathbf{N}_{1mp}(\mathbf{r})\mathbf{N}_{1mp}(\mathbf{r}) = \frac{h'^2}{(kr)^2}\mathbf{I}+\frac{4h^2-h'^2}{(kr)^2}\mathbf{e}_r\mathbf{e}_r, \tag{17}$$

with the notation $h\equiv h_1^{(1)}(kr)=-i(1-ikr)e^{ikr}/(kr)^2$ and $h'\equiv \mathrm{d}[krh_1^{(1)}(kr)]/\mathrm{d}(kr)$. By substituting these expressions into Eq. (10), the (equal-position) scattering Green tensor of a small sphere becomes

$$\begin{aligned}\mathbf{G}_S^{(1)}(\mathbf{r},\mathbf{r},\omega)=\frac{\mu e^{2ikr}}{4\pi k^2r^6}&\{[1-2ikr-3(kr)^2+2i(kr)^3+(kr)^4]\mathbf{I}\\&+[3-6ikr-(kr)^2-2i(kr)^3-(kr)^4]\mathbf{e}_r\mathbf{e}_r\}\\&\times\frac{\varepsilon_S-\varepsilon}{\varepsilon_S+2\varepsilon}R^3+\frac{\mu e^{2ikr}}{4\pi r^4}[1-2ikr-(kr)^2]\\&\times(\mathbf{I}-\mathbf{e}_r\mathbf{e}_r)\frac{\mu_S-\mu}{\mu_S+2\mu}R^3.\end{aligned} \tag{18}$$

Next, we relate our result to the Green tensor of the bulk medium without the sphere (cf., e.g., Ref. [44]),

$$\begin{aligned}\mathbf{G}(\mathbf{r},\mathbf{r}',\omega)=-\frac{\mu e^{ik\rho}}{4\pi k^2\rho^3}&\{[1-ik\rho-(k\rho)^2)]\mathbf{I}\\&-[3-3ik\rho-(k\rho)^2]\mathbf{e}_\rho\mathbf{e}_\rho\},\end{aligned} \tag{19}$$

which is valid for $\mathbf{r}\neq\mathbf{r}'$, where $\boldsymbol{\rho}=\mathbf{r}-\mathbf{r}'$, $\rho=|\boldsymbol{\rho}|$, and $\mathbf{e}_\rho=\boldsymbol{\rho}/\rho$. The Green tensor $\mathbf{G}_S^{(1)}(\mathbf{r},\mathbf{r},\omega)$ of the small sphere describes the propagation of the electric field from a source at $\mathbf{r}$ to the sphere, its scattering from the sphere (a polarizable and magnetizable point scatterer) at $\mathbf{r}_S=\mathbf{0}$, and its return to $\mathbf{r}$. It is therefore natural to try and compose $\mathbf{G}_S^{(1)}$ from products of $\mathbf{G}$, which describes the propagation of the electric field through the bulk medium to an electric scatterer, and $\mathbf{G}\times\overleftarrow{\nabla}$, which describes its propagation to a magnetic scatterer. Indeed, from Eq. (19), we find that

$$\begin{aligned}&\mathbf{G}(\mathbf{r},\mathbf{0},\omega)\cdot\mathbf{G}(\mathbf{0},\mathbf{r},\omega)\\&=\frac{\mu^2e^{2ikr}}{16\pi^2k^4r^6}\{[1-2ikr-3(kr)^2+2i(kr)^3+(kr)^4]\mathbf{I}\\&\quad+[3-6ikr-(kr)^2-2i(kr)^3-(kr)^4]\,\mathbf{e}_r\mathbf{e}_r\}\end{aligned} \tag{20}$$

and

$$\begin{aligned}&\mathbf{G}(\mathbf{r},\mathbf{r}_S,\omega)\times\overleftarrow{\nabla}_S\cdot\nabla_S\times\mathbf{G}(\mathbf{r}_S,\mathbf{r},\omega)|_{\mathbf{r}_S=\mathbf{0}}\\&=-\frac{\mu^2e^{2ikr}}{16\pi^2r^4}[1-2ikr-(kr)^2](\mathbf{I}-\mathbf{e}_r\mathbf{e}_r).\end{aligned} \tag{21}$$

A comparison with Eq. (18) shows that

$$\begin{aligned}\mathbf{G}_S^{(1)}(\mathbf{r},\mathbf{r},\omega)=4\pi\varepsilon R^3\frac{\varepsilon_S-\varepsilon}{\varepsilon_S+2\varepsilon}\frac{\omega^2}{c^2}&\mathbf{G}(\mathbf{r},\mathbf{0},\omega)\cdot\mathbf{G}(\mathbf{0},\mathbf{r},\omega)\\&-\frac{4\pi R^3}{\mu}\frac{\mu_S-\mu}{\mu_S+2\mu}\mathbf{G}(\mathbf{r},\mathbf{r}_S,\omega)\times\overleftarrow{\nabla}_S\\&\cdot\nabla_S\times\mathbf{G}(\mathbf{r}_S,\mathbf{r},\omega)|_{\mathbf{r}_S=\mathbf{0}}.\end{aligned} \tag{22}$$

Let us next consider a general background environment, which can involve different media or bodies, as sketched in Fig. 2. With the permittivity $\varepsilon(\mathbf{r},\omega)$ and permeability $\mu(\mathbf{r},\omega)$ of the environment now being functions of position, it is useful to introduce a notation for their values at the position of the sphere, $\varepsilon_\odot(\omega)\equiv\varepsilon(\mathbf{r}_S,\omega)$, $\mu_\odot(\omega)\equiv\mu(\mathbf{r}_S,\omega)$. In addition to the small-sphere limit $|k_SR|\ll1$, we assume the effective sphere radius $\sqrt{\varepsilon_S\mu_S}R$ to be much smaller than the distance from the sphere to any of the environment bodies. As demonstrated in Refs. [36,37], multiple scattering between sphere and environment can then be safely neglected to within a leading order of k_SR, and a result of the type (22) can be generalized from the bulk case to an arbitrary environment by adding the scattering Green tensor and replacing $\varepsilon\mapsto\varepsilon_\odot$ and $\mu\mapsto\mu_\odot$. This can be formally proven by treating both the sphere and the environment bodies using a Born expansion of the Green tensor [45] and discarding those terms in the Born series that involve multiple scattering between atom and environment. We obtain

$$\begin{aligned}\mathbf{G}_S^{(1)}(\mathbf{r},\mathbf{r},\omega)=\mathbf{G}^{(1)}(\mathbf{r},\mathbf{r},\omega)+\frac{\varepsilon_\odot}{\varepsilon_0}\alpha_S^\star\frac{\omega^2}{c^2}&\mathbf{G}(\mathbf{r},\mathbf{r}_S,\omega)\\&\cdot\mathbf{G}(\mathbf{r}_S,\mathbf{r},\omega)-\frac{\mu_0}{\mu_\odot}\beta_S^\star\mathbf{G}(\mathbf{r},\mathbf{r}_S,\omega)\times\overleftarrow{\nabla}_S\\&\cdot\nabla_S\times\mathbf{G}(\mathbf{r}_S,\mathbf{r},\omega),\end{aligned} \tag{23}$$

where we have introduced the polarizability

$$\alpha_S^\star=4\pi\varepsilon_0R^3\frac{\varepsilon_S-\varepsilon_\odot}{\varepsilon_S+2\varepsilon_\odot} \tag{24}$$

and the magnetizability

$$\beta_S^\star=\frac{4\pi R^3}{\mu_0}\frac{\mu_S-\mu_\odot}{\mu_S+2\mu_\odot} \tag{25}$$

of the sphere [46]. Note that $\alpha_S^\star$ is an excess or effective polarizability [47,48] and describes the electric response of the sphere with respect to that of the surrounding medium. It can take positive or negative values, depending on whether the sphere's permittivity is larger or smaller than that of the medium.

The relation (23) for $\mathbf{G}_S^{(1)}$ can be used to calculate the electric CP potential (6). In order to find the magnetic CP potential, Eq. (7), we also require the analogous relation for the magnetic Green tensor $\nabla\times\mathbf{G}_S^{(1)}\times\overleftarrow{\nabla}'$, which can be obtained by duality arguments. An electric/magnetic duality transformation $[\cdot]^\circledast$ corresponds to a global exchange of electric and magnetic properties, $\varepsilon^\circledast=\mu$ and $\mu^\circledast=\varepsilon$. As shown in Refs. [49,50], this results in the following changes to the Green tensor

for $\mathbf{r} \neq \mathbf{r}'$:

$$\frac{\omega^2}{c^2}\mathbf{G}^{\circledast}(\mathbf{r},\mathbf{r}',\omega) = -\frac{\nabla\times\mathbf{G}(\mathbf{r},\mathbf{r}',\omega)\times\overleftarrow{\nabla}'}{\mu(\mathbf{r},\omega)\mu(\mathbf{r}',\omega)}, \tag{26}$$

$$\nabla\times\mathbf{G}^{\circledast}(\mathbf{r},\mathbf{r}',\omega)\times\overleftarrow{\nabla}' = -\varepsilon(\mathbf{r},\omega)\frac{\omega^2}{c^2}\mathbf{G}(\mathbf{r},\mathbf{r}',\omega)\varepsilon(\mathbf{r}',\omega), \tag{27}$$

$$\nabla\times\mathbf{G}^{\circledast}(\mathbf{r},\mathbf{r}',\omega) = -\varepsilon(\mathbf{r},\omega)\frac{\mathbf{G}(\mathbf{r},\mathbf{r}',\omega)\times\overleftarrow{\nabla}'}{\mu(\mathbf{r}',\omega)}, \tag{28}$$

$$\mathbf{G}^{\circledast}(\mathbf{r},\mathbf{r}',\omega)\times\overleftarrow{\nabla}' = -\frac{\nabla\times\mathbf{G}(\mathbf{r},\mathbf{r}',\omega)}{\mu(\mathbf{r},\omega)}\varepsilon(\mathbf{r}',\omega). \tag{29}$$

In addition, Eqs. (24) and (25) imply that $\alpha_S^{\star\circledast} = \beta_S^{\star}/c^2$ and $\beta_S^{\star\circledast} = c^2\alpha_S^{\star}$. By applying the duality transformation to both sides of Eq. (23), one obtains the required relation

$$\begin{aligned}\nabla\times\mathbf{G}_S^{(1)}(\mathbf{r},\mathbf{r}',\omega)\times\overleftarrow{\nabla}'|_{\mathbf{r}'=\mathbf{r}} &= \nabla\times\mathbf{G}^{(1)}(\mathbf{r},\mathbf{r}',\omega)\times\overleftarrow{\nabla}'|_{\mathbf{r}'=\mathbf{r}} - \frac{\mu_0}{\mu_\odot}\beta_S^{\star}\nabla\times\mathbf{G}(\mathbf{r},\mathbf{r}_S,\omega)\times\overleftarrow{\nabla}_S \\ &\cdot\nabla_S\times\mathbf{G}(\mathbf{r}_S,\mathbf{r}',\omega)\times\overleftarrow{\nabla}'|_{\mathbf{r}'=\mathbf{r}} + \frac{\varepsilon_\odot}{\varepsilon_0}\alpha_S^{\star}\frac{\omega^2}{c^2} \\ &\times\nabla\times\mathbf{G}(\mathbf{r},\mathbf{r}_S,\omega)\cdot\mathbf{G}(\mathbf{r}_S,\mathbf{r}',\omega)\times\overleftarrow{\nabla}'|_{\mathbf{r}'=\mathbf{r}}.\end{aligned} \tag{30}$$

2. *Sphere inside an Onsager cavity*

Next, we consider a homogeneous magnetodielectric sphere with radius R centered around $\mathbf{r}_S$, with permittivity $\varepsilon_S(\omega)$ and permeability $\mu_S(\omega)$, which is not in immediate contact with the surrounding medium but is placed inside a small spherical cavity of radius R_C, also centered around $\mathbf{r}_S$ [Fig. 1(v)]. This enables us to compare and interpolate between the homogeneous sphere placed inside a medium (as considered in the previous section) and a local-field-corrected atom (i.e., a pointlike polarizable system surrounded by a cavity). The scattering Green tensor $\mathbf{G}_{S+C}^{(1)}$ of the sphere-plus-cavity system in a homogeneous bulk medium is again given by an equation of the form (10), in which the reflection coefficients take a more complex form. In particular, in the limit of a small effective cavity and sphere sizes $|k_S R|, |kR_C| \ll 1$, one has [44]

$$B_1^M = \frac{2i}{3}\left(\sqrt{\varepsilon\mu}\frac{\omega}{c}\right)^3\left[R_C^3\frac{1-\mu}{1+2\mu} + \frac{9\mu R^3(\mu_S-1)/(2\mu+1)}{(\mu_S+2)(2\mu+1)+2(\mu_S-1)(1-\mu)R^3/R_C^3}\right], \tag{31}$$

$$B_1^N = \frac{2i}{3}\left(\sqrt{\varepsilon\mu}\frac{\omega}{c}\right)^3\left[R_C^3\frac{1-\varepsilon}{1+2\varepsilon} + \frac{9\varepsilon R^3(\varepsilon_S-1)/(2\varepsilon+1)}{(\varepsilon_S+2)(2\varepsilon+1)+2(\varepsilon_S-1)(1-\varepsilon)R^3/R_C^3}\right]. \tag{32}$$

We can then follow exactly the same steps as in Sec. II A 1. We again arrive at Eqs. (23) and (30) with $S+C$ in place of S. A comparison of Eqs. (14) and (15) with Eqs. (31) and (32) shows that the relevant excess polarizability and magnetizability of the sphere-plus-cavity system are given by

$$\alpha_{S+C}^{\star} = 4\pi\varepsilon_0\left[R_C^3\frac{1-\varepsilon_\odot}{1+2\varepsilon_\odot} + \frac{9\varepsilon_\odot R^3(\varepsilon_S-1)/(2\varepsilon_\odot+1)}{(\varepsilon_S+2)(2\varepsilon_\odot+1)+2(\varepsilon_S-1)(1-\varepsilon_\odot)R^3/R_C^3}\right] \tag{33}$$

and

$$\beta_{S+C}^{\star} = \frac{4\pi}{\mu_0}\left[R_C^3\frac{1-\mu_\odot}{1+2\mu_\odot} + \frac{9\mu_\odot R^3(\mu_S-1)/(2\mu_\odot+1)}{(\mu_S+2)(2\mu_\odot+1)+2(\mu_S-1)(1-\mu_\odot)R^3/R_C^3}\right]. \tag{34}$$

One can easily verify that for $R = R_C$, Eqs. (33) and (34) reduce to the results (24) and (25) for the full sphere, as expected.

By introducing the free-space polarizability and magnetizability of the sphere,

$$\alpha_S = 4\pi\varepsilon_0 R^3\frac{\varepsilon_S-1}{\varepsilon_S+2} \tag{35}$$

and

$$\beta_S = \frac{4\pi R^3}{\mu_0}\frac{\mu_S-1}{\mu_S+2}, \tag{36}$$

as well as the excess polarizability and magnetizability of the cavity,

$$\alpha_C^{\star} = 4\pi\varepsilon_0 R_C^3\frac{1-\varepsilon_\odot}{1+2\varepsilon_\odot} \tag{37}$$

and

$$\beta_C^{\star} = \frac{4\pi R_C^3}{\mu_0}\frac{1-\mu_\odot}{1+2\mu_\odot}, \tag{38}$$

we can write Eqs. (33) and (34) more transparently as

$$\alpha_{S+C}^{\star} = \alpha_C^{\star} + \frac{\alpha_S}{\varepsilon_\odot}\left(\frac{3\varepsilon_\odot}{2\varepsilon_\odot+1}\right)^2 \times\frac{1}{1+\alpha_C^{\star}\alpha_S/\left(8\pi^2\varepsilon_0^2R_C^6\right)}, \tag{39}$$

$$\beta_{S+C}^{\star} = \beta_C^{\star} + \beta_S\mu_\odot\left(\frac{3}{2\mu_\odot+1}\right)^2 \times\frac{1}{1+\beta_C^{\star}\beta_S\mu_0^2/\left(8\pi^2R_C^6\right)}. \tag{40}$$

As we see, the response of the sphere-plus-cavity system to an electromagnetic field is due to reflection at the cavity surface from the outside ($\alpha_C^{\star}$,$\beta_C^{\star}$) plus reflections at the sphere ($\alpha_S^{\star}$,$\beta_S^{\star}$), in which the local-field correction factors in large round brackets account for the transmission of the field into and out of the cavity and the denominators account for multiple reflections between the cavity and sphere surfaces.

Note that in our leading-order approximation in terms of the cavity and sphere radii, the reflective properties of the cavity and the sphere as encoded via their dipole polarizabilities and magnetizabilities are proportional to the third

power of these radii. In contrast, the transmission properties of the cavity as described by the local-field correction factors become independent of R_C within leading order of kR_C.

B. Casimir-Polder potential

Consider a polarizable and magnetizable ground-state atom that interacts with a small magnetodielectric sphere in an arbitrary environment. We assume the atom-sphere separation r_{AS} to be much greater than the effective sphere and cavity radii, $\sqrt{\varepsilon_S\mu_S}R$, $\sqrt{\varepsilon_\odot\mu_\odot}R_C \ll r_{AS}$. For the frequency integral in Eq. (6), typically limited to values $\xi \leqslant c/r_{AS}$, the assumptions $|k_S R|, |kR_C| \ll 1$ made in Sec. II A hold. Hence, we can use our results for the electric and magnetic Green tensors $\mathbf{G}_S^{(1)}$ and $\nabla\times\mathbf{G}_S^{(1)}\times\overleftarrow{\nabla}'$ in the presence of a small magnetodielectric sphere to calculate the atom-sphere potential.

1. Full sphere

By substituting Eq. (23) into Eq. (6), the interaction of an electric atom with a magnetodielectric sphere is described by the potential

$$U_e(\mathbf{r}_A,\mathbf{r}_S) = U_{ee}(\mathbf{r}_A,\mathbf{r}_S) + U_{em}(\mathbf{r}_A,\mathbf{r}_S), \tag{41}$$

with

$$U_{ee}(\mathbf{r}_A,\mathbf{r}_S) = -\frac{\hbar\mu_0^2}{2\pi}\int_0^\infty \mathrm{d}\xi\ \xi^4\alpha_A(i\xi)\left[\frac{3\varepsilon_A(i\xi)}{2\varepsilon_A(i\xi)+1}\right]^2 \times \alpha_S(i\xi)\varepsilon_\odot(i\xi)\mathrm{Tr}[\mathbf{G}(\mathbf{r}_A,\mathbf{r}_S,i\xi)\cdot\mathbf{G}(\mathbf{r}_S,\mathbf{r}_A,i\xi)] \tag{42}$$

and

$$U_{em}(\mathbf{r}_A,\mathbf{r}_S) = -\frac{\hbar\mu_0^2}{2\pi}\int_0^\infty \mathrm{d}\xi\ \xi^2\alpha_A(i\xi)\left[\frac{3\varepsilon_A(i\xi)}{2\varepsilon_A(i\xi)+1}\right]^2 \times \frac{\beta_S(i\xi)}{\mu_\odot(i\xi)}\mathrm{Tr}[\mathbf{G}(\mathbf{r}_A,\mathbf{r}_S,i\xi)\times\overleftarrow{\nabla}_S\cdot\nabla_S \times \mathbf{G}(\mathbf{r}_S,\mathbf{r}_A,i\xi)] \tag{43}$$

being associated with the electric and magnetic properties of the sphere, respectively. Similarly, combining Eqs. (30) and (7) gives the CP interaction of a magnetic atom and a magnetodielectric sphere,

$$U_m(\mathbf{r}_A,\mathbf{r}_S) = U_{me}(\mathbf{r}_A,\mathbf{r}_S) + U_{mm}(\mathbf{r}_A,\mathbf{r}_S), \tag{44}$$

with

$$U_{me}(\mathbf{r}_A,\mathbf{r}_S) = -\frac{\hbar\mu_0^2}{2\pi}\int_0^\infty \mathrm{d}\xi\ \xi^2\beta_A(i\xi)\left[\frac{3}{2\mu_A(i\xi)+1}\right]^2 \times \alpha_S(i\xi)\varepsilon_\odot(i\xi)\mathrm{Tr}\{[\nabla_A\times\mathbf{G}(\mathbf{r}_A,\mathbf{r}_S,i\xi)] \cdot[\mathbf{G}(\mathbf{r}_S,\mathbf{r}_A,i\xi)\times\overleftarrow{\nabla}_A]\} \tag{45}$$

and

$$U_{mm}(\mathbf{r}_A,\mathbf{r}_S) = -\frac{\hbar\mu_0^2}{2\pi}\int_0^\infty \mathrm{d}\xi\beta_A(i\xi)\left[\frac{3}{2\mu_A(i\xi)+1}\right]^2 \times \frac{\beta_S(i\xi)}{\mu_\odot(i\xi)}\mathrm{Tr}\{[\nabla_A\times\mathbf{G}(\mathbf{r}_A,\mathbf{r}_S,i\xi)\times\overleftarrow{\nabla}_S] \cdot[\nabla_S\times\mathbf{G}(\mathbf{r}_S,\mathbf{r}_A,i\xi)\times\overleftarrow{\nabla}_A]\}. \tag{46}$$

Note that the electric and magnetic properties of the sphere completely decouple and give rise to the separate potentials U_{ee}, U_{me} and U_{em}, U_{mm}, respectively. However, this is only true in the small-sphere limit considered here.

As proven in Refs. [49,50], the local-field-corrected total CP potential of a magnetodielectric ground-state atom in the presence of an arbitrary arrangement of bodies as given by Eqs. (6) and (7) is always duality invariant. By using the transformation rules (26)–(29) for the Green tensor, together with $\alpha^{\star\circledast}=\beta^\star/c^2$, $\beta^{\star\circledast}=c^2\alpha^\star$, one sees that duality invariance also holds for the special case of a sphere, where $U_{ee}(\mathbf{r}_A,\mathbf{r}_S)^\circledast = U_{mm}(\mathbf{r}_A,\mathbf{r}_S)$ and $U_{em}(\mathbf{r}_A,\mathbf{r}_S)^\circledast = U_{me}(\mathbf{r}_A,\mathbf{r}_S)$. This property is ensured by the presence of the factors $\varepsilon_\odot$ and $1/\mu_\odot$ in Eqs. (42), (43), (45), and (46).

It is instructive to compare our findings with the vdW interaction between two magnetodielectric ground-state atoms A and B in the presence of an arbitrary magnetodielectric environment [37,42]. In order to reproduce those results, one has to perform the substitutions

$$\alpha_S\varepsilon_\odot \to \alpha_B\left(\frac{3\varepsilon_B}{2\varepsilon_B+1}\right)^2 \tag{47}$$

and

$$\frac{\beta_S}{\mu_\odot} \to \beta_B\left(\frac{3}{2\mu_B+1}\right)^2. \tag{48}$$

The differences between the cases of a sphere [left-hand sides of Eqs. (47) and (48)] and an atom [right-hand sides] are due to the microscopic and macroscopic nature of the two objects. The sphere consists of a large number of atoms whose magnetoelectric response can be described by an average permittivity and permeability. In this macroscopic picture, the sphere is in immediate contact with the surrounding medium (also characterized by permittivity and permeability), which leads to the factors $\varepsilon_\odot$ and $1/\mu_\odot$. In contrast, an atom is a microscopic object. In the microscopic picture, the interspace between the atom and the neighboring medium atoms needs to be taken into account; it gives rise to the local-field correction factors on the right-hand sides of Eqs. (47) and (48).

The second difference between the two cases is in the different explicit forms of polarizability and magnetizability. For a sphere, they are given in terms of the permeability and permittivity of the sphere in comparison to those of the surrounding medium [cf. Eqs. (24) and (25)]; they can be either positive or negative. For an atom, polarizability and magnetizability depend on the transition frequencies and dipole matrix elements [recall Eqs. (4) and (5)]; they are strictly positive on the positive imaginary frequency axis.

2. Sphere inside an Onsager cavity

In order to interpolate between the two extreme cases of a single atom and a sphere consisting of a very large number of atoms, we now consider the CP interaction of an atom with a sphere of radius R that is separated from the surrounding medium by a spherical free-space cavity of radius R_C, as introduced in Sec. II A2. Since expressions of the type (23) and (30) remain valid, their substitution into Eqs. (6) and (7) again leads to Eqs. (41)–(46), where now $\alpha^\star_{S+C}$ and $\beta^\star_{S+C}$ as given by Eqs. (33) and (34) appear in place of $\alpha^\star_S$ and $\beta^\star_S$.

In our model, the sphere may consist of an arbitrary number of atoms, whereas the cavity implements the interspace between the sphere's atoms and the surrounding medium atoms. As seen from Eqs. (39) and (40) for the polarizability and magnetizability of the sphere-plus-cavity system, the sphere is represented by its free-space polarizability and magnetizability, whereas the interspace gives rise to the cavity excess polarizability and magnetizability. In the purely electric case, the sphere gives rise to attractive forces and the cavity leads to a reduction of these forces.

For a sphere that consists of a very large number of atoms, the interspace between the sphere and medium atoms becomes irrelevant. In this case, which is implemented by the limit $R \to R_C$, the system's polarizability and magnetizability become equal to the excess polarizability and magnetizability of a full sphere (recall Sec. II A2), for which we recover Eqs. (41)–(46) in their original form.

In the opposite extreme case of a sphere that consists of very few atoms, the interspace becomes very large in comparison to the sphere, $R \ll R_C$. In this limit, the effect of multiple scattering between the surfaces of sphere and cavity becomes negligible, and the polarizability (39) and magnetizability (40) reduce to

$$\alpha^{\star}_{S+C} = \alpha^{\star}_{C} + \frac{\alpha_S}{\varepsilon_\odot}\left(\frac{3\varepsilon_\odot}{2\varepsilon_\odot+1}\right)^2 \tag{49}$$

and

$$\beta^{\star}_{S+C} = \beta^{\star}_{C} + \beta_S\mu_\odot\left(\frac{3}{2\mu_\odot+1}\right)^2. \tag{50}$$

When the sphere consists of only a single atom B, the Clausius-Mossotti laws [51]

$$\frac{\varepsilon_S-1}{\varepsilon_S+2} = \frac{\alpha_B}{3\varepsilon_0 V}, \qquad \frac{\mu_S-1}{\mu_S+2} = \frac{\mu_0\beta_B}{3V}, \tag{51}$$

where $V = (4\pi/3)R^3$, together with Eqs. (35) and (36), show that $\alpha_S = \alpha_B$ and $\beta_S = \beta_B$. When neglecting the backscattering from the outside surface of the cavity, we obtain

$$\alpha_{S+C}\varepsilon_\odot = \alpha_B\left(\frac{3\varepsilon_B}{2\varepsilon_B+1}\right)^2 \tag{52}$$

and

$$\frac{\beta_{S+C}}{\mu_\odot} = \beta_B\left(\frac{3}{2\mu_B+1}\right)^2, \tag{53}$$

where $\varepsilon_\odot = \varepsilon_B, \mu_\odot = \mu_B$, and substitution into Eqs. (41)–(46) leads to the local-field-corrected two-atom potentials [37,42]. It is in this limit $R \ll R_C, \sqrt{\varepsilon_\odot\mu_\odot}R_C \ll r_{AS}$ that the potential depends on the cavity radius only via its transmission properties and therefore becomes independent of R_C. Recall the discussion following Eq. (40).

For intermediate radii R, our sphere-plus-cavity model gives a good description of the interaction of a single atom with molecules or intermediate-size spherical clusters of atoms. Note that in this case the potential explicitly depends on both the sphere and cavity radii. The theory could be applied (e.g., in cell biology) to study the vdW-force-induced transfer of an atom or a very small molecule from one cell into another, where it is attracted to another bigger (spherical) cell component or molecule. Note that local-field effects are automatically included.

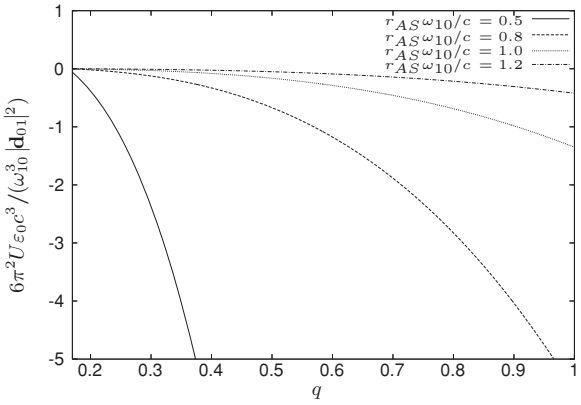

FIG. 3. CP potential $U(r_{AS})$ of a nonmagnetic atom in front of a dielectric sphere in an empty cavity embedded in bulk material vs. $q = R/R_C$ for different atom-sphere separations, $r_{AS}\omega_{10}/c$. Other parameters are $\omega_T/\omega_{10} = 1.03$, $\omega_{TS}/\omega_{10} = 1.0$, $\omega_{PS}/\omega_{10} = 6.0$, $\omega_P/\omega_{10} = 0.1$, and $\gamma_{(S)}/\omega_{10} = 0.001$.

As an example, let us consider the CP interaction of a nonmagnetic atom with a purely electric sphere (U_{ee}) in a bulk medium ($\varepsilon_\odot = \varepsilon_A = \varepsilon$). By substituting the required Green tensor (19) into Eq. (42), one easily finds

$$U(\mathbf{r}_A,\mathbf{r}_S) = -\frac{\hbar}{16\pi^3\varepsilon_0^2 r_{AS}^6}\int_0^\infty \mathrm{d}\xi\left[\frac{3\varepsilon(i\xi)}{2\varepsilon(i\xi)+1}\right]^2 \times \alpha_A(i\xi)\varepsilon(i\xi)\alpha^{\star}_{S+C}(i\xi)g[\sqrt{\varepsilon(i\xi)}\xi r_{AS}/c] \tag{54}$$

($r_{AS} = |\mathbf{r}_A - \mathbf{r}_S|$) with

$$g(x) = e^{-2x}(3+6x+5x^2+2x^3+x^4). \tag{55}$$

Figure 3 shows this potential for a two-level atom as a function of the relative sphere radius $q = R/R_C$ for various atom-sphere separations. We have used single-resonance models for the permittivities of the sphere and the medium:

$$\varepsilon_{(S)}(\omega) = 1 + \frac{\omega_{P(S)}^2}{\omega_{T(S)}^2 - \omega^2 - i\omega\gamma_{(S)}}. \tag{56}$$

In Fig. 4, we show the potential U_{ee} as a function of the atom-sphere separation for different relative sphere radii $q = R/R_C$. Both figures show that for the constant ε_S considered here, larger spheres with their corresponding larger polarizabilities lead to stronger vdW attraction between the atom and the sphere.

III. SUMMARY AND CONCLUSIONS

We have studied the CP interaction of an atom with a small magnetodielectric sphere in an arbitrary magnetoelectric environment. By employing a point-scattering technique, we were able to express the Green tensor in the presence of the sphere as a simple function of the Green tensor of the environment. Using this result, we have found closed general expressions for the CP potential of a magnetoelectric atom interacting with a small magnetodielectric sphere, which depend on the sphere's polarizability and magnetizability.

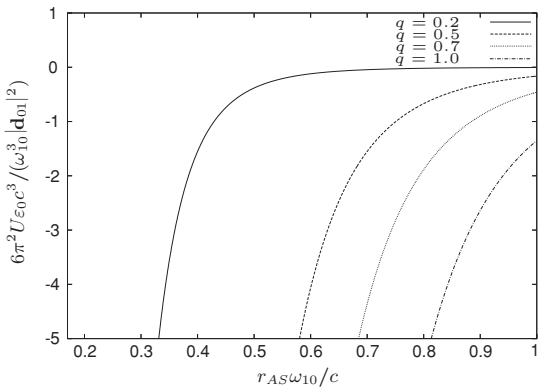

FIG. 4. $U(r_{AS})$ vs. $r_{AS}\omega_{10}/c$ for different ratios q. Other parameters are the same as in Fig. 3.

A comparison with the vdW potential between two ground-state atoms in the presence of the background medium has revealed how the different macroscopic and microscopic natures of atom versus sphere manifest themselves in the dispersion potentials: the immediate contact of a macroscopic sphere with the surrounding medium leads to the appearance of the permittivity and inverse permeability of the medium, whereas the coupling of the local electromagnetic field to the microscopic atom gives rise to local-field correction factors.

In order to interpolate between these two limiting cases, we have studied the potential of an atom with a sphere of variable radius located inside an Onsager cavity. The cavity represents the interspace between the particles contained in the sphere and those constituting the surrounding medium, so that our model can be used to study molecular systems of arbitrary size. Using similar techniques, we have derived the potential of an atom interacting with the sphere-plus-cavity system. We have shown that our result reduces to the atom-sphere or atom-atom potentials in the two limiting cases, in which the sphere radius is either much smaller than or equal to the cavity radius. As an example, we have considered the CP interaction between an electric atom and such a sphere-plus-cavity system, finding that the attractive potential diminishes as the sphere becomes smaller at a fixed cavity radius.

Our point-scattering method can also be used to calculate the Casimir force on a small sphere in an arbitrary environment and, in particular, the Casimir force between two small spheres. This problem will be subject of future work. A similar approach could be applied to dispersion interactions involving thin cylinders.

ACKNOWLEDGMENTS

This work was supported by the UK Engineering and Physical Sciences Research Council and the European Science Foundation Research Network CASIMIR. SYB is grateful for support by the Alexander von Humboldt Foundation.

[1] H. Margenau and N. R. Kestner, *Theory of Intermolecular Forces* (Pergamon Press, Oxford, 1969).
[2] J. Mahanty and B. W. Ninham, *Dispersion Forces* (Academic Press, London, 1976).
[3] G. Feinberg, J. Sucher, and C. K. Au, Phys. Rep. **180**, 83 (1989).
[4] P. W. Milonni, *The Quantum Vacuum* (Academic Press, New York, 1994).
[5] G. Compagno, R. Passante, and F. Persico, *Atom-Field Interactions and Dressed Atoms* (Cambridge University Press, Cambridge, 1995).
[6] V. A. Parsegian, *Van der Waals Forces: A Handbook for Biologists, Chemists, Engineers, and Physicists* (Cambridge University Press, New York, 2005).
[7] S. Y. Buhmann and D.-G. Welsch, Prog. Quantum Electron. **31**, 51 (2007).
[8] A. Salam, Int. Rev. Phys. Chem. **27**, 405 (2008).
[9] S. Scheel and S. Y. Buhmann, Acta Phys. Slovaka **58**, 675 (2008).
[10] M. B. Bordag, G. L. Klimchitskaya, U. Mohideen, and V. M. Mostepanenko, *Advances in the Casimir Effect* (Oxford University Press, Oxford, 2009).
[11] J. D. van der Waals, Ph.D. thesis, Universiteit Leiden, Leiden, 1873.
[12] F. London, Z. Phys. **63**, 245 (1930).
[13] H. B. G. Casimir and D. Polder, Phys. Rev. **73**, 360 (1948).
[14] A. Lambrecht, Phys. World **15**, 29 (2002).
[15] S. M. Gatica, M. W. Cole, and D. Velegol, Nano Lett. **5**, 169 (2005).
[16] H.-Y. Kim, J. O. Sofo, D. Velegol, M. W. Cole, and A. A. Lucas, Langmuir **23**, 1735 (2007).
[17] D. N. Thomas, S. J. Judd, and N. Fawcett, Water Res. **33**, 1579 (1999).
[18] J. W. Liu and E. Luijten, Phys. Rev. Lett. **93**, 247802 (2004).
[19] A. W. Rodriguez, J. N. Munday, J. D. Joannopoulos, F. Capasso, D. A. R. Dalvit, and S. G. Johnson, Phys. Rev. Lett. **101**, 190404 (2008).
[20] C. Hertlein, L. Helden, A. Gambassi, S. Dietrich, and C. Bechinger, Nature **451**, 172 (2008).
[21] J. Gregory, Water Sci. Technol. **27**, 1 (1993).
[22] Y. Liang, N. Hilal, P. Langston, and V. Starov, Adv. Colloid Interface Sci. **134–135**, 151 (2007).
[23] M. Fuchs and K. Schweizer, J. Phys. C: Condens. Matter. **14**, R239 (2002).
[24] V. A. Parsegian, A. Rev. Biophys. Bioeng. **2**, 221 (1973).
[25] J. N. Israelachvili, *Intermolecular and Surface Forces* (Academic Press, New York, 1991).
[26] M. V. Volkenstein, *Molecular Biophysics* (Academic Press, New York, 1977).
[27] J. N. Israelachvili, Q. Rev. Biophys. **6**, 341 (1974).
[28] S. Nir, Prog. Surf. Sci. **8**, 1 (1977).
[29] L. W. Bruch, Phys. Rev. B **72**, 033410 (2005).
[30] F. London, Trans. Faraday Soc. **33**, 8 (1937).
[31] H.-Y. Kim, J. O. Sofo, D. Velegol, M. W. Cole, and G. Mukhopadhyay, Phys. Rev. A **72**, 053201 (2005).
[32] H. Hamaker, Physica **4**, 1058 (1937).

[33] E. M. Lifshitz, Sov. Phys.—JETP **2** (1956).
[34] I. Dzyaloshinskii, E. M. Lifshitz, and L. Pitaevskii, Adv. Phys. **10**, 165 (1961).
[35] L. Onsager, J. Am. Chem. Soc. **58**, 1486 (1936).
[36] Ho Trung Dung, S. Y. Buhmann, and D.-G. Welsch, Phys. Rev. A **74**, 023803 (2006).
[37] A. Sambale, S. Y. Buhmann, D.-G. Welsch, and M. S. Tomaš, Phys. Rev. A **75**, 042109 (2007).
[38] R. Messina, D. A. R. Dalvit, P. A. M. Neto, A. Lambrecht, and S. Reynaud, Phys. Rev. A **80**, 022119 (2009).
[39] S. Y. Buhmann, Ho Trung Dung, and D.-G. Welsch, J. Opt. B: Quantum Semiclass. Opt. **6**, S127 (2004); J. Phys. B **39**, 3145(E) (2006).
[40] M. M. Taddei, T. N. C. Mendes, and C. Farina, e-print arXiv:0903.2091 (2009).
[41] M. Boustimi, J. Baudon, J. Robert, A. Semlali, and B. Labani, Phys. Rev. B **62**, 7593 (2000).
[42] H. Safari, D.-G. Welsch, S. Y. Buhmann, and S. Scheel, Phys. Rev. A **78**, 062901 (2008).
[43] L.-W. Li, P.-S. Kooi, M.-S. Leong, and T.-S. Yeo, IEEE Trans. Microwave Theory Tech. **42**, 2302 (1994).
[44] W. C. Chew, *Waves and Fields in Inhomogeneous Media* (IEEE Press, New York, 1995).
[45] S. Y. Buhmann and D.-G. Welsch, Appl. Phys. B **82**, 189 (2006).
[46] M. Xu and M. J. Dignam, J. Chem. Phys. **96**, 3370 (1992).
[47] L. D. Landau and E. M. Lifshitz, *Electrodynamics of Continuous Media*, 2nd ed. (Pergamon Press, Oxford, 1984), Vol. 8.
[48] A. D. McLachlan, Discuss. Faraday Soc. **40**, 239 (1965).
[49] S. Y. Buhmann and S. Scheel, Phys. Rev. Lett. **102**, 140404 (2009).
[50] S. Y. Buhmann and S. Scheel, Int. J. Mod. Phys. A **24**, 1796 (2009).
[51] J. D. Jackson, *Classical Electrodynamics*, 3rd ed. (Wiley, New York, 1998).

PHYSICAL REVIEW A **97**, 032507 (2018)

Lateral Casimir-Polder forces by breaking time-reversal symmetry

Ricardo R. Q. P. T. Oude Weernink
Theoretisch-Physikalisches Institut, Friedrich-Schiller-Universität Jena, Fröbelstieg 1, Jena 07743, Germany

Pablo Barcellona*
Physikalisches Institut, Albert-Ludwigs-Universität Freiburg, Hermann-Herder-Strasse 3, Freiburg 79104, Germany

Stefan Yoshi Buhmann†
Physikalisches Institut, Albert-Ludwigs-Universität Freiburg, Hermann-Herder-Strasse 3, Freiburg 79104, Germany
and Freiburg Institute for Advanced Studies, Albert-Ludwigs-Universität Freiburg, Albertstrasse 19, Freiburg 79104, Germany

(Received 12 December 2017; published 13 March 2018)

We examine the lateral Casimir-Polder force acting on a circular rotating emitter near a dielectric plane surface. As the circular motion breaks time-reversal symmetry, the spontaneous emission in a direction parallel to the surface is in general anisotropic. We show that a lateral force arises which can be interpreted as a recoil force because of this asymmetric emission. The force is an oscillating function of the distance between the emitter and the surface, and the lossy character of the dielectric strongly influences the results in the near-field regime. The force exhibits also a population-induced dynamics, decaying exponentially with respect to time on time scales of the inverse of the spontaneous decay rate. We propose that this effect could be detected measuring the velocity acquired by the emitter, following different cycles of excitation and spontaneous decay. Our results are expressed in terms of the Green's tensor and can therefore easily be applied to more complex geometries.

DOI: 10.1103/PhysRevA.97.032507

I. INTRODUCTION

Casimir-Polder (CP) forces are forces between atoms and magnetodielectric bodies originating from the quantum fluctuations of the electromagnetic field and the atomic charges [1,2]. Despite their generally low magnitude they have to be taken into account when working on nanoscales which today is common in experiments as well as applications [3].

Lateral Casimir forces are a relatively young topic, having been measured in 2002 [4]. They are characterized by their direction which is parallel to the surface instead of the usual normal direction, and have been suggested to facilitate contactless force transmissions [5]. Lateral forces are typically achieved by breaking the translational symmetry of the surface, using for example periodically structured surfaces [4,6–9] or corrugated surfaces [10–13]. A lateral force has also been realized by breaking the mirror symmetry, using chiral particles near a surface [14,15]. It is discriminatory since it pushes chiral particles with opposite handedness in opposite directions.

In this article we show that a lateral force can arise by breaking time-reversal symmetry via a rotating dipole which emits asymmetrically. A dipole moment is created with left-handed or right-handed circularly polarized light with spin parallel to the surface. More specifically we excite a cesium atom from the hyperfine ground state $|6^2\,S_{1/2}, F = 4, M_F = 4\rangle$ to the excited state $|6^2\,P_{3/2}, F' = 5, M'_F = 5\rangle$ using a resonant right-handed circularly polarized laser beam that propagates along the y direction, creating a dipole moment rotating in the x-z plane, where $\hat{z}$ is the direction normal to the surface. The excitation of guided and radiation modes that propagate in the $+x$ and $-x$ directions may be expected to be asymmetric in this case [16,17]. The asymmetric emission of guided modes has been extensively investigated in the literature and relies on spin-orbit coupling of light mediated by a particle near a surface [18–25]. The conservation of total momentum in the system in conjunction with the asymmetric emission suggests the existence of a lateral force opposite to the direction of stronger emission. This lateral force could be measured observing the asymmetric emission distribution. A similar effect has been studied for the same atomic system close to an optical nanofiber [16]. It is the circular polarization of the illuminating light that creates a rotating dipole moment which breaks time-reversal symmetry. Using linearly polarized light, the time-reversal symmetry is conserved and the force is purely normal to the surface.

Note that this system has been analyzed previously by classical methods, studying the interaction of the rotating dipole with the reflected field [26]. However, the excited atom will unavoidably decay to the ground state, for which the lateral force is forbidden by energy conservation. Hence the lateral force has a population-induced dynamics which can be captured only by quantum approaches to the atom-field coupling. It is the aim of this article to investigate this effect.

The problem can be solved by expanding the electric field into guided and radiation modes. However here we use a different approach which relies on the Green's tensor and permits us to study geometries different from the planar configuration as well the impact of dissipation [27,28]. Light

*pablo.barcellona@physik.uni-freiburg.de
†stefan.buhmann@physik.uni-freiburg.de

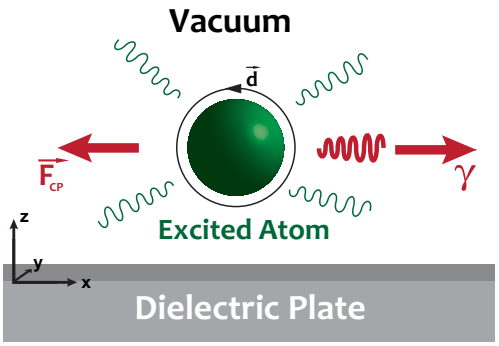

FIG. 1. Sketch of the system, expected lateral force and correlated asymmetric decay due to rotational dielectric moment.

modes confined inside the material are called guided modes. An incident wave hits the interface in such way there is total internal reflection and we have an evanescent wave behind the interface: it decays exponentially in the normal direction and hence propagates along the interface (evanescent waves have purely imaginary transverse wave vectors). By contrast radiation modes propagate also outside the material.

The article is organized as follows. In Sec. II we study the asymmetric emission of a multilevel circular emitter near a surface and investigate how the lateral force arises from this asymmetric emission. We also develop a dynamical approach to the atom-field coupling which gives the same expression for the lateral force. In Sec. III we consider a two-level cesium atom near a surface to quantify the order of magnitude of the force and compare it with previous findings.

II. LATERAL FORCE FROM THE ASYMMETRIC EMISSION

We consider a multilevel atom, with atomic frequencies $\omega_{nk} = (E_n - E_k)/\hbar$, and dipole moments $\boldsymbol{d}_{nk}$, near a homogeneous and isotropic dielectric plate (see Fig. 1). The atom is prepared in an incoherent superposition of energy eigenstates $|n\rangle$ with occupation $p_n(t)$ and is placed at position $\mathbf{r}_A = z_A\hat{\mathbf{z}}$ from the dielectric plate. We assume the atomic eigenstate $|n\rangle$ to exhibit a well-defined y component of angular momentum. It is then a circular emitter whose transitions matrix elements are not real, in general, but obey $\boldsymbol{d}_{kn} = \boldsymbol{d}^*_{nk}$ [27].

We first derive the lateral force using a dynamical approach to the atom-field coupling. According to the dynamical approach the Casimir-Polder force between the atom and the surface reads [28,29]

$$\mathbf{F}(\mathbf{r}_A,t) = \frac{\mu_0}{\pi}\lim_{\varepsilon\to 0^+}\sum_n p_n(t)\sum_k \int_0^\infty d\omega\omega^2 \frac{1}{\omega-\omega_{nk}-i\varepsilon} \times \nabla \boldsymbol{d}_{nk}\cdot \mathrm{Im}\mathbf{G}(\mathbf{r},\mathbf{r}_A,\omega)\cdot \boldsymbol{d}_{kn}|_{\mathbf{r}=\mathbf{r}_A} + \text{c.c.} \quad (1)$$

This integral can be rotated to the imaginary axis leading to the following nonresonant and resonant contributions:

$$\mathbf{F}^{\mathrm{nr}}(\mathbf{r}_A,t) = \frac{\mu_0}{\pi}\sum_n p_n(t)\sum_k \int_0^\infty d\xi\xi^2\left(\frac{1}{\omega_{nk}-i\xi}+\frac{1}{\omega_{nk}+i\xi}\right) \times \mathrm{Re}\{\nabla \boldsymbol{d}_{nk}\cdot \mathbf{G}(\mathbf{r},\mathbf{r}_A,i\xi)\cdot \boldsymbol{d}_{kn}\}|_{\mathbf{r}=\mathbf{r}_A}, \quad (2)$$

$$\mathbf{F}^{\mathrm{r}}(\mathbf{r}_A,t) = 2\mu_0\sum_n p_n(t)\sum_{k<n}\omega_{nk}^2 \times \mathrm{Re}\{\nabla \boldsymbol{d}_{nk}\cdot \mathbf{G}(\mathbf{r},\mathbf{r}_A,\omega_{nk})\cdot \boldsymbol{d}_{kn}\}|_{\mathbf{r}=\mathbf{r}_A}. \quad (3)$$

We first note that the lateral component of the nonresonant contribution vanishes, since $\partial_x\mathbf{G}^{(1)}(\mathbf{r},\mathbf{r}_A,i\xi)|_{\mathbf{r}=\mathbf{r}_A}$ is an antisymmetric tensor and $\mathbf{G}^{(1)}(\mathbf{r},\mathbf{r}_A,i\xi)$ is real. In fact the nonresonant term survives also for ground-state atoms, where the existence of a lateral force is forbidden by energy conservation: if it existed, one could accelerate the atom along the surface, leaving the atom and the field in the stationary ground states. A lateral force can arise only from the resonant contribution, which describes the atom recoil because of the asymmetric emission of the photon as we will show later.

Most importantly the force shows a population induced dynamics. For example if the atom is a two-level system initially excited in the state $|1\rangle$ the populations of the ground state and excited state satisfy the rate equations

$$\dot{p}_0 = \Gamma\, p_1, \quad \dot{p}_1 = -\Gamma\, p_1, \quad (4)$$

where Γ is the spontaneous decay rate for the transition $|1\rangle \to |0\rangle$($|0\rangle$ represents the ground state). The solutions, subject to the initial conditions $p_0(0) = 0$ and $p_1(0) = 1$, are

$$p_0(t) = 1 - e^{-\Gamma t}, \quad p_1(t) = e^{-\Gamma t}. \quad (5)$$

The lateral force for this two-level system hence reads

$$F_x(\mathbf{r}_A,t) = e^{-\Gamma t}2\mu_0\omega_{10}^2\mathrm{Re}\{\boldsymbol{d}_{10}\cdot\partial_x\mathbf{G}^{(1)}(\mathbf{r},\mathbf{r}_A,\omega_{10})\cdot\boldsymbol{d}_{01}\}|_{\mathbf{r}=\mathbf{r}_A}, \quad (6)$$

and decays exponentially with respect to time. Because of this force the particle will acquire some velocity in the lateral direction. Supposing that the initial velocity is zero, the mean velocity acquired reads

$$v = \int_0^\infty dt\frac{F_x(\mathbf{r}_A,t)}{m} = \frac{F_x(\mathbf{r}_A,0)}{m\Gamma}. \quad (7)$$

We next investigate the asymmetric emission of the circular emitter and how the lateral force arises from this asymmetry. The total emission rate Γ is the sum of the free-space emission rate $\Gamma^{(0)}$ and the surface-assisted emission rate $\Gamma^{(1)}$ where the photon is reflected by the dielectric surface. If the atom is prepared in the eigenstate $|n\rangle$ it will decay to lower lying energy levels, and the decay rate can be expressed in terms of the scattering Green's tensor $\mathbf{G}^{(1)}$ [28–30]:

$$\Gamma_n^{(1)}(z_A) = \frac{2\mu_0}{\hbar}\sum_{k<n}\omega_{nk}^2\mathrm{Im}\{\boldsymbol{d}_{nk}\cdot\mathbf{G}^{(1)}(\mathbf{r}_A,\mathbf{r}_A,\omega_{nk})\cdot\boldsymbol{d}_{kn}\}, \quad (8)$$

where we have used the property $\boldsymbol{d}_{nk}\cdot\mathrm{Im}\mathbf{G}(\mathbf{r},\mathbf{r},\omega)\cdot\boldsymbol{d}_{kn} = \mathrm{Im}\{\mathrm{d}_{nk}\cdot\mathbf{G}(\mathbf{r},\mathbf{r},\omega)\cdot\boldsymbol{d}_{kn}\}$.

The scattering Green's tensor for a dielectric reads ($z > 0, z' > 0$) [27,28]

$$\mathbf{G}^{(1)}(\mathbf{r},\mathbf{r}',\omega) = \int_0^{2\pi}d\varphi\int_0^\infty dk^\parallel k^\parallel\mathbf{G}^{(1)}(\mathbf{r},\mathbf{r}',\omega,\mathbf{k}^\parallel),$$

$$\mathbf{G}^{(1)}(\mathbf{r},\mathbf{r}',\omega,\mathbf{k}^\parallel) = \frac{i}{8\pi^2}\frac{1}{k^\perp}e^{i\mathbf{k}^\parallel\cdot(\mathbf{r}-\mathbf{r}')}e^{ik^\perp(z+z')} \times \sum_{\sigma=s,p} r_\sigma \mathbf{e}_{\sigma_+}\otimes\mathbf{e}_{\sigma_-}, \quad (9)$$

where $\mathbf{k}^{\parallel} = k^{\parallel}(\cos\varphi, \sin\varphi, 0)$ is wave vector parallel to the surface and $k^{\perp} = \sqrt{\omega^2/c^2 - k^{\parallel 2}}, k_m^{\perp} = \sqrt{\varepsilon(\omega)\omega^2/c^2 - k^{\parallel 2}}$ are the perpendicular components of the wave vector in vacuum and in the dielectric plate. The polarization vectors and Fresnel reflection coefficients for s-polarized and p-polarized waves read

$$\mathbf{e}_{s\pm} = (\sin\varphi, -\cos\varphi, 0), \tag{10}$$

$$\mathbf{e}_{p\pm} = \frac{c}{\omega}(\mp k^{\perp}\cos\varphi, \mp k^{\perp}\sin\varphi, k^{\parallel}), \tag{11}$$

$$r_s = \frac{k^{\perp} - k_m^{\perp}}{k^{\perp} + k_m^{\perp}}, \tag{12}$$

$$r_p = \frac{\varepsilon(\omega)k^{\perp} - k_m^{\perp}}{\varepsilon(\omega)k^{\perp} + k_m^{\perp}}. \tag{13}$$

Using Eq. (9) the assisted rate reads

$$\Gamma_n^{(1)}(z_{\mathrm{A}}) = \int_0^{2\pi} d\varphi \int_0^{\infty} dk^{\parallel} k^{\parallel} \gamma_n(z_{\mathrm{A}}, \mathbf{k}^{\parallel}), \tag{14}$$

where $\gamma_n(z_{\mathrm{A}}, \mathbf{k}^{\parallel})$ is the emission rate density:

$$\gamma_n(z_{\mathrm{A}}, \mathbf{k}^{\parallel}) = \frac{2\mu_0}{\hbar} \sum_{k<n} \omega_{nk}^2 \mathrm{Im}\{\boldsymbol{d}_{nk} \cdot \mathbf{G}^{(1)}(\mathbf{r}_{\mathrm{A}}, \mathbf{r}_{\mathrm{A}}, \omega_{nk}, \mathbf{k}^{\parallel}) \cdot \boldsymbol{d}_{kn}\}. \tag{15}$$

A lateral force may result from an unbalanced spontaneous emission into the $+x$ and $-x$ directions. According to the conservation of the total momentum the force is opposite to the momentum of the emitted photon. If the atom is prepared in an incoherent superposition of energy eigenstates $|n\rangle$ with population p_n the force reads

$$\begin{aligned} F_x(z_{\mathrm{A}}, t) &= -\int_0^{2\pi} d\varphi \int_0^{\infty} dk^{\parallel} k^{\parallel} \hbar k_x \sum_n p_n \gamma_n(z_{\mathrm{A}}, \mathbf{k}^{\parallel}) \\ &= 2\mu_0 \sum_n p_n(t) \sum_{k<n} \omega_{nk}^2 \\ &\quad \times \mathrm{Re}\{\boldsymbol{d}_{nk} \cdot \partial_x \mathbf{G}^{(1)}(\mathbf{r}, \mathbf{r}_{\mathrm{A}}, \omega_{nk}) \cdot \boldsymbol{d}_{kn}\}|_{\mathbf{r}=\mathbf{r}_{\mathrm{A}}}, \end{aligned} \tag{16}$$

where we have used the relation $\mathrm{Im}(ix) = \mathrm{Re}x$. The lateral force is associated with the recoil of the atom because of asymmetric emission. It vanishes if the atom is in the ground state or if the atomic dipole moments are real since $\partial_x \mathbf{G}^{(1)}(\mathbf{r}, \mathbf{r}_{\mathrm{A}}, \omega_{nk})|_{\mathbf{r}=\mathbf{r}_{\mathrm{A}}}$ is an antisymmetric tensor. Note that the bulk part of the Green's tensor gives no contribution to the lateral force since in the absence of the dielectric plate the emission is obviously symmetric.

III. APPLICATION: CESIUM ATOM

The aim of this section is to investigate the lateral force for a cesium atom near a dielectric plate and compare the orders of magnitude of the force to previous works in literature using cesium atoms near an optical nanofiber [16].

The cesium atom in its ground state can be excited to the excited state $|6^2P_{3/2}, F' = 5, M_F' = 5\rangle$ by using a right-handed circularly polarized laser beam. Since the beam is propagating along the y direction the resulting electric dipole moment is rotating in the x-z plane:

$$\boldsymbol{d}_{10} = d(i, 0, 1), \tag{17}$$

where $|1\rangle$ denotes the excited state and $|0\rangle$ the ground state. The magnitude of the dipole moment is $d = 1.9 \times 10^{-29}$ C m and the wavelength of the emitted photon is $\lambda_{10} = 852$ nm [16]. Furthermore $\boldsymbol{d}_{01} = \boldsymbol{d}_{10}^*$. The emitted photon carries the momentum and is responsible for the lateral force. There is only one decay channel to the ground state with the emission of a σ^+ photon; the atom hence can be treated as an effective two-level system.

Substituting the Green's tensor (9) into (6) and performing the trivial angular integrals we find

$$F_x(\mathbf{r}_{\mathrm{A}}, t) = -\frac{e^{-\Gamma t} d^2}{2\pi\varepsilon_0} \mathrm{Im}\left\{\int_0^{\infty} dk^{\parallel} k^{\parallel 3} e^{2ik^{\perp} z_{\mathrm{A}}} r_p\right\}. \tag{18}$$

Note that this system has been analyzed previously by classical methods [26]. However the classical result disregards the decay-induced dynamics of the force and it renders only half of our quantum result. The discrepancy can be understood from the fact that the other half of the lateral force is due to fluctuations of the electromagnetic field, which are absent in a classical description. Note also that our result contains a population-induced dynamics absent in classical models [31].

In the limit of short times the force does not vanish in the classical limit $\hbar \to 0$, showing that it could be described by classical methods [26]. Only the p-polarized components of the field affect the force, since the s-polarized components lead to an emission equal in the $+x$ and $-x$ half spaces.

The first interesting special case is a perfect conducting body, described by a unity reflection coefficient of p-polarized waves $r_p = 1$. In this case the integration over the parallel component of the wave vector can be performed analytically for any given distance:

$$\begin{aligned} F_x^{\mathrm{PC}}(\mathbf{r}_{\mathrm{A}}, t) = e^{-\Gamma t}\Bigg\{ &\frac{3d^2}{4\varepsilon_0\lambda_{10}} \frac{1}{z_{\mathrm{A}}^3} \cos\left(4\pi \frac{z_{\mathrm{A}}}{\lambda_{10}}\right) \\ &+ \frac{d^2}{\varepsilon_0}\left(\frac{\pi}{\lambda_{10}^2}\frac{1}{z_{\mathrm{A}}^2} - \frac{3}{16\pi}\frac{1}{z_{\mathrm{A}}^4}\right) \sin\left(4\pi \frac{z_{\mathrm{A}}}{\lambda_{10}}\right)\Bigg\}, \end{aligned} \tag{19}$$

where $k = \omega_{10}/c$ is the transition wave vector. This is depicted in Fig. 2 for short times.

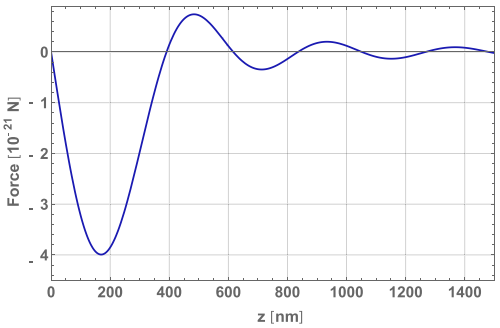

FIG. 2. Lateral CP force for a perfectly conducting half space.

We see that the force shows characteristic Drexhage-type oscillations [32,33]. Remarkably we note that the force can change sign depending on the distance between the emitter and the surface. This shows the importance of radiation modes to describe this effect. In fact, guided modes are excited strongly only in one direction giving a lateral force of constant sign.

Another interesting feature of this force is that it is not conservative. In fact if we take the curl of the total force we obtain a nonvanishing result:

$$\nabla \times \mathbf{F} = \frac{\partial F_x}{\partial z_A}\hat{y} = \frac{d^2}{\varepsilon_0}\left\{\left(\frac{4\pi^2}{\lambda_{10}^3 z_A^2} - \frac{3}{\lambda_{10} z_A^4}\right)\cos\left(\frac{4\pi z_A}{\lambda_{10}}\right) + \left(\frac{3}{4\pi z_A^5} - \frac{5\pi}{\lambda_{10}^2 z_A^3}\right)\sin\left(\frac{4\pi z_A}{\lambda_{10}}\right)\right\}\hat{y}. \tag{20}$$

Hence the Casimir-Polder force is not conservative and cannot be generally derived from a potential by just taking its gradient. Such class of forces, called curl forces, have been explored in the past [34].

We next consider the case of a dissipative dielectric medium described by a complex relative permittivity. An analytical expression can be derived in the nonretarded regimes when the distance between the emitter and the surface is much smaller than the atomic wavelength $z_A \ll \lambda_{10}$:

$$F_x^{\text{nret}}(\mathbf{r}_A,t) = -e^{-\Gamma t}\left(\frac{3d^2}{8\pi\varepsilon_0}\frac{1}{z_A^4}\frac{\text{Im}\,\varepsilon}{|\varepsilon+1|^2} + \frac{64\pi^4 d^2}{15\varepsilon_0\lambda_{10}^5} z_A \frac{|\varepsilon|^2-1}{|\varepsilon+1|^2}\right), \tag{21}$$

where $\varepsilon = \varepsilon(\omega_{10})$. In the nonretarded limit the main contribution comes from large values of $k^{\parallel}$, hence we set $k_m^{\perp} = k^{\perp}$ in the reflection coefficients [27]. The Fresnel coefficient (13) then simplifies to $r_p = (\varepsilon-1)/(\varepsilon+1)$. It shows a divergence when the emitter approaches the surface because of the lossy nature of the medium. Note that an analogous divergence is observed in the spontaneous emission of a real dipole moment near a lossy surface, where the emitter is excited with a linear-polarized resonant laser beam [35,36].

In the retarded regime, namely when the distance between the emitter and the surface is much greater than the atomic wavelength, $z_A \gg \lambda_{10}$, we have

$$F_x^{\text{ret}}(\mathbf{r}_A,t) = e^{-\Gamma t}\frac{d^2\pi}{\varepsilon_0\lambda_{10}^2}\frac{1}{z_A^2}\left\{\text{Re}\left[\frac{\sqrt{\varepsilon}-1}{\sqrt{\varepsilon}+1}\right] \times \sin\left(4\pi\frac{z_A}{\lambda_{10}}\right) + \text{Im}\left[\frac{\sqrt{\varepsilon}-1}{\sqrt{\varepsilon}+1}\right]\cos\left(4\pi\frac{z_A}{\lambda_{10}}\right)\right\}. \tag{22}$$

In the retarded limit the main contribution comes from $k_{\parallel} = 0$, hence we put $k^{\perp} \simeq \omega_{10}/c$ and $k_m^{\perp} \simeq \sqrt{\varepsilon}\omega_{10}/c$ in the reflection coefficients [27]. Hence, the Fresnel coefficient (13) simplifies to $r_p = (\sqrt{\varepsilon}-1)/(\sqrt{\varepsilon}+1)$.

The force is an oscillating function with period $\lambda_{10}/2$. This agrees with intuition. The atom emits at some time an electromagnetic field while having a specific dielectric moment orientation. The field is partially reflected by the surface and interacts with the dipole after some delay, when the dipole moment has a different orientation. If the distance between the emitter and the surface is incremented by $\lambda_{10}/4$ the delay is incremented by $\Delta t = \lambda_{10}/2c$, leading to an opposite orientation of the dipole $\boldsymbol{d} \to \boldsymbol{d}e^{i\omega_{10}\Delta t} = -\boldsymbol{d}$. This translates to a change of sign of the force.

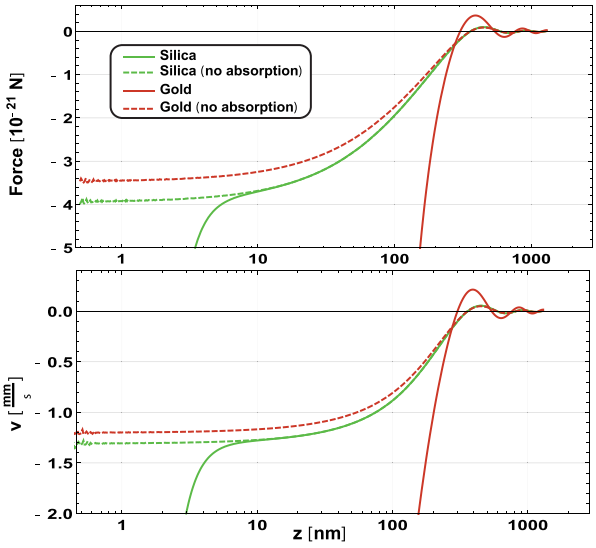

FIG. 3. Lateral CP force at initial time and long-time lateral velocity for an atom above silica and gold surfaces.

In Fig. 3 we display the lateral force at the initial time when the emitter is near a gold dielectric ($\varepsilon_{\text{Au}} \approx 1.40 + 1.35i$) [37] or silica ($\varepsilon_{\text{Si}} \approx 1.45 + 2.05 \times 10^{-7} i$). The force shows a strong increment in the near-field regime, having a magnitude of around 10^{-21} N. The same orders of magnitude have been obtained for a circular emitter near a nanofiber [16]. To judge the strength of the effect we consider the lateral velocity acquired by the atom due to the recoil, which is in the mm/s range.

The atom in the ground state can be excited also to the hyperfine level $|6^2P_{3/2}, F' = 5, M'_F = -5\rangle$ by using a left-handed circularly polarized laser beam. The atom will emit a σ^- photon and since the directionality depends on the polarization of the emitted light, the lateral force will change sign. This effect provides the opportunity to control the direction of the force changing the polarization of the illuminating light or in other words the quantum state of the emitter.

Note that for all materials considered so far, the force is directed in the $-\hat{x}$ direction in the near-field regime. This is a consequence of the right-hand rule in the lateral forces, already considered in the literature [38,39]. According to this rule the direction of the lateral force, the decay direction of the evanescent wave ($\hat{z}$ direction), and the atomic spin ($\hat{y}$ direction) follows a right-hand rule. This means that the lateral force is directed along the $-\hat{x}$ direction; see Fig. 1.

IV. EMISSION SPECTRUM

In this section we develop more closely the idea that the lateral force is a photon-recoil force. For this reason we consider the emission spectrum

$$\bar{\Gamma}(z_A,\varphi) = \int_0^{\infty} dk^{\parallel} k^{\parallel} \hbar k^{\parallel} \gamma(z_A,\mathbf{k}^{\parallel}), \tag{23}$$

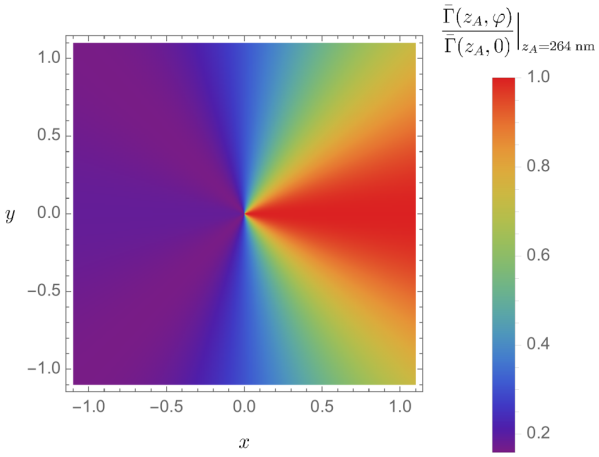

FIG. 4. Asymmetric emission spectrum at $z_A = 264$ nm for a gold dielectric ($\varepsilon_{Au} \approx 1.40 + 1.35i$).

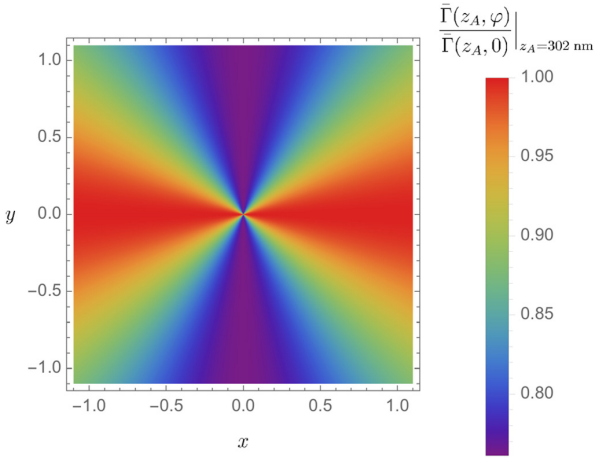

FIG. 5. Symmetric emission spectrum at distance $z_A = 302$ nm, also in the case of a gold dielectric.

which describes the scattering of a momentum $\hbar\mathbf{k}^{\parallel}$ along a particular direction parallel to the surface. Taking into account formula (15) we find the emission spectrum is in general asymmetric:

$$\bar{\Gamma}(z_A,\varphi) = A(z_A) + B(z_A)\cos\varphi + C(z_A)\cos^2\varphi + D(z_A)\sin^2\varphi, \tag{24}$$

where

$$A(z_A) = \frac{d^2}{4\pi^2\varepsilon_0}\mathrm{Re}\left[\int_0^\infty dk^{\parallel}\frac{k^{\parallel 4}}{k^{\perp}}e^{2ik^{\perp}z_A}r_p\right], \tag{25}$$

$$B(z_A) = \frac{d^2}{2\pi^2\varepsilon_0}\mathrm{Im}\left[\int_0^\infty dk^{\parallel}k^{\parallel 3}e^{2ik^{\perp}z_A}r_p\right], \tag{26}$$

$$C(z_A) = -\frac{d^2}{4\pi^2\varepsilon_0}\mathrm{Re}\left[\int_0^\infty dk^{\parallel}k^{\parallel 2}k^{\perp}e^{2ik^{\perp}z_A}r_p\right], \tag{27}$$

$$D(z_A) = \frac{d^2}{4\pi^2\varepsilon_0}\mathrm{Re}\left[\int_0^\infty dk^{\parallel}\frac{k^{\parallel 2}}{k^{\perp}}\frac{\omega^2}{c^2}e^{2ik^{\perp}z_A}r_s\right]. \tag{28}$$

The emission is in general asymmetric along the x direction because of the factor $B(z_A)$:

$$\int_{-\pi/2}^{\pi/2}d\varphi\bar{\Gamma}(z_A,\varphi) - \int_{\pi/2}^{3\pi/2}d\varphi\bar{\Gamma}(z_A,\varphi) = 4B(z_A) = \frac{2d^2}{\pi^2\varepsilon_0}\mathrm{Im}\left[\int_0^\infty dk^{\parallel}k^{\parallel 3}e^{2ik^{\perp}z_A}r_p\right]. \tag{29}$$

The comparison with Eq. (18) shows that if the emission is asymmetric along the x direction then the lateral force is finite. In Figs. 4 and 5 we show the emission spectrum for two atom-plate distances: $z_A = 264$ nm,302 nm. Figure 4 shows an asymmetric emission with stronger emission in the positive x direction; this suggests a negative lateral force as shown in Fig. 3. For $z_A = 302$ nm the emission spectrum is symmetric along the x direction suggesting that the lateral force is zero, as shown in Fig. 3.

V. CONCLUSION

We have predicted a lateral Casimir-Polder force for a circular excited emitter near a planar surface. The underlying reason for a nonvanishing force is the breaking of time-reversal symmetry. The sign of the force depends on the polarization of the emitted light and can be controlled by changing the quantum excited state of the emitter. We have also shown that the lateral force is an atom recoil force stemming from the asymmetric emission of the photon.

Our dynamical approach of the field-atom coupling shows that the lateral force has a population-induced dynamics, decaying exponentially with time, on time scales of the inverse of the spontaneous decay rate. Moreover it exhibits characteristic Drexhage-type oscillations when changing the distance between the emitter and the surface. The near-field regime is strongly influenced by the dissipative character of the medium: for short distances it converges to zero for a lossless medium, while it diverges if the medium has a complex dielectric permittivity. This effect could be detected measuring the velocity acquired by the atom after the recoil.

Our formalism which uses the scattering Green's tensor can be adopted for more complex geometries, like spheres, cylinders, or resonating planar cavities which can enhance the spatial oscillations of the force.

ACKNOWLEDGMENTS

We would like to thank M. Berry, F. J. Rodriguez-Fortuño, and S. Scheel for stimulating discussions. R.O.W., P.B., and S.Y.B. are grateful for support by the DFG (Grants No. BU 1803/3-1 and No. GRK 2079/1) and the Freiburg Institute for Advanced Studies (S.Y.B.).

[1] H. B. G. Casimir and D. Polder, Phys. Rev. **73**, 360 (1948).
[2] H. B. G. Casimir, Proc. K. Ned. Akad. Wet. **51**, 793 (1948).
[3] C. Genet, A. Lambrecht, and S. Reynaud, Eur. Phys. J.: Spec. Top. **160**, 183 (2008).
[4] F. Chen, U. Mohideen, G. L. Klimchitskaya, and V. M. Mostepanenko, Phys. Rev. Lett. **88**, 101801 (2002).
[5] A. Ashourvan, M. F. Miri, and R. Golestanian, Phys. Rev. Lett. **98**, 140801 (2007).
[6] H. Bender, C. Stehle, C. Zimmermann, S. Slama, J. Fiedler, S. Scheel, S. Y. Buhmann, and V. N. Marachevsky, Phys. Rev. X **4**, 011029 (2014).
[7] H.-C. Chiu, G. L. Klimchitskaya, V. N. Marachevsky, V. M. Mostepanenko, and U. Mohideen, Phys. Rev. B **80**, 121402 (2009).
[8] R. B. Rodrigues, P. A. M. Neto, A. Lambrecht, and S. Reynaud, Phys. Rev. Lett. **96**, 100402 (2006).
[9] A. Lambrecht and V. N. Marachevsky, Phys. Rev. Lett. **101**, 160403 (2008).
[10] D. A. R. Dalvit, P. A. M. Neto, A. Lambrecht, and S. Reynaud, J. Phys. A: Math. Theor. **41**, 164028 (2008).
[11] B. Dobrich, M. DeKieviet, and H. Gies, Phys. Rev. D **78**, 125022 (2008).
[12] R. Messina, D. A. R. Dalvit, P. A. M. Neto, A. Lambrecht, and S. Reynaud, Phys. Rev. A **80**, 022119 (2009).
[13] A. M. Contreras-Reyes, R. Guérout, P. A. M. Neto, D. A. R. Dalvit, A. Lambrecht, and S. Reynaud, Phys. Rev. A **82**, 052517 (2010).
[14] S. B. Wang and C. T. Chan, Nat. Commun. **5**, 3307 (2014).
[15] A. Hayat, J. P. B. Mueller, and F. Capasso, Proc. Natl. Acad. Sci. USA **112**, 13190 (2015).
[16] S. Scheel, S. Y. Buhmann, C. Clausen, and P. Schneeweiss, Phys. Rev. A **92**, 043819 (2015).
[17] Z. Xi, Y. Lu, P. Yao, W. Yu, P. Wang, and H. Ming, Opt. Express **21**, 30327 (2013).
[18] J. Lin, J. P. B. Mueller, Q. Wang, G. Yuan, N. Antoniou, X.-C. Yuan, and F. Capasso, Science **340**, 331 (2013).
[19] A. Manjavacas, F. J. Rodriguez-Fortuño, F. J. Garcia de Abajo, and A. V. Zayats, Phys. Rev. Lett. **118**, 133605 (2017).
[20] F. J. Rodriguez-Fortuño, G. Marino, P. Ginzburg, D. O'Connor, A. Martínez, G. A. Wurtz, and A. V. Zayats, Science **340**, 328 (2013).
[21] I. J. Luxmoore, N. A. Wasley, A. J. Ramsay, A. C. T. Thijssen, R. Oulton, M. Hugues, A. M. Fox, and M. S. Skolnick, Appl. Phys. Lett. **103**, 241102 (2013).
[22] M. Neugebauer, T. Bauer, P. Banzer, and G. Leuchs, Nano Lett. **14**, 2546 (2014).
[23] R. Mitsch, C. Sayrin, B. Albrecht, P. Schneeweiss, and A. Rauschenbeutel, Nat. Commun. **5**, 5713 (2014).
[24] J. Petersen, J. Volz, and A. Rauschenbeutel, Science **346**, 67 (2014).
[25] B. le Feber, N. Rotenberg, and L. Kuipers, Nat. Commun. **6**, 6695 (2015).
[26] F. J. Rodriguez-Fortuño, N. Engheta, A. Martínez, and A. V. Zayats, Nat. Commun. **6**, 8799 (2015).
[27] S. Y. Buhmann, *Dispersion Forces I* (Springer, Heidelberg, 2012).
[28] S. Y. Buhmann, *Dispersion Forces II* (Springer, Heidelberg, 2012).
[29] S. Y. Buhmann, L. Knoll, D. G. Welsch, and H. T. Dung, Phys. Rev. A **70**, 052117 (2004).
[30] S. Fuchs, J. A. Crosse, and S. Y. Buhmann, Phys. Rev. A **95**, 023805 (2017).
[31] D. Meschede, W. Jhe, and E. A. Hinds, Phys. Rev. A **41**, 1587 (1990).
[32] K. Drexhage, J. Lumin. **1-2**, 693 (1970).
[33] K. H. Drexhage, H. Kuhn, and F. P. Schäfer, Ber. Bunsenges. Phys. Chem. **72**, 329 (1968).
[34] M. V. Berry and P. Shukla, J. Phys. A: Math. Theor. **45**, 305201 (2012).
[35] S. Scheel, L. Knöll, and D.-G. Welsch, Acta Physica Slovaca **49**, 585 (1999).
[36] M. S. Yeung and T. K. Gustafson, Phys. Rev. A **54**, 5227 (1996).
[37] http://refractiveindex.info/?shelf=main&book=Au&page=McPeak, Access: 04/02/16.
[38] F. Kalhor, T. Thundat, and Z. Jacob, Appl. Phys. Lett. **108**, 061102 (2016).
[39] T. V. Mechelen and Z. Jacob, Optica **3**, 118 (2016).

PHYSICAL REVIEW A **94**, 012705 (2016)

van der Waals interactions between excited atoms in generic environments

Pablo Barcellona[*]
Physikalisches Institut, Albert-Ludwigs-Universität Freiburg, Hermann-Herder-Str. 3, 79104 Freiburg, Germany

Roberto Passante[†] and Lucia Rizzuto[‡]
Dipartimento di Fisica e Chimica, Università degli Studi di Palermo and CNISM, Via Archirafi 36, I-90123 Palermo, Italy and INFN, Laboratori Nazionali del Sud, I-95123 Catania, Italy

Stefan Yoshi Buhmann[§]
Physikalisches Institut, Albert-Ludwigs-Universität Freiburg, Hermann-Herder-Str. 3, 79104 Freiburg, Germany and Freiburg Institute for Advanced Studies, Albert-Ludwigs-Universität Freiburg, Albertstr. 19, 79104 Freiburg, Germany

(Received 20 May 2016; published 27 July 2016)

We consider the van der Waals force involving excited atoms in general environments, constituted by magnetodielectric bodies. We develop a dynamical approach studying the dynamics of the atoms and the field, mutually coupled. When only one atom is excited, our dynamical theory suggests that for large distances the van der Waals force acting on the ground-state atom is monotonic, while the force acting in the excited atom is spatially oscillating. We show how this latter force can be related to the known oscillating Casimir-Polder force on an excited atom near a (ground-state) body. Our force also reveals a population-induced dynamics: for times much larger that the atomic lifetime the atoms will decay to their ground states leading to the van der Waals interaction between ground-state atoms.

DOI: 10.1103/PhysRevA.94.012705

I. INTRODUCTION

Casimir and van der Waals (vdW) forces are interactions between neutral macroscopic bodies or atoms arising from the quantum fluctuations of both the electromagnetic field and the atomic charges [1,2]. They are responsible for many characteristic phenomena in physics, chemistry, and biology: the deviation from ideal-gas behavior in nonpolar gases [3], latent heat of liquids, capillary attraction, physical absorption, and cell adhesion [4]. Dispersion interactions have even played an important role during the early stages of planet formation [5], and they are also supposed to have a fundamental role in selective long-distance biomolecular recognition [6]. Due to their strong distance dependence, they become more and more important on the ever-decreasing scales of nanotechnology, where they lead to the unwanted stiction of small mobile components [7]. In a series of ground-breaking experiments, the vdW force between an excited barium ion and a mirror has been measured to high precision [8,9]. Such experiments show an oscillating dependence of the vdW force on the ion.

We will focus on the vdW force between two atoms, in excited states $|n\rangle$ and $|l\rangle$. The interaction in this case is different from the interaction between two ground-state atoms due to the possible exchange of a real photon between the atoms. In the well-understood nonretarded regime, that is, for distances r much smaller than the wavelength of atomic electronic transitions, one finds [10,11]

$$\mathbf{F}_{\rm nr}(r) = -\frac{\mathbf{e}_r}{4\pi^2\varepsilon_0^2 r^7}\sum_{k,p}\frac{\left|\mathbf{d}_{nk}^A\right|^2\left|\mathbf{d}_{pl}^B\right|^2}{E_k^A - E_n^A + E_p^B - E_l^B}, \qquad (1)$$

where $\mathbf{e}_r = \mathbf{r}/r$, $\mathbf{d}_{nm}^A$ are the matrix elements of the dipole operator, and E_k the energy relative to the state $|k\rangle$. For downward transitions, $E_k^A - E_n^A + E_p^B - E_l^B$ can be negative, yielding a repulsive interaction. Hence nonequilibrium situations can provide repulsive vdW interactions.

The interaction at larger separations has been the object of controversies. In a first group of works, it was predicted that the magnitude of the retarded potential oscillates as a function of interatomic distance [12–14]. In a later group of publications it was claimed that the retarded potential is nonoscillatory and proportional to $1/r^2$ [11,15–17]. The conflicting results are due to subtle differences in treating divergent energy denominators in the photon propagators: the poles in the real axis can be avoided using the principal value prescription or adding infinitesimal factors in the energy denominators and this leads to different results. Both procedures are mathematically correct, but they yield different physical results: a spatially oscillatory behavior of the interaction in the first case and a monotonically decreasing behavior in the second.

A group of recent works have used dynamical approaches to address the problem. By an appropriate time-averaging procedure [18] or in the limit of vanishing atomic linewidths [19], a third result, for the vdW interaction on the excited atom, was found that oscillates in magnitude and sign. Note that an earlier approach based on time-dependent perturbation theory yields a nonoscillatory result for the force on the ground-state atom that is however valid only for times shorter than the lifetime of the excited state [20]. Similar considerations about time scales hold for the diagrammatic nonequilibrium description used in Ref. [21].

A very recent work claims that both results, the monotonic and the oscillating, are valid, but they describe different physical processes [22]: the oscillating result is related to a coherent exchange of excitation between the atoms, while the monotonic result is associated to a fast loss of excitation

[*]pablo.barcellona@physik.uni-freiburg.de
[†]roberto.passante@unipa.it
[‡]lucia.rizzuto@unipa.it
[§]stefan.buhmann@physik.uni-freiburg.de

acquired from the initially excited atom. Another recent work finds that both forces can simultaneously arise in a single setup: the vdW interaction on the excited atom oscillates, in agreement with Refs. [18,19,22], but the vdW force acting on the ground-state atom is monotonic [23]. This result would imply an apparent violation of the action-reaction principle in excited systems in free space. However, it was shown that the momentum balance is restored when taking the photon emitted by the excited atom into account [24]. This emission being asymmetric due to the presence of the ground-state atom, the emitted photon carries some average momentum, so that the difference between forces on the excited versus ground-state atoms can be interpreted as a photon recoil force. The situation is somewhat similar to the lateral Casimir-Polder force on an atom near a nanofiber, which is also associated with asymmetric emission [25].

In this paper, we study the van der Waals interaction involving excited atoms by means of a dynamical approach on the basis of the Markov approximation. We show that the damped internal atomic dynamics uniquely determines the oscillatory or monotonic behavior of the retarded interaction for excited atoms. In our dynamical model, the poles in the real axis are automatically shifted to the upper or lower part of the complex plane, and no *ad hoc* choice for the imaginary shifts in the denominators is required. We will show that, when one atom is excited, the vdW force acting on the ground-state atom is monotonic and the vdW interaction of the excited atom is oscillating, in agreement with the most recent results in literature [22–24,26]. Our dynamical approach is an alternative to the time-dependent perturbation theory [23], where the behavior of the force is determined via a time average over rapid oscillations on time scales of the order of atomic transition frequencies. Instead, our model allows us to study the decay-induced dynamics on larger time scales of the order of the excited-state lifetimes. It reveals that the force is governed by population-induced dynamics on these scales, where for times much larger than the lifetime of the initial atomic state the vdW force converges to that between ground-state atoms. In addition, we are able to account for a general environment for the two atoms, via the classical Green tensor.

The article is organized as follows. In Sec. II, we present the basic formalism describing the coupled atom-field dynamics. It is used in Sec. III for calculating the force between two atoms in arbitrary excited initial states. In Sec. IV, we make the connection of our result with the Casimir-Polder force between an excited atom and a body of arbitrary shape. Some conclusions are given in Sec. V, while in the Appendix, we present some of the more cumbersome details of our general approach and our calculation.

II. ATOM-FIELD DYNAMICS

We consider the mutually coupled evolution of two atoms and the medium-assisted field. The field is prepared at zero temperature, and the atoms in generic internal states. The dynamics of the atoms can be described with time-dependent flip operators, defined by $\hat{A}_{mn} = |m^A\rangle\langle n^A|$, where $|n^A\rangle$ is an energy eigenstate, and similarly $\hat{B}_{pq} = |p^B\rangle\langle q^B|$.

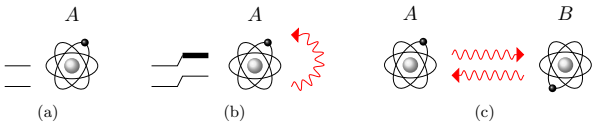

FIG. 1. Case (a) is the zero-order approximation: free field and free atom. Case (b) is the next-order approximation: the Lamb shift of an atom due to the emission and reabsorption of a photon. Case (c) is the dispersion interaction between two atoms due to the exchange of two photons.

In order to evaluate the force between the two atoms we must first solve the atom-field dynamics to obtain the flip operators and the field operators in the Heisenberg picture. The total Hamiltonian is the sum of three terms, the atomic and the field Hamiltonian and the interaction term in the multipolar coupling scheme within dipole approximation:

$$\begin{aligned}\hat{H} &= \hat{H}_A + \hat{H}_F + \hat{H}_{AF},\\ \hat{H}_A &= \sum_n E_n^A \hat{A}_{nn} + \sum_n E_n^B \hat{B}_{nn},\\ \hat{H}_F &= \sum_{\lambda=e,m} \int d^3r \int_0^\infty d\omega\, \hbar\omega \hat{\mathbf{f}}_\lambda^\dagger(\mathbf{r},\omega)\cdot\hat{\mathbf{f}}_\lambda(\mathbf{r},\omega),\\ \hat{H}_{AF} &= -\hat{\mathbf{d}}^A\cdot\hat{\mathbf{E}}(\mathbf{r}_A) - \hat{\mathbf{d}}^B\cdot\hat{\mathbf{E}}(\mathbf{r}_B),\end{aligned} \tag{2}$$

where $\hat{\mathbf{f}}_\lambda(\mathbf{r},\omega)$ is the annihilation operator for the elementary electric and magnetic excitations of the system [27].

Since the evolution of the whole system is unitary the commutator between two electric fields coincides with the commutator between free fields [28,29]

$$[\hat{\mathbf{E}}(\mathbf{r},\omega),\hat{\mathbf{E}}^\dagger(\mathbf{r}',\omega')] = \frac{\hbar\mu_0}{\pi}\mathrm{Im}\mathbf{G}(\mathbf{r},\mathbf{r}',\omega)\omega^2\delta(\omega-\omega'), \tag{3}$$

where $\mathbf{G}$ is the Green's tensor of the electromagnetic field and $\hat{\mathbf{E}}(\mathbf{r},\omega)$ is the Fourier component of the electric field $\hat{\mathbf{E}}(\mathbf{r}) = \int_0^\infty d\omega\,\hat{\mathbf{E}}(\mathbf{r},\omega) + \mathrm{H.c.}$, Heisenberg equations for the coupled atom-field dynamics read

$$\begin{aligned}\partial_t\hat{A}_{mn} &= i\omega_{mn}^A\hat{A}_{mn} + \frac{i}{\hbar}\hat{\mathbf{K}}_{mn}^A\cdot\hat{\mathbf{E}}(\mathbf{r}_A),\\ \partial_t\hat{\mathbf{E}}(\mathbf{r},\omega) &= -i\omega\hat{\mathbf{E}}(\mathbf{r},\omega) + \frac{i\mu_0}{\pi}\omega^2\\ &\quad\times[\mathrm{Im}\mathbf{G}(\mathbf{r},\mathbf{r}_A,\omega)\cdot\hat{\mathbf{d}}^A + \mathrm{Im}\mathbf{G}(\mathbf{r},\mathbf{r}_B,\omega)\cdot\hat{\mathbf{d}}^B],\end{aligned} \tag{4}$$

where $\hat{\mathbf{K}}_{mn}^A = [\hat{A}_{mn},\hat{\mathbf{d}}^A]$.

The electric field at the position of atom A consists of two terms: the radiation reaction and the field due to the other atom B. As shown in the literature [28,30], the radiation reaction field gives rise to frequency shifts and spontaneous decay for atom A; see Figs. 1(a) and 1(b). We thus renormalize the field by splitting off the radiation reaction

$$\begin{aligned}\langle\partial_t\hat{A}_{mn}\rangle &= \left[i\tilde{\omega}_{mn}^A - \left(\Gamma_n^A+\Gamma_m^A\right)/2\right]\langle\hat{A}_{mn}\rangle\\ &\quad + \frac{i}{\hbar}\langle\hat{\mathbf{K}}_{mn}^A\cdot\hat{\mathbf{E}}_{\not A}(\mathbf{r}_A)\rangle,\end{aligned} \tag{5}$$

where $m\neq n$ and the expectation value $\langle\cdots\rangle$ is taken over atomic state and the field thermal state. $\hat{\mathbf{E}}_{\not A}(\mathbf{r}_A,t)$ is the sum of

the free electric field and the source field of the atom B, $\tilde{\omega}^A_{mn}$ the (second-order) Lamb-shifted atomic frequencies, and Γ^A_n the decay rates.

III. VAN DER WAALS INTERACTION BETWEEN TWO EXCITED ATOMS

We consider two atoms A and B that are initially prepared in excited energy eigenstates $|i_A\rangle, |i_B\rangle$ of the free atomic Hamiltonian $[p^A_n(0) = \delta_{ni_A}, p^B_l(0) = \delta_{li_B}]$. These initial states are not eigenstates of the total Hamiltonian and thus the atomic states evolve in time yielding a time-dependent vdW force (population-induced dynamics). As time progresses, the lower lying levels $n \leqslant i_A$, $l \leqslant i_B$ will become populated.

To find the vdW force on, say, atom A, we calculate the Lorentz force in electric-dipole approximation acting on A which is due to the field $\mathbf{E}_{\not A}(\mathbf{r}_A,t)$ emitted by the other atom B:

$$\mathbf{F}_A(\mathbf{r}_A,\mathbf{r}_B,t) = \boldsymbol{\nabla}_A \langle \hat{\mathbf{d}}^A \cdot \hat{\mathbf{E}}_{\not A}(\mathbf{r}_A,t)\rangle, \tag{6}$$

where expectation value is taken over atomic and field states.

For weak atom-field coupling, corresponding in an expansion of the Hamiltonian in powers of the coupling strengths $\mathbf{d}$, we can apply the Markov approximation to find (see the Appendix):

$$\begin{aligned}\mathbf{F}_A(\mathbf{r}_A,\mathbf{r}_B,t) = {}& \frac{\mu_0^2}{2\pi^2\hbar} \sum_{n\leqslant i_A}\sum_{l\leqslant i_B} p^A_n(t) p^B_l(t) \sum_{k,p} \int_0^\infty d\omega \\ & \times \int_0^\infty d\omega' \omega^2 \omega'^2 \boldsymbol{\nabla}_A \big\{ \mathbf{d}^A_{nk} \cdot \mathrm{Im}\mathbf{G}(\mathbf{r}_A,\mathbf{r}_B,\omega) \cdot \mathbf{d}^B_{pl} \\ & \times \mathbf{d}^B_{lp} \cdot \mathrm{Im}\mathbf{G}(\mathbf{r}_B,\mathbf{r}_A,\omega') \cdot \mathbf{d}^A_{kn} \big\} \sum_{i=1}^{16} \frac{1}{D_i} + \text{H.c.},\end{aligned} \tag{7}$$

where $p^A_n(t) = \langle \hat{A}_{nn}(t)\rangle$ and $p^B_l(t) = \langle \hat{B}_{ll}(t)\rangle$ represent the atomic populations of states $|n\rangle$ and $|l\rangle$.

The energy denominators D_i are listed in Table I. Due to our dynamical treatment of the atom-field coupling, the result explicitly depends on atomic damping constants or linewidths, and also an infinitesimal damping for the photon of frequency ω. These factors uniquely ensure the convergence of time integrals.

For excited atoms the energy denominators can exhibit poles, for photon frequencies being resonant to the atomic ones. According to time-independent perturbation theory these poles would be situated on the real-frequency axis with the mentioned resulting ambiguities. In our dynamical approach, with the inclusion of the atomic linewidths, the poles are automatically shifted to the lower or upper part of the complex plane leading to unique resonant contributions.

The total vdW force acting on A consists in two terms, a nonresonant contribution arising from virtual photons exchange and a resonant contribution which corresponds to a possible emission of real photons by the excited atoms:

$$\mathbf{F}_A(\mathbf{r}_A,\mathbf{r}_B,t) = \mathbf{F}^{\mathrm{nr}}_A(\mathbf{r}_A,\mathbf{r}_B,t) + \mathbf{F}^{\mathrm{r}}_A(\mathbf{r}_A,\mathbf{r}_B,t). \tag{8}$$

In the limit of vanishing linewidths, the nonresonant contribution in an arbitrary magnetoelectric environment reads (see the Appendix)

$$\begin{aligned}\mathbf{F}^{\mathrm{nr}}_A(\mathbf{r}_A,\mathbf{r}_B,t) = {}& \frac{\hbar\mu_0^2}{2\pi} \int_0^\infty d\xi\, \xi^4 \boldsymbol{\nabla}_A \mathrm{Tr}\{\boldsymbol{\alpha}_A(i\xi) \\ & \cdot \mathbf{G}(\mathbf{r}_A,\mathbf{r}_B,i\xi) \cdot \boldsymbol{\alpha}_B(i\xi) \cdot \mathbf{G}(\mathbf{r}_B,\mathbf{r}_A,i\xi)\},\end{aligned} \tag{9}$$

where we have defined the following polarizabilities of the initially excited atoms:

$$\begin{aligned}\boldsymbol{\alpha}_A(\omega) &= \frac{1}{\hbar} \sum_{n\leqslant i_A} p^A_n(t) \sum_k \left(\frac{\mathbf{d}^A_{kn}\mathbf{d}^A_{nk}}{\omega^A_{kn} + \omega} + \frac{\mathbf{d}^A_{nk}\mathbf{d}^A_{kn}}{\omega^A_{kn} - \omega} \right), \\ \boldsymbol{\alpha}_B(\omega) &= \frac{1}{\hbar} \sum_{l\leqslant i_B} p^B_l(t) \sum_p \left(\frac{\mathbf{d}^B_{pl}\mathbf{d}^B_{lp}}{\omega^B_{pl} + \omega} + \frac{\mathbf{d}^B_{lp}\mathbf{d}^B_{pl}}{\omega^B_{pl} - \omega} \right).\end{aligned} \tag{10}$$

The resonant contribution reads

$$\begin{aligned}&\mathbf{F}^{\mathrm{r}}_A(\mathbf{r}_A,\mathbf{r}_B,t) \\ &= \mu_0^2 \sum_{n\leqslant i_A} p^A_n(t) \sum_{k<n} \boldsymbol{\nabla}_A \,\mathrm{Re}\left\{ \left(\omega^A_{nk}\right)^4 \right. \\ &\quad \left. \times \mathbf{d}^A_{nk} \cdot \mathbf{G}\left(\mathbf{r}_A,\mathbf{r}_B,\omega^A_{nk}\right) \cdot \boldsymbol{\alpha}_B\left(\omega^A_{nk}\right) \cdot \mathbf{G}\left(\mathbf{r}_B,\mathbf{r}_A,\omega^A_{nk}\right) \cdot \mathbf{d}^A_{kn} \right\} \\ &\quad + \mu_0^2 \sum_{l\leqslant i_B} p^B_l(t) \sum_{p<l} \boldsymbol{\nabla}_A \left\{ \left(\omega^B_{lp}\right)^4 \right. \\ &\quad \left. \times \mathbf{d}^B_{lp} \cdot \mathbf{G}\left(\mathbf{r}_B,\mathbf{r}_A,\omega^B_{lp}\right) \cdot \boldsymbol{\alpha}_A\left(\omega^B_{lp}\right) \cdot \mathbf{G}^*\left(\mathbf{r}_A,\mathbf{r}_B,\omega^B_{lp}\right) \cdot \mathbf{d}^B_{pl} \right\}.\end{aligned} \tag{11}$$

For large distances the resonant contribution dominates over the nonresonant one. Two terms, one oscillating and one

TABLE I. Energy denominators. In this table, ω^A_{kn} represents the transition frequency between the virtual state $|k\rangle$ and the excited state $|n\rangle$, while ω^B_{pl} represents the transition frequency between the virtual state $|p\rangle$ and $|l\rangle$. Furthermore, $\omega^{A(\pm)}_{kn} = \omega^A_{kn} \pm i(\Gamma^A_k + \Gamma^A_n)/2$, $\omega^{B(\pm)}_{pl} = \omega^B_{pl} \pm i(\Gamma^B_p + \Gamma^B_l)/2$, and $\omega^{(\pm)} = \omega \pm i\epsilon$ with ϵ infinitesimal factor. Γ is the atomic linewidth.

	Energy denominators
D_1	$\left(\omega^{(-)} + \omega^{A(-)}_{kn}\right)\left(\omega' + \omega^{B(-)}_{pl}\right)\left(\omega^{A(-)}_{kn} + \omega^{B(-)}_{pl}\right)$
D_2	$\left(\omega^{(-)} + \omega^{A(-)}_{kn}\right)\left(\omega' + \omega^{B(+)}_{pl}\right)\left(\omega^{A(-)}_{kn} - \omega^{B(+)}_{pl}\right)$
D_3	$\left(\omega^{(-)} - \omega^{A(+)}_{kn}\right)\left(\omega' + \omega^{B(-)}_{pl}\right)\left(\omega^{A(+)}_{kn} - \omega^{B(-)}_{pl}\right)$
D_4	$\left(\omega^{(-)} - \omega^{A(+)}_{kn}\right)\left(\omega' + \omega^{B(+)}_{pl}\right)\left(\omega^{A(+)}_{kn} + \omega^{B(+)}_{pl}\right)$
D_5	$\left(\omega^{(-)} + \omega^{A(-)}_{kn}\right)\left(\omega' + \omega^{A(-)}_{kn}\right)\left(\omega^{A(-)}_{kn} + \omega^{B(-)}_{pl}\right)$
D_6	$-\left(\omega^{(-)} - \omega^{A(+)}_{kn}\right)\left(\omega' + \omega^{A(+)}_{kn}\right)\left(\omega^{A(+)}_{kn} - \omega^{B(-)}_{pl}\right)$
D_7	$-\left(\omega^{(-)} + \omega^{A(-)}_{kn}\right)\left(\omega' + \omega^{A(-)}_{kn}\right)\left(\omega^{A(-)}_{kn} - \omega^{B(+)}_{pl}\right)$
D_8	$\left(\omega^{(-)} - \omega^{A(+)}_{kn}\right)\left(\omega' + \omega^{A(+)}_{kn}\right)\left(\omega^{A(+)}_{kn} + \omega^{B(+)}_{pl}\right)$
D_9	$\left(\omega^{(-)} + \omega'\right)\left(\omega^{(-)} + \omega^{A(-)}_{kn}\right)\left(\omega' + \omega^{B(-)}_{pl}\right)$
D_{10}	$\left(\omega^{(-)} - \omega'\right)\left(\omega^{(-)} + \omega^{A(-)}_{kn}\right)\left(\omega' + \omega^{B(+)}_{pl}\right)$
D_{11}	$-\left(\omega^{(-)} + \omega'\right)\left(\omega^{(-)} - \omega^{A(+)}_{kn}\right)\left(\omega' + \omega^{B(-)}_{pl}\right)$
D_{12}	$-\left(\omega^{(-)} - \omega'\right)\left(\omega^{(-)} - \omega^{A(+)}_{kn}\right)\left(\omega' + \omega^{B(+)}_{pl}\right)$
D_{13}	$\left(\omega^{(-)} + \omega'\right)\left(\omega^{(-)} + \omega^{A(-)}_{kn}\right)\left(\omega^{(-)} + \omega^{B(-)}_{pl}\right)$
D_{14}	$-\left(\omega^{(-)} - \omega'\right)\left(\omega^{(-)} + \omega^{A(-)}_{kn}\right)\left(\omega^{(-)} + \omega^{B(-)}_{pl}\right)$
D_{15}	$-\left(\omega^{(-)} + \omega'\right)\left(\omega^{(-)} - \omega^{A(+)}_{kn}\right)\left(\omega^{(-)} + \omega^{B(-)}_{pl}\right)$
D_{16}	$\left(\omega^{(-)} - \omega'\right)\left(\omega^{(-)} - \omega^{A(+)}_{kn}\right)\left(\omega^{(-)} + \omega^{B(-)}_{pl}\right)$

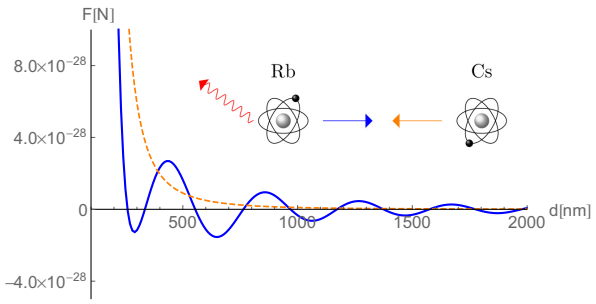

FIG. 2. vdW interaction between one cesium atom in the ground state ($5\,^2S_{1/2}$) and an excited rubidium atom ($5\,^2P_{1/2}$). The thick line represents the force on rubidium and the dashed one that on cesium.

monotonic, are involved in the resonant contribution. Their behavior can be seen explicitly for isotropic atoms in free space:

$$\begin{aligned}\mathbf{F}^{\mathrm{r}}_A(r,t) = &-\frac{1}{12\pi^2\varepsilon_0^2 r^7}\,\mathbf{e}_r \sum_{n\leqslant i_A} p_n^A(t) \sum_{k<n} \left|\mathbf{d}_{nk}^A\right|^2 \\ &\times \boldsymbol{\alpha}_B\left(\omega_{nk}^A\right)\left[\left(9-16x_{nk}^2+3x_{nk}^4\right)\cos(2x_{nk})\right. \\ &\left.+\left(18x_{nk}-8x_{nk}^3+x_{nk}^5\right)\sin(2x_{nk})\right] \\ &-\frac{1}{12\pi^2\varepsilon_0^2 r^7}\,\mathbf{e}_r \sum_{l\leqslant i_B} p_l^B(t) \sum_{p<l} \left|\mathbf{d}_{lp}^B\right|^2 \\ &\times \boldsymbol{\alpha}_A\left(\omega_{lp}^B\right)\left(9+2y_{lp}^2+y_{lp}^4\right), \end{aligned} \tag{12}$$

where $x_{nk} = r\omega_{nk}^A/c$ and $y_{lp} = r\omega_{lp}^B/c$, $\mathbf{e}_r = \mathbf{r}/r$. When both atoms are excited, the monotonic and oscillating results both contribute and can be attributed to different physical processes [22]: the oscillating result is related to a reversible exchange of excitation ("pendulation") and the monotonic form with an effectively irreversible (Forster) excitation transfer.

When only one atom is excited, the force acting on the excited atom is oscillating; on the other hand, the force acting on the ground-state atom is monotonic, consistent with the perturbative result in [20]. This implies a violation of the action-reaction principle in excited systems in free space. The interaction is accompanied by the transfer of linear momentum to the electromagnetic vacuum; this momentum is ultimately released through directional spontaneous emission of the excited atom [24].

In Fig. 2, we show the vdW force acting on a rubidium atom and on a cesium atom in free space, the rubidium atom being in the excited state $5\,^2P_{1/2}$ and the cesium atom in the ground-state $5\,^2S_{1/2}$ (see [31]); the force is represented for times much shorter than the atomic lifetime and much larger than the inverse of the atomic frequency, so that the populations of the states may be considered constant and the atomic dynamical self-dressing is not present. At large distances the resonant term dominates and the force on the excited atom shows Drexhage-type oscillations with an amplitude r^{-2}. The force acting on the ground-state atom is monotonic. At small distances, we find a nonoscillating repulsive force for both atoms.

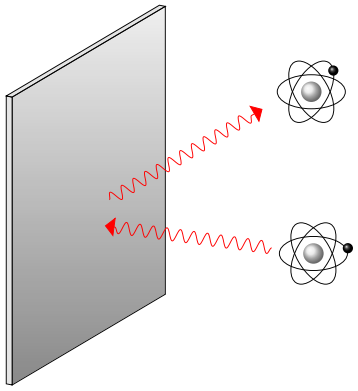

FIG. 3. Body-assisted vdW interaction: the exchanged photons can be reflected by the body's surface.

However our theory is more general because it includes the presence of general environments for the two atoms, like magnetodielectric bodies. Many differences arise in this more general case. First the interaction can be described as a two-photon process, where the photons can be reflected by the body's surface (see Fig. 3); this reflection is mathematically described in our formalism by the scattering Green tensor, which is known for many geometries and magnetodielectric properties. Secondly due to the presence of the additional body the action-reaction principle is also violated for ground-state atoms, with the interaction being accompanied by the transfer of linear momentum to the body. Lastly the total force acting on one molecule is not parallel to the interparticle separation vector.

We see that the resonant contribution vanishes for times much larger than the atomic lifetimes ($\mathbf{F}^{\mathrm{r}}_A \propto p_n^A(t) = e^{-\Gamma_n^A t}$), when the atoms have decayed to the ground state. Figure 4 represents this population-induced dynamics for the force acting on the excited rubidium at a given distance. We see that for time much larger than the atomic lifetime the force converges to the ground-state force, which is attractive. For times much smaller than the atomic lifetime the force is

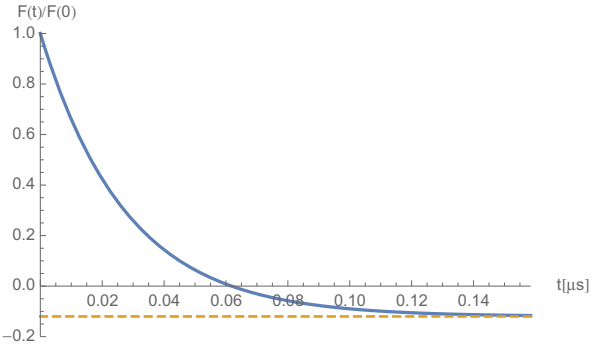

FIG. 4. Population-induced dynamics for the vdW force acting on the excited rubidium atom (thick line). The rubidium atom is in the $5\,^2P_{1/2}$ state, while the cesium is in the ground state. The distance between the atoms is $r = 10$ nm.

repulsive and roughly one order of magnitude larger than the ground-state force.

As stated above, the resonant force on the excited atom may be associated with photon recoil due to spontaneous emission. The fact that this force is stronger at small times can be understood from its ensemble-average nature: the probability of photon emission (and hence recoil) is highest for small times where a large fraction of the ensemble atoms are still in their excited state.

IV. COMPARISON TO CASIMIR-POLDER FORCE

Let us compare our result with the experimentally observed single-atom Casimir-Polder force. If an initially excited atom A is placed near a magnetodielectric body, the resonant contribution, associated with a possible emission of a real photon, reads [28]

$$\mathbf{F}_A^r(\mathbf{r}_A,t) = \mu_0 \sum_{n\leqslant i_A} p_n^A(t) \sum_{k<n} \left(\omega_{nk}^A\right)^2 \times \boldsymbol{\nabla}_A \mathrm{Re}\left\{\mathbf{d}_{nk}^A \cdot \mathbf{G}^1\left(\mathbf{r}_A,\mathbf{r}_A,\omega_{nk}^A\right)\cdot \mathbf{d}_{kn}^A\right\}, \quad (13)$$

where $\mathbf{G}^1$ is the body's scattering Green's tensor. If the body is made up of ground-state atoms with polarizability $\boldsymbol{\alpha}_B(\omega)$ and positions $\mathbf{r}_B$ and number density $\eta(\mathbf{r})$, it can be expressed in terms of a leading-order Born expansion [32]:

$$\mathbf{G}^1(\mathbf{r}_A,\mathbf{r}_A,\omega) = \mu_0\omega^2 \int d^3r_B\, \eta(\mathbf{r}_B)\mathbf{G}^0(\mathbf{r}_A,\mathbf{r}_B,\omega)\cdot\boldsymbol{\alpha}_B(\omega) \cdot \mathbf{G}^0(\mathbf{r}_B,\mathbf{r}_A,\omega) + \cdots, \quad (14)$$

where $\mathbf{G}^0$ is the free-space Green's tensor. The substitution of this expansion into the single-atom Casimir-Polder force leads to a resonant force

$$\begin{aligned}\mathbf{F}_A^r(\mathbf{r}_A,t) &= \int d^3r_B\, \eta(\mathbf{r}_B)\mathbf{F}_A^r(\mathbf{r}_A,\mathbf{r}_B)\\ &= \int d^3r_B\, \eta(\mathbf{r}_B)\mu_0^2 \sum_{n\leqslant i_A} p_n^A(t) \sum_{k<n} \boldsymbol{\nabla}_A\, \mathrm{Re}\left\{\left(\omega_{nk}^A\right)^4 \mathbf{d}_{nk}^A \cdot \mathbf{G}^0\left(\mathbf{r}_A,\mathbf{r}_B,\omega_{nk}^A\right)\cdot\boldsymbol{\alpha}_B\left(\omega_{nk}^A\right)\cdot \mathbf{G}^0\left(\mathbf{r}_B,\mathbf{r}_A,\omega_{nk}^A\right)\cdot \mathbf{d}_{kn}^A\right\}\end{aligned} \quad (15)$$

on the excited atom which is simply the sum over the (oscillating) resonant forces (11) on the excited atom due to the ground-state atoms constituting the body. Note that a monotonous force contribution is absent from the single-atom Casimir-Polder force (15), as the atoms in the body are not excited. In the present combination of an excited atom interacting with a ground-state atom, we would expect the force on the body to contain a monotonous Casimir-Polder force component. However, the force on the body is usually not considered in the context of Casimir-Polder physics due to the strongly asymmetric mass ratio.

V. CONCLUSIONS AND OUTLOOK

Our dynamical theory has allowed us to study the vdW force involving excited atoms in generic environments. It is able to give a unique answer to the old puzzle whether the respective interaction is oscillating or monotonic, without recourse to *ad hoc* assumptions or prescriptions.

When one atom is excited we have shown that the van der Waals force acting on the excited atom indeed shows Drexhage-type oscillations, while the force acting on the ground-state atom is monotonic. We have explicitly demonstrated that the oscillating force is consistent with the respective Casimir-Polder force between an excited atom and a ground-state body. On the contrary, the monotonic forces components cannot be deduced from the atom-body force in this way, because they act on the atoms inside the body, whereas Casimir-Polder calculations are usually restricted to calculating the force on the single atom in front of the body.

The oscillating force on the excited atom could have profound implications on the spatial correlations of excited atomic ensembles, in particular for Rydberg systems. In addition, both the oscillating and monotonous force components are expected to arise in waveguides as recently studied in Refs. [33–36]. It could be also interesting to generalize our model to include finite temperature, by changing the fluctuation relations of the electromagnetic field, and to consider many-body vdW forces.

ACKNOWLEDGMENTS

We thank M. Donaire, H. Haakh, J. Hemmerich, and P. W. Milonni for discussions. R.P. and L.R. gratefully acknowledge financial support by the Julian Schwinger Foundation and by MIUR. S.Y.B. and P.B. are grateful for support by the DFG (Grants No. BU 1803/3-1 and No. GRK 2079/1) and the Freiburg Institute for Advanced Studies (S.Y.B.).

APPENDIX

1. Perturbative expansion of the force operator

We consider the dynamics of an operator $\hat{\rho}(t)$, which is a superposition of operators $\hat{O}_n(t)$ with complex coefficients $f_n(t)$:

$$\hat{\rho}(t) = \sum_n f_n(t)\hat{O}_n(t) \quad (A1)$$

and we introduce a time limit which acts only on the operators:

$$\hat{\rho}(t)|_{t\to t_1} = \sum_n f_n(t)\hat{O}_n(t_1). \quad (A2)$$

The operators $\hat{O}_n(t)$ evolve dynamically according to the Heisenberg equations:

$$\partial_t \hat{O}_n(t) = \frac{1}{i\hbar}[\hat{O}_n(t),\hat{H}(t)], \quad (A3)$$

where $\hat{H}$ is the total Hamiltonian. This equation can be integrated from the initial time t_0 to a given time t:

$$\hat{O}_n(t) = \hat{O}_n(t_0) + \frac{1}{i\hbar}\int_{t_0}^{t} dt_1[\hat{O}_n(t_1),\hat{H}(t_1)]. \quad (A4)$$

This equation shows that the dynamical evolution of the operators $\hat{\rho}$ is

$$\hat{\rho}(t) = \hat{\rho}(t)\big|_{t\to t_0} + \frac{1}{i\hbar}\int_{t_0}^{t} dt_1\big[\hat{\rho}(t)\big|_{t\to t_1},\hat{H}(t_1)\big]. \quad (A5)$$

The vdW force operator acting on the atom A, due to the presence of other atoms, is

$$\hat{\mathbf{F}}_A(t) = \nabla[\hat{\mathbf{d}}_A \cdot \hat{\mathbf{E}}_{\not A}(\mathbf{r},t)]_{\mathbf{r}=\mathbf{r}_A}, \tag{A6}$$

where the field $\hat{\mathbf{E}}_{\not A}(\mathbf{r}_A,t)$ represents the total electric field, excluding the radiation reaction of atom A. Using Eq. (A5) we find the dynamical equation for the force:

$$\hat{\mathbf{F}}_A(t) = \hat{\mathbf{F}}_A(t)\big|_{t\to t_0} + \frac{1}{i\hbar}\int_{t_0}^{t} dt_1 \big[\hat{\mathbf{F}}_A(t)\big|_{t\to t_1}, \hat{H}(t_1)\big]. \tag{A7}$$

This equation can be reiterated considering now the dynamics of the commutator $[\hat{\mathbf{F}}_A(t)|_{t\to t_1}, \hat{H}(t_1)]$, which is a superposition of operators at the time t_1. Therefore, for weak coupling, we can construct a perturbative expansion $\hat{\mathbf{F}}_A(t)$ in terms of operators at the initial time t_0:

$$\begin{aligned}\hat{\mathbf{F}}_A(t) = \hat{\mathbf{F}}_A(t)\big|_{t\to t_0} &+ \frac{1}{i\hbar}\int_{t_0}^{t} dt_1 \big[\hat{\mathbf{F}}_A(t)\big|_{t\to t_1}, \hat{H}(t_1)\big]_{t_1\to t_0} \\ &+ \left(\frac{1}{i\hbar}\right)^2 \int_{t_0}^{t} dt_1 \int_{t_0}^{t_1} dt_2 \\ &\times \big[\big[\hat{\mathbf{F}}_A(t)\big|_{t\to t_1}, \hat{H}(t_1)\big]_{t_1\to t_2}, \hat{H}(t_2)\big]_{t_2\to t_0} + \cdots .\end{aligned} \tag{A8}$$

In our model the electric field and the flip operators of the two atoms are the dynamical variables of the system. Two different time scales are observed for the dynamical variables; there is a fast free dynamics and a much slower dynamics due to the interaction between the atoms and the field. For example, the free evolution of the flip operators is on time scales of $\omega_0^{-1} \approx 10^{-15}$ s, while the dynamics due to the interaction is on time scales of $\Gamma^{-1} \approx 10^{-9}$ s. We define new dynamical variables according the formulas:

$$\begin{aligned}\hat{\mathbf{E}}'(\mathbf{r},\omega,t) &= e^{i\omega t}\hat{\mathbf{E}}(\mathbf{r},\omega,t), \\ \hat{A}'_{mn}(t) &= f^A_{mn}(-t)\hat{A}_{mn}(t),\end{aligned} \tag{A9}$$

where

$$f^A_{mn}(t) = e^{[i\omega^A_{mn} - (\Gamma^A_n + \Gamma^A_m)/2]t}. \tag{A10}$$

The new dynamical variables change on the time scale of the interaction and have the following commutator with the total Hamiltonian [see Eqs. (4) and (5)]:

$$\begin{aligned}[\hat{\mathbf{E}}'_{\not A}(\mathbf{r},\omega,t), \hat{H}(t)] = &-\frac{\hbar\mu_0}{\pi} e^{i\omega t} \\ &\times \sum_{m,n} f^B_{mn}(t)\omega^2 \mathrm{Im}\mathbf{G}(\mathbf{r},\mathbf{r}_B,\omega)\cdot\mathbf{d}^B_{mn}\hat{B}'_{mn}(t),\end{aligned}$$

$$\begin{aligned}[\hat{A}'_{mn}(t), \hat{H}(t)] = -\int_0^\infty d\omega\, f^A_{mn}(-t)\big[&e^{-i\omega t}\hat{\mathbf{K}}^A_{mn}(t) \\ &\cdot \hat{\mathbf{E}}'_{\not A}(\mathbf{r}_A,\omega,t) + e^{i\omega t}\hat{\mathbf{E}}'^{\dagger}_{\not A}(\mathbf{r}_A,\omega,t) \\ &\cdot \hat{\mathbf{K}}^A_{mn}(t)\big],\end{aligned} \tag{A11}$$

where

$$\hat{\mathbf{K}}^A_{mn}(t) = \sum_k \big[\hat{A}'_{mk}(t) f^A_{mk}(t)\mathbf{d}^A_{nk} - \hat{A}'_{kn}(t) f^A_{kn}(t)\mathbf{d}^A_{km}\big] \tag{A12}$$

and a normal ordering prescription is used.

From Eqs. (A11) we see that the commutator between the Hamiltonian and a dynamical variable increases the number of electric dipole moments by one. Hence Eq. (A8) represents a perturbative expansion of the force with the dipole element as perturbative parameter. In particular, the electric vdW N-body force $\mathbf{F}_A(\mathbf{r}_A,\mathbf{r}_1,\ldots,\mathbf{r}_{N-1})$ acting on A due to the other atoms, with positions $\mathbf{r}_1,\ldots,\mathbf{r}_{N-1}$, contains $2N$ electric dipole matrix elements; this force results from the application of $2N-1$ commutators:

$$\begin{aligned}&\mathbf{F}_A(\mathbf{r}_A,\mathbf{r}_1,\ldots,\mathbf{r}_{N-1},t) \\ &= \left(\frac{1}{i\hbar}\right)^{2N-1} \int_{t_0}^{t} dt_1 \int_{t_0}^{t_1} dt_2 \cdots \int_{t_0}^{t_{2N-2}} dt_{2N-1} \\ &\quad\times \langle I|\big[\big[\cdots\big[\big[\hat{\mathbf{F}}_A(t)\big|_{t\to t_1}, \hat{H}(t_1)\big]_{t_1\to t_2}, \hat{H}(t_2)\big]_{t_2\to t_3}, \\ &\quad \ldots, \hat{H}(t_{2N-2})\big]_{t_{2N-2}\to t_{2N-1}}, \hat{H}(t_{2N-1})\big]_{t_{2N-1}\to t_0}|I\rangle,\end{aligned} \tag{A13}$$

where the expectation value is taken over the atomic+ field free state $|I\rangle$. This approximate solution to the coupled dynamics is equivalent to an iterative use of the atom-field equations, and it is valid for weak coupling between atoms and field.

The expectation value on free atomic and field states can be easily performed, since after the limit $t_{2N-1} \to t_0$ the resulting operators are evaluated at the same initial time t_0, which represents the time at which the electric field and the atoms are uncoupled.

2. van der Waals interaction between two atoms

We consider now the vdW interaction between two atoms. We suppose that the atomic states are incoherent superpositions of energy eigenstates $|n^A\rangle$ and $|l^B\rangle$ and the state of the field is the ground state.

In normal ordering, the force operator [see Eq. (A6)] can be expressed in terms of the new dynamical variables:

$$\hat{\mathbf{F}}_A(t) = \sum_{m,n}\int_0^\infty d\omega f^A_{mn}(t)e^{-i\omega t}\nabla\big\{\hat{A}'_{mn}(t)\mathbf{d}^A_{mn}\cdot\hat{\mathbf{E}}'_{\not A}(\mathbf{r},\omega,t)\big\}_{\mathbf{r}=\mathbf{r}_A} + \mathrm{H.c.} \tag{A14}$$

The two-body vdW interaction, which contains four electric dipole moments, involves three commutators:

$$\mathbf{F}_A(\mathbf{r}_A,\mathbf{r}_B,t) = \left(\frac{1}{i\hbar}\right)^3 \int_{t_0}^{t} dt_1 \int_{t_0}^{t_1} dt_2 \int_{t_0}^{t_2} dt_3 \big\langle\big[\big[\big[\hat{\mathbf{F}}_A(t)\big|_{t\to t_1}, \hat{H}(t_1)\big]_{t_1\to t_2}, \hat{H}(t_2)\big]_{t_2\to t_3}, \hat{H}(t_3)\big]_{t_3\to t_0}\big\rangle. \tag{A15}$$

With the help of Eqs. (A11), the commutators can be evaluated. For example, the application of one and two commutators gives

$$\begin{aligned}
\frac{1}{i\hbar}\big[\hat{\mathbf{F}}_A(t)\big|_{t\to t_1},\hat{H}(t_1)\big] &= \frac{i}{\hbar}\sum_{m,n}\int_0^\infty d\omega\int_0^\infty d\omega' e^{-i\omega t} f^A_{mn}(t-t_1)\nabla\big\{\big[e^{-i\omega' t_1}\hat{\mathbf{K}}^A_{mn}(t_1)\cdot\hat{\mathbf{E}}'_{\mathcal{A}}(\mathbf{r}_A,\omega',t_1)\\
&+ e^{i\omega' t_1}\hat{\mathbf{E}}'^{\dagger}_{\mathcal{A}}(\mathbf{r}_A,\omega',t_1)\cdot\hat{\mathbf{K}}^A_{mn}(t_1)\big]\mathbf{d}^A_{mn}\cdot\hat{\mathbf{E}}'_{\mathcal{A}}(\mathbf{r},\omega,t_1)\big\}_{\mathbf{r}=\mathbf{r}_A} + \frac{i\mu_0}{\pi}\sum_{m,n,r,s}\int_0^\infty d\omega\,\omega^2\\
&\times e^{-i\omega(t-t_1)} f^A_{mn}(t) f^B_{rs}(t_1)\nabla\big\{\hat{A}'_{mn}(t_1)\hat{B}'_{rs}(t_1)\mathbf{d}^A_{mn}\cdot\mathrm{Im}\,\mathbf{G}(\mathbf{r},\mathbf{r}_B,\omega)\cdot\mathbf{d}^B_{rs}\big\}_{\mathbf{r}=\mathbf{r}_A} + \mathrm{H.c.},\\
\left(\frac{1}{i\hbar}\right)^2\big[\big[\hat{\mathbf{F}}_A(t)\big|_{t\to t_1},\hat{H}(t_1)\big]_{t_1\to t_2},\hat{H}(t_2)\big] &= -\frac{\mu_0}{\pi\hbar}\sum_{m,n,r,s}\int_0^\infty d\omega\int_0^\infty d\omega' f^A_{mn}(t-t_1) f^B_{rs}(t_2)\\
&\times\nabla\big\{\omega'^2 e^{-i\omega t}\big[e^{-i\omega'(t_1-t_2)}\hat{\mathbf{K}}^A_{mn}(t_1)\big|_{t_1\to t_2}\cdot\mathrm{Im}\,\mathbf{G}(\mathbf{r}_A,\mathbf{r}_B,\omega')\cdot\mathbf{d}^B_{rs}\hat{B}'_{rs}(t_2)\\
&- e^{i\omega'(t_1-t_2)}\hat{B}'_{rs}(t_2)\mathbf{d}^B_{rs}\cdot\mathrm{Im}\,\mathbf{G}(\mathbf{r}_B,\mathbf{r}_A,\omega')\cdot\hat{\mathbf{K}}^A_{mn}(t_1)\big|_{t_1\to t_2}\big]\mathbf{d}^A_{mn}\cdot\hat{\mathbf{E}}'_{\mathcal{A}}(\mathbf{r},\omega,t_2)\\
&+\omega^2 e^{-i\omega(t-t_2)}\big[e^{-i\omega' t_1}\hat{\mathbf{K}}^A_{mn}(t_1)\big|_{t_1\to t_2}\cdot\hat{\mathbf{E}}'_{\mathcal{A}}(\mathbf{r}_A,\omega',t_2)\\
&+ e^{i\omega' t_1}\hat{\mathbf{E}}'^{\dagger}_{\mathcal{A}}(\mathbf{r}_A,\omega',t_2)\cdot\hat{\mathbf{K}}^A_{mn}(t_1)\big|_{t_1\to t_2}\big]\mathbf{d}^A_{mn}\cdot\mathrm{Im}\,\mathbf{G}(\mathbf{r},\mathbf{r}_B,\omega)\cdot\mathbf{d}^B_{rs}\hat{B}'_{rs}(t_2)\big\}_{\mathbf{r}=\mathbf{r}_A}\\
&-\frac{\mu_0}{\pi\hbar}\sum_{m,n,r,s}\int_0^\infty d\omega\int_0^\infty d\omega' e^{-i\omega(t-t_1)}\omega^2\nabla\big(\big\{f^A_{mn}(t-t_2) f^B_{rs}(t_1)\big[e^{-i\omega' t_2}\hat{\mathbf{K}}^A_{mn}(t_2)\\
&\cdot\hat{\mathbf{E}}'_{\mathcal{A}}(\mathbf{r}_A,\omega',t_2) + e^{i\omega' t_2}\hat{\mathbf{E}}'^{\dagger}_{\mathcal{A}}(\mathbf{r}_A,\omega',t_2)\cdot\hat{\mathbf{K}}^A_{mn}(t_2)\big]\hat{B}'_{rs}(t_2) + f^A_{mn}(t) f^B_{rs}(t_1-t_2)\hat{A}'_{mn}(t_2)\\
&\times\big[e^{-i\omega' t_2}\hat{\mathbf{K}}^B_{rs}(t_2)\cdot\hat{\mathbf{E}}'_{\mathcal{B}}(\mathbf{r}_B,\omega',t_2) + e^{i\omega' t_2}\hat{\mathbf{E}}'^{\dagger}_{\mathcal{B}}(\mathbf{r}_B,\omega',t_2)\cdot\hat{\mathbf{K}}^B_{rs}(t_2)\big]\big\}\\
&\times\mathbf{d}^A_{mn}\cdot\mathrm{Im}\,\mathbf{G}(\mathbf{r},\mathbf{r}_B,\omega)\cdot\mathbf{d}^B_{rs}\big)_{\mathbf{r}=\mathbf{r}_A} + \mathrm{H.c.}
\end{aligned}\tag{A16}$$

The commutators between $\hat{\mathbf{K}}_{mn}$ and the Hamiltonian have not been considered since they lead to higher-order corrections in the electric dipole $\mathbf{d}^A$ and $\mathbf{d}^B$.

We then evaluate the last commutator and take the expectation value on the atomic and field states. The thermal expectation value over the free-field variables can be performed with the help of the following fluctuation relations for zero temperature [10,28]:

$$\langle\hat{\mathbf{E}}^{(0)}(\mathbf{r},\omega,t)\hat{\mathbf{E}}^{(0)\dagger}(\mathbf{r}',\omega',t)\rangle = \frac{\hbar\mu_0}{\pi}\mathrm{Im}\mathbf{G}(\mathbf{r},\mathbf{r}',\omega)\omega^2\delta(\omega-\omega').\tag{A17}$$

After some algebra we obtain

$$\begin{aligned}
\mathbf{F}(\mathbf{r}_A,\mathbf{r}_B,t) &= -\frac{i\mu_0^2}{2\pi^2\hbar}\sum_{n,l}p^A_n(t)p^B_l(t)\sum_{k,p}\int_0^\infty d\omega\int_0^\infty d\omega'\omega^2\omega'^2\nabla_A\mathbf{d}^A_{nk}\cdot\mathrm{Im}\mathbf{G}(\mathbf{r}_A,\mathbf{r}_B,\omega)\cdot\mathbf{d}^B_{pl}\\
&\times\mathbf{d}^B_{lp}\cdot\mathrm{Im}\mathbf{G}(\mathbf{r}_B,\mathbf{r}_A,\omega')\cdot\mathbf{d}^A_{kn}\int_{t_0}^t dt_1\int_{t_0}^{t_1}dt_2\int_{t_0}^{t_2}dt_3\\
&\times\big\{e^{-i\omega(t-t_1)}\big[f^A_{nk}(t-t_2)-f^A_{kn}(t-t_2)\big]\big[e^{-i\omega'(t_2-t_3)}f^B_{lp}(t_1-t_3)-e^{i\omega'(t_2-t_3)}f^B_{pl}(t_1-t_3)\big]\\
&+e^{-i\omega(t-t_1)}\big[e^{-i\omega'(t_2-t_3)}f^A_{nk}(t-t_3)-e^{i\omega'(t_2-t_3)}f^A_{kn}(t-t_3)\big]\big[f^B_{lp}(t_1-t_2)-f^B_{pl}(t_1-t_2)\big]\\
&+e^{-i\omega(t-t_2)}\big[f^A_{nk}(t-t_1)-f^A_{kn}(t-t_1)\big]\big[e^{-i\omega'(t_1-t_3)}f^B_{lp}(t_2-t_3)-e^{i\omega'(t_1-t_3)}f^B_{pl}(t_2-t_3)\big]\\
&+e^{-i\omega(t-t_3)}[e^{-i\omega'(t_1-t_2)}-e^{i\omega'(t_1-t_2)}]\big[f^A_{nk}(t-t_1)-f^A_{kn}(t-t_1)\big]f^B_{lp}(t_2-t_3)\big\}+\mathrm{c.c.},
\end{aligned}\tag{A18}$$

where ∇_A is now applied to both Green's tensors (after exploiting their symmetry and introducing a factor $1/2$). The function f was defined in Eq. (A10) and $p^A_n(t)=\langle\hat{A}_{nn}(t)\rangle$ and $p^B_l(t)=\langle\hat{B}_{ll}(t)\rangle$ represent the atomic populations of the states $|n\rangle$ and $|l\rangle$. We have considered time-reversal symmetric systems, where $\mathbf{d}_{mn}$ is real ($\mathbf{d}_{mn}=\mathbf{d}_{nm}$), and reciprocal media [$\mathbf{G}^{\mathrm{T}}(\mathbf{r}_A,\mathbf{r}_B,\omega)=\mathbf{G}(\mathbf{r}_B,\mathbf{r}_A,\omega)$].

With the exception of resonant cavity-QED scenarios, we can assume the quantity $\omega^2\mathrm{Im}\mathbf{G}(\mathbf{r}_B,\mathbf{r}_A,\omega)$ to be sufficiently flat and to not exhibit any narrow peaks in the vicinity of any atomic frequency (weak coupling). For weak coupling, we may evaluate the time integral by means of the Markov approximation, extending the lower limit of the time integral to $t_0=-\infty$. The resulting integrals are not converging. In order to force the convergence we add an infinitesimal factor to the frequency ω, $\omega\to\omega-i\epsilon$, where $\epsilon>0$. Note that the opposite sign convention for this infinitesimal factor would lead to divergent integrals. Time integration leads to the energy denominators in Table I in the main text.

The frequency denominators can be combined:

$$
\begin{aligned}
1/D_2 + 1/D_7 + 1/D_{10} &= 1/(\omega^{(-)} - \omega')\big(\omega' + \omega_{kn}^{A(-)}\big)\big(\omega' + \omega_{pl}^{B(+)}\big),\\
1/D_3 + 1/D_6 + 1/D_{11} &= 1/(\omega^{(-)} + \omega')\big(\omega' + \omega_{kn}^{A(+)}\big)\big(\omega' + \omega_{pl}^{B(-)}\big),\\
1/D_1 + 1/D_9 &= \frac{1}{(\omega^{(-)} + \omega')\big(\omega_{kn}^{A(-)} + \omega_{pl}^{B(-)}\big)}\left(\frac{1}{\omega^{(-)} + \omega_{kn}^{A(-)}} + \frac{1}{\omega' + \omega_{pl}^{B(-)}}\right),\\
1/D_4 + 1/D_{12} &= \frac{1}{(\omega' - \omega^{(-)})\big(\omega_{kn}^{A(+)} + \omega_{pl}^{B(+)}\big)}\left(\frac{1}{\omega^{(-)} - \omega_{kn}^{A(+)}} - \frac{1}{\omega' + \omega_{pl}^{B(+)}}\right),\\
1/D_5 &= \frac{1}{(\omega^{(-)} - \omega')\big(\omega_{kn}^{A(-)} + \omega_{pl}^{B(-)}\big)}\left(\frac{1}{\omega' + \omega_{kn}^{A(-)}} - \frac{1}{\omega^{(-)} + \omega_{kn}^{A(-)}}\right),\\
1/D_8 &= \frac{1}{(\omega^{(-)} + \omega')\big(\omega_{kn}^{A(+)} + \omega_{pl}^{B(+)}\big)}\left(\frac{1}{\omega' + \omega_{kn}^{A(+)}} + \frac{1}{\omega^{(-)} - \omega_{kn}^{A(+)}}\right),
\end{aligned}
\tag{A19}
$$

which implies

$$
\sum_{i=1}^{16}\frac{1}{D_i} + \text{c.c.} = f_1(\omega')\left(\frac{1}{\omega^{(-)} + \omega'} + \frac{1}{\omega^{(+)} - \omega'}\right) + f_2(\omega^{(-)})\left(\frac{1}{\omega' + \omega^{(-)}} + \frac{1}{\omega' - \omega^{(-)}}\right) + \text{c.c.},
\tag{A20}
$$

where we have defined the following functions:

$$
\begin{aligned}
f_1(\xi) &= \frac{1}{\big(\omega_{kn}^{A(+)} + \omega_{pl}^{B(+)}\big)\big(\xi + \omega_{kn}^{A(+)}\big)} + \frac{1}{\big(\omega_{kn}^{A(-)} + \omega_{pl}^{B(-)}\big)\big(\xi + \omega_{pl}^{B(-)}\big)} + \frac{1}{\big(\xi + \omega_{kn}^{A(+)}\big)\big(\xi + \omega_{pl}^{B(-)}\big)},\\
f_2(\xi) &= \frac{1}{\big(\omega_{kn}^{A(+)} + \omega_{pl}^{B(+)}\big)\big(\xi - \omega_{kn}^{A(+)}\big)} + \frac{1}{\big(\omega_{kn}^{A(-)} + \omega_{pl}^{B(-)}\big)\big(\xi + \omega_{kn}^{A(-)}\big)} + \left(\frac{1}{\xi + \omega_{kn}^{A(-)}} - \frac{1}{\xi - \omega_{kn}^{A(+)}}\right)\frac{1}{\xi + \omega_{pl}^{B(-)}}
\end{aligned}
\tag{A21}
$$

and $\omega_{kn}^{A(\pm)} = \omega_{kn}^{A} \pm i(\Gamma_k^A + \Gamma_n^A)/2$, $\omega_{pl}^{B(\pm)} = \omega_{pl}^{B} \pm i(\Gamma_p^B + \Gamma_l^B)/2$, and $\omega^{(\pm)} = \omega \pm i\epsilon$.

For the first term in Eq. (A20) we integrate over ω and for the second term we integrate over ω'. We use the identity $\text{Im}\mathbf{G} = (\mathbf{G} - \mathbf{G}^*)/2i$ and the Schwarz reflection principle for the Green tensor:

$$
\int_0^\infty d\omega'\omega'^2\left(\frac{1}{\omega' + \omega^{(-)}} + \frac{1}{\omega' - \omega^{(-)}}\right)\text{Im}\mathbf{G}(\mathbf{r}_A,\mathbf{r}_B,\omega') = \frac{1}{2i}\int_{-\infty}^\infty d\omega'\omega'^2\left(\frac{1}{\omega' + \omega^{(-)}} + \frac{1}{\omega' - \omega^{(-)}}\right)\mathbf{G}(\mathbf{r}_A,\mathbf{r}_B,\omega').
\tag{A22}
$$

The Green's tensor is analytic in the upper half of the complex plane, including the real axis, and it is also finite at the origin. We close the path with an infinitely large half-circle in the upper complex half-plane and take the residuum inside the path. The integral along the infinite semicircle vanishes for $\mathbf{r}_A \neq \mathbf{r}_B$ because

$$
\lim_{|\omega|\to+\infty}\omega^2\,\mathbf{G}(\mathbf{r}_A,\mathbf{r}_B,\omega)\big|_{\mathbf{r}_A\neq\mathbf{r}_B} = 0.
\tag{A23}
$$

We thus find

$$
\int_0^\infty d\omega'\omega'^2\left(\frac{1}{\omega' + \omega^{(-)}} + \frac{1}{\omega' - \omega^{(-)}}\right)\text{Im}\mathbf{G}(\mathbf{r}_A,\mathbf{r}_B,\omega') = \pi\omega^2\mathbf{G}(\mathbf{r}_A,\mathbf{r}_B,-\omega).
\tag{A24}
$$

The total force can be expressed as the sum of two terms:

$$
\begin{aligned}
\mathbf{F}_A(\mathbf{r}_A,\mathbf{r}_B,t) &= \mathbf{F}_A^1(\mathbf{r}_A,\mathbf{r}_B,t) + \mathbf{F}_A^2(\mathbf{r}_A,\mathbf{r}_B,t),\\
\mathbf{F}_A^1(\mathbf{r}_A,\mathbf{r}_B,t) &= \frac{\mu_0^2}{2\pi\hbar}\sum_{n,l}p_n^A(t)p_l^B(t)\sum_{k,p}\int_0^\infty d\omega\,\omega^4\nabla_A\text{Im}\big\{\big[\mathbf{d}_{nk}^A\cdot\mathbf{G}(\mathbf{r}_A,\mathbf{r}_B,\omega)\cdot\mathbf{d}_{pl}^B\big]^2 g_1(\omega)\big\},\\
\mathbf{F}_A^2(\mathbf{r}_A,\mathbf{r}_B,t) &= \frac{\mu_0^2}{2\pi\hbar}\sum_{n,l}p_n^A(t)p_l^B(t)\sum_{k,p}\int_0^\infty d\omega\,\omega^4\nabla_A\big\{\big|\mathbf{d}_{nk}^A\cdot\mathbf{G}(\mathbf{r}_A,\mathbf{r}_B,\omega)\cdot\mathbf{d}_{pl}^B\big|^2 g_2(\omega)\big\},
\end{aligned}
\tag{A25}
$$

where

$$g_1(\omega) = f_1^*(\omega) + f_2^*(\omega) = \frac{1}{\omega + \omega_{pl}^{B(+)}}\left(\frac{1}{\omega + \omega_{kn}^{A(+)}} + \frac{1}{\omega + \omega_{kn}^{A(-)}} - \frac{1}{\omega - \omega_{kn}^{A(-)}}\right)$$
$$+ \frac{1}{\omega_{kn}^{A(+)} + \omega_{pl}^{B(+)}}\left(\frac{1}{\omega + \omega_{kn}^{A(+)}} + \frac{1}{\omega + \omega_{pl}^{B(+)}}\right) + \frac{1}{\omega_{kn}^{A(-)} + \omega_{pl}^{B(-)}}\left(\frac{1}{\omega + \omega_{kn}^{A(-)}} + \frac{1}{\omega - \omega_{kn}^{A(-)}}\right) \tag{A26}$$

and

$$g_2(\omega) = \mathrm{Im}[f_1(\omega) + f_2(\omega)] = 2\ \mathrm{Re}\left[\frac{1}{\omega_{kn}^{A(+)} + \omega} + \frac{1}{\omega_{kn}^{A(+)} - \omega}\right]\mathrm{Im}\frac{1}{\omega + \omega_{pl}^{B(-)}}. \tag{A27}$$

We consider then the limiting case of vanishing linewidths:

$$\varepsilon_A = \left(\Gamma_n^A + \Gamma_k^A\right)/2 \to 0^+, \quad \varepsilon_B = \left(\Gamma_l^A + \Gamma_p^B\right)/2 \to 0^+. \tag{A28}$$

In this limit the function g_1 can be simplified:

$$\lim_{\epsilon_{A,B}\to 0^+} g_1(\omega) = \frac{4\left(\omega - \omega_{kn}^A\right)\left(\omega + \omega_{kn}^A\right)}{\left[\left(\omega + \omega_{kn}^A\right)^2 + \varepsilon_A^2\right]\left(\omega - \omega_{kn}^A + i\varepsilon_A\right)}\frac{\left(\omega + \omega_{kn}^A + \omega_{pl}^B\right)}{\left(\omega + \omega_{pl}^B + i\varepsilon_B\right)\left(\omega_{kn}^A + \omega_{pl}^B\right)}. \tag{A29}$$

Using the property $\frac{1}{x \pm i\varepsilon} = \mathcal{P}\frac{1}{x} \mp i\pi\delta(x)$, where $\mathcal{P}$ is the principal value, we can also simplify g_2:

$$g_2(\omega) = 2\pi\ \mathrm{Re}\left[\frac{1}{\omega_{kn}^{A(+)} + \omega} + \frac{1}{\omega_{kn}^{A(+)} - \omega}\right]\delta\left(\omega - \omega_{lp}^B\right). \tag{A30}$$

With these results, after performing a Wick rotation on the imaginary axis we find the following nonresonant and resonant contributions to the $\mathbf{F}_A^1$:

$$\mathbf{F}_A^1(\mathbf{r}_A,\mathbf{r}_B,t) = \frac{\mu_0^2}{2\pi\hbar}\sum_{n,l} p_n^A(t)p_l^B(t)\sum_{k,p}\int_0^\infty d\xi\,\xi^4\frac{g_1(i\xi) + g_1^*(-i\xi)}{2}\nabla_A\left\{\left[\mathbf{d}_{nk}^A\cdot\mathbf{G}(\mathbf{r}_A,\mathbf{r}_B,i\xi)\cdot\mathbf{d}_{pl}^B\right]^2\right\}$$
$$+ \frac{\mu_0^2}{2\hbar}\sum_{n,l} p_n^A(t)p_l^B(t)\sum_{k,p}\nabla_A\left(\mathrm{Res}_1\left\{g_1(\omega)\omega^4\left[\mathbf{d}_{nk}^A\cdot\mathbf{G}(\mathbf{r}_A,\mathbf{r}_B,\omega)\cdot\mathbf{d}_{pl}^B\right]^2\right\}\right.$$
$$\left. - \mathrm{Res}_2\left\{g_1^*(-\omega)\omega^4\left[\mathbf{d}_{nk}^A\cdot\mathbf{G}(\mathbf{r}_A,\mathbf{r}_B,\omega)\cdot\mathbf{d}_{pl}^B\right]^2\right\}\right), \tag{A31}$$

where Res_1 indicates the sum of the residues in the first quadrant and Res_2 the sum of the residues in the second quadrant. Similarly, $\mathbf{F}_A^2$ reduces to

$$\mathbf{F}_A^2(\mathbf{r}_A,\mathbf{r}_B,t) = \mu_0^2\sum_l p_l^B(t)\sum_{p<l}\left(\omega_{lp}^B\right)^4\nabla_A\left\{\mathbf{d}_{lp}^B\cdot\mathbf{G}\left(\mathbf{r}_B,\mathbf{r}_A,\omega_{lp}^B\right)\cdot\boldsymbol{\alpha}_A\left(\omega_{lp}^B\right)\cdot\mathbf{G}^*\left(\mathbf{r}_A,\mathbf{r}_B,\omega_{lp}^B\right)\cdot\mathbf{d}_{pl}^B\right\}, \tag{A32}$$

where $\boldsymbol{\alpha}_A$ is the polarizability of the excited atom A. The sum of $\mathbf{F}_A^1$ and $\mathbf{F}_A^2$ gives the nonresonant and resonant contributions of the total vdW force; see Eqs. (9) and (11).

[1] H. B. G. Casimir, Proc. K. Ned. Akad. Wet. **51**, 793 (1948).
[2] H. B. G. Casimir and D. Polder, Phys. Rev. **73**, 360 (1948).
[3] T. Kihara, *Intermolecular Forces* (John Wiley & Sons, New York, 1977).
[4] S. Nir, Prog. Surf. Sci. **8**, 1 (1976).
[5] J. de Pater and J. J. Lissauer, *Planetary Sciences* (Cambridge University Press, Cambridge, UK, 2010).
[6] J. Preto, M. Pettini, and J. A. Tuszynski, Phys. Rev. E **91**, 052710 (2015).
[7] F. M. Serry, D. Walliser, and G. J. Maclay, J. Appl. Phys. **84**, 2501 (1998).
[8] M. A. Wilson, P. Bushev, J. Eschner, F. Schmidt-Kaler, C. Becher, R. Blatt, and U. Dorner, Phys. Rev. Lett. **91**, 213602 (2003).
[9] P. Bushev, A. Wilson, J. Eschner, C. Raab, F. Schmidt-Kaler, C. Becher, and R. Blatt, Phys. Rev. Lett. **92**, 223602 (2004).
[10] S. Y. Buhmann, *Dispersion Forces I* (Springer, Heidelberg, 2012).
[11] E. A. Power and T. Thirunamachandran, Phys. Rev. A **47**, 2539 (1993).
[12] L. Gomberoff, R. R. McLone, and E. A. Power, J. Chem. Phys. **44**, 4148 (1966).
[13] R. R. McLone and E. A. Power, Proc. R. Soc. London A **286**, 573 (1965).
[14] M. R. Philpott, Proc. Phys. Soc. London **87**, 619 (1966).
[15] E. A. Power and T. Thirunamachandran, Phys. Rev. A **51**, 3660 (1995).
[16] E. A. Power and T. Thirunamachandran, Chem. Phys. **171**, 1 (1993).

[17] Y. Sherkunov, Phys. Rev. A **75**, 012705 (2007).
[18] M. Donaire, R. Guérout, and A. Lambrecht, Phys. Rev. Lett. **115**, 033201 (2015).
[19] P. R. Berman, Phys. Rev. A **91**, 042127 (2015).
[20] L. Rizzuto, R. Passante, and F. Persico, Phys. Rev. A **70**, 012107 (2004).
[21] H. R. Haakh, J. Schiefele, and C. Henkel, Int. J. Mod. Phys.: Conf. Ser. **14**, 347 (2012).
[22] P. W. Milonni and S. M. H. Rafsanjani, Phys. Rev. A **92**, 062711 (2015).
[23] M. Donaire, Phys. Rev. A **93**, 052706 (2016).
[24] M. Donaire, arXiv:1604.07071.
[25] S. Scheel, S. Y. Buhmann, C. Clausen, and P. Schneeweiss, Phys. Rev. A **92**, 043819 (2015).
[26] H. Safari and M. R. Karimpour, Phys. Rev. Lett. **114**, 013201 (2015).
[27] S. Y. Buhmann and D. G. Welsch, Prog. Quantum Electron. **31**, 51 (2007).
[28] S. Y. Buhmann, *Dispersion Forces II* (Springer, Heidelberg, 2013).
[29] L. Knöll, S. Scheel, and D.-G. Welsch, in *Coherence and Statistics of Photons and Atoms*, edited by J. Peiřna (Wiley, New York, 2001), p. 1.
[30] J. R. Ackerhalt, P. L. Knight, and J. H. Eberly, Phys. Rev. Lett. **30**, 456 (1973).
[31] D. A. Steck, Rubidium 87D Line Data, Cesium D Line Data, http://steck.us/alkalidata.
[32] S. Y. Buhmann and D.-G. Welsch, Appl. Phys. B **82**, 189 (2006).
[33] E. Shahmoon and G. Kurizki, Phys. Rev. A **87**, 062105 (2013).
[34] E. Shahmoon, I. Mazets, and G. Kurizki, Proc. Natl. Acad. Sci. **111**, 10485 (2013).
[35] H. R. Haakh and S. Scheel, Phys. Rev. A **91**, 052707 (2015).
[36] R. de Melo e Souza, W. J. M. Kort-Kamp, F. S. S. Rosa, and C. Farina, Phys. Rev. A **91**, 052708 (2015).

RAPID COMMUNICATIONS

PHYSICAL REVIEW A **80**, 051801(R) (2009)

Impact of amplifying media on the Casimir force

Agnes Sambale,[1,*] Stefan Yoshi Buhmann,[2] Ho Trung Dung,[3] and Dirk-Gunnar Welsch[1]

[1]*Theoretisch-Physikalisches Institut, Friedrich-Schiller-Universität Jena, Max-Wien-Platz 1, D-07743 Jena, Germany*

[2]*Quantum Optics and Laser Science, Blackett Laboratory, Imperial College London, Prince Consort Road, London SW7 2BW, United Kingdom*

[3]*Institute of Physics, Academy of Sciences and Technology, 1 Mac Dinh Chi Street, District 1, Ho Chi Minh City, Vietnam*

(Received 10 February 2009; published 9 November 2009)

On the basis of macroscopic quantum electrodynamics, a theory of Casimir forces in the presence of linearly amplifying bodies is presented which provides a consistent framework for studying the effect of, e.g., amplifying left-handed metamaterials on dispersion forces. It is shown that the force can be given in terms of the classical Green tensor and that it can be decomposed into a resonant component associated with emission processes and an off-resonant Lifshitz-type component. We explicitly demonstrate that our theory extends additive approaches beyond the dilute-gas limit.

DOI: 10.1103/PhysRevA.80.051801 PACS number(s): 42.50.Wk, 12.20.−m, 34.35.+a, 42.50.Nn

I. INTRODUCTION

Among the vast body of literature related to Casimir forces [1–4] there is an almost complete lack of studies concerned with the influence of amplifying media. This is in stark contrast to the fact that Casimir forces between amplifying bodies may lead to far-reaching applications. To name just two examples, amplifying bodies may hold the key to enhancing the impact of novel (meta)material properties on dispersion forces and to realizing repulsive Casimir forces.

The problem of dispersion forces in the presence of metamaterials has recently attracted a lot of attention [5–11]. However, passive metamaterials suffer from high absorption which restricts desired metamaterial properties such as lefthandedness [12,13] to a narrow spectral bandwidth [14]; this may reduce or completely inhibit an influence of such properties on dispersion forces. It has been suggested that the influence of absorption can be mitigated via introducing active media [14]. In practice, gain may be introduced in a medium by optical parametric pumping [15] or quantum cascade lasing techniques [16,17]. The potential of amplifying bodies as a means of realizing repulsive Casimir forces has been pointed out recently [18,19]. It is already manifest in the Casimir-Polder (CP) forces acting on individual excited atoms [10,20–22]. Repulsive dispersion forces can help to suppress the unwanted phenomenon of stiction and allows for new classes of nanodevices [23]. Note that the repulsive Casimir forces recently measured in Refs. [24,25] require the interacting bodies to be embedded in medium. This is not necessary when realizing repulsive forces on the basis of amplification.

A recent calculation of Casimir forces on amplifying bodies [19] was based on the assumption that the well-known Lifshitz-type formula for the Casimir force as an integral over imaginary frequencies applies without change to amplifying media—an approach which neglects excited-state emission processes typical of amplification. As an alternative, the Casimir force between two dilute samples of excited atoms has been studied microscopically by summing over two-atom interactions [18]. Such an approach is limited to sufficiently dilute media, whereas a theory nonlinear in the magnetoelectric properties is indispensable in many applications such as superlens scenarios [26] or antistiction tools [27].

In this Rapid Communication, we present a macroscopic nonperturbative theory of Casimir forces on amplifying bodies that presents a consistent generalization of additive descriptions based on dispersion forces on atoms. We establish the consistency of our macroscopic body-body force with the theoretically [20,21] and experimentally [22] well-understood force between an excited atom and a body and show that relevant processes such as emission by the bodies are fully taken into account. We begin with an outline of the underlying quantisation scheme [28], which is an extension of macroscopic quantum electrodynamics (QED) to amplifying media, and then derive the Casimir force on an amplifying, polarisable body of arbitrary shape. Finally, contact to CP forces is established by applying the general formula to the case of a weakly polarisable medium.

II. QUANTIZATION SCHEME

Consider an arrangement of polarisable bodies whose linear, local and isotropic response is described by a spatially varying complex permittivity $\varepsilon(\mathbf{r},\omega)$ that fulfils the Kramers-Kronig relations. We allow for bodies that are (linearly) amplifying in some frequency range [Im $\varepsilon(\mathbf{r},\omega)=\varepsilon_I(\mathbf{r},\omega)<0$], assuming the amplifying medium to be pumped to a quasistationary excited state (for details, see [28]). Note that this inversion-type excitation is fundamentally different from thermal excitations. In particular, the amplifying bodies are explicitly not at (thermal) equilibrium with their environment.

The quantised electric field can be given as the solution to the inhomogeneous Helmholtz equation

$$[\boldsymbol{\nabla}\times\boldsymbol{\nabla}\times-\omega^2/c^2\varepsilon(\mathbf{r},\omega)]\underline{\hat{\mathbf{E}}}(\mathbf{r},\omega)=i\mu_0\omega\underline{\hat{\mathbf{j}}}_N(\mathbf{r},\omega), \quad (1)$$

$[\hat{\mathbf{O}}(\mathbf{r})=\int_0^\infty d\omega\hat{\mathbf{Q}}(\mathbf{r},\omega)+\text{H.c.}]$ according to

*agnes.sambale@uni-jena.de

$$\hat{\underline{\mathbf{E}}}(\mathbf{r},\omega) = i\omega\mu_0 \int d^3r' \mathbf{G}(\mathbf{r},\mathbf{r}',\omega)\cdot\hat{\underline{\mathbf{j}}}_N(\mathbf{r}',\omega), \tag{2}$$

where the classical Green tensor obeys the equation

$$[\boldsymbol{\nabla}\times\boldsymbol{\nabla}\times - \omega^2/c^2]\mathbf{G}(\mathbf{r},\mathbf{r}',\omega) = \boldsymbol{\delta}(\mathbf{r}-\mathbf{r}') + \omega^2/c^2[\varepsilon(\mathbf{r},\omega)-1]\mathbf{G}(\mathbf{r},\mathbf{r}',\omega) \tag{3}$$

together with the boundary condition at infinity. By exchanging the roles of creation and annihilation operators in the amplifying space and frequency regime [29], the noise current density can be given as

$$\hat{\underline{\mathbf{j}}}_N(\mathbf{r},\omega) = \omega\sqrt{\hbar\varepsilon_0\pi^{-1}|\varepsilon_I(\mathbf{r},\omega)|} \times\{\Theta[\varepsilon_I(\mathbf{r},\omega)]\hat{\mathbf{f}}(\mathbf{r},\omega) + \Theta[-\varepsilon_I(\mathbf{r},\omega)]\hat{\mathbf{f}}^\dagger(\mathbf{r},\omega)\} \tag{4}$$

[Θ: unit step function, $\Theta(0)\equiv 1$]. The dynamical variables $\hat{\mathbf{f}}(\mathbf{r},\omega)$ as introduced in Eq. (4) obey bosonic commutation relations such that the equal-time commutation relation characteristic of the electromagnetic field holds, $[\hat{\mathbf{E}}(\mathbf{r}),\hat{\mathbf{B}}(\mathbf{r}')] = i\hbar\varepsilon_0^{-1}\boldsymbol{\nabla}\times\boldsymbol{\delta}(\mathbf{r}-\mathbf{r}')$, where the electric and induction fields are given by Eq. (2) and

$$\hat{\underline{\mathbf{B}}}(\mathbf{r},\omega) = \mu_0\int d^3r'\boldsymbol{\nabla}\times\mathbf{G}(\mathbf{r},\mathbf{r}',\omega)\cdot\hat{\underline{\mathbf{j}}}_N(\mathbf{r}',\omega) \tag{5}$$

respectively. The vacuum state $|\{0\}\rangle$ of the electromagnetic field and the partially amplifying electric body is defined by $\hat{\mathbf{f}}(\mathbf{r},\omega)|\{0\}\rangle = \mathbf{0}\,\forall\,\mathbf{r},\omega$. The quantization procedure implies that the Hamiltonian $\hat{H} = \hat{H}_+ + \hat{H}_- = \int d^3r\int_0^\infty d\omega\hbar\omega\{\Theta[\varepsilon_I(\mathbf{r},\omega)] - \Theta[-\varepsilon_I(\mathbf{r},\omega)]\}\hat{\mathbf{f}}^\dagger(\mathbf{r},\omega)\cdot\hat{\mathbf{f}}(\mathbf{r},\omega)$ generates the correct Maxwell equations via the Heisenberg equations of motion.

III. CALCULATION OF THE CASIMIR FORCE

The Casimir force acting on a partially amplifying body of volume V in the presence of other bodies outside V can be identified as the average Lorentz force [30]

$$\mathbf{F} = \int_V d^3r\langle\hat{\rho}(\mathbf{r})\hat{\mathbf{E}}(\mathbf{r}') + \hat{\mathbf{j}}(\mathbf{r})\times\hat{\mathbf{B}}(\mathbf{r}')\rangle_{\mathbf{r}'\to\mathbf{r}} \tag{6}$$

on the body's internal charge and current densities

$$\hat{\underline{\rho}}(\mathbf{r},\omega) = \frac{i\omega}{c^2}\int d^3r'\,\boldsymbol{\nabla}\cdot\mathbf{G}(\mathbf{r},\mathbf{r}',\omega)\cdot\hat{\underline{\mathbf{j}}}_N(\mathbf{r}',\omega), \tag{7}$$

$$\hat{\underline{\mathbf{j}}}(\mathbf{r},\omega) = \left(\boldsymbol{\nabla}\times\boldsymbol{\nabla}\times - \frac{\omega^2}{c^2}\right)\int d^3r'\mathbf{G}(\mathbf{r},\mathbf{r}',\omega)\cdot\hat{\underline{\mathbf{j}}}_N(\mathbf{r}',\omega). \tag{8}$$

Note that the coincidence limit $\mathbf{r}'\to\mathbf{r}$ has to be performed such that (divergent) self-forces are discarded.

On using Eq. (4), the bosonic commutation relations for $\hat{\mathbf{f}}$, $\hat{\mathbf{f}}^\dagger$, and the definition of the vacuum state, we find the following nonvanishing expectation values:

$$\langle\hat{\underline{\mathbf{j}}}_N(\mathbf{r},\omega)\hat{\underline{\mathbf{j}}}_N^\dagger(\mathbf{r},\omega')\rangle = \hbar\omega^2\varepsilon_0\pi^{-1}\delta(\omega-\omega')\varepsilon_I(\mathbf{r},\omega) \times\boldsymbol{\delta}(\mathbf{r}-\mathbf{r}')\Theta[\varepsilon_I(\mathbf{r},\omega)], \tag{9}$$

$$\langle\hat{\underline{\mathbf{j}}}_N^\dagger(\mathbf{r},\omega)\hat{\underline{\mathbf{j}}}_N(\mathbf{r}',\omega')\rangle = -\hbar\omega^2\varepsilon_0\pi^{-1}\delta(\omega-\omega')\varepsilon_I(\mathbf{r},\omega) \times\boldsymbol{\delta}(\mathbf{r}-\mathbf{r}')\Theta[-\varepsilon_I(\mathbf{r},\omega)]. \tag{10}$$

We evaluate the force by combining Eqs. (2) and (5)–(10) and writing $\mathbf{a}\times\mathbf{b} = -\mathrm{Tr}(\mathbf{I}\times\mathbf{a}\otimes\mathbf{b})([\mathrm{Tr}\,\overline{\mathbf{T}}]_i = T_{kik})$ for the $\hat{\mathbf{j}}\times\hat{\mathbf{B}}$ term. Eliminating $\Theta[\varepsilon_I(\mathbf{s},\omega)]$ according to $\Theta[\varepsilon_I(\mathbf{s},\omega)] = 1-\Theta[-\varepsilon_I(\mathbf{s},\omega)]$, those spatial integrals not depending on $\Theta[-\varepsilon_I(\mathbf{s},\omega)]$ can be performed via

$$\frac{\omega^2}{c^2}\int d^3s\varepsilon_I(\mathbf{s},\omega)\mathbf{G}(\mathbf{r},\mathbf{s},\omega)\cdot\mathbf{G}^*(\mathbf{s},\mathbf{r}',\omega) = \mathrm{Im}\,\mathbf{G}(\mathbf{r},\mathbf{r}',\omega), \tag{11}$$

so the Casimir force can be given by $\mathbf{F} = \mathbf{F}^{\mathrm{r}} + \mathbf{F}^{\mathrm{nr}}$ with

$$\mathbf{F}^{\mathrm{nr}} = \frac{\hbar}{\pi}\int_0^\infty d\omega\int_V d^3r\left\{\frac{\omega^2}{c^2}\boldsymbol{\nabla}\cdot\mathrm{Im}\,\mathbf{G}(\mathbf{r},\mathbf{r}',\omega) + \mathrm{Tr}\left[\mathbf{I}\times\left(\boldsymbol{\nabla}\times\boldsymbol{\nabla}\times - \frac{\omega^2}{c^2}\right)[\mathrm{Im}\,\mathbf{G}(\mathbf{r},\mathbf{r}',\omega)]\times\overleftarrow{\boldsymbol{\nabla}}'\right]\right\}_{\mathbf{r}'\to\mathbf{r}} \tag{12}$$

and

$$\mathbf{F}^{\mathrm{r}} = -\frac{2\hbar}{\pi c^2}\int_V d^3r\int_0^\infty d\omega\omega^2\int d^3s\varepsilon_I(\mathbf{s},\omega)\Theta[-\varepsilon_I(\mathbf{s},\omega)] \times\mathrm{Re}\{\omega^2/c^2\,\boldsymbol{\nabla}\cdot\mathbf{G}(\mathbf{r},\mathbf{s},\omega)\cdot\mathbf{G}^*(\mathbf{s},\mathbf{r}',\omega) + \mathrm{Tr}[\mathbf{I}\times(\boldsymbol{\nabla}\times\boldsymbol{\nabla}\times - \omega^2/c^2)\mathbf{G}(\mathbf{r},\mathbf{s},\omega) \cdot\mathbf{G}^*(\mathbf{s},\mathbf{r}',\omega)\times\overleftarrow{\boldsymbol{\nabla}}']\}_{\mathbf{r}'\to\mathbf{r}}. \tag{13}$$

Equations (12) and (13) represent general expressions for the Casimir force acting on a linearly polarizable body of arbitrary shape and material in an arbitrary environment of additional bodies or media, where any of the bodies may be amplifying. The term $\mathbf{F}^{\mathrm{nr}}$ is a purely nonresonant Lifshitz-type contribution to the force. It can be rewritten as an integral over purely imaginary frequencies $\omega = i\xi$ and has exactly the same form as for purely absorbing bodies. In Ref. [19], the nonresonant term $\mathbf{F}^{\mathrm{nr}}$ is identified with the total Casimir force and it is shown that $\mathbf{F}^{\mathrm{nr}}$ may become repulsive in the presence of amplifying media as a consequence of the property $\varepsilon(i\xi)\leq 1$. The resonant term $\mathbf{F}^{\mathrm{r}}$ has never been given before. It only arises in the presence of amplifying bodies, in which case it can dominate the total Casimir force. As evident from the factor $\Theta[-\varepsilon_I(\mathbf{s},\omega)]$, the force component $\mathbf{F}^{\mathrm{r}}$ is associated with emission processes [the emission spectrum being related to $-\varepsilon_I(\mathbf{s},\omega)$].

IV. CONTACT TO CASIMIR-POLDER FORCES

We will next establish a relation between the Casimir force $\mathbf{F} = \mathbf{F}^{\mathrm{r}} + \mathbf{F}^{\mathrm{nr}}$ [with $\mathbf{F}^{\mathrm{r}}$ and $\mathbf{F}^{\mathrm{nr}}$ being given by Eqs. (12) and (13), respectively] and the well-understood CP force on excited atoms. In this way, we will be able to substantiate the role of emission mentioned above. To that end, we consider the Casimir force on an optically dilute amplifying body of volume V placed in a free-space region in an environment of purely absorbing bodies. We follow the procedure outlined in Ref. [30] for an absorbing dielectric body.

RAPID COMMUNICATIONS

We begin with the nonresonant force component $\mathbf{F}^{\mathrm{nr}}$, Eq. (12), and explicitly introduce the electric susceptibility $\chi(\mathbf{r},\omega)=\varepsilon(\mathbf{r},\omega)-1(\mathbf{r}\in V)$ of the body by invoking the relations,

$$\left(\boldsymbol{\nabla}\times\boldsymbol{\nabla}\times-\frac{\omega^2}{c^2}\right)\mathrm{Im}\,\mathbf{G}(\mathbf{r},\mathbf{r}',\omega)=\frac{\omega^2}{c^2}\mathrm{Im}[\chi(\mathbf{r},\omega)\mathbf{G}(\mathbf{r},\mathbf{r}',\omega)], \tag{14}$$

$$\boldsymbol{\nabla}\cdot\mathrm{Im}\,\mathbf{G}(\mathbf{r},\mathbf{r}',\omega)=-\mathrm{Im}[\boldsymbol{\nabla}\cdot\chi(\mathbf{r},\omega)\mathbf{G}(\mathbf{r},\mathbf{r}',\omega)], \tag{15}$$

which follow from Eq. (3). Expanding the resulting expression for $\mathbf{F}^{\mathrm{nr}}$ via $\mathrm{Tr}[\mathbf{I}\times\mathbf{G}\times\overleftarrow{\boldsymbol{\nabla}}']=\boldsymbol{\nabla}'\,\mathrm{Tr}\,\mathbf{G}-\boldsymbol{\nabla}'\cdot\mathbf{G}$ and exploiting the fact that terms involving a total divergence can be converted to a surface integral that vanishes for a body in free space, one obtains

$$\mathbf{F}^{\mathrm{nr}}=\frac{\hbar}{2\pi}\int_V d^3r\int_0^\infty d\omega\frac{\omega^2}{c^2}\mathrm{Im}[\chi(\mathbf{r},\omega)\,\boldsymbol{\nabla}\,\mathrm{Tr}\,\mathbf{G}^{(1)}(\mathbf{r},\mathbf{r},\omega)], \tag{16}$$

where the symmetry $\mathbf{G}(\mathbf{r}',\mathbf{r},\omega)=\mathbf{G}^{\mathrm{T}}(\mathbf{r},\mathbf{r}',\omega)$ of the Green tensor has been used. In addition, we have assumed the body to be homogeneous and performed the coincidence limit by simply replacing the Green tensor with its scattering part $\mathbf{G}^{(1)}$ (see the discussion in Ref. [30].). Next, we exploit the fact that the amplifying body is optically dilute and expand $\mathbf{F}^{\mathrm{nr}}$ as given by Eq. (16) to leading (linear) order in the susceptibility $\chi(\mathbf{r},\omega)$ of the amplifying body. We thus have to replace $\mathbf{G}$ with its zero-order approximation $\overline{\mathbf{G}}$, i.e., the Green tensor of the system in the absence of the amplifying body which is the solution to the Helmholtz equation (3) with

$$\bar{\varepsilon}(\mathbf{r},\omega)=\begin{cases}\varepsilon(\mathbf{r},\omega) & \text{for } \mathbf{r}\notin V,\\ 1 & \text{for } \mathbf{r}\in V.\end{cases} \tag{17}$$

in place of $\varepsilon(\mathbf{r},\omega)$. Finally, we assume that the amplifying body consists of a gas of isotropic atoms in an excited state $|n\rangle$ with polarizability

$$\alpha_n(\omega)=\lim_{\epsilon\to0}\frac{1}{3\hbar}\sum_k\left[\frac{|\mathbf{d}_{nk}|^2}{\omega+\omega_{kn}+i\epsilon}-\frac{|\mathbf{d}_{nk}|^2}{\omega-\omega_{kn}+i\epsilon}\right] \tag{18}$$

(ω_{kn}: transition frequencies, $\mathbf{d}_{nk}$: electric-dipole matrix elements), which can be related to the electric susceptibility of the body via the linearized Clausius-Mossotti law $\chi(\omega)=\varepsilon_0^{-1}\eta\alpha_n(\omega)$ (η: atomic number density). Transforming the frequency integral to the positive imaginary axis, we obtain $\mathbf{F}^{\mathrm{nr}}=-\int d^3r\,\eta\boldsymbol{\nabla}U_n^{\mathrm{nr}}(\mathbf{r})$, where

$$U_n^{\mathrm{nr}}(\mathbf{r})=\frac{\hbar\mu_0}{2\pi}\int_0^\infty d\xi\xi^2\alpha_n(i\xi)\mathrm{Tr}\,\overline{\mathbf{G}}^{(1)}(\mathbf{r},\mathbf{r},i\xi) \tag{19}$$

is the nonresonant CP potential of the excited body atoms [21]. It should be pointed out that there is an important difference to the case of the force on an absorbing object made of ground-state atoms: In the latter case, all of the frequencies ω_{kn} in Eq. (18) are positive so that the respective (virtual) transitions contribute to the nonresonant CP potential with the same sign. For excited atoms, upward as well as downward transitions are possible, so that positive and negative ω_{kn} occur and the overall sign of the nonresonant force can be reversed to make it repulsive.

Let us next consider the resonant force component $\mathbf{F}^{\mathrm{r}}$, Eq. (13), following similar steps as above. The linear approximation of $\mathbf{F}^{\mathrm{r}}$ can be obtained by using the zero-order approximation to Eq. (3) together with the identity $\omega^2/c^2\boldsymbol{\nabla}\cdot\mathbf{G}(\mathbf{r},\mathbf{r}',\omega)=-\boldsymbol{\nabla}\delta(\mathbf{r}-\mathbf{r}')$ and replacing $\mathbf{G}^*$ with $\overline{\mathbf{G}}^*$. Expanding the result according to $\mathrm{Tr}[\mathbf{I}\times\mathbf{G}\times\overleftarrow{\boldsymbol{\nabla}}']=\boldsymbol{\nabla}'\,\mathrm{Tr}\,\mathbf{G}-\boldsymbol{\nabla}'\cdot\mathbf{G}$ and discarding, for a body in free space, terms involving total divergences we derive

$$\mathbf{F}^{\mathrm{r}}=-\frac{\hbar}{\pi}\int_V d^3r\int_0^\infty d\omega\frac{\omega^2}{c^2}\Theta[-\varepsilon_I(\mathbf{r},\omega)]\varepsilon_I(\mathbf{r},\omega)\times\boldsymbol{\nabla}\,\mathrm{Tr}\,\mathrm{Re}\,\overline{\mathbf{G}}^{(1)}(\mathbf{r},\mathbf{r},\omega), \tag{20}$$

where we have again assumed the body to be homogeneous and performed the coincidence limit by replacing the Green tensor with its scattering part. Relating ε_I to the polarizability of the atoms by means of the linearized Clausius-Mossotti relation, we finally obtain $\mathbf{F}^{\mathrm{r}}=-\int d^3r\,\eta\boldsymbol{\nabla}U_n^{\mathrm{r}}(\mathbf{r})$, where

$$U_n^{\mathrm{r}}(\mathbf{r})=\frac{\hbar\mu_0}{\pi}\int_0^\infty d\omega\omega^2\Theta[-\mathrm{Im}\;\alpha_n(\omega)]\mathrm{Im}\;\alpha_n(\omega)\times\mathrm{Tr}\,\mathrm{Re}\,\overline{\mathbf{G}}^{(1)}(\mathbf{r},\mathbf{r},\omega) \tag{21}$$

is nothing but the resonant part of the CP potential of the excited atoms contained in the body. By using the relation

$$\alpha_I(\omega)=\frac{\pi}{3\hbar}\sum_k|\mathbf{d}_{nk}|^2[\delta(\omega+\omega_{nk})-\delta(\omega-\omega_{nk})], \tag{22}$$

which follow from definition (18) together with the identity $\lim_{\epsilon\to0}1/(x+i\epsilon)=\mathcal{P}/x-i\pi\delta(x)$ ($\mathcal{P}$: principal value), we can write it in the more familiar form [21],

$$U_n^{\mathrm{r}}(\mathbf{r})=-\frac{\mu_0}{3}\sum_k\Theta(\omega_{nk})\omega_{nk}^2|\mathbf{d}_{nk}|^2\,\mathrm{Tr}\,\mathrm{Re}\,\overline{\mathbf{G}}^{(1)}(\mathbf{r},\mathbf{r},\omega_{nk}). \tag{23}$$

Combining the results for $\mathbf{F}^{\mathrm{nr}}$ and $\mathbf{F}^{\mathrm{r}}$, we see that the Casimir force on an optically dilute, homogeneous, amplifying electric body is the sum of the CP forces on the excited atoms contained therein,

$$\mathbf{F}=\mathbf{F}^{\mathrm{nr}}+\mathbf{F}^{\mathrm{r}}=-\int d^3r\,\eta\boldsymbol{\nabla}U_n(\mathbf{r}) \tag{24}$$

$[U_n(\mathbf{r})=U_n^{\mathrm{nr}}(\mathbf{r})+U_n^{\mathrm{r}}(\mathbf{r})]$. This result generalizes similar findings for purely absorbing bodies (consisting of ground-state atoms) [30–33] to amplifying ones. In particular, the nonresonant and resonant components of the Casimir force, Eqs. (12) and (13), are directly related to the respective CP-potential terms which in turn are associated with virtual and real transitions of the atoms. Recall that for an atom in front of a plate at zero temperature, the nonresonant CP potential is proportional to $1/z^3$ and $1/z^4$ in the nonretarded and retarded limits (z: atom-plate separation), while the resonant potential as governed by a $1/z^3$ power law in the nonretarded regime makes way for a spatially oscillating $\cos(2\omega_{nk}z/c)/z$ asymptote for retarded distances [20]. As we have seen, the most important difference between forces on amplifying as opposed to absorbing bodies is the presence of a strong, resonant force contribution which is associated with real transi-

tions of the excited body atoms and hence with emission processes of the body.

V. SUMMARY AND PERSPECTIVE

On the basis of the consistent framework provided by macroscopic QED, we have developed an exact theory of Casimir forces in arrangements of linearly responding, electrically polarisable bodies of arbitrary shape, with special emphasis on amplifying bodies. Formulas (12) and (13) show that the Casimir force can be decomposed into two parts: a nonresonant Lifshitz-type component that looks formally the same as in the case of a purely absorbing body and a resonant component that is a direct consequence of the amplification in the system and contains an integration over bodies and frequencies where the imaginary part of the electric permittivity is negative. We have demonstrated that in the dilute-gas limit, the Casimir force on an amplifying body in the presence of absorbing bodies is given by a sum of CP forces over the excited body atoms; our theory is hence the natural generalization of additive approaches beyond their scope.

Two points to be addressed in more detail in the future are (i) the finite-temperature case and (ii) the relation of the excited atom-body force to atom-atom forces. (i) Finite temperature of the absorbing environment may be accounted for by introducing a thermal density matrix $\hat{\rho}_T = \exp[-\hat{H}_+/(k_B T)]/\mathrm{Tr}\{\exp[-\hat{H}_+/(k_B T)]\}$. This leads to a factor $[2n_T(\omega)+1]$ with thermal photon number $n_T(\omega)$ in Eq. (12), so the ξ-integral in Eq. (19) will be replaced with a Matsubara sum (cf. Ref. [34]). The $T \to 0$ limit of the nonresonant force being a nonuniform asymptotic expansion [35,36], the $T=0$ results are only valid for distances $z \ll \hbar c/(2\pi k_B T)$. (ii) The theoretically and experimentally established resonant and spatially oscillating forces between excited atoms and bodies are in contrast with the nonoscillating atom-atom forces found in the majority of theoretical works [37,38]. The discrepancy indicates that either the inclusion of atomic linewidth at the heart of excited atom-atom calculations has to be carefully reconsidered [39] or that microscopic atom-atom interactions are fundamentally different from the collective atom-body interaction.

Our results, which can be extended to magnetoelectric, anisotropic or nonlocally responding media in a straightforward way, present a reliable framework for enhancing the impact of metamaterial properties such as negative refraction on dispersion forces or realizing repulsive forces. In particular, perfect lens scenarios can be investigated by using the appropriate Green tensors. Note that the strategy employed in this Rapid Communication can also be employed to study CP forces on atoms in the presence of amplifying bodies, where a rich dynamics associated with the exchange of excitations is to be expected.

ACKNOWLEDGMENT

The work was supported by Deutsche Forschungsgemeinschaft. We gratefully acknowledge funding from the Alexander von Humboldt Foundation (S.Y.B.) and the Vietnam Education Foundation (H.T.D.). We acknowledge fruitful discussions with C. Raabe and M. Fleischhauer.

[1] M. Bordag *et al.*, Phys. Rep. **353**, 1 (2001).
[2] K. A. Milton, J. Phys. A **37**, R209 (2004).
[3] S. K. Lamoreaux, Rep. Prog. Phys. **68**, 201 (2005).
[4] S. Y. Buhmann and D.-G. Welsch, Progr. Quantum Electron. **31**, 51 (2007).
[5] S. Y. Buhmann, D. G. Welsch, and T. Kampf, Phys. Rev. A **72**, 032112 (2005).
[6] C. Henkel and K. Joulain, Europhys. Lett. **72**, 929 (2005).
[7] M. S. Tomaš, Phys. Lett. A **342**, 381 (2005).
[8] S. Spagnolo, D. A. R. Dalvit, and P. W. Milonni, Phys. Rev. A **75**, 052117 (2007).
[9] F. S. S. Rosa, D. A. R. Dalvit, and P. W. Milonni, Phys. Rev. Lett. **100**, 183602 (2008).
[10] A. Sambale, D. G. Welsch, Ho Trung Dung, and S. Y. Buhmann, Phys. Rev. A **78**, 053828 (2008).
[11] Y. Yang, R. Zeng, J. Xu, and S. Liu, Phys. Rev. A **77**, 015803 (2008).
[12] V. G. Veselago, Sov. Phys. Usp. **10**, 509 (1968).
[13] V. Veselago *et al.*, J. Comput. Theor. Nanosci. **3**, 189 (2006).
[14] B. Nistad and J. Skaar, Phys. Rev. E **78**, 036603 (2008).
[15] A. K. Popov and V. M. Shalaev, Opt. Lett. **31**, 2169 (2006).
[16] P. Ginzburg and M. Orenstein, J. Appl. Phys. **104**, 063513 (2008).
[17] J. Faist *et al.*, Sci. **264**, 553 (1994).
[18] Y. Sherkunov, Phys. Rev. A **72**, 052703 (2005).
[19] U. Leonhardt and T. G. Philbin, New J. Phys. **9**, 254 (2007).
[20] G. Barton, Proc. R. Soc. London, Ser. A **320**, 251 (1970).
[21] J. M. Wylie and J. E. Sipe, Phys. Rev. A **32**, 2030 (1985).
[22] P. Bushev *et al.*, Phys. Rev. Lett. **92**, 223602 (2004).
[23] H.-J. Butt *et al.*, Surf. Sci. Rep. **59**, 1 (2005).
[24] A. A. Feiler *et al.*, Langmuir **24**, 2274 (2008).
[25] J. N. Munday *et al.*, Nature (London) **457**, 170 (2009).
[26] V. A. Podolskiy *et al.*, Appl. Phys. Lett. **87**, 231113 (2005).
[27] Y. P. Zhao *et al.*, J. Adhes. Sci. Techol. **17**, 519 (2003).
[28] C. Raabe and D.-G. Welsch, Eur. Phys. J. Spec. Top. **160**, 371 (2008).
[29] S. Scheel, L. Knöll, and D.-G. Welsch, Phys. Rev. A **58**, 700 (1998).
[30] C. Raabe and D.-G. Welsch, Phys. Rev. A **73**, 063822 (2006); note erratum **74**, 019901(E) (2006).
[31] M. S. Tomaš, Phys. Rev. A **71**, 060101(R) (2005).
[32] S. Y. Buhmann *et al.*, Open Syst. Inf. Dyn. **13**, 427 (2006).
[33] S. Y. Buhmann and D.-G. Welsch, Appl. Phys. B: Lasers Opt. **82**, 189 (2006).
[34] S. Y. Buhmann and S. Scheel, Phys. Rev. Lett. **100**, 253201 (2008).
[35] B. W. Ninham and J. Daicic, Phys. Rev. A **57**, 1870 (1998).
[36] H. Wennerström, J. Daicic, and B. W. Ninham, Phys. Rev. A **60**, 2581 (1999).
[37] M. Boström *et al.*, Eur. Phys. J. D **22**, 47 (2003).
[38] Y. Sherkunov, Phys. Rev. A **75**, 012705 (2007).
[39] S. Y. Buhmann, L. Knöll, D.-G. Welsch, and Ho Trung Dung, Phys. Rev. A **70**, 052117 (2004).

PHYSICAL REVIEW A **78**, 052901 (2008)

Surface-induced heating of cold polar molecules

Stefan Yoshi Buhmann, M. R. Tarbutt, Stefan Scheel, and E. A. Hinds
Quantum Optics and Laser Science, Blackett Laboratory, Imperial College London, Prince Consort Road, London SW7 2AZ, United Kingdom

(Received 17 June 2008; published 11 November 2008)

We study the rotational and vibrational heating of diatomic molecules placed near a surface at finite temperature on the basis of macroscopic quantum electrodynamics. The internal molecular evolution is governed by transition rates that depend on both temperature and position. Analytical and numerical methods are used to investigate the heating of several relevant molecules near various surfaces. We determine the critical distances at which the surface itself becomes the dominant source of heating and we investigate the transition between the long-range and short-range behavior of the heating rates. A simple formula is presented that can be used to estimate the surface-induced heating rates of other molecules of interest. We also consider how the heating depends on the thickness and composition of the surface.

DOI: 10.1103/PhysRevA.78.052901 PACS number(s): 34.35.+a, 33.80.−b, 37.10.Mn, 42.50.Nn

I. INTRODUCTION

A number of techniques have recently been developed to cool polar molecules to low temperatures and to trap them for a second or longer. Using the switched electric field gradients of a Stark decelerator [1], polar molecules formed in a supersonic expansion have been decelerated to rest and then stored in electrostatic, magnetic, or electrodynamic traps [2–5]. An electrostatic trap has been continuously loaded by filtering out the slowest fraction of the molecules present in an effusive beam [6]. Polar molecules have also been cooled in a buffer gas of cold helium and then confined in a magnetic trap [7]. Extremely cold polar molecules such as RbCs can be produced by the photoassociation of two species of ultracold atoms, followed by laser-stimulated state transfer [8]. In all cases, the resulting molecules are typically far colder than their environments, and they may be heated by the absorption of blackbody radiation from that environment. Unlike atoms, the polar molecules can be rotationally or vibrationally excited by their interaction with this blackbody radiation, and in many cases this can severely limit the trapping lifetime of the molecules. Indeed, the blackbody heating rate for trapped OH and OD has already been measured experimentally and found to limit the trapping lifetime to just a few seconds when the environment is at room temperature [9]. Calculations of the free-space heating rates for several polar molecules have already been presented [10].

In most experiments so far, the cold polar molecules have been confined in macroscopic traps, with trap surfaces typically several mm from the molecules themselves. There is now a great deal of interest in confining and manipulating these molecules much closer to surfaces, so as to build a "molecule chip" technology analogous to that for atoms [11]. Fast-moving molecules have already been trapped in traveling potential wells formed approximately 25 μm above a microstructured surface [12]. This same structure can be used to decelerate the molecules to rest so that they can be trapped above the surface of the chip. Chip-based microtraps have been designed, along with schemes to interface the molecules with solid-state devices which could be used to cool, detect, and control them coherently [13]. Strong coupling to a superconducting stripline cavity is possible when the molecules are just a few microns from the surface, and then the molecules can be the long-lived quantum memory of a hybrid quantum information processor [14]. Recent developments also herald the prospect of integrated molecule detectors, based on optical microcavities [15] or ultrathin optical fibers [16].

These advances raise the question of the heating rates in the close vicinity of a surface. The influence of such a nontrivial environment on the internal atomic dynamics is commonly known as the Purcell effect [17]. Early theoretical studies were devoted to the zero temperature case where the evolution is governed by spontaneous decay. As shown by linear response theory, the decay rate for an arbitrary environment can be given in terms of the classical Green tensor for the respective geometry [18]. Alternative approaches have been developed on the basis of classical electrodynamics [19,20] and microscopic models [21] and have been applied to the case of an atom near a single surface or between two surfaces. Results for an arbitrary environment of electric [22] and magnetoelectric bodies [23], including local-field effects [24,25], have also been obtained on the basis of macroscopic quantum electrodynamics (QED) and have been used to study atoms in bulk material [22], outside [26] or inside a microsphere [24], inside a spherical cavity [27], and even in the presence of left-handed metamaterials [23,28,29]. The linear-response approach has been generalized to finite temperatures [30] where the internal dynamics is no longer governed by spontaneous decay alone, but stimulated emission and absorption of thermal photons also contribute. The respective environment-dependent transition rates can again be expressed in terms of the classical Green tensor; in addition, the thermal photon number comes into play. Ground-state heating rates of spinless atoms have been predicted to be very small near surfaces [31], in contrast to the case of atoms with spin which have been investigated for planar surfaces [31,32], wires [33], and carbon nanotubes [34].

In this paper, we calculate heating rates for a number of polar molecules currently favored by experimenters. On the basis of macroscopic QED (presented in Sec. II), we solve the internal molecular dynamics to obtain transition rates of a molecule in an arbitrary uniform-temperature environment

(Sec. III). In Sec. IV, the results are first used to calculate the rates in free space, and then as a function of distance from the surface of some common metals and dielectrics, as well as some unusual metamaterials.

II. MACROSCOPIC QUANTUM ELECTRODYNAMICS AT FINITE TEMPERATURE

Consider a molecule (or an atom) that is placed within an arbitrary environment of magnetoelectric bodies. The coupled dynamics of the molecule and the body-assisted electromagnetic field can be described by the Hamiltonian [23,35]

$$\hat{H} = \hat{H}_A + \hat{H}_F + \hat{H}_{AF}, \tag{1}$$

where

$$\hat{H}_A = \sum_n E_n |n\rangle\langle n| \tag{2}$$

(E_n, molecular eigenenergies; $|n\rangle$, molecular eigenstates) is the Hamiltonian of the molecule,

$$\hat{H}_F = \sum_{\lambda=e,m} \int d^3r \int_0^\infty d\omega \hbar\omega \hat{\mathbf{f}}_\lambda^\dagger(\mathbf{r},\omega)\cdot\hat{\mathbf{f}}_\lambda(\mathbf{r},\omega) \tag{3}$$

is the Hamiltonian of the electromagnetic field (including the internal charges present in the bodies) expressed in terms of the bosonic variables

$$[\hat{f}_{\lambda i}(\mathbf{r},\omega),\hat{f}_{\lambda' j}(\mathbf{r}',\omega')] = 0 = [\hat{f}^\dagger_{\lambda i}(\mathbf{r},\omega),\hat{f}^\dagger_{\lambda' j}(\mathbf{r}',\omega')], \tag{4}$$

$$[\hat{f}_{\lambda i}(\mathbf{r},\omega),\hat{f}^\dagger_{\lambda' j}(\mathbf{r}',\omega')] = \delta_{\lambda\lambda'}\delta_{ij}\delta(\mathbf{r}-\mathbf{r}')\delta(\omega-\omega') \tag{5}$$

(note that $\hat{\mathbf{f}}_e$ is associated with the polarization of the bodies and $\hat{\mathbf{f}}_m$ is related to their magnetization), and

$$\hat{H}_{AF} = -\sum_{m,n} \mathbf{d}_{mn}\cdot\hat{\mathbf{E}}(\mathbf{r}_A)\hat{A}_{mn} \tag{6}$$

($\mathbf{d}_{mn}=\langle m|\hat{\mathbf{d}}|n\rangle$, electric-dipole transition matrix elements of the molecule; $\mathbf{r}_A$, molecular center-of-mass position; $\hat{A}_{mn}=|m\rangle\langle n|$, molecular flip operators) is the molecule-field interaction Hamiltonian in electric-dipole approximation. The electric field can be expressed in terms of the bosonic variables according to

$$\hat{\mathbf{E}}(\mathbf{r}) = \int_0^\infty d\omega \underline{\hat{\mathbf{E}}}(\mathbf{r},\omega) + \text{H.c.}, \tag{7}$$

$$\underline{\hat{\mathbf{E}}}(\mathbf{r},\omega) = \sum_{\lambda=e,m}\int d^3r' \boldsymbol{G}_\lambda(\mathbf{r},\mathbf{r}',\omega)\cdot\hat{\mathbf{f}}_\lambda(\mathbf{r}',\omega), \tag{8}$$

with the coefficients $\boldsymbol{G}_\lambda$ being related to the classical Green tensor $\boldsymbol{G}$ by

$$\boldsymbol{G}_e(\mathbf{r},\mathbf{r}',\omega) = i\frac{\omega^2}{c^2}\sqrt{\frac{\hbar}{\pi\varepsilon_0}\,\mathrm{Im}\,\varepsilon(\mathbf{r}',\omega)}\boldsymbol{G}(\mathbf{r},\mathbf{r}',\omega), \tag{9}$$

$$\boldsymbol{G}_m(\mathbf{r},\mathbf{r}',\omega) = i\frac{\omega}{c}\sqrt{\frac{\hbar}{\pi\varepsilon_0}\frac{\mathrm{Im}\,\mu(\mathbf{r}',\omega)}{|\mu(\mathbf{r}',\omega)|^2}}[\boldsymbol{\nabla}'\times\boldsymbol{G}(\mathbf{r}',\mathbf{r},\omega)]^{\mathsf{T}}. \tag{10}$$

For a given environment of macroscopic bodies, described by their linear, local, and isotropic relative permittivity $\varepsilon(\mathbf{r},\omega)$ and permeability $\mu(\mathbf{r},\omega)$, the Green tensor is uniquely defined by the differential equation

$$\left[\boldsymbol{\nabla}\times\frac{1}{\mu(\mathbf{r},\omega)}\boldsymbol{\nabla}\times - \frac{\omega^2}{c^2}\varepsilon(\mathbf{r},\omega)\right]\boldsymbol{G}(\mathbf{r},\mathbf{r}',\omega) = \boldsymbol{\delta}(\mathbf{r}-\mathbf{r}') \tag{11}$$

together with the boundary condition

$$\boldsymbol{G}(\mathbf{r},\mathbf{r}',\omega)\to 0 \quad \text{for } |\mathbf{r}-\mathbf{r}'|\to\infty. \tag{12}$$

The above definitions imply the useful integral relation [23,35]

$$\sum_{\lambda=e,m}\int d^3s \boldsymbol{G}_\lambda(\mathbf{r},\mathbf{s},\omega)\cdot\boldsymbol{G}^+_\lambda(\mathbf{r}',\mathbf{s},\omega) = \frac{\hbar\mu_0}{\pi}\omega^2\,\mathrm{Im}\,\boldsymbol{G}(\mathbf{r},\mathbf{r}',\omega). \tag{13}$$

In thermal equilibrium at uniform temperature T, the electromagnetic field may be described by the density matrix

$$\hat{\rho}_T = \frac{e^{-\hat{H}_F/(k_\mathrm{B}T)}}{\mathrm{tr}[e^{-\hat{H}_F/(k_\mathrm{B}T)}]} \tag{14}$$

(k_B, Boltzmann constant). Thermal averages $\langle\ldots\rangle=\mathrm{tr}[\ldots\hat{\rho}_T]$ of the bosonic variables are thus given by

$$\langle\hat{\mathbf{f}}_\lambda(\mathbf{r},\omega)\rangle = \mathbf{0} = \langle\hat{\mathbf{f}}^\dagger_\lambda(\mathbf{r},\omega)\rangle, \tag{15}$$

$$\langle\hat{\mathbf{f}}_\lambda(\mathbf{r},\omega)\hat{\mathbf{f}}_{\lambda'}(\mathbf{r}',\omega')\rangle = \boldsymbol{0} = \langle\hat{\mathbf{f}}^\dagger_\lambda(\mathbf{r},\omega)\hat{\mathbf{f}}^\dagger_{\lambda'}(\mathbf{r}',\omega')\rangle, \tag{16}$$

$$\langle\hat{\mathbf{f}}^\dagger_\lambda(\mathbf{r},\omega)\hat{\mathbf{f}}_{\lambda'}(\mathbf{r}',\omega')\rangle = n(\omega)\delta_{\lambda\lambda'}\boldsymbol{\delta}(\mathbf{r}-\mathbf{r}')\delta(\omega-\omega'), \tag{17}$$

$$\langle\hat{\mathbf{f}}_\lambda(\mathbf{r},\omega)\hat{\mathbf{f}}^\dagger_{\lambda'}(\mathbf{r}',\omega')\rangle = [n(\omega)+1]\delta_{\lambda\lambda'}\boldsymbol{\delta}(\mathbf{r}-\mathbf{r}')\delta(\omega-\omega'), \tag{18}$$

where

$$n(\omega) = \frac{\Sigma_k k e^{-k\hbar\omega/(k_\mathrm{B}T)}}{\Sigma_k e^{-k\hbar\omega/(k_\mathrm{B}T)}} = \frac{1}{e^{\hbar\omega/(k_\mathrm{B}T)}-1} \tag{19}$$

is the average thermal photon number. Recalling definitions (7) and (8), the statistical properties of the electric field are found to be given by

$$\langle\underline{\hat{\mathbf{E}}}(\mathbf{r},\omega)\rangle = \mathbf{0} = \langle\underline{\hat{\mathbf{E}}}^\dagger(\mathbf{r},\omega)\rangle, \tag{20}$$

$$\langle\underline{\hat{\mathbf{E}}}(\mathbf{r},\omega)\underline{\hat{\mathbf{E}}}(\mathbf{r}',\omega')\rangle = \boldsymbol{0} = \langle\underline{\hat{\mathbf{E}}}^\dagger(\mathbf{r},\omega)\underline{\hat{\mathbf{E}}}^\dagger(\mathbf{r}',\omega')\rangle, \tag{21}$$

$$\langle\underline{\hat{\mathbf{E}}}^\dagger(\mathbf{r},\omega)\underline{\hat{\mathbf{E}}}(\mathbf{r}',\omega')\rangle = \frac{\hbar\mu_0}{\pi}n(\omega)\omega^2\,\mathrm{Im}\,\boldsymbol{G}(\mathbf{r},\mathbf{r}',\omega)\delta(\omega-\omega'), \tag{22}$$

$$\langle \hat{\underline{\mathbf{E}}}(\mathbf{r},\omega)\hat{\underline{\mathbf{E}}}^{\dagger}(\mathbf{r}',\omega')\rangle = \frac{\hbar\mu_0}{\pi}[n(\omega)+1]\omega^2 \,\mathrm{Im}\,\boldsymbol{G}(\mathbf{r},\mathbf{r}',\omega)\delta(\omega-\omega'), \quad (23)$$

where we have made use of the integral relation (13). Note that these relations are in accordance with the fluctuation-dissipation theorem [36],

$$\left\langle \frac{1}{2}[\hat{\underline{\mathbf{E}}}(\mathbf{r},\omega)\hat{\underline{\mathbf{E}}}^{\dagger}(\mathbf{r}',\omega')+\hat{\underline{\mathbf{E}}}^{\dagger}(\mathbf{r}',\omega')\hat{\underline{\mathbf{E}}}(\mathbf{r},\omega)]\right\rangle = \frac{\hbar\mu_0}{\pi}\left[n(\omega)+\frac{1}{2}\right]\omega^2 \,\mathrm{Im}\,\boldsymbol{G}(\mathbf{r},\mathbf{r}',\omega)\delta(\omega-\omega'), \quad (24)$$

where the thermal photon energy is given by

$$\hbar\omega\left[n(\omega)+\frac{1}{2}\right] \to \begin{cases} \frac{1}{2}\hbar\omega & \text{for } k_B T \ll \hbar\omega, \\ k_B T & \text{for } k_B T \gg \hbar\omega, \end{cases} \quad (25)$$

in the zero- and high-temperature limits, respectively.

III. INTERNAL MOLECULAR DYNAMICS

Consider a molecule which is prepared at initial time $t=0$ in an arbitrary internal state, represented by its internal density matrix $\hat{\sigma}(0)$. The environment of the molecule is initially taken to be at uniform temperature T, so that the electromagnetic field is in a thermal state $\hat{\rho}(0)=\hat{\rho}_T$.

The internal molecular dynamics can be determined by solving the coupled equations

$$\dot{\hat{A}}_{mn} = \frac{i}{\hbar}[\hat{H},\hat{A}_{mn}] = i\omega_{mn}\hat{A}_{mn} + \frac{i}{\hbar}\sum_k \int_0^\infty d\omega\Big[(\mathbf{d}_{nk}\hat{A}_{mk}-\mathbf{d}_{km}\hat{A}_{kn})\cdot\hat{\underline{\mathbf{E}}}(\mathbf{r}_A,\omega) + \hat{\underline{\mathbf{E}}}^{\dagger}(\mathbf{r}_A,\omega)\cdot(\mathbf{d}_{nk}\hat{A}_{mk}-\mathbf{d}_{km}\hat{A}_{kn})\Big], \quad (26)$$

and

$$\dot{\hat{\mathbf{f}}}_\lambda(\mathbf{r},\omega) = \frac{i}{\hbar}[\hat{H},\hat{\mathbf{f}}_\lambda(\mathbf{r},\omega)] = -i\omega\hat{\mathbf{f}}_\lambda(\mathbf{r},\omega) + \frac{i}{\hbar}\sum_{m,n}\mathbf{d}_{mn}\cdot\boldsymbol{G}^*_\lambda(\mathbf{r}_A,\mathbf{r},\omega)\hat{A}_{mn}, \quad (27)$$

as implied by the Hamiltonian (1) together with Eqs. (2), (3), and (6). The electromagnetic field can be eliminated by formally solving Eq. (27) and substituting the result into Eq. (26). For weak molecule-field coupling, the Markov approximation may then be employed to show that the dynamics of the internal density matrix of the molecule $\hat{\sigma}$ is given by the equations (Appendix A)

$$\dot{\sigma}_{nn}(t) = -\Gamma_n\sigma_{nn}(t) + \sum_k \Gamma_{kn}\sigma_{kk}(t), \quad (28)$$

$$\dot{\sigma}_{mn}(t) = \left[-i\tilde{\omega}_{mn} - \tfrac{1}{2}(\Gamma_m+\Gamma_n)\right]\sigma_{mn}(t) \quad \text{for } m\neq n \quad (29)$$

($\sigma_{mn}=\langle m|\hat{\sigma}|n\rangle=\langle\hat{A}_{nm}\rangle$). Here, the total loss rate Γ_n of a level n is given by

$$\Gamma_n = \Gamma_n(\mathbf{r}_A) = \sum_k \Gamma_{nk}, \quad (30)$$

and the individual intramolecular transition rates Γ_{nk} from level n to level k read

$$\Gamma_{nk} = \Gamma_{nk}(\mathbf{r}_A) \equiv \Gamma^0_{nk} + \Gamma^T_{nk} = \frac{2\mu_0}{\hbar}\tilde{\omega}^2_{nk}\mathbf{d}_{nk}\cdot\mathrm{Im}\,\boldsymbol{G}(\mathbf{r}_A,\mathbf{r}_A,|\tilde{\omega}_{nk}|)\cdot\mathbf{d}_{kn} \times\{\Theta(\tilde{\omega}_{nk})[n(\tilde{\omega}_{nk})+1]+\Theta(\tilde{\omega}_{kn})n(\tilde{\omega}_{kn})\} \quad (31)$$

[$\Theta(z)$, unit step function] where

$$\Gamma^0_{nk} = \frac{2\mu_0}{\hbar}\tilde{\omega}^2_{nk}\Theta(\tilde{\omega}_{nk})\mathbf{d}_{nk}\cdot\mathrm{Im}\,\boldsymbol{G}(\mathbf{r}_A,\mathbf{r}_A,\tilde{\omega}_{nk})\cdot\mathbf{d}_{kn} \quad (32)$$

and

$$\Gamma^T_{nk} = \frac{2\mu_0}{\hbar}\tilde{\omega}^2_{nk}\mathbf{d}_{nk}\cdot\mathrm{Im}\,\boldsymbol{G}(\mathbf{r}_A,\mathbf{r}_A,|\tilde{\omega}_{nk}|)\cdot\mathbf{d}_{kn} \times[\Theta(\tilde{\omega}_{nk})n(\tilde{\omega}_{nk})+\Theta(\tilde{\omega}_{kn})n(\tilde{\omega}_{kn})] \quad (33)$$

denote the zero-point and thermal contributions to these rates [recall Eq. (19)].

The intramolecular transition rates depend on the shifted molecular transition frequencies

$$\tilde{\omega}_{mn} = \tilde{\omega}_{mn}(\mathbf{r}_A) = \omega_{mn} + \delta\omega_m - \delta\omega_n, \quad (34)$$

where the frequency shift

$$\delta\omega_n = \delta\omega_n(\mathbf{r}_A) = \sum_k \delta\omega_{nk} \quad (35)$$

of a given level n has contributions

$$\delta\omega_{nk} = \delta\omega_{nk}(\mathbf{r}_A) \equiv \delta\omega^0_{nk} + \delta\omega^T_{nk} = \frac{\mu_0}{\pi\hbar}P\int_0^\infty d\omega\omega^2\left\{\mathbf{d}_{nk}\cdot\mathrm{Im}\,\boldsymbol{G}^{(1)}(\mathbf{r}_A,\mathbf{r}_A,\omega)\cdot\mathbf{d}_{kn} \times\left[\frac{n(\omega)+1}{\tilde{\omega}_{nk}-\omega}+\frac{n(\omega)}{\tilde{\omega}_{nk}+\omega}\right] + \frac{\omega|\mathbf{d}_{nk}|^2}{6\pi c}\left[\frac{n(\omega)}{\tilde{\omega}_{nk}-\omega}+\frac{n(\omega)}{\tilde{\omega}_{nk}+\omega}\right]\right\} \quad (36)$$

(P, principal value) due to all other levels k, which can again be separated into their zero-point and thermal parts,

$$\delta\omega_{nk}^0 = \delta\omega_{nk}^0(\mathbf{r}_A) = \frac{\mu_0}{\pi\hbar} P \int_0^\infty d\omega \omega^2 \frac{\mathbf{d}_{nk} \cdot \mathrm{Im}\, \boldsymbol{G}^{(1)}(\mathbf{r}_A, \mathbf{r}_A, \omega) \cdot \mathbf{d}_{kn}}{\tilde{\omega}_{nk} - \omega} \tag{37}$$

and

$$\begin{aligned}\delta\omega_{nk}^T &= \delta\omega_{nk}^T(\mathbf{r}_A) \\ &= \frac{\mu_0}{\pi\hbar} P \int_0^\infty d\omega \omega^2 \mathbf{d}_{nk} \cdot \mathrm{Im}\, \boldsymbol{G}(\mathbf{r}_A, \mathbf{r}_A, \omega) \cdot \mathbf{d}_{kn} \\ &\quad \times \left[\frac{n(\omega)}{\tilde{\omega}_{nk} - \omega} + \frac{n(\omega)}{\tilde{\omega}_{nk} + \omega} \right],\end{aligned} \tag{38}$$

respectively. Here, $\boldsymbol{G}^{(1)}$ denotes the scattering part of the Green tensor according to the decomposition

$$\boldsymbol{G}(\mathbf{r}, \mathbf{r}', \omega) = \boldsymbol{G}^{(0)}(\mathbf{r}, \mathbf{r}', \omega) + \boldsymbol{G}^{(1)}(\mathbf{r}, \mathbf{r}', \omega) \tag{39}$$

where the imaginary part of the bulk (free-space) part is given by [37]

$$\mathrm{Im}\, \boldsymbol{G}^{(0)}(\mathbf{r}, \mathbf{r}, \omega) = \frac{\omega}{6\pi c} \boldsymbol{I} \tag{40}$$

($\boldsymbol{I}$, unit tensor). The free-space zero-point frequency shifts associated with $\boldsymbol{G}^{(0)}$, i.e., the free-space Lamb shifts, are included in the bare transition frequencies ω_{mn} since they are determined experimentally in free space. The Green tensor being analytic in the upper half of the complex frequency plane, one can employ contour-integral techniques to rewrite the frequency-shift contributions as

$$\begin{aligned}\delta\omega_{nk} &= -\frac{\mu_0}{\hbar} \tilde{\omega}_{nk}^2 \mathbf{d}_{nk} \cdot \mathrm{Re}\, \boldsymbol{G}^{(1)}(\mathbf{r}_A, \mathbf{r}_A, \tilde{\omega}_{nk}) \cdot \mathbf{d}_{kn} \\ &\quad \times \{\Theta(\tilde{\omega}_{nk})[n(\tilde{\omega}_{nk}) + 1] - \Theta(\tilde{\omega}_{kn}) n(\tilde{\omega}_{kn})\} \\ &\quad + \frac{2\mu_0 k_B T}{\hbar^2} \sum_{N=0}^{\infty} (1 - \delta_{N0}) \xi_N^2 \tilde{\omega}_{kn} \\ &\quad \times \frac{\mathbf{d}_{nk} \cdot \boldsymbol{G}^{(1)}(\mathbf{r}_A, \mathbf{r}_A, \xi_N) \cdot \mathbf{d}_{kn}}{\tilde{\omega}_{kn}^2 + \xi_N^2} \\ &\quad + \frac{\mu_0 |\mathbf{d}_{nk}|^2}{6\pi^2 c\hbar} P \int_0^\infty d\omega \omega^3 \left[\frac{n(\omega)}{\tilde{\omega}_{nk} - \omega} + \frac{n(\omega)}{\tilde{\omega}_{nk} + \omega} \right]\end{aligned} \tag{41}$$

[note that $\mathrm{Re}\, \boldsymbol{G}(\mathbf{r}, \mathbf{r}', -\omega) = \mathrm{Re}\, \boldsymbol{G}(\mathbf{r}, \mathbf{r}', \omega)$ for real ω] with Matsubara frequencies

$$\xi_N = \frac{2\pi k_B T}{\hbar} N, \quad N = 0, 1, \ldots . \tag{42}$$

When neglecting the frequency shifts, the transition rates (30)–(33) obviously reduce to the well-known results given, e.g., in Ref. [30].

It is worth noting that the internal molecular dynamics described by Eqs. (28) and (29) obeys probability conservation,

$$\frac{d}{dt} \mathrm{tr}\, \hat{\sigma}(t) = \sum_n \dot{\sigma}_{nn}(t) = -\sum_{n,k} \Gamma_{nk} \sigma_{nn}(t) + \sum_{n,k} \Gamma_{kn} \sigma_{kk}(t) = 0, \tag{43}$$

where we have used Eq. (30). From the property

$$\Gamma_{nk} = e^{\hbar\tilde{\omega}_{nk}/(k_B T)} \Gamma_{kn} \tag{44}$$

of the transition rates [see Eq. (31)], it follows that in the long-time limit the molecule reaches a thermal state as its steady state

$$\hat{\sigma}(t \to \infty) = \hat{\sigma}_T = \frac{e^{-\Sigma_n \tilde{E}_n |n\rangle\langle n|/(k_B T)}}{\mathrm{tr}\left[e^{-\Sigma_n \tilde{E}_n |n\rangle\langle n|/(k_B T)} \right]} \tag{45}$$

with

$$\tilde{E}_n = \tilde{E}_n(\mathbf{r}_A) = E_n + \hbar\, \delta\omega_n \tag{46}$$

denoting the shifted molecular eigenenergies. This can be verified by noting that for this state the internal molecular evolution as given by Eqs. (28) and (29) becomes static,

$$\begin{aligned}\dot{\sigma}_{nn}(t \to \infty) &= -\Gamma_n \sigma_{nn,T} + \sum_k \Gamma_{kn} \sigma_{kk,T} \\ &= -\sum_k \Gamma_{nk} \sigma_{nn,T} + \sum_k e^{-\hbar\tilde{\omega}_{nk}/(k_B T)} \Gamma_n^k e^{\hbar\tilde{\omega}_{nk}/(k_B T)} \sigma_{nn,T} \\ &= 0,\end{aligned} \tag{47}$$

$$\sigma_{mn}(t \to \infty) = e^{\{-i\tilde{\omega}_{mn} - [\Gamma_m + \Gamma_n]/2\}(t - t_0)} \sigma_{mn,T} = 0 \quad \text{for } m \neq n. \tag{48}$$

According to Eqs. (30) and (31), the heating rate of a molecule prepared in its ground state $|0\rangle$ is given (initially) by

$$\begin{aligned}\Gamma_0 &= \sum_k \Gamma_{0k} \\ &= \sum_k \Gamma_{0k}^T \\ &= \frac{2\mu_0}{\hbar} \sum_k \tilde{\omega}_{k0}^2 n(\tilde{\omega}_{k0}) \mathbf{d}_{0k} \cdot \mathrm{Im}\, \boldsymbol{G}(\mathbf{r}_A, \mathbf{r}_A, \tilde{\omega}_{k0}) \cdot \mathbf{d}_{k0},\end{aligned} \tag{49}$$

due entirely to the absorption of thermal photons.

IV. APPLICATIONS

The energy associated with electronic excitation of molecules is typically large in comparison with thermal energy at room temperature, i.e., $\exp[-\hbar\omega_{n0}/(k_B T)] \ll 1$, so according to Eq. (44), the fully thermalized state effectively coincides with the electronic ground state. This argument does not apply to the rotational and vibrational excitations of polar molecules, which occur at much lower frequencies. In this section, we study the ground-state heating rates Γ_{0k} which provide a measure of the time scale on which this thermal excitation of the rotational and vibrational states takes place. We will assume that the frequency shifts induced by the en-

TABLE I. Properties of various diatomic radicals: electronic ground state, rotation and vibration constants, dipole moment and its derivative at equilibrium bond length, and reduced mass. For comparison with the constants used in [10], see [38].

Species	Ground state	B_e (GHz)	ω_e (THz)	μ_e (10^{-30} Cm)	μ_e' (10^{-21} C)	m (10^{-27} kg)[a]
LiH	$X\,^1\Sigma^+$	222 [40]	42.1 [10]	19.6 [41]	60.5 [10]	1.46
NH	$X\,^3\Sigma^-$	500 [42]	98.4 [42]	5.15 [43]	[b]	1.56
OH[c]	$X\,^2\Pi$	555 [45]	112 [47]	5.56 [48]	17.9 [49]	1.57
OD[c]	$X\,^2\Pi$	300 [50]	81.6 [50]	5.51 [48]	[b]	2.97
CaF	$X\,^2\Sigma^+$	10.5 [51]	18.4 [42]	10.2 [52]	172 [42]	21.4
BaF	$X\,^2\Sigma^+$	6.30 [10]	14.1 [10]	11.7 [10]	285 [10]	27.7
YbF	$X\,^2\Sigma^+$	7.20 [53]	15.2 [54]	13.1 [53]	195 [55]	28.4
LiRb	$X\,^1\Sigma^+$	6.60 [56]	5.55 [10]	13.5 [57]	21.4 [10,38]	10.8
NaRb	$X\,^1\Sigma^+$	2.03 [56]	3.21 [10]	11.7 [57]	12.6 [10]	30.0
KRb	$X\,^1\Sigma^+$	1.15 [58]	2.26 [10]	0.667 [57]	1.89 [10]	44.3
LiCs	$X\,^1\Sigma^+$	5.80 [59]	4.92 [10]	21.0 [57]	28.4 [10]	11.1
NaCs	$X\,^1\Sigma^+$	17.7 [59]	2.94 [10]	19.5 [57]	21.4 [10]	32.5
KCs	$X\,^1\Sigma^+$	92.8 [59]	1.98 [10]	8.61 [57]	6.93 [10]	50.0
RbCs	$X\,^1\Sigma^+$	0.498 [60]	1.48 [10]	7.97 [57]	4.41 [10]	86.0

[a]Reduced masses are given on the basis of the atomic masses (most abundant isotopes) of the molecular constituents as stated in Ref. [39].
[b]For NH and OD, the electric-dipole matrix elements for the transition between ground and first excited vibrational states can be given as $|\mathbf{d}_{0k}|=1.80\times10^{-31}$ Cm [42] and $|\mathbf{d}_{0k}|=7.54\times10^{-32}$ Cm [44], respectively.
[c]The spin-orbit coupling constants required for OH and OD are $A=-4.189$ THz [45] and $A=-4.174$ THz [46], respectively.

vironment are small enough to justify putting $\tilde{\omega}_{mn}=\omega_{mn}$. In this case the thermal excitation rate from the ground state to state k becomes

$$\Gamma_{0k}=\frac{2\mu_0}{\hbar}\omega_{k0}^2 n(\omega_{k0})\mathbf{d}_{0k}\cdot \mathrm{Im}\,\boldsymbol{G}(\mathbf{r}_A,\mathbf{r}_A,\omega_{k0})\cdot\mathbf{d}_{k0}. \quad (50)$$

This has the great virtue that the temperature appears only in the thermal photon number $n(\omega_{k0})$ [recall Eq. (19)], while the position enters only through the Green tensor $\boldsymbol{G}$. Therefore the dependence on temperature can be derived entirely from considering the free-space case, while the position-dependence can be understood completely from the behavior at zero temperature.

A. Molecules in free space

In free space, the Green tensor is given by Eq. (40), so the molecular transition rates become

$$\begin{aligned}\Gamma_{nk}&\equiv\Gamma_{nk}^{(0)}\\&\equiv\Gamma_{nk}^0+\Gamma_{nk}^T\\&=\frac{|\omega_{nk}|^3|\mathbf{d}_{nk}|^2}{3\pi\hbar\varepsilon_0c^3}\{\Theta(\omega_{nk})[n(\omega_{nk})+1]+\Theta(\omega_{kn})n(\omega_{kn})\}\end{aligned} \quad (51)$$

with

$$\Gamma_{nk}^0=\frac{\omega_{nk}^3|\mathbf{d}_{nk}|^2}{3\pi\hbar\varepsilon_0c^3}\Theta(\omega_{nk}) \quad (52)$$

and

$$\Gamma_{nk}^T=\frac{|\omega_{nk}|^3|\mathbf{d}_{nk}|^2}{3\pi\hbar\varepsilon_0c^3}[\Theta(\omega_{nk})n(\omega_{nk})+\Theta(\omega_{kn})n(\omega_{kn})]. \quad (53)$$

The total heating rate of a molecule initially prepared in its ground state thus reads

$$\Gamma_0=\sum_k\Gamma_{0k}=\sum_k\frac{\omega_{0k}^3|\mathbf{d}_{0k}|^2}{3\pi\hbar\varepsilon_0c^3}n(\omega_{k0}), \quad (54)$$

in agreement with Ref. [10].

The ground-state heating rate of polar molecules will be dominated by transitions to the adjacent excited rotational and vibrational states, so we restrict our attention to these in the following. We calculate the heating rates for the set of ground-state polar molecules listed in Table I, which also gives the required molecular constants.

We begin by considering rotational heating. To evaluate Eq. (54) we will calculate the matrix elements of the electric dipole operator using Hund's case (a) basis states [61]. In this coupling scheme, the orbital angular momentum $\hat{\mathbf{L}}$ is strongly coupled to the internuclear axis, and so is the electron spin $\hat{\mathbf{S}}$, due to a strong spin-orbit coupling. The total angular momentum is $\hat{\mathbf{J}}=\hat{\mathbf{L}}+\hat{\mathbf{S}}+\hat{\mathbf{R}}$, where $\hat{\mathbf{R}}$ is the angular momentum of the rotating nuclei and is necessarily perpendicular to the internuclear axis. The projections of $\hat{\mathbf{L}}$, $\hat{\mathbf{S}}$, and $\hat{\mathbf{J}}$ onto the internuclear axis are labeled by the quantum numbers Λ, Σ, and $\Omega=\Lambda+\Sigma$. The projection of $\hat{\mathbf{J}}$ onto the space-fixed z axis is M. The basis states are labeled by the quantum numbers S, Λ, Σ, Ω, J, and M.

For transitions between the rotational states, the matrix elements of the electric dipole operator are

$$\begin{aligned}\mathbf{d}_{mn} &= \langle \Omega JM|\hat{\mathbf{d}}|\Omega' J' M'\rangle \\ &= \mu_e \langle \Omega JM|\hat{\mathbf{u}}|\Omega' J' M'\rangle \\ &= \mu_e \left[(u_{mn}^{-1} - u_{mn}^{+1})\frac{\mathbf{e}_x}{\sqrt{2}} + (u_{mn}^{-1} + u_{mn}^{+1})\frac{i\mathbf{e}_y}{\sqrt{2}} + u_{mn}^{0}\mathbf{e}_z \right],\end{aligned} \tag{55}$$

where μ_e is the molecular dipole moment at the equilibrium internuclear separation, $\hat{\mathbf{u}} = \hat{\mathbf{r}}/|\hat{\mathbf{r}}|$, and

$$u_{mn}^{q} = (-1)^{M-\Omega}\sqrt{(2J+1)(2J'+1)} \times \begin{pmatrix} J & 1 & J' \\ -M & q & M' \end{pmatrix}\begin{pmatrix} J & 1 & J' \\ -\Omega & 0 & \Omega' \end{pmatrix}. \tag{56}$$

With this result, we obtain the selection rules for transitions between the basis states: $\Delta\Omega = 0$, $\Delta J = 0, \pm 1$, and $\Delta M = 0, \pm 1$. In this paper, we will not consider mixing of the electronic ground state with other electronic states, which leads to Λ doubling, because the energy splitting that is induced is very small compared with the rotational energies and so does not alter any of our results. In this approximation, the states $|\pm \Omega JM\rangle$ are degenerate, and since $\Delta\Omega = 0$ we can confine our attention to the positive values of Ω only. While our equations make it clear how to handle initial states of given M', we will consider the initial molecular state to be unpolarized, averaging over the possible values of M'.

The majority of the molecules listed in Table I have $\Lambda = 0$ ground states. These molecules are best described using Hund's coupling case (b) [61]. The spin is not coupled to the internuclear axis and neither Σ nor Ω is defined. The rotational eigenenergies are

$$E_N = hB_e N(N+1), \quad N = 0, 1, \ldots, \tag{57}$$

where B_e is the rotational constant and N is the rotational quantum number, $\hat{\mathbf{N}} = \hat{\mathbf{J}} - \hat{\mathbf{S}}$. The expansion of the Σ eigenstates in the case (a) basis is [61]

$$|S,N,J,M\rangle = \sum_{\Omega=-S}^{S} (-1)^{J-S}\sqrt{2N+1}\begin{pmatrix} J & S & N \\ \Omega & -\Omega & 0 \end{pmatrix}|\Omega,J,M\rangle. \tag{58}$$

Using Eqs. (55), (56), and (58), summing over the possible final states and averaging over initial states of different M', we find $\Sigma_k |\mathbf{d}_{0k}|^2 = \mu_e^2$ for $^1\Sigma$, $^2\Sigma$, and $^3\Sigma$ molecules. For $^2\Sigma$ molecules, the ground state $|N=0, J=1/2\rangle$ can be excited either to $|N=1, J=1/2\rangle$ or to $|N=1, J=3/2\rangle$, with branching ratios $1/3$ and $2/3$, respectively. The spin-rotation interaction lifts the degeneracy between these states, but this splitting is very small and we do not need to include it. For $^3\Sigma$ molecules, the ground state $|N=0, J=1\rangle$ can be excited to the three states with $N=1$ and $J=0,1,2$, with branching ratios $1/9$, $1/3$, and $5/9$, respectively. Again, we can neglect the small spin-rotation interaction that lifts the degeneracy between the three states.

The electronic ground states of OH and OD are $^2\Pi$ states and, for low values of J, are best described using Hund's coupling case (a). The Hamiltonian describing the fine structure contains a rotational part and a spin-orbit coupling, $\hat{H}_{fs} = hA\hat{\mathbf{L}}\cdot\hat{\mathbf{S}} + hB_e(\hat{\mathbf{J}} - \hat{\mathbf{L}} - \hat{\mathbf{S}})^2$. The rotational term couples states of the same J but different $|\Omega|$. Writing the matrix elements of the Hamiltonian as $m_{\Omega,\Omega'} = \langle \Omega JM|\hat{H}_{fs}|\Omega' JM\rangle$ we have [61]

$$m_{1/2,1/2}^{3/2,3/2} = \pm hA/2 + hB_e[J(J+1) - 3/4 \mp 1], \tag{59}$$

$$m_{3/2,1/2} = -hB_e\sqrt{(J+3/2)(J-1/2)}. \tag{60}$$

Diagonalizing this Hamiltonian gives a pair of energy eigenvalues for each value of $J > 1/2$,

$$E_J = hB_e[(J+1/2)^2 - 1 \pm \mathcal{Q}/2], \tag{61}$$

where

$$\mathcal{Q} = \sqrt{4(J+1/2)^2 + A/B_e(A/B_e - 4)}. \tag{62}$$

We will use the labels F_1 and F_2 to denote the states of lower and higher energy, respectively. For the low-J levels of OH and OD, the mixing of Ω states is small because $|A|$ is considerably larger than $B_e J$. Recalling that A is negative for these molecules, we can then identify F_1 as having predominantly $^2\Pi_{3/2}$ character, and F_2 as predominantly $^2\Pi_{1/2}$. For $J = 1/2$ there is only one level, which is of pure $\Omega = 1/2$ character. The eigenstates are

$$|F_1,J,M\rangle = c_+(J)|1/2,J,M\rangle + c_-(J)|3/2,J,M\rangle, \quad J = 3/2, 5/2, \ldots, \tag{63}$$

$$|F_2 J,M\rangle = c_+(J)|3/2,J,M\rangle - c_-(J)|1/2,J,M\rangle, \quad J = 1/2, 3/2 \ldots, \tag{64}$$

where

$$c_\pm(J) = \sqrt{1/2 \pm (A/B_e - 2)/(2\mathcal{Q})}. \tag{65}$$

Using the selection rules between the basis states, we see that the possible transitions out of the molecular ground state $|F_1, J=3/2\rangle$ are those to the states (a) $|F_1, J=5/2\rangle$, (b) $|F_2, J=1/2\rangle$, (c) $|F_2, J=3/2\rangle$, and (d) $|F_2, J=5/2\rangle$. Applying Eqs. (55) and (56) to each of these four transitions, summing over the M sublevels in the final state, and averaging over the M' sublevels in the initial state, we obtain

$$\sum_{k(a)} |\mathbf{d}_{0k}|^2 = \left[\frac{3}{5}c_+^2(3/2)c_+^2(5/2) + \frac{2}{5}c_-^2(3/2)c_-^2(5/2) + \frac{6}{5}\sqrt{\frac{2}{3}}c_+(3/2)c_+(5/2)c_-(3/2)c_-(5/2) \right]\mu_e^2, \tag{66}$$

$$\sum_{k(b)} |\mathbf{d}_{0k}|^2 = \frac{1}{3}c_+^2(3/2)\mu_e^2, \tag{67}$$

TABLE II. Free-space lifetimes for rotational heating out of the ground state at 293 K and 77 K. For OH and OD, the effects of the transitions (a)–(d) (see main text) are also shown separately. Also given are the frequency and the square of the dipole matrix element for each transition. For comparison with the results of [10], see [38].

Species	$\frac{\omega_{0k}}{2\pi}$ (GHz)	$\frac{\Sigma_k \lvert\mathbf{d}_{0k}\rvert^2}{\mu_e^2}$	$\tau^{(0)}$ (s)	
			293 K	77 K
LiH	444	1	2.1	9.1
NH	999	1	6.4	31
OH			2.1	17
(a)	2.51×10^3	0.405	2.4	18
(b)	3.80×10^3	0.00999	49	550
(c)	5.64×10^3	0.00775	34	720
(d)	8.67×10^3	0.00124	120	8400
OD			6.3	37
(a)	1.41×10^3	0.402	7.2	39
(b)	3.93×10^3	0.00381	120	1400
(c)	4.89×10^3	0.00302	110	1800
(d)	6.48×10^3	0.000636	340	10 000
CaF	21.0	1	3400	13 000
BaF	12.6	1	7200	28 000
YbF	14.4	1	4400	17 000
LiRb	13.2	1	4900	19 000
NaRb	4.05	1	70 000	260 000
KRb	2.30	1	6.7×10^7	2.5×10^8
LiCs	11.6	1	2600	10 000
NaCs	35.5	1	330	13 000
KCs	186	1	62	250
RbCs	0.995	1	2.5×10^6	9.5×10^6

$$\sum_{k(c)} |\mathbf{d}_{0k}|^2 = \frac{4}{15} c_+^2(3/2) c_-^2(3/2) \mu_e^2, \tag{68}$$

$$\sum_{k(d)} |\mathbf{d}_{0k}|^2 = \left[\frac{3}{5} c_+^2(3/2) c_-^2(5/2) + \frac{2}{5} c_-^2(3/2) c_+^2(5/2) - \frac{6}{5}\sqrt{\frac{2}{3}} c_+(3/2) c_-(3/2) c_+(5/2) c_-(5/2) \right] \mu_e^2. \tag{69}$$

With these preparations, we can now evaluate the rates for free-space rotational heating out of the ground state, for the molecules listed in Table I. The lifetimes, $\tau^{(0)}=(\Gamma^{(0)})^{-1}$, are given in Table II for environmental temperatures of 293 K and 77 K. Since there is little variation of the dipole moment, the lifetime is mainly determined by the power of the thermal spectrum at the transition frequency. Apart from the weakest transitions in OH and OD all these lines lie on the low side of the peak frequency in the thermal spectrum, which is 17 THz at 293 K or 5 THz at 77 K. Note that the rotational constant is roughly given by $B_e \approx \hbar/(4\pi m R_e^2)$, where R_e is the equilibrium internuclear separation and $m = m_1 m_2/(m_1+m_2)$ is the reduced mass, so as a rule of thumb, rotational heating is most severe for the light molecules. Strong heating is seen for LiH, NH, OH, OD, whose lifetimes are in the range of 2–6 seconds. For KCs and NaCs the heating is much less severe, and for the rest it is negligible for most practical purposes. Table II also shows that rotational heating of OH and OD is dominated by transition (a), with the other transitions providing small corrections to the heating rate, even though they are at higher frequencies. This behavior is due to the exceedingly small transition dipole moments of the latter transitions. The rotational excitation lifetimes of all these molecules can be extended by going to lower environmental temperatures. Figure 1 illustrates this temperature dependence in the light molecules LiH, NH, OH, OD, and KCs.

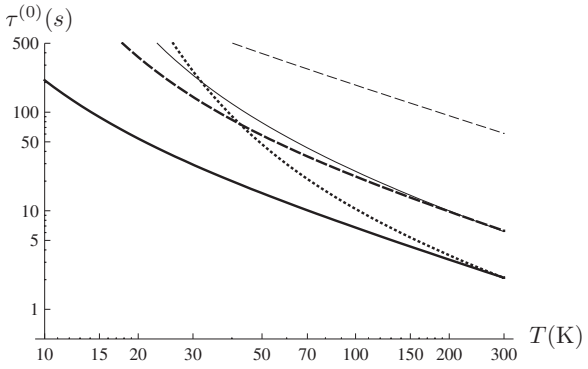

FIG. 1. Free-space lifetimes of the ground state against rotational heating as a function of environment temperature for LiH (thick solid line), NH (thick dashed line), OH(a) (thick dotted line), OD(a) (thin solid line), and KCs (thin dashed line).

Let us next turn our attention to vibrational heating. To a good approximation, the vibrational eigenenergies of the deeply-bound states of a diatomic molecule are

$$E_v = h\omega_e\left(v+\frac{1}{2}\right), \quad v=0,1,\ldots, \tag{70}$$

where ω_e is the vibrational constant and v is the vibrational quantum number. The corresponding eigenstates are

$$\langle q|v\rangle = \left(\frac{\alpha}{\pi}\right)^{1/4} \frac{1}{\sqrt{2^v v!}} H_v(\sqrt{\alpha} q) e^{-1/2\alpha q^2}, \tag{71}$$

where $q=R-R_e$, R being the internuclear separation, H_n are the Hermite polynomials and $\alpha=2\pi m\omega_e/\hbar$. Expanding the electric-dipole operator in a Taylor series about the equilibrium separation, $\hat{\mathbf{d}} \approx (\mu_e+\mu_e' \hat{q})\hat{\mathbf{u}}$, and recognizing that the first term cannot couple different vibrational states, we write the matrix elements for rovibrational transitions in the form

TABLE III. Lifetime against free-space vibrational heating out of the ground state for various polar molecules at 293 K and 77 K. For comparison with the results of [10], see [38].

Species	$\frac{\omega_{k0}}{2\pi}$ (THz)	$\tau^{(0)}$ (s)	
		$T=293$ K	$T=77$ K
LiH	42.1	25	6.5×10^{9}
NH	98.4	310 000	1.3×10^{25}
OH	112	9.8×10^{6}	2.2×10^{29}
OD	81.6	200 000	3.7×10^{21}
CaF	18.4	4.7	23 000
BaF	14.1	1.8	1300
YbF	15.2	4.1	4700
LiRb	5.55	128	2700
NaRb	3.21	1400	13 000
KRb	2.26	120 000	850 000
LiCs	4.92	80	1300
NaCs	2.94	580	4900
KCs	1.98	12 000	74 000
RbCs	1.48	63 000	350 000

$$\langle v\Omega JM|\hat{\mathbf{d}}|v'\Omega'JM'\rangle = \mu_e'\langle \Omega JM|\hat{\mathbf{u}}|\Omega'J'M'\rangle\langle v|\hat{q}|v'\rangle. \tag{72}$$

We see from this equation that the rovibrational transitions must satisfy the same rotational selection rules as already given above, and that to leading order in q, the vibrational selection rule is $\Delta v=\pm 1$. For transitions between $v'=0$ and $v=1$ we have

$$\langle v=1|\hat{q}|v'=0\rangle = \frac{1}{\sqrt{2\alpha}} = \sqrt{\frac{\hbar}{4\pi m\omega_e}}. \tag{73}$$

We neglect the contribution of rotational energy to the transition frequency since it is typically smaller than the vibrational energy by two orders of magnitude. This means that we can simply add up the contributions of transitions (a)–(d) in calculating the transition dipole moments for OH and OD. Thus we obtain

$$\sum_k |\mathbf{d}_{0k}|^2 = \frac{\hbar\mu_e'^2}{4\pi m\omega_e} f_{\rm rot}, \tag{74}$$

where $f_{\rm rot}=1$ for the Σ molecules, while for molecules with a $^2\Pi_{3/2}$ ground state,

$$f_{\rm rot} = \frac{14}{15}c_+^2(3/2) + \frac{2}{5}c_-^2(3/2) + \frac{4}{15}c_+^2(3/2)c_-^2(3/2). \tag{75}$$

The calculated lifetimes for free-space vibrational heating out of the ground state are given in Table III for $T=293$ K and $T=77$ K. These lifetimes are mainly determined by the vibrational transition frequencies. Since $\omega_e \propto 1/\sqrt{m}$, the lightest molecules have the highest vibration frequencies, which lie above the 17 THz peak of the room temperature spectrum, while the heaviest molecules vibrate well below this frequency. The vibrational transition frequencies of CaF, BaF, and YbF fall close to this maximum, and of the molecules considered these three also have the largest values of μ_e'. For both reasons, the ground-state lifetimes of these molecules are limited by vibrational heating to less than 5 s. For LiH and LiCs the vibrational heating is an order of magnitude slower, while it is exceedingly slow for all the other molecules. This slowness is mainly due to inefficient coupling with the thermal radiation which occurs both for the heavy molecules LiRb, NaRb, KRb, NaCs, KCs, and RbCs whose vibration frequencies are too low and, even more strikingly, for the light molecules NH, OH, and OD whose frequencies are too high. Due to the large transition frequencies, the impact of lowering the environment temperature is even more striking for vibrational heating than in the rotational case. This is illustrated in Fig. 2 where the temperature dependence of the lifetimes is displayed for the molecules LiH, CaF, BaF, and YbF, which are most strongly affected by vibrational heating.

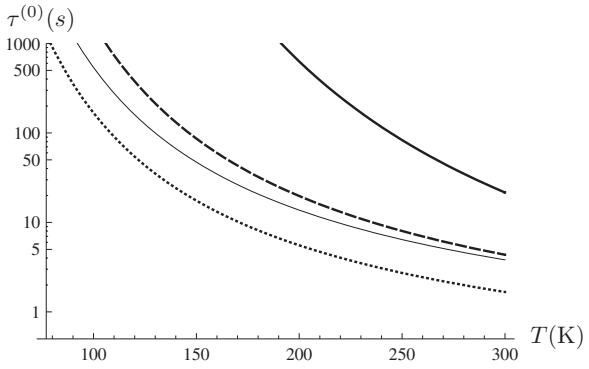

FIG. 2. Ground-state vibrational heating lifetimes in free space vs temperature for LiH (thick solid line), CaF (thick dashed line), YbF (thin solid line), and BaF (thick dotted line).

The relative importance of rotational vs vibrational heating varies from molecule to molecule. Rotational heating dominates for the hydrides and for NaCs and KCs, while vibrational heating is dominant for the fluorides in the list, and for the other alkali dimers.

We have confined our attention to the rates for rotational and vibrational excitation out of the ground state. The calculation is very easily adapted to the excited states, remembering that then there will be both excitation processes to higher lying states, and deexcitation processes to lower lying ones. For the latter processes, $n(\omega_{k0})$ should be replaced with $n(\omega_{k0})+1$ to account for spontaneous emission. The calculations also need to be modified if applied electric or magnetic fields are present, so as to account for the Stark or Zeeman shifted transition frequencies, and any associated change in the transition dipole moments.

B. Molecules near a surface

We turn now to the question of how proximity to a surface can affect the heating rate. Let us consider a molecule at distance z_A from the surface of a homogeneous magnetoelec-

tric body of (relative) permittivity $\varepsilon(\omega)$ and (relative) permeability $\mu(\omega)$. The body can be modeled by a semi-infinite half space provided it is close enough to the molecule and sufficiently smooth. The scattering part of the Green tensor is then given by

$$\boldsymbol{G}^{(1)}(\mathbf{r},\mathbf{r},\omega) = \frac{i}{8\pi}\int_0^\infty dq \frac{q}{\beta} e^{2i\beta z} \times \left[\left(r_s - \frac{\beta^2 c^2}{\omega^2} r_p\right)(\mathbf{e}_x\mathbf{e}_x + \mathbf{e}_y\mathbf{e}_y) + 2\frac{q^2 c^2}{\omega^2} r_p \mathbf{e}_z\mathbf{e}_z\right] \tag{76}$$

where

$$r_s = \frac{\mu(\omega)\beta - \beta_1}{\mu(\omega)\beta + \beta_1}, \quad r_p = \frac{\varepsilon(\omega)\beta - \beta_1}{\varepsilon(\omega)\beta + \beta_1} \tag{77}$$

are the reflection coefficients for s- and p-polarized waves,

$$\beta = \sqrt{\frac{\omega^2}{c^2} - q^2}, \quad \beta_1 = \sqrt{\frac{\omega^2}{c^2}\varepsilon(\omega)\mu(\omega) - q^2} \tag{78}$$

(Im β, Im $\beta_1 \geqslant 0$) denote the z component of the wave vector in free space (β) and inside the half space (β_1) and q is its component parallel to the surface. For computational purposes, it is often convenient to express the Green tensor as an integral over β,

$$\begin{aligned}\boldsymbol{G}^{(1)}(\mathbf{r},\mathbf{r},\omega) = {} & \frac{i}{8\pi}\int_0^{\omega/c} d\beta e^{2i\beta z}\left[\left(r_s - \frac{\beta^2 c^2}{\omega^2} r_p\right)(\mathbf{e}_x\mathbf{e}_x + \mathbf{e}_y\mathbf{e}_y) + 2\left(1 - \frac{\beta^2 c^2}{\omega^2}\right) r_p \mathbf{e}_z\mathbf{e}_z\right] \\ & + \frac{1}{8\pi}\int_0^\infty db e^{-2bz}\left[\left(r_s + \frac{b^2 c^2}{\omega^2} r_p\right)(\mathbf{e}_x\mathbf{e}_x + \mathbf{e}_y\mathbf{e}_y) + 2\left(1 + \frac{b^2 c^2}{\omega^2}\right) r_p \mathbf{e}_z\mathbf{e}_z\right]\end{aligned} \tag{79}$$

($\beta = ib$). Here, the first term represents the oscillating contributions due to traveling waves, while the second term contains the exponentially decaying contributions from evanescent waves.

Transition rates for a molecule near a half space can be obtained by substituting the scattering part of the Green tensor $\boldsymbol{G}^{(1)}$ [as given by Eq. (76) or Eq. (79)] together with its free-space part [Eq. (40)] into Eq. (31). The ground-state heating rates then take the particularly simple form

$$\begin{aligned}\Gamma(\mathbf{r}_A) &= \Gamma^{(0)} + \Gamma^{(1)}(\mathbf{r}_A) \\ &= \Gamma^{(0)}\left[1 + \frac{2\pi c}{\omega_{k0}} \operatorname{Im} \operatorname{tr} \boldsymbol{G}^{(1)}(\mathbf{r}_A,\mathbf{r}_A,\omega_{k0})\right].\end{aligned} \tag{80}$$

In general, the integral appearing in Eq. (76) or Eq. (79) has to be evaluated numerically, but analytic results can be obtained for sufficiently small or large molecule-surface separations. The nonretarded limit applies to short distances, where $z|\sqrt{\varepsilon\mu}|\omega/c \ll 1$, while the retarded limit holds for long distances such that $z\omega/c \gg 1$. For the materials we consider in this paper, $|\sqrt{\varepsilon\mu}|$ takes on values between 65 and 27 000 for rotational transitions and between 4.5 and 700 for vibrational transitions, depending on the molecule and the material. Consequently, there is quite a large range of intermediate distances where neither limit applies.

In the nonretarded limit, the Green tensor (79) is dominated by the integral over evanescent waves, which effectively extends up to a wave vector $b = 1/(2z)$. Over most of this region, $\beta \simeq \beta_1 \simeq iq$, allowing us to use the approximations

$$r_s \simeq \frac{\mu(\omega) - 1}{\mu(\omega) + 1}, \quad r_p \simeq \frac{\varepsilon(\omega) - 1}{\varepsilon(\omega) + 1}. \tag{81}$$

Performing the remaining integral and retaining only the leading order in $z\omega/c$, one finds that in this nonretarded limit, the Green tensor is well approximated by [31]

$$\boldsymbol{G}^{(1)}(\mathbf{r},\mathbf{r},\omega) = \frac{c^2}{32\pi\omega^2 z^3}\frac{\varepsilon(\omega) - 1}{\varepsilon(\omega) + 1}(\mathbf{e}_x\mathbf{e}_x + \mathbf{e}_y\mathbf{e}_y + 2\mathbf{e}_z\mathbf{e}_z). \tag{82}$$

Note that by retaining only the leading order in $z\omega/c$, the dependence on r_s and thus also that on μ has vanished. In any case, μ is close to 1 even for the ferromagnetic metals at the typical frequencies of interest here (i.e., $\omega/2\pi > 10$ GHz). On substituting Eq. (82) into Eq. (31), we obtain the approximate, near-field transition rate

$$\Gamma_{nk}(z_A) = \Gamma_{nk}^{(0)} + \frac{|\mathbf{d}_{nk}|^2 + |d_{nk,z}|^2}{8\pi\varepsilon_0\hbar z_A^3}\frac{\operatorname{Im}\varepsilon(\omega_{nk})}{|\varepsilon(\omega_{nk}) + 1|^2} \times \{\Theta(\omega_{nk})[n(\omega_{nk}) + 1] - \Theta(\omega_{kn})n(\omega_{kn})\}. \tag{83}$$

In particular, the ground-state heating rates (80) are approximated by

$$\Gamma(z_A) = \Gamma^{(0)}\left(1 + \frac{z_{\mathrm{nr}}^3}{z_A^3}\right) \tag{84}$$

where

$$z_{\mathrm{nr}} = \frac{c}{\omega_{k0}}\sqrt[3]{\frac{\operatorname{Im}\varepsilon(\omega_{k0})}{2|\varepsilon(\omega_{k0}) + 1|^2}} \tag{85}$$

is a scaling length that applies to calculations in the nonretarded limit. For a metal with permittivity

$$\varepsilon(\omega) = 1 - \frac{\omega_{\mathrm{P}}^2}{\omega(\omega + i\gamma)} \tag{86}$$

and for sufficiently small transition frequency, $\omega_{k0} \ll \gamma \leqslant \omega_{\mathrm{P}}$, z_{nr} may be estimated by the simple relation

$$z_{\mathrm{nr}} = c\sqrt[3]{\frac{\gamma}{2\omega_{\mathrm{P}}^2\omega_{k0}^2}}. \tag{87}$$

The plasma frequency, ω_{P}, and damping constant, γ, are given for various conductors in Table IV.

We stress that Eq. (84) applies only in the nonretarded limit, and that the distance z_{nr} typically lies well outside this limit. We define a second relevant length scale, z_{c}, the characteristic distance at which the surface-induced rate becomes equal to the free-space rate. This does not coincide with z_{nr},

TABLE IV. Drude parameters for various conductors. Values are taken from Ref. [62], with the exception of those for ITO (indium tin oxide) [63]. The list is in order of decreasing ω_P^2/γ, which corresponds to increasing surface heating rate.

Material	ω_P (rad/s)	γ (rad/s)	ω_P^2/γ (rad/s)
Au	1.37×10^{16}	4.12×10^{13}	4.53×10^{18}
Al	2.25×10^{16}	1.22×10^{14}	4.15×10^{18}
Pd	8.36×10^{15}	2.16×10^{13}	3.24×10^{18}
Ag	5.77×10^{15}	1.15×10^{13}	2.89×10^{18}
Cu	1.12×10^{16}	4.41×10^{13}	2.87×10^{18}
Mo	1.14×10^{16}	7.86×10^{13}	1.65×10^{18}
Fe	6.23×10^{15}	2.79×10^{13}	1.39×10^{18}
Co	1.18×10^{16}	1.07×10^{14}	1.29×10^{18}
W	9.72×10^{15}	8.53×10^{13}	1.11×10^{18}
Ni	7.44×10^{15}	6.53×10^{13}	8.49×10^{17}
Pt	7.75×10^{15}	1.04×10^{14}	5.75×10^{17}
ITO	3.33×10^{15}	1.68×10^{14}	6.63×10^{16}

because the nonretarded limit is not valid at this distance. We have calculated z_c by numerical integration of Eqs. (79) and (80) and we present the results for molecules near a gold surface in Table V, and for a range of other conductors in Appendix B. Table V also gives the corresponding values of z_{nr}, which are typically 2–5 times smaller.

Since Eq. (84) does not apply at length scales in the vicinity of the critical distance, we searched for an alternative formula by fitting to the numerical results obtained from the integration of Eqs. (79) and (80) at distances $z \leqslant z_c$. We find that for the molecules and surface materials studied, the heating rates throughout this range are well approximated by the empirical formula

$$\Gamma(z_A) = \Gamma^{(0)}\left(1 + \frac{z_c^2}{z_A^2} + \frac{z_{nr}^3}{z_A^3}\right). \tag{88}$$

Furthermore, a fit to the set of critical distances for rotational heating given in Appendix B, suggests the approximate formula

$$z_c \simeq \frac{3c}{4}\sqrt[4]{\frac{\gamma}{2\omega_P^2\omega_{k0}^3}}. \tag{89}$$

This empirical formula was found to be accurate to within 1% for all the surfaces and molecules considered, except in cases where the critical distances are particularly small (the hydrides and KCs), where deviations between 1% and 10% are more typical. The same formula does not accurately predict the critical distances for vibrational heating, but these are of less importance due to their very small values. We stress again that Eq. (88) is only empirical as the z_A^{-2} term has no physical interpretation.

The critical distances given in Table V show that the surface does not generate any significant heating when the molecules are more than a few hundred μm away. However, if the molecules are held a few μm from a surface, as they might be on a molecule chip, there is a substantial increase in the rotational heating for all the molecules considered, apart from the hydrides. Even in cases where the free-space rate is small, the enhanced rate can be very large because of the rapid inverse-power scaling. For example, in free space, the rotational heating time of CaF, 3400 s, is enormous compared with the vibrational lifetime of 4.7 s. However, at a distance of 1 μm from a room temperature gold surface the lifetime for rotational excitation drops to about 8 s and at smaller distances the rotational heating rate dominates over the vibrational rate. For the hydrides, the high rotational frequency that gives them rapid free-space heating also makes them relatively insensitive to the proximity of the surface except at submicron distances.

TABLE V. Nonretarded length scales and critical distances for surface enhancement of rotational and vibrational heating rates near a gold surface.

	Rotational		Vibrational	
Species	z_{nr} (μm)	z_c (μm)	z_{nr} (μm)	z_c (μm)
LiH	0.73	1.9	0.035	0.071
NH	0.42	1.0	0.020	0.042
OH			0.018	0.0039
(a)	0.23	0.50		
(b)	0.17	0.36		
(c)	0.13	0.27		
(d)	0.10	0.20		
OD			0.022	0.0048
(a)	0.34	0.78		
(b)	0.17	0.35		
(c)	0.15	0.30		
(d)	0.12	0.24		
CaF	5.5	19	0.061	0.12
BaF	7.8	27	0.072	0.14
YbF	7.1	25	0.069	0.14
LiRb	7.6	26	0.13	0.27
NaRb	17	64	0.19	0.41
KRb	24	98	0.24	0.54
LiCs	8.2	29	0.15	0.30
NaCs	3.9	13	0.21	0.44
KCs	1.3	3.6	0.27	0.60
RbCs	42	180	0.33	0.75

Figure 3(a) shows the critical distances for rotational heating of various molecules near a range of surfaces. It is seen that their frequency scaling follows quite nicely the $\omega^{-3/4}$ dependence given by Eq. (89), which is indicated by the solid line. This trend continues in Fig. 3(b), which shows the critical distances for vibrational heating. These are, of course, smaller because the vibrational frequencies are higher.

Equation (87) shows that the short-range heating depends on the surface material through the factor ω_P^2/γ. A low value of this ratio leads to a large critical distance and hence to more surface-induced heating. The values are displayed in the last column of Table IV for various metals in order of

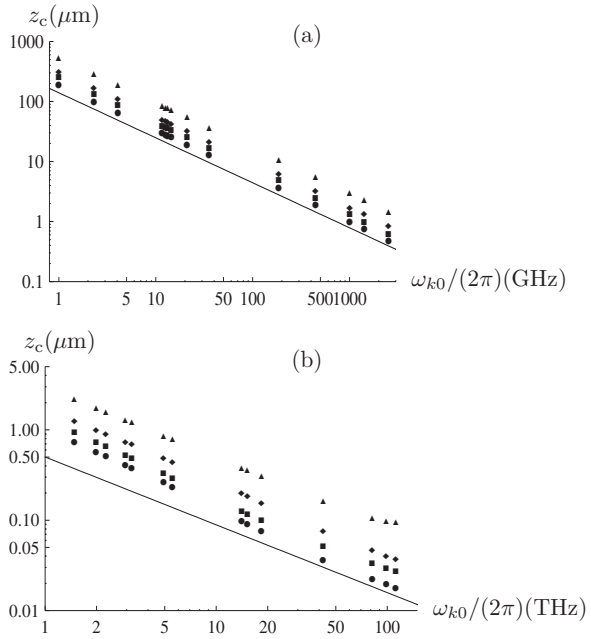

FIG. 3. Exact critical distances for surface-induced heating vs frequency of the molecular transition. (a) Rotational heating. (b) Vibrational heating. Surface materials are gold (circles), iron (squares), platinum (diamonds), and ITO (triangles). Frequencies of the plotted data points correspond (left to right) to RbCs, KRb, NaRb, LiCs, BaF, LiRb, YbF, CaF, NaCs, KCs, LiH, NH, OD(a), and OH(a). Solid lines indicate the slope corresponding to the $\omega^{-3/4}$ frequency dependence given by the empirical formula (89).

decreasing ω_P^2/γ. In this list, gold is the metal of choice when trying to minimize surface-induced heating of the molecules, as also indicated by the circles in Fig. 3. At the opposite extreme lies indium tin oxide (ITO), which we include here because of its attractive combination of conductivity and optical transparency. It has a low plasma frequency and a high damping rate γ and so generates stronger heating, as shown by the triangles in Fig. 3. The values for other metals generally obey the ω_P^2/γ scaling, though there are some exceptions where values of ω_P^2/γ are very similar.

As indicated by Eq. (85), the surface-induced heating will be particularly large in cases where $|\varepsilon|$ is not large, but ε has a significant imaginary part. This never happens for a conductor, but can occur for dielectric media that happen to be strong absorbers at the relevant frequency. As an example, consider borosilicate glass which has $\varepsilon=6.2+0.21i$ for frequencies in the tens of GHz range [64]. The critical distance for rotational heating of CaF near such a surface is about 620 μm, very much larger than for a metallic surface. The time scale for rotational heating, which is 3400 s in free space, is thus reduced to just 0.14 s when this molecule is 10 μm from such a glass surface.

Next, we turn to the retarded limit, where $z\omega/c \gg 1$, so the integrand in Eq. (79) is rapidly oscillating or decaying over most parts of the integration regime. The main contribution to the integral (79) comes from the region around the stationary-phase point $q=0$, so that we may approximate

$$r_s \simeq -r_p \simeq \frac{\sqrt{\mu(\omega)}-\sqrt{\varepsilon(\omega)}}{\sqrt{\mu(\omega)}+\sqrt{\varepsilon(\omega)}}. \tag{90}$$

The integral can then be performed, and upon retaining the leading order in $c/(z\omega)$, one finds that the Green tensor in the retarded limit reads

$$\boldsymbol{G}^{(1)}(\mathbf{r},\mathbf{r},\omega) = \frac{e^{2iz\omega/c}}{8\pi z}\frac{\sqrt{\mu(\omega)}-\sqrt{\varepsilon(\omega)}}{\sqrt{\mu(\omega)}+\sqrt{\varepsilon(\omega)}}(\mathbf{e}_x\mathbf{e}_x+\mathbf{e}_y\mathbf{e}_y). \tag{91}$$

Consequently, the transition rates (31) are given by

$$\Gamma_{nk}(z_A) = \Gamma_{nk}^{(0)} + \frac{\omega_{nk}^2(|d_{nk,x}|^2+|d_{nk,y}|^2)}{4\pi\varepsilon_0\hbar c^2 z_A} \times \mathrm{Im}\left(\frac{\sqrt{\mu(\omega_{nk})}-\sqrt{\varepsilon(\omega_{nk})}}{\sqrt{\mu(\omega_{nk})}+\sqrt{\varepsilon(\omega_{nk})}}e^{2iz_A\omega_{nk}/c}\right) \times\{\Theta(\omega_{nk})[n(\omega_{nk})+1]-\Theta(\omega_{kn})n(\omega_{kn})\}; \tag{92}$$

for a good conductor, $|\varepsilon| \gg |\mu|$, they further simplify to

$$\Gamma_{nk}(z_A) = \Gamma_{nk}^{(0)} - \frac{\omega_{nk}^2(|d_{nk,x}|^2+|d_{nk,y}|^2)}{4\pi\varepsilon_0\hbar c^2 z_A}\sin\left(\frac{2z_A\omega_{nk}}{c}\right) \times\{\Theta(\omega_{nk})[n(\omega_{nk})+1]-\Theta(\omega_{kn})n(\omega_{kn})\}. \tag{93}$$

In particular, the ground-state heating rates (80) are given by

$$\Gamma(z_A) = \Gamma^{(0)}\left[1+\frac{c}{2z_A\omega_{k0}} \times \mathrm{Im}\left(\frac{\sqrt{\mu(\omega_{k0})}-\sqrt{\varepsilon(\omega_{k0})}}{\sqrt{\mu(\omega_{k0})}+\sqrt{\varepsilon(\omega_{k0})}}e^{2iz_A\omega_{k0}/c}\right)\right] \simeq \Gamma^{(0)}\left[1-\frac{c}{2z_A\omega_{k0}}\sin\left(\frac{2z_A\omega_{nk}}{c}\right)\right]. \tag{94}$$

Thus, the surface-induced modification of the heating rates in the retarded limit is an oscillating function of distance, where the amplitude of the oscillation follows a z_A^{-1} power law. In particular, the heating rates approach their free-space values in the limit $z_A \to \infty$.

In order to see the entire distance dependence of the heating rate it is necessary to calculate the rates as given by Eqs. (79) and (80) numerically. The results are displayed in Fig. 4 where we show the total heating rates as a function of distance for OH, LiH, CaF, and NaCs molecules at distances in the range 1–500 μm from a gold surface. In all cases, the vibrational heating rate is dotted, the rotational rate is dashed, and the total rate is a solid line. For OH the heating is entirely dominated by the rotational transitions over the whole of this distance range, and the vibrational contribution does not even appear in the plot. The heating rate is modulated with a period of 60 μm just as expected in the retarded limit [Eq. (94)]. The heating rate is not greatly altered from its free space value, even at the shortest distance considered. For LiH, the heating is again dominated by the rotational transitions. The far-field oscillations modulate the rate and we see roughly one cycle with a period of 338 μm. The heating rate rises sharply inside the critical distance for rotational excitation, which is 1.9 μm, whereas the vibrational

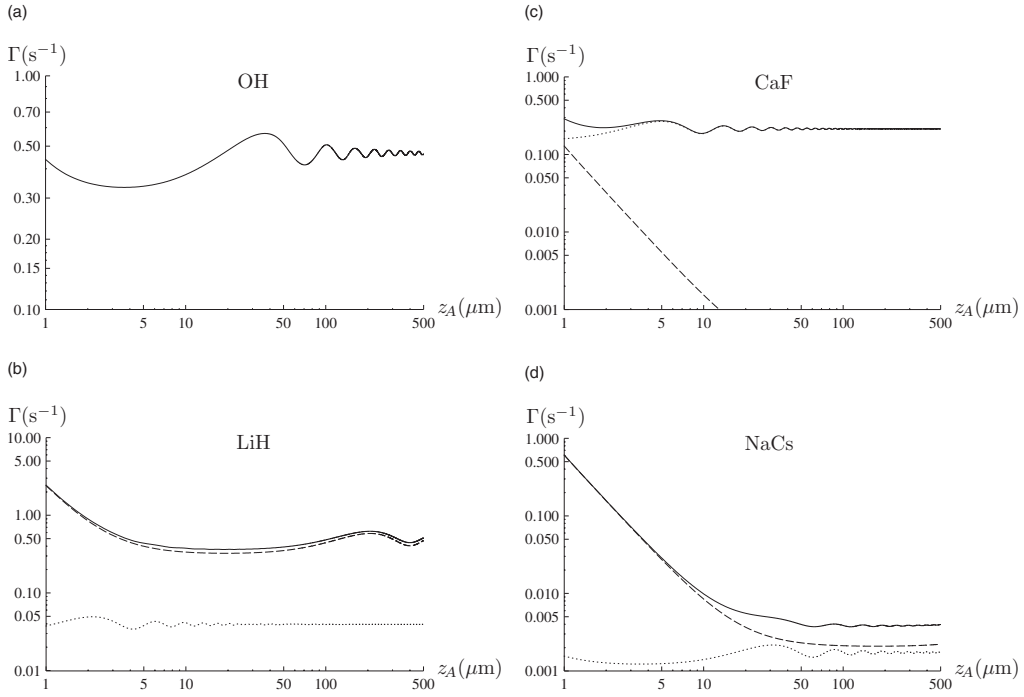

FIG. 4. Heating rates for (a) OH, (b) LiH, (c) CaF, and (d) NaCs vs distance from a gold surface. Solid lines: total heating rate. Dotted lines: vibrational excitation rate. Dashed lines: rotational excitation rate.

contribution, having a much shorter critical distance, remains essentially constant down to 1 μm. For CaF, the heating is dominated by vibrational excitation at 18.4 THz, corresponding to an oscillation period in the far field of 8 μm, which can clearly be seen. Inside the 19 μm critical distance for rotational heating, we see a dramatic increase in the rotational contribution to the rate, such that the two contributions are roughly equal at a distance of 1 μm from the surface. For NaCs, the two contributions are roughly equal in the far field and both are rather small. The 3 THz vibrational heating exhibits the expected far-field oscillations, while the rotational heating is at too low a frequency to show oscillations over this range. Inside the 13 μm critical distance, the rotational heating increases rapidly, becoming a thousand times faster at a distance of 1 μm.

In Fig. 5, we show once again the heating rate for NaCs as a function of distance from a gold surface (solid line). This figure also shows for comparison the heating rates near iron and ITO surfaces. At distances large enough for the retarded limit to apply, the heating rate given by Eq. (94) is independent of the particular metallic surface since these are all good conductors at the relevant excitation frequencies. At short range, however, where the near-field limit of Eq. (84) applies, the heating rate becomes proportional to γ/ω_P^2. As shown in Table IV, this ratio differs widely between these materials and is a hundred times larger for ITO than for gold. For this reason, the ITO surface produces a larger heating rate at short distance and exhibits a longer critical distance than gold, as seen in Fig. 5.

So far, we have discussed surface-enhanced heating in the presence of metallic and dielectric surfaces. It is also interesting to consider the heating rate for molecules in the vicinity of metamaterials, since these offer tunable magnetoelectric properties [65,66], and can even be left handed [67]. A left-handed medium is realized when the real parts of both ε and μ are simultaneously negative, leading to a negative index of refraction and a number of counterintuitive effects associated with the propagation of the electromagnetic field inside such a medium [67]. Since the surface-enhanced heating rate of a single interface depends solely on the reflected electromagnetic field, one would expect it to be insensitive to left handedness. For weakly absorbing media, the oscillations seen in the retarded limit are small when the signs of Re ε and Re μ are both positive or both negative. In the case where Re ε=Re μ, and the imaginary parts are small, there

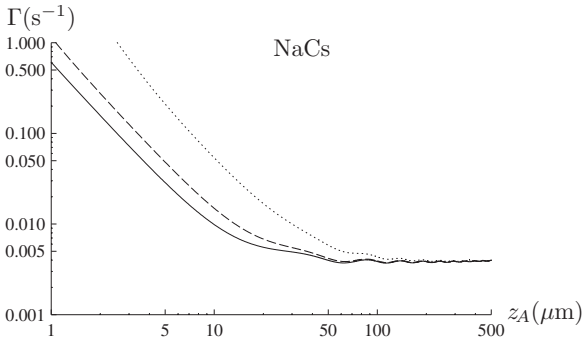

FIG. 5. Heating rate for ground-state NaCs as a function of the distance from gold (solid line), iron (dashed line), and ITO (dotted line) surfaces.

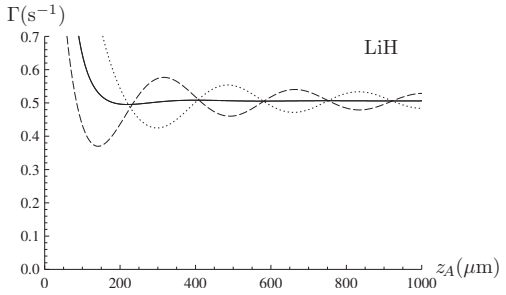

FIG. 6. Heating rate for ground state LiH as a function of distance from fictitious metamaterials with $\varepsilon(\omega_{k0})=\mu(\omega_{k0})=\pm 10+i$ (solid line), $\varepsilon(\omega_{k0})=10+i$, $\mu(\omega_{k0})=-10+i$ (dashed line), and $\varepsilon(\omega_{k0})=-10+i$, $\mu(\omega_{k0})=10+i$ (dotted line).

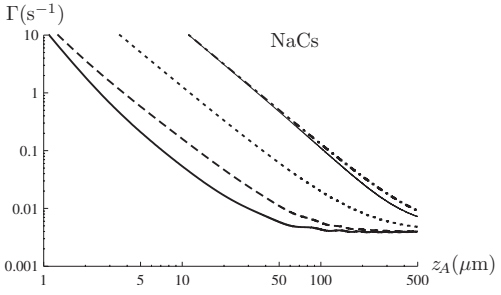

FIG. 7. Heating rate of NaCs as a function of distance from an ITO surface with thickness 10 μm (thick solid line), 1 μm (dashed line), 0.1 μm (dotted line), and 0.01 μm (dashed-dotted line). The thin solid line shows how the result changes for a 0.01 μm thick surface when the ITO is coated onto borosilicate glass.

are no oscillations at all since r_s and r_p are then very close to zero. The amplitude of the oscillations is greatest when these reflection coefficients have their maximum values of 1. As we have already seen, this occurs for metals because $|\varepsilon|$ is much larger than $|\mu|$. In the context of metamaterials, reflection coefficients close to unity are obtained for any weakly absorbing medium where Re ε and Re μ have opposite signs. Note that this result is insensitive to the magnitudes of Re ε, Re μ, which neither need to be equal nor particularly large; they need only be of opposite sign and considerably larger than the imaginary parts. A metamaterial engineered with these properties would produce large oscillations in the heating rate with a phase determined by the chosen values of Re ε, Re μ. Figure 6 shows the heating rate of a LiH molecule near fictitious weakly absorbing metamaterials with Re $\varepsilon=\pm$ Re μ. We see that the left-handed material (Re ε, Re $\mu<0$) gives rise to exactly the same heating rate as a comparable ordinary material with Re ε, Re $\mu>0$ (the two curves cannot be distinguished on the plot), and that the oscillations are suppressed. On the other hand, media with Re $\varepsilon=-$Re μ result in large oscillations of the heating rate in the long-distance regime, with a phase that depends on the material properties.

C. Surfaces of finite thickness

The results of the previous section have shown that metallic surfaces can considerably enhance surface-induced heating. In the context of chips, metal surfaces are often unavoidable since they are used in current-or charge-carrying structures. One possible strategy to reduce the associated molecular heating is to reduce the thickness of the metal substrates. For a slab of finite thickness d, coated onto an infinitely thick substrate of permittivity $\varepsilon_s=\varepsilon_s(\omega)$ and permeability $\mu_s=\mu_s(\omega)$, the surface-induced heating rate is still given by Eq. (80) together with Eq. (79), but the reflection coefficients are now given by

$$r_s=\frac{\mu^2\beta\beta_s-\mu_s\beta_1^2+i\mu\beta_1[\mu_s\beta-\beta_s]\cot(\beta_1 d)}{\mu^2\beta\beta_s+\mu_s\beta_1^2+i\mu\beta_1[\mu_s\beta+\beta_s]\cot(\beta_1 d)}, \quad (95)$$

$$r_p=\frac{\varepsilon^2\beta\beta_s-\varepsilon_s\beta_1^2+i\varepsilon\beta_1[\varepsilon_s\beta-\beta_s]\cot(\beta_1 d)}{\varepsilon^2\beta\beta_s+\varepsilon_s\beta_1^2+i\varepsilon\beta_1[\varepsilon_s\beta+\beta_s]\cot(\beta_1 d)}, \quad (96)$$

where

$$\beta_s=\sqrt{\frac{\omega^2}{c^2}\varepsilon_s(\omega)\mu_s(\omega)-q^2} \quad (97)$$

(Im $\beta_s\geqslant 0$).

Let us first consider the influence of the metal surface alone by letting $\varepsilon_s=\mu_s=1$. In the nonretarded limit, the reflection coefficients may then be approximated by

$$r_s\simeq\frac{\mu^2-1}{\mu^2+1+2\mu\coth(qd)}, \quad (98)$$

$$r_p\simeq\frac{\varepsilon^2-1}{\varepsilon^2+1+2\varepsilon\coth(qd)} \quad (99)$$

[recall the discussion above Eq. (81)]. Since $q\lesssim 1/(2z_A)$, the short-range heating rate will be identical to that of an infinitely thick plate provided $d\gg z_A$, since in this limit the above reflection coefficients reduce to those given in Eqs. (77). On the other hand, the reflection coefficients, and hence also the heating rate, must become very small when $d|\varepsilon|\ll z_A$. We note immediately that, for molecule-surface separations of interest, a conducting surface needs to be unfeasibly thin for this limit to be reached because of the enormously large values of $|\varepsilon|$ for a conductor. The behavior between the two limits has to be determined from a numerical analysis.

In the retarded limit, one may approximate

$$r_s\simeq -r_p\simeq\frac{\varepsilon-\mu}{\varepsilon+\mu+2i\sqrt{\varepsilon\mu}\cot(\sqrt{\varepsilon\mu}\omega d/c)}, \quad (100)$$

so for a good conductor, $|\varepsilon|\gg|\mu|$, the reflection coefficients and the heating rate become independent of the plate thickness at long range.

In Fig. 7, we display the surface-induced heating rate of a NaCs molecule near ITO plates of various thicknesses as a function of molecule-plate separation. At large separations, the heating rates are independent of the thickness, as predicted from Eq. (100). Over the entire range of distances calculated, the ITO plate of thickness 10 μm gives the same result as a plate of infinite thickness. Reducing the thickness below this value increases the heating rates at short distances, contrary to the expectation of reduced rates at short

range anticipated from Eqs. (98) and (99). A reduction of the short-range heating rates below the values observed for thick plates is eventually found but only once the coating is unfeasibly thin. Thus our calculations show that the heating at short-range cannot be reduced by reducing the material thickness. To understand the increase of the heating rate with decreasing thickness, note that in the nonretarded limit the heating is mainly due to the coupling of the molecule with the surface plasmons at the front face of the plate. As the thickness decreases, these couple to the plasmons at the back face of the plate, leading to mutual enhancement and thus to an increase of the heating rate [68]. To include the borosilicate glass substrate we took $\varepsilon_s(\omega_{k0})=6.2+0.21i$ for the rotational transitions [64] and $\varepsilon_s(\omega_{k0})=6.4+0.74i$ for the vibrational ones [69]. We find identical results whether or not this substrate is included, except for the thinnest coating, $d=0.01$ μm, where we find that the presence of the substrate slightly reduces the heating rate, as shown by the thin solid line in the figure.

V. SUMMARY AND CONCLUSIONS

Using macroscopic QED, we have calculated the internal dynamics of a molecule placed within an arbitrary environment of magnetoelectric bodies of uniform temperature. The internal time evolution is governed by the molecular transition frequencies and transition rates which depend on position and temperature. The dependence on temperature is due to the thermal photon number and can be completely understood from considering the free-space case, while the position-dependence, which enters via the classical Green tensor for the electromagnetic field in the environment, can be derived from the behavior at zero temperature.

We have used the general formulas to study the ground-state heating rates of several polar molecules of current experimental interest, as a function of the distance from various surfaces. We have given a simple approximate formula that can be used to estimate the heating rates for any other molecules at any distance from any surface of interest. For light molecules, particularly the hydrides, rotational heating dominates and limits the free-space lifetime of the ground state to a few seconds when the environment is at room temperature. For the metal fluorides we studied, vibrational heating dominates and again the room temperature free-space lifetime of the ground state is of the order of a few seconds. When the molecules approach a metallic surface, the heating rate can be greatly enhanced. This is particularly true for the rotational transitions where the critical distance at which the surface dominates the free-space rate is typically in the 1–100 μm range. For the hydrides, the free-space heating rate is large because the rotational frequencies are large, but this same fact also means that the critical distance for surface-induced heating is rather small. Therefore, these molecules could be trapped up to a few microns from a surface with little change in the heating rate. The effect of the surface on rotational heating is very much stronger for the heavier molecules, but since the rate in free space is typically very small for these molecules, they too have lifetimes of a second or more at distances up to 1 μm from the surface.

We have shown that, at long range, the heating rates become insensitive to the particular surface properties, while at short range the heating is faster for smaller values of the parameter ω_P^2/γ. Of the metals considered, gold induces the lowest heating rate. We have also shown that decreasing the thickness of the surface tends to increase the heating rate, particularly at short distances. Dielectric materials that are good absorbers at the relevant frequency result in large critical distances and hence very large heating rates at short range.

In the context of molecule chips, where confinement of molecules a few microns from the chip surface is envisaged, our work shows that surface-induced heating should be considered carefully when selecting appropriate molecules and surfaces, but that confinement for several seconds in single quantum states is quite feasible even when the surface is at room temperature. In all cases, lowering the environment temperature will allow for even longer lifetimes. For approach distances smaller than 1 μm, surface-induced heating becomes rapidly problematic, and cooling to cryogenic temperatures may be required.

ACKNOWLEDGMENTS

This work was supported by the Alexander von Humboldt Foundation, the Royal Society, and the UK Engineering and Physical Sciences Research Council. The research leading to these results has received funding from the European Community's Seventh Framework Programme No. FP7/2007-2013 under Grant No. 216774. S.Y.B. is grateful to W.L. Barnes, S. Franzen, C. Henkel, J. Kirkpatrick, G.J. McPhee, B.E. Sernelius, and M.S. Tomaš for discussions.

APPENDIX A: MARKOV APPROXIMATION

Substituting the formal solution

$$\hat{\mathbf{f}}_\lambda(\mathbf{r},\omega,t) = e^{-i\omega t}\hat{\mathbf{f}}_\lambda(\mathbf{r},\omega) + \frac{i}{\hbar}\sum_{m,n}\int_0^t d\tau e^{-i\omega(t-\tau)}\mathbf{d}_{mn}\cdot\boldsymbol{G}_\lambda^*(\mathbf{r}_A,\mathbf{r},\omega)\hat{A}_{mn}(\tau) \tag{A1}$$

to Eq. (27) into Eq. (26) and using the integral relation (13), one obtains

$$\dot{\hat{A}}_{mn}(t) = i\omega_{mn}\hat{A}_{mn}(t) + \frac{i}{\hbar}\sum_k\int_0^\infty d\omega \times\{e^{-i\omega t}[\mathbf{d}_{nk}\hat{A}_{mk}(t) - \mathbf{d}_{km}\hat{A}_{kn}(t)]\cdot\underline{\hat{\mathbf{E}}}(\mathbf{r}_A,\omega) + e^{i\omega t}\underline{\hat{\mathbf{E}}}^\dagger(\mathbf{r}_A,\omega)\cdot[\mathbf{d}_{nk}\hat{A}_{mk}(t) - \mathbf{d}_{km}\hat{A}_{kn}(t)]\} + \hat{Z}_{mn}(t) \tag{A2}$$

with

$$\hat{Z}_{mn}(t) = -\frac{\mu_0}{\hbar\pi}\sum_{k,l,j}\int_0^\infty d\omega\omega^2\int_0^t d\tau \times\{[e^{-i\omega(t-\tau)}\hat{A}_{mk}(t)\hat{A}_{lj}(\tau) - e^{i\omega(t-\tau)}\hat{A}_{lj}(\tau)\hat{A}_{mk}(t)] \times\mathbf{d}_{nk}\cdot\mathrm{Im}\,\boldsymbol{G}(\mathbf{r}_A,\mathbf{r}_A,\omega)\cdot\mathbf{d}_{lj}$$

$$- [e^{-i\omega(t-\tau)}\hat{A}_{kn}(t)\hat{A}_{lj}(\tau) - e^{i\omega(t-\tau)}\hat{A}_{lj}(\tau)\hat{A}_{nk}(t)]$$
$$\times \mathbf{d}_{km} \cdot \mathrm{Im}\, \boldsymbol{G}(\mathbf{r}_A, \mathbf{r}_A, \omega) \cdot \mathbf{d}_{lj}\} \quad \text{(A3)}$$

denoting the zero-point contribution to the internal molecular dynamics. This differential equation can be solved iteratively by substituting the self-consistent solution

$$\hat{A}_{mn}(t) = e^{i\tilde{\omega}_{mn}t}\hat{A}_{mn}(0) + \frac{i}{\hbar}\sum_k \int_0^\infty d\omega \int_0^t d\tau e^{i\tilde{\omega}_{mn}(t-\tau)}$$
$$\times \{e^{-i\omega\tau}[\mathbf{d}_{nk}\hat{A}_{mk}(\tau) - \mathbf{d}_{km}\hat{A}_{kn}(\tau)] \cdot \hat{\underline{\mathbf{E}}}(\mathbf{r}_A, \omega)$$
$$+ e^{i\omega\tau}\hat{\underline{\mathbf{E}}}^\dagger(\mathbf{r}_A, \omega) \cdot [\mathbf{d}_{nk}\hat{A}_{mk}(\tau) - \mathbf{d}_{km}\hat{A}_{kn}(\tau)]\} \quad \text{(A4)}$$

to the truncated Eq. (A2) without $\hat{Z}_{mn}(t)$ back into Eq. (A2), where at this level of approximation, the operator ordering in Eq. (A4) may be chosen arbitrarily. Taking expectation values according to Eqs. (15)–(18), one arrives at

$$\langle \dot{\hat{A}}_{mn}(t)\rangle = i\omega_{mn}\langle \hat{A}_{mn}(t)\rangle + \langle \hat{T}_{mn}(t)\rangle + \langle \hat{Z}_{mn}(t)\rangle \quad \text{(A5)}$$

where

$$\langle \hat{T}_{mn}(t)\rangle = -\frac{\mu_0}{\hbar\pi}\sum_{k,l}\int_0^\infty d\omega\omega^2 n(\omega)\int_0^t d\tau[e^{-i\omega(t-\tau)} + e^{i\omega(t-\tau)}]$$
$$\times \{e^{i\tilde{\omega}_{mk}(t-\tau)}[\langle \hat{A}_{ml}(\tau)\rangle \mathbf{d}_{nk} \cdot \mathrm{Im}\, \boldsymbol{G}(\mathbf{r}_A, \mathbf{r}_A, \omega) \cdot \mathbf{d}_{kl}$$
$$- \langle \hat{A}_{lk}(\tau)\rangle \mathbf{d}_{nk} \cdot \mathrm{Im}\, \boldsymbol{G}(\mathbf{r}_A, \mathbf{r}_A, \omega) \cdot \mathbf{d}_{lm}] - e^{i\tilde{\omega}_{kn}(t-\tau)}$$
$$\times \langle \hat{A}_{kl}(\tau)\rangle \mathbf{d}_{km} \cdot \mathrm{Im}\, \boldsymbol{G}(\mathbf{r}_A, \mathbf{r}_A, \omega) \cdot \mathbf{d}_{nl}$$
$$- \langle \hat{A}_{\mathrm{ln}}(\tau)\rangle \mathbf{d}_{km} \cdot \mathrm{Im}\, \boldsymbol{G}(\mathbf{r}_A, \mathbf{r}_A, \omega) \cdot \mathbf{d}_{lk}]\} \quad \text{(A6)}$$

denotes the thermal contribution to the internal molecular dynamics. For weak molecule-field coupling, the contributions $\langle \hat{T}_{mn}(t)\rangle$ and $\langle \hat{Z}_{mn}(t)\rangle$ may be evaluated by means of the Markov approximation, i.e., by letting $\langle \hat{A}_{mn}(\tau)\rangle \simeq e^{-i\tilde{\omega}_{mn}(t-\tau)}\langle \hat{A}_{mn}(t)\rangle$ and evaluating the remaining time integrals according to

$$\int_0^t d\tau e^{-i(\omega-\tilde{\omega}_{mn})(t-\tau)} \simeq \pi\delta(\omega - \tilde{\omega}_{mn}) + iP\frac{1}{\tilde{\omega}_{mn} - \omega}. \quad \text{(A7)}$$

Assuming the system to be nondegenerate, so that off-diagonal molecular density matrix decouple from each other as well as from the diagonal ones, we arrive at Eqs. (28) and (29), together with Eqs. (30)–(38).

APPENDIX B: CRITICAL DISTANCES

We have calculated the critical distances for surface-induced enhancement of ground-state heating rates for various combinations of molecules and materials on the basis of the data given in Tables I and IV. The results are summarized in Table VI.

TABLE VI. The exact critical distances z_c (μm) for the enhancements of ground-state heating rates of various polar molecules due to the presence of surfaces of various materials.

	Rotational											Vibrational										
Spe.	Al	Pd	Ag	Cu	Mo	Fe	Co	W	Ni	Pt	ITO	Al	Pd	Ag	Cu	Mo	Fe	Co	W	Ni	Pt	ITO
LiH	1.9	2.0	2.0	2.1	2.4	2.5	2.6	2.7	2.8	3.1	5.4	0.044	0.038	0.039	0.042	0.053	0.051	0.060	0.060	0.064	0.075	0.16
NH	1.0	1.0	1.0	1.1	1.3	1.3	1.4	1.4	1.5	1.7	2.9	0.021	0.022	0.023	0.023	0.028	0.029	0.031	0.032	0.035	0.040	0.097
OH												0.019	0.020	0.021	0.021	0.025	0.027	0.028	0.029	0.032	0.037	0.94
(a)	0.51	0.47	0.43	0.52	0.62	0.60	0.67	0.69	0.73	0.82	1.4											
(b)	0.36	0.32	0.29	0.37	0.45	0.41	0.48	0.49	0.52	0.59	1.0											
(c)	0.26	0.22	0.20	0.26	0.32	0.29	0.35	0.36	0.37	0.43	0.77											
(d)	0.18	0.15	0.13	0.17	0.22	0.29	0.24	0.25	0.25	0.30	0.55											
OD												0.025	0.024	0.026	0.026	0.032	0.033	0.035	0.036	0.039	0.046	0.11
(a)	0.79	0.77	0.73	0.84	0.98	0.97	1.1	1.1	1.2	1.3	2.2											
(b)	0.35	0.31	0.28	0.36	0.43	0.40	0.47	0.48	0.50	0.57	1.0											
(c)	0.30	0.25	0.23	0.29	0.36	0.33	0.39	0.40	0.42	0.48	0.86											
(d)	0.24	0.19	0.17	0.23	0.28	0.25	0.31	0.32	0.33	0.38	0.69											
CaF	19	20	21	21	24	25	26	26	28	31	53	0.094	0.074	0.071	0.086	0.11	0.098	0.13	0.13	0.13	0.15	0.30
BaF	28	30	31	31	35	37	37	39	42	46	78	0.12	0.093	0.088	0.11	0.14	0.12	0.16	0.16	0.16	0.20	0.37
YbF	25	27	28	28	32	33	34	35	38	41	71	0.11	0.087	0.083	0.10	0.13	0.12	0.15	0.15	0.15	0.18	0.35
LiRb	27	29	30	30	34	35	36	38	40	44	76	0.27	0.22	0.20	0.26	0.32	0.39	0.36	0.36	0.38	0.43	0.78
NaRb	66	70	72	72	82	86	88	91	97	110	180	0.42	0.37	0.34	0.43	0.51	0.48	0.55	0.57	0.60	0.68	1.2
KRb	100	110	110	110	130	130	130	140	150	160	280	0.55	0.51	0.47	0.57	0.68	0.65	0.73	0.75	0.79	0.89	1.6
LiCs	30	32	33	33	37	39	40	41	44	49	83	0.30	0.25	0.22	0.29	0.36	0.32	0.39	0.40	0.42	0.48	0.85
NaCs	13	14	14	14	16	17	17	18	19	21	36	0.45	0.40	0.37	0.46	0.55	0.52	0.59	0.61	0.64	0.73	1.3
KCs	3.7	3.9	4.0	4.0	4.6	4.8	4.9	5.1	5.5	6.0	10	0.61	0.58	0.54	0.64	0.75	0.73	0.81	0.83	0.88	0.99	1.7
RbCs	190	200	210	210	240	250	250	260	280	310	530	0.76	0.74	0.70	0.81	0.95	0.94	1.0	1.1	1.1	1.2	2.2

[1] H. L. Bethlem, G. Berden, and G. Meijer, Phys. Rev. Lett. **83**, 1558 (1999).

[2] H. L. Bethlem, G. Berden, F. M. H. Crompvoets, R. T. Jongma, A. J. A. van Roij, and G. Meijer, Nature (London) **406**, 491 (2000).

[3] S. Y. T. van de Meerakker, P. H. M. Smeets, N. Vanhaecke, R. T. Jongma, and G. Meijer, Phys. Rev. Lett. **94**, 023004 (2005).

[4] B. C. Sawyer, B. L. Lev, E. R. Hudson, B. K. Stuhl, M. Lara, J. L. Bohn, and J. Ye, Phys. Rev. Lett. **98**, 253002 (2007).

[5] J. van Veldhoven, H. L. Bethlem, and G. Meijer, Phys. Rev. Lett. **94**, 083001 (2005).

[6] T. Rieger, T. Junglen, S. A. Rangwala, P. W. H. Pinkse, and G. Rempe, Phys. Rev. Lett. **95**, 173002 (2005).

[7] J. D. Weinstein, R. deCarvalho, T. Guillet, B. Friedrich, and J. Doyle, Nature (London) **395**, 148 (1998).

[8] J. M. Sage, S. Sainis, T. Bergeman, and D. DeMille, Phys. Rev. Lett. **94**, 203001 (2005).

[9] S. Hoekstra, J. J. Gilijamse, B. Sartakov, N. Vanhaecke, L. Scharfenberg, S. Y. T. van de Meerakker, and G. Meijer, Phys. Rev. Lett. **98**, 133001 (2007).

[10] N. Vanhaecke and O. Dulieu, Mol. Phys. **105**, 1723 (2007).

[11] J. Fortágh and C. Zimmermann, Rev. Mod. Phys. **79**, 235 (2007).

[12] S. A. Meek, H. L. Bethlem, H. Conrad, and G. Meijer, Phys. Rev. Lett. **100**, 153003 (2008).

[13] A. André, D. DeMille, J. M. Doyle, M. D. Lukin, S. E. Maxwell, P. Rabl, R. J. Schoelkopf, and P. Zoller, Nat. Phys. **2**, 636 (2006).

[14] P. Rabl, D. DeMille, J. M. Doyle, M. D. Lukin, R. J. Schoelkopf, and P. Zoller, Phys. Rev. Lett. **97**, 033003 (2006).

[15] M. Trupke, J. Goldwin, B. Darquié, G. Dutier, S. Eriksson, J. Ashmore, and E. A. Hinds, Phys. Rev. Lett. **99**, 063601 (2007).

[16] F. Warken, E. Vetsch, D. Meschede, M. Sokolowski, and A. Rauschenbeutel, Opt. Express **15**, 11952 (2007).

[17] E. M. Purcell, H. C. Torrey, and R. V. Pound, Phys. Rev. **69**, 681 (1946).

[18] G. S. Agarwal, Phys. Rev. A **12**, 1475 (1975).

[19] R. R. Chance, A. Prock, and R. Silbey, J. Chem. Phys. **60**, 2744 (1974).

[20] R. R. Chance, A. Prock, and R. Silbey, J. Chem. Phys. **62**, 771 (1975).

[21] M. S. Yeung and T. K. Gustafson, Phys. Rev. A **54**, 5227 (1996).

[22] S. Scheel, L. Knöll, and D.-G. Welsch, Phys. Rev. A **60**, 4094 (1999).

[23] H. T. Dung, S. Y. Buhmann, L. Knöll, D.-G. Welsch, S. Scheel, and J. Kästel, Phys. Rev. A **68**, 043816 (2003).

[24] Ho Trung Dung, S. Y. Buhmann, and D.-G. Welsch, Phys. Rev. A **74**, 023803 (2006).

[25] A. Sambale, S. Y. Buhmann, D.-G. Welsch, and M. S. Tomaš, Phys. Rev. A **75**, 042109 (2007).

[26] Ho Trung Dung, L. Knöll, and D.-G. Welsch, Phys. Rev. A **64**, 013804 (2001).

[27] Ho Trung Dung, L. Knöll, and D.-G. Welsch, Phys. Rev. A **62**, 053804 (2000).

[28] J. Kästel and M. Fleischhauer, Phys. Rev. A **71**, 011804(R) (2005).

[29] A. Sambale, S. Y. Buhmann, D.-G. Welsch, and Ho Trung Dung, Phys. Rev. A (to be published), e-print arXiv:0711.3369.

[30] J. M. Wylie and J. E. Sipe, Phys. Rev. A **30**, 1185 (1984).

[31] C. Henkel and M. Wilkens, Europhys. Lett. **47**, 414 (1999).

[32] C. Henkel, S. Pötting, and M. Wilkens, Appl. Phys. B: Lasers Opt. **69**, 379 (1999).

[33] P. K. Rekdal, S. Scheel, P. L. Knight, and E. A. Hinds, Phys. Rev. A **70**, 013811 (2004).

[34] R. Fermani, S. Scheel, and P. L. Knight, Phys. Rev. A **75**, 062905 (2007).

[35] S. Y. Buhmann and D.-G. Welsch, Prog. Quantum Electron. **31**, 51 (2006).

[36] R. Kubo, Rep. Prog. Phys. **29**, 255 (1966).

[37] L. Knöll, S. Scheel, and D.-G. Welsch, in *Coherence and Statistics of Photons and Atoms*, edited by J. Peřina (Wiley, New York, 2001), p. 1.

[38] In comparing the results of Ref. [10] with the free space limit of our results, there are several comments worth making. (i) *Constants*. Because we have used measured values where possible, there are small discrepancies between some of our value of μ_e and those used in Ref. [10]. For KRb the difference is large. These affect the rotational but not the vibrational heating rates. Our values of μ_e' are the calculated ones presented in Table I of Ref. [10]. Note that the value given there for LiRb should read 0.34 (Da_0^{-1}), not 0.14 (Da_0^{-1}). (ii) *Heating*. We take room temperature as 293 K, rather than 300 K, resulting in small differences throughout. Table II of Ref. [10] gives lifetimes that are too long for NaCs and KCs because they neglect rotational excitation, which is the dominant effect. Our rotational heating rate for LiH differs from the rate given in Table II of Ref. [10] because our initial state is $J=0$, whereas theirs is $J=1$.

[39] I. Mills, T. Cvitaš, K. Homann, N. Kallay, and K. Kuchitsu, *Quantities, Units and Symbols in Physical Chemistry* (Blackwell Scientific Publications, Oxford, 1993).

[40] M. Bellini, P. De Natale, M. Inguscio, T. D. Varberg, and J. M. Brown, Phys. Rev. A **52**, 1954 (1995).

[41] E. Rothstein, J. Chem. Phys. **50**, 1899 (1969).

[42] R. S. Ram, P. F. Bernath, and K. H. Hinkle, J. Chem. Phys. **110**, 5557 (1999).

[43] W. C. Campbell, G. C. Groenenboom, Hsin-I. Lu, E. Tsikata, and J. M. Doyle, Phys. Rev. Lett. **100**, 083003 (2008).

[44] D. E. Osterbrock, J. P. Fulbright, P. C. Cosby, and T. A. Barlow, Publ. Astron. Soc. Pac. **110**, 1499 (1998).

[45] G. H. Dieke and H. M. Crosswhite, J. Quant. Spectrosc. Radiat. Transf. **2**, 97 (1962).

[46] J. A. Coxon, J. Mol. Spectrosc. **58**, 1 (1975).

[47] J. P. Maillard, J. Chauville, and A. W. Mantz, J. Mol. Spectrosc. **63**, 120 (1976).

[48] W. L. Meerts and A. Dynamus, Chem. Phys. Lett. **23**, 45 (1973).

[49] D. D. Nelson, Jr., A. Schiffmann, D. J. Nesbitt, J. J. Orlando, and J. B. Burkholder, J. Chem. Phys. **93**, 7003 (1990).

[50] W. L. Meerts and A. Dynamus, Astrophys. J. **180**, L93 (1973).

[51] L. A. Kaledin, J. C. Bloch, M. C. McCarthy, and R. W. Field, J. Mol. Spectrosc. **197**, 289 (1999).

[52] W. J. Childs, L. S. Goodman, U. Nielsen, and V. Pfeufer, J. Chem. Phys. **80**, 2283 (1984).

[53] B. E. Sauer, J. Wang, and E. A. Hinds, J. Chem. Phys. **105**, 7412 (1996).

[54] R. F. Barrow and A. H. Chojnicki, J. Chem. Soc., Faraday Trans. 2 **71**, 728 (1975).

[55] M. Dolg, H. Stoll, and H. Preuss, Chem. Phys. **165**, 21 (1992).
[56] M. Korek, A. R. Allouche, M. Kobeissi, A. Chaalan, M. Dagher, K. Fakherddin, and M. Aubert-Frécon, Chem. Phys. **256**, 1 (2000).
[57] V. Tarnovsky, M. Bunimovicz, L. Vušković, B. Stumpf, and B. Bederson, J. Chem. Phys. **98**, 3894 (1993).
[58] A. J. Ross, C. Effantin, P. Crozet, and E. Boursey, J. Phys. B **23**, L247 (1990).
[59] M. Korek, A. R. Allouche, K. Fakhreddine, and A. Chaalan, Can. J. Phys. **78**, 977 (2000).
[60] C. E. Fellows, R. F. Gutteres, A. P. C. Campos, J. Vergès, and C. Amiot, J. Mol. Spectrosc. **197**, 19 (1999).
[61] J. Brown and A. Carrington, *Rotational Spectroscopy of Diatomic Molecules* (Cambridge University Press, Cambridge, 2003).
[62] *Handbook of Optical Constants of Solids II*, edited by E. D. Palik (Academic Press, New York, 1991).
[63] S. Franzen (private communication).
[64] R. Grignon, M. N. Asfar, Y. Wang, and S. Butt, Proceedings of the 20th IEEE Instrumentation and Measurement Technology Conference (IEEE, Piscataway, NJ, 2003), Vol. 1, p. 865
[65] J. B. Pendry, A. J. Holden, D. J. Robbins, and W. J. Stewart, IEEE Trans. Microwave Theory Tech. **47**, 2075 (1999).
[66] D. R. Smith, W. J. Padilla, D. C. Vier, S. C. Nemat-Nasser, and S. Schultz, Phys. Rev. Lett. **84**, 4184 (2000).
[67] V. G. Veselago, Sov. Phys. Usp. **10**, 509 (1968).
[68] Z. Lenac and M. S. Tomaš, Surf. Sci. **215**, 299 (1989); R. M. Amos and W. L. Barnes, Phys. Rev. B **55**, 7249 (1997).
[69] M. Naftaly and R. E. Miles, Proc. IEEE **95**, 1658 (2007).

PRL 100, 253201 (2008) PHYSICAL REVIEW LETTERS week ending 27 JUNE 2008

Thermal Casimir versus Casimir-Polder Forces: Equilibrium and Nonequilibrium Forces

Stefan Yoshi Buhmann and Stefan Scheel

Quantum Optics and Laser Science, Blackett Laboratory, Imperial College London, Prince Consort Road, London SW7 2AZ, United Kingdom

(Received 5 March 2008; revised manuscript received 30 April 2008; published 26 June 2008)

We critically discuss whether and under what conditions Lifshitz theory may be used to describe thermal Casimir-Polder forces on atoms or molecules. An exact treatment of the atom-field coupling reveals that for a ground-state atom (molecule), terms associated with virtual-photon absorption lead to a deviation from the traditional Lifshitz result; they are identified as a signature of nonequilibrium dynamics. Even the equilibrium force on a thermalized atom (molecule) may be overestimated when using the ground-state polarizability instead of its thermal counterpart.

DOI: 10.1103/PhysRevLett.100.253201 PACS numbers: 34.35.+a, 12.20.−m, 42.50.Ct, 42.50.Nn

Dispersion forces such as Casimir and Casimir-Polder (CP) forces are of increasing relevance in nanophysics [1]; recent successes include the chemical identification of surface atoms via atomic force microscopy [2] as well as the construction of novel biomimetic dry adhesives [3]. They become important in efforts to miniaturize atom chips [4] and play a key role in experiments placing upper bounds on nonstandard gravitational forces [5].

In all of these areas, a thorough understanding of dispersion forces under realistic conditions must account for their temperature dependence induced by thermal photons [6]. A series of high-precision experiments [7] has triggered a renewed interest in this thermal Casimir force [8] by opening the perspective of its experimental investigation [9]. It was noticed that, depending on the model chosen to describe the metal response, Lifshitz theory can yield different answers for the temperature dependence of the Casimir energy between two metal plates [10]. The resulting debate concerning the correct description of the thermal Casimir force [11] will ultimately have to be settled by experiments. Nonequilibrium situations of two plates of different temperatures have recently been suggested as sensitive probes to the quantum electrodynamics (QED) of the Casimir effect [12].

The CP force on single atoms can be measured indirectly via spectroscopic means; clear evidence for thermal frequency shifts has been found for atoms inside a cavity [13] and their signature has been detected in the interaction of atoms with a sapphire surface [14]. The novel nonequilibrium CP forces predicted for the case of different surface and environment temperatures [15] have recently been observed via their effect on the center-of-mass oscillations of a trapped Bose-Einstein condensate [16]. While some theoretical studies of the thermal CP force are based on a QED treatment of the atom-field coupling [17,18], the vast majority of investigations invokes a macroscopic calculation using Lifshitz theory [6,19,20] or a linear-response description of the atom [15,21] (leading to equivalent results).

The macroscopic approach to the CP force is based on a very close relation between Casimir and CP forces. It is the validity of this one-to-one correspondence and its results for the CP force that we intend to investigate in this Letter, so let us briefly recount the argument in its traditional form: Generalizing the famous Lifshitz result for two plates [6], the thermal Casimir force on a homogeneous body of arbitrary shape occupying a volume V in free space due to the presence of another body can be given as a Matsubara sum [22,23]

$$\boldsymbol{F} = 2k_BT \int_V d^3r \sum_{N=0}^{\infty}{}' \left(1 - \frac{1}{2}\delta_{N0}\right) \times [\mathrm{Tr}\{\mathbf{I} \times [\boldsymbol{\nabla} \times \boldsymbol{\nabla} \times + (\xi_N/c)^2]\mathbf{G}^{(1)}(\boldsymbol{r}, \boldsymbol{r}', i\xi_N) \times \overleftarrow{\boldsymbol{\nabla}}'\}_{\boldsymbol{r}=\boldsymbol{r}'} - (\xi_N/c)^2 \boldsymbol{\nabla} \cdot \mathbf{G}^{(1)}(\boldsymbol{r}, \boldsymbol{r}, i\xi_N)] \quad (1)$$

with Matsubara frequencies $\xi_N = 2\pi k_B T N/\hbar$. Here, $\mathbf{G}^{(1)}$ is the scattering part of the classical Green tensor

$$[\boldsymbol{\nabla} \times \boldsymbol{\nabla} \times - (\omega/c)^2 \varepsilon(\boldsymbol{r}, \omega)]\mathbf{G}(\boldsymbol{r}, \boldsymbol{r}', \omega) = \boldsymbol{\delta}(\boldsymbol{r} - \boldsymbol{r}') \quad (2)$$

associated with the bodies that are characterized by their dielectric permittivity $\varepsilon(\boldsymbol{r}, \omega)$. The result (1) can be obtained from the zero-temperature force by applying the simple replacement rule

$$\frac{\hbar}{\pi} \int_0^{\infty} d\xi f(i\xi) \mapsto 2k_BT \sum_{N=0}^{\infty}{}' \left(1 - \frac{1}{2}\delta_{N0}\right) f(i\xi_N) \quad (3)$$

which is equivalent to replacing the zero-point energy $\frac{1}{2}\hbar\omega$ by a thermal spectrum $[n(\omega) + \frac{1}{2}]\hbar\omega$ with photon number $n(\omega) = 1/[e^{\hbar\omega/(k_BT)} - 1]$. To derive the CP force, one assumes that one body consists of a dilute gas (number density η) of atoms with polarizability $\alpha(\omega)$, so that its permittivity may be approximated by $\varepsilon(\omega) = 1 + \eta\alpha(\omega)/\varepsilon_0$. After a linear expansion in α, it follows that the thermal CP force is given by [22,23]

$$\boldsymbol{F}(\boldsymbol{r}_A) = -\mu_0 k_B T \sum_{N=0}^{\infty}{}' \left(1 - \frac{1}{2}\delta_{N0}\right) \xi_N^2 \alpha(i\xi N) \times \boldsymbol{\nabla}_A \mathrm{Tr}\mathbf{G}^{(1)}(\boldsymbol{r}_A, \boldsymbol{r}_A, i\xi_N). \quad (4)$$

As an immediate consequence of its macroscopic derivation, this force expression is very similar in structure to the respective Casimir force. In particular, the replacement

PRL 100, 253201 (2008) PHYSICAL REVIEW LETTERS week ending 27 JUNE 2008

rule (3) is again valid which often serves as a starting point for studies of the thermal CP force [24].

In view of the high precision of modern experiments, the current widespread use of the macroscopic result (4) and the replacement rule (3) for calculating thermal CP forces calls for a critical discussion of their validity. In this Letter we clarify the extent to which Eq. (4) can be used on the basis of a direct calculation of the time-dependent thermal CP force from the atom-field coupling Hamiltonian. We will demonstrate that force components associated with thermal-photon absorption will generically lead to deviations from Eq. (4). As we will show, the macroscopic result provides a reasonable approximation to the force on a fully thermalized atom, provided that the atomic polarizability is correctly interpreted.

In electric dipole approximation, the force on an atom or a molecule (called atomic system in the following) prepared in an incoherent superposition of internal eigenstates $|n\rangle$ is given by [23,25]

$$\boldsymbol{F}(\boldsymbol{r}_A, t) = \langle [\nabla \hat{\boldsymbol{d}} \cdot \hat{\boldsymbol{E}}(\boldsymbol{r})]_{\boldsymbol{r}=\boldsymbol{r}_A} \rangle, \tag{5}$$

where it is assumed that the internal and translational motion of the atomic system decouple in the spirit of Born-Oppenheimer approximation. In order to evaluate this expression, one needs to solve the coupled dynamics of the electromagnetic field and the atomic system, which is governed by the Hamiltonian [26]

$$\hat{H} = \int d^3r \int_0^\infty d\omega \hbar\omega \hat{\boldsymbol{f}}^\dagger(\boldsymbol{r}, \omega) \cdot \hat{\boldsymbol{f}}(\boldsymbol{r}, \omega) + \sum_n E_n \hat{A}_{nn} - \sum_{m,n} \hat{A}_{mn} \boldsymbol{d}_{mn} \cdot \hat{\boldsymbol{E}}(\boldsymbol{r}_A) \tag{6}$$

($\boldsymbol{d}_{mn} = \langle m|\hat{\boldsymbol{d}}|n\rangle$, $\hat{A}_{mn} = |m\rangle\langle n|$). The bosonic dynamical variables $\hat{\boldsymbol{f}}^\dagger$ and $\hat{\boldsymbol{f}}$, which describe the elementary excitations of the body-assisted electromagnetic field, can be used to construct an expansion of the electric-field operator $\hat{\boldsymbol{E}}(\boldsymbol{r}) = \int_0^\infty d\omega \hat{\boldsymbol{E}}(\boldsymbol{r}, \omega) + \text{H.c.}$ according to

$$\hat{\boldsymbol{E}}(\boldsymbol{r}, \omega) = i\sqrt{\hbar/(\pi\varepsilon_0)}(\omega/c)^2 \int d^3r' \times \sqrt{\text{Im}\varepsilon(\boldsymbol{r}', \omega)} \mathbf{G}(\boldsymbol{r}, \boldsymbol{r}', \omega) \cdot \hat{\boldsymbol{f}}(\boldsymbol{r}', \omega). \tag{7}$$

The expansion coefficients are given in terms of the classical Green tensor (2) which obeys the integral relation

$$\frac{\omega^2}{c^2} \int d^3s \text{Im}\varepsilon(\boldsymbol{s}, \omega) \mathbf{G}(\boldsymbol{r}, \boldsymbol{s}, \omega) \cdot \mathbf{G}^*(\boldsymbol{s}, \boldsymbol{r}', \omega) = \text{Im}\mathbf{G}(\boldsymbol{r}, \boldsymbol{r}', \omega). \tag{8}$$

The Hamiltonian (6) implies that the atom-field dynamics is governed by the system of equations

$$\dot{\hat{A}}_{mm} = i\omega_{mn}\hat{A}_{mn} + \frac{i}{\hbar}\sum_k (\boldsymbol{d}_{nk}\hat{A}_{mk} - \boldsymbol{d}_{km}\hat{A}_{kn}) \cdot \hat{\boldsymbol{E}}(\boldsymbol{r}_A), \tag{9}$$

$$\dot{\hat{\boldsymbol{f}}}(\boldsymbol{r}, \omega) = -i\omega\hat{\boldsymbol{f}}(\boldsymbol{r}, \omega) + \sqrt{\text{Im}\varepsilon(\boldsymbol{r}, \omega)/(\hbar\pi\varepsilon 0)}(\omega/c)^2 \times \sum_{m,n} \hat{A}_{mn}\boldsymbol{d}_{mn} \cdot \mathbf{G}^*(\boldsymbol{r}_A, \boldsymbol{r}, \omega). \tag{10}$$

We eliminate the field by formally integrating Eq. (10) and substituting the result back into Eq. (9), which we arrange in normal ordering. After using the integral relation (8), we obtain

$$\dot{\hat{A}}_{mn}(t) = i\omega_{mn}\hat{A}_{mn}(t) + \hat{Z}_{mn}(t) + \frac{i}{\hbar}\sum_k \int_0^\infty d\omega \{e^{i\omega t}\hat{\boldsymbol{E}}^\dagger(\boldsymbol{r}_A, \omega) \cdot [\boldsymbol{d}_{nk}\hat{A}_{mk}(t) - \boldsymbol{d}_{km}\hat{A}_{kn}(t)] + e^{-i\omega t}[\hat{A}_{mk}(t)\boldsymbol{d}_{nk} - \hat{A}_{kn}(t)\boldsymbol{d}_{km}] \cdot \hat{\boldsymbol{E}}(\boldsymbol{r}_A, \omega)\} \tag{11}$$

where

$$\hat{Z}_{mn}(t) = \frac{\mu_0}{\hbar\pi}\sum_{j,k,l} \int_0^\infty d\omega\omega^2 \boldsymbol{d}_{kl} \cdot \text{Im}\mathbf{G}(\boldsymbol{r}_A, \boldsymbol{r}_A, \omega) \times \int_0^t d\tau \cdot \{e^{-i\omega(t-\tau)}[\boldsymbol{d}_{jm}\hat{A}_{jn}(t) - \boldsymbol{d}_{nj}\hat{A}_{mj}(t)]\hat{A}_{kl}(\tau) + e^{i\omega(t-\tau)}\hat{A}_{kl}(\tau)[\boldsymbol{d}_{nj}\hat{A}_{mj}(t) - \boldsymbol{d}_{jm}\hat{A}_{jn}(t)]\} \tag{12}$$

denotes the zero-point contribution to the internal atomic dynamics. The thermal contribution can be determined iteratively by substituting the self-consistent solution

$$\hat{A}_{mn}(t) = e^{i\tilde{\omega}_{mn}t}\hat{A}_{mn} + \frac{i}{\hbar}\sum_k \int_0^\infty d\omega \times \int_0^t d\tau e^{i\tilde{\omega}_{mn}(t-\tau)}[\hat{A}_{mk}(\tau)\boldsymbol{d}_{nk} - \hat{A}_{kn}(\tau)\boldsymbol{d}_{km}] \cdot [\hat{\boldsymbol{E}}(\boldsymbol{r}_A, \omega)e^{-i\omega\tau} + \text{H.c.}] \tag{13}$$

into the truncated Eq. (11) [without the zero-point contribution $\hat{Z}_{mn}(t)$] back into itself and taking expectation values. With the field initially being prepared in a thermal state $\hat{\rho}_T = \exp[-\hat{H}_F/(k_BT)]/\text{Tr}\{\exp[-\hat{H}_F/(k_BT)]\}$, $\hat{H}_F = \int d^3r \int_0^\infty d\omega\hbar\omega \hat{\boldsymbol{f}}^\dagger(\boldsymbol{r}, \omega) \cdot \hat{\boldsymbol{f}}(\boldsymbol{r}, \omega)$, the nonvanishing averages of the field operators are

$$\langle \hat{\boldsymbol{E}}^\dagger(\boldsymbol{r}, \omega)\hat{\boldsymbol{E}}(\boldsymbol{r}', \omega')\rangle = (\hbar\mu_0/\pi)n(\omega)\omega^2 \text{Im}\mathbf{G}(\boldsymbol{r}, \boldsymbol{r}', \omega) \times \delta(\omega - \omega') \tag{14}$$

[recall Eqs. (7) and (8)]. One thus obtains a closed system of equations for the internal atomic dynamics

$$\langle \dot{\hat{A}}_{mn}\rangle = i\omega_{mn}\langle \hat{A}_{mn}\rangle + \langle \hat{Z}_{mn}\rangle + \langle \hat{T}_{mn}\rangle, \tag{15}$$

with the thermal contribution being given by

$$\langle \hat{T}_{mn}(t)\rangle = \frac{\mu_0}{\hbar\pi}\sum_{k,l} \int_0^\infty d\omega\omega^2 n(\omega) \int_0^t d\tau [e^{-i\omega(t-\tau)} + e^{i\omega(t-\tau)}]\{e^{i\tilde{\omega}mk(t-\tau)}\boldsymbol{d}_{nk} \cdot \text{Im}\mathbf{G}(\boldsymbol{r}_A, \boldsymbol{r}_A, \omega) \cdot [\boldsymbol{d}_{lm}\langle \hat{A}_{lk}(\tau)\rangle - \boldsymbol{d}_{kl}\langle \hat{A}_{ml}(\tau)\rangle] + e^{i\tilde{\omega}kn(t-\tau)}\boldsymbol{d}_{km} \cdot \text{Im}\mathbf{G}(\boldsymbol{r}_A, \boldsymbol{r}_A, \omega) \cdot [\boldsymbol{d}_{nl}\langle \hat{A}_{kl}(\tau)\rangle - \boldsymbol{d}_{lk}\langle \hat{A}_{\text{ln}}(\tau)\rangle]\}. \tag{16}$$

For weak atom-field coupling, this system can be solved in Markov approximation using the relations $\langle \hat{A}_{mn}(\tau)\rangle \simeq e^{-i\tilde{\omega}_{mn}(t-\tau)}\langle \hat{A}_{mn}(t)\rangle$ and $\int_0^t d\tau e^{ix(t-\tau)} \simeq \pi\delta(x) + i\mathcal{P}/x$.

PRL 100, 253201 (2008) PHYSICAL REVIEW LETTERS week ending 27 JUNE 2008

For a nondegenerate system, the off-diagonal elements of the atomic density matrix $\hat{\sigma}$ decouple from one another as well as from the diagonal elements, and one finds that the internal atomic dynamics follows the rate equations

$$\dot{\sigma}_{nn}(t) = -\Gamma_n \sigma_{nn}(t) + \sum_k \Gamma_{kn} \sigma_{kk}(t), \tag{17}$$

$$\dot{\sigma}_{mn}(t) = \left[-i\tilde{\omega}_{mn} - \frac{1}{2}(\Gamma_m + \Gamma_n) \right] \sigma_{mn}(t), \quad m \neq n \tag{18}$$

($\sigma_{mn} = \langle m|\hat{\sigma}|n\rangle = \langle \hat{A}_{nm} \rangle$). Here, the total loss rates read

$$\Gamma_n = \sum_k \Gamma_{nk} = \frac{2\mu_0}{\hbar} \sum_k \tilde{\omega}_{nk}^2 \{\Theta(\tilde{\omega}_{nk})[n(\tilde{\omega}_{nk}) + 1] + \Theta(\tilde{\omega}_{kn}) n(\tilde{\omega}_{kn})\} \boldsymbol{d}_{nk} \cdot \mathrm{Im}\mathbf{G}(\boldsymbol{r}_A, \boldsymbol{r}_A, |\tilde{\omega}_{nk}|) \cdot \boldsymbol{d}_{kn} \tag{19}$$

and the shifts of the atomic transition frequencies $\tilde{\omega}_{mn} = \omega_{mn} + \delta\omega_m - \delta\omega_n$ are given by

$$\delta\omega_n = \sum_k \delta\omega_{nk} = \frac{\mu_0}{\pi\hbar} \sum_k \mathcal{P} \int_0^\infty d\omega\, \omega^2 \times \left[\frac{n(\omega) + 1}{\tilde{\omega}_{nk} - \omega} + \frac{n(\omega)}{\tilde{\omega}_{nk} + \omega} \right] \boldsymbol{d}_{nk} \cdot \mathrm{Im}\mathbf{G}(\boldsymbol{r}_A, \boldsymbol{r}_A, \omega) \cdot \boldsymbol{d}_{kn}; \tag{20}$$

they reduce to the perturbative result derived in Ref. [18] upon setting $\tilde{\omega}_{nk} \simeq \omega_{nk}$ in the denominators.

With these preparations, we evaluate the CP force (5) with the help of Eqs. (7), (13), and (14) and the solution to Eq. (10) as

$$\boldsymbol{F}(\boldsymbol{r}_A, t) = \frac{i\mu_0}{\pi} \sum_{n,k} \int_0^\infty d\omega\, \omega^2 \boldsymbol{\nabla} \boldsymbol{d}_{nk} \cdot \mathrm{Im}\mathbf{G}^{(1)}(\boldsymbol{r}, \boldsymbol{r}_A, \omega) \cdot \boldsymbol{d}_{kn}|_{\boldsymbol{r}=\boldsymbol{r}_A} \int_0^t d\tau \langle \hat{A}_{nn}(\tau) \rangle \{ n(\omega) \times e^{[i(\omega+\omega_{nk}) - (\Gamma_n + \Gamma_k)/2](t-\tau)} + [n(\omega) + 1] \times e^{[-i(\omega-\omega_{nk}) - (\Gamma_n + \Gamma_k)/2](t-\tau)} \} + \text{c.c.} \tag{21}$$

Here we have used the correlation function

$$\langle \hat{A}_{mn}(t) \hat{A}_{kl}(\tau) \rangle = \delta_{nk} \langle \hat{A}_{ml}(\tau) \rangle e^{[i\tilde{\omega}_{mn} - (\Gamma_m + \Gamma_n)/2](t-\tau)} \tag{22}$$

which follows from Eq. (18) by means of the quantum regression theorem [27]. Evaluating the τ integral in Markov approximation and the ω integral by means of contour-integral techniques (cf. Ref. [25]), one finds that the thermal CP force on an atomic system prepared in an incoherent superposition of energy eigenstates is given by $\boldsymbol{F}(\boldsymbol{r}_A, t) = \sum_n \sigma_{nn}(t) \boldsymbol{F}_n(\boldsymbol{r}_A)$ with force components

$$\boldsymbol{F}_n(\boldsymbol{r}_A) = -\mu_0 k_B T \sum_{N=0}^\infty \left(1 - \frac{1}{2}\delta_{N0} \right) \xi_N^2 \boldsymbol{\nabla} \mathrm{Tr} \{ [\boldsymbol{\alpha}_n(i\xi_N) + \boldsymbol{\alpha}_n(-i\xi_N)] \cdot \mathbf{G}^{(1)}(\boldsymbol{r}_A, \boldsymbol{r}, i\xi_N) \}|_{\boldsymbol{r}=\boldsymbol{r}_A} + \mu_0 \sum_k \{ \Theta(\tilde{\omega}_{nk}) \Omega_{nk}^2 [n(\Omega_{nk}) + 1] \boldsymbol{\nabla} \boldsymbol{d}_{nk} \cdot \mathbf{G}^{(1)}(\boldsymbol{r}, \boldsymbol{r}_A, \Omega_{nk}) \cdot \boldsymbol{d}_{kn}|_{\boldsymbol{r}=\boldsymbol{r}_A} - \Theta(\tilde{\omega}_{kn}) \Omega_{kn}^{*2} n(\Omega_{kn}^*) \times \boldsymbol{\nabla} \boldsymbol{d}_{nk} \cdot \mathbf{G}^{(1)}(\boldsymbol{r}, \boldsymbol{r}_A, \Omega_{kn}^*) \cdot \boldsymbol{d}_{kn}|_{\boldsymbol{r}=\boldsymbol{r}_A} + \text{c.c.} \} \tag{23}$$

[$\Omega_{nk} = \tilde{\omega}_{nk} + i(\Gamma_n + \Gamma_k)/2$] and atomic or molecular polarizability

$$\boldsymbol{\alpha}_n(\omega) = \frac{1}{\hbar} \sum_k \left[\frac{\boldsymbol{d}_{nk} \boldsymbol{d}_{kn}}{-\Omega_{nk} - \omega} + \frac{\boldsymbol{d}_{kn} \boldsymbol{d}_{nk}}{-\Omega_{nk}^* + \omega} \right]. \tag{24}$$

This result generalizes the zero-temperature force calculated in Ref. [25].

In order to compare this force with the macroscopic result (4), we consider an isotropic atomic system in the perturbative limit $\Omega_{nk} \simeq \omega_{nk}$, whereby Eq. (23) simplifies to

$$\boldsymbol{F}_n(\boldsymbol{r}_A) = -\mu_0 k_B T \sum_{N=0}^\infty \left(1 - \frac{1}{2}\delta_{N0} \right) \xi_N^2 \alpha_n(i\xi_N) \times \boldsymbol{\nabla}_A \mathrm{Tr} \mathbf{G}^{(1)}(\boldsymbol{r}_A, \boldsymbol{r}_A, i\xi_N) + \frac{\mu_0}{3} \sum_k \omega_{nk}^2 \{ \Theta(\omega_{nk})[n(\omega_{nk}) + 1] - \Theta(\omega_{kn}) n(\omega_{kn}) \} |\boldsymbol{d}_{nk}|^2 \boldsymbol{\nabla}_A \mathrm{Tr}\, \mathrm{Re}\mathbf{G}^{(1)}(\boldsymbol{r}_A, \boldsymbol{r}_A, \omega_{nk}) \tag{25}$$

and coincides with the negative gradient of the frequency shift (20) given in Ref. [18]. In addition to the Matsubara sum, the thermal CP force has resonant contributions proportional to $n(\omega_{nk})$ and $n(\omega_{nk}) + 1$, respectively, which are due to the absorption and emission of photons by the atomic system. Even the force $\boldsymbol{F}_0(\boldsymbol{r}_A)$ on a ground-state atom or molecule exhibits resonant force components $-\frac{1}{3}\mu_0 \omega_{k0}^2 n(\omega_{k0}) |\boldsymbol{d}_{0k}|^2 \boldsymbol{\nabla}_A \mathrm{Tr}\, \mathrm{Re}\mathbf{G}^{(1)}(\boldsymbol{r}_A, \boldsymbol{r}_A, \omega_{k0})$ associated with thermal-photon absorption which lead to a discrepancy with the macroscopic result (4). These resonant forces can be observed on time scales which are short with respect to the inverse ground-state heating rates Γ_{0k}^{-1}, and their magnitude scales with the number of thermal photons at the respective transition frequency $n(\omega_{k0})$. Polar molecules thus present an ideal candidate for studying them, since their heating time can be of the order of several seconds, and the thermal-photon number at the relevant vibrational and rotational transition frequencies in the microwave regime can reach values of up to a few hundred at room temperature [28]. As discussed in Ref. [14], the enhanced frequency shifts observed very recently via selective reflection spectroscopy of cesium in the far infrared might be due to a resonant thermal effect of this kind.

Our approach allows us to discuss the full dynamics of the CP force. It reveals that resonant force components associated with absorption and stimulated or spontaneous

emission of photons are a genuine nonequilibrium effect: According to Eq. (17), the atomic system reaches thermal equilibrium with its environment in the long-time limit and is described by the thermal state $\hat{\sigma}_T = e^{-\sum_n \tilde{E}_n \hat{A}_{nn}/(k_B T)}/\mathrm{Tr}[e^{-\sum_n \tilde{E}_n \hat{A}_{nn}/(k_B T)}]$ $(\tilde{E}_n = E_n + \hbar\delta\omega_n)$. In thermal equilibrium, all resonant force components cancel and the force can be written in the form of Eq. (4) only if the atomic polarizability has been identified as the thermal polarizability, $\alpha_T(\omega) = \sum_n \sigma_{T,nn}\alpha_n(\omega)$. In the limit of a single dominant transition, this equilibrium force is smaller than that resulting from Eq. (4) with $\alpha_0(\omega)$ by a factor $r_T = \tanh[\hbar\tilde{\omega}_{10}/(2k_B T)] = [2n(\tilde{\omega}_{10}) + 1]^{-1}$. The force on ground-state atoms, which is dominated by electronic transitions, is insensitive to this effect at room temperature due to the very small thermal-photon number: For Rb ($\omega_{10} = 2.37 \times 10^{15}$ Hz rad [29]), one obtains $r_T = 1 - 1.3 \times 10^{-26}$ at $T = 300$ K. As in the case of the nonequilibrium force discussed above, a noticeable deviation from the Lifshitz result is to be expected for polar molecules: For CaF, force components associated with vibrational transitions ($\omega_{10} = 1.15 \times 10^{14}$ Hz rad [30]) are reduced by a factor $r_T = 0.90$, those associated with rotational transitions ($\omega_{10} = 1.32 \times 10^{11}$ Hz rad [31]) even by a factor $r_T = 0.0017$—they are thus strongly reduced with respect to the prediction from Lifshitz theory.

In conclusion, a full quantum-mechanical treatment of the atom-field interaction has revealed that the thermal CP force on a ground-state atom or molecule cannot be obtained from a macroscopic calculation while the force on a fully thermalized atom can—provided that one uses its correct finite-temperature polarizability. As shown, the force on thermalized molecules is considerably smaller than suggested by Lifshitz theory. The resonant contributions to the force that occur for a ground-state atom are due to the absorption of thermal photons and manifest a nonequilibrium effect. In particular, they may dominate the thermal CP force on polar molecules, where they present both a considerable limiting factor for the miniaturisation of molecular surface traps and a novel probe to the surface-assisted thermal dynamics of these molecules. The discussion presented here immediately generalizes to scenarios such as those suggested in Ref. [15] where different parts of the environment are held at different temperatures.

This work was supported by the Alexander von Humboldt Foundation and the UK Engineering and Physical Sciences Research Council.

[1] H. G. Craighead, Science **290**, 1532 (2000).
[2] Y. Sugimoto *et al.*, Nature (London) **446**, 64 (2007).
[3] M. T. Northen and K. L. Turner, Nanotechnology **16**, 1159 (2005).
[4] J. Fortágh and C. Zimmermann, Rev. Mod. Phys. **79**, 235 (2007).
[5] R. S. Decca *et al.*, Ann. Phys. (Leipzig) **318**, 37 (2005).
[6] E. M. Lifshitz, Sov. Phys. JETP **2**, 73 (1956); I. E. Dzyaloshinskii, E. M. Lifshitz, and L. P. Pitaevskii, Adv. Phys. **10**, 165 (1961).
[7] S. K. Lamoreaux, Phys. Rev. Lett. **78**, 5 (1997); U. Mohideen and A. Roy, *ibid.* **81**, 4549 (1998); R. S. Decca *et al.*, *ibid.* **91**, 050402 (2003); for reviews, see M. Bordag, U. Mohideen, and V. M. Mostepanenko, Phys. Rep. **353**, 1 (2001); S. K. Lamoreaux, Rep. Prog. Phys. **68**, 201 (2005).
[8] C. Genet, A. Lambrecht, and S. Reynaud, Phys. Rev. A **62**, 012110 (2000); G. L. Klimchitskaya and V. M. Mostepanenko, *ibid.* **63**, 062108 (2001).
[9] M. Boström and B. E. Sernelius, Phys. Rev. Lett. **84**, 4757 (2000).
[10] M. Bordag *et al.*, Phys. Rev. Lett. **85**, 503 (2000); J. S. Høye *et al.*, Phys. Rev. E **67**, 056116 (2003).
[11] V. M. Mostepanenko *et al.*, J. Phys. A **39**, 6589 (2006); I. Brevik, S. A. Ellingsen, and K. A. Milton, New J. Phys. **8**, 236 (2006).
[12] M. Antezza *et al.*, Phys. Rev. Lett. **97**, 223203 (2006); V. B. Bezerra *et al.*, Eur. Phys. J. C **52**, 701 (2007).
[13] M. Marrocco *et al.*, Phys. Rev. Lett. **81**, 5784 (1998).
[14] P. C. d. S. Segundo *et al.*, Laser Phys. **17**, 983 (2007).
[15] M. Antezza, L. P. Pitaevskii, and S. Stringari, Phys. Rev. Lett. **95**, 113202 (2005).
[16] J. M. Obrecht *et al.*, Phys. Rev. Lett. **98**, 063201 (2007).
[17] T. Nakajima, P. Lambropoulos, and H. Walther, Phys. Rev. A **56**, 5100 (1997); S.-T. Wu and C. Eberlein, Proc. R. Soc. A **456**, 1931 (2000).
[18] M.-P. Gorza and M. Ducloy, Eur. Phys. J. D **40**, 343 (2006).
[19] M. Antezza, L. P. Pitaevskii, and S. Stringari, Phys. Rev. A **70**, 053619 (2004).
[20] J. F. Babb, G. L. Klimchitskaya, and V. M. Mostepanenko, Phys. Rev. A **70**, 042901 (2004); M. Bordag *et al.*, Phys. Rev. B **74**, 205431 (2006); E. V. Blagov, G. L. Klimchitskaya, and V. M. Mostepanenko, Phys. Rev. B **75**, 235413 (2007).
[21] A. D. McLachlan, Proc. R. Soc. A **274**, 80 (1963); C. Henkel *et al.*, J. Opt. A: Pure Appl. Opt. **4**, S109 (2002).
[22] C. Raabe and D.-G. Welsch, Phys. Rev. A **73**, 063822 (2006).
[23] S. Y. Buhmann and D.-G. Welsch, Prog. Quantum Electron. **31**, 51 (2007).
[24] J. N. Israelachvili, Q. Rev. Biophys. **6**, 341 (1974); V. M. Nabutovskiĭ, V. R. Belosludov, and A. M. Korotkikh, Sov. Phys. JETP **50**, 352 (1979); M. Boström and B. E. Sernelius, Phys. Rev. A **61**, 052703 (2000); T. H. Boyer, *ibid.* **11**, 1650 (1975).
[25] S. Y. Buhmann *et al.*, Phys. Rev. A **70**, 052117 (2004).
[26] L. Knöll, S. Scheel, and D.-G. Welsch, in *Coherence and Statistics of Photons and Atoms*, edited by J. Peřina (Wiley, New York, 2001), p. 1.
[27] W. Vogel and D.-G. Welsch, *Quantum Optics* (Wiley-VCH, Berlin, 2006), 3rd ed.
[28] N. Vanhaecke and O. Dulieu, Mol. Phys. **105**, 1723 (2007).
[29] J. E. Sansonetti, J. Phys. Chem. Ref. Data **35**, 301 (2006).
[30] M. Pelegrini *et al.*, Braz. J. Phys. **35**, 950 (2005).
[31] L. A. Kaledin *et al.*, J. Mol. Spectrosc. **197**, 289 (1999).

PRL 104, 223003 (2010) PHYSICAL REVIEW LETTERS week ending 4 JUNE 2010

Temperature-Independent Casimir-Polder Forces Despite Large Thermal Photon Numbers

Simen Å. Ellingsen,[1,*] Stefan Yoshi Buhmann,[2] and Stefan Scheel[2]

[1]*Department of Energy and Process Engineering, Norwegian University of Science and Technology, N-7491 Trondheim, Norway*
[2]*Quantum Optics and Laser Science, Blackett Laboratory, Imperial College London, Prince Consort Road, London SW7 2AZ, United Kingdom*

(Received 2 March 2010; published 2 June 2010)

We demonstrate that Casimir-Polder potentials can be entirely independent of temperature even when allowing for the relevant thermal photon numbers to become large. This statement holds for potentials that are due to low-energy transitions of a molecule placed near a plane metal surface whose plasma frequency is much larger than any atomic resonance frequencies. For a molecule in an energy eigenstate, the temperature independence is a consequence of strong cancellations between nonresonant potential components and those due to evanescent waves. For a molecule with a single dominant transition in a thermal state, upward and downward transitions combine to form a temperature-independent potential. The results are contrasted with the case of an atom whose potential exhibits a regime of linear temperature dependence. Contact with the Casimir force between a weakly dielectric and a metallic plate is made.

DOI: 10.1103/PhysRevLett.104.223003 PACS numbers: 31.30.jh, 12.20.−m, 34.35.+a, 42.50.Nn

Dispersion forces between polarizable objects were originally predicted by Casimir and Polder as a consequence of quantum zero-point fluctuations [1]. Recent measurements of both Casimir-Polder (CP) forces between atoms and surfaces [2] and Casimir forces between macroscopic bodies [3,4] typically operate at room temperature, where thermal fluctuations also come into play [5–8]. The temperature dependence of dispersion forces is of relevance for both fundamental and practical reasons.

On the theoretical side, the correct description of the Casimir force between metals at finite temperature is subject to an ongoing debate [4,9]. To wit, predictions differ for the high-temperature behavior of the Casimir force between metals, for which employing a standard dissipative description of the surfaces fails to reproduce the experimental observations [10]. This suggests that progress can be made by directly observing the variation of the Casimir force with temperature.

On the practical side, CP forces become increasingly relevant when trying to trap and coherently manipulate cold atoms near surfaces [11]. Current endeavours aim at extending these techniques to more complex systems such as polar molecules [12]. Such systems typically exhibit long-wavelength transitions so that CP forces become increasingly long-ranged. This raises the question of whether they can be controlled by lowering the ambient temperature and hence suppressing thermal force components.

Thermal contributions to the CP potential are governed by the photon number $n(\omega) = [e^{\hbar\omega/(k_B T)} - 1]^{-1}$. A noticeable deviation of the potential from its zero-temperature value is to be expected when $n(\omega) \gtrsim 1$ in the relevant frequency range. This is the case, for instance, for molecules with small transition frequencies, $|\omega_{kn}| \lesssim k_B T/\hbar = 3.93 \times 10^{13}$ rad/s at room temperature (300 K). The associated wavelengths are much larger than typical experimental molecule-surface separations in the nanometer to micrometer range [2], $z_A \ll c/|\omega_{kn}|$. Furthermore, experimental realizations typically involve metal surfaces with $|\varepsilon(\omega_{kn})| \gg 1$ which act like perfect reflectors.

As we will show in this Letter, the above three conditions combined result in potentials which are independent of temperature over the entire range from zero to room temperature and beyond. We will first discuss the case of a molecule prepared in an energy eigenstate and then consider molecules at thermal equilibrium with their environment, comparing our results with those for atoms whose transitions involve higher energies.

Molecule vs atom in an eigenstate.—As shown in Ref. [13], the CP potential of a molecule prepared in an isotropic energy eigenstate $|n\rangle$ at distance z_A from the plane surface of a metal,

$$U_n(z_A) = U_n^{\mathrm{nr}}(z_A) + U_n^{\mathrm{ev}}(z_A) + U_n^{\mathrm{pr}}(z_A), \tag{1}$$

may be separated into three contributions: a nonresonant term U_n^{nr} due to virtual photons that is formally similar to that produced by the Lifshitz theory [5], and a resonant contribution due to real photons which may be further split into contributions from evanescent (U_n^{ev}) and propagating (U_n^{pr}) waves. The nonresonant potential is given by [13]

$$U_n^{\mathrm{nr}}(z_A) = -\frac{\mu_0 k_B T}{6\pi\hbar} \sum_k |\boldsymbol{d}_{nk}|^2 {\sum_{j=0}^{\infty}}' \frac{\omega_{kn}}{\omega_{kn}^2 + \xi_j^2} \int_{\xi_j/c}^{\infty} db \times e^{-2bz_A} \{2b^2 c^2 r_p(i\xi_j) - \xi_j^2 [r_s(i\xi_j) + r_p(i\xi_j)]\} \tag{2}$$

[$\omega_{kn} = (E_k - E_n)/\hbar$, transition frequencies; $\boldsymbol{d}_{nk}$, dipole matrix elements; $\xi_j = j\xi$ with $\xi = 2\pi k_B T/\hbar$, Matsubara frequencies; and the primed summation indicates half-weight for the term $j = 0$] and the evanescent one reads

$$U_n^{\mathrm{ev}}(z_A) = \frac{\mu_0}{12\pi} \sum_k n(\omega_{kn}) |\boldsymbol{d}_{nk}|^2 \int_0^{\infty} db e^{-2bz_A} \times \{2b^2 c^2 \mathrm{Re}[r_p(\omega_{kn})] + \omega_{nk}^2 \mathrm{Re}[r_s(\omega_{kn}) + r_p(\omega_{kn})]\}; \tag{3}$$

note that $n(\omega_{kn}) = -[n(\omega_{nk}) + 1]$ for downward transi-

tions. These two contributions dominate in the region $z_A|\omega_{kn}|/c \ll 1$ that we are interested in, while the spatially oscillating U_n^{pr} becomes relevant only in the far-field range $z_A|\omega_{kn}|/c \gg 1$. The reflection coefficients of the surface for s- and p-polarized waves are given by $r_s(\omega) = (b - b_1)/(b + b_1)$ and $r_p(\omega) = [\varepsilon(\omega)b - b_1]/[\varepsilon(\omega)b + b_1]$ with $b_1 = \sqrt{b^2 - [\varepsilon(\omega) - 1]\omega^2/c^2}$, $\mathrm{Re}(b_1) > 0$.

For our analytical investigations, we will model the metal surface by a perfect reflector with frequency-independent reflection coefficients $r_s \approx -1$ and $r_p \approx 1$. This is well justified, as the plasma frequency is typically much larger than the molecular transition frequency ω_{kn}, and hence $|\varepsilon(\omega)| \gg 1$ in the relevant frequency range. The b integrals can then be performed to give

$$U_n^{nr}(z_A) = -\frac{k_B T}{12\pi\varepsilon_0\hbar z_A^3}\sum_k |\boldsymbol{d}_{nk}|^2 {\sum_{j=0}^{\infty}}' \frac{\omega_{kn} e^{-2jz_A\xi/c}}{\omega_{kn}^2 + j^2\xi^2} \times\left[1 + 2j\frac{z_A\xi}{c} + 2j^2\frac{z_A^2\xi^2}{c^2}\right], \quad (4)$$

$$U_n^{ev}(z_A) = \frac{1}{24\pi\varepsilon_0 z_A^3}\sum_k n(\omega_{kn})|\boldsymbol{d}_{nk}|^2. \quad (5)$$

The asymptotic temperature dependence of the potential for a given distance z_A is governed by two characteristic temperatures: The molecular transition frequency defines a spectroscopic temperature $T_\omega = \hbar|\omega_{kn}|/k_B$, which is roughly the temperature required to noticeably populate the upper level. Similarly, the distance introduces a geometric temperature $T_z = \hbar c/(z_A k_B)$, i.e., the temperature of radiation whose wavelength is of the order z_A.

We will now show that the total potential becomes independent of temperature in both the geometric low-temperature limit $T \ll T_z$ and the spectroscopic high-temperature limit $T \gg T_\omega$. For a typical molecule with its long-wavelength transitions, the potential is nonretarded for typical molecule-surface distances, $z_A|\omega_{kn}|/c \ll 1$. As depicted in Fig. 1 (i), this implies $T_\omega \ll T_z$; hence, the two regions of constant potential overlap and the potential is constant for all temperatures. For an atom, on the contrary, the transition wavelengths are much shorter, so that we may have $z_A|\omega_{kn}|/c \gg 1$. In this case, an intermediate regime $T_z \ll T \ll T_\omega$ exists where the potential increases linearly with temperature, cf. Fig. 1 (ii).

We begin with a typical molecule with $z_A|\omega_{kn}|/c \ll 1$. In the geometric low-temperature limit $T \ll T_z$, we have $z_A\xi/c \ll 1$; hence, the sum in Eq. (4) is densely spaced. The factor $1/(\omega_{kn}^2 + j^2\xi^2)$ restricts it to values where $jz_A\xi/c \leq z_A|\omega_{kn}|/c \ll 1$. With this approximation, the summation can be performed as

$${\sum_{j=0}^{\infty}}' \frac{1}{a^2 + j^2} = \frac{\pi}{2a}\coth(\pi a) \quad (6)$$

and we find

$$U_n^{nr}(z_A) \overset{T\ll T_z}{=} -\frac{1}{24\pi\varepsilon_0 z_A^3}\sum_k\left[n(\omega_{kn}) + \frac{1}{2}\right]|\boldsymbol{d}_{nk}|^2, \quad (7)$$

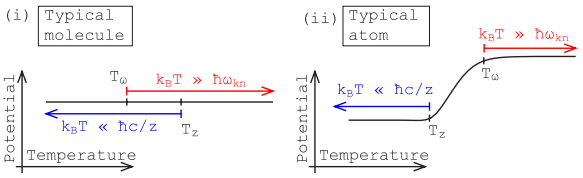

FIG. 1 (color online). Sketch of the temperature dependence of the CP potential for a typical molecule vs a typical atom.

noting that $\coth[\hbar\omega_{kn}/(2k_BT)] = 2n(\omega_{kn}) + 1$. Adding the evanescent contribution (5), we find the temperature-independent total potential

$$U_n(z_A) \overset{T\ll T_z}{=} -\frac{\sum_k |\boldsymbol{d}_{nk}|^2}{48\pi\varepsilon_0 z_A^3} = -\frac{\langle\hat{\boldsymbol{d}}^2\rangle_n}{48\pi\varepsilon_0 z_A^3}, \quad (8)$$

in agreement with the well-known nonretarded zero-temperature result [1].

In the spectroscopic high-temperature limit $T \gg T_\omega$, we have $\xi/|\omega_{kn}| \gg 1$. Because of the denominator $\omega_{kn}^2 + j^2\xi^2$, the $j = 0$ term strongly dominates the sum in Eq. (4) and we find

$$U_n^{nr}(z_A) \overset{T\gg T_\omega}{=} -\frac{1}{24\pi\varepsilon_0 z_A^3}\sum_k \frac{k_B T}{\hbar\omega_{kn}}|\boldsymbol{d}_{nk}|^2. \quad (9)$$

Under the condition $T \gg T_\omega$, i.e., $k_BT \gg \hbar|\omega_{kn}|$, the evanescent contribution (5) reduces to

$$U_n^{ev}(z_A) \overset{T\gg T_\omega}{=} \frac{1}{24\pi\varepsilon_0 z_A^3}\sum_k\left(\frac{k_B T}{\hbar\omega_{kn}} - \frac{1}{2}\right)|\boldsymbol{d}_{nk}|^2. \quad (10)$$

Adding the two results, the total potential is again temperature independent and given by Eq. (8). This limit is just the high-temperature saturation found in Refs. [7,13].

The thermal CP potential of a typical molecule with its long-wavelength transitions has thus been found to be temperature independent in the geometric low-temperature and spectroscopic high-temperature regimes. Because of the condition $z_A|\omega_{kn}|/c \ll 1$, at least one of the conditions $T \ll T_z$ or $T \gg T_\omega$ always holds, implying that the potential is constant for all temperatures and it agrees with its zero-temperature value. The independence of the total potential in both regimes is a result of cancellations between nonresonant and evanescent potential components, which both strongly depend on temperature. This is illustrated in Fig. 2, where we display the total temperature-independent potential as well as its nonresonant and evanescent parts for a ground-state LiH molecule in front of a Au surface for various temperatures. It is seen that very strong cancellations occur, especially at high temperatures. Note that, while our theoretical arguments are based on the perfect-conductor limit, all numerical examples use the reflectivities of real metals.

We now turn to the case of atoms, whose electronic wavelengths are short compared to typical experimental separations: $z_A|\omega_{kn}|/c \gg 1$. The exponential restricts the sum in Eq. (4) to terms with $j\xi \lesssim c/z_A \ll |\omega_{kn}|$, so the

PRL 104, 223003 (2010) PHYSICAL REVIEW LETTERS week ending 4 JUNE 2010

term $j^2\xi^2$ in the denominator may be neglected. The sum can then be performed according to

$$\sum_{j=0}^{\infty}{}' e^{-2ja}(1+2ja+2j^2a^2) \to \begin{cases} 3/(2a) & a \ll 1 \\ 1/2 & a \gg 1. \end{cases} \quad (11)$$

In the geometric low-temperature regime $T \ll T_z$, we further have $z_A\xi/c \ll 1$, i.e., $a \ll 1$ in Eq. (11); hence

$$U_n^{\mathrm{nr}}(z_A) \overset{T\ll T_z}{=} -\frac{c}{16\pi^2\varepsilon_0 z_A^4}\sum_k \frac{|\boldsymbol{d}_{nk}|^2}{\omega_{kn}}, \quad (12)$$

in agreement with the famous zero-temperature result of Casimir and Polder [1]. Moreover, the condition $z_A|\omega_{kn}|/c \gg 1$ implies that $T \ll T_z \ll T_\omega$: The geometric low-temperature regime is also a spectroscopic one, and hence the evanescent potential reduces to

$$U_n^{\mathrm{ev}}(z_A) \overset{T\ll T_z}{=} -\frac{1}{24\pi\varepsilon_0 z_A^3}\sum_k \Theta(\omega_{nk})|\boldsymbol{d}_{nk}|^2. \quad (13)$$

[$\Theta(x)$ is the unit step function.] Adding the two contributions, we find the temperature-independent total potential

$$U_n(z_A) \overset{T\ll T_z}{=} -\frac{1}{24\pi\varepsilon_0 z_A^3}\sum_k \left[\frac{3c}{2z_A\omega_{kn}} + \Theta(\omega_{nk})\right]|\boldsymbol{d}_{nk}|^2 \quad (14)$$

in the geometric low-temperature regime.

For intermediate temperatures $T_z \ll T \ll T_\omega$, we have $z_A\xi/c \gg 1$, so using $a \gg 1$ in the sum (11), the nonresonant potential (4) is found to read as in Eq. (9). The evanescent contribution is still given by Eq. (13), so the total potential varies linearly with temperature,

$$U_n(z_A) \overset{T_z\ll T\ll T_\omega}{=} -\frac{1}{24\pi\varepsilon_0 z_A^3}\sum_k \left[\frac{k_B T}{\hbar\omega_{kn}} + \Theta(\omega_{nk})\right]|\boldsymbol{d}_{nk}|^2. \quad (15)$$

In the spectroscopic high-temperature limit $T \gg T_\omega$, the evanescent contribution is given by Eq. (10) as already shown. It cancels with the nonresonant contribution, still agreeing with Eq. (9), to give a saturated potential of the form (8). However, with, e.g., $T_\omega \approx 18.000$ K for Rb, this saturation is unobservable. Moreover, as the electronic transition frequencies can be comparable to the plasma frequency of the metal, the assumptions $r_s \approx -1$ and $r_p \approx 1$ do not hold. As a consequence, the cancellations required to achieve saturation do not occur for atoms near realistic metal surfaces.

We have thus seen that for an atom with $z_A|\omega_{kn}|/c \gg 1$, separate geometric low-temperature and spectroscopic high-temperature regimes exist, with the potential exhibiting a linear temperature dependence between these two regions. The difference between the thermal CP potentials of typical atoms vs molecules is illustrated in Fig. 3, where we show the temperature dependence of the potential at fixed distance from a Au surface for different species. The potentials associated with the long-wavelength, rotational transitions of LiH and OH are virtually temperature independent, while the short-wavelength electronic transition of Rb shows a linear increase over a large range of temperatures. YbF, with its dominant vibrational transition, lies in between the two extremes of typical long-wavelength molecular and short-wavelength atomic transitions; its potential increases by about 30% in the displayed temperature range. In contrast to the other examples, the potential of YbF noticeably deviates from the corresponding ideal conductor result due to imperfect reflection. Note that contributions to the molecular CP potentials due to electronic transitions are smaller than the rotational and vibrational ones (8) by factors $c/(z_A\omega_{kn}) \ll 1$ (14) or $k_BT/(\hbar\omega_{kn}) \ll 1$ (15) within the displayed temperature range and are hence negligible.

Molecule at thermal equilibrium.—The proven temperature independence immediately generalizes to molecules in incoherent superpositions of energy eigenstates with temperature-independent probabilities $p_n \neq p_n(T)$ and total potential $U(z_A) = \sum_n p_n U_n(z_A)$. The situation is different for a molecule at thermal equilibrium with its environment because the respective probabilities $p_n(T) = \exp[-E_n/(k_BT)]/\sum_k \exp[-E_k/(k_BT)]$ do depend on T. At thermal equilibrium, all resonant potential components

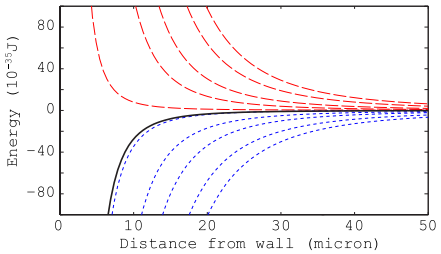

FIG. 2 (color online). CP potential of a ground-state LiH molecule in front of a Au surface. We show the total potential (solid line) as well as its evanescent (dashed line) and nonresonant (dotted line) contributions for temperatures 10 K, 50 K, 100 K, 200 K, 300 K (left to right).

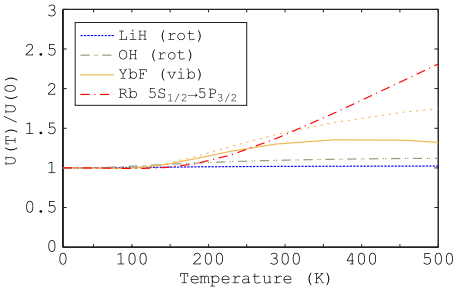

FIG. 3 (color online). Temperature dependence of the CP potential of various ground-state atoms and molecules at distance $z_A = 5$ μm from a Au surface. The transition frequencies of these species are such that $z_A\omega_{kn}/c = 0.046$ (LiH), 0.26 (OH), 1.59 (YbF), 40.2 (Rb). For comparison, the perfect-conductor result for YbF is also shown (dotted line).

cancel pairwise [8]. Introducing potential components U_{nk} due to a particular transition $n \leftrightarrow k$ (such that $U_n = \sum_k U_{nk}$) and the associated statistical weights $p_{nk} = p_n + p_k$, and exploiting the fact that $U_{kn} = -U_{nk}$, we can write the total potential in the form

$$U(z_A) = \sum_{n<k} (p_n - p_k) U^{nr}_{nk}(z_A) = \sum_{n<k} p_{nk} \tanh\left(\frac{\hbar\omega_{kn}}{2k_BT}\right) U^{nr}_{nk}(z_A). \quad (16)$$

The behavior of this potential in the two limits relevant for a molecule with $z_A|\omega_{kn}|/c \ll 1$ follows immediately from the asymptotes given in the previous section. For $T \ll T_z$, U^{nr}_{nk} from Eq. (7) leads to

$$U(z_A) \overset{T\ll T_z}{=} -\frac{1}{48\pi\varepsilon_0 z_A^3} \sum_{n<k} p_{nk} |\boldsymbol{d}_{nk}|^2, \quad (17)$$

where $n(\omega_{kn}) + 1/2 = \coth[\hbar\omega_{kn}/(2k_BT)]/2$ has been used once more. For $T \gg T_\omega$, we recall U^{nr}_{nk} from Eq. (9) and note that $\tanh[\hbar\omega_{kn}/(2k_BT)] \approx \hbar\omega_{kn}/(2k_BT)$ to again find the potential (17).

Combining the two results, we may use the main argument of the previous section to conclude that the potential components U_{nk} associated with a particular transition $n \leftrightarrow k$ are independent of temperature for all temperatures. The independence is a result of cancellations between the purely nonresonant contributions from lower state n and upper state k. Note, however, that the statistical weights p_{nk} introduce a weak temperature dependence, in general: The total potential is only strictly temperature independent when dominated by a single transition. For instance, when accounting for the presence of the first vibrational transition in LiH (labeled as 2), the weight p_{01} for the dominant rotational transition varies from its zero-temperature value unity to $p_{01}(T) = (1 + e^{-\hbar\omega_{10}/k_BT})/(1 + e^{-\hbar\omega_{10}/k_BT} + e^{-\hbar\omega_{20}/k_BT}) = 0.9994$ at room temperature.

Relevance to Casimir forces.—To illustrate the relevance of the demonstrated temperature independence to the Casimir force, let us consider an infinite dielectric halfspace filled with molecules of number density η at a distance z from a metal plane. For a weakly dielectric medium, the Casimir energy per unit area is given by $E(z) = \int_z^\infty dz_A \eta U(z_A)$ [14]. Using Eq. (17), we find that

$$E(z) = \frac{\eta}{96\pi\varepsilon_0 z^2} \sum_{n<k} p_{nk} |\boldsymbol{d}_{nk}|^2, \quad (18)$$

which is temperature independent under the conditions mentioned above. Note that Lifshitz's expression only agrees with this statement if the correct thermal permittivity is used [8]. If the ground-state permittivity is used, one describes a system out of equilibrium, and the Lifshitz formula does not apply.

For dielectrics with a stronger response (such that $\varepsilon - 1 \ll 1$ does not hold), many-body effects will lead to temperature-dependent corrections of higher order in the molecular polarizability. They are suppressed in the spectroscopic high-temperature limit $T \gg T_\omega$, since they are of higher order in $\tanh[\hbar\omega_{kn}/(2k_BT)] \ll 1$. Our results hence remain valid in this latter limit even for moderately strong dielectrics. On the contrary, they do not immediately generalize to the force between two metals.

Summary.—The temperature independence encountered for molecules with long-wavelength transitions shows that CP forces on such systems cannot be altered via the ambient temperature. Instead, the original zero-temperature results of Casimir and Polder apply universally across the whole temperature range. It is worth emphasizing that a "classical" regime of linear temperature dependence is never reached. Our results further indicate that when accounting for the thermal excitation of the media, the temperature dependence of Casimir forces involving dielectrics may be weaker than previously thought.

We have benefited from discussions with I. Brevik, A. Lambrecht, and S. Reynaud. This work was supported by the U.K. Engineering and Physical Sciences Research Council. Support from the European Science Foundation within the activity "New Trends and Applications of the Casimir Effect" is gratefully acknowledged.

*simen.a.ellingsen@ntnu.no

[1] H. B. G. Casimir and D. Polder, Phys. Rev. **73**, 360 (1948).
[2] C. I. Sukenik *et al.*, Phys. Rev. Lett. **70**, 560 (1993); M. Marrocco *et al.*, Phys. Rev. Lett. **81**, 5784 (1998); H. Failache *et al.*, Phys. Rev. Lett. **83**, 5467 (1999); V. Druzhinina and M. DeKieviet, Phys. Rev. Lett. **91**, 193202 (2003); H. Kübler *et al.*, Nat. Photon. **4**, 112 (2010).
[3] S. de Man *et al.*, Phys. Rev. Lett. **103**, 040402 (2009); F. Capasso *et al.*, IEEE J. Sel. Top. Quantum Electron. **13**, 400 (2007) and references therein.
[4] M. Bordag *et al.*, *Advances in the Casimir Effect* (Oxford University Press, Oxford, 2009).
[5] E. M. Lifshitz, Sov. Phys. JETP **2**, 73 (1956).
[6] T. Nakajima, P. Lambropoulos, and H. Walther, Phys. Rev. A **56**, 5100 (1997); S.-T. Wu and C. Eberlein, Proc. R. Soc. A **456**, 1931 (2000); Y. Sherkunov, Phys. Rev. A **79**, 032101 (2009).
[7] M.-P. Gorza and M. Ducloy, Eur. Phys. J. D **40**, 343 (2006).
[8] S. Y. Buhmann and S. Scheel, Phys. Rev. Lett. **100**, 253201 (2008).
[9] I. Brevik *et al.*, New J. Phys. **8**, 236 (2006).
[10] R. S. Decca *et al.*, Ann. Phys. (N.Y.) **318**, 37 (2005).
[11] Y. J. Lin *et al.*, Phys. Rev. Lett. **92**, 050404 (2004).
[12] J. van Veldhoven, H. L. Bethlem, and G. Meijer, Phys. Rev. Lett. **94**, 083001 (2005).
[13] S. Å. Ellingsen, S. Y. Buhmann, and S. Scheel, Phys. Rev. A **79**, 052903 (2009).
[14] C. Raabe and D.-G. Welsch, Phys. Rev. A **73**, 063822 (2006).

PHYSICAL REVIEW LETTERS **121,** 083603 (2018)

Nonadditivity of Optical and Casimir-Polder Potentials

Sebastian Fuchs,[1] Robert Bennett,[1] Roman V. Krems,[2] and Stefan Yoshi Buhmann[1,3]
[1]*Physikalisches Institut, Albert-Ludwigs-Universität Freiburg, Hermann-Herder-Straße 3, 79104 Freiburg, Germany*
[2]*Department of Chemistry, University of British Columbia, Vancouver, British Columbia V6T 1Z1, Canada*
[3]*Freiburg Institute for Advanced Studies, Albert-Ludwigs-Universität Freiburg, Albertstraße 19, 79104 Freiburg, Germany*

(Received 28 November 2017; revised manuscript received 30 May 2018; published 22 August 2018)

An atom irradiated by an off-resonant laser field near a surface is expected to experience the sum of two fundamental potentials, the optical potential of the laser field and the Casimir-Polder potential of the surface. Here, we report a new nonadditive potential, namely, the laser-induced Casimir-Polder potential, which arises from a correlated coupling of the atom with both the laser and the quantum vacuum. We apply this result to an experimentally realizable scenario of an atomic mirror with an evanescent laser beam leaking out of a surface. We show that the nonadditive term is significant for realistic experimental parameters, transforming potential barriers into potential wells, which can be used to trap atoms near surfaces.

DOI: 10.1103/PhysRevLett.121.083603

In experiments involving an applied electromagnetic field and particles trapped in or near material objects, two forces of very different origin arise. One is the Casimir-Polder (CP) force [1] arising from the interaction between an atom and the electromagnetic vacuum field, which is restricted and modified by the presence of nearby surfaces [2]. The other is the optical force stemming from the direct interaction between the applied electromagnetic field and the atom. The latter was first applied in experiments where micron-size dielectric spheres were trapped by two laser beams [3], eventually leading to the first observation of optical trapping of atoms by a single strongly focused Gaussian laser beam [4]. Atoms can also be reflected by an evanescent laser field at a surface, as shown, for example, in Ref. [5] where state-selective reflection of Na atoms was demonstrated using an evanescent field.

The CP force has been studied extensively. It is well described by many established theoretical approaches, ranging from a quantum-mechanical linear-response formalism [6,7] to macroscopic extensions of quantum electrodynamics that incorporate material properties, see, e.g., Ref. [8]. There are also several experimental techniques to investigate this force. Almost fifty years after its theoretical prediction, the CP force was first measured by observing the deflection of atoms passing through a V-shaped cavity [9]. Later, it was demonstrated that the scattering of slowly moving atoms from a surface can also be used to deduce the CP potential [10]. Recently, approaches involving a single Rb atom optically trapped close to a surface have been employed [11]. There, the sum of the trapping potential and the CP potential determines the equilibrium position of the atom, so that for a known trapping potential the CP potential can be determined.

This technique has recently been used to make a first direct measurement of CP forces between solid surfaces and atomic gases in the transition regime between short distances (nonretarded) and long distances (retarded) [11,12]. In this experiment, ultracold ground-state Rb atoms are reflected from an evanescent wave barrier at a glass prism.

The question arises whether the two fundamentally different ingredients, the CP potential (U_{CP}) and the light-induced optical potential (U_{L}), can be simply added to obtain the total potential. Being inherently related to universal scaling laws of dispersion potentials [13], this question is of fundamental importance. In this Letter we report a new nonadditive laser-induced CP potential. We show that it plays an important role under specific experimental conditions.

The CP potential can be viewed as the modification of a fluctuating dipole moment due to the electric field those fluctuations induce. It is clear that this is a recursive process; the dipole induces a field, which in turn interacts with the dipole, changing the field it produces, which then interacts again with the dipole and so on. Normally, only the first step in this process is considered, where the fluctuations of the dipole moment are taken to come from the field that would be present if the dipole were not there. This electric field could come from the vacuum field or a laser field depending on the specific context. This leads to the usual approach taken when considering atoms subject to vacuum and laser fields; the two potentials are simply added (cf. Ref. [14]). Here we consider and take into account the effect of the laser field on the CP potential.

Quantum vacuum forces between an atom in its ground state and a surface are attractive and in general not suitable to create a stable position for the atom [15]. Nevertheless, Ref. [16] describes the possibility of trapping ground-state atoms by dressing them with an excited state whose potential is repulsive in a laser field. This method is similar in spirit to our work, especially because the laser-induced

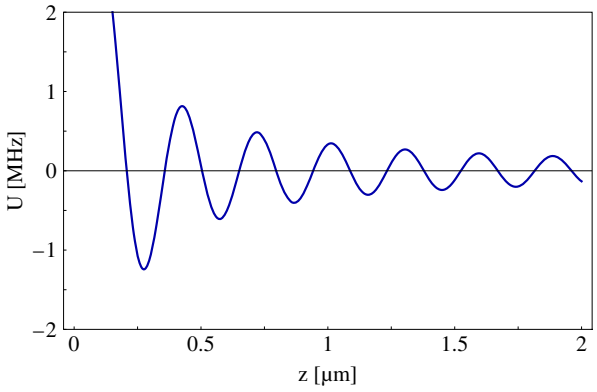

FIG. 1. Difference $\Delta U = U_{\mathrm{CP}} - U_{\mathrm{LCP}}$ for a perfectly conducting mirror with reflective coefficients $r_s = -1$ and $r_p = 1$. The laser intensity is $I = 5\ \mathrm{W/cm^2}$ used for Rb atoms with a transition frequency of $\tilde{\omega}_{10} = 2.37 \times 10^{15}$ rad/s. The detuning is $\Delta = 2\pi \times 10^8$ rad/s. The angle between the z axis and the orientation of the field $\mathbf{E}(\mathbf{r}_A)$ is $\theta = \pi/2$.

CP potential for the atomic ground state resembles the excited-state CP potential (cf. Fig. 1), but has a major difference in its assumption of a position-independent Rabi frequency.

We describe the system using a Hamiltonian that governs the coupling of the atom to the electric field and consequently consists of a field part, an atomic part, and a multipolar dipole-field coupling. The field Hamiltonian $\hat{H}_F$ can be expressed as

$$\hat{H}_F = \sum_{\lambda=\mathrm{e,m}} \int d^3r \int_0^\infty d\omega \hbar\omega \hat{\mathbf{f}}_\lambda^\dagger(\mathbf{r},\omega) \cdot \hat{\mathbf{f}}_\lambda(\mathbf{r},\omega), \quad (1)$$

where $\hat{\mathbf{f}}_\lambda$ and $\hat{\mathbf{f}}_\lambda^\dagger$ are creation and annihilation operators for composite field-matter excitations. Here we model a driving laser as being a result of a source occupying a volume V_S in space. This leads us to represent field states as a product

$$|\psi\rangle_F = |\{\mathbf{f}_\lambda(\mathbf{r},\omega)\}\rangle_{\mathbf{r}\in V_S} \otimes |\{0\}\rangle_{\mathbf{r}\notin V_S} \quad (2)$$

of coherent excitations $|\{\mathbf{f}_\lambda(\mathbf{r},\omega)\}\rangle$ in the source region and the vacuum state $|\{0\}\rangle$ for all other regions. If the annihilation operator $\hat{\mathbf{f}}_\lambda(\mathbf{r},\omega)$ acts on the state (2), there are, consequently, two contributions

$$\hat{\mathbf{f}}_\lambda(\mathbf{r},\omega)|\psi\rangle_F = \begin{cases} \mathbf{f}_\lambda(\mathbf{r},\omega)|\psi\rangle_F & \text{if } \mathbf{r} \in V_S \\ 0 & \text{if } \mathbf{r} \notin V_S \end{cases}. \quad (3)$$

The atom-field Hamiltonian $\hat{H}_{\mathrm{AF}} = -\hat{\mathbf{d}} \cdot \hat{\mathbf{E}}(\mathbf{r}_A)$ in the multipolar coupling scheme is determined by the electric field at the atom's position $\mathbf{r}_A$ and the dipole operator $\hat{\mathbf{d}}$. The electric field is given by the respective classical Green's tensor $\mathbf{G}(\mathbf{r},\mathbf{r}_A,\omega)$ and the field operator $\hat{\mathbf{f}}_\lambda(\mathbf{r},\omega)$. Solving the Heisenberg equation of motion for the field operator using the field Hamiltonian $\hat{H}_F$ (1) and the coupling Hamiltonian $\hat{H}_{\mathrm{AF}}$ and inserting this back into the electric field, the final expression for the time-dependent electric field operator yields

$$\begin{aligned} \hat{\mathbf{E}}(\mathbf{r},\omega,t) &= \hat{\mathbf{E}}_{\mathrm{free}}(\mathbf{r},\omega,t) + \hat{\mathbf{E}}_{\mathrm{ind}}(\mathbf{r},\omega) \\ &= \hat{\mathbf{E}}(\mathbf{r},\omega)e^{-i\omega(t-t_0)} \\ &\quad + \frac{i\mu_0}{\pi}\omega^2 \int_{t_0}^{t} dt' e^{-i\omega(t-t')} \mathrm{Im}\mathbf{G}(\mathbf{r},\mathbf{r}_A,\omega) \cdot \hat{\mathbf{d}}(t'), \end{aligned} \quad (4)$$

where μ_0 is the permeability of free space. The induced contribution represents the inhomogeneous part of the solution and couples the Green's tensor to the atomic dipole moment as shown in Ref. [17]. The state (3) can be inserted into Eq. (4) where the free component is modeled as a classical laser driving field of frequency ω_L at the atom's position, $\mathbf{E}(\mathbf{r}_A,t) = \mathbf{E}(\mathbf{r}_A)\cos(\omega_L t)$. In a similar way, one can compute the Heisenberg equation of motion for the atomic flip operator $\hat{A}_{mn}(t)$ [18] defined in such a way that the atomic part of the Hamiltonian is $\hat{H}_{\mathrm{A}} = \sum_n E_n \hat{A}_{nn}$.

We first assume that the atom-field coupling is weak and that the field is far-detuned from the atomic resonance. This assumption is later relaxed to obtain a more general result, as described in Ref. [19]. The electric field (4) is evaluated using the Markov approximation for weak atom-field coupling and we discard slow nonoscillatory dynamics of the flip operator by setting $\hat{A}_{mn}(t') \simeq e^{i\tilde{\omega}_{mn}(t'-t)}\hat{A}_{mn}(t)$ for the time interval $t_0 \le t' \le t$. To apply the Markov approximation we have assumed that the atomic transition frequency $\tilde{\omega}_{10}$ is not close to any narrowband resonance mode of the medium. If there were such a mode, the atom would mostly interact with it, similar to a cavity. In this case the mode could be modeled by a Lorentzian profile [18,20,21].

The parameters entering the dynamics are the shifted frequency $\tilde{\omega}_{mn} = \omega_{mn} + \delta\omega_{mn}$, where ω_{mn} is the atom's pure eigenfrequency and the CP frequency shift $\delta\omega_{mn}$ due to the presence of the surface, and the rate of spontaneous emission Γ_{mn}. The fast-oscillating nondiagonal parts $\hat{A}_{mn}(t)$ can be decoupled from the slowly oscillating diagonal operator terms $\hat{A}_{mm}(t)$ by assuming that the atom does not have quasidegenerate transitions. Moreover the atom is unpolarized in each of its energy eigenstates so that $\mathbf{d}_{mm} = \mathbf{0}$, which is guaranteed by atomic selection rules [18]. Finally, we assume the atom stays in its initial state with $\langle\hat{A}_{kl}(t')\rangle \approx \langle\hat{A}_{kl}(t)\rangle \approx \delta_{kn}\delta_{ln}$. Consequently, to compute the dipole moment we only need the nondiagonal elements of the atomic flip operator

$$\langle \dot{\hat{A}}_{mn}(t)\rangle = \mathrm{i}\tilde{\omega}_{mn}\langle \hat{A}_{mn}(t)\rangle - \frac{1}{2}[\Gamma_n + \Gamma_m]\langle \hat{A}_{mn}(t)\rangle + \frac{\mathrm{i}}{\hbar}\sum_k [\langle \hat{A}_{mk}(t)\rangle \mathbf{d}_{nk} - \langle \hat{A}_{kn}(t)\rangle \mathbf{d}_{\mathrm{km}}]\cdot \mathbf{E}(\mathbf{r}_\mathrm{A}, t). \tag{5}$$

Similar to the electric field (4), the equation for the time evolution of the dipole operator $\hat{\mathbf{d}}(t)$ can be split into free and induced (electric field dependent) parts $\hat{\mathbf{d}}_{\mathrm{free}}(t)$ and $\hat{\mathbf{d}}_{\mathrm{ind}}(t)$, given, respectively, by the first and second lines of Eq. (5).

In the Markov approximation, we use the expression of the complex atomic polarizability for an atom in a spherically symmetric state with negligible damping

$$\alpha_n(\omega) = \frac{2}{3\hbar}\sum_k \frac{\tilde{\omega}_{kn}|\mathbf{d}_{nk}|^2}{\tilde{\omega}_{kn}^2 - \omega^2}\mathbf{1}, \tag{6}$$

where $\mathbf{1}$ is the unit matrix. The dipole moment in the time domain reads

$$\langle \hat{\mathbf{d}}_{\mathrm{ind}}(t)\rangle_n = \frac{1}{2}[\alpha_n(\omega_L)\mathbf{E}(\mathbf{r}_A)e^{-i\omega_L t} + \mathrm{H.c.}], \tag{7}$$

which oscillates with the laser frequency ω_L. An equivalent expression for the induced electric field $\hat{\mathbf{E}}_{\mathrm{ind}}(\mathbf{r}, t)$ is obtained in a similar way.

The quantity we are interested in is the total potential $U = -\frac{1}{2}\langle \hat{\mathbf{d}}(t)\cdot\hat{\mathbf{E}}(\mathbf{r}_A, t)\rangle$, which consists of various contributions as shown in Table I. The order of the terms is determined by the number of dipole moments. At leading order, the induced part of the field (dipole moment) depends on the free part of the dipole moment (field), given by the first iteration of Eq. (4). This leads to two well-known potentials, namely, the laser-light potential and the standard, undriven CP potential. Going one iteration further yields an additional contribution containing four dipole moments in total, the CP potential under the influence of the driving laser field. This contribution is nonadditive; i.e., the total potential experienced by the atom can no longer be obtained simply by summing the Casimir-Polder potential and the laser-induced potential. We will show that this nonadditive contribution can be significant under certain circumstances.

TABLE I. Summary of contributions to the total potential U. The contributions to lowest order (yellow) form the ordinary CP potential U_{CP} and the laser-light potential U_{L}. Higher-order terms (green) build up the nonadditive laser-induced CP potential U_{LCP}, with certain terms vanishing as explained in the main text.

	$\hat{\mathbf{d}}^{(1)}_{\mathrm{free}}$	$\hat{\mathbf{d}}^{(2)}_{\mathrm{ind}}$	$\hat{\mathbf{d}}^{(3)}_{\mathrm{ind}}$	$\hat{\mathbf{d}}^{(4)}_{\mathrm{ind}}$	...
$\hat{\mathbf{E}}^{(0)}_{\mathrm{free}}$	0	U_{L}	0	$\frac{1}{2}U_{\mathrm{LCP}}$	
$\hat{\mathbf{E}}^{(1)}_{\mathrm{ind}}$	U_{CP}	0	$U^{(2)}_{\mathrm{CP}}$		
$\hat{\mathbf{E}}^{(2)}_{\mathrm{ind}}$	0	$\frac{1}{2}U_{\mathrm{LCP}}$			
$\hat{\mathbf{E}}^{(3)}_{\mathrm{ind}}$	$U^{(2)}_{\mathrm{CP}}$				
⋮					

The term of lowest order $\langle \hat{\mathbf{d}}_{\mathrm{free}}(t)\cdot\hat{\mathbf{E}}_{\mathrm{free}}(\mathbf{r}_\mathrm{A}, t)\rangle$ contains the free dipole moment and the free electric field. For $\mathbf{r}' \in V_\mathrm{S}$, this expression leads to the vanishing expectation value of the free dipole moment $\langle \hat{\mathbf{d}}_{\mathrm{free}}(t)\rangle = 0$. In the case of $\mathbf{r}' \notin V_\mathrm{S}$, this term vanishes as well according to Eqs. (2) and (3). The occurrence of a free dipole moment is the reason for the terms of odd order to vanish. The standard, undriven CP potential is obtained from the term $\langle \hat{\mathbf{d}}_{\mathrm{free}}(t)\cdot\hat{\mathbf{E}}_{\mathrm{ind}}(\mathbf{r}_\mathrm{A}, t)\rangle$ [22]

$$U_{\mathrm{CP}}(\mathbf{r}_A) = \frac{\hbar\mu_0}{2\pi}\int_0^\infty d\xi\xi^2\alpha_n(i\xi)\mathrm{Tr}\mathbf{G}^{(S)}(\mathbf{r}_A, \mathbf{r}_A, \mathrm{i}\xi) - \frac{\mu_0}{3}\sum_{k<n}\tilde{\omega}_{nk}^2|\mathbf{d}_{nk}|^2\mathrm{Tr}[\mathrm{Re}\mathbf{G}^{(\mathrm{S})}(\mathbf{r}_A, \mathbf{r}_A, \tilde{\omega}_{nk})]. \tag{8}$$

$\mathbf{G}^{(S)}(\mathbf{r}_\mathrm{A}, \mathbf{r}_A, \tilde{\omega}_{nk})$ is the scattering part of the classical Green's tensor $\mathbf{G}(\mathbf{r}_A, \mathbf{r}_A, \tilde{\omega}_{nk})$. The CP potential can be split into resonant and off-resonant contributions, where the ground state only shows the latter. The third term of the total potential U results in the laser-light potential $\langle \hat{\mathbf{d}}_{\mathrm{ind}}(t)\cdot\hat{\mathbf{E}}_{\mathrm{free}}(\mathbf{r}_A, t)\rangle = \langle \hat{\mathbf{d}}_{\mathrm{ind}}(t)\rangle\cdot\mathbf{E}(\mathbf{r}_A, t)$ from the coherent time-averaged electric field ($\mathbf{r}' \in V_S$),

$$U_{\mathrm{L}}(\mathbf{r}_A) = -\frac{1}{4}\alpha_n(\omega_L)\mathbf{E}^2(\mathbf{r}_A), \tag{9}$$

and the fourth term of the total potential $\langle \hat{\mathbf{d}}_{\mathrm{ind}}(t)\cdot\hat{\mathbf{E}}_{\mathrm{ind}}(\mathbf{r}_A, t)\rangle$ vanishes again both for $\mathbf{r}' \in V_S$ and $\mathbf{r}' \notin V_S$.

We are interested in a higher-order iteration, where the induced part of the dipole moment itself depends on the induced part of the electric field, while the induced electric field itself contains the induced dipole moment. Combining the two high-order perturbative expressions for $\hat{\mathbf{d}}$ and $\hat{\mathbf{E}}$ leads to the final result for the driven CP potential

$$U_{\mathrm{LCP}}(\mathbf{r}_A) = -\frac{1}{2}\langle \hat{\mathbf{d}}_{\mathrm{ind}}(t)\cdot\hat{\mathbf{E}}^{(2)}_{\mathrm{ind}}(\mathbf{r}_A, t)\rangle - \frac{1}{2}\langle \hat{\mathbf{d}}^{(2)}_{\mathrm{ind}}(t)\cdot\hat{\mathbf{E}}_{\mathrm{free}}(\mathbf{r}_A, t)\rangle = -\frac{\mu_0\omega_L^2}{2}\alpha_n^2(\omega_L)\mathbf{E}(\mathbf{r}_A)\cdot\mathrm{Re}\mathbf{G}^{(\mathrm{S})}(\mathbf{r}_A, \mathbf{r}_A, \omega_L)\cdot\mathbf{E}(\mathbf{r}_A). \tag{10}$$

This expression contains induced dipole moments and induced electric fields, both of second order. The CP force corresponding to the potential (10) is computed by taking

the gradient of the potential $\mathbf{F}_{\mathrm{LCP}}(\mathbf{r}_A) = -\nabla_A U_{\mathrm{LCP}}(\mathbf{r}_A)$ and can be expressed using the two contributions $\nabla\langle\hat{\mathbf{d}}^{(2)}_{\mathrm{ind}} \cdot \hat{\mathbf{E}}_{\mathrm{free}}(\mathbf{r})\rangle_{\mathbf{r}=\mathbf{r}_A} + \nabla\langle\hat{\mathbf{d}}_{\mathrm{ind}} \cdot \hat{\mathbf{E}}^{(2)}_{\mathrm{ind}}(\mathbf{r})\rangle_{\mathbf{r}=\mathbf{r}_A}$, where one can use the relation $\nabla\mathbf{E}(\mathbf{r}_A)\cdot\mathbf{E}(\mathbf{r})|_{\mathbf{r}=\mathbf{r}_A} = \frac{1}{2}\nabla_A\mathbf{E}^2(\mathbf{r}_A)$ and the symmetry of the Green's tensor $\nabla\mathbf{G}^{(S)}(\mathbf{r},\mathbf{r}_A)|_{\mathbf{r}=\mathbf{r}_A} = \frac{1}{2}\nabla_A\mathbf{G}^{(S)}(\mathbf{r}_A,\mathbf{r}_A)$.

Figure 1 shows the difference between the laser-induced CP potential and the standard CP potential U_{CP} for a perfectly conducting mirror, whose Green's tensor is well known. The laser-induced potential for a constant laser potential is similar to the CP potential of an excited atom. The strongest addition effect of U_{LCP} is seen in the nonretarded regime, which we investigate further for a more realistic evanescent laser field.

For simplicity we first consider a two-level, isotropically polarized atom a distance z away from a dielectric half-space described by s (transverse electric: TE) and p

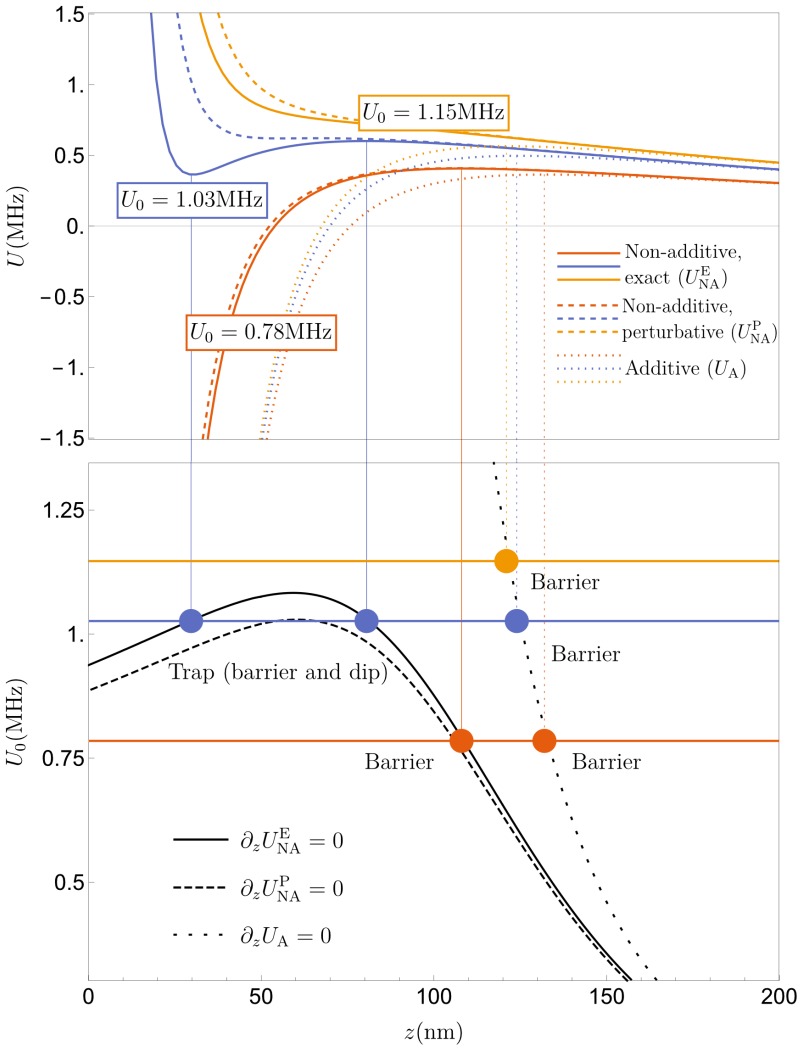

FIG. 2. Upper figure: Total potential with (solid lines) and without (dotted lines) the nonadditive term calculated here, for three different values of the potential scale U_0. The dashed lines are the total potential using the perturbative result, as opposed to the nonperturbative one. The parameters taken from Refs. [11,12] are as follows: decay length $z_0 = 430$ nm, detuning $\Delta = 2\pi \times 10^8$ Hz, dipole moment $d = 2.53 \times 10^{-29}$ Cm, transition frequency $\tilde{\omega}_{10} = 2.37 \times 10^{15}$ rad/s and quality factor $Q = 37.5 = -\mathrm{Re}(r_p)$. As reported in Ref. [11] the potential scale is given by $U_0 \sim P(\mathrm{W}) \times 10^{-23}$ J/W, meaning the range of values chosen for this quantity are commensurate with milliwatt laser power. The lower figure shows the positions of the minima and maxima of the additive potential U_A (dotted), the perturbative potential U^P_{NA} (dashed) and exact nonadditive potential U^E_{NA} (solid) as a function of the potential scale U_0 and the distance. This demonstrates that the nonadditive potential undergoes a transition from a traplike to barrierlike as a function of the atom-surface distance, while the additive potential remains barrierlike for all parameters shown here.

(transverse magnetic: TM) polarized reflection coefficients r_s and r_p. We display our formulas in the nonretarded (small z) limit, but all plots are produced including the effects of retardation. We find,

$$U_{\mathrm{LCP}} = -\frac{|\mathbf{d}_{nk}|^2}{192\pi\epsilon_0^2 z^3}\frac{\Omega^2}{\Delta^2}\mathrm{Re}r_p = U_{\mathrm{CP}}U_{\mathrm{L}}\frac{\mathrm{Re}r_p}{\hbar\Delta}, \qquad (11)$$

where we have defined $\Omega \equiv \mathbf{E}(\mathbf{r}_{\mathrm{A}})\cdot\mathbf{d}_{nk}/\hbar$ and $\Delta = \omega_L - \tilde{\omega}_{10}$, and on the right-hand side we have written the result in a suggestive form. This tells us that the laser-assisted Casimir-Polder potential is given by the product of the laser potential and the Casimir-Polder potential, modulated by the detuning Δ and the reflection coefficient r_p.

So far we have used a perturbative approach that is valid for a large detuning Δ. As we shall see later, this is not reliably satisfied for the particular application to the evanescent laser field, since the detuning and Rabi frequency Ω turn out to be of the same order of magnitude. Repeating the calculation by solving the optical Bloch equations, we find a more general nonperturbative result (see Ref. [19] for details);

$$U_{\mathrm{LCP}}^{\mathrm{NP}} = -\frac{|\mathbf{d}_{nk}|^2}{192\pi\epsilon_0^2 z^3}\frac{\Omega^2}{\Delta^2+\Omega^2}\mathrm{Re}r_p, \qquad (12)$$

which is seen to reduce to the perturbative result (11) in the large-detuning limit. The potential arising from an evanescent laser field can be written as $U_{\mathrm{L}} = U_0 e^{-2z/z_0}$, where U_0 is a constant that sets the scale of the interaction, and z_0 is its range. The electric field that is associated with this potential satisfies $E_L^2 = 6\hbar\Delta U_{\mathrm{L}}/d^2$, which gives the Rabi frequency as $\Omega_L^2 = 6\Delta U_{\mathrm{L}}/\hbar$.

The final ingredient we require is the electromagnetic response of the surface, described by a permittivity ε, which enters into Eq. (12) through the nonretarded limit of the p-polarized reflection coefficient: $r_{\mathrm{p}} = (\varepsilon-1)/(\varepsilon+1)$. By taking the Drude-Lorentz model as a basis, the reflection coefficient becomes $r_p \approx \omega_S/2\gamma$ with the plasmon resonance frequency $\omega_S = \sqrt{\omega_0^2 + \omega_P^2/2}$, which in turn depends on the absorption line frequency ω_0, the plasma frequency ω_P and the damping constant γ, cf. Ref. [16]. It is important to note that the real part of the reflection coefficient has both positive and negative wings around its resonance frequency, so that when viewed as a quality factor $\mathrm{Re}(r_p) = \pm Q$. As shown in Refs. [23–26], surface plasmon resonances, connected in the context of CP potentials, can be used to produce a maximum Purcell enhancement factor (or quality factor Q) of up to 60.

In order to produce concrete predictions, we consider the setup of Refs. [11,12], where an evanescent wave is created close to a surface creating a repulsive dipole potential into which a rubidium atom is placed. In order to assess the contribution of our nonadditive term U_{LCP} we compare the "additive" potential $U_A = U_{\mathrm{CP}} + U_{\mathrm{L}}$ to that with the exact nonadditive term included: $U_{\mathrm{NA}}^E = U_{\mathrm{CP}} + U_{\mathrm{L}} + U_{\mathrm{LCP}}^{\mathrm{NP}}$. Our results are shown in Fig. 2, and demonstrate that the nonadditive term calculated here has a drastic effect on even the qualitative character of the potential. The perturbative version $U_{\mathrm{NA}}^P = U_{\mathrm{CP}} + U_{\mathrm{L}} + U_{\mathrm{LCP}}$ of the laser-assisted Casimir-Polder potential is shown for reference, it is seen that the qualitative character of the effect is captured in the perturbative regime, but precise predictions require the nonperturbative result.

In this Letter we have derived and theoretically evaluated a nonadditive laser-induced CP potential. The electric field and the dipole moment were each split into a free contribution and an induced contribution, each of which depends on the other. In this way the laser light potential and the standard CP potential are reproduced as lowest-order terms. The higher-order correction term leads to the nonadditive potential which we have derived in both a perturbative and nonperturbative approach. We have shown that this term makes a significant contribution under certain experimental conditions. If the laser power is high enough and in combination with an additional enhancement by a surface plasmon resonance, the occurrence and position of barriers and minima in the total potential can significantly change, leading to local minima, which can be used to trap atoms near surfaces.

We acknowledge helpful discussions with Diego Dalvit, Francesco Intravaia, and Ian Walmsley. This work was supported by the German Research Foundation (DFG, Grants No. BU 1803/3-1 and No. GRK 2079/1). S. Y. B is grateful for support by the Freiburg Institute of Advanced Studies.

[1] H. Casimir and D. Polder, Phys. Rev. **73**, 360 (1948).
[2] In this work we use the convention where "Casimir-Polder" refers to atom-surface interactions in all distance regimes, with van der Waals forces appearing as a special case for short distances.
[3] A. Ashkin, Phys. Rev. Lett. **24**, 156 (1970).
[4] S. Chu, J. E. Bjorkholm, A. Ashkin, and A. Cable, Phys. Rev. Lett. **57**, 314 (1986).
[5] V. I. Balykin, V. S. Letokhov, Y. B. Ovchinnikov, and A. I. Sidorov, Phys. Rev. Lett. **60**, 2137 (1988).
[6] J. M. Wylie and J. E. Sipe, Phys. Rev. A **32**, 2030 (1985).
[7] J. M. Wylie and J. E. Sipe, Phys. Rev. A **30**, 1185 (1984).
[8] S. Scheel and S. Y. Buhmann, Acta Phys. Slovaca **58**, 675 (2008).
[9] C. I. Sukenik, M. G. Boshier, D. Cho, V. Sandoghdar, and E. A. Hinds, Phys. Rev. Lett. **70**, 560 (1993).
[10] F. Shimizu, Phys. Rev. Lett. **86**, 987 (2001).
[11] H. Bender, P. W. Courteille, C. Marzok, C. Zimmermann, and S. Slama, Phys. Rev. Lett. **104**, 083201 (2010).
[12] H. Bender, C. Stehle, C. Zimmermann, S. Slama, J. Fiedler, S. Scheel, S. Y. Buhmann, and V. N. Marachevsky, Phys. Rev. X **4**, 011029 (2014).

[13] S. Y. Buhmann, S. Scheel, and J. Babington, Phys. Rev. Lett. **104**, 070404 (2010).
[14] J. D. Perreault, M. Bhattacharya, V. P. A. Lonij, and A. D. Cronin, Phys. Rev. A **77**, 043406 (2008).
[15] S. J. Rahi, M. Kardar, and T. Emig, Phys. Rev. Lett. **105**, 070404 (2010).
[16] D. Chang, K. Sinha, J. Taylor, and H. Kimble, Nat. Commun. **5**, 4343 (2014).
[17] J. Dalibard, J. Dupont-Roc, and C. Cohen-Tannoudji, J. Phys. France **43**, 1617 (1982).
[18] S. Y. Buhmann, *Dispersion Forces II—Many-Body Effects, Excited Atoms, Finite Temperature and Quantum Friction* (Springer, Berlin, Heidelberg, 2012).
[19] S. Fuchs, R. Bennett, and S. Y. Buhmann, Phys. Rev. A **98**, 022514 (2018).
[20] S. Haroche, M. Brune, and J. Raimond, Europhys. Lett. **14**, 19 (1991).
[21] S. Y. Buhmann and D.-G. Welsch, Phys. Rev. A **77**, 012110 (2008).
[22] S. Y. Buhmann, L. Knöll, D.-G. Welsch, and H. T. Dung, Phys. Rev. A **70**, 052117 (2004).
[23] T. Esslinger, M. Weidemüller, A. Hemmerich, and T. W. Hänsch, Opt. Lett. **18**, 450 (1993).
[24] N. Bartolo, R. Messina, D. A. R. Dalvit, and F. Intravaia, Phys. Rev. A **93**, 042111 (2016).
[25] C. Stehle, C. Zimmermann, and S. Slama, Nat. Phys. **10**, 937 (2014).
[26] H. T. Dung, L. Knöll, and D.-G. Welsch, Phys. Rev. A **64**, 013804 (2001).

A Letters Journal Exploring the Frontiers of Physics

November 2018

EPL, **124** (2018) 34003 www.epljournal.org
doi: 10.1209/0295-5075/124/34003

Purcell-Dicke enhancement of the Casimir-Polder potential

Sebastian Fuchs[1] and Stefan Yoshi Buhmann[1,2]

[1] *Physikalisches Institut, Albert-Ludwigs-Universität Freiburg - Hermann-Herder-Straße 3, 79104 Freiburg, Germany*
[2] *Freiburg Institute for Advanced Studies, Albert-Ludwigs-Universität Freiburg - Albertstraße 19, 79104 Freiburg, Germany*

received 9 July 2018; accepted in final form 19 October 2018
published online 4 December 2018

PACS 42.50.Lc – Quantum fluctuations, quantum noise, and quantum jumps
PACS 42.50.Nn – Quantum optical phenomena in absorbing, amplifying, dispersive and conducting media; cooperative phenomena in quantum optical systems
PACS 12.20.-m – Quantum electrodynamics

Abstract – The emission by an initially completely inverted ensemble of two-level atoms in the long-wavelength regime is simultaneously enhanced by both collective effects (Dicke effect) and dielectric environments (Purcell effect), thus giving rise to a combined Purcell–Dicke effect. We study this effect by treating the ensemble of N atoms as a single effective $N+1$-level "Dicke atom" which couples to the environment-assisted quantum electrodynamic field. We find that an environment can indeed alter the superradiant emission dynamics, as exemplified using a perfectly conducting plate. As the emission acquires an additional anisotropy in the presence of the plate, we find an associated resonant Casimir-Polder potential for the atom that is collectively enhanced and that exhibits a superradiant burst in its dynamics. An additional tuneability of the effect is introduced by applying an external driving laser field.

Introduction. – Recent studies of atom-light interactions in non-trivial environments have increasingly focused on collective effects [1,2]. In such efforts, two very distinct phenomena can potentially lead to a complex interplay: the Casimir-Polder potential of a single atom near a surface mediated by the vacuum fluctuations [3] and the associated change of the atom's spontaneous emission rate due to the surface's presence (Purcell effect [4]) on the one hand, and the collective enhancement of radiation in an atomic ensemble (Dicke effect [5]) on the other.

The Casimir-Polder potential and its associated force are part of the field of dispersion forces, which are pure quantum forces in a sense that they stem from zero-point fluctuations of the quantized electromagnetic field. There are a variety of theoretical frameworks to describe the Casimir-Polder potential [6,7]. We use macroscopic quantum electrodynamics (QED), cf. *e.g.* ref. [8], an extension of vacuum QED incorporating material properties by macroscopic response functions such as permittivity or permeability. Experimentally, Casimir-Polder forces can be made visible directly via the change of the atomic motion under the influence of the potential, *e.g.*, by measuring the deflection angle of atoms passing a macroscopic object such as a V-shaped cavity [9], or in an indirect approach using spectroscopy to detect the shift of the atomic transition frequency [10].

Originally defined as the enhancement of the rate of spontaneous decay of an atom coupled to a single-mode resonant cavity [4,11], the term Purcell effect can also be extended to a situation where the atom is in the vicinity of a single surface providing a large density of states and thus an enhancement of the radiative decay [12,13]. This has been exploited, *e.g.* by increasing light emission of quantum wells in InGaN light-emitting diodes by means of surface plasmons [14].

Superradiance is another effect which enhances light emission, in this case by a collective mechanism in an ensemble of atoms [15]. The characteristics of the emerging superradiant burst for a total number of N atoms are the proportionality of its height to N^2 and its width to $1/N$. The first experimental verification of superradiance was realized in an optically pumped hydrogen fluoride gas [16]. After this first detection, superradiance was studied for several systems, *e.g.* in quantum dots [17], single diamond nanocrystals [18], Rydberg atoms [19], or artificial atoms in a cavity [1]. As a further development, collective effects have recently been demonstrated to impact atom-light interactions near surfaces [2]. There, by

studying the cooperative coupling of ultracold atoms to surface plasmons propagating on a plane gold surface a Purcell enhancement of the atomic fluorescence caused by the surface plasmons was found. In this context, ref. [20] studies superradiance as the collective decay rate additionally enhanced by surface plasmons. References [21–23] report the Purcell-Dicke enhancement of the decay rate of a multitude of atoms enclosed in a spherical metal shell. Collective effects in a ground-state ensemble were studied in ref. [24], where a quantum field theory for the Casimir-Polder interaction of a Bose-Einstein condensate with a surface was developed.

This article reports on the superradiant intensity of atomic emitters in arbitrarily structured environments, illustrated for the example of a perfectly conducting planar surface (see fig. 1). In addition, we demonstrate how the Dicke effect is manifested in an enhanced Casimir-Polder interaction between the atomic ensemble and the surface.

Note that ref. [25], which was developed in parallel to our work, studies the collective Casimir-Polder force in a different approach; the two works can be considered as complementary.

Collective atom-field coupling. – We are going to study the influence of a nearby surface on the superradiant emission burst of an atomic cloud and derive the associated collective Casimir-Polder potential due to photon recoil. The Hamiltonian of this system $\hat{H} = \hat{H}_{\rm F} + \hat{H}_{\rm A} + \hat{H}_{\rm AF}$ consists of the surface-assisted field contribution $\hat{H}_{\rm F}$, the collective atomic Hamiltonian $\hat{H}_{\rm A}$ and the interaction term coupling the atoms to the electromagnetic field $\hat{H}_{\rm AF}$. In the framework of macroscopic QED [26,27], spontaneously fluctuating noise currents are described by polariton-like annihilation and creation operators $\hat{\mathbf{f}}(\mathbf{r},\omega)$ and $\hat{\mathbf{f}}^\dagger(\mathbf{r},\omega)$, which form the Hamiltonian of the medium-assisted electromagnetic field $\hat{H}_{\rm F}$, where we restrict our attention to non-magnetic media. The frequency components of the electric field $\hat{\mathbf{E}}(\mathbf{r},\omega)$ are given by [28]

$$\hat{\mathbf{E}}(\mathbf{r},\omega) = \mathrm{i}\mu_0\omega^2 \int \mathrm{d}^3 r' \sqrt{\frac{\hbar\epsilon_0}{\pi}\mathrm{Im}\epsilon(\mathbf{r},\omega)}\mathbf{G}(\mathbf{r},\mathbf{r}',\omega)\cdot\hat{\mathbf{f}}(\mathbf{r}',\omega), \tag{1}$$

where the classical Green's tensor $\mathbf{G}(\mathbf{r},\mathbf{r}',\omega)$ is the formal solution of the Helmholtz equation for the electromagnetic field [28].

The electric field $\hat{\mathbf{E}}(\mathbf{r}_i)$ at the position $\mathbf{r}_i$ of each atom i couples to the respective dipole moments $\hat{\mathbf{d}}_i$ according to the multipolar coupling, yielding the interaction Hamiltonian $\hat{H}_{\rm AF}$

$$\hat{H}_{\rm AF} = -\sum_{i=1}^{N}\hat{\mathbf{d}}_i\cdot\hat{\mathbf{E}}(\mathbf{r}_i) = -\left(\sum_{i=1}^{N}\hat{\mathbf{d}}_i\right)\cdot\hat{\mathbf{E}}(\mathbf{r}_{\rm A}), \tag{2}$$

where N is the total number of atoms in the cloud. According to the Dicke model [5], the atoms are assumed to be motionless and confined to a volume much smaller than the wavelength λ of the applied or emitted fields. In essence all atoms then feel the same average electromagnetic field $\hat{\mathbf{E}}(\mathbf{r}_{\rm A})$.

As outlined in ref. [15], one can then establish the Dicke states as symmetric eigenstates of the atomic ensemble. All atoms are considered as identical two-level systems with an excited state $|e\rangle$ and a ground state $|g\rangle$ separated by an energy $\hbar\omega_{\rm A}$ and coupled by the single-atom dipole moment $\mathbf{d} = \langle e|\hat{\mathbf{d}}_i|g\rangle$. Initially, the atoms are prepared in the maximally excited state

$$|\psi(0)\rangle = |e,e,\ldots,e\rangle. \tag{3}$$

Here, we assume that the atoms interact only with the electromagnetic field, and atomic collisions or other relaxation processes are discarded. All atomic states being involved in the subsequent evolution have to be invariant with respect to an exchange of any two atoms. This property is represented by a symmetric superposition of N spin-1/2 states, which is an eigenstate of the angular momentum operator $\hat{J}$ at its maximal eigenvalue $J = N/2$. These $N+1$ collective Dicke states can be obtained by successive application of the symmetric collective deexcitation operator to the initial state (3)

$$|J,M\rangle = \sqrt{\frac{(J+M)!}{N!(J-M)!}}\left(\sum_{i=1}^{N}\hat{\sigma}_i^-\right)^{(J-M)}|e,e,\ldots,e\rangle \tag{4}$$

with $-J \le M \le J$. A general Dicke state $|J,M\rangle$ for N atoms can be represented as

$$|J,M\rangle = \hat{\mathcal{S}}|\underbrace{e,e,\ldots,e}_{J+M},\underbrace{g,g,\ldots,g}_{J-M}\rangle, \tag{5}$$

where there are $(J+M)!$ possibilities to arrange the excited atoms and $(J-M)!$ possibilities for the ground-state atoms. Making use of the normalized symmetrization operator $\hat{\mathcal{S}}$ the totally symmetrical state $|J,M\rangle$ (4) has

$$\binom{N}{J+M} = \frac{N!}{(J-M)!(J+M)!} \tag{6}$$

distinct contributions. The square root of this expression serves as normalizing factor for the completely symmetric state $|J,M\rangle$.

Collective operators can be introduced by

$$\hat{J}^\pm = \sum_{i=1}^{N}\hat{\sigma}_i^\pm; \quad \hat{J}^z = \sum_{i=1}^{N}\hat{\sigma}_i^z \tag{7}$$

and are analogous to the operators of angular momentum with $J = N/2$. The Pauli spin operators are given by $\hat{\sigma}^+ = |e\rangle\langle g|$, $\hat{\sigma}^- = |g\rangle\langle e|$ and $\hat{\sigma}^z = |e\rangle\langle e| - |g\rangle\langle g|$ and fulfill the commutation relations $[\hat{\sigma}^+,\hat{\sigma}^-] = \hat{\sigma}^z$ and $[\hat{\sigma}^z,\hat{\sigma}^\pm] = \pm 2\hat{\sigma}^\pm$, cf. ref. [29]. Using eq. (7), the atomic Hamiltonian $\hat{H}_{\rm A}$ can be written as $\hat{H}_{\rm A} = \frac{1}{2}\hbar\sum_{i=1}\omega_{\rm A}\hat{\sigma}_i^z = \frac{1}{2}\hbar\omega_{\rm A}\hat{J}^z$. Making use of the collective operators (7) the atomic cloud

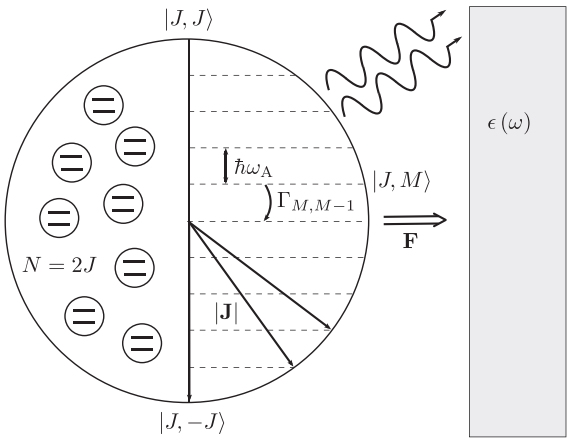

Fig. 1: Purcell-Dicke effect: N identical two-level atoms form a "Dicke atom" with equidistant Dicke states $|J,M\rangle$ (4) separated from each other by $\hbar\omega_{\rm A}$, and decay rates to the neighboring states $\Gamma_{M,M-1}$. The presence of the surface with permittivity $\epsilon(\omega)$ alters the radiation properties of the "Dicke atom" causing an attractive Casimir-Polder force.

of identical two-level atoms may be regarded as one single "Dicke atom" having dipole transitions only between neighboring states, which are all separated by $\hbar\omega_{\rm A}$. Figure 1 depicts the Dicke states $|J,M\rangle$ (4) as eigenstates of angular momentum. The interaction Hamiltonian $\hat{H}_{\rm AF}$ can be expressed as $\hat{H}_{\rm AF} = -(\hat{J}^+ + \hat{J}^-)\mathbf{d}\cdot\hat{\mathbf{E}}(\mathbf{r}_{\rm A})$ with the single-atom dipole moment $\mathbf{d}$.

Collective emission. – One can then define the rate of photon emission in state $|J,M\rangle$ decaying to state $|J,M-1\rangle$ in the Dicke picture based on the decay rate of a single atom [27,30] as

$$\Gamma_{M,M-1} = \frac{2\mu_0}{\hbar}\omega_{\rm A}^2 \mathbf{d}_{M,M-1}\cdot{\rm Im}\mathbf{G}(\mathbf{r}_{\rm A},\mathbf{r}_{\rm A},\omega_{\rm A})\cdot\mathbf{d}_{M-1,M}. \tag{8}$$

Next, we express the collective dipole moments $\mathbf{d}_{M,M-1}$ and $\mathbf{d}_{M-1,M}$ in eq. (8) by single-atom dipole moments $\mathbf{d}$, which contribute to the single-atom decay rate Γ. The atom-field coupling (2) for N dipole operators contains N single-atom dipole operators, which need to act between a ground state $|g\rangle$ and an excited state $|e\rangle$ at the same position to have a dipole moment with non-zero contribution, whereas the $N-1$ atoms at the other positions have to be in the same state. This results in a number of permutations given by the product of N and the number of permutations for $J+M-1$ excited atoms in $N-1$ atoms in total, cf. eq. (6), yielding a general expression for the Dicke state dipole moment

$$\begin{aligned}\mathbf{d}_{M,M-1} &= \langle J,M|\sum_{i=1}^{N}\hat{\mathbf{d}}_i|J,M-1\rangle \\ &= \sqrt{(J+M)(J-M+1)}\mathbf{d}.\end{aligned} \tag{9}$$

The decay rate of the Dicke state $|J,M\rangle$ (8) contains the two dipole moments $\mathbf{d}_{M,M-1}$ (9) and $\mathbf{d}_{M-1,M}$, resulting in an expression for the decay rate of $\Gamma_{M,M-1} = (J+M)(J-M+1)\Gamma$, which is formally identical to the free-space result from ref. [15]. These scaling properties represent an intrinsic connection between Dicke states (4) and decay rates (8) and is the fundamental difference between one single atom with N quantum states and a collection of N atoms in the Dicke approximation. As we will see, this further leads to a superradiance-like scaling behavior of the collective Casimir-Polder potential for the atomic cloud. In contrast to the macroscopic treatment of ref. [21], the collective decay rate (8) depends explicitly on the number of atoms N.

As mentioned above, the surface's presence modifies the collective decay rate (8) by a Purcell factor $F_{\rm P}$

$$\Gamma_{M,M-1} = (J+M)(J-M+1)F_{\rm P}\Gamma^{(0)}. \tag{10}$$

This can be seen by decomposing the Green's tensor into $\mathbf{G}(\mathbf{r}_{\rm A},\mathbf{r}_{\rm A},\omega_{\rm A}) = \mathbf{G}^{(0)}(\mathbf{r}_{\rm A},\mathbf{r}_{\rm A},\omega_{\rm A}) + \mathbf{G}^{(1)}(\mathbf{r}_{\rm A},\mathbf{r}_{\rm A},\omega_{\rm A})$ with the bulk part $\mathbf{G}^{(0)}(\mathbf{r}_{\rm A},\mathbf{r}_{\rm A},\omega_{\rm A})$ responsible for the free-space decay rate

$$\Gamma^{(0)} = \frac{\omega_{\rm A}^3|\mathbf{d}|^2}{3\pi\epsilon_0\hbar c^3} \tag{11}$$

and the scattering part $\mathbf{G}^{(1)}(\mathbf{r}_{\rm A},\mathbf{r}_{\rm A},\omega_{\rm A})$ yielding the Purcell factor

$$F_{\rm P} = 1 + \frac{6\pi c}{\omega|\mathbf{d}|^2}\mathbf{d}\cdot{\rm Im}\mathbf{G}^{(1)}(\mathbf{r}_{\rm A},\mathbf{r}_{\rm A},\omega_{\rm A})\cdot\mathbf{d}^*. \tag{12}$$

This is a general expression and applies to all kinds of geometries and materials, such as dielectric surfaces or resonator structures. We illustrate our results for the specific case of a perfectly conducting mirror in the following. At this point, it is worth checking the long-wavelength assumption of the Dicke model. To this end, we consider two atoms to be located at slightly different positions. Beside the symmetric superradiant state (4), an anti-symmetric subradiant state, which would be the singlet state if there were only two atoms, will emit radiation in this case. As shown in ref. [31] the decay process is governed by a joint decay rate of the two atoms $i=1$ and $i=2$: $\Gamma^{12} = \frac{2\mu_0\omega_{\rm A}^2}{\hbar}\mathbf{d}\cdot{\rm Im}\mathbf{G}(\mathbf{r}_1,\mathbf{r}_2,\omega_{\rm A})\cdot\mathbf{d}^*$.

To see if the conditions of superradiance hold, we need to check if the decay rate $\Gamma_{M=1,M=0} = \Gamma + \Gamma^{12}$ of the superradiant two-atom state is indeed equal to 2Γ as suggested by eq. (8). This is the case if $F = \Gamma^{12}/\Gamma \simeq 1$. We display the general results of the superradiance fidelity for the specific case of two atoms near a perfectly conducting surface [32] where we fix the position of one atom and vary the position of the other. In fig. 2(b), the atom is located close to the surface. One observes that the fidelity F is indeed close to unity in a corridor around atom 1, which is particularly narrow in the normal direction, $|z_{\rm B}-z_{\rm A}| \ll z_{\rm B}$. This anisotropy of the superradiance region is induced by the presence of the surface, as seen by

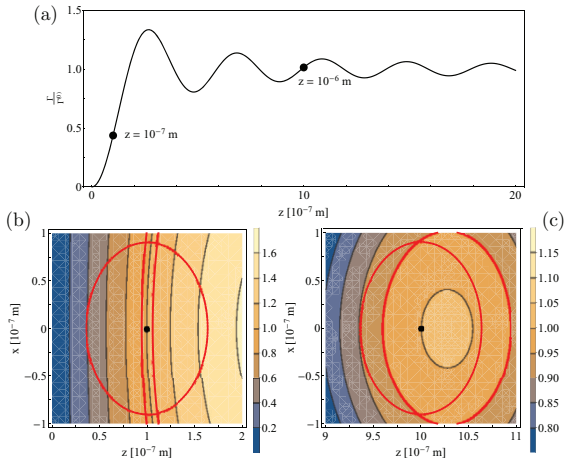

Fig. 2: (Colour online) Superradiant fidelity. (a) Single-atom decay rate $\Gamma/\Gamma^{(0)}$ near a perfectly conducting plate along the z-axis ($x = 0$). The atomic dipole moment is polarized along the x-direction. Γ is composed of the bulk rate and the scattered rate from an image dipole and thus vanishes at the boundary $z = 0$. (b) We indicate regions where $F = \Gamma^{12}/\Gamma = (100 \pm 5)\%$ (red corridor) for the atomic position $x_\mathrm{A} = 0$, $z_\mathrm{A} = 10^{-7}\,\mathrm{m}$ and (c) the atomic position $x_\mathrm{A} = 0$, $z_\mathrm{A} = 10^{-6}\,\mathrm{m}$. For comparison, we also display the fidelity in free space $F^{(0)} = \Gamma^{12(0)}/\Gamma^{(0)} = (100 \pm 5)\%$ (red dashed circle). The shape and width of the corridors depend on the orientation of the dipole.

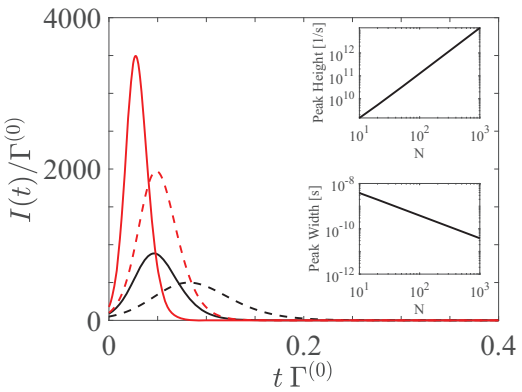

Fig. 3: (Colour online) Total photon emission rate $I(t)$ (13) scaled by the free-space decay rate $\Gamma^{(0)}$ (11) for $N = 50$ (black curves) and $N = 100$ atoms (red curves) under the influence of a perfectly conducting surface. All atoms are located at $x_\mathrm{A} = 0$, $z_\mathrm{A} = 10^{-7}\,\mathrm{m}$ and are polarized along the z-direction. The dashed lines show the respective total photon emission rate for $N = 50$ and $N = 100$ atoms in the absence of the surface. The insets show the burst height and the full width at half-maximum (FWHM) as a function of the number of atoms N. We obtain the relations: burst height $\propto N^{2.00}$ and FWHM $\propto N^{-1.00}$.

comparison with the free-space case. Figure 2(c) sheds light on this scenario with a greater distance between the atom and the surface. The surface does not influence the radiative behavior of the atom so strongly and the fidelity is close to unity in a broad region around the atom, $|\mathbf{r}_\mathrm{B} - \mathbf{r}_\mathrm{A}| \ll c/\omega_\mathrm{A}$.

In the following, we assume that all atoms are sufficiently close to one another, so that superradiance occurs. The time-dependent total photon emission rate $I(t)$ is then given by the sum of photon emission rates for state $|J, M\rangle$, $\Gamma_{M,M-1}$ (8), weighted by respective time-dependent probabilities $p_M(t)$

$$I(t) = \sum_{M=-J+1}^{J} p_M(t)\Gamma_{M,M-1}. \tag{13}$$

A set of rate equations for the probabilities is set up by computing the decay rate for each collective atomic state $|J, M\rangle$ (8)

$$\dot{p}_M(t) = -\Gamma_{M,M-1}p_M(t) + \Gamma_{M+1,M}p_{M+1}(t) \tag{14}$$

for $-J \leq M \leq J$. This set of rate equations is solved numerically using a Runge-Kutta algorithm. Figure 3 shows the emitted intensity for an atomic ensemble of $N = 50$ and $N = 100$ atoms at a distance of $z_\mathrm{A} = 10^{-7}\,\mathrm{m}$ from the surface scaled by the single-atom vacuum decay rate $\Gamma^{(0)}$. The superradiant emission burst is very pronounced especially for a large number of atoms. The presence of the surface enhances this effect even further thus giving a Purcell-Dicke enhancement. The perfectly conducting mirror can cause an enhancement factor of at most 2. Materials showing plasmonic resonances can exceed this value by far. In the context of the Casimir-Polder potential, a Purcell enhancement factor of 60 is reported in ref. [33]. The insets show logarithmic plots of the burst height and the burst width as a function of the number of atoms N. We observe the well-known properties for the burst height of $\propto N^2$ and the burst width of $\propto 1/N$.

Collective Casimir-Polder potential. – The collective emission by the atomic ensemble is intrinsically related to the Casimir-Polder potential of the atomic ensemble, where we further allow for the presence of a monochromatic coherent driving laser field $\mathbf{E}(\mathbf{r}_\mathrm{A}, t) = \mathbf{E}(\mathbf{r}_\mathrm{A})\cos(\omega_\mathrm{L}t)$ of frequency ω_L. Based on the analysis of the Casimir-Polder potential for one laser-driven atom [34], this formalism is readily extended to an arbitrary number of atoms in the form of an atomic cloud by using the respective Dicke states $|J, M\rangle$ and their transition dipole matrix elements (9) in place of the single-atom states and matrix elements. It has non-resonant parts, which are not considered in our analysis. The remaining resonant potential represents a sum of potentials for each energy level weighted by the respective probabilities

$$U(\mathbf{r}_\mathrm{A}, t) = \sum_{i=1}^{N} U(\mathbf{r}_i) = \sum_{M=-J+1}^{J} p_M(t)U_M(\mathbf{r}_\mathrm{A}) \tag{15}$$

with

$$U_M(\mathbf{r}_\mathrm{A},t) = (J+M)(J-M+1)U(\mathbf{r}_i), \quad (16)$$

$$U(\mathbf{r}_i) = -\mu_0\omega_\mathrm{L}^2\mathbf{d}\cdot\mathrm{Re}\mathbf{G}^{(1)}(\mathbf{r}_i,\mathbf{r}_i,\omega_\mathrm{L})\cdot\mathbf{d}^*. \quad (17)$$

All damping terms are assumed to be much smaller than the laser frequency and the transition frequency: $\Gamma \ll \omega_\mathrm{L}, \omega_\mathrm{A}$. As described in ref. [34], the potential terms depend on the driving frequency of the laser ω_L. A detailed analysis would reveal the occurrence of Mollow triplets [35], which is discarded for our choice of laser intensity and detuning, cf. ref. [36].

In the absence of a driving field, the probabilities $p_M(t)$ are given by eq. (14). The presence of the laser field causes the coupling of the expectation value of the diagonal elements of the atomic flip operator (14) to the non-diagonal elements, whose differential equation reads

$$\begin{aligned}\langle\dot{\hat{A}}_{M,N}(t)\rangle &= \mathrm{i}[M-N]\omega_\mathrm{A}\langle\hat{A}_{M,N}(t)\rangle \\ &+ \frac{\mathrm{i}}{\hbar}\sum_{K=N\pm1}\mathbf{d}_{N,K}\cdot\mathbf{E}(\mathbf{r}_\mathrm{A},t)\langle\hat{A}_{M,K}(t)\rangle \\ &- \frac{\mathrm{i}}{\hbar}\sum_{K=M\pm1}\mathbf{d}_{K,M}\cdot\mathbf{E}(\mathbf{r}_\mathrm{A},t)\langle\hat{A}_{K,N}(t)\rangle \\ &+ [\Gamma_{M+1,M,N,N+1}+\Gamma_{N,N+1,M+1,M}]\langle\hat{A}_{M+1,N+1}(t)\rangle \\ &- [\Gamma_{N,N-1,N-1,N}+\Gamma_{M-1,M,M,M-1}]\langle\hat{A}_{M,N}(t)\rangle. \quad (18)\end{aligned}$$

The respective differential equation of the diagonal elements of the atomic flip operator $\langle\hat{A}_{M,M}(t)\rangle$ is given by

$$\begin{aligned}\langle\dot{\hat{A}}_{N,N}(t)\rangle &= \frac{\mathrm{i}}{\hbar}\sum_{K=N\pm1}\mathbf{d}_{N,K}\cdot\mathbf{E}(\mathbf{r}_\mathrm{A},t)\langle\hat{A}_{N,K}(t)\rangle \\ &- \frac{\mathrm{i}}{\hbar}\sum_{K=N\pm1}\mathbf{d}_{K,N}\cdot\mathbf{E}(\mathbf{r}_\mathrm{A},t)\langle\hat{A}_{K,N}(t)\rangle \\ &+ \Gamma_{N+1,N}\langle\hat{A}_{N+1,N+1}(t)\rangle - \Gamma_{N,N-1}\langle\hat{A}_{N,N}(t)\rangle \quad (19)\end{aligned}$$

and is identical with the rate equation for the probability $p_M(t)$ (14) with the additional term from the driving laser field. The decay rates having four indices are defined by $\Gamma_{M,K,N,L} = \frac{2\mu_0}{\hbar}\omega_\mathrm{A}^2\mathbf{d}_{M,K}\cdot\mathrm{Im}\mathbf{G}(\mathbf{r}_\mathrm{A},\mathbf{r}_\mathrm{A},\omega_\mathrm{A})\cdot\mathbf{d}_{N,L}$. The dipole moment operator in the Dicke picture is given by

$$\hat{\mathbf{d}}(t) = \sum_{i=1}^{N}\hat{\mathbf{d}}_i(t) = \sum_{K=M\pm1}\mathbf{d}_{M,K}\hat{A}_{M,K}(t) \quad (20)$$

in terms of collective atomic flip operators $\hat{A}_{M,M-1} = |J,M\rangle\langle J,M-1|$. To calculate the laser-driven Casimir-Polder potential, the dipole correlation $\langle\hat{\mathbf{d}}(t)\hat{\mathbf{d}}(\tau)\rangle$ is required. Like the set of rate equations (14), this system is solved numerically by a Runge-Kutta algorithm. The probabilities can also be computed using a master equation [25] with a system Hamiltonian consisting of the atomic Hamiltonian $\hat{H}_\mathrm{A}$ and the driving Hamiltonian, which is explained in ref. [37]. The Lindblad Liouvillian describes spontaneous emission with the collective operators (7).

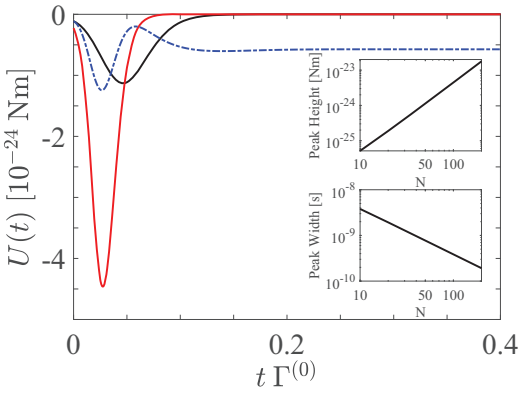

Fig. 4: (Colour online) Casimir-Polder potential of an atomic ensemble of $N = 50$ atoms (black line) and $N = 100$ atoms (red line) for Rb atoms with atomic transition frequency of $\omega_\mathrm{A} = 2.37\times10^{15}$ rad/s and dipole moment $|\mathbf{d}| = 2.53\times10^{-29}$ Cm. All atoms are located at $x_\mathrm{A} = 0$, $z_\mathrm{A} = 10^{-7}$ m and are polarized along the z-direction. The blue dot-dashed line shows the Casimir-Polder burst for a laser-driven ensemble of $N = 50$ atoms with an intensity of $I = 30000\,\mathrm{W/m^2}$ and a detuning between the laser frequency ω_L and the atomic frequency ω_A of $\Delta = \omega_\mathrm{L} - \omega_\mathrm{A} = 2\pi\times10^8$ rad/s, which gives physical results only in the regime $\Gamma t \ll 1$. The insets show the burst height and the full width at half-maximum (FWHM) as a function of the number of atoms N. We obtain the relations: burst height $\propto N^{1.958}$ and FWHM $\propto N^{-0.999}$.

Figure 4 shows the collective Casimir-Polder potential (15) of an atomic ensemble of $N = 50$ and $N = 100$ atoms. As shown in the insets, the burst height and the burst width exhibit the typical superradiant scalings with N^2 and $1/N$, respectively and the burst position is thus given by $t = 1/(N\Gamma)$. We want to emphasize that the total momentum transferred to the atomic cloud as obtained by an integration in time agrees with the result found in an additive approach found for incoherent, individual atoms. However, the effect is achieved on a considerably shortened timescale. This is very relevant for all experiments and theoretical proposals, where an effect accumulates over a finite interaction region. Examples are the measurement of the Casimir-Polder force, where sodium atoms pass through a parallel-plate cavity [9], the interferometry of large molecules such as C_{70} at gold gratings [38] or a Poisson-spot experiment with neutral deuterium molecules [39].

By applying an electric driving field, the timescale is additionally governed by the Rabi frequency $\Omega = \mathbf{d}\cdot\mathbf{E}(\mathbf{r}_\mathrm{A})/\hbar$. If $N\Gamma > \Omega$, a pronounced burst remains, the Rabi oscillations are not visible and the curve resembles that without applied electric field. In case of $N\Gamma < \Omega$, Rabi oscillations are superposed on the burst. Figure 4 shows the Casimir-Polder potential with applied electric field in the regime $N\Gamma \approx \Omega$, where the burst structure is significantly altered. The application of an electric field causes a longer-term persistence of the Casimir-Polder potential and significantly alters the dynamics, as can be seen in

fig. 4. This might be helpful for the experimental detection of these effects.

Conclusion. – In this article, we have studied the enhancement of the total photon emission rate and the Casimir-Polder potential due to collective effects and the presence of a surface in a combined Purcell-Dicke effect. We show the connection of the decay rate in the Dicke picture with the single-atom rate via the atomic dipole moments using the symmetric Dicke states. The long-wavelength approximation according to the Dicke model is checked by comparing the joint decay rate of two atoms placed slightly away from each other with the respective Dicke decay rate. The enhancement due to the presence of the surface is described in the form of a Purcell fidelity given by the surface-induced decay rate $\Gamma^{(1)}$ relative to the free-space decay rate $\Gamma^{(0)}$. This enhancement effect is depicted for the total photon emission rate and the collective Casimir-Polder potential for the specific case of a moderate number of atoms in the vicinity of a perfectly conducting mirror, showing burst heights and widths which fulfill the criteria of superradiance. As shown, an external driving laser can be used to manipulate the dynamics of the potential.

The Dicke enhancement of the Casimir-Polder force can be exploited to significantly increase sensitivity without having to extend interaction times or interaction regions (*e.g.* for atoms passing a plate). In this way, such forces can be used as sensitive probes of atomic or surface properties such as chirality [40] or *CP* violation [41] or even facilitate the (spectroscopic) detection of quantum friction [42,43].

* * *

We acknowledge helpful discussions with Miguel Bastarrachea, Robert Bennett, Diego Dalvit, Francesco Intravaia, Björn Kubala and Ian Walmsley. This work was supported by the German Research Foundation (DFG, Grants BU 1803/3-1 and GRK 2079/1). SYB is grateful for support by the Freiburg Institute of Advanced Studies (FRIAS).

REFERENCES

[1] Mlynek J. A., Abdumalikov A. A., Eichler C. and Wallraff A., *Nat. Commun.*, **5** (2014) 5186.
[2] Stehle C., Zimmermann C. and Slama S., *Nat. Phys.*, **10** (2014) 937.
[3] Casimir H. and Polder D., *Phys. Rev.*, **73** (1948) 360.
[4] Purcell E. M., Torrey H. C. and Pound R. V., *Phys. Rev.*, **69** (1946) 37.
[5] Dicke R. H., *Phys. Rev.*, **93** (1954) 99.
[6] Barton G., *Proc. R. Soc. Lond. A*, **320** (1970) 251.
[7] Wylie J. M. and Sipe J. E., *Phys. Rev. A*, **30** (1984) 1185.
[8] Scheel S. and Buhmann S. Y., *Acta Phys. Slovaca*, **58** (2008) 675.
[9] Sukenik C. I., Boshier M. G., Cho D., Sandoghdar V. and Hinds E. A., *Phys. Rev. Lett.*, **70** (1993) 560.
[10] Failache H., Saltiel S., Fichet M., Bloch D. and Ducloy M., *Phys. Rev. Lett.*, **83** (1999) 5467.
[11] Fox M., *Quantum Optics: An Introduction* (Oxford University Press) 2006.
[12] Iwase H., Englund D. and Vučković J., *Opt. Express*, **18** (2010) 16546.
[13] Cohen-Tannoudji C., Dupont-Roc J. and Grynberg G., *Atom-Photon Interactions* (Wiley-VCH Verlag) 2004.
[14] Okamoto K., Niki I., Shvartser A., Narukawa Y., Mukai T. and Scherer A., *Nat. Mater.*, **3** (2004) 601.
[15] Gross M. and Haroche S., *Phys. Rep.*, **93** (1982) 301.
[16] Skribanowitz N., Herman I. P., MacGillivray J. C. and Feld M. S., *Phys. Rev. Lett.*, **30** (1973) 309.
[17] Scheibner M., Schmidt T., Worschech L., Forchel A., Bacher G., Passow T. and Hommel D., *Nat. Phys.*, **3** (2007) 106.
[18] Bradac C., Johnsson M. T., van Breugel M., Baragiola B. Q., Martin R., Juan M. L., Brennen G. K. and Volz T., *Nat. Commun.*, **8** (2017) 1205.
[19] Grimes D. D., Coy S. L., Barnum T. J., Zhou Y., Yelin S. F. and Field R. W., *Phys. Rev. A*, **95** (2017) 043818.
[20] Choquette J. J., Marzlin K.-P. and Sanders B. C., *Phys. Rev. A*, **82** (2010) 023827.
[21] Friedberg R. and Manassah J. T., *Phys. Rev. A*, **86** (2012) 023804.
[22] Manassah J. T., *Laser Phys.*, **22** (2012) 738.
[23] Friedberg R. and Manassah J. T., *Chem. Phys. Lett.*, **539-540** (2012) 118.
[24] Schiefele J. and Henkel C., *Phys. Rev. A*, **82** (2010) 023605.
[25] Sinha K., Venkatesh B. P. and Meystre P., *Phys. Rev. Lett.*, **121** (2018) 183605.
[26] Buhmann S. Y., *Dispersion Forces I - Macroscopic Quantum Electrodynamics and Ground-State Casimir, Casimir-Polder and van der Waals Forces* (Springer, Berlin, Heidelberg) 2012.
[27] Buhmann S. Y., *Dispersion Forces II - Many-Body Effects, Excited Atoms, Finite Temperature and Quantum Friction* (Springer, Berlin, Heidelberg) 2012.
[28] Buhmann S. Y., Knöll L., Welsch D.-G. and Dung H. T., *Phys. Rev. A*, **70** (2004) 052117.
[29] Sakurai J. J. and Napolitano J. J., *Modern Quantum Mechanics* (Pearson Education) 2014.
[30] Agarwal G. S., *Phys. Rev. A*, **12** (1975) 1475.
[31] Dzsotjan D., Sørensen A. S. and Fleischhauer M., *Phys. Rev. B*, **82** (2010) 075427.
[32] Palacino R., Passante R., Rizzuto L., Barcellona P. and Buhmann S. Y., *J. Phys. B*, **50** (2017) 154001.
[33] Esslinger T., Weidemüller M., Hemmerich A. and Hänsch T. W., *Opt. Lett.*, **18** (1993) 450.
[34] Fuchs S., Bennett R. and Buhmann S. Y., *Phys. Rev. A*, **98** (2018) 022514.
[35] Mollow B. R., *Phys. Rev.*, **188** (1969) 1969.
[36] Ge R.-C., Van Vlack C., Yao P., Young J. F. and Hughes S., *Phys. Rev. B* , **87** (2013) 205425.

[37] Breuer H.P. and Petruccione F., *The Theory of Open Quantum Systems* (Oxford University Press) 2002.
[38] Brezger B., Hackermüller L., Uttenthaler S., Petschinka J., Arndt M. and Zeilinger A., *Phys. Rev. Lett.*, **88** (2002) 100404.
[39] Reisinger T., Patel A. A., Reingruber H., Fladischer K., Ernst W. E., Bracco G., Smith H. I. and Holst B., *Phys. Rev. A*, **79** (2009) 053823.
[40] Barcellona P., Safari H., Salam A. and Buhmann S. Y., *Phys. Rev. Lett.*, **118** (2017) 193401.
[41] Buhmann S. Y., Marachevsky V. N. and Scheel S., *Phys. Rev. A*, **98** (2018) 022510.
[42] Milton K. A., Høye J. S. and Brevik I., *Symmetry*, **8** (2016) 29.
[43] Klatt J., Bennett R. and Buhmann S. Y., *Phys. Rev. A*, **94** (2016) 063803.

PHYSICAL REVIEW A **80**, 042902 (2009)

Casimir-Polder forces on moving atoms

Stefan Scheel* and Stefan Yoshi Buhmann
Quantum Optics and Laser Science, Blackett Laboratory, Imperial College London, Prince Consort Road, London SW7 2AZ, United Kingdom

(Received 7 August 2009; published 22 October 2009)

Polarizable atoms and molecules experience the Casimir-Polder force near magnetoelectric bodies, a force that is induced by quantum fluctuations of the electromagnetic field and the matter. Atoms and molecules in relative motion to a magnetoelectric surface experience an additional velocity-dependent force. We present a full quantum-mechanical treatment of this force and identify a generalized Doppler effect, the time delay between photon emission and reabsorption, and the Röntgen interaction as its three sources. For ground-state atoms, the force is very small and always decelerating, hence commonly known as quantum friction. For atoms and molecules in electronically excited states, on the contrary, both decelerating and accelerating forces can occur depending on the magnitude of the atomic transition frequency relative to the surface-plasmon frequency.

DOI: 10.1103/PhysRevA.80.042902 PACS number(s): 34.35.+a, 12.20.−m, 42.50.Nn, 42.50.Wk

I. INTRODUCTION

The ground-state fluctuations of the electromagnetic field lead to several inherently quantum effects such as the spontaneous decay of excited atoms and molecules as well as dispersion forces [1]. Forces between isolated atoms that are mediated by the quantum vacuum are known as van der Waals forces [2], while forces between macroscopic bodies are referred to as Casimir forces [3]. The third type of dispersion (in a sense an interpolation between these two extreme cases) is the Casimir-Polder (CP) force exerted on single atoms near macroscopic bodies [4].

For a two-level atom with transition frequency ω_A and electric-dipole moment d located at a distance z_A away from a perfectly conducting plate, the short-distance (nonretarded) [4] and long-distance (retarded) [5] limits of the CP potential take the well-known forms

$$U_{\mathrm{nret}}(z_A) = -\frac{d^2}{48\pi\varepsilon_0 z_A^3}, \quad U_{\mathrm{ret}}(z_A) = -\frac{cd^2}{16\pi^2\varepsilon_0\omega_A z_A^4}. \quad (1)$$

These potentials, acting on atoms at rest, lead to conservative forces perpendicular to the plate's surface. CP forces (as well as all other dispersion forces) play important roles as limiting factors in efforts to miniaturize atom-optical devices [6] and have been measured at distances as small as 6 μm [7].

Casimir-Polder forces are well understood far beyond the aforementioned special case of a perfectly conducting plate, with magnetoelectric materials of arbitrary shape [8] and finite temperature being investigated theoretically [9,10] as well as experimentally [11]. While most theoretical investigations are based on Lifshitz's macroscopic treatment [12] or a linear-response description [13], full quantum theories based on electromagnetic-field quantization in magnetoelectrics have also been developed [8]. In the latter approach, the operator-valued Lorentz force

$$\hat{\mathbf{F}} = \int d^3r[\hat{\rho}_A(\mathbf{r})\hat{\mathbf{E}}(\mathbf{r}) + \hat{\mathbf{j}}_A(\mathbf{r}) \times \hat{\mathbf{B}}(\mathbf{r})] \quad (2)$$

on the atomic charge and current densities due to the body-assisted electromagnetic fields is computed. In the long-wavelength approximation, it leads to the well-known expression

$$\hat{\mathbf{F}} = \boldsymbol{\nabla}_A[\hat{\mathbf{d}} \cdot \hat{\mathbf{E}}(\mathbf{r}_A)] + \frac{d}{dt}[\hat{\mathbf{d}} \times \hat{\mathbf{B}}(\mathbf{r}_A)] \quad (3)$$

with $\hat{\mathbf{d}}$ denoting the atomic electric-dipole moment operator.

Intuitively, dispersion forces can be understood as dipole-dipole forces generated by spontaneous polarization due to the electric-field fluctuations. Therefore, CP forces on atoms at rest act either toward (attractively) or away (repulsively) from the macroscopic body. For atoms in motion, retardation delays the dipole response, and a force component emerges along the direction of motion. In most cases, this force component acts against the motion and is thus the origin of quantum friction.

Quantum friction forces have traditionally been studied within a linear-response formalism [14–17]. Evaluating the correlated quantum fluctuations of moving atom and dielectrics, the friction force on ground-state atoms can be obtained in this way. However, the predicted forces are typically very small. For the stationary case it is well known that CP forces can be resonantly enhanced for excited atoms [8,18]. For such nonequilibrium situations, linear-response methods cannot be applied and a more detailed investigation of the atom-field dynamics becomes necessary.

In this paper, we develop a full quantum theory of the velocity-dependent CP force. In particular, we will show that for atoms and molecules in electronically excited states, both decelerating and accelerating forces can occur depending on the relative magnitude of the frequencies of the atomic transition and the surface plasmon. The paper is organized as follows. After briefly reviewing the formalism of macroscopic quantum electrodynamics in Sec. II, we study the atom-field dynamics in Sec. III A before investigating the resulting force in Sec. III B and applying our results to the

*s.scheel@imperial.ac.uk

quantum friction scenario in Sec. III C. We illustrate the theory with representative examples in Sec. IV, followed by a summary in Sec. V.

II. BASIC FORMULAS

Let us assume an arbitrary arrangement of dispersing and absorbing magnetoelectric bodies, characterized by their complex-valued Kramers-Kronig consistent permittivity $\varepsilon(\mathbf{r},\omega)$ and permeability $\mu(\mathbf{r},\omega)$. The Hamiltonian of the quantum electromagnetic field and the bodies can be given as (for a recent review, see Ref. [19])

$$\hat{H}_F = \sum_{\lambda=e,m} \int d^3r \int_0^\infty d\omega\, \hbar\omega \hat{\mathbf{f}}_\lambda^\dagger(\mathbf{r},\omega)\cdot\hat{\mathbf{f}}_\lambda(\mathbf{r},\omega), \tag{4}$$

where the fundamental variables $\hat{\mathbf{f}}_\lambda^\dagger(\mathbf{r},\omega)$ and $\hat{\mathbf{f}}_\lambda(\mathbf{r},\omega)$ are creation and annihilation operators for the elementary electric ($\lambda=e$) and magnetic ($\lambda=m$) excitations of the system; they obey the bosonic commutation relations

$$[\hat{\mathbf{f}}_\lambda(\mathbf{r},\omega),\hat{\mathbf{f}}_{\lambda'}^\dagger(\mathbf{r}',\omega')] = \delta_{\lambda\lambda'}\boldsymbol{\delta}(\mathbf{r}-\mathbf{r}')\delta(\omega-\omega'). \tag{5}$$

The electric and magnetic fields can be expanded in terms of the fundamental variables according to

$$\begin{aligned}\hat{\mathbf{E}}(\mathbf{r}) &= \int_0^\infty d\omega \underline{\hat{\mathbf{E}}}(\mathbf{r},\omega) + \text{H.c.}\\ &= \sum_{\lambda=e,m}\int d^3r' \int_0^\infty d\omega \boldsymbol{G}_\lambda(\mathbf{r},\mathbf{r}',\omega)\cdot\hat{\mathbf{f}}_\lambda(\mathbf{r}',\omega) + \text{H.c.},\end{aligned} \tag{6}$$

$$\begin{aligned}\hat{\mathbf{B}}(\mathbf{r}) &= \int_0^\infty d\omega \underline{\hat{\mathbf{B}}}(\mathbf{r},\omega) + \text{H.c.}\\ &= \sum_{\lambda=e,m}\int d^3r' \int_0^\infty \frac{d\omega}{i\omega}\boldsymbol{\nabla}\times\boldsymbol{G}_\lambda(\mathbf{r},\mathbf{r}',\omega)\cdot\hat{\mathbf{f}}_\lambda(\mathbf{r}',\omega) + \text{H.c.},\end{aligned} \tag{7}$$

with coefficients

$$\boldsymbol{G}_e(\mathbf{r},\mathbf{r}',\omega) = i\frac{\omega^2}{c^2}\sqrt{\frac{\hbar}{\pi\varepsilon_0}\text{Im}\,\varepsilon(\mathbf{r}',\omega)}\boldsymbol{G}(\mathbf{r},\mathbf{r}',\omega), \tag{8}$$

$$\boldsymbol{G}_m(\mathbf{r},\mathbf{r}',\omega) = i\frac{\omega}{c}\sqrt{\frac{\hbar}{\pi\varepsilon_0}\frac{\text{Im}\,\mu(\mathbf{r}',\omega)}{|\mu(\mathbf{r}',\omega)|^2}}[\boldsymbol{\nabla}'\times\boldsymbol{G}(\mathbf{r}',\mathbf{r},\omega)]^{\mathsf{T}}. \tag{9}$$

Here, $\boldsymbol{G}$ is the classical Green tensor as uniquely defined by the inhomogeneous Helmholtz equation,

$$\left[\boldsymbol{\nabla}\times\frac{1}{\mu(\mathbf{r},\omega)}\boldsymbol{\nabla}\times - \frac{\omega^2}{c^2}\varepsilon(\mathbf{r},\omega)\right]\boldsymbol{G}(\mathbf{r},\mathbf{r}',\omega) = \boldsymbol{\delta}(\mathbf{r}-\mathbf{r}'), \tag{10}$$

together with the boundary condition

$$\boldsymbol{G}(\mathbf{r},\mathbf{r}',\omega)\to\boldsymbol{0} \quad \text{for } |\mathbf{r}-\mathbf{r}'|\to\infty. \tag{11}$$

The Green tensor is an analytic function in the upper half of the complex frequency plane and it has the following useful properties:

$$\boldsymbol{G}(\mathbf{r},\mathbf{r}',-\omega^*) = \boldsymbol{G}^*(\mathbf{r},\mathbf{r}',\omega), \tag{12}$$

$$\boldsymbol{G}(\mathbf{r}',\mathbf{r},\omega) = \boldsymbol{G}^{\mathsf{T}}(\mathbf{r},\mathbf{r}',\omega), \tag{13}$$

$$\sum_{\lambda=e,m}\int d^3s \boldsymbol{G}_\lambda(\mathbf{r},\mathbf{s},\omega)\cdot\boldsymbol{G}_\lambda^{*\mathsf{T}}(\mathbf{r}',\mathbf{s},\omega) \tag{14}$$

$$= \frac{\hbar\mu_0}{\pi}\omega^2\,\text{Im}\,\boldsymbol{G}(\mathbf{r},\mathbf{r}',\omega). \tag{15}$$

The Hamiltonian describing the internal dynamics of an atom with eigenenergies E_n and eigenstates $|n\rangle$ can be given as

$$\hat{H}_A = \sum_k E_k\hat{A}_{kk} \tag{16}$$

($\hat{A}_{kk}=|k\rangle\langle k|$ are the atomic flip operators). Throughout this paper, we will assume that the center-of-mass motion is sufficiently slow so that it separates from the internal dynamics in the spirit of a Born-Oppenheimer approximation. The interaction of the atom with the body-assisted electromagnetic field is then adequately described by the atom-field coupling Hamiltonian for given center-of-mass position $\mathbf{r}_A$ and velocity $\mathbf{v}_A$, which in the multipolar coupling scheme and electric-dipole approximation reads

$$\begin{aligned}\hat{H}_{AF} &= -\hat{\mathbf{d}}\cdot\hat{\mathbf{E}}(\mathbf{r}_A) - \hat{\mathbf{d}}\cdot\mathbf{v}_A\times\hat{\mathbf{B}}(\mathbf{r}_A)\\ &= -\sum_{kl}\mathbf{d}_{kl}\cdot\hat{\mathbf{E}}(\mathbf{r}_A)\hat{A}_{kl} - \sum_{kl}\mathbf{d}_{kl}\cdot\mathbf{v}_A\times\hat{\mathbf{B}}(\mathbf{r}_A)\hat{A}_{kl}\end{aligned} \tag{17}$$

($\mathbf{d}_{kl}=\langle k|\hat{\mathbf{d}}|l\rangle$). The first term is the familiar electric-dipole interaction, while the second term is the Röntgen interaction associated with the center-of-mass motion. Combining Eqs. (4), (16), and (17), the total Hamiltonian of the atom-body-field system reads

$$\hat{H} = \hat{H}_A + \hat{H}_F + \hat{H}_{AF}. \tag{18}$$

Finally, the total Lorentz force on the atomic charge and current distribution can in electric-dipole approximation be given as

$$\begin{aligned}\hat{\mathbf{F}} &= \boldsymbol{\nabla}_A[\hat{\mathbf{d}}\cdot\hat{\mathbf{E}}(\mathbf{r}_A) + \hat{\mathbf{d}}\cdot\mathbf{v}_A\times\hat{\mathbf{B}}(\mathbf{r}_A)] + \frac{d}{dt}[\hat{\mathbf{d}}\times\hat{\mathbf{B}}(\mathbf{r}_A)]\\ &= \boldsymbol{\nabla}_A\sum_{kl}[\mathbf{d}_{kl}\cdot\hat{\mathbf{E}}(\mathbf{r}_A)\hat{A}_{kl} + \mathbf{d}_{kl}\cdot\mathbf{v}_A\times\hat{\mathbf{B}}(\mathbf{r}_A)\hat{A}_{kl}]\\ &\quad + \frac{d}{dt}\sum_{kl}[\mathbf{d}_{kl}\times\hat{\mathbf{B}}(\mathbf{r}_A)\hat{A}_{kl}].\end{aligned} \tag{19}$$

III. CASIMIR-POLDER FORCE ON A MOVING ATOM

The Casimir-Polder force on an atom is the quantum average of the Lorentz force (19) with the body-assisted field being in its ground state. To evaluate this expression, we first need to solve the coupled atom-field dynamics.

A. Atom-field dynamics

Using Hamiltonian (18), the Heisenberg equations of motion of the atomic and field operators are found to be

$$\dot{\hat{A}}_{mn} = i\omega_{mn}\hat{A}_{mn} + \frac{i}{\hbar}\sum_k (\mathbf{d}_{nk}\hat{A}_{mk} - \mathbf{d}_{km}\hat{A}_{kn})\cdot\hat{\mathbf{E}}(\mathbf{r}_A) + \frac{i}{\hbar}\sum_k (\mathbf{d}_{nk}\hat{A}_{mk} - \mathbf{d}_{km}\hat{A}_{kn})\cdot\mathbf{v}_A\times\hat{\mathbf{B}}(\mathbf{r}_A), \tag{20}$$

where $\omega_{mn}=(E_m-E_n)/\hbar$, and

$$\dot{\hat{\mathbf{f}}}_\lambda(\mathbf{r},\omega) = -i\omega\hat{\mathbf{f}}_\lambda(\mathbf{r},\omega) + \frac{i}{\hbar}\sum_{k,l} \boldsymbol{G}^{*\mathbf{T}}_\lambda(\mathbf{r},\mathbf{r}_A,\omega)\cdot\mathbf{d}_{kl}\hat{A}_{kl} + \frac{1}{\hbar\omega}\sum_{k,l}[\boldsymbol{G}^{*\mathbf{T}}_\lambda(\mathbf{r},\mathbf{r}_A,\omega)\times\overleftarrow{\boldsymbol{\nabla}}']\times\mathbf{v}_A\cdot\mathbf{d}_{kl}\hat{A}_{kl} \tag{21}$$

(by convention, $\boldsymbol{\nabla}$ and $\boldsymbol{\nabla}'$ only act on the first or second argument of the Green tensor, respectively). The latter equation is formally solved by

$$\hat{\mathbf{f}}_\lambda(\mathbf{r},\omega,t) = \hat{\mathbf{f}}_{\lambda,\mathrm{f}}(\mathbf{r},\omega,t) + \hat{\mathbf{f}}_{\lambda,\mathrm{s}}(\mathbf{r},\omega,t), \tag{22}$$

where

$$\hat{\mathbf{f}}_{\lambda,\mathrm{f}}(\mathbf{r},\omega,t) = e^{-i\omega t}\hat{\mathbf{f}}_\lambda(\mathbf{r},\omega), \tag{23}$$

$$\hat{\mathbf{f}}_{\lambda,\mathrm{s}}(\mathbf{r},\omega,t) = \frac{i}{\hbar}\sum_{k,l}\int_0^t d\tau\, e^{-i\omega(t-\tau)}\boldsymbol{G}^{*\mathbf{T}}_\lambda[\mathbf{r},\mathbf{r}_A(\tau),\omega]\cdot\mathbf{d}_{kl}\hat{A}_{kl}(\tau) - \frac{1}{\hbar\omega}\sum_{k,l}\int_0^t d\tau e^{-i\omega(t-\tau)} \times\{\boldsymbol{G}^{*\mathbf{T}}_\lambda[\mathbf{r},\mathbf{r}_A(\tau),\omega]\times\overleftarrow{\boldsymbol{\nabla}}'\}\times\mathbf{v}_A\cdot\mathbf{d}_{kl}\hat{A}_{kl}(\tau) \tag{24}$$

determine the free and source parts of the electromagnetic field.

We assume that the atom moves with uniform nonrelativistic speed ($v_A \ll c$) and we are seeking a solution to the system of Eqs. (20) and (21) within linear order of $\mathbf{v}_A$. We may hence write

$$\mathbf{r}_A(\tau) = \mathbf{r}_A(t) - (t-\tau)\mathbf{v}_A, \tag{25}$$

and after substituting Eqs. (22)–(24) into Eq. (6), using the integral relation (14), and applying a linear Taylor expansion in $\mathbf{v}_A$, the time-dependent frequency components of the electric field are given by

$$\hat{\underline{\mathbf{E}}}(\mathbf{r},\omega,t) = \hat{\underline{\mathbf{E}}}_\mathrm{f}(\mathbf{r},\omega,t) + \hat{\underline{\mathbf{E}}}_\mathrm{s}(\mathbf{r},\omega,t) \tag{26}$$

with

$$\hat{\underline{\mathbf{E}}}_\mathrm{f}(\mathbf{r},\omega,t) = e^{-i\omega t}\hat{\underline{\mathbf{E}}}(\mathbf{r},\omega), \tag{27}$$

$$\hat{\underline{\mathbf{E}}}_\mathrm{s}(\mathbf{r},\omega,t) = \frac{i\mu_0}{\pi}\omega^2\int_0^t d\tau e^{-i\omega(t-\tau)}\sum_{k,l}\mathrm{Im}\,\boldsymbol{G}(\mathbf{r},\mathbf{r}_A,\omega)\cdot\mathbf{d}_{kl}\hat{A}_{kl}(\tau) - \frac{i\mu_0}{\pi}\omega^2\int_0^t d\tau(t-\tau)e^{-i\omega(t-\tau)} \times\sum_{k,l}\mathrm{Im}\,\boldsymbol{G}(\mathbf{r},\mathbf{r}_A,\omega)\cdot\mathbf{d}_{kl}(\overleftarrow{\boldsymbol{\nabla}}'\cdot\mathbf{v}_A)\hat{A}_{kl}(\tau) - \frac{\mu_0}{\pi}\omega\int_0^t d\tau e^{-i\omega(t-\tau)} \times\sum_{k,l}\mathrm{Im}[\boldsymbol{G}(\mathbf{r},\mathbf{r}_A,\omega)\times\overleftarrow{\boldsymbol{\nabla}}']\times\mathbf{v}_A\cdot\mathbf{d}_{kl}\hat{A}_{kl}(\tau) \tag{28}$$

[$\mathbf{r}_A=\mathbf{r}_A(t)$]. The magnetic field (7) only enters the equations of motion in conjunction with a factor $\mathbf{v}_A$, so we only require its zero-order expansion in the velocity,

$$\hat{\underline{\mathbf{B}}}(\mathbf{r},\omega,t) = \hat{\underline{\mathbf{B}}}_\mathrm{f}(\mathbf{r},\omega,t) + \hat{\underline{\mathbf{B}}}_\mathrm{s}(\mathbf{r},\omega,t) \tag{29}$$

with

$$\hat{\underline{\mathbf{B}}}_\mathrm{f}(\mathbf{r},\omega,t) = e^{-i\omega t}\hat{\underline{\mathbf{B}}}(\mathbf{r},\omega), \tag{30}$$

$$\hat{\underline{\mathbf{B}}}_\mathrm{s}(\mathbf{r},\omega,t) = \frac{\mu_0}{\pi}\omega\int_0^t d\tau e^{-i\omega(t-\tau)} \times\sum_{k,l}\boldsymbol{\nabla}\times\mathrm{Im}\,\boldsymbol{G}(\mathbf{r},\mathbf{r}_A,\omega)\cdot\mathbf{d}_{kl}\hat{A}_{kl}(\tau). \tag{31}$$

We can next substitute our solutions (27)–(31) for the time-independent electromagnetic fields into the equation of motion (20) for the atomic flip operators. Noting that the total field operators $\hat{\underline{\mathbf{E}}}(\mathbf{r},\omega,t)$ and $\hat{\underline{\mathbf{B}}}(\mathbf{r},\omega,t)$ commute with the atomic flip operators at equal times, we arrange all products such that creation operators $\hat{\mathbf{f}}^\dagger_\lambda(\mathbf{r},\omega)$ are always at the left and annihilation operators $\hat{\mathbf{f}}_\lambda(\mathbf{r},\omega)$ are always at the right. Assuming the field to be initially prepared in its vacuum state and taking expectation values, all contributions from the source fields vanish. For weak atom-field coupling, the time integrals can be evaluated with the aid of the Markov approximation,

$$\int_0^t d\tau e^{-i\omega(t-\tau)}\langle\hat{A}_{ij}(t)\hat{A}_{kl}(\tau)\rangle \simeq \langle\hat{A}_{ij}(t)\hat{A}_{kl}(t)\rangle\int_{-\infty}^t d\tau e^{-i(\omega-\tilde{\omega}_{lk})(t-\tau)} = \langle\hat{A}_{il}(t)\rangle\delta_{jk}\left[\pi\delta(\omega-\tilde{\omega}_{lk}) - i\mathcal{P}\frac{1}{\omega-\tilde{\omega}_{lk}}\right] \tag{32}$$

(here $\mathcal{P}$ represents the principal value); similarly we have

$$\int_0^t d\tau(t-\tau)e^{-i\omega(t-\tau)}\langle \hat{A}_{ij}(t)\hat{A}_{kl}(\tau)\rangle \simeq \langle \hat{A}_{il}(t)\rangle \delta_{jk}\frac{d}{d\omega}\left[\mathcal{P}\frac{1}{\omega-\tilde{\omega}_{lk}}+i\pi\delta(\omega-\tilde{\omega}_{lk})\right], \quad (33)$$

where the shifted atomic transition frequencies

$$\tilde{\omega}_{mn}=\omega_{mn}+\delta\omega_m-\delta\omega_n \quad (34)$$

have yet to be determined.

For a nondegenerate atom, the resulting equations of motion for the off-diagonal atomic flip operators decouple from each other as well as from the diagonal ones. In addition, we consider an atom whose internal Hamiltonian (16) is time-reversal invariant, so that we may assume real dipole-matrix elements. After a lengthy but straightforward calculation, we finally obtain the following equations of motion for the internal atomic density matrix elements $\sigma_{mn}=\langle \hat{A}_{nm}\rangle$:

$$\dot{p}_n=-\Gamma_n p_n+\sum_k \Gamma_k^n p_k, \quad (35)$$

$$\dot{\sigma}_{mn}=[-i\tilde{\omega}_{mn}-(\Gamma_m+\Gamma_n)/2]\sigma_{mn} \quad \text{for } m\neq n, \quad (36)$$

where we have introduced the probabilities $p_n=\sigma_{nn}$. The equations of motion for a moving atom have exactly the same form as for an atom at rest: the population of the diagonal density matrix elements is governed by spontaneous decay, while the off-diagonal ones undergo damped oscillations. However, the respective transition rates

$$\Gamma_n=\sum_k \Gamma_n^k \quad (37)$$

and frequency shifts

$$\delta\omega_n=\sum_k \delta\omega_n^k \quad (38)$$

are affected by the atomic motion,

$$\delta\omega_n^k=\delta\omega_n^k(\mathbf{r}_A)+\delta\omega_n^k(\mathbf{r}_A,\mathbf{v}_A), \quad (39)$$

$$\delta\omega_n^k(\mathbf{r}_A)=\frac{\mu_0}{\pi\hbar}\mathcal{P}\int_0^\infty d\omega\frac{\omega^2\mathbf{d}_{nk}\cdot \mathrm{Im}\,\boldsymbol{G}^{(1)}(\mathbf{r}_A,\mathbf{r}_A,\omega)\cdot\mathbf{d}_{kn}}{\tilde{\omega}_{nk}-\omega}, \quad (40)$$

$$\delta\omega_n^k(\mathbf{r}_A,\mathbf{v}_A)=\frac{\mu_0}{2\hbar}\Theta(\tilde{\omega}_{nk})(\mathbf{v}_A\cdot\boldsymbol{\nabla}_A)\times[\omega^2\mathbf{d}_{nk}\cdot \mathrm{Im}\,\boldsymbol{G}(\mathbf{r}_A,\mathbf{r}_A,\omega)\cdot\mathbf{d}_{kn}]'_{\omega=\tilde{\omega}_{nk}}, \quad (41)$$

$$\Gamma_n^k=\Gamma_n^k(\mathbf{r}_A)+\Gamma_n^k(\mathbf{r}_A,\mathbf{v}_A), \quad (42)$$

$$\Gamma_n^k(\mathbf{r}_A)=\frac{2\mu_0}{\hbar}\Theta(\tilde{\omega}_{nk})\tilde{\omega}_{nk}^2\mathbf{d}_{nk}\cdot \mathrm{Im}\,\boldsymbol{G}(\mathbf{r}_A,\mathbf{r}_A,\tilde{\omega}_{nk})\cdot\mathbf{d}_{kn}, \quad (43)$$

$$\Gamma_n^k(\mathbf{r}_A,\mathbf{v}_A)=-\frac{\mu_0}{\pi\hbar}(\mathbf{v}_A\cdot\boldsymbol{\nabla}_A)\mathcal{P}\int_0^\infty d\omega\times\frac{[\omega^2\mathbf{d}_{nk}\cdot \mathrm{Im}\,\boldsymbol{G}^{(1)}(\mathbf{r}_A,\mathbf{r}_A,\omega)\cdot\mathbf{d}_{kn}]'}{\tilde{\omega}_{nk}-\omega} \quad (44)$$

(the primes indicate derivatives with respect to ω). Here, we have decomposed the Green tensor into its bulk (free-space) and scattering parts according to

$$\boldsymbol{G}(\mathbf{r},\mathbf{r}',\omega)=\boldsymbol{G}^{(0)}(\mathbf{r},\mathbf{r}',\omega)+\boldsymbol{G}^{(1)}(\mathbf{r},\mathbf{r}',\omega) \quad (45)$$

and have discarded the Lamb-shift contribution due to $\boldsymbol{G}^{(0)}$ from the frequency shift $\delta\omega_n^k(\mathbf{r}_A)$ (as the free-space Lamb shift is assumed to be already included in the bare transition frequencies ω_{mn}). We have further exploited the symmetry (13) of the Green tensor which implies $\boldsymbol{\nabla}'\mapsto\frac{1}{2}\boldsymbol{\nabla}_A$, showing that the translationally invariant bulk Green tensor does not contribute to the velocity-dependent shifts and rates.

It is worth noting that for real dipole-matrix elements, the contributions from the Röntgen interaction exactly cancel. As a result, the velocity dependence of these quantities is entirely due to the fact that the moving atom emits and receives the electromagnetic field at different positions. The velocity-dependent contributions are proportional to the total derivative of the scattering Green tensor along the direction of motion. As a consequence, the decay rates and frequency shifts are unaffected by uniform motion in a direction along which the environment is translationally invariant (e.g., motion parallel to a plate or a cylinder). It is worth pointing out that such a vanishing of velocity-dependent frequency shifts does not necessarily imply that the velocity-dependent part of the CP force must also be zero. One should bear in mind that all of the above have only been shown within linear order in the velocity.

B. Casimir-Polder force

Having solved the coupled atom-field dynamics, we can now evaluate the quantum average of the Lorentz force (19). We restrict our attention to the pure dispersion force by again assuming the field to be initially prepared in its ground state. The atom may initially be in an arbitrary incoherent superposition of internal energy eigenstates. For an atom at rest, it has been found that the third term in Eq. (19), which involves a total time derivative, does not contribute to the force on atoms in incoherent internal states. We have explicitly checked that the same is true here, so that we only need to consider the force

$$\mathbf{F}=\boldsymbol{\nabla}_A\langle\hat{\mathbf{d}}\cdot\hat{\mathbf{E}}(\mathbf{r}_A)+\hat{\mathbf{d}}\cdot\mathbf{v}_A\times\hat{\mathbf{B}}(\mathbf{r}_A)\rangle=\boldsymbol{\nabla}_A\sum_{kl}[\mathbf{d}_{kl}\cdot\langle\hat{\mathbf{E}}(\mathbf{r}_A)\hat{A}_{kl}\rangle+\mathbf{d}_{kl}\cdot\mathbf{v}_A\times\langle\hat{\mathbf{B}}(\mathbf{r}_A)\hat{A}_{kl}\rangle]. \quad (46)$$

We begin by substituting the time-dependent electromagnetic fields (26)–(31) where again we retain only terms up to linear order in $\mathbf{v}_A$ and we arrange all products such that the contributions from the free fields vanish. The source fields give rise to intra-atomic correlation functions. By virtue of

the quantum regression theorem, Eq. (36) implies that the relevant correlation functions are of the form

$$\langle \hat{A}_{nk}(t)\hat{A}_{ln}(\tau)\rangle = \delta_{kl} e^{i\Omega_{nk}(t-\tau)}\sigma_{nn}(\tau) \tag{47}$$

with

$$\Omega_{nk} = \tilde{\omega}_{nk} + i(\Gamma_n + \Gamma_k)/2. \tag{48}$$

We evaluate time integrals in the spirit of the Markov approximation

$$\int_0^t d\tau\, e^{-i\omega(t-\tau)}\langle \hat{A}_{nk}(t)\hat{A}_{ln}(\tau)\rangle \simeq \sigma_{nn}(t)\,\delta_{kl}\int_{-\infty}^{t} d\tau\, e^{-i(\omega-\Omega_{nk})(t-\tau)}$$

$$= -\frac{\sigma_{nn}(t) i\,\delta_{kl}}{\omega-\Omega_{nk}} \tag{49}$$

and similarly

$$\int_0^t d\tau (t-\tau) e^{-i\omega(t-\tau)}\langle \hat{A}_{nk}(t)\hat{A}_{ln}(\tau)\rangle \simeq -\frac{\sigma_{nn}(t)\,\delta_{kl}}{(\omega-\Omega_{nk})^2}. \tag{50}$$

Again assuming real dipole-matrix elements, the resulting expression for the CP force can be written in the form

$$\mathbf{F}(t) = \sum_n p_n(t)\mathbf{F}_n \tag{51}$$

with

$$\mathbf{F}_n = \frac{\mu_0}{\pi}\sum_k \int_0^\infty d\omega\omega^2 \frac{\nabla \mathbf{d}_{nk}\cdot \mathrm{Im}\, \boldsymbol{G}^{(1)}(\mathbf{r}_A,\mathbf{r}_A,\omega)\cdot \mathbf{d}_{kn}}{\omega-\Omega_{nk}} + \frac{i\mu_0}{\pi}\sum_k \int_0^\infty d\omega\omega^2 \frac{\nabla(\mathbf{v}_A\cdot\nabla')\mathbf{d}_{nk}\cdot \mathrm{Im}\, \boldsymbol{G}^{(1)}(\mathbf{r}_A,\mathbf{r}_A,\omega)\cdot \mathbf{d}_{kn}}{(\omega-\Omega_{nk})^2}$$

$$+ \frac{i\mu_0}{\pi}\sum_k \int_0^\infty d\omega\omega \frac{(\nabla'-\nabla)\mathbf{d}_{nk}\cdot \mathbf{v}_A \times [\nabla \times \mathrm{Im}\, \boldsymbol{G}^{(1)}(\mathbf{r}_A,\mathbf{r}_A,\omega)]\cdot \mathbf{d}_{kn}}{\omega-\Omega_{nk}} + \text{c.c.} \tag{52}$$

Note that the two contributions from the Röntgen interaction have been collected in a single term as given on the second line of the above equation by making use of the symmetry (13) of the Green tensor. In addition, the (vanishing) contributions from the free-space Green tensor have been discarded.

Next, let us separate the forces $\mathbf{F}_n$ into their position- and velocity-dependent parts. The shifted and broadened atomic transition frequencies Ω_{nk} are velocity dependent, so that the first term in Eq. (52) also contributes to the velocity-dependent part of the force. Again retaining only terms up to linear order in the velocity, we find

$$\mathbf{F}_n = \mathbf{F}_n(\mathbf{r}_A) + \mathbf{F}_n(\mathbf{r}_A,\mathbf{v}_A), \tag{53}$$

with

$$\mathbf{F}_n(\mathbf{r}_A) = \frac{\mu_0}{2\pi}\sum_k \int_0^\infty d\omega\omega^2 \times \frac{\nabla_A \mathbf{d}_{mk}\cdot \mathrm{Im}\, \boldsymbol{G}^{(1)}(\mathbf{r}_A,\mathbf{r}_A,\omega)\cdot \mathbf{d}_{kn}}{\omega-\Omega_{nk}} + \text{c.c.} \tag{54}$$

and

$$\mathbf{F}_n(\mathbf{r}_A,\mathbf{v}_A) = \frac{\mu_0}{\pi}\sum_k \int_0^\infty d\omega\omega^2 \frac{\Omega_{nk}(\mathbf{v}_A)\,\nabla\, \mathbf{d}_{nk}\cdot \mathrm{Im}\, \boldsymbol{G}^{(1)}(\mathbf{r}_A,\mathbf{r}_A,\omega)\cdot \mathbf{d}_{kn}}{(\omega-\Omega_{nk})^2}$$

$$+ \frac{i\mu_0}{\pi}\sum_k \int_0^\infty d\omega\omega^2 \frac{\nabla(\mathbf{v}_A\cdot\nabla')\mathbf{d}_{nk}\cdot \mathrm{Im}\, \boldsymbol{G}^{(1)}(\mathbf{r}_A,\mathbf{r}_A,\omega)\cdot \mathbf{d}_{kn}}{(\omega-\Omega_{nk})^2}$$

$$+ \frac{i\mu_0}{\pi}\sum_k \int_0^\infty d\omega\omega \frac{(\nabla'-\nabla)\mathbf{d}_{nk}\cdot \mathbf{v}_A \times [\nabla \times \mathrm{Im}\, \boldsymbol{G}^{(1)}(\mathbf{r}_A,\mathbf{r}_A,\omega)]\cdot \mathbf{d}_{kn}}{\omega-\Omega_{nk}} + \text{c.c.}, \tag{55}$$

where $\Omega_{nk} \equiv \Omega_{nk}(\mathbf{r}_A)$ and $\Omega_{nk}(\mathbf{v}_A) \equiv \Omega_{nk}(\mathbf{r}_A,\mathbf{v}_A)$. The velocity-independent force (54) is just the well-known CP force on an atom at rest. We will in the following restrict our attention to the velocity-dependent force (55), which consists

of three terms: The first generalized Doppler term is due to the velocity dependence of the atomic transition frequencies. The second delay term is associated with the time interval between emission and reabsorption of the electromagnetic field. The third Röntgen term is due to the coupling of the current density associated with the moving atom to the magnetic field.

In close analogy to the case of an atom at rest, the force can be separated into its resonant and nonresonant parts using contour-integral techniques. Writing $\mathrm{Im}\,\boldsymbol{G}=(\boldsymbol{G}-\boldsymbol{G}^*)/(2i)$, using the property (12) of the Green tensor, and employing Cauchy's theorem to transform integrals along the real axis to integrals along the positive imaginary axis plus contributions from the poles, one can show that

$$\int_0^\infty d\omega \frac{\omega\,\mathrm{Im}\,\boldsymbol{G}^{(1)}(\mathbf{r},\mathbf{r}',\omega)}{\omega-\Omega_{nk}} = \int_0^\infty d\xi \frac{\xi^2 \boldsymbol{G}^{(1)}(\mathbf{r},\mathbf{r}',i\xi)}{\xi^2+\Omega_{nk}^2} + \pi\Omega_{nk}\boldsymbol{G}^{(1)}(\mathbf{r},\mathbf{r}',\Omega_{nk})\Theta(\tilde{\omega}_{nk}), \tag{56}$$

$$\int_0^\infty d\omega \frac{\omega^2\,\mathrm{Im}\,\boldsymbol{G}^{(1)}(\mathbf{r},\mathbf{r}',\omega)}{(\omega-\Omega_{nk})^2} = -\int_0^\infty d\xi \frac{\xi^2(\Omega_{nk}^2-\xi^2)\boldsymbol{G}^{(1)}(\mathbf{r},\mathbf{r}',i\xi)}{(\xi^2+\Omega_{nk}^2)^2} + \pi[\omega^2\boldsymbol{G}^{(1)}(\mathbf{r},\mathbf{r}',\omega)]'_{\omega=\Omega_{nk}}\Theta(\tilde{\omega}_{nk}). \tag{57}$$

Substituting these results into Eq. (55), one finds

$$\mathbf{F}_n(\mathbf{r}_A,\mathbf{v}_A) = \mathbf{F}_n^{\mathrm{nr}}(\mathbf{r}_A,\mathbf{v}_A) + \mathbf{F}_n^{\mathrm{r}}(\mathbf{r}_A,\mathbf{v}_A) \tag{58}$$

with

$$\begin{aligned}\mathbf{F}_n^{\mathrm{nr}}(\mathbf{r}_A,\mathbf{v}_A) = &-\frac{\hbar\mu_0}{2\pi}\int_0^\infty d\xi\xi^2\,\boldsymbol{\nabla}\,\mathrm{tr}\{[\boldsymbol{\alpha}_n(\mathbf{v}_A,i\xi)+\boldsymbol{\alpha}_n(\mathbf{v}_A,-i\xi)]\cdot\boldsymbol{G}^{(1)}(\mathbf{r}_A,\mathbf{r}_A,i\xi)\}\\ &-\frac{i\hbar\mu_0}{2\pi}\int_0^\infty d\xi\xi^2\,\boldsymbol{\nabla}\,(\mathbf{v}_A\cdot\boldsymbol{\nabla}')\mathrm{Tr}\{[\boldsymbol{\alpha}_n'(i\xi)+\boldsymbol{\alpha}_n'(-i\xi)]\cdot\boldsymbol{G}^{(1)}(\mathbf{r}_A,\mathbf{r}_A,i\xi)\}\\ &+\frac{\hbar\mu_0}{2\pi}\int_0^\infty d\xi\xi(\boldsymbol{\nabla}'-\boldsymbol{\nabla})\mathrm{Tr}\{[\boldsymbol{\alpha}_n(i\xi)-\boldsymbol{\alpha}_n(-i\xi)]\cdot\mathbf{v}_A\times[\boldsymbol{\nabla}\times\boldsymbol{G}^{(1)}(\mathbf{r}_A,\mathbf{r}_A,i\xi)]\}\end{aligned} \tag{59}$$

and

$$\begin{aligned}\mathbf{F}_n^{\mathrm{r}}(\mathbf{r}_A,\mathbf{v}_A) = &\,\mu_0\sum_k\,\Theta(\tilde{\omega}_{nk})\Omega_{nk}(\mathbf{v}_A)[\omega^2\,\boldsymbol{\nabla}\,\mathbf{d}_{nk}\cdot\boldsymbol{G}^{(1)}(\mathbf{r}_A,\mathbf{r}_A,\omega)\cdot\mathbf{d}_{kn}]'_{\omega=\Omega_{nk}}\\ &+i\mu_0\sum_k\,\Theta(\tilde{\omega}_{nk})[\omega^2\,\boldsymbol{\nabla}\,(\mathbf{v}_A\cdot\boldsymbol{\nabla}')\mathbf{d}_{nk}\cdot\boldsymbol{G}^{(1)}(\mathbf{r}_A,\mathbf{r}_A,\omega)\cdot\mathbf{d}_{kn}]'_{\omega=\Omega_{nk}}\\ &+i\mu_0\sum_k\,\Theta(\tilde{\omega}_{nk})\Omega_{nk}(\boldsymbol{\nabla}'-\boldsymbol{\nabla})\mathbf{d}_{nk}\cdot\mathbf{v}_A\times[\boldsymbol{\nabla}\times\boldsymbol{G}^{(1)}(\mathbf{r}_A,\mathbf{r}_A,\Omega_{nk})]\cdot\mathbf{d}_{kn}+\mathrm{c.c.}\end{aligned} \tag{60}$$

Here,

$$\boldsymbol{\alpha}_n(\omega) = \frac{1}{\hbar}\sum_k\left[\frac{\mathbf{d}_{kn}\mathbf{d}_{nk}}{\omega-\Omega_{nk}^*}-\frac{\mathbf{d}_{nk}\mathbf{d}_{kn}}{\omega+\Omega_{nk}}\right] \tag{61}$$

is the polarizability for an atom at rest and

$$\boldsymbol{\alpha}_n(\mathbf{v}_A,\omega) = \frac{1}{\hbar}\sum_k\left[\frac{\Omega_{nk}^*(\mathbf{v}_A)\mathbf{d}_{kn}\mathbf{d}_{nk}}{(\omega-\Omega_{nk}^*)^2}+\frac{\Omega_{nk}(\mathbf{v}_A)\mathbf{d}_{nk}\mathbf{d}_{kn}}{(\omega+\Omega_{nk})^2}\right] \tag{62}$$

is the correction to this polarizability for a moving atom within linear order of the atomic velocity.

It is instructive to consider the perturbative limit $\Omega_{nk}\to\omega_{nk}$ (i.e., $\delta\omega_{n/k}$, $\Gamma_{n/k}\to 0$). The resonant force can be represented by its zero-order approximation in $\delta\omega_{n/k}$ and $\Gamma_{n/k}$ which reads

$$\mathbf{F}_n^{\mathrm{r}}(\mathbf{r}_A,\mathbf{v}_A) = 2\mu_0 \sum_k \Theta(\omega_{nk})[\delta\omega_n(\mathbf{v}_A) - \delta\omega_k(\mathbf{v}_A)][\omega^2 \boldsymbol{\nabla}\, \mathbf{d}_{nk} \cdot \mathrm{Re}\, \boldsymbol{G}^{(1)}(\mathbf{r}_A,\mathbf{r}_A,\omega) \cdot \mathbf{d}_{kn}]'_{\omega=\omega_{nk}}$$
$$- \mu_0 \sum_k \Theta(\omega_{nk})[\Gamma_n(\mathbf{v}_A) + \Gamma_k(\mathbf{v}_A)][\omega^2 \boldsymbol{\nabla}\, \mathbf{d}_{nk} \cdot \mathrm{Im}\, \boldsymbol{G}^{(1)}(\mathbf{r}_A,\mathbf{r}_A,\omega) \cdot \mathbf{d}_{kn}]'_{\omega=\omega_{nk}}$$
$$- 2\mu_0 \sum_k \Theta(\omega_{nk})[\omega^2 \boldsymbol{\nabla}\, (\mathbf{v}_A \cdot \boldsymbol{\nabla}')\mathbf{d}_{nk} \cdot \mathrm{Im}\, \boldsymbol{G}^{(1)}(\mathbf{r}_A,\mathbf{r}_A,\omega) \cdot \mathbf{d}_{kn}]'_{\omega=\omega_{nk}}$$
$$- 2\mu_0 \sum_k \Theta(\omega_{nk})\omega_{nk}(\boldsymbol{\nabla}' - \boldsymbol{\nabla})\mathbf{d}_{nk} \cdot \mathbf{v}_A \times [\boldsymbol{\nabla} \times \mathrm{Im}\, \boldsymbol{G}^{(1)}(\mathbf{r}_A,\mathbf{r}_A,\omega_{nk})] \cdot \mathbf{d}_{kn}. \tag{63}$$

The nonresonant velocity-dependent force vanishes to zeroth order in the frequency shifts and decay rates in contrast to the force observed for an atom at rest. The leading nonvanishing contribution is linear in these quantities and it reads

$$\mathbf{F}_n^{\mathrm{nr}}(\mathbf{r}_A,\mathbf{v}_A) = -\frac{2\mu_0}{\pi} \sum_k \int_0^\infty d\xi \xi^2 \frac{[\delta\omega_n(\mathbf{v}_A) - \delta\omega_k(\mathbf{v}_A)](\omega_{kn}^2 - \xi^2)}{(\omega_{kn}^2 + \xi^2)^2} \boldsymbol{\nabla}\, \mathbf{d}_{nk} \cdot \boldsymbol{G}^{(1)}(\mathbf{r}_A,\mathbf{r}_A,i\xi) \cdot \mathbf{d}_{kn}$$
$$+ \frac{2\mu_0}{\pi} \sum_k \int_0^\infty d\xi \xi^2 \frac{\omega_{kn}(\Gamma_n + \Gamma_k)(\omega_{kn}^2 - 3\xi^2)}{(\omega_{kn}^2 + \xi^2)^3} \boldsymbol{\nabla}\, (\mathbf{v}_A \cdot \boldsymbol{\nabla}')\mathbf{d}_{nk} \cdot \boldsymbol{G}^{(1)}(\mathbf{r}_A,\mathbf{r}_A,i\xi) \cdot \mathbf{d}_{kn}$$
$$- \frac{2\mu_0}{\pi} \sum_k \int_0^\infty d\xi \xi^2 \frac{\omega_{kn}(\Gamma_n + \Gamma_k)}{(\omega_{kn}^2 + \xi^2)^2} (\boldsymbol{\nabla}' - \boldsymbol{\nabla})\mathbf{d}_{nk} \cdot \mathbf{v}_A \times [\boldsymbol{\nabla} \times \boldsymbol{G}^{(1)}(\mathbf{r}_A,\mathbf{r}_A,i\xi)] \cdot \mathbf{d}_{kn}. \tag{64}$$

For an isotropic atom, these results reduce to

$$\mathbf{F}_n^{\mathrm{r}}(\mathbf{r}_A,\mathbf{v}_A) = \frac{2\mu_0}{3} \sum_k \Theta(\omega_{nk})|\mathbf{d}_{nk}|^2[\delta\omega_n(\mathbf{v}_A) - \delta\omega_k(\mathbf{v}_A)][\omega^2 \boldsymbol{\nabla}\ \mathrm{Tr}\, \mathrm{Re}\, \boldsymbol{G}^{(1)}(\mathbf{r}_A,\mathbf{r}_A,\omega)]'_{\omega=\omega_{nk}}$$
$$- \frac{\mu_0}{3} \sum_k \Theta(\omega_{nk})|\mathbf{d}_{nk}|^2[\Gamma_n(\mathbf{v}_A) + \Gamma_k(\mathbf{v}_A)][\omega^2 \boldsymbol{\nabla}\ \mathrm{Tr}\, \mathrm{Im}\, \boldsymbol{G}^{(1)}(\mathbf{r}_A,\mathbf{r}_A,\omega)]'_{\omega=\omega_{nk}}$$
$$- \frac{2\mu_0}{3} \sum_k \Theta(\omega_{nk})|\mathbf{d}_{nk}|^2[\omega^2 \boldsymbol{\nabla}\, (\mathbf{v}_A \cdot \boldsymbol{\nabla}')\mathrm{Tr}\, \mathrm{Im}\, \boldsymbol{G}^{(1)}(\mathbf{r}_A,\mathbf{r}_A,\omega)]'_{\omega=\omega_{nk}}$$
$$- \frac{2\mu_0}{3} \sum_k \Theta(\omega_{nk})\omega_{nk}|\mathbf{d}_{nk}|^2(\boldsymbol{\nabla}' - \boldsymbol{\nabla})\mathrm{Tr}\{\mathbf{v}_A \times [\boldsymbol{\nabla} \times \mathrm{Im}\, \boldsymbol{G}^{(1)}(\mathbf{r}_A,\mathbf{r}_A,\omega_{nk})]\} \tag{65}$$

and

$$\mathbf{F}_n^{\mathrm{nr}}(\mathbf{r}_A,\mathbf{v}_A) = -\frac{2\mu_0}{3\pi} \sum_k |\mathbf{d}_{nk}|^2 \int_0^\infty d\xi \xi^2 \frac{[\delta\omega_n(\mathbf{v}_A) - \delta\omega_k(\mathbf{v}_A)](\omega_{kn}^2 - \xi^2)}{(\omega_{kn}^2 + \xi^2)^2} \boldsymbol{\nabla}\ \mathrm{Tr}\, \boldsymbol{G}^{(1)}(\mathbf{r}_A,\mathbf{r}_A,i\xi)$$
$$+ \frac{2\mu_0}{3\pi} \sum_k |\mathbf{d}_{nk}|^2 \int_0^\infty d\xi \xi^2 \frac{\omega_{kn}(\Gamma_n + \Gamma_k)(\omega_{kn}^2 - 3\xi^2)}{(\omega_{kn}^2 + \xi^2)^3} \boldsymbol{\nabla}\, (\mathbf{v}_A \cdot \boldsymbol{\nabla}')\mathrm{Tr}\, \boldsymbol{G}^{(1)}(\mathbf{r}_A,\mathbf{r}_A,i\xi)$$
$$- \frac{2\mu_0}{3\pi} \sum_k |\mathbf{d}_{nk}|^2 \int_0^\infty d\xi \xi^2 \frac{\omega_{kn}(\Gamma_n + \Gamma_k)}{(\omega_{kn}^2 + \xi^2)^2} (\boldsymbol{\nabla}' - \boldsymbol{\nabla})\mathrm{Tr}\{\mathbf{v}_A \times [\boldsymbol{\nabla} \times \boldsymbol{G}^{(1)}(\mathbf{r}_A,\mathbf{r}_A,i\xi)]\}. \tag{66}$$

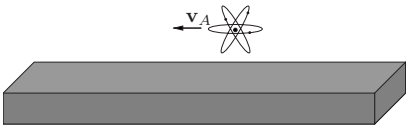

FIG. 1. Atom moving with a velocity $\mathbf{v}$ near a planar surface.

C. Motion parallel to a planar interface

Up until this point, all results are valid for arbitrary geometries. In order to gain physical insight, we restrict ourselves to the generic quantum friction scenario of an atom moving parallel $[\mathbf{v}_A = \mathbf{v}_\parallel = (v_x, v_y, 0)^{\mathbf{T}}]$ to a homogeneous dielectric or metal of permittivity $\varepsilon(\omega)$ whose plane surface defines the (x,y) plane (see Fig. 1). The Weyl expansion of the Green tensor,

$$\boldsymbol{G}(\mathbf{r},\mathbf{r}',\omega)=\int\frac{d^2k_\parallel}{(2\pi)^2}e^{i\mathbf{k}_\parallel\cdot(\boldsymbol{\rho}-\boldsymbol{\rho}')}\boldsymbol{G}(\mathbf{k}_\parallel,z,z',\omega),\tag{67}$$

with $\mathbf{r}=(\boldsymbol{\rho},z)$ can then be used to calculate explicit expressions for the terms that contribute to the velocity-dependent force. The relevant Weyl components $\boldsymbol{G}(\mathbf{k}_\parallel,z,z',\omega)$ of the Green tensor for $z,z'>0$ are given by $[G_{ij}\equiv G_{ij}(\mathbf{k}_\parallel,z,z',\omega)]$

$$G_{xx}=\frac{i}{2k_z}e^{ik_z(z+z')}\left[r_s\frac{k_y^2}{k_\parallel^2}-r_p\frac{k_z^2k_x^2}{k^2k_\parallel^2}\right],\tag{68}$$

$$G_{xy}=\frac{i}{2k_z}e^{ik_z(z+z')}\left[-r_s\frac{k_xk_y}{k_\parallel^2}-r_p\frac{k_z^2k_xk_y}{k^2k_\parallel^2}\right],\tag{69}$$

$$G_{xz}=-\frac{i}{2k_z}e^{ik_z(z+z')}r_p\frac{k_zk_x}{k^2},\tag{70}$$

$$G_{zz}=\frac{i}{2k_z}e^{ik_z(z+z')}r_p\frac{k_\parallel^2}{k^2},\tag{71}$$

with

$$r_s=\frac{k_z-k_{1z}}{k_z+k_{1z}},\quad r_p=\frac{\varepsilon(\omega)k_z-k_{1z}}{\varepsilon(\omega)k_z+k_{1z}}\tag{72}$$

being the Fresnel reflection coefficients of the surface for s- and p-polarized waves $[k^2=\omega^2/c^2,\ k_1^2=\varepsilon(\omega)\omega^2/c^2,\ k_{(1)z}^2=k_{(1)}^2-k_\parallel^2]$. The other components of the Green's tensor can be obtained by using the reciprocity condition $\boldsymbol{G}(\mathbf{r},\mathbf{r}',\omega)=\boldsymbol{G}^T(\mathbf{r}',\mathbf{r},\omega)$, which translates into $\boldsymbol{G}(\mathbf{k}_\parallel,z,z',\omega)=\boldsymbol{G}^T(-\mathbf{k}_\parallel,z',z,\omega)$, and the replacement rules $G_{yy}=G_{xx}(k_x\leftrightarrow k_y)$, $G_{yz}=G_{xz}(k_x\leftrightarrow k_y)$.

For the assumed motion parallel to the surface, the velocity-dependent shifts and rates vanish $\delta\omega_n^k(\mathbf{r}_A,\mathbf{v}_A)=\Gamma_n^k(\mathbf{r}_A,\mathbf{v}_A)=0$ (cf. the remark at the end of Sec. III A) and so do the generalized Doppler contributions to the resonant force (65) (first two terms) and the nonresonant force (66) (first term). To calculate the delay and Röntgen contributions, we require second derivatives of the Green's tensor as given above. It is useful to note that derivatives vanish unless they contain an even number for each of the Cartesian indices (x,y,z). For example, terms such as $\partial_x\partial_yG_{xx}$ or $\partial_y\partial_yG_{xz}$ will not contribute, whereas terms such as $\partial_x\partial_yG_{xy}$ or $\partial_y\partial_yG_{zz}$ will. For simplicity, we restrict our attention to the nonretarded or near-field limit, where the dominant contribution to the Green's tensor is due to evanescent waves with $k_{1z}\simeq k_z\simeq ik_\parallel$. With this replacement, we have

$$r_s=0,\quad r_p=\frac{\varepsilon(\omega)-1}{\varepsilon(\omega)+1}\tag{73}$$

and Eqs. (67)–(71) lead to

$$\boldsymbol{\nabla}(\mathbf{v}_\parallel\cdot\boldsymbol{\nabla}')\mathrm{Tr}\,\boldsymbol{G}^{(1)}(\mathbf{r}_A,\mathbf{r}_A,\omega)=\frac{3c^2\mathbf{v}_\parallel}{16\pi\omega^2z_A^5}\frac{\varepsilon(\omega)-1}{\varepsilon(\omega)+1},\tag{74}$$

$$(\boldsymbol{\nabla}'-\boldsymbol{\nabla})\mathrm{Tr}\{\mathbf{v}_\parallel\times[\boldsymbol{\nabla}\times\boldsymbol{G}^{(1)}(\mathbf{r}_A,\mathbf{r}_A,\omega)]\}=\mathbf{0}.\tag{75}$$

In the near-field limit, the Röntgen contribution hence also vanishes and quantum friction is entirely due to the delay effect.

Substituting Eqs. (76) and (75) into Eqs. (65) and (66), we find the friction forces,

$$\mathbf{F}_n^{\mathrm{r}}(\mathbf{r}_A,\mathbf{v}_\parallel)=-\frac{\mathbf{v}_\parallel}{4\pi\varepsilon_0z_A^5}\sum_k\Theta(\omega_{nk})|\mathbf{d}_{nk}|^2\left[\frac{\mathrm{Im}\,\varepsilon(\omega)}{|\varepsilon(\omega)+1|^2}\right]'_{\omega=\omega_{nk}}\tag{76}$$

and

$$\mathbf{F}_n^{\mathrm{nr}}(\mathbf{r}_A,\mathbf{v}_\parallel)=-\frac{\mathbf{v}_\parallel}{8\pi\varepsilon_0z_A^5}\sum_k|\mathbf{d}_{nk}|^2\omega_{kn}(\Gamma_n+\Gamma_k)\times\int_0^\infty d\xi\frac{\omega_{kn}^2-3\xi^2}{(\omega_{kn}^2+\xi^2)^3}\frac{\varepsilon(i\xi)-1}{\varepsilon(i\xi)+1}.\tag{77}$$

If we further assume a single-resonance Drude-Lorentz model for the permittivity,

$$\varepsilon(\omega)=1+\frac{\omega_\mathrm{P}^2}{\omega_\mathrm{T}^2-\omega^2-2i\gamma\omega},\tag{78}$$

with plasma frequency ω_P, transverse resonance frequency ω_T, and linewidth γ, we find that for a weakly absorbing medium ($\gamma\ll\omega_{\mathrm{P,T}}$) the resonant and nonresonant forces are given by

$$\mathbf{F}_n^{\mathrm{r}}(\mathbf{r}_A,\mathbf{v}_\parallel)=\frac{\mathbf{v}_\parallel}{8\pi\varepsilon_0z_A^5}\sum_k\Theta(\omega_{nk})|\mathbf{d}_{nk}|^2\frac{\gamma\omega_\mathrm{P}^2(\omega_\mathrm{S}^2+3\omega_{nk}^2)}{(\omega_{nk}^2-\omega_\mathrm{S}^2)^3}\tag{79}$$

and

$$\mathbf{F}_n^{\mathrm{nr}}(\mathbf{r}_A,\mathbf{v}_\parallel)=-\frac{\mathbf{v}_\parallel}{32\pi\varepsilon_0z_A^5}\sum_k|\mathbf{d}_{nk}|^2\frac{\mathrm{sgn}(\omega_{kn})(\Gamma_n+\Gamma_k)\omega_\mathrm{P}^2}{\omega_\mathrm{S}(|\omega_{kn}|+\omega_\mathrm{S})^3}\tag{80}$$

($\omega_\mathrm{S}=\sqrt{\omega_\mathrm{T}^2+\omega_\mathrm{P}^2/2}$ is the surface-plasmon frequency).

Let us discuss our results. We first note that in a quantum friction scenario of an atom moving parallel to a plane surface, a generalized Doppler effect does not contribute to the velocity-dependent force; this will be different for an atom moving perpendicularly toward the surface. In the near-field limit, the magnetic Röntgen coupling becomes negligible as well; it will become relevant for larger distances. Near-field quantum friction forces are hence dominantly caused by a delay effect.

For a ground-state atom, only a nonresonant force component (80) is present. With both ω_{k0} and Γ_k being positive quantities, $\mathbf{F}_n^{\mathrm{nr}}(\mathbf{r}_A,\mathbf{v}_\parallel)$ is strictly antiparallel to the velocity and hence presents a genuine friction force. Note that this force is proportional to the rates of spontaneous decay Γ_k, the absorption parameters of the atom. In the near-field limit, these decay rates are given by [20–22]

$$\Gamma_n = \sum_k \Gamma_{nk} = \sum_k \Theta(\omega_{nk}) \frac{|\mathbf{d}_{nk}|^2}{6\pi\hbar\varepsilon_0 z_A^3} \frac{\mathrm{Im}\ \varepsilon(\omega_{nk})}{|\varepsilon(\omega_{nk})+1|^2}$$

$$= \sum_k \Theta(\omega_{nk}) \frac{|\mathbf{d}_{nk}|^2}{12\pi\hbar\varepsilon_0 z_A^3} \frac{\gamma\omega_{nk}\omega_P^2}{(\omega_{nk}^2-\omega_S^2)^2}. \quad (81)$$

Inserting this into Eq. (80) yields a friction force that is extremely short ranged and falls off as z_A^{-8}. This is in contrast to previous theories [14] that predict a z_A^{-5} scaling, resulting from a disregard of the distance dependence of the spontaneous decay rate.

For an excited atom, resonant forces arise as a consequence of possible transitions to lower lying atomic energy levels. They will dominate the velocity-dependent force in particular if one of them is near resonant with the surface-plasmon frequency ω_S. Depending on whether the respective atomic transition frequency ω_{nk} is smaller or greater than the surface-plasmon frequency, the velocity-dependent resonant force will either be a decelerating friction force antiparallel to the velocity or it may be a quantum acceleration force parallel to the velocity. This can be qualitatively understood from an energy consideration. The energy $\hbar\omega_{nk}$ emitted during a downward transition of the atom is resonantly absorbed by the surface and leads to the excitation of a surface plasmon with energy $\hbar\omega_S$. The energy difference between these two reservoirs leads to a change in the atom's kinetic energy. If the emitted energy is smaller than the absorbed one, the atom has to decelerate; if the emitted energy is greater than the absorbed one, the atom will accelerate. Note also that the off-resonant contribution (80) consists of strictly accelerating downward contributions as well as strictly decelerating upward contributions which, as before, have a z_A^{-8} scaling and can be safely neglected with regard to the z_A^{-5} scaling of the resonant forces. It is known from previous studies [23] that the rate of spontaneous decay increases for atoms in motion. This mechanism leads to a more rapid dissipation of the internal energy initially stored in the atom, restricting the lifetime of resonant forces; it needs to be taken into account in a more quantitative analysis of energy conservation.

IV. EXAMPLES

In order to illustrate the effect of velocity-dependent forces on atoms, we present a selection of numerical examples. We will concentrate on forces that are dominated by a single atomic transition between a ground state $|0\rangle$ and an excited state $|1\rangle$ with frequency ω_A and (isotropic) dipole-matrix element d. In this case, the nonresonant ground-state force (80) reduces to the simpler expression

$$\mathbf{F}_0(\mathbf{r}_A, \mathbf{v}_\parallel) = -\frac{\mathbf{v}_\parallel d^2}{32\pi\varepsilon_0 z_A^5} \frac{\Gamma\omega_P^2}{\omega_S(\omega_A+\omega_S)^3}, \quad (82)$$

where the decay rate . (81) now reads

$$\Gamma = \frac{d^2}{12\pi\hbar\varepsilon_0 z_A^3} \frac{\gamma\omega_A\omega_P^2}{(\omega_A^2-\omega_S^2)^2}. \quad (83)$$

The excited-state force is dominated by the resonant force component, $\mathbf{F}_1(\mathbf{r}_A, \mathbf{v}_\parallel) = \mathbf{F}_1^{\mathrm{nr}}(\mathbf{r}_A, \mathbf{v}_\parallel) + \mathbf{F}_1^{\mathrm{r}}(\mathbf{r}_A, \mathbf{v}_\parallel) \approx \mathbf{F}_1^{\mathrm{r}}(\mathbf{r}_A, \mathbf{v}_\parallel)$,

$$\mathbf{F}_1(\mathbf{r}_A, \mathbf{v}_\parallel) = \frac{\mathbf{v}_\parallel d^2}{8\pi\varepsilon_0 z_A^5} \frac{\gamma\omega_P^2(\omega_S^2+3\omega_A^2)}{(\omega_A^2-\omega_S^2)^3}. \quad (84)$$

As a first example, we consider a ground-state ^{87}Rb atom moving parallel to a gold surface. We consider the lowest electronic transition $D_2(5^2S_{1/2} \rightarrow 5^2P_{3/2})$ with wavelength $\lambda_A = 780$ nm ($\omega_A = 2.41 \times 10^{15}$ rad s^{-1}) [24] and dipole moment $d = 4.23ea_0 = 3.58 \times 10^{-29}$ C m [25]. The permittivity of gold may be characterized by a plasma frequency $\omega_P = 1.37 \times 10^{16}$ rad s^{-1} and an absorption parameter $\gamma = 4.12 \times 10^{13}$ rad s^{-1} [22]. Note that the transverse resonance frequency vanishes for metals, $\omega_T = 0$, so that the surface-plasmon resonance is located at $\omega_S = \omega_P/\sqrt{2}$. With these parameters, we find a deceleration of the rubidium atom as ($m_{^{87}\mathrm{Rb}} = 1.44 \times 10^{-25}$ kg)

$$\mathbf{a}_\parallel = -\mathbf{v}_\parallel (9.6\ \mathrm{s}^{-1}) \left[\frac{1\ \mathrm{nm}}{z_A}\right]^8. \quad (85)$$

The force is extremely short ranged and is negligible for any reasonable values of the velocity and atom-surface distance.

In contrast, for an excited rubidium atom with the same data as above, the deceleration becomes

$$\mathbf{a}_\parallel = -\mathbf{v}_\parallel (5.0 \times 10^4\ \mathrm{s}^{-1}) \left[\frac{1\ \mathrm{nm}}{z_A}\right]^5. \quad (86)$$

In comparison to the ground-state force, excited-state quantum friction is strongly enhanced and has a much longer range. For an atomic velocity of $v = 200$ ms^{-1}, the deceleration at an atom-surface distance $z_A = 10$ nm can be as large as $a = -100$ ms^{-2}. Even at $z_A = 100$ nm the deceleration is still $a = -10^{-3}$ ms^{-2}.

Results for other atoms and metallic surfaces can be easily obtained by noting that in most cases, the relevant atomic transition frequency is much smaller than the surface-plasmon frequency of the metal, hence $\omega_A \ll \omega_S$. Under this approximation, the excited-state force (84) and the decay rate (83) read as

$$\mathbf{F}_1(\mathbf{r}_A, \mathbf{v}_\parallel) \approx -\frac{\mathbf{v}_\parallel d^2}{2\pi\varepsilon_0 z_A^5} \frac{\gamma}{\omega_P^2} \quad (87)$$

and

$$\Gamma \approx \frac{d^2\omega_A}{3\pi\hbar\varepsilon_0 z_A^3} \frac{\gamma}{\omega_P^2}. \quad (88)$$

Typical values for the material parameter ω_P^2/γ are tabulated in Ref. [22]. Note that unless the excitation is maintained by continuous repumping, the excited-state force only acts during a time interval $\Delta t \approx \Gamma^{-1}$. The relative velocity change during this time is approximately

$$\frac{\Delta v}{v} \approx \frac{F_1}{\Gamma m v} \approx -\frac{3\hbar}{m_A z_A^2} \frac{1}{2\omega_A}. \quad (89)$$

In this limit ($\omega_A \ll \omega_S$), the relative change in velocity is independent of the strength of the atomic dipole transition and all material parameters.

Upon inspection of the excited-state force (84) one notices that this force can be resonantly enhanced if an atomic

transition matches the frequency of a surface-plasmon resonance. An example of such a close match has been pointed out in Refs. [26,27] and involves a sapphire substrate with its principal surface plasmon at $\lambda_S=12.21$ μm ($\omega_S=1.54\times10^{14}$ rad s^{-1}) and the $6D_{3/2}\rightarrow 7P_{1/2}$ transition in ^{133}Cs with a wavelength of $\lambda_A=12.15$ μm ($\omega_A=1.55\times10^{14}$ rad s^{-1}). Near this plasmon resonance, the permittivity of sapphire is well approximated by [27]

$$\varepsilon_{\text{sapphire}}(\omega)=\eta+\frac{\eta\omega_P^2}{\omega_T^2-\omega^2-2i\gamma\omega} \tag{90}$$

with $\eta=2.71$, $\omega_P=0.84\omega_S=1.29\times10^{14}$ rad s^{-1}, $\omega_T=0.70\omega_S=1.08\times10^{14}$ rad s^{-1}, and $\gamma=7.5\times10^{-3}\omega_S=1.16\times10^{12}$ rad s^{-1}; note that $\omega_S=\sqrt{\omega_T^2+\omega_P\eta/(\eta+1)}$. With this model and introducing the atom-plasmon detuning $\delta=\omega_A-\omega_S$, we find that the force (76) and the decay rate (81) in the vicinity of the surface-plasmon resonance may be given as ($|\delta|,\gamma\ll\omega_S$)

$$\mathbf{F}_1(\mathbf{r}_A,\mathbf{v}_\parallel)\approx\frac{\mathbf{v}_\parallel d^2}{4\pi\varepsilon_0 z_A^5}\frac{\eta}{(\eta+1)^2}\frac{\omega_P^2}{\omega_S}\frac{\gamma\delta}{(\delta^2+\gamma^2)^2} \tag{91}$$

and

$$\Gamma\approx\frac{d^2}{12\pi\hbar\varepsilon_0 z_A^3}\frac{\eta}{(\eta+1)^2}\frac{\omega_P^2}{\omega_S}\frac{\gamma}{\delta^2+\gamma^2}. \tag{92}$$

With the dipole moment of the above-mentioned transition being $d=5.85\times10^{-29}$ C m [28], one finds ($m_{^{133}\text{Cs}}=2.21\times10^{-25}$ kg)

$$\mathbf{a}_\parallel=+\mathbf{v}_\parallel(7.1\times10^{11}\ \text{s}^{-1})\left[\frac{1\ \text{nm}}{z_A}\right]^5. \tag{93}$$

Compared with the result (86) for the excited-state force near a metal, we find a significantly enhanced force. Note also that, because $\omega_A>\omega_S$ (i.e., $\delta>0$), the force is accelerating rather than decelerating. As a numerical example, for a particle velocity of $v=100$ ms^{-1} and an atom-surface distance of $z_A=100$ nm, one would observe an acceleration of $a=7\times10^4$ ms^{-2}. As before, without continuous repumping this force acts only for a very short time, leading to a net relative change in velocity

$$\frac{\Delta v}{v}\approx\frac{3\hbar}{mz_A^2}\frac{\delta}{\delta^2+\gamma^2}. \tag{94}$$

V. SUMMARY

We have shown that atoms or molecules in relative motion with respect to an electric surface experience velocity-dependent CP forces. Solving the coupled atom-field dynamics for a slowly moving atom, we have found an expression for the linearized velocity-dependent force on an atom in an arbitrary incoherent internal quantum state moving near an arbitrary arrangement of magnetoelectric bodies. In general, three effects contribute to the velocity-dependent Casimir-Polder force: a generalized Doppler effect due to the velocity dependence of the atomic transition frequencies; the delay between the emission and reabsorption of photons by the atom; and the Röntgen interaction, i.e., the coupling of the current density associated with the atomic motion to the magnetic field.

In order to illustrate the general theory, we have studied the near-field force on an atom that moves parallel to a planar dielectric or metallic surface. Due to the translational invariance of the system, the Doppler term does not contribute in this case. Furthermore, the delay term dominates over the Röntgen term. For a ground-state atom the force is a genuine friction force, i.e., a force antiparallel to its velocity. It is proportional to the atomic linewidth and hence very small. In contrast, excited-state atoms can be either decelerated or accelerated depending on the relative magnitude of their transition frequency with respect to the characteristic frequency of the substrate material. For metals, the force is always decelerating while for dielectric substrates with sufficiently small surface-plasmon frequency, acceleration of excited-state atoms can be realized.

In addition, the force on such atoms is strongly enhanced when atom and substrate are near resonant. Much stronger enhancement can be achieved when the atom moves through resonator structures, in close analogy to the stationary case [29].

ACKNOWLEDGMENTS

The authors gratefully acknowledge discussions with T. Freegarde and P. Horak. This work was supported by the Engineering and Physical Sciences Research Council (UK) and the Alexander von Humboldt Foundation.

[1] P. W. Milonni, *The Quantum Vacuum* (Academic Press, New York, 1994).
[2] J. D. van der Waals, Ph.D. thesis, Leiden University, 1873.
[3] H. G. B. Casimir, Proc. K. Ned. Akad. Wet. **51**, 793 (1948).
[4] H. G. B. Casimir and D. Polder, Phys. Rev. **73**, 360 (1948).
[5] J. E. Lennard-Jones, Trans. Faraday Soc. **28**, 333 (1932).
[6] R. Fermani, S. Scheel, and P. L. Knight, Phys. Rev. A **75**, 062905 (2007).
[7] D. M. Harber, J. M. Obrecht, J. M. McGuirk, and E. A. Cornell, Phys. Rev. A **72**, 033610 (2005).
[8] S. Y. Buhmann, L. Knöll, D.-G. Welsch, and Ho Trung Dung, Phys. Rev. A **70**, 052117 (2004).
[9] M. Antezza, L. P. Pitaevskii, and S. Stringari, Phys. Rev. A **70**, 053619 (2004).
[10] S. Y. Buhmann and S. Scheel, Phys. Rev. Lett. **100**, 253201 (2008).
[11] J. M. Obrecht, R. J. Wild, M. Antezza, L. P. Pitaevskii, S. Stringari, and E. A. Cornell, Phys. Rev. Lett. **98**, 063201 (2007).
[12] E. M. Lifshitz, Sov. Phys. JETP **2**, 73 (1956).

[13] A. D. McLachlan, Proc. R. Soc. London, Ser. A **274**, 80 (1963).
[14] A. A. Kyasov and G. V. Dedkov, Surf. Sci. **463**, 11 (2000); G. V. Dedkov and A. A. Kyasov, Nucl. Instrum. Methods Phys. Res. B **183**, 241 (2001); Phys. Solid State **44**, 1809 (2002); A. A. Kyasov and G. V. Dedkov, Nucl. Instrum. Methods Phys. Res. B **195**, 247 (2002); G. V. Dedkov and A. A. Kyasov, Phys. Lett. A **339**, 212 (2005); Nucl. Instrum. Methods Phys. Res. B **237**, 507 (2005); G. V. Dedkov, Phys. Solid State **48**, 1387 (2006).
[15] I. Dorofeyev, H. Fuchs, B. Gotsmann, and J. Jersch, Phys. Rev. B **64**, 035403 (2001).
[16] A. I. Volokitin and B. N. J. Persson, Phys. Rev. B **65**, 115419 (2002).
[17] B. L. Hu, A. Roura, and S. Shresta, J. Opt. B: Quantum Semiclassical Opt. **6**, S698 (2004).
[18] J. M. Wylie and J. E. Sipe, Phys. Rev. A **32**, 2030 (1985).
[19] S. Scheel and S. Y. Buhmann, Acta Phys. Slov. **58**, 675 (2008).
[20] M. S. Yeung and T. K. Gustafson, Phys. Rev. A **54**, 5227 (1996).
[21] C. Henkel and M. Wilkens, Europhys. Lett. **47**, 414 (1999).
[22] S. Y. Buhmann, M. R. Tarbutt, S. Scheel, and E. A. Hinds, Phys. Rev. A **78**, 052901 (2008).
[23] L. G. Boussiakou, C. R. Bennett, and M. Babiker, Phys. Rev. Lett. **89**, 123001 (2002).
[24] C. E. Moore, *Atomic Energy Levels: As Derived from the Analyses of Optical Spectra* (U.S. Government Printing Office, Washington, D.C., 1971), Vol. II.
[25] D. A. Steck, Cesium D Line Data, 2009, http://steck.us/alkalidata
[26] M. Fichet, F. Schuller, D. Bloch, and M. Ducloy, Phys. Rev. A **51**, 1553 (1995).
[27] M.-P. Gorza and M. Ducloy, Eur. Phys. J. D **40**, 343 (2006).
[28] A. Lindgård and S. E. Nielsen, At. Data Nucl. Data Tables **19**, 533 (1977).
[29] S. Å. Ellingsen, S. Y. Buhmann, and S. Scheel, Phys. Rev. A **80**, 022901 (2009).

PHYSICAL REVIEW A **94**, 063803 (2016)

Spectroscopic signatures of quantum friction

Juliane Klatt,[1] Robert Bennett,[1] and Stefan Yoshi Buhmann[1,2]
[1]*Physikalisches Institut, Albert-Ludwigs-Universität Freiburg, Hermann-Herder-Strasse 4, D-79104, Freiburg im Breisgau, Germany*
[2]*Freiburg Institute for Advanced Studies, Albert-Ludwigs-Universität Freiburg, Albertstrasse 19, D-79104 Freiburg im Breisgau, Germany*
(Received 11 January 2016; published 1 December 2016)

We present a formula for the spectroscopically accessible level shifts and decay rates of an atom moving at an arbitrary angle relative to a surface. Our Markov formulation leads to an intuitive analytic description whereby the shifts and rates are obtained from the coefficients of the Heisenberg equation of motion for the atomic flip operators but with complex Doppler-shifted (velocity-dependent) transition frequencies. Our results conclusively demonstrate that for the limiting case of parallel motion the shifts and rates are quadratic or higher in the atomic velocity. We show that a stronger, linear velocity dependence is exhibited by the rates and shifts for perpendicular motion, thus opening the prospect of experimentally probing the Markovian approach to the phenomenon of quantum friction.

DOI: 10.1103/PhysRevA.94.063803

I. INTRODUCTION

How does an atom with a fluctuating dipole moment behave when moving relative to a surface? Given the recent resurgence of interest in short-range fluctuation-induced forces brought about by advances in micro- and nanoscale technology, one would expect this question to have a clear-cut, unambiguous answer. Indeed the intuition for the effect is clear—the properties of a fluctuating atomic dipole depend on the distance to an image dipole [1], meaning that a relative motion between the two should cause velocity-dependent dynamical corrections. However, even for relatively simple and idealized models of atoms and surfaces there are significant disagreements between different approaches to calculating, for instance, the frictional force that an atom may experience while moving parallel to a surface. For example, Refs. [2,3] disagree with Refs. [4–6] about the power law governing the velocity dependence of the effect at zero temperature; it is even argued in Ref. [7] that the effect does not exist at all, or in Ref. [8] that some methods (e.g., Ref. [9]) are very sensitive to the initial velocity preparation. These discrepancies arise largely because several different and incompatible formalisms have been used in calculating the velocity-dependent force. These include linear-response theory [10], Born-Markov approximations [6], time-dependent perturbation theory [8], and appeals to a generalized fluctuation-dissipation theorem [2]. As in all physics, the only real validation of a successful approach is via experiments, which are sorely lacking in atomic friction. This is because the forces involved are extremely small, and there are serious experimental challenges concerning precision measurements of forces on atoms near surfaces [11,12], meaning that it is difficult to confirm or exclude particular theoretical approaches.

Here, we take a different route and consider the much more experimentally accessible internal dynamics of the atom, which in principle can be measured spectroscopically, thus providing a testable prediction of a velocity-dependent quantum-vacuum effect. We present results for the paradigmatic setup of a zero-temperature neutral atom with dipole moment $\mathbf{d}$ and nonrelativistic velocity $\mathbf{v}$ moving next to a perfectly smooth macroscopic surface, as shown in Fig. 1. For an atom at rest, the interaction of the atom's fluctuating dipole moment with its image causes the Casimir-Polder corrections to the atom's levels and decay rates [1]. If the atom is allowed to move relative to the surface, fields induced by images at *previous* times reach the atom; in other words, the motion of the atom causes it to "see" its image as being at a different position than where it is currently, resulting in dynamical effects.

II. MODEL

The dynamics shown in Fig. 1 consists of three mutually coupled parts: (i) the atom's center-of-mass motion, (ii) the internal dynamics of the atom, and (iii) the dynamics of the medium-assisted electromagnetic field which surrounds the atom. The center-of-mass motion may be separated from the other degrees of freedom in the spirit of the Born-Oppenheimer approximation. Accordingly, the coupled atom-field dynamics are solved for a fixed atomic velocity. For the description of the dynamics of the composite field-matter system consisting of the electromagnetic field coupled to the charges making up the medium, we use the framework of macroscopic quantum electrodynamics [13,14]. The latter is a prescription for the quantization of the electromagnetic field interacting with macroscopic, dispersive, and absorbing bodies. As a consequence, the field-matter system is represented by a bosonic field with elementary excitations $\mathbf{f}_\lambda$ for each electric or magnetic-type excitation $\lambda = \{e,m\}$, with position $\mathbf{r}$ and frequency ω. The Hamiltonian H_F describing this part of the dynamics is then simply the canonical form integrated over all space:

$$H_\mathrm{F} = \hbar \int d^3\mathbf{r} \int_0^\infty d\omega\omega\, \mathbf{f}_\lambda^\dagger(\mathbf{r},\omega)\cdot\mathbf{f}_\lambda(\mathbf{r},\omega). \tag{1}$$

The free atom of mass m and center-of-mass momentum $\mathbf{p}$ is described by a Hamiltonian

$$H_\mathrm{A} = \frac{\mathbf{p}^2}{2m} + \sum_n E_n |n\rangle\langle n|, \tag{2}$$

where n indexes an atomic level of energy E_n. The third and final part of the Hamiltonian comprises the interaction between the macroscopic QED electric field $\mathbf{E}(\mathbf{r})$ and the atom. This interaction is described in the dipole approximation

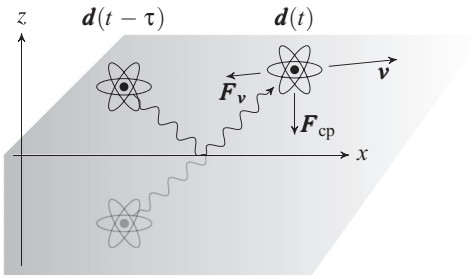

FIG. 1. Atom moving next to a surface with velocity $\mathbf{v}$. Its electric dipole $\mathbf{d}(t)$ fluctuates about zero. The atom may have emitted a photon at time $t-\tau$ which is reabsorbed at time t.

by a Hamiltonian

$$H_{\mathrm{AF}} = -\sum_{mn} |m\rangle\langle n|\,\mathbf{d}_{mn}\cdot\mathbf{E}(\mathbf{r}_{\mathrm{A}}), \tag{3}$$

furnishing us with the total Hamiltonian $H = H_{\mathrm{F}} + H_{\mathrm{A}} + H_{\mathrm{AF}}$. Note that magnetic contributions to the interaction are omitted since they play a minor role in close proximity to the surface. The macroscopic QED electric field in a region with permittivity $\varepsilon(\mathbf{r},\omega)$ and permeability $\mu(\mathbf{r},\omega)$ is given explicitly in terms of the bosonic operators $\mathbf{f}_\lambda(\mathbf{r},\omega)$ introduced above by

$$\mathbf{E}(\mathbf{r}) = \sum_\lambda \int d^3\mathbf{r}' \int_0^\infty d\omega\, \mathbf{G}_\lambda(\mathbf{r},\mathbf{r}',\omega)\cdot\mathbf{f}_\lambda(\mathbf{r}',\omega) + \mathrm{H.c.} \tag{4}$$

with

$$\mathbf{G}_{\mathrm{e}}(\mathbf{r},\mathbf{r}',\omega) = i\frac{\omega^2}{c^2}\sqrt{\frac{\hbar\varepsilon_0}{\pi}\mathrm{Im}\varepsilon(\mathbf{r}',\omega)}\mathbf{G}(\mathbf{r},\mathbf{r}',\omega), \tag{5}$$

$$\mathbf{G}_{\mathrm{m}}(\mathbf{r},\mathbf{r}',\omega) = i\frac{\omega}{c}\sqrt{\frac{\hbar}{\pi\mu_0}\frac{\mathrm{Im}\mu(\mathbf{r}',\omega)}{|\mu(\mathbf{r}',\omega)|^2}}\mathbf{G}(\mathbf{r},\mathbf{r}',\omega), \tag{6}$$

where $\mathbf{G}(\mathbf{r},\mathbf{r}',\omega)$ is the Green's function for the Helmholtz equation

$$\left[\nabla\times\frac{1}{\mu(\mathbf{r},\omega)}\nabla\times - \frac{\omega^2}{c^2}\varepsilon(\mathbf{r},\omega)\right]\mathbf{G}(\mathbf{r},\mathbf{r}',\omega) = \delta(\mathbf{r}-\mathbf{r}'). \tag{7}$$

This Green's function describes the propagation of field-matter excitations of frequency ω from $\mathbf{r}'$ to $\mathbf{r}$ thereby encoding all the information about the environment, i.e., its geometry as well as its dispersive and absorptive properties.

Using Eq. (4) in our Hamiltonian H, we have for the Heisenberg equations of motion,

$$\dot{A}_{mn}(t) = i\omega_{mn} + \frac{1}{i\hbar}[A_{mn}(t),\, H_{\mathrm{AF}}(t)], \tag{8}$$

for the atomic flip operators $A_{mn} \equiv |m\rangle\langle n|$ a differential equation which can be formally solved in a Dyson-like expansion in the square of the electric dipole moment $\mathbf{d}$ of the atom. The dipole operator $d_{mn}A_{mn}$ induces an atomic transition from one electronic level to another, which will necessarily be accompanied by the emission or absorption of a body-assisted field excitation given the form of the atom-field coupling in Eq. (3). Hence, restricting to quadratic order in $\mathbf{d}$ corresponds to considering (at most) two emission or absorption events, which—if a surface is present—means neglecting multiple reflections. Doing this, we find for the dynamics of the $\mathbf{d}^2$ approximation $A^{(2)}_{mn}(t)$ to the atomic flip operator

$$\dot{A}^{(2)}_{mn}(t) = \dot{A}^{(0)}_{mn}(t) - \frac{1}{i\hbar}\sum_{ij}\left[A^{(0)}_{mn}(t),\, A^{(0)}_{ij}(t)\mathbf{d}_{ij}\cdot\mathbf{E}^{(1)}(\mathbf{r}_{\mathrm{A}},t)\right], \tag{9}$$

where $\mathbf{E}^{(1)}$ is the free field plus that induced by an atom described via the $\mathbf{d}^0$ approximation $A^{(0)}_{mn}(t)$ to the atomic flip operator. Taking the normal-ordered vacuum expectation value of (9) and utilizing the Heisenberg equation of motion for the $\mathbf{f}_\lambda(\mathbf{r},\omega)$ one arrives at

$$\left\langle\dot{A}^{(2)}_{mn}(t)\right\rangle = \{i\omega_{mn} - [C_n(t) + C^*_m(t)]\}\left\langle A^{(2)}_{mn}(t)\right\rangle, \tag{10}$$

where we have replaced $A^{(0)}_{mn}(t) \to A^{(2)}_{mn}(t)$ on the right-hand side. The resulting error will be of order $\mathbf{d}^4$, as can be easily seen from the coefficients $C_n = \sum_k C_{nk}$ given explicitly by [15]

$$C_{nk} = \frac{\mu_0}{\pi\hbar}\int_{t_0}^{t} dt' \int_0^\infty d\omega\omega^2\mathbf{d}_{nk}\cdot[\mathrm{Im}\mathbf{G}(\mathbf{r}_{\mathrm{A}},\mathbf{r}'_{\mathrm{A}},\omega)]\cdot\mathbf{d}_{kn} \times e^{-i(\omega-\omega_{nk})(t-t')}, \tag{11}$$

where $\mathbf{r}_{\mathrm{A}} = \mathbf{r}_{\mathrm{A}}(t)$ and $\mathbf{r}'_{\mathrm{A}} = \mathbf{r}_{\mathrm{A}}(t')$ are the current and previous positions of the atom, respectively. Here we have used a well-known integral relation for electromagnetic dyadic Green's functions [15]:

$$\sum_\lambda\int d^3\mathbf{s}\,\mathbf{G}_\lambda(\mathbf{r},\mathbf{s},\omega)\cdot\mathbf{G}^*_\lambda(\mathbf{s},\mathbf{r}',\omega) = \frac{\hbar\mu_0}{\pi}\omega^2\mathrm{Im}\mathbf{G}(\mathbf{r},\mathbf{r}',\omega). \tag{12}$$

Inspection of Eq. (10) shows that the real and imaginary parts of C_n deliver respectively the rate of spontaneous decay, Γ_n, and the level shift $\hbar\delta\omega_n$ with respect to the bare level E_n of the state n via

$$\Gamma_n = 2\sum_{k<n}\mathrm{Re}C_{nk}, \quad \delta\omega_n = \sum_k \mathrm{Im}C_{nk}. \tag{13}$$

Having set up the model, we now present our main results, which are the first predictions of level shifts and decay rates for an atom moving in an arbitrary direction near a surface. In order to produce concrete numbers for the level shifts and decay rates, we employ a Markov approximation in which the coefficients in Eq. (10) are presupposed to be time independent. In other words, we assume clear separation of the three time scales involved. First, the both the field dynamics and the internal dynamics of the atom are assumed to happen at a much faster pace than the atomic center-of-mass motion. Hence, the atom's position and velocity may be treated as instantaneous and fixed—eliminating implicit time dependencies in the C_{nk}. Second, typical time scales of the field's dynamics—given by its memory, i.e., autocorrelation time—are presupposed to be very small compared to the time scales on which electronic transitions in the atom take place. Therefore, any residual time dependence—saturated on the scale of the field's memory—will not be resolved in the internal atomic dynamics. This is the well-known coarse-graining effect the Markov approximation relies on. Consistency with such an approximation requires that we assume approximately uniform motion $\mathbf{r}_{\mathrm{A}} - \mathbf{r}'_{\mathrm{A}} \approx \mathbf{v}(t-t') \equiv \mathbf{v}\tau$.

We take advantage of translational invariance parallel to the surface to take the Fourier transform $\underline{\mathrm{Im}\mathbf{G}}$ of the imaginary part of the Green's function appearing in Eq. (11). Similarly, we split up the atomic velocity $\mathbf{v}$ and the wave vector $\mathbf{k}$ into components parallel to the surface $\{\mathbf{v}_\parallel,\mathbf{k}_\parallel\}$ and perpendicular to it $\{\mathbf{v}_\perp,\mathbf{k}_\perp\}$, giving for Eq. (11)

$$C_{nk} = \frac{\mu_0}{\pi\hbar}\int_0^\infty d\tau \int_0^\infty d\omega\omega^2 \int d^2\mathbf{k}_\parallel \times \mathbf{d}_{nk}\cdot[\underline{\mathrm{Im}\mathbf{G}}(\mathbf{k}_\parallel,z_\mathrm{A},\omega)]\cdot\mathbf{d}_{kn}e^{-i(\omega-\omega'_{nk})\tau}, \tag{14}$$

where a Doppler-shifted frequency $\omega'_{nk}\equiv\omega_{nk}+\mathbf{k}\cdot\mathbf{v}$ has naturally arisen and we have made use of a shorthand $\mathbf{G}(\mathbf{k}_\parallel,z,\omega)\equiv\mathbf{G}(\mathbf{k}_\parallel,z,z,\omega)$. Finally, we have taken the limit $t_0\to-\infty$, which is justified as long as t_0 is significantly larger than the width of the field's memory kernel, consistent with the Markov approximation.

Since we ultimately want to determine the shifts $\delta\omega_n$ and rates Γ_n given in Eq. (13) and accordingly aim to identify the real and imaginary parts of Eq. (14), it is useful to further simplify $\underline{\mathrm{Im}\mathbf{G}}$ (the Fourier transform of the imaginary part of $\mathbf{G}$) as this quantity has no obvious separation into real-valued and imaginary components. To this end, we note that for real $\mathbf{d}_{nk}$ only the symmetric portion $\mathcal{S}\underline{\mathbf{G}}$ of the Fourier-transformed Green's tensor $\underline{\mathbf{G}}$ contributes, which, for a half-space geometry described by $\mathbf{G}=\mathbf{G}^\mathrm{HS}$ that we use later on, is precisely the part for which Fourier transforming and taking the imaginary part commute: $\mathcal{S}[\underline{\mathrm{Im}\mathbf{G}^\mathrm{HS}}]=\mathcal{S}[\mathrm{Im}\underline{\mathbf{G}^\mathrm{HS}}]$. Now we have the imaginary part of the Fourier transform (rather than vice versa) which is manifestly real. Thus we now have a clear separation of real and imaginary parts in Eq. (14), enabling us to easily identify level shifts and rates of spontaneous decay via Eq. (13).

Furthermore, we specialize to the nonretarded (i.e., near-field) regime where the atom-surface distance z_A is short enough that the finite round-trip time of a reflected photon is negligible compared to atomic time scales. This regime is defined by $\omega_{nk}z_\mathrm{A}/c\ll 1$. Under these conditions, $k_\perp\approx(-k_\parallel^2)^{1/2}$ and the Doppler-shifted atomic transition frequencies become $\omega'_{nk}\to\omega_{nk}+\mathbf{k}_\parallel\cdot\mathbf{v}_\parallel-ik_\parallel v_\perp$, where we have made the physical choice of branch of the square root such that evanescent waves are decaying away from the surface as $z\to\infty$.

Finally, let us spell out in more detail the connection between contributions stemming from a finite atomic center-of-mass velocity $\mathbf{v}$ to the internal atomic dynamics on the one hand and quantum friction, i.e., finite-$\mathbf{v}$ contributions to the Casimir-Polder force, on the other hand. An agreed-upon feature of the various approaches to quantum friction mentioned in the introduction is the following expression for the Casimir-Polder force:

$$\mathbf{F}_\mathrm{CP}(t) = \frac{i\mu_0}{4\pi^3}\nabla\int_0^t dt'\int d^2\mathbf{k}_\parallel\int_0^\infty d\omega\omega^2 e^{-i\omega(t-t')} \times\mathrm{tr}\{\mathcal{C}_d(t,t';\mathbf{v})\cdot[\mathrm{Im}\mathbf{G}(\mathbf{k}_\parallel,z_\mathrm{A},\omega)]\}e^{i\mathbf{k}_\parallel\cdot(\mathbf{r}_\mathrm{A}-\mathbf{r}'_\mathrm{A})}, \tag{15}$$

where $\mathcal{C}_d$ is the two-time correlator of the atomic dipole moment,

$$\mathcal{C}_d(t,t';\mathbf{v}) = \langle\mathbf{d}(t)\mathbf{d}(t')\rangle. \tag{16}$$

The Casimir-Polder force (15) experienced by an atom which moves parallel to a macroscopic surface comprises the aforementioned dynamical contributions in twofold manner: first, *explicitly* via the distance $\mathbf{r}_\mathrm{A}-\mathbf{r}'_\mathrm{A}$ traveled by the atom during emission at time t and reabsorption at time t' of a photon, and second, *implicitly*, via the time evolution of the dipole operator which evolves according to the entire Hamiltonian which naturally includes the atomic center-of-mass motion and hence $\mathbf{v}$. This implicit dependence is indicated by the third argument of the correlator $\mathcal{C}_d$ and corresponds exactly to the finite-velocity contributions to the internal dynamics provided by Eqs. (13) and (14).

There is consensus that the leading-order-in-$\mathbf{v}$ contributions to the friction force acting on an atom moving parallel to the surface stem from the *explicit* velocity dependence rather than the *implicit* one in the correlator. Noncompatible assumptions on the precise long-time behavior of the latter are nevertheless believed to bring about the contradicting results for that very leading order in relative velocity of the friction force. While Intravaia *et al.*, for instance, assume a power-law decay of correlations for very large times [2], the Markovian approach presupposes exponential decay of correlations on all time scales [6]. This large-time behavior strongly influences the low-frequency contributions to quantum friction, which are the ones most sensitive to the *explicit*, Doppler-shift-like, corrections in Eq. (15).

While *not* lending our voice to either of the contradicting assumptions, we solely focus on the fact that the Markov approach—in contrast to the generalized fluctuation-dissipation approach—does not only render a prediction for dynamical corrections to the static Casimir-Polder force, but moreover predicts dynamical corrections on the level of the internal dynamics of the atom, associated with the implicit velocity dependence of that force. The latter can be probed spectroscopically—which, though challenging, is less demanding than a force measurement. Hence, the question whether the Markov approximation is legitimate for a Casimir-Polder setup subject to relative motion may in principle be answered by means of spectroscopy. The remainder of this work focuses on exactly that venture.

III. RESULTS

In order to arrive at physical predictions, we now make use of the explicit nonretarded half-space Green's function (see, for example, Ref. [16])

$$\mathbf{G}^\mathrm{HS}(\mathbf{r},\mathbf{r}',\omega) = \frac{r_p(\omega)c^2}{8\pi^2\omega^2}\int_0^{2\pi}d\phi\int_0^\infty d\kappa\kappa^2 \times e^{i\mathbf{k}_\parallel\cdot(\mathbf{r}_\parallel-\mathbf{r}'_\parallel)}e^{-\kappa(z+z')}\mathbf{a}\otimes\mathbf{a}, \tag{17}$$

where $\mathbf{a}=(\cos\phi,\sin\phi,i)$ and $r_p(\omega)=\frac{\varepsilon(\omega)-1}{\varepsilon(\omega)+1}$ is the nonretarded limit of the Fresnel reflection coefficient for p-polarized (transverse magnetic) radiation of frequency ω incident upon a nonmagnetic $[\mu(\mathbf{r},\omega)=1]$ half-space of permittivity $\varepsilon(\omega)$. We have written the frequency integral in Eq. (17) in polar coordinates $\mathbf{k}_\parallel=(\kappa\cos\phi,\kappa\sin\phi)$. Defining a weighted squared dipole moment $d_{nk}^{2(\phi)}\equiv\mathbf{d}_{nk}\cdot[\mathbf{a}\otimes\mathbf{a}]\cdot\mathbf{d}_{kn}$ and inserting Eq. (17) into Eq. (14) with $\mathbf{G}=\mathbf{G}^\mathrm{HS}$ and making

use of the the Heaviside step function $\Theta(x)$ we find

$$C_{nk} = -\frac{i}{8\pi^2\epsilon_0\hbar}\int_0^\infty d\kappa\kappa^2\int_0^{2\pi} d\phi\Big[r_p(\omega'_{nk})\Theta[\mathrm{Re}(\omega'_{nk})] - \frac{1}{\pi}\int_0^\infty d\xi\,\frac{\omega'_{nk}r_p(i\xi)}{\xi^2+\omega'^2_{nk}}\Big]e^{-2\kappa z}d^{2(\phi)}_{nk}, \quad (18)$$

which is our main result. Its detailed derivation (see the Appendix) proves that Eq. (18) is valid for either sign of $v_\perp$, as long as the component of velocity away from the interface is not too large, as then the atom would "remember" having emerged from inside the medium, where our model does not apply. We also note that, in practice, the argument $\mathrm{Re}[\omega'_{nk}]$ of the step function in Eq. (18) is dominated by ω_{nk}, because $\omega_{nk} \gg k_\parallel v_\parallel$. To see this we note that the $k_\parallel$ integral in Eq. (18) is effectively cut off at $\sim 1/z$. Then one can easily check that the resulting condition $\omega_{nk} \gg v_\parallel/z$ is comfortably satisfied for all nonrelativistic velocities and distances greater than a few nanometers. Equation (18) contains a remarkable amount of information—the decay rates and frequency shifts for an atom with any velocity vector $\mathbf{v}$ can be obtained from it simply by taking real and imaginary parts via Eqs. (13).

Physical insight can be gained from expanding our formula (18) in a Taylor series for low atomic velocities:

$$C^{\parallel\mathrm{res}}_{nk} \simeq \frac{-i}{32\pi\epsilon_0\hbar z^3}\Big[d^{(i)2}_{nk}r_p(\omega_{nk}) + \frac{3d^{(a)2}_{nk}v^2_\parallel}{8z^2}r''_p(\omega_{nk})\Big], \quad (19)$$

$$C^{\perp\mathrm{res}}_{nk} \simeq \frac{-id^{(i)2}_{nk}}{32\pi\epsilon_0\hbar z^3}\Big[r_p(\omega_{nk}) - \frac{3iv_\perp}{2z}r'_p(\omega_{nk})\Big], \quad (20)$$

where $d^{(i)2}_{nk}=d^2_{nk,x}+d^2_{nk,y}+2d^2_{nk,z}$ and $d^{(a)2}_{nk}=3d^2_{nk,x}+d^2_{nk,y}+4d^2_{nk,z}$ and the primes denote derivatives with respect to frequency. Here we have presented only the resonant part of the interaction since the nonresonant part is orders of magnitude smaller, as shown more explicitly later on.

If applied to parallel motion and a plasma-model medium, Eq. (19) exactly coincides with known results [17]. We immediately see from Eq. (19) [via Eq. (13)] that the lowest-order velocity-dependent corrections to the resonant level shifts $\delta\omega^\parallel_n$ and decay rates $\Gamma^\parallel_n$ for parallel motion are *quadratic* in the atomic velocity; in fact all odd-order terms vanish. This is expected given that the sign of the velocity should not matter for motion parallel to the surface, since the system is translationally invariant along those directions. Turning our attention to perpendicular motion, we observe from Eq. (20) that the leading velocity-dependent corrections are linear in the velocity. This is physically reasonable as the system is not translationally invariant along the direction perpendicular to the surface, so that changing the sign of the velocity in that direction *should* matter. Note that the vanishing of all even orders in velocity in the case of parallel motion is by no means a contradiction to the fact that the friction force [Eq. (15)] must be odd in relative velocity. As mentioned when this force was introduced, its leading-order-in-$\mathbf{v}$ contribution does *not* stem from the internal dynamics of the atom, i.e., the shifts and rates we studied in this section. Instead, leading-order dynamical contributions to the friction force rather stem from an explicit, Doppler-shift-like $\mathbf{v}$ dependence attributed to the distance $\mathbf{r}_A - \mathbf{r}'_A$ traveled by the atom during emission and reabsorption of a photon.

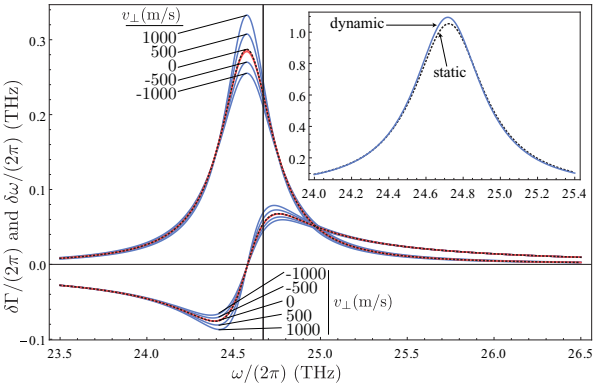

FIG. 2. Dependence of shifts $\delta\omega$ and decay rates Γ (relative to the respective free-space values) on possible atomic transition frequencies of a ^{133}Cs atom moving parallel (red) or perpendicular (blue) to a sapphire surface. The actual $6D_{3/2} \to 7P_{1/2}$ transition is indicated by the vertical axis. The parameters describing the surface and the atom are $z_A = 10$ nm; $v = \pm 500, \pm 1000$ m/s, $\eta = 2.71, \omega_T = 1.56 \times 10^{14}$ s^{-1}, $\omega_P = 1.2\omega_T$, $\gamma = 0.02\omega_T$, and $d = 5.85 \times 10^{-29}$ Cm and isotropic. We also include the static shifts and rates as dashed lines. The vertical line marks the actual transition frequency. The inset shows the emission-line profile for static (dashed) and moving (blue) atoms at $v_\perp = 500$ m/s after averaging over 5 nm $< z_A <$ 1 μm. For parallel motion the corrections are much smaller than for the perpendicular one and have no visible effect on the line profile.

IV. EXPERIMENTAL RELEVANCE

As a concrete example, consider ^{133}Cs whose far infrared $6D_{3/2} \to 7P_{1/2}$ transition is near resonant with the 12.21-μm phononic resonance of ordinary sapphire [18] which strongly enhances resonant Casimir-Polder effects. We describe the sapphire with a dominant-resonance Drude-Lorentz model, $\varepsilon(\omega) = \eta[1 - \omega_P^2/(\omega^2 - \omega_T^2 + i\gamma\omega)]$, where ω_P is the plasma frequency, ω_T is an absorption line frequency, γ is the damping parameter, and η accounts for the small background stemming from other atomic transitions. By means of Eq. (18) we can now determine the velocity-dependent shifts and rates corresponding to this ^{133}Cs transition in front of a sapphire surface. In Fig. 2 we plot the dependence of these shifts and rates on the atomic transition frequency for a selection of center-of-mass velocities. For parallel motion the dynamical corrections are much smaller than those for perpendicular motion. Hence, the inset in Fig. 2 depicts a spatially averaged (5 nm $< z_A <$ 1 μm) profile of the mentioned emission line—as, e.g., obtained by evanescent-wave spectroscopy—of atoms moving *perpendicularly towards* the surface at 500 m/s. Compared to the static profile it is slightly shifted and clearly more peaked. An observation of the latter effect is demanding but much more in reach than measurement of quantum friction forces. Similar experiments have already been carried out in order to measure the static Casimir-Polder shift [19]. In Fig. 3 we show the velocity dependence of the decay rate for a ^{133}Cs atom moving arbitrarily with respect to the sapphire surface.

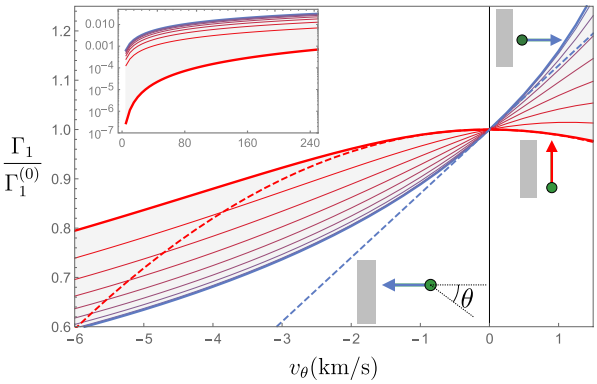

FIG. 3. Velocity dependence of the decay rate for parallel (thick red line, $\theta = \pm\pi/2$) and perpendicular (thick blue line, $\theta = 0, \pi$) motion of a ^{133}Cs atom in front of sapphire in units of the static decay rate $\Gamma_1^{(0)}$, alongside the leading-order-in-v expressions (dashed lines, with the parallel motion asymptote being barely distinguishable from the exact result at this scale). The thin lines between these extremal cases are for intermediate $0 < \theta < \pi/2$ evenly spaced in steps of $\pi/16$. All parameters chosen here are the same as in Fig. 2, and the transition frequency is taken as ω_L as indicated in Fig. 2. Inset: Detail of low-velocity region.

The nonresonant shifts and rates are a factor of $(\omega_P^2 + \omega_T^2)^{1/2}/\gamma \approx 100$ smaller than the resonant shifts for any realistic choice of parameters, meaning that we can safely ignore them here. The known static, resonant, Casimir-Polder shifts and rates emerge from the terms zero order in velocity in Eqs. (19) and (20). For an atom whose dipole moment is aligned along the positive **z** direction they read

$$\delta\omega^{(0)}_{n,\Omega_+} = \frac{d_z^2}{16\pi\epsilon_0\hbar}\frac{\eta}{(\eta+1)}\frac{\omega_p^2}{\omega_L\gamma}\frac{1}{z_A^3}, \tag{21}$$

$$\Gamma^{(0)}_{n,L} = \frac{d_z^2}{4\pi\epsilon_0\hbar}\frac{\eta}{(\eta+1)}\frac{\omega_p^2}{\omega_L\gamma}\frac{1}{z_A^3}, \tag{22}$$

when evaluated at their respective maxima Ω_+ and ω_L (see Table I) and taken at leading order in $\gamma \ll \omega_T$.

In Table I we summarize the lowest-order velocity-dependent contributions to the level shifts and decay rates, expressed as ratios to the static quantities (21) and (22). One can estimate the radius of convergence of the Taylor expansion by finding the ratios of successive orders. So from Table I one can see that the series converge for $v_{\parallel,\perp} \lesssim \gamma z_A \approx 1$ THz $\times$ 1 nm $= 10^3$ m/s. Typical velocities of atomic beams generated through thermal effusion are in the range 1×10^2–1×10^3 m/s (see, for example, Ref. [20]), meaning that even the simple asymptotic formulas in Table I are immediately relevant to experiment.

TABLE I. Leading-order contributions $\delta\omega_n^{loc}$ and Γ_n^{loc} to resonant level shifts and rates for an atom moving with velocity $v < \gamma z_A$ next to a surface, with its dipole moment aligned along the positive **z** direction. We have reported only the leading terms in γ since the next terms will be smaller by a similar factor as the nonresonant parts, which we have ignored here. Each quantity is evaluated at the maximal points of the static quantities; that is, decay rates are evaluated at $\omega_L = \sqrt{\eta\omega_P^2/(\eta+1) + \omega_T^2}$ and level shifts at $\Omega_+ = \omega_L + \gamma/2$.

	Perpendicular motion	Parallel motion
$\delta\omega_n^{loc}/\delta\omega_{n,\Omega_+}^{(0)}$	$\pm\frac{3v_\perp}{\gamma z_A}$	$-\frac{3v_\parallel^2}{\gamma^2 z_A^2}$
$\Gamma_n^{loc}/\Gamma_{n,L}^{(0)}$	$\frac{3v_\perp}{\gamma z_A}$	$-\frac{6v_\parallel^2}{\gamma^2 z_A^2}$

Finally, let us discuss our assumptions and associated errors. Nonrelativistic ($v/c \simeq 1 \times 10^{-5}$), nonretarded ($\omega_T z/c \simeq 1 \times 10^{-3}$), and single-reflection ($d^2\omega_T^2/\hbar\varepsilon_0 c^3 \simeq 1 \times 10^{-8}$) approximations lead to a relative error of about 1×10^{-3}, which is not detectable for the class of experiments we compare to here. The Born-Oppenheimer and Markov approximations assume separation of field autocorrelation time, $\tau_F = \gamma^{-1}$, internal atomic time scales, $\tau_A = \Gamma^{-1}$, and center-of-mass time scales, τ_C, respectively. The significant difference between the masses of the electron and the nucleus causes τ_C to clearly separate from internal atomic as well as field time scales ($\tau_C \gg \tau_A, \tau_F$). However, the separation of the latter ($\tau_A \gg \tau_F$) strongly depends on z_A. The proposed experiment may hence serve to confirm or refute the applicability of the Markov approximation in this crossover regime. Finally, finite temperature enhances both static and dynamic effects by a factor $n(\omega_A) + 1$, where $n(\omega_A)$ is the thermal occupation number of the mode ω_A corresponding to the atomic transition of interest. For the aforementioned transition of ^{133}Cs at room temperature, $n(\omega_A) \lesssim 0.02$.

V. SUMMARY

Here we have presented spectroscopically accessible analytical predictions of the dynamical corrections to the internal structure of an atom as it moves in an arbitrary direction near a surface. We have obtained the general formula (18) that gives the full set of level shifts and decay rates for an obliquely moving, possibly excited, atom near a half-space with results shown in Fig. 3. Our asymptotic results show that the relevant expansion parameter for small velocities is $v/(\gamma z_A)$, which is large compared to, for example, v/c or $v/(\omega_T z_A)$. This, alongside the fact that the results we have presented for perpendicular motion are linear in this parameter (in contrast to the quadratic dependence for parallel motion), means that these quantities are larger than previously thought, and therefore more easily measurable. In addition to being a velocity-dependent vacuum effect in its own right, our results constitute a testable prediction related to the less-accessible phenomenon of quantum friction. Our results represent a test-bed for the applicability of the Markov approximation in this setting. Refuting Markovianity by experiments would rule out one of the contradicting standpoints in the quantum friction debate.

ACKNOWLEDGMENTS

We would like to thank D.A.R. Dalvit, M.B. Farías, S. Scheel, and B. von Issendorff for discussions. This work was supported by the DFG (Grants No. BU 1803/3-1476 and No. GRK 2079/1) and the Freiburg Institute for Advanced Studies.

APPENDIX: DERIVATION OF EQ. (18)

Starting with the Heisenberg coefficients (6), substituting the nonretarded scattering Green's function for a half-space (7), and performing the κ integration, one arrives at

$$C_{nk} = \frac{1}{4\pi^3\hbar\varepsilon_0}\int_0^T d\tau \int_0^\infty d\omega \int_0^{2\pi} d\phi\, \boldsymbol{d}_{nk}^{(\phi)2}\,\mathrm{Im}r_\mathrm{p}(\omega)e^{-i(\omega-\omega_{nk})\tau}(2z_\mathrm{A} - v\tau\cos\theta - iv\tau\sin\theta\cos\phi)^{-3}. \tag{A1}$$

Here, without loss of generality, the coordinate system is chosen such that the y component of the atom's velocity is zero. Expanding the denominator of Eq. (13) in the unitless parameter $s = v\tau/2z_\mathrm{A}$ around zero and abbreviating $f_{\phi,\theta} = \cos\theta + i\sin\theta\cos\phi$ yields

$$C_{nk} = \frac{1}{64\pi^3\hbar\varepsilon_0 z_\mathrm{A}^3}\int_0^T d\tau \int_0^\infty d\omega \int_0^{2\pi} d\phi\, \boldsymbol{d}_{nk}^{(\phi)2}\mathrm{Im}r_\mathrm{p}(\omega)e^{-i(\omega-\omega_{nk})\tau}\sum_{j=0}^\infty \frac{(j+2)!}{j!}s^j f_{\phi,\theta}^j. \tag{A2}$$

Due to the oscillating nature of the integrand, the latter does not contribute to the integral for $\tau \gg \omega_{nk}$. Hence, the domain where the above series is convergent, i.e., for $v\omega_{nk} \ll 2z_\mathrm{A}$, matches the domain where the integrand contributes. The powers of τ can be rewritten as derivatives with respect to ω which, via partial integration, may be shifted onto the reflection coefficient $r_\mathrm{p}(\omega)$. Afterwards, the τ integral can be solved, giving

$$C_{nk} = \frac{1}{64\pi^3\hbar\varepsilon_0 z_\mathrm{A}^3}\sum_{j=0}^\infty \frac{(j+2)!}{j!}\int_0^\infty d\omega \int_0^{2\pi} d\phi\, \boldsymbol{d}_{nk}^{(\phi)2}\mathrm{Im}r_\mathrm{p}^{(j)}(\omega)\left(-\frac{ivf_{\phi,\theta}}{2z_\mathrm{A}}\right)^j\left[\pi\delta(\omega-\omega_{nk}) - i\mathcal{P}\frac{1}{\omega-\omega_{nk}}\right]. \tag{A3}$$

Carrying out the complex-frequency integration separates resonant (pole) and nonresonant contributions:

$$C_{nk}^\mathrm{res} = -\frac{i}{64\pi^2\hbar\varepsilon_0 z_\mathrm{A}^3}\sum_{j=0}^\infty \frac{(j+2)!}{j!}\int_0^{2\pi} d\phi\, \boldsymbol{d}_{nk}^{(\phi)2}\left(-\frac{ivf_{\phi,\theta}}{2z_\mathrm{A}}\right)^j r_\mathrm{p}^{(j)}(\omega_{nk}), \tag{A4}$$

$$C_{nk}^\mathrm{nres} = \frac{i}{128\pi^3\hbar\varepsilon_0 z_\mathrm{A}^3}\sum_{j=0}^\infty (j+2)!\int_0^{2\pi} d\phi\, \boldsymbol{d}_{nk}^{(\phi)2}\left(\frac{ivf_{\phi,\theta}}{2z_\mathrm{A}}\right)^j\int_0^\infty d\xi\, \frac{(\omega_{nk}+i\xi)^{(j+1)} + (\omega_{nk}-i\xi)^{(j+1)}}{(\omega_{nk}^2+\xi^2)^{(j+1)}}r_\mathrm{p}(i\xi). \tag{A5}$$

This can be rewritten as

$$C_{nk}^\mathrm{res} = -\frac{i\,\Theta(\omega_{nk})}{8\pi^2\hbar\varepsilon_0}\int_0^{2\pi} d\phi \int_0^\infty d\kappa\kappa^2 e^{-2\kappa z_\mathrm{A}}\boldsymbol{d}_{nk}^{(\phi)2}r_\mathrm{p}(\omega'_{nk}), \tag{A6}$$

and

$$C_{nk}^\mathrm{nres} = \frac{i}{8\pi^3\hbar\varepsilon_0}\int_0^{2\pi} d\phi \int_0^\infty d\kappa\kappa^2 e^{-2\kappa z_\mathrm{A}}\boldsymbol{d}_{nk}^{(\phi)2}\int_0^\infty d\xi\, \frac{\omega'_{nk}r_\mathrm{p}(i\xi)}{\omega'^2_{nk}+\xi^2}. \tag{A7}$$

The above derivation demonstrates that Eq. (18) is valid for either sign of $v_\perp$, as long as the component of velocity away from the interface is not too large—more precisely as long as $v\omega_{nk} \ll 2z_\mathrm{A}$.

[1] H. B. G. Casimir and D. Polder, Phys. Rev. **73**, 360 (1948).
[2] F. Intravaia, R. O. Behunin, and D. A. R. Dalvit, Phys. Rev. A **89**, 050101 (2014).
[3] J. S. Høye, I. Brevik, and K. A. Milton, J. Phys. A Math. Theor. **48**, 365004 (2015).
[4] B. Persson and A. Volokitin, J. Chem. Phys. **103**, 8679 (1995).
[5] W. L. Schaich and J. Harris, J. Phys. F **11**, 65 (1981).
[6] S. Scheel and S. Y. Buhmann, Phys. Rev. A **80**, 042902 (2009).
[7] T. G. Philbin and U. Leonhardt, New J. Phys. **11**, 033035 (2009).
[8] F. Intravaia, V. Mkrtchian, S. Buhmann, S. Scheel, D. A. R. Dalvit, and C. Henkel, J. Phys. Condens. Matter **27**, 214020 (2015).
[9] G. Barton, New J. Phys. **12**, 113045 (2010).
[10] G. V. Dedkov and A. A. Kyasov, Tech. Phys. Lett. **28**, 346 (2002).
[11] F. Sorrentino, A. Alberti, G. Ferrari, V. V. Ivanov, N. Poli, M. Schioppo, and G. M. Tino, Phys. Rev. A **79**, 013409 (2009).
[12] M. G. Tarallo, A. Alberti, N. Poli, M. L. Chiofalo, F.-Y. Wang, and G. M. Tino, Phys. Rev. A **86**, 033615 (2012).
[13] T. Gruner and D.-G. Welsch, Phys. Rev. A **53**, 1818 (1996).
[14] S. Scheel and S. Y. Buhmann, Acta Physica Slovaca **58**, 675 (2008).
[15] S. Y. Buhmann, L. Knöll, D.-G. Welsch, and H. T. Dung, Phys. Rev. A **70**, 052117 (2004).
[16] C.-T. Tai, *Dyadic Green Functions in Electromagnetic Theory* (IEEE, Piscataway, NJ, 1994).
[17] T. L. Ferrell and R. H. Ritchie, Phys. Rev. A **21**, 1305 (1980).
[18] M. Fichet, F. Schuller, D. Bloch, and M. Ducloy, Phys. Rev. A **51**, 1553 (1995).
[19] M. Chevrollier, M. Fichet, M. Oria, G. Rahmat, D. Bloch, and M. Ducloy, J. Phys. II **2**, 631 (1992).
[20] *Atom Interferometry*, edited by P. R. Berman (Academic Press, San Diego, CA, 1997).

PHYSICAL REVIEW X **4,** 011029 (2014)

Probing Atom-Surface Interactions by Diffraction of Bose-Einstein Condensates

Helmar Bender, Christian Stehle, Claus Zimmermann, and Sebastian Slama[*]
Physikalisches Institut and Center for Collective Quantum Phenomena in LISA+, Universität Tübingen, Auf der Morgenstelle 14, D-72076 Tübingen, Germany

Johannes Fiedler, and Stefan Scheel
Institut für Physik, Universität Rostock, Universitätsplatz 3, D-18055 Rostock, Germany

Stefan Yoshi Buhmann[†]
Quantum Optics and Laser Science, Blackett Laboratory, Imperial College London, Prince Consort Road, London SW7 2AZ, United Kingdom

Valery N. Marachevsky[‡]
Department of Physics, Saint Petersburg State University, Ulianovskaya 1, Petrodvorets, 198504 St. Petersburg, Russia

(Received 8 May 2013; revised manuscript received 7 October 2013; published 27 February 2014)

In this article, we analyze the Casimir-Polder interaction of atoms with a solid grating and the repulsive interaction between the atoms and the grating in the presence of an external laser source. The Casimir-Polder potential is evaluated exactly in terms of Rayleigh reflection coefficients and via an approximate Hamaker approach. The laser-tuned repulsive interaction is given in terms of Rayleigh transmission coefficients. The combined potential landscape above the solid grating is probed locally by diffraction of Bose-Einstein condensates. Measured diffraction efficiencies reveal information about the shape of the potential landscape in agreement with the theory based on Rayleigh decompositions.

DOI: 10.1103/PhysRevX.4.011029

Subject Areas: Atomic and Molecular Physics, Nanophysics, Optics

The Casimir-Polder (CP) interaction is one of a class of examples where fluctuating electromagnetic fields give rise to (normally attractive) forces between matter [1,2]. For infinitely extended plane surfaces, CP forces can be readily calculated from the polarizability of the atom and the dielectric properties of the substrate [3] and have been measured in a number of experiments [4–11]. However, of particular importance is the influence of the surface geometry [12–14]. Nontrivial geometries can have a large impact on the exact force profile and can potentially be used for manipulating the closely related Casimir forces [15]. The possibility of tailoring the Casimir force is also of importance for applications in the microelectromechanical systems (MEMS) and nanoelectromechanical systems (NEMS) industry, where it is one of the limiting factors in the miniaturization of micromachines and microsensors [16].

[*]sebastian.slama@uni-tuebingen.de
[†]s.buhmann@imperial.ac.uk
[‡]maraval@mail.ru

One class of nontrivial geometries that have been investigated theoretically, both in the framework of atom-surface and surface-surface interactions, are periodic structures such as gratings [17–19]. Please note that the reflection of fast atoms from crystalline planar surfaces can also be understood as diffraction caused by the periodic shape of the attractive Casimir-Polder interaction. Corresponding experiments with hot atomic beams were reported some time ago [20]. In recent experiments, CP forces above gratings were measured by different methods [21–25]. In those experiments, the power-law coefficients describing the CP potential in the electrostatic and in the retarded regimes were determined. Recently, theoretical proposals have been put forward to measure the CP potential at corrugated surfaces with Bose-Einstein condensates [26].

In this article, we present both theoretical simulations and experimental measurements of the potential landscape for a single atom that is positioned at a submicron distance from a grating of metal nanowires. The potential landscape is composed of an attractive contribution due to the CP force and a repulsive contribution due to an evanescent light wave (EW) at the surface. The quantitative agreement between theory and experiment in the absence of free parameters demonstrates that complex surface-assisted

potentials resulting from a combination of geometric structure and tunable evanescent laser potentials are now well understood both theoretically and experimentally. Whereas in previous experiments the measured values of the CP potential represent only an average over the complicated potential landscape above the structures, in this work we fully account for the dependence of the potential on the lateral position above such a surface.

The evanescent light wave is generated by the internal total reflection of a laser beam in the dielectric substrate carrying the grating. A repulsion from the surface is achieved by a laser ($\lambda = 765$ nm) that is blue detuned with respect to the transition frequency of the atoms (Rb: $\lambda_0 = 780$ nm). Recently, we used this setup and enhanced the evanescent waves by exciting surface plasmon polaritons at the surface [27]. In a similar way, nanoobjects have been optically trapped in a patterned light field above a structured metallic film [28]. Here, we exploit the fact that the exact shape of the total potential landscape can be tuned by the strength of the optical dipole potential via the laser intensity. This allows us to acquire spatially resolved information of the surface potentials: Fig. 1 shows a simulation of the potential landscape for a typical laser power of $P = 211$ mW, including the optical dipole potential of the evanescent wave and the Casimir-Polder potential.

The CP potential with its strong attraction towards the gold stripes and the repulsive EW potential with its maximal repulsion above the sapphire surface combine to a periodic potential landscape that resembles a chain of hills in front of the grating surface with valleys that lead to the centers of the gold stripes. The heights and widths of the hills depend on the laser power (Fig. 2), with larger powers resulting in higher and broader hills.

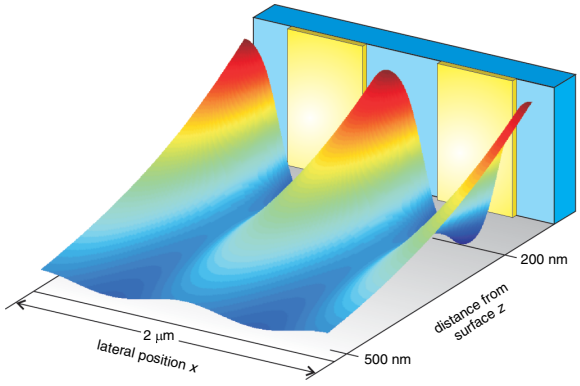

FIG. 1 Simulation of the combined potential landscape, including the evanescent-wave potential and Casimir-Polder landscape as calculated from Eqs. (1) and (2) for a laser power of $P = 211$ mW. The repulsive evanescent-wave potential is generated by a laser beam that is reflected by the total internal reflection in the substrate. The gold stripes weaken the intensity of the evanescent wave and thus modulate the strength of the repulsion. The attractive Casimir-Polder potential reaches its maximum value above the gold stripes and further increases this modulation. At a distance of $z = 200$ nm, the potential is laterally modulated with an amplitude of $\Delta E/k_B = 14$ μK.

The EW potential

$$U_{\mathrm{EW}}(\boldsymbol{r}) = \sum_{i=1,2} \frac{|\boldsymbol{d}_i|^2 |\boldsymbol{E}(\boldsymbol{r})|^2}{3\hbar\Delta_i} \tag{1}$$

is the potential due to the external monochromatic electric field $\boldsymbol{E}$ with its frequency ω close to a specific set of atomic transitions of Rb with dipole matrix elements $\boldsymbol{d}_i$ and detunings $\Delta_i = \omega - \omega_i$. It is dominated by these atomic transitions and the transmission properties of the grating at a single laser frequency ω. The EW potential is expressed in terms of Rayleigh transmission coefficients in the Appendix.

In the simulations, the ground-state CP potential of the Rb atoms is calculated to lowest order in their isotropic ground-state polarizability as [29]

$$U_{\mathrm{CP}}(\boldsymbol{r}) = \frac{\hbar\mu_0}{2\pi} \int_0^\infty d\xi \xi^2 \alpha(\mathrm{i}\xi) \mathrm{Tr}\mathbf{G}^{(1)}(\boldsymbol{r}, \boldsymbol{r}, \mathrm{i}\xi). \tag{2}$$

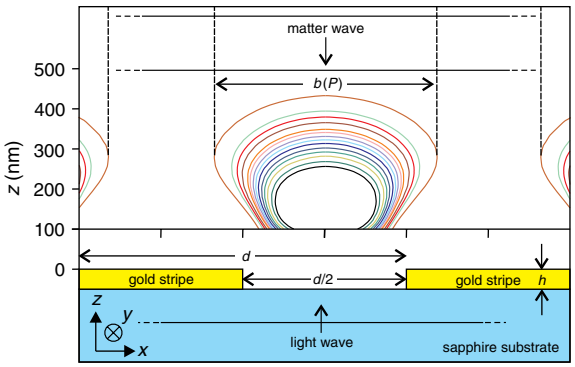

FIG. 2 Geometry of the metal grating. Approximately 200 gold stripes with $h = 50$ nm height and 500 nm width are deposited on a sapphire substrate and form a grating with a $d = 1$ μm period. A laser beam impinges under an angle of $\theta = 35.50°$ from the sapphire substrate onto the interface to vacuum (respectively, gold) with its k vector in the (y, z) plane. The laser beam is internally reflected and generates an evanescent wave. The combination of the repulsive potential due to the evanescent wave with the Casimir-Polder interaction forms a potential landscape above the grating. The colored lines (black to brown, corresponding to laser powers $P = 120$, 126, 133, 138, 144, 151, 156, 162, 169, 174, 187, 198, 211, 247 mW) are simulations of equipotential lines using exact theory based on Rayleigh decompositions for a ^{87}Rb atom moving towards the surface with velocity $v = 3.4$ cm/s. From those, we deduce the width $b(P)$ where atoms are reflected. The two horizontal lines at the top represent the incoming matter wave and are drawn at a distance given by the de Broglie wavelength $\lambda_{\mathrm{dB}} = \frac{2\pi\hbar}{mv} = 135$ nm, with atomic mass m.

Here, the polarizability $\alpha(i\xi)$ is approximated by an eight-line model (see the Appendix), and $\mathbf{G}^{(1)}$ is the scattering Green tensor, which, for the grating structure in Fig. 2, can be given as a Rayleigh decomposition in terms of Rayleigh reflection coefficients. Because of the integral over all imaginary frequencies as a result of the vacuum fluctuations of the electromagnetic field, the CP potential depends on all atomic transition frequencies and all eigenfrequencies of the macroscopic system (grating).

From the theoretical point of view, it is quite interesting to perform a comparison of an exact approach to the calculation of CP potentials near gratings with an approximate Hamaker approach [30,31], which is based on a pairwise summation of van der Waals forces between volume elements of one body with those of the other. However, such an approach neglects many-body interactions that can lead to wrong results, in particular, for complex geometric structures [32,33]. The nonadditivity of Casimir forces induced by many-body interactions [34] implies that the position, shape, and material dependencies of such forces are intertwined in a complicated way. Nevertheless, the Hamaker approach is widely used in applications such as colloid science and biology [35]. The most prominent example is the adhesive force of gecko feet [36].

Surprisingly, so far not a single experiment has addressed the accuracy of the Hamaker approach in atom-surface interactions, despite there being a large amount of work that has addressed deviations of the proximity force approximation (PFA) from the exact calculations, taking diffraction into account in the context of surface-surface interactions [33,37–41]. In our case, the CP potential contribution to the combined potential (CP + EW) is relevant at given separations, and one can discern the difference between the result of exact simulation of the Casimir-Polder potential expressed in terms of Rayleigh coefficients and the result of an approximate Hamaker approach.

The CP potential in the Hamaker approach is calculated in the local-field-corrected first-order Born approximation as

$$\mathbf{G}^{(1)}(\boldsymbol{r},\boldsymbol{r},\omega) = \frac{\omega^2}{c^2}\frac{\chi(\omega)}{1+\chi(\omega)/3} \times \int \mathrm{d}^3 s \mathbf{R}^{(0)}(\boldsymbol{r},\boldsymbol{s},\omega)\mathbf{R}^{(0)}(\boldsymbol{s},\boldsymbol{r},\omega), \quad (3)$$

where $\mathbf{R}^{(0)}(\boldsymbol{r},\boldsymbol{s},\omega)$ is the regular part of the Green tensor, $\chi(\omega)$ is the susceptibility of the gold stripes, and the integration extends over the total volume V of the grating. Details of all the calculations are contained in the Appendix.

Experimentally, we probe the width b of the reflection zones in Fig. 2 by reflecting Bose-Einstein condensates (BEC) from the surface. The experiment is carried out as follows. A BEC is prepared in a magnetic trap at a distance of several hundred μm from the grating and accelerated such that it moves towards the surface with a constant velocity $v = 3.4$ cm/s. Thereby, the cloud is ballistically expanding and transforms its interaction energy in velocity spread. For that reason, interaction effects do not play a role during reflection from the surface. The experimental details of this preparation are contained in the Appendix. The atoms reflect from the surface only at those lateral positions where the potential height exceeds the kinetic energy of the atoms. This happens in a zone with width b in each lattice site (see Fig. 2). Note that considerable quantum reflection of Rb atoms at the CP potential of a solid surface would require atomic velocities below a few mm/s [9]. For the velocity of $v = 3.4$ cm/s, it is completely negligible. By tuning the laser power, the reflection zone width b is changed and different distances from the surface are probed. Each atom of the BEC approaching the surface constitutes a matter wave with a lateral extension that is given by the size of the BEC on the order of several tens of microns. This size is much larger than the grating period; thus, the matter wave is diffracted from the periodic structure of reflection zones in a direction x of period d.

In a simplified model that neglects the curvature of the equipotential lines, we consider reflection of the matter wave from the same reflection zones of width b as for a single atom. The resulting atomic momentum distribution in the far field is analogous to Fraunhofer diffraction. For an arrangement of rectangular stripes as shown in Fig. 2, the occupation p_n of diffraction order n (normalized to p_0) is given by

$$p_n = \left|\mathrm{sinc}\left(\pi n \cdot \frac{b}{d}\right)\right|^2. \quad (4)$$

It depends only on the ratio b/d. This is illustrated in the theoretical curves in Fig. 3, where we plot the relative occupations (normalized to $\sum p_n$) of the diffraction orders as determined from Eq. (4). In the limit of $b/d \to 0$, the situation resembles the emission of waves from a chain of pointlike sources, in which all diffraction orders are equally occupied. In contrast, the limit $b/d \to 1$ corresponds to a reflection from a surface with a constant density profile. Here, the atomic cloud remains fully in the diffraction order $n = 0$.

In the experiment, we analyze the relative occupation of individual diffraction orders by measuring the momentum distribution $p_x = \hbar k_x$ of the atoms. This is done by taking an absorption image of the cloud after ballistic expansion for a time of flight of $t_{\mathrm{tof}} = 21.5$ ms after reflection from the surface. A typical image is shown in the inset of Fig. 3. From the image, the atom numbers N_n corresponding to diffraction orders n with momentum $p_{x,n} = n\hbar\frac{2\pi}{d}$ are counted within the yellow boxes and are scaled to the total number of reflected atoms. This provides us data

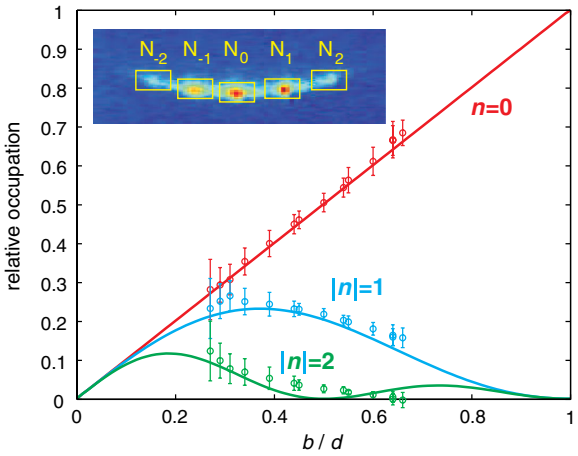

FIG. 3 Matter-wave diffraction. Relative occupation of diffraction orders as a function of the relative width of the reflection zone b/d. The curves are obtained from Eq. (4). Data points represent the measured occupation of diffraction orders as shown in the inset. The horizontal position of each triple of data points (its value b/d) is obtained from a fit to the theoretical curves.

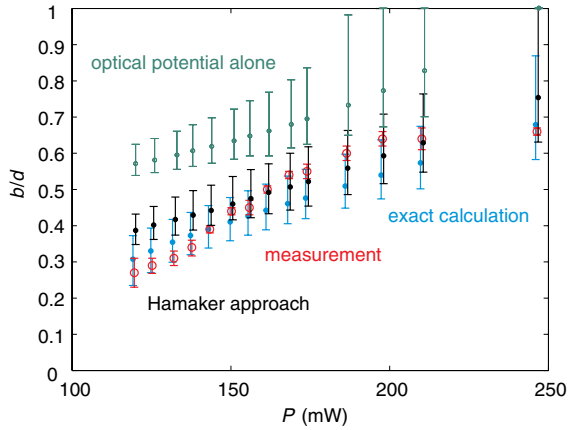

FIG. 4 Comparison between theory and experiment. Width of the reflection zone b/d versus laser power P. Red circles are experimental data points obtained from the fit in Fig. 3. Error bars of the data points are due to the combined statistic and systematic uncertainties in the atom-number measurement. Blue dots show the theoretical values taken from the equipotential lines in Fig. 2 and represent the result of the exact calculation based on Rayleigh decompositions. Black points are the corresponding results based on a Hamaker approach. Green points stem from a simulation of the optical potential alone, neglecting any influence of the Casimir-Polder potential. Error bars of the theoretical points represent the systematic error due to the uncertainty in the laser intensity at the surface $\Delta I = \pm 5\%$ and the velocity of the atoms $\Delta v = \pm 0.3$ cm/s. Please note that the data points are horizontally shifted one line width ($\lesssim 1$ mW) for clarity.

triples of relative populations of diffraction orders $n = 0$, ± 1, ± 2 for each value of laser power. The populations for $n \neq 0$ are averaged over the populations of the orders with $\pm n$. Each triple is individually fitted by the theoretical curves in Fig. 3 and is thus attributed a certain value of b/d.

Although all data points coincide with the corresponding theory curves very well, it is notable that the model used is valid only for the lower laser powers used, corresponding to the small values of b/d. The model is based on amplitude modulation only and thus neglects phase modulation of the reflected matter wave. As shown in the Appendix, this approximation is valid for laser powers $P \lesssim 140$ mW, whereas phase imprinting becomes an important effect for the large laser powers used. Because a complete calculation of the diffraction problem is more difficult than electromagnetic diffraction and would not affect the overall meaning of the results presented here, we restrict the conclusions of this work to the data points with small laser power.

The fitted values of b/d are now compared with the theoretical prediction that is accessible from the width of the equipotential lines shown in Fig. 2. As can be seen in Fig. 4, the measured diffraction cannot be explained by the spatial modulation of the optical potential alone. Thus, the experiment is sensitive to the Casimir-Polder potential. Moreover, it can partly discriminate between different theoretical models: The data points agree with exact theory based on Rayleigh decompositions within their statistic and systematic errors. The Hamaker approach underestimates the strength of the Casimir-Polder potential. The corresponding values of b/d for low values of P in Fig. 4 are thus larger than the observed data points and deviate from them by more than 1 standard deviation. In the range of large P in Fig. 4, the optical potential dominates over the CP potential and reduces the difference between exact theory and the Hamaker model.

It is obvious from Fig. 4 that the functional profile of the data points differs from that of the simulations for laser powers $P \gtrsim 140$ mW. In particular, the value of b/d of the measured data points saturates for large laser powers. This observation is caused by the growing influence of phase imprinting for increasing laser power, as shown in the Appendix. This leads to a principally different behavior of the scattered field, which manifests e.g., in the absence of missing orders [42]. Qualitatively, for high reflectivity, the assumption of instantaneous reflection is not justified. Instead, the interaction time of the atoms with the surface potential and the strength of the latter depend on the lateral position x; i.e., depending on the lateral position, the matter wave acquires a different phase. A periodic potential imprints a phase that leads to a substantial diffraction even when all atoms are reflected and thus simulates a saturation of b/d for large laser powers [43–45].

It is worth considering the possible influence of surface potential generated by Rb atoms adsorbed to our grating. As reported in Ref. [46], surface potentials are primarily

generated on metal surfaces such as the grating bars. The authors report an electric field of 1 μV/cm per adsorbed atom at a distance $z = 10\ \mu$m, with a $1/z^{2.3}$ distance dependence, corresponding to roughly 0.1 V/m at a distance of 430 nm. At this distance, adsorbed atoms from a surface area of about $1\ \mu\text{m} \times 1\ \mu\text{m} = 1\ \mu\text{m}^2$ contribute to the field. The 2×10^5 atoms involved in a single run of the experiment are spread out over a cloud of dimensions $100\,\mu\text{m} \times 50\,\mu\text{m} = 5000\,\mu\text{m}^2$ so that $2 \times 10^5 \times (1/5000) \times (1/2) = 20$ atoms potentially impinge on this area, where the factor $1/2$ represents the filling factor of the grating. With the small sticking probability of 0.8% as observed in Ref. [47], 1600 atoms could accumulate in the relevant surface area in the course of 10000 runs of the experiment. This would lead to a total electric field of the order of 2×10^2 V/m, much smaller than the value of the evanescent laser field of about 3×10^4 V/m at the same distance calculated for a laser power of 247 mW. Alternative measurements [48] predict even smaller values of the electric fields due to adsorbed atoms.

In conclusion, we have experimentally probed surface potential landscapes that are composed of Casimir-Polder forces and optical dipole forces above metallic nanostructures. We have used matter-wave diffraction of Bose-Einstein condensates as a measuring tool, which, in principle, can be applied to arbitrary surfaces. Complementary to previous experiments in which spatial averages of the Casimir-Polder coefficients were determined, we obtain additional spatial information by analyzing the occupation of individual diffraction orders. Our data agree quantitatively with numerical calculations of the surface potentials (1) and (2) based on exact theory where potentials are expressed in terms of Rayleigh coefficients, whereas a Hamaker approach leads to incompatible results for low laser powers. The difference is so large that an experiment can distinguish between both approaches. From the theoretical point of view, the main result is the first comparison of exact theoretical results for atom-surface potentials above a structured surface (based on Rayleigh decompositions) and experimental data used to measure the structure of the potential landscape. The results open a wide range of possibilities for exact theoretical simulations and design of atomic-surface potentials in the vicinity of nanostructured and microstructured surfaces.

The fact that we understand these potentials very well is crucial for the design and realization of nanoscale surface traps for surface quantum optics experiments with cold atoms. Our analysis demonstrates the possibility to couple atoms to light near structured surfaces in a controlled way. Moreover, the metallic parts of the surface can give rise to spectrally broad surface plasmon resonances in the optical-frequency range. Related phonon polariton resonances in the infrared frequency range have e.g., led to the observation of repulsive Casimir-Polder forces of highly excited Cs atoms [49]. A plasmon-based repulsive Casimir-Polder force would give a perspective on fascinating scenarios for controlling CP forces [50] and for generating surface traps for cold atoms that do not require external magnetic or optical fields.

C. S. was supported by Carl-Zeiss Stiftung Baden-Württemberg. Support from the European Science Foundation (ESF) within the activity "New Trends and Applications of the Casimir Effect" is gratefully acknowledged. This work was financially supported by the UK EPSRC. The research leading to these results has received funding from the European Union Seventh Framework Programme (FP7-PEOPLE-2010-IRSES) under Grant Agreement No. PIRSES-GA-2010-268717. V. N. M was partially supported by the Saint Petersburg State University Grant No. 11.38.660.2013. Furthermore, we acknowledge support by the Deutsche Forschungsgemeinschaft within the European Collaborative Research program of the European Science Foundation.

APPENDIX

1. Simulation of the Casimir-Polder potential

The ground-state CP potential of an atom or molecule can be given as [29]

$$U_{\text{CP}}(\boldsymbol{r}) = \frac{\hbar\mu_0}{2\pi}\int_0^\infty d\xi\xi^2 \text{Tr}[\boldsymbol{\alpha}(\text{i}\xi)\cdot\mathbf{G}^{(1)}(\boldsymbol{r},\boldsymbol{r},\text{i}\xi)]. \quad \text{(A1)}$$

To allow for potentially anisotropic molecules, we have included the ground-state polarizability tensor $\boldsymbol{\alpha}(\text{i}\xi)$; $\mathbf{G}^{(1)}$ is the scattering Green tensor. We are neglecting thermal contributions to the CP force, which is a good approximation for the distances considered in this work. For the structure in Fig. 2, the scattering Green tensor can be given in a Rayleigh decomposition as

$$\begin{aligned}\mathbf{G}^{(1)}(\boldsymbol{r},\boldsymbol{r}',\omega) = \frac{\text{i}}{8\pi^2}\int_{-\pi/d}^{\pi/d}\text{d}k_x\sum_{m,n=-\infty}^{\infty}\int_{-\infty}^{\infty}\text{d}k_y \\ \times\sum_{\sigma,\sigma'=E,H}\frac{\text{e}^{\text{i}(k_x^m x - k_x^n x') + \text{i}k_y(y-y') + \text{i}(k_z^m z + k_z^n z')}}{k_z^n} \\ \times \boldsymbol{e}_{m+}^{\sigma}(k_x,k_y,\omega)R_{mn}^{\sigma\sigma'}(k_x,k_y,\omega)\boldsymbol{e}_{n-}^{\sigma'}(k_x,k_y,\omega).\end{aligned} \quad \text{(A2)}$$

Here, $\boldsymbol{k} = (k_x^m, k_y, k_z^m)$ is the wave vector; its x and z components read $k_x^m = k_x + mq$ ($q = 2\pi/d$: lattice vector of the grating) and $k_z^m = \sqrt{\omega^2/c^2 - (k_x^m)^2 - k_y^2}$, with Im $k_z^m > 0$. The polarization unit vectors for upward or downward moving waves are defined by

$$\boldsymbol{e}^{E}_{m\pm}(k_x,k_y,\omega)=\frac{c}{\omega\sqrt{\omega^2/c^2-k_y^2}}\begin{pmatrix}k_x^m k_y\\ k_y^2-\omega^2/c^2\\ \pm k_y k_z^m\end{pmatrix}, \quad \text{(A3)}$$

$$\boldsymbol{e}^{H}_{m\pm}(k_x,k_y,\omega)=\frac{1}{\sqrt{\omega^2/c^2-k_y^2}}\begin{pmatrix}\mp k_z^m\\ 0\\ k_x^m\end{pmatrix}. \quad \text{(A4)}$$

The latter are chosen such that the y components of the electric or magnetic fields vanish for $\sigma = H,\ E$. The Rayleigh reflection coefficients $R^{\sigma\sigma'}_{mn}(k_x,k_y,\omega)$ are calculated by numerically integrating the Maxwell equations within the grating ($0<z<h$) and imposing conditions of continuity at its upper (free-space) and lower (sapphire) boundaries [17]. They are even functions of k_y and obey the following symmetries: $R^{\sigma\sigma'}_{mn}(k_x,k_y,\mathrm{i}\xi)=\pm R^{\sigma\sigma'*}_{-m-n}(-k_x,k_y,\mathrm{i}\xi)$ and $R^{\sigma\sigma'}_{mn}(k_x,k_y,\mathrm{i}\xi)\beta^n_z=\pm R^{\sigma'\sigma*}_{-n-m}(k_x,k_y,\mathrm{i}\xi)\beta^m_z$, with $\beta^n_z=\sqrt{\xi^2/c^2+(k_x^n)^2+k_y^2}$, the sign $+$ for $\sigma\sigma'=EE,HH$, and the sign $-$ otherwise. Our theory is able to allow for anisotropic atoms or molecules. For a sufficiently anisotropic molecule, we find a repulsive CP potential in particular spatial locations, similar to the repulsive Casimir force predicted in Ref. [15] (see also Refs. [51–53]). Note that for the isotropic atoms used in the current experiment, $\boldsymbol{\alpha}=\alpha\mathbf{l}$ ($\mathbf{l}$: unit tensor), Eq. (A1) simplifies to Eq. (1) and our formalism reduces to that of Ref. [18].

2. Simulation of the evanescent-wave potential

The evanescent-wave potential is generated by an incoming wave of (free-space) wavelength $\lambda = 765$ nm, which impinges on the sapphire-grating interface at an incidence angle $\theta = 35.50° = 0.6196$ rad, with the plane of incidence being parallel to the grating bars. The components of the wave vector in the sapphire layer are hence $k_x^m=0$, $k_y=k\sin\theta=8.39\times10^6\ \mathrm{m}^{-1}$, $k_z^{0+}=k\cos\theta=1.18\times10^7\ \mathrm{m}^{-1}$ ($k=\mathrm{Re}n_{\mathrm{sapp}}\omega/c$, with $\mathrm{Re}n_{\mathrm{sapp}}=1.76$ and $\omega=2\pi c/\lambda=2.46\times10^{15}$ rad/s). The incoming field is polarized such that its component perpendicular to the grating vanishes; it can hence be written as $\boldsymbol{E}_{\mathrm{in}}(\boldsymbol{r})=E_{\mathrm{sapp}}\boldsymbol{e}^{E}_{0+}(0,k_y,\omega)\mathrm{e}^{\mathrm{i}(k_y y+k_z^{0+}z)}$. The field amplitude inside sapphire can be related to the respective laser power P_{sapp} and beam waist w_{sapp} via $\frac{1}{2}\epsilon_0 n_{\mathrm{sapp}}cE^2_{\mathrm{sapp}}=I_{\mathrm{sapp}}=P_{\mathrm{sapp}}/(2\pi w^2_{\mathrm{sapp}})$. The laser power is in turn related to its free-space value by $P_{\mathrm{sapp}}=T_{\text{free-space}\to\mathrm{sapp}}P_{\text{free-space}}$, where $T_{\text{free-space}\to\mathrm{sapp}}=0.88$ has been determined experimentally from a setup with symmetric light paths. The measured beam waist of 170 μm in free space results in an effective beam waist $w_{\mathrm{sapp}}=182.9$ μm in sapphire after transitions through the free-space–glass and glass-sapphire interfaces. After transmission through the grating, the external laser leads to a field

$$\boldsymbol{E}(\boldsymbol{r})=E_{\mathrm{sapp}}\sum_{n=-\infty}^{\infty}\sum_{\sigma=E,H}\mathrm{e}^{\mathrm{i}(nqx+k_y y)-\kappa_z^{n+}z}\times\boldsymbol{e}^{\sigma}_{n+}(nq,k_y,\omega)T^{\sigma E}_{n0}(0,k_y,\omega) \quad \text{(A5)}$$

with $\kappa_z^{n+}=\sqrt{k_y^2-\omega^2/c^2+n^2q^2}$, where the Rayleigh transmission coefficients $T^{\sigma\sigma'}_{mn}(k_x,k_y,\omega)$ are found from numerical integration in the same way as the respective reflection coefficients. When interacting with a Rb atom, this evanescent field generates an optical potential

$$\begin{aligned}U_{\mathrm{EW}}(\boldsymbol{r})&=\sum_{i=1,2}\frac{|\boldsymbol{d}_i|^2|\boldsymbol{E}(\boldsymbol{r})|^2}{3\hbar\Delta_i}\\&=\sum_{i=1,2}\frac{|\boldsymbol{d}_i|^2E^2_{\mathrm{sapp}}}{3\hbar\Delta_i}\\&\quad\times\sum_{m,n=-\infty}^{\infty}\sum_{\sigma,\sigma'=E,H}\mathrm{e}^{\mathrm{i}(m-n)qx-(\kappa_z^{m+}+\kappa_z^{n+*})z}\\&\quad\times\boldsymbol{e}^{\sigma}_{m+}(mq,k_y,\omega)\cdot\boldsymbol{e}^{\sigma'*}_{n+}(nq,k_y,\omega)\\&\quad\times T^{\sigma E}_{m0}(0,k_y,\omega)T^{\sigma' E*}_{n0}(0,k_y,\omega).\end{aligned} \quad \text{(A6)}$$

3. Details of calculations

The potential $U_{\mathrm{EW}}(\boldsymbol{r})$ (1) was evaluated using transition frequencies $\omega_1=2.37\times10^{15}$ rad/s, $\omega_2=2.41\times10^{15}$ rad/s and dipole-matrix elements $d_1=2.53\times10^{-29}$ Cm, $d_2=3.57\times10^{-29}$ Cm for the D_1 ($5^2S_{1/2}\to5^2P_{1/2}$) and D_2 ($5^2S_{1/2}\to5^2P_{3/2}$) lines of the isotropic Rb atom [54,55]; one can neglect the contribution of other transition lines in Eq. (1).

In the calculation of the CP potential (2), the polarizability

$$\alpha(i\omega)=\sum_{i=1}^{8}\frac{2\omega_i|\boldsymbol{d}_i|^2}{3\hbar(\omega_i^2+\omega^2)} \quad \text{(A7)}$$

for the isotropic Rb atom was evaluated within a model, taking into account eight transition frequencies [54]: $\omega_1=2.37\times10^{15}$ rad/s, $d_1=2.53\times10^{-29}$ Cm, $\omega_2=2.41\times10^{15}$ rad/s, $d_2=3.57\times10^{-29}$ Cm, $\omega_3=4.468\times10^{15}$ rad/s, $d_3=0.200\times10^{-29}$ Cm, $\omega_4=4.482\times10^{15}$ rad/s, $d_4=0.324\times10^{-29}$ Cm, $\omega_5=5.245\times10^{15}$ rad/s, $d_5=0.069\times10^{-29}$ Cm, $\omega_6=5.251\times10^{15}$ rad/s, $d_6=0.121\times10^{-29}$ Cm, $\omega_7=5.622\times10^{15}$ rad/s, $d_7=0.035\times10^{-29}$ Cm, $\omega_8=5.625\times10^{15}$ rad/s, $d_8=0.067\times10^{-29}$ Cm.

Distances in the range $\lambda_8\sim300\ \mathrm{nm}\lesssim z\lesssim\lambda_1\sim800\ \mathrm{nm}$ are in between the Casimir-Polder regime ($z\gg\lambda_i$) and the nonretarded van der Waals regime ($z\ll\lambda_i$) of the CP potential. In the range of separations $100\ \mathrm{nm}\le z\lesssim\lambda_i$ used in the calculations, the frequencies $\omega\lesssim\omega_i$ yield the leading contribution to the integral (2).

The numerical error in the evaluation of the combined potential (which is the sum of the Casimir-Polder and evanescent-wave potentials) is 0.1%. The number of Rayleigh coefficients used was selected to obtain the needed accuracy; $N = 30$ ($2N + 1$ terms in every Rayleigh expansion) is sufficient to obtain the potential with the required accuracy even at closest separations from the grating, as shown in Fig. 2.

4. Casimir-Polder potential using the Hamaker approach

The scattering Green tensor $\mathbf{G}^{(1)}(\boldsymbol{r},\boldsymbol{r},\omega)$ in Eq. (A1) can be expanded in a Born series with respect to a known reference Green tensor $\mathbf{G}^{(0)}(\boldsymbol{r},\boldsymbol{r},\omega)$ as [3,56]

$$\mathbf{G}^{(1)}(\boldsymbol{r},\boldsymbol{r},\omega)=\frac{\omega^2}{c^2}\int \mathrm{d}^3 s\,\mathbf{G}^{(0)}(\boldsymbol{r},\boldsymbol{s},\omega)\delta\epsilon(\omega)\mathbf{G}^{(0)}(\boldsymbol{s},\boldsymbol{r},\omega) + \left(\frac{\omega^2}{c^2}\right)^2\int \mathrm{d}^3 s\mathrm{d}^3 s'\mathbf{G}^{(0)}(\boldsymbol{r},\boldsymbol{s},\omega)\delta\epsilon(\omega) \times\mathbf{G}^{(0)}(\boldsymbol{s},\boldsymbol{s}',\omega)\times\delta\epsilon(\omega)\mathbf{G}^{(0)}(\boldsymbol{s}',\boldsymbol{r},\omega)+\cdots, \tag{A8}$$

where the integration range covers the volume of the material under investigation. The perturbation $\delta\epsilon(\omega) = \epsilon^{(1)}(\omega) - \epsilon^{(0)}(\omega)$ denotes the deviation from the reference permittivity. In the case of the free-space Green tensor as our reference, the difference permittivity simply equals the susceptibility [here, $\delta\epsilon(\omega) = \chi_{\mathrm{Au}}(\omega)$] of the material. The free-space Green tensor can be written as ($\boldsymbol{\varrho} = \boldsymbol{r} - \boldsymbol{s}$, $\varrho = |\boldsymbol{\varrho}|$) [3]

$$\mathbf{G}^{(0)}(\boldsymbol{\varrho},\omega) = -\frac{c^2}{3\omega^2}\boldsymbol{\delta}(\boldsymbol{\varrho}) + \frac{\omega}{4\pi c}\left[f\left(\frac{c}{\omega\varrho}\right)\mathbf{I} - g\left(\frac{c}{\omega\varrho}\right)\frac{\boldsymbol{\varrho}\otimes\boldsymbol{\varrho}}{\varrho^2}\right]\mathrm{e}^{\mathrm{i}\varrho\omega/c} \tag{A9}$$

with $f(x) = x + \mathrm{i}x^2 - x^3$ and $g(x) = x + 3\mathrm{i}x^2 - 3x^3$.

The Hamaker approach only uses the first term of the Born series expansion. Because the Born series is a perturbative expansion in the susceptibility $\chi(\omega)$, it converges badly for materials with a large susceptibility such as gold. To improve this convergence, and to implement a local-field correction, the reference Green tensor is separated into a regular $\mathbf{R}$ and a singular part $\mathbf{D} = -\frac{c^2}{3\omega^2}\boldsymbol{\delta}(\boldsymbol{\varrho})$. Inserting this into Eq. (A8) and performing the integrals over the δ distributions yields the local-field-corrected first-order scattering Green tensor

$$\mathbf{G}^{(1)}(\boldsymbol{r},\boldsymbol{r},\omega) = \frac{\omega^2}{c^2}\chi(\omega)\sum_{n=0}^{\infty}\left(-\frac{1}{3}\chi(\omega)\right)^n \times\int \mathrm{d}^3 s\,\mathbf{R}^{(0)}(\boldsymbol{r},\boldsymbol{s},\omega)\mathbf{R}^{(0)}(\boldsymbol{s},\boldsymbol{r},\omega), \tag{A10}$$

which leads to

$$\mathbf{G}^{(1)}(\boldsymbol{r},\boldsymbol{r},\omega) = \frac{\omega^2}{c^2}\frac{\chi(\omega)}{1+\chi(\omega)/3} \times\int \mathrm{d}^3 s\,\mathbf{R}^{(0)}(\boldsymbol{r},\boldsymbol{s},\omega)\mathbf{R}^{(0)}(\boldsymbol{s},\boldsymbol{r},\omega) \tag{A11}$$

with ($\boldsymbol{\varrho} = \boldsymbol{r} - \boldsymbol{s}$, $\varrho = |\boldsymbol{\varrho}|$)

$$\mathbf{R}^{(0)}(\boldsymbol{\varrho},\omega) = \frac{\omega}{4\pi c}\left[f\left(\frac{c}{\omega\varrho}\right)\mathbf{I} - g\left(\frac{c}{\omega\varrho}\right)\frac{\boldsymbol{\varrho}\otimes\boldsymbol{\varrho}}{\varrho^2}\right]\mathrm{e}^{\mathrm{i}\varrho\omega/c}. \tag{A12}$$

Equation (A11) has to be evaluated numerically. Because of the smooth shape of the potential, numerical integration methods converge quickly, with errors proportional to, at most, the curvature of the potential, which is small in the range of investigation.

In the Hamaker approach (pairwise summation), the potential is clearly additive. The total potential can be separated into three parts: one related to the evanescent field, one related to the dispersion interaction between Rb and Au, and one part for the Casimir-Polder interaction between the Rb atoms and the sapphire substrate. The latter can be neglected because the interaction with the gold stripes by far dominates every other CP interaction, as we have explicitly checked.

5. BEC preparation

The BEC is prepared in an ultrahigh vacuum chamber. After precooling and trapping ^{87}Rb atoms in a magneto-optic trap, the atoms are adiabatically transferred into a highly compressed magnetic trap, where they are further cooled by forced radio-frequency evaporation by which Bose-Einstein condensates with, typically, 2×10^5 atoms are generated. This is done at a distance of several hundred μm from the surface of a glass prism. A thin sapphire substrate containing the gold grating investigated in this paper is glued to the top of this prism. After preparation of the BEC, we suddenly displace the magnetic trapping minimum by a distance Δz, thereby raising the potential energy of the atoms by $\Delta E = \frac{1}{2}m\omega^2\Delta z^2$, with atomic mass m and magnetic trapping frequency ω. The BEC is accelerated towards the new trapping minimum. After a quarter of the oscillation period $\delta t = \frac{\pi}{2\omega}$, we switch off the magnetic trap and apply a constant magnetic-field gradient of $B' = 15\ \mathrm{Gcm}^{-1}$, which compensates the gravitational force. Thus, the atoms are not further accelerated or

decelerated because of gravitation while moving towards the grating. We measure the actual velocity of the atoms by taking absorption images of the cloud at several time intervals of 1 ms after the acceleration.

6. Comparison between amplitude and phase modulation

Experimental data are evaluated in this paper, for simplicity, only with an amplitude modulation model. This is, as will be shown below, a good approximation for the small laser powers used, whereas for large laser powers, the phase of the matter wave is also significantly modulated, leading to an increased diffraction as compared to amplitude modulation alone. For a normal incidence of the matter wave on the grating (like in the experiment—see also Fig. 2), the diffracted intensity is given within the Fraunhofer limit as [57]

$$I(\kappa) = I_0 k^2 \left| \int_{-\infty}^{\infty} e^{-i\kappa x} r(x) dx \right|^2, \qquad \text{(A13)}$$

where $k = 2\pi/\lambda_{dB}$ with de Broglie wavelength $\lambda_{dB} = \frac{h}{mv}$ of the matter wave and $\kappa = k \cdot \sin(\theta_r)$ with angle θ_r of the reflected wave. Diffraction order n is reflected at the angle $\theta_r^{(n)} \approx n\frac{\lambda_{dB}}{d}$. For the estimation of the relevance of phase imprinting, only relative occupations are important. Thus, neglecting prefactors in Eq. (A13), we calculate the Fourier transform $\hat{r}(\kappa)$ of the complex reflection function $r(x)$ and evaluate $\hat{r}(\kappa)$ at the values corresponding to the diffraction orders. The reflection function $r(x) = r_A(x) \cdot e^{i\phi(x)}$ contains both amplitude and phase modulation. The phase at a certain lateral position x is calculated from the simulated combined EW and CP potential landscape via [58]

$$\phi(x) = -\frac{2}{\hbar v} \int_{+\infty}^{z_R(x)} (U_{\mathrm{EW}}(x) + U_{\mathrm{CP}}(x)) dz, \qquad \text{(A14)}$$

where the integral is evaluated from distances far from the surface ($z \to +\infty$) to the distance $z_R(x)$, where the potential energy $U_{\mathrm{EW}} + U_{\mathrm{CP}}$ equals the kinetic energy of the atoms $E_{\mathrm{kin}} = \frac{1}{2}mv^2$. The factor of 2 before the integral stems from the fact that the incoming and the reflected matter wave acquire the same phase. The amplitude of the reflection function is $r_A(x) = 1$ for those lateral positions where atoms are reflected and $r_A(x) = 0$ for those positions where they are transmitted. Please note that Eq. (A14) is the phase along the classical path in the eikonal approximation and that it neglects the influence of the curvature of the potential on the path. The expressions above are thus not a full solution to the scattering problem, but they are a reasonable approximation in the limit of small scattering angles ($\theta_r^{(1)} \approx 8°$). Solving Eq. (A13), we deduce the influence of phase imprinting on the diffraction by comparing the results of the full reflection function $r(x)$ with those where the phase is artificially set to be constant, $\phi(x) = 0$. The corresponding occupations are shown in Fig. 5. For laser powers $P < 140$ mW, the deviation is $\lesssim 20\%$ such that the diffraction can be described in some approximation by amplitude modulation alone. In contrast, this approximation is not valid for the high laser powers used where the deviation exceeds 50%.

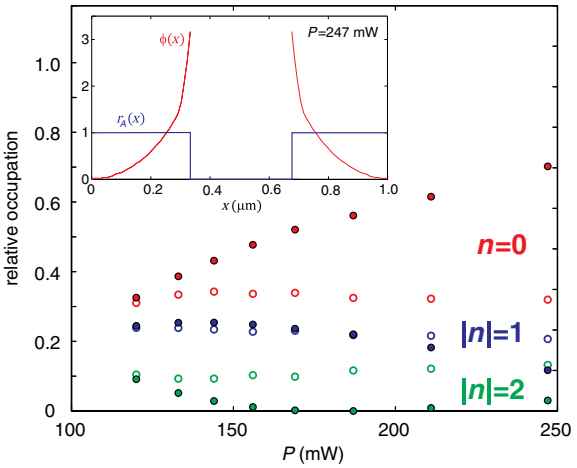

FIG. 5 Occupation of diffraction orders including phase imprinting (open circles) as compared to amplitude imprinting alone (dots). The deviation due to phase imprinting is increasing with the laser power. The inset shows the spatial dependence of the amplitude $r_A(x)$ and the phase $\phi(x)$ of the reflection function for a laser power of $P = 247$ mW, exemplarily.

[1] J. E. Lennard Jones, *Processes of Adsorption and Diffusion on Solid Surfaces*, Trans. Faraday Soc. **28**, 333 (1932).

[2] H. B. G. Casimir and D. Polder, *The Influence of Retardation on the London-van der Waals Forces*, Phys. Rev. **73**, 360 (1948).

[3] S. Scheel and S. Y. Buhmann, *Macroscopic Quantum Phenomena—Concepts and Applications*, Acta Phys. Slovaca **58**, 675 (2008).

[4] C. I. Sukenik, M. G. Boshier, D. Cho, V. Sandoghdar, and E. A. Hinds, *Measurement of the Casimir-Polder Force*, Phys. Rev. Lett. **70**, 560 (1993).

[5] A. Landragin, J.-Y. Courtois, G. Labeyrie, N. Vansteenkiste, C. I. Westbrook, and A. Aspect, *Measurement of the van der Waals Force in an Atomic Mirror*, Phys. Rev. Lett. **77**, 1464 (1996).

[6] A. Landragin, L. Cognet, G. Zs. K. Horvath, C. I. Westbrook, N. Westbrook, and A. Aspect, *A Reflection Grating for Atoms at Normal Incidence*, Europhys. Lett. **39**, 485 (1997).

[7] F. Shimizu, *Specular Reflection of Very Slow Metastable Neon Atoms from a Solid Surface*, Phys. Rev. Lett. **86**, 987 (2001).

[8] V. Druzhinina and M. DeKieviet, *Experimental Observation of Quantum Reflection Far from Threshold*, Phys. Rev. Lett. **91**, 193202 (2003).

[9] T. A. Pasquini, Y. Shin, C. Sanner, M. Saba, A. Schirotzek, D. E. Pritchard, and W. Ketterle, *Quantum Reflection from a Solid Surface at Normal Incidence*, Phys. Rev. Lett. **93**, 223201 (2004).

[10] J. M. Obrecht, R. J. Wild, M. Antezza, L. P. Pitaevskii, S. Stringari, and E. A. Cornell, *Measurement of the Temperature Dependence of the Casimir-Polder Force*, Phys. Rev. Lett. **98**, 063201 (2007).

[11] H. Bender, P. W. Courteille, C. Marzok, C. Zimmermann, and S. Slama, *Direct Measurement of Intermediate-Range Casimir-Polder Potentials*, Phys. Rev. Lett. **104**, 083201 (2010).

[12] R. Messina, D. A. R. Dalvit, P. A. Maia Neto, A. Lambrecht, and S. Reynaud, *Dispersive Interactions between Atoms and Nonplanar Surfaces*, Phys. Rev. A **80**, 022119 (2009).

[13] A. W. Rodriguez, F. Capasso, and S. G. Johnson, *The Casimir Effect in Microstructured Geometries*, Nat. Photonics **5**, 211 (2011).

[14] V. N. Marachevsky, *The Casimir Effect: Medium and Geometry*, J. Phys. A **45**, 374021 (2012).

[15] M. Levin, A. P. McCauley, A. W. Rodriguez, M. T. Homer Reid, and S. G. Johnson, *Casimir Repulsion between Metallic Objects in Vacuum*, Phys. Rev. Lett. **105**, 090403 (2010).

[16] F. W. DelRio, M. P. de Boer, J. A. Knapp, E. D. Reedy Jr., P. J. Clews, and M. L. Dunn, *The Role of van der Waals Forces in Adhesion of Micromachined Surfaces*, Nat. Mater. **4**, 629 (2005).

[17] A. Lambrecht and V. N. Marachevsky, *Casimir Interaction of Dielectric Gratings*, Phys. Rev. Lett. **101**, 160403 (2008); *Theory of the Casimir Effect in One-Dimensional Periodic Dielectric Systems*, Int. J. Mod. Phys. A **24**, 1789 (2009).

[18] A. M. Contreras-Reyes, R. Guérout, P. A. Maia Neto, D. A. R. Dalvit, A. Lambrecht, and S. Reynaud, *Casimir-Polder Interaction between an Atom and a Dielectric Grating*, Phys. Rev. A **82**, 052517 (2010).

[19] P. S. Davids, F. Intravaia, F. S. S. Rosa, and D. A. R. Dalvit, *Modal Approach to Casimir Forces in Periodic Structures*, Phys. Rev. A **82**, 062111 (2010).

[20] D. Farías and K.-H. Rieder, *Atomic Beam Diffraction from Solid Surfaces*, Rep. Prog. Phys. **61**, 1575 (1998).

[21] T. A. Pasquini, M. Saba, G.-B. Jo, Y. Shin, W. Ketterle, D. E. Pritchard, T. A. Savas, and N. Mulders, *Low Velocity Quantum Reflection of Bose-Einstein Condensates*, Phys. Rev. Lett. **97**, 093201 (2006).

[22] B. S. Zhao, S. A. Schulz, S. A. Meek, G. Meijer, and W. Schöllkopf, *Quantum Reflection of Helium Atom Beams from a Microstructured Grating*, Phys. Rev. A **78**, 010902 (R) (2008).

[23] R. E. Grisenti, W. Schöllkopf, J. P. Toennies, G. C. Hegerfeldt, and T. Köhler, *Determination of Atom-Surface van der Waals Potentials from Transmission-Grating Diffraction Intensities*, Phys. Rev. Lett. **83**, 1755 (1999).

[24] H. Oberst, D. Kouznetsov, K. Shimizu, J. I. Fujita, and F. Shimizu, *Fresnel Diffraction Mirror for an Atomic Wave*, Phys. Rev. Lett. **94**, 013203 (2005).

[25] J. D. Perreault and A. D. Cronin, *Observation of Atom Wave Phase Shifts Induced by van der Waals Atom-Surface Interactions*, Phys. Rev. Lett. **95**, 133201 (2005).

[26] G. A. Moreno, D. A. R. Dalvit, and E. Calzetta, *Bragg Spectroscopy for Measuring Casimir-Polder Interactions with Bose-Einstein Condensates above Corrugated Surfaces*, New J. Phys. **12**, 033009 (2010).

[27] C. Stehle, H. Bender, C. Zimmermann, D. Kern, M. Fleischer, and S. Slama, *Plasmonically Tailored Micropotentials for Ultracold Atoms*, Nat. Photonics **5**, 494 (2011).

[28] M. Righini, A. S. Zelenina, C. Girard, and R. Quidant, *Parallel and Selective Trapping in a Patterned Plasmonic Landscape*, Nat. Phys. **3**, 477 (2007).

[29] S. Y. Buhmann, L. Knöll, D. G. Welsch, and H. T. Dung, *Casimir-Polder Forces: A Nonperturbative Approach*, Phys. Rev. A **70**, 052117 (2004).

[30] J. H. de Boer, *The Influence of van der Waals' Forces and Primary Bonds on Binding Energy, Strength and Orientation, with Special Reference to Some Artificial Resins*, Trans. Faraday Soc. **32**, 10 (1936).

[31] H. C. Hamaker, *The London van der Waals Attraction between Spherical Particles*, Physica (Amsterdam) **4**, 1058 (1937).

[32] S. N. Thennadil and L. H. Garcia-Rubio, *Approximations for Calculating van der Waals Interaction Energy between Spherical Particles - A Comparison*, J. Colloid Interface Sci. **243**, 136 (2001).

[33] H.-C. Chiu, G. L. Klimchitskaya, V. N. Marachevsky, V. M. Mostepanenko, and U. Mohideen, *Demonstration of the Asymmetric Lateral Casimir Force between Corrugated Surfaces in the Nonadditive Regime*, Phys. Rev. B **80**, 121402(R) (2009); *Lateral Casimir Force between Sinusoidally Corrugated Surfaces: Asymmetric Profiles, Deviations from the Proximity Force Approximation, and Comparison with Exact Theory*, **81**, 115417 (2010).

[34] S. Y. Buhmann and D.-G. Welsch, *Born Expansion of the Casimir-Polder Interaction of a Ground-State Atom with Dielectric Bodies*, Appl. Phys. B **82**, 189 (2006).

[35] V. A. Parsegian, *Van der Waals Forces: A Handbook for Biologists, Chemists, Engineers, and Physicists* (Cambridge University Press, New York, 2005).

[36] K. Autumn, Y. A. Liang, S. T. Hsieh, W. Zesch, W. P. Chan, T. W. Kenny, R. Fearing, and R. J. Full, *Adhesive Force of a Single Gecko Foot-Hair*, Nature (London) **405**, 681 (2000).

[37] R. B. Rodrigues, P. A. Maia Neto, A. Lambrecht, and S. Reynaud, *Lateral Casimir Force beyond the Proximity-Force Approximation*, Phys. Rev. Lett. **96**, 100402 (2006).

[38] A. Rodriguez, M. Ibanescu, D. Iannuzzi, F. Capasso, J. D. Joannopoulos, and S. G. Johnson, *Computation and Visualization of Casimir Forces in Arbitrary Geometries: Nonmonotonic Lateral-Wall Forces and the Failure of Proximity-Force Approximations*, Phys. Rev. Lett. **99**, 080401 (2007).

[39] Y. Bao, R. Guérout, J. Lussange, A. Lambrecht, R. A. Cirelli, F. Klemens, W. M. Mansfield, C. S. Pai, and H. B. Chan, *Casimir Force on a Surface with Shallow Nanoscale Corrugations: Geometry and Finite Conductivity Effects*, Phys. Rev. Lett. **105**, 250402 (2010).

[40] L. P. Teo, M. Bordag, and V. Nikolaev, *Corrections beyond the Proximity Force Approximation*, Phys. Rev. D **84**, 125037 (2011).

[41] G. Bimonte, T. Emig, R. L. Jaffe, and M. Kardar, *Casimir Forces beyond the Proximity Approximation*, Europhys. Lett. **97**, 50001 (2012).

[42] A. D. Cronin and J. D. Perreault, *Phasor Analysis of Atom Diffraction from a Rotated Material Grating*, Phys. Rev. A **70**, 043607 (2004).

[43] C. Henkel, J.-Y. Courtois, and A. Aspect, *Atomic Diffraction by a Thin Phase Grating*, J. Phys. II France **4**, 1955 (1994).

[44] A. Günther, S. Kraft, C. Zimmermann, and J. Fortágh, *Atom Interferometer Based on Phase Coherent Splitting of Bose-Einstein Condensates with an Integrated Magnetic Grating*, Phys. Rev. Lett. **98**, 140403 (2007).

[45] A. D. Cronin, J. Schmiedmayer, and D. E. Pritchard, *Optics and Interferometry with Atoms and Molecules*, Rev. Mod. Phys. **81**, 1051 (2009).

[46] J. M. McGuirk, D. M. Harber, J. M. Obrecht, and E. A. Cornell, *Alkali-Metal Adsorbate Polarization on Conducting and Insulating Surfaces Probed with Bose-Einstein Condensates*, Phys. Rev. A **69**, 062905 (2004).

[47] C. Stehle, H. Bender, F. Jessen, C. Zimmermann, and S. Slama, *Ad- and Desorption of Rb Atoms on a Gold Nanofilm Measured by Surface Plasmon Polaritons*, New J. Phys. **12**, 083066 (2010).

[48] A. Tauschinsky, R. M. T. Thijssen, S. Whitlock, H. B. van Linden van den Heuvell, and R. J. C. Spreeuw, *Spatially Resolved Excitation of Rydberg Atoms and Surface Effects on an Atom Chip*, Phys. Rev. A **81**, 063411 (2010).

[49] H. Failache, S. Saltiel, M. Fichet, D. Bloch, and M. Ducloy, *Resonant van der Waals Repulsion between Excited Cs Atoms and Sapphire Surface*, Phys. Rev. Lett. **83**, 5467 (1999).

[50] F. Intravaia, C. Henkel, and A. Lambrecht, *Role of Surface Plasmons in the Casimir Effect*, Phys. Rev. A **76**, 033820 (2007).

[51] K. A. Milton, E. K. Abalo, P. Parashar, N. Pourtolami, I. Brevik, and S. Å. Ellingsen, *Casimir-Polder Repulsion near Edges: Wedge Apex and a Screen with an Aperture*, Phys. Rev. A **83**, 062507 (2011).

[52] K. A. Milton, P. Parashar, N. Pourtolami, and I. Brevik, *Casimir-Polder Repulsion: Polarizable Atoms, Cylinders, Spheres, and Ellipsoids*, Phys. Rev. D **85**, 025008 (2012).

[53] C. Eberlein and R. Zietal, *Casimir-Polder Interaction between a Polarizable Particle and a Plate with a Hole*, Phys. Rev. A **83**, 052514 (2011).

[54] M. S. Safronova, C. J. Williams, and C. W. Clark, *Relativistic Many-Body Calculations of Electric-Dipole Matrix Elements, Lifetimes, and Polarizabilities in Rubidium*, Phys. Rev. A **69**, 022509 (2004).

[55] D. A. Steck, Rubidium 87D Line Data, http://steck.us/alkalidata (2009).

[56] A. A. Maradudin and D. L. Mills, *Scattering and Absorption of Electromagnetic Radiation by a Semi-infinite Medium in the Presence of Surface Roughness*, Phys. Rev. B **11**, 1392 (1975); D. L. Mills and A. A. Maradudin, *Surface Roughness and the Optical Properties of a Semi-infinite Material: The Effect of a Dielectric Overlayer*, Phys. Rev. B **12**, 2943 (1975).

[57] R. E. Grisenti, W. Schöllkopf, J. P. Toennies, J. R. Manson, T. A. Savas, and H. I. Smith, *He-atom Diffraction from Nanostructure Transmission Gratings: The Role of Imperfections*, Phys. Rev. A **61**, 033608 (2000).

[58] V. P. A. Lonij, W. F. Holmgren, and A. D. Cronin, *Magic Ratio of Window Width to Grating Period for van der Waals Potential Measurements Using Material Gratings*, Phys. Rev. A **80**, 062904 (2009).

PHYSICAL REVIEW A **94**, 023621 (2016)

Impact of Casimir-Polder interaction on Poisson-spot diffraction at a dielectric sphere

Joshua L. Hemmerich,[1] Robert Bennett,[1] Thomas Reisinger,[2] Stefan Nimmrichter,[3] Johannes Fiedler,[1] Horst Hahn,[2] Herbert Gleiter,[2] and Stefan Yoshi Buhmann[1,4]

[1]*Physikalisches Institut, Albert-Ludwigs-Universität Freiburg, Hermann-Herder-Strasse 4, D-79104 Freiburg im Breisgau, Germany*
[2]*Institute of Nanotechnology, Karlsruhe Institute of Technology, Hermann-von-Helmholtz-Platz 1, D-76344 Karlsruhe, Germany*
[3]*Centre for Quantum Technologies, National University of Singapore, 3 Science Drive 2, Singapore 117543, Singapore*
[4]*Freiburg Institute for Advanced Studies, Albert-Ludwigs-Universität Freiburg, Albertstrasse 19, D-79104 Freiburg im Breisgau, Germany*

(Received 30 June 2016; published 17 August 2016)

Diffraction of matter waves is an important demonstration of the fact that objects in nature possess a mixture of particlelike and wavelike properties. Unlike in the case of light diffraction, matter waves are subject to a vacuum-mediated interaction with diffraction obstacles. Here we present a detailed account of this effect through the calculation of the attractive Casimir-Polder potential between a dielectric sphere and an atomic beam. Furthermore, we use our calculated potential to make predictions about the diffraction patterns to be observed in an ongoing experiment where a beam of indium atoms is diffracted around a silicon-dioxide sphere. The result is an amplification of the on-axis bright feature, which is the matter-wave analog of the well-known "Poisson spot" from optics. Our treatment confirms that the diffraction patterns resulting from our complete account of the sphere Casimir-Polder potential are indistinguishable from those found via a large-sphere nonretarded approximation in the discussed experiments, establishing the latter as an adequate model.

DOI: 10.1103/PhysRevA.94.023621

I. INTRODUCTION

Matter-wave diffraction around material objects is one of the most compelling demonstrations of the particle-wave duality. Beginning from the classic electron diffraction experiments of the 1920s [1,2], particles of progressively higher mass have had their wavelike nature revealed. This process began in the 1930s and 1940s with the diffraction of atoms and molecules [3], as well as neutrons [4], from various crystal surfaces. More recently the diffraction of atoms [5] and simple molecules [6] from lithographically fabricated grating structures has been demonstrated. These experiments paved the way for grating diffraction experiments with complex organic molecules such as fullerenes [7] and porphyrin derivates [8]. Scaling of diffraction experiments to even larger objects such as macromolecules or even living organisms like viruses or bacteria presents some considerable difficulties but has the potential to shed light on the question if quantum mechanics applies unmodified to such increasingly macroscopic systems [9]. The latter used a Talbot-Lau arrangement of three gratings, with the middle grating realized by a standing light wave to eliminate the problem of molecule-grating interaction.

As the diffracting molecules become larger, a number of difficulties arise. The immediate reduction in de Broglie wavelength can be counteracted, for example, by a reduction in the molecular speeds or the use of gratings with smaller grating constants, which both present significant technological challenges. In addition, interaction with the environment, for example, via thermal emission of radiation [10], can lead to decoherence [11]. More practically, the buildup of unwanted contaminants (from the beam or elsewhere) upon the grating itself over time can result in a reduction in the interference visibility or even cause the slits to become blocked. Additionally, Talbot-Lau interferometers impose relatively loose restrictions on the width of the beam's wavelength distribution, which may, however, become limiting for sources of objects of increasing mass such as, for example, cluster sources. Furthermore, the gratings must have very uniform grating constants and must be aligned with high precision.

Finally, the problem addressed in the present study stems from the fact that extended particles undergoing diffraction have a nonzero electromagnetic polarizability in general, meaning they experience Casimir-Polder or van der Waals (CP or vdW) dispersion forces originating from the grating itself. The result is an effective reduction in the slit width in addition to a coherent phase shift [12], which increasingly obscures the distinction between particle and wave nature [11,13]. The current mass record is held by a setup that reduces this problem through the use of a standing light-wave phase grating as the middle diffraction grating in a Talbot-Lau interferometer arrangement [14]. Another approach has the potential to eliminate the problem entirely by using three pulsed laser-ionization gratings [15]. Aside from these developments, an accurate knowledge of the CP or vdW incurred phase shifts is highly desirable, but remains challenging. The dispersion forces can exhibit intricate spatial dependence in complex geometries (see, for example, [16–21]), but in many far-field diffraction experiments the effect is reduced to an effective slit narrowing fitted to the data after the experiment [22]. Dispersion forces near gratings are extremely difficult to model accurately [12,16–21,23–30], especially when sharp edges are involved [31]. This, coupled to the fact that gratings necessarily have a large number of sharp edges spaced closely together, means that progress in detailed accounts of this effect has stalled.

Here we investigate a different type of diffraction scheme: the "Poisson spot" interferometer. There waves in general are diffracted around a circular or spherical object, resulting in an on-axis bright spot, called Poisson's spot or spot of Arago [32,33]. This effect was first predicted by Poisson when looking for evidence against Fresnel's wave theory of light in the early 1800s. Poisson described it as an absurd prediction of Fresnel's theory, but experiments by François Arago proved that the effect is real, accelerating the shift away from Newton's "corpuscular" theory [34]. The matter-wave

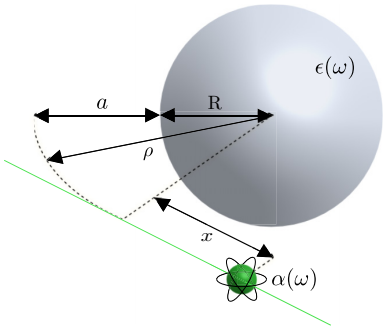

FIG. 1. Schematic representation of the system we consider, where an atom of polarizability $\alpha(\omega)$ passes near a sphere of permittivity $\epsilon(\omega)$. The resulting Casimir-Polder or van der Waals interaction will cause the atomic wave function to pick up a phase shift, which is observable in matter-wave diffraction experiments.

version of this experiment [35] avoids some of the problems that appear in the grating experiments discussed above (e.g., blocking of the grating, or alignment). However, the inevitable contribution from CP or vdW forces remains. These have been accounted for using a relatively simple model for the disk-based experiments of [35] in [13]. The question of whether this approach is valid is part of the motivation for the study presented here.

The current article covers an approach related to [35], where a dielectric sphere (see Fig. 1) replaces the disks used as diffraction obstacles in the aforementioned studies. The lack of sharp edges in spherical diffraction obstacles makes this approach ideally suited to accurate modeling of the CP or vdW interaction; see, for example [36]. The focus is, in particular, directed at a specific experiment that is currently being conducted at the Karlsruhe Institute of Technology, the parameters of which will be used throughout this article. The experiment aims at recording diffraction patterns in the shadow of submicron-sized silica particles cast by thermally evaporated indium atoms. The choice of these two materials is motivated in the following ways.

The Stöber process [37] enables the controlled growth of monodispersed spheres composed of amorphous silicon dioxide via condensation of silicic acid in alcoholic solutions. The advantage in preparing these silica spheres, which are to be used as diffraction obstacles, using a bottom-up approach as opposed to a top-down lithographic process is the close-to-optimal spherical shape that can be achieved in this way. Specifically the low surface corrugation of the particles is crucial [35] for achieving the Poisson-spot visibilities reported here. Furthermore, the resulting huge quantities of diffraction obstacles of uniform size are compatible with a simple parallelization of the experiment in order to average over large numbers of recorded diffraction images.

The choice of indium is largely due to its high vapor pressure, which enables the realization of a thermal-oven-based point source of sufficient brightness. It also sets the experiment apart from matter-wave diffraction aimed at measuring CP or vdW forces with beams composed of alkali-metal atoms [12,38] and seeks to demonstrate in this way a compatibility with a large number of condensable atom and molecular species. Thus, a wide variety of CP or vdW potentials could be studied using the same experimental approach.

In the following section we review the derivation of CP or vdW potentials and apply it to the particular materials and geometry used in the experiment. Then, in Sec. III we derive the resulting phase shifts affecting the matter-wave diffraction experiment. Finally, a numerical solution of the Fresnel-diffraction integral is used in Sec. IV to predict the Poisson-spot diffraction intensities in the presence of the CP or vdW potential followed by a discussion and the conclusion.

II. CASIMIR-POLDER POTENTIAL

In this section we outline a general derivation for the CP interaction for a dielectric sphere and a single ground-state atom and show that it reduces to well-known results in asymptotic cases.

Perturbation theory

We consider an atomic dipole $\hat{\mathbf{d}}$ interacting with the electric field $\hat{\mathbf{E}}$ of macroscopic QED [39,40], which includes all the information about geometry and dielectric functions in the electromagnetic environment surrounding the atom. We work in the long-wavelength approximation, where one can restrict to the first term in the multipole expansion of the atom-field interaction, meaning that the interaction Hamiltonian is

$$H = -\hat{\mathbf{d}} \cdot \hat{\mathbf{E}}(\mathbf{r}_\mathrm{A}), \tag{1}$$

with

$$\hat{\mathbf{E}}(\mathbf{r}) = \int d^3\mathbf{r}' \int_0^\infty d\omega \mathbf{G}(\mathbf{r},\mathbf{r}',\omega) \cdot \hat{\mathbf{f}}(\mathbf{r}',\omega) + \mathrm{H.c.}, \tag{2}$$

where $\hat{\mathbf{f}}(\mathbf{r}',\omega)$ is a bosonic field operator that describes the fundamental excitations of the composite matter-field system and $\mathbf{G}(\mathbf{r},\mathbf{r}',\omega)$ is the electromagnetic Green's tensor solving

$$\nabla \times \nabla \times \mathbf{G}(\mathbf{r},\mathbf{r}',\omega) - \varepsilon(\mathbf{r},\omega)\frac{\omega^2}{c^2}\mathbf{G}(\mathbf{r},\mathbf{r}',\omega) = \delta(\mathbf{r}-\mathbf{r}'), \tag{3}$$

where $\varepsilon(\mathbf{r},\omega)$ is the position and frequency-dependent permittivity of the system. Application of second-order perturbation theory to the ground state of the atom-field system yields an expression for the CP potential in terms of a complex frequency $\omega = i\xi$ [41,42],

$$U(\boldsymbol{r}) = \frac{\hbar\mu_0}{2\pi}\int_0^\infty d\xi\ \xi^2\alpha(i\xi)\,\mathrm{Tr}\,\mathbf{G}^{(1)}(\boldsymbol{r},\boldsymbol{r},i\xi), \tag{4}$$

where $\mathbf{G}^{(1)}(\boldsymbol{r},\boldsymbol{r}',i\xi)$ is the scattering part of the Green's tensor for the geometry at hand, which is obtained from the full Green's tensor at each point by subtracting the Green's tensor of a homogenous material with the same permittivity as the point in question. In this work we are only interested in the case when the atom is in the vacuum region outside a sphere, so for our purposes the scattering Green's tensor is obtained simply by subtracting the vacuum Green's tensor from that of a sphere. The quantity $\alpha(\omega)$ in Eq. (4) is the atomic polarizability for a transition from the ground state to state k with dipole moment d_{0k} and frequency ω_{0k};

$$\alpha(\omega) = \frac{2}{3\hbar(2J_0+1)}\sum_k \frac{\omega_{0k}d_{0k}^2}{\omega_{0k}^2-\omega^2}, \tag{5}$$

where J_0 is the total angular momentum quantum number of the ground state, which here appears as a weighting factor accounting for its degenerate levels.

The Green's tensor outside a sphere can be written as [42–44]

$$\begin{aligned}\mathbf{G}^{(1)}(\mathbf{r},\mathbf{r}',\omega) = \frac{ik}{4\pi}\sum_{l=1}^{\infty}\sum_{m=0}^{l}\sum_{\sigma=\mathrm{TE,TM}}(2-\delta_{m0})\\ \times\frac{2l+1}{l(l+1)}\frac{(l-m)!}{(l+m)!}r_{l\sigma}\\ \times[\mathbf{a}_{lm+\sigma}(\mathbf{r})\otimes\mathbf{a}_{lm+\sigma}(\mathbf{r}')\\ +\mathbf{a}_{lm-\sigma}(\mathbf{r})\otimes\mathbf{a}_{lm-\sigma}(\mathbf{r}')],\end{aligned} \tag{6}$$

where $\otimes$ denotes the dyadic product $(\mathbf{A}\otimes\mathbf{B})_{ij}=A_iB_j$, $\mathbf{a}_{lm\pm\sigma}$ are spherical wave-vector functions as listed in Appendix A, and $r_{l\sigma}$ are the Mie reflection coefficients for a sphere of radius R, given by

$$\begin{aligned}r_{lTE} &= -\frac{j_l(z_1)[z_2j_l(z_2)]' - [z_1j_l(z_1)]'j_l(z_2)}{h_l^{(1)}(z_1)[z_2j_l(z_2)]' - [z_1h_l^{(1)}(z_1)]'j_l(z_2)},\\ r_{lTM} &= -\frac{\varepsilon(i\xi)j_l(z_2)[z_1j_l(z_1)]' - j_l(z_1)[z_2j_l(z_2)]'}{\varepsilon(i\xi)[z_1h_l^{(1)}(z_1)]'j_l(z_2) - h_l^{(1)}(z_1)[z_2j_l(z_2)]'},\end{aligned} \tag{7}$$

where $z_i\equiv k_iR$, $k_1=\omega/c$, $k_2=\omega\sqrt{\varepsilon(\omega)}/c$, and the primes denote derivatives with respect to z_1, z_2, respectively; e.g., $[xf(x)]'\equiv\frac{d}{dx}[xf(x)]$. The quantities $j_l(z_i)$ and $h_l^{(1)}(z_i)$ are the spherical Bessel and Hankel functions of the first kind, respectively.

Using addition theorems for spherical harmonics [45], the potential for a sphere can be rewritten in the form [46] (see Appendix B)

$$\begin{aligned}U(r) = -\frac{\hbar\mu_0}{8\pi^2c}\int_0^\infty d\xi\xi^3\alpha(i\xi)\sum_{l=1}^{\infty}(2l+1)\\ \times\left(r_{lTE}\left[h_l^{(1)}(kr)\right]^2 + r_{lTM}\left\{l(l+1)\frac{\left[h_l^{(1)}(kr)\right]^2}{(kr)^2}\right.\right.\\ \left.\left.+\frac{\left[krh_l^{(1)}(kr)\right]'^2}{(kr)^2}\right\}\right),\end{aligned} \tag{8}$$

in agreement with [47,48]. We now investigate Eq. (8) in several asymptotic regimes, both as a consistency check and as a useful point of comparison later on. First, we consider atom-sphere distances $r-R$ much smaller than the atomic transition wavelengths $\lambda_A=2\pi c/\omega_A$, which means that the atom-sphere interaction can be considered to be instantaneous and so is termed the nonretarded regime. This renders the nonretarded CP potential $U_{NR}(r)\equiv U(r\ll\lambda_A)$ [42,47,48]:

$$\begin{aligned}U_{NR}(r) = -\frac{\hbar}{8\pi^2\varepsilon_0}\sum_{l=1}^{\infty}(2l+1)(l+1)\\ \times\frac{R^{2l+1}}{r^{2l+4}}\int_0^\infty d\xi\,\alpha(i\xi)\frac{\varepsilon(i\xi)-1}{\varepsilon(i\xi)+[(l+1)/l]}.\end{aligned} \tag{9}$$

It is worth noting that this expression does not depend on the spherical Bessel and Hankel functions j_l and $h_l^{(1)}$, which means the convergence of the sum over l is much more robust than for the full potential (8). Considering, furthermore, the sphere radius R to be much greater than the distance r from the surface of the sphere to the atom $|R-r|=z\ll R$, the terms with large l dominate and yield a $1/z^3$ dependence,

$$U_{BNR} = -\frac{\hbar}{16\pi^2\varepsilon_0}\frac{1}{z^3}\int_0^\infty d\xi\,\alpha(i\xi)\frac{\varepsilon(i\xi)-1}{\varepsilon(i\xi)+1}\equiv-\frac{C_3}{z^3}, \tag{10}$$

where the coefficient C_3 has been defined for later use. Equation (10) is the well-known Lennard-Jones formula [49] for the potential near a half space, which is indeed the expected limiting case for an atom a small distance from a large sphere.

Separately, we can consider a small sphere radius compared to the distance to the atom $r\gg R$. Beginning again from the general formula (8), one finds that the leading-order term in this expansion for small R/r comes from the first spherical harmonic $l=1$, which leads to the small-sphere potential,

$$\begin{aligned}U_S(r) = -\frac{\hbar}{4\pi^2\varepsilon_0}\frac{R^3}{r^6}\int_0^\infty d\xi\,\alpha(i\xi)\frac{\varepsilon(i\xi)-1}{\varepsilon(i\xi)+2}\exp(-2\xi r/c)\\ \times[3+6(\xi r/c)+5(\xi r/c)^2\\ +2(\xi r/c)^3+(\xi r/c)^4],\end{aligned} \tag{11}$$

which can again be further simplified in the nonretarded regime $U_{SNR}(r)\equiv U_S(r\ll\lambda)$,

$$U_{SNR}(r) = -\frac{3\hbar c}{4\pi^2\varepsilon_0}\frac{R^3}{r^6}\int_0^\infty d\xi\,\alpha(i\xi)\frac{\varepsilon(i\xi)-1}{\varepsilon(i\xi)+2}, \tag{12}$$

which is the well-known van der Waals potential between two microscopic polarisable objects [50].

Finally, considering the limit of strong retardation of the electromagnetic field $\lambda_A\ll r$ and a pointlike sphere as before, the retarded CP potential is obtained [47,48,51,52]:

$$U_{SR}(r) = -\frac{23\hbar c}{16\pi^2\varepsilon_0}\frac{R^3}{r^7}\alpha(0)\frac{\varepsilon(0)-1}{\varepsilon(0)+2}. \tag{13}$$

So far our considerations have been for a sphere of unspecified permittivity and a general (ground state) atom. In order to calculate this potential explicitly, one needs to use particular values of the atomic polarizability and the permittivity for the sphere as functions of imaginary frequency ξ.

III. NUMERICAL INVESTIGATION OF A REAL SYSTEM

A. Material response functions

As mentioned in the Introduction, we specifically consider amorphous silicon dioxide (SiO_2) for the sphere and indium for the atom. To determine the permittivity $\varepsilon(i\xi)$ of (SiO_2) as a function of imaginary frequencies $i\xi$, we used tabulated data for the real-frequency refractive index [53], which was then converted to that for imaginary frequencies via the Kramers-Kronig relations (see, for example, [45]). Amorphous SiO_2 has two main groups of resonances at frequencies $\omega_{T,1}$ and $\omega_{T,2}$, to which we fitted a two-line Drude model on the imaginary

TABLE I. Fit parameters for a two-line Drude-Lorentz model [Eq. (14)] for the permittivity of SiO_2.

Parameter	Value (Hz)	Error (%)	Parameter	Value (Hz)	Error (%)
$\omega_{P,1}$	1.75×10^{14}	0.37	$\omega_{P,2}$	2.96×10^{16}	0.45
$\omega_{T,1}$	1.32×10^{14}	0.34	$\omega_{T,2}$	2.72×10^{16}	0.43
γ_1	4.28×10^{13}	2.07	γ_2	8.09×10^{15}	3.40

frequency axis,

$$\varepsilon(i\xi) = 1 + \frac{\omega_{P,1}^2}{\omega_{T,1}^2 + \gamma_1\xi + \xi^2} + \frac{\omega_{P,2}^2}{\omega_{T,2}^2 + \gamma_2\xi + \xi^2}, \quad (14)$$

where $\omega_{P,i}$ are the plasma frequencies of the two effective resonances and γ_i their decay width. The explicit values of the parameters of our fit are shown in Table I. The properties of the atom enter into the CP potential (8) via the polarizability (5), which in turn depends on the dipole matrix elements d_{0k} and frequencies ω_{0k} describing transitions from the ground state to level k. These parameters (obtained from [54], where they are found by combining experimental data and computational chemistry) are listed in Table II for each possible transition. The polarizability $\alpha(i\xi)$ for indium in its ground state ($5P_{1/2}$, i.e., $J_0 = 1/2$) was then calculated from the data from Table II via (5).

B. Numerical calculations

Given the material response functions (14) and the tabulated optical data in Tables I and II, we now have everything needed to calculate the CP potential Eq. (8) of an indium atom near a silicon-dioxide sphere. However, the sum over spherical harmonics cannot, in general, be done analytically, so the series has to be truncated at value of l large enough to keep errors within acceptable bounds. Calculating the potential for extremely large l is very time consuming computationally, so, based on the desired accuracy of our simulations, we decide upon a point at which the potential can be replaced by its half-space asymptote Eq. (10). We choose this accuracy to be at the 3% level, because beyond this the errors in the material response functions would dominate. Carrying out this replacement procedure, one finds the CP potential shown in Fig. 2.

C. CP-induced phase shift in matter-wave diffraction

In this section we discuss the impact of the CP interaction on matter-wave diffraction, in particular on the Poisson spot.

TABLE II. Transition frequencies ω_{0k} in 10^{15} rad/s and dipole matrix elements D_{0k} in 10^{-30} C m for indium [54]. Each k represents one degenerate manifold of internal states.

k	Transition	ω_{0k}	D_{0k}
1	$5P_{1/2} \to 6S_{1/2}$	4.594	16.092
2	$5P_{1/2} \to 5D_{3/2}$	6.200	22.048
3	$5P_{1/2} \to 7S_{1/2}$	6.843	4.587
4	$5P_{1/2} \to 6D_{3/2}$	7.360	7.910
5	$5P_{1/2} \to 8S_{1/2}$	7.659	2.518
6	$5P_{1/2} \to 7S_{3/2}$	7.886	3.582

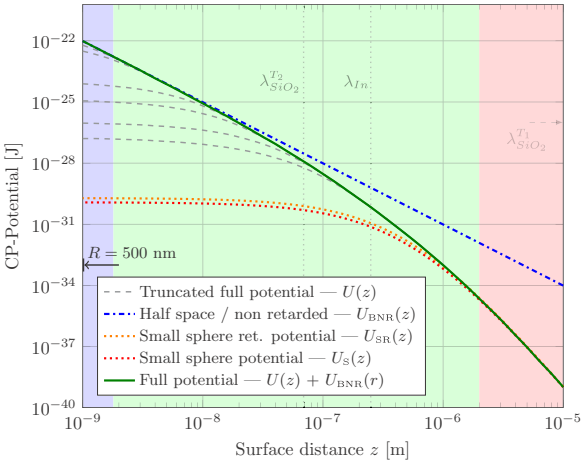

FIG. 2. CP potential for a 500 nm SiO_2 (amorphous) sphere and a ground-state indium atom. The dotted lines from top (orange) to bottom (red) are the retarded- and full-small sphere potentials respectively. The dashed (gray) lines are the solutions from the full potential (8) for different truncation values of the angular momentum $l\max = 10,20,50,100,500,800$. This shows that truncation in l is an especially delicate problem if the atom is in close proximity to the sphere, where the error induced by truncation of the l-series is largest. The solid (green) line is the full solution (with $l_{\max} = 800$) up to where the convergence to the half space is $U_{BNR}(r_l)/U(r_l) \simeq 3\%$, there it is replaced with the half-space potential. The vertical dotted lines represent the main resonances from SiO_2 ($\lambda^{T_1}_{SiO_2}$ and $\lambda^{T_2}_{SiO_2}$) and the dominant transition wavelength of indium (λ_{In}).

The Poisson spot is a bright spot which appears in the shadow region of a circular or spherical object due to diffraction. An approximate analogy with the double-slit experiment can be made by realizing that a circular (or spherical) diffracting object may be thought of as pairs of double slits arranged around a circle. The central maximum of the diffraction pattern for each pair of slits is on the axis, resulting in a bright spot. In other words, its appearance can be understood by the fact that the atomic paths from the point source via the rim of the spherical object to any specific point on the optical axis all have the same length. The quantum-mechanical phases of the atoms thus positively interfere at the optical axis which results in Poisson's spot.

In order to quantify the effects of the CP potential on the Poisson spot, we use the Wentzel-Kramers-Brillouin (WKB) approximation, where the potential is assumed to change slowly relative to the de Broglie wavelength associated with the matter wave. Explicitly, the WKB approximation holds if the spatial derivative of the position-dependent wave vector $k(x)$ satisfies

$$k'(x) \ll k^2(x), \quad (15)$$

which can be recast as

$$\frac{d}{dx}\sqrt{2m[E - U(x)]} \ll \frac{2m[E - U(x)]}{\hbar}, \quad (16)$$

where $E = \frac{1}{2}mv^2$ is the kinetic energy a particle of mass m and velocity v and U is the potential it is subject to. To check that

the approximation is valid here, we consider an indium atom ($m = 114.8\,\mathrm{u}$) and SiO_2, as discussed in the previous section. For these materials we have the large-sphere nonretarded potential $U = U_{\mathrm{BNR}}(r) = C_3/z^3$ given by Eq. (10) with

$$C_3 = \frac{\hbar}{16\pi^2\varepsilon_0}\int_0^\infty d\xi\ \alpha(i\xi)\frac{\varepsilon(i\xi)-1}{\varepsilon(i\xi)+1} \approx 9.77\times 10^{-50}\ \mathrm{J\,m^3}. \tag{17}$$

Using this potential and an approximate velocity of the indium atoms of 500 m/s (see Sec. IV) in Eq. (16), one finds that for nanometer distances the left-hand side is approximately nine orders of magnitude smaller than the right-hand side, meaning that for (at least) the case of the large-sphere nonretarded potential we are comfortably within the conditions of validity of the WKB approximation.

We describe the trajectory in our specific system through the coordinates x and $\rho = a + R$, as indicated in Fig. 1. This means that the CP-induced phase shift $\Delta\varphi_{\mathrm{CP}}$ (also known as the eikonal phase) is given by [38]

$$\Delta\varphi_{\mathrm{CP}}(\rho) = -\frac{1}{\hbar v}\int_{-\infty}^{\infty} dx\ U(x,\rho). \tag{18}$$

Given this phase shift, one can then calculate a diffraction pattern using the Fresnel approximation (where the wavelength of the beam undergoing diffraction is much smaller than the dimensions of the diffracting object). The amplitude $A(P)$ of the signal at a point P in the image plane (see Fig. 5) is given by [13,55]

$$A(P) = -\frac{i}{\lambda g b}\int_0^{2\pi} d\phi\ \int_0^\infty d\rho\ G(\phi,\rho)\rho e^{i[\varphi_g(\rho)+\Delta\varphi_{\mathrm{CP}}(\rho)]}, \tag{19}$$

where $\varphi_g(\rho) = \frac{\pi}{\lambda}(\frac{1}{g}+\frac{1}{b})\rho^2$ is the phase shift induced by the geometry of the object in Fresnel approximation and $\varphi_{\mathrm{CP}}(\rho)$ is the CP-induced phase shift given by Eq. (18), with $U(x,\rho)$ the lateral CP potential (see Fig. 3). The function $G(\phi,\rho)$ is the aperture function representing the circular cross section of the sphere. It is 0 for points that are located within the blocked cross section and 1 otherwise. To calculate the amplitude for an arbitrary point P in the detection plane, the origin used in the integral (19) is shifted to the intersection point of the line connecting the source and image points with the integration plane, resulting in the new radial coordinate $\overline{\rho}$. The numerical evaluation of $|A|^2$, which is equal to the intensities in the imaging plane, is discussed in Sec. IV.

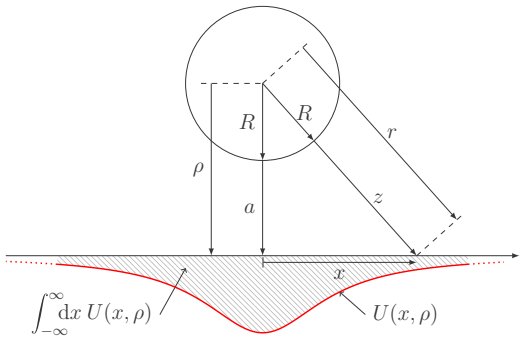

FIG. 3. Sketch of the lateral CP potential. The curve corresponds to the CP interaction of an atom flying in a straight line parallel to the optical axis nearby the sphere surface.

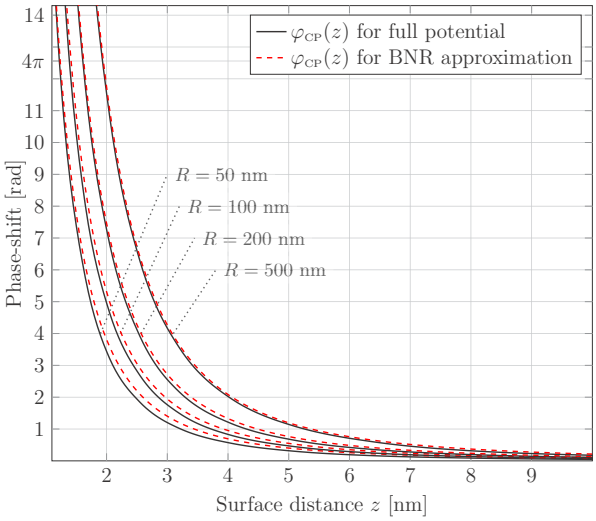

FIG. 4. CP potential-induced phase shift for spheres with different radii (50, 100, 200, and 500 nm). The solid (black) line is the phase shift where the full solution for the CP potential from Eq. (18) has been used. The dashed (red) line is the phase shift for the leading order of the half-space approximation. Note that the approximation improves for larger spheres, in line with the intuition that a sphere with a larger radius is more similar to a half space.

The Fresnel approximation is accurate in the discussed experiment since the object and image distances g and b are large compared to the size of the diffraction object R and the wavelength λ is much smaller than R. In addition, note that although Fresnel theory only applies to two-dimensional objects, the "volume" of the sphere is implicitly taken into account by the accumulated phase shift Eq. (18).

For distances of less than approximately 10 nm the phase shift is well approximated by the large-sphere potential of Eq. (10), as shown in Fig. 4. The potential takes a particular simple form in this limit [56], namely,

$$U_{\mathrm{BNR}}(r) = -\frac{C_3}{z^3} = -\frac{C_3}{[\sqrt{(a+R)^2+x^2}-R]^3}, \tag{20}$$

as shown in Fig. 3. This means that if this potential is used in the phase-shift integral, the result can, in fact, be found analytically,

$$\begin{aligned}\Delta\varphi_{\mathrm{CP,BNR}}(a) &= \frac{C_3}{2\hbar v}\frac{1}{a^2(2R+a)^2}\\ &\quad\times\left(6R^2+8Ra+4a^2+\frac{3R(R+a)^2}{\sqrt{a(2R+a)}}\right.\\ &\quad\left.\times\left\{2\arctan\left[\frac{R}{\sqrt{a(2R+a)}}\right]+\pi\right\}\right)\\ &\approx \frac{C_3}{2\hbar v}\frac{3\pi\sqrt{R}}{2\sqrt{2}a^{5/2}} \quad \text{for } a\ll R,\end{aligned} \tag{21}$$

with $C_3 \approx 9.77\times 10^{-50}\,\mathrm{J\,m^3}$, as explained above. Finally, we define for later convenience the quantity $C_{52} \equiv \frac{C_3}{2\hbar v}\frac{3\pi\sqrt{R}}{2\sqrt{2}}$

so that

$$\Delta\varphi_{\mathrm{CP,BNR}}(a \ll R) = \frac{C_{52}}{a^{5/2}}. \tag{22}$$

IV. CALCULATION OF DIFFRACTION IMAGES

In this section the derived Casimir-Polder phase shift is used in a numerical solution of the Fresnel-diffraction integral in order to predict the effect of the Casimir-Polder interaction on the relative intensity of Poisson's spot. With relative intensity I_{rel} we refer to the ratio between the intensity at the center of Poisson's spot in the detection plane and the intensity of the undisturbed beam, also in the detection plane. These predicted relative intensities can then be compared to intensity data from the aforementioned matter-wave experiments.

The parameters assumed in the calculations, and detailed in the following lines, are chosen according to the setup used in the experiment. The oven source consists of a closed molybdenum crucible with a nominally 20-μm-diameter orifice and is kept at a temperature of $T_s = 1200\,^{\circ}\mathrm{C}$. The temperature is chosen this high to generate a substantial partial pressure of indium (about 87 Pa) within the crucible, resulting in the high source brightness needed to observe Poisson's spot. The orifice diameter is also small enough to avoid any increase in the virtual source size [57,58]. In spite of the relatively high pressure, the speed of the exiting indium atoms is expected to be characterized by the thermal speed distribution inside the source, with an approximate mean velocity given by $\bar{v} = \sqrt{8k_bT_s/(\pi m)} \approx 521$ m/s, where k_b is Boltzmann's constant and m is the atomic mass of indium ($m = 114.8$ u). This corresponds to a mean de Broglie wavelength of 6.67 pm, which is the wavelength used in the calculations described below. The speed of the atoms affects the relative intensity in two ways. (1) Higher atomic speed results in smaller wavelengths and thus in a thinner point-source Poisson spot which is equivalent to lower relative intensity for extended sources. (2) Higher atomic speed also results in shorter Casimir-Polder interaction times and thus a reduced phase shift, which also results in a reduction of the relative Poisson-spot intensity [13,36], as can be seen below. The spread in wavelengths is neglected as its effect on the relative intensity of Poisson's spot is expected to average out. A clear sign of the wave nature is the presence of the side maxima (as, for example, visible in Fig. 9), unlike the Poisson spot itself, which has a classical analog due to particle deflection in the CP potential [13,36]. The visibility of these side maxima is, however, affected by the spread in wavelengths, which are therefore hard to detect in practice. Three different sphere diameters of the silicon-dioxide particles will be assumed ($R = 50,\ 100,\ 200$ nm) and a fixed distance between the source and the sphere of $g = 600$ mm. The image distance b between the sphere and the detection plane is varied in the range $b = 0.05$–1.05 mm.

The disturbance $A(P)$ at a point P in the detection plane can be expressed by Eq. (19), which makes use of the Fresnel approximation and already incorporates the phase shift expected from the Casimir-Polder interaction [27].

The phase shift $\varphi_{\mathrm{CP}}(r)$ is only non-negligible in an annular region in the integration plane between radii $R_{i,\mathrm{CP}}$ and $R_{o,\mathrm{CP}}$ (see Fig. 5). Very close to the sphere the phase shift starts to oscillate increasingly fast as a function of z. It is safe to neglect contributions originating from an annular region of radius $R_{i,CP}$ and inward, i.e., immediately adjacent to the sphere. This is because, from a classical point of view, trajectories passing within $R_{i,CP}$ result in large particle deflections or even particle capture by the sphere and thus do not contribute to the diffraction image close to the optical axis. In the calculations presented here, $R_{o,\mathrm{CP}}$ and $R_{i,\mathrm{CP}}$ are set such that the phase shift equals $\pi/1000$ and 4π, respectively (this turns out to be more efficient and accurate than the absolutely fixed boundaries used in Ref. [13]). For the sphere radii $R = 50$, 100, and 200 nm, for which results are reported below, the phase-shift constants defined by Eq. (22) are $C_{52} = 6.622 \times 10^{-22}$, 9.365×10^{-22}, and 13.244×10^{-22} $\mathrm{m}^{5/2}$, respectively, and the boundary radii are $[R_{i,\mathrm{CP}}, R_{o,\mathrm{CP}}] = [51.2, 83.8]$, $[101.4, 138.9]$, and $[201.6, 244.7]$ nm, respectively, for the given beam parameters.

The surface integral is solved numerically following the general approach discussed in Ref. [55] and explained schematically in Fig. 5. The integral is replaced by two sums.

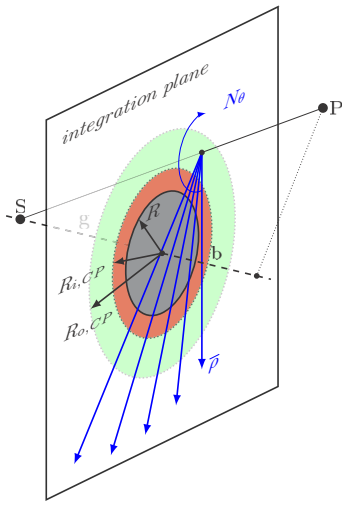

FIG. 5. Schematic indicating numerical solution of Fresnel integral. In order to calculate the amplitude $A(P)$ at point P due to a point source at S, the surface integral from Eq. (19) in the indicated integration plane needs to be solved. Note that to calculate the amplitude for an arbitrary point P in the detection plane the origin used in the integral is shifted to the intersection point of the line $\overline{SP}$ and the integration plane, resulting in the new radial coordinate $\overline{\rho}$. The circular cross section of the sphere is shown in gray with a solid circumference. The adjacent annular zone in orange with an outer radius $R_{i,\mathrm{CP}}$ indicates the region where the CP or vdW phase shift is larger than 4π. This zone was therefore neglected entirely in any of the radial line integrals, which are indicated by the blue arrows. Further away from the optical axis the annular zone shown in green corresponds to the region where the CP or vdW phase shift is in the range $[\frac{\pi}{1000}, 4\pi]$ with an outer radius of $R_{o,\mathrm{CP}}$. In this region each radial line integral was solved numerically, taking into account the surface distance a at each numerical integration step. Outside of it, the CP or vdW phase shift is neglected and the contribution to the line integrals simplifies to two terms corresponding to the intersection point(s) with the circle of radius $R_{o,\mathrm{CP}}$ with the radial integration line and a point at infinity (see Ref. [55]).

The first solves the integral in the θ variable, corresponding to N_θ radially equally spaced rays. We choose $N_\theta = 19\,997$ (a prime number) to avoid artificial fringes from symmetry in the numerical evaluation. The second sum, which corresponds to line integrals in the radial direction, reduces to a few summands that are evaluated at the intersection points of each particular ray with the edges of transmitting regions. In the annular region where the CP potential is non-negligible, this simplification does not hold. Therefore, whenever a ray traverses this region the corresponding part of the radial line integral is computed using a simple trapezoidal rule, taking into account the local phase shift. The resolution of this numerical line integration was fixed at 0.1 nm. For each image distance b and sphere radius R the intensities corresponding to a row of 2000 pixels reaching from the optical axis to the radius R in the image plane is computed with this method. The complete 4000×4000-pixel two-dimensional point-source diffraction image is inferred from symmetry and interpolation. Finally, the image is convoluted with the demagnified image of the source of width $20b/g$ μm.

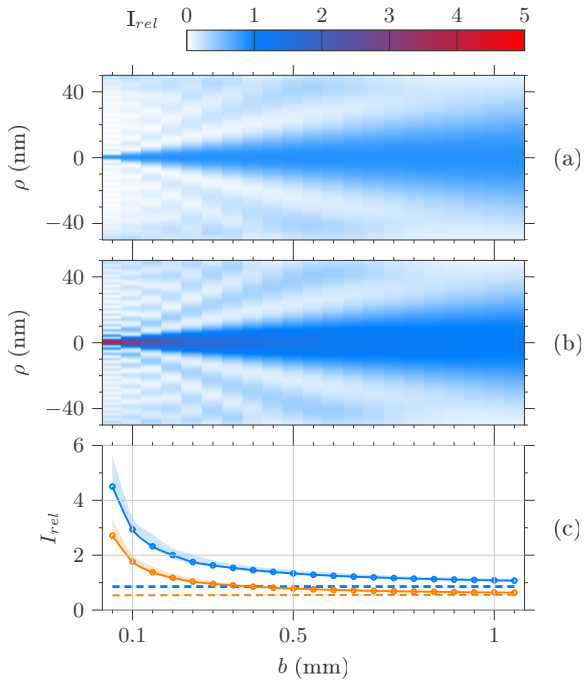

FIG. 6. Relative diffraction intensity for sphere radius $R = 50$ nm. The plots in this figure show the calculated relative intensity of an atomic indium beam in the shadow region behind a silicon-dioxide sphere with a diameter of 100 nm. The formation of Poisson's spot about the optical axis (horizontal) can be clearly seen. The beam originates from a 20-μm-diameter source at a distance of 600 mm from the sphere. $I_{\rm rel}$ is given in intensity units of the undisturbed wave front (without the sphere, the plot would show $I_{\rm rel} = 1$). Here ρ denotes the distance from the optical axis and b is the distance between sphere and detection plane. For comparison, we display results for the case of no interaction between the sphere and the beam (a) and including the Casimir-Polder-induced phase shifts using the large-sphere nonretarded potential (b). In (c) the relative intensity on the optical axis is shown. The upper dashed and upper solid lines (blue) correspond to the data in (a) and (b), respectively, which means that the solid lines include the CP potential, while the dashed lines do not. The lower dashed and lower solid lines (orange) show the trend for the same parameters, but assume a 40-μm-diameter beam source. The shaded region about the solid lines give an approximate error margin due to a thin layer of indium forming on the sphere (see text).

V. DISCUSSION AND OUTLOOK

As can be seen in Fig. 4, the change in the phase shift due to retardation or the size of the sphere is negligible for the experiment discussed here. For this reason we have limited the Fresnel-diffraction simulations to the simpler half-space, nonretarded approximation.

The resulting relative intensities as a function of ρ and b are plotted in Figs. 6, 7, and 8 for three different sphere diameters. For better comparison the lateral relative intensity distributions are shown at the image distance $b = 0.1$ mm in Fig. 9. The relative intensity of Poisson's spot is increasingly amplified at smaller distances b due to the CP interaction. In addition, a small shift of the side maxima toward the optical axis can be noted [see especially Fig. 9(a)], which we attribute to an increasing effective sphere diameter for stronger CP interaction. The plot of the on-axis intensity for two different source sizes shows that increased spatial coherence leads to a more pronounced sensitivity of the Poisson-spot intensity to the CP potential. By comparing Figs. 6, 7, and 8 one can see that an increase in sphere diameter both increases $I_{\rm rel}$ due to the longer time the particle spends in the vicinity of the sphere, but also decreases it, as expected from Fresnel diffraction. In other words, there are two competing effects, which is why

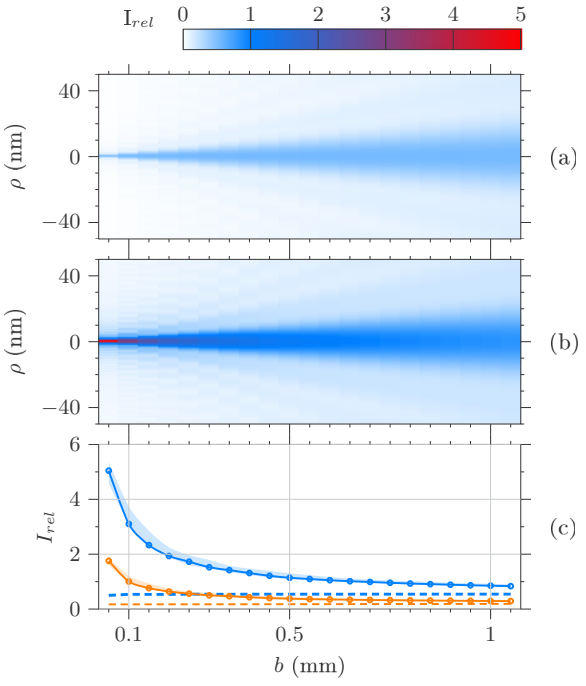

FIG. 7. Relative diffraction intensity for sphere radius $R = 100$ nm. The graphs are analogous to Fig. 6.

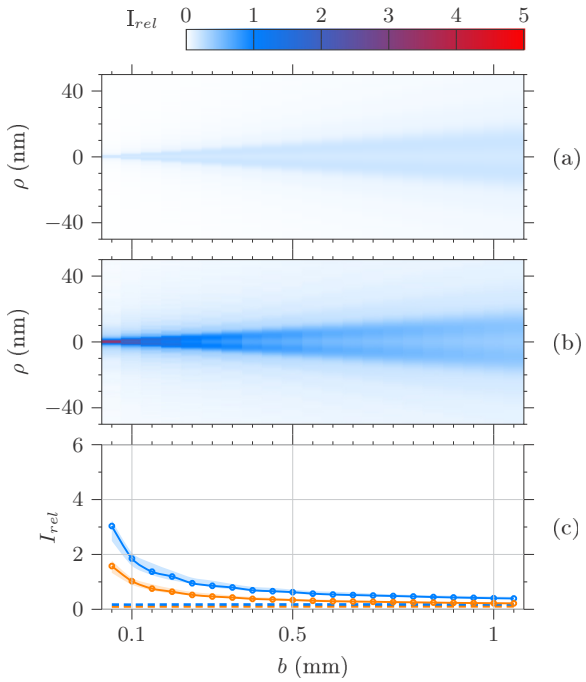

FIG. 8. Relative diffraction intensity for sphere radius $R = 200$ nm. The graphs are analogous to Fig. 6.

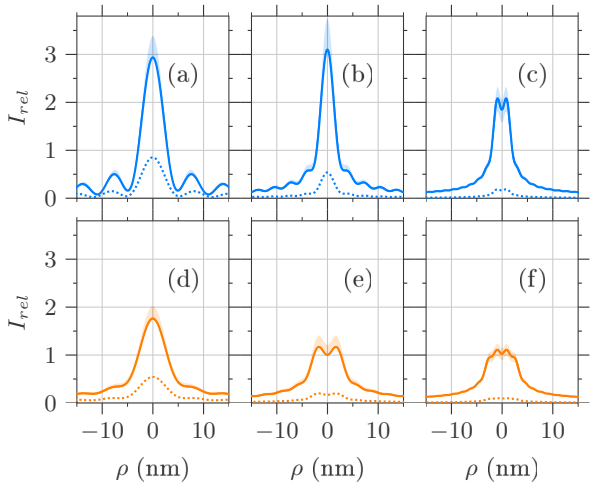

FIG. 9. Lateral relative intensity at $b = 0.1$ mm assuming a source diameter of 20 μm (a)–(c) and 40 μm (d)–(f). The assumed sphere diameter is $R = 50$ nm (a), (d), $R = 100$ nm (b), (e), and $R = 200$ nm (c), (f). The model including the large-sphere nonretarded CP-phase shift is depicted using solid lines and the Fresnel-diffraction-only model using dotted lines. The shaded regions around the solid lines give an approximate error margin stemming from the formation of a thin indium layer on the sphere (see Sec. V B).

I_{rel} is at a maximum for the medium sphere diameter (only in case of the 20-μm source).

To ensure the reliability of our results, we compared them to those found using a completely different numerical approach. As discussed in the caption of Fig. 5, the results plotted in Figs. 6, 7, 8, and 9 were computed in a similar way to [55], i.e., by direct numerical implementation of the Fresnel integral. That method is equivalent to the phase-space treatment outlined in [36] using Wigner functions (see [59] for details). The phase-space framework is ideally suited to account for environmental decoherence effects [11,60], e.g., by background gas collisions, and to juxtapose the predictions of the matter-wave model and a classical ballistic treatment of the atom trajectories. We have checked our numerical results against this framework and find agreement at the percent level, with the dominant contribution to the difference being our use of the approximate expression in the final line of (21). Another consistency check between our work and that of [36] is that the latter can predict which (semi-)classical trajectories physically collide with the sphere due to deflection by the potential. This can be determined simply by imposing conservation of energy and momentum, then minimizing the resulting function to find the smallest impact parameter a_{min} that escapes the potential. For the cases $R = 50$, 100, 200 nm considered here, we find $a_{\mathrm{min}} = 1.0$, 1.2, and 1.4 nm, respectively, which is consistent with the values $R_{i,\mathrm{CP}}$ [61] derived from our phase criteria in Sec. IV.

There are three more effects that we have not addressed so far, but which we discuss in the following sections.

A. Surface corrugation

The calculation neglects any surface corrugation of the sphere, for which a reduction in Poisson-spot intensity is expected at small distances b behind the sphere from the zero-interaction Fresnel-Kirchhoff integral. This effect can be estimated using an analytic dampening factor [62] that can be applied to the on-axis intensities. The relative intensity of Poisson's spot will be close to zero if the amplitude of the surface corrugation is approximately equal to the width of the adjacent Fresnel zone $w_{fz} = \sqrt{R^2 + \frac{\lambda g b}{(g+b)}} - R$. Assuming a corrugation amplitude of about 1 nm, we have $w_{fz} \approx 1$ nm at distances $b = 0.015$, 0.03, and 0.06 nm for sphere radii $R = 50$, 100, and 200 nm, respectively. A corrugation amplitude of 10 nm entails approximately a tenfold increase in the values of b at which the Poisson spot is no longer visible. This illustrates the importance of avoiding surface corrugation in the experiment as much as possible.

Furthermore, surface corrugation can influence the CP potential in the vicinity of the sphere in nontrivial ways [16–19,30,63]. In practice, we expect that the presence of CP interaction effectively mitigates the requirements on surface corrugation to some degree, especially if the corrugation amplitude is less than $R_{i,\mathrm{CP}} - R$. Accurate accounting of this influence could help in the future to distinguish between quantum and classical behavior of mesoscopic particles [13]. The details of this, however, we anticipate to be an interesting route for further study.

B. Formation of a metallic thin film on the sphere

One more reason for a deviation of experimental data from the results presented above is the possible buildup of

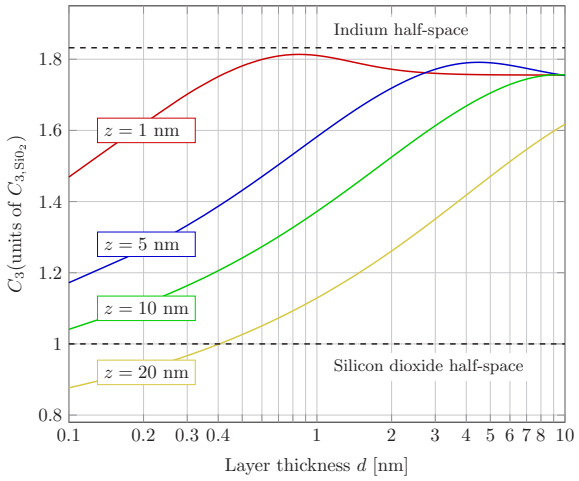

FIG. 10. Variation of the nonretarded, half-space CP constant C_3 as a function of deposited indium film thickness, with z being the distance from the sphere surface to the atom.

an indium film on the silicon-dioxide sphere. In our large-sphere approximation this would manifest itself as a thin layer deposited on top of a half space, for which estimates of its influence on the effective Casimir-Polder potential can be obtained relatively easily. We present a preliminary investigation of this in Fig. 10, where an effective C_3 at various distances from the coated sphere is shown as a function of indium film thickness. For thin layers a screening effect can be noted far from the surface. As the film grows in thickness the half-space CP potential of a pure indium surface is reached. The graph suggests that the effect can be accounted for by a modification of the effective C_3 of the system by approximately a factor in the range 0.8–1.8 (depending on layer thickness). This would result in an exposure-time-dependent diffraction pattern as the indium continuously accumulates upon the sphere. We show the deviation in the relative intensity of Poisson's spot approximately possible due to the thin film in the form of an error corridor (see shaded region in the plots of Figs. 6–9). The boundaries of the corridors were calculated by assuming constant effective CP constants of $0.8\,C_3$ and $1.8\,C_3$. The variation of the effective C_3 as a function of distance from the sphere z, as predicted in Fig. 10, can lead to even stronger attenuation or amplification depending on the resulting CP phase shift relative to the geometrical phase shift. However, we expect the error to be of the same order of magnitude as depicted by the shaded error corridors. The results suggest that the change in intensity of Poisson's spot due to a metallic thin film can be observed, but may be, in practice, hard to quantify. The main reasons for this are additional modifications of I_{rel} to be expected from changing surface corrugation as the thin film is deposited.

C. Temperature

1. Temperature of indium atoms

The effect of the CP interaction on the relative intensity of Poisson's spot depends on the temperature T_s of the indium atoms, at which they emerge from the oven source, in two distinct ways. First, T_s determines the speed distribution of the atoms and thus the accumulated CP phase shift [see Eq. (21)]. The speed distribution also affects the geometrical Fresnel phase shift via the de Broglie wavelength of the atoms. Both of these manifestations of finite T_s have been accounted for in the presented calculations. Second, at T_s any number of internal degrees of freedom of the atom maybe excited, which would alter the atom's polarizability and thus the CP potential. The occupation probability of the lowest excited state of the indium atoms at temperature $T_s = 1200\,^{\circ}\mathrm{C}$ can be estimated using the Boltzmann factor $e^{-\frac{\hbar\omega_{01}}{k_B T_s}}$ with the transition frequency ω_{01} from Table II and the reduced Planck constant $\hbar$ and Boltzmann's constant k_B. This evaluates to approximately 5×10^{-11}, which makes the assumption that all indium atoms reside in the ground state an extremely good one. Even at higher temperatures accessible with a standard oven heater, this ratio remains negligible. However, an artificial excitement using a laser at one of the specific indium wavelengths could be an appealing route to probing the CP interaction with excited atoms.

2. Ambient temperature

The ambient temperature of the experimental apparatus floods the interaction region between atom and dielectric sphere with thermal photons. These additional excitations of the electromagnetic field affect the CP potential only at distances of the order of the wavelengths of the thermal photons [64–66] (approximately 48 μm at room temperature). Since we determined that the CP phase shift in the discussed experiment is completely negligible at distances exceeding about 50 nm, it is safe to ignore any contributions from ambient thermal photons.

3. Temperature of the silicon-dioxide sphere

While it is not practicable to change the temperature of the apparatus significantly, the temperature of the diffraction obstacle could be raised to about $1000\,^{\circ}\mathrm{C}$ and higher for alternative obstacle materials. A reason for heating the obstacle could be to prevent the deposition of a thin film of the beam species, as discussed above. This would result in immediate re-evaporation of beam particles captured by the sphere, reflecting them diffusely in the general direction of the source. The influence of such states of thermal nonequilibrium on the CP potential is a topic of current research [67–69], and its possible influence on the present experiment should be the subject of further study.

VI. CONCLUSION

We have presented a detailed treatment of the CP potential between indium atoms and a silicon-dioxide sphere and its influence in the case of Poisson-spot matter-wave diffraction experiments. The main feature of our results is that the makeshift models of Casimir-Polder potentials, which neglect retardation and surface curvature and were used so far in matter-wave diffraction experiments, are, in fact, completely adequate. We have shown this by making a detailed account of the situation for a realistic and ongoing Poisson-spot experiment. This has allowed us to make verifiable predictions of diffraction patterns and relative intensities of the Poisson spot, backed up by a proper account of geometry- and

material-dependent dispersion forces. We found that the diameter of the silicon-dioxide sphere mainly affects the relative intensity of Poisson's spot due to the related change in length of the interaction region. Furthermore, we have estimated the effect from surface corrugation of the silicon-dioxide sphere and the possible deposition of indium on the diffraction obstacle. Finally, there remain a few more minor idealizations that are not included in our model thus far, for example that the sphere is at thermal equilibrium with the indium beam. On the whole, we expect that the predictions for the relative intensity of Poisson's spot made here provide solid ground for tests of the CP potential as predicted by macroscopic quantum electrodynamics in the ongoing experiments.

ACKNOWLEDGMENTS

We thank Stefan Scheel for fruitful discussions. S.Y.B. and R.B. acknowledge support from the Deutsche Forschungsgemeinschaft (Grant No. BU 1803/3-1), and S.Y.B. additionally acknowledges support from the Freiburg Institute for Advanced Studies (FRIAS). J.F. and S.Y.B. acknowledge support by the Research Innovation Fund of Freiburg University. T.R. acknowledges support by the Ministry of Science, Research and Art of Baden-Württemberg via a Research Seed Capital (RISC) grant. T.R., H.G., and H.H. acknowledge support by the Helmholtz Association. S.N. is supported by the National Research Foundation, Prime Minister's Office, Singapore and the Ministry of Education, Singapore under the Research Centres of Excellence programme.

APPENDIX A: VECTOR WAVE FUNCTIONS

The vector wave functions entering into (6) are given by

$$\mathbf{a}_{lm\pm TE}(\mathbf{r}) = \mp h_l^{(1)}(k_j r) m \frac{P_l^m(\cos\theta)}{\sin\theta} \begin{matrix}\sin(m\phi)\\ \cos(m\phi)\end{matrix} \mathbf{e}_\theta + h_l^{(1)}(k_j r) \frac{d}{d\theta}\left[P_l^m(\cos\theta)\right] \begin{matrix}\cos(m\phi)\\ \sin(m\phi)\end{matrix} \mathbf{e}_\phi, \quad \text{(A1)}$$

$$\mathbf{a}_{lm\pm TM}(\mathbf{r}) = l(l+1)\frac{h_l^{(1)}(k_j r)}{k_j r} P_l^m(\cos\theta) \begin{matrix}\cos(m\phi)\\ \sin(m\phi)\end{matrix} \mathbf{e}_r + \frac{[k_j r h_l^{(1)}(k_j r)]'}{k_j r} \frac{d}{d\theta}\left[P_l^m(\cos\theta)\right] \begin{matrix}\cos(m\phi)\\ \sin(m\phi)\end{matrix} \mathbf{e}_\theta \mp \frac{[k_j r h_l^{(1)}(k_j r)]'}{k_j r} m \frac{P_l^m(\cos\theta)}{\sin\theta} \begin{matrix}\sin(m\phi)\\ \cos(m\phi)\end{matrix} \mathbf{e}_\phi, \quad \text{(A2)}$$

where the primes are to be understood in the same sense as detailed below Eq. (7). The notation $\begin{matrix}x\\ y\end{matrix}$ here means that its upper or lower entries should be taken consistent with corresponding entries of the relevant $\pm$.

APPENDIX B: GREEN'S TENSOR SIMPLIFICATIONS

The trace of the scattering Green's tensor (6) reads

$$\begin{aligned}\mathrm{Tr}\,\mathbf{G}^{(1)}(\mathbf{r},\mathbf{r},i\xi) = -\frac{\xi}{4\pi c}\sum_{l=1}^{\infty}\sum_{m=0}^{l}(2-\delta_{m0})\frac{2l+1}{l(l+1)}\frac{(l-m)!}{(l+m)!} \times \Bigg\{ r_{lTE}\left[h_l^{(1)}(kr)\right]^2 \Bigg[m^2\left[\frac{P_l^m(\cos\theta)}{\sin\theta}\right]^2 + \left[\frac{dP_l^m(\cos\theta)}{d\theta}\right]^2\Bigg] + r_{lTM}\Bigg[\left(l(l+1)P_l^m(\cos\theta)\frac{h_l^{(1)}(kr)}{kr}\right)^2 + \frac{\left[kr h_l^{(1)}(kr)\right]'^2}{(kr)^2}\Bigg(m^2\left[\frac{P_l^m(\cos\theta)}{\sin\theta}\right]^2 + \left[\frac{dP_l^m(\cos\theta)}{d\theta}\right]^2\Bigg)\Bigg]\Bigg\}. \quad \text{(B1)}\end{aligned}$$

To carry out the sum over m, we use the addition theorem for spherical harmonics [45]:

$$P_l(\cos\gamma) = \sum_{m=0}^{l}(2-\delta_{m0})\frac{(l-m)!}{(l+m)!} \times P_l^m(\cos\theta)P_l^m(\cos\theta')\cos[m(\phi-\phi')]. \quad \text{(B2)}$$

The trace can therefore be rewritten as

$$\begin{aligned}\mathrm{Tr}\,\mathbf{G}^{(1)}(\mathbf{r},\mathbf{r},i\xi) = -\frac{\xi}{4\pi c}\sum_{l=1}^{\infty}(2l+1)\Bigg\{ r_{lTE}\left[h_l^{(1)}(kr)\right]^2 + r_{lTM}\Bigg[l(l+1)\frac{\left[h_l^{(1)}(kr)\right]^2}{(kr)^2} + \frac{\left[kr h_l^{(1)}(kr)\right]'^2}{(kr)^2}\Bigg]\Bigg\}, \quad \text{(B3)}\end{aligned}$$

which together with Eq. (4) renders the CP potential (8) for a sphere and a ground-state atom.

[1] C. Davisson and L. H. Germer, Nature (London) **119**, 558 (1927).
[2] G. P. Thomson and A. Reid, Nature (London) **119**, 890 (1927).
[3] I. Estermann and O. Stern, Z. Phys. **61**, 95 (1930).
[4] C. G. Shull and E. O. Wollan, Science **108**, 69 (1948).
[5] D. W. Keith, M. L. Schattenburg, H. I. Smith, and D. E. Pritchard, Phys. Rev. Lett. **61**, 1580 (1988).
[6] W. Schöllkopf and J. P. Toennies, Science **266**, 1345 (1994).
[7] M. Arndt, O. Nairz, J. Vos-Andreae, C. Keller, G. van der Zouw, and A. Zeilinger, Nature (London) **401**, 680 (1999).
[8] S. Gerlich, S. Eibenberger, M. Tomandl, S. Nimmrichter, K. Hornberger, P. J. Fagan, J. Tüxen, M. Mayor, and M. Arndt, Nat. Commun. **2**, 263 (2011).
[9] A. Bassi, K. Lochan, S. Satin, T. P. Singh, and H. Ulbricht, Rev. Mod. Phys. **85**, 471 (2013).
[10] L. Hackermueller, K. Hornberger, B. Brezger, A. Zeilinger, and M. Arndt, Nature (London) **427**, 711 (2004).

[11] K. Hornberger, J. E. Sipe, and M. Arndt, Phys. Rev. A **70**, 053608 (2004).
[12] J. D. Perreault and A. D. Cronin, Phys. Rev. Lett. **95**, 133201 (2005).
[13] T. Reisinger, G. Bracco, and B. Holst, New J. Phys. **13**, 065016 (2011).
[14] S. Eibenberger, S. Gerlich, M. Arndt, M. Mayor, and J. Tüxen, Phys. Chem. Chem. Phys. **15**, 14696 (2013).
[15] P. Haslinger, N. Dörre, P. Geyer, J. Rodewald, S. Nimmrichter, and M. Arndt, Nat. Phys. **9**, 144 (2013).
[16] C. Henkel and V. Sandoghdar, Opt. Commun. **158**, 250 (1998).
[17] R. Messina, D. A. R. Dalvit, Paulo A. Maia Neto, A. Lambrecht, and S. Reynaud, Phys. Rev. A **80**, 022119 (2009).
[18] A. M. Contreras-Reyes, R. Guérout, Paulo A. Maia Neto, D. A. R. Dalvit, A. Lambrecht, and S. Reynaud, Phys. Rev. A **82**, 052517 (2010).
[19] R. Bennett, Phys. Rev. A **92**, 022503 (2015).
[20] A. Rodriguez, M. Ibanescu, D. Iannuzzi, F. Capasso, J. D. Joannopoulos, and S. G. Johnson, Phys. Rev. Lett. **99**, 080401 (2007).
[21] C. Eberlein and R. Zietal, Phys. Rev. A **83**, 052514 (2011).
[22] O. Nairz, M. Arndt, and A. Zeilinger, Am. J. Phys. **71**, 319 (2003).
[23] R. E. Grisenti, W. Schöllkopf, J. P. Toennies, G. C. Hegerfeldt, and T. Köhler, Phys. Rev. Lett. **83**, 1755 (1999).
[24] R. E. Grisenti, W. Schöllkopf, J. P. Toennies, J. R. Manson, T. A. Savas, and H. I. Smith, Phys. Rev. A **61**, 033608 (2000).
[25] I. Brevik, M. Lygren, and V. Marachevsky, Ann. Phys. (NY). **267**, 134 (1998).
[26] A. D. Cronin and J. D. Perreault, Phys. Rev. A **70**, 043607 (2004).
[27] A. D. Cronin and J. D. Perreault, J. Phys. Conf. Ser. **19**, 48 (2005).
[28] P. A. Maia Neto, A. Lambrecht, and S. Reynaud, Europhys. Lett. **69**, 924 (2005).
[29] G. Bimonte, T. Emig, and M. Kardar, Phys. Rev. D **90**, 081702 (2014).
[30] H. Bender, C. Stehle, C. Zimmermann, S. Slama, J. Fiedler, S. Scheel, S. Y. Buhmann, and V. N. Marachevsky, Phys. Rev. X **4**, 011029 (2014).
[31] H. Gies and K. Klingmüller, Phys. Rev. Lett. **97**, 220405 (2006).
[32] J. E. Harvey and J. L. Forgham, Am. J. Phys. **52**, 243 (1984).
[33] E. Hecht, *Optics*, 4th international ed. (Addison Wesley, Boston, 2002).
[34] D. Gooding, T. Pinch, and S. Schaffer, *The Uses of Experiment: Studies in the Natural Sciences* (Cambridge University Press, Cambridge, UK, 1989).
[35] T. Reisinger, A. A. Patel, H. Reingruber, K. Fladischer, W. E. Ernst, G. Bracco, H. I. Smith, and B. Holst, Phys. Rev. A **79**, 053823 (2009).
[36] T. Juffmann, S. Nimmrichter, M. Arndt, H. Gleiter, and K. Hornberger, Found. Phys. **42**, 98 (2012).
[37] W. Stöber, A. Fink, and E. Bohn, J. Colloid Interface Sci. **26**, 62 (1968).
[38] J. D. Perreault, A. D. Cronin, and T. A. Savas, Phys. Rev. A **71**, 053612 (2005).
[39] T. Gruner and D.-G. Welsch, Phys. Rev. A **53**, 1818 (1996).
[40] S. Scheel and S. Y. Buhmann, Acta Physica Slovaca **58**, 675 (2008).
[41] S. Y. Buhmann, L. Knöll, D.-G. Welsch, and H. T. Dung, Phys. Rev. A **70**, 052117 (2004).
[42] S. Buhmann, *Dispersion Forces I: Macroscopic Quantum Electrodynamics and Ground-State Casimir, Casimir-Polder and van der Waals Forces*, Springer Tracts in Modern Physics (Springer, Berlin, Heidelberg, 2013).
[43] Le-Wei Li, Pang-Shyan Kooi, Mook-Seng Leong, and Tat-Soon Yee, IEEE Trans. Microwave Theory Tech. **42**, 2302 (1994).
[44] C.-T. Tai, *Dyadic Green Functions in Electromagnetic Theory* (Institute of Electrical and Electronics Engineers, New York, 1994).
[45] J. Jackson, *Classical Electrodynamics* (Wiley, New York, 1998).
[46] S. Y. Buhmann, H. T. Dung, and D.-G. Welsch, J. Opt. B **6**, S127 (2004).
[47] W. Jhe and J. Kim, Phys. Lett. A **197**, 192 (1995).
[48] W. Jhe and J. W. Kim, Phys. Rev. A **51**, 1150 (1995).
[49] J. E. Lennard-Jones, Trans. Faraday Soc. **28**, 333 (1932).
[50] R. Eisenschitz and F. London, Z. Phys. **60**, 491 (1930).
[51] H. B. G. Casimir and D. Polder, Phys. Rev. **73**, 360 (1948).
[52] V. M. Nabutovskii, V. R. Belosludov, and A. M. Korotkikh, Zh. Eksp. Teor. Fiz. **77**, 700 (1979) [J. Exp. Theor. Phys. **50**, 352 (1979)].
[53] Edited by E. Palik, *Handbook of Optical Constants of Solids* (Academic Press, San Diego, 1998).
[54] M. S. Safronova, U. I. Safronova, and S. G. Porsev, Phys. Rev. A **87**, 032513 (2013).
[55] D. E. Dauger, Comput. Phys. **10**, 591 (1996).
[56] K. Hornberger, S. Gerlich, P. Haslinger, S. Nimmrichter, and M. Arndt, Rev. Mod. Phys. **84**, 157 (2012).
[57] T. Reisinger, G. Bracco, S. Rehbein, G. Schmahl, W. E. Ernst, and B. Holst, J. Phys. Chem. A **111**, 12620 (2007).
[58] T. Reisinger, M. M. Greve, S. D. Eder, G. Bracco, and B. Holst, Phys. Rev. A **86**, 043804 (2012).
[59] S. Nimmrichter, *Macroscopic Matter Wave Interferometry*, Springer Theses (Springer International, Cham, Switzerland, 2014).
[60] K. Hornberger, S. Uttenthaler, B. Brezger, L. Hackermüller, M. Arndt, and A. Zeilinger, Phys. Rev. Lett. **90**, 160401 (2003).
[61] Note that the $R_{i,\mathrm{CP}}$ values quoted in Sec. IV include the sphere radii R.
[62] T. Reisinger, P. Leufke, H. Gleiter, and H. Hahn (unpublished).
[63] S. Y. Buhmann, V. N. Marachevsky, and S. Scheel, Int. J. Mod. Phys. A **31**, 1641029 (2016).
[64] M.-P. Gorza and M. Ducloy, Eur. Phys. J. D **40**, 343 (2006).
[65] P. Chaves de Souza Segundo, I. Hamdi, M. Fichet, D. Bloch, and M. Ducloy, Laser Phys. **17**, 983 (2007).
[66] C. Henkel, K. Joulain, J.-P. Mulet, and J.-J. Greffet, J. Opt. A Pure Appl. Opt. **4**, S109 (2002).
[67] M. Antezza, L. P. Pitaevskii, and S. Stringari, Phys. Rev. A **70**, 053619 (2004).
[68] J. M. Obrecht, R. J. Wild, M. Antezza, L. P. Pitaevskii, S. Stringari, and E. A. Cornell, Phys. Rev. Lett. **98**, 063201 (2007).
[69] S. Y. Buhmann and S. Scheel, Phys. Rev. Lett. **100**, 253201 (2008).

nature COMMUNICATIONS

ARTICLE

DOI: 10.1038/s41467-018-05091-x OPEN

The influence of retardation and dielectric environments on interatomic Coulombic decay

Joshua Leo Hemmerich[1], Robert Bennett[1] & Stefan Yoshi Buhmann[1,2]

Interatomic Coulombic decay (ICD) is a very efficient process by which high-energy radiation is redistributed between molecular systems, often producing a slow electron, which can be damaging to biological tissue. During ICD, an initially-ionised and highly-excited donor species undergoes a transition where an outer-valence electron moves to a lower-lying vacancy, transmitting a photon with sufficient energy to ionise an acceptor species placed close by. Traditionally the ICD process has been described via ab initio quantum chemistry based on electrostatics in free space, which cannot include the effects of retardation stemming from the finite speed of light, nor the influence of a dispersive, absorbing, discontinuous environment. Here we develop a theoretical description of ICD based on macroscopic quantum electrodynamics in dielectrics, which fully incorporates all these effects, enabling the established power and broad applicability of macroscopic quantum electrodynamics to be unleashed across the fast-developing field of ICD.

[1] Physikalisches Institut, Albert-Ludwigs-Universität Freiburg, Hermann-Herder-Str. 3, 79104 Freiburg, Germany. [2] Freiburg Institute for Advanced Studies (FRIAS), Albertstr. 19, 79104 Freiburg, Germany. These authors contributed equally: Joshua Leo Hemmerich, Robert Bennett, Stefan Yoshi Buhmann Correspondence and requests for materials should be addressed to R.B. (email: robert.bennett@physik.uni-freiburg.de)

ARTICLE NATURE COMMUNICATIONS | DOI: 10.1038/s41467-018-05091-x

Exactly one century ago, Einstein showed[1] that the existence of a thermal equilibrium between matter and radiation implies a process by which atoms can indiscriminately release energy—now known as spontaneous emission. Its origin is the coupling of the atom to the quantum electrodynamical vacuum field that permeates all of space, so while being originally thought of as a fundamental atomic property, spontaneous emission can in fact be tuned by placing the emitter in an environment that modifies the vacuum state—between mirrors, for example. This was first pointed out by Purcell[2], who predicted that the rate of spontaneous decay could be dramatically enhanced by confining an emitter to a small volume. At a similar time, Casimir and Polder[3] found that the finite speed of light can impact the London-van der Waals force, originally thought of as an instantaneous and fundamental interaction between particles. In both cases, the explanation of a previously known effect in terms of a more fundamental theory, quantum electrodynamics (QED), led to the prediction of new physics, later verified in experiments. This is the blueprint we wish to follow in the present study of interatomic Coulombic decay (ICD)

ICD was first predicted in 1997 by L.S. Cederbaum and coworkers[4] and experimentally observed shortly afterwards[5–8]. The details of the ICD process are shown in Fig. 1, where in our terminology the interaction-mediating photon is in fact a generalised polariton-like field-matter excitation, containing both radiative (long-range) and non-radiative (short-range) contributions. It is worth noting that the electron left in the continuum is usually of a relatively low energy[9], as most of the energy the photon transfers to the acceptor is spent freeing the electron. It has been shown that such low-energy electrons can have detrimental effects on biological matter[10], meaning that ICD is of more than fundamental interest.

Comparison of ICD observations with theory is usually made by elaborate ab initio quantum chemistry approaches[11]—a trend that continues in the recently proposed superexchange[12], surface-based[13] and doubly-ionised[14] ICD variants. These methods are well-suited to dealing with the complex consequences of orbital overlap between donor and acceptor. However, they cannot easily deal with the effects of retardation stemming from the finite speed of light. Furthermore, while a simple dielectric background or extended host molecule can be taken into account with molecular dynamics techniques[15,16] or via numerical quantum chemistry[17–19], the full effects of dispersion, absorption, relativistic retardation and sharp boundaries remain computationally beyond reach. This means that such approaches are not able to account for the effects of a complex environment, such as that of a helium nanodroplet[20–23] or those found in biological settings[10,24,25].

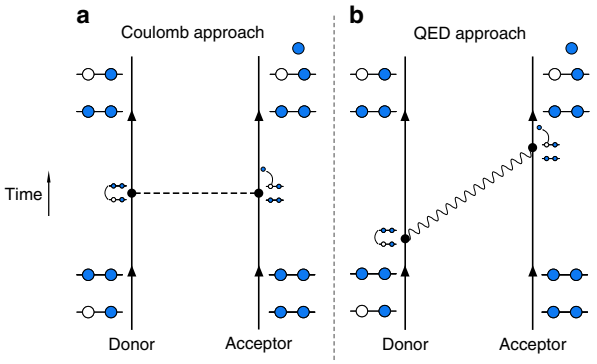

Fig. 1 Interatomic Coulombic decay process. Illustration of the interatomic Coulombic decay process in terms of **a** the traditional language of Coulomb interactions and **b** our quantum electrodynamics approach. An ionised, excited atom or molecule (donor) with an inner-valence vacancy (sometimes known as hollow) makes a transition where that vacancy is filled and a photon is emitted. If that photon has an energy higher than the photoionisation threshold of a neighbouring atom or molecule (acceptor), its absorption may be accompanied by an electron being freed into the continuum. The resulting pair of ions then undergoes a 'Coulomb explosion', which is one of the experimental signatures of ICD

In the following we present a theoretical description of ICD that systematically includes all of the latter effects, for which we use a framework known as macroscopic QED[26–29]. In this formalism the quantised electromagnetic field in dispersive and absorbing media is described by a dyadic Green's tensor $\mathbb{G}(\mathbf{r}, \mathbf{r}', \omega)$ governing propagation of field-matter excitations (medium-assisted photons) of frequency ω between a source at position $\mathbf{r}'$ and an observation point $\mathbf{r}$. Various QED quantities such as spontaneous decay rates and Casimir forces can then be expressed entirely in terms of this Green's tensor, which is known in closed form for simple geometries[30] and can be approximated for more complex ones[31]. This allows the computation of such QED quantities in any desired environment, with vacuum emerging as a special case. In this work we use this formalism to show that the range of ICD may be much larger than expected from purely electrostatic considerations, and that an environment such as liquid water can significantly alter the efficiency of ICD. For donor and acceptor situated near a macroscopic body, we predict that the ICD rate can be enhanced or suppressed due to resonant interactions with surface plasmons.

Results

Macroscopic QED approach to ICD. Using the formalism of macroscopic QED, we have calculated a general expression for the ICD rate in arbitrary dispersive and absorbing environments, valid at any donor–acceptor distance where orbital overlap can be neglected[32]. We begin with the interaction Hamiltonian of the dipole moments $\hat{\mathbf{d}}_\mathrm{D}$of the donor and $\hat{\mathbf{d}}_\mathrm{A}$ of the acceptor,

$$\hat{H}_\mathrm{int} = -\hat{\mathbf{d}}_\mathrm{D} \cdot \hat{\mathbf{E}}(\mathbf{r}_\mathrm{D}) - \hat{\mathbf{d}}_\mathrm{A} \cdot \hat{\mathbf{E}}(\mathbf{r}_\mathrm{A}) \quad (1)$$

where the quantised electric field operator $\hat{\mathbf{E}}(\mathbf{r})$ excites polariton-like field-matter excitations through an appropriate set of bosonic operators. We then evaluate the ICD rate Γ using the interaction Hamiltonian (1) in time-dependent perturbation theory with causal adiabatic coupling. It is important to note that viewing the ICD process as the exchange of virtual photons means that twice as many orders of perturbation theory are needed compared to an instantaneous Coulomb-like picture, as illustrated in Fig. 1.This is because the Coulomb approach considers the donor and acceptor as essentially a single object, which then undergoes ICD as a one-step process (the two interactions in Fig. 1 occur simultaneously). By contrast, the virtual photon approach considers the donor and acceptor completely separately, so that the finite time delay associated with propagation from one to the other is fully taken into account. This doubling of the number of interactions means that in contrast to Coulomb approaches where second order perturbation theory suffices (see, for example ref.[11]), we need to use fourth-order time-dependent perturbation theory. Using the Hamiltonian (1) and expanding the transition matrix element that links our initial and final states in a Dyson series keeping terms up to fourth order in the interaction (see Methods section), we extract the ICD decay rate as;

$$\Gamma = 2\pi^2 \sum_{\text{channels}} \gamma_\mathrm{D}\sigma_\mathrm{A}(\hbar\omega_\mathrm{A})\mathrm{Tr}[\mathbb{G}(\mathbf{r}_\mathrm{A}, \mathbf{r}_\mathrm{D}, \omega_\mathrm{D}) \cdot \mathbb{G}^*(\mathbf{r}_\mathrm{D}, \mathbf{r}_\mathrm{A}, \omega_\mathrm{D})], \quad (2)$$

NATURE COMMUNICATIONS | DOI: 10.1038/s41467-018-05091-x ARTICLE

where $\mathbf{r}_A$ and $\mathbf{r}_D$ are, respectively, the positions of the acceptor and donor, ω_D is the transition frequency of the donor and $\hbar\omega_A = \hbar\omega_D - U_{coul}$, where U_{coul} is the Coulomb energy of the system. The allowed channels in the above expression are those satisfying $\hbar\omega_D \geq U_{coul} + U_{ion}$, where U_{ion} is the ionisation potential of the acceptor. We make use of the following shorthands; γ_D is the free-space single-atom decay rate of the donor, given explicitly by

$$\gamma_D = \frac{\omega_D^3 |\mathbf{d}_D|^2}{3\pi\hbar c^3 \varepsilon_0}, \tag{3}$$

and $\sigma_A(E)$ is the photoionization cross section of the acceptor

$$\sigma_A(E) = \frac{\pi E}{3\varepsilon_0 c\hbar} \frac{\mathrm{d}}{\mathrm{d}E} |\mathbf{d}_A|^2, \tag{4}$$

which is expressed as a function of the energy E of the incident photon. We see from equations (3) and (4) that formula (2) contains four dipole moments, each of which corresponds to an interaction vertex in our fourth-order perturbation theory.

Formula (2) can be physically understood as the product of three factors. The first is the free-space decay rate γ_D of the donor, which is simply a measure of how strongly its coupling to the vacuum causes it to emit, even in the absence of the acceptor or an environment. The second factor is the trace over Green's tensors, describing the impact of the environment between and around donor and acceptor on the transmission of energy between them. The final factor is the photoionisation cross section σ_A of the acceptor, evaluated at the photon frequency $\hbar\omega_D$. This factor corresponds to how likely it is that a photon arriving at the acceptor will cause a photoionisation event, freeing an electron from the acceptor. This means the three factors each loosely correspond to a probability of a step in the process (emission, propagation and then absorption), meaning that their product represents an overall rate for ICD.

Relativistic retardation in ICD. The first consequence of Eq. (2) that we will highlight is the effect of retardation originating from the finite speed of light (note that the related process of two-centre resonant photoionisation has also been shown to be affected by retardation in free space[33]). The consequences of this are expected to be the most dramatic at large donor–acceptor distances—systems with this character have been the focus of recent experimental work[34,35]. Using the vacuum Green's tensor [see, for example, ref.[29] or the Methods section] in our formula (2) we find;

$$\Gamma_{vac} = \frac{1}{4} \sum_{channels} \frac{\gamma_D \sigma_A(\hbar\omega_A)}{(2\pi/\lambda_D)^4 \rho^6} \left[3 + \left(\frac{2\pi\rho}{\lambda_D}\right)^2 + \left(\frac{2\pi\rho}{\lambda_D}\right)^4 \right], \tag{5}$$

where $\rho = |\mathbf{r}_D - \mathbf{r}_A|$ is the donor–acceptor separation and $\lambda_D = 2\pi c/\omega_D$ is the wavelength of the photon emitted from the donor. In the limit of short distances only the first term in the square brackets of (5) remains, this is is the non-retarded vacuum rate Γ_{vac}^{NR};

$$\Gamma_{vac}^{NR} = \frac{3}{4} \sum_{channels} \frac{\gamma_D \sigma_A(\hbar\omega_A)}{(2\pi/\lambda_D)^4 \rho^6}. \tag{6}$$

This is the only part of Eq. (5) accessible without using our theory, and as such is reproduced by the more traditional instantaneous Coulomb approach[32,36], and its inverse sixth power of distance can be understood as coming from the ρ^{-3} dependence of the near-field limit of the electric field of a dipole, which is then squared during calculation of dipole–dipole coupling. The second and third terms of Eq. (5) are new and come from the inclusion of the far-field of the dipole which decays as ρ^{-1}. The new terms are proportional to ρ^{-4} and ρ^{-2}, which obviously means they decay much more slowly at large distances than the ρ^{-6} found without including retardation. This can cause dramatic enhancement relative to the rate expected from the non-retarded theory if the condition $2\pi\rho > \lambda_D$ is satisfied, as shown in Fig. 2.

Systems undergoing ICD are typically separated by around 3–10 Å, meaning that the condition $\rho > \lambda_D/2\pi$ is comfortably satisfied by, for example, taking Ne^{9+} (nine-fold ionised neon) as a donor species. There the transition energy from the $2P_{1/2} \rightarrow 2S_{1/2}$ levels is around 1.02 keV, corresponding to $\lambda_D/2\pi$ of approximately 1.9 Å.

The importance of retardation is not limited to small, extreme systems such as hydrogen-like ions—even large, multi-electron ions can be near enough to each other to undergo ICD $(\lesssim 10\,\text{Å})$, while also being far enough for the assumption of negligible orbital overlap to be applicable. The degree of orbital overlap depends strongly on specific choice of donor and acceptor species, so here we refer to the specific example studied in ref.[32], where it was shown that the effects of orbital overlap become negligible in Ne–Mg ICD if the separation is above ~6–7 Å. In that system the transition wavelength is far too long for retardation to play a role. However, if one replaces the neon donor with a neon-like ion, the transition wavelength will be much shorter, but the degree of orbital overlap should to remain similar, meaning its influence will still become negligible at at about 6–7 Å. We have included in the inset of Fig. 2 the ICD rate for three selected neon-like donors, with arbitrary acceptor species. While one would have to carefully consider the degree of orbital overlap for a neon-like donor and a specific acceptor species in order to decide in which specific distance range our model applies, the preceding discussion and the inset of Fig. 2 together show that ICD between large, multi-electron systems can in principle also be subject to significant retardation corrections.

ICD in a host medium. The second application of our formula (2) is to ICD processes in a medium. A naive approach to calculating the ICD rate in this situation would be simply changing the optical path length of the photon, but this is not an adequate description of interatomic processes in media, as discussed in ref.[37]. Such an approach misses the fact that an atom embedded in a medium has a small region of empty space around it, meaning the field it experiences is different from that found in the bulk medium—this is known as the local-field effect (LFE). Our approach to ICD can include this by using the appropriate Green's tensor in Eq. (2), in particular that described in ref.[38] where the local-field corrected Green's tensor is calculated for arbitrary media described by a frequency-dependent permittivity $\varepsilon(\omega)$. For illustrative purposes we concentrate on the small-distance limit of our formula (2), but we emphasise that our general theory can take into account retardation and medium effects simultaneously. Using the local-field corrected Green's tensor (see Methods) in the non-retarded limit of our formula (2) we find the rate for a single ICD channel in a bulk medium as;

$$\Gamma_{bulk}^{NR} = \Gamma_{vac}^{NR} \cdot \eta \cdot \eta_{LFE} \quad \eta_{LFE} = \left| \frac{3\varepsilon(\omega_D)}{2\varepsilon(\omega_D) + 1} \right|^4 \tag{7}$$

where $\eta = |\varepsilon(\omega_D)|^{-2}$ is the correction factor that arises in the simple bulk model, η_{LFE} is the correction due to the LFE, and we have expressed the rate in terms of Γ_{vac}^{NR} as given by Eq. (6). In order to assess the impact of the LFE, we have also shown in Eq. (7) the result that is found if the LFE is ignored ($\eta_{LFE} = 1$). For quantitative analysis of (7) we have used the measured

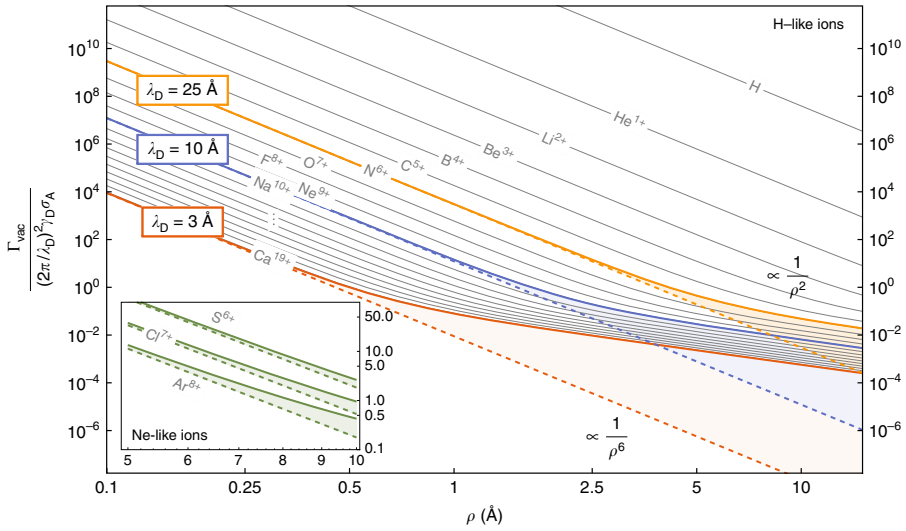

Fig. 2 Effect of retardation on interatomic Coulombic decay rate: Main plot: position-dependence of the interatomic Coulombic decay rate for arbitrary acceptor species and a variety of donors, as a function of their mutual separation ρ. Shown with thick solid lines are the rates for a selection of donor transition wavelengths λ_D. In the near-field (non-retarded) limit the rate is proportional to ρ^{-6} (dashed straight lines), while in the far-field (retarded) limit it becomes proportional to ρ^{-2}, drastically enhancing the rate relative to that which is found if retardation is ignored. For reference we have shown as thin lines the ICD rates if the donor is taken to be a hydrogen-like ion undergoing a $2P_{1/2} \rightarrow 2S_{1/2}$ transition[48]. The rates for the first twenty such ions are shown (labels for Mg^{11+} to K^{18+} are replaced by '...' for formatting reasons) demonstrating that, for example, an ICD process whose donor is a Na^{10+} ($\lambda_D = 10.05$ Å) ion will experience significant retardation at typical ICD distances (3–10 Å). Inset: Same axes as the main plot, instead displaying data relevant to the $1P^o \rightarrow 1S$ transition in selected neon-like ions

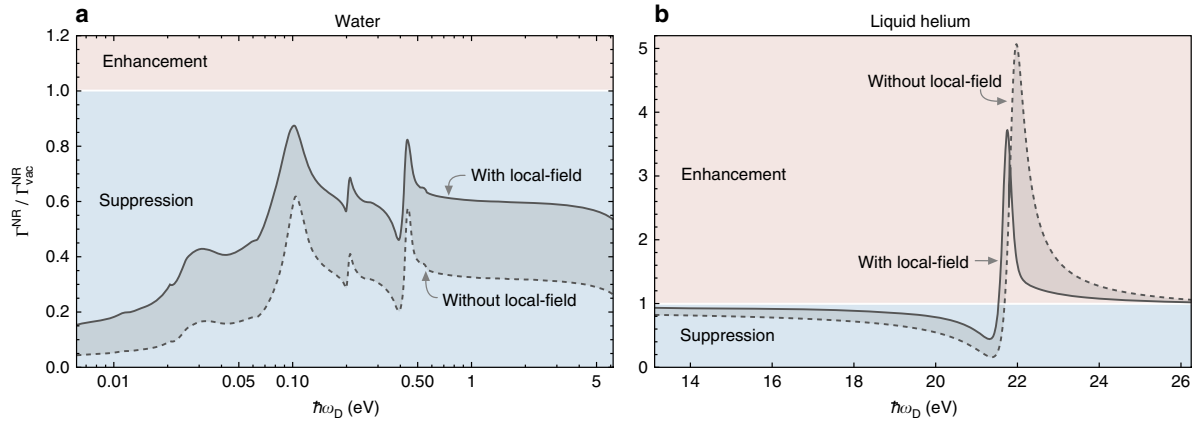

Fig. 3 Effect of solvent media on interatomic Coulombic decay rate. Non-retarded interatomic Coulombic decay rate Γ^{NR} in **a** liquid water and **b** liquid helium, using tabulated optical data[40, 41]. The results are normalised to the non-retarded rate Γ^{NR}_{vac} encountered in vacuum, given by Eq. (6). As explained in the main text, the bulk medium can enhance or suppress the ICD rate, and the local-field effect can cause an additional suppression or enhancement relative to the results without the local-field effect

permittivities for water[40] and liquid helium[41], relevant to biological processes and experiments on nanodroplets[22], respectively. Our results are shown in Fig. 3 where we make a comparison with the rate that would be predicted if LFEs were not taken into account. There we see that inclusion of the LFE can cause enhancement or suppression of the ICD rate, on top of the suppression or enhancement that the simple bulk (that is, without the LFE) causes. The LFE-corrected bulk causes suppression when $\eta \cdot \eta_{LFE} < 1$, which is satisfied when, for example, $\varepsilon < 1$ as is the case near the absorption resonance of helium, which is the origin of the enhancement there. For water in the displayed frequency range, the ICD rate is always suppressed by the solvent medium where the neglect of the LFE leads to an overestimation of this suppression. For helium, the LFE significantly narrows the frequency window where the ICD rate is enhanced. The experiment reported in ref.[22] reveals an ICD signal at 21.6 eV inside a He nanodroplet. Our calculations as shown in Fig. 3 predict an enhancement of the respective ICD rate by a factor 1.7 due to the

presence of the bulk nanodroplet medium. To confirm this quantitatively, one has to first use our Eq. (2) in conjunction with the known Green's tensor of the spherical nanodroplet (see, for example ref.[42]) to calculate the ICD rate for arbitrary donor and acceptor positions with respect to the droplet, a similar study of the effect of a dielectric sphere on the van der Waals interaction between two atoms has been carried out in ref.[43]. Subsequently, the geometric distributions of donors and acceptors, as well as additional decay channels and processes, have to be accounted for to generate a predicted experimental signal. Finally, we note that in this discussion we have concentrated on the effects that the medium has on field propagation between donor and acceptor. In addition, the medium has an impact on the donor and acceptor's properties such as transition frequencies and dipole moments. This could be studied alternatively using molecular dynamics or macroscopic QED[44].

ICD near a dielectric surface. Another demonstration of the power of our general formula (2) is calculation of the effect an inhomogenous environment has on ICD, taking inspiration from the Purcell enhancement of the spontaneous decay rate. Similarly to our presentation of the rates in a bulk medium, we will concentrate on the short-distance limit of our formula (2), but again emphasise that our general theory can simultaneously take into account all the effects discussed so far. Using the dyadic Green's tensor for a dielectric surface[29,30] with frequency-dependent permittivity $\varepsilon(\omega)$ occupying the region $z<0$ (see Methods) in our formula (2), we find the following rate in the non-retarded regime;

$$\Gamma^{\mathrm{NR}}_{\mathrm{plate}} = \frac{3}{4}\sum_{\mathrm{channels}} \frac{\gamma_{\mathrm{D}}\sigma_{\mathrm{A}}(\hbar\omega_{\mathrm{A}})}{\omega_{\mathrm{D}}^4/c^4} \times \left\{\frac{1}{\rho^6} + 2\mathrm{Re}[R(\omega_{\mathrm{D}})]\left[\frac{1}{3\rho^3\bar{\rho}^3} - \frac{\rho^2+\bar{\rho}^2}{2\rho^5\bar{\rho}^5}\rho_{||}^2\right] + \frac{|R(\omega_{\mathrm{D}})|^2}{\bar{\rho}^6}\right\}, \tag{8}$$

where $\bar{\rho} = \rho(z_D \to -z_D)$, $\rho_{||}^2 = (x_D - x_A)^2 + (y_D - y_A)^2$ and $R(\omega) = (\varepsilon(\omega)-1)/(\varepsilon(\omega)+1)$ is the Fresnel reflection coefficient of the surface. In order to make quantitative predictions we assume a permittivity of the Drude–Lorentz form,

$$\varepsilon(\omega) = 1 - \frac{\omega_p^2}{\omega^2 - \omega_{\mathrm{T}}^2 + i\gamma\omega}, \tag{9}$$

where ω_p is the plasma frequency, ω_{T} is a transition frequency and γ is a damping constant. This choice of dielectric function causes the reflection coefficient $R(\omega)$ defined above to exhibit a resonance at a frequency $\omega_{\mathrm{S}} = \sqrt{\omega_{\mathrm{T}}^2 + \omega_p^2/2}$, commonly known as the surface plasmon frequency. In Fig. 4 we display the plate-dependent ICD rate (normalised to that for free space) for a donor at a fixed position near the interface while allowing the position of the acceptor to vary. We choose a range of transition frequencies for the donor, both above and below the resonance frequency of the material. It is seen that the medium-dependent ICD rate has an intricate dependence on both the relative positions of the donor and acceptor, and the relationship between the ICD photon frequency and that of the material resonance. For example, at frequencies below the material resonance and with $\mathbf{r}_{\mathrm{A}} - \mathbf{r}_{\mathrm{D}}$ aligned parallel to the surface, the ICD rate is suppressed by a factor of up to 2. This placement of donor and acceptor could be envisaged in a biological context as two molecules sitting on a cell membrane, our theory predicts that the ICD rate between the two will be slower due to the presence of the membrane. Similarly, if the frequency remains below resonance but now $\mathbf{r}_{\mathrm{A}} - \mathbf{r}_{\mathrm{D}}$ is aligned perpendicular to the surface, the ICD rate can be enhanced by a similar factor. This could arise in a biological setting as an aid to efficient energy transport; our theory predicts that the presence of an interface at the end of a linear arrangement of emitters and absorbers would cause a noticeable enhancement of energy transfer between neighbours.

Finally, we emphasise that although we have separately presented three ICD-modifying effects (retardation, immersion in a bulk medium and placement near a surface) in order to maintain a clear conceptual divide between each, all of these and more can be taken into account simultaneously in our framework simply by using the appropriate well-known Green's tensors (c.f. ref.[29]). As an example, we report here the ICD rate found from Eq. (2) for donor and acceptor embedded in an absorbing medium of complex refractive index $\bar{n}(\omega) = \sqrt{\varepsilon(\omega)} = n(\omega) + i\kappa(\omega)$, simultaneously including local-field corrections and relativistic retardation. To do this we use the retarded bulk Green's tensor and the local-field prescription (both of which are found in the Methods section) in Eq. (2), finding;

$$\Gamma_{\mathrm{bulk}} = \sum_{\mathrm{channels}} \Gamma^{\mathrm{NR}}_{\mathrm{bulk}} e^{-2\kappa\rho\omega_{\mathrm{D}}/c} \times \left[1 + 2\kappa\zeta + \frac{\zeta^2}{3}\left(4\kappa^2 + |\bar{n}|^2\right) + \frac{2\kappa\zeta^3}{3}|\bar{n}|^2 + \frac{\zeta^4}{3}|\bar{n}|^4\right], \tag{10}$$

where $\zeta = \rho\omega_{\mathrm{D}}/c$. The material parameters $n(\omega)$ and $\kappa(\omega)$ are both evaluated at the donor frequency ω_{D}, and we have used the rate defined by (7) as a shorthand. From Eq. (10) it is evident that there is a complex interplay between the various factors discussed so far, including an exponential screening factor that depends on the extinction coefficient κ, as well as polynomial dependence on various combinations of distance and material parameters. In Fig. 5 we plot the separation-dependence of the rate (10) in vacuum and in helium, both with and without local-field corrections. The rates (5) and (7) emerge from Eq. (10) in its vacuum ($n \to 1$, $\kappa \to 0$), and non-retarded ($\rho\omega_{\mathrm{D}}/c \ll 1$) limits, respectively.

In conclusion, we have presented a description of the ICD rate in arbitrary environments that are described via the electromagnetic Green's tensor. We have demonstrated some of the explicit consequences of our main result (2), the first being the fundamental importance of retardation which can cause ICD rates to be orders of magnitude higher than expected from any previous theory. We have also studied local-field corrections in a bulk medium, as well as the intricate dependence of the ICD rate upon a nearby macroscopic body. All of these effects should be taken into account when calculating the impact of ICD in the non-idealised, messy situations found in the life sciences, as well as to more fundamental research into medium-dependent ICD. We emphasise that every calculation here proceeded analytically from the same very general formula (2), which was derived using the established power and broad applicability of macroscopic QED, which can now be unleashed across the fast-developing field of ICD.

Methods

Derivation of ICD rate. In this section we derive our central result (2), which is the ICD rate Γ in arbitrary environments. We will calculate Γ from Fermi's golden rule;

$$\Gamma = \sum_f \frac{2\pi}{\hbar}\left|M_{fi}\right|^2 \delta\left(E_i - E_f\right). \tag{11}$$

where M_{fi} is a transition matrix element and E_i, E_f are the energy eigenvalues of the unperturbed Hamiltonian for the initial and final states $|i\rangle$ and $|f\rangle$, respectively. The transition matrix element arising from a time-dependent perturbation $\hat{V}$ can be calculated using time-dependent perturbation theory. In the causal adiabatic

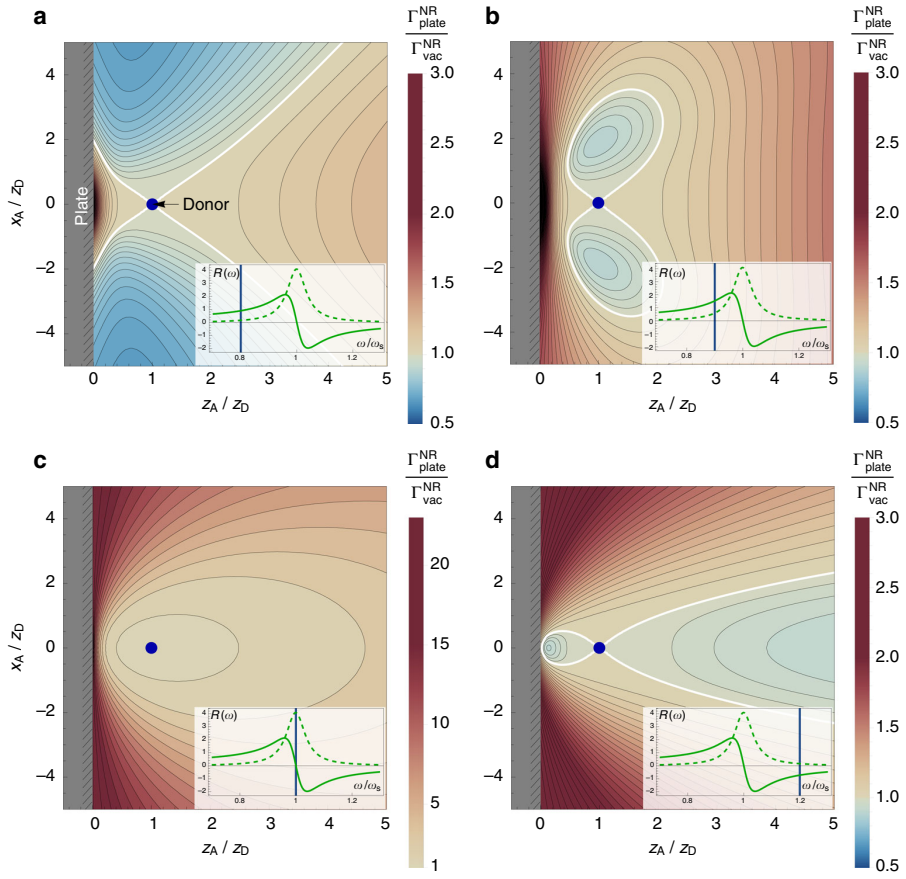

Fig. 4 Interatomic Coulombic decay rate near a dielectric surface. Non-retarded interatomic Coulombic decay rate Γ^{NR}_{plate} in vacuum near a dielectric surface with Drude–Lorentz permittivity as given by Eq. (9), normalised to the free-space non-retarded rate Γ^{NR}_{vac}. The donor is at a fixed position on the z-axis a distance z_D from the dielectric, which occupies the region $z < 0$. The acceptor is at position $(x_A,0,z_A)$, which is varied and the rate shown at each position in the $x-z$ plane. All distances are normalised to z_D, and the Drude–Lorentz parameters are $\omega_p = \omega_S$ and $\gamma = \omega_S/10$. The white contours represent the position at which the free-space and surface-modified rates are equal. In the insets we plot the behaviour of the reflection coefficient R as a function of frequency near its resonance ω_S, and show with a vertical line the ICD frequency ω_D chosen in the corresponding plot. The off-resonance plots (**a**, **b** and **d**) share the same scale, while the on-resonance plot (**c**) has a much larger range due to the strong enhancement of the rate if the ICD and material resonance frequencies are equal

coupling approach (see, for example ref.[45]) one has;

$$M_{fi} = \lim_{\varepsilon\to 0^+} \sum_k \frac{\langle f|\hat{V}|k\rangle\langle k|\hat{V}|i\rangle}{E_i - E_k + \mathrm{i}\hbar\varepsilon} \tag{12}$$

where E_k is the energy eigenvalue of the intermediate state k. In writing Eq. (12) we have assumed that all diagonal elements of $\hat{V}$ vanish, which is true for the perturbation we shall consider here. The leading-order processes supported by our interaction Hamiltonian (1) are shown in Fig. 6.

We will use δ, γ and α, β to represent the states of the donor D and acceptor A, respectively. The donor and acceptor may each be atoms, ions or molecules, though for brevity we describe their states simply as atomic in the rest of this section. In general the states of the acceptor can either be bound or belong to the continuum. During the ICD process the donor decays ($\delta \to \gamma$), while the acceptor becomes excited ($\alpha \to \beta$). In terms of product states $|\mathrm{a}\rangle\otimes|\mathrm{b}\rangle \equiv |\mathrm{a},\mathrm{b}\rangle$ we can therefore write the ICD process as $|\delta,\alpha\rangle \to |\gamma,\beta\rangle$. Then the contributions to the sum over intermediate states k in Eq. (12) are simply the two possible time-orderings of a process where a single polariton-like field-matter excitation (coinciding with the usual notion of a photon if the process takes place in vacuum) $|\mathbf{1}(\mathbf{r},\omega)\rangle$ at position $\mathbf{r}$ with frequency ω is exchanged, as shown in Fig. 6. We can hence write the following initial, intermediate and final product states for the composite system of the donor and acceptor coupled to the medium-assisted field whose ground state is $|\{0\}\rangle$

$$\begin{aligned} &\text{Initial :} && |i\rangle = |\delta,\alpha\rangle|\{0\}\rangle, \\ &\text{Intermediate :} && |k^{(1)}\rangle = |\gamma,\alpha\rangle|\mathbf{1}(\mathbf{r},\omega)\rangle \quad \text{or} \quad k^{(2)} = |\delta,\beta\rangle|\mathbf{1}(\mathbf{r},\omega)\rangle, \\ &\text{Final :} && |f\rangle = |\gamma,\beta\rangle|\{0\}\rangle. \end{aligned} \tag{13}$$

Combining the contributions from both diagrams yields the following expression for the coupling matrix element

$$M_{fi} = -\lim_{\varepsilon\to 0^+} \sum_{\gamma,\alpha} \int d^3\mathbf{r} \int_0^\infty d\omega \left[\frac{\langle f|\hat{\mathbf{d}}_A\cdot\hat{\mathbf{E}}(\mathbf{r}_A)|k^{(1)}\rangle\langle k^{(1)}|\hat{\mathbf{d}}_D\cdot\hat{\mathbf{E}}(\mathbf{r}_D)|i\rangle}{\hbar\left(\omega - \omega_{\delta\gamma} - \mathrm{i}\varepsilon\right)} + \frac{\langle f|\hat{\mathbf{d}}_D\cdot\hat{\mathbf{E}}(\mathbf{r}_D)|k^{(2)}\rangle\langle k^{(2)}|\hat{\mathbf{d}}_A\cdot\hat{\mathbf{E}}(\mathbf{r}_A)|i\rangle}{\hbar\left(\omega + \omega_{\beta\alpha} - \mathrm{i}\varepsilon\right)} \right], \tag{14}$$

where $\omega_{ab} \equiv (E_a - E_b)/\hbar$ are all positive. We can use the dipole operators $\hat{\mathbf{d}}$ to directly evaluate the atomic part of each term, for example the numerator of the first term becomes;

$$\begin{aligned} &\langle f|\hat{\mathbf{d}}_A\cdot\hat{\mathbf{E}}(\mathbf{r}_A)|k^{(1)}\rangle\langle k^{(1)}|\hat{\mathbf{d}}_D\cdot\hat{\mathbf{E}}(\mathbf{r}_D)|i\rangle \\ &= \left(\mathbf{d}_{\alpha\beta}\cdot\langle\{0\}|\hat{\mathbf{E}}(\mathbf{r}_A)|\mathbf{1}(\mathbf{r},\omega)\rangle\right)\left(\mathbf{d}_{\delta\gamma}\cdot\langle\mathbf{1}(\mathbf{r},\omega)|\hat{\mathbf{E}}(\mathbf{r}_D)|\{0\}\rangle\right) \end{aligned} \tag{15}$$

with $\mathbf{d}_{\delta\gamma} \equiv \langle\gamma|\hat{\mathbf{d}}_D|\delta\rangle$ and $\mathbf{d}_{\alpha\beta} \equiv \langle\beta|\hat{\mathbf{d}}_A|\alpha\rangle$. To evaluate the field-dependent part

NATURE COMMUNICATIONS | DOI: 10.1038/s41467-018-05091-x ARTICLE

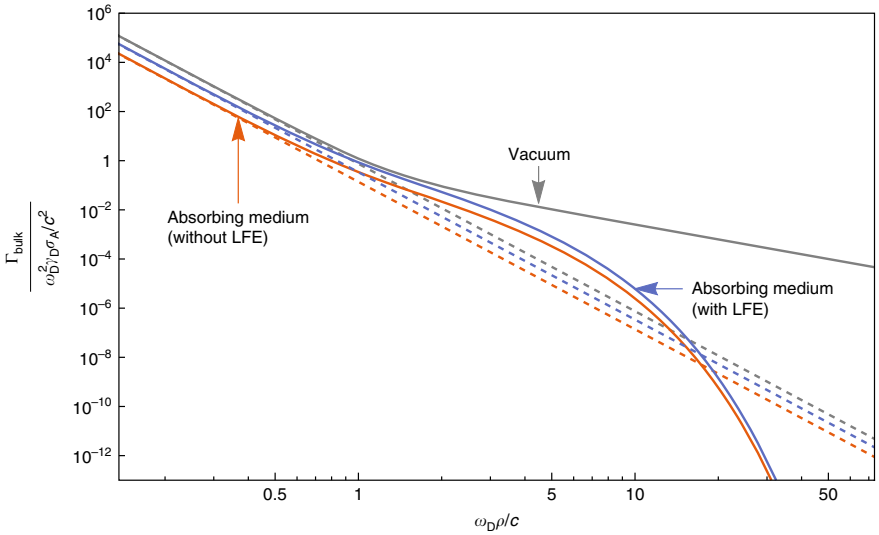

Fig. 5 Interplay of medium and retardation effects on interatomic Coulombic decay rate. Shown here is the interatomic Coulombic decay rate for arbitrary donor and acceptor, including medium and retardation effects as given by Eq. (10), as a function of the dimensionless parameter $\omega_D\rho/c$. The vertical axis is normalised in the same way as that of Fig. 2, and the dashed lines correspond to the non-retarded limits of the three rates shown. The material parameters chosen for the absorbing medium are $n(\omega_D) = 1.49$ and $\kappa(\omega_D) = 0.35$, corresponding to the first absorption line of helium[41]

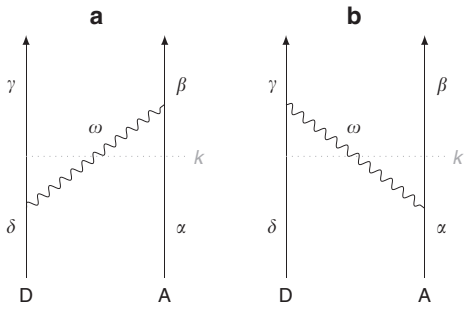

Fig. 6 Feynman diagrams for the ICD process. Diagrammatic illustration of the two processes (**a**) and (**b**) supported by our interaction Hamiltonian, for donor D and acceptor A

of each term, we use the definition of the macroscopic QED electric field[26,29]

$$\hat{\mathbf{E}}(\mathbf{r}) = \mathrm{i}\int_0^\infty d\omega \int d^3\mathbf{r}' \frac{\omega^2}{c^2}\sqrt{\frac{\hbar}{\pi\varepsilon_0}\mathrm{Im}\varepsilon(\mathbf{r}',\omega)}\mathbb{G}(\mathbf{r},\mathbf{r}',\omega)\cdot\hat{\mathbf{f}}(\mathbf{r}',\omega) + \mathrm{H.c.} \quad (16)$$

where $\hat{\mathbf{f}}$ and $\hat{\mathbf{f}}^\dagger$ are a set of bosonic operators that create and annihilate combined matter-field excitations[26,29]. For the field evaluated at a general position $\boldsymbol{r}_a$ we have;

$$\begin{aligned}\langle\{0\}|\hat{\mathbf{E}}(\mathbf{r}_a)|\mathbf{1}(\mathbf{r},\omega)\rangle &= \int d^3\mathbf{r}'\int_0^\infty d\omega \mathrm{i}\frac{\omega^2}{c^2}\sqrt{\frac{\hbar}{\pi\varepsilon_0}\mathrm{Im}\varepsilon(\mathbf{r}',\omega)}\mathbb{G}(\mathbf{r}_a,\mathbf{r}',\omega)\delta(\mathbf{r}-\mathbf{r}')\delta(\omega-\omega')\\ &= \mathrm{i}\frac{\omega^2}{c^2}\sqrt{\frac{\hbar}{\pi\varepsilon_0}\mathrm{Im}\varepsilon(\mathbf{r},\omega)}\mathbb{G}(\mathbf{r}_a,\mathbf{r},\omega).\end{aligned} \quad (17)$$

Using this result in (14) we find;

$$\begin{aligned}M_{fi} = &-\sum_{\gamma,\alpha}\frac{\mu_0}{\pi}\lim_{\varepsilon\to0^+}\Big\{\int_0^\infty d\omega\frac{\omega^2}{\omega-\omega_{\delta\gamma}-\mathrm{i}\varepsilon}\int d^3\mathbf{r}\frac{\omega^2}{c^2}\mathrm{Im}\varepsilon(\mathbf{r},\omega)\\ &\times\left[\mathbf{d}_{\alpha\beta}\cdot\mathbb{G}(\mathbf{r}_A,\mathbf{r},\omega)\right]\left[\mathbf{d}_{\delta\gamma}\cdot\mathbb{G}^*(\mathbf{r}_D,\mathbf{r},\omega)\right]\\ &+\int_0^\infty d\omega\frac{\omega^2}{\omega+\omega_{\beta\alpha}-\mathrm{i}\varepsilon}\int d^3\mathbf{r}\frac{\omega^2}{c^2}\mathrm{Im}\varepsilon(\mathbf{r},\omega)\left[\mathbf{d}_{\gamma\delta}\cdot\mathbb{G}(\mathbf{r}_D,\mathbf{r},\omega)\right]\left[\mathbf{d}_{\alpha\beta}\cdot\mathbb{G}^*(\mathbf{r}_A,\mathbf{r},\omega)\right]\Big\}.\end{aligned} \quad (18)$$

We can now use the following integral relation for the Green's tensor[26,29]

$$\frac{\omega^2}{c^2}\int d^3\mathbf{s}\,\mathrm{Im}[\varepsilon(\mathbf{s},\omega)]\mathbb{G}(\mathbf{r},\mathbf{s},\omega)\cdot\mathbb{G}^*(\mathbf{s},\mathbf{r}',\omega) = \mathrm{Im}[\mathbb{G}(\mathbf{r},\mathbf{r}',\omega)], \quad (19)$$

to carry out the position integral in (18), obtaining

$$\begin{aligned}M_{fi} = -\frac{\mu_0}{\pi}\lim_{\varepsilon\to0^+}\sum_{\gamma,\alpha}\int_0^\infty d\omega\Big[&\frac{\omega^2}{\omega-\omega_{\delta\gamma}-\mathrm{i}\varepsilon}\mathbf{d}_{\delta\gamma}\cdot\mathrm{Im}\mathbb{G}\left(\mathbf{r}_D,\mathbf{r}_A,\omega_{\delta\gamma}\right)\cdot\mathbf{d}_{\alpha\beta}\\ &+\frac{\omega^2}{\omega+\omega_{\alpha\beta}-\mathrm{i}\varepsilon}\mathbf{d}_{\delta\gamma}\cdot\mathrm{Im}\mathbb{G}\left(\mathbf{r}_D,\mathbf{r}_A,\omega_{\beta\alpha}\right)\cdot\mathbf{d}_{\alpha\beta}\Big]\end{aligned} \quad (20)$$

where we have assumed that the dipole moments are real. Deforming the integration contour into the upper half of the complex frequency plane we pick up a resonant term from a pole at $\omega_{\delta\gamma}$ and an off-resonant contribution along the positive imaginary axis. Taking the limit $\varepsilon\to0^+$ we find;

$$\begin{aligned}M_{fi} = -\mu_0\sum_{\gamma,\alpha}\mathbf{d}_{\delta\gamma}\cdot\Big\{&\omega_{\delta\gamma}^2\left[\mathbb{G}\left(\mathbf{r}_D,\mathbf{r}_A,\omega_{\delta\gamma}\right)+\mathbb{F}\left(\mathbf{r}_D,\mathbf{r}_A,\omega_{\delta\gamma}\right)\right]\\ &-\omega_{\beta\alpha}^2\mathbb{F}\left(\mathbf{r}_D,\mathbf{r}_A,\omega_{\beta\alpha}\right)\Big\}\cdot\mathbf{d}_{\alpha\beta}\end{aligned} \quad (21)$$

where

$$\mathbb{F}(\mathbf{r},\mathbf{r}',\omega) \equiv \int_0^\infty d\xi\frac{\omega\xi^2\mathbb{G}(\mathbf{r},\mathbf{r}',\mathrm{i}\xi)}{\omega^2+\xi^2} \quad (22)$$

is the off-resonant contribution. This expression is now suitable for substitution into Fermi's golden rule (11), giving the rate $\Gamma_{\delta\alpha}$ for one particular choice of initial state $|\delta,\alpha\rangle$;

$$\begin{aligned}\Gamma_{\delta\alpha} = &\sum_{\beta,\gamma}\frac{2\pi}{9\hbar}\mu_0^2\left|\mathbf{d}_{\alpha\beta}\right|^2\left|\mathbf{d}_{\delta\gamma}\right|^2\mathrm{Tr}\left[\mathbb{G}\left(\mathbf{r}_A,\mathbf{r}_D,\omega_{\delta\gamma}\right)\mathbb{G}^*\left(\mathbf{r}_D,\mathbf{r}_A,\omega_{\beta\alpha}\right)\right]\\ &\times\delta\left(\hbar\omega_{\delta\gamma}-\hbar\omega_{\beta\alpha}\right),\end{aligned} \quad (23)$$

where we have taken isotropically averaged dipole moments,

$$\mathbf{d}\otimes\mathbf{d} = \frac{1}{3}|\mathbf{d}|^2\mathbb{I} \quad (24)$$

where $\mathbb{I}$ is the identity matrix.

In evaluating the sum over final states in (23), one must be mindful of the fact that the transition $|\alpha\rangle \to |\beta\rangle$ is a photoionisation process, meaning that its final state is part of the continuum. This means that the relevant observable is the photoionisation cross section σ_α at a certain incident energy E, rather than the

dipole moment **d**. The two quantities can however be related;[46,47]

$$\sum_{\beta\in\mathcal{C}}\frac{\mathrm{d}}{\mathrm{d}\omega}\left|\mathbf{d}_{\alpha\beta}(\omega)\right|^2=\frac{3\varepsilon_0 c\hbar}{\pi\omega}\sigma_\alpha(E). \tag{25}$$

Similarly, the continuum nature of the final states means that the formal sum over β is in a fact sum over discrete states $\beta\in\mathcal{D}$ corresponding to distinct ICD channels, as well as an integral over continuum states $\beta\in\mathcal{C}$ for each individual channel. We use the following rule for converting a sum over discrete states with energies $\hbar\omega'_i$ to an integral over a continuous variable ω';

$$\begin{aligned}\sum_{\beta\in\mathcal{C}}\left|\mathbf{d}_{\alpha\beta}(\omega')\right|^2 f(\omega')\delta(\hbar\omega-\hbar\omega')\rightarrow\int_0^\infty \mathrm{d}\omega'\frac{\mathrm{d}}{\mathrm{d}\omega'}\frac{\left|\mathbf{d}_{\alpha\beta}(\omega')\right|^2}{\hbar}f(\omega')\delta(\omega-\omega')\\ =\frac{3\varepsilon_0 c}{\pi\omega}\sigma_\alpha(\hbar\omega)f(\omega)\end{aligned} \tag{26}$$

where $f(\omega)$ is an arbitrary smooth function. This finally gives;

$$\Gamma_{\delta\alpha}=2\pi^2\sum_\gamma\gamma_{\delta\gamma}\sigma_\alpha\left(\hbar\omega_{\delta\gamma}\right)\mathrm{Tr}\left[\mathbb{G}\left(\mathbf{r}_\mathrm{A},\mathbf{r}_\mathrm{D},\omega_{\delta\gamma}\right)\cdot\mathbb{G}^*\left(\mathbf{r}_\mathrm{D},\mathbf{r}_\mathrm{A},\omega_{\delta\gamma}\right)\right], \tag{27}$$

with $\gamma_{\delta\gamma}$ being the free-space decay rate of the donor;

$$\gamma_{\delta\gamma}=\frac{\omega_{\delta\gamma}^3\left|\mathbf{d}_{\delta\gamma}\right|^2}{3\pi\hbar c^3\varepsilon_0}. \tag{28}$$

In the main text we make use of the fact that the sum in Eq. (27) represents a sum over allowed ICD channels for a given initial state $|\delta,\alpha\rangle$, so that we write $\sum_{\mathrm{channels}}$ instead of $\sum_\gamma$. Upon using the shorthands $\mathbf{d}_\mathrm{D}\equiv\mathbf{d}_{\delta\gamma}$, $\omega_\mathrm{D}=\omega_{\delta\gamma}$ and $\Gamma_{\delta\alpha}=\Gamma$, and renaming $\sigma_\alpha=\sigma_\mathrm{A}$, the derivation of Eq. (2) in the main text is now complete.

Green's tensors. In this section we specify the Green's tensors $\mathbb{G}(\mathbf{r},\mathbf{r}',\omega)$ used to derive the ICD rates (5), (7), (8) and (10) in the main text. Subject to appropriate boundary conditions, these are defined to solve;

$$\nabla\times\nabla\times\mathbb{G}(\mathbf{r},\mathbf{r}',\omega)-\frac{\omega^2}{c^2}\varepsilon(\mathbf{r},\omega)\mathbb{G}(\mathbf{r},\mathbf{r}',\omega)=\mathbb{I}\delta^{(3)}(\mathbf{r}-\mathbf{r}'), \tag{29}$$

where $\varepsilon(\mathbf{r},\omega)$ is relative permittivity, which in general depends on both position $\boldsymbol{r}$ and frequency ω. Here we denote the 3×3 identity matrix as $\mathbb{I}$.

Bulk medium. A translationally-invariant medium has $\varepsilon(\mathbf{r},\omega)=\varepsilon(\omega)$, for which the Green's tensor is (see, for example ref.[29]):

$$\begin{aligned}\mathbb{G}^{(0)}(\mathbf{r},\mathbf{r}',\omega)=-\frac{\mathbb{I}}{3k^2}\delta^{(3)}(\boldsymbol{\rho})\\ -\frac{e^{ik\rho}}{4\pi k^2\rho^3}\left\{\left[1-\mathrm{i}k\rho-(k\rho)^2\right]\mathbb{I}-\left[3-3\mathrm{i}k\rho-(k\rho)^2\right]\mathbf{e}_\rho\otimes\mathbf{e}_\rho\right\},\end{aligned} \tag{30}$$

where $k=(\omega/c)\sqrt{\varepsilon(\omega)}$, $\boldsymbol{\rho}=\mathbf{r}-\mathbf{r}'$, $\rho=|\boldsymbol{\rho}|$, and $\mathbf{e}_\rho=\boldsymbol{\rho}/\rho$. The vacuum Green's tensor $\mathbb{G}^{(0)}_{\mathrm{vac}}(\mathbf{r},\mathbf{r}',\omega)$ is found from this by setting $\varepsilon(\omega)=1$.

Local-field corrections. Local-field corrections can be introduced on the level of the Green's tensor. Ultimately, the LFE leads to a correction factor for the bulk Green's tensor, which amounts to a replacement;

$$\mathbb{G}^{(0)}(\mathbf{r},\mathbf{r}',\omega)\quad\rightarrow\quad\left(\frac{3\varepsilon(\omega)}{2\varepsilon(\omega)+1}\right)^2\mathbb{G}^{(0)}(\mathbf{r},\mathbf{r}',\omega), \tag{31}$$

as discussed in detail in ref.[39].

Dielectric half-space. Here we consider a dielectric medium of permittivity $\varepsilon(\omega)$ filling the region $z<0$, with $z>0$ being vacuum. We are interested in the non-retarded (near-field) limit defined by $\omega\rho/c\ll1$, for which the half-space Green's tensor $\mathbb{G}_{\mathrm{HS}}(\mathbf{r},\mathbf{r}',\omega)$ in the region $z>0$ can be obtained by an image construction based on the non-retarded vacuum Green's tensor above. One finds, in agreement with ref.[48];

$$\mathbb{G}_{\mathrm{HS}}(\mathbf{r},\mathbf{r}',\omega)=\mathbb{G}^{(0)}_{\mathrm{vac,NR}}(\mathbf{r},\mathbf{r}',\omega)+\frac{\varepsilon(\omega)-1}{\varepsilon(\omega)+1}\mathbb{G}^{(0)}_{\mathrm{vac,NR}}(\mathbf{r},\bar{\mathbf{r}}',\omega)\cdot\begin{pmatrix}-1&0&0\\0&-1&0\\0&0&1\end{pmatrix}, \tag{32}$$

where $\bar{\mathbf{r}}=(x,y,-z)$, and

$$\mathbb{G}^{(0)}_{\mathrm{vac,NR}}(\mathbf{r},\mathbf{r}',\omega)=\frac{\mathbb{I}c^2}{3\omega^2}\delta(\boldsymbol{\rho})-\frac{c^2}{4\pi\omega^2\rho^3}\left(\mathbb{I}-3\mathbf{e}_\rho\otimes\mathbf{e}_\rho\right) \tag{33}$$

is the non-retarded limit of the vacuum Green's tensor. Given relations (30), (31) and (32) it is then a matter of algebra to arrive at the ICD rates (5), (7), (8) and (10).

Data availability. All data contained within the figures are generated solely from the formulae in the manuscript using the given parameters, with the exception of Fig. 3 where optical data from refs.[40,41] were used. The transition frequencies of hydrogen- and neon-like ions are publicly available in the NIST Atomic Spectra Database[37].

Received: 18 January 2018 Accepted: 13 June 2018
Published online: 26 July 2018

References

1. Einstein, A. Zur Quantentheorie der Strahlung. *Phys. Z.* **18**, 121 (1917).
2. Purcell, E. M. Spontaneous emission probabilities at radio frequences. *Proc. Am. Phys. Soc.* **69**, 674–674 (1946).
3. Casimir, H. B. G. & Polder, D. The influence of retardation on the London-van der Waals forces. *Phys. Rev.* **73**, 360–372 (1948).
4. Cederbaum, L. S., Zobeley, J. & Tarantelli, F. Giant intermolecular decay and fragmentation of clusters. *Phys. Rev. Lett.* **79**, 4778–4781 (1997).
5. Thissen, R., Lablanquie, P., Hall, R., Ukai, M. & Ito, K. Photoionization of argon, krypton and xenon clusters in the inner valence shell region. *Eur. Phys. J. D. - Atom. Mol. Opt. Phys.* **4**, 335–342 (1998).
6. Thomas, T. D. et al. Anomalous natural linewidth in the 2p photoelectron spectrum of SiF_4. *Phys. Rev. Lett.* **89**, 223001 (2002).
7. Marburger, S., Kugeler, O., Hergenhahn, U. & Möller, T. Experimental evidence for Interatomic Coulombic decay in Ne clusters. *Phys. Rev. Lett.* **90**, 203401 (2003).
8. Jahnke, T. et al. Experimental observation of Interatomic Coulombic decay in neon dimers. *Phys. Rev. Lett.* **93**, 163401 (2004).
9. Gokhberg, K., Kolorenč, P., Kuleff, A. I. & Cederbaum, L. S. Site- and energy-selective slow-electron production through intermolecular Coulombic decay. *Nature* **505**, 661–663 (2014).
10. Boudaiffa, B., Cloutier, P., Hunting, D., Huels, M.A., Sanche, L. Resonant formation of DNA strand breaks by low-energy (3 to 20 eV) electrons.*Science* **287**, 1658–1660 (2000).
11. Santra, R. & Cederbaum, L. S. Non-Hermitian electronic theory and applications to clusters. *Phys. Rep.* **368**, 1–117 (2002).
12. Miteva, T., Kazandjian, S., Kolorenč, P., Votavová, P. & Sisourat, N. Interatomic Coulombic decay mediated by ultrafast superexchange energy transfer. *Phys. Rev. Lett.* **119**, 083403 (2017).
13. Wilhelm, R. A. et al. Interatomic Coulombic decay: the mechanism for rapid deexcitation of hollow atoms. *Phys. Rev. Lett.* **119**, 103401 (2017).
14. Takanashi et al. Time-resolved measurement of interatomic coulombic decay induced by two-photon double excitation of Ne_2. *Phys. Rev. Lett.* **118**, 033202 (2017).
15. Meyer, H.-D., Manthe, U. & Cederbaum, L. The multi-configurational time-dependent Hartree approach. *Chem. Phys. Lett.* **165**, 73–78 (1990).
16. Meyer, H.-D., Gatti, F. & Worth, G. *Multidimensional quantum dynamics: MCTDH theory and applications* (Wiley-VCH, Germany, 2009).
17. Ahlrichs, R., Bär, M., Häser, M., Horn, H. & Kölmel, C. Electronic structure calculations on workstation computers: the program system turbomole. *Chem. Phys. Lett.* **162**, 165–169 (1989).
18. Shao, Y. et al. Advances in molecular quantum chemistry contained in the Q-Chem 4 program package. *Mol. Phys.* **113**, 184–215 (2015).
19. Javani, M. H. et al. Resonant Auger–intersite-Coulombic hybridized decay in the photoionization of endohedral fullerenes. *Phys. Rev. A* **89**, 063420 (2014).
20. Kryzhevoi, N. V., Averbukh, V. & Cederbaum, L. S. High activity of helium droplets following ionization of systems inside those droplets. *Phys. Rev. B* **76**, 094513 (2007).
21. Kryzhevoi, N. V., Mateo, D., Pi, M., Barranco, M. & Cederbaum, L. S. Probing the interface of doped isotopically mixed helium droplets by the directional anisotropy of Interatomic Coulombic decay. *Phys. Chem. Chem. Phys.* **15**, 18167 (2013).
22. LaForge, A. C. et al. Enhanced ionization of embedded clusters by electron-transfer-mediated decay in helium nanodroplets. *Phys. Rev. Lett.* **116**, 203001 (2016).
23. Shcherbinin, M. et al. Interatomic Coulombic decay in helium nanodroplets. *Phys. Rev. A* **96**, 013407 (2017).

24. Kim, J. et al. Enhanced proton treatment in mouse tumors through proton irradiated nanoradiator effects on metallic nanoparticles. *Phys. Med. Biol.* **57**, 8309–8323 (2012).
25. Jeon, J. et al. Coulomb nanoradiator-mediated, site-specific thrombolytic proton treatment with a traversing pristine Bragg peak. *Sci. Rep.* **6**, 37848 (2016).
26. Gruner, T. & Welsch, D.-G. Green-function approach to the radiation-field quantization for homogeneous and inhomogeneous Kramers-Kronig dielectrics. *Phys. Rev. A* **53**, 1818–1829 (1996).
27. Scheel, S. & Buhmann, S. Y. Macroscopic QED—concepts and applications. *Acta Phys. Slov.* **58**, 675–809 (2009).
28. Philbin, T. G. Canonical quantization of macroscopic electromagnetism. *New J. Phys.* **12**, 123008 (2010).
29. Buhmann, S. Y. Dispersion Forces I - Macroscopic Quantum Electrodynamics and ground-state Casimir, Casimir-Polder and van der Waals Forces. *Springer Tracts in Modern Physics* **247** (Springer, Berlin, 2012).
30. Chew, W. *Waves and fields in inhomogeneous media* (IEEE Press, New Jersey, 1995).
31. Buhmann, S. Y. & Welsch, D.-G. Born expansion of the Casimir-Polder interaction of a ground-state atom with dielectric bodies. *Appl. Phys. B* **82**, 189–201 (2006).
32. Averbukh, V., Müller, I. B. & Cederbaum, L. S. Mechanism of Interatomic Coulombic decay in clusters. *Phys. Rev. Lett.* **93**, 263002 (2004).
33. Najjari, B., Voitkiv, A. B. & Müller, C. Two-center resonant photoionization. *Phys. Rev. Lett.* **105**, 153002 (2010).
34. Fasshauer, E., Förstel, M., Pallmann, S., Pernpointner, M. & Hergenhahn, U. Using ICD for structural analysis of clusters: a case study on NeAr clusters. *New J. Phys.* **16**, 103026 (2014).
35. Förstel, M. et al. Long-range interatomic coulombic decay in ArXe clusters: experiment and theory. *J. Phys. Chem. C.* **120**, 22957–22971 (2016).
36. Matthew, J. & Komninos, Y. Transition rates for interatomic Auger processes. *Surf. Sci.* **53**, 716–725 (1975).
37. Scheel, S., Knöll, L. & Welsch, D.-G. Spontaneous decay of an excited atom in an absorbing dielectric. *Phys. Rev. A* **1**, 4094–4104 (1999).
38. Dung, H. T., Buhmann, S. Y. & Welsch, D.-G. Local-field correction to the spontaneous decay rate of atoms embedded in bodies of finite size. *Phys. Rev. A* **74**, 023803 (2006).
39. Hale, G. M. & Querry, M. R. Optical constants of water in the 200-nm to 200-µm wavelength region. *Appl. Opt.* **12**, 555 (1973).
40. Lucas, A. A., Vigneron, J. P., Donnelly, S. E. & Rife, J. C. Theoretical interpretation of the vacuum ultraviolet reflectance of liquid hehum and of the absorption spectra of helium microbubbles in aluminum. *Phys. Rev. B* **28**, 2485–2496 (1983).
41. Tai, C.-T. *Dyadic Green functions in electromagnetic theory* (IEEE Press, New Jersey, 1994).
42. Safari, H., Welsch, D.-G., Dung, H. T. & Buhmann, S. Y. Interatomic van der Waals potential in the presence of a magnetoelectric sphere. *Phys. Rev. A* **77**, 053824 (2008).
43. Wylie, J. M., Sipe, J. E. Quantum electrodynamics near an interface. II. *Phys. Rev. A Gen Phys.* **32**, 2030–2043 (1985).
44. Sakurai, J. *Modern Quantum Mechanics* (Addison-Wesley, Massachusetts, 1994).
45. Gokhberg, K. et al. Molecular photoionization cross sections by Stieltjes-Chebyshev moment theory applied to Lanczos pseudospectra. *J. Chem. Phys.* **130**, 064104 (2009).
46. Hilborn, R. C. Einstein coefficients, cross sections, f values, dipole moments, and all that. *Am. J. Phys.* **50**, 982 (1982).
47. Palacino, R., Passante, R., Rizzuto, L., Barcellona, P. & Buhmann, S. Y. Tuning the collective decay of two entangled emitters by means of a nearby surface. *J. Phys. B At. Mol. Opt. Phys.* **50**, 154001 (2017).
48. Kramida, A., Ralchenko, Y. & Reader, J. NIST Atomic Spectra Database (ver. 5.5.1). (National Institute of Standards and Technology, Gaithersburg, MD, 2017) https://physics.nist.gov/asd. [Last accessed 25/05/2018]

Acknowledgements

The authors would like to thank Pablo Barcellona, Lorenz Cederbaum, Kirill Gokhberg, Alexander Kuleff, Aaron LaForge, Marcel Mudrich, Alberto Rodriguez, Carsten Müller and Akbar Salam for fruitful discussions and suggestions. Financial support from the Deutsche Forschungsgemeinschaft (DFG grant BU1803/3-1), the Alexander von Humboldt Foundation and the Freiburg Institute for Advanced Studies (FRIAS) is gratefully acknowledged.

Additional information

Competing interests: The authors declare no competing interests.

Bibliography

Books

[P1] S. Y. Buhmann, *Dispersion forces I: Macroscopic quantum electrodynamics and ground-state Casimir, Casimir–Polder and Van der Waals forces*, Springer Tracts in Modern Physics 247 (Heidelberg: Springer, 2012).

[P2] S. Y. Buhmann, *Dispersion forces II: Many-body effects, excited atoms, finite temperature and quantum friction*, Springer Tracts in Modern Physics 248 (Heidelberg: Springer, 2012).

Book chapters (physics)

[P3] S. Y. Buhmann, Normal-mode quantum electrodynamics: The quantum vacuum and its consequences, in W. Simpson and U. Leonhardt (eds), *Forces of the quantum vacuum: An introduction to Casimir physics* (London: World Scientific Press, 2015), 7–59.

[P4] W. Simpson, U. Leonhardt, R. Decca, and S. Y. Buhmann, Casimir forces at the cutting edge, in W. Simpson and U. Leonhardt (eds), *Forces of the quantum vacuum: An introduction to Casimir physics* (London: World Scientific Press, 2015), 227–249.

Book chapters (learning and teaching)

[P5] I. M. Kinchin, M. Kingsbury, and S. Y. Buhmann, Research as pedagogy in academic development: A case study, in E. Medland, R. Watermeyer, A. Hosein, I. M. Kinchin, and S. Lygo-Baker (eds), *Academic peculiarities: Conversations at the edge of university teaching and learning* (Leiden: Brill Sense, 2018), 49–67.

Review articles

[P6] S. Scheel and S. Y. Buhmann, Macroscopic quantum electrodynamics: Concepts and applications, *Acta Phys. Slovaka*, 58/5 (2008), 675–809.

[P7] S. Y. Buhmann and D.-G. Welsch, Dispersion forces in macroscopic quantum electrodynamics, *Prog. Quantum Electron.*, 31/2 (2007), 51–130.

Feature articles

[P8] S. Y. Buhmann, Steifigkeit des leeren Raums, *Phys. J.*, 18/3 (2019), 21.

Refereed articles (physics)

[P9] M. Boström, R. Corkery, E. R. A. Lima, O. I. Malyi, S. Y. Buhmann, C. Persson, I. Brevik, D. F. Parsons, and J. Fiedler, Dispersion forces stabilise ice coatings at certain gas hydrate interfaces which prevent water wetting, *ACS Earth Space Chem.*, in press (2019).

[P10] R. Bennett, P. Votavová, P. Kolorenč, T. Miteva, N. Sisourat, and S. Y. Buhmann, The virtual photon approximation for three-body interatomic Coulombic decay, *Phys. Rev. Lett.*, in press (2019).

[P11] S. Esfandiarpour, H. Safari, and S. Y. Buhmann, Cavity-QED interactions of several atoms, *J. Phys. B*, 52/8 (2019), 085503.

[P12] F. Suzuki, T. Momose, and S. Y. Buhmann, Stern–Gerlach separator of chiral enantiomers based on the Casimir–Polder potential, *Phys. Rev. A*, 99/1 (2019), 012513.

[P13] T. Haug, S. Y. Buhmann, and R. Bennett, Casimir–Polder potential in the presence of a Fock state, *Phys. Rev. A*, 99/1 (2019), 012508.

[P14] S. Fuchs and S. Y. Buhmann, Purcell–Dicke enhancement of the Casimir–Polder potential, *Europhys. Lett.*, 124/3 (2018), 34003.

[P15] F. Lindel, G. W. Hanson, M. Antezza, and S. Y. Buhmann, Inducing and controlling rotation on small objects using photonic topological materials, *Phys. Rev. A*, 98/14 (2018), 144101.

[P16] G. Winstone, R. Bennett, M. Rademacher, M. Rashid, S. Y. Buhmann, and H. Ulbricht, Direct measurement of the electrostatic image force of a levitated nanoparticle close to a surface, *Phys. Rev. A*, 98/5 (2018), 053831.

[P17] S. Fuchs, R. Bennett, R. V. Krems, and S. Y. Buhmann, Nonadditivity of optical and Casimir–Polder potentials, *Phys. Rev. Lett.*, 121/8 (2018), 083603.

[P18] R. Bennett, S. Y. Buhmann, and C. Eberlein, Distinguishing models of surface response through the self-energy of an electron, *Phys. Rev. A*, 98/2 (2018), 022515.

[P19] S. Fuchs, R. Bennett, and S. Y. Buhmann, Casimir–Polder potential of a driven atom, *Phys. Rev. A*, 98/2 (2018), 022514.

[P20] S. Y. Buhmann, V. N. Marachevsky, and S. Scheel, Charge–parity-violating effects in Casimir–Polder potentials, *Phys. Rev. A*, 98/2 (2018), 022510.

[P21] S. Y. Buhmann and A. Salam, Three-body dispersion potentials involving electric octupole coupling, *Symmetry*, 10/8 (2018), 343.

[P22] J. L. Hemmerich, R. Bennett, and S. Y. Buhmann, The influence of retardation and dielectric environments on interatomic Coulombic decay, *Nature Commun.*, 9 (2018), 2934.

[P23] P. Thiyam, J. Fiedler, S. Y. Buhmann, C. Persson, I. Brevik, M. Boström, and D. F. Parsons, Ice particles sink below the water surface due to a balance of salt, Van der Waals, and buoyancy forces, *J. Phys. Chem. C*, 122/27 (2018), 15311.

[P24] J. Fiedler, C. Persson, M. Boström, and S. Y. Buhmann, Orientational dependence of the Van der Waals interactions for finite-sized particles, *J. Phys. Chem. A*, 122/19 (2018), 4663.

[P25] S. Esfandiarpour, H. Safari, R. Bennett, and S. Y. Buhmann, Cavity-QED interactions of two correlated atoms, *J. Phys. B*, 51/9 (2018), 094004.

[P26] S. Rode, R. Bennett, and S. Y. Buhmann, Casimir effect for perfect electromagnetic conductors (PEMCs): A sum rule for attractive/repulsive forces, *New J. Phys.*, 20/4 (2018), 043024.

[P27] R. R. Q. P. T. Oude Weernink, P. Barcellona, and S. Y. Buhmann, Lateral Casimir–Polder forces by breaking time-reversal symmetry, *Phys. Rev. A*, 97/3 (2018), 032507.

[P28] P. Barcellona, R. Bennett, and S. Y. Buhmann, Manipulating the Coulomb interaction: A Green's function perspective, *J. Phys. Commun.*, 2/3 (2018), 035027.

[P29] F. A. Burger, J. Fiedler, and S. Y. Buhmann, Zero-point electromagnetic stress tensor for studying Casimir forces on colloidal particles in media, *Europhys. Lett.*, 121/2 (2018), 24004.

[P30] J. Fiedler, P. Thiyam, A. Kurumbail, F. A. Burger, M. Walter, C. Persson, I. Brevik, D. F. Parsons, M. Boström, and S. Y. Buhmann, Effective polarizability models, *J. Phys. Chem. A*, 121/51 (2017), 9742.

[P31] S. Fuchs, F. Lindel, R. V. Krems, G. W. Hanson, M. Antezza, and S. Y. Buhmann, Casimir–Lifshitz force for nonreciprocal media and applications to photonic topological insulators, *Phys. Rev. A*, 96/6 (2017), 062505.

[P32] R. Palacino, R. Passante, L. Rizzuto, P. Barcellona, and S. Y. Buhmann, Tuning the collective decay of two entangled emitters by means of a nearby surface, *J. Phys. B*, 50/15 (2017), 154001.

[P33] M. Könne, R. Bennett, T. Reisinger, and S. Y. Buhmann, Impact of dispersion forces on matter-wave scattering near a dielectric disk, *Phys. Rev. A*, 96/1 (2017), 013626.

[P34] J. Klatt, M. B. Farías, D. A. R. Dalvit, and S. Y. Buhmann, Quantum friction in arbitrarily directed motion, *Phys. Rev. A*, 95/5 (2017), 052510.

[P35] P. Barcellona, H. Safari, A. Salam, and S. Y. Buhmann, Enhanced chiral discriminatory Van der Waals interactions mediated by chiral surfaces, *Phys. Rev. Lett.*, 118/19 (2017), 193401.

[P36] J. Klatt, P. Barcellona, R. Bennett, O. S. Bokareva, H. Feth, A. Rasch, P. Reith, and S. Y. Buhmann, Strong Van der Waals adhesion of a polymer film on rough substrates, *Langmuir*, 33/21 (2017), 5298.

[P37] S. Fuchs, J. A. Crosse, and S. Y. Buhmann, Casimir–Polder shift and decay rate in the presence of nonreciprocal media, *Phys. Rev. A*, 95/2 (2017), 023805.

[P38] J. Klatt, R. Bennett, and S. Y. Buhmann, Spectroscopic signatures of quantum friction, *Phys. Rev. A*, 94/6 (2016), 063803.

[P39] F. Armata, R. Vasile, P. Barcellona, S. Y. Buhmann, L. Rizzuto, and R. Passante, Dynamical Casimir–Polder force between an excited atom and a conducting wall, *Phys. Rev. A*, 94/4 (2016), 042511.

[P40] V. A. Yerokhin, S. Y. Buhmann, S. Fritzsche, and A. Surzhykov, Electric dipole polarizabilities of Rydberg states of alkali-metal atoms, *Phys. Rev. A*, 94/3 (2016), 032503.

[P41] J. L. Hemmerich, R. Bennett, T. Reisinger, S. Nimmrichter, J. Fiedler, H. Hahn, H. Gleiter, and S. Y. Buhmann, Impact of Casimir–Polder interaction on Poisson-spot diffraction at a dielectric sphere, *Phys. Rev. A*, 94/2 (2016), 023621.

[P42] P. Barcellona, R. Passante, L. Rizzuto, and S. Y. Buhmann, Van der Waals interactions between excited atoms in generic environments, *Phys. Rev. A*, 94/1 (2016), 012705.

[P43] P. Barcellona, R. Passante, L. Rizzuto, and S. Y. Buhmann, Dynamical Casimir–Polder interaction between a chiral molecule and a surface, *Phys. Rev. A*, 93/3 (2016), 032508.

[P44] P. Thiyam, E. R. A. Lima, O. I. Malyi, D. F. Parsons, S. Y. Buhmann, C. Persson, and M. Boström, Effects of Van der Waals forces and salt ions on the growth of water films on ice and the detachment of CO_2 bubbles, *Europhys. Lett.*, 113/4 (2016), 43002.

[P45] S. Y. Buhmann, V. N. Marachevsky, and S. Scheel, Impact of anisotropy on the interaction of an atom with a one-dimensional nanograting, *Int. J. Mod. Phys. A*, 31/2–3 (2016), 1641029.

[P46] P. Thiyam, O. I. Malyi, C. Persson, S. Y. Buhmann, D. F. Parsons, and M. Boström, Effective Lennard-Jones parameters for CO_2–CO_2 dispersion interactions in water and near amorphous silica–water interfaces, in *Progress In Electromagnetics Research Symposium Proceedings* (Prague, 2015), 1289.

[P47] J. A. Crosse, S. Fuchs, and S. Y. Buhmann, Electromagnetic Green's function for layered topological insulators, *Phys. Rev. A*, 92/6 (2015), 063831.

[P48] S. Scheel, S. Y. Buhmann, C. Clausen, and P. Schneeweiss, Directional spontaneous emission and lateral Casimir–Polder force on an atom close to a nanofiber, *Phys. Rev. A*, 92/4 (2015), 043819.

[P49] F. Intravaia, V. E. Mkrtchian, S. Y. Buhmann, S. Scheel, D. A. R. Dalvit, and C. Henkel, Friction forces on atoms after acceleration, *J. Phys. Condens. Matter*, 27/21 (2015), 214020.

[P50] S. Ribeiro, S. Y. Buhmann, T. Stielow, and S. Scheel, Casimir–Polder interaction from exact diagonalization and surface-induced state mixing, *Europhys. Lett.*, 110/5 (2015), 51003.

[P51] K. A. Milton, E. K. Abalo, P. Parashar, N. Pourtolami, I. Brevik, S. Å. Ellingsen, S. Y. Buhmann, and S. Scheel, Casimir–Polder repulsion: Three-body effects, *Phys. Rev. A*, 91/4 (2015), 042510.

[P52] P. Thiyam, C. Persson, D. F. Parsons, D. Huang, S. Y. Buhmann, and M. Boström, Trends of CO_2 adsorption on cellulose due to Van der Waals forces, *Colloids Surf. A*, 470 (2015), 360.

[P53] M. Boström, P. Thiyam, C. Persson, D. F. Parsons, S. Y. Buhmann, I. Brevik, and B. E. Sernelius, Nonperturbative theory of dispersion interactions, *Phys. Scr.*, 90/3 (2015), 035405.

[P54] B. W. Ninham, M. Boström, C. Persson, I. Brevik, S. Y. Buhmann, and B. E. Sernelius, Casimir forces in a plasma: Possible connections to Yukawa potentials, *Eur. Phys. J. D*, 68/10 (2014), 328.

[P55] H. Bender, C. Stehle, C. Zimmermann, S. Slama, J. Fiedler, S. Scheel, S. Y. Buhmann, and V. N. Marachevsky, Probing atom–surface interactions by diffraction of Bose–Einstein condensates, *Phys. Rev. X*, 4 (2014), 011029.

[P56] S. Ribeiro, S. Y. Buhmann, and S. Scheel, Second-order coupling between excited atoms and surface polaritons, *Phys. Rev. A*, 87/4 (2013), 042508.

[P57] S. Y. Buhmann, H. Safari, S. Scheel, and A. Salam, Body-assisted dispersion potentials of diamagnetic atoms, *Phys. Rev. A*, 87/1 (2013), 012507.

[P58] D. T. Butcher, S. Y. Buhmann, and S. Scheel, Casimir–Polder forces between chiral objects, *New J. Phys.*, 14/11 (2012), 113013.

[P59] S. Y. Buhmann, D. T. Butcher, and S. Scheel, Macroscopic quantum electrodynamics in nonlocal and nonreciprocal media, *New J. Phys.*, 14/8 (2012), 083034.

[P60] S. Y. Buhmann, S. Scheel, S. Å. Ellingsen, K. Hornberger, and A. Jacob, Casimir–Polder interaction of fullerene molecules with surfaces, *Phys. Rev. A*, 85/4 (2012), 042513.

[P61] S. Scheel and S. Y. Buhmann, Path decoherence of charged and neutral particles near surfaces, *Phys. Rev. A*, 85/3 (2012), 030101(R).

[P62] S. Å. Ellingsen, S. Y. Buhmann, and S. Scheel, Casimir–Polder energy-level shifts of an out-of-equilibrium particle near a microsphere, *Phys. Rev. A*, 85/2 (2012), 022503.

[P63] S. Å. Ellingsen, S. Y. Buhmann, and S. Scheel, Temperature-independent Casimir–Polder forces in arbitrary geometries, *Phys. Rev. A*, 84/6 (2011), 060501(R).

[P64] H. Safari, S. Azizi, M. R. Karimpour, and S. Y. Buhmann, Chirality contribution in dispersion potential of a ground state atom the presence of magnetoelectric media, in *Proceedings of 17th Iranian Conference on Optics and Photonics* (Tehran, 2011).

[P65] S. Å. Ellingsen, S. Y. Buhmann, and S. Scheel, Casimir–Polder potential and transition rate in resonating cylindrical cavities, *Phys. Rev. A*, 82/3 (2010), 032516.

[P66] J. A. Crosse, S. Å. Ellingsen, K. Clements, S. Y. Buhmann, and S. Scheel, Thermal Casimir–Polder shifts in Rydberg atoms near metallic surfaces, *Phys. Rev. A*, 82/1 (2010), 010901(R).

[P67] S. Å. Ellingsen, S. Y. Buhmann, and S. Scheel, Temperature-invariant Casimir–Polder forces despite large thermal photon numbers, *Phys. Rev. Lett.*, 104/22 (2010), 223003.

[P68] A. Sambale, D.-G. Welsch, S. Y. Buhmann, and D. T. Ho, Casimir force on amplifying bodies, *Opt. Spectrosc. (USSR)*, 108/3 (2010), 391.

[P69] S. Y. Buhmann, S. Scheel, and J. Babington, Universal scaling laws for dispersion interactions, *Phys. Rev. Lett.*, 104/7 (2010), 070404.

[P70] A. Sambale, S. Scheel, and S. Y. Buhmann, Casimir–Polder interaction between an atom and a small magnetodielectric sphere, *Phys. Rev. A*, 81/1 (2010), 012509.

[P71] S. Å. Ellingsen, Y. Sherkunov, S. Y. Buhmann, and S. Scheel, Casimir–Polder potential in thermal nonequilibrium, in K. A. Milton and M. Bordag (eds), *Proceedings of the Ninth Conference on Quantum Field Theory Under the Influence of External Conditions* (New Jersey: World Scientific, 2010), 168.

[P72] A. Sambale, S. Y. Buhmann, D.-G. Welsch, and D. T. Ho, Impact of amplifying media on the Casimir force, *Phys. Rev. A*, 80/5 (2009), 051801(R).

[P73] S. Scheel and S. Y. Buhmann, Casimir–Polder forces on moving atoms, *Phys. Rev. A*, 80/4 (2009), 042902.

[P74] S. Å. Ellingsen, S. Y. Buhmann, and S. Scheel, Enhancement of thermal Casimir–Polder potentials of ground-state polar molecules in a planar cavity, *Phys. Rev. A*, 80/2 (2009), 022901.

[P75] S. Y. Buhmann and S. Scheel, Nonequilibrium thermal Casimir–Polder forces, *Phys. Scripta T*, 135 (2009), 014013.

[P76] A. Sambale, S. Y. Buhmann, D. T. Ho, and D.-G. Welsch, Resonant Casimir–Polder forces in planar metamaterials, *Phys. Scripta T*, 135 (2009), 014019.

[P77] S. Å. Ellingsen, S. Y. Buhmann, and S. Scheel, Dynamics of thermal Casimir–Polder forces on polar molecules, *Phys. Rev. A*, 79/5 (2009), 052903.

[P78] S. Y. Buhmann, S. Scheel, H. Safari, and D.-G. Welsch, Dispersion forces and duality, *Int. J. Mod. Phys. A*, 24/8–9 (2009), 1796.

[P79] S. Y. Buhmann and S. Scheel, Macroscopic quantum electrodynamics and duality, *Phys. Rev. Lett.*, 102/14 (2009), 140404.

[P80] A. Sambale, D.-G. Welsch, D. T. Ho, and S. Y. Buhmann, Local-field-corrected Van der Waals potentials in magnetodielectric multilayer systems, *Phys. Rev. A*, 79/2 (2009), 022903.

[P81] H. Safari, D.-G. Welsch, S. Y. Buhmann, and S. Scheel, Van der Waals potentials of paramagnetic atoms, *Phys. Rev. A*, 78/6 (2008), 062901.

[P82] S. Y. Buhmann, M. R. Tarbutt, S. Scheel, and E. A. Hinds, Surface-induced heating of cold polar molecules, *Phys. Rev. A*, 78/5 (2008), 052901.

[P83] A. Sambale, D.-G. Welsch, D. T. Ho, and S. Y. Buhmann, Van der Waals interaction and spontaneous decay in a superlens-type geometry, *Phys. Rev. A*, 78/5 (2008), 053828.

[P84] S. Y. Buhmann and S. Scheel, Thermal Casimir–Polder forces: Equilibrium and nonequilibrium forces, *Phys. Rev. Lett.*, 100/25 (2008), 253201.

[P85] H. Safari, D.-G. Welsch, D. T. Ho, and S. Y. Buhmann, Interatomic Van der Waals potential in the presence of a magnetoelectric sphere, *Phys. Rev. A*, 77/5 (2008), 053824.

[P86] S. Y. Buhmann and D.-G. Welsch, Casimir–Polder forces on excited atoms in the strong atom–field coupling regime, *Phys. Rev. A*, 77/1 (2008), 012110.

[P87] S. Y. Buhmann, H. Safari, D. T. Ho, and D.-G. Welsch, Two-atom Van der Waals interaction between polarizable/magnetizable atoms near magnetodielectric bodies, *Opt. Spectrosc. (USSR)*, 103/3 (2007), 374.

[P88] A. Sambale, S. Y. Buhmann, D.-G. Welsch, and M. S. Tomaš, Local-field correction to one- and two-atom Van der Waals interactions, *Phys. Rev. A*, 75/4 (2007), 042109.

[P89] S. Y. Buhmann, H. Safari, D.-G. Welsch, and D. T. Ho, Microscopic origin of Casimir–Polder forces, *Open Sys. Inf. Dyn.*, 13/4 (2006), 427.

[P90] H. Safari, S. Y. Buhmann, D.-G. Welsch, and D. T. Ho, Body-assisted Van der Waals interaction between two atoms, *Phys. Rev. A*, 74/4 (2006), 042101.

[P91] D. T. Ho, S. Y. Buhmann, and D.-G. Welsch, Local-field correction to the spontaneous decay rate of atoms embedded in bodies of finite size, *Phys. Rev. A*, 74/2 (2006), 023803.

[P92] S. Y. Buhmann and D.-G. Welsch, Born expansion of the Casimir–Polder interaction of a ground-state atom with dielectric bodies, *Appl. Phys. B*, 82/2 (2006), 189.

[P93] S. Y. Buhmann, D. T. Ho, T. Kampf, L. Knöll, and D.-G. Welsch, Atoms near magnetodielectric bodies: Van der Waals energy and the Casimir–Polder force, *Opt. Spectrosc. (USSR)*, 99/3 (2005), 466.

[P94] S. Y. Buhmann, T. Kampf, and D.-G. Welsch, Ground-state Van der Waals forces in planar multilayer magnetodielectrics, *Phys. Rev. A*, 72/3 (2005), 032112.

[P95] S. Y. Buhmann, D. T. Ho, T. Kampf, and D.-G. Welsch, Casimir–Polder interaction of atoms with magnetodielectric bodies, *Eur. Phys. J. D*, 35/1 (2005), 15.

[P96] S. Y. Buhmann, D. T. Ho, L. Knöll, and D.-G. Welsch, Casimir–Polder forces: A nonperturbative approach, *Phys. Rev. A*, 70/5 (2004), 052117.

[P97] S. Y. Buhmann, D. T. Ho, and D.-G. Welsch, The Van der Waals energy of atomic systems near absorbing and dispersing bodies, *J. Opt. B*, 6/3 (2004), S127.

[P98] D. T. Ho, S. Y. Buhmann, L. Knöll, D.-G. Welsch, S. Scheel, and J. Kästel, Electromagnetic-field quantization and spontaneous decay in left-handed media, *Phys. Rev. A*, 68/4 (2003), 043816.

[P99] S. Y. Buhmann, D. T. Ho, L. Knöll, S. Scheel, and D.-G. Welsch, Spontaneous decay in left-handed material, in H. Moya-Cessa, R. Jáuregui, S. Hacyan, and O. Castaños (eds), *Proceedings of the 8th International Conference on Squeezed States and Uncertainty Relations* (New Jersey: Rinton Press, 2003), 110.

[P100] S. Y. Buhmann, V. A. Dzuba, and O. P. Sushkov, Enhancement of the electron electric dipole moment in Gd^{3+}, *Phys. Rev. A*, 66/4 (2002), 042109.

Refereed articles (learning and teaching)

[P101] S. Y. Buhmann and M. Kingsbury, A standardised, holistic framework for concept-map analysis combining topological attributes and global morphologies, *Knowledge Management & E-Learning*, 7/1 (2014), 20.

Theses

[P102] S. Y. Buhmann, 'When "light" dawns upon them: Mapping the essence of conceptual understanding of physics learners', MEd thesis, Imperial College London, London, 2014.

[P103] S. Y. Buhmann, 'Casimir–Polder forces on atoms in the presence of magnetoelectric bodies', PhD thesis, University of Jena, Jena, 2007.

[P104] S. Y. Buhmann, 'Enhancement factor for the electron electric dipole moment in gadolinium 3+', BSc (Hons) thesis, University of New South Wales, Sydney, 2001.

[P105] S. Y. Buhmann, 'Late time spectra of type II supernovae', BSc (Hons) thesis, University of New South Wales, Sydney, 2001.

References

[1] P. A. M. Dirac, The quantum theory of the emission and absorption of radiation, *Proc. R. Soc. London A*, 114/767 (1927), 243.

[2] S. S. Schweber, *QED and the men who made it: Dyson, Feynman, Schwinger, and Tomonaga* (Princeton: Princeton University Press, 1994).

[3] M. E. Peskin and D. V. Schroeder, *An introduction to quantum field theory* (Boulder: Westview Press 1995).

[4] S. Weinberg, *The quantum theory of fields: Volume I—Foundations* (Cambridge: Cambridge University Press, 1995).

[5] C. Cohen-Tannoudji, R. Dupont-Roc, and G. Grynberg, *Photons and atoms* (New York: Wiley, 1989).

[6] R. Loudon, *The quantum theory of light* (3rd edn, Oxford: Oxford University Press, 2000).

[7] R. R. Puri, *Mathematical methods of quantum optics* (Berlin: Springer, 2001).

[8] D. P. Craig and T. Thirunamachandran, *Molecular quantum electrodynamics*, (New York: Dover, 1998).

[9] A. Salam, *Molecular quantum electrodynamics: Long-range intermolecular interactions* (Hoboken: Wiley, 2010).

[10] S. Haroche, Cavity quantum electrodynamics, in S. Haroche, J. Dalibard, J. M. Raimond, and J. Zinn-Justin (eds), *Fundamental systems in quantum optics, Les Houches summer school session LIII* (Amsterdam: North-Holland, 1992), 767.

[11] E. T. Jaynes and F. W. Cummings, Comparison of quantum and semiclassical radiation theories with application to the beam maser, *Proc. IEEE*, 51/1 (1963), 89.

[12] T. F. Gallagher, *Rydberg atoms* (Cambridge: Cambridge University Press, 1994).

[13] A. Perot and C. Fabry, On the application of interference phenomena to the solution of various problems of spectroscopy and metrology, *Astrophys. J.*, 9 (1899), 87.

[14] J. M. Raimond, M. Brune, and S. Haroche, Manipulating quantum entanglement with atoms and photons in a cavity, *Rev. Mod. Phys.*, 73/3 (2001), 565.

[15] I. I. Rabi, Space quantization in a gyrating magnetic field, *Phys. Rev.*, 51/8 (1937), 652.

[16] R. J. Glauber and M. Lewenstein, Quantum optics of dielectric media, *Phys. Rev. A*, 43/1 (1991), 467.

[17] J. D. Jackson, *Classical electrodynamics* (3rd edn, New York: Wiley, 1998).

[18] G. S. Agarwal, Quantum electrodynamics in the presence of dielectrics and conductors: I. Electromagnetic-field response functions and black-body fluctuations in finite geometries, *Phys. Rev. A*, 11/1 (1975), 230.

[19] J. M. Wylie and J. E. Sipe, Quantum electrodynamics near an interface, *Phys. Rev. A*, 30/3 (1984), 1185.

[20] W. C. Chew, *Waves and fields in inhomogeneous media* (New York: IEEE Press, 1994).

[21] H. B. Callen and T. A. Welton, Irreversibility and generalized noise, *Phys. Rev.*, 83/1 (1951), 34.

[22] R. Kubo, The fluctuation–dissipation theorem, *Rep. Prog. Phys.*, 29/1 (1966), 255.

[23] B. Huttner and S. M. Barnett, Quantization of the electromagnetic field in dielectrics, *Phys. Rev. A*, 46/7 (1992), 4306.

[24] U. Fano, Atomic theory of electromagnetic interactions in dense materials, *Phys. Rev.*, 103/5 (1956), 1202.

[25] M. Wubs and L. G. Suttorp, Transient QED effects in absorbing dielectrics, *Phys. Rev. A*, 63/4 (2001), 043809.

[26] L. G. Suttorp and A. J. van Wonderen, Fano diagonalization of a polariton model for an inhomogeneous absorptive dielectric, *Europhys. Lett.*, 67/5 (2004), 766.

[27] L. G. Suttorp and M. Wubs, Field quantization in inhomogeneous absorptive dielectrics, *Phys. Rev. A*, 70/1 (2004), 013816.

[28] O. Di Stefano, S. Savasta, S., and R. Girlanda, Microscopic calculation of noise current operators for electromagnetic field quantization in absorbing material systems, *J. Opt. B*, 3/4 (2001), 288.

[29] L. Knöll, S. Scheel, and D.-G. Welsch, QED in dispersing and absorbing dielectric media, in J. Peřina (ed.), *Coherence and statistics of photons and atoms* (New York: Wiley, 2001), 1.

[30] R. Matloob, R. Loudon, S. M. Barnett, and J. Jeffers, Electromagnetic field quantization in absorbing dielectrics, *Phys. Rev. A*, 52/6 (1995), 4823.

[31] R. Matloob, Electromagnetic field quantization in a linear isotropic dielectric, *Phys. Rev. A*, 69/5 (2004), 052110.

[32] R. Matloob, Electromagnetic field quantization in a linear isotropic permeable dielectric medium, *Phys. Rev. A*, 70/2 (2004), 022108.

[33] A. Tip, Linear absorptive dielectrics, *Phys. Rev. A*, 57/6 (1998), 4818.

[34] A. Tip, L. Knöll, S. Scheel, and D.-G. Welsch, Equivalence of the Langevin and auxiliary-field quantization methods for absorbing dielectrics, *Phys. Rev. A*, 63/4 (2001), 043806.

[35] T. G. Philbin, Canonical quantization of macroscopic electromagnetism, *New J. Phys.*, 12/12 (2010), 123008.

[36] S. A. R. Horsley, Canonical quantization of the electromagnetic field interacting with a moving dielectric medium, *Phys. Rev. A*, 86/2 (2012), 023830.

[37] W. Heisenberg, Über den anschaulichen Inhalt der quantentheoretischen Kinematik und Mechanik, *Z. Phys.*, 43/3–4 (1927), 172.

[38] J. Schwinger, On quantum-electrodynamics and the magnetic moment of the electron, *Phys. Rev.*, 73/4 (1948), 416.

[39] P. Kusch and H. M. Foley, The magnetic moment of the electron, *Phys. Rev.*, 74/3 (1948), 250.

[40] H. A. Bethe, The electromagnetic shift of energy levels, *Phys. Rev.*, 72/4 (1947), 339.

[41] W. E. Lamb and R. C. Retherford, Fine structure of the hydrogen atom by a microwave method, *Phys. Rev.*, 72/3 (1947), 241.

[42] J. D. van der Waals, 'Over de Continuiteit van den Gas- en Vloeistoftoestand', PhD thesis, University of Leiden, Leiden, 1873.

[43] R. Eisenschitz and F. London, Über das Verhältnis der van der Waalsschen Kräfte zu den homöopolaren Bindungskräften, *Z. Phys.*, 60/7–8 (1930), 491.

[44] H. B. G. Casimir and D. Polder, The influence of retardation on the London–Van der Waals forces, *Phys. Rev.*, 73/4 (1948), 360.

[45] A. Einstein, Zur Quantentheorie der Strahlung, *Phys. Z.*, 18 (1917), 121.

[46] P. W. Milonni, *The quantum vacuum* (New York: Academic Press, 1994).

[47] S. Weinberg, The cosmological constant problem, *Rev. Mod. Phys.*, 61/1 (1989), 1.

[48] H. B. G. Casimir, On the attraction of two perfectly conducting plates, *Proc. K. Ned. Akad. Wetensch.*, 51 (1948), 793.

[49] E. M. Purcell, H. C. Torrey, and R. V. Pound, Resonance absorption by nuclear magnetic moments in a solid, *Phys. Rev.*, 69/1–2 (1946), 37.

[50] K. H. Drexhage, H. Kuhn, and F. P. Schäfer, Variation of the fluorescence decay time of a molecule in front of a mirror, *Ber. Bunsenges. phys. Chem.*, 72/2 (1968), 329.

[51] G. Barton and N. S. J. Fawcett, Quantum electromagnetics of an electron near mirrors, *Phys. Rep.*, 170/1 (1988), 1.

[52] J. B. Pendry, Shearing the vacuum: Quantum friction, *J. Phys. Condens. Mat.*, 9/47 (1997), 10301.

[53] P. C. W. Davies, Scalar production in Schwarzschild and Rindler metrics, *J. Phys. A*, 8/4 (1975), 609.

[54] W. G. Unruh, Notes on black-hole evaporation, *Phys. Rev. D*, 14/4 (1976), 870.

[55] S. A. Fulling and P. C. W. Davies, Radiation from a moving mirror in two dimensional space-time: Conformal anomaly, *Proc. R. Soc. Lond. A*, 348/1654 (1976), 393.

[56] C. M. Wilson, G. Johansson, A. Pourkabirian, M. Simoen, J. R. Johansson, T. Duty, F. Nori, and P. Delsing, Observation of the dynamical Casimir effect in a superconducting circuit, *Nature*, 479/7373 (2011), 376.

[57] S. W. Hawking, Black hole explosions?, *Nature*, 248/5443 (1974), 30.

[58] E. M. Lifshitz, The theory of molecular attractive forces between solids, *Sov. Phys. JETP*, 2/1 (1956), 73.

[59] P. W. Milonni and M.-L. Shih, Source theory of the Casimir force, *Phys. Rev. A*, 45/7 (1992), 4241.

[60] D. Meschede, W. Jhe, and E. A. Hinds, Radiative properties of atoms near a conducting plane: An old problem in a new light, *Phys. Rev. A*, 41/3 (1990), 1587.

[61] A. S. Moskalenko, C. Riek, D. V. Seletskiy, G. Burkard, and A. Leitenstorfer, Paraxial theory of direct electro-optic sampling of the quantum vacuum, *Phys. Rev. Lett.*, 115/26, 263601 (2015).

[62] A. S. Moskalenko, C. Riek, D. V. Seletskiy, G. Burkard, and A. Leitenstorfer, Paraxial theory of direct electro-optic sampling of the quantum vacuum, *Phys. Rev. Lett.*, 115/26, 263601 (2015).

[63] J. Mahanty and B. W. Ninham, *Dispersion forces* (London: Academic Press, 1976).

[64] J. N. Israelachvili, *Intermolecular and surface forces* (London: Academic Press, 1991).

[65] G. Compagno, R. Passante, and F. Persico, *Atom–field interactions and dressed atoms* (Cambridge: Cambridge University Press, 1995).

[66] V. A. Parsegian, *Van der Waals forces: A handbook for biologists, chemists, engineers, and physicists*, (Cambridge: Cambridge University Press, 2005).

[67] M. B. Bordag, G. L. Klimchitskaya, U. Mohideen, and V. M. Mostepanenko, *Advances in the Casimir effect* (Oxford: Oxford University Press, 2009).

[68] D. Dalvit, P. Milonni, D. Roberts, and F. da Rosa (eds), *Casimir physics* (Berlin: Springer, 2011).

[69] L. M. Woods, D. A. R. Dalvit, A. Tkatchenko, P. Rodriguez-Lopez, A. W. Rodriguez, and R. Podgornik, Materials perspective on Casimir and Van der Waals interactions, *Rev. Mod. Phys.*, 88/4 (2016), 045003.

[70] J. E. Lennard-Jones, On the determination of molecular fields, *Proc. R. Soc. Lond. A*, 106/738 (1924), 463.

[71] L. Boinovich and A. Ermelyanenko, Wetting behaviour and wetting transitions of alkanes on aqueous surfaces, *Adv. Colloid Interface Sci.*, 147 (2009), 44.

[72] L. W. Bruch, M. W. Cole, and E. Zaremba, *Physical adsorption: Forces and phenomena* (Oxford: Clarendon Press, 1997).

[73] R. Schmid, Recent advances in the description of the structure of water, the hydrophobic effect, and the like-dissolves-like rule, *Monatsh. Chem.*, 132/11 (2001), 1295.

[74] Y. A. Freiman and J. J. Jodl, Solid oxygen, *Phys. Rep.*, 401/1–4 (2004), 1.

[75] B. V. Derjaguin and L. D. Landau, Theory of stability of highly charged lyophobic sols and adhesion of highly charged particles in solutions of electrolytes, *Acta Physicochim. USSR*, 14 (1941), 633.

[76] E. J. W. Verwey and J. T. G. Overbeek, *Theory of the stability of lyophobic colloids* (Amsterdam: Elsevier, 1948).

[77] J. Blum, G. Wurm, S. Kempf, T. Poppe, H. Klahr, T. Kozasa, M. Rott, T. Henning, J. Dorschner, R. Schräpler, H. U. Keller, W. J. Markiewicz, I. Mann, B. A. S. Gustafson, F. Giovane, D. Neuhaus, H. Fechtig, E. Grün, B. Feuerbacher, H. Kochan, L. Ratke, A. El Goresy, G. Morfill, S. J. Weidenschilling, G. Schwehm, K. Metzler, and W. H. Ip, Growth and form of planetary seedlings: Results from a microgravity aggregation experiment, *Phys. Rev. Lett.*, 85/12 (2000), 2426.

[78] D. J. Scheeres, C. M. Hartzella, P. Sáncheza, and M. Swift, Scaling forces to asteroid surfaces: The role of cohesion, *Icarus*, 210/2 (2010), 968.

[79] K. Autumn, M. Sitti, Y. A. Liang, A. M. Peattie, W. R. Hansen, S. Sponberg, T. W. Kenny, R. Fearing, J. N. Israelachvili, and R. J. Full, Evidence for Van der Waals adhesion in gecko setae, *P. Natl. Acad. Sci. USA*, 99/19 (2002), 12252.

[80] F. M. Serry, D. Walliser, and G. J. Maclay, The role of the Casimir effect in the static deflection and stiction of membrane strips in microelectromechanical systems (MEMS), *J. Appl. Phys.*, 84/5 (1998), 2501.

[81] E. Buks and M. L. Roukes, Stiction, adhesion energy, and the Casimir effect in micromechanical systems, *Phys. Rev. B*, 63/3 (2001), 033402.

[82] G. Binnig, C. F. Quate, and C. Gerber, Atomic force microscope, *Phys. Rev. Lett.*, 56/9 (1986), 930.

[83] Y.-j. Lin, I. Teper, C. Chin, and V. Vuletić, Impact of the Casimir–Polder potential and Johnson noise on Bose–Einstein condensate stability near surfaces, *Phys. Rev. Lett.*, 92/5 (2004), 050404.

[84] H. Oberst, M. Morinaga, F. Shimizu, and K. Shimizu, One-dimensional focusing of an atomic beam by a flat reflector, *Appl. Phys. B*, 76/8 (2003), 801.

[85] S. K. Lamoreaux, Demonstration of the Casimir force in the 0.6 to 6 μm range, *Phys. Rev. Lett.*, 78/1 (1997), 5.

[86] U. Mohideen and A. Roy, Precision measurement of the Casimir force from 0.1 to 0.9 μm, *Phys. Rev. Lett.*, 81/21 (1998), 4549.

[87] R. S. Decca, D. Lopez, E. Fischbach, and D. E. Krause, Measurement of the Casimir force between dissimilar metals, *Phys. Rev. Lett.*, 91/5 (2003), 050402.

[88] A. A. Banishev, G. L. Klimchitskaya, V. M. Mostepanenko, and U. Mohideen, Casimir interaction between two magnetic metals in comparison with nonmagnetic test bodies, *Phys. Rev. B*, 88/15 (2013), 155410.

[89] G. Bressi, G. Carugno, R. Onofrio, and G. Ruoso, Measurement of the Casimir force between parallel metallic surfaces, *Phys. Rev. Lett.*, 88/4 (2002), 041804.

[90] H. B. Chan, Y. Bao, J. Zou, R. A. Cirelli, F. Klemens, W. M. Mansfield, and C. S. Pai, Measurement of the Casimir force between a gold sphere and a silicon surface with nanoscale trench arrays, *Phys. Rev. Lett.*, 101/3 (2008), 030401.

[91] R. S. Decca, D. López, H. B. Chan, E. Fischbach, D. E. Krause, and C. R. Jamell, Constraining new forces in the Casimir regime using the isoelectronic technique, *Phys. Rev. Lett.*, 94/24 (2005), 240401.

[92] A. O. Sushkov, W. J. Kim, D. A. R. Dalvit, and S. K. Lamoreaux, Observation of the thermal Casimir force, *Nature Phys.*, 7/3 (2011), 230.

[93] J. N. Munday, F. Capasso, and V. A. Parsegian, Measured long-range repulsive Casimir–Lifshitz forces, *Nature*, 457/7226 (2009), 170.

[94] F. Chen, U. Mohideen, G. L. Klimchitskaya, and V. M. Mostepanenko, Demonstration of the lateral Casimir force, *Phys. Rev. Lett.*, 88/10 (2002), 101801.

[95] D. A. T. Somers, J. L. Garrett, K. J. Palm, and J. N. Munday, Measurement of the Casimir torque, *Nature*, 564/7736 (2018), 386.

[96] D. Raskin and P. Kusch, Interaction between a neutral atomic or molecular beam and a conducting surface, *Phys. Rev.*, 179/3 (1969), 712.

[97] M. Oria, M. Chevrollier, D. Bloch, M. Fichet, and M. Ducloy, Spectral observation of surface-induced Van der Waals attraction on atomic vapour, *Europhys. Lett.*, 14/6 (1991), 527.

[98] C. I. Sukenik, M. G. Boshier, D. Cho, V. Sandoghdar, and E. A. Hinds, Measurement of the Casimir–Polder force, *Phys. Rev. Lett.*, 70/5 (1993), 560.

[99] H. Failache, S. Saltiel, M. Fichet, D. Bloch, and M. Ducloy, Resonant Van der Waals repulsion between excited Cs atoms and sapphire surface, *Phys. Rev. Lett.*, 83/26 (1999), 5467.

[100] J. M. Obrecht, R. J. Wild, M. Antezza, L. P. Pitaesvkii, S. Stringari, and E. A. Cornell, Measurement of the temperature dependence of the Casimir–Polder force, *Phys. Rev. Lett.*, 2007, 98/6 (2007), 063201.

[101] H. Gies and K. Klingmüller, Casimir effect for curved geometries: Proximity-force-approximation validity limits, *Phys. Rev. Lett.*, 96/22 (2006), 220401.

[102] T. Emig, N. Graham, R. L. Jaffe, and M. Kardar, Casimir Forces between arbitrary compact objects, *Phys. Rev. Lett.*, 99/17 (2007), 170403.

[103] A. Canaguier-Durand, P. A. Maia Neto, A. Lambrecht, and S. Reynaud, Thermal Casimir effect in the plane–sphere geometry, *Phys. Rev. Lett.*, 104/4 (2010), 040403.

[104] M. H. Reid, A. W. Rodriguez, J. White, and S. G. Johnson, Efficient computation of Casimir interactions between arbitrary 3D objects, *Phys. Rev. Lett.*, 103/4 (2009), 040401.

[105] O. Kenneth, I. Klich, A. Mann, and M. Revzen, Repulsive Casimir forces, *Phys. Rev. Lett.*, 89/3 (2002), 033001.

[106] A. G. Grushin and A. Cortijo, Tunable Casimir repulsion with three-dimensional topological insulators, *Phys. Rev. Lett.*, 106/2 (2011), 020403.

[107] O. Kenneth and I. Klich, Opposites attract: A theorem about the Casimir force, *Phys. Rev. Lett.*, 97/16 (2006), 160401.

[108] S. J. Rahi, M. Kardar, and T. Emig, Constraints on stable equilibria with fluctuation-induced (Casimir) forces, *Phys. Rev. Lett.*, 105/7 (2010), 070404.

[109] M. Levin, A. P. McCauley, A. W. Rodriguez, M. H. Reid, and S. G. Johnson, Casimir repulsion between metallic objects in vacuum, *Phys. Rev. Lett.*, 105/9 (2010), 090403.

[110] M. Boström and B. E. Sernelius, Thermal effects on the Casimir force in the 0.1–5 μm range, *Phys. Rev. Lett.*, 84/20 (2000), 4757.

[111] I. Brevik, S. A. Ellingsen, and K. A. Milton, Thermal corrections to the Casimir effect, *New J. Phys.*, 8/10 (2006), 236.

[112] H. B. G. Casimir, Introductory remarks on quantum electrodynamics, *Physica*, 1953, 19/1–12 (1953), 846.

[113] G. Barton, Perturbative check on the Casimir energies of nondispersive dielectric spheres, *J. Phys. A*, 32/3 (1999), 525.

[114] I. Brevik, V. N. Marachevsky, and K. A. Milton, Identity of the Van der Waals force and the Casimir effect and the irrelevance of these phenomena to sonoluminescence, *Phys. Rev. Lett.*, 82/20 (1999), 3948.

[115] J. B. Pendry, A. J. Holden, D. J. Robbins, and W. J. Stewart, Magnetism from conductors and enhanced nonlinear phenomena, *IEEE T. Microw. Theory*, 47/11 (1999), 2075.

[116] D. R. Smith, W. J. Padilla, D. C. Vier, S. C. Nemat-Nasser, and S. Schultz, Composite medium with simultaneously negative permeability and permittivity, *Phys. Rev. Lett.*, 84/18 (2000), 4184.

[117] B. A. Bernevig, T. L. Hughes, and S.-C. Zhang, Quantum spin Hall effect and topological phase transition in HgTe quantum wells, *Science*, 314/5806 (2006), 1757.

[118] M. König, S. Wiedmann, C. Brüne, A. Roth, H. Buhmann, L. W. Molenkamp, X.-L. Qi, and S.-C. Zhang, Quantum spin Hall insulator state in HgTe quantum wells, *Science*, 318/5851 (2007), 766.

[119] S. Raghu and F. D. M. Haldane, Analogs of quantum-Hall-effect edge states in photonic crystals, *Phys. Rev. A*, 78/3 (2008), 033834.

[120] A. B. Khanikaev, S. H. Mousavi, W. K. Tse, M. Kargarian, A. H. MacDonald, and G. Shvets, Photonic topological insulators, *Nature Mater.*, 12/3, (2013), 233.

[121] C. Raabe, S. Scheel, and D.-G. Welsch, Unified approach to QED in arbitrary linear media, *Phys. Rev. A*, 75/5 (2007), 053813.

[122] H. A. Lorentz, The theorem of Poynting concerning the energy in the electromagnetic field and two general propositions concerning the propagation of light, *Amst. Akad. Wetensch.*, 4 (1896), 176.

[123] P. Doyeux, S. A. H. Gangaraj, G. W. Hanson, and M. Antezza, Giant interatomic energy-transport amplification with nonreciprocal photonic topological insulators, *Phys. Rev. Lett.*, 119/17 (2019), 173901.

[124] L. Zhu and S. Fan, Persistent directional current at equilibrium in nonreciprocal many-body near field electromagnetic heat transfer, *Phys. Rev. Lett.*, 117/13 (2016), 134303.

[125] F. H. Hehl and Yu. N. Obukhov, *Foundations of classical electrodynamics: Charge, flux, and metric* (Boston: Birkhäuser, 2003).

[126] I. V. Lindell and A. H. Sihvola, Perfect electromagnetic conductor, *J. Electromagnet. Wave.*, 19/7 (2005), 861.

[127] L. W. Li, P. S. Kooi, M. S. Leong, and T. S. Yeo, On the eigenfunction expansion of dyadic Green's function in planarly stratified media, *J. Electromagnet. Wave.*, 8/6 (1994), 663.

[128] M. S. Tomaš, Green function for multilayers: Light scattering in planar cavities, *Phys. Rev. A*, 51/3 (1995), 2545.

[129] L.-W. Li, P.-S. Kooi, M.-S. Leong, T.-S. Yee, Electromagnetic dyadic Green's function in spherically multilayered media, *IEEE Trans. Microw. Theory Tech.*, 42/12 (1994), 2302.

[130] L.-W. Li, M.-S. Leong, T.-S.Yeo, and P.-S. Kooi, Electromagnetic dyadic Green's functions in spectral domain for multilayered cylinders, *J. Electromagnet. Wave.*, 14/7 (2000), 961.

[131] H. Weyl, Ausbreitung elektromagnetischer Wellen über einem ebenen Leiter, *Ann. Phys. (Leipzig)*, 365/21 (1919), 481.

[132] A. Fresnel, *Oeuvres complètes d'Augustin Fresnel*, ed. H. de Senarmont, E. Verdet, and L. Fresnel, 3 vols (Paris: Imprimerie Impériale, 1866–70), i, 773.

[133] Ld Rayleigh, On the dynamical theory of gratings, *Proc. Roy. Soc A*, 79/532 (1907), 399.

[134] A. Lambrecht and V. N. Marachevsky, Casimir interaction of dielectric gratings, *Phys. Rev. Lett.*, 101/16 (2008), 160403.

[135] A. M. Contreras-Reyes, R. Guérout, P. A. Maia Neto, D. A. R. Dalvit, A. Lambrecht, and S. Reynaud, Casimir–Polder interaction between an atom and a dielectric grating, *Phys. Rev. A*, 82/5 (2010), 052517.

[136] C. Raabe and D.-G. Welsch, Casimir force acting on magnetodielectric bodies embedded in media, *Phys. Rev. A*, 71/1 (2005), 013814.

[137] F. S. S. Rosa, D. A. R. Dalvit, and P. W. Milonni, Casimir interactions for anisotropic magnetodielectric metamaterials, *Phys. Rev. A*, 78/3 (2008), 032117.

[138] T. H. Boyer, Van der Waals forces and zero-point energy for dielectric and permeable materials, *Phys. Rev. A*, 9/5 (1974), 2078.

[139] S. J. van Enk, Casimir torque between dielectrics, *Phys. Rev. A*, 52/4 (1995), 2569.

[140] J. C. Torres-Guzmán and W. L. Mochán, Casimir torque, *J. Phys. A*, 39/21 (2006), 6791.

[141] B. S. Lu, Van der Waals torque and force between anisotropic topological insulator slabs, *Phys. Rev. B*, 97/4 (2018), 045427.

[142] R. B. Rodrigues, P. A. Maia Neto, A. Lambrecht, and S. Reynaud, Vacuum-induced torque between corrugated metallic plates, *Europhys. Lett.*, 76/5 (2006), 822.

[143] M. T. Northen and K. L. Turner, A batch fabricated biomimetic dry adhesive, *Nanotechnology*, 16/8 (2005), 1159.

[144] B. V. Derjaguin, I. I. Abrikosova, and E. M. Lifshitz, Direct measurement of molecular attraction between solids separated by a narrow gap, *Q. Rev. Chem. Soc.*, 10/3 (1956), 295.

[145] H. C. Hamaker, The London–Van der Waals attraction between spherical particles, *Physica*, 4/10 (1937), 1058.

[146] E. A. Power and S. Zienau, Coulomb Gauge in non-relativistic quantum electrodynamics and the shape of spectral lines, *Philos. Trans. R. Soc. Lond. A*, 251/999 (1959), 427.

[147] W. P. Healy, Centre of mass motion in non-relativistic quantum electrodynamics, *J. Phys. A*, 10/2 (1977), 279.

[148] C. Baxter, M. Babiker, R. Loudon, Canonical approach to photon pressure, *Phys. Rev. A*, 47/2 (1993), 1278.

[149] E. Lenz, Über die Bestimmung der Richtung der durch elektodynamische Vertheilung erregten galvanischen Ströme, *Ann. Phys. Chem.*, 107/31 (1834), 483.

[150] S. P. Lloyd, 2^{L-1}-magnetic 2^L-electric interference terms in γ–γ-angular correlations *Phys. Rev.*, 81/1 (1951), 161.

[151] L. Rosenfeld, Quantenmechanische Theorie der natürlichen optischen Aktivität von Flüssigkeiten und Gasen, *Z. Phys*, 52/3-4) (1929), 161.

[152] I. B. Khriplovich and S. K. Lamoreaux, *CP violation without strangeness: Electric dipole moments of particles, atoms, and molecules* (Berlin: Springer, 2012).

[153] R. P. Feynman, Space-time approach to quantum electrodynamics, *Phys. Rev.*, 76/6 (1949), 769.

[154] C. Mavroyannis and M. J. Stephen, Dispersion forces, *Mol. Phys.*, 5/6 (1962), 629.

[155] G. Feinberg and J. Sucher, General theory of the Van der Waals interaction: A model-independent approach, *Phys. Rev. A*, 2/6 (1970), 2395.

[156] A. Salam, Retarded intermolecular interactions involving diamagnetic molecules, *Int. J. Quantum Chem.*, 78/6, (2000), 437.

[157] J. K. Jenkins, A. Salam, and T. Thirunamachandran, Retarded dispersion interaction energies between chiral molecules, *Phys. Rev. A*, 50/6, (1994), 4767.

[158] B. M. Axilrod and E. Teller, Interaction of the Van der Waals type between three atoms, *J. Chem. Phys.*, 11/6, (1943), 299.

[159] P. Curie, On symmetry in physical phenomena, symmetry of an electric field and of a magnetic field, *J. Phys. (Paris)*, 3 (1894), 401.

[160] L. Onsager, Electric moments of molecules in liquids, *J. Am. Chem. Soc.*, 58/8 (1936), 1486.

[161] M. Abraham, On the electrodynamics of moving bodies, *Rend. Circ. Mat. Palermo*, 28 (1909), 1.

[162] I. E. Dzyaloshinskii, E. M. Lifshitz, and L. P. Pitaevskii, The general theory of Van der Waals forces, *Adv. Phys.*, 10/38 (1961), 165.

[163] L. P. Pitaevskii, Comment on 'Casimir force acting on magnetodielectric bodies embedded in media', *Phys. Rev. A*, 73/4, (2006), 047801.

[164] C. Raabe and D.-G. Welsch, Reply to "Comment on 'Casimir force acting on magnetodielectric bodies embedded in media' ", *Phys. Rev. A*, 73/4 (2006), 047802.

[165] M. S. Tomaš, Medium-modified Casimir forces, *J. Phys. A*, 39/21 (2006), 6785.

[166] T. G. Philbin, Casimir effect from macroscopic quantum electrodynamics, *New J. Phys.*, 13/6 (2001), 063026.

[167] I. Brevik and S. A. Ellingsen, Comment on 'Casimir force acting on magnetodielectric bodies embedded in media', *Phys. Rev. A*, 79/2 (2009), 027801.

[168] H. Yukawa, On the interaction of elementary particles. I., *Proc. Phys.-Math. Soc. Jpn. 3rd Ser.*, 17 (1935), 48.

[169] J. M. Wylie and J. E. Sipe, Quantum electrodynamics near an interface. II, *Phys. Rev. A*, 32/4 (1985), 2030.

[170] G. Barton, Quantum electrodynamics of spinless particles between conducting plates, *Proc. R. Soc. Lond. A*, 320/1541 (1970), 251.

[171] M. A. Wilson, P. Bushev, J. Eschner, F. Schmidt-Kaler, C. Becher, R. Blatt, and U. Dorner, Vacuum-field level shifts in a single trapped ion mediated by a single distant mirror, *Phys. Rev. Lett.*, 91/21 (2003), 213602.

[172] P. Bushev, A. Wilson, J. Eschner, C. Raab, F. Schmidt-Kaler, C. Becher, and R. Blatt, Forces between a single atom and its distant mirror image, *Phys. Rev. Lett.*, 92/22 (2004), 223602.

[173] F. J. Rodríguez-Fortuño, G. Marino, P. Ginzburg, D. O'Connor, A. Martínez, G. A. Wurtz, and A. V. Zayats, Near-field interference for the unidirectional excitation of electromagnetic guided modes, *Science*, 340/6130 (2013), 328.

[174] J. Lin, J. B. Mueller, Q. Wang, G. Yuan, N. Antoniou, X. C. Yuan, and F. Capasso, Polarization-controlled tunable directional coupling of surface plasmon polaritons, *Science*, 340/6130 (2013), 331.

[175] M. Neugebauer, T. Bauer, P. Banzer, and G. Leuchs, Polarization tailored light driven directional optical nanobeacon, *Nano Lett.*, 14/5 (2015), 2546.

[176] R. Mitsch, C. Sayrin, B. Albrecht, P. Schneeweiss, and A. Rauschenbeutel, Quantum state-controlled directional spontaneous emission of photons into a nanophotonic waveguide, *Nature Commun.*, 5 (2014), 5713.

[177] T. van Mechelen and Z. Jacob, Universal spin-momentum locking of evanescent waves, *Optica*, 3/2 (2016), 118.

[178] M. V. Berry and P. Shukla, Classical dynamics with curl forces, and motion driven by time-dependent flux, *J. Phys. A*, 45/30 (2012), 305201.

[179] A. Manjavacas, F. J. Rodríguez-Fortuño, F. J. G. de Abajo, and A. V. Zayats, Lateral Casimir force on a rotating particle near a planar surface, *Phys. Rev. Lett.*, 118/13 (2017), 133605.

[180] R. R. McLone and E. A. Power, Long range Van der Waals forces between nonidentical systems, *Proc. R. Soc. Lond. A*, 286/1407 (1965), 573.

[181] M. R. Philpott, Retarded interaction between electronically excited molecules, *Proc. Phys. Soc. Lond.*, 87/3 (1966), 619.

[182] H. Safari and M. R. Karimpour, Body-assisted Van der Waals interaction between excited atoms, *Phys. Rev. Lett.*, 114/1 (2015), 013201.

[183] E. A. Power and T. Thirunamachandran, Quantum electrodynamics with nonrelativistic sources. V. Electromagnetic field correlations and intermolecular interactions between molecules in either ground or excited states, *Phys. Rev. A*, 47/4 (1993), 2539.

[184] Yu. Sherkunov, Casimir–Polder interaction between an excited atom and a gas dielectric medium, *Phys. Rev. A*, 75/1 (2007), 012705.

[185] P. R. Berman, Interaction energy of nonidentical atoms, *Phys. Rev. A*, 91/4 (2015), 042127.

[186] P. W. Milonni and S. M. H. Rafsanjani, Distance dependence of two-atom dipole interactions with one atom in an excited state, *Phys. Rev. A*, 92/6 (2015), 062711.

[187] M. Donaire, Two-atom interaction energies with one atom in an excited state: Van der Waals potentials versus level shifts, *Phys. Rev. A*, 93/5 (2016), 052706.

[188] M. Donaire, Net force on an asymmetrically excited two-atom system from vacuum fluctuations, *Phys. Rev. A*, 94/6 (2016), 062701.

[189] S. Scheel, L. Knöll, and D.-G. Welsch, QED commutation relations for inhomogeneous Kramers–Kronig dielectrics, *Phys. Rev. A*, 58/1 (1998), 700.

[190] C. Raabe and D.-G. Welsch, QED in arbitrary linear media: Amplifying media, *Eur. Phys. J. Spec. Top.*, 160/1 (2008), 371.

[191] Yu. Sherkunov, Van der Waals interaction of excited media, *Phys. Rev. A*, 72/5 (2005), 052703.

[192] U. Leonhardt and T. G. Philbin, Quantum levitation by left-handed metamaterials, *New J. Phys.*, 9/8 (2007), 254.

[193] S. N. Bose, Plancks Gesetz und Lichtquantenhypothese, *Z. Phys.*, 26/1 (1924), 178.

[194] A. Einstein, Quantentheorie des einatomigen idealen Gases, *Sitzungsber. Preuss. Akad. Wiss.*, 245 (1924).

[195] J. Brown and A. Carrington, *Rotational spectroscopy of diatomic molecules* (Cambridge: Cambridge University Press, 2003).

[196] T. A. Matsubara, New approach to quantum-statistical mechanics, *Prog. Theor. Phys.*, 14/4 (1955), 351.

[197] M.-P. Gorza and M. Ducloy, Van der Waals interactions between atoms and dispersive surfaces at finite temperature, *Eur. Phys. J. D*, 40/3 (2006), 343.

[198] M. Antezza, L. P. Pitaevskii, and S. Stringari, New asymptotic behaviour of the surface–atom force out of thermal equilibrium, *Phys. Rev. Lett.*, 95/11 (2005), 113202.

[199] A. Ashkin, Trapping of atoms by resonance radiation pressure, *Phys. Rev. Lett.*, 40/12 (1978), 729.

[200] S. Chu, J. E. Bjorkholm, A. Ashkin, and A. Cable, Experimental observation of optically trapped atoms, *Phys. Rev. Lett.*, 57/3 (1986), 314.

[201] J. P. Dowling and J. Gea-Banacloche, Evanescent light-wave atom mirrors, resonators, waveguides, and traps, *Adv. At. Mol. Opt. Phys.*, 37 (1996), 1.

[202] A. Landragin, J.-Y. Courtois, G. Labeyrie, N. Vansteenkiste, C. I. Westbrook, and A. Aspect, Measurement of the Van der Waals force in an atomic mirror, *Phys. Rev. Lett.*, 77/8 (1996), 1464.

[203] H. Bender, P. W. Courteille, C. Marzok, C. Zimmermann, and S. Slama, Direct measurement of intermediate-range Casimir–Polder potentials, *Phys. Rev. Lett.*, 104/8 (2010), 083201.

[204] A. M. Guzmán, The London–Van der Waals interaction in the presence of evanescent waves, in A. O. Marcano and J. L. Paz (eds), *5th Iberoamerican Meeting on Optics and 8th Latin American Meeting on Optics, Lasers, and Their Applications* (Bellingham: SPIE, 2004), 348.

[205] J. D. Perreault, M. Bhattacharya, V. P. Lonij, and A. D. Cronin, Modifying atom–surface interactions with optical fields, *Phys. Rev. A*, 77/4 (2008), 043406.

[206] T. Thirunamachandran, Intermolecular interactions in the presence of an intense radiation field, *Mol. Phys.* 40/2 (1980), 393.

[207] M. M. Burns, J.-M. Golovchenko, and J. A. Golovchenko, Optical binding, *Phys. Rev. Lett.*, 63/12 (1989), 1233.

[208] R. H. Dicke, Coherence in spontaneous radiation processes, *Phys. Rev.*, 93/1 (1954), 99.

[209] M. Gross and S. Haroche, Superradiance: An essay on the theory of collective spontaneous emission, *Phys. Rep.*, 93/5 (1982), 301.

[210] J. T. Manassah, The Purcell–Dicke effect in the emission from a coated small sphere of resonant atoms placed inside a matrix cavity, *Laser Phys.*, 22/4 (2012), 738.

[211] K. Sinha, B. P. Venkatesh, and P. Meystre, Collective effects in Casimir–Polder forces, *Phys. Rev. Lett.*, 121/18 (2018), 183605.

[212] T. G. Philbin and U. Leonhardt, No quantum friction between uniformly moving plates, *New J. Phys.*, 11/3 (2009), 033035.

[213] J. B. Pendry, Quantum friction—fact or fiction?, *New J. Phys.*, 12/3 (2010), 033028.

[214] K. Milton, J. Høye, I. Brevik, The reality of Casimir friction, *Symmetry*, 8/5 (2016), 29.

[215] M. S. Tomassone and A. Widom, Electronic friction forces on molecules moving near metals, *Phys. Rev. B*, 56/8 (1997), 4938.

[216] A. A. Kyasov and G. V. Dedkov, Electromagnetic fluctuation forces on a particle moving near a surface, *Surf. Sci.*, 463/1 (2000), 11.

[217] A. I. Volokitin and B. N. J. Persson, Dissipative Van der Waals interaction between a small particle and a metal surface, *Phys. Rev. B*, 65/11 (2002), 115419.

[218] G. Barton, On Van der Waals friction. II: Between atom and half-space, *New J. Phys.*, 12/11 (2010), 113045.

[219] F. Intravaia, R. O. Behunin, and D. A. R. Dalvit, Quantum friction and fluctuation theorems, *Phys. Rev. A*, 89/5 (2014), 050101.

[220] F. Intravaia, R. O. Behunin, C. Henkel, K. Busch, and D. A. R. Dalvit, Non-Markovianity in atom–surface dispersion forces, *Phys. Rev. A*, 94/4 (2016), 042114.

[221] P. Horak, G. Hechenblaikner, K. M. Gheri, H. Stecher, and H. Ritsch, Cavity-induced cooling in the strong coupling regime, *Phys. Rev. Lett.*, 79/25 (1997), 4974.

[222] M. Ducloy and M. Fichet, General theory of frequency-modulated selective reflection. Influence of atom surface interactions, *J. Phys. II*, 1/12 (1991), 1429.

[223] K. Hornberger, J. E. Sipe, and M. Arndt, Theory of decoherence in a matter wave Talbot–Lau interferometer, *Phys. Rev. A*, 70/5 (2004), 053608.

[224] S. Gerlich, S. Eibenberger, M. Tomandl, S. Nimmrichter, K. Hornberger, P. J. Fagan, J. Tüxen, M. Mayor, and M. Arndt, Quantum interference of large organic molecules, *Nature Commun.*, 2 (2011), 263.

[225] M. Born and E. Wolf, *Principles of optics* (7th edn, Cambridge: Cambridge University Press, 1999).

[226] G. E. Grisenti, W. Schöllkopf, J. P. Toennies, G. C. Hegerfeldt, and T. Köhler, Determination of atom–surface Van der Waals potentials from transmission-grating diffraction intensities, *Phys. Rev. Lett.*, 83/9 (1999), 1755.

[227] C. Brand, J. Fiedler, T. Juffmann, M. Sclafani, C. Knobloch, S. Scheel, Y. Lilach, O. Cheshnovsky, and M. Arndt, A Green's function approach to modeling molecular diffraction in the limit of ultra-thin gratings, *Ann. Phys. (Berlin)*, 527/9–10 (2015), 580.

[228] J. E. Harvey and J. L. Forgham, The spot of Arago: New relevance for an old phenomenon, *Am. J. Phys.*, 52/3 (1984), 243.

[229] D. F. J. Arago, Rapport fait par M. Arago à l'Académie des Sciences, au nom de la Commission qui avait été chargée d'examiner les Mémoires envoyés au concours pour le prix de la diffraction, *Ann. Chim. Phys. 2nd Ser.*, 11 (1819), 5.

[230] G. Wentzel, Eine Verallgemeinerung der Quantenbedingungen für die Zwecke der Wellenmechanik, *Z. Phys.*, 38/6–7 (1926), 518.

[231] H. A. Kramers, Wellenmechanik und halbzahlige Quantisierung, *Z. Phys.*, 39/10 (1926), 828.

[232] L. Brillouin, La mécanique ondulatoire de Schrödinger: une éthode générale de resolution par approximations successives, *C. R. Acad. Sci.*, 183 (1926), 24.

[233] J. D. Perreault, A. D. Cronin, and T. A. Savas, Using atomic diffraction of Na from material gratings to measure atom–surface interactions, *Phys. Rev. A*, 71/5 (2005), 053612.

[234] T. Juffmann, S. Nimmrichter, M. Arndt, H. Gleiter, and K. Hornberger, New prospects for de Broglie interferometry, *Found. Phys.*, 42/1 (2012), 98.

[235] T. Reisinger, G. Bracco, and B. Holst, Particle–wave discrimination in Poisson spot experiments, *New J. Phys.*, 13/6 (2011), 065016.

[236] T. Reisinger, A. A. Patel, H. Reingruber, K. Fladischer, W. E. Ernst, G. Bracco, H. I, Smith, and B. Holst, Poisson's spot with molecules, *Phys. Rev. A*, 79/5 (2009), 053823.

[237] P. Sonnentag and F. Hasselbach, Measurement of decoherence of electron waves and visualization of the quantum–classical transition, *Phys. Rev. Lett.*, 98/20 (2007), 200402.

[238] F. Impens, R. O. Behunin, C. C. Ttira, and P. A. Maia Neto, Non-local double-path Casimir phase in atom interferometers, *Europhys. Lett.*, 101/6 (2013), 60006.

[239] L. S. Cederbaum, J. Zobeley, and F. Tarantelli, Giant intermolecular decay and fragmentation of clusters, *Phys. Rev. Lett.*, 79/24 (1997), 4778.

[240] R. Thissen, P. Lablanquie, R. I. Hall, M. Ukai, M., and K. Ito, Photoionization of argon, krypton and xenon clusters in the inner valence shell region, *Eur. Phys. J. D*, 4/3 (1998), 335.

[241] K. Gokhberg, P. Kolorenč, A. I. Kuleff, and L. S. Cederbaum, Site- and energy-selective slow-electron production through intermolecular Coulombic decay, *Nature*, 505/7485 (2014), 661.

[242] R. Santra and L. S. Cederbaum, Non-hermitian electronic theory and applications to clusters, *Phys. Rep.*, 368/1 (2002), 1.

[243] M. Shcherbinin, A. C. LaForge, V. Sharma, M. Devetta, R. Richter, R. Moshammer, T. Pfeifer, and M. Mudrich, Interatomic Coulombic decay in helium nanodroplets, *Phys. Rev. A*, 96/1 (2017), 013407.

[244] T. Förster, Zwischenmolekulare Energiewanderung und Fluoreszenz, *Ann. Phys. (Leipzig)*, 437/1–2 (1948), 55.

[245] D. L. Andrews, A unified theory of radiative and radiationless molecular energy transfer, *Chem. Phys.*, 135/2 (1998), 195.

[246] H. T. Dung, L. Knöll, and D.-G. Welsch, Intermolecular energy transfer in the presence of dispersing and absorbing media, *Phys. Rev. A*, 65/4 (2002), 043813.

[247] D. P. Craig and T. Thirunamachandran, Third-body mediation of resonance coupling between identical molecules, *Chem. Phys.*, 135/1 (1989), 37.

[248] A. Salam, Mediation of resonance energy transfer by a third molecule, *J. Chem. Phys.*, 136/1 (2012), 014509.

[249] J. S. Ford and D. L. Andrews, Geometrical effects on resonance energy transfer between orthogonally-oriented chromophores, mediated by a nearby polarisable molecule, *Chem. Phys. Lett.*, 591 (2014), 88.

[250] T. Miteva, S. Kazandjian, P. Kolorenč, P. Votavová, and N. Sisourat, Interatomic Coulombic decay mediated by ultrafast superexchange energy transfer, *Phys. Rev. Lett.*, 119/8 (2017), 083403.